RUPAC XXII
Russian Particle Accelerator Conference
IHEP PROTVINO 2010
September 27 - October 1

Russian Academy of Sciences
State Corporation for Atomic Energy "ROSATOM"
Institute for High Energy Physics (IHEP)

RuPAC-2010
ИФВЭ IHEP

http://www.ihep.su/rupac2010/

PREFACE

The XXIInd Russian Particle Accelerator Conference (RuPAC-2010) was held in Protvino, Moscow region, September 27 - October 1, 2010. It was hosted by Institute for High Energy Physics (IHEP) and organized jointly by IHEP, Scientific Council for Accelerators of the Russian Academy of Science, Joint Institute for Nuclear Research (JINR), and Budker Institute of Nuclear Physics (BINP) of Siberian Branch of the Russian Academy of Science. The Conference was supported in part by the State Corporation for Atomic Energy ROSATOM. Goal of the event was to facilitate information interchange and discussion of various aspects of accelerator science and technology, beam physics, new accelerator development, upgrade of existing facilities, and use of accelerators for basic and applied research. The scientific program included topics to follow:

- Circular Colliders
- Linear Colliders, Lepton Accelerators and New Acceleration Techniques
- Hadron Accelerators
- Synchrotron Light Sources and FELs
- Cooler Storage Rings
- Particle Dynamics in Accelerators and Storage Rings, Cooling Methods, New Methods of Acceleration
- Accelerator Technologies
- Applications of Accelerators
- Radiation Problems in Accelerators
- Instrumentation, Controls, Feedback, and Operational Aspects

During the RuPAC-2010, the Accelerator Conference Prizes for young physicists and engineers for the best works presented at the Conference have been nominated for the second time since the previous RuPAC-2008. The First Prize was attributed to Dmitry Shwartz (BINP, Novosibirsk) who presented the report "Present Status of VEPP–2000". Two Second Prizes went to Mariya Gusarova (NRNU MEPhI, Moscow) for her report "MultP-M Code Expansions" and to Andrey Kobets (JINR, Dubna) for his report "Advance in the LEPTA Project". The Prizes were awarded by solution of the ad hoc Selection Committee chaired by Vasily Parkhomchuk, Corresponding Member of the Russian Academy of Sciences.

The Conference Proceedings are published only electronically in the format of a CD-ROM. Processing of the electronic files of the contributions prior to, during and short after the Conference was fulfilled by the RuPAC editing team headed by Maxim Kuzin (BINP) and comprising persons experienced in preparation of the Proceedings of several other Conferences (RuPAC, EPAC, and others), which are members of the Joint Accelerator Conferences Website (JACoW) collaboration. The final version was published at the JACoW website in November 2010.

The success of the RuPAC-2010 can be attributed to the collaborative efforts of the Program and Organizing Committees, the local staff of the host institution – IHEP-Protvino, and, of course, to all of the participants.

Nikolay Tyurin, Chair of Organizing Committee of the RuPAC-2010 Conference

Sergey Ivanov, Co-Chair of Organizing Committee

Igor Meshkov, Co-Chair of Program Committee

Contents

Contents

Appendices **415**

Contents

Program Committee

Chairman	A. Skrinsky	BINP SB RAS
Co-Chairman	I. Meshkov	JINR
Members:		
	A. Lebedev	LPI RAS
	A. Agafonov	LPI RAS
	B. Sharkov	ITEP/FAIR
	P. Zenkevich	ITEP
	S. Ivanov	IHEP
	G. Shirkov	JINR
	E. Levichev	BINP SB RAS
	V. Parkhomchuk	BINP SB RAS
	L. Kravchuk	INR RAS
	M. Vorogushin	SRI of EPA
	V. Romanov	IPPE

Organizing Committee

Chairman	N. Tyurin	IHEP
Co-Chairman	S. Ivanov	IHEP
Co-Chairman	I. Meshkov	JINR
Members:		
	O. Patarakin	ROSATOM
	A. Lebedev	LPI RAS
	B. Sharkov	ITEP/FAIR
	N. Alexeev	ITEP
	O. Lebedev	IHEP
	G. Shirkov	JINR
	G. Trubnikov	JINR
	E. Levichev	BINP SB RAS
	Yu. Shatunov	BINP SB RAS
	M. Kuzin	BINP SB RAS
	V. Matveev	INR RAS
	L. Kravchuk	INR RAS
	A Feschenko	INR RAS
	M. Vorogushin	SRI of EPhA

PRESENT STATUS OF VEPP-2000*

Dmitry Shwartz, Dmitry Berkaev, Alexander Kirpotin, Ivan Koop, Alexander Lysenko, Igor Nesterenko, Evgeny Perevedentsev, Yury Rogovsky, Alexander Romanov, Petr Shatunov, Yuri Shatunov, Alexander Skrinsky, Ilya Zemlyansky BINP SB RAS, 630090 Novosibirsk, Russia

Abstract

VEPP-2000 electron-positron collider has been completed in the Budker INP in 2007. First beam was captured in a special lattice with switched off final focus solenoids. This regime is used for all machine subsystems test and calibration as well as vacuum chamber treatment by synchrotron radiation with electron beam current up to 150 mA. Another special low-beta lattice with solenoids switched on partially was used for the first test of the round beam option at the energy of 508 MeV. Studies of the beam-beam interaction were done in "weak-strong" and "strong-strong" regimes. Measurements of the beam sizes in both cases have indicated beam behaviour similar to expectations for the round colliding beams. Also the first collider energy calibration at the phi-meson resonance was performed with SND detector. Since the end of 2009 VEPP-2000 started first experimental work with both particle detectors SND and CMD-3 at the energies of 500-950 MeV range with the lattice mode close to project. The precise energy calibration via resonant depolarization method is in progress.

INTRODUCTION

At BINP for more than quarter of century the electron-positron collider VEPP-2M has been operated in the energy range of $0.4 \div 1.4$ GeV. For a long time its results were the main source of information about hadrons production in this energy range. On the other hand, a whole number of events collected by different experimental groups in the energy span above VEPP-2M (up to 2 GeV) doesn't exceed 10 % of the data accumulated by VEPP-2M. These motivations caused a decision to create instead of VEPP-2M collider a new machine with higher luminosity (up to 10^{32} cm^{-2}s^{-1}) and the beam energy up to 2×1 GeV.

To achieve the final goals (luminosity and energy), the Round Beam Concept was applied in design of the machine optics [1]. The main feature of this concept is rotational symmetry of the kick from the round opposite beam. Together with the x − z symmetry of the betatron transfer matrix between the collisions, it results in particle's angular momentum conservation ($M = xz' - zx' = const$). As a consequence, it yields an enhancement of dynamical stability, even with nonlinear effects from the beam-beam force taken into account.

Computer simulations of the beam-beam interaction in "weak-strong" and "strong-strong" situations confirmed these expectations [2, 3].

COLLIDER OVERVIEW

The accelerator complex consists of VEPP-2000 collider itself and injection system including 900 MeV booster of electrons and positrons BEP and injection channels also designed for energy of 900 MeV.

Magnetic structure of VEPP-2000 [4] has the 2-fold symmetry. It includes two (3 m long) experimental straight sections, two straights (2.5 m) for beams injection and RF cavity and 4 short technical straights with 4 triplets of quadrupole magnets. Each triplet together with two 2.4 T bending magnets forms an 90° achromat.
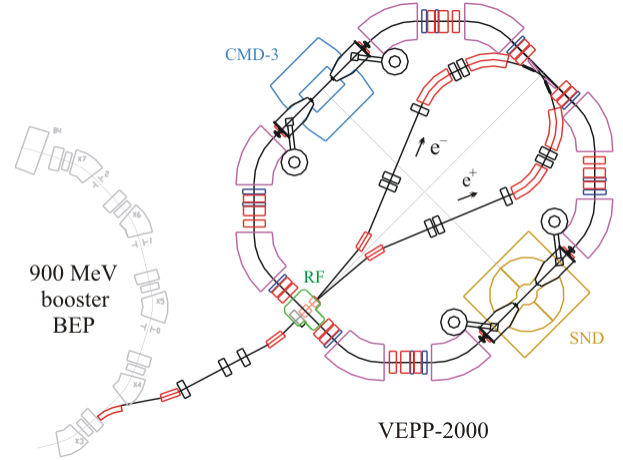
Figure 1: VEPP-2000 layout.

The RBC at VEPP-2000 was implemented by placing into Interaction Regions two pairs of superconducting solenoids symmetrically with respect to collision points.

Table 1: VEPP-2000 Main Parameters (at $E = 1$ GeV)

Parameter	Value
Circumference, Π	24.39 m
Betatron functions at IP, $\beta^*_{x,z}$	10 cm
Betatron tunes, $\nu_{x,z}$	4.1, 2.1
Beam emittance, $\varepsilon_{x,z}$	1.4×10^{-7} m rad
Momentum compaction, α	0.036
Synchrotron tune, ν_s	0.0035
Energy spread, $\sigma_{\Delta E/E}$	6.4×10^{-4}
RF frequency	172 MHz
RF harmonic number, q	14

1

RF voltage	100 kV
Number of particles per bunch, N	10^{11}
Beam-beam parameters, $\xi_{x,z}$	0.075
Luminosity, L	10^{32} cm^{-2}s^{-1}

The strong solenoid focusing provides equal beta-functions of the horizontal and vertical betatron oscillations. There are two combinations of solenoid polarities $(+ +\ - -)$ and $(+ +\ + +)$, that rotate the betatron oscillation plane by ±90 degrees and give alternating horizontal orientation of the normal betatron modes. It results in equal tunes and equal radiation emittances of the betatron oscillations. But the simplest case $(+ -\ + -)$ with an additional small decompensation of solenoid fields also gives round colliding beams and satisfies the RBC requirements.

Superconducting Solenoids

Each solenoid is designed in two sections: main 13 T solenoid 50 cm in length, and 10 cm anti-solenoid (8 T). In part, the main solenoid consists of two identical units each of these has an inner coil wound with Nb$_3$Sn wire and an outer coil wound with NbTi wire. To feed the solenoid, we use separate power supplies for the outer and inner coils and for the anti-solenoid. All coils are embedded in the iron yoke located in a common LHe cryostat. During first run 2007/2008 the LHe consumption appeared to be surprisingly high. After the modernization of all solenoids in 2008 consumption decreased from 6 to 4 l/h. The investigations for further consumption decrease are in progress.

LATTICE OPTIONS

Several lattice schemes are available at VEPP-2000 all of them being useful for operation.

Switched off Solenoids

At the first stage the optics of VEPP-2000 was simplified to the conventional option without solenoids. This "soft" optics ($\nu_x = 2.4$; $\nu_z = 1.4$) is quite different from the round beam lattice (see Fig. 2, 4). But a part of the lattice near injection is preserved similar to the project one to produce proper betatron phase advance between injection and kicker. Optics without solenoids is available only at energy range below 600 MeV due to gradient limitation in weak F-lenses situated in IR.
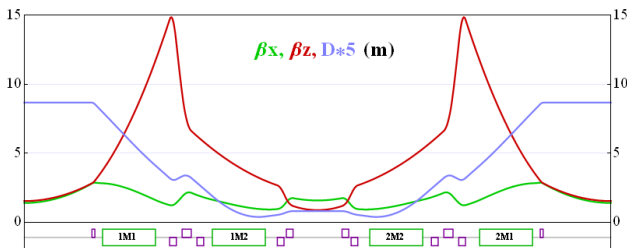
Figure 2: Half period lattice functions. "Soft" optics.

"Soft" lattice was used for the first beam capture, beam transfer efficiency tuning, calibration of the beam diagnostic system, etc. The procedure of vacuum chamber treatment by the synchrotron radiation was also done in this optics scheme, with electron beam in both directions, with several RF-buckets being populated. Beam current, while few days training, raised up to 150 mA and the beam lifetime achieved 1000 sec. At that condition, the lifetime of low beam current (about 1mA) exceeds 10 hours.

To start the round beam operation, first of all, we had to align the cooled solenoids. It was done in the same "weak focusing" regime by the CO deviation measurements as a response to the solenoids coils excitation (see Fig. 3). Each section of all 4 solenoids has been tested with magnetic field level up to 4 T. So, coordinates of each i-th solenoid section center (x_i, z_i, x'_i, z'_i) have been obtained from the Orbit Response Matrix analysis, and necessary mechanical adjustments of the solenoids have been done.
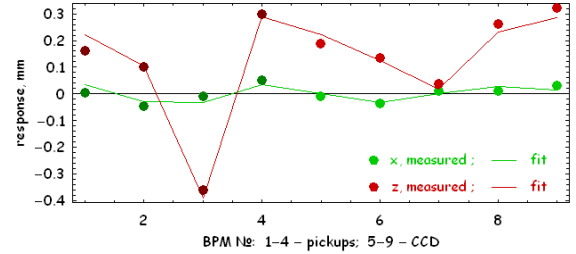
Figure 3: An example of fitted CO response exited by solenoid's coil field.

Short Solenoids

Round beams optics introduces solenoid focusing, but at low energy of two main solenoid's units it is possible to use only one, closest to IP. It requires 10 T field at 500 MeV and allow to produce β-function at IP as small as $\beta^* = 4.5$ cm. This optics in the simplest round beam regime $(+ -\ + -)$ was used for the first round colliding beam tests in 2008. The colliding beam sizes measurements vs. beam current in "strong-weak" and "strong-strong" cases showed the behavior close to simulations results [5]. The space charge parameter defined by expression

$$\xi = \frac{N\, r_e \beta^*}{4\pi\gamma\sigma_0^2} \quad (1)$$

achieved the value of ~0.1 and the corresponding maximum peak luminosity expressed as

$$L = \frac{f_0 N^2}{4\pi\sigma^2} \quad (2)$$

or

$$L = \frac{4\pi\gamma^2 f_0}{r_e} \frac{\varepsilon}{\beta^*} \xi^2 \quad (3)$$

was equal to $L = 1\times10^{31}$ cm^{-2}s^{-1}. In the end of 2008/2009 run VEPP-2000 worked in this optics with collecting the

data SND detector that allowed to make first absolute energy calibration at the φ-meson resonance.

Full Solenoids

Operation at higher energy requires the full solenoid use. Lattice functions for this option are presented at Fig. 4. This optics corresponds to almost twice larger $\beta^* = 8.5\ cm$, while the beam emittance is almost the same. That means that for the same beam currents the luminosity (2, 3) should be near twice lower.

Figure 4: Half period lattice functions. Regular optics with full solenoids.

In the beginning of 2009/2010 run CMD-3 detector became ready for operation. After it's installation together with VEPP-2000 final focus solenoids into the IR of the ring, to compensate longitudinal field of the detector ($B = 1\ T$, $L = 1\ m$) anti-solenoids' coils were switched on.

Up to now round beams at VEPP-2000 were always carried out in simple mode where solenoids in each IR have opposite polarity ($+-\ \ +-$). This corresponds to usual betatron modes, horizontal and vertical elsewhere except IR, where they are rotated on the large angle (roughly π/4). Equal beam emittances required for RBC are produced by finite betatron coupling and betatron tunes being at the coupling resonance $\nu_x - \nu_z = 2$. We plan to try another optic schemes ($++\ \ --$) and ($++\ \ ++$) during the next experimental run 2010/2011, but expect difficulties with smaller dynamic aperture.

RESPONSE MATRIX TECHNIQUES

The ORM analysis is widely applied at VEPP-2000 complex. It was used in "soft" optics for rough alignment of cooled solenoids. The precision of coils' position and tilt restored from measured CO response at BPMs does not exceed 0.1 mm and 1 mrad correspondingly. More precise experiments of solenoid position determination with respect to CO was done in regular "round beam" optics also with use of ORM measurements [7].

Another ORM routine application is the measurement and correction of CO distortions at BEP and VEPP-2000 rings. Varying the gradient strength of each quadrupole one can get the CO distortion value there by comparison of measured CO response to model one. This technique is the only one for BEP, where the number of BPMs is poor, but it is also necessary for VEPP-2000 since 16 CCD cameras registering beam synchrotron radiation have high precision of 1 μm but haven't absolute calibration.

The use of SVD technique for ORM inversion also allows us to minimize steering coils currents for given CO.

This is important for dynamic aperture optimization since many dipole correctors being embedded in quadrupole lenses have strong nonlinear field components.

Finally, the analysis of orbit responses to dipole correctors variation became a routine but powerful instrument for lattice correction at VEPP-2000 [6, 7]. In Fig. 5 the lattice functions for low-beta optics are presented before lattice correction and after 4-th iteration of the procedure.

Figure 5: Lattice functions restored from ORM analysis before and after lattice correction.

LUMINOSITY INTEGRAL

In 2009/2010 first experimental run with both detectors SND and CMD-3 was carried out. Rude energy scan was done from 500 MeV to 950 MeV. The total luminosity integral collected by both detectors amounts to $\int L \sim 10\ pb^{-1}$. In Fig. 6 one can see the luminosity integral collected by SND at each point of energy scan. The integral collected by CMD-3 is ~1.6 times smaller.

Figure 6: Integrated luminosity collected by SND.

Although the peak luminosity with given beam-beam parameter (3) should grow rapidly with energy ($L \propto \varepsilon \gamma^2$),

at present several restrictions exists which do not allow us to provide maximum beam currents at high energy. First one is the insufficient positrons production by the old injection system (part of VEPP-2M complex). It would be fixed after the start up of new VEPP-5 injection complex at BINP. Another problem is low maximum energy of booster BEP and injection channels (900 MeV). In fact the energy ramping in VEPP-2000 was introduced for operation over 800 MeV due to head-tail instabilities in BEP at the higher energies. Firstly ramping inevitably causes large dead time. Moreover, even with enough positrons production the beam currents couldn't be on the beam-beam limit after ramping due to strong energy dependence of space charge parameter (1). In the case of ramping the luminosity dependence $L(E)$ is defined by (2) but with fixed beam current N and thus degrade with energy. Due to mentioned restrictions together with β^* change the luminosity value decreased during 2009/2010 run from 1×10^{31} $cm^{-2}s^{-1}$ at 500 MeV to 1.5×10^{30} $cm^{-2}s^{-1}$ at 950 MeV. The project luminosity would be achieved only after BEP upgrade up to 1 GeV. The designing of upgrade is already in progress.

ENERGY CALIBRATION

The requirement on the beam energy measurement precision is $\Delta E/E \leq 10^{-4}$. All VEPP-2000 bending dipoles are equipped with 2 NMR probes each. Probes themselves have high accuracy and show good stability of magnetic field ($\sim10^{-5}$). At the same time they are situated in the dipole gap, but outside of the vacuum volume i.e. rather far from the CO. Rude calibration of the NMR probes was done through the maps of magnetic field obtained from the magnetic measurements. For higher accuracy we use two methods.

Phi-meson

The φ-meson mass is known with high precision $M_\varphi = 1019.455 \pm 0.020$ MeV (PDG). So, the first absolute VEPP-2000 energy calibration was done at the φ-meson resonance with SND detector. It showed an error of previous calibration as large as 3.5 MeV (see Fig.7).
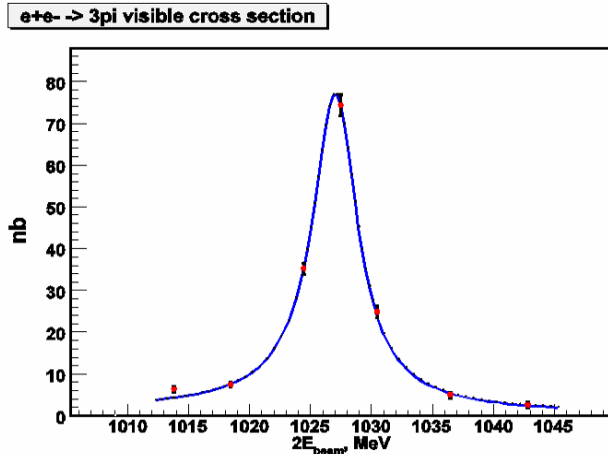
Figure 7: φ-meson resonance before energy calibration (SND data).

Resonant Depolarization

For more precise energy measurement in addition available at other energy values the method of resonance depolarization is assumed. At the end of 2009/2010 run two weeks were spent for polarization experiments at VEPP-2000. Two counters were installed into one of the technical straights to detect scattered particles. Counters are positioned in horizontal plane one from inner side and another from outer side at some distance from CO. At high energies the main contribution to counting rate is done by Intra Beam Scattering. By comparison of beam lifetime for the case of one bunch and two bunches with the same total beam current it was shown that IBS gives more than 80% of counting rate at 800 MeV. Moreover, to select precisely only good Touschek events only coincident data from two counters was taken. Since the Touschek effect depends on beam polarization the jump in the counting rate should happen during the polarization destruction. The special RF depolarizator was installed into center of injection straight.
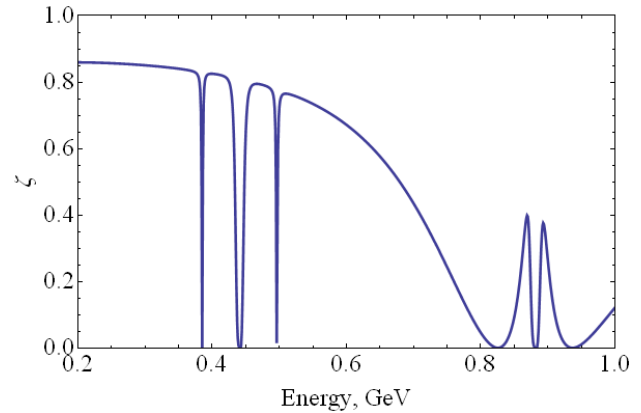
Figure 8: Calculated polarization degree vs. beam energy. Solenoids polarity scheme for low energy experiments.
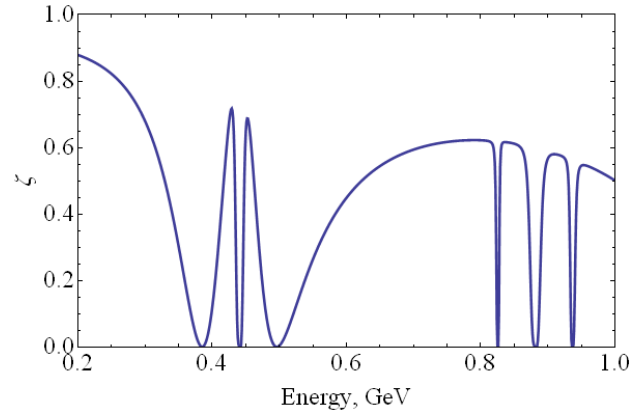
Figure 9: The case of solenoids polarity scheme for high energy polarization experiments.

According to theoretical calculations [8] the jump in Touschek scattering rate depends on the beam emittances ratio being suppressed for the round beam case

comparatively to the flat one. So, experiments were held with flat beam: opposite solenoids polarity in each IR; betatron tunes away from coupling resonance; betatron coupling suppressed with skew quadrupole correctors family. To avoid problems with beam parameters drift due to ion cloud focusing the positron beam was chosen for experiments. Radiative polarization time at experiment energy of 750 MeV amounts to ~ 45 minutes according to calculations.

Simulations made with ASPIRRIN code [9] show the great difference for solenoids polarity schemes. In Fig. 8 the beam polarization degree is shown for the $(+ - \ \ + -)$ scheme. This scheme includes 2-nd harmonic of longitudinal field that provide strong integer spin resonance at 880 MeV that destroy the polarization at this energy. Thus, such a polarity is suitable for beam polarization only at low energy. Narrow resonance at 440 MeV with two betatron satellites appears in case of solenoids detuning ($\Delta B_s/B \sim 10^{-3}$ at Fig. 8, 9) that is inevitable for real operation. Another scheme $(+ - \ \ - +)$ generates the first longitudinal field harmonic, and provide ~60% polarization at 700-800 MeV energy span (see Fig. 9). This scheme was used in attempts of energy calibration at 750 MeV.

Experimental results were dramatically obtained only last night before the complex shut down in the end of July 2010. The first results for the counting rate jump are shown in Fig.10. One can see three scans with the $2.5 \div 3$ % jump in counting rate. The energy obtained is 750.67 ± 0.03 MeV.
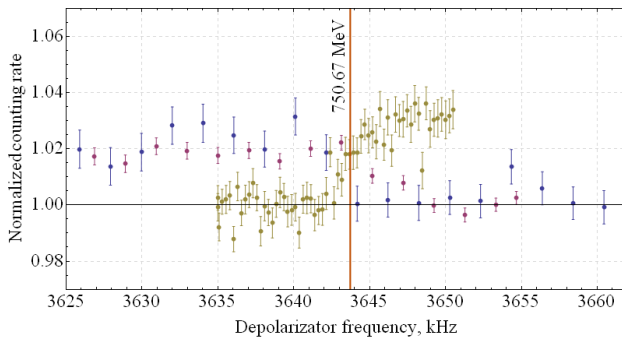
Figure 10: The jump in counting rate.

We plan to continue polarization activity at the beginning of the next run.

CONCLUSION

VEPP-2000 started up the data taking. First energy scan was done. All subsystems were tested at the energies up to 950 MeV. Different optics regimes were tried: technical solenoids-free option; regular round beam optics with $\beta^* = 8.5$ cm and CMD field switched on; low beta optics with higher luminosity; flat beam lattice for resonance depolarization method implementation.

The experimental results of the beam-beam study in the round beams mode have confirmed our expectations for the beam size behaviour in the "weak-strong" and "strong-strong" situations. In the "weak-strong" case the

space charge parameter achieved the value of $\xi = 0.1$. The peak luminosity $L = 1 \times 10^{31} \ cm^{-2} s^{-1}$ has been achieved at energy of 500 MeV with beam currents $I^+ \times I^- = 40 \times 40 \ mA^2$. To reach the target luminosity (1×10^{32}) at high energy (1 GeV) more positrons are required and booster BEP upgrade is need.

Energy calibration is in progress. NMR probes system was calibrated at the φ-meson resonance. First results of energy measurements via resonance depolarization method were obtained.

REFERENCES

[1] V.V.Danilov et al., in Proc of the EPAC 1996, Sitges, vol. 2, p.1149.
[2] Yu.M.Shatunov at. al., in Proc. of the EPAC 2000, Vienna, p.439.
[3] A.A.Valishev et al., in Proc. of the PAC 2003, Oregon, p.3398.
[4] P.Yu.Shatunov et. al., in Proc. of the EPAC 2006, Edinburg p. 628.
[5] D.E.Berkaev, et. al., in Proc. of the EPAC 2008, Genoa, p. 956.
[6] A.L.Romanov, et. al., in Proc. of the RuPAC 2008, Zvenigorod, p. 64.
[7] A.L.Romanov, et. al., in Proc. of the IPAC 2010, Kyoto, p. 4542.
[8] V.M.Strakhovenko, e-Print: arXiv:0912.5429 [physics.acc-ph], 2009.
[9] E.A.Perevedentsev, et al., AIP Conf. Proc. vol.675, p.761, 2003.

01 Circular Colliders

CRAB WAIST APPROACH: FROM DAΦNE TO SUPERB

M. Zobov, INFN LNF, Frascati, Italy

on behalf of the DAΦNE Collaboration Team[*] and the SuperB Accelerator Team[#]

Abstract

The crab waist collision scheme (CW) was proposed and successfully tested at the Φ-factory DAΦNE. At present this scheme is considered to be most attractive for the next generation lepton factories. In particular, the novel scheme is a key element of the SuperB project, a new SuperB-factory with luminosity about two orders of magnitude higher than that achieved at the present B-factories (KEKB and PEPII). In this paper we summarize the results achieved at DAΦNE after implementation of the CW collision scheme and discuss the status of the SuperB project.

INTRODUCTION

Pushing the luminosity of storage-ring colliders to unprecedented levels opens up unique opportunities for precision measurements of rare decay modes and extremely small cross sections, which are sensitive to new physics beyond the Standard Model.

Present generation lepton factories have been very successful in achieving their design luminosity performances [1]. However, new ideas were required in order to achieve a further substantial luminosity increase. Indeed, several novel collision concepts and new collision schemes have been proposed to provide such a qualitative step in the luminosity increase. The most known are the following: round beam collision preserving an additional integral of motion [2]; crab crossing [3, 4]; collision with large Piwinski angle [5] ("superbunch" in hadron colliders [6, 7]); longitudinal strong RF focusing [8]; collision with travelling waist [9]; crab waist collision [10, 11].

Now the crab waist collision scheme is considered to be most prominent for the next generation factories since it holds the promise of increasing the luminosity of the storage-ring colliders by 1-2 orders of magnitude beyond the current state-of-art, without any significant increase in beam current and without reducing the bunch length.

The CW scheme has been successfully tested at the electron-positron collider DAΦNE [12], the Italian Φ-factory operating at the energy of 1020 MeV in the center of mass. After an upgrade including the implementation of this novel collision scheme, the specific luminosity at low beam currents has been boosted by more than a factor of 4, while the present peak luminosity, 4.53×10^{32} cm^{-2}s^{-1}, is a factor of 3 higher than the maximum value obtained with the original configuration based on the standard collision scheme. The achieved peak luminosity is close (within 10%) to the design value in good agreement with numerical simulations [13].

The successful test has provided the opportunity to continue the DAΦNE Physics program. Moreover, advantages of the CW collision scheme have triggered several collider projects exploiting its potential [14, 15, and 16]. In particular, an international collaboration is pursuing the SuperB project [14] aiming at constructing in Italy a very high luminosity asymmetric collider at the Y(4S) energy in the center of mass. The new SuperB factory is expected to reach a luminosity as high as 10^{36} cm^{-2}s^{-1}, i.e. 2 orders of magnitude higher than that achieved at present B-factories (KEKB and PEPII).

In the first section of this paper we discuss the basic concept and advantages of the CW scheme. In the following section we briefly describe results of the CW experimental test at DAΦNE. Finally, we overview the status of the SuperB accelerator project.

CRAB WAIST COLLISION SCHEME

The CW scheme can substantially increase collider luminosity since it combines several potentially advantageous ideas: collisions with a large Piwinski angle, micro-beta insertions and suppression of beam-beam resonances using dedicated ("crab waist") sextupoles. Let us consider two bunches colliding under a horizontal crossing angle θ (as shown in Fig. 1a). Then, the CW principle can be explained, somewhat artificially, in three basic steps.

[*]DAΦNE Team: D.Alesini, M.E.Biagini, C.Biscari, A.Bocci, R.Boni, M.Boscolo, F.Bossi, B.Buonomo, A.Clozza, G.O.Delle Monache, T.Demma, E.Di Pasquale, G.Di Pirro, A.Drago, A.Gallo, A.Ghigo, S.Guiducci, C.Ligi, F.Marcellini, G.Mazzitelli, C.Milardi, F.Murtas, L.Pellegrino, M.A.Preger, L.Quintieri, P.Raimondi, R.Ricci, U.Rotundo, C.Sanelli, M.Serio, F.Sgamma, B.Spataro, A.Stecchi, A.Stella, S.Tomassini, C.Vaccarezza, M.Zobov (LNF INFN); M.Schioppa (INFN,Cosenza); M.Esposito (La Sapienza); P.Branchini (INFN, Rome 3); F.Iacoangeli, P.Valente (INFN,Rome); E.Levichev, P.Piminov, D.Shatilov, V.Smaluk (BINP); N.Arnaud, D.Breton, L.Burmistrov, A.Stocchi, A.Variola, B.F.Viaud (LAL); S.Bettoni (CERN); K.Ohmi (KEK); D.Teytelman (Dimtel Inc.).

[#]SuperB Team: M.E.Biagini, R.Boni, M.Boscolo, B.Buonomo, T.Demma, A.Drago, S.Guiducci, G.Mazzitelli, L.Pellegrino, M.A.Preger, P.Raimondi, R.Ricci, C.Sanelli, M.Serio, A.Stella, S.Tomassini, M.Zobov (LNF INFN); K.Bertsche, A.Brachmann, A.Chao, R.Chestnut, M.Donald, C.Field, A.Fisher, D.Kharakh, A.Krasnykh, K.Moffeit, Y.Nosochkov, A.Novokhatski, M.Pivi, J.Seeman, M.K.Sullivan, A.Weidemann, J.Weisend, U.Wienands, W.Wittmer, M.Woods (SLAC); A.Bogomiagkov, I.Koop, E.Levichev, S.Nikitin, I.Okunev, P.Piminov, S.Siniyatkin, D.Shatilov, P.Vobly (BINP); F.Bosi, S.Liuzzo, E.Paoloni (Pisa University); J.Bonis, R.Chehab, O.Dadoun, G.Le Meur, P.Lepercq, F.Letellier-Cohen, B.Mercier, F.Poirier, C.Prevost, C.Rimbault, F.Touze, A.Variola (LAL); B.Bolzon, L.Brunetti, A.Jeremie (LAPP, Annecy); M.Baylac, O.Bourrion, J.M.DeConto, Y.Gomez, F.Meot, N.Monseu, D.Tourres, C.Vescovi (LPSC, Grenoble); A.Chancé, O.Napoly (CEA Saclay); D.P.Barber (DESY, Cockcroft Institute, Universty of Liverpool); S.Bettoni, D.Quatraro (CERN).

The **first one** is large Piwinski angle. For collisions with $\Phi = \theta\sigma_z/2\sigma_x \gg 1$ the luminosity L and the beam-beam tune shifts scale as (see, for example, [17]):

$$L \propto \frac{N\xi_y}{\beta_y^*}; \quad \xi_y \propto \frac{N\sqrt{\beta_y^*/\varepsilon_y}}{\sigma_z\theta}; \quad \xi_x \propto \frac{N}{(\sigma_z\theta)^2}$$

Clearly, in such a case, if it were possible to increase N proportionally to $\sigma_z\theta$, the vertical tune shift ξ_y would remain constant, while the luminosity would grow proportionally to $\sigma_z\theta$. Moreover, the horizontal tune shift would drop as $1/(\sigma_z\theta)$.

Differently from [6, 7], in the crab waist scheme the Piwinski angle is increased by decreasing the horizontal beam size and increasing the crossing angle. In this way we can gain in luminosity as well, and the horizontal tune shift decreases. Moreover, parasitic collisions (PC) become negligible since with higher crossing angle and smaller horizontal beam size the beam separation at the PC is large in terms of σ_x. But the most important effect is that the length of the overlap area of the colliding bunches is reduced, since it is proportional to σ_x/θ (see Fig. 1).

Then, as the **second step**, the vertical beta function β_y can be made comparable to the overlap area size (i.e. much smaller than the bunch length):

$$\beta_y^* \approx \frac{2\sigma_x}{\theta} \cong \frac{\sigma_z}{\Phi} \ll \sigma_z$$

It is worth noting that usually it is assumed that ξ_y (see the expression for L in (1)) always reaches the maximum allowed value, the so called "beam-beam limit". So, reducing β_y at the IP gives us several advantages:

- Luminosity increase with the same bunch current;
- Possibility of bunch current increase (if it is limited by ξ_y), thus further increasing the luminosity;
- Suppression of the vertical synchrobetatron resonances [18];
- Reduction of the vertical tune shift with the synchrotron oscillation amplitude [18].
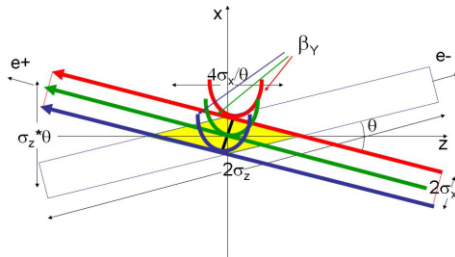
a) Crab sextupoles OFF.
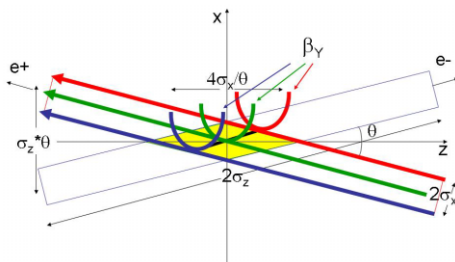
b) Crab sextupoles ON.

Figure 1: Crab Waist collision scheme.

Besides, there is an additional advantage in such a collision scheme: there is no need to decrease the bunch length to increase the luminosity as proposed in standard upgrade plans for B- and Φ-factories. This certainly helps in solving the problems of HOM heating, coherent synchrotron radiation of short bunches, excessive power consumption, etc.

However, implementation of these two steps introduces new beam-beam resonances which may strongly limit the maximum achievable tune shifts. At this point the crab waist transformation enters the game boosting the luminosity. This is the **third step**. As can be seen in Fig. 1b, the beta function waist of one beam is oriented along the central trajectory of the other one. In practice the CW vertical beta function rotation is provided by sextupole magnets placed on both sides of the IP in phase with the IP in the horizontal plane and at $\pi/2$ in the vertical one (as shown in Fig. 2). The crab sextupole strength should satisfy the following condition depending on the crossing angle and the beta functions at the IP and the sextupole locations:

$$K = \frac{1}{\theta}\frac{1}{\beta_y^*\beta_y}\sqrt{\frac{\beta_x^*}{\beta_x}}$$
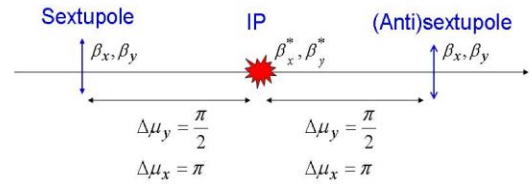
Figure 2: Crab sextupole locations.

The crab waist transformation gives a small geometric luminosity gain due to the vertical beta function redistribution along the overlap area. It is estimated to be of the order of several percent. However, the dominating effect comes from the suppression of betatron (and synchrobetatron) resonances arising (in collisions without CW) from the vertical motion modulation by the horizontal betatron oscillations [19].

Figure 3 demonstrates the resonances suppression applying the frequency map analysis (FMA) for the beam-beam interaction in CW collisions [20]. It shows the beam-beam footprint for DAΦNE with CW sextupoles off (left) and on (right).
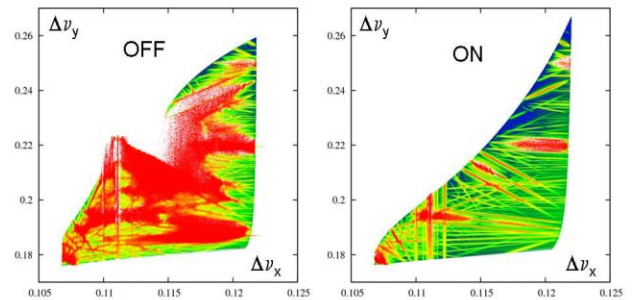
Figure 3: Beam-beam footprint with crab sextupoles off (left) and on (right) obtained by FMA techniques [20].

EXPERIMENTAL TEST AT DAΦNE

In 2007 the Φ-factory DAΦNE was upgraded implementing the crab waist collision scheme. This required major changes in the design of the mechanical and magnetic layout of both collider interaction regions [21]. Table 1 shows a comparison of the main beam parameters for the DAΦNE upgrade with those of the previous runs for the KLOE and FINUDA experiments.

As one can see from Table 1 the Piwinski angle was increased and the collision region length reduced by doubling the crossing angle, decreasing the horizontal beta function almost by an order of magnitude and slightly decreasing the horizontal emittance. In turn, the vertical beta function at the interaction point was decreased by a factor 2. The crab waist transformation is provided by two electromagnetic sextupoles installed at both ends of the experimental interaction region with the required phase advances between them and the IP. Their integrated gradient is about a factor 5 higher than that of normal sextupoles used for chromaticity correction.

Right from the start of commissioning, the effectiveness of the new collision scheme was confirmed by several measurements and qualitative observations of the beam-beam behavior. The simplest and most obvious test consisted in switching off the crab waist sextupoles of one of the colliding beams. This blew up both horizontal and vertical transverse beam sizes of that beam and created non-gaussian tails of the beam distribution, seen on the synchrotron light monitors (Fig. 4). At the same time, a luminosity reduction was recorded by all the luminosity monitors. This behavior is compatible with the prediction of additional beam-beam resonances when the crab sextupoles are off.

Table 1. DAΦNE best luminosity and respective IP parameters for three experimental runs.

Parameters	KLOE	FINUDA	Siddharta
Date	Sept 05	Apr 07	June 09
Luminosity, $cm^{-2}s^{-1}$	$1.53x10^{32}$	$1.60x10^{32}$	$4.53x10^{32}$
e– current, A	1.38	1.50	1.43
e+ current, A	1.18	1.10	1.00
Number of bunches	111	106	105
ε_x, mm mrad	0.34	0.34	0.25
β_x, m	1.5	2.0	0.25
β_y, cm	1.8	1.9	0.93
Crossing angle, mrad	2x12.5	2x12.5	2x25
Tune shift, ξ_y	0.0245	0.0291	0.044
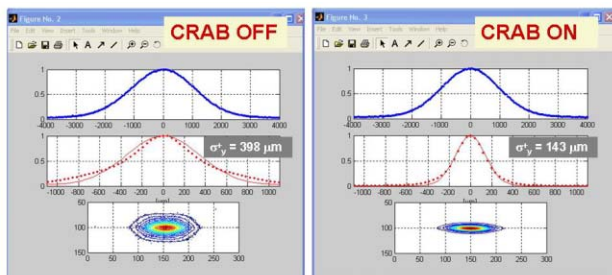
Figure4: Transverse beam profiles with crab on and off.

The best peak luminosity of $4.53x10^{32}$ $cm^{-2}s^{-1}$ was obtained in June 2009 together with a daily integrated luminosity exceeding $15pb^{-1}$. As one can see from Table 1, the best present luminosity is by a factor 3 higher than that in the runs before the upgrade. The maximum peak luminosity is already very close to the design value of $5x10^{32}$ $cm^{-2}s^{-1}$, and work is still in progress to achieve this ultimate goal. The vertical tune shift parameter has been significantly improved and it is now as high as 0.044 (a factor 1.5 higher than before). It is worth mentioning that in weak-strong collisions when the electron beam current is much higher than the positron one the tune shift has reached almost 0.09, in a perfect agreement with numerical simulations [13].

SUPERB ACCELERATOR PROJECT

The crab waist collision is the basic concept of the SuperB project [14] aimed at the construction of a very high luminosity asymmetric e+e- flavour factory with a possible location either near the campus of the University of Rome at Tor Vergata or at the site of the INFN Frascati National Laboratories. Figure 5 shows the SuperB layout at the Frascati (INFN LNF) site.

Figure 5: SuperB footprint at LNF.

The SuperB accelerator is being designed to satisfy the following requirements:

- Very high luminosity, $> 10^{36}$ $cm^{-2}s^{-1}$;
- Longitudinally polarized beam (e-) at IP (>80%);
- Ability to collide at charm threshold (3.8 GeV c.m.);
- Flexible parameter choice;
- Flexible lattice.

Column 1 of Table 2 shows the baseline parameter set that relies on the following criteria:

- to maintain wall plug power, beam currents, bunch lengths, and RF requirements comparable to present B-Factories, with parameters as close as possible to those achieved or under study for the ILC Damping Ring and at the ATF ILC-DR test facility;
- to reuse as much as possible of the PEP-II hardware;
- to simplify the IR design as much as possible, reducing the synchrotron radiation in the IR, HOM power and increasing the beam stay-clear;

- to eliminate the effects of the parasitic beam crossing, at the same time relaxing as much as possible the requirements on the beam demagnification at the IP;
- to design a Final Focus (FF) system to follow as closely as possible existing systems, and integrating it as much as possible into the ring design.

The machine is designed to have flexibility for the parameters choice with respect to the baseline: the horizontal emittance can be decreased by a factor of ~2 in both rings by changing the partition number (by changing the RF frequency, as done in LEP, or the orbit in the arcs) and the natural emittance by readjusting β functions.

Moreover the FF system has a built-in capability for decreasing the IP β functions by a factor of ~2, and the RF system will be able to support higher beam currents than the baseline, when all the available PEP RF units will be installed.

Based on these considerations, columns 2 and 3 in Table 2 show different parameters options:

- "Low Emittance" case relaxes RF requirements and problems related to high current operations (including wall-plug power) but puts more strain on the optics and the tuning capabilities;
- "High Current" case relaxes requirements on vertical emittance and IP β functions, but high currents issues are enhanced in terms of instabilities, HOM, synchrotron radiation, wall-plug power, etc.

The cases considered have several parameters kept as much constant as possible (bunch length, IP stay clear etc…), in order to reduce their impact on other unwanted effects (Detector background, HOM heating etc…).

SuperB can also operate at lower cm energy (τ/charm threshold energies near 3.8 GeV) with a somewhat reduced luminosity and minimal modifications to the machine: the beam energies will be scaled, maintaining the nominal energy asymmetry ratio used for operation at the cm energy of the Y (4S). The last column in Table 2 shows preliminary parameters for the run at the τ/charm.

Table 2: SuperB parameters for baseline, low emittance and high current options, and for τ/charm running.

Parameter	Units	Base Line		Low Emittance		High Current		τ-charm	
		HER (e+)	LER (e-)	HER (e+)	LER (e-)	HER (e+)	LER (e-)	HER (e+)	LER (e-)
LUMINOSITY	cm^{-2} s^{-1}	1.00E+36		1.00E+36		1.00E+36		1.00E+35	
Energy	GeV	6.7	4.18	6.7	4.18	6.7	4.18	2.58	1.61
Circumference	m	1258.4		1258.4		1258.4		1258.4	
X-Angle (full)	mrad	66		66		66		66	
β$_x$ @ IP	cm	2.6	3.2	2.6	3.2	5.06	6.22	6.76	8.32
β$_y$ @ IP	cm	0.0253	0.0205	0.0179	0.0145	0.0292	0.0237	0.0658	0.0533
Coupling (full current)	%	0.25	0.25	0.25	0.25	0.5	0.5	0.25	0.25
Emittance x (with IBS)	nm	2.00	2.46	1.00	1.23	2.00	2.46	5.20	6.4
Emittance y	pm	5	6.15	2.5	3.075	10	12.3	13	16
Bunch length (full current)	mm	5	5	5	5	4.4	4.4	5	5
Beam current	mA	1892	2447	1460	1888	3094	4000	1365	1766
RF frequency	MHz	476.		476.		476.		476.	
Number of bunches	#	978		978		1956		1956	
Tune shift x		0.0021	0.0033	0.0017	0.0025	0.0044	0.0067	0.0052	0.0080
Tune shift y		0.097	0.097	0.0891	0.0892	0.0684	0.0687	0.0909	0.0910
Total RF Wall Plug Power	MW	16.38		12.37		28.83		2.81	

RINGS LATTICE

The SuperB HER and LER ring lattices need to comply with several constraints: first of all extremely low emittances and IP beam sizes, needed for the high luminosity, damping times, beam lifetimes and polarization for the electron beam. The rings can be basically considered as two Damping Rings (similar to ILC and CLIC ones) with the constraint to include a FF section for collisions. So, the challenge is not only how to achieve low emittance beams but how to choose the other beam parameters to be able to reach design luminosity with reasonable lifetimes and small beams degradation. For this purpose a new "Arc cell" design has been adopted for SuperB [22]. The extremely low-β in the FF system, together with the Crab Waist scheme, requires a special optics that provides the necessary beam demagnification at the IP, corrects its relative chromaticity and provides the necessary conditions and constraints for the "Crab Waist" optics.

Both rings are located in the horizontal plane. The FF is combined with the two arcs in two half-rings (one inner, one outer) and a straight section on the opposite side, which comes naturally to close the ring and readily accommodate the RF system and other necessities (e.g. injection). In this utility region crossing without collisions for the two rings will be provided. More details on the lattice can be found in Ref [22].

INTERACTION REGION

The high luminosity is achieved primarily with the implementation of very small β_x^* and β_y^* values at IP. These conditions are principal driving terms in the design of the IR. The FF doublet (QD0 and QF1) must be as close as possible to the IP in order to minimize chromatic and other higher-order aberrations from these magnet fields. The present IR design with a crossing angle of +/- 33 mrad uses separate focusing elements for each beam. The QD0 magnet is now a twin design of side-by-side super-conducting quadrupoles. The magnet windings are designed so that the fringe field of the neighbouring magnet can be cancelled maintaining high quality quadrupole fields for both beams. Further details about the IR design can be found in the Ref [23].

POLARIZATION

SuperB will achieve polarized beams by injecting polarized electrons into the LER. We chose the LER rather than the HER because the spin rotators employ solenoids which scale in strength with energy.

In SuperB at high luminosity the beam lifetime will be only 3…5 minutes and continuous-injection ("trickle-charge") operation is a key component of the proposal. By injecting at a high rate with a polarized beam one can overcome the depolarization in the ring as long as the spin diffusion is not too rapid. In the ring arcs the polarization must be close to vertical to minimize depolarization. In order to obtain longitudinal polarization at the IP, a rotation of the spin by 90° about the radial axis is required. A rotation of 90° in a solenoid followed by a spin rotation of 90° in the horizontal plane by dipoles also provides the required net rotation about the radial axis without vertical bending and was therefore adopted. The solenoid field integral required is 21.88 Tm for 90° spin rotation, well within the technical capabilities of superconducting solenoids of the required aperture. After the IP, the polarization has to be restored to vertical by a second spin rotator. Due to the low beam lifetime, it turns out that a symmetric spin-rotator scheme is feasible and can achieve 70% polarization or better. More details on these studies can be found in Ref [24].

INJECTION SYSTEM

The injection system for SuperB [25] is capable of injecting electrons and positrons into their respective rings at full energies. The HER requires positrons at 6.7 GeV and the LER 4.18 GeV polarized electrons. At full luminosity and beam currents, up to 4 A, the HER

and LER have expected beam lifetimes in the range of 3÷5 minutes. Thus, the injection process must be continuous, to keep nearly constant beam current and luminosity. Multiple bunches are injected on each linac pulse into one or the other of the two rings. Electrons from the gun source are longitudinally polarized: the spins are rotated to the vertical plane in a special transport section downstream the gun. The spins then remain vertical for the rest of the injection system and injected in this vertical state into the LER. Positron bunches are generated by striking a high charge electron bunch onto a positron converter target and collecting the emergent positrons. Electron to positron conversion is done at about 0.6 GeV using a newly designed capture section to produce a yield of more than 10% [26]. The transverse and longitudinal emittances of both beams are larger than the LER and HER acceptances and must be pre-damped. A specially designed Damping Ring at 1 GeV, shared by both beams to reduce costs, is used to reduce the injected beam emittances.

REFERENCES

[1] ICFA Beam Dynamics Letter 48, April 2009.

[2] V.V.Danilov et al., EPAC96, p.1149.

[3] R.B.Palmer, SLAC-PUB-4707, 1988.

[4] K.Oide, K.Yokoya, Phys.Rev.A40:315-316, 1989.

[5] K.Hirata, Phys.Rev.Lett.74:2228-2231,1995.

[6] K.Takayama et al., Phys.Rev.Lett.88:144801,2002.

[7] F.Ruggiero, F.Zimmermann, Phys. Rev. ST Accel. Beams 5:061001, 2002.

[8] A.Gallo et al., e-Print:physics/0404020, 2004. A.Gallo et al., e-Print:physics/0309066, 2003.

[9] Y.Ohnishi, ICFA Beam Dyn.Newslett.48:252, 2009.

[10] P.Raimondi, in 2nd SuperB Workshop, 2006.

[11] P.Raimondi et al., e-Print:physics/0702033, 2007.

[12] M.Zobov et al., Phys.Rev.Lett.104:174801, 2010. C.Milardi et al., Nuovo Cim.32C:379-382, 2009. C.Milardi et al., Int.J.Mod.Phys.A24:360-368, 2009.

[13] M.Zobov, e-Print: arXiv:1006.1207, 2010. M.Zobov et al., ICFA Beam Dyn.Newslett. 48, p.34, 2009.

[14] SuperB CDR, e-Print: arXiv:0709.0451, 2007. M.E.Biagini et al., Nuovo Cim.123B:987-990, 2008.

[15] M.Masuzawa, IPAC10, p. 4764.

[16] E.Levichev, Phys.Part.Nucl.Lett.5:554-559, 2008.

[17] D.Shatilov, M.Zobov, ICFA Beam Dyn.Newslett. 37, p.99, 2005.

[18] D.V.Pestrikov, Nucl.Instrum.A336:427-437, 1993.

[19] P.Raimondi, D.Shatilov and M.Zobov, EPAC08, p.2620.

[20] E.Levichev at al., e-Print: arXiv:1002.3733, 2010.

[21] C.Milardi et al., e-Print: arXiv:0803.1450.

[22] M.Biagini et al., IPAC10, p.1521.

[23] M.K.Sullivan et al., IPAC10, p.1581.

[24] U.Wienands et al., IPAC10, p.1587.

[25] R.Boni et al., IPAC10, p.3685.

[26] F. Poirier et al., IPAC10, p.1650.

ACCELERATOR ASPECTS OF THE PRECISION MASS MEASUREMENT EXPERIMENTS AT THE VEPP-4M COLLIDER WITH THE KEDR DETECTOR *

Sergei Nikitin† for the VEPP-4 Team, BINP SB RAS, Novosibirsk

Abstract

Two methods for particle energy measurement are realized at the electron-positron collider VEPP-4M: one based on the resonant depolarization technique and another using the Back Compton Scattering. KEDR detector measurements of the J/Psi-, Psi' mesons and the tau-lepton masses performed with the help of these methods is better in accuracy now in the world. Peculiarities of the beam energy calibraton as well as of the mass measurement experiments are represented in the viewpoint of requirements on beam parameters and accelerator systems.

INTRODUCTION

The VEPP-4 accelerator facility with electron-positron colliding beams is known by the experiments on high precision calibration of the fundamental mass scale since the early eighties [1]. In 2002, the new series of similar experiments was started at VEPP-4M, the modernized collider ring, with the KEDR versatile magnetic detector. We improved the J/ψ and $\psi(2s)$ mass accuracy by a factor of 3-4 as compared with the world average one which had been based on our resuts of 80s. Owing to this fact, the J/Psi and Psi(2s) meson masses are now among the ten most accurate elementary particle masses measured over the entire history of physics. The measurement of the tau-lepton mass at its production threshold performed at the VEPP-4M collider is most accurate to date [2]. We obtained the D^0- and $D^\pm$-meson mass values (the second and the best results in accuracy, respectively) matching with the world average data.

The following activities at VEPP-4 contributed to so high precise results:
- the beam polarization measurement and beam energy monitoring methods including the new ones were developed and applied;
- the problems on accuracy of energy calibration by spin precession frequency were studied at new level;
- the questions on optimal tuning of VEPP-4 systems and operation modes for obtaining and application of beam polarization in mass measurements were set and resolved.

BEAM ENERGY CALIBRATION

Resonant Depolarization technique

The Resonant Depolarization (RD) technique for measuring the beam energy was proposed and implemented for the first time at BINP [3]. This approach was widely used thereafter both at the BINP and in other laboratories throughout the world.

In an ideal storage ring with the planar orbits, the average energy of electrons in a beam E is related to the average spin precession frequency Ω by the simple equation

$$E = mc^2\gamma = mc^2 \cdot \frac{q_0}{q'} \cdot \left(\frac{\Omega}{\omega_0} - 1\right) = 440.64843(3) \cdot \nu,$$

with q' and q_0, the anomalous and normal parts of the gyromagnetic ratio; ω_0, the revolution frequency; $\nu = \gamma q'/q_0$, the spin tune parameter. Limiting accuracy of the energy determination by the spin frequency $\delta E/E \approx 7.8 \cdot 10^{-8}$ is due to errors in knowledge of the fundamental constants. To measure Ω one needs to have a polarized beam in a storage ring, a system to observe the beam polarization as well as a system for enforced beam depolarization at the external spin resonance.

State of the VEPP-4M beam polarization at energies up to 2 GeV is observed by comparison of the Touschek electron/positron counting rate from the polarized and unpolarized bunches separated by a half turn ("two bunch method") [4]. The system of scintillation counters installed at several azimuths and put into the dynamic aperture provides a total counting rate ~ 1 MHz/mA at the distance of counters to the beam orbit ≈ 1 cm. The relative counting rate experiences a jump $\sim 1\%$ at the moment of depolarization proportional to squared level of polarization.

The two matched striplines of the VEPP-4 kicker are used to create a TEM wave propagating towards the beam. The signal source is a frequency synthesizer with a minimal frequency step of 0.35 mHz [4]. Scan rate and the TEM wave amplitude are tuned to provide the depolarization time ~ 1 second. The reference frequency signal for the synthesizer as well as for the VEPP-4M RF system is generated by the rubidium frequency standard (10^{-10}). Typical behavior of the measured effect in a time and the depolarization jump are shown in Fig.1. Absolute energy RD calibration accuracy is of a record level: $\delta E/E \sim 10^{-6}$. It is determined by the spin tune spread $\delta\nu/\nu \sim 5 \cdot 10^{-7}$ due to quantum diffusion of particle trajectories taking into account a quadratic non-linearity of the VEPP-4M guide field. To date more than 3000 RD calibrations has been performed.
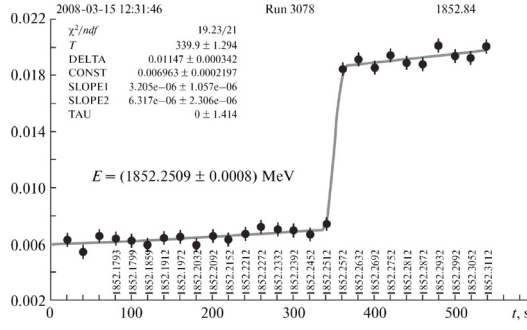
Figure 1: The ratio of counting rates from polarized and unpolarized bunches. Statistical error for the energy found is 0.8 keV.

Figure 2: Fragment of the energy spectrum of backscattered photons measured by the HPGe detector.

Compton Backscattering monitor

First beam energy measurements based on the Compton Back Scattering (CBS) was made at the BESSY-I and BESSY-II SR storage rings in Berlin. In 2005 this method was realized at VEPP-4M, for the first time for colliders. Since then, it is a routine instrument for monitoring the VEPP-4M beam energy. At $E \leq 2$ GeV it was achieved a record accuracy about $5 \cdot 10^{-5}$ in determination of the energy by this method for a half hour of scattered photon statistics acquisition. The method consists in measurement of the CBS spectrum edge (ω_{max}) related to the electron beam energy:

$$ E = \frac{\omega_{max}}{2} \left(1 + \sqrt{1 + \frac{m^2}{\omega_{inc}\omega_{max}}} \right), $$

ω_{inc} is the incident photon energy. The infrared CO_2 laser with the wave length 10.6 μm and 50 W CW power is used for radiation generation. The laser spot size in the interaction area is approximately 10 times larger than the electron beam horizontal transverse size to provide a correct measurement of average beam energy. Maximal energy of γ-quanta scattered towards the High Purity Germanium (HPGe) detector lies in the range 4-6 MeV. At first, the available γ-ray sources provided the HPGe energy scale calibration only in the $0.5 - 3$ MeV range. Calibration at the 6000 keV edge was made by extrapolation of the low energy data or using RD data of the VEPP-4M energy. Extrapolation gave ~ 100 keV difference between CBS and RD energy measurements. At present, we have the 6.13 MeV γ-quanta source in conjunction with a precise pulse generator. It solves a problem of the independent energy scale calibration. In Fig.2 the experimental spectrum is shown with the fitting applied to its edge. The "edge place" parameter is determined with a relative statistical accuracy $< 3 \cdot 10^{-5}$, while the "edge width" parameter has a statistical uncertainty of about 3%. These parameters together with the energy scale calibration are used to obtain the online data of the VEPP-4M beam energy and beam energy spread.

01 Circular Colliders
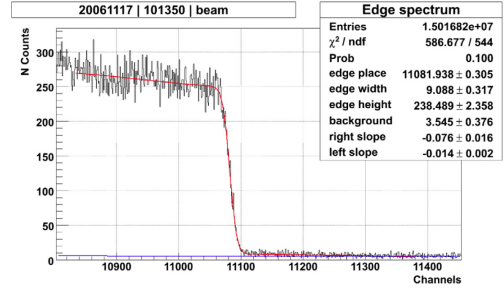
BEAM POLARIZATION

Polarized beams are obtained in the VEPP-3 booster storage ring owing to the natural radiative mechanism. Polarization rise time $\tau_p \propto E^{-5}$ amounts about 30 min at $E = 1.85$ GeV. For comparison, at VEPP-4M $\tau_p = 70$ hr at the same energy. It makes impossible to obtain the beam polarization in the collider ring. At the same time, it allows to have an acceptable polarization life-time in VEPP-4M even at small off-tunings from the spin resonances. VEPP-3 and VEPP-4M tunes ν_x, ν_y are kept in free cells of the spin resonanse grid $\nu + m \cdot \nu_x + n \cdot \nu_y = k$ up to the $|m| + |n| = 10$ order. Feed back system on the VEPP-3 work point stabilization with an accuracy $\delta(\nu_x, \nu_y) = \pm 0.002$ is applied to control the betatron tunes during the radiative polarization process.

VEPP-3 beam polarization degree vs. the beam energy (see Fig.3) was measured in 2003 using a method realized for the first time [6]. New method is based on measuring the asymmetry in scattering of polarized beam electrons on the internal polarized gas jet target. The internal target with the thickness of $\sim 5 \cdot 10^{11}$electron/cm^2 is formed by the jet of polarized deuterium atoms from the Atomic Beam Source of Deuteron Facility. The polarization appeared to be small in a wide range below 1840 MeV down to the threshold energy of τ-lepton production (1777 MeV) because of the spin resonances: $E \approx 1815$ ($\nu_x - \nu = 1$), $E \approx 1825$ MeV ($\nu_y - \nu = 1$) and $E = 1763$ MeV ($\nu = 4$). Taking into account this fact, a scenario of τ-mass measurement experiment near the threshold energy was elaborated. Radiative polarization in VEPP-3 and the injection into VEPP-4M of the polarized and unpolarized bunches, needed for RD calibration, occur at $E = 1.85$ GeV. Then the circulating particles are deaccelerated down to the experiment energy with a rate ≈ 10 MeV/sec.

Because of the integer spin resonance $\nu = 4$ closeness, a depolarizing effect of quantum fluctuations related to the field imperfections is enhanced that leads to decrease of a polarization life-time (PLT). Influence of different sources of such imperfections on PLT was numerically analyzed. Statistically, PLT is estimated to be most likely about or more than 1 hr at energies nearby the "τ- threshold", that is enough for the RD energy calibrations. At first, never-

theless, a rather small PLT, about several hundreds of seconds, was observed [7]. PLT grew to a level ≥ 1 hr after we turned off the vertical orbit bumps in the parasitic interaction points and carried out the global vertical orbit correction. As a whole, it may indicate the existance of an additional factor, for instance, the out of control spin resonant diffusion. Recently, it was suggested to consider from this point of view the second harmonic of the 12.5 kHz ripples in the magnetic correction coils supplied by PWM-generators (an off-tuning from the integer spin resonance at the "τ- threshold" makes up about 27 kHz; the instant spin tune spread is 1.4 kHz).

The vertical spin projection of polarized positrons injected at 1.85 GeV is 1.5 times less than that of electrons (having the analogous projection close to 1). It gives a design decrease of depolarization jump in the RD technique by a factor of 2.5. With the aim to eliminate this defect we installed and applied the 2.5 T·m pulse solenoid at the VEPP-3-VEPP-4M beam-line section before the outlet $90°$ bend magnets. As result, the depolarization jump for positrons increased by a factor 2. This contributed to improvement of an accuracy in the electron-positron energy gap measurement (~ 1 keV) which is important for the systematic error study.

ACCURACY AND STABILITY

We studied and resolved the different questions concerning the instant absolute energy calibration accuracy, the central mass (CM) energy determination errors as well as the collider energy stability.

Suppression of 50 Hz and 100 Hz ripples in the non-linearity corrections improved the RD calibration accuracy from 10^{-4} to 10^{-6}. To avoid the error related to depolarization at the modulation spin resonances we thoroughly calculate the depolarizer efficiency and properly tune the scan mode [8].

Spin tune shift due to a compensation error of the KEDR detector longitudinal field integral does not conserve the "spin tune - energy" ratio. We measured this spin tune shift vs. the anti-solenoid strength [9]. It resulted in minimization of the KEDR field compensation error with an accuracy $\sim 1\%$ and in reduction of the RD systematic energy error down to 1 keV.

Another source of the systematic error is the vertical orbit distortions [10]. The spin tune shift can be writen as a quadratic form of the vertical orbit deflection angles composed of two terms: non-correlation and correlation ones. We performed the analytical estimates and Monte-Carlo simulation for the statistically independent perturbations model. It was found that the correlation term can play a determinant role. Correct estimate of the systematic error at the 1.5 mm rms orbit distortions, $E = 1777$ MeV is $\delta E = 1.5 \pm 1.5$ keV, but it is ~ 100 keV when excluding the correlation.

Taking into account the non-uniform distribution of radiative energy losses over the ring, the systematic error in

01 Circular Colliders

the CM energy determination by the RD calibration of a single beam can be found in a special experiment as a difference of electron and positron energies. According to our tentative experiments on simultaneous RD calibrations with electron and positron beams their energy gap is ~ 1 keV. We also studied the contributions to the CM energy error from the IP chromaticity, the beam potential, the orbit separation in parasitic IPs and others [11]. At the begin-
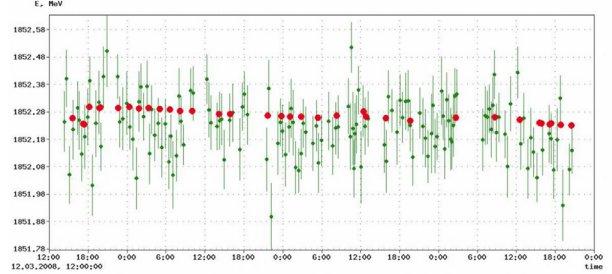
Figure 3: RD (circles blown-up to show) and CBS (dots with dispersion) energy data during 3 days and nights.

ning of regular RD calibrations at the 1.5 GeV VEPP-4M without the water cooling of magnets, the round-the-clock energy oscillations with a several tens of keV amplitude were found caused, presumably, by the tunnel temperature variations. Later on, the system for heatset of the distilled water for cooling of magnets was created [1]. If operating with the heatset system and no changes in VEPP-4M magnet settings the round-the-clock energy drift is $\sim$ one or more keV. In Fig.3 the long-term energy stability run with RD and CBS data is presented.

To improve the energy stability in our most precise RD experiments with the depolarization frequency resolution of $\sim 10^{-9}$ we developed the NMR magnetometer-based field stabilization system [5]. It reduces the field ripples with a period of more than 10 seconds by a factor of ten.

REFERENCES

[1] O.V. Anchugov et al. Instruments and Experimental Techniques, 2010, Vol. 53, No. 1, pp. 152

[2] A.G. Shamov, KEDR Collab., Nucl. Phys. B, Proc. Suppl. 181182, 311 (2008).

[3] A.D.Bukin et al., Proc. of V Int.Symp.High Energy and Particle Physics, Dubna, 1975, p. 138.

[4] V.E. Blinov et al. / NIMA 598 (2009) 2330.

[5] V.E.Blinov et al. Beam Dynamics Newsletter, 2009, No. 48, pp. 207-217.

[6] M.V. Dyug et al. NIMA 536 (2005) 338-343

[7] A.Bogomyagkov et al.,Proc. of EPAC 2004, pp.737-739.

[8] S.A.Nikitin. BINP Preprint 2005-54 (russ.).

[9] S.A. Nikitin. RUPAC 2006 Proceedings.

[10] A.V. Bogomyagkov, S.A. Nikitin, A.G. Shamov. RUPAC 2006 Proceedings.

[11] A.Bogomyagkov et al., PAC 2007 Proceedings, MOOBI01, p.63.

PROJECT OF THE NUCLOTRON-BASED ION COLLIDER FACILITY (NICA) AT JINR

G. Trubnikov, N. Agapov, V. Alexandrov, A. Butenko, E. Donets, A. Eliseev, V.V.Fimushkin, Yu. Filatov, A.Govorov, V.Karpinsky, T. Katayama, V. Kekelidze, H. Khodzhibagiyan, V. Kobets, S.Kostromin, A. Kovalenko, O. Kozlov, A. Kuznetsov, I. Meshkov, V. Mikhaylov, V. Monchinsky, V. Shevtsov, A. Sidorin, A. Sissakian, A. Smirnov, A. Sorin, V. Toneev, V. Volkov, V. Zhabitsky, O. Brovko, JINR, Dubna, Russia

Abstract

The Nuclotron-based Ion Collider fAcility (NICA) is the new accelerator complex being constructed at JINR aimed to provide collider experiments with heavy ions up to uranium at the center of mass energy from 4 to 11 GeV/amu. It includes 6 MeV/amu heavy ion linac, 600 MeV/amu booster, upgraded Super Conducting (SC) synchrotron Nuclotron and collider consisting of two SC rings, which provide average luminosity of the level of 10^{27}cm^{-2}s^{-1}.

INTRODUCTION

The goal of the NICA project is construction at JINR of the new accelerator facility that consists of (see Fig.1)

- cryogenic heavy ion source of Electron String type (ESIS),
- source of polarized protons and deuterons,
- the existing linac LU-20,
- a new heavy ion linear accelerator (HILAc) [1],
- a new SC Booster-synchrotron (that will be placed inside the decommissioned Synchrophasotron yoke),
- the existing proton and heavy ion synchrotron Nuclotron (located in the basement of the Synchrophasatron building) [2],
- two new SC storage rings of the collider,
- a new system of beam transfer channels.

The facility will have to provide ion-ion (1÷4.5 GeV/amu of the ion kinetic energy), ion-proton collisions and polarized proton-proton (5÷12.6 GeV) and deuteron-deuteron (2÷5.8 GeV/amu) beams collisions.

As a result of the project realization, the potential of the Nuclotron accelerator complex will be sufficiently increased in all the fields of its current physics program. The fixed target experiments with slow extracted Nuclotron beams are presumed the experiments with internal target as well. The Booster will be equipped with a slow extraction system to perform radio-biological and applied researches using heavy ion beams.

The collider will have two interaction points. The Multi Purpose Detector (MPD), aimed for experimental study of hot and dense strongly interacting QCD matter and search for possible manifestation of signs of the mixed phase and critical endpoint in heavy ion collisions, is located in one of them. The second one is used for the Spin Physics Detector (SPD).

Main goal of the NICA facility construction is to provide collider experiment with heavy ions like Au, Pb or U at luminosity above $1\cdot10^{27}$ cm$^{-2}\cdot$s^{-1} at the energy of 3.5 GeV/amu. It was decided to choose the Gold nuclei ^{197}Au^{79+} as the reference particles for the heavy ion collider mode. In the collisions of polarized beams the luminosity above $1\cdot10^{31}$ cm$^{-2}\cdot$s^{-1} is planned to be achieved in the total energy range.
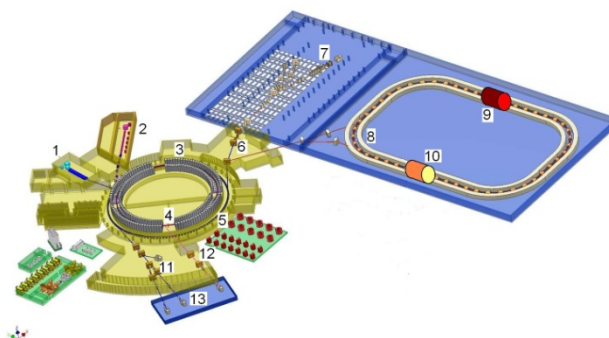
Fig. 1. Scheme of NICA facility: 1 – light and polarized ion sources and "old" Alvarez-type linac; 2 – ESIS source and new RFQ linac; 3 – Synchrophasotron yoke; 4 – Booster; 5 – Nuclotron; 6 – beam transfer line; 7 – Nuclotron beam lines and fixed target experiments; 8 – Collider; 9 – MPD; 10 – SPD; 11, 12 – transfer lines; 13 – new research

The essential features of the project permitting to minimize its cost, the construction period and to realize a wide experimental program are the following:

- Collider facility does allow independent carrying out the fixed target experiments;
- The facility can be used for collider experiments with light and middle weight ions including polarized deuterons;
- The required modifications of the Nuclotron ring including development of the ion sources are realizing within the project of the Nuclotron upgrade, which will be completed in 2010 [3];
- Choice of optimal Booster design based on a few possible versions made before;
- Application of recent world data obtained at BNL, CERN and GSI for achievement of a high collider luminosity;
- Wide co-operation with JINR Member State

01 Circular Colliders

institutions and active participation of Russian institutions;

- Application of relevant experience available at JINR in superconducting magnets design and fabrication (the magnet cryostating systems of the collider rings and Booster can be made by the institute workshops).

NICA OPERATION

Collider will be operated at a fixed energy without acceleration of an injected beam. Correspondingly the maximum energy of the experiment is determined by the Nuclotron magnetic rigidity that is equal to about 45 T·m at the field value of about 2 T. The collider rings will be placed one above the other one and elements of SC magnetic system are being design as a "twin bore" magnets. For luminosity preservation in the heavy ion collision mode an electron and stochastic cooling systems are planned to be used. To cover the total ion energy range the electron energy of the electron cooling system has to be varied from 0.5 to 2.4 MeV. For optimum operation of the stochastic cooling system the collider optic structure is designed to permit variation of the ring critical energy [4].

To achieve the maximum design energy the Nuclotron has to accelerate fully stripped ions. To provide the ion stripping at high efficiency the ions have to be accelerated to the energy of a few hundreds of MeV/amu. For this goal is used a new synchrotron ring – the Booster. To obtain maximum ion number after single turn injection the Booster has to have a circumference as long as possible. It is realized at the Booster location inside the Synchrophasotron yoke. The yoke will provide also a necessary radiation shielding of the Booster ring.

The heavy ion beam accumulation in the collider rings will be realized with application of RF barrier bucket technique. Intensity of the injected portion influences on the stacking process duration only and could be arbitrary in principle. The required beam emittance is formed during the stacking by the cooling application. The maximum bunch number in the collision mode is limited by requirement to avoid parasitic collisions in the interaction region. The collider will be equipped with Barrier Bucket RF system and two sinusoidal RF systems – one of them is operated at the harmonics number coinciding with the bunch number at the collisions (it is used for the bunching of the stacked beam), another one is operated at significantly larger harmonics number that is necessary to keep a short bunch length at reasonable RF voltage value.

The suggested Project allows one to collide mass asymmetric beams including proton-ion (pA) collisions. Alongside of proper physics meaning, it is quite important as a reference point for comparison with heavy ion data. The experiment will be performed at the same MPD detector therefore the luminosity significantly larger than 10^{27} cm^{-2}·s^{-1} is not necessary. This level is achievable

quite easily because of large proton number in the beam comparing with heavy ions.

In this mode the collider injection chain has to be switched fast (during a time of a few seconds) from acceleration of heavy ions to acceleration of protons. Two acceleration and stacking chains of heavy ions and protons (or light polarized ions) are proposed:

- ESIS → HILAc → Booster → Nuclotron → Collider
- Duoplasmatron (polarized ions source) → LU-20 → Nuclotron → Collider

For the proton acceleration the Booster is not necessary. The proton beam generated by duoplasmatron source is accelerated by LU-20 up to energy of 20 MeV. Single-turn injection allows Nuclotron to have more than 10^{11} protons. After adiabatic bunching they are accelerated at the 5-th harmonic of the revolution frequency to the experimental energy and transferred, bunch by bunch, to the collider ring. If necessary the accelerated proton beam can be rebunched in the Nuclotron after the acceleration to form a single bunch of larger intensity.

Another mode of the facility operation will be proton-proton and deuteron-deuteron polarized colliding beams in the energy range 5 ÷ 12.6 GeV for protons and 2 ÷ 5.8 GeV/amu for deuterons. The luminosity above $1·10^{31}$ cm^{-2}·s^{-1} is required over the total energy range.

For the spin physics program the Booster is not used because it has only four super periods instead of 8 in the Nuclotron. The polarized particles are accelerated with LU-20, single-turn injected into the Nuclotron where accelerated up to the experiment energy.

In the Nuclotron ring the deuteron depolarization resonances are absent in the total achievable energy range. The possibility of acceleration and extraction of polarized deuterons in the Nuclotron has been demonstrated a few years ago. The measurements of polarization degree performed by three independent groups on internal and extracted beams in November 2003 gave the value of 65 % agreed with the expected value.

For acceleration of the polarized proton beam the Nuclotron has to be equipped with insertion devices for the spin tune control to cross the depolarization resonances without loose of the polarization degree. Preliminary design of such devices was prepared and the Nuclotron straight section length is sufficiently long to place them.

Presently the maximum achieved intensity of polarized beam in the Nuclotron is about $2·10^8$ particles per cycle. The main direction of work aimed at increase of the intensity is connected with the design and construction of a new high current polarized ion source with charge-exchanged plasma ionizer (IPSN) based on the equipment of CIPIOS polarized proton and deuteron source transferred to Dubna from Bloomington (Indiana

University, USA). The work is carried out in collaboration with INR (Troitsk). Some parts of suitable equipment for the new source were presented by DAPHNIA (Saclay). The IPSN will provide the output beam current up to 10 mA of $\uparrow$p and $\uparrow$d$^+$ ions. $\uparrow$d$^+$ ion polarization of 90% of the nominal vector mode +/-1 and tensor mode +1,-2 is expected. That will result in increase of the accelerated polarized beam intensity at the Nuclotron up to above 10^{10} particle/cycle.

The collider operational cycle assumes feeding the collider with ions during a few minutes after that the collision experiment will be provided during a few hours at almost constant luminosity without additional injections. At this time the Booster and Nuclotron will be used for independent experimental programs. The Nuclotron with LU-20 as injector will provide light ion beams for internal target experiments and its slow extraction system will be used for fixed target experiments and test of the MPD elements. The Booster will be used as a heavy ion synchrotron. Its designed magnetic rigidity of 25 T·m allows providing the wide range of radio-biological and applied experiments as well as cancer therapy researches with carbon and heavy ions.

PLANS FOR REALISATION

The Nuclotron upgrade program considered as a first stage of the NICA project [5] is in the final stage now. Main goal of the program is to prepare the synchrotron for operation as a part of the NICA collider injection chain. To the moment the upgrade of the Nuclotron vacuum system is completed, deep reconstruction of the liquid helium factory was provided during 2008-2009, modernization of the magnetic system power supply and energy evacuation system will be completed this year. As a result of the works at the Nuclotron run in March 2010 the ions Xe^{42+} were successfully accelerated up to energy of about 1.5 GeV/amu, and the magnetic system was operated at the dipole magnetic field of about 1.8 T (the designed value is 2 T). Development of the new heavy ion source and the polarized ion source is the part of the Nuclotron upgrade as well.

In parallel with the accelerator modernization the technical design of the collider injection chain elements (HILAc, Booster, LU-20 upgrade program) was prepared. One of the most important problems determining the facility construction period is the possibility of the collider location close to the Nuclotron with minimum civil constructions. The collider ring circumference has to be about 550 m. But it is not possible to locate such a ring in the existing experimental building. The project of the new location of the collider (see Fig.1) is under development by State Specialized Design Institution (Moscow) and we expect it the completion at the end of 2010. As a result the price and the required reconstruction period will be determined.

The structural dipole and quadrupole magnets for the collider, as well as for the Booster, will be based on the design developed during the Nuclotron construction. The Nuclotron superconducting magnets are based on a cold-iron window frame type yoke and low inductance winding made of a hollow composite superconductor. The magnetic field distribution is formed by the iron yoke. The Nuclotron magnet fabrication has brought a great experience to the Institute staff in the field of SC magnet design and manufacturing. Such type of magnets one plans to use for construction of SIS-100 synchrotron of the FAIR project. The collider dipole magnet will be about 2 m long, the distance between apertures is about 30 cm. Construction of the magnet model based on the preliminary design has been started in 2010.

To construct the Booster and collider rings we need to fabricate more than two hundreds of the dipole magnets and lenses during short period of time. The working area for the magnet fabrication and test benches required for the magnet commissioning are under preparation now.

A few elements of the facility (such as electron and stochastic cooling) require R&D works and long term of the construction (HILAc).

Taking into account all these problems the beginning of the facility element commissioning in 2015 looks realistic at the moment. In the optimistic expectations the experiments with circulating beam in the collider rings can be started at the end of 2015. At the first stage of the collider operation the heavy ion collisions will be realized and the design luminosity level can be achieved to 2017. After upgrade of the ring optics in the vicinity of the collision point the heavy ion–proton collisions will be performed. Collisions of light polarized ions are scheduled for the third stage of the collider operation.

REFERENCES

[1] V.Kobets, A.Sidorin et al., Injector Complex of the NICA Facility, These Proceedings.

[2] A.Butenko, V.Mikhaylov et al., Design of the Nuclotron Booster in the NICA Project, These Proceedings.

[3] A.Butenko, G.Trubnikov et al., Status of the Nuclotron. "Nuclotron-M" Project, These Proceedings.

[4] S.Kostromin, O. Kozlov et al., Lattice of the NICA Collider Rings, These Proceedings.

[5] I.Meshkov, A.Sisakian, G.Trubnikov, Heavy Ion Programs for Applications and Fundamental Research at JINR, These Proceedings.

01 Circular Colliders

OPTICS DESIGN FOR NICA COLLIDER

S.Kostromin, O.Kozlov, I.Meshkov, V.Mikhailov, A.Sidorin, G. Trubnikov, JINR, Dubna
V.Lebedev, S.Nagaitsev, FNAL, Batavia, Illinois, USA, Yu.Senichev, IKP, Juelich, Germany

Abstract

The Nuclotron-based Ion Collider fAcility (NICA) [1] is a new accelerator complex being constructed at JINR. It is designed for collider experiments with ions and protons and has to provide ion-ion (Au^{79+}) and ion-proton collisions in the energy range 1÷4.5 GeV/n and collisions of polarized proton-proton and deuteron-deuteron beams.

Collider conceptions with constant γ_{tr} and with possibility of its variation are considered. The ring has the racetrack shape with two arcs and two long straight sections. Its circumference is about 450m. The straight sections are optimized to have $\beta^* \sim 35cm$ in two IPs and a possibility of final betatron tune adjustment.

INTRODUCTION

NICA collider lattice development has a number of challenges which must be overcome in the design process. The requirements set by physics goals are: changeable energy of the Au-ions collision in the range 1÷4.5 GeV/n, operation with different ion mass (Au^{79+}, deuterons and protons), the peak luminosity up to $5 \cdot 10^{27}$ cm^{-2}s^{-1} at 4.5 GeV/n, and, additionally, the collider rings must fit into existing JINR infrastructure.

The ring lattice is based on super-ferric magnets with 2T bending field. The technology of fabrication of such magnets operating at 4.5K with hollow composite NbTi cable is well established in JINR.

The main luminosity limitation is set by the direct space charge tune shift. In this case the luminosity is proportional to the beam emittance and, consequently, to the collider acceptance. Thus, good optics for NICA implies that in addition to the standard requirement of small beta-function in IP, β^*, there is a requirement of maximizing the machine acceptance.

INTRA-BEAM SCATTERING STUDY

The intra-beam scattering (IBS) is one of the main factors which have to be taken into account in a collider ring design. For operation below transition IBS is significantly reduced if the local beam temperatures averaged over the ring are equal. In this case the emittance growth rate due to IBS is equal to zero for a perfectly smooth lattice. Beta-function and dispersion variations destroy this thermal equilibrium resulting in an emittance growth in all three planes: larger variations excite faster emittance growth.

First, the IBS rates were computed for the ideal rings (without straight sections) constructed from ODFDO - and FODO -cells [2]. For the same number of particles the beam emittances were adjusted to have the same growth rates for all planes (thermal equilibrium) and to have the same vertical space charge tune shift (bunch density). Due to "smother" optics the IBS heating rate,

τ_{IBS}^{-1}, for the ring based on the triplet cells is ~5 times smaller than for the singlet cells ring with the same phase advance per cell. Therefore the ODFDO-cell ring was chosen as a reference for the collider optics.

A transition from the ideal ring to the collider optics with low-β straight sections increases β-function and dispersion variations and yields an increase of IBS rates. Finally, the collider ring lattice based on FODO-cells has only ~1.5 times larger rates: the growth time of ~890 s versus ~1350 s for the luminosity of $6 \cdot 10^{27}$ cm^{-2}s^{-1}.

Table 1: Main parameters of the collider rings optics

Beam species and energy	Au^{79+}, 4.5 GeV/n
Ring circumference	454 m
Gamma-transition, γ_{tr}	6.22
Betatron tunes	9.46 / 9.46
Particles per bunch (of 20 bunches)	$5.3 \cdot 10^9$
Acceptance	40 π mm mrad
Longitudinal acceptance, $\Delta p/p$	+/- 0.0125
RMS emittance, $\varepsilon_x/\varepsilon_y$	1.1/0.6 π mm mrad
Beta function at IP, β^*	35 cm
Rms bunch length	60 cm
IBS growth time	1350 s
Luminosity (for Au^{79+} 4.5 GeV/n)	$6 \cdot 10^{27}$ cm^{-2} s^{-1}
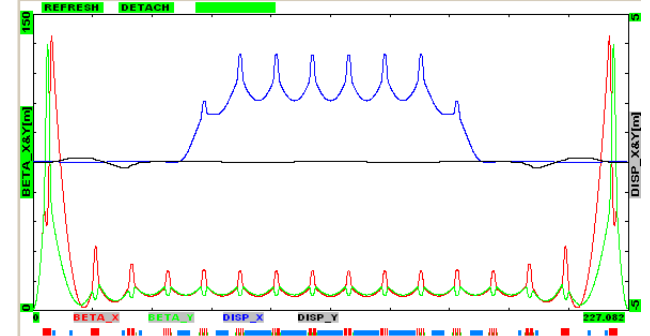
Figure 1: β-function & dispersions for half of the ring.

COLLIDER RING OPTICS STRUCTURE

Two main options of the NICA optics were considered.

Triplet based racetrack with γ_{tr}=6.22

This option was considered in Ref. [3] (see Fig.1). The objectives for the optics design are: (1) small β*, (2) an operation near thermal equilibrium where IBS rates can be minimized, (3) large transverse and momentum acceptances, (4) small circumference, (5) optimal location of collider tune and (6) two IPs. That determined the following design choices: (1) mirror symmetric racetrack with IP in each straight section, (2) triplet focusing through the entire machine (including IPs), (3) phase

advance of 90° per cell, (4) dispersion zeroing in the straight sections by a half-dipole without changing phase advance per cell, and (5) vertical beam separation at IPs with two-step vertical elevation for zeroing the vertical dispersion in IPs. The ring parameters are listed in Table 1.

Important to note, that a relative smoothness of the optics resulted in a 3.5 times difference between the heating of all degrees of freedom and the temperature exchange time between different planes ($\tau_{exchange} \approx 380$ s).
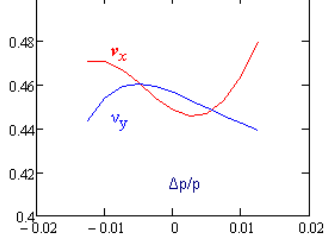
Figure 2: Tune dependence on the momentum offset.
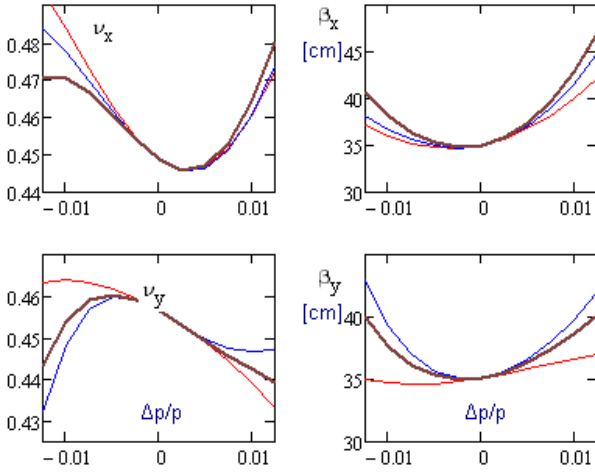
Figure 3: Dependence of the tune and β^* on $\Delta p/p$ with different sextupoles strength.

A chromaticity correction includes 4 families of sextupoles (2 focusing and 2 defocusing ones). It allows one to correct both the tune chromaticity and the beta-function chromaticity excited by IP quadrupoles. Sextupoles of each family are located with 180° betatron phase advances for their nonlinearity compensation. The dependence of the collider tune on $\Delta p/p$ is shown in Fig. 2. It is very nonlinear due to large β^* which excites large tune and β-function chromaticity. The natural chromaticity of the ring are: $\xi_x = -27.1$, $\xi_y = -23.2$ ($\Delta\xi_{x,y} \sim -17$ from two IPs). Corrected chromaticities are: $\xi_x = -1.54$, $\xi_y = -1.50$. The sextupole strength is ~0.35 kG/cm². A non-linear dependence of tunes and β-functions on $\Delta p/p$ and the optics smoothness requirement do not allow the perfect chromaticity correction. However sextupole settings making reasonably good compensation were found (see Fig. 3). That allowed us to avoid adding octupoles. Note also that the nonlinearity of tunes is actually profitable. It allows us to have large tune chromaticity required for transverse instabilities suppression with moderate tune variation across the momentum aperture.

The stochastic cooling system is assumed to be used in the collider. The slip-factor was chosen for optimal cooling at 4.5 GeV/n. The cooling time is ~200 s which is significantly smaller than the IBS heating time. The slip factor is increasing fast with beam energy decrease. For fixed momentum spread and bunch length it would result in an unacceptably high RF voltage. However, the beam thermal equilibrium yields a momentum spread decrease with energy decrease as the beam emittance is determined by the ring acceptance and stays constant. That results in that the maximum RF voltage of 0.9 MV is achieved at 2.5 GeV/n. This is only 2 times larger than at 4.5 GeV/n – the energy where optics was optimized.

FODO-cell based racetrack with changeable γ_{tr}

To meet the NICA requirements of operation with Au-ions in range 1÷4.5 GeV/u and with proton 6÷13 Ge lattice with changeable transition energy is considered. Such lattice has to be capable to operate with the minimum IBS heating for Au-ions, to provide increased transition energy for operation with protons [4] and ensure slippage factor in a range 0.01÷0.05 for acceptable RF-voltage and efficient stochastic cooling.

Table 2: Main Parameters of optics with changeable γ_{tr}

Energy of the experiment	Ion-ion and ion-proton collisions			Polarized protons
	1.5 GeV/n	3.5 GeV/u	4.5 GeV/u	5÷12 GeV
Ring circumference, m	534.2			
Transition energy, γ_{tr}	3.2	5.8	7.6	68
Phase advance per cell, °	30	60	90	varied
Slippage factor, η_ω	0.051	0.015	0.013	0.004
Betatron tune Q_x/Q_y	8.44/ 7.44	10.44/ 10.44	12.44/ 12.44	12.44/ 12.44
Number of bunches, n_{bunch}	26			
Total chromaticity of the ring(before correction) ξ_x/ξ_y	-28.8/ -27.5	-29.6/ -32.4	-38.3/ -36.6	-37.2/ -33.5
Ring acceptance, π·mm·mrad	200/ 300	200/ 200	40/40	40/70
Ring long. acceptance, $\Delta p/p$	±0.005			±0.005
Maximum acceptable RMS emittance, $\varepsilon_x/\varepsilon_y$ π·mm·mrad	1.1/0.5	1.1/0.6	1.2/ 0.6	1.1/0.6
RMS momentum spread	$0.6\cdot10^{-3}$	$1.3\cdot10^{-3}$	$1.7\cdot10^{-3}$	$1.2\cdot10^{-3}$
Particle per bunch corresponding to tune shift $(\Delta Q + \xi) = 0.05$	$0.4\cdot10^9$	$2.5\cdot10^9$	$4.9\cdot10^9$	$2.5\cdot10^{11}$
β^*, cm	35			35
Bunch length, cm	60	60	60	60
IBS growth time, s	110	600	710	8700
Maximum achievable luminosity, cm⁻² s⁻¹	$1.8\cdot10^{25}$	$2.0\cdot10^{27}$	$4.2\cdot10^{27}$	$4.2\cdot10^{31}$

The ring optics (Table 2) is optimized for operation with Au^{79+} ions at the energy of 4.5 GeV/u. Increasing of $_{tr}$ was carried out by adjusting gradients in structural lenses [4]. Decrease of $_{tr}$ was fulfilled by decrease of the phase advance in each FODO-cell in the arcs.

Optics structure of the ring for different regimes of operation is presented in Fig. 4.
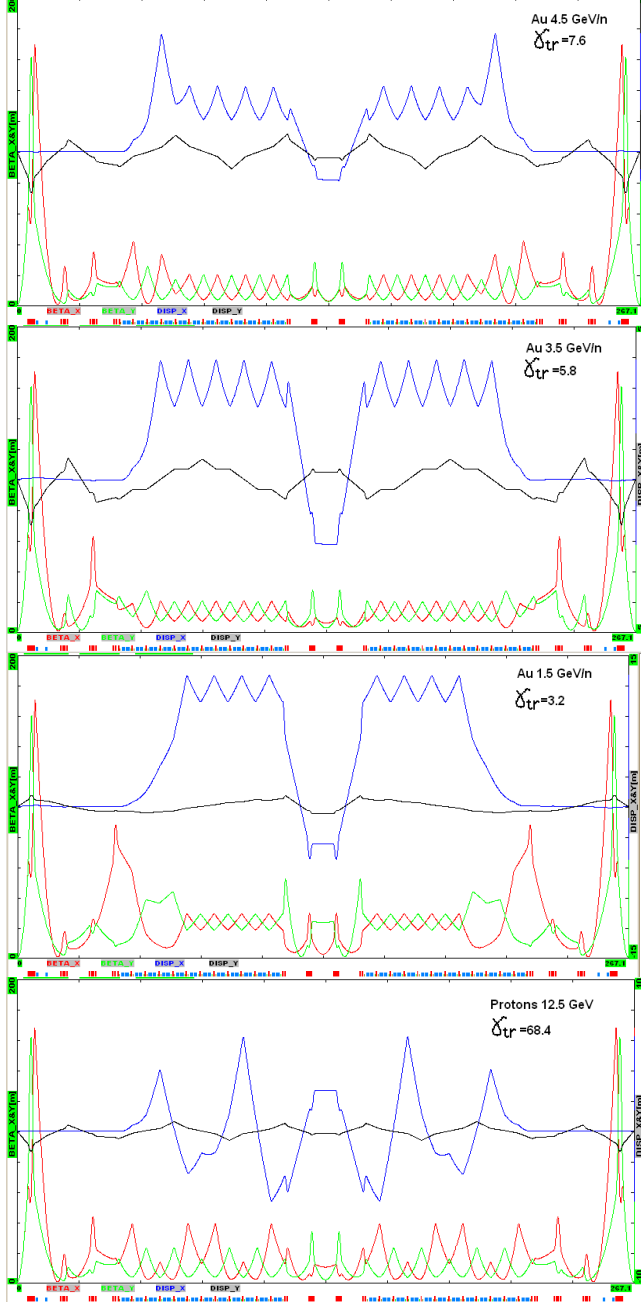
Figure 4: β-function & dispersions for half of the ring.

The horizontal dispersion suppression was provided by adjusting of focusing gradients in cells near the entrance to the straight section. Such a choice allows tuning of the suppressor at different lattice options when phase advance per cell is changed.

In the proton mode the number of cells in one superperiod N_{cell} and the number of superperiods S_{arc} per

arc are dictated by the required betatron phase advance in the horizontal plane. Horizontal betatron phase advance in the arc v_{arc} is close to the number of superperiods S_{arc} as possible keeping them both being integers. This means that the phase advance in one superperiod should be $2\pi v_{arc}/S_{arc}$, and the phase advance of radial oscillations between the cells located in different superperiods and separated by $S_{arc}/2$ superperiods is $2\pi \cdot \dfrac{v_{arc}}{S_{arc}} \cdot \dfrac{S_{arc}}{2} = 2\pi \cdot \dfrac{v_{arc}}{2} = \pi + 2\pi n$. It corresponds to the condition of first-order compensation for the nonlinear effects of sextupoles in the arcs. Considering all implications arc consist from 12 FODO cells. They are grouped into 4 superperiods by gradient modulation in the case of proton mode and remain a regular periodic structure (no modulation) for Au-ions (see fig.4). A transition from one option to another is done by gradient change in two focusing quadrupole families in the arcs and then by optics match to the straight sections.

The horizontal dispersion suppression was provided by adjusting of focusing gradients in cells near the entrance to the straight section. Such a choice allows tuning of the suppressor at different lattice options when phase advance per cell is changed. In the proton mode the dispersion in the straight sections is suppressed due to the 2π integer betatron phase advance in the arc.

Straight sections were designed to provide β*~35 cm, to bring minimum chromaticity into the ring, to ensure total ring tune adjustment, and to have space for non-structural equipment positioning.

Nevertheless due to two IP the NICA has sufficiently high normalised chromaticity value $\xi_{x,y}/v_{x,y} \sim 3.5$, and use of quite strong sextupole magnets for chromaticity correction sharply restricts the dynamic aperture (see Table 2). The ring tunes have non-linear dependence on $\Delta p/p$ especially for Au 1.5 GeV/n and Protons options. Thus, may be, adding of the octupoles is needed. However in the region of momentum acceptance $\Delta p/p$ ±0.005 the tunes have acceptable values to avoid crossing of dangerous resonances (especially half-integer).

REFERENCES

[1] G. Trubnikov et al., "Project of the Nuclotron-based Ion Collider fAcility (NICA) at JINR, Proceedings of RuPAC 2008, Zvenigorod, Russia.

[2] S. Nagaitsev, "Intrabeam scattering formulas for fast numerical evaluations", Physical Review Special Topics – Accelerators and Beams, 8, 064403, (2005) and V. Lebedev, OptiM - Computer code for linear and non-linear optics calculations, 2009.

[3] V. Lebedev, "NICA: Conceptual proposal for collider", MAC2010, January, 2010.

[4] Yu. Senichev and A. Chechenin, Theory of "Resonant" Lattices for Synchrotrons with Negative Momentum Compaction Factor, Journal of Experimental and Theoretical Physics, December 2007, vol. 105, No. 5, pp. 1127–1137.

01 Circular Colliders

MUON COLLIDER DESIGN STATUS*

Y. Alexahin, FNAL, Batavia, IL 60510, U.S.A.

Abstract

Muon Collider (MC) - proposed by G.I. Budker and A.N. Skrinsky a few decades ago [1, 2] - is now considered as the most exciting option for the energy frontier machine in the post-LHC era. A national Muon Accelerator Program (MAP) is being formed in the USA with the ultimate goal of building a MC at the Fermilab site with c.o.m. energy in the range 1.5-3 TeV and luminosity of ~1-5·10³⁴ cm⁻²s⁻¹. As the first step on the way to MC it envisages construction of a Neutrino Factory (NF) for high-precision neutrino experiments. The baseline scheme of the NF-MC complex is presented and possible options for its main components are discussed.

INTRODUCTION

As was already clear in 60s [1, 2] muons provide an intriguing alternative to electrons and positrons in TeV energy range: due to practical absence of synchrotron radiation the collider ring can be very compact fitting on existing laboratory sites, the collision energy spread is significantly smaller due to negligible beamstrahlung and can be made as small as a few units by 10^{-4} by applying a monochromatization scheme. Another obvious advantage is by $(m_\mu/m_e)^2$ times larger s-channel cross-section which makes muon collider potentially a more effective tool in search for scalar particles, such as the Higgs boson.

However, short lifetime of muons – 2.2 μsec in the rest frame – makes a muon collider very challenging technologically. In his talk at Morges seminar in 1971 [2] A.N.Skrinsky briefly outlined four major requirements to render such a machine feasible: high-intensity proton driver, efficient muon production and collection scheme (so-called front-end), ionization cooling channel and, finally, fast acceleration of muons.

In a later paper [3] devoted to various cooling techniques (including the ionization cooling) it was proposed to use cooled muon beams also as the source of neutrino beams for high-precision neutrino experiments – a concept which became later known as the Neutrino Factory. The modern look at physics possibilities at a NF and MC is presented in [4].

Since mid-90s there has been some theoretical and experimental effort in the framework of international Neutrino Factory and Muon Collider Collaboration (NFMCC) which lead to successful completion of MERIT experiment at CERN on pion production in Hg jet target [5] and launching of the Muon Ionization Cooling Experiment (MICE) now under construction at RAL [6].

A significant technological progress which was achieved during the past decade and better understanding of the underlying accelerator physics made the muon collider idea look more realistic and resulted in formation of a national Muon Accelerator Program (MAP) [7] on the basis of the American part of NFMCC and the Fermilab Muon Collider Task Force created in 2006. The goal of MAP is to provide by 2015 a Design Feasibility Study Report (DFSR) which would lay the groundwork for a full-scale project aimed at the MC construction at the Fermilab site in 2020s.
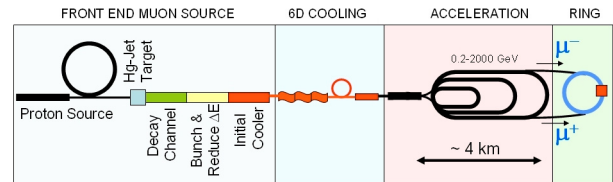
Figure 1: Schematic view of the Muon Collider complex.

GENERAL SCHEME

A simplified scheme of a Muon Collider is shown in Fig. 1. The high-power proton beam for pion production will be provided by a chain of accelerators including those to be constructed under the Fermilab Project-X [8]. A 3 GeV 1mA CW beam from Project-X accelerators will be accumulated and re-bunched in a ring for further acceleration to 8 GeV in a pulsed linac or even up to 21 GeV if a Rapid Cycling Synchrotron option will be adopted. A possibility is also considered to accelerate the proton beam in the Main Injector up to 60 GeV to substantially reduce the required number of protons per bunch.

The accelerated proton beam should then be longitudinally compressed in another ring to be finally delivered to the pion production target with the repetition rate of the complex (10-15Hz). The pions are confined transversely by strong longitudinal magnetic field (20T at the target) lowering to 1.5-2 T in the decay channel.
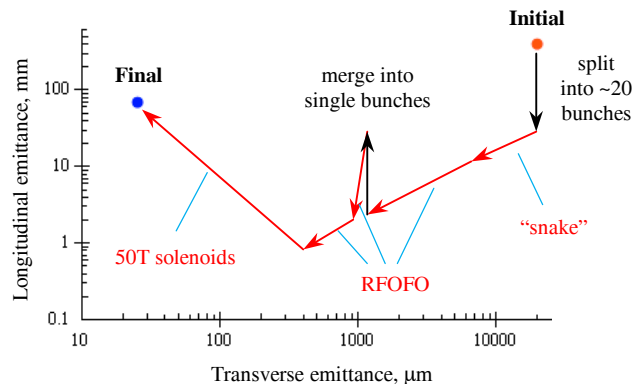
Figure 2: Evolution of muon beam emittance.

01 Circular Colliders

Table 1: Baseline MC parameters

Parameter	Unit	Value
Beam energy	TeV	0.75
Average luminosity / IP	$10^{34}\text{cm}^{-2}\text{s}^{-1}$	1.25
Number of IPs, N_{IP}	-	2
Circumference, C	km	2.5
β^*	cm	1
Momentum compaction, α_p	10^{-5}	-1.5
Normalized emittance, $\varepsilon_\perp$	$\pi\cdot$mm$\cdot$mrad	25
Momentum spread	%	0.1
Bunch length, σ_s	cm	1
Number of muons / bunch	10^{12}	2
Beam-beam parameter / IP	-	0.09
RF voltage at 800 MHz	MV	16
Synchrotron tune	-	0.0006
Repetition rate	Hz	15
P-driver power	MW	4

Muons produced by decaying pions are bunched in RF field with varying in time phase velocity (see next section) and then the energy of the bunches is equalised in RF rotator. The normalised r.m.s. emittance of muons captured in a bunch is ~2cm in all planes.

To cool the muons a number of steps is envisaged, the emittance evolution being plotted in Fig. 2. Both μ+ and μ- are first cooled together in a "FOFO snake" [9], then the two signs are separated and cooled individually in either "Guggenheim" RFOFO channels [10] or Helical Cooling Channels (HCC) [11] until their emittance is small enough to allow for longitudinal merging of 12-15 most populated bunches in each beam into just one bunch per beam.

After the merge 6D cooling continues until the normalised emittances reach $\varepsilon_\perp \approx 0.4$ mm, $\varepsilon_\parallel \approx 1$ mm. The final stage provides only transverse cooling while the longitudinal emittance is allowed to grow, the final values being $\varepsilon_\perp \approx 25$ μm, $\varepsilon_\parallel \approx 7$ cm.

With such longitudinal emittance, momentum spread $\sigma_p / p \approx 3\%$ and $p \approx 40$ MeV/c the bunch length will be ~ 6m so that the initial acceleration will be carried out by induction linac. After that the NF accelerating system will be used which consists of a 201 MHz linac, two RLAs and FFAG (Fig. 3). Acceleration to the final energy will be performed by a tandem of Rapid Cycling Synchrotrons (RCS).

The baseline parameters of the 1.5 TeV c.o.m. energy MC are given in Table 1.

Neutrino Factory

The Neutrino Factory will share the p-driver and front end with the MC. The main difference is in the packaging

of protons: they will be delivered at the target in groups by 3 bunches with 50 Hz reprate. With the same average beam power the number of protons per bunch will be 10 times smaller.
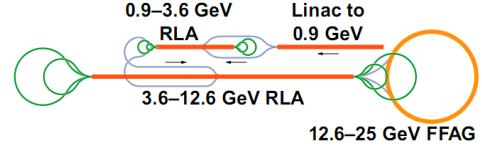
Figure 3. Layout of NF accelerators.

Another possible difference is employing of a straight FOFO channel instead of a snake: the NF does not need small longitudinal emittance so that only transverse cooling can be implemented but with acceleration of muons above 300 MeV to avoid excessive longitudinal heating.

MAIN SYSTEMS

Front End
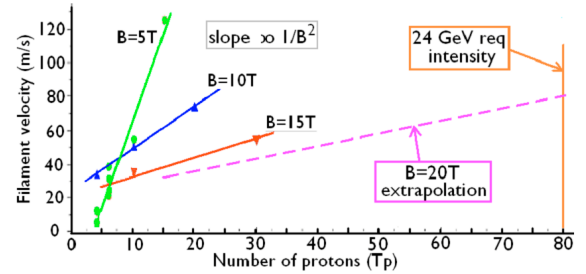
Figure 4: Observed Hg splash velocities at indicated magnetic field and their extrapolation to 20 T [12].

The use of a Hg jet as pion production target was successfully demonstrated in MERIT experiment [5]. The main issue to study was the jet explosion due to heat deposition by powerful proton beam. Fig. 4 shows the observed filament velocities vs. 24 GeV proton beam intensity and magnetic field. Projection of the measured data to 20T shows that at required proton intensities the mercury splash will be sufficiently suppressed [12].

The p-beam power which a mercury jet target can accept is estimated as 8 MW – twice the required value. There is a problem however with evacuation of energy deposited by spallation particles downstream of the target.
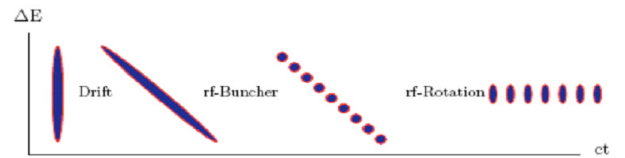
Figure 5: Muon capture in a bunch train.

In the decay channel a correlation between momentum and longitudinal position of muons is developed which is used to capture muons in wide momentum range 100-600

01 Circular Colliders

MeV/c [13]. The idea is illustrated by Fig. 5. RF bunching and then energy rotation is achieved with the help of RF cavities of 30 different frequencies ranging from 360 MHz at the start of the buncher to 201.25 MHz at the end of the rotator. μ+ and μ- bunches are interleaved with 180° separation in RF phase.

6D Ionization Cooling Channel

The major obstacle in application of ionization cooling is rapid falloff of ionization losses with particle energy leading to longitudinal heating. There are three systems under considerations with different mechanisms of the longitudinal cooling restoration.
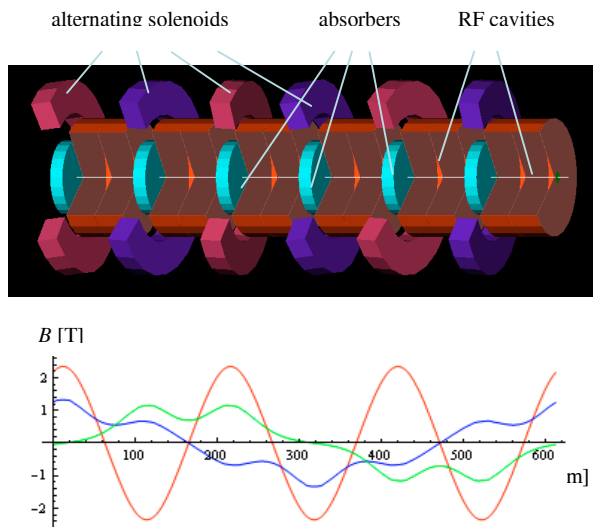
Figure 6: FOFO snake layout and magnetic field.

FOFO snake

The first scheme – "FOFO snake" – employs dispersion in trajectory slope through a flat absorber for muons with different momenta [9]. To produce the dispersion a rotating dipole field is generated by periodically inclining the solenoids. The schematic view of one period of the channel and the magnetic field distribution along the axis are shown in Fig. 6.

Since the FOFO snake is a linear channel with flat absorbers it can cool both μ+ and μ- simultaneously. However, the amount of cooling which can be obtained in this channel is limited by relatively high beta-function value at the absorbers: 0.75 m with current design. The emittances at the snake exit – $\varepsilon_\perp \approx 6$ mm, $\varepsilon_\parallel \approx 10$ mm – are small enough to allow for charge separation without significant losses for subsequent cooling in RFOFO or HCC channels.

Guggenheim RFOFO

The RFOFO (reversed FOFO) channel utilizes wedge absorbers and dispersion rather than its derivative which is created by bending the channel into a ring or a helix ("Guggenheim" RFOFO) [10]. The side view of three RFOFO cells is shown in Fig. 7. Like in the FOFO snake the solenoids have alternating polarity but owing to the unequal spacing between them the beta-function has deep

minima at the absorbers – 0.4 m in the 201 MHz section – allowing to achieve smaller emittances.
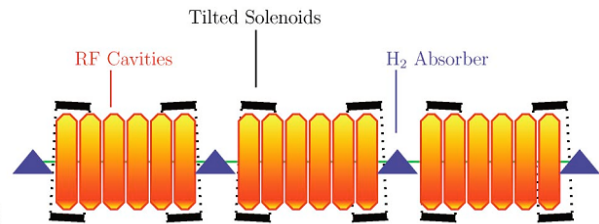
Figure 7: Schematic view of three RFOFO cells.
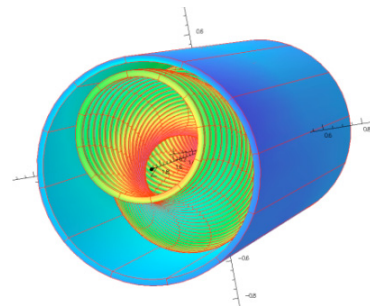
Figure 8: HCC solenoids.

Helical Cooling Channel

The main issue with the RFOFO channel – and to lesser extent with the FOFO snake – is possible RF breakdown in strong magnetic field.

This difficulty is practically eliminated in the Helical Cooling Channel [11] which uses high-pressure H_2 gas filling throughout the channel as the absorber. HCC employs yet another mechanism of longitudinal cooling: large positive momentum compaction of helical orbits created by the superposition of constant longitudinal and rotating dipole fields. The right ratio of field components is obtained by using two solenoids: a helical inner solenoid and straight outer counter-solenoid (Fig. 8).

Theoretically, the existence of a continuous group of symmetry (translation + twist) makes the HCC resonance-free promising excellent dynamic properties. However, its practical implementation is quite cumbersome since the RF cavities have to be placed inside two solenoids. Another unresolved issue with HCC is RF loading with plasmas created by passing beam.
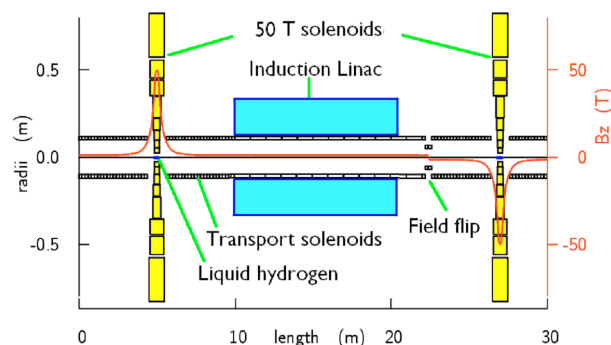
Figure 9: Concept of the 50 T solenoid chanel

Final Cooling

To attain the required final transverse emittance, $\varepsilon_\perp \approx 25$ μm, much stronger focusing is required than can be achieved in the 6D cooling lattices. It can be obtained using high-field solenoids [12]. Progress with high temperature superconductors makes feasible magnetic fields as high as 40-50 T.

Figure 9 shows schematically a piece of such channel including two solenoids of opposite polarity. Energy lost in hydrogen absorber inside the first solenoid is replenished by induction linac which – by virtue of special waveform – also rotates the phase of the bunch so as to keep the momentum spread at minimum. The total of 13 solenoids are necessary if μ+ and μ- can be cooled in the same channel which would require the induction linac operate in bipolar regime.

Other possibilities for the final cooling are also considered including a channel with Li lenses and the so-called Parametric resonance Ionization Cooling (PIC). However, technological limitations of Li lenses and difficulties with correction of chromatic and spherical aberrations in PIC channel make them less attractive candidates than the high-field solenoids.
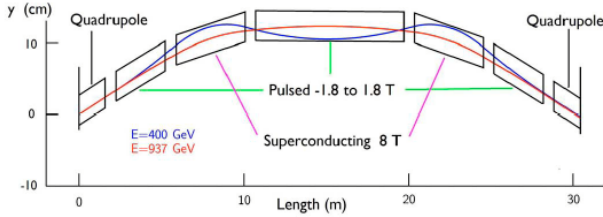
Figure 10 (color): Closed orbit through the RCS half-cell at low energy (blue) and final energy (red).

Table 2: Muon transmission for various steps.

Step	Transmission	Cumulative
Best 12 bunches	0.7	0.7
Charge separation	0.9	0.63
6D cooling before merge	0.47	0.3
Merge	0.88	0.26
6D cooling after merge	0.48	0.12
Final cooling	0.65	0.08
Acceleration	0.7	0.057

Acceleration

After induction linacs at the very early stage of acceleration the MC will use the NF accelerator chain depicted in Fig. 3. For the subsequent acceleration to final energy it is planned to use Rapid Cycling Synchrotrons to maximize the number of passes through RF cavities.

To make the RCS compact and fast it is proposed to use combination of fixed-field superconducting magnets and warm AC magnets with yokes of grain-oriented silicon steel [14]. A half-cell layout is shown in Fig. 10. The

01 Circular Colliders

University of Mississippi is building 400 Hz 1.8 T prototype magnets with tests scheduled for 2011-2012.

A RLA is also being designed (as shown in Fig. 1), but it is significantly more costly and therefore considered only as a fallback solution.

The expected efficiency of all stages of muon beam manipulations is presented in Table 2. For the front end yield of 0.2μ per 8 GeV proton the required p-driver power is 3.4 MW, so there is a good margin.
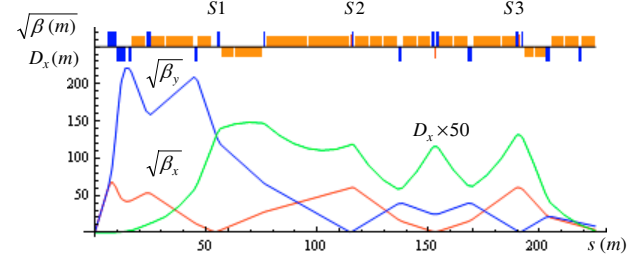
Figure 11 (color): IR layout and optics functions.

Collider Ring

To obtain large momentum acceptance for very small β^* a new scheme for IR chromaticity correction – called a three-sextupole scheme – was developed [15]. It includes strong dipoles in the close vicinity of IP (Fig. 11 orange boxes) to generate dispersion and at the same time to sweep decay electrons away from the detector. The design is based on the existing Nb3Sn magnet technology. MARS simulations show tolerable levels of energy deposition in magnets and detector backgrounds [16].

REFERENCES

[1] G.I. Budker, *in* Proc. VII Intern. Conf. on High Energy Accelerators, Yerevan, 1969, v.I, pp.33-39

[2] A.N. Skrinsky, talk at 1971 Morges seminar published in AIP Conf. Proc. 352, 6, (1996)

[3] A.N. Skrinsky, V.V. Parchomchuk, Sov. J. Part. Nucl. 12 (1981) 223

[4] S. Geer, Ann. Rev. Nucl. Part. Sci. 59 (2009) 347

[5] K.T. McDonald, H.G. Kirk, H. Park *et al.* PAC09, Vancouver, 2009, TU4GRI03.

[6] See http://mice.iit.edu and references therein.

[7] http://map.fnal.gov

[8] http://projectx.fnal.gov

[9] Y. Alexahin, AIP Conf. Proc. 1222, 313 (2009)

[10] R. Palmer *et al.*, Proc. Science PoS (Nufact08) 019.

[11] Y. Derbenev and R. P. Johnson, PRSTAB 8, 041002 (2005).

[12] R. Palmer, PAC09, Vancouver, 2009, TU1GRI03

[13] D. Neuffer, C. Yoshikawa, ibid, TU1GRC05

[14] D. Summers *et al.*, *in* Proc. 2007 Particle Accelerator Conf., Albuquerque, 2007, p. 3178.

[15] Y. Alexahin, E. Gianfelice-Wendt and A. Netepenko, IPAC10, Kyoto, 2010, TUPEB021.

[16] Y. Alexahin, V.Y. Alexakhin, E. Gianfelice-Wendt *et al.*, ibid, TUPEB022.

CONCEPTS FOR RASING RF BREAKDOWN THRESHOLD BY USING MULTI-MODED CAVITIES

S.V. Kuzikov[#], M.E. Plotkin, A.A. Vikharev, Institute of Applied Physics, Russian Academy of Sciences, Nizhny Novgorod, 603950, Russia.
J.L. Hirshfield, Omega-P, Inc., New Haven, CT 06510, U.S.A.
S.Yu. Kazakov, Fermi National Accelerator Laboratory, Batavia, 60510 IL, U.S.A.
Y. Jiang , Yale University, New Haven, 06520 CT, U.S.A.

Abstract

Multi-mode accelerating structures aimed at increasing accelerating gradient are described. Such structures operating in several resonant, equidistantly-spaced, axisymmetric, TM-like eigenmodes allow reduction of exposure time to surface fields, reduction of high-field areas and reduction of those fields which are responsible for electron emission. These effects are planned for use in studying the physics of RF breakdown phenomenon with the goal of designing new high-gradient accelerating structures.

ACCELERATION IN A STRUCTURE OF MULTI-FREQUENCY CAVITIES

Because rf breakdown is a strong limiting factor towards increase acceleration gradient, one needs first of all to prevent the initiation of breakdown. To follow this aim, let us consider a particle beam to be accelerated as a periodic sequence of tight bunches that move along a straight path with a velocity close to the speed of light. High accelerating fields need exist only during the narrow time intervals when test bunches traverse the cavities that comprise the accelerator structure. During time intervals between bunches, fields in each cavity should preferably be as small as possible. In each cavity, fields localized in space should periodically move between the structure axis when a bunch to be accelerated arrives, and at other times to move away from the axis and generally weaken (Fig. 1a) [1]. This principle automatically requires that cavity should contain equidistant spectrum of modes. The ideal electric field seen by bunches along the structure is sketched in Fig. 1b (curve 1—in green), in comparison with field behaviour in a single-frequency structure (curve 2—in red). In the case of a limited number of modes the resulted field would look like that in curve 3—in blue. It is widely accepted that thresholds increase for rf breakdown and thermal fatigue, as one decreases the exposure time to intense rf. It is thus natural to anticipate that a cavity in which the peak fields are present only during transit of the bunches - rather than during a substantial fraction of the interbunch period - should be capable of sustaining higher peak. An acceleration structure based on these main principles can be built either as a sequence of rectangular copper cavities driven in two-beam scheme [2-3], or as a sequence of axisymmetric cavities operated with alternating drive and accelerated bunches [4, 6].

[#]kuzikov@appl.sci-nnov.ru

a)

b)
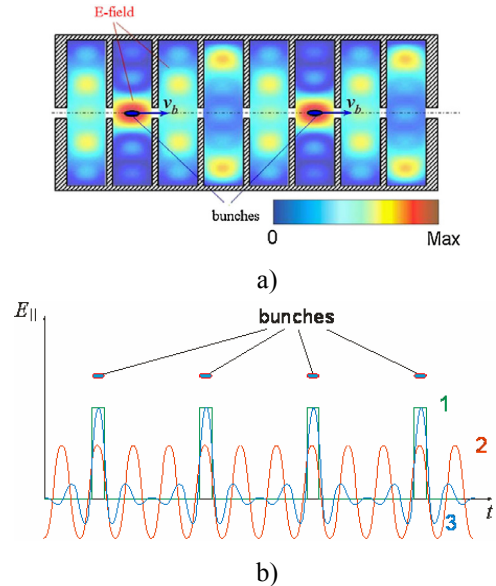
Figure 1: Principles of acceleration of moving periodic bunches in multi-mode structure. a - accelerating structure scheme, b - time dependence of fields: in ideal multi-mode structure (curve 1 in green), in single-frequency structures (curve 2 in red), in a multi-mode structure operating in a limited number of modes (curve 3 in blue).

CRITERIA OF RF BREAKDOWN TRIGGERING

RF breakdown is a complicated, multi-stage phenomenon, which can be viewed as a continuous sequence of several stages. A modern theory is based on priority of electron field emission, describing how RF electric field produces electrons to tunnel from metal, surface heating causes growth of the protrusions and surface material evaporation [7-8]. Experimental data obtained for many accelerating structures show that the breakdown probability I is dependent on electric field threshold E and also on exposure time τ by the scaling law [8]:

$$I \sim E^6 \cdot \tau. \qquad (1)$$

Second, new experimental results obtained recently show that breakdown probability may depend by the rf magnetic field, i.e. by the surface temperature rise [9-10]. The model underlying (1) does not explain why magnetic

field plays a role. That stimulates attempts to develop a breakdown theory and to modify the scaling law (1). In particular, a so-called modified Poynting vector [8], pulse heating temperature rise, and the stored rf energy in an accelerating structure are considered to formulate criteria of breakdown initiation [8-9]. The mentioned criteria are based on squared field values: E^2, H^2, or $E \times H$. In a multi-mode structure in comparison with a single mode structure of the same acceleration gradient (accelerating field is constituted only by phase synchronous modes) all these values are by factor N smaller, where N is the number of modes; i.e. breakdown threshold is higher in multi-mode case. An absolutely alternative criterion is based principally on nanoclusters evaporation, rather than electron field emission [10]. From this point the disscissing in this paper "anode-cathode" effect could be used to test the validity of this criterion experimentally, and perhaps to increase acceleration gradient.

EFFECTS TO INCREASE ACCELERATING GRADIENT

The initial idea to apply multi-mode cavities was based on *exposure time reduction effect*. Further studies of multi-mode structures resulted in understanding that there are at least two complementary effects: *high-field area reduction* and so-called *"anode-cathode" effect*.

In order to compare the exposure time in a multi-mode accelerating cavity with that in a single-mode accelerating cavity we analysed time dependencies of fields in both mentioned cases [6]. As a result we obtained a ratio of the exposure time for the multi-mode structure and single mode accelerating structure:

$$\Delta\tau_s/\Delta\tau_m = \sqrt{\sum_{n=0}^{n=N-1}(\omega_0 + n\cdot\Delta\omega)^2} \Big/ \omega_0\cdot\sqrt{N}, \quad (2)$$

where N- is a number of modes, ω_0 is the frequency of the lowest (fundamental) mode, $\Delta\omega$ is a frequency distance between modes, and n is a positive integer. In (2) it was also assumed that in a multi-mode cavity and in a single mode cavity we have the same field maximum. In concordance with the scaling law (1) we see that we can increase the accelerating field in comparison with the single-mode structure by a factor $E^*/E = \sqrt[6]{\Delta\tau_s/\Delta\tau_m}$ without increasing of the breakdown probability. In the two-mode case with modes at ω_0 and $3\omega_0$ we find $E^*/E=1.14$, while in the three-mode case (ω_0, $3\omega_0$ and $5\omega_0$) we find $E^*/E=1.23$.

Modern theory considers initiation of rf breakdown as a random process. That is why the frequently used and experimentally-proven scaling law (1) should also depend upon the number of initiation centres, which is proportional to the area of cavity surface exposed to high fields. In the modified form we should just multiply

probability of the breakdown I in (1) by S, where S is an area which is being exposed to high enough fields. As seen in Fig. 1a in multi-mode case the effective exposed area is much less than in single-mode case. Results of rigorous numerical analysis are that the ratio of the breakdown probabilities for the three-mode case and the single mode case is about 1/25 [6]. This provides the field enhancement factor $E^*/E=1.70$ calculated in accordance with the modified scaling law.
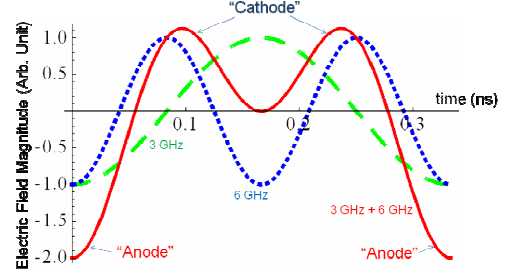
Figure 2: Time-dependence for a composite field (red-solid) excited at 3 (green-dashed) and 6 GHz (blue-dotted) with equal amplitudes and zero phase difference. Negative anode-like fields have twice the magnitude of positive cathode-like fields.

In an arbitrary single mode cavity, the rf field oscillates symmetrically between positive and negative maxima. In a multi-mode cavity, the situation could be strongly asymmetrical. As shown in Fig. 2, two harmonically related modes (at 3 GHz and 6 GHz, for example) excited in a cavity are able to produce a cathode-like field which is almost two times smaller than the maximum anode-like field. This property of a multi-mode cavity might be used to increase acceleration gradient. Since cathode phenomena such as electron emission and positive ion sputtering probably initiate breakdown, a cavity like in that in Fig. 3 with modes having non-equal fields on the left and on the right walls might be able to increase accelerating gradient. In this cavity the field on the right wall has maximum $+2E_0$. This value $+2E_0$ is actually an anode-like field, the cathode-like field on the right wall is approximately two times less i.e. $-E_0$, where E_0 is a breakdown threshold value in this case. The field on the left wall at all times has its maximum to be less than E_0 due to the assumed asymmetrical field structures of the eigenmodes. The cavity shown in Fig. 3 was investigated in detail in [5-6], where the calculated ratio of acceleration gradient to maximum surface field is by a factor of 1.55 higher in the designed multi-mode cavity than in a single mode pillbox cavity.
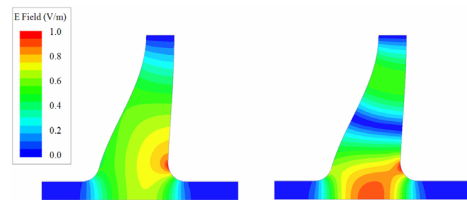
Figure 3: Electric field maps for the 3.0 GHz TM_{010} (left) and 6.0 GHz TM_{020} (right) modes.

03 Linear Colliders, Lepton Accelerators and New Acceleration Techniques

POSSIBLE EXPERIMENTS WITH MULTI-MODE ACCELERATING STRUCTURES

Methodology of experiments naturally assumes comparison of breakdown probabilities in 1-, 2-and 3-mode cavities having the same surface *E*-fields. Two kinds of tests can be discussed, namely cavities powered by a drive beam like CTF3, and cavities powered by more than one phase-locked RF sources.

Preliminary calculations for CTF3 based experiment were carried out for three axisymmetric cavities: 3 GHz (single mode); 3 and 6 GHz (two-mode); 3, 6, and 9 GHz (three-mode). The first design issue, to obtain an equidistant mode spectrum, has been solved by a specific cavity shape. Field maps for the three mode cavity are shown in Fig. 4. In the two-mode cavity the highest mode is detuned, in single-mode cavity both higher modes are out of the resonant excitation condition. Calculations show that the CTF3 bunch parameters allow easily to excite several modes simultaneously and to achieve *E*-field level ~1 MV/cm in each cavity. Plan of the experiment assumes that surface fields in each cavity should be equal to one another. Roughly it is reached by cavity shape design. In order to provide fine tuning of fields, the bunch current could be varied.
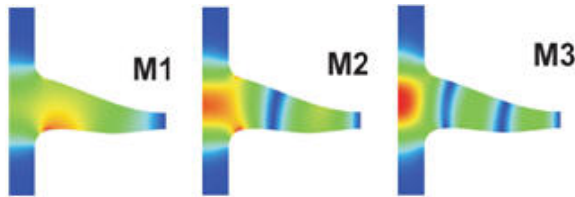
Figure 4: Modes of three-mode cavity: M1 – 3 GHz, M2 – 6 GHz, M3 – 9 GHz.

Experiments with several phase-locked high-power RF sources are attractive due to a possibility to easily vary amplitudes and phases of different modes. Such experiments are ideally acceptable to test anode-cathode effect, where two modes only are enough in order to demonstrate the expected essential increase of acceleration gradient. An asymmetric cavity concept and possible experimental scheme have been already described in [5]. The proposed bimodal cavity has two (3 GHz- and 6 GHz) coupling waveguides. This design (Fig. 5) provides that higher frequency radiation is not leaking through and being transmitted back towards the lower frequency source. A coupling design to accomplish this property uses a high-frequency choke. Loading *Q*-factor ($Q \approx 6 \times 10^3$) is two times less than coupling *Q*-factor for both modes, in order to avoid undesirable reflection. Experimental goals could include obtaining a theoretically-predicted 55% increase of acceleration gradient in comparison with conventional pillbox cavity. It seems also very important that due to a flexibility of this experiment we could (by changing phases of RF sources) to test regimes where either the cathode-like field reaches its absolute maximum or where anode-like field is highest. This should allow an experimental answer

to the critical question: Do cathode or anode phenomena have a leading role in RF breakdown?
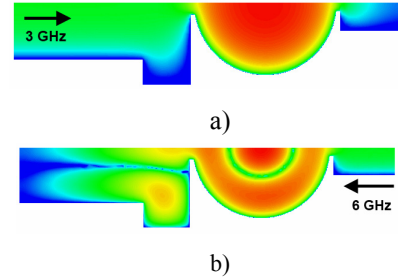
Figure 5: Power coupling into multi-mode cavity from waveguide at the left side at 3 GHz (a) and at right side at 6 GHz (b).

SUMMARY

We have described several means for increasing accelerating gradients in structures consisted of multi-mode cavities; namely time exposure reduction effect, high field area reduction effect, and anode-cathode effect. We have also proposed experiments with the axisymmetric multi-mode cavities, in order to prove the main principles of multi-mode acceleration and to study a nature of rf breakdown.

REFERENCES

[1] S.V. Kuzikov and M. E. Plotkin, Proc. of Joint 32nd International Conference on Infrared and Millimeter Waves, 2007 and the 15th International Conference on Terahertz Electronics, pp. 797–798.

[2] S.Yu. Kazakov, S.V. Kuzikov, V.P. Yakovlev, and J.L. Hirshfield, CP1086, Adv. Accel. Concepts, 13th Workshop, pp. 373-379.

[3] S.V. Kuzikov, S.Yu. Kazakov, J.L. Hirshfield, M.E. Plotkin, A.A. Vikharev, V.P. Yakovlev, 2009 CLIC Workshop.
http://indico.cern.ch/sessionDisplay.py?sessionId=7&sloId=0&confId=45580#2009-10-14

[4] S.V. Kuzikov, S.Yu. Kazakov, Y. Jiang, and J. L. Hirshfield, Phys. Rev. Lett. Vol. 13, No.7, 071303 (2010).

[5] S.V. Kuzikov, S.Yu. Kazakov, Y. Jiang, and J. L. Hirshfield, Phys. Rev. Lett. 104, 214801 (2010).

[6] Y. Jiang, S.Yu. Kazakov, S.V. Kuzikov, and J.L. Hirshfield, Adv. Accel. Concepts, 14th Workshop, 2010. (in print)

[7] A. Descoeudres, T. Ramsvik, S. Calatroni, M. Taborelli, and W. Wuensch. Phys. Rev. ST Accel. Beams 12, 032001 (2009).

[8] A. Grudiev, S. Calatroni, and W. Wuensch. Phys. Rev. ST Accel. Beams 12, 102001 (2009).

[9] V.Dolgashev. 2009 CLIC Workshop, http://indico.cern.ch/contributionDisplay.py?sessionId=7&contribId=138&confId=45580

[10] Z. Insepov, J. H. Norem, and A. Hassanein, Phys. Rev. ST Accel. Beams 7, 122001 (2004).

ACCELERATOR COMPLEX U70 OF IHEP: PRESENT STATUS AND RECENT UPGRADES

S. Ivanov, on behalf of the U70 staff[#]

Institute for High Energy Physics (IHEP), Protvino, Moscow Region, 142281, Russia

Abstract

The report overviews status of the U70, accelerator complex of IHEP-Protvino comprising four machines (2 linear accelerators and 2 synchrotrons). Particular emphasis is put on the recent upgrades implemented since the previous conference RuPAC-2008.

GENERALITIES

Layout and technical specification of the entire Accelerator complex U70 of IHEP-Protvino was specified in the previous status report [1] whose general part remains up-to-date.

On December 30, 2009, the Russian Federal Government issued an executive order enrolling the complex into the national List-Register of Unique Nuclear-Physics Facilities. It constitutes a prerequisite for an awaited revision of a funding scheme to maintain special and general-purpose engineering infrastructure of the IHEP facilities.

Efforts were continued to attain the following goals:

1. to ensure stable operation and high beam availability during the regular machine runs,
2. to improve proton beam quality,
3. to implement a program to accelerate light ions with a charge-to-mass ratio $q/A = 0.4$–0.5, and
4. to put forward a sound long-range option to diversify and develop accelerator and experimental facilities on the IHEP grounds, with a bias towards fixed-target research beyond elementary particle physics.

ROUTINE OPERATION

Since RuPAC-2008, the U70 complex worked for four runs in total. Table 1 lists their calendar data (end of the text). The first run of a year is shorter and solves, mainly, developmental and methodological tasks.

Dedicated machine development (MD) activity is split into two sessions per a run. One takes about a week prior to delivering beam to experimental facilities. Another (2-day long) occurs amidst the fixed-target physics program, under conditions of a smooth sustained operation of the machines thus facilitating R&D on beam physics.

Fig. 1 shows beam availability data during MDs and a fixed-target experimental physics program (XPh) with averages over 2002–10. Run 2009-2 has set a record with experimental facilities acquiring the extracted beam with its availability exceeding 90%.

During the runs, all the beam extraction systems available in the U70 were engaged — fast single-turn, slow 3rd-order resonant, internal targets, and deflectors made of

---

04 Hadron Accelerators

bent silicon crystals. Fig. 2 demonstrates a period of smooth operation of the U70. Fig. 3 presents operation of slow extraction system.
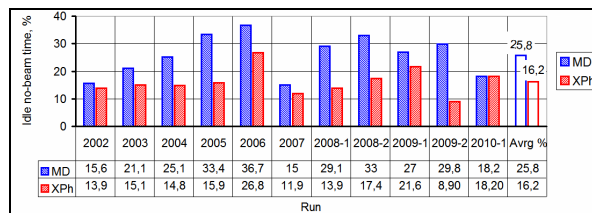
Figure 1: Beam availability statistics.
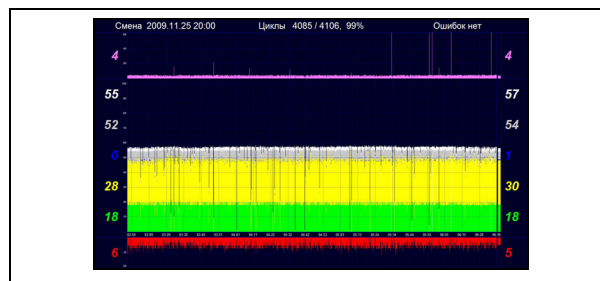
Figure 2: Screenshot of the on-line monitoring over the U70 operation. Time interval (abscissa) extends over 3 hr, or 1000 cycles of acceleration. Yellow trace slows intensity of stochastic extraction, green trace — operation of internal targets. Red (inverted) trace indicates spent beam remains damped onto internal absorber.

MACHINE DEVELOPMENT

This Section reports on recent updates in equipment.

New Septum Magnet SM26

In 2008, a new septum magnet SM26, manufactured at IHEP workshops, was installed in 4.9 m long straight section SS#26 of the U70 lattice, see Fig. 4. It was a step in upgrade of the slow extraction system aimed at enlarging vertical gap for extracted beam from 25 to 35 mm.
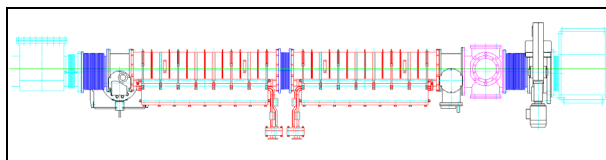
Figure 4: Layout of equipment in SS26 of the U70.

SM26 is sectioned into 2 identical units. Other auxiliary equipment housed in SS#26 (beam diagnostics, vacuum pumps and valves, bellows) was rearranged to a new configuration which also accommodated an universal 3-port docking box (right block in Fig. 4) suitable for inserting diagnostics devices or, say, bent-silicon-crystal deflectors.
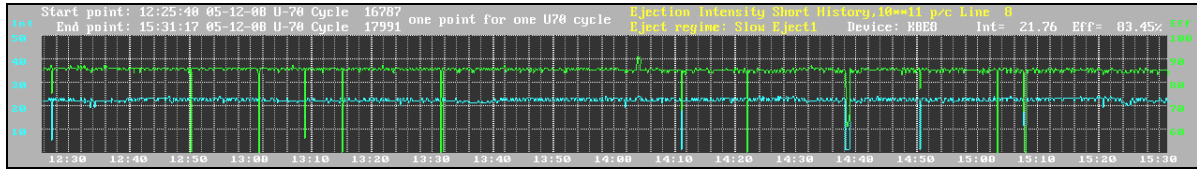
Figure 3: Efficiency factor of slow extraction (90–95%), upper trace. Slowly extracted beam current, lower trace.

Table 1: Four runs of the U70 in between RuPAC-2008 and -2010

Run	2008-2	2009-1	2009-2	2010-1
Launching linac URAL30, booster U1.5 and U70 sequentially	October, 10	March, 10	October, 12	March, 15
Proton beam in the U70 ring since	November, 3	April, 1	November, 5	April, 7
Fixed-target physics program with extracted beams	November, 19 – December, 10, 28 days	April 6–21, 14½ days	November, 12 –December, 9, 25 days	April, 12–22, 10 days
No. of multiple beam users (of which the 1st priority ones)	11 (8)	8 (5)	10 (6)	9 (6)
MD sessions and R&D on beam and accelerator physics, days	9	6 ½	11	7
Light-ion acceleration MD program	December, 10–12, 2 ½ days	April, 21–25, 3 ½ days	December, 11–15, 3 ½ days	April , 24–27, 3 ½ days

Wide-Band Transverse Feedback

It is a fast bunch-by-bunch 1-turn delay feedback employing variable delay line ($\Delta\tau/\tau$ is about –10%) and the "virtual pickup" concept, see Fig. 5. In 2008, the former analogue delay was traded for an up-to-date digital delay clocked at the 16th harmonic of radiofrequency.
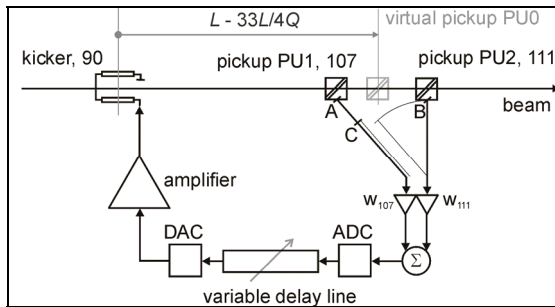
Figure 5: Layout of the wide-band feedback.

A natural byproduct of going to DSP is flexibility in implementation of various feedback algorithms, from linear proportional to nonlinear "bang-bang", sensitive to sign of the beam offset. In practice, an intermediates regime constituting a combination of the two was found most effective with its factor of 50 in shortening decay time of coherent transverse oscillations. Details of the technical solutions adopted by now are reported in [2].

Our intent is to continue efforts in this direction and test a promising one-pickup 3-turn digital delay feedback solution that behaves as a 3-tap periodical notch FIR filter and imposes a purely imaginary coherent tune shift [3].

Intensity of Proton Beam

For the first time in many years, we have run the U70 complex with a high intensity and 29 bunches injected. Here is a summary of beam parameters in the run 2009-1.

Proton synchrotron U70 has achieved operating intensity of 0.7–$1.1\cdot10^{13}$ protons per pulse. Beam top energy is 50 GeV (kinetic). Beam losses over cycle are 2–3%. Bunch length through a cycle is 96 ns (injection) – 17 ns (transition) – 20 ns (extraction). Horizontal beam size is 9–11 mm at 50 GeV. Slow stochastic extraction to beamline #21 to the OKA experimental facility (study of rare kaon decays) yielded 6–$9.5\cdot10^{12}$ protons per a low-ripple 1.4–1.85 s long spill. Booster synchrotron U1.5 has attained top intensity of $5.3\cdot10^{11}$ protons per a (single) bunch under a very reliable operation (relative idle time 6%). Fig. 6 illustrates operation of the U70.

On going to higher beam intensities, mainly, due to uniform orbit filling patterns involved, we have encountered problems with transition crossing. They were tentatively evaded by switching back the 200 MHz spill cavity that dilutes longitudinal phase volume (notice a kink in the peak-current trace of Fig. 6). Still, efforts were and are being spent to better understand transition crossing with compact bunches (high local density) and work out appropriate working point, betatron resonance- and chromaticity-correction scenarios close to γ_t.
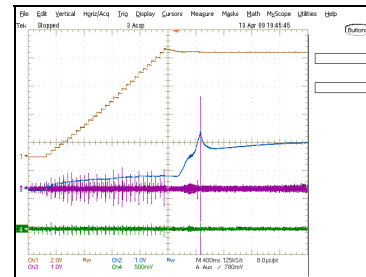
Figure 6: Aaccumulated beam intensity (upper trace, DCCT monitor, 29 bunches) and peak current of beam (second trace). Lower traces show transverse beam offset signals (H/V injection errors).

04 Hadron Accelerators

Slow Stochastic Extraction

Fig. 7 illustrates operation of slow extraction system delivering beam to the OKA experimental facility. It shows both, technological signals acquired in the U70 ring and readouts of front-end counters in the OKA setup proper (courtesy of the OKA team). Distance between these two data acquisition points is around 1 km.
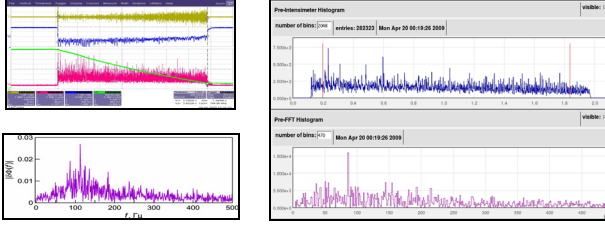
Figure 7: Left, signals from the U70. (1, brown) AM-modulated extraction noise. (2, blue) Feedback signal to modulate noise amplitude. (3, green) Population of waiting beam stack monitored with a DCCT. (4, red) Spill current measured with a BLM in SS#106. (5, purple) Amplitude Fourier spectrum of spill. Right, slowly extracted beam seen at the OKA facility. (1, blue) Spill current. (2, purple) Amplitude Fourier spectrum of spill.

Left-side spill trace (4) in Fig. 7 originates from the beam loss monitor in the ring hall that sees secondary particles emerging due to interception of extracted beam halo by a wire septum of electro-static deflector ESD106. Right-side signal shows intensity of the slowly extracted beam core delivered to the terminal beam consumer.

The data confirms that the U70 now possesses a high-intensity low-ripple long-spill slow extraction system.

Fast Extraction below Flattop

To meet the demand of beam users, we have successfully tested a fast 1-turn extraction of bunches at 50 GeV (B-field 0.8590 T) during a ramp with $dB/dt \neq 0$ and flat-top 1.0331 T corresponding to beam energy 60 GeV.

To this end, new cable traces in the ring hall of the U70 were laid that allowed reshaping horizontal closed-orbit bump near deflecting magnets DM62, 64 from a half- to a full-wavelength (cancellation of electromotive force due to $dB/dt \neq 0$ at bump-coil power supply outlets). Beam trace angle at entry to transfer line has required adjusting with a dipole corrector DCH66 (switched polarity).
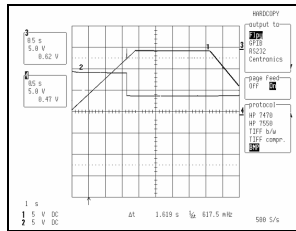
Figure 8: Fast extraction from the U70 during B-field ramp (trace 1). Intensity of circulating bean is shown by trace 2

Fig. 8 shows experimental data. Stability of operation of fast-extraction synchronization (especially, in its up-

dated configuration) and reproducibility of the extracted beam energy was confirmed in runs 2009-1 and 2009-2.

The similar goal — to diversify extracted beams available in a given magnetic cycle of the U70 — was pursued during tests of acceleration with an intermediate plateau of the B-field. The first plateau (flat bottom) at .0.03537 T corresponds to injection energy 1.32 GeV. The second (new) plateau at 0.8590 T accepts 50 GeV beam, while the third plateau (flattop) is at 1.0330 T and 60 GeV.
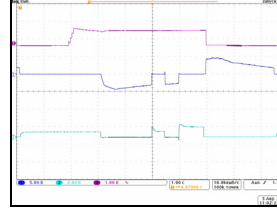
Figure 9: Here and on the right, traces are listed from top to bottom. (1) Beam current (DCCT). (2) Derivative dB/dt, inverted. (3) Feedback signal to stabilize level of plateau.
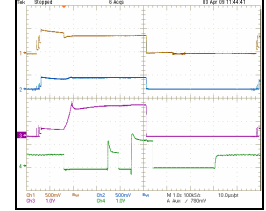
Figure 10: (1) Beam intensity (pickup). (2) Beam current (DCCT). (3) Peak current of bunches. (4) Feedback signal to stabilize level of plateau.

On the one hand, this task constitutes a backup alternative to the on-the-fly fast extraction mentioned above. On the other hand, it set a sound work-pad to Department of Power Engineering Facilities of the U70 to develop and test a new set of tools to control, synchronize and stabilize magnetic cycle, with both 3 and 2 (routine) plateaus.

This regime was safely implemented in the run 2009-1. There were no beam loss observed in course of (a well adiabatic) traversal of the intermediate plateau. Experimental signals acquired from ring magnet supplies and beam monitors are shown in Fig. 9 and 10.

Both the tasks in question related to fast extraction below flattop put forward new options for a more flexible operation of the U70 in the future.

Proton Linear Accelerator URAL30

This machine stands in the start position in the Accelerator complex U70. Its stable operation is crucial to maintain high overall beam availability.
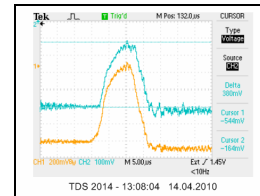
Figure 11: Beam pulse in the URAL30. Pulse current is 25–40 mA.
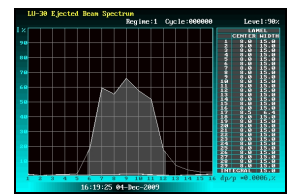
Figure 12: Bunch distribution over momentum at exit from the URAL30.

To maintain stable operation of the proton ion source (duoplasmatron), its vacuum pumping system was renovated. To this end, a pair of new high-tech turbo molecular pumps SHIMADZU 3203LM (speed 3200 l/s (in N_2), 2400 l/s (in H_2)) was mounted. Since then, no failures of

04 Hadron Accelerators

ion source due to vacuum conditions were observed. Reproducibility of bunches has improved, witch can ne noticed, say, as a linear slope of the upper, beam accumulation trace in Fig. 6. Fig. 11, 12 show other beam data.

The upgrade plans foresee renewal of pulsed power supplies in the ion gun, of RF powering scheme of the fist two sections, and installing a commercially available subsystem to stabilize temperature of cooling water.

Digital Master Oscillator

A new DDS master oscillator for the U70 proton synchrotron was developed and tested in the run 2010-1. This activity pursues many goals. These are (in priority order):

1. To attain more flexibility in generating "B-field–radiofrequency" law allowing acceleration of protons and light ions with charge-to-mass ratio about ½.
2. To provide a tool for coordinated variation through cycle of gains in radial and phase-frequency feedback loops around the maser oscillator.
3. To introduce, as a routine, bunch-rotation RF gymnastics prior to de-bunching at flattop for prompt control over momentum spread in circulating beam.
4. To introduce a straightforward procedure of bunch smoothing and lengthening with an off-line digitally synthesized and uploaded phase noise samples of accelerating voltage.

All items of this list were beam-tested successfully. The capabilities of the DDS master oscillator are very promising, though an in-depth study of the newly opened options is yet to be completed. Figs. 13–15 present a few experimental results on the items in question.
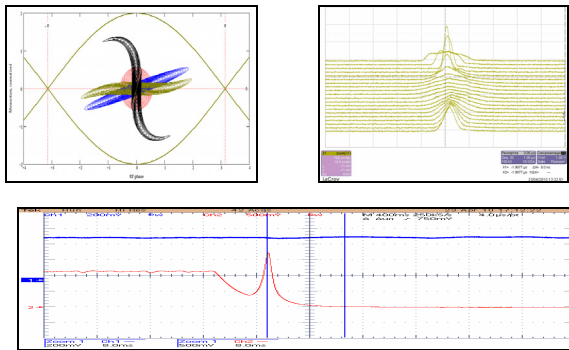
Figure 13: Bunch rotation in the longitudinal phaseplane. Top left – calculation, right– observed "mountain range" display, bottom – peak current of beam. Notice a fast 1.5 ms de-bunching with no symptoms of a spurious re-bunching due to a widened $\pm\Delta p/p_0$.
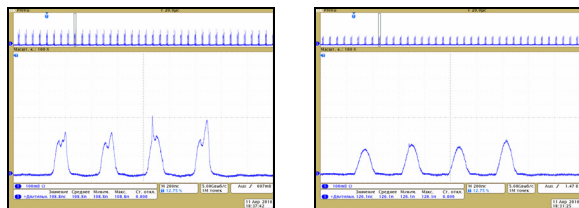
Figure 14: Bunch smoothing and lengthening with external phase noise.
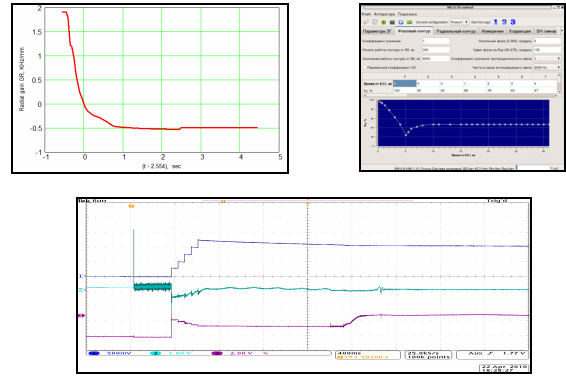
Figure 15: Variable gains in feedback loops. Top left – calculated optimal gain in radial loop for a fixed gain 0.15 kHz/deg in phase-frequency loop, right– its view in a control screen of the DDS MO, sign reversal at transition is implied. Bottom – traces of beam intensity, radial position, and beam phase about RF voltage.

Light-Ion Program

This program proceeds at a steady pace. By the last run 2010-1, deuterons were accelerated to 23.6 GeV per nucleon (kinetic) through a chain of the Γ100, U1.5, and U70 proper. Chronology of the progress is reported in [4].

Crystal Deflectors

These types of beam transverse deflectors are extensively employed for routine technological purposes and in a dedicated R&D program accomplished with beams of the U70. Ref. [5] reports on details of this activity.

AC-IHB

Generalities

This acronym stands for Accelerator Complex of Intense Hadron Beams. It is a multi-purpose mega-project discussed at IHEP now [6]; refer to Fig. 16. The proposal offers a long-range plan to develop accelerator and experimental facilities on the IHEP grounds for fixed-target research, within and beyond elementary particle physics.
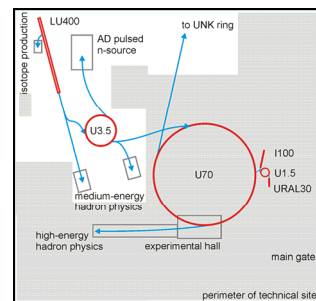
Area of a dense civil engineering and utility infrastructure existing is shadowed. Blue arrows show directions of beam transfer.

Figure 16: Layout of the AC-IHB facility.

The base-line design foresees construction of a pulsed facility having more than 1 MW of proton beam average power, a pulse rate of 25 Hz, pulse width ≤ 1.5 μs, clear staging, site-specific integration and upgrade plans, and a reduced technical risk (use of proven technologies).

04 Hadron Accelerators

The facility comprises a non-SC 400 MeV linear accelerator LU400 followed by a 3.5 GeV rapid cycled proton synchrotron (RC PS) U3.5.

Staging

A particular stage of the project addresses either applied or fundamental science (see Fig. 16).

Stage-1 assumes construction of a short-pulse accelerator-driven 1 MW neutron source for applied research (material and life sciences).

Goal of the next stage-2 is to develop the second direction of fast extraction from the U3.5 to feed a new experimental zone dedicated to intense-beam medium-energy hadron physics.

At a later stage, the U3.5 is engaged as a new injector to the existing U70 PS, or its updated successor. To this end, orbit length and RF harmonic number of the U3.5 amount to 3/10 of those in the U70. It facilitates, at most, a 3-train bunch-to-bucket transfer from U3.5 to the U70 ring thus yielding a beam pattern $3 \times (9$ filled $+ 1$ empty) bunches there. Apart from the lower-energy mode of a 3.5 GeV proton beam stretcher delivering slow spills, the U70 will accelerate intense beam to higher energies.

This staging does not intervene drastically into the present operation of the URAL30(I100)/U1.5/U70 chain. Even more, at stage-0, the existing machines will be beam test benches and pilot consumers of the key project-related technologies (like source of H⁻ ions, RFQ linac, stripping-foil insertion, ferrite-loaded RF cavities, etc).

RC PS U3.5

Core of the AC-IHB project constitutes a new 3.5 GeV rapid cycled proton synchrotron U3.5 ramped at 25 Hz (sinusoidal) and yielding $7.5 \cdot 10^{13}$ ppp. Other specifications of the machine are listed in Table 2.

Table 2: Specifications of U3.5 (project)

Energy (kinetic), E	0.4–3.5	GeV
Orbit length, L	445.11	m
Curvature radius, ρ	15.28	m
Magnetic rigidity, $B\rho$	3.18–14.47	T·m
Compaction factor, α	0.0173	
Transition gamma, γ_t	7.60	
Intensity, N	$7.5 \cdot 10^{13}$	ppp
Ramping time, t_R	0.020	s
Cycle period, T	0.040	s
Average beam current	300	μA
Beam power, P	>1	MW
RF harmonic, h	9	
Radio frequency, f_{RF}	4.322–5.925	MHz
Net RF voltage, V_{RF}	720	kV/turn
Lattice period	FODO(90°)	
No. of periods	36	
No. of super periods	6	
Betatron tune (H/V)	9.15/7.20	

A multi-turn (145 turns around) charge-exchange injection into the RC PS U3.5 is performed at 400 MeV from a new linear accelerator LU400 (H⁻, 40 mA).

Lattice of the U3.5 is based on a synthesis of a plain FODO stricture, "missing dipole" and "quadruple-bent achromat" (QBA) concepts with 6 dispersion-free straights half-the-ring long totally, Fig. 17.

The lattice has 24 dipole magnets (length 4 m, field 0.95 T, and gap 150 mm). There are 72 identical quadrupole lenses (length 0.6 m, gradient < 5.6 T/m, and bore radius 102.8 mm). The quads are arranged into three families (36 QF, 30 QD, and 6 QD1 at arc mid-points).
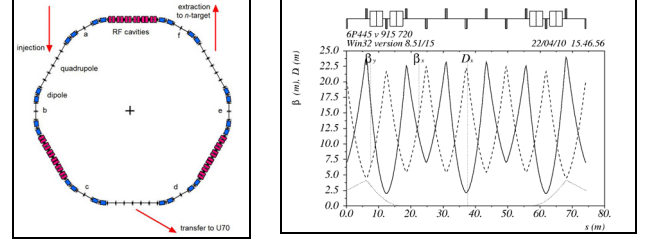
Figure 17: Backbone equipment and optical functions of the U3.5 RC PS ring.

Aperture margin is set at a conservative $\pm 4\sigma$ level. The betatron acceptance is about 660/160 π·mm·mrad (horizontal/vertical). Momentum acceptance is $\pm 3.1\%$ (pencil beam), or $\pm 1.6\%$ (full beam).

Coulomb tune shift at injection is –0.08/–0.15 (horizontal/vertical).

Protons are accelerated by 36 two-gap ferrite-loaded cavities yielding 20 kV peak voltage each. An RF station occupies < 2.5 m of a dispersion-free straight flange-to-flange. Stable phase angle is ≥ 55–56° (cosine convention). Estimated power consumption is around 130 kW per a cavity. Beam loading factor (ratio of beam fundamental RF harmonic to peak current through shunting resistance) is 3.8 ca, which is manageable.

Outline for other subsystems is being elaborated, [6].

CONCLUSION

Accelerator complex U70 of IHEP-Protvino is the sole national proton facility running for the fixed-target research in high-energy physics. It is a subject of an ongoing upgrade program affecting the key technological systems and promising still better beam quality. To maintain and develop expertise available at IHEP in hadron beam accelerators and experimental physics, a new AC-IHB project is put forward and is under development.

REFERENCES

[1] S. Ivanov and the U70 staff, Proc. of RUPAC-2008, Zvenigorod, 2008, p. 130–133.
[2] O. Lebedev et al, these Proceedings.
[3] S. Ivanov, Preprint IHEP 97–64, Protvino, 1997.
[4] S. Ivanov et al, these Proceedings.
[5] A. Afonin et al, these Proceedings.
[6] Accelerator Complex of Intense Hadron Beams, IHEP Internal Rep., September 2010.

MAINTENANCE OF ITEP-TWAC FACILITY OPERATION AND MACHINE CAPABILITIES DEVELOPMENT

N.N.Alexeev, P.N.Alekseev,V.A.Andreev, A.N.Balabaev,V.I.Nikolaev,A.S.Rjabtsev, Yu.A.Satov, V.S.Stolbunov,V.A.Schegolev, B.Yu.Sharkov, A.V.Shumshurov, V.P. Zavodov, ITEP, Moscow, Russia,

Abstract

The ITEP-TWAC facility operation with proton and heavy ion beams for ~4000 hours per year in several modes of beam acceleration and accumulation is determined by present-day demands of different beam users in the frame of current machine resources. Displacement of state interests from fundamental research to strictly-practical tasks as the spirit of the time stimulates multimode operation of accelerators with tendency of beam using for applications on the basis of modern beam technologies development. Mastering of Ag^{19+} ions acceleration in the UK ring up to the energy of 100 MeV/u and Fe^{26+} beam stacking in the U-10 ring at the energy of >200 MeV/u in addition to routine operation with C^{6+} beam at energy of 200-400 MeV/u with fast and slow extraction of circulating beam clear the way to beam using for a lot of applications requiring extension of the facility experimental area. Development of laser ion source (LIS) technology takes aim at high current and high charge state ions generation to get ratio of Z/A up to 0.4 for elements with A ~ 60 to be effectively stacked in the U-10 ring with multiple charge exchange injection technique at the beam energy of ~700 MeV/u. The machine maintenance efforts and current results of activities aiming at both subsequent improvement of beam parameters and extending of beam applications are presented.

INTRODUCTION

The ITEP-TWAC Facility consisting of main synchrotron-accumulator U-10 with 25 MeV proton injector I-2 and linked to U-10 ring booster synchrotron UK with 4 MV ion injector I-3 runs now in several operation modes accelerating protons in the energy range of 0.1-9.3 GeV, accelerating ions in the energy range of 0.1-4 GeV/u and accumulating nuclei at the energy of 200-300 MeV/u. Accelerated beams are used in several modes: secondary beams generated in internal targets of U-10 ring are transferred for experiments to Big experimental hall (BEH); beams extracted from U-10 ring in one turn are transferred to Target hall (TH); and proton beam bunch extracted from U-10 ring is transferred to Biological research hall (BRH). Some of secondary beam transfer lines are used now for transferring of slow extracted beams from U-10 ring.

MACHINE OPERATION

Next year will be 50-th anniversary of ITEP Ring Accelerator was started for operation that continues up today in parallels with machine modernization.

Statistic of ITEP-TWAC operation time is shown on Fig.1. The total machine run time of near 4000 hours per year is divided between three operation modes: acceleration of protons (~50%), acceleration of ions to relativistic energy (~10%) and nuclei stacking (~40%). Statistic of beam using for different research fields shows the tendancy of machine operation time increase for applications as proton and ion beams using in biology, medicine and radiation treatment of electronics for cosmic apparatus. The required beam time for users exceeds the possible one by factor of two. This discrepancy has to be cardinally reduced in a result of machine infrastructure development and extension of its experimental area.
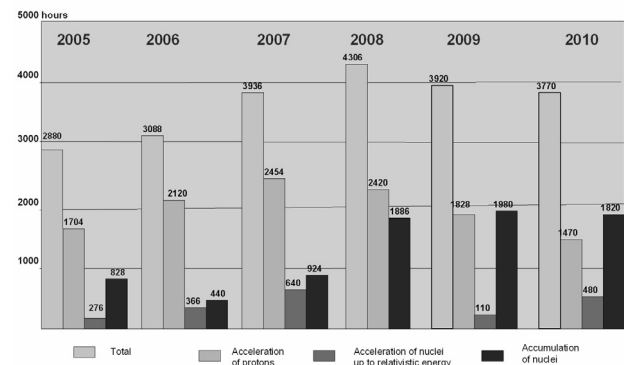
Fig.1. Statistic of ITEP-TWAC operation time

New modes of Fe-nuclei acceleration up to the energy of 3.6 GeV/u and of Ag^{19+}-ions acceleration up to the energy of 100 MeV/u realized in 2008-2009 are illustrated by oscillograms in Fig.2 and Fig.3. In the mode of Ag^{19+}-ions acceleration from very low level of injection energy as 0.7 MeV/u at vacuum in the beampipe as 1×10^{-9} Torr, particle losses at acceleration exceeds 90%.
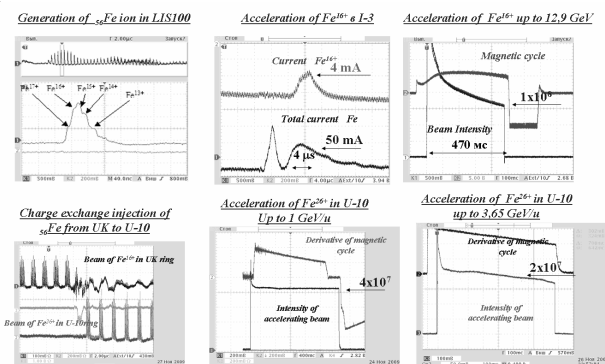
Fig.2. Acceleration of Fe-nuclei up to relativistic energy

04 Hadron Accelerators

Generation of $_{109}$Ag in L100   *Acceleration of Ag^{19+} in I-3*   *Circulation of Ag^{19+} in UK ring*

Acceleration of Ag^{19+} in UK ring up to energy of 10,9 GeV (100 MeV/u)
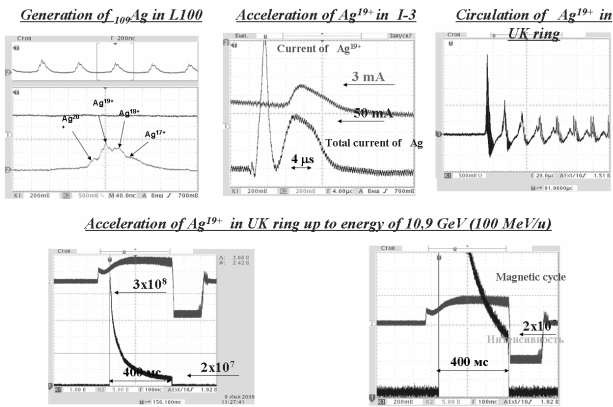
Figure 3: Acceleration of Ag^{19+} ions in UK Ring.

EXPERIENCE WITH LIS OPERATION

First compact configuration of LIS with 5J CO_2 laser L5 [1] has been in operation at injector I-3 until 2006 when it was reconstructed under using in the frame of a new universal optical scheme the 100J CO_2 laser L100 which was assembled and prepared for operation [2]. Old LIS was used for generation of C-ions only (Fig.4) and maximal charge state specie C^{5+} had been observed in this beam which shows that ionization potential (IP) in the laser plasma exceeds 374 V.

Beam parameters
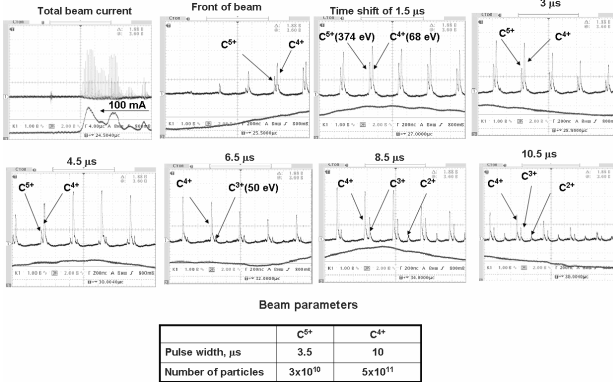
	C^{5+}	C^{4+}
Pulse width, µs	3.5	10
Number of particles	3×10^{10}	5×10^{11}

Figure 4: C-ions generation in old LIS with L5 (2006).

Beam parameters
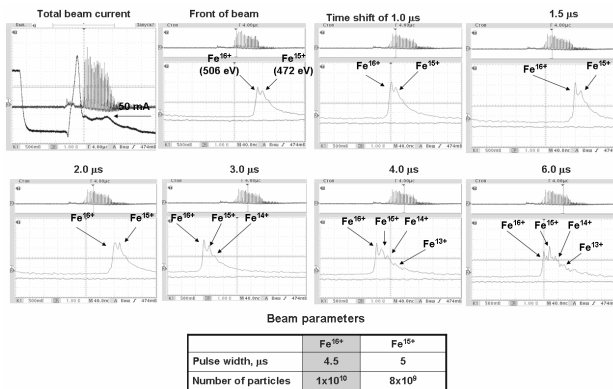
	Fe^{16+}	Fe^{15+}
Pulse width, µs	4.5	5
Number of particles	1×10^{10}	8×10^{9}

Figure 5: Fe-ions generation in new LIS with laser L100.

The new LIS with laser L100 is in operation from 2008 and it's used with target materials of Al, Fe and Ag. Generation of Fe-ions (Fig.5) shows maximal charge state specie Fe^{16+} with IP= 506 V. The higher level of charge state specie Fe^{17+} with IP=1168 V has been also observed

in some measurements but in very few quantity. Generation of Ag-ions (Fig.6) shows maximal charge state specie Ag^{20+} with IP= 816 V and very few specie Ag^{21+} with IP= 960 V has been also observed in some measurements. Summarizing results of ion generation in old and new configurations of LIS at injector I-3 is shown on Fig.7 with another data obtained from different publications [3-6].

Ag beam parameters
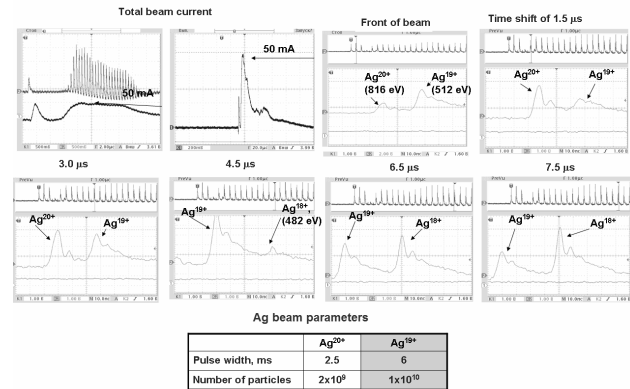
	Ag^{20+}	Ag^{19+}
Pulse width, ms	2.5	6
Number of particles	2×10^{9}	1×10^{10}

Figure 6: Ag-ions generation in new LIS with laser L100
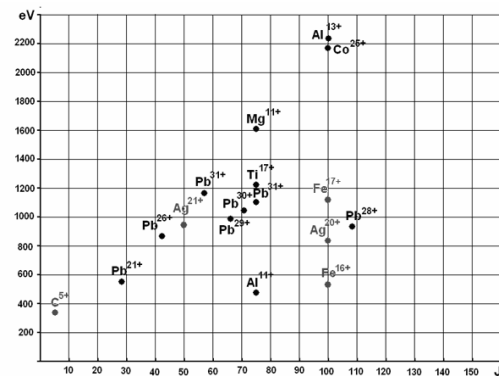
Figure 7: Ionization potentials reached in LIS stand tests from different publications (black points) and in LIS at injector I-3 (red points) from laser used radiation energy.

DEVELOPMENT OF HEAVY NUCLEI STACKING TECHNIQUE

The charge exchange injection technique is used now with stacking factor of 70 for C-nuclei stacking at the beam energy of 300 MeV/u [7]. The efficiency of Fe-nuclei stacking at the energy of 230 MeV/u is limited on the level of stacking factor 10 due to disturbing effects of beam interaction with stripping foil. Efficiency of beam stacking for nuclei of mass number A~60 will be increased many times with increasing of injected beam energy up to 600-700 MeV/u. For nuclei with A<30, disturbing effects of beam interaction with stripping foil are small enough and efficiency of beam stacking is a function of injection scheme parameters and of storage ring dynamic aperture. We are planning to start experiments on the beam stacking process optimization at the end of this year with stacking of $Si^{12+}=>Si^{14+}$ ions at the energy of >500 MeV/u. Expected results of stacking process improvement are shown on Fig.8.

04 Hadron Accelerators

Parameters of beam stacking with laser L5
(L100 for Si) and 4MV injector I-3

Parameters	Reached for $C^{4+} \Rightarrow C^{6+}$	Expected for $C^{4+} \Rightarrow C^{5+}$	Expected for $Si^{12+} \Rightarrow Si^{14+}$
Energy	300 MeV/u	400 MeV/u	650 MeV/u
Injected beam intensity	6×10^8	$\sim 5 \times 10^9$	$\sim 5 \times 10^9$
Cycle time , s	3	2	2
Acceptance, $A_{x,}$ π mm mrad	10	30-50	30-50
Vacuum, Torr	$\sim 1 \times 10^8$	$\sim 1 \times 10^9$	$\sim 1 \times 10^9$
Stacking factor	~70	~200	~200
Stacked beam intensity	4×10^{10}	$\sim 10^{12}$	$\sim 10^{12}$

Figure 8: Optimization of beam stacking at A<30.

DEVELOPMENT OF ITEP-TWAC INFRASTRUCTURE

Elaborated strategy of ITEP-TWAC infrastructure development is aimed to redouble beam time for physical experiments and applications extending of functionality of UK synchrotron for protons acceleration too and for generation of slow extracted beams to the area of beam using for applications. Layout of expanded Injection Complex with additional beam lines from injectors both I-2 and I-4 to UK Ring is shown on Fig.9.
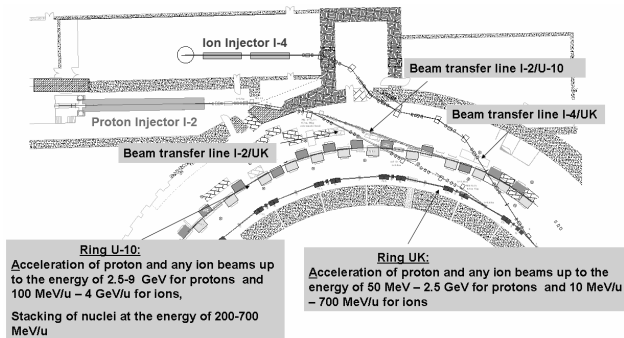
Figure 9: Expanding of ITEP-TWAC Injection Complex
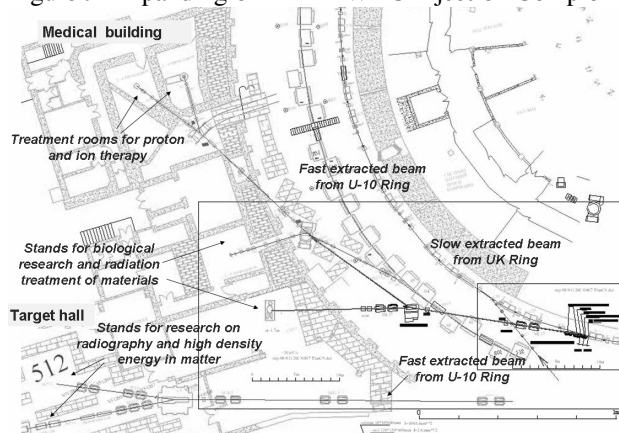
Figure 10: Expanding of beam area for applications.

Layout of beam using area for applications is shown on Fig.10. New projected beam line for slow extracted beam from UK Ring is directed to free space of Target hall (where stand will be installed for biological research) and

linked with beam line from U10 Ring used now for proton therapy.

We consider also possibility of construction the second slow extraction system for U-10 Ring to BEH [8] for the beam of maximal beam momentum of 10Z GeV/c. Area of this beam using in the corner of BEH has to be rounded by radiation shielding.

CONCLUSION

The ITEP Accelerator Facility is in operation by ~4000 hours yearly accelerating proton and ion beams and stacking nuclei for physics experiments, methodical research and radiation technologies.

The progress has been achieved in acceleration of heavy ion: specie of Ag^{19+} have been generated in LIS and accelerated in synchrotron UK up to the energy 100 MeV/u with intensity of 2×10^7; nuclei of Fe^{26+} have been accelerated using three stage scheme I-3/UK/U-10 up to record energy of 3.6 GeV/u or 200 GeV per particle with intensity of 5×10^7.

Experiments on the ion beam generation in LIS with 100J CO_2 laser L100 give evidence of optic used imperfection reducing the laser radiation power density on the target surface by factor of more than ten. New focusing scheme for target station is elaborated on a base of parabolic short focusing mirror to increase the power density by factor of three. Next factor of power density increase will be achieved replacing windows by them of better quality.

Construction of the new heavy ion injector I-4 is in progress: the RFQ section for the energy of 1.5 MeV/u of Z/A=0.3 ions is constructed and successfully tested for resonator parameters measuring and RF power loading [9]. Preparations of RFQ section for the beam test is now started to be carried out in the first quarter of next year.

The progress in intensity of heavy ion beam stacked in U-10 Ring using multiple charge exchange injection technique is expected in the experiments planned for the end of this year with ions $Si^{12+} \Rightarrow Si^{14+}$ stacking at the energy of 500 MeV/u.

Development of ITEP-TWAC facility Infrastructure is aimed to redouble beam time for physical experiments and applications making operation of both U-10 and UK synchrotrons in parallels .

REFERENCES

[1] N.Alexeev, et al., EPAC -2000, 1283-1285.
[2] N.Alexeev, et al., EPAC -2008, 352-354
[3] Yu.Satov, et al. Journal of Russian Laser Reasearch, V.25, N.3 (2), 205-210.
[4] S.Kondrashev, A.Balabaev, K.Konukov, et al. Procidings of EPAC 2004, 1402-1404.
[5] S.Kondrashev, N.Mescheryakov, B.Sharkov, et al. Rev.Sci. Ins., 71, 3, 1409–1412, (2000)
[6] V.V.Appolonov et al. Pisma JETF, v.11 (1970), p.377
[7] N.Alexeev, et al., EPAC -2006, 243-245.
[8] N.Alexeev, et al., RuPAC-2008, 134-136
[9] V.Andreev, et al., IPAC-2010, 801-803

04 Hadron Accelerators

COMPENSATION OF NONLINEARITIES IN NICA COLLIDER OPTICS

S.Kostromin, O.Kozlov, I.Meshkov, V.Mikhailov, A.Sidorin, JINR, Dubna, V.Lebedev,
S.Nagaitsev, FNAL, Batavia, Illinois, USA, Yu.Senichev, IKP, Juelich, Germany

Abstract

The Nuclotron-based Ion Collider fAcility (NICA) [1] is a new accelerator complex being constructed at JINR. It is designed for collider experiments with ions and protons and has to provide ion-ion (Au^{79+}) and ion-proton collisions in the energy range $1 \div 4.5$ GeV/n and collisions of polarized proton-proton and deuteron-deuteron beams.

Different chromaticity correction schemes involving several families of sextupoles are considered for two collider conceptions: with constant γ_{tr} and with changeable one.

INTRODUCTION

The collider rings has the racetrack shape and consist from two arcs and two long dispersionless straight sections with two IPs. The normalized chromaticity reaches a high value ~4.

Therefore the quite strong chromatic sextupoles magnets on arcs are required which in turn bring significant non-linear distortions in beam dynamics. Different schemes involving several families of sextupoles and are tested. Optimization of the chromaticity correction scheme was carried out to increase the dynamic aperture.

CHROMATICITY CORRECTION SCHEMES

Triplet based racetrack with $\gamma_{tr}=6.22$

This option was considered in Ref. [2] (see Fig.1).
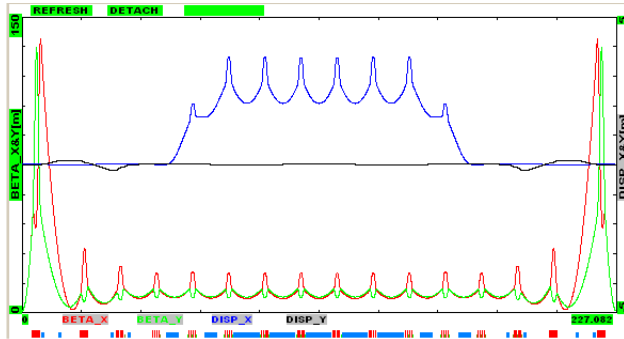
Figure 1: β-function & dispersions for half of the ring.

A chromaticity correction includes 4 families of sextupoles (2 focusing and 2 defocusing ones). It allows one to correct both the tune chromaticity and the beta-function chromaticity excited by IP quadrupoles. Sextupoles of each family are located with 180° betatron phase advances for their nonlinearity compensation. The dependence of the collider tune on Δp/p is shown in Fig. 2. It is very nonlinear due to large β* which excites large tune and β-function chromaticity.
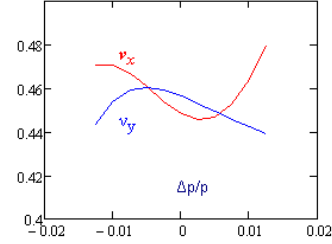
Figure 2: Tune dependence on the momentum offset.

The natural chromaticity of the ring are: ξ_x=-27.1, ξ_y=-23.2 ($\Delta\xi_{x,y} \sim -17$ from two IPs). Corrected chromaticities are: $\xi_x = -1.54$, $\xi_y = -1.50$. The sextupole strength is ~0.35 kG/cm². A non-linear dependence of tunes and β-functions on Δp/p and the optics smoothness requirement do not allow the perfect chromaticity correction. However sextupole settings making reasonably good compensation were found (see Fig. 3).
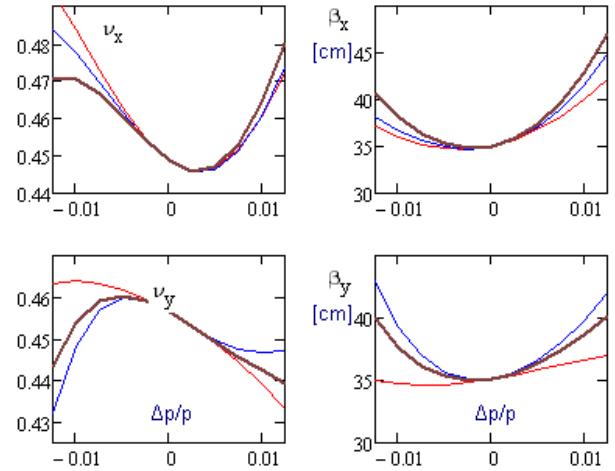
Figure 3: Dependence of the tune and β* on Δp/p with different sextupoles strength.

That allowed us to avoid adding octupoles. Note also that the nonlinearity of tunes is actually profitable. It allows us to have large tune chromaticity required for transverse instabilities suppression with moderate tune variation across the momentum aperture.

FODO-cell based racetrack with changeable γ_{tr}

To meet the NICA requirements of operation with different magnetic rigidity beams, Au-ions in range $1 \div 4.5$ GeV/u and with proton $6 \div 13$ GeV lattice with changeable transition energy was considered.

1. Au 4.5 Gev/u mode (see Fig. 4)
Only sextupoles located in two central superperiods (without dispersion supressors) plus four additional sextupoles (instead of multipole correctors) are used for correction (see Fig. 5).

01 Circular Colliders
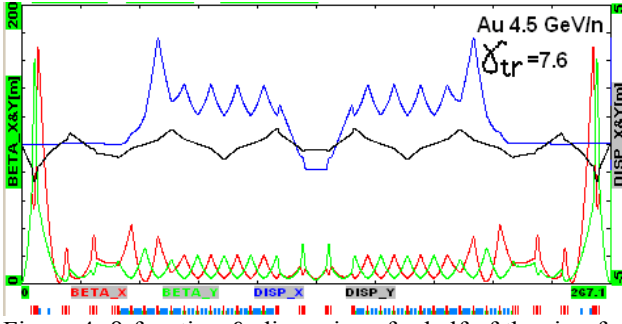
Figure 4: β-function & dispersions for half of the ring for Au 4.5 GeV/n
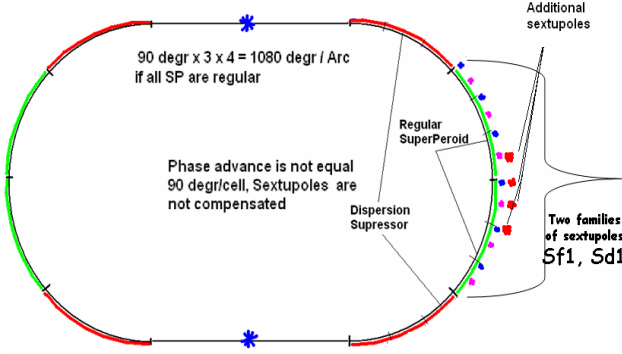
Figure 5: Chromaticity correction scheme for Au 4.5 GeV/u option (arcs without straight insertions)

2. Au 3.5 GeV/u, Au 1.5 GeV/u modes (see Fig 6)
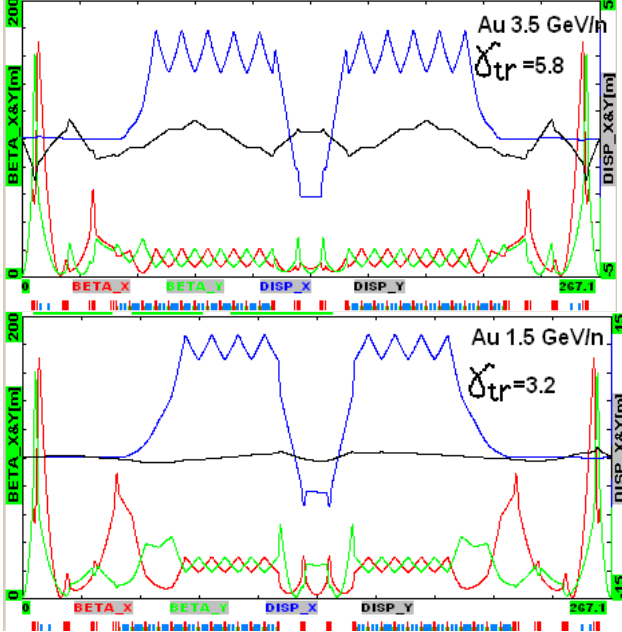
Figure 6: β-function & dispersions for half of the ring for Au 3.5 & 1.5 GeV/u

All sextupoles in the arc (near each quad) are used for chromaticity correction.

3. Protons 12.45 GeV mode (see Fig 7)

In the proton mode the number of cells in one superperiod N_{cell} and the number of superperiods S_{arc} per arc are dictated by the required betatron phase advance in the

horizontal plane. Following the theory of resonant lattices [4], we construct a lattice with the horizontal betatron phase advance in the arc v_{arc} as close to the number of superperiods S_{arc} as possible keeping them both being integers. This means that the phase advance in one superperiod should be $2\pi v_{arc}/S_{arc}$, and the phase advance of radial oscillations between the cells located in different superperiods and separated by $S_{arc}/2$ superperiods is $2\pi \cdot \dfrac{v_{arc}}{S_{arc}} \cdot \dfrac{S_{arc}}{2} = 2\pi \cdot \dfrac{v_{arc}}{2} = \pi + 2\pi n$. It corresponds to the condition of first-order compensation for the nonlinear effects of sextupoles in the arcs.

Only sextupoles near central lenses (four families) in each superperiod (where dispersion function of the lattice are positive) are used (see Fig 8).
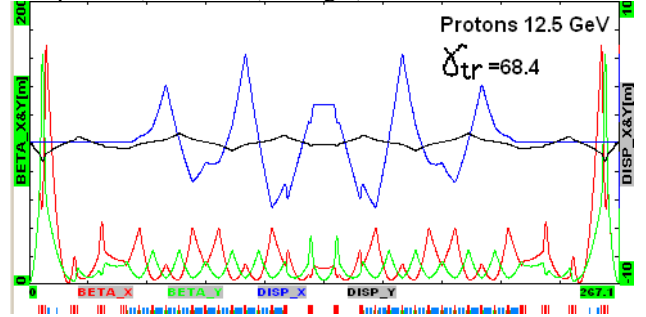
Figure 7: β-function & dispersions for half of the ring for 12.45 GeV Protons option
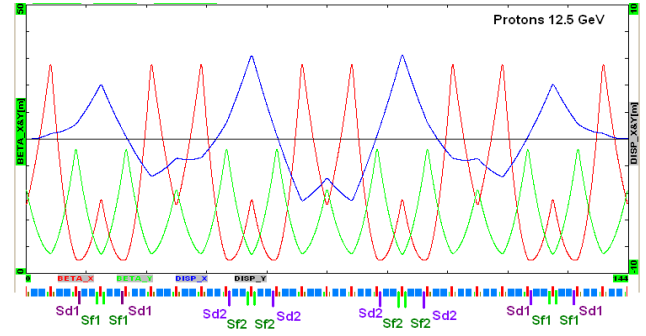
Figure 8: Chromaticity correction scheme for proton 12.45 GeV option (arc without straight insertion)

Parameters of the sextupoles are shown in the Table 1.

Table 1. Parameters of sextupole lenses

	Sextupoles strength [kG/cm²] /Number per arc				Ring crom (before corr), ξ_x / ξ_y	Ring crom (after corr), ξ_x / ξ_y
	Sf		**Sd**			
Au 4.5 GeV/n	0.154 / 8		-0.264 / 8		-38.3 / -36.6	0.11 / -0.15
Au 3.5 GeV/n	0.054 / 12		-0.085 / 12		-29.6 / -32.4	0.12 / -0.18
Au 1.5 GeV/n	0.011 / 12		-0.130 / 12		-28.8 / -27.5	0.24 / 0.04
Proton 12.45 GeV	**Sf1**	**Sf2**	**Sd1**	**Sd2**	-37.2 / -33.5	-0.005 / -0.27
	0.072 /4	0.110 /4	-0.207 /4	-0.284 /4		

Dependences of the ring tune via Δp/p are presented in Fig. 9.
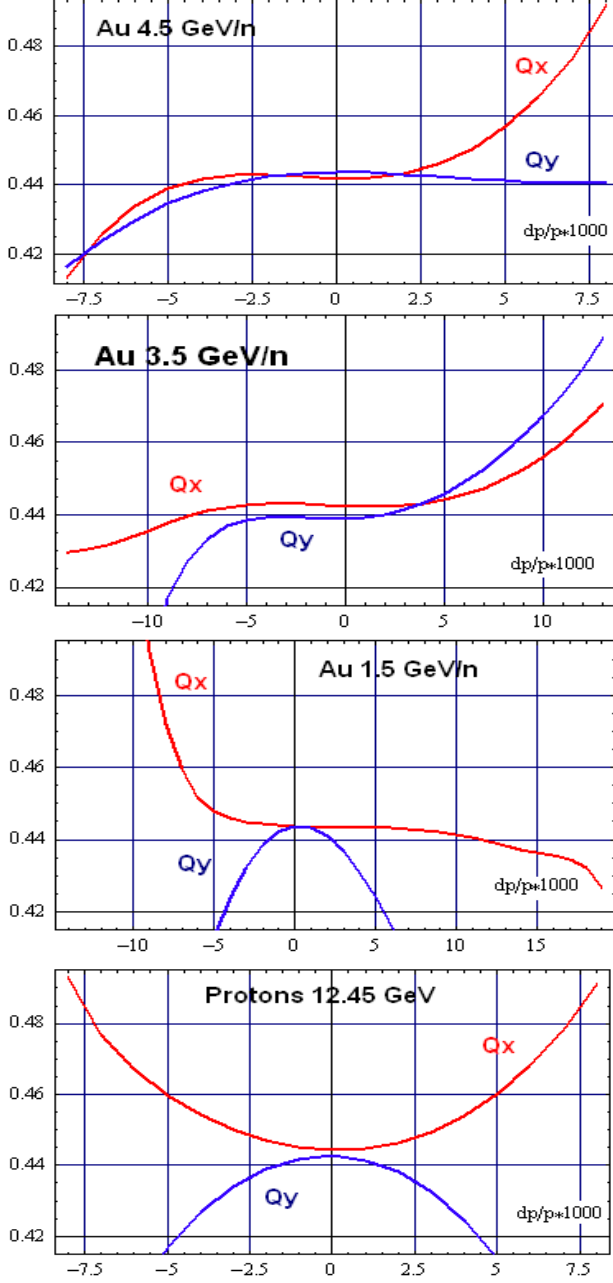
Figure 9: Collider rings tune via *dp/p*

The ring tunes have non-linear dependence on Δp/p especially for Au 1.5 GeV/n and Protons options. Thus, may be, adding of the octupoles is needed. However in the region of momentum acceptance Δp/p ±0.005 the tunes have acceptable values to avoid crossing of dangerous resonances (especially half-integer).

Due to high total length of straight sections (relatively to all ring perimeter) NICA collider has sufficiently high normalised chromaticity value $\xi_{x,y}/\nu_{x,y} \sim 4$, and use of quite strong sextupole magnets for chromaticity correction sharply restricts the dynamic aperture.

Dynamic aperture of the collider is calculated by tracking through the ring optics in MAD and OptiM codes.
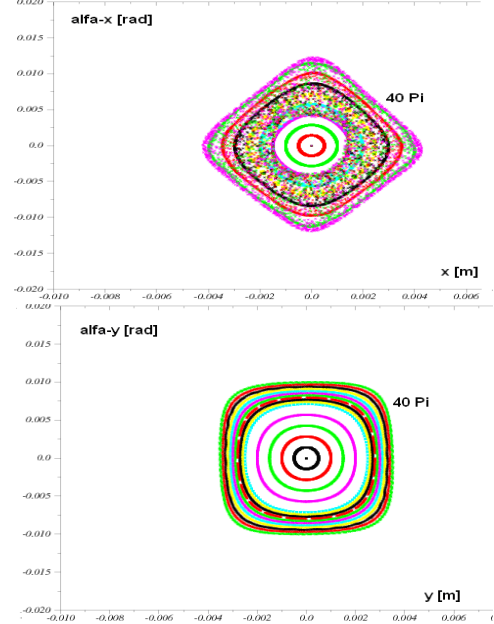
Figure 10: Dynamic aperture in the transverse phase planes for *Au 4.5 GeV/n*

Thus the scheme of chromaticity compensation for all working options of NICA collider is presented. Ist developed to reduce the sextupole nonlinearities in the ring as much as possible, ensures achievable values of the sextupole magnets strength and acceptable dynamic aperture of the collider to get the desirable luminostity 10^{27} cm^{-2}s^{-1} for Au- collisions and 10^{30} cm^{-2}s^{-1} for proton collisions.

REFERENCES

[1] G. Trubnikov et al., "Project of the Nuclotron-based Ion Collider fAcility (NICA) at JINR, Proceedings of RuPAC 2008, Zvenigorod, Russia.

[2] V. Lebedev, "NICA: Conceptual proposal for collider", MAC2010, January, 2010.

[3] Yu. Senichev and A. Chechenin, Theory of "Resonant" Lattices for Synchrotrons with Negative Momentum Compaction Factor, Journal of Experimental and Theoretical Physics, December 2007, vol. 105, No. 5, pp. 1127–1137.

STUDY OF EFFICIENCY OF BEAM COLLIMATION AT U-70 ACCELERATOR BY USE OF CRYSTAL TARGETS

A.G. Afonin, V.T. Baranov, S. Belov, V.N. Chepegin, Yu. Chesnokov, P.N. Chirkov, A. Ermolaev, V. Gorlov, I. Ivanova, D. Krylov, V. Maisheev, D. Savin, E. Syshikov, V. Terekhov, I.A. Yazynin

IHEP Protvino, Russia.

Abstract

New crystal technique – bent crystal array and veer – type reflector based on straight crystals were used like first stage in collimation system at U-70 accelerator. Efficiency of collimation was enhanced up to 90% in two-stage collimation system which included first crystal stage and long steel absorber like second stage. For data taking and analysis of information modified modern beam diagnostic system was applied.

INTRODUCTION

The phenomenon of deflection of a charged particle beam in a bent crystal is well investigated and successfully applied at energies of about 10 GeV and higher [1,2,3]. However, the task of bending and extraction of charged particles with energies below 1 GeV presents a big practical interest, for example for the production of ultra stable beams of low emittance for medical and biological applications. There exists a big experimental problem in steering such energy beams, which is connected with the small size of the bent crystal samples. Potentially suitable tools in this case can be the bent quasimosaic crystals such as in [5], or thin straight crystals [6,7], but in both these cases it is necessary to increase a deflection angle of particles in some times.

CRYSTAL DEVICES

In this article we propose a novel crystal technique, which can effectively work in a wide energy range and is especially perspective for low energy below 1 GeV.

The first option is based on use of array of shot bent channeling crystals (Fig.1) with sub – millimeter length (special thin silicon wafers about 100 micron thickness were used for the production of such samples). Thus the bend of array occurs also, as a bend of the single well investigated silicon strip [8].
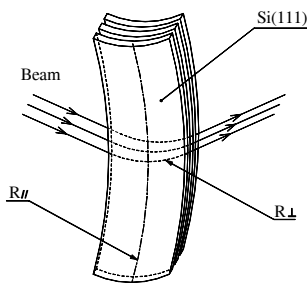
Figure 1: The array of bent silicon strips for beam deflection due to channeling.

The second option is based on the reflection of particles on very thin straight crystal plates with thickness, which is equal to an odd number of half-lengths of channeling oscillation waves $L = (2n+1)/2 \times \lambda$, where $\lambda = \pi d/\theta_c$, $d = 2.3 A^0$ – interplanar distance in silicon. It means, for example, that the optimum length of a crystal should be 10 microns for particles with energy 50 GeV. For the enhancement of the deflection angle, a few aligned plates placed like a veer are foreseen (Fig.2).
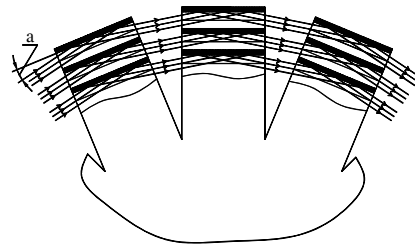
Figure 2: Veer-type reflector for bending of particle beam with use of thin straight crystals.

For an optimum deflection of a beam in this design each following crystal is unwrapped on angle $2\theta_c$. Then the total bend angle of beam can reach the value $2\theta_c \times N$, where N – is the amount of crystal plates. If the unwrap of a fan and thickness of plates are not optimal, the lower bend of particles occurs, and this picture is more difficult for interpretation. On Fig.3 for understanding the process of Monte Carlo calculations for unitary passage of a beam through a fan are submitted at its different parameters.
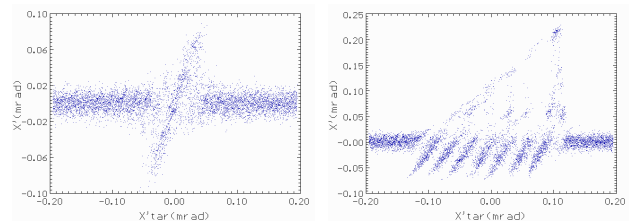
$$dx' = 0\,\mu rad, \quad L = 10\,\mu m, \qquad dx' = 30\,\mu rad.$$

Figure 3: Distribution of protons with energy 50 GeV on scattering angles after passage of a crystal fan from seven plates depending on its angular orientation X'tar with respect to the beam. The parameter dx' means a turn of the next plates of a fan in microradians.

Three different devices have been prepared for accelerator experiment: a usual crystal strip (the technology is described in [8]), a crystal array (Fig. 1),

and assembly of veer - type (Fig. 2). The realized schemes of crystal devices are shown in photos Fig. 4. Parameters of crystals are submitted in the table.

Crystal type	Length, mm	Thickness, mm	Bend angle, mrad
Strip	1	0.3	1.0
Array	0.9	7×0.2	1.1
Veer	7×0.25	3	~7×0.05
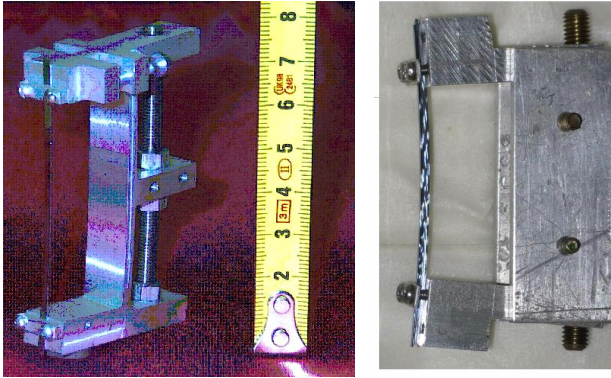
Figure. 4: The realized schemes of devices (left to right): the bent strip and array of strips.

DESCRIPTION OF ACCELERATOR EXPERIMENT

Experiment was performed during two runs of U-70 operation in 2009 and 2010. In experiment 3 crystals in high-vacuum goniometers were serially entered in a circulating accelerated. The angle of bending is sufficient to separate the circulating and deflected (by the crystal) beams in space. The beam deflection effect due to channeling was measured by secondary emission detector (SEM), located in vacuum chamber of an accelerator near to circulating beam. Parameters of the accelerator are described in [9]. Details of the experimental equipment are shown on Fig. 5.
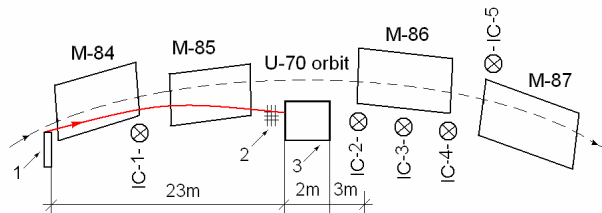
Figure. 5: An arrangement of the equipment in the U-70 accelerator: 1– crystal station, 2– profilometer, 3– absorber, IC – ionization chambers (loss monitors 1-5), M– magnetic blocks of the accelerator.

For carrying out of experiment the new automated diagnostic system of the beam, including 5 monitors of losses based on ionization chambers and 2 plane stationary profilometer has been created on basis of the

secondary emission, established directly ahead of an absorber in vacuum volume and recording parameters of the deserted beam in horizontal and vertical planes.

The system of data taking and acquisition is based on use of an industrial computer with trunk PCI. In the tunnel of the accelerator two skeletons of preliminary electronics for integration of signals from electrodes of profilometer are placed. The first skeleton contains 24 measuring channels for registration of horizontal distribution of density of a beam and 8 channels for integration of signals from loss monitors. The second skeleton with 32 measuring channels is intended for 32 channel vertical profilometer. In each skeleton signals from integrators are multiplexed and on the common coaxial cables act on 2 inputs of 8-channel ADC, integrated in an industrial computer. On other inputs of ADC other necessary auxiliary information, somehow acts: intensity of a beam before its dump on an absorber, the voltage values proportional to currents of bump-magnets, to positions of crystals, etc. The software for data taking and acquisition has been based on application of platform LabVIEW.

RESULTS OF MEASUREMENTS

Measurements were carried out at two energies of the accelerated beam of protons: 50 GeV and 1.3 GeV (kinetic energy).

First measurements have been lead at energy of protons 50 GeV. For definition of collimation efficiency calibration of the detector with the help of fast kicker - magnet has been lead. In Fig. 6 the sums of signals of the detector are shown when the beam deflected by different crystals in comparison with effect of one-turn brought of a beam by fast kicker (in this last case whole beam with 6 mm size gets in the aperture of the detector).
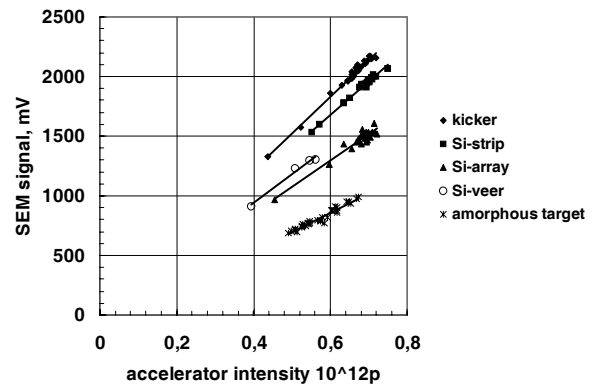
Figure 6: Comparison of the sum of profilometer signals at work of different crystals with effect of particle brought towards absorber by kicker.

Measured collimation efficiencies for three mentioned crystals are equal 91, 77 and 82%. The amount of particles in channeling peak is accordingly equal 86, 72 and 70%. That is all crystals well deflected 50 GeV proton beam. The received data are in agreement with computer simulation with use of program SCRAPER [10]

which is taking into account multi-turn character of movement of particles in real structure of the accelerator and repeated their interaction with a crystal.

On the Fig. 7 the orientation dependences of collimation and channeling efficiencies are shown for crystal strip.
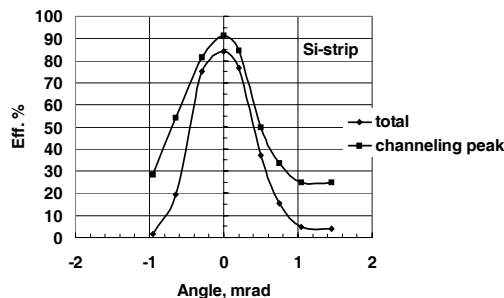
Figure 7: Collimation efficiency depending on angular orientation of a crystal strip with respect to the beam.

On the Fig. 8 are shown orientation curves of particle losses, measured on signals of 5 ionization chambers located in a vicinity of an absorber (see Fig.5).
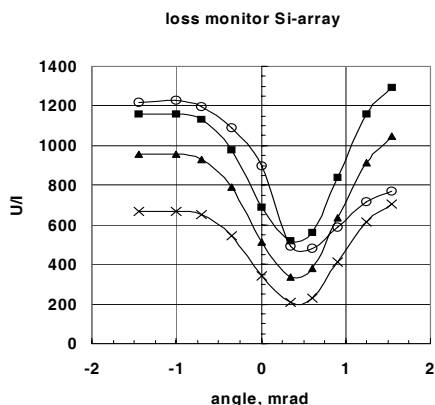
Figure 8: Orientation dependences of loss monitors for array of strips.

Particle losses at optimum alignment of crystals decrease in 2-3 times in comparison with disoriented crystals that corresponds to calculation. Approximately in as much time intensity of muon torch behind an absorber far from the accelerator should decrease that is the important factor at achievement of high intensity of beam of circulating protons in the accelerator.

At energy of a beam 1.3 GeV results of efficiency are much lower (see the table). The best result, channeling peak of about 20 %, has shown array from seven thin strip crystals. The big loss of efficiency is explained by non-optimal tuning of circulating beam towards the crystal by bump-magnet. At low energy because of sizable beam, about 50 mm, there is a drift of an incident angle about a half milliradian that should be removed at prompting a beam by high-frequency noise (this work is planned). In Fig. 9 the profile of 1.3 GeV beam deflected by silicon array is shown. The fraction of channeling peak is

allocated by a thick line (channeling peak is well separated from a circulating beam and approximately corresponds to efficiency of a possible beam extraction from the accelerator).
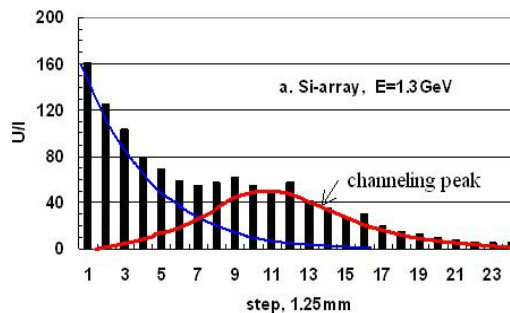
Figure 9: The 1.3 GeV proton beam profile at the absorber entry deflected by array of silicon strips.

CONCLUSION

Thus, it is shown, that the created crystal devices can work in a wide range of energy and have prospects for the organization of low energy medical beams on U-70 accelerator. For optimization of crystal devices for low energy experiments in a test area of laboratory LNF are planned where accessible beam of particles with 50-700 MeV energies exist [4].

Reduction of particle losses in 2-3 times on the accelerator was observed also at application of different crystals in comparison with the usual one-stage scheme of beam collimation by steel absorber. Approximately in as much time intensity of muon torch behind an absorber far from the accelerator should decrease that is the important factor for achievement of higher intensity of a circulating beam in U-70.

REFERENCES

[1] V.M. Biryukov, Yu.A. Chesnokov, and V.I. Kotov, Crystal Channeling and Its Application at High-Energy Accelerators (Springer: Berlin, 1997).
[2] W.Scandale, et al., Phys.Rev.Lett. 98,154801 (2007).
[3] N.V. Mokhov, et al. PAC 2009, Canada, 2009.
[4] S.Bellucci, et al., Nucl.Instrum.Meth.B252:3-6, 2006.
[5] Yu.M.Ivanov, et al, JETP Letters 81 (2005) 99
[6] A.Taratin, et al, SSCL-545, 1991.
[7] S.Strokov,et al,Nucl.Instrum.Meth.B252:16-19,2006.
[8] A.G.Afonin, et al, Phys. Rev. Lett. 87,094802 (2001).
[9] A.G.Afonin, et al, Phys.Part.Nucl.36:21-50,2005
[10] I.I.Degtyarev, O.A.Liashenko, I.A Yazynin, Applications of Coupled SCRAPER-RTS&T Code in Radiation Therapy, EPAC 2000, p.2506-2508.

SUPERCONDUCTING MAGNETS FOR THE NICA ACCELERATOR COMPLEX IN DUBNA

H. Khodzhibagiyan, P. Akishin, A. Bychkov, A. Kovalenko, O. Kozlov, G. Kuznetsov, I. Meshkov, V. Mikhaylov, E. Muravieva, A. Shabunov, A. Starikov, and G. Trubnikov, JINR, Dubna, Russia

Abstract

NICA is the new accelerator complex being under design and construction at JINR. The facility is aimed at providing collider experiments with heavy ions up to Uranium in a center of mass energy range from 4 to 11 GeV/u and an average luminosity up to 10^{27} cm-2s-1.The facility includes a new superconducting Booster synchrotron, the existing 6A·GeV superconducting synchrotron – Nuclotron, and the new superconducting Collider .The status of the design and construction of the full size model magnets for the Booster synchrotron as well as for the NICA Collider is presented.

INTRODUCTION

The flagship of the Joint Institute for Nuclear Research in Dubna is now the NICA/MPD project [1, 2] started in 2007. The general goal of the project is to start experimental study of hot and dense strongly interacting quantum chromodynamics matter in the coming 5-7 years. This goal is proposed to reach by: 1) upgrade of the existing superconducting synchrotron – the Nuclotron [3] as a basis for generation of intense beams over the atomic mass range from protons to uranium and light polarized ions; 2) design and construction of the facility to provide collider experiments with heavy ions like Au, Pb or U at luminosity of 10^{27} cm-2-s-1 at the kinetic energy range of 1 - 4.5 GeV/amu; 3) design and construction of the Multi Purpose Detector (MPD). The NICA facility (see Figure 1) includes two injector chains, a new 600MeV/u superconducting Booster synchrotron, the 6A·GeV superconducting synchrotron – Nuclotron, and the new superconducting Collider consisting of two rings of about 500m circumference each.

MAGNETIC SYSTEM OF THE BOOSTER SYNCHROTRON

The main goals of the Booster [4] are the following: accumulation of $4 \cdot 10^9$ Au^{32+} ions; acceleration of the heavy ions up to the energy of 600 MeV/u that is sufficient for stripping the Au ions up to the highest charge state of 79+; forming of the required beam emittance with an electron cooling system. The present layout makes it possible to place the Booster having 211 m circumference and a four fold symmetry lattice inside the yoke of the Synchrophasotron (shut down in 2002). Four large straight sections of the Booster will be used for injection from the linac, single turn extraction to transfer the beams into the Nuclotron, placing of the acceleration cavity and the electron cooler. With a maximum dipole field of 1.8 T, energy of above 600 MeV/u can be reached

allowing the stripping of heavy ions up to the bare nucleus state. The magnetic system of the Booster consists of 4 quadrants and each of them has 10 dipole magnets, 6 focusing and 6 defocusing lenses. The multipole
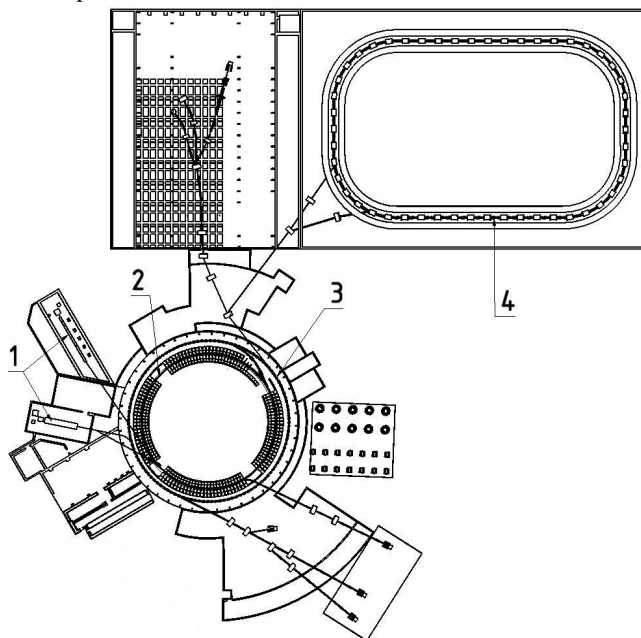
Figure 1: Schematic view of the NICA accelerator complex: 1 - injector chains; 2 - Booster synchrotron; 3 - existing superconducting accelerator Nuclotron; 4 – Collider with two superconducting rings.

correctors are also used to compensate the errors of both the main (dipole, quadrupole) and higher (sextupole, octupole) harmonics of the magnetic field. The required magnetic field in aperture is 1.8 T at the maximum rigidity. The increased aperture of both the lattice dipole and quadrupole magnets is one of the main design features.

The Nuclotron-type design [5] based on a window frame iron yoke and a saddle-shaped superconducting winding has been chosen for the Booster magnetic system. The Nuclotron magnets include a cold (4.5K) window frame iron yoke and a superconducting winding made of a hollow NbTi composite superconducting cable cooled with a two-phase helium flow.

Further development of the technology was proposed [6] to increase the efficiency of the magnetic system. A cross-section view of the Booster dipole and quadrupole magnets is shown in Figs. 2 and 3, correspondingly.
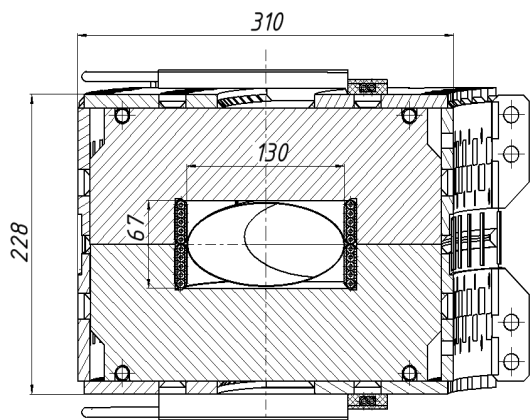
Figure 2: Cross-section view of the Booster dipole magnet.
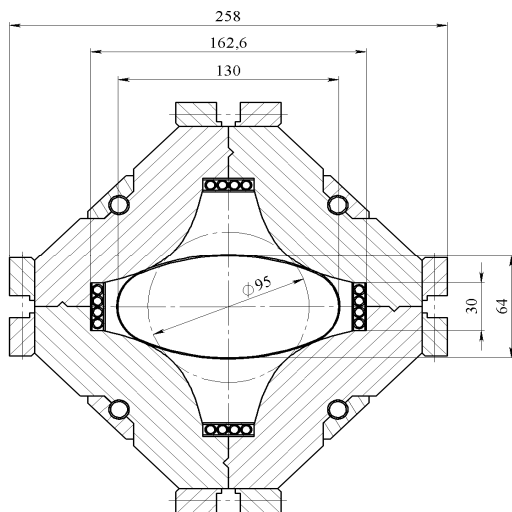
Figure 3: Cross-section view of the Booster quadrupole magnet.

In accordance with this proposal the single-layer winding bent dipole will be built to decrease the magnet cross section and AC losses in comparison with the straight double-layer winding dipole at the same aperture budget by means of the doubled structural current density in a winding. The use of curved (sector) dipoles instead of the straight ones in circular accelerators makes possible the reduction the horizontal size of the magnet useful aperture leading to less AC losses.

MAGNETIC SYSTEM OF THE NICA COLLIDER

The Nuclotron-type design based on a cold, window-frame iron yoke and a saddle-shaped winding of the hollow superconductor was chosen for the NICA Collider. The design of the Collider dipole magnet is shown in Figure 4. Two identical single-layer windings are located in the common straight iron yoke one over the other. Lorenz forces in the windings are supported by the yoke. The yoke consists of three parts made of laminated isotropic 0.65 mm thick electrical steel sheets. They are held together by longitudinal steel plates welded with

laminations and frontal sheets. The distance between the beams is 320 mm. The windings are made of a hollow superconducting cable. Sixteen SC strands are spirally wound on a copper-nickel tube 4 mm in diameter. The cable is wrapped with two layers of 0.04 mm Kapton tape and two layers of 0.1 mm epoxy impregnated glass-fiber tape. The bending field in the iron-dominated magnets is limited to approximately 2 T. The field geometry is formed by the iron yoke; therefore at the maximum field of 1.8 T the relative imperfection is less than $2 \cdot 10^{-4}$. The winding current at the maximum field is designed to be 10.8 kA. The NICA Collider will be operated at constant magnetic field, but the power supply system is designed to provide a maximum field ramp of 0.5 T/s. The design of the regular collider twin bore quadrupole lens with hyperbolic poles is in progress. The production technology, assembling and cooling of the dipole and quadrupole magnets are similar.
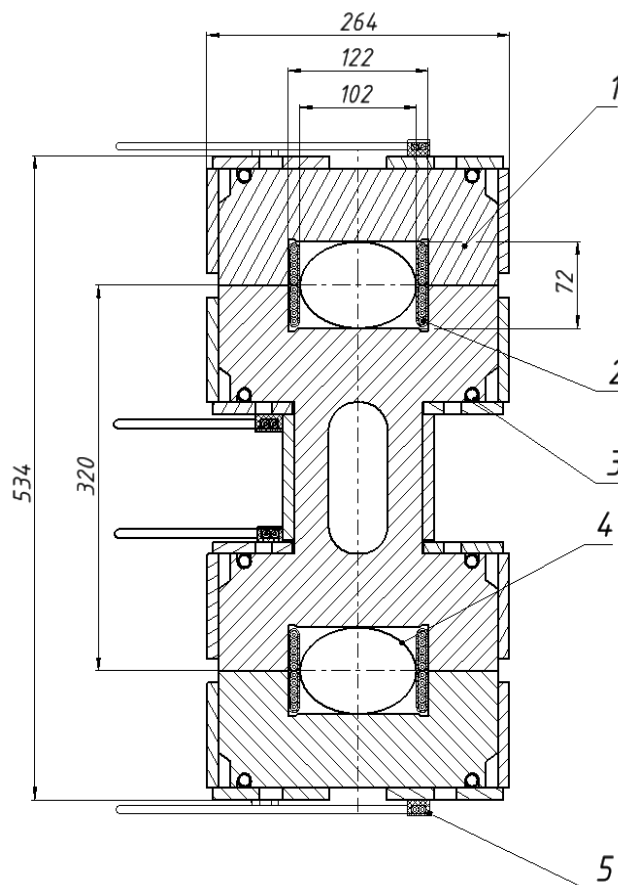
Figure 4: Cross-section view of the NICA Collider dipole magnet: 1 – iron yoke; 2 – SC winding; 3 – tubes for cooling the iron yoke; 4 – beam pipe; 5 – bus bars.

The dipole and quadrupole magnets are cooled with a two-phase helium flow [7] which in series passes from the supply header through the cooling channels of the bus bars, lower and upper windings, iron yoke and then - enters the return header. Each twin bore dipole or quadrupole magnet is connected in parallel to the supply and return helium headers. The cooling of the magnets

01 Circular Colliders

with a two-phase helium flow is justified because it was checked and confirmed by the long-term Nuclotron operation. The mass vapor content of helium at the inlet is kept approximately equal to zero. Hydraulic resistance of the cooling channels of magnets are adjusted so that the mass vapor content of helium at the outlet of the dipole and two type quadrupoles should be identical and equal to 90%. The estimated value of the total heat input to liquid helium in the Collider is 1100 W. The consumption of liquid helium for cooling the current leads is approximately 1.2 g/s.

STATUS OF THE PRODUCTION PROTOTYPE MAGNET

Making a full-scale prototype dipole magnet for the Booster synchrotron is about to be completed. All the components of the magnet yoke (lamination sheets, brackets, and end plates) were manufactured in the industry. Approximately 7000 sheets of isotropic electrical steel 0.65 mm thick were manufactured with high precision using a laser cutting machine.

The yoke assembly and its final machining have been carried out at the LHEP, JINR, in July - August 2010 (see Figure 6). The superconducting wire was made at the Bochvar Research Institute in July 2010. Now the device for winding a curved coil is being manufactured at JINR.

The production of SC cable and winding of the coil at LHEP JINR is planned for September and October 2010.
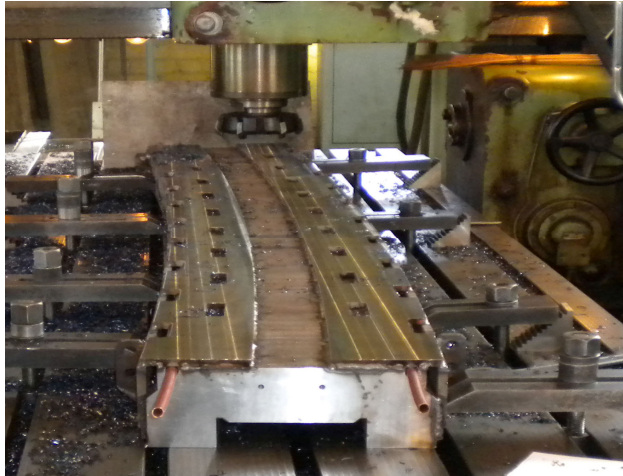
Figure 6: View of the Booster magnet yoke during processing on the milling machine.

The design of the twin bore straight dipole magnet prototype for the Collider was completed and the manufacturing process was started in August of this year. Completion of the full-size Collider magnet production is planned by the end of 2010. Cryogenic tests of both the prototype dipoles and production of the quadrupole magnet prototype for the Booster and the Collider are planned for 2011.

CONCLUSION

In accordance with our R&D program the design and manufacturing of the first NICA Booster and Collider full-size dipole prototype magnets are close to completion which is planned for October and December 2010, respectively. Cryogenic tests of both the dipole prototypes and production of the quadrupole magnet prototype for the Booster and the Collider are planned in 2011.

REFERENCES

[1] A. N. Sissakian et al., "The Project NICA/MPD at JINR: Search for the mixed phase of strongly interacting matter at Nuclotron-based ion collider facility" XXIII Int. Symposium on lepton and photon interaction at high energy, LP07, Daegu, Korea, 2007.

[2] Nuclotron-based ion collider facility. Available: http://nica.jinr.ru/

[3] A.M. Baldin, et al., "Nuclotron status report", IEEE Trans. Nucl. Sci., vol.NS-30, N4, 1983, pp.3247-3249.

[4] A. Butenko N. et al., "Design of the Nuclotron booster in the NICA project", Proc. of IPAC'10, Kyoto, Japan, 2010, pp. 681-683.

[5] H.G. Khodzhibagiyan, A.A. Smirnov "The concept of a superconducting magnet system for the Nuclotron", Proc. of the Twelfth Int. Cryogen. Eng. Conf., ICIC12, Southampton, 1988, pp.841-844.

[6] H. Khodzhibagiyan, N. Agapov, A. Kovalenko, A. Smirnov, A. Starikov "Development of fast-cycling superconducting magnets at JINR", Proc. of the Twenty First Int. Cryogen. Eng. Conf., ICIC21, CRYOPrague 06, vol.1, Prague, Czech Republic, 2006, pp. 113-116.

[7] A.M. Baldin, N.N. Agapov, V.A. Belushkin, E.I. D'yachkov, H.G. Khodzhibagiyan, A.D. Kovalenko, L.G. Makarov, E.A. Matushevskiy, A.A. Smirnov "Cryogenic System of the Nuclotron – a new superconducting synchrotron", Advances in Cryogenic Engineering N39, 1994, pp.501-508.

A 12 GHZ PULSE COMPRESSOR AND COMPONENTS FOR CLIC TEST STAND

A.A. Bogdashov, G.G. Denisov, S.V. Kuzikov[#], A.A. Vikharev, Institute of Applied Physics,
Russian Academy of Sciences, Nizhny Novgorod, 603950, Russia.
K.M. Schirm, I. Syratchev, CERN, 1211 Geneva 23, Switzerland.

Abstract

The X-band power test stand needed for preprocessing and testing of key CLIC RF components is being installed in the test facility CTF3. The test stand includes several 12 GHz XL5 klystrons (50 MW, 1.5 μs) and a pulse compressor (PC) of the SLED-I type to obtain over 120 MW peak power at 230 ns pulse length. A compact compressor of this type based on TE_{01}-TE_{02} beating wave in high Q-factor compressor's cavities has been designed, produced, and tested at low power level. For testing accelerating structures and so-called "CLIC recirculation principle" of its operation several -3 dB couplers, tuneable phase shifters, and variable power attenuators were also produced and tested.

DESIGN OF SLED-I PC

In order to provide at 12 GHz an efficient compression of rf pulses with parameters P_{inp}=50 MW, τ_{inp}=1.5μs, aimed to obtain P_{out}=120 MW, τ_{out}=230 ns, it is proposed to use a compact SLED-I pulse compressor [1]. The scheme of the well-known SLED-I is to be modified in order to provide necessary Q-factor of a storage cavity (Q_l≈25·10^4, Q_0≈1.5·10^5), because Q-factors of spurious modes in an oversized cavity could be comparable with that for operating mode. The compressor of such modified scheme consists of two identical cavities coupled by -3 dB couplers [2], each cavity is based on TE_{01}-TE_{02} beating wave waveguide which starts from single-mode TE_{01} waveguide and finishes by a waveguide of a big enough radius which is necessary in order to provide the mentioned high Q-factors (Fig. 1). The use of the beating wave due to inserted absorbers allows simple solutions for spurious mode suppression. Indeed, these absorbers

made of ceramics are placed out of the operating mode field while spurious mode fields are to penetrate perhaps in these absorbers. The design also naturally solves a problem of pumping ports which also play a role of selective elements and do not spoil Q-factor of the operating TE_{01}-TE_{02} mode (Fig. 2). Similar principle based on beating wave was used in 30 GHz TE_{01} mitre bends produced several years ago for CTF3 [3].

The beating wave (to provide deep modulation of surface field) consists of approximately 80% of the TE_{01} mode and only 20% of the TE_{02} mode. This mode mixture is produced sequentially by TE_{10} − TE_{01} "serpent-like" mode converter [3], and then the resulted TE_{01} mode is converted into the desired mode mixture by specially profiled horn (Fig, 3) which provides excitation level of other than TE_{01} and TE_{02} axisymmetric modes less than -30 dB (Fig. 3a). Mutual phase of the TE_{01} and TE_{02} modes at horn output is zero (this corresponds to flat phase front of a field localized out of waveguide wall) as it is seen in Fig. 3b.

The cavities in each channel are based on ∅100 mm copper waveguides. Length of each cavity corresponds to 3 beating periods (~600 mm).

The mentioned pumping port consists of a ring vacuum vessel which has a set of the 24 circular holes to pump a whole volume of the PC. The mentioned vessel is also partially filled by absorbers.

Fine frequency tuning in each of two channels is organized by means of independent, electric, stepping motors which allowed also manual control.
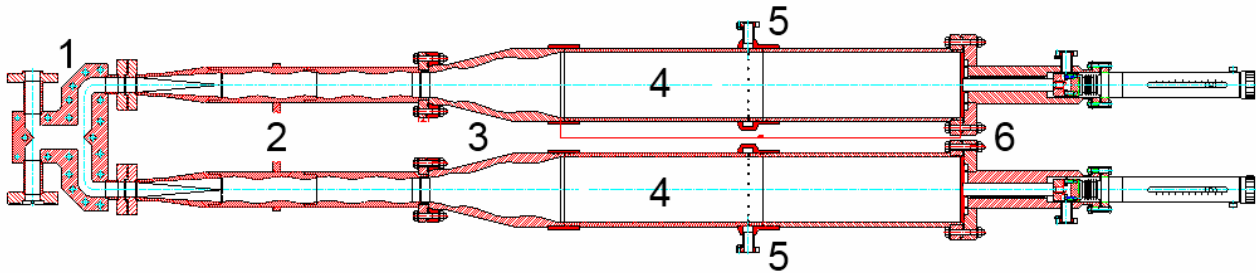
Figure 1: Technical drawing of 12 GHz PC: 1 - -3 dB coupler, 2- TE_{10} rectangular waveguide to TE_{01} of circular waveguide mode converters, 3 - TE_{01} to TE_{01}+TE_{02} mode converters (horns) with coupling irises in the beginning, 4 - circular waveguide cavities, 5- pumping ports, 6- plungers with stepping motors.

[#]kuzikov@appl.sci-nnov.ru

03 Linear Colliders, Lepton Accelerators and New Acceleration Techniques
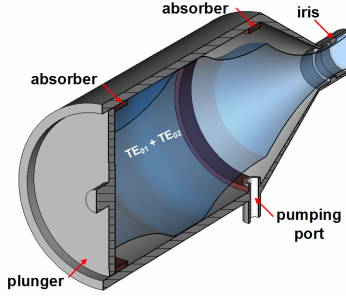
Figure 2: Internal view of PC cavity at TE_{01}-TE_{02} beating wave.

a)

b)
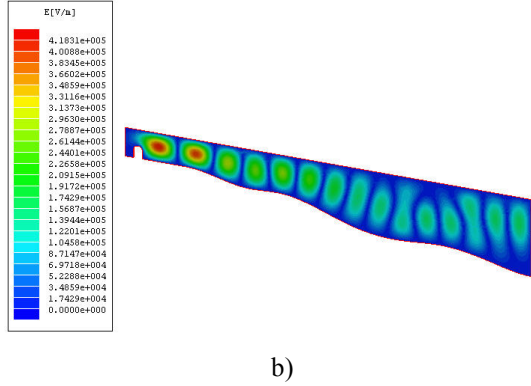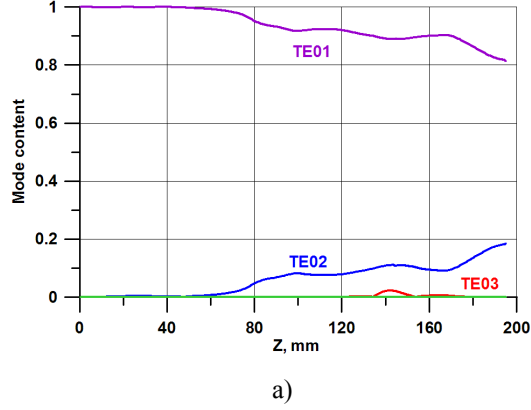
Figure 3: Mode content in TE_{01} – $TE_{01}+TE_{02}$ mode converter along its length (a) and field in storage cavity at horn and coupling iris (b).

PC LOW POWER TESTS

The described 12 GHz PC was produced (Fig. 4) and tested at low power level.
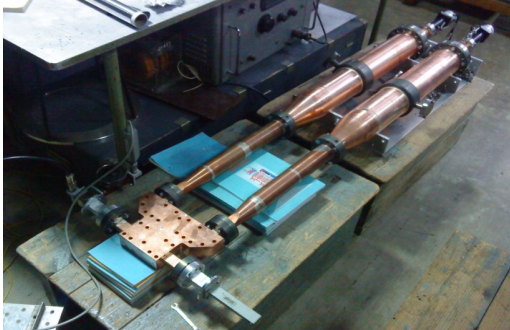
Figure 4: SLED-I type pulse compressor at cold testing.

The measured transmission characteristic S_{12} of the PC is shown in Fig. 5 by red curve. In order to find Q-factors and to simulate pulse compression we decided to fit the obtained measured curve by theoretical curve (blue curve in Fig. 5):

$$S_{12} = B \cdot \left(r - \frac{(1-r^2) \cdot \rho \cdot \exp(i2\pi \cdot n \cdot \Delta f / f_0)}{1 - \rho \cdot r \cdot \exp(i2\pi \cdot n \cdot \Delta f / f_0)} \right) \quad (1)$$

where f_0 =12 GHz is a central frequency, $1-r^2$ – is a coupling coefficient (transmission through coupling iris), ρ - is an attenuation in a PC cavity, n=80 – is a longitudinal number of variations of the eigen mode, B describes attenuation in waveguide network outside cavity.

The found parameters B, ρ, and r allowed to conclude that in fact the loaded Q-factor was Q_l=22·10^4-25·10^4. The own Q-factor was $Q_0 \approx 1.5 \cdot 10^5$, while the Ohmic Q-factor was estimated as $4 \cdot 10^5$. This difference is caused by diffraction losses in cavities (due to not perfect axial performance). On a base of the found parameters we also numerically simulated a pulse compression process (Fig. 6).
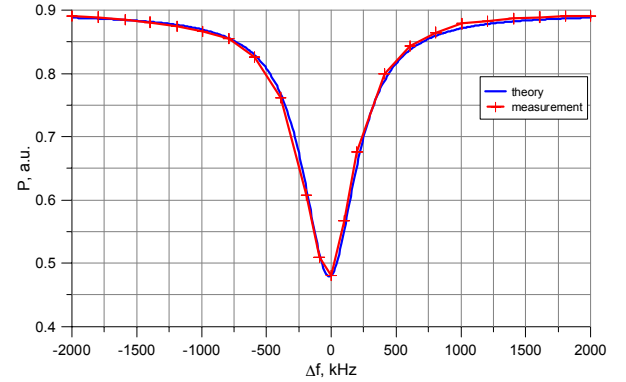
Figure 5: Fitting of the measured S_{12} PC characteristic by theoretical formula.
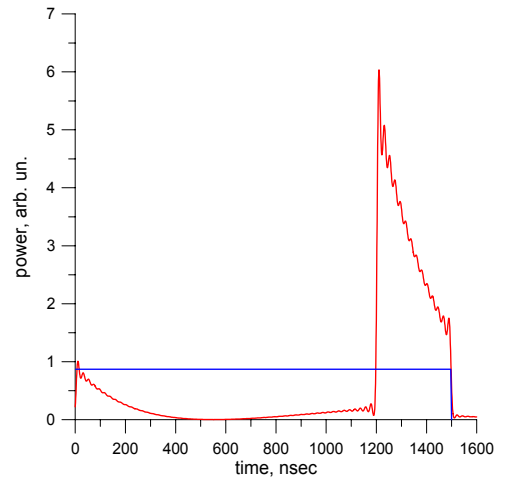
Figure 6: Simulation of pulse compression using the found PC parameters: input pulse (blue) and output compressed pulse (red).

03 Linear Colliders, Lepton Accelerators and New Acceleration Techniques

TUNEABLE PHASE SHIFTER AND VARIABLE POWER ATTENUATOR

Schemes of high-power phase shifter and variable power attenuator are shown in Fig. 7a and b correspondingly. Both components are based on so-called -3 dB coupler (phase shifter), or several such couplers (attenuator), and previously described mode converters. These allow to change phase (phase shifter) or to switch powers between output ports (attenuator). In order to provide tune ability, the components have electrically controlled plungers based on cut off waveguides with absorbing ceramics inside for mode selection. The plungers work at TE_{01} mode of a circular waveguide in order to avoid breakdown at high power level which could be caused by inevitable holes between plungers and a waveguide where its move.

a)

b)
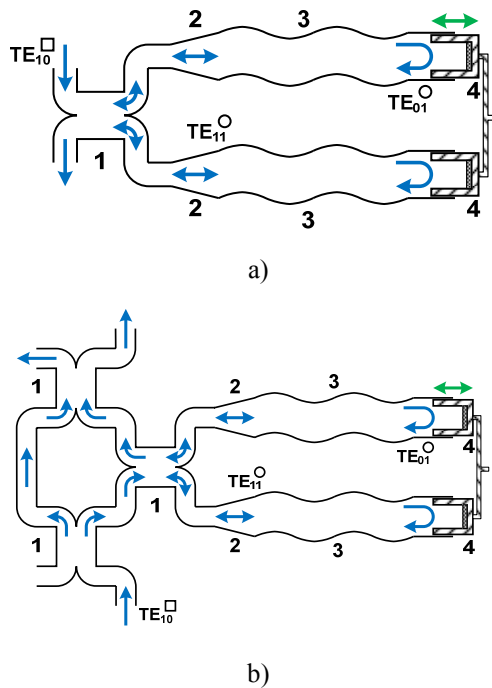
Figure 7: Scheme of phase shifter (a) and scheme of attenuator (b). 1 – -3 dB coupler, 2 – transducers of TE_{10} mode in rectangular waveguide to TE_{11} of circular waveguide, 3 – TE_{11} to TE_{01} mode converter, 4 – movable plungers.

Both components were produced of oxygen free copper in vacuum versions and were tested at low power level.

The measured, inserted phase of the phase shifter in dependence on position of the plungers is shown in Fig. 8, where it is seen that this phase can be varied between 0° and 400°. The measured S_{11} parameter was less than -24 dB.

Measurements of the attenuator were aimed to investigate powers as a function of plunger's position in all 4 ports (Fig. 9). One can see that output power can be switched between two output ports in region 1% - 90%. Total losses (Ohmic and diffraction) do not exceed 10%.

High-power experiments are being carried out now.
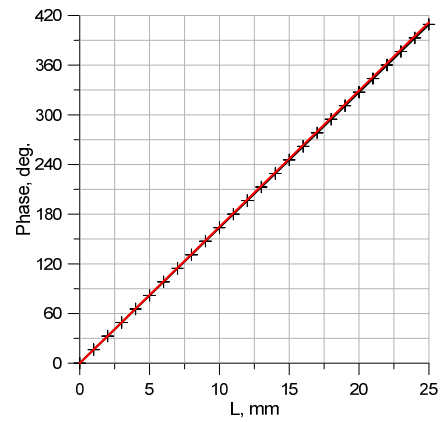
Figure 8: Measured (black crosses) and theoretical (red line) inserted phase by phase shifter.
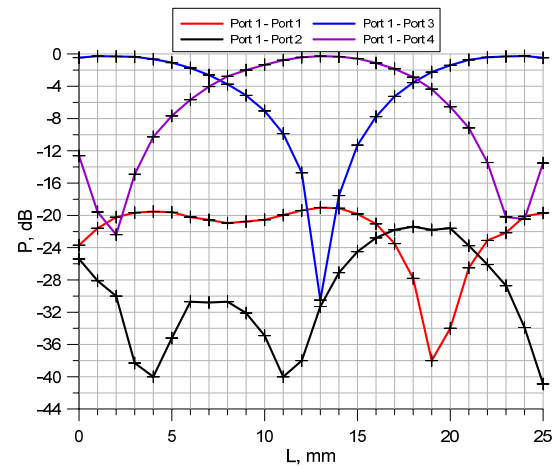
Figure 9: Measured powers in ports of the tested attenuator.

SUMMARY

The produced 12 GHz pulse compressor, phase shifters and variable power attenuators are acceptable for the CLIC high power test program.

REFERENCES

[1] F. Peauger, A. Hamdi, S. Curt, S. Doebert, G. McMonagle, G. Rossat, K.M. Schirm, I. Syratchev, L. Timeo, S. Kuzikov, A.A. Vikharev, A. Haase, D. Sprehn, A. Jensen, E.N. Jongewaard, C.D. Nantista, A. Vlieks, A 12 GHz RF Power Source for the CLIC Study, Proceedings of IPAC'10, Kyoto, Japan, THPEB053, pp. 3990-3992 (2010).

[2] S.V. Kuzikov, Status of CLIC activity at IAP, 2009 CLIC Workshop, (2009); http://indico.cern.ch/contributionDisplay.py?contribId=129&confId=45580

[3] Kuzikov S.V., Denisov G.G., Heikkenen S. et al. Study of Ka-Band High-Power Transmission Lines, AIP Conf. Proc., 7th Workshop on High Energy Density and High Power RF, Ed. by D.K. Abe and G. Nusinovich. Greece, Vol. 807. pp. 424–430, (2006).

03 Linear Colliders, Lepton Accelerators and New Acceleration Techniques

EXPERIMENT ON RF HEATING OF THE COPPER CAVITY – THE IMITATOR OF THE CLIC HIGH-GRADIENT ACCELERATING STRUCTURE*

S.N.Sedykh, E.V.Gorbachev, A.K.Kaminsky, N.I.Lebedev, E.A.Perelstein, N.V.Pilyar, T.V.Rukoyatkina, V.V.Tarasov, JINR, Dubna, Russsia
S.V.Kuzikov, N.Yu.Peskov, M.I.Petelin, A.A.Vikharev, IAP RAS, N.Novgorod, Russia

Abstract

The facility for joint experiments of JINR-IAP RAS has been commissioned to investigate the lifetime dependence of the CLIC high-gradient accelerating structure on the surface damage by repetitive high-power RF pulses. The facility is based on the 30 GHz JINR free-electron maser, which uses an electron beam of the induction linear accelerator LIU-3000.

Intermediate optical observations of the central ring allowed us to control the process of the damage evolution. The first damage of the copper surface have been observed after $1.6*10^4$ pulses with the pulse heating of 250ºK. After $6*10^4$ pulses the damage of the surface of the oxygen-free copper cavity became strong enough to cause regular breakdowns inside the test cavity.

INTRODUCTON

The project of the compact electron-positron collider CLIC with room-temperature accelerating structure is now developed by international collaboration headed by CERN [1]. The damage of the wall of the accelerating structure due to very intensive cyclic heating by short high-power RF pulses can be one of the most severe limits on the accelerating gradient or serve as a criterion for choice the materials for structure manufacturing [2]. Several experimental groups around the world have started investigations of this effect using different methods. Collaboration of JINR and IAP RAS has developed the experimental facility creating the RF pulse heating with temperature rise more than 200ºK. The expected lifetime of the copper cavity at such high temperatures was not more than $2*10^5$ pulses.

EXPERIMENTAL FACILITY

The facility is based on the 30 GHz 20 MW free-electron maser (FEM), which uses an electron beam of the induction linear accelerator LIU-3000 [3]. Radiation spectrum width does not exceed 10 MHz at pulse duration of 180 ns, repetition rate is 0.5-1 pulse per second.

The Gaussian wave beam from the FEM output waveguide is passing through the thin diagnostic film to the symmetrical two-mirror quasi-optical transmission line. After the oversized waveguide with an input vacuum window the radiation is transformed by the input horn from the Gaussian distribution into the TE_{11} mode and then – into TE_{01} mode by a specialized mode converter.

After the output horn the radiation is monitored by a detector with a dielectric waveguide and then it is fully accepted by the calorimeter (figure 1).

A specially designed test cavity- imitator of the CLIC accelerating structure - operates at the mode TE_{011} with zero electric field near the wall to prevent the inner discharge. It consists of two diaphragms and the inner ring with a rather thin edge. The most heated area is the inner edge of the ring. The quality factor of the cavity is 1500. The precise frequency matching of the cavity with the FEM oscillator can be achieved by changing the distance between the diaphragms. The test cavity module has its own vacuum system.

DATA ACQUISITION AND CONTROL SYSTEM

The distributed data acquisition system was constructed several years ago [4, 5] and it demonstrates her versatility and reliability. Recently the some new possibilities were added. The automatic stabilization sub-system [6], being exploited in test regime with local control during 1 year, is now installed inside the accelerator hall and completely switched to the remote control. The electron beam focusing system consists of 12 magnetic lenses along the accelerator and beam-line. Each magnetic lens is fed by individual stabilized current supply. Controller is connected to the PC and current supplies by means of RS-485 protocol, allowing controlling the individual lenses currents. Another new feature of the control system is an active automatic start-times control for the modulators of the induction linear accelerator. It means the local feedback between the synchronization sub-system (which was operating previously only in human-controlled regime) and modulator pulse control sub-system. The hardware core of the pulse control subsystem is a set of fast ADC with memory buffers and input multiplexors. The server program is now supplied by a module of pulse shape recognition, which calculates a time when a flat top of pulse is started. TCP server module of this subsystem is ready to send this data to the client module in synchronization subsystem. The synchronization program calculates the difference between measured value and desired one, and then sends the correction to the synchronization channel connected with corresponding modulator. The list of channels taking part in this regime can be corrected by the operator in on-line regime.

03 Linear Colliders, Lepton Accelerators and New Acceleration Techniques
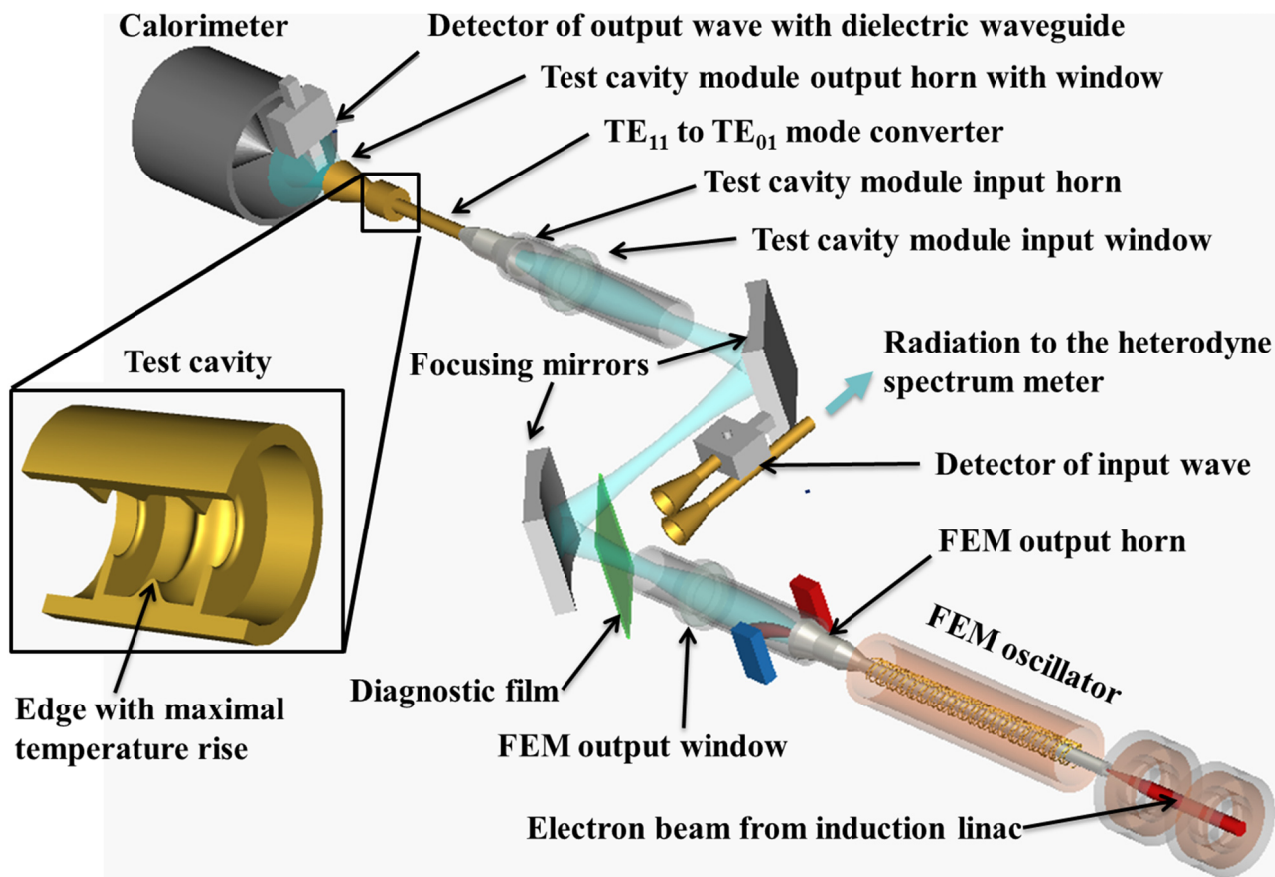
Figure 1. The layout of the experiment on 30 GHz copper cavity heating

EXPERIMENTAL RESULTS

Several full-scale experiments have been performed using created facility. Inner rings of the test cavity, which imitates the CLIC accelerating structure, have been manufactured from oxygen-free copper by turning with a diamond tool. Temporal and space variation of surface temperature inside the test cavity has been simulated numerically taking into account radiation parameters after the output horn. We have controlled a heating regime in each pulse, RF mode purity and the absence of the vacuum breakdown inside the test cavity. The maximal pulse temperature rise in different experiments was varied from 220ºK up to-250ºK with well-known decreasing along the surface according the distribution of near-surface magnetic field.

One feature of our experiments was the investigation of the dynamics of the surface damages appearance and development. We had controlled visually the surface of the inner ring after $1.6*10^4$, $3.2*10^4$, $4.8*10^4$ and $6*10^4$ pulses using optical microscope. After the experiment each ring has been cut into 6 sectors and investigated carefully by electron microscope. The first damages of a copper surface were observed after $1.6*10^4$ pulses [7]. After $6*10^4$ pulses the damage of the surface of the oxygen-free copper cavity became considerable enough to cause regular breakdowns inside the test cavity.

CONCLUSION

The experimental facility have been created consisting of the linear induction accelerator LIU-3000, the 30 GHz free-electron maser with the output power 15-20 MW, the wave transmission line, the diagnostics of an electron beam and RF radiation, the modernized system of data acquisition and control. The goal of these experiments was a correct choice of the material for the accelerating structure of the future electron-positron collider CLIC.

The distributed data acquisition system was constructed several years ago and demonstrated her versatility and reliability. Recently the some new possibilities were added, such as a remote control of the magnetic lenses power supplies and an active automatic start times control for the modulators.

The series of experiments have been fulfilled to investigate a copper cavity damages due to the repetitive action of the high-power RF radiation. A damage of a copper surface was observed after $1.6*10^4$ pulses with the pulse heating of 220ºK -250ºK. After $6*10^4$ pulses with a temperature rise of 250°K the surface of the oxygen-free copper cavity has been damaged strong enough to initiate the regular breakdowns inside the cavity.

03 Linear Colliders, Lepton Accelerators and New Acceleration Techniques
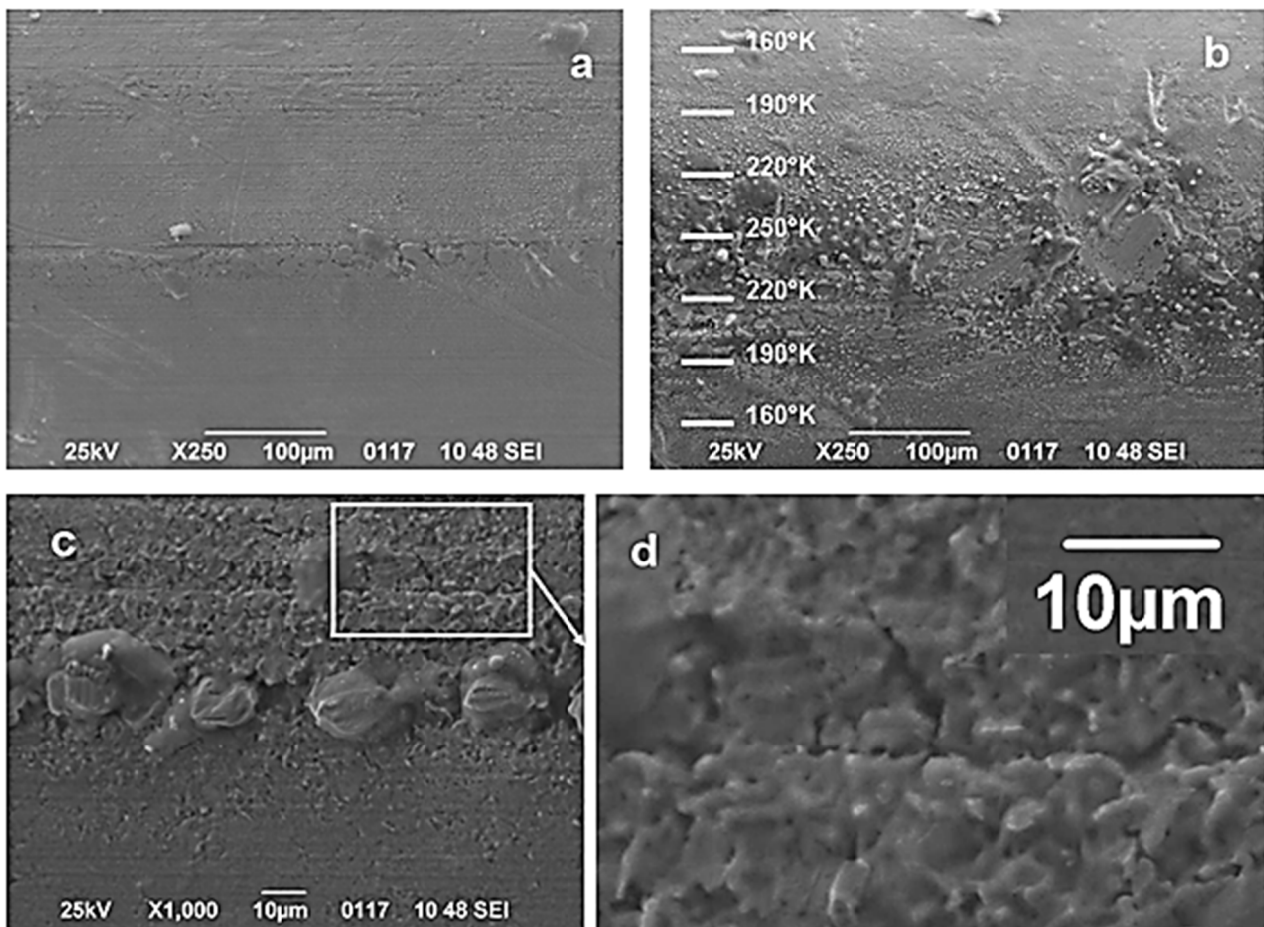
Figure 2. Scanning microscope image of the central ring surface before irradiation (a) and after = $4.8*10^4$ pulses with temperature rise up to 250°K (b). Images (c) and (d) show cracks observed after $6*10^4$ pulses with temperature rise up to 250°K.

The experimental results obtained using the facility can be useful not only for correct choice of the material for the CLIC accelerating structure, but for development of high-power microwave generators of any types if the magnetic field near the wall causes its high pulse heating [8].

REFERENCES

[1] I.Wilson - The compact linear collider CLIC – CERN AB-2004-100, CLIC Note 617, Dec. 2004, 12pp.

[2] D.P.Pritzkau, R.H.Siemann – Experimental study of RF pulsed heating on oxygen free electronic copper – Physical review special topics – accelerators and beams, 2002, vol. 5, p. 112002.

[3] A.V.Elzhov, N.S.Ginzburg, A.K.Kaminsky et al. - Test facility for investigation of heating of 30 GHz accelerating structure imitator for the CLIC project. - Nuclear Instruments and Methods in Physical Research, A, Volume A528, 2004, pp.78-82.

[4] N.I.Lebedev, A.V.Pilyar, N.V.Pilyar, et al. - Data acquisition system for lifetime investigation of CLIC accelerating structure - Dubna, Proceedings of NEC`2005, Dubna, JINR, 2006, pp.181-187.

[5] D.E.Donets, N.I.Lebedev, T.V.Rukoyatkina, S.N.Sedykh - Distributed control systems for modernization of JINR linear accelerators and HV power supplies of polarized deuteron source POLARIS – Proceedings of NEC'2007, Dubna: JINR, 2008.-pp.181-186.

[6] E.V.Gorbachev, V.V.Tarasov, A.A.Kaminsky, S.N.Sedykh - The Focusing Magnetic Field Stabilization System for LIU-3000 Accelerator – Proceedings of NEC'2007,- Dubna, JINR, 2008, pp.29-30.

[7] Yu.Yu.Danilov, N.S.Ginzburg, I.I.Golubev et al. - First full-scale result in CLIC-JINR-IAP RAS experiment on 30 GHz copper cavity heating -:Strong Microwaves: sources and applications, IAP RAS, Nizhny Novgorod, 2009, v.1, pp.230-235.

[8] M.Petelin, A.Fix – Comparison of metals in their steadiness to pulse-periodic microwave heating fatique – Vacuum Electronics Conference, 2009, IVEC 2009, p.163-164.

THERMAL BALANCE OF MULTILAYERED TUNABLE DIELECTRIC LOADED WAKEFIELD ACCELERATING STRUCTURE*

I.L. Sheynman[#], Saint-Petersburg ElectroTechnical University «LETI», Saint-Petersburg, Russia
I. Ya. Sheynman, St. Petersburg State Polytechnic University, St. Petersburg
A. Kanareykin, Euclid TechLabs, LLC, Solon, Ohio, U.S.A.

Abstract

Thermal balance of a cylindrical tuneable multilayer dielectric-filled accelerating structure is considered. One ceramic layer of the structure possesses ferroelectric properties, which allow the waveguide frequency spectrum to be tuned by varying the permittivity of the ferroelectric layer. Dielectric and induction losses in ferroelectric layer and a metal shell leads to a structure warming up and increasing temperature of the ferroelectric layer. Because of a temperature sensitivity of dielectric permittivity of ferroelectric layer this effect may detune the accelerating structure. On the basis of the analysis of a thermal regime of multilayered wakefield structure the medium and pulse temperature deviations are determined. A repetition rate of electronic bunch series should be chosen to limit temperature detuning.

INTRODUCTION

The method of dielectric wakefield acceleration of electrons is one of perspective directions of creation high gradient structures of modern linear accelerators. The methods based on the concept of wakefield acceleration in structures with dielectric filling, are now one of the most perspective in sense of possibility of creation высокоградиентных accelerating structures for the future generation of linear colliders. These structures which are object of intensive studying last years, can be excited both a high current electronic bunch, and an external source of powerful microwave radiation. At wakefield acceleration method high current (as a rule, 20–80 nC), short (1–4 mm) the leading electronic bunch, moving in the vacuum channel of the dielectric wave guide concluded in spending metal cover, generates TM01 mode of Vavilov-Cherenkov radiation which is used for acceleration of an electronic bunch of high energy, moving behind a leading bunch on the distance, corresponding to an accelerating phase of a wave.

In work [1] the structure analysis of wake fields and also induction losses in a metal cover was spent with reference to single-layered dielectric structure with the vacuum channel of rectangular geometry. In [2, 3] it is resulted experimental demonstration of tuneable structure with two-layer filling (a dielectric with dielectric permeability ε = 10 and a ferroelectric material with ε =500), and the maximum observable shift of frequency has made 160 MHz for accelerating TM01 fashions with frequency of 11.424 GHz. The analysis of losses of energy and a method of their decrease in structure is resulted in [4]. Research of possibility of creation of tuneable waveguides is conducted in work [5] with ferroelectric layers of cylindrical geometry.

Introduction of a ferroelectric layer between dielectric ceramic plates and a metal surrounding cover in a wave guide leads to management possibility its frequency spectrum. For the appendix of an external field operating a ferroelectric material the electrode serves. The choice of parameters of the ferroelectric layer – dielectric permeability and a thickness – is defined demanded for compensation of technological and temperature shifts by controllability of base frequency of a waveguide. Last is $\delta f = 2\Delta f / f_0$, where Δf – the greatest possible deviation of base frequency from settlement frequency f_0.

Presence located between a dielectric and a metal cover the ferroelectric layer with high value of dielectric permeability ε and rather big tangent of dielectric losses angle results as in increase of a share of the energy disseminated in the ferroelectric layer, and to additional induction losses in a metal cover of structure.

Last fact is caused by sharp growth tangential components of intensity of a magnetic field on a surface of a metal cover of the wave guide caused by rather high values of dielectric permeability of a ferroelectric material. As a result the contribution ferroelectrics and induction losses in the general losses of energy in system appears defining, and losses sharply accrue with growth of dielectric permeability of a ferroelectric material that limits an admissible thickness ferroelectric layer and limits possibilities of operative adjustment of frequency of accelerating structure with dielectric filling.

Total capacity of dielectric losses of energy in a ferroelectric material and a dielectric, and also the Joule losses connected with prompting of induction currents in a metal cover, can be presented as

$$w_s = \omega\varepsilon \tan\delta \int_V \mathbf{E}\cdot\dot{\mathbf{E}}\, dV + \frac{1}{2\sigma_m\Delta}\oint_{S_m} H_\tau^2 ds,$$

where $\varepsilon, \tan\delta, V$ are dielectric permeability, tangents of corners of dielectric losses and volumes of the dielectric and the ferroelectric material, H_τ is a tangential component of intensity of a magnetic field on border with an area S_m conductor, and depth of a skin-layer $\Delta = c / \sqrt{2\pi\omega\mu\sigma_m}$ is defined by frequency of an electromagnetic field ω and conductivity of metal σ_m, the point means complex interface.

THERMAL CALCULATION OF A MULTILAYERED WAVEGUIDE

For calculation of heat transfer in multilayered waveguide with an additional ferroelectric layer we will consider stationary distribution of temperature in the established periodic mode of gating of beams with the set period in time. We will accept following basic assumptions:

1. Heat generation doesn't depend on time and coordinate and is equal to the value in the given layer which is averaged on time.

2. The waveguide is infinitely long ($l >> R_w$)

3. Heat conductivity of separate layers of a waveguide λ_i are constant.

4. The transient behaviour isn't considered, only the stationary mode is calculated.

5. The beam moves along an axis of a waveguide and its electromagnetic field is axisymmetric. So, the temperature field is axisymmetric too.

In this case the temperature field is described by the stationary equation of heat conductivity with a heat generation source:

$$\frac{1}{r}\frac{\partial}{\partial r} r\lambda \frac{\partial T}{\partial r} + Q = 0 ,$$

where r – radial coordinate, λ – heat conductivity, $W/(m\cdot K)$, T is absolute temperature, Q is volume heat generation, W/m3.

Internal surface of a waveguide on border with the vacuum channel of radius R_c is heat-insulated:

$$-\lambda \left.\partial T/\partial r\right|_{r=R_c} = 0 .$$

The ideal contact condition is set between layers i and $i+1$ with different heat conductivity:

$$-\lambda_i \left.\partial T_i/\partial r\right|_{r=R_i} = -\lambda_{i+1} \left.\partial T_{i+1}/\partial r\right|_{r=R_i} .$$

On an external surface of a waveguide the boundary condition of 3rd type (heat exchange under Newton's law) is set:

$$-\lambda \left.\partial T/\partial r\right|_{r=R_{ex}} = \alpha\left(\left.T\right|_{r=R_{ex}} - T_{env}\right),$$

where α is heat transfer coefficient $W/(м^2 \cdot K)$, index «env» corresponds to ambient parameters (air in our case).

Heat transfer to environment it is carried out by free convection and radiation: $\alpha = \alpha_{conv} + \alpha_{rad}$ For a free convection on a horizontal surface of the cylinder the following formula is applied [8]: $Nu = A(Gr \cdot Pr)^n$, where

– $Nu = A(Gr \cdot Pr)^n$ where Nu is Nusselt number, R_{ex} is external radius of a metal cover of a wave guide λ_{env} – heat conductivity of air, Gr is Grashof number, Pr is Prandtl number, A and n is empirical constants. Constants A and n calculated by following correlations:

for $Gr \cdot Pr < 1 \cdot 10^{-1}$ $A = 0.5$; $n = 0$,

for $1 \cdot 10^{-1} < Gr \cdot Pr < 5 \cdot 10^2$ $A = 1.18$; $n = 0.125$,   for

$5 \cdot 10^2 \le Gr \cdot Pr < 2 \cdot 10^7$ $A = 0.54$; $n = 0.25$,   for

$2 \cdot 10^7 \le Gr \cdot Pr$ $A = 0.135$; $n = 0.333$.

Grashof number and Prandtl number are defined by

$$Gr = \frac{g\beta_T (2R_{ex})^3 \Delta T}{\nu^2} ; \qquad Pr = \frac{\nu}{a} = \frac{\nu C_p p \mu}{\lambda_{env} R T_{env}} ,$$

where g is a gravitational acceleration, β_T – thermal expansion coefficient (for ideal gas $\beta_T = 1/T_{env}$), ν – kinematics viscosity, м²/c; $a = \lambda_{env}/(\rho C_p) = \lambda_{env} R T_{env}/(p\mu C_p)$ – air heat diffusivity, ρ – air density, C_p – air heat capacity under constant pressure, J/kg·K; μ – molar mass, kg/mol; R – gas constant, J/mol·K; $\Delta T = T_{ex} - T_{env}$ – typical temperature drop.

For a characteristic range of differences of temperatures from 0.1 to 500 K which will be coordinated with the settlement data received more low $A = 0.54$; $n = 0.25$, whence we receive:

$$\alpha_{conv} = A\left(\frac{\lambda_{env}^3 g C_p p \mu \Delta T}{2R_{ex} R T_{env}^2 \nu}\right)^{\frac{1}{4}} .$$

For an estimation of radiating factor heat transfer we will use the Stefan –Boltsman law:

$$\frac{\partial W_{изл.}}{S_{ex}\partial t} = \sigma\varepsilon\left(T_{ex}^4 - T_{env}^4\right) = \sigma\varepsilon\left(T_{ex}^2 + T_{env}^2\right)\left(T_{ex} + T_{env}\right)\Delta T ,$$

whence we will receive $\alpha_{rad} = \sigma\varepsilon\left(T_{ex}^2 + T_{env}^2\right)\left(T_{ex} + T_{env}\right)$.

In case of the compelled water cooling by means water current through the helicoid tube wound on outer side of a wave guide, $\alpha_f = Nu\,\lambda/d$, where $Nu = 0.021 Re^{0.8} Pr^{0.43} \delta$, $Re = vd/\nu$, $Pr = \nu\rho c_p/\lambda$, $\delta = \left(Pr(T)/Pr(T_c)\right)^{1/4}$, d is diameter of a heat-removing tube, v is a speed of a water current on a tube, ν, ρ, c_p are a kinematical factor of viscosity, m²/s; density and a water thermal capacity.

The decision of the stationary equation of heat conductivity looks like:

$$u_i = u_{0i} - Q_i(r^2 - r_{0i}^2)/(2\lambda_i) ;$$

$$T_i = T_{i0} + \left(u_{i0} + \frac{Q_i r_{0i}^2}{2\lambda_i}\right)\ln\left(\frac{r}{r_{0i}}\right) - \frac{Q_i r^2}{4\lambda_i} + \frac{Q_i r_{0i}^2}{4\lambda_i} ,$$

where $u_i = r\,\partial T_i/\partial r$. Considering boundary conditions, for temperature gradients and absolute temperatures on borders of layers we will receive

$$u_{i0} = -\frac{1}{2\lambda_i}\sum_{j=1}^{i} Q_j \left(R_j^2 - R_{(j-1)}^2\right) ;$$

$$T_{i0} = T_{(i+1)0} - \left(u_{i0} + \frac{Q_i R_i^2}{2\lambda_i}\right)\ln\left(\frac{R_{(i+1)}}{R_i}\right) + \frac{Q_i\left(R_{(i+1)}^2 - R_i^2\right)}{4\lambda_i} .$$

On fig. 6 dependences of temperature on distance on the centre of a waveguide in the conditions of natural heat

03 Linear Colliders, Lepton Accelerators and New Acceleration Techniques

emission from a waveguide surface are shown. Calculations are spent for different repetition rates ν at the same thickness of a metal cover $\Delta_m = 10$ mm (fig. 1).
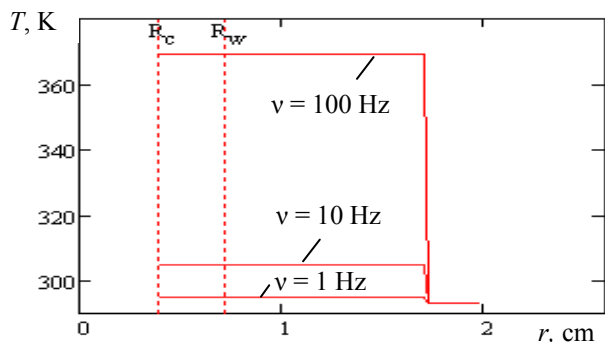
Figure 1: The dielectric waveguide with additional ferroelectric layer

From fig. 1 it is visible that distribution of temperature in dielectric and ferroelectric layers almost in regular intervals and essentially depends on factors: thickness of a metal cover of a waveguide and frequency of following of impulses series. The thermal emission in waveguide layers (especially in a ferroelectric material and on border with a metal cover) at passage of bunches considerably changes equilibrium temperature of structure. Considering that the ferroelectric material is a nonlinear material with dielectric permeability essentially depending on temperature, the obligatory preliminary analysis and the account of a thermal mode is necessary for waveguide calculation on the set of repetition rate of excitation multilayered wakefield structures.
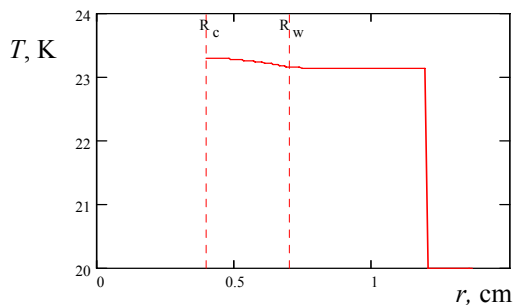
Figure 2: Dependence of temperature in cylindrical structure in the conditions of compelled heat emission

Temperature change on 10 K at repetition rate ν = 10 Hz and a thickness of a metal cover $\Delta_m = 15$ mm leads to change of dielectric permeability on 5 % and to respective alteration of the basic frequency of a waveguide on 1.6%. At repetition rate ν = 100 Hz and a thickness of a metal cover $\Delta_m = 10$ mm temperature change reaches 80 K that leads to change of dielectric permeability on 25% and to corresponding shift of the basic frequency of a wave guide on 4.9 %. Last value exceeds a range of adjustment of frequency of a waveguide the constant electric field enclosed to a ferroelectric material (2.92%) and can't be compensated.

The overheat of an internal part of accelerating structure in comparison with ambient temperature at repetition rate ν = 10 Hz and a thickness of a metal cover Δ_m=10 mm makes 15 K. Overheat of an internal part of accelerating structure in comparison with ambient temperature at repetition rate ν = 100 Hz and to a thickness of a metal cover Δ_m=10 mm makes 82 K. That is, at increase in repetition rate natural convective cooling of the waveguide appears insufficient and compulsory liquid cooling is required.

On fig. 2 dependence of temperature on distance on the centre of a waveguide in the conditions of compelled heat emission from a surface of a waveguide by means of the helicoids metal tube wound on outer side of the waveguide on which water proceeds is shown. Calculations are spent at repetition rate ν = 100 Hz, a thickness of a metal cover of the waveguide Δ_m = 5 mm, internal diameter of a heat-removing tube d = 2 mm, speeds of a current of water on a tube 1 m/s and length of cooled section of a waveguide 1 m.

The maximum overheat in relation to ambient temperature makes 3.8 K that practically doesn't render influence on dielectric properties of the ferroelectric material.

CONCLUSION

The analysis of a thermal mode multilayered wakefield structures shows that at designing wakefield accelerating structure on high current and high acceleration gradient the preliminary account of thermal balance of the waveguide is necessary for excitation. At increase in repetition rate for correct adjustment of a waveguide of natural cooling of accelerating structure insufficiently use of compulsory water cooling also is required.

REFERENCES

[1] Liling Xiao, Wei Gai, Xiang Sun. Field Analysis of a Dielectric-Loaded Rectangular Waveguide Accelerating Structure. Physical Review E, Volume 65, 2001, № 5 (1-9).

[2] A. Kanareykin, W. Gai, J. Power et al. Experimental Investigation of an X-band Tunable Dielectric Accelerating Structure. Proceedings Particle Accelerator Conference, PAC-2005, pp. 3529-3532, (2005).

[3] C.-J. Jing, A. Kanareykin, W. Gai, W. Liu, J. G. Power. 34.272 GHz Multilayered Dielectric-Loaded Accelerating Structure. Proceedings Particle Accelerator Conference , PAC-2005, pp. 1592-1594, (2005)

[4] A.D. Kanareykin, I.L. Sheinman. Analysis of Losses in a Rectangular Multilayer Dielectric-Filled Tunable Accelerating Structure // Technical Physics Letters, 2007, Vol. 33, No. 4, pp. 344–346.

[5] A. M. Altmark, A. D. Kanareykin, and I. L. Sheinman. Tunable Wakefield Dielectric-Filled Accelerating Structure // Technical Physics, Vol. 50, No. 1, 2005, pp. 87–95.

[6] V. P. Isachenko, V. A. Osipova, A. S. Sukomel. Heat transfer, Moscow, «Energy», 1975, 488 p.

03 Linear Colliders, Lepton Accelerators and New Acceleration Techniques

INTERBUNCH ENERGY EXCHANGE IN THE ACCELERATING SCHEME WITH UNIFORM CHARGE DISTRIBUTION*

I. Sheynman[#], Saint-Petersburg ElectroTechnical University «LETI», Saint-Petersburg, Russia
A. Kanareykin, Euclid TechLabs, LLC, Solon, Ohio, U.S.A.

Abstract

The efficiency of energy transformation in multi bunch accelerating schema with uniform charge distribution is considered. The transmitted energy to accelerated bunch taking into account driving bunch exit of relativism and settling them on the walls of the waveguide is determined. It is shown that accounting losses charge of generator beam increases passed accelerated bunch energy by eliminating exhaust bunches.

INTRODUCTION

The method of dielectric wakefield acceleration of electrons is one of perspective directions of creation high gradient structures of modern linear accelerators.

The basic element of a wakefield accelerator represents the cylindrical metal waveguide filled inside with a dielectric with the vacuum channel along an axis. The short electronic bunch with the big charge and concerning small energy of particles at flight on the vacuum channel generates a Cherenkov radiations TM01 mode with longitudinal component of electric field up to 100 MV/m. Following for it with a delay selected from the requirement of the coordination with the accelerating phase of a wake field, the accelerated bunch with a small charge is accelerated by it wake field. The given principle of acceleration has been successfully experimentally shown in Argonne National laboratory of the USA (ANL) and now intensively develops in a number of laboratories [1, 2].

The size of a charge of a driving bunch which can be passed through a waveguide, is limited by technical possibilities of the photoinjector, a created by a bunch spatial charge a Coulomb field and the sizes of the vacuum channel of a waveguide. In this connection to increase in an accelerating field in a waveguide instead of a single bunch apply a chain of electronic bunches. The accelerating scheme with a flat profile of bunches sequence (flat bunch train – FBT) is used for coherent addition of fields of separate bunches and increase in a total accelerating field.

Increase of efficiency of the accelerator is connected with increase in a share of energy of a driving bunch which is transferred to particles of an accelerated bunch [3] – [6]. The factor of transformation of energy R is defined as the ratio of the maximum increment of energy electron in an accelerated bunch to the maximum decrease of energy of driving bunches

$$R = \Delta W^+ / \left(\max \left| \Delta W^- \right| \right).$$

For maximization of factor of transformation of energy R the accelerating scheme with a triangular profile of a chain Gaussian bunches with the sequence period $d = m\lambda + \lambda/2$, where λ – base frequency of accelerating structure (Ramped Bunch Train – RBT) is used. Charges in a chain a profiled so that the first bunch in sequence possesses the least charge, and last – the greatest. All driving bunches in a chain are affected identical on amplitude concerning the small braking field E_z^-, however the accelerating field behind a chain E_z^+ – is considerable above. This factor provides high efficiency of transmission of energy from driving bunches sequence to an accelerated bunch that reflects numerically increase in factor of transformation which ideally one mode regime excitation of a waveguide, exact positioning of bunches and exact selection of charges can reach values $R = 2N$ where N – the number of driving bunches in a chain. High efficiency of transmission of energy from a chain of driving bunches to a field in a RBT-method is reached by considerable range of flight on which there is a selection of energy from driving bunches.
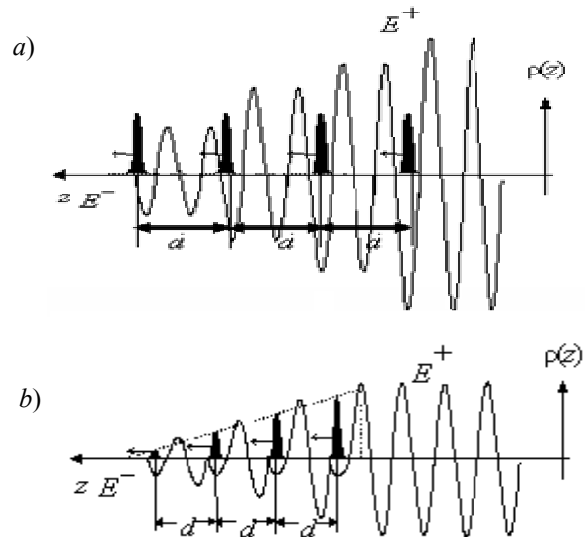
Figure 1: Multibunch acceleration schemes:
(a) FBT, (b) RBT

THE ANALYSES OF FBT

---

03 Linear Colliders, Lepton Accelerators and New Acceleration Techniques

ACCELERATION SCHEME

Unlike RBT scheme, in FBT scheme the braking fields operating on driving bunches, located on distance $d = m\lambda$ from each other, quickly increase with growth of bunch number in a chain, and, thus distance on which there is an energy extraction, much less, than in RBT scheme. The rate of acceleration reached in FBT scheme, exceeds rate of acceleration RBT scheme at equal maximum charges of driving bunches in 2N−1 time, and in N time at equal total charges of a chain, where N is quantity of driving bunches. At the same time FBT scheme shows much lower, than in RBT scheme, transformer ratio traditionally found as $R \approx 1 + 1/(2N+1)$, [4-6].

The reason of low value of transformer ratio in FBT scheme is coherent summation of the fields operating not only on the accelerated bunch, but also on driving bunches, in particular on the last from them.

Taking into account of radial dynamics of a bunch allows achieving in FBT scheme fuller energy extraction from a chain of driving bunches $\Delta W^- = \int eE^- dl$, at increase energy transferred to an accelerated bunch ΔW^+. The specified criterion demands some increase in range of flight L on which the bunch interacts with accelerating structure. This range however, appears much less, than in case of RBT.

The analysis of transverse dynamics high current bunches shows defining influence of a radial deviation of a bunch on restriction of range of flight L of bunches in a waveguide [2, 4-6]. Presence, along with longitudinal fields, transverse fields rejecting a bunch leads to a contact a bunch of walls of a waveguide, loss at first separate particles, and then and all bunch. Transverse instability limits longitudinal length of accelerating structure, and also defines distance on which transmission of energy from a driving bunch to an accelerated bunch is possible. At introduction of external focusing partially suppress transverse instability that leads to increase in range of flight.

At ultrarelativistic speed of particles of driving bunches influence of rejecting fields is expressed more weakly. In a case when longitudinal components of a field considerably exceed transverse fields, and also in the presence of external focusing, influence of rejecting field starts to be shown only near to an exit of bunches from a relativity, fig. 2a. Thus the greatest deviation undergoes last driving bunch of a chain, fig. 2b. As consequence, the particles which have left a relativity of the last driving bunch almost completely give the energy to an accelerated bunch and, as a result of action of rejecting fields, "sit down" on a waveguide wall.
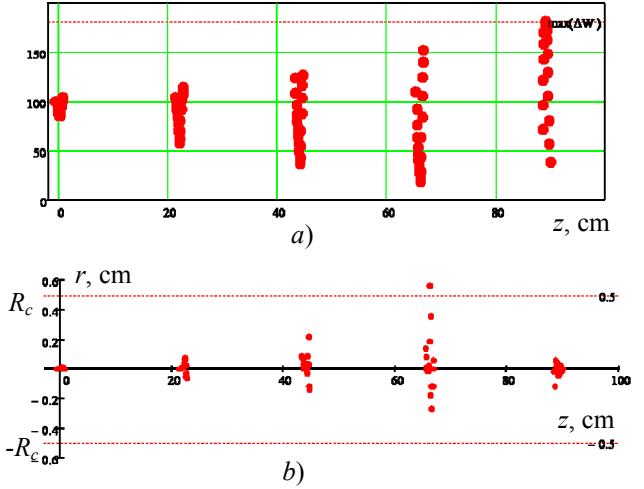
Figure 2: Energy (a) and displacement of bunches from a structure axis (b) at the moment of a contact of a waveguide wall

As a result after braking of last bunch we receive again FBT scheme, but already with $N-1$ driving bunch. Process repeats, yet won't give the energy the very first driving bunch.

For simplification of estimations we will consider that initial energy of driving bunches $W_0 \gg m_0 c^2$. Thus in the qualitative description of process of braking resulted more low we will neglect residual energy of bunches after their exit from a relativity.

In one mode regime of waveguide excitation intensity of a field, for Gaussian bunch in 2 times exceeds a field in a bunch, slowing down it movement. In FBT scheme the subsequent driving bunches are located on distance of an integer of lengths of waves of waveguide base frequency.

At the moment of an exit from a relativity of the last driving bunch, the energy transferred to an accelerated bunch makes $W_{1,ac} = 2NW_0/(2N-1)$. The distance passed by bunches makes

$$l_1 = \frac{W_0}{(2N-1)eE_1^-} = \frac{2W_0}{(2N-1)eE_1},$$ where $E_1^- = E_1/2$ is a field, braking the first driving bunch, E_1 is a field behind a single driving bunch, e – is an electron charge.

The remained energy in driving bunches of a chain at equal starting energy of bunches W0 forms sequence $W_{1,i} = 2W_0(N-i)/(2N-1)$, where i is a number of a driving bunch in a chain. Thus last driving bunch loses the energy W0 almost completely. The ratio of the energy transferred to the accelerated bunch $W_{1,ac}$, to the maximum loss of energy of particles of a driving bunch W_0 makes traditionally counted for FBT schemes transformer ratio $R_1 \approx 1 + 1/(2N+1)$, [4-6].

After loss of last driving bunch we receive again FBT scheme, but already with $N-1$ driving bunch. Transmission of energy to an accelerated bunch proceeds further while the remained energy will be not given by a penultimate driving bunch of a chain. In this time bunches pass distance $l_2 = \dfrac{W_{N-1}}{eE_{N-1}^-} = \dfrac{4W_0}{(2N-1)(2N-3)eE_1}$. The energy of an accelerated bunch received on this step makes $W_{2,ac} = (N-1)E_1 l_2 = \dfrac{4W_0(N-1)}{(2N-1)(2N-3)}$. Remained in driving bunches of a chain energy forms sequence $W_{2,i} = 2W_0\left(N-i-1\right)/\left(2N-3\right)$.

The specified process repeats consistently with other driving bunches of a chain. After braking of last of driving bunches the accelerated bunch gets energy

$$W_{ac} = \frac{2NW_0}{2N-1} + 4W_0 \sum_{j=2}^{N} \frac{(N-j+1)}{(2(N-j)+3)(2(N-j)+1)}\ .$$

The distance, demanded to a chain of bunches to full energy extraction, makes $l = 2W_0/\left(eE_1\right)$ and it is equal to distance on which completely loses energy the very first driving bunch.

Thus, the factor of transformation of energy at the fullest extraction of energy in FBT to the scheme makes

$$R = \frac{W_{ac}}{W_0} = \frac{2N}{2N-1} + 4\sum_{j=2}^{N} \frac{(N-j+1)}{(2(N-j)+3)(2(N-j)+1)}\ .$$

In case of a chain of four bunches full transformer ratio makes $R = 3.35$ that considerably exceeds calculated on a site of a way to an exit from relativity of last driving bunch $R_1 = 1.14$.

The rate of acceleration reached in FBT scheme with full extraction of energy of a chain of driving bunches, exceeds rate of acceleration RBT scheme at equal maximum charges of driving bunches in $(2N-1)R/(2N)$ time that for a chain of 4 bunches makes 2.93 times, and in $R/2$ time at equal total charges of a chain that for a chain of 4 bunches makes 1.676 times.

Thus, defined taking into account bunch dynamics the efficiency of FBT scheme appears considerably above, than by traditional consideration of movement till the contact moment a driving bunch of a wall of a waveguide.

REFERENCES

[1] Experimental demonstrations of wake-field effects in dielectric structures / W. Gai, P. Schoessow, B. Cole et al. // Phys. Rev. Lett. 1988. Vol. 61, № 24. P. 2756–2760.

[2] Wei Gai, Manoel Conde, John Gorham Power, Chunguang Jing. Considerations for a Dielectric-Based Two-Beam Accelerator Linear Collider. Proceedings of IPAC'10, Kyoto, Japan 2010. p. 3428-3430.

[3] Bane K. L., Chen P., Wilson P. B. IEEE Trans. Nucl. Sci. 1985. Vol. 32, № 11. P. 3524–3534.

[4] Laziev E. M., Tsakanov V. M., Vahanian S. S. Electromagnetic Wave generation with High Transformation Ratio by Intense Charged Particle Bunches // Preprint YerPhI–1040(3)–88, Yerevan. 1988.

[5] С. С. Ваганян, Э. М. Лазиев, В. М. Цаканов, Вопросы атомной науки и техники. Сер. Ядерно-физические исследования. Вып. 7 (15) 1990 г.

[6] Power, J.G.; Gai, W.; Sun, X.; Kanareykin, A. Transformer Ratio Enhancement Using A Ramped Bunch Train In A Collinear Wakefield Accelerator Particle Accelerator Conference, 2001. PAC 2001. v.1. p. 114-116.

[7] I. L. Sheinman and A. D. Kanareykin, Technical Physics, 53 (2008) 10.

ATTOSECOND AND FEMTOSECOND ELECTRON BUNCHES OBTAINABLE UPON FIELD EMISSION IN A COMBINED QUASI-STATIC AND LASER ELECTRIC FIELD

V. A. Papadichev*

Lebedev Physical Institute, RAS, Leninsky Prospect 53, Moscow 119991, Russia

Abstract

Short pulses of electrons of femtosecond and attosecond duration are necessary for numerous applications: studying fast processes in physics, chemistry, biology and medicine. Heating of spikes for single-pulse regime is several degrees and therefore it is possible to generate a sequence of electron bunches (up to 100–500 pulses). They can be used in diffractometry and after acceleration to 3–4 MeV for generation of short pulses of VUV and soft X-ray radiation in periodic fields or as a relativistic mirror.

INTRODUCTION

Modulation of electron beams at optical frequencies is promising for numerous applications in physics, chemistry, and biology [1-5]. As it was shown earlier [6 - 9], placing a needle cathode biased with a quasi-static potential into the laser focus permits to obtain a train of electron bunches of femtosecond and attosecond duration at the frequency of the laser (e.g., carbon dioxide or neodymium lasers).

The number of bunches in the train can be varied from one to dozens or hundreds by changing the envelope of the laser pulse. Such electron bunches can be used for time-resolved diffraction analysis of expansion, deformation and destruction of solids under high-power thermal and mechanical loads [4].

After additional acceleration, electron bunches can be applied for generation of tunable, coherent UV and X-ray electromagnetic radiation in the periodic structure of the electromagnetic field.

Moreover, such trains of electron bunches could serve as a relativistic mirror [5]. Interacting with a counter-propagating pulse of electromagnetic radiation (even wide-band), the mirror will select radiation at resonant frequencies and reflect it with frequency multiplication of $4\gamma^2$, where γ is a relativistic factor of accelerated electrons.

Small longitudinal dimensions of bunches (nm) and negligible energy spread $10^{-4} - 10^{-3}$ allow to obtain tunable, coherent UV and X-ray radiation of acceptable power for experiments with micro- and nanoscale objects.

It was shown in previous papers [6 - 9] that it is possible to obtain ≈ 10 as pulses with a laser of 1 μm wavelength if space-charge forces are negligible . Currents of

10 mA to 10 A can be obtained from single-spike cathode and upto 10 kA with a multi-spike cathode. Further bunching occurs due to velocity modulation in the bunch by laser electric field. In this paper, electron dynamics is analyzed more thoroughly for various emission velocities as the main cause of dispersion. Quasi-static and laser fields and emission velocity influence phase distribution of electrons in a bunch so their strengths were varied to reveal it.

Bunch evolution in a space-charge dominated regime was also studied for two cases: a plane (sheet) bunch and a spherical one corresponding to multi-spike and single-spike cathodes respectively.

CATHODE GEOMETRIES AND REGIMES OF OPERATION

Wide known Fowler-Nordheim formula was used to calculate currents one can obtain from needle cathode. In the field strength range $3 \cdot 10^7 - 2 \cdot 10^8$ V/cm the density of current from the cathode follows the Fowler-Nordheim law quite well and in the case of a copper cathode for the given field strength range is $1 - 7 \cdot 10^8 A/cm^2$. The formula was obtained for static field but can be applied for variable fields as well if the time of electron tunneling is much less than a period of a periodic electric field [10]. In the case of a combined quasi-static and variable electric field obtaining the exact solution of the Schrödinger equation is very difficult, but the criteria of validity of Fowler- Nordheim formula is the same: the tunneling time of electron should be much less than duration of variable field period.

Evaluating the field strength for copper cathode (barrier height 4.3 eV) and carbon dioxide laser ($\lambda = 10\mu m$) gives $E_{sum} > 10^8$ and $E_{sum} > 10^9$ for neodymium laser ($\lambda = 1\mu m$).

It should be noted that real applied laser fields may be much lower because of field enhancement on the spike tip with small radius of curvature [11].

Fig. 1, 2 and 3 are schematic representation of three types of devices. In 1 a single spike device: a cathode having a spike with a curvature radius ρ_c is at the focus of a laser. A quasi-static voltage V_0 is applied to the cathode. This creates at the spike a high-intensity electric field $E_{0n} \approx V_0/\rho_c$, where E_{0n} is the field perpendicular to the cathode surface (the distance between the cathode and the anode here is considered to be much greater than the curvature radius ρ_c).

---

* papadich@sci.lebedev.ru

03 Linear Colliders, Lepton Accelerators and New Acceleration Techniques
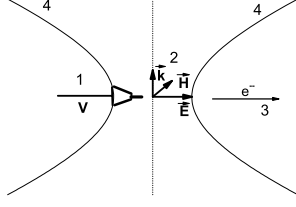
Figure 1: Schematic drawing of the device: 1 - cathode, 2 - EM-wave focus, k - wave-vector, E and H - electric and magnetic vectors of the wave, respectively, 3 - electron beam, 4 - focus surface where E = 0.

The schematic drawing of a multi-spike cathode is shown in Fig. 2. The spikes are placed with a period equal to laser wavelength λ in the direction of laser wave propagation in order to synchronize all electron bunches.
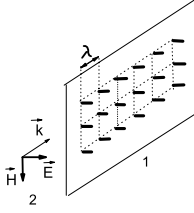
Figure 2: Schematic drawing of the multi-spike cathode: 1 - cathode, 2 - EM-wave , k - wave-vector, E and H - electric and magnetic vectors of the wave, respectively.
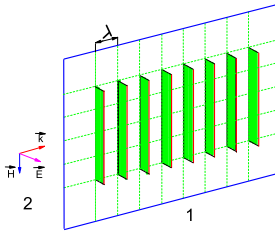
Figure 3: Schematic drawing of the blade cathode: 1 - cathode, 2 - EM-wave , k - wave-vector, E and H - electric and magnetic vectors of the wave, respectively.

BEAM DYNAMICS IN A COMBINED QUASI-STATIC AND LASER ELECTRIC FIELD

The length of an electron bunch near the cathode depends mainly on the ratio of amplitude of variable field to the value of quasi-static field, E_v/E_0. The duration τ for small laser electric field compared to quasi-static field $E_v << E_{st}$ may be nearly laser half-period $\tau \approx T/2$, and $\tau \approx T/8$ in the case $E_v >> E_{st}$. The mean propagation (directed) velocity depends mainly on E_{st}, so one can estimate initial bunch length

$$l_b \approx T\sqrt{\frac{2eV_0}{m}}, \qquad (1)$$

where e, m are electron charge and mass, V_0 is the voltage applied to the spike. One can see this in Fig. 4 as well as bunching of a part of the beam.
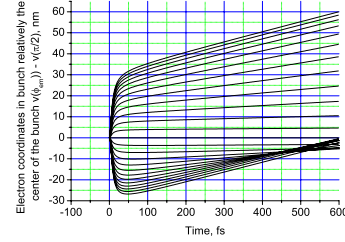
Figure 4: Bunching in the second half of the beam. $E_{st} = 1 \cdot 10^8$, $E_v = 5 \cdot 10^7$, $\lambda = 1\ \mu m$, $v_0 = 2 \cdot 10^3$ cm/s.

Laser electric field produces velocity modulation in the bunch depending on the phase variation from front to back electron emission. Main velocity dispersion is obtained during one-two periods of laser oscillations. Further, there are much smaller changes in velocity spread. This can be seen in Fig. 5, where velocities of electrons versus time in coordinate system of their electrostatic motion are shown.
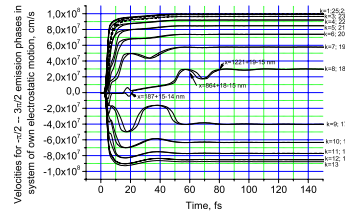
Figure 5: Time dependence of velocities of electrons emitted at various laser oscillation phases; k = 1 corresponds to $\phi = -\pi/2$, k = 25 - $\phi = 3\pi/2$. Field parameters are the same as in Fig4.

It should be noted that a formula given in [12] can not be applied because the condition that laser period should be much smaller than the period T_{st} of motion in potential field $2\pi/\omega << T_{st}$ is not satisfied. Quasi-static field falls sharply $E_{st} = E_0(\rho_c/r)^2$ with $\rho_c \approx \lambda/10$, i.e., by the factor 3 in 20 fs equal to 6 periods of neodymium laser.

It is necessary to take into account two factors when choosing an optimal set of parameters. First, the minimal bunch length in real beams depends also on instantaneous

03 Linear Colliders, Lepton Accelerators and New Acceleration Techniques

velocity dispersion. Form.2 [9] shows that the most favorable may be low velocities. Integration of the equation of motion shows that the time shift between $v_F = 1 \cdot 10^7$ and $v_F = 1.05 \cdot 10^7$ cm/s cases is less than 1 as. Small emission velocities require application of semiconductors for spike material, larger - metals.

Second, curves minima move to larger phases with increasing emission velocity. This means (especially for large E_v/E_{st} values) that useful phase region starting from curve minimum slips somewhat out of the most favorable region of bunch current curve $(0-\pi)$. One can use $\pi/2-\pi$ phase interval with small emission velocities and $1/3-1/5$ of it with large ones. Bunch current at emission for small E_v/E_{st} values has large duration $\approx T/2$ and not big variation of I_{max}/I_{min}. In this case, $\pi/2 - \pi$ interval is also useful. Subsequent bunching compensates bunch lengthening at emission.

SPACE-CHARGE EFFECTS

Two models can be studied analytically as the initial step. The first is one-dimensional treatment adequate to multi-spike or multi-blade cathodes which generates a plane (sheet) bunch. The second model is also one-dimensional and suitable for a one-spike cathode. A short emitted bunch can be approximated as a uniformly charged sphere, and this problem has also an easy solution.

The problem for a spherical bunch was treated in [9]. The total beam/bunch current with a multi-spike cathode of area S is S/λ^2 times larger than for a single-spike cathode, e.g., $\approx 10^3 I_b$ for $S = 30 \times 30 \mu m^2$. If a blade-type cathode is used, the current is $I_b S/(\rho\lambda)$, i.e., 10 times larger than for a multi-spike one. The longitudinal dimension of a plane bunch decreases faster and to a smaller value than for a spherical bunch because space-charge force does not increase during bunching contrary to the spherical bunch. Evolution of bunch duration is shown in Fig. 6 for initial bunch peak current $I_b = 10$ A of one beamlet (one spike).
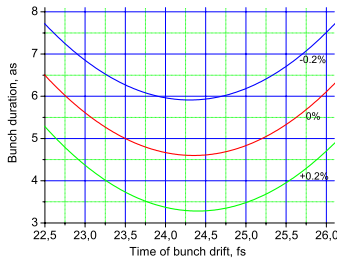
Figure 6: Final stage of plane bunch contraction. $E_0 = 4 \cdot 10^8$, $E_v = 8 \cdot 10^7$, $\lambda = 1\ \mu m$, initial one-spike current 10 A of 0.4 fs duration, $\delta v/v = \pm 0.2\%$.

POSSIBLE APPLICATIONS

Trains of short electron bunches may be useful for various applications. First, they can be applicable directly for excitation of atoms, molecules and micro- and nano-structures in researches in physics, chemistry, biology and medicine. By varying two-spike cathode geometry, one can obtain two successive bunches with regulated time interval between them to implement the pump-and-probe method.

Second, such beams can be used for time-resolved diffractometry of fast processes of thermal expansion or destruction in high-power-load experiments.

Third, it is possible to generate tunable coherent electromagnetic radiation of UV and X-ray spectra. Such options could be very effective if bunches were accelerated to MeV energies of electrons. This may be done by using modern schemes of acceleration by lasers. One can use further two ways: generation of coherent radiation by bunches in a periodic structure of electromagnetic field created by laser or using such a periodic structure of bunches as a multi-layer flying relativistic mirror.

Counterpropagating coherent radiation with wavelength λ will be reflected to produce coherent radiation with wavelength $\lambda_r = \lambda/(4\gamma_e^2)$. The necessary requirement for phasing radiation from all bunches is that in an electron co-moving system $d' = n\lambda'$, where d' is the distance between the bunches, λ' is the wavelength of radiation $\lambda' = \lambda/(2\gamma)$, and n is an integer.

REFERENCES

[1] P.Emma,Issues and challenges for short pulse radiation production, Proceedings of EPAC 2004.

[2] V.A.Lobastov,R.Srinivasan, and A.H.Zewail, Proc. National Acad. Sci. USA 102,7069 (2005).

[3] M.Merano, S.Sonderegger, A.Crottini et al., Nature 438(2005),p. 479.

[4] Time-resolved diffraction, Oxford University Press, 1997, ed. J.R.Helliwell and P.M.Rentzepis.

[5] S.V.Bulanov et al., Brief Physics Lett., LPI, 6 (1991) 9. T.Zh.Esirkepov, S.V.Bulanov, M.Kando et al.,PRL 103, 025002 (2009).

[6] V.A.Papadichev, A mathod to obtain modulated electron beam, Patent RU 2 269 877 C1, publ. 10.02.06, Bulletin 4.

[7] V.A.Papadichev, Femtosecond and attosecond bunches of electrons upon field emission in a combined quasi-static and laser electric field, Proceedings of EPAC08, p.2812.

[8] V.A.Papadichev, Accelerating and transporting attosecond and femtosecond bunches of electrons, Proceedings of EPAC08, p.2815.

[9] V.A.Papadichev, Evolution of electron bunches in a combined quasi-static and laser electric field, Proceedings of IPAC'10, Kyoto, Japan, p. 4372.

[10] L.V.Keldysh, JETP,47(1964),1945.

[11] Y.C.Martin, H.F.Hamann, and H.K.Wickramasinghe , Journal of Applied Physics 89, 5774 (2001).

[12] L.D.Landau and E.M.Lifshits, Course of theoretical physics, v. 1, chapter 5, sect. 30.

HOLLOW PHOTOCATHODE CONCEPT FOR E-GUN

M. A. Nozdrin[#], N. I. Balalykin, V. Ph. Minashkin, E. M. Syresin, G. V. Trubnikov, G.D. Shirkov,
JINR, Dubna, Russia
J. Huran, IEE SAS, Bratislava, Slovakia

Abstract

Photocathodes are the key devices for high-quality electron bunches generation. Such bunches are needed as initial electron source in contemporary linear accelerators. In all cases there are several important parameters: fast response time, quantum efficiency, long lifetime, low thermal emittance, minimal effect on RF properties of the accelerating system. In this paper the new concept of the photocathode is proposed – hollow (absolutely transparent for the laser beam) photocathode. Such cathode geometry allows quantum efficiency rising due to surface photoelectric effect which is concerned with normal to material surface wave electric field multiplier. Usability investigation experimental results for both hollow photocathodes made of bulk materials (Nb, Cu) and by thin-film technology (CsITe and diamond-like carbon as film on copper substrate) are given. After Nb hollow photocathode irradiation by a laser beam (λ = 266 nm, τ_{pulse} = 15 ns, frequency 1 Hz) a charge of 64nC was extracted. Backside irradiation radically simplifies laser beam targeting on emitting surface, accelerator equipment adjustment and allows photocathode working surface laser cleaning.

INTRODUCTION

Despite that fact that today considerable results in effective photocathodes (RF, SRF, DC) development and creation are achieved, the work on this line is underway [1, 2, 3].

Progress in basic photocathode parameters is possible by optimal usage of photoemission initializing laser beam potential.

Response time and emittance of electron beam increase upon thermoemission current appearing and rising, so there are several signatures that distinguish photoemission from thermoemission.

- Since upon photoelectric effect electron output is inertialless so current pulse lateness relative to laser pulse is absent. At that, for one-photon process, current pulse length is equal to laser pulse length. Lateness is absent at intensities less than 4 MW/cm^2 [4]. At intensities above 4 MW/cm^2 lateness is observed and photocurrent pulse broadening occurs, what is evidence of thermoemission process appearing. For impulses shorter than 10^{-11} s coverage of the photoelectric effect against a background of thermoemission can be expanded to intensities of $10 \div 100$ GW/cm^2 [4, 5]. In the picosecond range of pulse duration

thermoemission nature changes severely. With such durations electron subsystem is isolated out of the lattice and in view of small thermal capacity warms up nearly inertialless. So, for thermoemission under the picosecond pulses influence, current lateness against laser pulse is absent. Such thermoemission almost can not be observed separately from photoemission but can cause emittance increasing.

- As is well known, surface photoelectric effect is a typical vector phenomenon. Current magnitude is concerned with normal to surface wave electric field multiplier and dramatically depends on laser beam hade and polarizing angle. From the other side, thermoemission current completely depends on metal surface temperature which depends on accepted power.

It is interesting to investigate the following questions:

- Thermoemission minimization degree by cathode accepted power decreasing (by close to 90° laser beam to work surface hade using).
- Quantum efficiency increasing due to normal to cathode work surface electric field multiplier.

HOLLOW HOTOCATHODE AND EXPERIMENTAL RESULTS

Investigations were done by a stand [6] (Fig. 1) with a chamber vacuum of $2 \cdot 10^{-9}$ torr and gun anode voltage of 6 kV.

Monopulse YAG:Nd3+ (yttrium-aluminium garnet alloyed with neodymium) laser was used for cathode irradiation. Wavelength of generated UV-radiation was 266 nm, beam Ø6 mm, pulse energy less than 15 mJ.

Figure 1: Photocathode stand overview

[#]nozdrin@sunse.jinr.ru

03 Linear Colliders, Lepton Accelerators and New Acceleration Techniques

In this article the new concept is proposed: hollow photocathode – transparent for the laser beam cathode made like a washer with the width of 4-6 mm with a cone or cylinder aperture in the middle (Fig. 2). Work surface of the photocathode is the cone (or cylinder) generatrix. In the case of a cone obliquity is 1:50. Outcome diameter is ~2 mm.
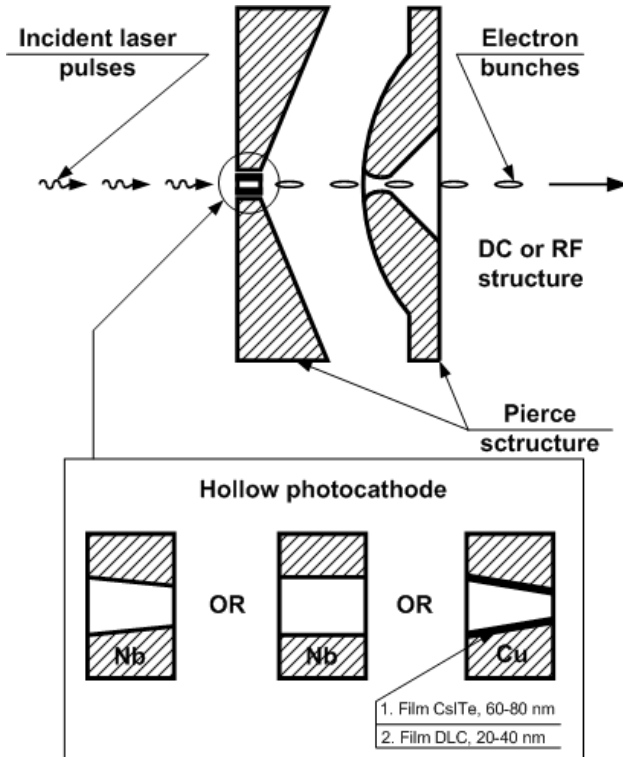
Figure 2: Scheme of the hollow photocathode operation.

Backside irradiation radically simplifies laser beam targeting on emitting surface, accelerator equipment adjustment and allows photocathode work surface laser cleaning.
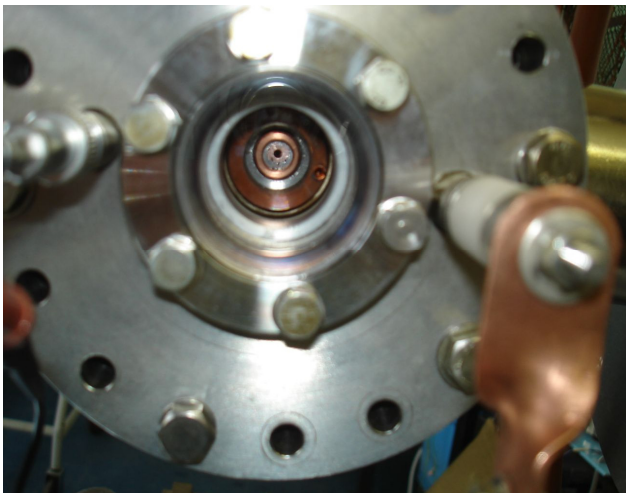
Figure 3: E-gun with hollow photocathode (back view).

Test cathode was made mechanically of niobium with purity 99.97. Work surface was grinded but not polished

and chemical etched. Before investigations all cathodes was laser cleaned by a Ø3 mm focused laser beam with 5-6 MW/cm^2 intensity.

Preliminary emission characteristics of common photocathode (Nb, Ø10 mm disk 1 mm thick, normal hade) investigations were done. Radiant flux density (intensity) was changed from 0.8 MW/cm^2 to 4.1 MW/cm^2 for unfocused beam and from 3.2 MW/cm^2 to 16.4 MW/cm^2 for focused beam, cathode surface was laser cleaned.

During unfocused beam irradiation up to obtainable intensity no thermoemission was observed.

As shown in Fig. 4, thermoemission is almost absent by intensity under 4.2 MW/cm^2. From intensity about 4,8 MW/cm^2 thermoemission appears – photocurrent pulse duration increases.
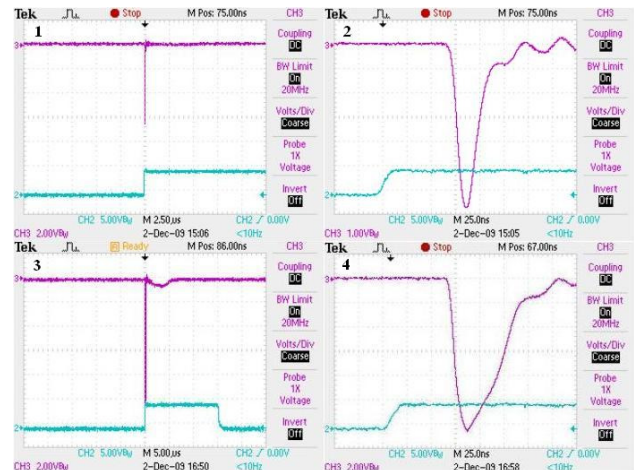
Figure 4. Nb solid photocathode photocurrent oscillograms: 1, 2 – 4.2 MW/cm^2 intensity, unfocused (for different time scales); 3, 4 – 4.8 MW/cm^2 intensity, focused (for different time scales).

Quantum efficiency was defined as a ratio of numbers of emitted electrons and injected laser photons. QE of common photocathode without thermoemission was not exceeded $2 \cdot 10^{-6}$ ($2 \cdot 10^{-4}$ %).

As shown in Fig. 5, QE of hollow Nb photocathode is not less than $6 \cdot 10^{-5}$ ($6 \cdot 10^{-3}$ %).

Figure 5. Quantum efficiency of hollow Nb photocathode

03 Linear Colliders, Lepton Accelerators and New Acceleration Techniques

Current density on the cathode was ≈ 70 A/cm^2. Extracted charge was Q $\approx$ 90 nC (I $\approx$ 6 A).

For the demonstration purpose hollow photocathodes with film work surface on copper substrate were produced (by plasmachemical precipitation in vacuum): CsITe (film thickness 80 nm) and DLC (film thickness 40 nm). After laser cleaning was measured QE of $7\cdot10^{-5}$ ($7\cdot10^{-3}$%) for CsITe and $1\cdot10^{-5}$ ($1\cdot10^{-3}$%) for DLC.

CONCLUSION AND OUTLOOK

Investigations have shown that hollow photocathode usage radically simplifies laser beam targeting on emitting surface, accelerator equipment adjustment and allows photocathode working surface laser cleaning.

Quantum efficiency of investigated hollow photocathodes is at least ten times more then QE of solid ones. So it seems to be interesting to continue experiments with hollow photocathodes.

In future it is planned to investigate:

- Hollow photocathodes with polished work surface;
- Operation life of the thin-film photocathodes. We can expect cathode lifetime increasing both because of cathode accepted power decreasing due to sliding beam incidence and because of back ion bombardment effect decreasing.

REFERENCES

[1] S. I. Anisimov, V. A. Benderskij, D. Farkash, Nelinejnyj fotojelektricheskij jeffekt v metallah pod dejstviem lazernogo izluchenija, UFN 122, vyp.2 (1977).

[2] S. I. Anisimov, B. L. Kapeliovich, T. L. Perel'man, ZhJeTF 66, 776 (1974).

[3] Xiangyun Chang et al. Recent progress on the diamond amplified photo-cathode experiment, PAC07, June 2007, p. 2044.

[4] Ilan Ben-Zvi et al. Superconducting photoinjector. Proceedings of FEL 2007, Novosibirsk, Russia.

[5] T. Rao et al. Photoemission studies on BNL/AES/JLAB all niobium, superconducting RF injector. Proceedings of 2005 Particle Accelerator Conference, Knoxville, Tennessee.

[6] N. I. Balalykin, V. Ph. Minashkin, M. A. Nozdrin, G. D. Shirkov, V. G. Shabratov. The stand for research of characteristics of photo- and thermoemission cathodes. Proceedings of International Workshop on Charged Particle Accelerators, NSC KIPT, Alushta, Ukraine.

[7] D. H. Dowelli et al. Cathode R&D for future light sources. SLAC-PUB-14002.

03 Linear Colliders, Lepton Accelerators and New Acceleration Techniques

TBA SCHEME WITH ION/PROTON DRIVING BEAM

E.G. Bessonov, FIAN LPI, Moscow, Russia

A.A.Mikhailichenko[#], Cornell University, LEPP, Ithaca, NY 14853, U.S.A.

Abstract

We are considering a two-beam accelerator (TBA) scheme with ion or proton beam as a driver. By comparison of the proposed scheme and the one with electron driver, we concluded, that TBA with ion/proton driver beam looks preferable. Existence of big proton accelerators in a few laboratories gives a boost for reconsideration of the baseline for post-LHC era. These Labs are FERMILAB, BNL, CERN and IHEP at Protvino, Moscow region. Protvino could emerge as one advantageous location and get stimulus for recovering the $600 GeV$-proton synchrotron in the existing $\sim 20 km$-long tunnel. This synchrotron was planned as a booster for $3 \times 3 TeV$ storage ring.

OVERVIEW

Many authors have developed TBA during the last decades [1]. CLIC is the mostly advanced representative of this kind [2]. The CLIC team does not give up even after International Technology Recommendation Panel made their decision in a favour of SC technology in August 2004. This is a good indication that some positive aspects are present in this idea. Obvious difficulty of TBA scheme associated with generation of electron driving beam (which forced recent change of CLIC operational frequency, by the way). To be useful for excitation of accelerating structure, the driving beam should have maximal content of spectral component of the driving current at the operational frequency. To some extent, TBA scheme with electron beam as a driver uses low impedance beam for transferring its energy to a high impedance one.

On the other hand, an idea of energy accumulation in a beam circulating in a storage ring and further usage of it for excitation of RF structure is an old one, discussed by G.I.Budker [3]. Later the idea to use the proton beam for excitation of the accelerating structure of electron linac was revealed in [4]. Here the proton beam excites *the same structure*, which is used for acceleration of electrons (or positrons). Naturally, this narrows the freedom of optimization of RF generation and further transferring it to the accelerating beam, as the transfer structure should take only a small fraction of power from the drive beam, while the accelerating structure should deliver as much power to the beam as possible. Usage of different structures for extraction of energy and for acceleration, linked together by the waveguides solves this problem.

The proton/ion drive beam is more advantageous, than the electron one is as follows: first advantage of the ion/proton beams is associated with their much lower emittance. These beams (or plans to have them) already

exist–that is another advantage. Other positive moment associated with lower gamma factor γ for the same energy $\sim mc^2\gamma$. Lower gamma factor allows easier manipulation of the beam in a longitudinal phase space, $\sim 1/\gamma^2$. High stored energy in the proton beam (up to few MJ) is more than enough for excitation of RF structure. For fixed radius of accelerator the intensity of synchrotron radiation $\sim \gamma^2$, which excludes the losses associated with SR for protons. These losses prohibit usage of electron beam with high-energy as a driver. On the other hand, the energy of proton beam is high, so the ratio of impedances of the driving beam to the main beam is closer to unity for the proton/ion driver. The longitudinal component of the transport current is the only important parameter in a process of RF generation in a transfer structure. Lower γ makes bunching with chicane easier $\sim 1/\gamma^2$ and decreases the longitudinal mass $\sim m\gamma^3$.

Basically, we raise the question for revision of TBA scheme in a favour of proton/ion driver beam. We shall use 30GHz-CLIC parameters as the reference ones [11]. All components developed for this project can be used for our scheme, delivering substantial savings.

PRINCIPAL SCHEME

Principal scheme of TBA driven by the Ion/Proton beams is represented in Fig.1.
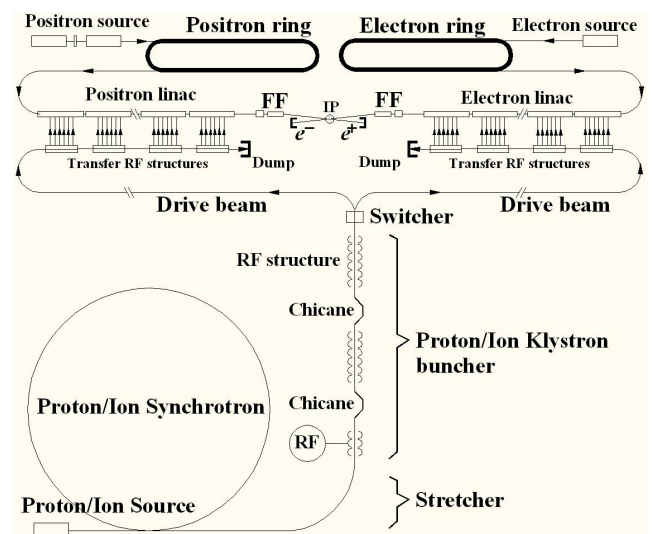
Figure 1: Principal scheme of the Complex proposed. FF stands for the Final Focus, IP-interaction point. RF stands for the RF generator feeding the first bunching structure.

Positron source with undulator could be easily introduced here in the same style as the one for ILC [5]. We consider the possibility of stacking polarized

_____

[#]aam10@cornell.edu

03 Linear Colliders, Lepton Accelerators and New Acceleration Techniques

positrons obtained by conversion of polarized electrons in a thin target as well [6].

Below we describe the key elements of this scheme.

Proton/Ion klystron buncher

Operation of the Proton/Ion klystron buncher is basically the same as a buncher in usual klystron. As the beam is relativistic, the drift space replaced by the chicanes with a big value of $R_{56} = \kappa = \gamma(\partial l / \partial \gamma)$. This is actually a multi-cavity klystron, where the accelerating structures serve as cavities. The ratio of DC to AC current could reach a factor of 2 with a multi-frequency bunching.

Details of klystron operation one can find anywhere, we will underline here some key points. Distribution of particles (protons/ions) in the longitudinal phase space $\{\Delta E, \vartheta\}$ can be characterized by a function of these two variables $f(\Delta E, \vartheta)$, where the energy deviation ΔE and the phase $\vartheta = \omega t$ are canonically conjugated; ⍵ stands for the frequency, t –for the time. These variables are so called characteristics of the equations of the longitudinal motion. Motion in a phase space could be described by the generation function, which is action, cinematically transferring these variables from one time slice to another one $(\Delta E, \vartheta)_1 \rightarrow (\Delta E, \vartheta)_2$ [7],[8]. Function $f(\Delta E, \vartheta)$ stays invariant under these transformations. Therefore, for description of the phase distribution in actual point, one needs cinematically transform the coordinates of individual particle to this point. In a good assumption, the distribution function could be factorized as $f(\Delta E, \vartheta) = f(\Delta E) \cdot f(\vartheta)$, and the Fourier component of current at the second point is

$$i_m = \iint f(\Delta E) f(\vartheta_2) e^{-im\vartheta_2} v\, d\vartheta_2 d\Delta E \qquad (1)$$

where v is a speed of particle. Initially, $f = 1/2\pi$, and $f(\Delta E) = \frac{1}{\sqrt{2\pi}\sigma_E} exp(-\Delta E^2 / 2\sigma_E^2)$, where σ_E stands for the local energy spread in the beam, variable $\vartheta_2 = \omega t_2$ is an actual phase at the second point. Integral (1) can be transferred as the following

$$i_m = \frac{1}{2\pi} I_0 \int |\partial \vartheta / \partial \vartheta_2| e^{-im\vartheta_2} f(\Delta E) d\vartheta_2 d\Delta E =$$
$$= \frac{1}{2\pi\sqrt{2\pi}\sigma_E} I_0 \iint e^{-im\vartheta_2} exp(-\Delta E^2 / 2\sigma_E^2) d\vartheta_2 d\Delta E \qquad (2)$$

where I_0 is the local current at the start point, $(\Delta E / E)_\sigma$ is the relative energy deviation. By introduction $X_{12} = k\kappa(eU_{eff}/E)$, $k = \omega / v$, $\vartheta_{12} = \omega l / v = kl$, U_{eff} is effective voltage of the first cavity (structure) one can rewrite (2)

$$i_m = \frac{1}{2\pi} I_0 e^{i\vartheta_{12}} \int exp(im(\vartheta_1 - X_{12}Cos\,\vartheta_1)) d\vartheta_1 \times$$
$$\times \frac{1}{\sqrt{2\pi}\sigma_E} \int exp(ik\kappa(\Delta E / E) - (\Delta E)^2 / 2\sigma_E^2) \cdot d\Delta E \qquad (3)$$

By integration one can find finally

$$i_m / I_0 = J_m(X_m) exp(-\tfrac{1}{2}(mk\kappa\sigma_E / E)^2) \qquad (4)$$

where $X_m = mX_{12}$, J_m is a Bessel function of m-th order.

The term with exponent reflects the reduction of AC current due to the energy spread in the bunch. The first harmonic, $m=1$ is the subject of interest; $J_1(X_1)$ has a maximum at $X_1 = 1.82$, $J_1 = 0.57$. For $\sigma_E/E \cong 0.001$, $E \approx 600 GeV$, $\lambda \sim 1cm$; debunching due to energy spread being low so the efficiency of this system will be ~57%. If the beam comes to the second cavity at the phase ωt_2, then the modulation provided by the second cavity becomes

$$|\Delta E / E|_2 Cos(\omega t_1 + \vartheta_{12} + X_{12} \cdot Cos(\omega t_1)) \qquad (5)$$

It is clear from (5) that many frequencies are generated, due to appearance of the cosine function as an argument of a cosine. The main result from this is the presence of second harmonic in the phase modulation due to *cascade* bunching. In fact, the second harmonic can be obtained in a dedicated RF structure (cavity) with second harmonic feed by the additional RF generator. As a result, the level of the first harmonic becomes 28% higher than in a case with single-stage bunching, brining efficiency to ~75%. The voltage in a bunching cavity required for obtaining the bunching coefficient ~1 defined from the equity

$$1 \cong X \cong k\kappa \cdot (eU_{eff} / E) \cong (2\pi / \lambda) \cdot \kappa \cdot (eU_{eff} / E). \quad (6)$$

The last expression gives the energy eU_{eff} ~3 MeV only. If we suggest that the length of RF structure is 3 m, then the electric field strength should be 1MeV/m, which could easily be realized (even with Superconducting RF). Practically there is no beam loading here.

The 600GeV beam can transfer its energy with ~75% efficiency to RF. If we suggest that the proton bunch population is $2 \cdot 10^{11}$ (see Table 1), then the energy of electron bunch with population $\sim 10^{10}$ can reach $\sim 1 TeV$ with 12% beam loading.

Chicane

Instead of straight section like in an ordinary klystron, used here is a chicane, with significant parameter

$$\kappa = \gamma(\partial l / \partial \gamma) = \int_0^s (D(s)/\rho(s)) \cdot ds, \qquad (7)$$

where $D(s)$ is a dispersion, $\rho(s)$ is a local bending radius in the magnets. For a three-magnet scheme [7]

$$\kappa = \frac{(2\pi)^2}{48}(1 + K_{bend}^2) \cdot s / \gamma^2 \qquad (8)$$

where $K_{bend} \approx eH_0 s / 2\pi n_p c^2$, H_0 is the bending field in the magnet, the s is a total length of the chicane. For example, if s=10m, $H_\perp = 2T$, then $K_{bend} \cong 2$ $\gamma \cong 600$, and $\kappa \cong 0.01m$. The lengthening due to the natural energy spread in the beam will be $\Delta l \cong \lambda_{ac} / 100$. The lengthening due to finite emittance can be made small as well.

Stretcher

At the stretcher, Fig.1, value of R_{56} allows reduction of local energy spread by controllable enlargement of the bunch length. The beam structure can be any, even as long the circumference of synchrotron, if RF turned on at the top. Each bunch allowed expansion of its length while

03 Linear Colliders, Lepton Accelerators and New Acceleration Techniques

the local energy spread is decreasing in the same proportion as the length growth.

Switcher

The switcher serves for re-direction of bunch-trains to the electron/positron wings of collider. It is basically, a fast kicker. Switcher located in a slightly asymmetric position with respect to the IP, for proper phasing.

Electron/Positron rings

Electron/Positron rings use the same ideology as the ring suggested in [9]. They have long straight sections filled with the wigglers circled with the multi-magnet bends. Wigglers have linear piecewise field dependence for reduction of nonlinearities [10].

Proton/Ion Synchrotron

In UNK, Protvino, the booster synchrotron was planned

for installation in the same main tunnel. That is why it has such a big circumference, very much desirable for our purposes, however. Parameters of existing synchrotrons represented in a Table 1. One other possibility is to fit a newly built synchrotron in existing main tunnel of appropriate Laboratory (IHEP-22.7km; CERN-26.67km; FERMILAB -6.28km; BNL-3.834km).

Stretcher

Typical bunch length in a proton accelerator is~1nsec (see Table 1). It is interesting that for 30GHz-CLIC scheme, the driving bunch train of 22 bunches was planned to be ~0.72 nsec long [11]. With the stretcher, the length of the train can be adjusted to any necessary value. Many designs can be found elsewhere, (see section *Chicane* above).

Table 1. Parameters of proton/ion synchrotrons

Laboratory/location	IHEP/Protvino	CERN/Geneva	FERMILAB/Batavia	BNL/Brookhaven
Installation	UNK-600	SPS	Main Injector	AGS
Energy	600 GeV	450 GeV	150 GeV	24.5(28) GeV
Circumference	20.77km	6.9km	3.319 km	0.807 km
Acceleration/flattop	11/20 s	4/3 s	2.5/<0.1 s	(0.1-2)/0.03 s
$\Delta E / E$ (4σ)	$2 \cdot 10^{-3}$	$1.16 \cdot 10^{-3}$	$6 \cdot 10^{-3}$	$2 \cdot 10^{-3}$
Population/bunch	$4.0 \cdot 10^{11}$	$1.15 \cdot 10^{11}$	$(0.6-1.2) \cdot 10^{11}$	$4.0 \cdot 10^{13}$
Number of bunches	30x12	72x4 (4200)	498/588 (max)	8(24)
Bunch length/c	-	1.8 ns	10 ns	1 ns
Bunch spacing/c	160 ns	25 ns	19 ns	224(336) ns
RF Voltage max	8 MV	7 MV	4 MV	147 kV
Emittance transv.	30 μm(norm)	3.5μm (450GeV)	40 μm (norm)	50 μm(norm)
Emittance longitud.	1 eV-s	1 eV-s	0.2 eV-s	0.3 eV-s

SUMMARY

Existences of big proton/ion synchrotrons in few laboratories give a new boost for reconsidering the baseline for the post LHC era. These Labs are FERMILAB, BNL, CERN and IHEP at Protvino, Moscow region. Protvino could emerge as the most advantageous place for recovery of the developed proton synchrotron in existing ~ 20 km-long tunnel. This synchrotron was planned to be a booster for 3x3TeV UNK complex [12].

REFERENCES

[1] K.Hubner, "*Two Beam Linear Colliders*", CERN/PS 92-43(DI), CLIC Note No.176, In Proc. of XVth Int. Conf. On High Energy Accelerators, Hamburg, July 20-24, 1992.

[2] W.Schnell," *The CLIC Study of an Electron-positron Collider",* CERN SL/92-51(RFL), CLIC Note 184, LC92 ECFA Workshop on e+e- Colliders, Garmisch-Partenkirchen, 25 July-2 August 1992.

[3] G.I Budker, In the Proceedings of Int. Symposium on Electron and Positron Storage Rings, Saclay, p.II-1-1; AE22, 346, 1967.

[4] E.A. Perevedentsev, A.N. Skrinsky, "*On the Possible Use of Intense Beams of the Big Proton Accelerators*

for Excitation of a Linear Accelerator Structure", Preprint BINP 79-80, Novosibirsk, 1979.

[5] ILC-REPORT-2007-001.

[6] E.G.Bessonov, A.A.Mikhailichenko, "*A Method of Polarized Positron Beam Production***",** EPAC96, Barcelona, June 9-14, 1996, Proceedings, p.1516.

[7] A.A.Mikhailichenko, "*Particle Acceleration in Microstructures Excited by Laser Radiation: Basic Principles",* CLNS-00-1662, Feb 2000. 89pp.

[8] E.G. Bessonov, "*The Evolution of the Phase Space Density of Particle Beams in External Fields*", Proceedings of COOL 2009, p. 91, Lanzhou, China; http://arxiv.org/ftp/arxiv/papers/0808/0808.2342.pdf.

[9] A.Mikhailichenko, "*Damping Ring for Generation of Positroniums and Investigation of Fermi Degeneration in Moving Beams",* PAC03-TPPG007, CBN-03-10, May 2003, 3pp.

[10] A.Mikhailichenko, "*Ideal Wiggler*", CBN-05-1, 12pp; PAC-2005-MPPT061, Proc. of PAC2005, Knoxville, Tennessee, 16-20 May 2005, p. 3511.

[11] B.Autin *et al, "CLIC Drive Beam Generation. A Feasibility Study",* CERN-PS-94-16-LP, CLIC-NOTE-228, 1994. 4pp., Proc EPAC94, p.43.

[12] UNK status, EPAC96, Sitges (Barcelona), 10-14 June, Proceedings, pp.407-409 (1996).

THE CDS PARAMETERS FOR PROTON LINAC WITH MODERATE HEAT LOADING

V.V. Paramonov[*]

Institute for Nuclear Research of the RAS, Moscow, Russia

Abstract

The Cut Disk Structure (CDS) was originally proposed for high energy linac in L-band or S-band frequency range. CDS combines simultaneously high coupling coefficient, high efficiency and small transverse dimensions. For lower particle velocity ($\beta < 1$) the structure loses in the effective shunt impedance Z_e value due to relatively thick partition with internal cooling channels. For moderate heat loading internal cooling is not necessary and partition thickness is limited only by mechanical rigidity. The structure equalizes in Z_e value with another bi-periodical structures and original CDS advantages come in front. Calculated CDS parameters for proton linac are presented.

INTRODUCTION

For high energy part ($\beta \geq 0.4$) of proton linac such well known normal conducting accelerating structures as Side Coupled Stricture (SCS) [1], Disk and Washer Structure (DAW), Annular Coupled Structure (ACS) [2] are realized. Topologically these structures can be considered as External Coupling Cell (ECC) structures, Fig. 1a with coupling cells removed from the beam axis. The septum thickness t_1 between adjacent accelerating cells is defined by structure rigidity and placement of cooling channels.

The Cut Disk Structure (CDS) has been proposed [3] ini-
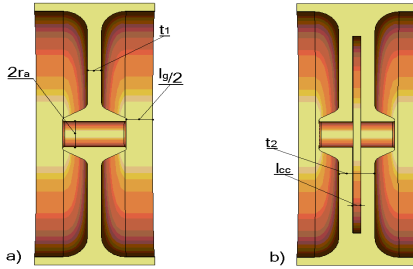
Figure 1: Accelerating cells in structures with External (a) and Internal (b) Coupling Cells - ECC and ICC.

tially for electron $\beta \approx 1$ linac with S-band and L-band operating frequency to join both high Z_e and coupling coefficient k_c values. Topologically initial CDS is the structure with Internal Coupling Cells (ICC), Fig. 1b. The coupling cell with the length l_{cc} is placed in the septum between accelerating cells. Cooling of the drift tube region is required for intense linacs with high heat loading at the structure. If internal cooling channels are required, the effective septum

thickness $\frac{2t_2}{\beta\lambda}$ is still high for ($\beta \sim 0.4 \div 0.5$) and CDS loses in Z_e value with respect to another structures.

Further CDS development [4] has shown preference of the four windows CDS option (CDS4W, Fig. 2c), as compared to two (CDS2W, Fig. 2b) or three windows - sufficient $k_c \approx (10 \div 15)\%$ value, a higher vacuum conductivity, a simpler cooling scheme, slightly higher Z_e value, absence of transversal field for coupling mode, strongly reduced possibility of multipactor discharge in coupling cells. For lower operating frequency $f_0 \geq 700MHz$ the
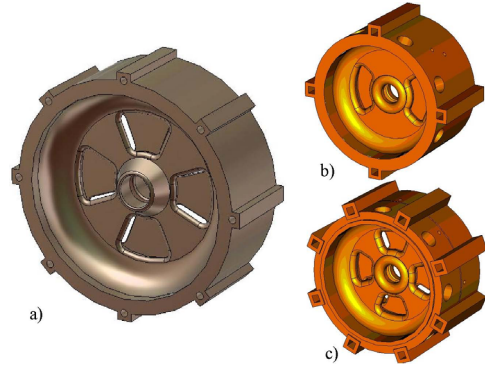
Figure 2: CDS structure for proton linac (a) and for electron intense linac, (b) - CDS2W, (c) -CDS4W.

relative septum thickness becomes smaller and CDS with internal cooling is competitive with another structures [5] in Z_e value and has big advantage of small transverse dimensions.

With the moderate average heat loading to the structure $\sim 3kW/m$ internal cooling is not strongly necessary. The septum thickness in CDS can be reduced.

CDS RF PARAMETERS FOR THIN SEPTUM

The CDS RF parameters were calculated for operating frequency $f_0 = 991MHz$ with aperture radius $r_a = 17mm$ and septum thickness $t_2 = 14mm$ for particle velocity range $0.4 \leq \beta \leq 0.8$. Results are plotted in Fig. 3. The CDS coupling value $k_c \approx (14 \div 17)\%$ appears naturally, due to original concept [3] and is well balanced with respect DAW coupling $k_c \approx 50\%$ and SCS-ACS one, $k_c \approx 5\%$.

Comparison with another structures in Z_e value is presented in Fig. 4. Coupling windows in CDS4W are placed in the region of the maximal magnetic field for accelerating mode, resulting in th surface decreasing and related

04 Hadron Accelerators
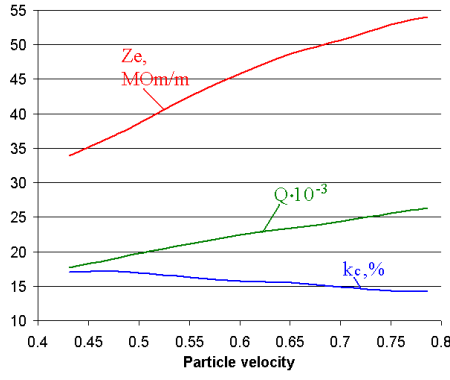
Figure 3: CDS RF parameters Z_e, k_c and Q for $0.4 \leq \beta \leq 0.8$ and thin septum $t_2 = 14mm$.

RF loss reduction. The calculated and the measured Z_e value for CDS4W is higher, than for ECC, Fig. 1a, without windows $k_c = 0$ (zero coupling) even for more thick CDS4W septum (Ze value for ESS, Fig. 1a, is calculated for $t_1 = 10mm$). The magnetic field enhancement at windows ends is not so strong, as compared to field enhancement at coupling slots in ACS, SCS, and higher coupling k_c is not connected with Z_e reduction, which normally takes place in SCS, ACS with the rate $\frac{\partial Z_e}{Z_e} \sim -2\%$ for $\delta k_c = 0.01$. In Fig. 4 Z_e valus for SCS and ACS are estimated with respect directly calculated Z_e for ECC (Fig. 1a) assuming this rate for Z_e reduction.

The calculated Z_e value for DAW in INR linac is from [6].
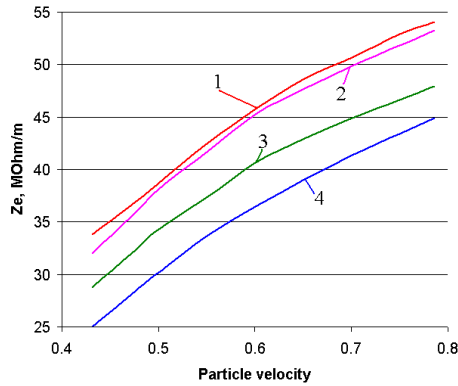
Figure 4: Z_e value for CDS (1), ECC $k_c = 0, t_1 = 10mm$ (2), SCS and ACS assuming $k_c = 5\%, t_1 = 10mm$ (3) and DAW (4).

The lower Z_e value, as compared to Z_e in SCS, is due to L-stems for washer support. Three L-stems in each DAW period do not disturb the electric field distribution for accelerating mode, but are placed in the region with a high magnetic field value and provide additional RF losses.

As comparison shows, see Fig. 4, the CDS4W with relatively thin septum exceeds equivalent structures in efficiency together with very good k_c value.

Calculated dispersion curves for operating and High Order Modes (HOM) are shown for CDS4W in frequency
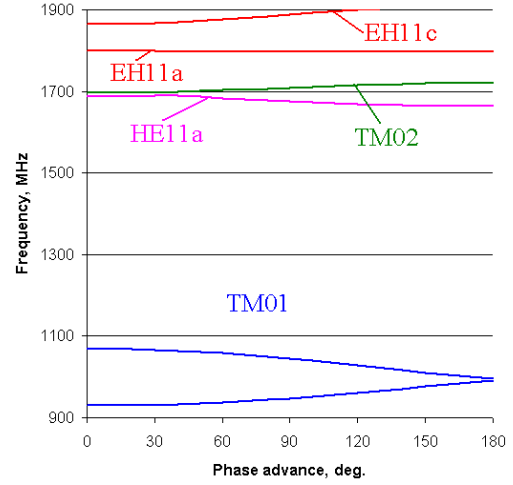
Figure 5: Calculated dispersion curves in CDS4W for operating and high order modes in frequency range $2f_0$.

range $f < 2f_0$ in Fig. 5. Due to small transverse dimensions $r_c \sim 0.33\lambda_0 \approx 110mm$ the nearest curve for HE_{11a} modes is well separated from the pass band of operating TM_{01} modes. Due to original CDS coupling concept, only operating TM_{01} modes are coupled significantly. The nearest HOMs are twice degenerated in frequency, due to CDS4W symmetry, and have field distributions concentrated either in accelerating cells (HE_{11a}, EH_{11a}) or in coupling cells, (EH_{11c}). In comparison with another structures, mentioned in this report, CDS has no HOM problem.

CDS4W EXTERNAL COOLING

The complete thermal-structural analysis for CDS4W with the thin septum has been performed according [7]. The moderate for modern intense proton linac value of average heat dissipation in the structure $3kW/m$ is assumed with $+10\%$ safety margins. In the consideration, the cooling circuit consists from 8 cylindrical cooling channels at outer cylindrical wall, Fig. 2a. The water flow velocity is $V = 1.5\frac{m}{sec}$, corresponding to the value of heat exchange coefficient $h = 9200\frac{W}{K^o m^2}$ and input water temperature $T_i = 27C^o$. The results of thermal-stress analysis are summarized in the Table 1.

The example of RF loss power distribution at the surface of the CDS cell is presented in Fig. 6a and shows not so essential heat flux enhancement at the ends of coupling windows. Corresponding temperature distribution is shown in Fig. 6b. The maximal surface temperature T_m is at drift tubes and exceeds the input water temperature at $\delta T_m = T_m - T_i \approx 10C^o$. Coupling windows in CDS reduce the own septum heat conductivity and δT_m value is approximately two times higher, as compared to ideal ECC cell, Fig. 1a, for the same cooling conditions. But the value $\delta T_m \approx 10C^o$ is well tolerable for stable structure operation.

The example of internal stress distribution, induced by
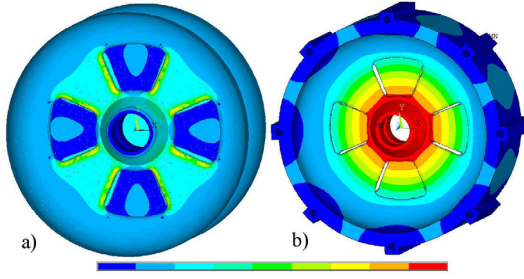
Figure 6: RF loss density (a) and temperature (b) distributions in CDS4W, $\beta = 0.6$.

Table 1: Summary for CDS thermal-stress analysis.

β	$\delta T_m, C^o$	σ_m, MPa	$\delta z_m, \mu m$	$\delta f_0, kHz$
0.43	8.5	0.21	9.8	-193.6
0.60	10.8	0.28	12.5	-199.4
0.78	12.6	0.36	14.9	-189.5

the temperature distribution in Fig. 6b, is shown in Fig. 7a. The maximal stress value σ_m, as one can see from the Table 1, is well below the yield stress σ_y for the annealed Oxygen Free Copper (OFC), $\sigma_y \approx 34 MPa$ [8]. The thermal induced distribution of longitudinal displacements with respect the cell center is shown in Fig. 8b. The maximal δz_m value is at the drift tube nose tip and $\delta z_m \approx 10 \mu m$, as one can see form the Table 1. This value consists from two parts. The first part is the own thermal expansion of the half drift tube and is of $\approx (3 \div 5) \mu m$. The second part is the displacement of the half drift tube as a whole due to thermal web deformation, see Fig. 8b. The second part dominates in the total drift tube displacement. As the result, the shift of operating frequency due to thermal structure expansion is rather significant, $\delta f_0 \approx -190 kHz$, see Table 1. It is not drastic value, but lower δf_0 is more convenient, because initial artificial structure heating for the first RF pulse input will be lower. The CDS cell shape can be changed slightly to provide such drift tube displacement, when two parts of displacement will compensate each other.

The thermal - stress analysis for CDS without internal
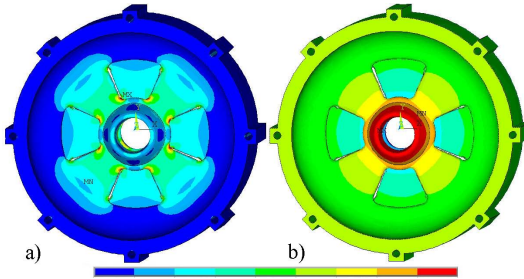
Figure 7: Internal stress (a) and longitudinal displacements (b) distributions in CDS4W, $\beta = 0.6$

cooling shows acceptable results for reliable operation with moderate average heat dissipation in the structure.

04 Hadron Accelerators

SUMMARY

Consideration shows, that CDS structure with the thin septum overlaps the equivalent structures for the same destination in all essential RF properties. In application with moderate average heat loading the thermal condition inside CDS cell are tolerable even without internal cooling. Internal stress values are well below the yield stress limit for OFC copper. The thermal induced shift of operating frequency is acceptable and can be reduced by further CDS shape optimization.

CDS transverse dimensions in comparison with another
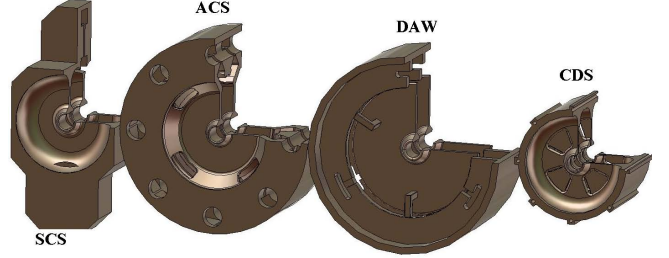
Figure 8: Comparison for transverse dimensions of SCS, ACS, DAW and CDS structures, $f_0 = 991 MHz, \beta = 0.6$

structures one can estimate from Fig. 8.
At present time consideration of RF superconductivity for the high energy part of the hadron linacs is usual. But may be the possibility of normal conducting structure application due to 'special purpose'. This case CDS structure is the promising candidate for further consideration.

REFERENCES

[1] E.A. Knapp et al., Standing wave accelerating structures for high energy linacs. Rev. Sci. Instr. v.39, p.31, 1968

[2] V.G. Andreev et al., Study of high-energy proton linac structures. Proc. 1972 Proton Linac Conf., p.114

[3] V.V. Paramonov. The Cut Disk Accelerating Structure for High Energy Linacs. Proc. 1997 PAC, v.3, p.2959, 1997.

[4] V.V. Paramonov et al., Design Parameters of the NC Booster Cavity for PITZ-2 Test Stand. Proc. 2004 Linac, p. 204, 2004

[5] V.V. Paramonov, The CDS Parameters for Medium Proton Energy Range. Proc. 2008 Linac, p. 924, 2008

[6] A.N. Liharev, V.M. Piroshenko, Calculated parameters of accelerating sections for second part of the meson facility linac. Proc. RTI AS USSR, n. 25, Moscow, 1976 (in Russian)

[7] A. Skassyrskaya et al., The complete 3-D coupled rf-thermal-structural-rf analysis procedure for normal conducting structures. Proc. 2002 Linac, p. 216, 2002

[8] D.P. Pritzkau, RF Pulsed Heating, SLAC-R-577, 2001

DESIGN OF THE NUCLOTRON BOOSTER IN THE NICA PROJECT

Andrey Butenko, Nikolay Agapov, Alexey Eliseev, Viktor Karpinsky, Hamlet Khodzhibagiyan, Alexander Kovalenko, Grigory Kuznetsov, Igor Meshkov, Vladimir Mikhaylov, Valery Monchinsky, Anatoly Sidorin, Alexander Smirnov, Grigoriy Trubnikov, Bogdan Vasilishin, JINR, Dubna, Russia

Abstract

NICA is the new complex being constructed on the JINR aimed to provide collider experiments with ions up to uranium at energy of 3.5x3.5 GeV/u. The NICA layout includes Electron String Ion Source, 6.2 Mev/u linac, 600 MeV/u booster synchrotron, upgraded Nuclotron and ion collider with average luminosity of 10^{27} cm^{-2} s^{-1}. The main goals of the Booster are the following: accumulation of $4\cdot10^9$ Au^{32+} ions; acceleration of the heavy ions up to energy required for effective stripping; forming of the required beam emittance with electron cooling system. The present layout makes it possible to place the Booster having 211 m circumference and four fold symmetry lattice inside the yoke of the Synchrophasotron (shut down in 2002). The features of this booster, the requirement to the main synchrotron systems and their parameters are presented in this paper.

INTRODUCTION

General challenge of the NICA facility is to achieve a high luminosity level of heavy ion collisions in a wide energy range starting with about 1 GeV/u. To reach this goal the NICA injection chain has to deliver a single bunch of fully stripped heavy ions (Au^{79+}) at intensity of about $1\div1.5\cdot10^9$ ions [1]. An effective stripping of the ions before injection into the Nuclotron requires their preliminary acceleration to an energy of a few hundreds of MeV/u. Therefore, realization of the NICA project presumes design and construction an intermediate booster synchrotron as new element of the NICA collider injection chain.

Before injection into the collider ring the Nuclotron RF system has to provide compression of the accelerated bunch. The beam parameters providing by linac-injector do not permit to realize the bunch compression with required efficiency. Thus a beam cooling at some stage of its acceleration is necessary. The Nuclotron ring has no convenient straight sections for location of the cooling system. Therefore the booster is only the place where the beam cooling can be realized. Additionally, the larger beam energy at the injection simplifies requirements to vacuum conditions in the Nuclotron beam pipe.

Correspondingly, the main functions of the intermediate heavy ion synchrotron, the Booster of the Nuclotron, are the following:

- Accumulation of $4\cdot10^9$ Au^{32+} ions that necessary to have after acceleration and stripping the beam intensity of $1\div1.5\cdot10^9$ ions ;

- Decrease of the ion beam longitudinal emittance at the energy of 100 MeV/u approximately by application of the electron cooling;

- Acceleration of the ions up to energy of 600 MeV/u that is sufficient for stripping of the Gold ions up to the charge state of 79+;

- Simplification of the requirements to the vacuum conditions in the Nuclotron owing to higher energy and charge state of the injected ions.

MAIN PARAMETERS OF THE BOOSTER

The huge yoke of the Synchrophasotron – the old 10 GeV proton synchrotron that was decommissioned in 2002, after the magnet winding is removed, gives a free tunnel of 4 x 2.3 m. The present layout of the Nuclotron and existing injection and extraction systems make it possible to place the Booster having 211 m circumference and four fold symmetry inside the yoke (Fig. 1).

Four large straight sections of the Booster will be used for injection from the linac, single turn extraction to transfer the beams into the Nuclotron, placing of the acceleration cavity and electron cooler. At the maximum field of dipole magnets of 1.5 T one can reach for heavy ions the energy of above 600 MeV/u that is sufficient for stripping of the ions up to the bare nucleus state (Table 1).

Table 1. Main parameters of the Booster

Ions	Au^{32+}
Circumference, m	211 m
Fold symmetry	4
Quadrupole periodicity	24
Injection/extr. energy Au^{32+}, MeV/u	6.2/600
Magnetic rigidity, T·m	$2.2 \div 25.0$
Dipole field, T	$0.17 \div 1.8$
Pulse repetition rate, Hz	0.25
Magnetic field ramp, T/s	1.2
Beam Injection type	Twice repeated, single turn
Beam extraction type	Single turn
Injection store duration, s	0.02
Vacuum, Torr	10^{-11}
Au^{79+} beam intensity, ions per pulse	1.5×10^9
Transition energy, GeV/u	3.98
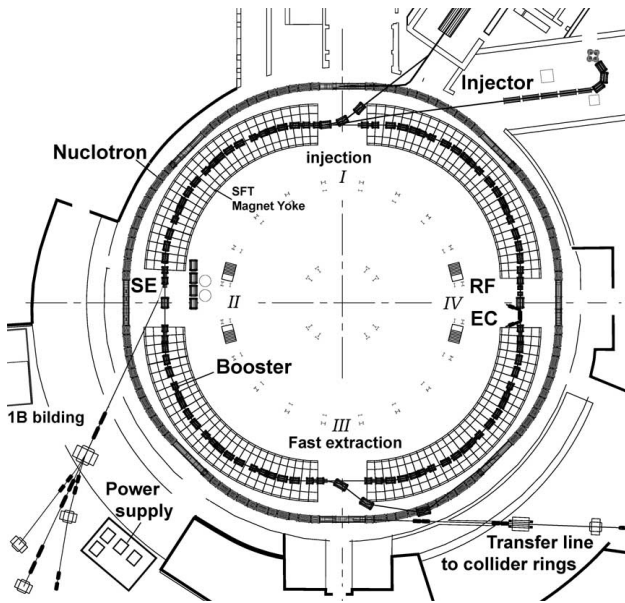
Figure 1. The Booster layout.

The Booster cycle (Fig. 2) is composed of five parts:
- the adiabatic trapping at fixed frequency (flat bottom),
- the beam acceleration at the forth harmonics of the revolution frequency up to 100 MeV/u and debunching,
- electron cooling during 1 s in the order to form the beam emittance required for successive acceleration and extraction from the Nuclotron,
- the beam bunching at the first harmonics of the revolution frequency together with the electron cooling,
- the beam acceleration at the first harmonics of the revolution frequency up to 600 MeV/u.
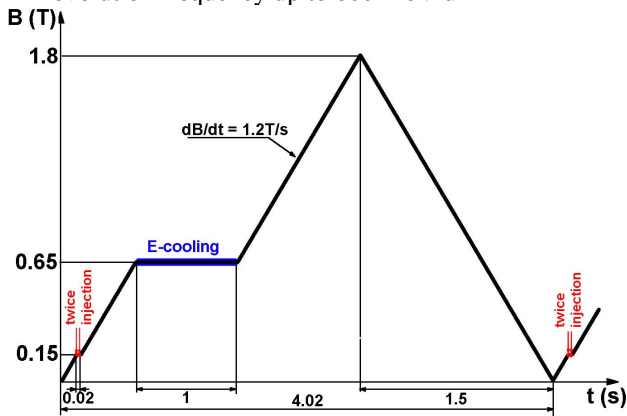
Figure 2. Booster cycle diagram, time is in seconds

The cycle duration is chosen to be approximately equal to the Nuclotron one, which is optimum for the collider feeding.

LATTICE & BEAM DYNAMICS

The chosen lattice (Table 2 and Fig. 3) contains 4 arcs. Each arc consists of 5 regular FODO cells with dipoles and one without them. One regular cell includes focusing and defocusing quadrupoles, one sector dipole and small

04 Hadron Accelerators

drift section used for location of magnetic correctors, beam position monitors, collimators and so on. The equipment of injection, ejection and acceleration are placed in the four large straight sections. In the vicinity of the working point there are only two systematic betatron difference resonances of the forth order: $3Q_x - Q_y = 12$ and $3Q_y - Q_x = 12$. Both are quite distant from the chosen tunes of $Q_{x,y} \approx 5.8$.
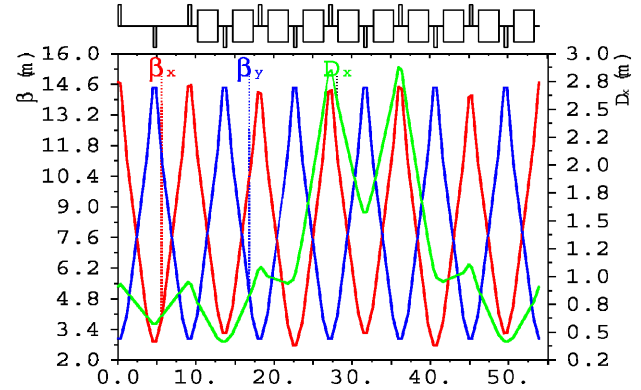
Figure 3. Betatron and dispersion functions for one SP.

Table 2. Lattice parameters of the Booster

Fold symmetry	4
Number of the FODO lattice cells per arc	6
Length of large straight sections, m	4.1×2
Length of small straight sections, m	0.65
Betatron tunes	5.8/5.85
Amplitude of β-functions, m	14.6
Maximum dispersion function, m	2.9
Momentum compaction factor	0.038
Chromaticity	-7.0
Horizontal acceptance, π·mm·mrad	400
Vertical acceptance, π·mm·mrad	70

The twice repeated single turn injection has duration of 7 μs per pulse with a betatron stacking in the horizontal plane. The injection scheme includes three bump magnets BM 1 ÷ 3 and one septum magnet SM (Fig. 4.). The bump magnets form the necessary local distortion of the closed orbit that decreases by two steps during injection time. The time interval between injection pulses is of 0.1 s.
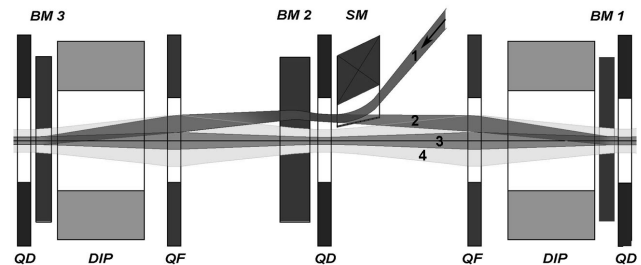
Figure 4. Injection system layout and beam orbits and envelopes: 1 – injected beam, 2 – 'bumped' one, 3 – circulated beam after first turn injection, 4 – after accumulation; BM 1÷ 3 – magnets for the bump formation, SM – injection septum magnet.

BOOSTER MAGNETS

The magnetic system of the booster consists of 4 quadrants. There are 10 dipole magnets, 6 focusing and 6 defocusing lenses in each one. The multipole correctors are also used to compensate the errors of both main (dipole, quadrupole) and higher (sextupole, octupole) harmonics of the magnetic field. The needed magnetic field induction in aperture is 1.8 T at maximum rigidity (Table 3). The increased aperture of both lattice dipole and quadrupole magnets is one of the main design features.

Table 3. Lattice magnets

Dipoles	
Number of dipoles	40
Maximum magnetic field, T	1.8
Effective field length, m	2.2
Bending angle, deg	9.0
Curvature radius , m	14.09
Vacuum chamber, mm^2	128 x 64
Quadrupoles	
Number of quadrupoles	48
Field gradient, T/m	19.7/-20.3
Effective field length, m	0.4

The requirements for dipole and quadrupole magnets of the Booster can be met using either – normal conducting or superconducting windings. The Nuclotron-type design based on a window-frame iron yoke and a saddle-shaped superconducting winding is chosen for the Booster.

The Nuclotron magnets include a cold (4.5K) window frame iron yoke and a superconducting winding made of a hollow NbTi composite superconducting cable cooled with two-phase helium flow at T = 4.5 K [2]. A further development of the technology was proposed [3] to increase the efficiency of the magnetic system (Fig. 5).
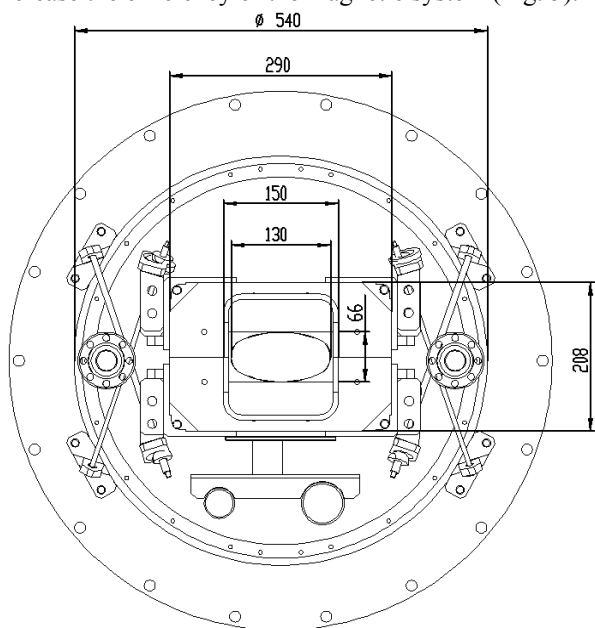
Fig. 5. Cross-section of the dipole magnet in cryostat.

04 Hadron Accelerators

In accordance with this proposal the single-layer winding bent dipole will be built to reduction the magnet cross section and AC losses in comparison with the straight double-layer winding dipole at the same aperture budget by means of the doubled structural current density in a winding. The use of curved (sector) dipoles instead of the straight ones in circular accelerators makes it possible to reduce the horizontal size of the magnet useful aperture that leads, in particular, to less AC losses.

ELECTRON COOLING

An optimal energy value for electron cooling was chosen with account the following effects:
1) beam lifetime limitation due to interaction with the rest gas ;
2) beam lifetime limitation due to recombination on the cooling electrons;
3) space charge effects appearing due to ion beam shrinking at cooling;
4) sufficiently short cooling time (≤1 sec);
5) space charge effect of electron beam on ion cooling;
6) an optimal use of the RF station;
7) cost of the electron cooler.

Numerical simulations of the cooling process showed that the cooling section of 4 m of the total length and electron current of 1 A provides required ion beam parameters at the ion energy of 100 MeV/u. The parameters are typical for conventional electron cooling systems, the energy corresponds to minimum range of the RF frequency variation (0.6 ÷ 2.4 MHz) during the Booster working cycle [4]. To adjust the cooling section with the SC magnetic system at minimum length, one plan to use a superconducting solenoid for the electron beam transportation, that is main technical peculiarity of the Booster cooler.

Design and construction of the Booster electron cooling system as well as the RF systems for the NICA rings will be provided in co-operation with BINP (Novosibirsk).

REFERENCES

[1] NICA Conceptual Design Report, JINR, January 2008. http://www.jinr.ru/
[2] Khodzhibagiyan H.G., Smirnov A.A., The concept of a superconducting magnet system for the Nuclotron, *Proc. of the 12th Int. Cryogen. Eng. Conf.*, pp. 841-844, 1988.
[3] H. Khodzhibagiyan, N. Agapov, A. Kovalenko, A. Smirnov, A. Starikov, Development of fast-cycling superconducting magnets at JINR» *Proc. of the CRYOPrague 06*, Prague, July 2006.
[4] I.Meshkov, A.Sidorin, Electron cooling, NIM A 532 (2004), pp. 19-25.

INJECTOR COMPLEX OF THE NICA FACILITY

A.O.Sidorin, A.V.Butenko, E.E.Donets, E.D.Donets, A.I.Govorov, V.V.Kobets, V.A.Monchinsky, I.N.Meshkov, G.V.Trubnikov, V.V.Fimushkin, JINR, Dubna, Russia, A.Belov, INR, Moscow, Russia, O.K.Belyaev, A.P.Maltsev, Yu.A.Budanov, I.A.Zvonarev, IHEP, Protvino, Russia, V.V.Kapin, MEPhI, Moscow, Russia

Abstract

The injector complex of the NICA facility consists of existing Alvarez-type linac LU-20 and new heavy ion linac HILac. The LU-20 is under modernization now, the HILac will be constructed during coming years. Parameters of the accelerators are presented.

INTRODUCTION

General goal of the NICA/MPD project under realization at JINR is to start in the coming 5÷7 years an experimental study of hot and dense strongly interacting QCD matter and search for possible manifestation of signs of the mixed phase and critical endpoint in heavy ion collisions. The Nuclotron-based Ion Collider fAcility (NICA) and the Multi Purpose Detector (MPD) are proposed for these purposes. The NICA collider is aimed to provide experiment with heavy ions like Au, Pb or U at the kinetic energy range from 1 to 4.5 GeV/u with average luminosity of 10^{27} cm^{-2}·s^{-1} and to provide collisions of light ions in the total energy range available with the Nuclotron.

The goal of the NICA project is construction at JINR of the new accelerator facility that consists of [1]:

- cryogenic heavy ion source of Electron String type (ESIS),

- source of polarized protons and deuterons,

- the "old" linac LU-20,

- a new heavy ion linear accelerator (HILac),

- a new superconducting Booster-synchrotron,

- the existing proton synchrotron Nuclotron,

- two new superconducting storage rings of the collider,

- new set of transfer channels.

Two acceleration and stacking chains of heavy ions and polarized protons and deuterons are pressumed:

- ESIS →HILac →Booster →Nuclotron → Collider

- Source of polarized ions→L U-20 →Nuclotron →Collider

The main elements of the NICA injection complex (source of polarized ions, LU-20, ESIS and HILac) are described in this paper.

POLARIZED ION SOURCE

Presently the maximum achieved intensity of polarized beam in the Nuclotron is about $2 \cdot 10^8$ particles per cycle.

The main direction of work aimed at increase of the intensity is connected with the design and construction of a new high current polarized ion source with charge-exchanged plasma ionizer (IPSN) based on the equipment of CIPIOS polarized proton and deuteron source transferred to Dubna from Bloomington (Indiana University, USA) [2]. The work is carried out in collaboration with INR (Troitsk). Some parts of suitable equipment for the new source were presented by DAPHNIA (Saclay). The IPSN will provide the output beam current up to 10 mA of d^+ and ↑p ions. d^+ ion polarization of 90% of the nominal vector mode +/-1 and tensor mode +1,-2 is expected. That will result in increase of the accelerated polarized beam intensity at the Nuclotron up to above 10^{10} part/cycle.

ALVAREZ-TYPE LINAC LU-20

LU-20 Linac Status

At present time, the injector of the Nuclotron is the Alvarez-type linac LU-20 (Fig. 1), which was built in 1974 as a proton injector with output energy of 20 MeV. Main parameters of LU-20 were presented in paper [3]. LU-20 was originally designed as so-called the $L = \beta\lambda$ Alvarez drft-tube linac (DTL).

Fig. 1. Inner view of LU-20 resonator.

It can also operate in the second harmonic mode as the $L = 2\beta\lambda$ DTL allowing acceleration of light ions with output energy of 5 MeV/u, it was experimentally proved that it is also possible to accelerate ions with $Z/A \geq 1/3$ ions at increased levels of RF field. In the middle of nineties, the front part of the LU-20 was upgraded in order to ensure acceleration of ions with

$Z/A \approx 0.28$ [4]. At that time, the first 11 drift tubes of LU-20 were replaced by new ones.

LU-20 Parameters for proton acceleration

The linac LU-20 accelerates protons from 600 keV to 20 Mev. Its resonator with the length of 14.4 m and the diameter of 1.4 m operates at the frequency f_0 =144.5 MHz and consists of 58 accelerating cells with the length $L = \beta\lambda$.

Fig. 2 shows the parameters of LU-20 for proton acceleration at constant average accelerating field along the resonator of E_0 =1.8 MV/m. At connection of 11 upgraded front cells with rest original cells the parameters have some jumps: the gap factor α changes from 0.20 to 0.25; the slightly growing transit-time factor T becomes almost constant; the energy gain ΔW changes its growing rate, and synchronous phase φ after linear growth comes to its constant value.
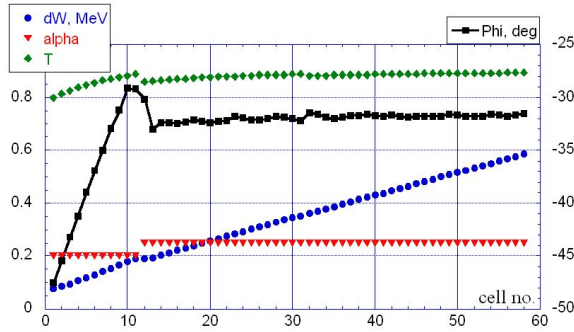
Fig. 2. Parameters of LU-20 vs the cell number.

Upgrade of LU-20 drift-tubes

Due to ageing of LU-20, it is necessary to replace and upgrade its most critical components. It is presently discussed to replace all drift tubes with new ones. Every drift tube of existing linac contains the magnetic quadrupole lens operating in CW mode. To ensure more reliable operation of LU-20, the pulsed magnetic quadrupoles will be used. In the seventies, the cell sizes were approximately calculated with simplified model (R_{int} =0, R_{out} =0) with some available at that time code. Afterwards, precise tuning of the accelerating cells was ensured by tuning rings located on the drift tube outer surfaces. These rings bring a lot of operational troubles.

In order to preserve existing accelerator parameters of LU-20, all longitudinal sizes of the drift tubes are kept without modifications, while other accelerating cell sizes can be varied to adjust resonance frequency of every cell to f_0 =144.5 MHz. The cells of upgraded LU-20 have been recalculated with the Superfish-code [5], which simulates axially-symmetrical cells with a real

configuration including the drift-tube chamfer radii R_{int} and R_{out}. As results, tuning rings are not needed anymore. As example, a typical sketch of half cell used in numerical simulations with Superfish-code is shown in Fig. 3. The cells of existing LU-20 have a simple cylindrical configuration with α_f =0. This configuration is still assumed for the new drift tubes. The tuning of each accelerating cell to the resonant frequency f_0 is realized by varying the drift-tube diameter d.

At first step, the cells have been simulated with the tuning program DTLfish of the Superfish code, assuming a symmetric location of the gap in the cell. The DTLfish sets up Superfish runs for only half the cell as shown in Fig. 3. The drift-tube diameters for symmetric cells have been calculated at f_0 =144.50 MHz. At the second step, the full cells using actual positions of gaps have been simulated with a direct usage of Superfish. The resonant frequencies for full cells are equal to about f_0 =144.38 MHz. Such deviation of the resonant frequency is negligible.
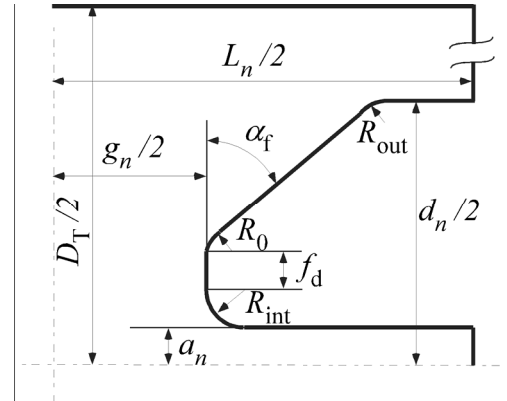
Fig. 3. The DTL half cell set up by the code DTLfish.

Every drift-tube is supported by pair of cylindrical stems of radius R_{stem} =0.04 m. Calculation of the frequency perturbations due to the drift-tube supporting stems have shown that f_0 deviates withing +- 0.2 MHz along the whole structure that is acceptable for LU-20. Another option with conical drift-tubes ($\alpha_f \neq 0$) allowing unification of magnetic quadrupoles is now under discussion.

ESIS

Electron beam ion sources (EBIS) invented at JINR [6] are used widely in many accelerator centers for production of highly charged ions. In the reflex mode of the EBIS operation the electrons do not reach electron collector after one pass through the drift space of the source. Instead they are reflected back towards the

electron gun, where are reflected again near the gun cathode, travel one more to the reflector, and so on. Thus, the electrons are bouncing between the cathode and the reflector of the source and can be used for generation of highly charged ions much as a direct electron beam does.

It was found that in certain conditions the "cloud" consisting of the multiply reflected electrons confined in a strong solenoid magnetic field exhibits properties similar to a phase transition. It leads to a stepwise increase of the confined electron plasma density in a new steady state called "the electron string". Various highly charged ion beams have been produced with the ESIS "KRION-2" constructed at JINR (Fig. 4) and used in three Nuclotron runs during recent years [7].

Fig. 4. ESIS "KRION-2" operated at JINR.

New stand ESIS "KRION-6T" aimed to achieve parameters required for NICA (Table 1) is under construction now.

Table 1. Main parameters of the ESIS sources

	"KRION-2" achieved to date	"KRION-6T" expected
Magnetic field, T	≤ 3	≤ 6
Electron energy, keV	≤ 8	≤ 25
Ions	Au^{30+}	Au^{32+} (U^{32+})
Ionization time, s	$2 \cdot 10^{-2}$	0.015
Work frequency, Hz	40	50
Number of ions per pulse (at given charge state)	$5 \cdot 10^8$	$2 \cdot 10^9$
Extraction time, μs	8	6 - 8

RFQ AND RFQ DTL

The RFQ section was chosen as the initial part of the HILac. At low ion velocity RFQ permits a continuous acceleration and perfect adiabatic conditions to produce a very good bunching efficiency (~ 100%).
For the main part of the HILac we considered four versions:
1) Alvarez-type accelerator,
2) an accelerator with the Alternative Phase Focusing (APF),
2) hybrid type of the focusing proposed at GSI,
4) RFQ DTL developed in IHEP (Protvino) [8].
At the moment, *the 4^d version* - RFQ DTL is chosen as the basis for the main part of the HILac design and construction. In operation it is simpler than the Alvarez-type linac, in contrast to the APF structures utilizes

focusing by quadrupole components of the RF field and provides a strong focusing in both longitudinal and transverse planes. As result, the maximum ion beam current can reach of about 100 mA. Conceptual design of the RFQ and the RFQ DTL [9] was prepared by the IHEP group (founded by one of the inventors of the RFQ accelerator Vladimir Teplyakov), wich has more than 30 years experience in design and construction of such structures.

The RF in both accelerators - the RFQ and the RFQ DTL - is equal to 75 MHz. The accelerator is designed to accelerate the beam of initial normalized rms emittance of 0.1 π·mm·mrad and the emittance growth during acceleration does not exceed two times. To avoid electron load of the cavity (cold emission) the maximum electric field at the electrode surface is chosen to be limited by the value about 350 kV/cm for RFQ DTL and about 220 kV/cm for RFQ . The accelerator consists of the RFQ section (of the length of about 7 m) and four RFQ DTL sections (of the length of about 5 m). The section number and length are determined by technological reasons. The RF, water cooling, vacuum systems and the beam diagnostics along the accelerator will be designed and constructed on the basis of the IHEP long experience in the design, construction and exploitation of RFQ structures.

REFERENCES

[1] NICA Conceptual Design Report, JINR, January 2008. http://www.jinr.ru/

[2] V. V. Fimushkin et al., *Eur. Phys. J., Special Topics* 162 275 (2008), V. P. Derenchuk, A. S. Belov, in *Proceedings of the 2001 Particle Accelerator Conference* Chicago (2001) p.2093, A. S. Belov et al., *Nucl. Instrum. and Meth.* A333 256 (1993).

[3] A.I. Govorov et al, "Linac LU-20 as Injector of Nuclotron", Proc. 1996 Linear Accelerator Conf, pp. 349-451.

[4] A.M. Baldin et al, Upgrades of the Nuclotron Injector for Acceleration of Ions with Z/A=0.28, Proc. 1996 Linear Accelerator Conf, pp. 352-454.

[5] K. Halbach and R.F. Holsinger, Part. Accel. 7, No.4, pp. 213-222 (1976).

[6] E.D.Donets, in "Physics and Technology of Ion Sources", Ed. by I.G. Brown, Wiley &Sons, NY, 1989, p. 245.

[7] E.D. Donets et al., Electron string source of highly charged ions: Studies and the first test on a synchrotron, in Proc. of EPAC-2002, Paris, June 3-7, 2002 p.1700-1702.

[8] O.K. Belyaev A.P. Maltsev,, V.B. Stepanov, et. al., RFQ Drift-Tube proton linacs in IHEP, Proceedings of LINAC 2004, Lübeck, Germany

[9] V.V.Kobets, A.I.Govorov, G.V.Trubnikov, et. al., Heavy ion injector for NICA/MPD project, Proceedings of LINAC08, Victoria, BC, Canada, p.121-123

STOCHASTIC COOLING SYSTEM PROTOTYPE FOR NUCLOTRON

I. Meshkov, V. Seleznev, N.Shurkhno, A. Sidorin, G. Trubnikov, JINR, Dubna, Moscow Region

R.Stassen, IKP FZ Juelich, Germany

Abstract

Joint Institute for Nuclear Research (JINR) initiated the creation of a new and unique heavy-ion collider – Nuclotron-based Ion Collider Facility (NICA), which is planned to be operational in 2016 [1]. The luminosity in the colliding beams of Au^{79+} ions is expected to reach 10^{27} $cm^{-2}s^{-1}$. By met estimates it will mainly be determined by the intra-beam scattering effect. To suppress one, it was proposed to use the cooling of the beam. For the medium and high-energy heavy ions, such as NICA collider, stochastic cooling will be more efficient, then electron cooling, so this system will be used in the collider. In the coming years it's planned to build stochastic cooling system prototype at presently working accelerator Nuclotron to test different working modes at an early stage of NICA project. Main results of the development of stochastic cooling system at Nuclotron are presented.

INTRODUCTION

The Veksler and Baldin Laboratory of High Energy Physics (VB LHEP) of JINR is a pioneer in designing, constructing and commissioning the world first fast cycling synchrotron based on low-field iron dominated electromagnets with superconducting coils. This accelerator named Nuclotron was commissioned in 1993 [2]. Superconductive ring of 251,5 m in circumference is located in the tunnel with a cross-section of 2,5x3 m that was a part of the Synchrophasotron infrastructure. Since 1993 it was performed 41 beam runs at the accelerator. Presently the Nuclotron delivers ion beams for experiments on internal targets and for fixed target experiments using slow extraction system. Achieved energy of protons is 5.7 GeV, deuterons – 3.8 GeV/u and nucleons - 2.2 GeV/u.

The Nuclotron lattice is typical for a strong-focusing separated function synchrotron. It contains 8 superperiods. Each superperiod consists of three regular FODO cells. The fourth cell has not a dipole magnet. The regular cell includes F- and D-quadrupole magnets, four dipole magnets and two small drift spaces for the installation of correcting magnets, beam monitors, etc. In total the ring contains 96 dipole, 64 quadrupole, 32 correcting multipole SC-magnets. The betatron tunes are $Q_x \sim Q_y \approx 6.75$.

There are two straight sections on the direct opposite sides of the ring (Fig.1) where the pick-up and kicker can be installed.

The main argument to have operating stochastic cooling system prototype at Nuclotron - is to test different working modes of the machine. The first stage includes longitudinal cooling of the coasting deutron or light ion (lithium, carbon) beam using notch filter technique [3] for the cooling.
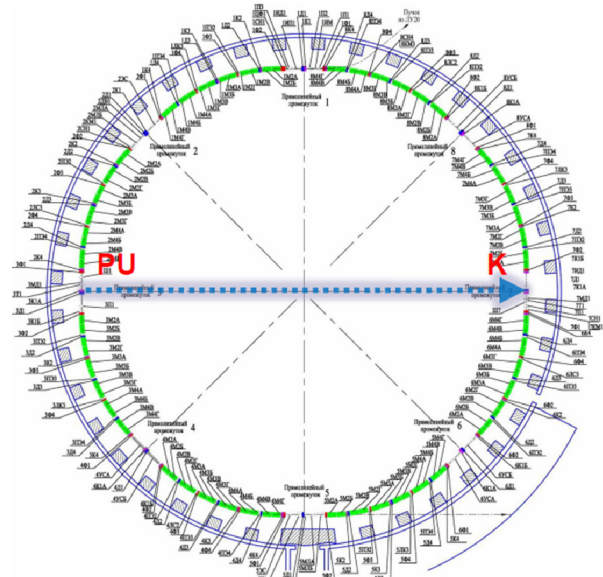
Figure 1. Nuclotron ring configuration.

Regular operation cycle duty of the machine is from 5 to 10 seconds, the flat-top time is around 80% of the duty cycle, therefore period available to get effect of the stochastic cooling process is limited to characteristic flat-top time. Main parameters of the accelerator summarized in Table 1.

Table 1. Nuclotron ring parameters

Circumference, m	251.5
Ions	up to A = 124
Energy, GeV/u	6
Rev.frequency, MHz	1.2
Vacuum, Torr	10^-10
Intensity	10^11(p)-10^9(C12)
dp/p	10^-3
Ring slippage factor	0.0322

SCHEME OF THE PROPOSED STOCHASTIC COOLING SYSTEM

The first step in realization of stochastic cooling experiment is longitudinal cooling of the coasting beam.

The dispersion value is too small in the section, where pick-up is placed, so Palmer method can not be implemented. Instead there is going to be installed a scheme with a notch filter. Octave band of 2-4 GHz was chosen for the system. The schematical picture of the assembly is shown on Fig.2
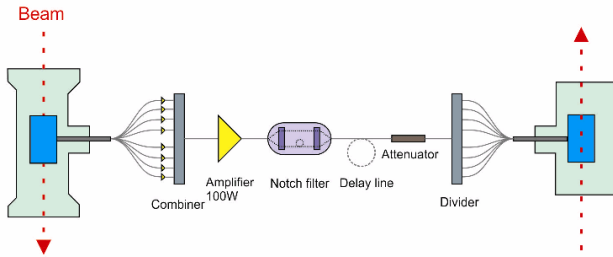
Figure 2. Scheme of the stochastic cooling system. Pick-up is on the left side, kicker is on the right.

The signal from the beam is measured with pick-up, installed in a specially designed vacuum chamber inside cryostat. Eight outputs for the beam signal from the pick-up are amplified with 40 dB preamplifiers and then combined together. The summarized signal is amplified after with 100W amplifier. Afterwards the signal follows to the notch filter which rejects the harmonics of revolution frequency and inverts phase of the signal. After is transported via variable delay line and variable phase-independent attenuator. Then the signal is divided by eight equal outputs, which are applied at the kicker for correction of the particle angle.

DESIGN AND CONSTRUCTION OF ELEMENTS

Installation includes the following components: pick-up and kicker electrodes assembly, pre-amplifier and amplifier, notch filter and delay line. For pick-up and kicker it is planned to use well-proved ring-slot couplers initially developed at COSY as a prototype for HESR ring [4]. Both pick-up and kicker have absolute similar design: assembly of 16 rings of 90mm aperture with 8 gold plated electrodes each (Fig 3).
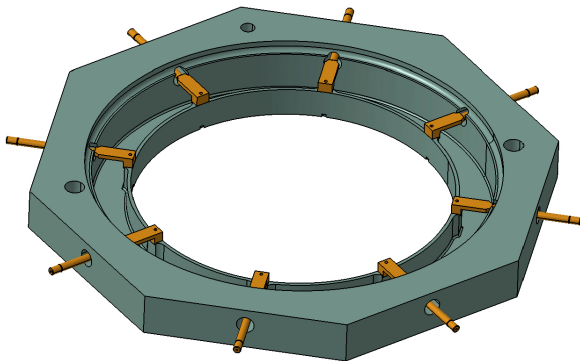
Figure 3. Design of the ring for slot-coupler

The basic principle of the beam signal formation at pick-up is the following. The total image current passes the surrounding uninterrupted gap formed by two adjacent rings. The round cell is somewhat like a classical iris loaded linac cell which is heavily loaded with the eight 50Ohm coaxial lines to obtain the octave bandwidth.

Each cell (ring) has eight shorted electrodes. The signal from different rings is gathered with the combiner boards, which have properly adjusted delays for different rings, so that the signal propagates in boards synchronously with the beam. Thus such a structure has correspondingly eight outputs, which are combined at dedicated board together afterwards for longitudinal signal.

The modular design of this structure allows an easy increase of the number of rings. Number of rings for kicker depends on the power required for delivery to the beam. Together with very good longitudinal coupling impedance it makes this device a good choice not only for Nuclotron, but for NICA as well.

Pick-up will be installed in the cold section of the ring (3rd stright section) using special pick-up tank designed for installation In order to provide optimal operation of the pick-up (stability, signal sensitivity, noise reduction) it has to be placed in the cold section of the ring. Dedicated designed cryostat is under manufacturing now for installation of the pick-up structure at Nuclotron for operation at temperature close to 10K. This structure is an adapted version of pick-up tank presently using at COSY. The upper dome of the tank is made short as possible to prevent energy loss in cables.
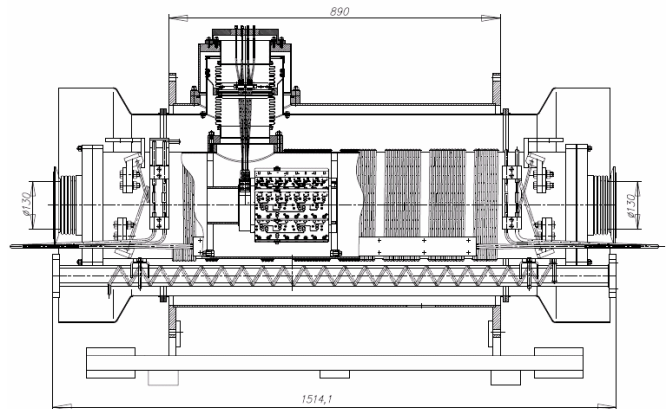
Figure 4. Pick-up assembly in Nuclotron cryostat.

Eight outputs from combiner boards will be delivered using special cables to 2 feedthrough flanges on the top of cryostat with 4 SMA connectors on each. Each output will be equipped with preamplifier.

Kicker slot-coupler assembly will be installed in the dedicated vacuum tank and located in the warm gap of Nuclotron (7th straight section)

Optical notch filter

It is planned to construct notch filter with both optical legs, which gives advantages in gain value, regularity and uniformity of notches (Fig. 5).
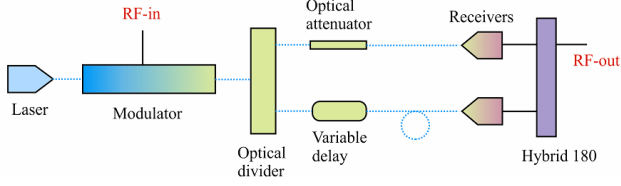
Figure 5. Notch filter layout.

Laser light is modulated by a RF signal from the longitudinal pick-up. After that the infrared signal is divided in two legs: in the 1st leg the attenuator is installed for power adjustments; in the 2nd leg the signal is delayed by a fibre optic coil and stretcher for precision adjustments. Afterwards RF signal is reconstructed by receivers and is combined by a hybrid. The basic scheme of such optical notch filter was initially proposed and tested in COSY [4].

COOLING PROCESS SIMULATIONS

Impedances of the pick-up and kicker are calculated through modeling the electro-magnetic field inside of the ring electrodes. Then the process of stochastic cooling is fully described with the Fokker-Planck equation[5, 6]:

$$\frac{\partial \Psi(E,t)}{\partial t} + \frac{\partial}{\partial E}(F(E)\Psi(E,t) - D(E,t)\frac{\partial \Psi(E,t)}{\partial E}) = 0$$

Where $\Psi(E,t) = \dfrac{dN}{dE}$ is a particle distribution function, and
$F(E) = f_0 \Delta E_c$

$$D(E,t) = \frac{1}{2}f_0 \left\langle \Delta E_{ic}^2 \right\rangle$$

$F(E)$ and $D(E,t)$ are coherent (cooling) and incoherent (heating) terms respectively. $\Delta E_c(E)$ - is the correction energy per turn, and ΔE_{ic}^2 - the incoherent noise effects for the particle.

Solving numerically this equation with introduced parameters of the real system, we can get the evolution of particle distribution function, evolution of momentum spread and value of power for the beam, required for cooling.

Simulations have been performed for different types of particles: protons and carbon ions C(6+). The results are presented at Figs. 6 and 7.

The results of the simulation give the following requirements for the system: in case of proton coasting beam, the power required for performing this experiment lays in 30-40W margins and gain is approximately 140dB. If the C(+12) beam will be used, the power requirements significantly decreases to 10W and 130dB gain correspondingly.

04 Hadron Accelerators
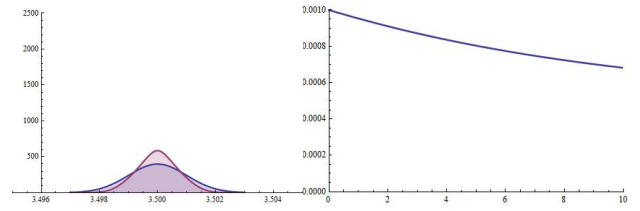
Figure 6. Expected evolution of particle distribution function and rms value of momentum spread for potons.
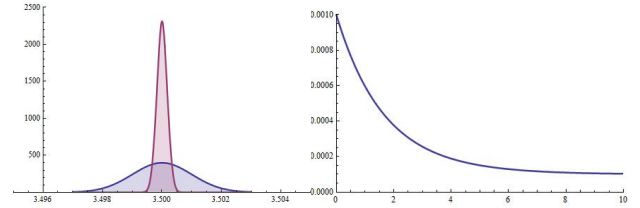
Figure 7. Expected evolution of particle distribution function and rms value of momentum spread for carbon ions (C6+)

CONCLUSIONS

Detailed design of stochastic cooling system prototype for Nuclotron have been performed: all components of the system were chosen and fixed. Design of vacuum and cryogenic vessels is completed. Within several months it is planned to start construction of the system in several stages. The first stage will include assembly of the dedicated test bench for producing and testing the notch filter. Second stage involves installing pick-up and kicker tanks with ring-slot couplers inside and measuring parameters of the system at warm test bench. The third stage includes installing the assembled stochastic cooling system and testing its work for longitudinal cooling.

ACKNOWLEDGMENTS

REFERENCES

[1] A.N.Sisakian et al. XXIII Int. Symposium. on Lepton and Photon Interactions at High Energy, LP07, Daegu, Korea. (2007).

[2] A.A.Smirnov, A.D.Kovalenko, "Nuclotron-superconducting accelerator of nuclei at LHE JINR (Creation, Operation, Development)" Particles and Nuclei, Letters, 2004, v.1, №6 (123), p.11-40.

[3] Optical Notch Filter for the Stochastic Cooling System of COSY, PAC, 1999.

[4] Recent developments for the HESR stochastic cooling system, Proceedings of COOL 2007, Bad Kreuznach, Germany, p. 191.

[5] D. Mohl, G. Petrucci, L. Thorndahl, and S. van der Meer, Phys. Rept. 58 (1980), 76.

[6] T. Katayama and N. Tokuda, Part. Accel. 21 (1987), 99.

PROJECT OF JINR SUPERCONDUCTING SYNCHROTRON FOR HADRON THERAPY

E.M. Syresin[#], V.A. Mikhaylov, A.V. Tuzikov, N.N. Agapov, A.V. Eliseev,
G.G. Khodzhibagiyan, V.N. Karpinsky, A.D. Kovalenko, A.I. Malakhov, I.N. Meshkov,
A.G. Olshevsky, G. D. Shirkov, S.G. Shirkov, G.V. Trubnikov,
Joint Institute for Nuclear Research, Dubna, Russia

Abstract

The project of the medical carbon synchrotron at maximal ion energy of 400 MeV/n was developed in JINR. The project goal is accumulation of the superconducting technology at construction of the carbon synchrotron with a circumference of 65 m on basis of the Nuclotron type magnet elements. For injection of the carbon ions it is proposed to use IH linac of C^{4+} at energy 4 MeV/n. The superconducting gantry is developed for patient treatment at a weight of 150 t.

INTRODUCTION

Today, the cancer is the second highest cause of death in developed countries. Its treatment still presents a real challenge. Protons and carbon ions allow depositing the radiation dose more precisely in a cancer tumor, reducing greatly the amount of dose received by healthy tissue surrounding the tumor with respect to electrons. But in addition to the ballistic accuracy of protons, the carbon ion beams have an extra advantage in radiation therapy: they have a different biological interaction with cells and are very effective even against some type of cancerous cells which resist to usual radiations. That is why the last years have seen increasing interest in particle therapy based on $^{12}C^{6+}$ ions. A project of the medical superconducting synchrotron dedicated for the carbon therapy has been designed in JINR.

The basis of this medical accelerator is the superconducting JINR synchrotron – Nuclotron [1,2] (Fig.1).

Figure. 1: JINR superconducting synchrotron- Nuclotron.

The Nuclotron type straight dipole magnets [2] (Fig.2) were adopted for the optic of the medical synchrotron and beam delivery system. The superconducting magnets permit to reduce the accelerator electrical consumption, the size and weight of the accelerator. Especially the superconducting technology is important at design of the carbon gantry. A superconducting gantry was developed for tumor treatment at a weight of 150 t.
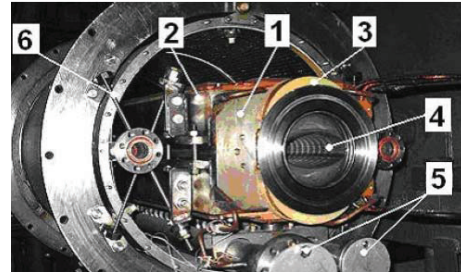
Figure. 2: The Nuclotron type dipole magnets

INJECTION

The superconducting electron string ion source [3] is planed to use for $^{12}C^{4+}$ injection in the carbon linac. Additionally this source can applied for formation of primary radioactive carbon ion beams $^{11}C^{4+}$ in ISOLDE scheme. The intensive primary radioactive $^{11}C^{4+}$ ion beams can be used simultaneously for cancer treatment and on-line PET. The compact IH linac [4] (Table 1) will applied as synchrotron injector. The injection channel consists from two sections: the discharge section, where accelerated in IH linac ions C^{4+} are discharged to ions C^{6+}, and the section of injection of ions C^{6+} in the synchrotron.

Table 1. Parameters of carbon IH linac.

Parameters	RFQ	IH-DTL
Injection energy, MeV/u	0.01	0.61
Extraction energy, MeV/u	0.61	4
Operation frequency, MHz	200	200
Charge-mass ratio	1/3	1/3
Cavity length, m	2.5	3.4
Cavity outer diameter, m	0.42	0.44
Power, kW	120	360
Normalized 90% emittance, $\pi \cdot mm \cdot mrad$	0.85	1.1
Normalized 90% longitudinal emittance, $\pi \cdot ns \cdot keV/n$	1	1.2
Energy spread,%		±0.4
Maximal beam current, eμA	392	390

---

04 Hadron Accelerators

CARBON SYNCHROTRON

The FODO structure (Fig.3) is more preferable for injection and extraction schemes and corrections of the closed orbit distortions. The basic parameters of the carbon synchrotron are given in Table 2. The synchrotron magnetic system (Table 3) consists of 4 superperiods, which involves 8 straight dipole magnets, 8 quadrupole lenses and multipole correctors. The maximum magnetic field in dipole magnets corresponds to 1.8 T.
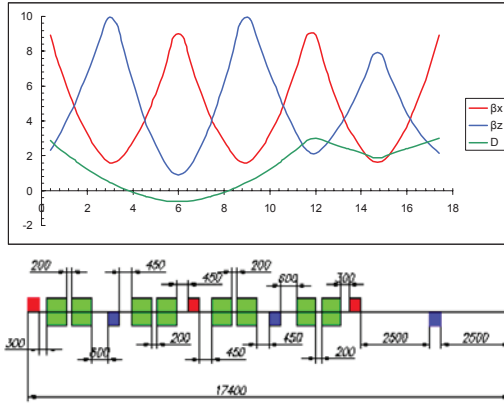
Figure 3: Synchrotron super period characteristics.

Table 2. Basic parameters of carbon synchrotron.

Injection/maximal energy	4,2/400 MeV/u
Maximal/ injection magnetic rigidity	6,36/0.59 T·m
Circumference	69,6 м
Column limit of intensity at injection	$6 \cdot 10^9$ p/cycle
Betatron tune shift	0,02
Revolution time at injection	2,37 μs
Number of turns at injection	20
Injection efficiency	50 %
Time of synchrotron acceleration	0.5 s
Slow extraction time	(0,5 -10) s
Energy of extracted beam	(170 – 400) MeV/u
Extraction efficiency	96%
Critical energy	3.1 GeV/u

The multiturn injection (Fig.4) is realized at fulfilling of the horizontal acceptance during 10-15 ion turns. The stored beam intensity is equal to 10^{10} ions C^{6+} per pulse. The working point corresponds to betatron tunes $Q_{x,z} \approx 3.25$. Nonlinear 3 order resonance $3Q_x=10$ is used for slow beam extraction (Fig.5). The extraction time is varied from 0.5 s to 10 s. The intensity of extracted beam is equal to 10^9 pps.

Table 2. Structure and magnetic elements.

Number of superperiods/FODO periods	4/12
Number of dipole magnets/ quadrupole lenses	32/24
Magnetic field at injection/maximal field	0,17/1,8 T
Rate of magnetic field	3,26 T/s
Maximal/injection gradients in F lenses	8,5/0.8 T/m
Maximal/injection gradients in D lenses	−7,5/−0,7 T/m
Curvature radius in dipole magnets	3,53 m
Sagitta in dipole magnets	8,7 mm
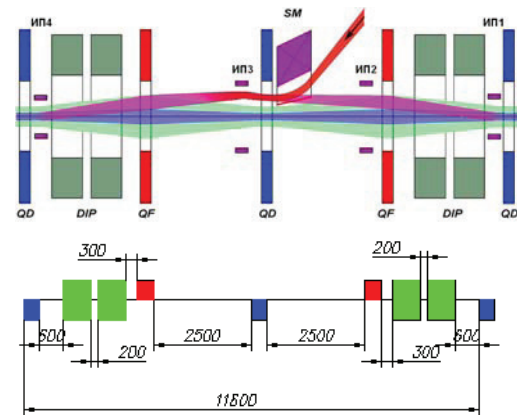
Figure 4: Multiturn injection scheme, orbit and beam envelope: red – injected beam, violet – deflected beam, blue – circulated beam after first injection, green - circulated beam.

Table 4 Beam and synchrotron structure dynamic characteristics.

Betatron tunes	3,25
Chromaticity $\Delta Q_x/(\Delta p/p)$	-3,1
$\Delta Q_z/(\Delta p/p)$	-3,2
Parameter of orbit compaction	0,053
COD, mm	3
Horizontal/Vertical acceptance, π·mm·mrad	180/70
Emittance of injected beam, π·mm·mrad	10
Emittances of accelerated beam $\varepsilon_x/\varepsilon_z$, π·mm·mrad	20/1,5
Emittance of extracted beam $\varepsilon_x/\varepsilon_z$, π·mm·mrad	0.5/1,5
Relative momentum spread	$\pm 10^{-3}$
Relative maximal momentum spread	$\pm 2\times 10^{-3}$

04 Hadron Accelerators
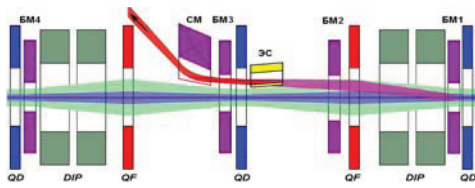
Figure 5: Scheme of slow beam extraction.

BEAM DELIVERY SYSTEM

The   beam delivery system (Fig.6) consists of following sections: the extraction section; the foil section provided equal beam emittances in both transverse planes; the   accommodation   section;   the   section   for   beam delivery in the cabin; the section of beam transportation between the medical cabins; the isocentric gantry;   the channel with fixed beam position cabin. The beam delivery system should provide the fixed transverse beam sizes in the gantry isocenter. These sizes do not depend on the gantry rotation angle, the extracted ion energy, emittance of the extracted carbon ion beam.
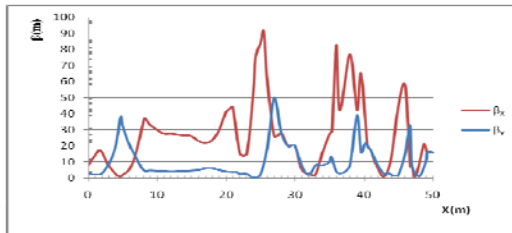
Figure 6: Beta-functions of beam delivery system.

The extracted carbon beam has non symmetric horizontal and vertical emittances, the vertical emittance is few times larger horizontal one. A special scattering foil is installed in the beam delivery system to provide both equal horizontal and vertical beam emittances. The accommodation section is used to provide same optical beam characteristic in the vertical and horizontal directions at exit. It accommodates the beam optic to the gantry for any its rotation angles. The section for beam delivery in cabin consists of the chopper, the achromatic bend and 2 triplets.   The chopper involves 4 dipole magnets. The beam is pick-upped by an absorber trap, when dipoles switch off. The beam is transported in the channel when magnets switch on. The section of beam transportation between cabins has the horizontal betatron phase shift 2π and vertical one π. The optic of the isocentric gantry is achromatic at beam transportation to the tumor target. The gantry optic provides equal horizontal and vertical beta functions and zero alpha-function on the tumor target. The parameters of gantry optic is adjusted to obtain the equal vertical and horizontal beta and alpha functions at the gantry entrance at variation of extracted beam emittances and sizes.

SUPERCONDUCTING CARBON GANTRY

The JINR-IBA collaboration develops superconducting cyclotron C400 and carbon gantry (Table 4) in frame work of Archade project [5,6]. This gantry is planed to use in JINR carbon synchrotron complex.   The gantry provides rotation around the patient on an angle 0-180^0. The positioner also rotates together with patient on an angle 180^0-360^0. The main gantry superconducting dipole magnet has aperture 20×20 cm at magnetic field homogeneity of 10^{-4}. The magnetic field rate corresponds to 1 T/min.   The magnet is cooled by 4 He-free criocoolers.   The distance from dipole magnet exit to isocenter corresponds 2 m.

Table 4. Superconducting carbon gantry

Gantry	
Weight, t	156
Diameter, m	9.2
Length, m	12,7
Scanning area in isocenter, cm	20×20
Gantry rotation angle, degree	180
Positioner rotation angle, degree	180
Main dipole magnet	
Magnetic field, T	3.2
Bending radius, m	2
Weight, t	28
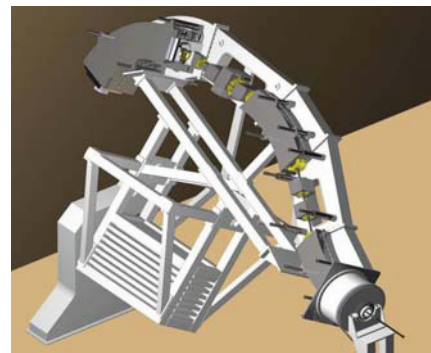
Figure 7: Superconducting carbon gantry.

REFERENCES

[1] A.D. Kovalenko UPhN, v.177, №8, (2007) 914.

[2] A.A. Smirnov, A.D. Kovalenko, Nuclear Particle Letters, v.1, №6 (2004) 11.

[3] E.D. Donets et al., Review of Scientific Instruments, v71, N2, part II, (2000) 896.

[4] K.Noda et al., Radiation Res. 48 suppll. (2007) A43.

[5] Y. Jongen et al., HIAT09, D9 (2009).

[6] Y. Jongen, Design of a K=1600 SC cyclotron for Carbon therapy, ECPM, Nice (2006).

INTERCATION OF THE BIOMOLECULAR IONS WITH THE ELECTRON TARGET IN THE ELECTROSTATIC STORAGE RING

Syresin E.M., Shirkov S.G.,

Joint Institute for Nuclear Research, Dubna, Russia

Abstarct

A nanostructure of the radiation damages is formed at an interaction of carbon ions with DNA molecules at hadron therapy. A local interaction of the ion beam with the bimolecular structures in the human cells is defined mainly by parameters of the ion tracks. The track core is connected with ionization properties of the charged ion, its cross-section sizes are defined by the delta-electrons. The delta-electron energy varies statistically from several eV to few keV therefore they lead to substance ionization along their trajectory on a distance several nanometers from that point where they were produced.

Interaction of the delta-electrons with DNA molecules and other biological structures is one of the important mechanisms realized in process of the hadron therapy. A study of interaction of the accelerated biomolecular ions with an electron target in the electrostatic storage ring was performed for modeling of an input of the delta-electrons in processes of the hadron therapy.

INTRODUCTION

The realization of carbon therapy on a microscopic level is connected with a nanostructure of local radiation damages produced along trajectories of ions with a characteristic cross dimension of a few nanometers and a root-mean-square distance between the damages several hundred nanometers (Fig. 1), covering the structure of DNA molecules in the tumor cells with a probability around of 80%. The arising two-strand breaks of DNA molecules are irreversible because of high linear energy transfer (LET) for particles stopped in the tumor, while the structure of radiation damages in normal tissues at low LET ensures less than 10–20% probability of complications in these tissues, producing damages (predominantly single-strand DNA breaks) that allow cell functioning to be restored after irradiation.

At carbon therapy the ions produce the double-strand breaks of DNA molecules by the direct ionization. The delta-electrons are formed also at this ionization. It leads to additional DNA breaks along the electron trajectories. As a result, the radiation damages arise in the region of ion track with the lateral dimensions of the order of nm comparable with the DNA transverse dimensions. Majority of the delta-electrons have energy lower 30 eV.

The interaction of the electrons with an energy of 0.5-100 eV with the biomulecular ions at a mass of 1000-66000 a.m. accelerated up to energy of 30 keV/Z in the KEK (Japan) electrostatic ring is discussed below.
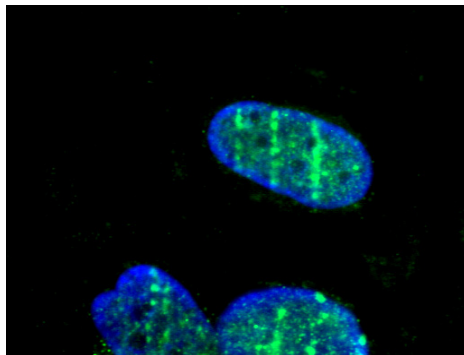
Fig.1. Photo of irradiated human cells taken at the fluorescent microscope. Fluorescent markers demonstrate nanostructured double-strand breaks of the DNA molecules caused by the carbon ions.

ELECTROSTATIC STORAGE RINGS

The magnetic rigidity $B\rho$ of the ion storage ring is determined by the ion mass M: $B\rho=(2E_iM/q_i^2)^{1/2}$, where E_i and q_i is ion energy and charge. Consequently, the biomolecular ions of proteins, amino acids or DNA ions with a mass of 10^3-10^6 a.m. can not accelerated in the ion storage rings with a magnetic structure. In this regard, in recent years a new class of electrostatic storage rings [1-4] was constructed. The rigidity of electrostatic ring $E\rho$ does not depend on ion mass: $E\rho=2E_i/q_i$. These storage rings were effectively used for the formation and accumulation of the biomolecular ion beams [1-4].

The circumference of the KEK electrostatic ring is equal to 8.1 m. The accumulated current of biomolecular ions was 50-500 nA. The lifetime of biomolecular ions with masses up to 66 000 in the KEK electrostatic storage ring is 10-20 s at a pressure of $(3-5)\times10^{-11}$ Torr. The ring acceptance corresponds to 50 $\pi\cdot$mm$\cdot$mrad. The emittance of stored ion beam is equal to 15 $\pi\cdot$mm$\cdot$mrad, the ion beam diameter is about 6 mm in the electron target. The relative momentum spread corresponds to 10^{-3}.

The biomolecular ions are produced in the electrospray ion source [2]. Then they are stored in the ion trap to increase by one order of magnitude the

ion beam intensity. The bunched ions accelerated up to energy of 20 keV/Z pass through the mass analyzing system with a mass-resolving power 10^3. Finally, the biomolecular ions are injected in the electrostatic ring.

ELECTRON TARGET

The main peculiarity of the KEK electrostatic ring is related to the electron target [3,5-9] developed in KEK-JINR-NIRS collaboration. This target is applied for study of biomolecular ion-electron interaction at an electron energy of 0.5-100 eV.

The electron target design is similar to a design of the electron cooling system with a high magnetic expansion factor. The magnetic expansion factor in KEK electron target can be varied in the range of 10-100. The gun magnetic field corresponds to1 kG, the magnetic field in the interaction region is equal to 10-100 G. The electron beam is formed in three electrode gun (Fig.2). The cathode diameter corresponds to 3.5 mm. The electron beam in the interaction region is varied in range of 11-35 mm. The length of electron-ion interaction erea is equal to 20 cm. The maximum electron current corresponds to 2 mA.
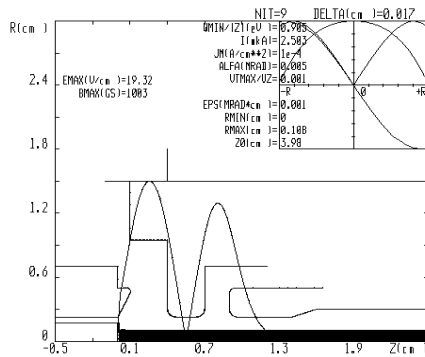
Fig.2. Electron beam formation in the three electrode gun with variable emission spot size.

The energy of accelerated electrons is defined by several parameters [6,8]:

$$E_e/e = V_{cath} + U_{min} - A/e - IR - kI/E_e^{1/2},$$

where V_{cath} is the cathode voltage, U_{min} is the potential minimum produced near the cathode surface, A is the work function of the cathode material, IR is a voltage related to the active resistance R of the emitter layer, $kI/E_e^{1/2}$ corresponds to the electron space-charge effects.

TRANSVERSE COHERENT OSCILLATIONS AT TARGET ELECTRON-ION INTERACTION

The proton lifetime reduction in KEK electrostatic ring [6] can be related to excitation of the dipole coherent oscillations produced by ion interaction

with the electron target or at the so-called electron heating effect [10].

The proper choice of working point reduces the ion-beam losses caused by the excitation of the transverse coherent oscillations. In the KEK electrostatic ring there are 4 stable working points with different amplitude functions and tunes: point A (Q_x/Q_y=2.68/0.78), point B (Q_x/Q_y=3.28/0.53), point C (Q_x/Q_y=2.71/1.38) and point D (Q_x/Q_y=3.28/1.35) [2]. The interaction of the protons with the electron target is rather weak at working point C. The ion lifetime is reduced by about 10-20% at the electron-target interaction. The simulated cooling and ion coherent-oscillation rates are equal to 2 s^{-1} and 0.5 s^{-1} for the proton beam at working point C.

The increment of the instability has a maximum at a coupling resonance Q_x-Q_y=n [10]. This resonance is realized in a region around points A and D. The simulated rate of the transverse coherent oscillations is high by one order of magnitude for points A and D, compared with point C. The resonance width is of $\delta Q \approx 0.04$.

The interaction of the stored ions with a highly intensive electron target also leads to excitation of ion transverse coherent oscillations an ion lifetime reduction [6]. The resonance width of the betatron tune is rather small for the simulated ions: $\delta Q \approx 0.015$ at $I_e = 0.1$ mA (Fig.3) and $\delta Q \approx 0.05$ at $I_e = 0.5$ mA. The increment of the instability has a maximum at an ion intensity of $2 \cdot 10^7$ ppp. It oscillates at a high ion intensity, which is caused by the electron drift resonances.
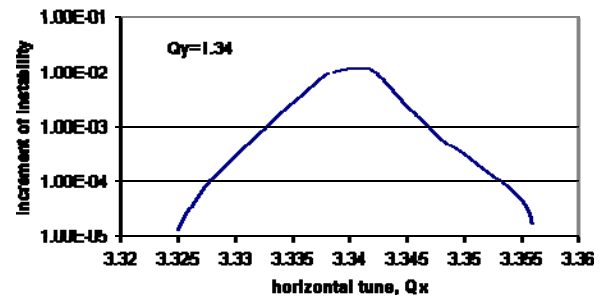
Fig. 3 Dependence of the increment of instability on the horizontal tune at Q_y=1.34, I_e=0.1 mA, E_e =40 eV, B=30 G, Z=4, A=1200, Ni=10^7 ppp, FWHM=6 mm.

INTERACTION OF BIOMOLECULAR IONS WITH THE TARGET'S ELECTRONS

The results of biomolecular ion-target electron interactions are presented in Fig. 4 [6-7]. Fig. 4 shows the yields of neutral radicals formed at interaction of the target electrons and the ions of the basic amino argenina (mass 0.17 kDa) and ions of the peptide bradykihina (mass 1.06 kDa) with a one-dimensional structure and consisting of 9 amino acids. The interaction of electrons with biomolecular ions, became to the damage of the intermolecular bonds, resulting from the ions come off the free radicals, and whose output is recorded in the

experiment. The growth yield of neutral radicals and the relative energy of the electrons below 2 eV is associated with the contribution of dissociative recombination. For the basic amino acid Arg at electron energies greater than 2 eV yield of the neutrals increases linearly with electron energy. At the same time for bradykihina peptide consisting of 9 basic amino acids, cross section, and accordingly, the yield of the neutrals has a pronounced maximum at the relative energy of the electrons and ions of 6.5 eV. The peak in the cross section associated with breakage of peptide bonds.
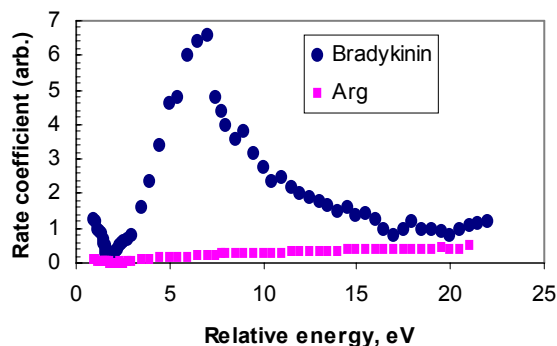
Fig.4. Dependence of the neutral radical production rate on the electron-ion relative energy.

Similar form has a cross section at the interaction of the target electrons and DNA (oligonucleotide - d (AAA)) ions. The maximum cross section of such interaction corresponds to the relative electron- ion energy of 4.5 eV (Fig. 5).
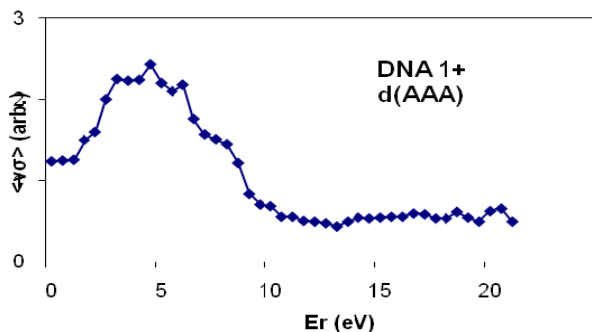
Fig. 5 Dependence of the yield of neutral radicals on relative electron–ion energy at interaction of the target electrons with the DNA ions.

ELECTRON INTERACATION WITH BIOMOLECULAR ANIONS

A collective mechanism of a plasmon excitation by DNA valence electrons at electron-DNA anion interaction is proposed in [11]. The plasma oscillations lead to break of the DNA anion bounds and the neutral particle emission. The threshold electron energy corresponds to 10 eV, when the neutral particles are produced at electron collisions with DNA anions. The threshold target electron energy is increased almost linearly with DNA anion charge [11] (Fig. 6).
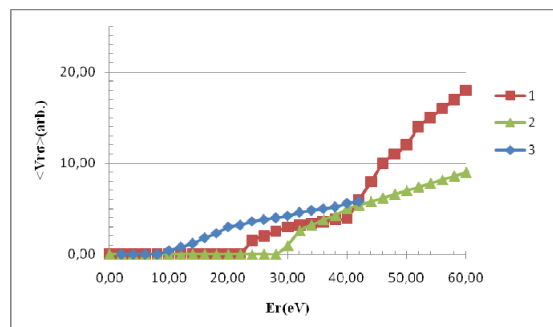
Fig. 6 Dependence of the yield of neutral radicals on relative anion-electron energy at different DNA anion charges, 1-Z=-1, 2-Z=-2, 3-Z=-3.

At small impact parameter $\rho_{min} \cong n_v^{-1/3}$ three-body and/or collective interactions of the target electron, anion and valence electron can lead to transformation of kinetic energy of the target electron into the energy of the valence electron and excitation of the collective plasma oscillations [12,8]. The plasma oscillations brake the DNA bonds and produce the neutral molecular emission. The critical target electron energy is defined by the electron-anion interaction at small impact parameter $\rho_{min} \cong n_v^{-1/3} \cong$ 1.5A: $E_{cr} = Ze^2 n_v^{1/3} \cong Z \times 10$ eV, where n_v is the density of valence electrons.

The yield of neutral radicals corresponds to [12] $N_{rad} = (N_e N_i / \tau_{life}) \times (\rho_{min}/\rho)^2 \cong 2$ s^{-1}, where $N_i \approx 10^7$ ppp is the number of stored anions , $N_e \approx 3 \cdot 10^6$ is the number of fresh target electrons collided with anion during its lifetime of $\tau_{life} \approx 10$ s, , $\rho \cong 0.2$ mm is the average impact parameter at electron-DNA anion collisions.

REFERENCES
[1] S.P. Moller NIM A 394 (1997), p.281.
[2] T. Tanabe et al, NIM A 482 (2002), p.595.
[3] T. Tanabe, K. Noda, E. Syresin, et al, EPAC 2002, p. 632.
[4] S. Jinno et al, NIM A 532 (204), p. 477.
[5].E. Syresin, K.Noda, T.Tanabe, Physica Scripta, 2003, v.T104, p.185.
[6].E.Syresin, K.Noda, T.Tanabe, in Proc. of EPAC 2004, p. 162.
[7].T.Tanabe, K.Noda, E.Syresin, NIM A, 532, 2004, p.105.
[8].E.Syresin, in Proc. of EPAC 2006, p.1645.
[9] E.Syresin, S. Shirkov, III Europe-Asian Congress of Medical Physics and Engineering, 2010, v.2, p.117.
[10]V.V.Parkhomchuk, V.B.Reva, J. of Experimental and Theoretical Physics, v. 91, N5 (2000) 975.
[11] T.Tanabe, K.Noda, M.Saito, E.B. Starikov, M. Tateno Phys. Rev. Letters, v. 93, N.4, 043201 (2004).
[12] E. Syresin, K. Noda, T. Tanabe, HIMAC-098, 2004.

04 Hadron Accelerators

POWER SUPPLY AND PROTECTION SYSTEM OF THE NUCLOTRON BOOSTER IN THE NICA PROJECT

A. Kudashkin, V. Karpinsky, H. Khodzhibagiyan, A. Sidorin, JINR, Dubna, Russia

Abstract

The Nuclotron Booster in NICA project [1] is aimed to accelerate heavy ions up to 600 MeV/u to provide effective stripping before injection into the Nuclotron. The Booster power supply system consists of one powerful unit, providing maximum current of 12 kA and field ramp up to 1.2 T/s, and two additional units, that are used for the ring working point adjustment. The quench protection system is based on thyristor switches. Structure and parameters of the power supply system are presented.

THE SYSTEM STRUCTURE AND DESTINATION

The Nuclotron-type design based on a window-frame iron yoke and a saddle-shaped superconducting winding is chosen for the Booster. The Nuclotron magnets include a cold (4.5K) window frame iron yoke and a superconducting winding made of a hollow NbTi composite superconducting cable cooled with two-phase helium flow at T = 4.5 K [2]. A further development of the technology was proposed [3] to increase the efficiency of the magnetic system. In accordance with this proposal the single-layer winding bent dipole will be built to reduction the magnet cross section and AC losses in comparison with the straight double-layer winding dipole at the same aperture budget by means of the doubled structural current density in a winding.

At design of the Booster power supplies system (fig. 1) the requirement of consecutive connection of structural dipole magnets (total inductance 16.4 mH), quadrupole focusing (total inductance 0.6 mH) and defocusing (total inductance 0.6 mH) lenses is accepted for a basis. The main powerful source of the power supply system forms a demanded current (up to 12.1 kA) with the required magnetic field ramp of 1.2 T/s in the general chain according to a demanded cycle.

The powerful power supply source consists of connected in parallel thyristor rectifiers PS1, 2, powered from a high-voltage net 6 kV. Each of sources "PS" is a 12 phase rectifier with nominal parameters of 180 V x 6.3 kA, and phase shift between voltages of 15 degree. Together PS1, 2 form 24 phases regulated thyristor rectifier with nominal output parameters 180 V x 12.6 кА, that allows to receive the magnetic field ramp of 1.2 T/s. The peak power of a source is 2.5 MW.

Two additional power supply sources of essentially smaller power are intended for flexible adjustment of an working point of the accelerator. One of them allows to change simultaneously a field gradient in focusing and defocusing lenses, another only in defocusing ones.

The power supply system includes also equipment of regulation, management and diagnostics.
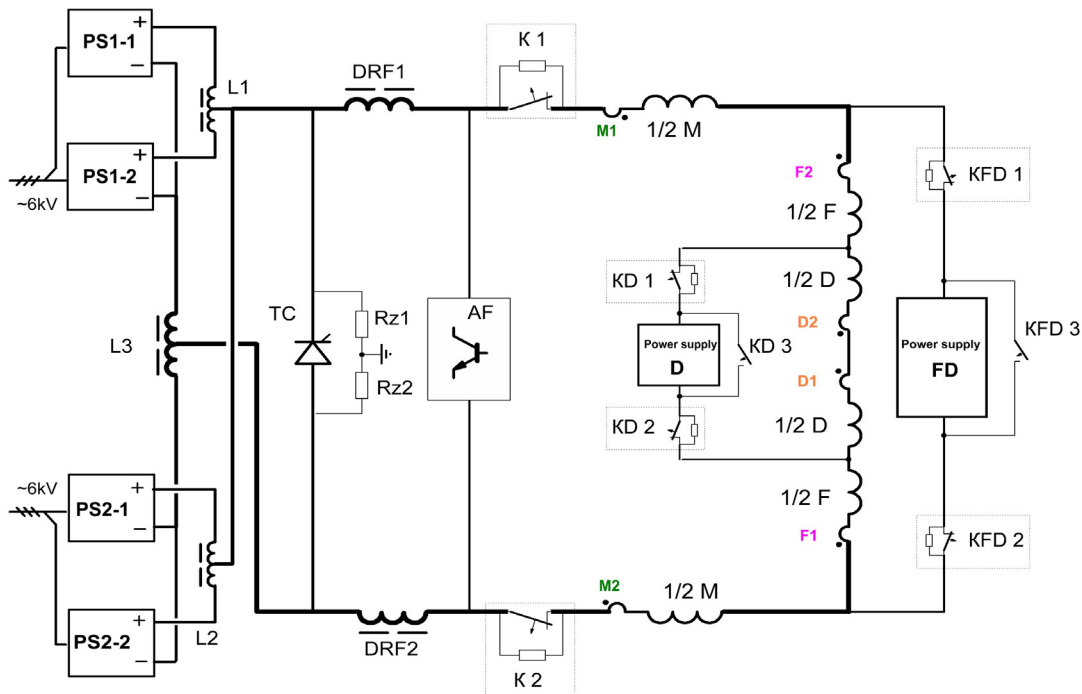
Fig. 1. The schematic diagram of the Booster power supply system (the explanation in the text).

04 Hadron Accelerators

QUENCH PROTECTION SYSTEM

The "switches" connected consistently with a chain of magnets and lenses are applied to evacuation of the accumulated energy from superconducting elements in case of superconductivity quench. They are controlled by a signal from detecting system that reacts on the occurrences of a normal phase in a superconductor. On the arrival of a control signal the switch is disconnected, and the energy, which has been saved up in the magnets, dissipates in resistors of the field dump, connected in parallel to the switches (fig. 2).
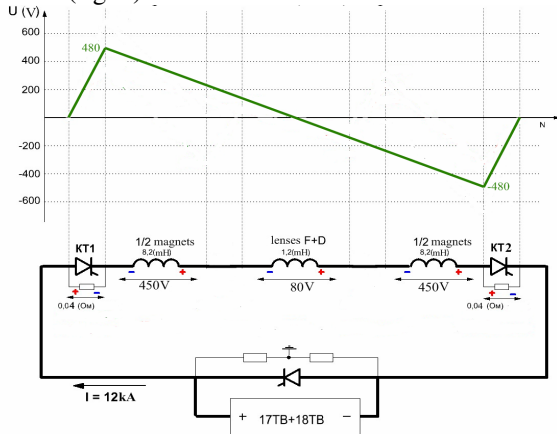
Rated characteristics in the process of energy evacuation:
- The constant time output of energy 220ms,
- Total field damping resistance 0,08Om,
- The voltage in the process of current output 980V.

Fig. 2. Potential on magnets and lenses

The dipole magnets (2 chains 1/2M) and quadrupole lenses (on 2 chains 1/2 F and 1/2 D) are connected through the switches of energy evacuation (К1, К2) to a source under the symmetric scheme concerning voltage supply. Inductance of groups and nominal resistance of dumping resistors are chosen so that the voltage on the current feed through concerning the ground potential have not exceed 500 V at the moment of energy evacuation. At the total voltage of U = 1000 V (±500 V); and maximum current of I = 12 kA the resistance have to be equal to

$$R = \frac{U}{I} = 83 mOm \cdot$$

At the total inductance of the magnetic system of L = 17.6 mH that corresponds to the evacuation process characteristic time of

$$t = \frac{L}{R} = 220 ms,$$

It is sufficient from the safety requirements.

THE SYSTEM ARAANGEMENT

Induction sensors of a magnetic field are established in the measuring magnets M 1, 2, lenses F 1, 2 and D 1, 2 (fig. 3). They are located near the Booster in the Sinchrophasatron building. Their output signals go to
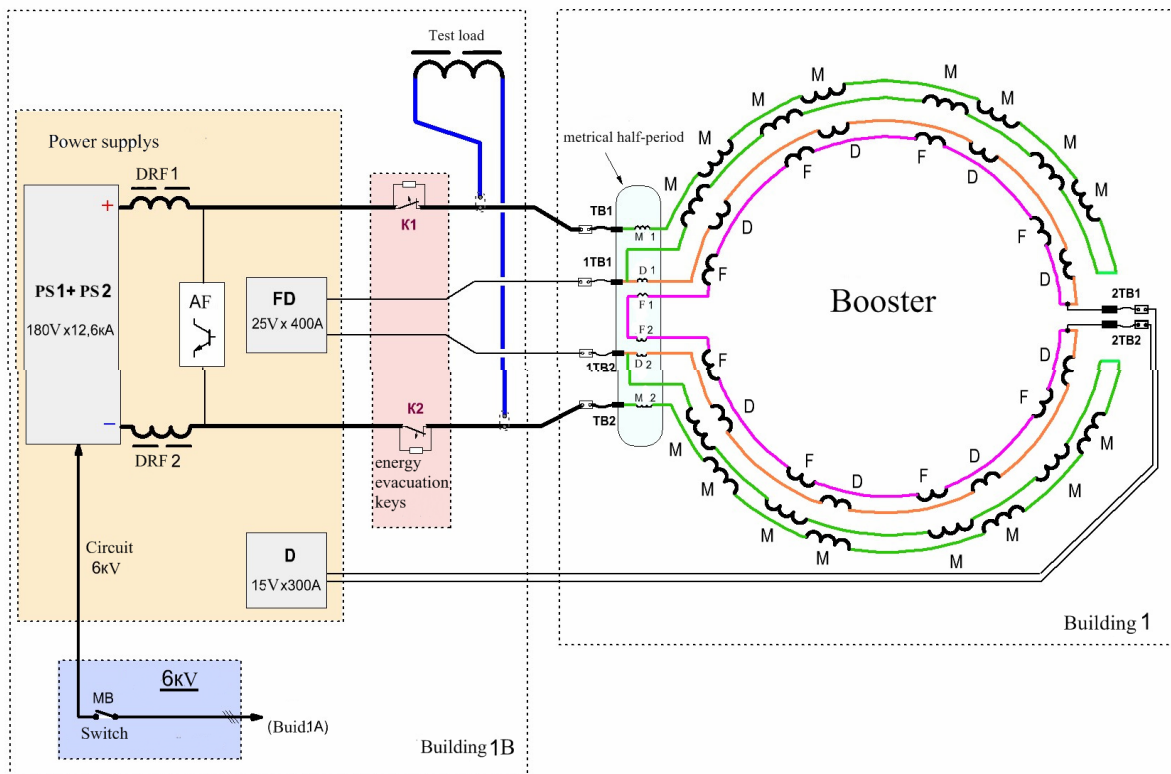
Fig. 3. The scheme of power supply system equipment arrangement.

04 Hadron Accelerators

All powerful equipment and the energy evacuation keys are located in the building 1B.

   Filter throttles DRF1, DRF2 together with the active filter (AF) reduce level of current pulsations to the demanded level. Resistors Rz1 and Rz2 symmetrize the output voltage of the source concerning ground. Thyristor switch shunts the power supply source at the moment of energy evacuation. Additional source FD of addition current in to lenses with output parameters 25 V x 400 A is connected through the switches of energy evacuation KFD1, 2 to a chain of consistently connected lenses. The source of addition in to the lenses D with output parameters 15 V x 300 A is similarly connected to a chain of defocusing lenses through switches KD1, 2.

REFERENCES

[1] NICA Conceptual Design Report, JINR, January 2008. http://www.jinr.ru/

[2] Khodzhibagiyan H.G., Smirnov A.A., The concept of a superconducting magnet system for the Nuclotron, *Proc. of the 12th Int. Cryogen. Eng. Conf.*, pp. 841-844, 1988.

[3] H. Khodzhibagiyan, N. Agapov, A. Kovalenko, A. Smirnov, A. Starikov, Development of fast-cycling superconducting magnets at JINR» *Proc. of the CRYOPrague 06*, Prague, July 2006.

04 Hadron Accelerators

DEVELOPMENT OF INJECTOR FOR ITEP HEAVY ION SINCHROTRON BASED ON LASER PLASMA GENERATOR

N. Alekseev, A. Balabaev, A. Belokurov, I. Khrisanov, A. Vasilyev,
Yu. Satov, B. Sharkov, A. Shumshurov, *ITEP, Moscow, 117259, Russia.*

Abstract

A schematic diagram of heavy ion injector based on laser ion sources is described. Two different basic laser configurations used in ITEP synchrotron. First laser excels in simplicity and consists of CO_2 free-running laser that is applied for carbon target plasma heating and ionization at laser power density $q=3 \cdot 10^{12} W/cm^2$ to create high current C^{4+} ion beam. Second master oscillator-amplifier laser configuration intends for production super high laser intensity at a target to provide considerable charge state in a plasma of heavy elements (Al, Fe, Ag etc). This laser configuration is founded on original physical principle[*] that simplifies the installation and ensures high reliability for long term operation.

Laser characteristics for the different laser scheme and ion current for injector outlet beam of C^{4+} and Ag^{+19} are shown in this paper. The latter was accelerated in synchrotron for energy up to 100 MeV/u.

[*] K. N. Makarov et al. Quantum Electronics (Russian), 2001, 31 (1), pp. 23÷29

INTRODUCTION

The fundamental knowledge of the high charge state ion generation with lasers was obtained in the frame of laser-plasma interaction researches. In Russia such investigations were carried out in leading physical institutes with different types of laser. In particular, it was shown that high intensity laser radiation focused on the material allows creation of high temperature powerful stream of plasma having small phase volume. The following separation of electron and ion components produces a pulsed ion source with superior luminosity. Basing on known in literature laser-plasma investigation publications one might say that there are no crucial distinctions for laser-plasma ion generators using different types (different wavelength) of lasers. Nevertheless, CO_2 lasers are mainly used in the practice due to their high output energy with comparative technical simplicity for the repetition rate operation, cheapness of the installation and ecological compatibility. These preferences of CO_2 lasers ensure adapting them in a laser-plasma ion source for an ion accelerator injector. The use of such injectors in a heavy ion synchrotron simplifies the accelerator scheme due to momentary (by a single pulse) ring filling by the particles of proper mass and charge state number.

The investigations of the ion generation from plasma produced by CO_2 laser pulses with a target power density q up to $q \leq 5 \cdot 10^{13} W/cm^2$ and the laser-plasma generators (LPG) development were realized by ITEP-CERN-TRINITI collaboration [1-9]. In the frame of lead ion generation measurements it was shown that, in particular:

1. The total ion current is proportional to the laser pulse energy while the other parameters remain unchanged.

2. The average ion charge state number is proportional to logarithm of the laser flux at a target, at least, for the case of ionization of external atomic shells.

3. For an effective laser-plasma heating it is necessary to use the laser pulse duration τ_p less than the characteristic plasma expansion time τ_{exp} ($\tau_p < \tau_{exp}$). The latter is defined by the ion velocity and the characteristic plasma thickness which depend finally on the target laser pulse density. Otherwise, the process of laser-plasma interaction for long high power density pulses is complicated due to the refraction of the laser beam in the plasma corona, self-focusing of laser radiation and generation of shock waves distorting the expanding plasma flow. As a result, the laser heating efficiency drops and useful part of ions near expansion axis is decreased.

The experimental data allow choosing the laser driver scheme with such general considerations. It is known, for example, that the free-running CO_2 generator provides the laser pulses with duration $\tau_p \leq 40ns$. That allows to use efficiently such a laser for ion generation up to $q \leq 10^{11} \div 10^{12} W/cm^2$ and, correspondingly, for the plasma expansion velocity $V_{exp} < 10^6 cm/s$. In these conditions the plasma extension is not to be significant during the laser heating $V_{exp} \cdot \tau_p < 0.4mm$. The ion generation for a higher laser flux requires using more complicate optical laser scheme such as master-oscillator power amplifier (MOPA) configuration. The shortest pulse duration is to be $\tau_p \approx 150$ ps correspondingly the amplification line width of 7GHz for the typical gas mixture of an atmospheric pressure CO_2 laser [10]. The ITEP heavy ion accelerator injector is based on both the free-running and the MOPA CO_2 lasers (LPG-1,2) to carry out scientific program devoted to fundamental researches and medical applications. Now the heavy ion acceleration program is basically founded on two laser systems: effective free-running generator "Malish" and wide aperture laser L-100 that operates in two modes, either a free-running generator [11] or a master oscillator-power amplifier configuration. The laser-plasma ion source with the MOPA scheme is directed to generate extremely ionized heavy particles, similar to Al, Fe, Ag, Pb, etc. The free-running CO_2 laser is used in the injector of carbon ions.

DEVELOPMENTS OF LPG-1 AND LPG-2

Laser plasma generator LPG-1 including the free-running laser "Malish" was developed to increase output laser intensity as a main parameter. The improvement consists of modernization of an electrical scheme for formation of volume discharge basing on the techniques described

in [12]. The concept is to try to separate the stages of the discharge volume ionization and the energy input to the discharge similar to the non-self-maintained discharge techniques. To do this a specially profiled voltage pulse is generated to apply on the discharge electrodes simultaneously with UV-preionization of gas volume. This is provided by introduction of additional `shock' LC-circuit to the HV pulse generator. Finally, it results in a growth of the energy input to the uniform discharge and to raise the molecular gas content in the active mixture of the laser. As a result, it was obtained superior laser specific output laser power of 105 MW/l that corresponds to peak laser pulse of about 60 MW [13] as shown in Fig.1.
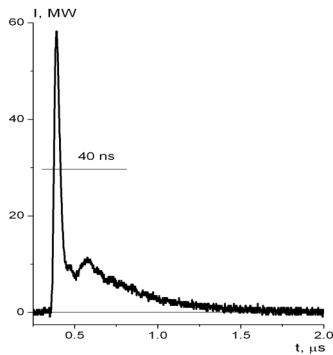
Figure 1: Oscilloscope trace of pulse intensity for laser driver in LPG-1.

A numerical calculations shows that laser target power density reach for focal spot center value of $5 \cdot 10^{11}$ W/cm^2 . This laser beam intensity level allows reliable creation of C^{4+} particles in plasma and production about 100mA of total ion current after extraction system.

MOPA laser driver produces now laser pulse with duration of ~30ns (see Fig.3) that corresponds to peak power density $q=10^{13}$W/cm^2 in the focal spot.
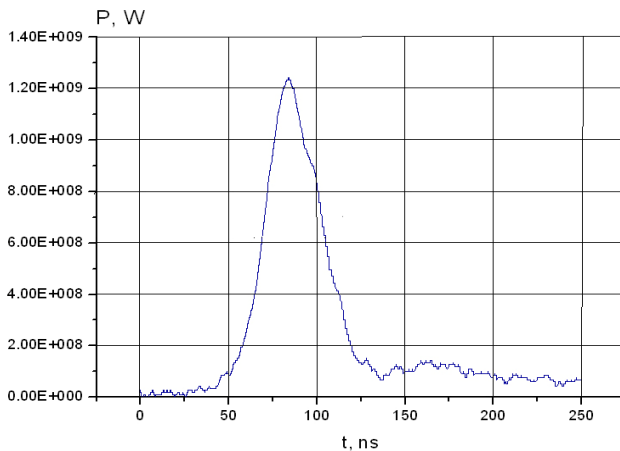
Figure 2: Oscilloscope trace of pulse intensity for laser driver in LPG-2.

In the frame of heavy ion injector development it is intended to improve the laser driver for LPG-2 to reach

for higher laser target flux. The main modification of the MOPA scheme is including of two-module preamplifier that allows proper formation of the laser special form and the temporal shape of the MO beam at the power amplifier entrance. At present, the preamplifier with active volume of 3 liters has been manufactured and is under testing (see Fig.3). Second modification of the ion injector concerning both LPG-1 and LPG-2 generators is a perfection of focusing mirror. The idea is to install off-axis parabolic mirror instead of present spherical one.

As a result of modifications, the laser target power density might reach for value of $5 \cdot 10^{14}$ W/cm^2 in accordance with estimations that could ensure more wide investigations of heavy ion production, acceleration and application.
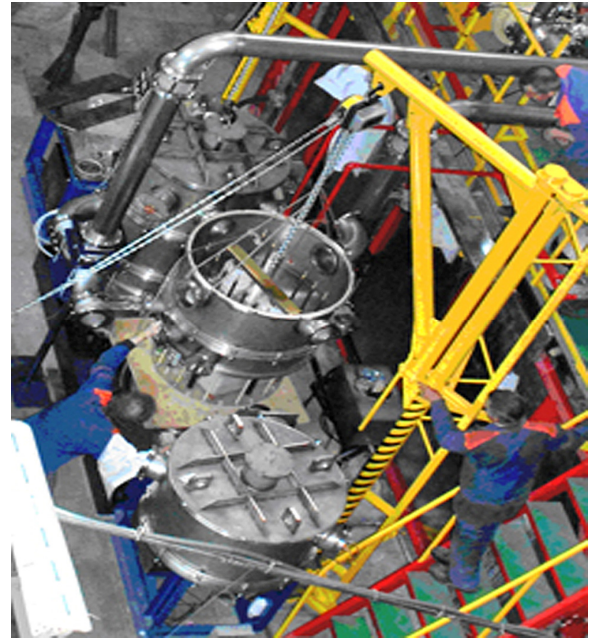
Figure 3: The view of two-module preamplifier.

SCHEMATIC DIAGRAM OF ITEP HEAVY ION INJECTOR

The synchrotron injector scheme based on the laser-plasma ion generator is shown in Fig.4. The laser beams created by different systems are converted in the optical scheme to adjust with a common focusing objective with aperture F/10 (diameter of the laser beam is 160mm). The plasma jet expanded after the target heating comes up to the HV extraction system where separation of charged particles occurs and the ion beam is created. The ion beam comes into a buncher operated at frequency of 2.5~MHz after low energy transport line consisted of three electrostatic lenses and then goes to the resonance two-gap (2MeV per gap) accelerator I-3.
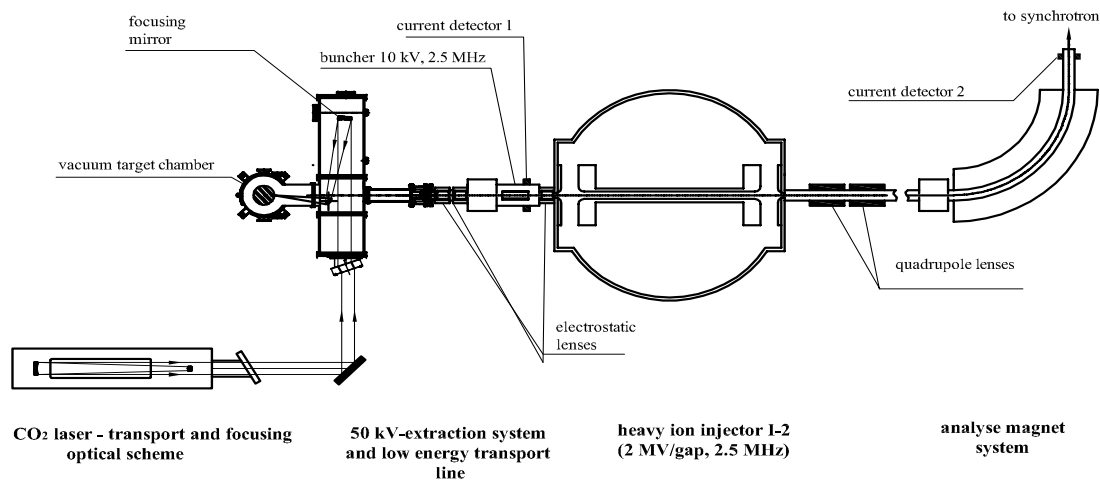
Figure 4: ITEP heavy ion injector scheme based on laser-plasma generator.
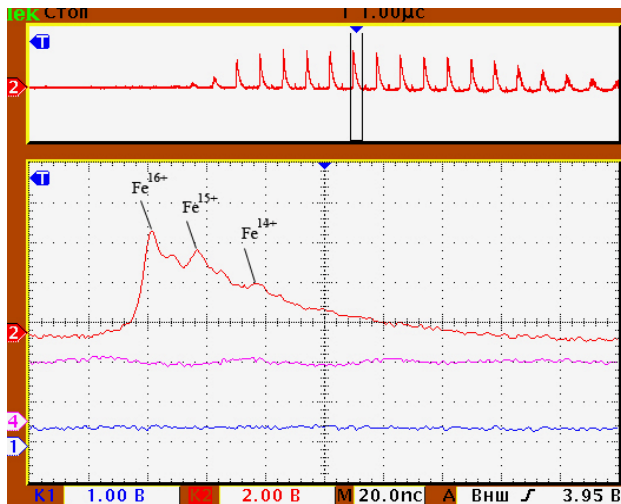
Figure 5: Bunched structure of iron ion beam at the outlet of I-3 (upper trace) and charge state content (lower trace).

The oscilloscope trace of bunched iron ion beam at the outlet of I-3 and charge state structure is shown in Fig. 5. The magnet analyzer is situated at the injector output so, finally, the ion beam is separated for one charge state number as shown, for example, in Fig. 6 for the beam of C^{4+}.
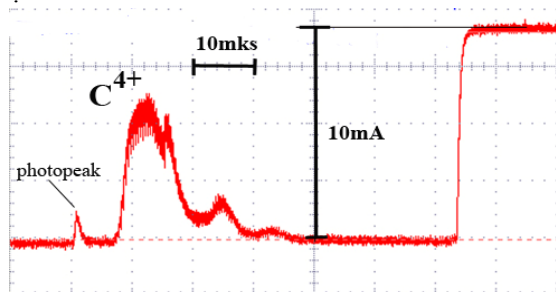
Figure 6: C^{4+} ion current signal at outlet of injector.

ITEP acceleration complex operated this year 630 hours in accumulation mode of carbon nuclei for energy of 200-300 MeV/u, 480 hours in acceleration mode up to energy of 4GeV/u, 60 hours for acceleration of silver nuclei with energy 100 MeV/u and 228 hours for iron nuclei acceleration for energy up to 230 MeV/u. During these periods experiments devoted to high energy density physics, radiation biology, fundamental nuclear physics and their applications were carried out.

REFERENCES

 [1] K. Makarov, et al., Zh. Eksp. Teor. Fiz.(Russian), 106(6), 1994, pp.164-1662.
[2] S. Kozochkin, et al., Fiz. Plazmy (Russian), 20(1), 1994, pp.110-114.
[3] S. Kondrashev, N. Mescheryakov, B. Sharkov, et al., Rev. Sci. Instrum. 71(3), 1994, pp.1409-1412.
[4] V. Baranov, et al. Laser and Particle beams. 14(3), 1996, pp.347-368.
[5] K. Makarov, et al. Pis'ma Zh. Eksp. Teor. Fiz. 71(1), 2000, pp.13-17.
[6] A. Stepanov, et al., Pis'ma Zh. Eksp. Fiz. 29(5), 2003, 36-41.
[7] A. Stepanov, et al., Plasma Phys. Control Fusion. 45, 2003, pp.1261-1281.
[8] Yu. Satov, et al. J. of Russian Laser Research. 25(6), 2004, pp.524-534.
[9] Yu. Satov, et al. J. of Russian Laser Research. 25(3), 2004, pp.205-216.
[10] R.L. Abrams, Appl. Phys. Lett., 25, 1974, pp. 609.
[11] B. Sharkov, et al., Proceedings of EPAC08, Genoa, Italy, 352-355.
[12] Yu. Satov, et al., Russian Federation Patent #RU2096881-C1, H01S-003/097, 199828, 1997.
[13] Yu. Satov, et al., Institute of Theoretical and Experimental Physics 2009, preprint #3-09, Moscow, 2009-09, 32p.

04 Hadron Accelerators

88

SIMULATION OF Au^{32+} BEAM LOSSES DUE TO CHARGE EXCHANGE AND DYNAMIC VACUUM IN NUCLOTRON BOOSTER

A.V. Philippov$^{\#}$, A.B. Kuznetsov , V.A. Mikhaylov , A.O. Sidorin , G.V. Trubnikov

JINR, Veksler and Baldin Laboratory of High Energy Physics Dubna, Russia

P. Puppel , P. Spiller

GSI Helmholtzzentrum für Schwerionenforschung GmbH, Darmstadt, Germany

Abstract

The StrahlSim code [1] was used to simulate the beam loss and the dynamic vacuum for the proposed Nuclotron booster [2]. The Nuclotron booster will accelerate Au32+ ions from 6.2 MeV/u to 600 MeV/u. The simulations have been carried out considering systematic injection (0% to 10%) and RF-capture losses (5% to 15%). Furthermore the influence of an ion catcher system on the beam loss has been investigated, in order to estimate, if such a system could stabilize the beam loss. Without an ion catcher system, zero systematic losses, and a static pressure of 10^{-11} mbar ($7.5 \cdot 10^{-12}$ Torr), the transmission was calculated to be 83%. The presence of an ion catcher system would stabilize the transmission at a considerably higher level than without such a system for all scenarios.

BOOSTER PARAMETERS LIST

The main functions of the Nuclotron booster are the following [2]:

- Accumulation of $4 \cdot 10^9$ Au^{32+} ions in the booster;
- Acceleration of the ions up to energy of 600 MeV/u that is sufficient for stripping the gold ions up to the charge state of 79+;
- Simplification of the requirements to the vacuum conditions in the Nuclotron owing to higher energy and charge state of the ions injected into the Nuclotron;
- Decrease of the ion beam longitudinal emittance at the energy of approximately 100 MeV/u by application of electron cooling.

The FODO lattice was considered for further investigation as the more preferable lattice design. The parameters for the booster are listed in tables 1, 2, and 3. A diagram of the booster cycle and a scheme of the booster vacuum system are shown in Fig. 1, 2.

SIMULATION SETUP

The acceleration ramp had to be divided into two parts, because StrahlSim is not capable of simulating a waiting time in the middle of the ramp, as it is foreseen in the Nuclotron booster cycle. The division of the simulation is shown in Fig. 1 (left and middle) and was used for all calculations. First part (red line): injection at 6.2 MeV/u, acceleration with 1 T/s to 100 MeV/u and 1 s waiting time (electron cooling) at this energy. Second part (green line): acceleration with 1 T/s to a beam energy of 600 MeV/u,

followed by a fast extraction at this energy, and ramping down. The beam losses due to electron cooling were not simulated, because StrahlSim is unfortunately not able to consider these losses. So the simulated beam losses during the cooling time are only due to charge exchange processes, and therefore less than the beam loss that can be expected.

Table 1: Parameter list for the Nuclotron booster lattice.

Fold symmetry	4
Number of the FODO lattice cells per arc	6
Length of lattice cell, m	9
Length of straight sections per cell, m	4
Betatron tunes	5.8/5.85
Phase advance per cell	1.51
Amplitude of β-functions, m	17
Maximum dispersion function, m	2.9
Dipole	
Beam horizontal/vertical emittance, π·mm·mrad	10/10
Effective field length, m	2.2
Curvature radius, m	14
Quadrupole	
Bending angle, degree	9
Effective field length, m	0.4
Average aperture	
Chamber shape	elliptical
Vacuum chamber, m^2	0.065×0.032

Unfortunately there are no charge exchange cross sections for Au^{32+}. Therefore the cross sections for Au^{31+} have been used for all simulations discussed in this work. The differences between these cross sections are considered to be negligible.

Table 2: Parameter list for the Nuclotron booster.

Ions	Au^{32+}
Circumference, m	211
Injection/extraction energy, MeV/u	6.2/600
Magnetic rigidity, T·m	2.4÷25

$^{\#}$philippov@jinr.ru

05 Beam Dynamics and Electromagnetic Fields

Table 2: Parameter list for the Nuclotron booster (continue).

Dipole field, T	0.17÷1.8
Quadrupole gradient, T/m	20
Pulse repetition rate, Hz	0.25
Magnetic field ramp, T/s	1
Harmonic number	4, after cooling 1
Number of bunches	4, after cooling 1
Beam injection/extraction type	one turn/one turn
Time for injection or number of turns, s	$7 \cdot 10^{-6}$
Injection store duration, s	0.02
Start-up time for the ramp, s	0.02
Vacuum, Torr	10^{-11}
Beam intensity, ions per pulse	$2 \div 4 \cdot 10^{9}$

Table 3: Vacuum system: gauge, pumps and gates.

Cold cathode gauge head, IKR 060, DN40 CF	36
Robust thermal conductivity gauge, Pirani gauge	6
Roughing-down pump Varian TriScroll 300	42
TM pump, Pfeiffer TMU 071 YP DN63 CF	28
TM pump, Pfeiffer TMU 521 YP DN160 CF	14
Adsorption pump, speed 80 l/s	22
Magnetic-discharge pump, speed 80 l/s	6
Titanium sublimation pump, speed 80 l/s	6
High vacuum gate, 10836-CE44 DN63	56
High vacuum gate, 10848-CE44 DN160	14

The types of pumps that were considered for beam loss simulations due to dynamic vacuum effects include the following: adsorption, magnetic-discharge and titanium sublimation pumps (see Fig. 2). For the simulation a total pumping speed of about 1.3 m³/s was assumed.

RESULTS

The Au^{33+} ions appear in the booster as a result of charge exchange interaction of the circulating beam ions of Au^{32+} with residual gas (electron loss process). The other process, i.e. ionization of circulating beam ions of Au^{32+}, occurs due to interaction with residual gas as well. A collimation of Au^{31+} and Au^{33+} ions would stabilize the dynamic vacuum.

In order to investigate the influence of an ion catcher system on the stability of the vacuum system and the beam loss, ion catchers have been placed in the lattice.

The tracking simulations by StrahlSim give a total catching efficiency for each charge exchange channel. Here we give only the values for the collimation efficiency of the two considered charge exchange channels: about 86% for $Au^{32+} \rightarrow Au^{31+}$ and about 91% for

$Au^{32+} \rightarrow Au^{33+}$. These values were obtained with a theoretical catcher system.
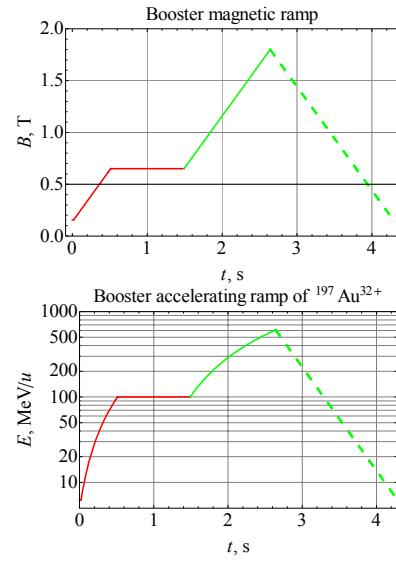
Figure 1: Nuclotron booster acceleration ramp for Au^{32+} magnetic ramp (top), accelerating ramp (bottom).

If such high collimation efficiencies can be reached in the real machine, has to be investigated separately. The collimation screenshots are shown in Fig. 3.
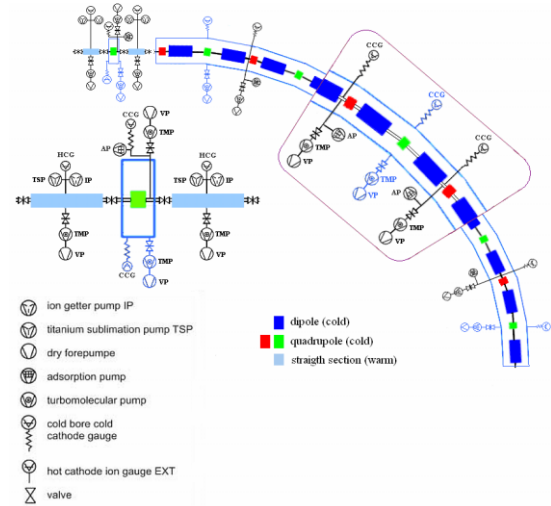
Figure 2: The Nuclotron booster vacuum system.

Tables 4 and 5 show the main simulation results. Simulations with extraction losses have been performed as well, but these results are not shown, because the pressure rise due to extraction losses would only have an influence on the simulation, if multiple cycles in a row would have been simulated. The transmission of simulations considering extraction losses only (5% to 15%), was stable at about 40% (with a static pressure of 10^{-10} mbar).

05 Beam Dynamics and Electromagnetic Fields

Table 4: Losses of Au^{32+} ion beams in the Nuclotron booster, with collimation.

Injection losses	Pressure, mbar		
	10^{-12}	10^{-11}	10^{-10}
0%	1%	6%	45%
5%		42%	64%
10%		61%	75%
RF capture losses	Pressure, mbar		
	10^{-12}	10^{-11}	10^{-10}
5%		41%	63%
10%		60%	75%
15%		72%	82%

Table 5: Losses of Au^{32+} ion beams in the Nuclotron booster, without collimation.

Injection losses	Pressure, mbar		
	10^{-12}	10^{-11}	10^{-10}
0%	2%	17%	73%
5%		77%	89%
10%		89%	94%
RF capture losses	Pressure, mbar		
	10^{-12}	10^{-11}	10^{-10}
5%		71%	87%
10%		85%	92%
15%		91%	95%
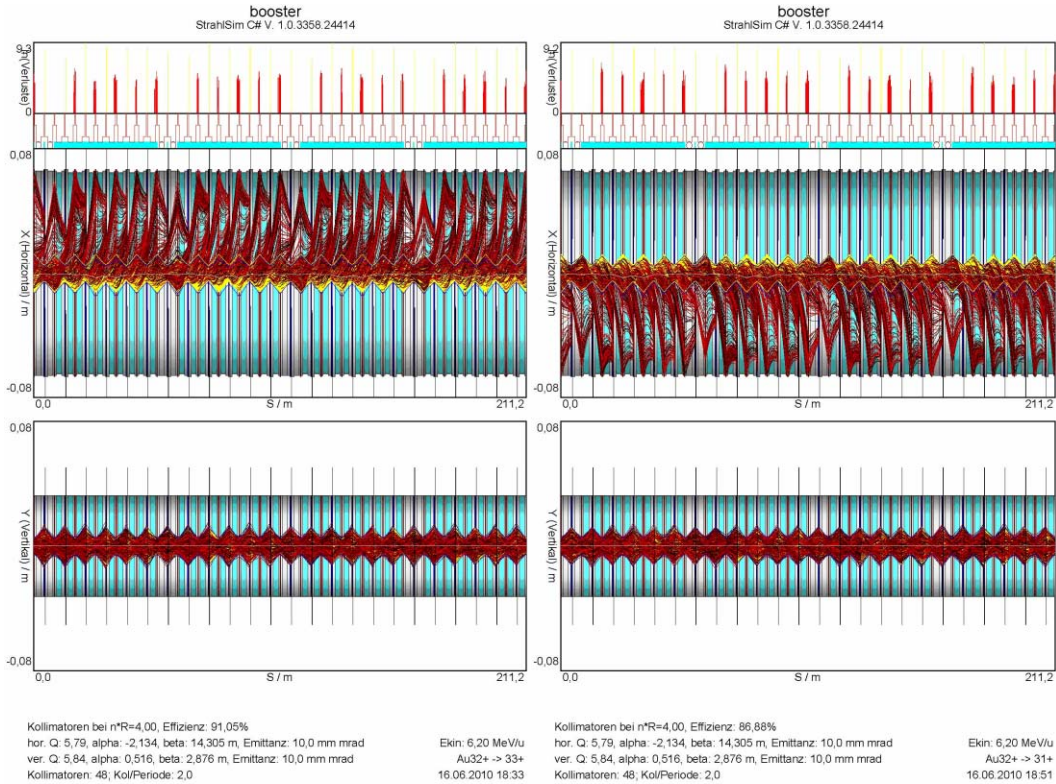
Figure 3: Collimation of Au^{32+} ions in the Nuclotron booster. Charge exchange channel: Au^{32+}→ Au^{33+} (left) and Au^{32+}→ Au^{31+} (right).

In total more that 100 simulations with different parameters have been taken out.

DISCUSSIONS

The simulation results show a strong dependence of the losses on the static pressure.

For a static pressure of 10^{-10} mbar the losses of all scenarios with (without ion catchers) is more than 40÷80% (70÷90%). As the Nuclotron booster is a cold machine, it is likely, that the static pressure is better than 10^{-10} mbar (7.5·10^{-11} Torr).

Furthermore the simulation results show, that the reduction of systematic losses to an absolute minimum is curtail for a stable operation of the Nuclotron booster with Au^{32+} ions.

REFERENCES

[1] C. Omet. Kollimatorsystem zur Stabilisierung des dynamischen Restgasdrucks im Schwerionensynchrotron SIS18: Ph. D. thesis. 2008.
[2] Conceptual Design Report of Nuclotron-based Ion Collider fAcility (NICA). JINR. 2008.

05 Beam Dynamics and Electromagnetic Fields

RTS&T CODE STATUS

I.I. Degtyarev*, O.A. Liashenko , F.N. Novoskoltsev , I.A. Yazynin , IHEP, Protvino, Russia
A.I. Blokhin, IPPE, Obninsk, Russia

Abstract

The paper describes the main features of the RTS&T2010 the modern version of the RTS&T (Radiation Transport Simulation and Isotopes Transmutation problem) code system [1]. The RTS&T code performs detailed Monte Carlo simulations of many type of particles transport in complex spatial geometries with composite materials in the energy range from thermal energy up to 100 TeV. The RTS&T code considers interaction of low-, intermediate-, and high-energy particles with condensed matter, including hadron-nucleus interactions inside the target, generation and transportation of secondary particles, deposition of energy and production of radionuclides in the target. Recently, the transfer of ions was added and tested. The modern version of the RTS&T code supports a researches in the fields of accelerator and reactor technologies, radiotherapy, space radiation, and in many other fields which are related to particle and ion transport phenomena.

INELASTIC HADRONIC AND PHOTONIC INTERACTIONS

Inelastic hadronic and photonic interactions are simulated within RTS&T code by several energy-dependent models based on the different microscopic and macroscopic approaches (Fig. 1) [2].
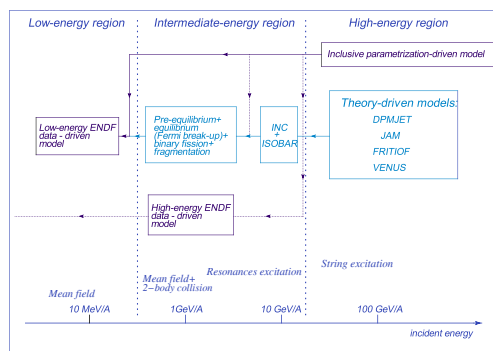
Figure 1: Inelastic hadronic and photonic interactions are simulated within RTS&T code by several energy-dependent models based on the different microscopic and macroscopic approaches.

High-Energy Region

To simulate of hadron(nucleus)-nucleus inelastic collisions at $E > 5$ GeV the modified versions of some micro-models (DPMJET-II/III, JAM, FRITIOF,VENUS, RQMD) or an inclusive parametrization-driven model can be used. These codes has been completed with a simulation of the nuclear destruction at fast stage of the interaction, with a calculation of the excitation energy of the nuclear residual nuclei and with a simulation of the nuclear relaxation stage in the framework of the statistical evaporation model to calculate the characteristics of the inelastic hadron-nucleus and nucleus-nucleus interactions at the energies higher 3-5 GeV per nucleon.

Intermediate-energy region

In the RTS&T calculations, the hadron-induced nuclear reaction process in the energy region about 20 MeV to 5 GeV is assumed to be a three-step process of spallation (intranuclear cascade stage), pre-equilibrium decay of residual nucleus and the compound nucleus decay process (evaporation/high-energy fission competition). To calculate the intranuclear cascade stage, the Dubna-version of intra-nuclear cascade model coupled with the Lindenbaum-Sternheimer isobar model for single- and double-pion production in nucleon-nucleon collisions and single-pion production in pion-nucleon collisions was provided. Recently, an addition of multiple-pion channels was included in code package to simulate up to 5 pions emission. The pre-equilibrium stage of nuclear reaction simulation is based on the exciton model. The initial exciton configuration for pre-equilibrium decay is calculated at the cascade stage of reaction or postulated in general input. The equilibrium stage of reaction (evaporation/fission processes competition) is performed according to the Weisskopf-Ewing statistical theory of particle emission and Bohr and Wheeler or Fong theories of fission. To calculate the quantities determining the total fission width, Atchison prescriptions are used.

Low-Energy Region

The RTS&T code uses continuous-energy nuclear and atomic evaluated data files to simulate of radiation transport and discrete interactions of the particles in the energy range from thermal energy up to 20/150/3000 MeV. In contrast with is a well-known and widely used Monte Carlo code MCNP [4, 5] for neutron, photon, and electron transport simulations, the ENDF-data driven model of the RTS&T code does access the evaluated data directly. In current model development, all data types provided by ENDF-6 format can be used in the coupled multy-particle radiation

* Igor.Degtyarev@ihep.ru

08 Applications of Accelerators, Technology Transfer and Industrial Relations

transport modeling. Universal data reading and preparation procedure allows us to use various data library written in the ENDF-6 format (ENDF/B VI/VII,JENDL, JENDL-HE, FENDL, CENDL, JEF, BROND, LA150, ENDF-HE/VI, IAEA Photonuclear Data Library etc.). ENDF data pre-processing (linearization, restoration of the resolved resonances, temperature dependent Doppler broadening of the cross sections and checking and correcting of angular distributions and Legendre coefficients for negative values are produced automatically with the Cullen's ENDF/B Pre-processing codes [3] LINEAR, RECENT, SIGMA1 and LEGEND rewritten in ANSI standard FORTRAN-90.

ISOTOPES TRANSMUTATION PART OF THE RTS&T CODE

The isotopes transmutation process is described by a system of balance ordinary differential equations. For the isotopes concentration N_i, where $i = 1, M$ (M is the total number of nuclides which to participate in connected transitions) the given system of equations is the following:

$$\frac{dN_i(t)}{dt} = -N_i \cdot \left(\lambda_i + \sum_k \int_0^{E_0^k} \sigma_i^k(E) \cdot \phi^k(E,t)dE \right)$$
$$+ \sum_{j \neq i} N_j \cdot \left(\lambda_{ji} + \sum_k \int_0^{E_0^k} \sigma_{ji}^k(E) \cdot \phi^k(E,t)dE \right) \quad (1)$$
$$N_i(0) = N_i^0,$$

where $\sigma_i^k(E)$ is summary cross section of reactions presenting the change of i-th nucleus structure, $\sigma_{ji}^k(E)$ is the partial cross sections of i-th isotopes formation reactions from j-th mother nucleuses under action of particles of grade k with the energy E, λ_i - disintegration constant of the i-th isotopes, λ_{ji} - disintegration constant of the j-th isotopes on the channels were presented to i-th nuclide formation; $\phi^k(E,t)$ is the particles of grade k with the energy E total flux, maximum significance of which is E_0^k. Breaking a period of exposition of a material on a number of temporary sessions with $\phi^k(E,t) \equiv \phi^k(E)$, we receive from (1) the independent system of equations with constant factors:

$$\begin{cases} \frac{dN_1}{dT} = C_{11}N_1 + C_{12}N_2 + ...C_{1n}N_n \\ \frac{dN_2}{dT} = C_{21}N_1 + C_{22}N_2 + ...C_{2n}N_n \\ \quad .... \\ \frac{dN_n}{dT} = C_{n1}N_1 + C_{n2}N_2 + ...C_{nn}N_n \end{cases}$$

with

$$C_{ij} = \begin{cases} - \left(\lambda_i + \sum_k \int_0^{E_0^k} \sigma_i^k(E) \cdot \phi^k(E)dE \right), i = j \\ \\ \lambda_{ij} + \sum_k \int_0^{E_0^k} \sigma_{ij}^k(E) \cdot \phi^k(E)dE, i \neq j \end{cases}$$

Given system of equations can be recorded in a matrix kind:

$$\frac{dN}{dt} = CN, \quad N(0) = N_0. \quad (2)$$

Analytical decision (2) is

$$N(t) = \exp(Ct)N_0, \text{ where} \quad (3)$$

$$\exp(Ct) = \sum_{s=0}^{\infty} \frac{C^s t^s}{s!}, C^0 = E.$$

We shall note a number of the equation system (2) features:

1. Practically at any modes of exposition or endurance of any material the isotopes transmutation process contains both fast and slow making, and the distinction between them can reach 20 and more orders. Such spread of significance's of elements of a matrix results to its bad conditionally $[cond(C) >> 1]$ and allows to assume, that a system of equations (2) is "stiff". Correctly the definition of "stiffness" of the equation system requires the calculation of own significance's λ of matrix C, that reasonably is a difficult problem for large-size matrixes. Usually for these purposes a ODE system use the following criterion - the system is "stiff" if inequalities are executed:

$$||C||_1^{-1} << H \quad |Cp(C)|^{-1} << H \quad (4)$$

where H is the duration of exposition session or endurance, $||C||_1$ and $Sp(C)$ is the norm and trace of matrix C respectively: $||C||_1 = \max\limits_{1 \leq i \leq n} \sum\limits_{j=1}^n |c_{ij}|$, $Sp(C) = \sum\limits_{i=1}^n c_{ii} = \sum\limits_{i=1}^n \lambda_i$. Numerical integration of "stiff" systems any obvious discrete methods (Runge-Kutta, Adams and etc.) results in effect "error explosion" at the chosen step $h \geq \max(||C||_1^{-1}, |Sp(C)|^{-1})$. Given restriction from above on a integration step can result in unreal times of account when connected transitions (chains combined with nuclear reactions of radiation disintegration) contain nuclides with strongly distinguished life-times. Hence, application of standard methods of numerical integration non-stiff systems in an isotopes transmutation problem unacceptably.

2. The majority of specialized methods of numerical integration of "stiff" systems of equations are based on implicit discrete methods (Rosenbrok, Kollahan and etc.), which in case of a system with constant factors require calculations of a return matrix $(E + hC)^{-1}$, where h is the integration step, E - unit matrix. As the overwhelming majority of matrix C elements is considerably less than 1, reference (manipulation) of a given matrix is made with a large error, which grows with an increase of its size and with a reduction of

the integration step. Using of arithmetic with a floating point of double accuracy to isotopes transmutation problem solution does not remove this problem (for example, at radioactive disintegration of ^{235}U nuclei, $C_{ii} = 3 \cdot 10^{-17}$ and, in case of small h, even the operation of summation the diagonal elements of matrices E and hC already passes on limit of allowable accuracy by use of the 64 bits computers).

The marked specific of an isotopes transmutation problem limits the applicability discrete methods of numerical integration of ODE systems, that makes the their universal settlement circuit unsuitable for construction. Direct use of the analytical decision (3) at large times and bad conditionality of the matrix C results in unjustified quantity terms at calculation exhibitor and high error. For the decision of a system of equations (2) in RTS&T code the circuit of calculation $exp(Ct)$ was applied recurrent, which gives satisfactory results even in case of brightly expressed "stiffness" of a equations system (2) in a wide range of intervals of time h.

To construct recurrent of the calculation circuit $exp(CH)$, where H is the duration of the exposition session, the interval H is broken into a number of any uniform sections h. Then isotopes concentration in each discrete moment of time $tn = nh, n = 0, 1, ...$ are defined by the formula:

$$N_{n+1} = N_n \exp(Ch) \quad n = 0, 1... \qquad (5)$$

To the exponential $exp(Ch)$ calculating the additional recurrent matrix equation construction is required. Such step h' is chosen, which satisfied to following conditions:

$$h' = \frac{h}{2^K}, \qquad h' \ll \min(\|C\|^{-1}, |Sp(C)|^{-1})$$

where K is any integer value. Having calculated on (3) $exp(Ch')$, we can find $exp(Ch)$, applying consistently formulas:

$$\exp(2Ch') = \exp(Ch') \exp(Ch'),$$

$$....$$
$$\exp(2^K Ch') = \exp(2^{K-1} Ch') \exp(2^{K-1} Ch').$$

We shall record these equations as the recurrent matrix equation:

$$\phi_{k+1} = \phi_k^2, \text{ where } \phi_k = \exp(2^k Ch'), \quad k = 0, 1, ..., K; \qquad (6)$$

Thus, it is possible to choose so small size h', that high accuracy of representation $exp(Ch')$ by decomposition (3) with small number of the members (s) is provided no matter how. On the other hand, the use recurrent of equations (5) and (6) for the decision of a system (1) considerably reduces number of steps of integration for the given interval H:

$$\frac{H}{h} = 2^{-K} \frac{H}{h'}.$$

That removes a "large times" problem in any isotopes mixes. Valuation of a relative error of the numerical circuit of the decision of an equation system (1) to be made according to the Runge rule: i.e. results received for the steps $h'(K)$ and $h'/2(K+1)$ are compared. As indicative isotopes transmutation process with brightly expressed "stiffness" of equation system the spontaneous disintegration of ^{235}U nuclei is chosen, where in connected transitionse both short-period with a half-life period $T_{1/2}$ about 1 sec (^{211}Po, ^{215}Po), and long-period (^{231}Pa, ^{235}U) isotopes participate. Besides the chain-length of U transitions makes more than 10 links, that can also demonstrate reliability of a settlement method at the "extreme stiff situation" (see Fig. 2).
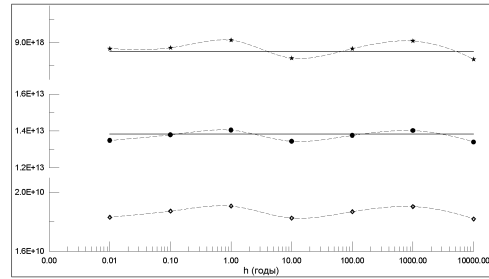
Figure 2: Dependence of settlement nuclear concentration of $^{211}Pb(\diamond)$, $^{227}Th(\bullet)$ and $^{231}Pa(\star)$ from a step of integration h at ^{235}U disintegration in current of 10000 years.

REFERENCES

[1] I.I. Degtyarev, A.E. Lokhovitskii, M.A. Maslov and I.A. Yazynin, "RTS&T Monte Carlo Code (Facilities and Computation Methods)", Proc. of the Third Workshop on Simulating Accelerator Radiation Environments (SARE-3), May 1997, KEK, Tsukuba, Japan.

[2] I.I. Degtyarev, O.A. Liashenko, I.A. Yazynin, A.I. Blokhin and V.I. Belyakov-Bodin, "Simulation of Relativistic Hadronic Interactions in the Framework of the RTS&T-2004 Code", Proc. of RuPAC XIX Conf., Dubna, 2004.

[3] D.E. Cullen, "The 1996 ENDF/B Pre-Processing Codes", The International Atomic Energy Agency, Vienna, Austria, IAEA-NDS-39, Rev. 9, November, 1996.

[4] J.F. Briesmeister, Ed., "MCNP A General Monte Carlo N-Particle Transport Code Version 4C", LA-13709-M, Los Alamos National Laboratory, March, 2000.

[5] F.B. Brown, A.C. Kahler, G.W. McKinney, R.D. Mosteller, M.C.White, "MCNP+DATA+MCNPX Workshop", LA-UR-07-2053, Los Alamos National Laboratory, 2007.

08 Applications of Accelerators, Technology Transfer and Industrial Relations

THE COMPACT FARADAY CUP FOR RADIOBIOLOGICAL RESEARCHES IN IHEP ACCELERATORS BEAMS

Yu. Antipov, N. Anferov, G. Dantsevich, A. Koshelev, A. Larionov, V. Seleznev, A. Sytin,
Institute for High Energy Physics, Protvino, Moscow region, Russia

Abstract

IHEP's experts are currently working on the creation of a medical irradiation centre with beams of protons and carbon ions on the basis of IHEP acceleration complex. Already existing IHEP accelerators I-100 - U-1,5 - U-70 are forming a complete chain capable of accelerating not only protons, but also, due to certain modifications, light ions: deuterons and carbon. The compact autonomic Faraday cup which works in the atmospheric environment has been developed to measure currents in the accelerators beams. The device has a good electromagnetic protection. It is compact and allows to make measurements on any (from 600 mm long) open site of a beam line. Vacuum tests and work with biological samples on a beam of protons of I-100 accelerator have proved that the Faraday cup is meeting all the requirements.

INTRODUCTION

IHEP's experts are currently working on the creation of a medical irradiation centre with beams of protons and carbon ions on the basis of IHEP acceleration complex. Already existing IHEP accelerators I-100 - U-1,5 - U-70 are forming a complete chain capable of accelerating not only protons, but also, due to certain modifications, light ions: deuterons and carbon.

In collaboration with scientists of the Medical radiological scientific centre (MRSC, Obninsk, Kaluga region), IHEP experts make biological researches in IHEP accelerators, with existing beams. Possible places of making researches on complex IHEP are shown on fig. 1 by red colour.

The parameters of beams in these sections [2] are shown in the Table 1.

Table 1: Parameters of beams at 3 points of IHEP accelerators

	Ions	Kinetic energy, MeV/u	Range in water, mm	Z/A	Pulse duration, current	
I-100 (point 1)	$_1H^{+1}$	72	43	1	1÷50 µs	1-50 mA
	$_2H^{+1}$	16,7	4	1/2	1÷50 µs	15 mA
	$_{12}C^{+6}$	16,7	1,0	1/2	3 µs	1.5 mA
U-1,5 (point 2)	$_1H^{+1}$	<1320	<4700	1	≈0.2 µs	400 mA
	$_2H^{+1}$	<440	<2000	1/2		80 mA
	$_{12}C^{+6}$	<440	<300	1/2		8 mA
U-70 (point 3)	$_1H^{+1}$	<1320	<4700	1	Slow extraction	
	$_2H^{+1}$	<440	<2000	1/2		
	$_{12}C^{+6}$	<440	<300	1/2		

06 Instrumentation, Controls, Feedback and Operational Aspects
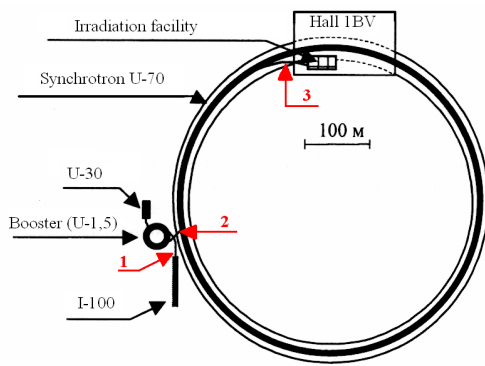
Figure 1: The layout of linear accelerator I-100, synchrotron-booster U-1.5, main ring U-70 and experimental hall 1BV.

THE FARADAY CUP`S DESIGN

The device (Fig. 2) has been made with the classical scheme of Faraday Cup (FC) [3, 4]. It has following features:

- works under atmospheric conditions;
- working aperture - Ø 69 mm;
- external dimensions of pipe: diameter - 100 mm, length
- 550 mm;
- weight - 11 kg;
- weight of magnetic system (3) – 12 kg;
- entrance window is made of 0.1 mm thickness
  mylar, covered with aluminum from two sides;
-the carbon (density of ~2 g/sm3) core's (8) of
  length 200мм provides full absorption of
  different beams of tab. 1;
-induced activity from an absorber, because of
 nuclear interactions with a beam, has a half-life
 period of ~20 minutes that is important for the
 portable device;
- aluminum collimator (5), attached to FC`s body, can be
fast replaced with an other one in case of need.
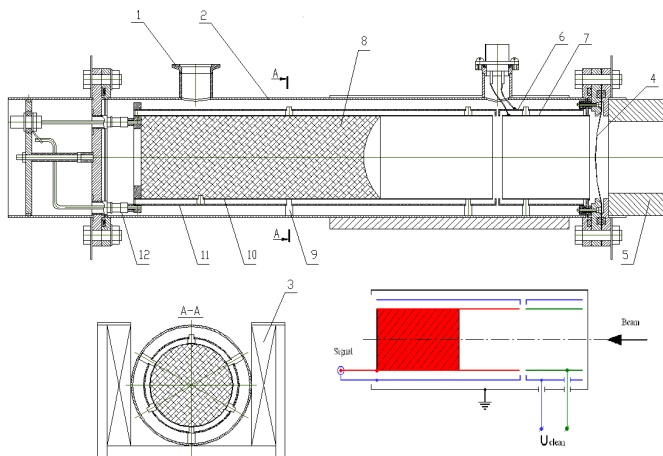
Figure 2: Compact autonomic Faraday cup.

Because of strong electromagnetic hindrances there has been chosen 3-cylinder coaxial design, for minimizing influence of hindrances and breakthroughs. All cylinders

are made from stainless steel. The external cylinder (2) forms a closed and grounded vacuum volume. Two inner pipes are divided on length on two unequal parts and are suspended on ceramic insulators (9). The beam enters to the cylinder from the right side (in the drawing). The first parts of cylinders (on a course of a beam) form "clearing" electrodes (6, 7) length of 70 mm. The internal cylinder has positive potential. The purpose of this part of FC is to gather secondary electrons which been emitted with a beam from an entrance window. The second parts of pipes (10, 11) form "the measuring" section. Inner pipe is covered from inside with a copper and electrically contacted to the 70 mm diameter carbon core (8). The charge, formed by a beam of ions in a core is read out through vacuum ceramic-metal feedthrough (12) and HF socket. The stream of secondary electrons, arising from the core and moving back (towards to a beam), is going to the internal surface of the same "measuring" pipe (10). Such effect is caused by a cross-section constant magnetic field from external system (3) on the basis of SmCo. The same magnetic system helps to improve a gathering of secondary electrons, arising from an entrance window, on "clearing" electrode (7). Vacuum inside the cylinder is $3*10^{-3}$ torr. It prevents ionization effect.

FC TESTS AND RESULTS

Manufacturing, clearing of details and vacuum tests of FC were spent in IHEP at the high- vacuum stand [5]. One of the important specificities of the device is ability to work without pumping out for a long time. Changing of pressure in the device from time has been measured with different entrance windows.

FC has been tested for tightness with leak founder with sensitivity ~$1 \cdot 10^{-12}$ L·mbar/s. No leaks has been found during the test. It means, that pressure changing inside FC is defined by gas evolution from internal surfaces of cylinders, mylar window and graphite. Pumping out for working during the day was made at the vacuum stand. Then the device was transferred to the beam. For longer period of work FC has been constantly attached to the ceolitic sputter pump.

Electric tests of FC have confirmed high quality of used ceramic insulators and a socket: leakage currents have not exceeded 1 pA.

Working tests of FC were made in accelerator I-100 with a proton beam with energy of 72 MeV (fig. 3) at small (duration of a current's impulse is 1.5 μs) and big (20 μs) irradiation doses.

06 Instrumentation, Controls, Feedback and Operational Aspects
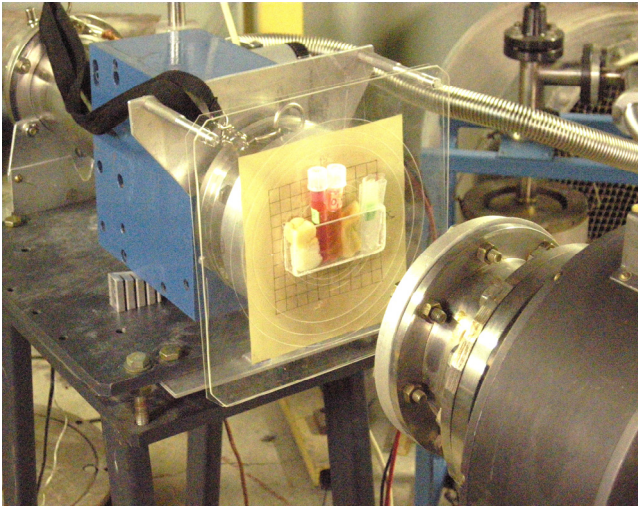
Figure 3: FC with biological samples is mounted on a beam of I-100

On the following fig. 4 there are oscillograms of a beam current from the Beam Current Transformer (BCT) mounted in vacuum system of the accelerator and from FC, standing in atmosphere on exit of I-100.
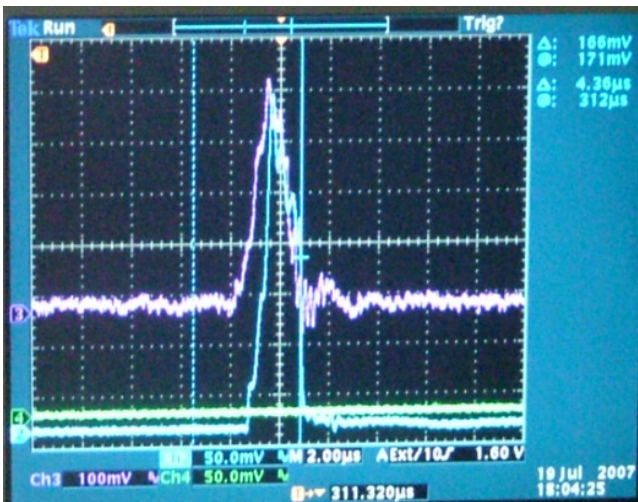
Figure 4: Oscillograms of signals from BCT (the top ray) and FC (the bottom ray). Coincidence within 10 %.

Signal's monotonous dependence from "clearing" electric field (in limits ±200 V), has smooth character and can change indications of FC for 4 %. The "correct" value of a clearing bias voltage is +200 V.

Installation of a constant magnet in a forward part of the cylinder increases a signal for 4 %.

In the end of tests there has been made irradiation of thermo luminescent dosimeters, which were fixed on a target flange in front of the cylinder. The range of measurements of doses was from 1 to 10 Gray (through 1 Gray) and further 20, 50, 150, 300, 500 and 1000 Gray.

Results of measurements of these dosimeters have been compared with FC`s indications. The data are correlated with 10 %.

REFERENCES

[1] Antipov Yu.M., Vasilevskij A.V., Vorobev A.P., etc. *The medical irradiation centre with a beam of ions of carbon on the basis of IHEP accelerating complex.* In "Proceedings of XVI Conference for accelerators of the charged particles", Protvino, 1999, volume 2, p. 212-219.

[2] Antipov Yu.M., Ivanov S.V. *Acceleration of ions in IHEP accelerators: a state of affairs and prospects*. News and problems of the fundamental physics, 3 (3), Protvino, 2008, p. 1-11.

[3] Moskalev V. A, Sergeev G. I. *Measurement of parameters of beams of charged particles*. Energoatomizdat, Moscow, 1992, p. 11-19 (rus).

[4] Ziegler J.F., Saunders P.A., Zabel T.H. *Portable Faraday cup for non - vacuum proton beams*. IBM J. RES. DEVELOP. Vol. 40 No1, 1996, pp. 73-76.

[5] Asanov V. N, Galjaev N.A., Grishin V. N, etc. Set up for vacuum clearing and filling of ionization chambers (beam loss monitors). The Engineering Physics, №3, 2007, p. 1-5 (rus).

06 Instrumentation, Controls, Feedback and Operational Aspects

CALIBRATION OF THE ELECTROSTATIC BEAM POSITION MONITOR FOR VEPP-2000

Yu. A. Rogovsky, I. N. Nesterenko, BINP SB RAS, 630090 Novosibirsk, Russia

Abstract

The basic requirement for the VEPP-2000 Beam Position Monitor (BPM) is the measurement of the beam orbit with 0.1 mm precision. To improve the measurement accuracy, the response of the electrostatic BPMs (pickups) were mapped in the laboratory before they were installed in the VEPP-2000 ring. The wire method for the sensitivity calibration and position-to-signal mapping is used. The test stand consists of high frequency coaxial switches to select each pickup electrode, movable antenna to simulate the beam, signal source, spectrum analyzer to measure the pickup signals, and analysis software. This calibration showed possibility of required accuracy. During calibration the electrical center of the different BPMs was measured with respect to the mechanical center. Conversion between the BPM signal and the actual beam position is done by using polynomial expansions fit to the mapping data within ± 6 mm square. Results for these portions of the calibration are presented.

INTRODUCTION

A beam position monitor system is operated for two kinds of orbit measurements, a relative measurement and an absolute measurement. The former is to measure the orbit displacement from the initial or standard orbit when some optics perturbation is applied. The latter case is to measure orbit position relative to the geometrical monitor center. This function will be essential for maintaining stable operations in a ring where the optics depends strongly on the orbit, particularly at nonlinear optics elements.

Closed orbit stabilization and correction is routine operation for VEPP-2000 ring [1, 2]. To stabilize the beam orbit, the absolute beam position should be measured. The output data from a position monitor system usually shows the orbit position relative to the electric monitor center, not the geometrical center. So we should calibrate each beam position monitor to know the location of the electric center with respect to geometrical one i.e. relative to the reference frame of each BPM.

Moreover the system needs calibrating not only because of pickup characteristics (center displacement, sensitivity and nonlinearity) caused by machining, installment, cable matching, and signal processing circuits, but in order to meet the requirements on the accuracy of the measured beam position.

Basically there are 4 BPMs installed in VEPP-2000 ring, but there is reserve one. In order to test characterize, align, and provide data for calibration, a general purpose test stand was designed and constructed in 2006. All BPMs needed for operations was calibrated and data analyzed in

06 Instrumentation, Controls, Feedback and Operational Aspects

the same year, and last one was processed in 2009 because of some replacement actions.

CALIBRATION TEST STAND

BPM Block

The electrostatic BPM for VEPP-2000 ring consist of four 15 mm diameter button style electrodes are mounted on the diagonals of its housing and are centered symmetrically. Buttons orientation is 45 degrees to avoid the fan of synchrotron radiation. All parts precisely machined from solid stainless steel blocks, isolated the electrodes and feedthroughs with ceramic material. The electrode surface is smoothed with that of the vacuum chamber, so the impedance induced by the electrode may be reduced greatly. The vacuum chamber of VEPP-2000 is
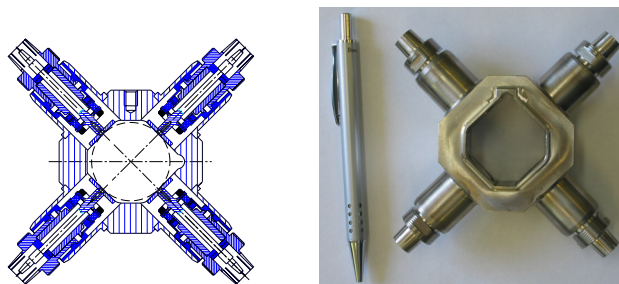
Figure 1: The electrostatic BPM for VEPP-2000 ring.

not the same along the ring. With exception of the bending magnets, it has approximately square form (35 mm inscribed circle diameter). The BPM is integral part of the quadrupole vacuum chamber of the technical strait section, which in turn is referenced to the magnet axis by means of supporting arms, and assembled on the vacuum chamber by welding, assuring no gas leak. To reduce the mechanical surveyment for the BPM with the same vacuum chamber dimensions, BPM housing has the same cross section form and dimensions, and coincides with the vacuum chamber within ± 0.2 mm. Fig. 1 shows a transverse section and common view of the pickup before assembling.

Test Stand and Data Collection

The approach used to determine the position of the electron beam is to treat the effect of the beam as a two dimensional electrostatic problem. An electron beam passing through a BPM induces a charge on the buttons, which uniquely depends on the position of the beam. Due to the lack of longitudinal variation, the electron beam appears to be essentially a line charge. Using the voltage on the buttons, one can solve for the position of the electron beam.

In order to calibrate different BPMs, a general purpose test stand was designed and constructed. The picture of the test stand is shown in Fig. 2. To simulate the real beam traveling through the BPM more accurately, we send a continuous signal down a movable antenna with stretched wire through the BPM. In this case, we believe that the low-frequency measurement yields the same information as the real beam using the usual subtrac/sum algorithm. The wire, which diameter is $100 \ \mu$m, is made of tungsten material is driven from an Agilent 4402B Network Analyzer RF out port. The $1 \div 200$ MHz RF signal (sweep time 100 ms) is amplified to about 3dB and delivered to the stretched wire through the coaxial cable. The RF signal on the wire induces signal on the four buttons of the pickup at the test. Each button is connected sequentially to the analyzers RF in through the same coaxial cable. The antenna is placed in-
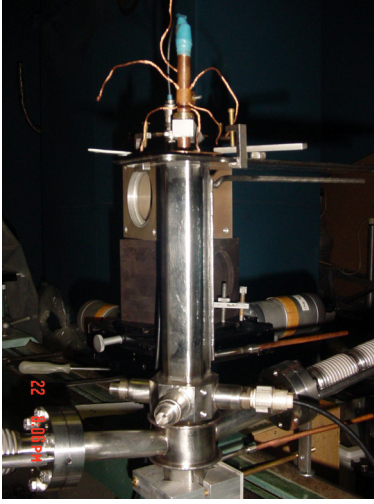
Figure 2: Test stand view.

side the BPM and is straightened along the vacuum chamber, and can be manually moved by the $x - y$ positioning tables in a grid patten, while the BPM block is fixed by the BPM mounting fixtures. The $x - y$ positioning tables have a position resolution of 0.01 mm (half step mode) and 0.001 mm repeatability.

The vacuum chamber was scanned along constant lines and measurements were made with the antenna positioned at $x = 0, \pm2, \pm4, \pm6$ mm and $y = 0, \pm2, \pm4, \pm6$ mm grid-points, where $x = y = 0$ corresponds to the geometrical center. Fig. 3 shows a nomograph of measured h and v, as defined in (3). The horizontal lines drawn at constant Y position, while the vertical lines corresponds to X constant. The distance between lines is 2 mm. It shows that there is a good linearity in the central area of BPM, while pin cushion distortion appears clearly far from the central.

CALIBRATION AND ERROR ANALYSIS

Calibration of all monitors was made in the laboratory at a test bench. Now the voltages (A, B, C, D) on the BPM buttons as a function of wire position are known and posi-
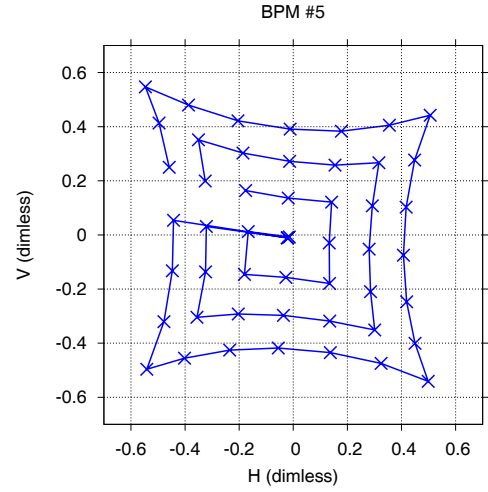
Figure 3: The H and V distribution from four buttons.

tion is the desired variable. The challenge is to invert the function and solve for the position of the wire as a function of the voltage on the electrodes.

$$V(A, B, C, D) \rightarrow P(x, y) \qquad (1)$$

A simplistic approximation, involves linearization of summing over the differences

$$x = K_x * h, y = K_y * v \qquad (2)$$

where K_x and Ky are calibration factors set by the geometry of the BPM, and signals (A, B, C, D) normalized as defined in (3).

$$
\begin{aligned}
h &= \frac{A - B - C + D}{A + B + C + D} \\
v &= \frac{A + B - C - D}{A + B + C + D}
\end{aligned}
\qquad (3)
$$

Though accurate when the wire beam is close to the center of the BPM, these equations are not accurate at large deviations from the center. The lack of accuracy is unfortunate because the need for the BPMs is the most acute when the wire is not near the center. So one have to use nonlinear least-square fitting method.

After calibration data are obtained, the mapping data are fitted by least-square method to fourth polynomials of (4), where $0 \leqslant i, j \leqslant 4, 0 \leqslant i + j \leqslant 4$.

$$
\begin{aligned}
x &= \sum a_{ij} * h^i * v^j \\
y &= \sum b_{ij} * h^i * v^j
\end{aligned}
\qquad (4)
$$

In these expression, $a_{0,0}$ and $b_{0,0}$ gives the deviation of the electrical center from the geometrical one, and $a_{1,0}$ and $b_{0,1}$ one can interpreter as the sensitivity of BPM in the x and y direction, respectively. Special code in C language using GNU Scientific Library (GSL) was written to do fit and calculate all coefficients. We obtain the offset (x_0, y_0) between the geometrical center and the electrical

center ($h = 0, v = 0$), and the coefficients (K_x, K_y) for position from the full mapping data. Fig. 4 shows mapping plot of one of the BPMs.
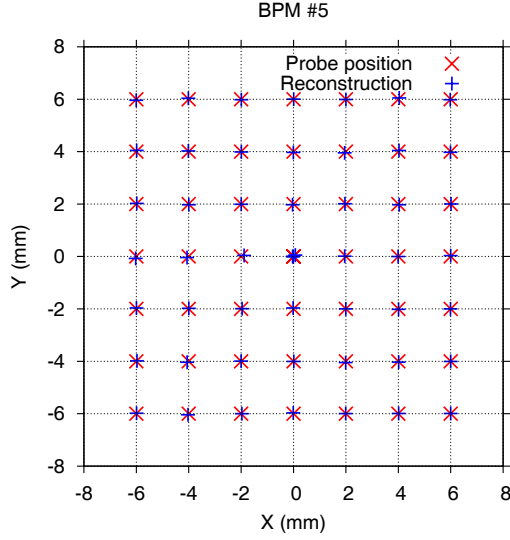
Figure 4: Reconstructed probe position with respect to real one.

The maximum fitting rms error is found as follows:

$$\sigma_k = \sqrt{\frac{\sum_{i=0}^{n-1}(k_{fi} - k_{mi})^2}{n}}, \qquad (5)$$

where k stands for x or y respectively, and x_{mi} and y_{mi} are the values from the probe position i-th measure point, while x_{fi} and y_{fi} are the values calculated by the least-square method.

The typical values of the offset, position coefficients, fitting rms error of data collection are summarized in Table 1 and Fig. 5. Mean rms error values all over BPMs:

$$\sigma_x = 4.5 * 10^{-2} mm, \sigma_y = 3.8 * 10^{-2} mm \qquad (6)$$

Table 1: Individual BPM parameters.

♯	Offset		Coeeficient		Error	
	$a_{0,0}$	$b_{0,0}$	$a_{1,0}$	$b_{0,1}$	σ_x	σ_x
1	0.037	-0.011	12.732	12.874	0.071	0.055
2	-0.258	0.081	12.331	13.203	0.058	0.046
3	1.088	-0.302	12.467	12.942	0.031	0.029
4	0.482	0.306	12.443	13.056	0.041	0.035
5	0.245	0.176	12.556	13.204	0.029	0.028

The repeatable accuracy of the scheme has been measured. Wire was placed in the same position after every 10 wire movements, and differences of the buttons voltages was compared. The iterances of these results were no more than $(3-5)$ μV. These results show the accuracy of electronics system is about 3 μm.

06 Instrumentation, Controls, Feedback and Operational Aspects
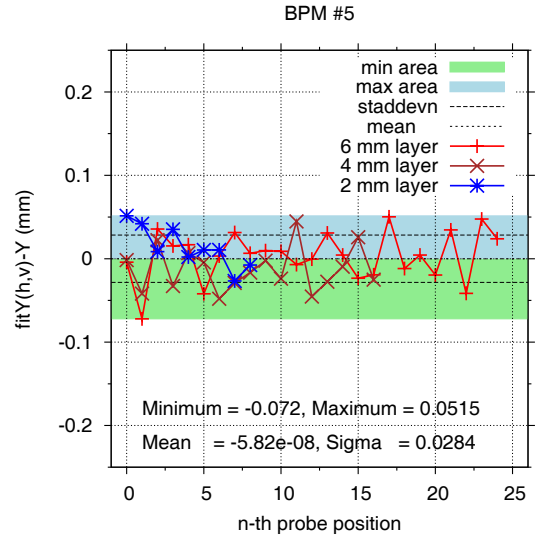
Figure 5: Difference between reconstructed and real probe position.

SUMMARY AND CONCLUSION

The BPM calibration system has been established and tested. It has a theoretical resolution capability of 0.01 mm, as limited by the movable stage system. We designed a new calibration scheme, measuring the power on each pickup electrode sequentially by the spectrum analyzer. Although we have not verified to this accuracy, we have obtained the clear BPM mapping using 2 mm step of wire movement. The calibration of the BPM system has been shown to be better than the requirements which VEPP-2000 BPM system wants. All calibration results saved as a tables of polynomial coefficients appropriate for using in software or other calculations.

ACKNOWLEDGMENTS

REFERENCES

[1] Yu. M. Shatunov et al.. Project of a New Electron-Positron Collider VEPP-2000, in: Proc. 7th European Particle Accelerator Conf. (EPAC 2000), Vienna, Austria, 439-441.

[2] http://vepp2k.inp.nsk.su/ avaliable at 30.09.2009.

[3] W.M. Zhou Y.Z. Chen K.R.Ye W.X.Cheng Y.Yang. THE CALIBRATION OF SSRF BPM. Proceedings of the Second Asian Particle Accelerator Conference, Beijing, China, 2001

[4] M.Tejima et al., "BEAM POSITION MONITOR SYSTEM for KEKB", Proc. 1997 the 11th symp. on Accel. Sci. and Tech., SPring 8, Hyogo, Japan.

[5] Eva S. Bozoki, Jung-Yun Huang, John W. Bittner, A NONITERATIVE METHOD FOR CALCULATING BEAM POSITON FROM INDUCED ELECTRIC SIGNALS, Brookhaven National Laboratory.

PICKUP BEAM MEASUREMEN SYSTEM AT THE VEPP-2000 COLLIDER

Yu. A. Rogovsky, E. A. Bekhtenev, BINP SB RAS, 630090 Novosibirsk, Russia

Abstract

This paper reviews the present state of electromagnetic beam position monitors (pickups) at VEPP-2000 collider. It includes descriptions of position monitors, typical interfaces for these monitors and their system characteristics (resolution, stability, bandwidth and problems or limitations) are discussed. The paper also reviews several types of diagnostic measurements using beam position monitors which are useful in improving accelerator operations.

INTRODUCTION

The new electron-positron collider VEPP-2000 ring is a part of VEPP-2000 complex [1, 2] at BINP has been successfully commissioned and has been delivering luminosity at energy close to 508 MeV since June 2007. VEPP-2000 is a new machine with luminosity up to 10^{32} cm^{-2}s^{-1} and the beam energy from hadron production threshold up to 2×1 GeV. Small ring size and sophisticated optics lay on limitation on beam quality and operations. Therefore such modern machines requires various beam diagnostics for perfect tuning and ask us to monitor the beam status quickly and accurately.

The measurement and control of the closed orbit is one of the basic functions of any accelerator beam instrumentation and control systems. A beam position monitor (BPM) system is operated for two kinds of orbit measurements, a relative measurement and an absolute measurement. The former is to measure the orbit displacement from the initial or standard orbit when some optics perturbation is applied. The latter case is to measure orbit position relative to the geometrical monitor center. This function will be essential for maintaining stable operations in a ring where the optics depends strongly on the orbit, particularly at nonlinear optics elements.

The VEPP-2000 electrostatic BPMs system is not only used to monitor the beam orbit and correct the closed orbit distortion (COD), but also used to perform the interaction point (IP) beam steering along the detectors, control and adjustment of the beam oscillation amplitude during the injection, measure the dispersion functions and the betatron frequencies.

SYSTEM HARDWARE

The VEPP-2000 collider ring is equipped with a system of beam position diagnostics based on 4 electrostatic BPMs, frontend electronics located near BPMs and readout electronics in CAMAC standard. A set of low loss coaxial

06 Instrumentation, Controls, Feedback and Operational Aspects

cables brings up the BPM signals of each detector to the local control room where the signal readout and processing electronics is located. The lengths of cables vary from 15 to 25 meters depending on the locations of the detectors in the storage ring. Each BPM is placed in the center of the technical strait section surrounded with two quadrupole magnets, very close to them. Before installation, electrical zero point of pickup electrode for each BPM is calibrated by a calibration bench with a wire method [3].

BPM Block

The beam position monitor for VEPP-2000 ring consist of four 15 mm diameter button style pickups are mounted on the diagonals of its housing and are centered symmetrically. The button type electrodes, which are capacitive coupled to the beam, are most popular with electron-positron rings because they occupy very little longitudinal space and the coupling impedance is small. Buttons orientation is 45 degrees to avoid the fan of synchrotron radiation. All parts precisely machined from solid stainless steel blocks, isolated the electrodes and feedthroughs with ceramic material. The electrode surface is smoothed with that of the vacuum chamber, so the impedance induced by the electrode may be reduced greatly. Fig. 1 shows a transverse section and common view of the BPM before assembling.
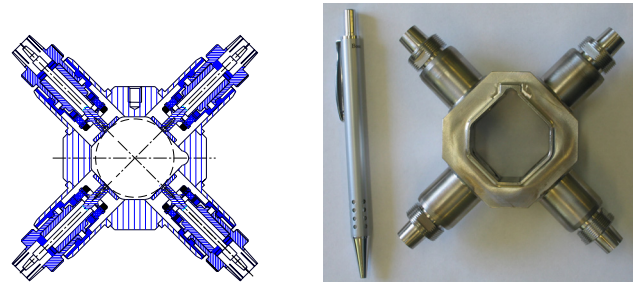
Figure 1: The beam position monitor for VEPP-2000 ring.

Electronics

The signals from four BPM electrodes are simultaneously processed with four channels of processing electronics. Each channel consist of LPF with cut-off frequency of 110 MHz, programmable gain amplifier and 12-bit ADC.

Time interval between electron and positron bunches is about 20 ns for each BPM. Analog electronics bandwidth of 110 MHz allows us to decrease the crosstalk of electron and positron bunches signals at level of 0.5 dB. Timing circuit provides ADC samples at the top of BPM signal. It is achieved by means of programmable delay of reference
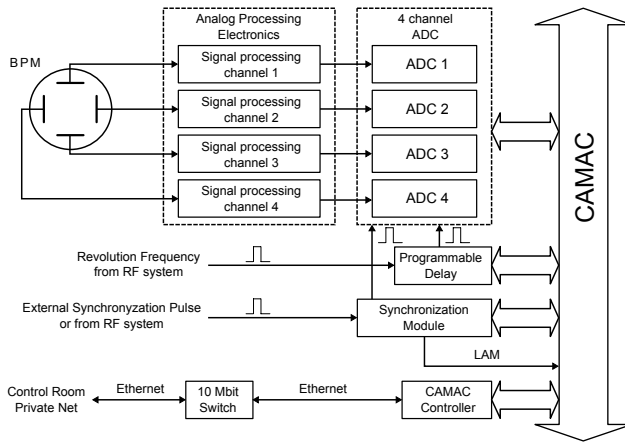
Figure 2: Structure of VEPP-2000 electronics.

pulses with revolution frequency. Delay range covers all revolution period. Delay range covers all revolution period with step equal $0,25$ ns. Amplifier range of 45 dB allow us operate with $1 - 100$ mA beam current.

DATA ACQUISITION SYSTEM

The data acquisition system is based on client-server model over TCP/IP protocol. PowerPC embedded CAMAC controller, which running Linux operating system [4], is used to initialize electronics and perform the data acquisition operation. Such choice is caused by heavy traffic limitation and high rate response requirements. Two level server scheme is used: there main server works on PC and its main goal is to receive incoming requests and initiate measurements; slave server works on CAMAC controller and its main goal is hardware serving and returning measured data to the master server as fast as possible (actually speed is limited only by hardware carrying capacity). The controller communicates with the electronics via CAMAC bus by using compiled command system for programmable instruments. All software uses the CX libraries set [5]. The user interface is developed under X-Windows/Qt/TclTk environment.

The acquired signals from button electrodes are filled into the memory of the ADC with a revolution clock of the ring ($f_0 = 12.191$ MHz). The memory depth of the digitizer is up to 32 Kwords (i.e. beam position is measured at each turn with maximum record length is about 2.5 msec). So one can measure betatron frequencies using FFT technique, or obtain slow data with averaging of results for any chosen number of turns (say 2048 points average @ 10 Hz). Synchronization of the system with beam injection gives the possibility of the beam position measurements for the first turn and measurements of the betatron frequencies after injection. Although the system allows measurements of the betatron frequencies after external excitation.

The raw data, the calculated beam position, the betatron tune and the phase space plot are presented on the screen in interactive basis. The experimental data can also be stored

on mass storage devices for off-line analysis

ACCURACY OF THE SYSTEM

During storage ring commissioning precision and stability of the BPM system has been measured [6]. There are number sources of errors during beam position measurements: temperature instability, time jitter of the ADC trigger pulses, quantization noise of ADC, interferences in BPMs and cables connecting BPMs with processing electronics and so on. Temperature instability of the processing channels gains and time delays formed with Delay lines leads to temperature instability of the beam position measurements. Experimental examination gave the temperature stability value 2μm/$^\circ$C. Then temperature instability of the time delays leads to temperature instability of the beam position measurements mainly due to the differences in BPM cables lengths and gain-frequency characteristics of the processing channels. So electrical length of each cable was measured and made equal ones for each BPM. Another experimental investigations have shown that major contribution to coordinate error is brought by interferences in the cables connecting BPMs with processing electronics. Some measures and efforts have been made to reduce these interferences. One of them is using of double-shielded coaxial cables. The main reason of beam position from

Table 1: BPM system parameters.

Beam Current	Resolution	
	Turn by turn	256 turns average
$0,1 - 1$ mA	$150 - 500\ \mu$m	$10 - 30\ \mu$m
$1 - 10$ mA	$50 - 150\ \mu$m	$3 - 10\ \mu$m
> 10 mA	$< 50\ \mu$m	$< 3\ \mu$m

beam current dependence is nonlinearity of programmable attenuators, amplifiers and multipliers. Some results and parameters are present in Table 1.

APPLICATIONS

Beam position and Tune monitor

The flexibility of the system allows to perform a series of turn-by-turn measurements, while FFT can be moved over the data by a user defined step to generate a "spectrum movie" and see dynamic processes in the beams during injection or other operations. The signal-to-coordinate coversion, tune calculation with specific filtering and approximation [7] are made on the client side. Examples of user-end application presented on Fig. 3. Beam injection is one of the significant task for any accelerator. You can see horizontal beam oscillation after injection, caused beam energy mismatch on Fig. 4. Tune measurements became routine operations since the end of 2009 then VEPP-2000 started first experimental work with both particle detectors SND
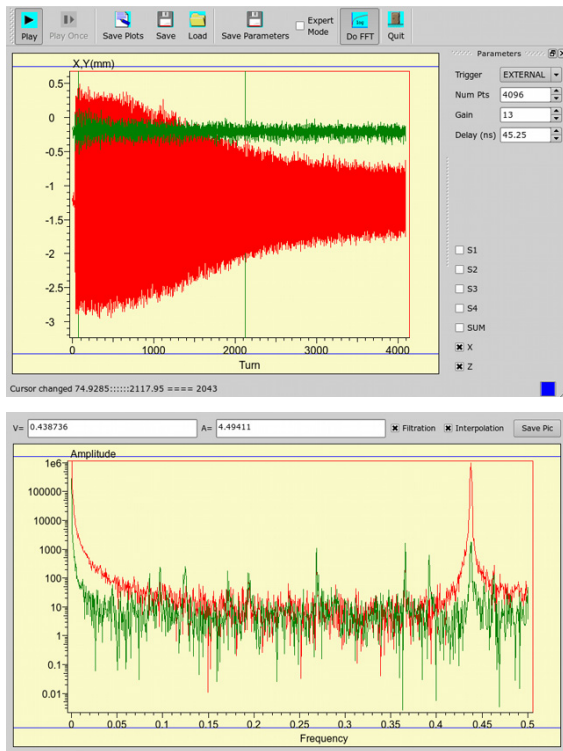
Figure 3: Beam oscillation after external kick during 4000 turns and their betatron spectra.
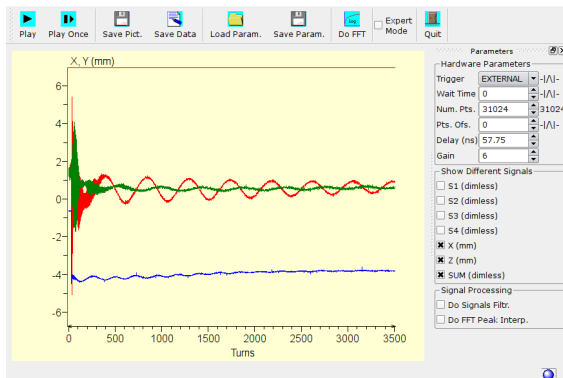
Figure 4: Beam oscillation after injection.

and CMD-3 at the energies of 500-950 MeV range with the lattice mode close to project. Together with Response Matrix Techniques [8] it became a powerful instrument for lattice and optical functions correction at VEPP-2000. The BPM system is very sensitive for dispersion function measurements, because our BPMs located in the places with maximum dispersion function. Fig. 5 shows the dispersion measured before and after applying of calculated corrections for quadrupoles gradients and solenoids fields.

06 Instrumentation, Controls, Feedback and Operational Aspects
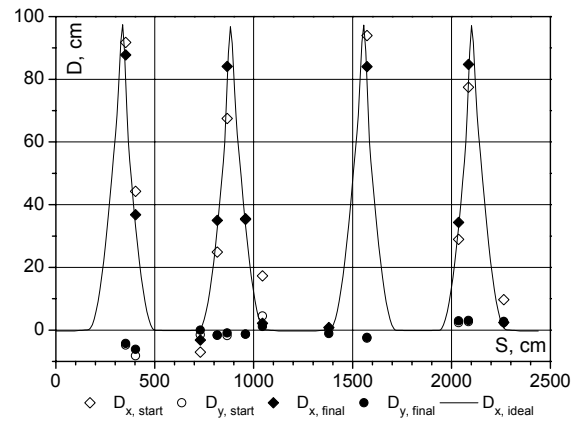
Figure 5: Dispersion function. Point near picks maximums is the BPM measurements.

Intensity and Lifetime measurements

A DC Beam Transformer (DCBT) is used to measure the bunched or unbunched circulating beam current. Because DCBT can measure only total charge amount and there are two beams with different charge rotating together, so we need some additional information about relative beam intensities during operations with higher intensity ($\sim 10^{10}$) circulating beams. This information one can obtain from the BPM system, because total signal from all BPM's tablets is proportional to the beam current. So one can calculate beam lifetime.

REFERENCES

[1] Yu. M. Shatunov et al.. Project of a New Electron-Positron Collider VEPP-2000, in: Proc. 7th European Particle Accelerator Conf. (EPAC 2000), Vienna, Austria, 439-441.

[2] http://vepp2k.inp.nsk.su/ avaliable at 30.09.2009.

[3] Yu. A. Rogovsky et al.. Calibration of the Electrostatic Beam Position Monitors for VEPP-2000. This Procceedings: TUPSA028.

[4] http://www.inp.nsk.su/activity/automation/ avaliable at 30.09.2009.

[5] D. Bolkhovityanov, "VEPP-5 Injection Complex Control System Software", 2007, Ph.D. thesis (in russian), avaliable at 30.08.2010,
http://www.inp.nsk.su/~bolkhov/publs/←
bolkhov_phd_final.pdf

[6] D. E. Bekhtenev, Yu. A. Rogovsky at al.. Beam Position Mesasurement System for the VEPP-2000 Collider. Proceedings of RuPAC 2008, Zvenigorod, Russia

[7] Bartolini. R, et al.., Algorithms For A Precise Determination Of The Betatron Tune, 5th European Particle Accelerator Conference, Sitges, Barcelona, Spain, 10 - 14 Jun 1996, pp.e-proc. 1329-1331

[8] A. L. Romanov et al.., Correction the Round Beam Lattice of VEPP-2000 Collider Using Orbit Response Technique, 11th European Particle Accelerator Conference, Genoa, Italy, 23 - 27 Jun 2008, pp.THPC034

BEAM MEASUREMENTS WITH VISIBLE SYNCHROTRON LIGHT ON VEPP-2000 COLLIDER*

Yu. A. Rogovsky, D. E. Berkaev, A. N. Kyrpotin, I. N. Nesterenko,
A. L. Romanov, BINP SB RAS, 630090 Novosibirsk, Russia

Abstract

This paper describes beam diagnostics at VEPP-2000 collider, based on visible synchrotron light analysis. These beam instruments include: SR beamline and optics; acquisition tools and high resolution CCD cameras distributed around the storage ring to measure the transverse beam profile and its position in vacuum chamber; photomultiplier tubes (PMT) which enables beam current measurements; video system. Some applications of these measurement systems and their measurement results are presented.

INTRODUCTION

The new electron-positron collider VEPP-2000 ring is a part of VEPP-2000 complex [1, 2] at BINP has been successfully commissioned and has been delivering luminosity at energy close to 508 MeV since June 2007. VEPP-2000 is a new machine with luminosity up to 10^{32} cm^{-2}s^{-1} and the beam energy from hadron production threshold up to 2×1 GeV. Small ring size and sophisticated optics lay on limitation on beam quality and operations. Therefore such modern machines requires various beam diagnostics for perfect tuning and ask us to monitor the beam status quickly and accurately.

The measurement and control of the closed orbit is one of the basic functions of any accelerator beam instrumentation and control systems. A beam position monitor (BPM) system is operated for two kinds of orbit measurements, a relative measurement and an absolute measurement. The VEPP-2000 optical BPM system equipped with 16 CCD cameras registering beam synchrotron radiation have high precision of 1 μm, and used to monitor the beam orbit and correct the closed orbit distortion (COD), but hasn't absolute calibration.

BEAM ORBIT AND TRANSVERSE PROFILE MONITOR

SR acquisition system

Beam parameters in the VEPP-2000 collider measured by the Synchrotron Radiation (SR) at 8 points along the ring for both (e$^+$e$^-$) directions. Polished copper plates installed in the vacuum chamber, are used for output the SR from the bending magnets. The SR after passing through vacuum glass window comes to the optical diagnostics station and then is distributed by the half-transmitting mirrors Fig. 1-2.

Each station equipped with two CCD cameras (for positron and electron beams) for measurements the beam
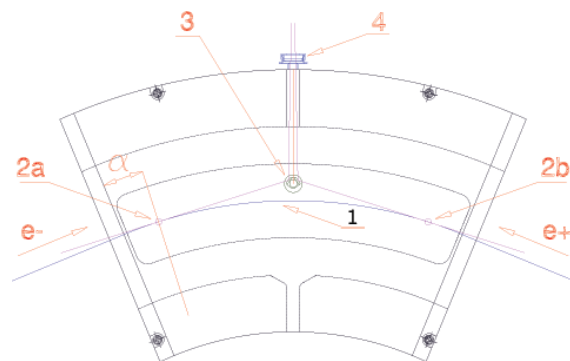
(a) 1-beam orbit, (2a, 2b)-radiation point of e$^+$e$^-$ beams, 3-copper mirror, 4-output window, $\alpha = 4°47'$.

(b) Vacuum chamber and mirror after assembling. Additional mirror is placed in the center for comparison.

Figure 1: SR output in bending magnet.

size and position. Because the SR outputs are located in orbital positions with very small dispersion function, four additional places are foreseen for dispersion and its symmetry control, and the beam position is measured in these points with pick-ups. In some stations the SR are used for beam current measurement (by the PMT) and will be used for the longitudinal beam sizes control in future (by the dissectors).

CCD camera

Processing of optical part of the SR in circular accelerators allows one to obtain various beam parameters – vertical and radial sizes, axes tilt, position in a vacuum chamber. There is non-perturbative diagnostics that can work with super small beam currents. The essential nonlinearity (gamma correction) and low spatial resolution put some limitations on "TV camera + videograbber" system. In the case of a cheap digital TV camera the limitations ap-

06 Instrumentation, Controls, Feedback and Operational Aspects

Figure 2: Optical bench with system of movable mirrors and SR diagnostic station with two CCD cameras.

pear due to space between camera and a computer. Typical values for this distance are about 100 m. Therefore the decision of development special camera based on b/w CCD of the type *ILX084AL* was taken from the very beginning. This CCD in 1/3-inch format has in working area 494 rows of 659 elements (i.e. about 330,000 active diode target cells) and uses so-called line-to-line transfer, when diode columns alternate with light-proof vertical storage registers. For high sensitive to obtain a matrix of light-collecting microlenses is placed on the CCD surface. Saturation charge of the cell is about 40000 carriers, a noise charge is about $30-40$ carriers.

The camera structure is developed under Ethernet 100 MHz standard. Usage of this standard allows one not to have in the camera internal memory unit and to real-time transfer the information from the camera to a computer. Reading rate is about 1/12 sec per frame. It is possible to install in the camera 3-channel ADC AD922. This 14-bit ADC has a double correlated sampling regime as well as independent correction of sensitivity and offset for each channel. In a standard configuration only one ADC channel is connected to the main CCD, but it is possible to use two channels as is needed in case of VEPP-2000 collider (electron and positron monitors is placed together).

Software

The subsystem software is based on client-server model over TCP/IP protocol. All cameras have own unique MAC addresses and are connected to the special private subnet, because of traffic limitation. It may be more than 150 Mbytes/sec, so CCDs subnet is insulated to another subnets (control room private net). Only a special program, "CCD-server" has immediate access to CCD cameras; all other programs, "clients", sent their measure requests to the server; and the server provides for requests optimal execu-

tion and primary development of CCDs frames. Elliptical beam profile model is fitted to the real data - and position, axes main sizes and axes tilt are calculating. For the optimized algorithm it takes about 10 mksec to approximate a frame (300000 pixels $\times$ 16 bits) on (Athlon 64, 1.8 MHz) machine. Also, the server provides clients for more detailed information, such as beam profiles, along X,Y-axes; or a compressed picture with level lines marked by pseudocolors. According their purposes, clients may request any type of data. The user interface is developed under X-Windows/Motif/Qt environment.

Applications

The system widely used for routine operations: common control, measurement and correction of closed orbit (CO) distortions, specific beam measurements. More precise experiments of solenoid position determination with respect to CO was done in regular "round beam" optics also with use of ORM measurements [3]. There is regime for the system with external synchronization to perform some specific measurements. Synchronization of the system with beam injection gives the possibility of the beam position measurements for the first turn after injection or external signal. Fig. 3 shows X-profiles of injected beam, measured in different moments of time.
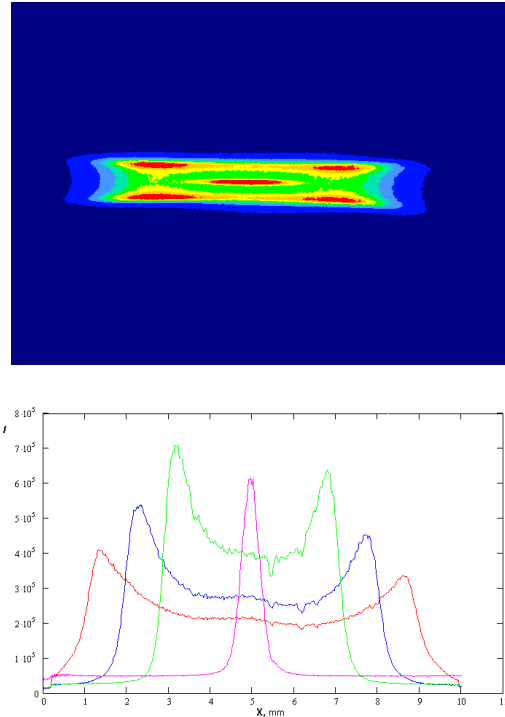
Figure 3: Transverse beam profile and its longitudinal cross-section.

Transverse Profile Monitor application, providing to the operator online picture of the beam, presented at Fig. 4.

The program can store pictures in different formats and allows online hardware configuration.
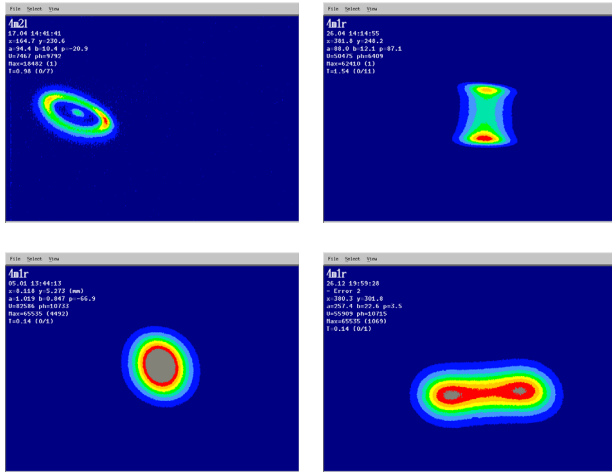
Figure 4: Beam profile at different moments.
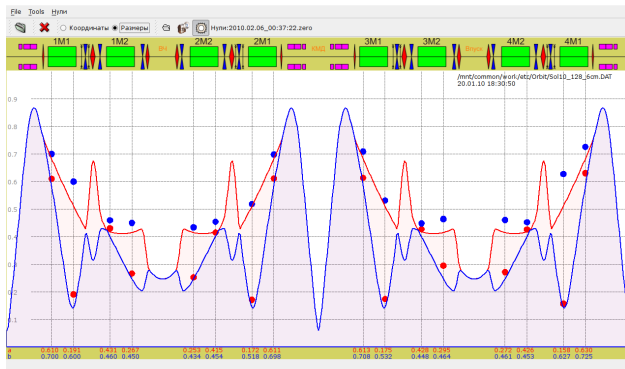
Figure 5: Beam sizes along the ring vs. current lattice model.

BEAM CURRENT AND LIFETIME MONITOR

Low Intensity $(\sim 10^8)$ circulating beam

A DC Beam Transformer (DCBT) is used to measure the bunched or unbunched circulating beam current. As mentioned above the SR intensity measurement is used for beam current measurements in case of low beam intensity. Signal from PMT measured by the integrating 8-bit ADC is proportional to the real beam current. So the DCBT values with sufficient electron beam are used to cross-calibrate the low intensity PMT-based measurement system. This system was used in early stage of VEPP-2000 commissioning, and now days used in some specific cases for tuning, because adequate optical intensity attenuation system is under construction.

06 Instrumentation, Controls, Feedback and Operational Aspects
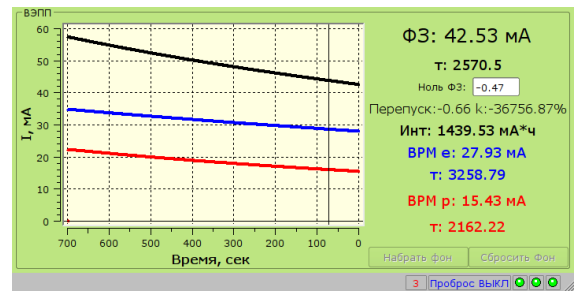
Figure 6: Beam currents and life time monitor.

OTHER SYSTEMS

There are a number analog TV cameras distributed around the ring for both e^+, e^- beam diagnostics. The cameras and display monitor are connected through a matrix video switcher, which can be control either local, or by the control system. Video switch also provides stamped title for each video signal. Since the title display is synchronized with incoming video signal, it is also often used for simple and fast diagnostics. Fig. 7 shows positron vertical beam size blow up in the presence of strong electron beam. There are couple scintillation screens in the VEPP-
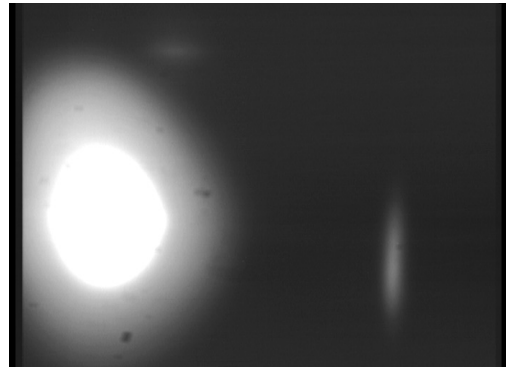
Figure 7: Both colliding beams beams: electron - left, positron - right.

2000 injection channels, used for beam observation with TV cameras. For specific tune measurements the swept Beam Transfer Function (BTF) measurements is used. All systems are integrated in common VEPP-2000 Collider Control System.

REFERENCES

[1] Yu. M. Shatunov et al.. Project of a New Electron-Positron Collider VEPP-2000, in: Proc. 7th European Particle Accelerator Conf. (EPAC 2000), Vienna, Austria, 439-441.

[2] http://vepp2k.inp.nsk.su/ avaliable at 30.09.2009.

[3] A. L. Romanov et al.., Correction the Round Beam Lattice of VEPP-2000 Collider Using Orbit Response Technique, 11th European Particle Accelerator Conference, Genoa, Italy, 23 - 27 Jun 2008, pp.THPC034

PROFILES AND INTENSITIES MEASUREMENTS IN THE DIAGNOSTIC SYSTEM OF THE EXTRACTED BEAMS OF THE U-70 ACCELERATOR

N. Ivanova, V.Kovaltsov, A.Koshelev, A.Lukyantsev, S.Makonin, A.Matyushin, V.Milyutkin, V.Seleznev, A.Sotnikov, IHEP, Protvino, Russia

Abstract

Diagnostic system for the extracted beams of the U-70 accelerator is a hardware-software complex with profilometers, intensimeters and electronic crates at the lower level, VME-crates with ADC-modules and MVME-167 processors (vxWorks operating system, basic EPICS tools, home made software) at the middle level, personal computers used as workstation at the upper level.

In this report we consider:
- The approaches to the system adaptation problems during the U-70 runs and solutions to these problems
- Data acquisition and hardware-sofware levels of data processing for non-standard profilometers
- The tools for the beam intensity measurement and presentation, the intensimeter calibration procedure.

INTRODUCTION

The diagnostic system for the extracted beams of the U-70 was operated since the 2001. The basic principles of the system and its original structure were described in [1].

The main tasks of the system are:
- the acquisition of beam related data and its primary processing;
- various on-line and off-line presentation of the information;
- data archiving and access to data.

The system does have a flexible adjustment mechanism, but it cannot solve all the problems. Since physicists and beam specialists are doing scientific research, an alteration of the software and hardware is sometimes needed. We will consider the ways of the non-standard measurement hardware integration into the system as well as the system adaptation to special operation modes.

LOWER AND MIDDLE LEVELS OF THE DIAGNOSTIC SYSTEM

The diagnostic system is a three-level hardware-software complex. The software for the upper and middle levels is based on the EPICS toolkit [2].

The layout of the middle and lower levels is shown in Figure 1. The signals related to beam particles are registered at the lower level. VME-crates with crate controllers and ADC-modules make up the middle level. This is the IOC (Input-Output Controller) in EPICS terms. In the considered configuration IOC consists of VTG, VSA, VCT modules and Motorola MVME-167 controller. VTG is the timing module, VSA is 12-bit ADC for 16 channels and VCT is 8-channel counter module.
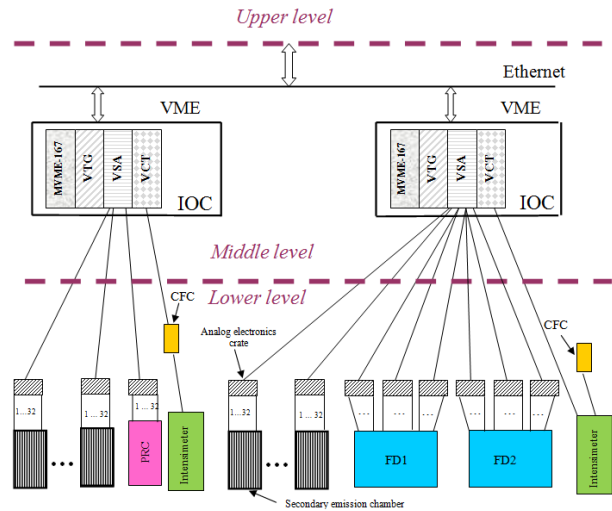
Figure 1: The layout of the lower and middle levels of the diagnostic system. The new components are marked by colors. PRC – the proportional chamber before beamstopper. FD1 and FD2 – the ionization chambers in the area of FODS setup.

IOC operates in the real time mode in accordance with the U-70 accelerator supercycles which are 8-9 seconds long. Within this time interval data should be acquired and processed and transferred to the upper level.

For IOC start-up one needs to load several files from the upper level via Ethernet. The files contain vxWorks operating system [3], EPICS base software, developed in IHEP special software and various setup parameters.

THE NONSTANDARD HARDWARE IMPLEMENTATION

All "standard" diagnostic system profilometers have 16 measurement channels in the horizontal plane and 16 – in the vertical one. The chambers are connected to the analog electronic crates.

The profilometer located before the beamstopper which is needed for OKA setup has a different structure. It is a proportional chamber with 32 signal electrodes in the particle separation plane. In order to make usage of this chamber as close as possible to the standard way the first 16 channels were connected to analog electronics as correspondent to the horizontal plane, and the other 16 channels – as correspondent to the vertical plane. This prevents any changes on the IOC level. The transfer of the information and its processing were the same as for the "standard" orthogonal chambers.

The ionization chambers located in the FODS setup area have 40 channels for the beam profile measurement in each plane. Also, these chambers have different distances between electrodes, in contrast to the other profilometers which have the constant distances. This is why the standard method for the integration in the diagnostic system was not suitable. At first the connection of these chambers to new electronics was performed merely by hardware. Only the central parts of the chambers were employed. It was a good decision for the quick implementation. The next iteration involved the complete solution of the problem, when all channels were connected and data presentation was made by software in IOC.

The beam profiles measuring devices are linked to the system through the analog electronics. But diagnostic system allows for the other method of connection, too. Figure 1 shows the intensimeter implementation: it connects to VCT via current-frequency convertor (CFC).

INTENSITY MEASUREMENT

The intensity value detection of the slowly extracted beams is performed by the intensimeter, which is a secondary emission chamber or a gas-filled ionization chamber. The intensimeter has one output channel for connection to the VCT module of the VME crate. The readings of this device are relative, so it needs calibration.

The activation foil methods were used for the absolute calibration of the intensimeter. During the specified time periods for each accelerator cycle the value of the intensity measured by the intensimeter was fixed. By summarizing these values the total charge of the beam was calculated. At the same time the foil was irradiated by this beam. Then the charge of the foil cumulated during the exposition time was found by means of dosimetry. Thereby there were two sets of measurements. Assuming that the dosimetry data were "true" (with an error of 5%) the proportionality coefficient was calculated by the formula of the least square method :

$$K = \frac{\sum X_i Y_i}{\sum X_i} \qquad (1)$$

where K represented the needed coefficient; X_i – sum of intensimeter data values, Y_i – total charge of the protons passed through the foil for the i-th time period respectively.

The comparison of the intensimeter measurements and the dozimetry measurements make it possible to detect only the compliance of the cumulative charges. However, the important device characteristic is the dynamic correspondence of its measurements and the real value of intensity. Such comparison may be carried out by using the common charge of one of the planes of the profilometer that is the first in the beam course. This charge gives the approximate estimate of the current

intensity with some coefficient. Fig. 2 shows the intensimeter data (the upper graph) and total charge of all the channels of the first profilometer in the vertical plane (the lower graph). It is seen that the graphs' shapes are very similar. This method of comparison was used for the preliminary estimation of the workability of the implemented device.
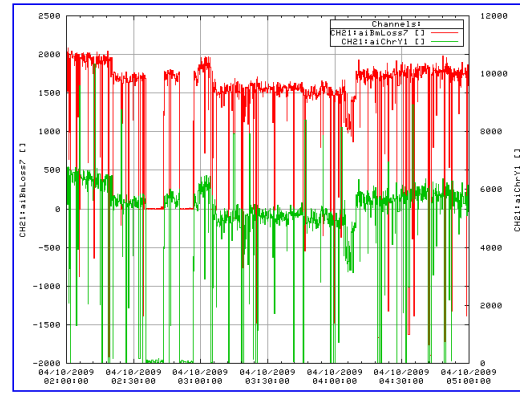
Figure 2: The comparison of the intensimeter measurements and the common charge of the Y-plane of the first profilometer.

SOFRWARE FOR IOC AND PROCESS DATABASE

Software for the middle and upper levels was developed by means of EPICS tools. The main program components of the middle level are shown in Fig. 3. They are Channel Access (CA), the process database, the means for database maintenance and the driver for hardware and software interface. CA provides the communication between IOC and the middle level support.

CA and the process database maintenance are the "staff" parts of EPICS. Besides these, the IOC software includes a process database and a driver-program both developed in IHEP. The process database contains the results of the current measurements and specifies the algorithms for data processing and control. Record is the database element. When implementing new devices in the diagnostic system one or several records for parameters setup are always added to database – ao-records (analog output). For each profilometer, these parameters are orientation and "step", and for the intensimeter, it is the proportionality coefficient (1). For the data acquired by profilometers the wf-records (waveform) and ai-records (analog input) were added to database. wf-records contain the arrays of profile measurements, ai-records contain the calculated beam characteristic. ai-record for the intensimeter data was added to the database too.

2
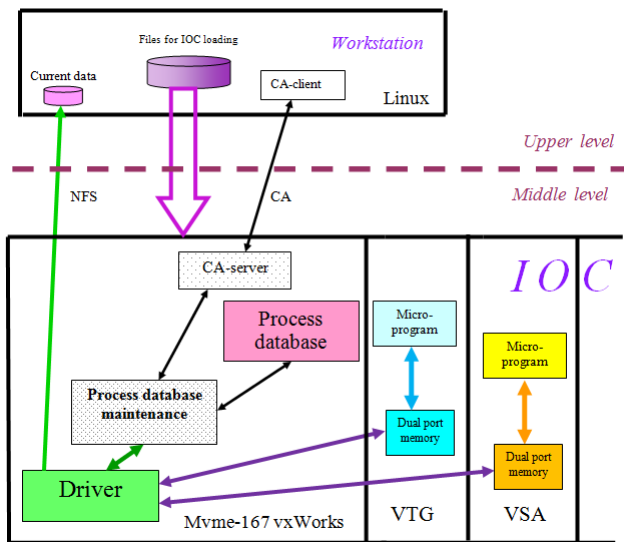
Figure 3: Some parts of IOC software and their links. The homemade components are colored.

In the recent accelerator runs there were two IOCs in operation, both designed for the beam profiles and intensity measurements. The separate databases were composed for each IOC. The total number of records for each IOC is about 900.

DRIVER FOR HARDWARE SUPPORT IN IOC

Driver is a multifunctional homemade program which provides the software support for all VME-modules and complicated data processing in IOC.

The driver functions include data reading from VSA, VTG and VCT and their processing, communication with database maintenance software, initializing and reconfiguration of the VME modules, data transfer to the upper level, etc.

When driver designing the special attention was paid to the data organization. The data were put in the hierarchical structures (in the sense of C language) that are common for all parts of the driver. In line with the diagnostic system logic, the structures contain measurements, descriptions of devices, processing parameters, current states of the diagnostic system components.

The vxWorks operating system ensures the parallel running of several tasks. It gives the driver functions the possibility to work simultaneously and independently. So the driver guarantees regular data refreshing and data presentation at the same time.

The driver performs the data transformation for the non-standard ionization chambers.

CONCLUSION

The diagnostic system is used in the U-70 accelerator runs for the tuning of the channels' magnetic optics in order to deliver beams to the experimental setups.

The generally accepted hardware design and software orientation on the EPICS allow rather quick and effective adaptation of the diagnostic system to the various requirements of the physics experiments.

REFERENCES

[1] V.Kovaltsov, A.Matyushin, V.Milyutkin, I.Romanov, V.Seleznev, A.Sytin, M.Clausen. Upgrading of the beam diagnostic system of U-70 beam transfer lines. Proceedings of ICALEPCS-2001, San Jose, California, USA, Oct. 2001.

[2] http://www.aps.anl.gov/epics, 'EPICS Home Page'.

[3] VxWorks Programmers's Guide, WindRiver Systems, 1994.

THE TNK BEAM POSITION MONITOR SYSTEM

E.A.Bekhtenev, G.V.Karpov, E.I.Shubin, Budker Institute of Nuclear Physics, Novosibirsk, Russia

Abstract

New second generation synchrotron radiation source TNK is being built in Zelenograd, Russia. The new FPGA-based beam position monitor (BPM) system for TNK has been developed and produced in BINP. The BPM system requirements for second generation light sources are not as severe as for the third generation light sources. Nevertheless the system is able to perform turn-by-turn measurements and has micron level accuracy. The TNK light source is intended for work both in multiple and in single bunch mode. In the second case the charge of one bunch can achieve the value of 60 nK, which results in high peak voltages at BPM electrodes. Design features of the BPM system, its parameters and testing results are presented in this paper.

INTRODUCTION

Second generation synchrotron radiation source TNK ("Zelenograd") is presently under construction in Zelenograd, Russia [1]. Storage ring main parameters are given in Table 1.

Table 1: Main parameters of the TNK storage ring

Beam energy	2 GeV
Revolution frequency F_0	2.59 MHz
RF frequency	181.3 MHz
Beam current in multiple bunch mode	300 mA
Beam current in single bunch mode	150 mA

For beam orbit measurements Beam position monitor (BPM) system has been designed and fabricated at BINP. The system includes 24 button-type Beam Position Monitors (BPMs) and BPM electronics. Requirements to BPM electronics are:
-    possibility of turn-by-turn measurements
-    measurements of injected beam trajectory (first turn)
-    resolution for nominal beam currents not worse than 1-2 microns
-    relative accuracy for nominal beam currents at ~10 microns
-    measurement rate is ~10 Hz, fast data acquisition is not required.

Slow data acquisition (~10 Hz) will be used for slow orbit feedback. Fast orbit feedback is not planned at TNK.

SYSTEM STRUCTURE

One of the methods which combine turn-by-turn measurements with high accuracy is method based at the use of an array of switches [2]. We choose this method for our BPM electronics. One of the problems associated with the use of semiconductor switches was high peak voltages at pickup buttons. In single bunch mode the charge of one bunch can achieve the value of 60 nK which gives peak voltage of tens of volts after passing through Low Pass Filter with cut-off frequency of 500-600 MHz.

Acceptable solution of this problem is employment of RF band pass Filters (BPF) directly after pickup buttons [3]. For this purpose a special printed-circuit BPF with frequency 362 MHz (doubled RF frequency) had been developed at BINP. The measured parameter S_{21} of the filter is shown in Fig.1,2. The measured bandwidth is ~10 MHz, insertion loss is ~6 dB.
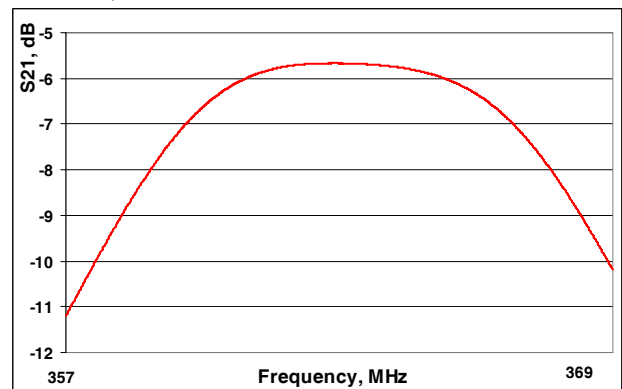
Fig.1. Measured S_{21} of BPF, narrow frequency span.
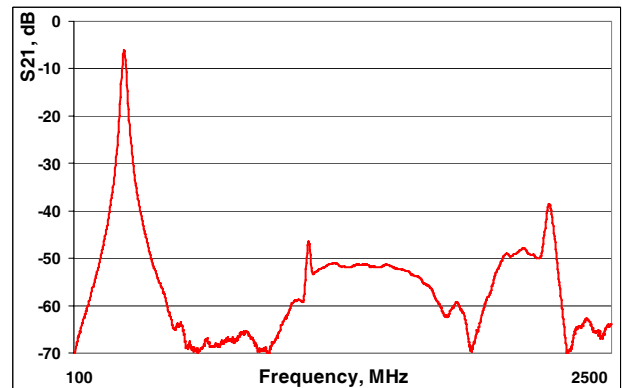
Fig.2. Measured S_{21} of BPF, wide frequency span.

Inequality of Band Pass Filters results in static measurement error therefore calibration of electronics is needed.

The structure of the BPM electronics is presented in Fig.3.
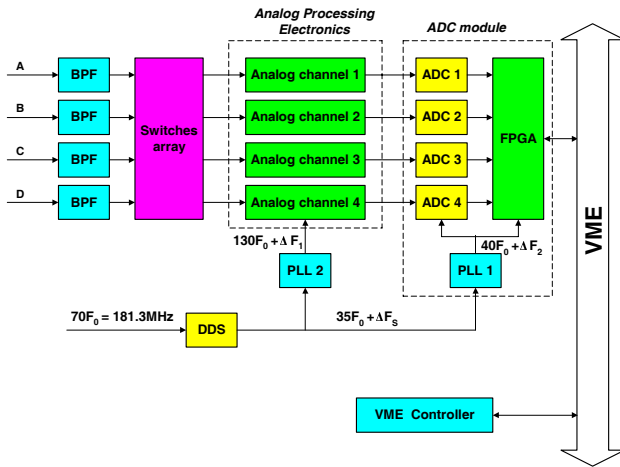
Fig.3. The structure of the BPM electronics.

Second harmonic of RF frequency $140F_0$ (362.6 MHz) is extracted from BPM signal and used for measurements.

GaAs switches provide 4 combinations of connections between 4 pickup buttons and 4 analog channels. Channel to channel crosstalk is less than -60 dB.

Analog Processing electronics occupy 1U 19" chassis. After analog processing the signals via 50 Ohm cables come to ADC module (made in VME standard) where are sampled. One ADC module contains four 14-bits ADCs, FPGA and clock generator (PLL).

Digital signal processing is performed in FPGA. The results are transmitted via VME bus to VME Controller.

ANALOG AND DIGITAL SIGNAL PROCESSING

A functional diagram of the analog signal processing channel is presented in Fig.4.
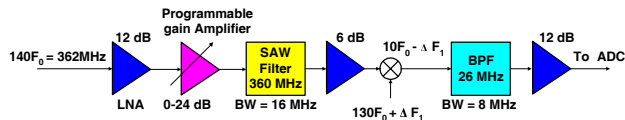
Fig.4. Functional diagram of the analog processing channel.

The signals with a frequency of $140F_0$ after amplification by Low Noise Amplifier (LNA) and Programmable Gain Amplifier are mixed with heterodyne signal. Band Pass Filter (SAW filter) with bandwidth of 16 MHz minimizes noise and distortions and provides additional suppression of mirror components. The heterodyne frequency differs from $130F_0$ by a small value of ΔF_1 (a few kHz), so after mixing the signal frequency becomes $10F_0 - \Delta F_1$. Offset of the heterodyne frequency from integer multiple of revolution frequency provides insensitivity of result from signal phase. The signals selected by Band Pass Filter with central frequency of 26 MHz and bandwidth of 8 MHz are then amplified and pass to ADC module where they are sampled at frequency of $40F_0 + \Delta F_2$.

ADC sampling frequency also slightly differs from integer multiple of revolution frequency. This compensates some of the undesirable effects caused by nonlinearity of ADC and other components [3]. Offsets ΔF_1 and ΔF_2 improve resolution of measurements, decrease fill-pattern dependence and make the result insensitive to signal phase. It is especially important for single bunch mode.

Heterodyne and sampling frequencies are generated by low jitter Phase Locked Loop (PLL) oscillators AD9516. Specified time jitter of this oscillator in a bandwidth of 0.01-20 MHz is 0.275 ps. Reference frequency for both PLLs is generated by Direct Digital Synthesizer (DDS) AD9958. DDS frequency ($35F_0 + \Delta F_S$) defines ΔF_1 and ΔF_2 values. Reference frequency for DDS is RF frequency 181.3 MHz. Because of comparatively large DDS phase noise PLL loop bandwidth is chosen 1 kHz. As a consequence DDS phase noise at frequencies more than 1 kHz is not transferred to oscillators. Measured heterodyne jitter in bandwidth 0.1-100 MHz is less than 1 ps.

Digital signal processing chain in FPGA is shown in Fig.5.
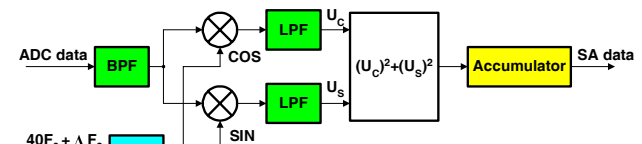
Fig.5. Digital signal processing chain.

Numerically Controlled Oscillator (NCO) frequency slightly differs from $10F_0$. It is calculated on base of ΔF_1 and ΔF_2 values so that data after synchronous detector is a DC value. A sum of squares of Sin and Cos components is calculated for each turn. Then these values are accumulated for specified number of turns to form Slow data acquisition (SA). As a consequence low frequency phase noise (less than 100 kHz) does not worsen resolution of measurements.

EXPERIMENTAL TESTS RESULTS

BPM electronics had been tested at test stand and at BINP storage ring VEPP-4M.

At test stand Agilent Signal Generator and Agilent Pulse Generator where used as signal sources modeling multi bunch and single bunch modes. The signals of these generators where split into four lines. A -3dB attenuator was inserted into one of the lines to imitate beam displacement. Five main parameters where measured at test stand:

- Resolution
- Temperature instability of the beam position measurements
- Beam-current dependence
- Fill-pattern dependence

06 Instrumentation, Controls, Feedback and Operational Aspects

- Dependence on the signal phase for single bunch mode

All BPM electronics hade been investigated. Results are given in Table 2. Geometric factors of BPMs: $K_X = K_Z = 20$ mm.

Table 2: BPM system parameters defining accuracy of measurements ($K_X = K_Z = 20$ mm) for average beam current 50÷300mA (pickup signal level: -14÷2 dBm).

Resolution of slow measurements (SA data)	μm	0.2-0.5
Resolution of turn-by-turn data	μm	8-10
Beam-current dependence	μm	< 10
Fill-pattern dependence	μm	< 15
Dependence on bunch phase for single bunch mode	μm	< 5
Temperature dependence	μm/°C	1.5-2

Relatively large dependence of the result on temperature (1.5-2 μm/°C) is caused by two reasons:

- Inequality of the Band Pass Filters (input BPF)
- Inequality of Ga As switches.

Different temperature dependencies of insertion loss of different BPFs and switches results in temperature dependence of the measurement result. Nevertheless these results satisfy of machine requirements. Special thermal stabilization is not needed.

Results of measurements during 2 hours at test stand for one of sets of electronics are given in Fig.6. Resolution of ~0.2 µm was achieved. Slow changing of result is caused by temperature instability.
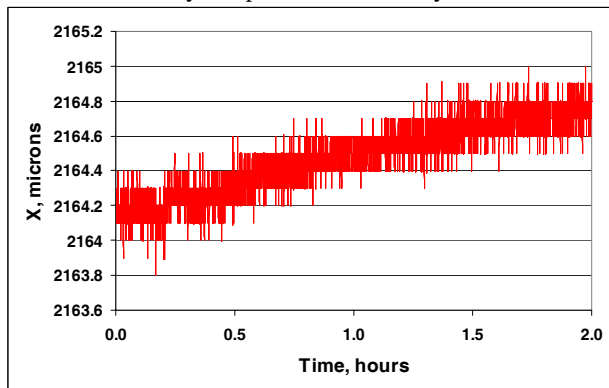
Fig.6. Results of measurements at test stand with signal level of -10 dBm.

Results of measurements during 1 hour at VEPP-4M storage ring with small beam current ~2 mA and data rate 1 Hz are presented in Fig.7 ($K_X = K_Z = 43$ mm).

Root-mean-squire deviations of measured horizontal and vertical positions are ~3 µm and ~1 µm correspondingly. Some part of these values is caused by real beam position instability.
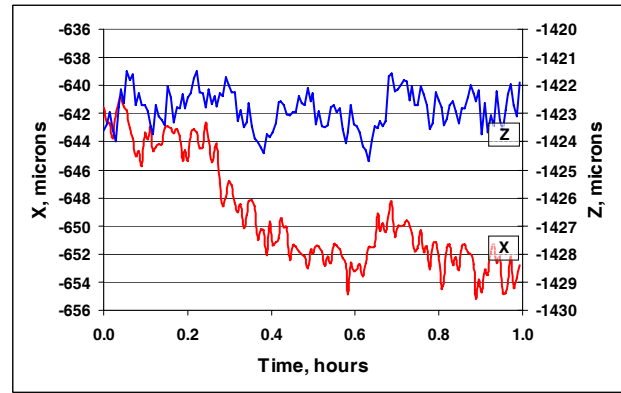
Fig.7. Results of beam position measurements at VEPP-4M with beam current ~2 mA (signal level of -45 dBm).

STATUS

At present all 24 BPMs have been manufactured and installed at TNK storage ring. All electronics has also been made, tested and calibrated at test stand. 80 % of electronics satisfy machine requirements. Remaining part needs additional tuning. Commissioning of BPM system at TNK is planned at first half of 2011.

REFERENCES

[1] Salashenko at al. "Status of "Zelenograd" storage ring". Nuclear Instruments and methods in Physics research. Volume 603, p.4-6.
[2] A.Cosicek. "Libera electron beam position processor". Proceeding of PAC-2005, Knoxville, p.4284-4286.
[3] F.Epaud, B.K.Scheidt. "Installation and commissioning of a complete upgrade of the BPM system for the ESRF storage ring". Proceeding of DIPAC-2009, Basel, p.50-52.

TRANSITION RADIATION DETECTOR WHICH USED DIHEDRAL ANGLE AS RADIATOR

A.V.Koltsov and A.V.Serov. P.N.Lebedev Physical Institute RAS

Abstract

The spatial distribution of the field of transition radiation generated by a relativistic particle flying into a dihedral angle formed by perfectly conducting plane surfaces is determined. The angular distributions of radiation intensity in dihedral angles of different values are calculated. It has been shown that the dependence of the angular distributions of radiation intensity in a dihedral angle on the energy and on the direction of motion of particles is stronger than a similar dependence in the case of transition radiation on a plane interface.

Transition radiation possesses certain properties that make this radiation useful for solving various problems [1]. One of the simplest and important particular cases in the theory of transition radiation is the radiation generated when a particle is incident on a perfectly conducting plane. This problem was considered in the first paper by Ginzburg and Frank on the theory of transition radiation [2]. They pointed out that the transition radiation on a perfectly conducting plane can be considered as radiation from two particles: a real particle with charge q and its image with charge $-q$.

The study of radiation on dihedral angle has shown that the spectral-angular distributions of radiation in this case exhibit new features that enhance the applicability of transition radiation. The properties of transition radiation generated when a particle passes through a dihedral angle have been investigated both theoretically [3-5] and experimentally [6].

In the present paper, we consider the specific features of transition radiation in a dihedral angle that enhance the applicability of this transition radiation to the measurement of the parameters of charged particles.

The geometry of the problem is shown in Fig.1. Let us introduce a cylindrical system of coordinates (ρ, φ, z).
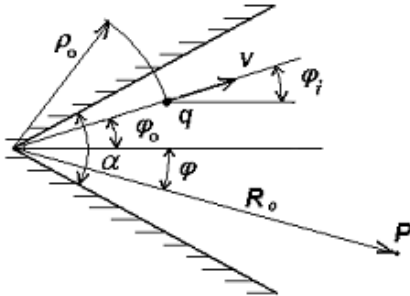
Figure1: Geometry of the problem.

The value of the dihedral angle is α. The z-axis is directed along the edge of the dihedral angle, and the planes that form the dihedral angle coincide with the planes $\varphi = \alpha/2$. The charged particle with charge q flies out from a point (ρ_0, φ_0) on the edge of dihedral angle and moves at constant velocity v. The velocity vector of the particle lies in the plane $z=0$ and is directed at an angle φ_t.

In this paper the method of images is used to describe transition radiation. Fig.2 illustrates the dispositions and velocity vectors of real and additional charges in dihedral angles of $\alpha = \pi/2$ and $\alpha = \pi/3$. The dihedral angles are shown in Fig.2 by solid lines, while the complementary angles are shown by dashed lines. The original charge q_1 moves on dihedral angle and additional image charges move on complementary angles.
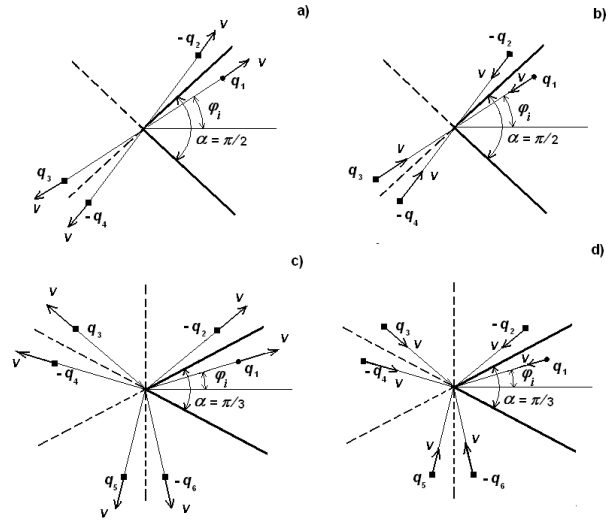
Figure2: The disposition and the velocity vector of the given and additional charges in dihedral angles of $\alpha = \pi/2$ and $\alpha = \pi/3$.

In the case of a dihedral angle of $\alpha = \pi/n$, where $n=0,1,2..$, Fourier component of the field of transition radiation can be expressed as

$$E_\omega = \frac{q\,v}{2\pi} \frac{exp(-ikR_o)}{R_o} \sum_{j=0}^{n-1} \Big[\frac{sin(\varphi - \varphi_t - 2j\alpha)}{1 - \beta \cos(\varphi - \varphi_t - 2j\alpha)} x$$

$$exp(ik\rho_o \cos(\varphi - \varphi_t - 2j\alpha)) - \frac{sin(\varphi + \varphi_t - (2j-1)\alpha)}{1 - \beta \cos(\varphi + \varphi_t - (2j-1)\alpha)} x$$

$$exp(ik\rho_o \cos(\varphi + \varphi_t - (2j-1)\alpha))\Big] \qquad (1)$$

where $k=2\pi/\lambda$, λ - wave length.

The angular distribution of the radiation intensity in the plane $z=0$ has been considered. Fig.3 shows the

distributions of intensity for various values of the dihedral angle. Particles are injected along the bisector of the dihedral angle. One can see that decrease of α up to value $\alpha=\pi/\gamma$ leads to increase of maximum of the intensity. Further decrease of α causes intensity reduces.
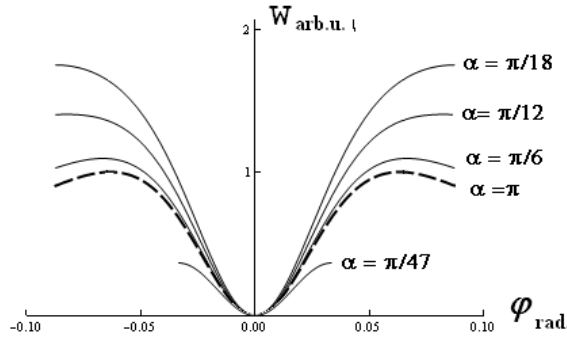
Figure3: Angular distribution of radiation intensity for various α. Particles with energy $\gamma=15$ are injected along the bisector of dihedral angle.

The impact of shifting the injection point along one of the conducting plane surfaces and change of angle of injection on angular distribution of radiation intensity has been investigated. The results of calculations are presented in Fig.4. Distributions have been calculated for different α. For all pictures dashed lines are used for distributions for $\alpha=\pi$, thin lines – for $\alpha=\pi/3$ and thick lines – for $\alpha=\pi/6$.
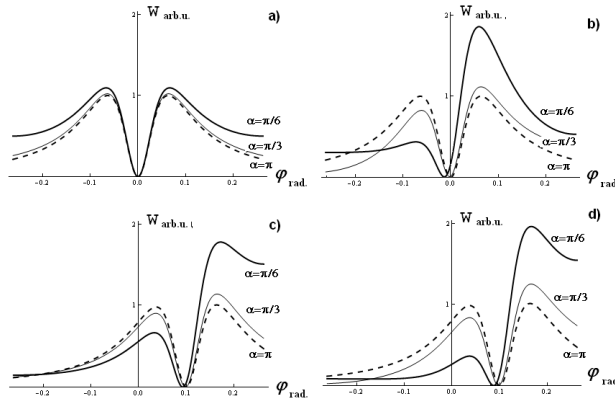
Figure4: Angular distribution of radiation intensity as function of φ for various directions of injection, injection points and α. $\rho_0=0$; a) $d=0$, $\varphi_t=0$; b) $d/\lambda=0.5$, $\varphi_t=0$; c) $d=0$, $\varphi_t=0.1$; d)) $d/\lambda=0.5$, $\varphi_t=0.1$.

It can be seen that shifting the injection point leads to asymmetry of angular distribution. Increase of sensibility caused by using of dihedral angle is explained by field in the dihedral angle is formed as a result of interference of radiation fields of many particles (real particle and its images).

To determine particles parameters pickup where transition radiation intensity is measured in two directions can be used. Pickup scheme is shown in the upper left corner of the Fig.5. Indicators D_1 and D_2 measure radiation lengthwise both sides of the dihedral angle. Difference between D_1 and D_2 values characterises shifting of injection point. In Fig.5 dependence of $\Delta W=W_1 - W_2$ on shifting value d for different α is presented.
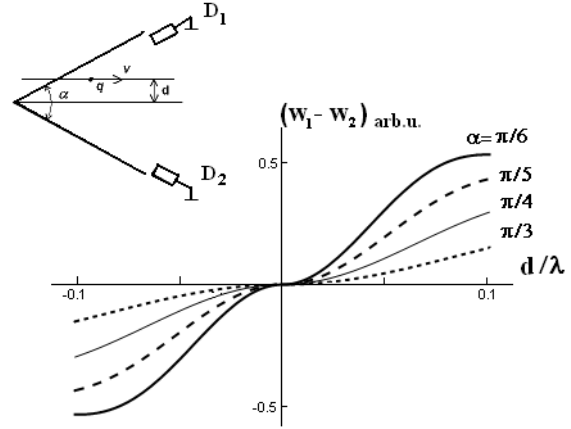
Figure5: Dependence of radiation intensities difference along sides of the dihedral angle W_1-W_2 on shifting d of injection point.

Let us mention one more property of transition radiation in a dihedral angle. For this purpose angular distributions of radiation for two cases should be compared: when the particle injects out of dihedral angle and when the particle falls on the dihedral angle. Let's particle trajectory is directed under angle $\varphi_t\neq0$. In Fig.6 dependence $W=f(\varphi)$ for angles $\alpha=\pi, \pi/2, \pi/3, \pi/4$ is presented. In Fig.6a distributions of radiation intensities when the particle injects out of dihedral angle and in Fig. 6b - when it falls on the dihedral angle are demonstrated.

In both cases particles move under $\varphi_t=0.3$. It can be seen in the figures that change of angle α impacts to the angular distribution of radiation intensity differently.

When a particle injects out of the boundary surface of the dihedral angle, decrease of the angle increases asymmetry of distribution relatively to particle movement direction (Fig. 6a), but for any α radiation is concentrated under angles close to a trajectory of the particle.

Change of the dihedral angle has qualitatively other influence on angular distribution in a case when the particle falls on the boundary surface. For angles $\alpha=\pi/n$, corresponding to even n, distributions of radiation when the particle injects out of the boundary surface and when the particle falls on this surface coincide (dependences for $\alpha=\pi/2$ and for $\alpha=\pi/4$ are in Fig. 6a and Fig. 6b). For odd n - angular distributions of injecting out and falling particles are symmetric relatively to a bisector of the

dihedral angle $\varphi=0$ (curves for $\alpha=\pi$ and $\alpha=\pi/3$ are in Fig. 6a and Fig. 6b).

To explain such feature of angular distribution of intensity of the transition radiation of the particle calculation schemes using a method of images should be considered (Fig. 2).

Remember that the relativistic particle at start and at stop radiates mainly in a direction its movement in an interval of angles $\Delta\varphi=\pm\gamma^{-1}$. Therefore when particle starts main contribution to a field of radiation of the dihedral angle is given by the real charge q_1 (Fig. 2a and Fig. 2c), and when the particle falls – by the image charge. For $\alpha=\pi/2$ the image charge is q_3 (Fig.2b), and for $\alpha=\pi/3$ the image charge is $-q_4$ (Fig.2d).

It can be seen in figures that for $\alpha=\pi/2$, i.e. when n is even, trajectories of the real charge q_1 and of the image charge q_3 are situated on one straight line, even when $\varphi_t\neq0$. Therefore both at a start and at stop radiation is concentrated under angles close to a trajectory of the real charge.

For odd n, when $\varphi_t\neq0$, value of the angle between trajectories of the real charge and the image charge is $2\varphi_t$. Therefore radiation is concentrated under angles $\varphi\approx-\varphi_t$, i.e. close to the trajectory of the image charge. Angular distribution of radiation of the particle injecting out of the dihedral angle and the particle falling on the dihedral angle will be mirror - symmetric.

Figure6: Angular distributions of radiation intensities for particles injecting out of (a) and falling to (b) the dihedral angle.

REFERENCES

[1] V.L.Ginzburg and V.N.Tsytovich, "Transition Radiation and Transition Scattering", Adam Hilger, Bristol, 1990.

[2] V.L.Ginzburg and I.M.Frank, Zh. Ekap. Teor. Fiz. (1944) 16, 15.

[3] M.I.Ryazanov and S.N.Safronov, Lazer Phys. ,(1996) 6, 708.

[4] A.V.Serov and B.M.Bolotovskii, Zh.Eksp.Teor.Fis. (2007) 131, 6, 994.[JETP (2007) 104, 6, 866.]

[5] A.V.Kol'tsov and A.V.Serov. Zh.Eksp.Teor.Fis. (2009) 136, 1, 44, [JETP (2009) 109, 1, 35.]

[6] A.V.Serov. Zh.Eksp.Teor.Fis. (2009) 135, 4, 678, [JETP (2009) 108, 4, 593.]

DISTORTIONS OF PROTON BEAM 2-D IMAGES AND PROFILES DUE TO BEAM SPACE CHARGE

P. Reinhardt-Nickoulin[1,#], S. Gavrilov[1,2], A. Feschenko[1,2], I. Vasilyev[1]
1) Institute for Nuclear Research of RAS, Moscow, Russia
2) Moscow Institute of Physics and Technology, Moscow, Russia

Abstract

The special residual gas ion cross section monitor is used at Proton LINAC INR RAS output to provide measurements of beam parameters. There are distortions and errors of measurements which are caused by various external and internal factors during the formation of beam cross section images. Below estimations of these distortions and results of numerical simulation of registration process of images are resulted, resolution of the detector and accuracy of measurements are discussed.

INTRODUCTION

Beam cross section monitor (BCSM) of accelerated protons is installed at an output of INR linac about in 4 m behind last accelerating resonator. It gives the possibility to observe the next beam parameters during adjustment and exploitation of the linac: form of beam cross section (BCS), form of current impulse, beam position and its displacement concerning linac axis. Besides due to computer processing of images BCSM allows to observe distribution of density of the accelerated particles in BCS and beam profiles. Double dimension distribution of accelerated beam particles in BCS is more informative characteristic in comparison with profiles of a beam [1].
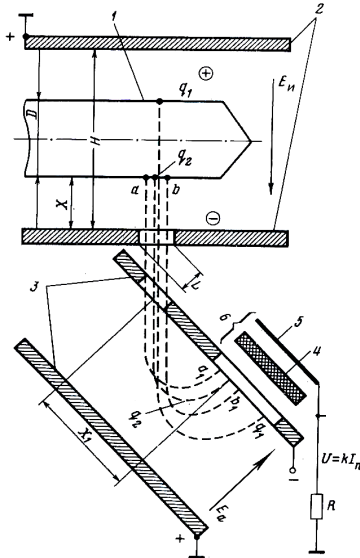
Fig. 1. Configuration design of the monitor:
1) Investigated beam   2) Condenser extracting ions
3) Analyzer of ions   4) Microchannel plates
5) Phosphor screen   6) Electro-optical converter

#petrein@inr.ru

The beam of the accelerated protons moves in the vacuum chamber of the accelerator and ionizes residual gas. Formed positive ions are extracted by homogeneous field of flat electrostatic condenser (extracting condenser) through a special slit in lower electrode of the condenser (Fig. 1). Accelerated gas ions pass the slit and form the taped beam. Then ions are rotated by a field of electrostatic energy analyzer (analyzing condenser) which electrodes are placed under 45 degrees to a direction of extraction of ions and to the plane of the extracting electrode. After that ions get to a double microchannel plate (MCP) of the electro-optical converter (EOC) with the coordinates depending on coordinates of an ionization point, creating the image of beam cross section registered TV-camera. Calculation of ion motion trajectory in homogeneous electrostatic fields shows that all kinds of positive ions compose the image [2].

THEORETICAL DESCRIPTION OF IONS DYNAMICS

Indeed nascent positive ion is under the influence of several kinds of fields (Fig. 2):
1) electrostatic field of the extracting condenser $E_{ext} = 1{,}2$ kV/cm (force F_{ext})
2) electromagnetic field of the beam which consists of radial electric field E_b (force F_E) and azimuth magnetic field B_b (force F_B).

The vector of the resultant force F_{Ion} isn't perpendicular to axis Y that causes broadening of BCS image (ΔY) along this axis under the influence of the beam space charge. In addition it is necessary to take into account ΔY-errors because of the finite width of the slit and nonzero initial velocities of the ions.

In our case the proton beam coasts at the interval L and expands significantly (by several digits) in a longitudinal direction under the law $\Delta\varphi = \dfrac{360 \cdot L}{\lambda \cdot \beta \cdot \gamma^2}\dfrac{\Delta p}{p}$ because of different value of impulses of accelerated particles $\Delta p / p \approx \pm 2 \cdot 10^{-3}$.

Therefore the beam length σ_z is much large than the transverse radii σ_x and σ_y. The appropriate charge distribution in this case is a Gaussian distribution in two dimensions with the constant line number density n:

$$\rho(x,y) = \frac{nq}{2\pi\sigma_x\sigma_y}\exp\left(-\frac{x^2}{2\sigma_x^2}-\frac{y^2}{2\sigma_y^2}\right).$$

In case of such azimuthally symmetric beam with two-dimensional charge Gaussian distribution the approximate

formula for unique nonzero radial component of force acting upon an ion in a beam electromagnetic field was received in work [3]:

$$F_r(r) = \frac{nqQ\left(1 \pm \dfrac{v_0\beta}{c}\right)}{2\pi\varepsilon_0 r}\left[1 - \exp\left(-\frac{r^2}{2\sigma^2}\right)\right],$$

where the sign depends on a relative direction of speeds of an ion v_0 and a beam.

The beam in the detector point has the elliptic form with parameters $\sigma_x \approx 2$ mm, $\sigma_y \approx 1$ mm, $\beta = 0,575$, $n \approx 3,625\cdot10^8$ protons/m.

In this connection we shall assume that initial resultant force acting upon an ion from the beam has exclusively radial direction, but the absolute magnitude of this force is estimated in view of existing X, Y-axes normal distributions of charges. Such simplifications allow to execute the most realistic simulation in using of azimuthally symmetric beam model with two-dimensional Gaussian distribution of charge.
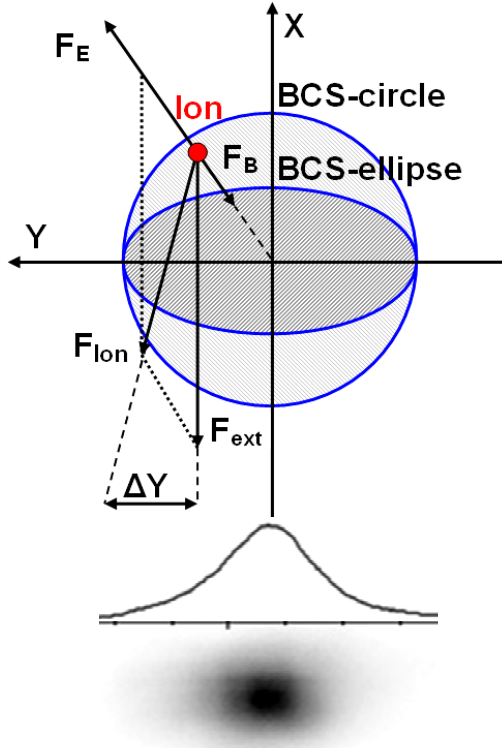
Fig. 2. Forces acting upon an ion and BCS with profile

The formed ions have various energy from 0 up to 0,025 eV. During modeling we shall assume, that initial velocities of hydrogen ions are evenly distributed to X, Y, Z-axes in the interval (–500 m/s, 500 m/s).

Besides we shall consider motion of only positive hydrogen ions (protons), because errors appearing at variation of weight and charge of an ion are negligibly small (around 0,1 percent at transition from a proton to fully ionized atom of nitrogen).

In our case force of the beam magnetic field is less than force of the beam electric field by six digits, therefore its influence on formed ions can be neglected.

Subject to using of various Gaussian distributions in calculations we shall consider, that the zone of ions formation in the residual gas is limited by 3σ.

Taking into consideration all foregoing approximations we shall consider that there are two forces acted upon a formed ion in the extracting condenser:

$$F_x(x,y) = -qE_{ext} + \frac{nq^2}{2\pi\varepsilon_0}\frac{x}{\left[x^2+y^2\right]}\left[1 - \exp\left(-\frac{x^2}{2\sigma_x^2} - \frac{y^2}{2\sigma_y^2}\right)\right],$$

$$F_y(x,y) = \frac{nq^2}{2\pi\varepsilon_0}\frac{y}{\left[x^2+y^2\right]}\left[1 - \exp\left(-\frac{x^2}{2\sigma_x^2} - \frac{y^2}{2\sigma_y^2}\right)\right],$$

which define distortions BCS images under influence of the beam space charge.

NUMERICAL SIMULATION

Program IonTrace with classical numerical Runge-Kutt method of 4-th order of accuracy and adaptive step was written for simulation. As required solutions are smooth enough adaptive step control provides the calculation of an approximate solution at fine mesh when solution changes quickly, and at crude mesh when it changes slowly. It allows to raise accuracy and to reduce time required for solution of the equations.

The primary goal of the program is an estimation of the errors in received BCS image in relation to the ideal image when there is no influence of a beam space charge and all initial velocities of ions are equal to zero.

Let's consider Y-axis distortions. We shall accept that during simulation Z-coordinate of all ions is equal to zero at birth. Final ΔY-distortions depending on ions birth coordinates in the vacuum chamber in case of nonzero initial velocities are presented in fig. 3 (Y-direction deflections up to ±160 μm).
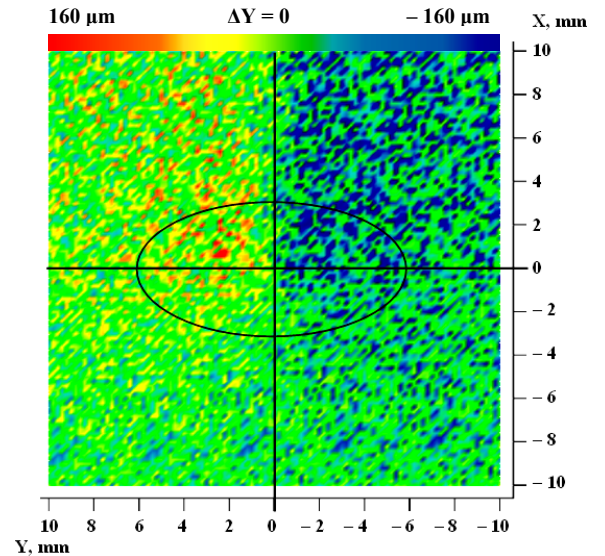
Fig. 3. Y-direction deflections ΔY of ions subject to born coordinates (X, Y)

The color spectrum from green to red corresponds to increasing of the deflections ΔY in a positive Y-direction, from green to violet – in a negative Y-direction, that is color in figure characterizes final deflection of the formed ion with birth coordinates X, Y. Such gradation of colors allows to allocate zones of the least and the greatest deflections of ions at MCP depending on their birth coordinates in relation to the center of a proton beam (marked by ellipse). Average deflections at Y-axis because of influence of the beam space charge are in the range of 100÷150 microns.

The maximum Y-deflection about 160 microns corresponds to an ion with birth coordinates from the zone of the greatest deflections and the worst vector of velocity (500, – 500, – 500) that is when the ion moves upwards against a beam motion that increases time of its staying in the detector.
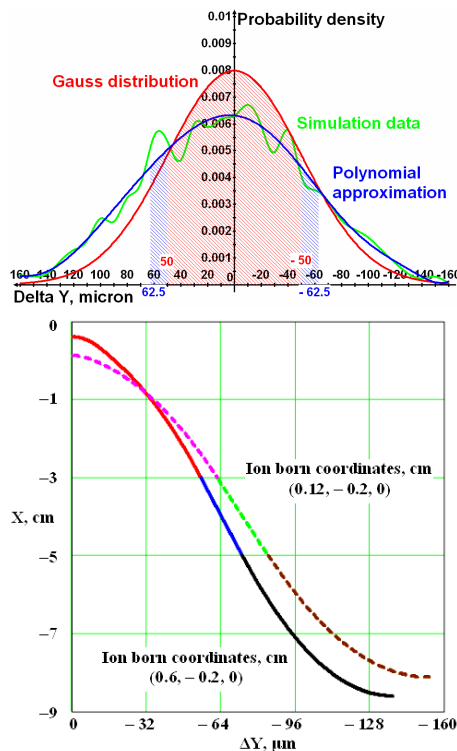
Fig. 4. Ions trajectories with max ΔY subject to born coordinates (X, Y)

Now we shall consider Z-axis errors. According to simulation average total time of an ion motion in the detector is less than 180 ns and time of motion in the extracting condenser is around 80 ns.

For such times ions with thermal velocities are shifted by Z-direction no more than 100 microns. However as shown in fig. 1 the finite width of the slit causes making of two parallel layers «a» and «b» of extracted ions.

Thus we receive several BCS imposed each other. Nevertheless as shown in [4] from the point of view of statistics, it gives small error under the law $\sigma^2_{measured} = \sigma^2_{beam} + L^2/12$, where L – width of the slit (L = 1 mm in the present version).

Resolution of the image is defined by resolution of a chevron MCP assembly in EOC (Fig. 5) which is estimated around 50 micron [5]. Thus we visual recognize final images of two ions if their hit coordinates at MCP differ in 50 microns at X, Y-axes.
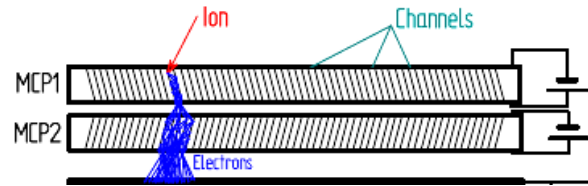
Fig. 5. Image formation mechanism in EOC

CONCLUSION

Considering the simulation data it is possible to tell with confidence that upper limit of the total error in BCS image received on MCP assembly doesn't exceed 30 microns. It is mainly defined by three independent parameters: a beam space charge, initial velocities of formed ions of residual gas and the split influence.

Thus Beam cross section monitor allows to register BCS images with inaccuracy around of 1% that is quite admissible result for the decision of problems of the operative visual control, diagnostics and correction of various parameters of a beam. Possible reduction of the slit size down to 0,1 mm will allow to receive BCS images similar to ideal: at a level of errors less than 1% and final image resolution of 50 microns.

REFERENCES

[1] *P. Reinhardt-Nickoulin, A. Feschenko, S. Gavrilov, I. Vasilyev*, Development of ion transverse section monitor for proton beam of INR LINAC. // Problems of Atomic Science and Technology, VANT №2 (53), p. 39–43, 2010.

[2] *V. G. Mihailov, V. V. Leonov, V. A. Rezvov et al.*, Multivariate ionization detectors for the control of beams of the accelerated particles. // Instruments and Experimental Techniques, №6, p. 39–53, 1995.

[3] *E. Keil*, Beam-beam dynamics. // CERN SL/94-78 (AP), Geneva, 1994.

[4] *E. S. Ventcel*, Theory of probability. «Science», Moscow, 1969.

[5] *J. L. Wiza*, Microchannel plate detectors. // Nuclear Instruments and Methods, 162 (1979), p. 587–601.

SHAPES OF NUCLEAR INDUCTION SIGNALS UNDER INHOMOGENEOUS MAGNETIC FIELDS

B. Makarov, V. Ryzhov, Federal State Unitary Enterprise "The Moscow Radio Institute of the Russian Academy of Sciences", Moscow, Russia

INTRODUCTION

The shape of the nuclear induction signal is determined by structural types and dynamic processes in the analizable substance. It depends on the conditions of observation: temperature, a radio-frequency (RF) impulse sequence type, a spatial inhomogeneity of the RF field and so on [1, 2]. The magnetic polarizing field inhomogeneity exerts essential influence on nuclear induction signal parameters. The form and the orientation of the sample have also effect. F. Bloch equations describing the motion of the macroscopic nuclear magnetization vector have been solved in case of the homogeneous magnetic field. The inhomogeneity influence is taken into account under the assumption that the real distribution of the magnetic field is known [3 – 5].

SHAPES OF NUCLEAR INDUCTION SIGNALS

In the inhomogeneous magnetic field B_0 ($\vec{B}_0$ is axial $\vec{z}$) and the absence of the electromagnetic field ($\vec{B}_1 = 0$) the x-component (M_x) of the macroscopic nuclear magnetization vector $\vec{M}$ is

$$M_x(t) = M_x(0)\exp(-t/T_2)\cos(\omega_0 t),\qquad(1)$$

where $M_x(0)$ − initial value of the transversal component of the magnetization vector, $\omega_0 = \gamma B_0$ the resonant value of the nuclear frequency in the field B_0, γ - gyromagnetic ratio, T_2 − the transverse relaxation time of nuclear spins.

The sample is divided into elementary volumes. The field inside of them is considered to be homogeneous. The signal from the elementary volume is a two-variable function: of time t and of $\Delta\omega_0 = \gamma\Delta B_0$ - a frequency deviation of a nuclear precession from its average value $\omega_0 = \gamma B_0$, where ΔB - induction deviation from its average value B_0 inside the volume element (the spot). In that case

$$M_x(t,\alpha) = M_x(0)\exp(-t/T_2)\cos(\omega^{\bullet}t),\qquad(2)$$

here

$$\omega^{\bullet} = (1-\sigma)\omega == (1-\sigma)(\omega_0 + \Delta\omega) =$$
$$= (1-\sigma)(\omega_0 + \alpha) = \gamma(1-\sigma)(B_0 + \Delta B)$$

− a precessional frequency in the elementary volume taking into account the screening magnetic effect, σ - constant of the magnetic screening, $\alpha = \Delta\omega$. Since field deviations from the average value B_0 are small value M(0) − a weak dependence function from inhomogeneity. This dependence is neglected.

The total precession signal from the simple is

$$F_x(t) = \int_{-\infty}^{+\infty} f(\alpha)M_x(t,\alpha)d\alpha =$$
$$= M_x(0)\exp(-t/T_2)\int_{-\infty}^{+\infty} f(\alpha)\cos\,\omega^*(\alpha)t d\alpha \qquad(3)$$

In case of the exponential distribution

$$f(\alpha) = \frac{1}{2\beta}\cdot\exp(-|\alpha|/\beta)\qquad(4)$$

the total signal with the initial amplitude normalized to unity is

$$F_N(t) = \frac{M_x(t)}{M_x(0)} = \frac{\exp(-t/T_2)}{\sqrt{1+(\beta^*t)^2}}\cdot\cos(\omega_0^*t+\phi),\qquad(5)$$

where $\phi = arctg\,(\beta^*t)$, $\beta^* = (1-\sigma)\beta$, $\omega_0^* = (1-\sigma)\omega_0$, this and below index "x" is omitted. The phase of the induction signal is time-depended. Therefore the frequency of total precession signal is changing.

Selecting the field triangular distribution

$$f(\alpha) = \begin{cases} h(1+h\alpha) & by \quad -1/h < \alpha < 0 \\ h(1-h\alpha) & by \quad 1/h > \alpha > 0 \\ 0 & by \quad |\alpha| > 1/h \end{cases}, \quad h > 0$$

it is getting

$$F_N(t) = \left[\frac{\sin(h^*t)}{(h^*t)}\right]^2 \exp(-t/T_2)\cos(\omega_0^*t),\qquad(6)$$

where $h^* = (1-\sigma)/2h$.

In case the Lorentz, the Gaussian, the triangular, the impulse (rectangular) field distributions the frequency is $\omega_0^* = const$. Amplitude expressions for the Lorentz, the Gaussian and impulse distributions published in [5] agree with those which we deduced in special case of $\sigma = 0$.

Let's examine the pulse distribution with finite acceleration time. If the leading edge curve changes by Lorentz law

$$f(\alpha) = \begin{cases} \dfrac{1}{pa} & by \quad |\alpha| \le \dfrac{a}{2} \\[4mm] \dfrac{(p-1)T_2^{'}}{p\pi\{1+[(|\alpha|-\dfrac{a}{2})T_2^{'}]^2\}} & by \quad |\alpha| > \dfrac{a}{2} \end{cases},$$

$$p \ge 1$$

the nuclear induction signal is

$$F_N(t) = A\exp(-t/T_2)\cos(\omega_0^*t+\phi),\qquad(7)$$

where

$$A = \frac{1}{p}\sqrt{B(B+C)+(p-1)^2 D},$$

$B = \dfrac{\sin(a^* t)}{a^* t}$,

$C = 2(p-1)\sqrt{D}\cos(a^* t + \theta)$,

$D = \exp(-2t/T_2^*) + G_M^2/\pi$,

G_M - Meijer G-function of the kind

$MeijerG\ [\{\{\tfrac{1}{2}\},\{\}\}, \{\{\tfrac{1}{2},\tfrac{1}{2}\},\{0\}\}, \left(\dfrac{t}{2T_2^*}\right)^2]sign\left[\dfrac{t}{T_2^*}\right]$,

$\theta = arctg\left\{\dfrac{G_M \exp(t/T_2^*)}{\pi}\right\}$,

$\phi = arctg\left[\dfrac{2(p-1)D\sin(a^* t + \theta)}{2B + C}\right]$,

$a^* = (1-\sigma)a/2$, $1/T_2^* = (1-\sigma)/T_2'$.

For a continuously curve it needs $p = 1 + \pi/(aT_2^*)$.

If pulse "wings" modify by Gaussian law

$f(\alpha) = \begin{cases} \dfrac{1}{pa} & by\ |a| \le a/2 \\[2mm] \dfrac{p-1}{p\sigma_1\sqrt{2\pi}}\exp\left(\dfrac{(|\alpha| - a/2)^2}{2\sigma_1^2}\right) & by\ |a| > a/2 \end{cases}$,

$p \ge 1$

the nuclear induction signal is

$F_N(t) = A\exp\left(-t/T_2\right)\cos(\omega_0^* t + \phi)$,   (8)

where

$A = \dfrac{1}{pa^* t}\sqrt{B^2 + \sqrt{1 + (2B)^2}\sin a^* t \cos(a^* t - \theta_1)}$,

$B = (p-1)a^* t \exp(-(\sigma_1^* t)^2)$,

$\theta_1 = arctg\left[\dfrac{\exp(\sigma_1^* t)^2}{2(p-1)a^* t}\right]$,

$\phi = arctg\left[\dfrac{B\sin(a^* t)}{\cos(a^* t - \theta_2)\cdot\sqrt{1 + B^2}}\right]$,

$\theta_2 = arctg\left[\left(\dfrac{\exp\left((\sigma_1^* t)^2\right)}{(p-1)a^* t}\right)\right]$,

$\sigma_1^* = \sqrt{2}(1-\sigma)\sigma_1$, $a^* = (1-\sigma)a/2$.

There are not ruptures of the function if

$p = 1 + \sqrt{\pi}\sigma_1^*/a$.

If leading edges modify by exponential law

$f(\alpha) = \begin{cases} \dfrac{1}{pa} & by\ |\alpha| \le \dfrac{a}{2} \\[2mm] \dfrac{p-1}{2\beta p}\exp\left(\dfrac{|\alpha| - a/2|}{\beta}\right) & by\ |\alpha| \ge \dfrac{a}{2} \end{cases}$

$p \ge 1$

the formula is given by

$F_N(t) = A\exp\left(-t/T_2\right)\cos\left(\omega_0^* t + \phi\right)$,   (9)

where

$A = \dfrac{1}{p}\sqrt{[B + C\cos(a^* t + \theta_1)]^2 + [C\cos(a^* t - \theta_2)]^2}$,

$B = (\sin a^* t)/(a^* t)$, $C = (p-1)/\sqrt{1 + (\beta^* t)^2}$,

$\theta_1 = arctg(\beta^* t)$, $\theta_2 = arctg(1/\beta^* t)$,

$\phi = arctg\left[\dfrac{C\cos(a^* t - \theta_2)}{B + C\cos(a^* t + \theta_1)}\right]$.

There are not jumps of the function if

$p = 1 + (2\beta \exp(\ \|\alpha| - a/2|)/\beta)/a$.

If leading edges modify by the linear law (the trapezoidal distribution)

$f(\alpha) = \begin{cases} f_1(\alpha) & by & -1/h - a/2 < \alpha < -a/2 \\ f_2(\alpha) & by & |\alpha| \le a/2 \\ f_3(\alpha) & by & 1/h + a/2 > \alpha > a/2 \\ f_4(\alpha) & by & |\alpha| > 1/h + a/2 \end{cases}$

where

$f_1(\alpha) = [(p-1)(h + h^2(\alpha + a/2)]/p$,

$f_2(\alpha) = 1/pa$,

$f_3(\alpha) = [(p-1)[h - h^2(\alpha - a/2)]/p$,

$f_4(\alpha) = 0$,

$p \ge 1$

the expression is given by

$F_N(t) = (A + B)\exp(-t/T_2)\cos\omega_0^* t$.   (10)

At this point

$A = \dfrac{1}{p}[\dfrac{\sin(a^* t)}{a^* t} + \dfrac{p-1}{2(h^* t)^2}\sqrt{1 + (a^* t)^2}\cos(a^* t - \theta_1)]$,

$B = \dfrac{p-1}{p}\{\dfrac{C\sin(h^* t)}{(h^*)^2 t}\cos[(C - h^*)t] -$

$-\dfrac{1}{2(h^* t)^2}\sqrt{1 + (Ct)^2}\cos(Ct - \theta_2)\}$,

$h^* = (1-\sigma)/(2h)$, $C = a^* + 2h^*$, $\theta_1 = arctg(a^* t)$,

$\theta_2 = arctg(Ct)$.

Let's consider two sites system (a and b) of the same nuclear spins with a chemical shift $\Delta\omega_{ab} \ne 0$. We will consider fast exchange between components a and b. In this case [6] $C_a, C_b \gg 1/T_{2a}, 1/T_{2b}, |\omega_a - \omega_b|$ and

$(\omega_a - \omega_b)^2 \gg (1/T_{2a} - 1/T_{2b})$ the nuclear magnetization is

$M_x = M'(0)\exp(-t/T_2)\sin\omega_{av} t$,

where $M'(0) = k_1 M(0)$, $k_1 \le 1$, $\omega_{av} = P_a\omega_a + P_b\omega_b$,

$\dfrac{1}{T_{2a}} = \dfrac{P_a}{T_{2a}} + \dfrac{P_b}{T_{2b}} + \dfrac{[1 - (P_b - P_a)^2](\omega_a - \omega_b)^2}{4(C_a + C_b)}$.

Then an average frequency with a gradient is

$\overline{\omega_{abG}^c} = P_a\omega_{aG}^c + P_b\omega_{bG}^c = m(\omega_0 + \alpha)$,

where $m = P_a(1 - \sigma_a) + P_b(1 - \sigma_b)$.

1.   For the Gaussian distribution of the field

$f(\alpha) = \dfrac{1}{\sigma_1\sqrt{2\pi}}\cdot\exp(-\alpha^2/2\sigma_1^2)$

the signal is

$F_N(t) = A\exp(-Bt - Ct^2)\sin(D\omega_0 t)$,   (11)

here

$A = \dfrac{1}{\sigma_1\sqrt{2d}}$, $B = n + k\omega_0^2$, $C = \dfrac{m^2 - 4k^2\omega_0^2}{4d}$,

$D = \left(1 - \dfrac{kt}{d}\right)m$, $d = \dfrac{1}{2\sigma_1^2} + kt$, $n = \dfrac{P_a}{T_{2a}} + \dfrac{P_b}{T_{2b}}$,

$k = \dfrac{1 - (P_b - P_a)^2}{4(C_a + C_b)}(\sigma_b - \sigma_a)^2$.

2. For the exponential distribution (4) the formula is

$$F_N(t) = A \exp(-nt) \sin(m\omega_0 t),$$ (12)

where

$$A = \frac{\left(\dfrac{1}{\beta} + 2k\omega_0 t\right)\left[\sqrt{\pi} \exp\left(-\dfrac{m^2}{4k}t\right) + 2\sqrt{kt}\right]}{2\beta\left[\left(\dfrac{1}{\beta} + 2k\omega_0 t\right)^2 + (mt)^2\right]\sqrt{kt}},$$

n, m, k are the similar as above.

Similar expressions have a place for the component of the longitudinal magnetization $M_z(t)$, if in foregoing formulas $M_x(t, \alpha)$ is replaced by $[M_z^0 - M_z(t, \alpha)]$ and $F_N(t)$ is replaced by $F(t)/[M_z^0 - M_z(0)]$, where M_z^0, $M_z(0) = M_z(t=0)$ - equilibrium and initial values of the longitudinal magnetization M_z.

Now work out the shape of the nuclear induction signal from the cylinder sample under the field with the constant gradient G. Let the gradient is directed along the coil axis coinciding with ꞁ (B=B_0 – Gx). If the coil has got radius r_0, the amount of turns N uniformly distributing among the length l the electromotive force (emf) induced in the coil is

$$E(t) = E(0)\frac{e^{-t/T_2}}{2\delta^*\omega_0^* t}\{\frac{2}{T_2}\sin(\delta^* t)\cos[(\omega_0^* - \delta^*)t] +$$
$$+ (\omega_0^* - 2\delta^*)\cos[(\omega_0^* - 2\delta^*)t] - \omega_0^*\cos(\omega_0^* t) +$$ (13)
$$+ \frac{2}{t}\sin(\delta^* t)\cos[(\omega_0^* - \delta^*)t]\}$$

where the precession initial amplitude is

$$E(0) = \frac{4\pi}{c} NM(0)\omega_0^* S = \frac{4\pi^2}{c} NM(0)\omega_0^* r_0^2,$$

the cross-section area (circle) is $S = \pi r_0^2$ and

$$\delta^* = \frac{1}{2}\gamma(1-\sigma)Gl .$$

In case $\omega_0^* \gg \delta^*$

$$E(t) = E(0)e^{-t/T_2}\frac{\sin(\delta^* t)}{\delta^* t}\{\frac{\cos\omega_0^* t}{\omega_0^* T_2} +$$
$$+ \frac{\sqrt{1 + (\omega_0^* t)^2}}{\omega_0^* t}\cos(\omega_0^* t - \theta)\}$$ (14)

In extreme case $\omega_0^* \gg \delta^*$ and $\omega_0^* T_2 \gg 1$

$$E(t) = E(0)\frac{\sqrt{1 + (\omega_0^* t)^2}}{\omega_0^* t}\frac{\sin(\delta^* t)}{\delta^* t}\cos(\omega_0^* t - \theta),$$ (15)

where $\theta = arctg(\omega_0^* t)$.

If $\omega_0^* t \gg 1$ the second factor $\dfrac{\sqrt{1 + (\omega_0^* t)^2}}{\omega_0^* t} \cong 1$ and

$$E(t) = E(0)\frac{\sin(\delta^* t)}{\delta^* t}\sin\omega_0^* t ,$$ (16)

because $\theta \to \dfrac{\pi}{2}$ at $\omega_0^* t \to \infty$.

If the field gradient direction is perpendicular to the coil axis (B=B_0 – Gz or B=B_0 – Gy) the emf value induced in the coil is

$$E(t) = A \exp(-t/T_2)\cos(\omega_0^* t - \psi) ,$$ (17)

where

$$A = 2E(0)\sqrt{B^2 + \left[kr_0 C + \frac{B}{\omega_0^* T_2}\right]^2} ,$$

$$B = \frac{J_1(\vartheta t)}{\vartheta t}, \quad C = \frac{J_2(\vartheta t)}{\vartheta t} .$$

Here $J_1(\vartheta^* t)$ - Bessel's function of the first order of the first kind, $J_2(\vartheta^* t)$ - Bessel's function of the second order of the first kind, $\vartheta^* = \gamma G^* r_0$, $k = G/B_0$,

$$\psi = arctg\left(\frac{B}{kr_0 C + B/\omega_0^* T_2}\right).$$

At $\omega_0^* T_2 \gg 1$

$$E(t) = A_1 \exp\left(-\frac{t}{T_2}\right)\cos(\omega_0^* t - \psi_1) ,$$ (18)

$$A_1 = 2E(0)\sqrt{B^2 + [kr_0 C]^2} ,$$

$$\psi_1 = arctg\left(\frac{B}{kr_0 C}\right).$$

In the limit case $\omega_0^* T_2 \gg 1$ and $kr_0 \ll 1$

$$E(t) = 2E(0)\frac{J_1(\vartheta t)}{\vartheta t}\exp\left(-\frac{t}{T_2}\right)\sin\omega_0^* t ,$$ (19)

because $\psi_1 \to \dfrac{\pi}{2}$ at $\dfrac{J_1(\vartheta t)}{kr_0 J_2(\vartheta t)} \to \infty$.

CONCLUSIONS

The shapes of the nuclear induction signals depend on the inhomogeneity type of the magnetic polarizing field. It is possible to perform effective filtrating of the magnetic resonance signals by the deduced expressions. It enables to increase a precision of the data processing and decrease experimental time.

REFERENCES

[1] Abragam A., "The principals of nuclear magnetism", Oxford at the Claredon Press, 1961.
[2] Farrar T.C. and Becker E.D., "Pulse and Fourier transform NMR introduction to the theory and methods", Academic Press, New York and London, 1971.
[3] Gabillard R., "A steady state transient technique in nuclear resonance", Phys.Rev., 1952, v.85, p. 694 - 695.
[4] Carr H. Y. and Purcell E. M., "Effects of diffusion on free precession in nuclear magnetic resonance experiments", Phys. Rev., 1954, v.94, No. 3, p.630 – 638.
[5] Pfeifer H., "Möglichkeiten der Spin-Echo-Methoden", Hochfrequenzspektroskopie", Berlin, 1961, p.31 - 39.
[6] Woessner D.E., "Nuclear transfer effects in nuclear magnetic resonance pulse experiments", J. Chem. Phys., 1961, v. 35, Nu. 1, p.41 – 48.

ADVANCE OF MARGINAL OSCILLATOR

B. Makarov, V. Ryzhov, Federal State Unitary Enterprise "The Moscow Radio Institute of the Russian Academy of Sciences", Moscow, Russia

INTRODUCTION

The marginal oscillator is used for detecting nuclear magnetic resonance (NMR) signals. This scheme is convenient for search of resonant absorption of energy by atomic nuclei so it is prevalent in the NMR magnetometers. At present the valve and the transistor oscillators are developed [1 - 5].

In this article is briefly considered the theory of operation and concrete schemes of the marginal on basis of a field-effect transistor (FET).

BASES OF THEORY

A sample containing nuclear spins is placed in the coil of an oscillatory circuit of the marginal. In this case inductance of the coil is equal

$$L = \mu L_0 = L_0(1 + 4\pi\chi\xi), \tag{1}$$

where L_0 - self inductance of the coil, μ - magnetic permeability of substance of the sample, χ - dynamic nuclear susceptibility, ξ - factor of filling of the coil [2].

The impedance of the circuit is changed at the moment of the resonant absorption of the high-frequency energy by spins. The real component of the impedance of the parallel circuit is

$$\frac{\Delta R}{R} = 1 - \frac{1}{(1 + 4\pi\chi'\xi)(1 - 4\pi Q\chi''\xi)}, \tag{2}$$

and the phase angle is

$$tg\,\varphi = -\frac{4\pi Q\chi'\xi}{1 + 4\pi Q\chi''\xi}. \tag{3}$$

Here Q is the quality of the oscillatory circuit, χ', χ'' are the real and the imaginary parts of dynamic nuclear susceptibility $\chi = \chi' - j\chi''$.

The contribution to (2) by real part of the magnetic susceptibility approximately in Q times is less than the one of its imaginary part. Therefore only as a first approximation it is possible to consider that in the case amplitude detecting the marginal oscillators develop the signal proportional to the absorption. Simultaneously according to (3) the operating frequency is changed. Mainly this change is caused by the imaginary part of the dynamic susceptibility. Thereby the imaginary part of the nuclear susceptibility is responsible for absorption of energy of the radio-frequency circuit at the resonance, and phase and the frequency changes are caused by its real part.

Except the aforesaid staggering of the oscillatory circuit the phenomenon of frequency capturing is observed at changing (modulating) the invariable magnetic field through the resonant value analogous picking-up the oscillations in the tube or the transistor oscillator by exter-

nal force. In this case the system of the nuclear magnetic moments acts like the external force. It is possible to consider it as the high-Q resonant circuit which interacts with the marginal oscillatory circuit. However, in this case there is no the perfect analogy. This interaction differs from that of two connected oscillatory circuits. Therefore frequency deviation connected with magnetic field change allows comparing this phenomenon with frequency capturing instead of frequency pulling observed in two connected oscillatory systems [6].

The marginal is an oscillator operating under the scheme of "an induction three-point (Hartley oscillator)" or of "a capacitor three-point (Colpitts oscillator)" [1 - 5] theory which is well developed [7, 8]. According to the theory for generating the self-oscillation a two-pole net with negative differential resistance is necessary to be connected to the oscillatory circuit

$$I(u) = S_1 u + S_3 u^3 + ... , \tag{4}$$

where $S_1 < 0$.

From this theory it also known that stable inherent oscillations arise at increase of factor of feedback β to some critical value β_{cr}, i.e. at

$$\beta > \beta_{cr} = \frac{R_0 C}{S_1 L_0} = \frac{1}{S_1 R}, \tag{5}$$

here R_0 and C - parameters of the parallel oscillatory circuit, R_0 - (real) resistance of the coil, R - entering (equivalent) resistance of the circuit at the resonance. (The expression (5) doesn't consider transistor influence.) As appears from (2) at the nuclear magnetic resonance equivalent resistance of the parallel circuit decreases. According to expression (5) it leads to increase in critical value of feedback factor β_{cr}. So for the value of feedback factor β_0 established in the generator the amplitude of oscillations will decrease.

And under the influence of destabilizing factors the self-oscillations in oscillators are the oscillations with random amplitudes and phases

$$u(t) = A(t)\cos(\omega t + \varphi(t)), \tag{6}$$

where $A(t)$ and $\varphi(t)$ are time stochastic functions.

The marginal scheme feature is that its sensitivity increases when the oscillation amplitude reduces [2, 7]

$$E(t) \approx \frac{dA(t)}{dS_1} \propto \frac{1}{A(t)}. \tag{7}$$

As consequence there are fluctuations of the sensitivity and the NMR signal amplitude.

The feature of the marginal is that it generates voltage with small amplitude (therefore it is still named the oscillator of small oscillations). In this operating mode even very small changes of parameters of an oscillatory circuit

lead to considerable variations of voltage amplitude generated by the marginal.

The phase locked-loop (PLL) is tuning the frequency of the parallel oscillatory circuit to its resonance value and conductivity of the circuit at the resonance is

$$G \approx \frac{1}{R}(1 - 4\pi Q \chi^{"} \xi)\,, \tag{8}$$

here R is a resonant resistance of the circuit without NMR sample

From this formula it is obvious that PLL allows to exclude influence of the real part of susceptibility $\chi^{'}$, there-fore there will be no impurity of a dispersion component in the output signal.

The phase and amplitude locked-loops are included with the purpose of increasing the stability of the scheme function and carrying out the precision magnetic measurements.

It is necessary to notice there is an optimum frequency of invariant magnetic field modulation for each HF oscillation level. Application also of higher frequency modulation (in the range $10 - 100$ kHz) promotes suppression of noise of a kind 1/f [1 – 3, 6, 8].
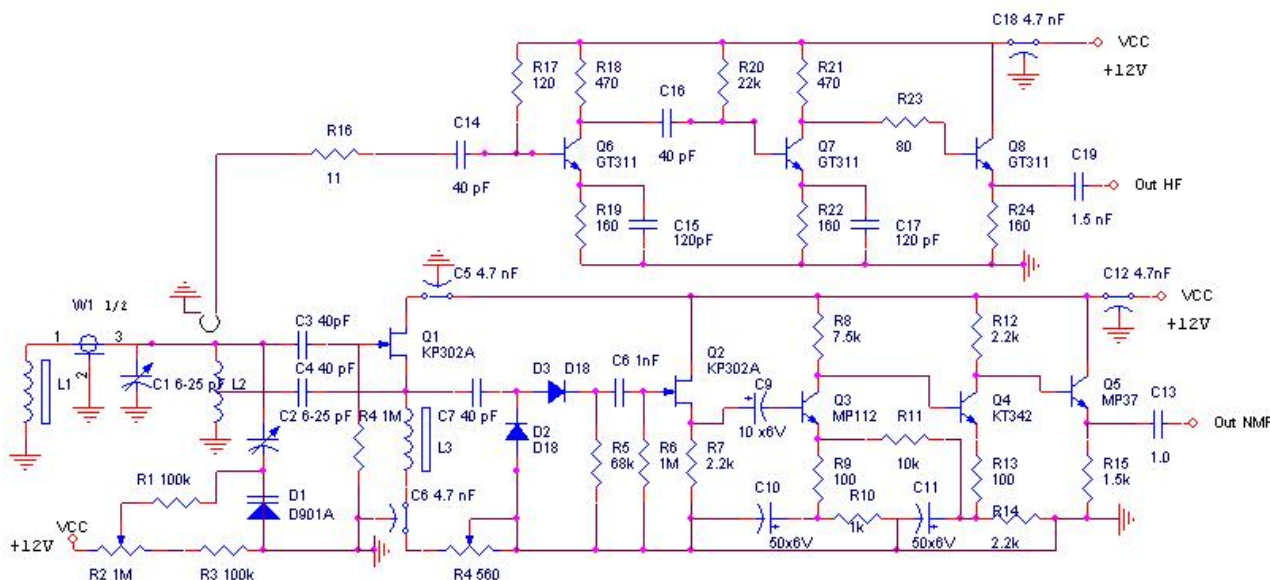
Figure1: The NMR magnetometer on the base the marginal oscillator with using FET.

FET MARGINAL SCHEMES

The nuclear magnetic resonance magnetometer (Fig. 1) is one of the first magnetometers on a basis of the marginal with application field-effect transistors [10]. It is developed in 1973 for field control in the superconducting solenoid made for use in the proton polarized target which is applied to research of spin effects in the high energy physics. It is the classical scheme. Actually the marginal oscillator functions on the transistor Q1. The peak detector is assembled with application diodes D1 and D2, on transistors Q2 - Q5 the amplifier of low frequency is designed, on transistors Q6 - Q8 the high-frequency amplifier is built. The probe is connected to the device by cable RC-50 which length l/2 = 2.5 meters, operating frequency F =30 - 40 MHz. At increase in values of circuit elements it is possible to lower working frequency to ~ 5 MHz. Further the transistors possessing the best characteristics (KP 303, KP 307) were applied. In this case at corresponding reduction of length of a cable operating frequency can be considerable above.

The signal of electron spin resonance (ESR) received by this scheme in ⍺-diphenyl-β-pikrilgidrazil (DPhPG) containing free radicals is shown on Fig. 2. The alternating magnetic field with frequency 50 Hz is created by the coil, the working frequency of the marginal is f = 30 MHz, the signals ESR arise in the field ~10 Gauss.
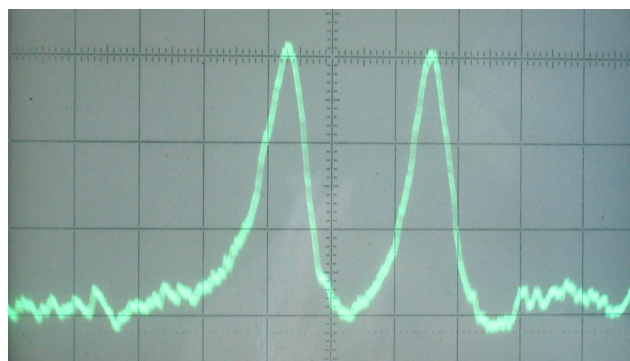
Figure 2: The signal of electron spin resonance in alternating magnetic field obtained by the scheme on fig. 1. Substance of the probe is ⍺-diphenyl-β-pikrilgidrazil (DPhPG).

06 Instrumentation, Controls, Feedback and Operational Aspects

Fig. 3 is presented the scheme of the simplest spin detector with operating frequency 150 MHz [11]. The resulted length (L = 0.32 m) of the connecting cable of type RC-75 is equal to a quarter of the length wave (L = λ/4) in it. The device distinguishes the minimum quantity of units.

On the basis of scheme Pound - Knight marginal is developed the device with the phase and amplitude locked-loops (Fig. 4). The Pound - Knight oscillator is collected on transistors Q1 - Q3. The amplitude locked-loop consists from the HF amplifier A1, the peak detector AD, the amplifier of direct current U1, Q2 − Q4 transistors. The phase locked-loop includes the HF amplifiers A1, A2, the phase detector PD, the stable (quartz) generator SF.
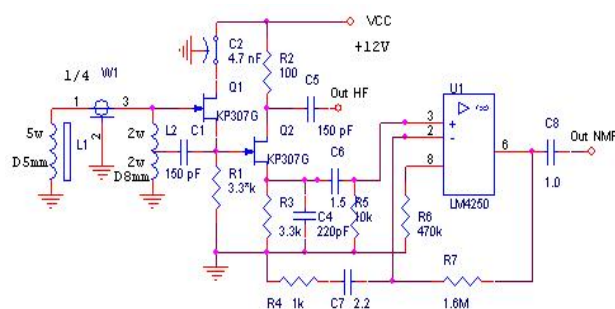
Figure 3: The elementary marginal detector.
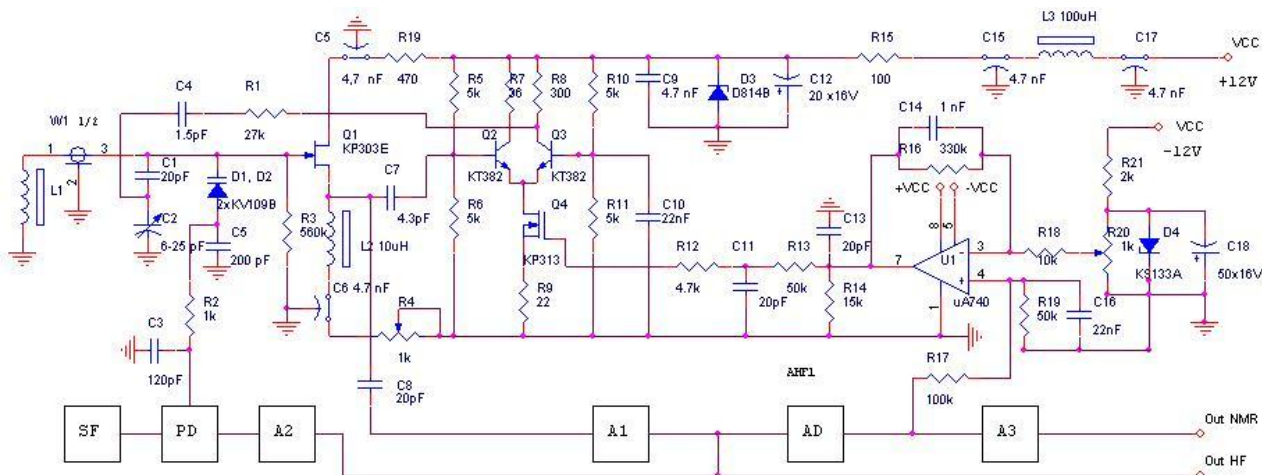
Figure 4: The NMR magnetometer on the base Pound - Knight marginal. A1 is HF amplifier, A2 - HF amplifier-terminator, AD - peak detector, PD - phase detector, SF − frequency synthesizer.

Operating frequencies range is 30 − 50 MHz, at replacement of inductance and capacity in the oscillatory circuit it is decreased to ~2 MHz. Long-term (~6 − 8 hours) stability of frequency is better 10^{-7} if the frequency synthesizer Ch6-31 is used. The generation minimum level is ~ 5 mV.

CONCLUSIONS

FET marginal facilities are the third generation of oscillators after tube schemes and bipolar transistor schemes.

Advantage of this scheme is high input resistance FET which as well as in case of tubes shunts an oscillatory loop a little and so its quality is reduced only a little. High quality oscillatory circuit causes the maximum modulation HF carrier.

PLL application of the oscillatory circuit allows to obtain the pure signal of the absorption which have been not deformed by dispersion. The amplitude locked-loop raises the relation of a signal to noise. It allows to increase accuracy of magnetic induction measurements.

The further improvement of device characteristics is connected with application of methods: synchronous detecting, digital accumulation and averaging of signals, improvement of processing algorithms.

REFERENCES

[1] Andrew E.R., "Nuclear magnetic resonance", Cambridge at the University Press, 1965.

[2] Lösche A., "Kerninduction", Veb Deutscher Verlag Der Wissenschaften, Berlin, 1957.

[3] Howling D.H., "Signal and noise characteristics of the PKW marginal oscillator spectrometer.", Rev. Sci. Instrum., 1965, v.36, No.5, p. 660-667.

[4] Pierce W.L. and Hicks J.C., "Improved NMR prober for magnetic field measurements", Rev. Sci. Instrum., 1965,v. 36, No. 2, p.202-203.

[5] Idoine John D., Brandenberger Jr. and J.R., "FET mardinal oscillator circuit", Rev. Sci. Instrum., 1971, v.42, No.5, p. 715-717.

[6] Pomerantsev N.M., Ryzhkov V.M., Scrotsky G.V. "Physical bases of quantum magnetometry.", (in Russia), "Science", Moscow, 1972, p.448.

[7] Tietze U., Schenk Ch., "Halbleiter-Schaltungstechnik", Springer-Verlag, Berlin-Heidelberg-New York, 1980.

[8] Zernov N.V. and Karpov V.G., "Theory of radio engineering networks", (in Russia), "Energy", Leningrad, 1972, p.816.

[9] Adler M.S., Senturia S.D. and Hewes C.R., "Sensitivity of marginal oscillator spectrometers.", Rev. Sci. Instrum., 1971, v.42, No.5, p. 704-712.

[10] Parphenov L.B. , Ryzhov V.G., Unpublished data.

[11] Maximov A.Yu., Ryzhov V.G., Unpublished data.

06 Instrumentation, Controls, Feedback and Operational Aspects

HV ELECTRON COOLER FOR THE NICA COLLIDER

E.V.Ahmanova, A.G.Kobets[**], I.N.Meshkov[#], R.V.Pivin, A.U.Rudakov, A.V.Shabunov, A.V. Smirnov, N.D.Topilin, Yu.A.Tumanova, S.L.Yakovenko, JINR, Dubna
A.A.Filippov, L.M.Fisher, M.M.Pashin, AREI, Moscow,

Abstract

The goal of the cooling system of the NICA collider is to meet the required parameters of ion beams in energy range of $1 \div 4.5$ GeV/u that corresponds to the $0.5 \div 2.5$ of the electron MeV. The electron cooler is developed according to the available world practice of manufacturing of similar systems [1] The main peculiarity of the electron cooler for the NICA collider is use of two cooling electron beams (one electron beam per each ring of the collider) that never has been done. The acceleration and deceleration of the electron beams is produced by common high-voltage generator. The cooler consist of three tanks. Two of them contain acceleration/deceleration tubes and are immersed in superconducting solenoids. The third one contains HV generator. The scheme of the electron cooler, its main parameters and operation regime are presented.

CONCEPTUAL DESIGN OF THE COOLER

The electron cooler (Fig. 1) consists of three tank filled with SF6 gas under pressure of 8 at. Tanks 1 and 3 contain acceleration tube and electron gun for one of the electron beam and deceleration tube and electron collector for another one. The tank 2 houses the HV generator
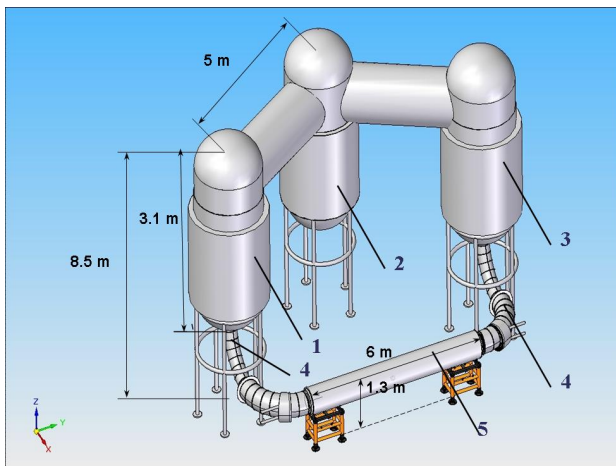
Fig.1. General view of the electron cooler. 1, 3 – tanks with electron gun and acceleration tube and deceleration tube + collector for electron beam of opposite direction, 2 – tank with HV generator, 4 – beam transportation solenoids, 5- electron cooling section.

The magnetic field is formed by a set of straight and toroidal superconducting solenoids. The solenoids

forming the magnetic field in the region of acceleration/deceleration tubes are placed outside of the tanks that resolve the problem of HV insulation.

Table 1. Cooler parameters

Electron energy, MeV	$0.5 \div 2.5$
Electron beam current , A	$0.1 \div 1,0$
Beam diameter, cm	1,0
SC solenoid magnetic field, T	$0.1 \div 0.2$
HV PS current, mA	1
Collector PS, kW	2×2
HV PS stability	1×10^{-4}
SF6 gas pressure, at	$5 \div 8$

Both acceleration and deceleration systems consist of three main subsystems (Fig. 2): acceleration vacuum tube with electron gun or collector mounted on the upper end of the tube, high pressure tank, solenoid forming longitudinal magnetic field. Acceleration vacuum tube with electron gun or collector mounted on the upper end of the tube. Electron gun design (Fig.3) has three main elements: cathode with the Pierce electrode, control (steering) electrode, anode connected with first (upper) flange of acceleration tube. Electron collector (Fig.3) consists of three elements as well: collector anode connected with upper flange of deceleration tube, suppressor ("repeller") electrode, electron collecting vessel. The last one is cooled by water circulating at high potential. The design of collector cooling system is under construction.
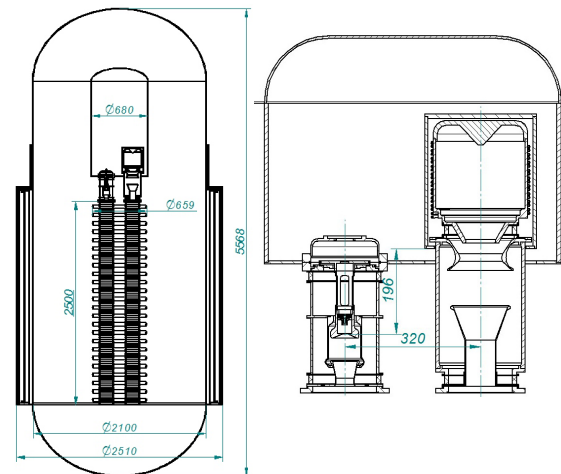
Fig.2. Acceleration and deceleration systems of two beams of opposite directions.

_____
** Joint Institute for Nuclear Research, Russia,
     Institute of Electrophysics and Radiation Technologies, Ukraine
meshkov@jinr.ru

01 Circular Colliders

Fig.3. Electron gun and electron collector design.

MAGNETIC FIELDS SIMULATION
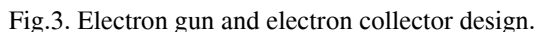
The simulation of magnetic field at the cathode and collector region of two beams of opposite directions was performed (Fig.4, Fig.5). The optimal configuration of the magnetic screen was found.

Fig.4. Magnetic field distribution at the solenoid axis in the cathode vicinity.

Fig.5.Magnetic field distribution at the solenoid axis in the collector (permanent magnet of opposite field direction is placed on the top of the collector).

HIGH VOLTAGE GENERATOR
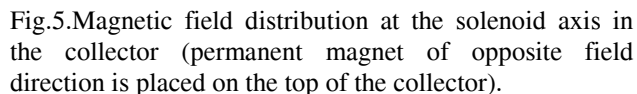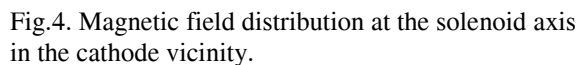
High voltage (HV) generator (Fig.6) is based on the principle of the cascade scheme. The chosen scheme has three diode column and twelve multiplying levels. At the

working frequency of 20 kHz the total number of diodes (type 2Ц106Г in Russian standard) is equal to 2500, the capacitors (type С2-29В-2 in Russian standard) is of 8316. The dimensions of the tank for generator accommodation in this case are of 6000×1200 mm.

Fig.6. The HV generator electric scheme.

CONCLUDING REMARKS

The scheme of the HV e-cooler has been chosen. Simulation of magnetic field formation in acceleration columns, electron beam formation and recuperation has been done. Design of SC magnetic system, the electron gun and collector, the system of power transmission to high potential is in progress.

REFERENCES

[1] Electron cooling of 8 GeV antiprotonsat Fermilab's Recycler: Results and operational implications, to be published in Proc. of HB2006, Tsukuba, Japan, May 29-June 2, 2006

[2] S. Nagaitsev *et al*., Phys. Rev. Lett. **96**, 044801 (2006)

01 Circular Colliders

STATUS OF THE NUCLOTRON

A. Sidorin, N. Agapov, V. Alexandrov, O. Brovko, V.Batin, A. Butenko, E.D. Donets, A. Eliseev, A.Govorov, V. Karpinsky, V. Kekelidze, H. Khodzhibagiyan, A.Kirichenko, A. Kovalenko, O. Kozlov, I. Meshkov, V. Mikhaylov, V. Monchinsky, S.Romanov, V. Shevtsov, V. Slepnev, I. Slepnev, A. Sissakian, G. Trubnikov, B.Vasilishin, V. Volkov, JINR, Dubna, Moscow Region

Abstract

The "Nuclotron-M" project started in 2007 is considered as the key point of the first stage of the NICA/MPD project. General goal of the "Nuclotron-M" project is to prepare all the systems of the Nuclotron for its long and reliable operation as a part of the NICA collider injection chain. Additionally the project realization will increase the Nuclotron ability for realization of its current experimental program. Results of the last runs of the Nuclotron operation are presented.

INTRODUCTION

The project "Nuclotron-M" is considered as a key part of the first stage of the JINR general project NICA/MPD (**N**uclotron-based **I**on **C**ollider f**A**cility and **M**ulty **P**urpose **D**etector) [1]. The extension of JINR basic facility capabilities for generation of intense heavy ion and high intensity light polarized nuclear beams, including design and construction of heavy ion collider aimed at reaching the collision energy of $\sqrt{s_{NN}} = 4 \div 11$ GeV and averaged luminosity of $1 \cdot 10^{27}$ cm^{-2}s^{-1} is necessary for realization of the NICA/MPD.

The first stage of the NICA/MPD realization includes the following tasks:

- upgrade the Nuclotron facility (the "Nuclotron-M" project);
- elaboration of the NICA technical design report;
- development of the laboratory infrastructure aimed for long term stable operation of the accelerator complex and preparation for construction of the NICA elements;
- R&D works for MPD elements.

The "Nuclotron-M" program includes all necessary works on the development of the existing Nuclotron accelerator complex [2] to the facility for generation of relativistic ion beams over atomic mass range from protons to gold and uranium ions at the energies corresponding to the maximum design magnetic field (2 T) in the lattice dipole magnets. Realization of the project will make it possible to reach new level of the beam parameters and to improve substantially reliability and efficiency of the accelerator operation, renovate or replace some part of the equipment that have been under operation since 1992-93 as well.

As an element of the NICA collider injection chain the Nuclotron has to accelerate single bunch of fully stripped heavy ions (U^{92+}, Pb^{82+} or Au^{79+}) from 0.6 to about 4.5 GeV/u. The required bunch intensity is about $1 \div 1.5 \cdot 10^9$ ions. The particle losses during acceleration have to be minimized and do not exceed 10%. The magnetic field ramp has to be ≥ 1 T/s. To demonstrate the ability of the Nuclotron complex to satisfy these requirements, the general milestones of the project are specified as an acceleration of heavy ions (at atomic number larger than 100) and stable and safety operation at 2 T of the dipole magnet field. The project has been started in 2007. During the project realization almost all the Nuclotron systems were modernized and 5 runs of the Nuclotron operation were carried out. During the last run performed from 25 of February to 25 of March 2010 the Xe ions were accelerated and the magnetic system was operated at 1.8 T. Completion of the project is scheduled for the fall of 2010.

STATUS AND MAIN PARAMETERS OF THE NUCLOTRON

The first run at the Nuclotron (the superconducting synchrotron intended to accelerate nuclei and multi charged heavy ions) was performed in March 1993. Presently the Nuclotron delivers ion beams for experiments on internal targets and for fixed target experiments using slow extraction system. Achieved energy of protons is 5.7 GeV, deuterons – 3.8 GeV/u and nucleons - 2.2 GeV/u. The maximum achieved energy is limited by the system of the energy evacuation of the Nuclotron SC magnets and power supply of the lattice magnets.

Main elements and systems of the Nuclotron facility (Fig. 1) are the following:

1. superconducting synchrotron Nuclotron, which magnetic-cryostat system of the circumference of 251,5 m is located in the tunnel surrounding the Synchrophasotron basement;
2. cryogenic supply system consisting of two helium refrigerators KGU-1600/4.5 with required infrastructure for storage and circulation of the gaseous helium, liquid helium transfer lines, tanks for the liquid nitrogen storage and nitrogen tranfer lines for thermal screens of the Nuclotron lattice magnets;
3. the injection complex consisting of HV fore-injector and Alvarez-type linac LU-20. The fore-injector voltage up to 700 kV is produced by pulsed transformer. The LU-20 accelerates the protons up to the energy of 20 MeV and ions at Z/A $\geq$ 0.33 up to the energy of 5 MeV/u. The wide range of the ion species is provided by the heavy ion source "KRION-2", duoplasmatron ion source, polarized deuteron source

POLARIS and laser ion source.

4. beam transport line from LU-20 to the Nuclotron ring including equipment for the beam injection onto the orbit;
5. system of the resonant slow extraction of the accelerated beam in the direction to main experimental hall (bld. 205);
6. transport lines for the extracted beam;
7. power supply units for the Nuclotron lattice magnets and the transport lines to the experimental facilities located in the separated building 1A (it does not shown in the Fig. 1);
8. control system, diagnostics of the beam and the accelerator complex parameters;
9. RF system for the beam acceleration in the Nuclotron;
10. radiation shielding and automatic system for the radiation measurements.
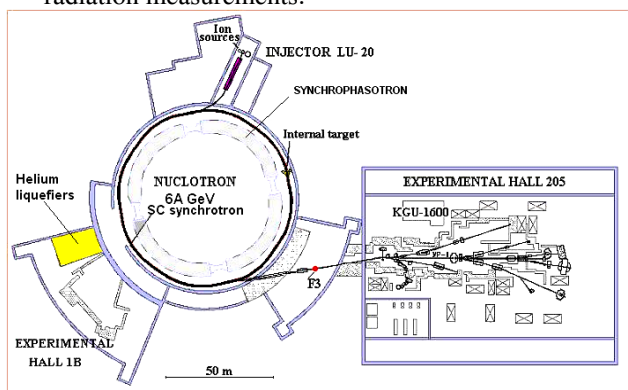
Figure 1. Schematics of the Nuclotron facility.

NUCLOTRON-M PROJECT

General goal of the project is to prepare all the existing systems of the Nuclotron for its long and reliable operation as a part of the NICA facility. Additionally the project realization will increase the Nuclotron ability for realization of its current experimental program. The project working program includes the next main tasks:

1. Development of the heavy ion source.
2. Development of the polarized deuteron source.
3. Sufficient improvement of the vacuum conditions in the Nuclotron beam pipe and linear accelerator-injector.
4. Development of the power supply system and energy evacuation system in order to reach magnetic field in dipole magnets of 1.8 - 2 T.
5. Upgrade of the Nuclotron RF system, realization of the adiabatic trapping into acceleration.
6. Development of the slow extraction system.
7. Development of the beam transfer lines and radiation shielding.
8. Beam dynamics investigations, minimizations of the particle loss at all stages of the acceleration.
9. Preparation of the KRION-2 ion source for generation of the ion beam at A > 100 and q/A > 0.33.
10. Design of new heavy ion linear injector.

04 Hadron Accelerators

Sufficient part of the first run performed after beginning of the project - #37 (November of 2007) - was devoted to the test of the status of the Nuclotron systems and machine development experiments. During this run experimental estimate of average vacuum in the Nuclotron was made based on the studies of $^2H^+$ and deuteron beam circulation at the injection energy (5 MeV/u). It was shown, the beam pipe pressure scaled to equivalent concentration of N_2 molecules at T = 300 K is measured to about p ≈ 2·10^{-8} Torr, that is not sufficient for heavy ion acceleration. To start modernization of the system for orbit position measurements and the orbit correction the existing PU stations and correctors were tested and calibrated. Preliminary test of new scheme of the structural magnet supply based on the consequent magnet connection was performed. It was demonstrated that the large inductivity sufficiently suppresses the magnetic field ripple. It leads to stable acceleration process and improve the quality of slow extracted beam.

RESULTS OF LAST RUNS

During the "Nuclotron-M" project realization four runs of the Nuclotron operation were carried out - #38 (June of 2008), #39 (June of 2009), #40 (November 2009) and #41 (March 2010). Sufficient part of them was devoted to the test of new equipment installed at the Nuclotron accelerator complex. Within this period two stages of the ring vacuum system upgrade were completed. Deep reconstruction of the cryogenic system was performed. New supply system for electrostatic septum of the slow extraction system was constructed and tested at a test bench and at the ring. New power supplies for the closed orbit corrector magnets were designed and first 4 units were tested at the ring. Partial upgrade of the ring RF system aiming to increase RF voltage and realize the adiabatic trapping into acceleration was performed. A set of works at LU-20 accelerator was performed to improve the vacuum conditions and to increase the acceleration efficiency.

In parallel with the Nuclotron modernization a good progress was achieved in design and construction of the new heavy ion and polarized light ion sources.

Upgrade of the Nuclotron ring vacuum system

The Nuclotron vacuum system consists of two sub-systems: insulation vacuum system of the cryostat and high vacuum system for the beam pipe. Insulation vacuum system satisfied to all the requirements of the accelerator operation and its serious upgrade is not necessary. Before beginning of the "Nuclotron-M" project the Nuclotron beam pipe had no effective pumping of gaseous hydrogen and helium, while gaseous helium can to penetrate into the pipe due to diffusion from insulation vacuum volume of the cryostat through non welded connection between beam extraction channel and circulating beam chamber.

Upgrade of the vacuum system was performed in two stages:

- reconstruction of a few sections of the ring and installation of new vacuum pumps and diagnostic equipment;
- creation of automatic control system for the vacuum equipment.

The first stage was realized in a general between the runs #37 and #38. Installed vacuum equipment was tested and put into operation during the run #38 and its application was resulted in improvement of the vacuum conditions by about one order of magnitude.

The automatic control system was put into operation during the runs #40 and #41 that permitted to provide experimental study of evolution of the residual gas pressure and composition during long period of the ring operation. At the moment the vacuum conditions in the beam pipe satisfies to requirements of the NICA project that was additionnaly demonstrated during the #41 run in acceleration of Xe ions.

Upgrade of the cryogenic system

Starting from August of 2008 the Nuclotron cryogenic system was deeply reconstructed. Almost all the equipment was dismounted, transferred to specialized factories, repaired and transferred back into JINR. From the February of 2009 the equipment was tested and step by step put into operation.

Heavy ion acceleration

During the run #41 the ions of $_{124}Xe^{42+}$ were accelerated up to about 1.5 GeV/u. At 1 GeV/u the slow extraction of the accelerated beam was used for a few methodical and physics experiments. To reach this goal the following works were performed during 2009 and first month of 2010:

- four stand runs (five weeks each) at multi charged heavy ion source Krion-2 have been done in order to optimize operational parameters;
- modernization of power supply system of the beam transfer line from LU-20 to the Nuclotron;
- readjustment of the LU-20 accelerating-focusing system in order to improve the acceleration efficiency;
- three runs at LU-20 dedicated to test all the systems at acceleration of deuteron, C^{+4} and heavy ion beams.

During LU-20 run performed in January – February of 2010 the following ions were obtained with Krion-2 source in the pulse of 6.7 μs of duration:

- a) $_{84}Kr^{28+}$ $3.5 \cdot 10^7$ ions per pulse,
- b) $_{84}Kr^{29+}$ $3.2 \cdot 10^7$ ions per pulse,
- c) $_{84}Kr^{30+}$ $3.0 \cdot 10^7$ ions per pulse,
- d) $_{124}Xe^{41+}$ $3.0 \cdot 10^7$ ions per pulse,
- e) $_{124}Xe^{42+}$ $3.0 \cdot 10^7$ ions per pulse,
- f) $_{124}Xe^{43+}$ $2.7 \cdot 10^7$ ions per pulse,
- g) $_{124}Xe^{44+}$ $1.5 \cdot 10^7$ ions per pulse.

The beams of $_{84}Kr^{29+}$ and $_{124}Xe^{42+}$ ions were accelerated with LU-20 up to 5 MeV/u.

The Nuclotron run #41 was started with laser ion source. All the ring systems were tested and tuned with deuteron beam initially. Thereafter initial part of the beam acceleration was optimized for acceleration of ions at charge to mass ration closed to 1/3 with C^{+4} beam. The C^{+4} beam life-time due to stripping on residual gas is not long enough to accelerate them to energy of the range of 1 GeV/u. The slow extraction system was tuned with Xe ions after change of the ion source. The Xe beam intensity during the acceleration was measured with the ionization monitor and even relative change of the intensity is complicated to estimate due to variation of the ionization cross-section. Intensity of the accelerated beam was at the sensitivity threshold therefore accurate tuning of the slow extraction was not provided. Even at these conditions the beam intensity at the exit of the ring was about a few thousands ions per pulse. Most likely the source of the ion loss during the acceleration was interaction with the residual gas. As a part of the NICA injection chain the Nuclotron will be operated for acceleration of fully striped gold ions from 600 MeV/u up to 4.5 GeV/u. During Xe ion acceleration it was demonstrated that the vacuum conditions in the Nuclotron beam pipe is sufficient for this goal.

FURTHER DEVELOPMENT

During # 41 run the magnetic system was operated at 1.8 T of the dipole magnetic field for a few hundred of cycles. It was demonstrated that after more than 15 years of the operation a degradation of the magnet properties is practically absent. The long and safe operation of the accelerator magnetic system at maximum design level of the magnetic field (2 T) is related to the following modifications of the power supply system:

- manufacturing, assembling and put into operation seven units of the new switches for energy damp from the magnets in a case of quench for both the dipoles and the quadrupoles power supply circuits;
- upgrade of the quench detection system;
- development of scheme of the Nuclotron magnet power supply.

The works are in the final stage, and beginning of the commissioning of the new power supply and quench protection systems is scheduled for the Autumn Nuclotron run in 2010. After that the Nuclotron upgrade project will be completed. The next stage of the development is connected with construction of the NICA facility elements.

REFERENCES

[1] NICA Conceptual Design Report, JINR, January 2008. http://www.jinr.ru/

[2] A.A.Smirnov, A.D.Kovalenko, "Nuclotron-superconducting accelerator of nuclei at LHE JINR (Creation, Operation, Development)" Particles and Nuclei, Letters, 2004, v.1, №6 (123), p.11-40

ACCELERATION OF DEUTERONS UP TO 23.6 GEV PER NUCLEON THROUGH I100, U1.5, AND U70 OF IHEP

S. Ivanov, on behalf of the U70 light-ion task team[#]

Institute for High Energy Physics (IHEP), Protvino, Moscow Region, 142281, Russia

Abstract

The paper reports on the recent progress en route of implementing the program of accelerating light ions in the Accelerator Complex U70 of IHEP-Protvino. The crucial milestone of guiding the deuteron beam through entire cascade of three accelerators available to a specific kinetic energy of 23.6 GeV per nucleon was accomplished in April 2010, which confirms feasibility of the project goal to diversify our main proton machine U70 to a light-ion synchrotron as well.

INTRODUCTION

The program to accelerate light ions with a charge-to-mass ratio $q/A = 0.4$–0.5 in the Accelerator complex U70 of IHEP-Protvino aims at diversification and development of our accelerator facilities. The ion mode of operation involves a sequence of Alvarez DTL I100, rapid cycled synchrotron U1.5, and the main synchrotron U70 proper.

Refs. [1, 2] reported on the first attempts of operation with a deuteron beam of a yet truncated cascade comprising I100 and U1.5. Since then, consisted efforts were continued to adapt and upgrade technological systems of the proton machines to better accommodate the ion beam. This report chronologically overviews the progress achieved since the previous conference RuPAC-2008.

RUN 2008-2

During this run, in the period of 10–12.12.08, acceleration of deuterons from 16.7 to 455 MeV per nucleon was accomplished for the second time in the U1.5 record of service (Fig. 1). Achieving this goal was hampered by improper vector adding at beam of RF voltages from 8 accelerating ferrite-loaded cavities whose start frequency is lowered from 0.747 (design value) to 0.563 MHz.
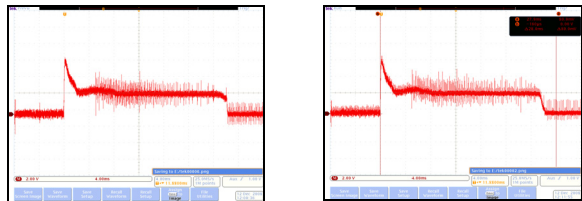
Figure 1: Deuteron beam in the U1.5 seen by a DCCT.

A bit earlier, while being in a proton mode, the U70 was trained to accept the ions. To this end, 1.32 GeV proton beam accumulation and circulation on flat-bottom was studied. The lattice magnets were powered a stand-alone

DC power supply (131.1 A, 354 G). Coasting beam circulation (with RF off) and injection of bunches populated by as small as $3 \cdot 10^{10}$ ppb (imitation of a low-intensity deuteron bunch) were tried.

Attempts to transfer a full deuteron beam to the U70 ring and get a circulation there were not successful. Still, first deuterons in the U70 were observed with scintillating screen in straight section #10 indicating beam traversal through at least 4 of 120 combined-function magnets.

RUN 2009-1

In the closing days of this run (on April 25, 2010), the first ever stable circulation of a light-ion beam (ions of deuterium) at flat-bottom values of magnetic guide field of the main synchrotron U70 was obtained.

To start with, the Alvarez DTL I100 safely accelerated deuterons to 16.7 MeV per nucleon at the 4π-mode. The gas ion source yielded 16–17 mA of pulsed current at 40 µs pulse width with chopper off, and 15 mA; 5 µs with chopper on.

Specific kinetic energy was then ramped in the U1.5 ring from 16.7 to 448.6 MeV per nucleon. Overall in-out transfer efficiency through the machine amounted to 50%. The output intensity of $4.5 \cdot 10^{10}$ dpb complies with design expectations. Beam observation over the regime is shown in Fig. 2.
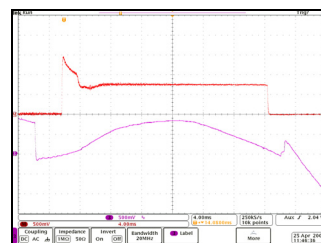
Figure 2: Ramping rate of the U1.5 guide field (lower trace) and deuteron beam intensity monitored with a DCCT (upper trace). Acceleration is accomplished in 26 ms. Compare with Fig. 1 to notice much improved performance of beam diagnostics made free of EM interferences.

Finally, the deuterons at 448.6 MeV per nucleon were transferred onto the waiting flat-bottom of the U70 ring (field 350.9 G, DC PSU current 128.4 A).

As a result, the U70 got a stable circulation of a coasting deuteron beam for about 7.5 s. This limit was imposed by an operational constraint in the existing timing system rather than by any physical reason. Momentum spread of the bunch injected is equal to $\pm 3.6 \cdot 10^{-3}$, bunch full length at base is about 100 ns, intensity is $4.5 \cdot 10^{10}$ dpb.

Estimated decay time of de-bunched beam (RF field off) is about 30–40 s.

Beam signals observed are shown in Figs. 3, 4.
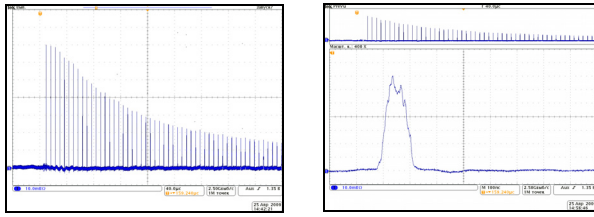
Figure 3: Circulation of a deuteron beam in the U70. (Left) AC beam current acquired by a pickup electrode. Rotation period is 6.72 μs. The same guide field would have forced lighter and faster protons rotate with 5.44 μs recurrence. The signal decays due to de-bunching given RF accelerating field switched off. Envelope of this signal bears data about beam momentum spread. (Right) First-turn shape of a deuteron bunch injected.
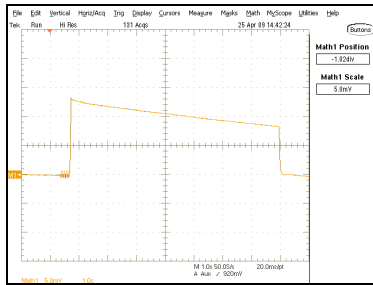
Figure 4: Deuteron beam intensity monitored with a DCCT. It dyes out much slower than beam peak current shown in Fig. 3. Scan tome base is 10 s.

RUN 2009-2

In course of maintenance activity for this run, 8 (of 40 available) ferrite-loaded RF cavities in the U70 ring were accommodated to an extended band of radiofrequency 2.6–6.1 MHz (essentially, reset to the factory default). These and only these cavities were fit to operate with the light-ion beam. To this end, they were driven to the top gap voltages feasible to compensate for a deficit in an overall number of cavities adapted.

This group of cavities had lower frequency sufficient to capture light-ion beam longitudinally at the flat-bottom guide field of the U70.

A new digital (DDS) RF master oscillator was put into service and coded to start from a lower RF of 4.46 MHz.

On taking full advantage of these hardware updates, we have continued with light-ion acceleration program during closing days of the run (December 11–15, 2010).

The injector cascade comprising ion source, Alvarez DTL I100 and transfer line to the booster ring U1.5 operated reliably, as is shown in Figs. 5, 6.

Troubles with vector summing of RF voltages in accelerating system of the U1.5 persisted. They were even aggravated by a certain misbalance of performances of a

renovated Automated Frequency Control (in 8 cavities of 8), well adapted for light-ion program, and an out-dated wide-band intermediate amplifiers (in 7 of 8) that stayed yet beyond the upgrade activity by the run in question.
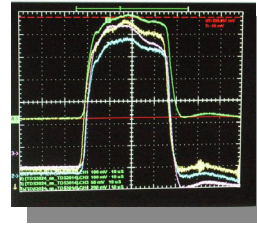
Figure 5: Deuterons in the DTL I100. Pulsed current 19 mA, pulse width 40 μs. Beam chopper is off.
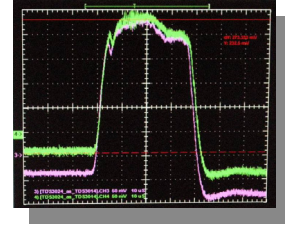
Figure 6: Beam current at entry to and exit from beam transfer line from I100 to U1.5. In-out transfer efficiency is 90% ca.

In spite of the obstacles encountered, we have managed to get circulation of both, an azimuthally uniform beam (like in run 2009-1) and capture deuterons into RF buckets to get circulation of deuteron bunches in the U70.

Then, after a smooth ramp of RF by +10 kHz in 3 s we have safely tried the fixed-field mode of acceleration of a deuteron bunch (the so called phasotron regime). This way, kinetic energy was ramped by +3.8 MeV per nucleon unless deuterons had been lost at the outer wall of the vacuum chamber (Fig. 7).

Formally, this exercise might be recorded as the first ever attempt of *acceleration of light ions* in the U70.
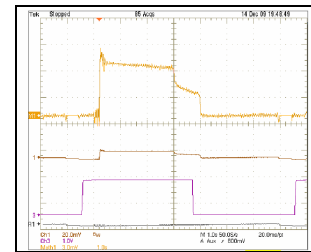
Figure 7: Acceleration of deuterons in the U70, fixed-field regime. Upper trace is beam intensity. First step down occurs when the captured beam fraction goes to outer radii and impacts horizontal aperture limitation. The surviving residual is azimuthally continuous fraction that is intercepted later on by internal beam dump target. Meander shows RF voltage amplitude program.

RUN 2010-1

This run succeeded on April 27, 2010 in the first acceleration to specific kinetic energy 23.6 GeV per nucleon of a light-ion beam (deuterons) in the main ring U70.

Booster U1.5 ramped the beam energy, as usual, from 16.7 to 448.6 MeV per nucleon. Top intensity observed amounted to $2 \cdot 10^{11}$ and $1.2 \cdot 10^{11}$ dpb at start and end of a cycle, respectively. In-out transfer efficiency improved to 60% thus exceeding that of the previous runs.

Lattice magnets of the U70 were powered via the conventional scheme, by rotor machine generators (guide

field 351–8441 G, cycle period (shortened) 7.5 s). Ultimately, the transition energy (at 8.0 GeV per nucleon) was safely crossed, and U70 accelerated deuterons to 23.6 GeV per nucleon. Maximum beam intensity observed was $7 \cdot 10^{10}$ and $5 \cdot 10^{10}$ dpb at start and end of a cycle, respectively.

The top energy of 23.6 GeV per nucleon was imposed by the particular magnet cycle inherited from a preceding regular 50 GeV proton mode of the U70. Going to the top magnetic field of 12 kG would have resulted in a deuteron beam having 34.1 GeV per nucleon which energy now seems surely attainable from the technical viewpoint.

Figs. 8, 9 and 10 present beam observations along the cascade of machines engaged.
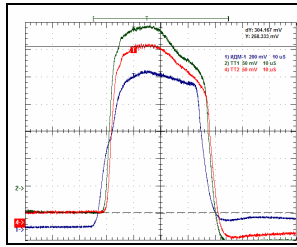
Figure 8: Acceleration of deuterons in the Alvarez DTL I100. Lower trace — beam pulse at exit from the fore injector. First and second traces from top — beam current at entry to and exit from beam transfer line I100/U1.5, respectively. In-out transfer factor is 91%. Top-pulsed current at exit from I100 amounted to 21 mA. All the pulses are 40 μs wide.
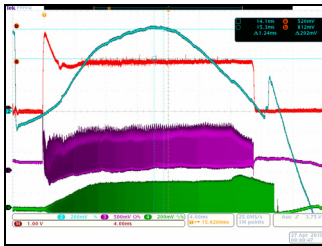
Figure 9: Acceleration of deuterons in the booster U1.5. Traces are listed from top to bottom. First (blue) signal is ramp rate of guide field. Second (red) signal is beam intensity monitored with a DCCT. It stands for $1.4 \cdot 10^{11}$ dpb at start and $8.6 \cdot 10^{10}$ dpb at end of acceleration. Third (purple) ray is a signal from pickup electrode that sees combination of longitudinal and transverse beam motions. Fourth (green) trace is envelope of the net accelerating field. Ramping time is 26 ms, cycle period is 60 ms long.
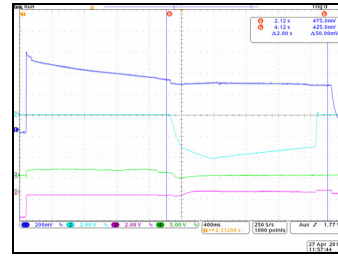
Figure 10: Acceleration of a deuteron bunch in the main ring U70. Traces are listed from top to bottom. First (blue) signal is acquired from an electrostatic pickup. It stands for $4 \cdot 10^{10}$ dpb at start and $2.5 \cdot 10^{10}$ dpb at end of acceleration. Second (cyan) trace shows ramping rate of magnetic field. Third (green) ray is a technological signal from beam radial position detector. Fourth (purple) ray is a technological signal from beam phase detector. Phase jump occurs at transition crossing (at 8 GeV per nucleon).

CONCLUSION

The important milestone of the program to accelerate beams of light ions in the Accelerator complex U70 of IHEP-Protvino was achieved in April of 2010 by accelerating deuterons to 23.6 GeV per nucleon in the U70 ring.

The main accelerator faculty of IHEP— its proton synchrotron U70 can now be substantially referred to as an ion (to be more precise, a light-ion) synchrotron as well.

Next step planned for the end of 2010, or beginning of 2011, is to accumulate and accelerate carbon ions and to put on trial a new slow extraction system delivering spills at the flat-bottom energies of the U70.

REFERENCES

[1] S. Ivanov and the U70 staff, Proc. of RUPAC-2008, Zvenigorod, 2008, p. 130–133.
[2] Yu. Antipov et al, ibid, p. 104–106.

STATUS AND PROSPECTS OF THE NOVOSIBIRSK FEL FACILITY

N.A. Vinokurov[#], E.N. Dementyev, B.A. Dovzhenko, A.A. Galt, Ya.V. Getmanov, B.A. Knyazev, E.I. Kolobanov, V.V. Kubarev, G.N. Kulipanov, L.E. Medvedev, S.V. Miginsky, L.A. Mironenko, V.K. Ovchar, B.Z. Persov, V.M. Popik, T.V. Salikova, M.A. Scheglov, S.S. Serednyakov, O.A. Shevchenko, A.N. Skrinsky, V.G. Tcheskidov, M.G. Vlasenko, P.D. Vobly, N.S. Zaigraeva, Budker INP, Novosibirsk, Russia

Abstract

Multiturn energy recovery linacs (ERL) looks very promising for making ERLs less expensive and more flexible, but have serious intrinsic problems. At this time only one multiturn ERL exists. This Novosibirsk ERL operates with two orbits and two free electron lasers now. The Novosibirsk terahertz radiation user facility provides 0.5 kW average power at 50 - 240 micron wavelength range. Different users work at six stations. Two another orbits and third free electron laser are under construction. The operation experience revealed specific problems of ERLs(especially, of multiturn ones). Some solutions were proposed recently.

THE FIRST ORBIT FEL

A source of terahertz radiation was commissioned in Novosibirsk in 2003 [1]. It is CW FEL based on an accelerator–recuperator, or an energy recovery linac (ERL). It differs from other ERL-based FELs [2, 3] in the low frequency non-superconducting RF cavities and longer wavelength operation range. The one-turn ERL (which is the first stage of the full-scale four-turn ERL) parameters are listed in Table 1, and its scheme is shown in Fig. 1.

Table 1: Parameters of the first stage of Novosibirsk ERL.

Beam energy, MeV	11
Maximum average electron current, mA	30
RF frequency, MHz	180.4
Maximum bunch repetition rate, MHz	22.5
Bunch length, ps	100
Normalized emittance, mm·mrad	30
Charge per bunch, nC	1.5
RF cavities Q factor	$4 \cdot 10^4$
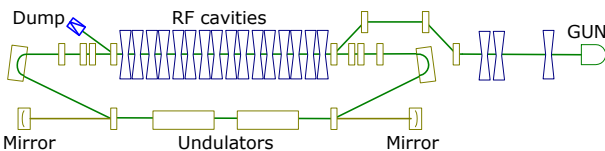
This first stage of the Novosibirsk free electron laser generates coherent radiation tunable in the range 120-240 micron as a continuous train of 40-100 ps pulses at the repetition rate of 2.8 - 22.5 MHz. Maximum average output power is 500 W, the peak power is more than 1 MW [4,5]. The minimum measured linewidth is 0.3%, which is close to the Fourier-transform limit. The third harmonics lasing was obtained recently. It was achieved by suppression of the first harmonics lasing using aperture-decreasing scrapers.

Five user stations are in operation now. Two other are in progress.

THE SECOND STAGE OF ERL AND FEL

Full-scale Novosibirsk free electron laser facility is to be based on the four-orbit 40 MeV electron accelerator-recuperator (see Fig. 2). It is to generate radiation in the range from 5 micrometer to 0.24 mm [6, 7].

Manufacturing, assembly, and commissioning of the full-scale four-turn ERL are underway. The orbit of the first stage with the terahertz FEL lies in the vertical plane. The new four turns are in the horizontal one. One FEL will be installed at the fourth orbit (40 MeV energy), and the second one is already installed and works at the bypass of the second orbit (20 MeV energy).

The bypass provides about 0.7 m lengthening of the second orbit. Therefore, when the bypass magnets are switched on, the deceleration of beam take place at the third passing through the accelerating system, and after that electrons come to the first orbit and, after the second deceleration, to the beam dump.

All 180-degree bends are achromatic. To reduce sensitivity to the power supply ripples, all magnets are connected in series. To simplify the mechanical design, all non-round (small) magnets are similar and parallel-edge. Water-cooled vacuum chambers are made from aluminium.

Figure 1: Scheme of the Novosibirsk terahertz free electron laser.

[#]vinokurov@inp.nsk.su
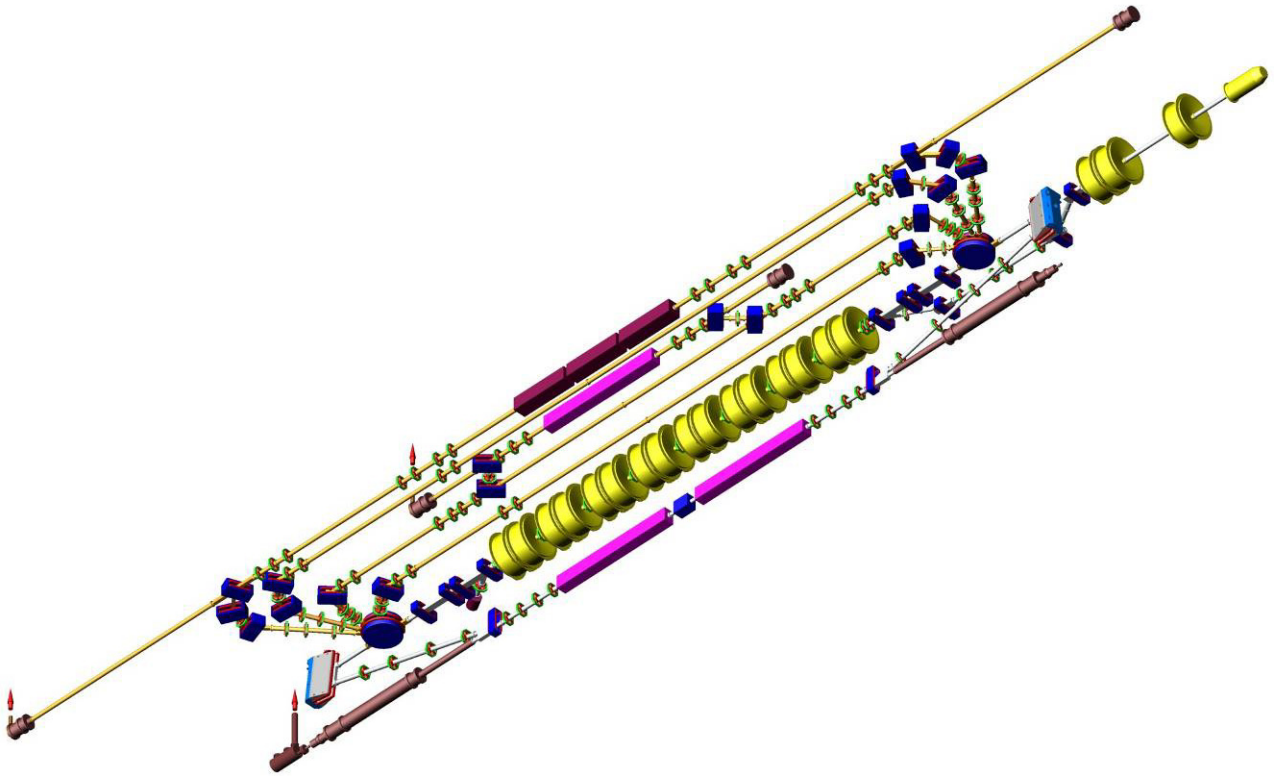
Figure 2: The full-scale Novosibirsk ERL with 3 FELs (bottom view).

The bypass magnetic system contains four bending magnets, quadrupoles, and undulator. The second orbit undulator is very similar to the old undulators of the first-orbit FEL, but its gap is lower. It is fixed-gap electromagnetic undulator. The main parameters of the undulator are listed in Table 2.

Table 2: Parameters of the second orbit undulator.

Period, mm	120
Gap, mm	70
Maximum field amplitude, T	0.12
Total length, m	3.9
Maximum bus current, kA	2.2
Maximum power consumption, kW	30

The undulator poles have the concave shape to equalize focusing in both transverse coordinates. It is necessary, as at 20 MeV this focusing is strong (matched beta function at the 0.12 T field amplitude is 1.1 m only).

The optical resonator length is 20 m (12 RF wavelengths). Therefore the bunch repetition rate for initial operation is 7.5 MHz (24th subharmonics of the RF frequency). Mirrors are made of copper, water-cooled, and covered by gold. Outcoupling holes (3 and 4 mm diameter) serve also for alignment by visible reference laser.

The location of two FELs in accelerator hall is shown in Fig.3. The first lasing of the FEL at bypass was achieved in 2009. The radiation wavelength range is 40 - 80 micron. The maximum gain was about 40%. The significant (percents) increase of beam losses took place during lasing. Therefore sextupole corrections were installed to some of quadrupoles to make the 180-degree bends second-order achromatic. It increased the energy acceptance for used electron beam.
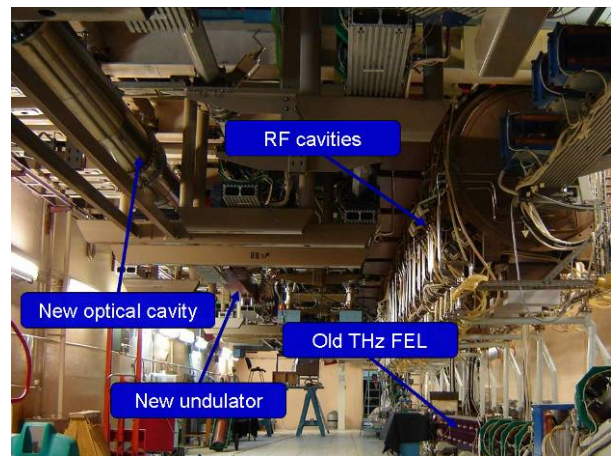
Figure 3: The location of two FELs in accelerator hall.

The beamline (Fig. 4), which delivered radiation from new FEL to existing user stations, is assembled and commissioned. The output power is about 0.5 kW at the 9 mA ERL average current. Thus, the first in the world multiturn ERL operates for the far infrared FEL.

02 Synchrotron Light Sources and FELs

Figure 4: The optical beamline which transport the radiation of the second FEL to the user stations.

THE PROSPECTS

The assembly of third and fourth orbits is in progress. The four-orbit ERL commissioning will start the next year.

REFERENCES

[1] E. A. Antokhin et al. NIM A528 (2004) p.15.

[2] G.R. Neil et al. Phys. Rev. Lett. 84 (2000), p. 662.

[3] E.J. Minehara. NIM A483 (2002) p. 8.

[4] V.P. Bolotin et al. NIM A 557 (2006) p.23.

[5] E.A.Antokhin et al., Problems of Atomic Science and Technology, p.3, №1, 2004.

[6] N.G. Gavrilov et al. IEEE J. Quantum Electron., QE-27, p. 2626, 1991.

[7] V.P.Bolotin et al. Proc. of FEL-2000, Durham, USA, p. II-37 (2000).

KURCHATOV SYNCHROTRON RADIATION SOURCE FACILITIES MODERNIZATION

M.Blokhov, V.Leonov, E.Fomin, G.Kovachev, V.Korchuganov, M.Kovalchuk, Yu.Krylov, V.Kvardakov, V.Moryakov, D.Odintsov, N. Smoliakov, S.Tomin, Yu.Tarasov, V.Ushkov, A.Valentinov, A.Vernov,Yu.Yupinov, A.Zabelin, RRC Kurchatov Institute, Moscow 123182, Russia

Abstract

Kurchatov Synchrotron Radiation Source (KSRS) operates in the range of SR from VUV up to hard X-ray. Technical modernization of KSRS systems is under way. It includes a replacement of the power supplies and the nano- and micro-second generators by the new ones, the installation of the new third RF accelerator cavity on 2.5 GeV storage ring SIBERIA-2. The projects of the feedback system for the longitudinal coherent multi-bunch instabilities dumping and of the new sensitive electronics for pick-up stations on Siberia-2 storage ring start in 2010. Three 7.5 T wiggler beam lines were mounted and tested with SR beam in December 2009. The 7.5 T (19+2) poles SC wiggler and new 3 RF cavities are doing the KSRS spectrum harder and intensive. The program tools for KSRS operation are introduced in accelerator control system with a new electronics. The new scheme of top-up energy injection placed outside of Siberia-2 storage ring tunnel is carried out. The report describes a statistics works and plans on KSRS facilities.

INTRODUCTION

The accelerator complex of KSRS consists of the linear accelerator and two storage rings [1]. Main parameters of the KSRS accelerator facilities are shown in Table 1.

Table 1: Parameters of KSRS facilities

Linac	SIBERIA-1	SIBERIA-2
E = 80 MeV	E = 80÷450 MeV	E = 0.45÷2.5 GeV
I = 0.2 A	I = 0.2÷0.3 A (singlebunch)	I = 0.1÷0.3 A (multibunch)
L = 6 m	C = 8.68 m	C = 124.13 m
DE/E = 0.005	B = 1.5 T	B = 1.7 T
ε_0=300 nm·rad	ε_{x0}=800 nm·rad	ε_{x0}=78÷100 nm·rad
T = 18 ns	T_0 = 29 ns	T_0 = 414 ns
f_{rep} = 1 Hz	T_{rep} = 25 s	τ =10÷25 hrs
	λ_c=61 Å , BMs	λ_c=1.75 Å, BMs λ_c=0.40 Å, SCW
Forinjector	Booster, VUV and soft X-ray source	Dedicated SR source 0.1-2000Å [1]

Possible number of photon beam lines from BMs equals to 24, SR sources like SC wigglers and warm wigglers (undulators) are planed to offer 6-8 SR beam lines from IR to hard X-ray radiation.

KSRS FACILITIES WORK

The work of SIBERIA-2 on experiments is carried out with use of SR from bending magnets in energy range of photons 4-40 keV and spectral flux $(10^{13}$-$10^{11})$ ph/s/mrad/0.1%BW during week runs in a round-the-clock mode. Within one week 9 working 12-hour shifts are presented.

Table 2 shows the integral time devoted for SR experimental work in 2005 - 2009 years. Fig.1 contains some statistics of the time which was spent on experiment, injection and tuning of SR source.

Table 2: SR Experimental time in 2005-2009 years

	2005	2006	2007	2008	2009
Siberia-1: experiment, hrs	238	236	205	471	634
Integral, A-hrs	16.1	21.1	13.4	41.7	67.4
Siberia-2: experiment, hrs	1292	2035	1629	1437	1527
Integral, A-hrs	94.9	165.5	126.2	56.3	77.5
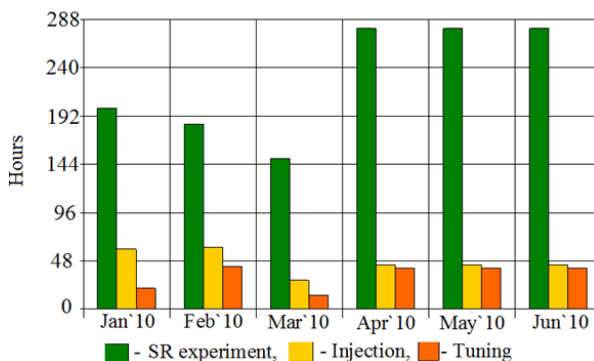
Figure 1: The Siberia-2 work in 2010.

MODERNIZATION OF 2008-2010

New septum-magnet of Siberia -1(KCSR-INP)

The new pulse septum-magnet was installed with aim to increase the effectiveness of electron beam ejection from Siberia -1 into the electron transport line - ETL-2. The new septum-magnet is the modified version of the old one that worked during previous 8 years. It has more homogeneous magnetic field distribution. The results are obtained: stable control of the pulse generator

of the septum-magnet, an increase in the coefficient of the release of electron beam from the Siberia-1 storage ring into the ETL-2 up to 70%.

New SR beamline at Siberia-1 (KCSR – NIIOFI)

SR from 3^d BM of Siberia-1 was conducted in VUV experimental hall after the completion of mechanical and vacuum works on the new beamline D3.2. First metrology experiments were made by NIIOFI and KCSR staff.

RF system of Siberia-2 upgrade

The RF system upgrade was target to increased reliability of the machine operation and to adapt Siberia-2 storage ring to operate with new high magnetic field sc wigglers. Now RF system of Siberia-2 has two channels. Each channel includes 200 kW RF generator (with two GU-101A thetrodes), a waveguide and one or two 181 MHz cavity with own feeders. Three bi-metal cavities (7 mm of stainless steel and 8 mm of copper joint together by diffusion bonding) were installed in the storage ring upon completion of the upgrade. Initially, on December 2007 one old cavity has been replaced by a section of two new cavities. Second old cavity was replaced by a single new bi-metal cavity on October 2009.

So total accelerating voltage is increased up to 1.5 (1.8 MV max). New set of parameters of the storage ring and its RF system is listed in Table 3.

Table 3. Parameters of Siberia-2 and its RF system [9].

Parameters of the Siberia-2 storage ring	Energy of electrons	E_{MAX}	GeV	2.5
	SR losses with BMs and wigglers	ΔE_{BMs} ΔE_{BM+WIG}	keV/turn	681 1021
	Beam current	$I_{B\,MAX}$	A	0.29
	Total accelerating voltage	$2U_1+U_2$	kV	1500
First RF channel : 200 kW generator, two cavities (№1, №3)	Accelerating voltage	$2U_1$	kV	820
	Shunt impedance	$2ZT^2$	MOhm	8.6
	Power dissipated in the cavities	$2P_1$	kW	39
	Power transferred to the beam	$2P_{1b}$	kW	157
Second RF channel: 200 kW generator, one cavity (№2)	Accelerating voltage	U_1	kV	680
	Shunt impedance	ZT^2	MOhm	4.3
	Power dissipated in the cavity	P_2	kW	54
	Power transferred to the beam	P_{2b}	kW	139

A new 2 feeders connected with the waveguide of RF generator №1 deliver RF power to the lateral cavities (№1 and №3). The middle cavity (№2) is fed by the RF generator №2, see Fig.2.

At the moment we observe the mutual influence of two RF generator control systems through the electron beam which leads to unstable operation of the RF generators.
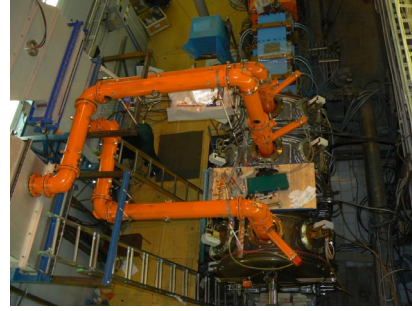
Figure 2: New cavities and feeders at SIBERIA-2 ring.

According to a simulation, the stability will grow with tuning the RF feeders and the waveguides at a wavelength of $(n+1/8)\mathtt{l}$. We plane to do it to the end of 2010.

The synchrotron oscillations collective modes appear after injection of first four or five bunches. The energy ramping of the electrons with current in many bunches exceeding 150 mA is characterized by synchrotron motion in coherent modes and possible losses of the beam part. The losses depend on the number of bunches and modulate the particles numbers in bunches correspondingly with the synchrotron mode number, see Fig.3.
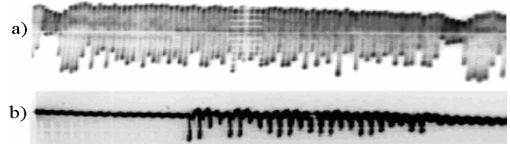
Figure 3: The modulation of bunches with different filling due to collective mode instability losses.

The decision was made to carry out "Bunch-to-bunch longitudinal feedback" to dump the coherent synchrotron oscillation. It will include a wide-band cavity as a kiker, a wide-band pick-up electrode, a phase detector, a modulator, RF control electronics, a wide-band power amplifier.

New nanosecond generator (KCSR)

The prototype of new low voltage sin-like pulse nanosecond generator with 100-200 ns semi-period was created at a base of the pseudo-spark thyratron "ТПИ1-10К/50"with the cold cathode. Maximum anode amplitude is of 25-30 kV. It was successfully tested with the electron beam. The short-circuited plates of the Siberia-2 inflector were switched on as parallel electrical loads of the new ns generator (<1.5kA, 14 kV). In result, the high temporary stability of capture of electrons was reached in the regime of injection in Siberia-2 with high efficiency (up to 70- 75%). The features of new device are low voltage, absence of spark discharge and a work only with magnetic field between the kiker plates. It will be a real alternative to high voltage existing inflector and

02 Synchrotron Light Sources and FELs

preinflector nanosecond generators of Siberia-2, which work on the electric spark dischargers.

New SR beam lines from BMs of Siberia-2

Currently under construction are 3 experimental stations and 3 SR beamlines from the 1.7.T bending magnets of Siberia-2: "PES" - Photoelectron Spectroscopy (PES, ARPES, NEXAFS) - K6.5, "PHASE"- X-Ray precision optic-2 - K2.3, "NANOFAB-2" – micro- and nano-electro-mechanical systems researches (MEMS and NEMS)- K2.6. These SR beamlines and experimental stations are producing with a firm "NT-MDT", Zelenograd.

New SC wiggler beam lines

We note the production and the consequent mounting of wiggler`s beam lines elements were effectuated according to KCSR`s drawings with the help of a firm «Megaterm», Briansk...

In the first half-year 2009 the installation of three SC wiggler`s beam lines elements was first executed inside the tunnel of Siberia-2, then they were conducted through the shielding wall and installed in the experimental hall. A specially designed 100 kW SR absorber–distributor was mounted near the ring of Siberia-2. Inside its vacuum volume it contains one stationary and three movable absorbers for each of three separate SR beam lines. Before 100 kW absorber the DU250 shatter was posed for the separation of the vacuum systems of the X-ray beam lines and Siberia-2. These works were alternated with the work on SR experiments.

In September - October 2009, the work was carried out with the opening of the vacuum chamber of Siberia-2. A new camera with three SR absorbers to limit sc wiggler`s SR divergence was installed in the triplet following 7.5T wiggler. A refinement was also made of the existing pumping unit and diagnosis (PDU), located after the first bending magnet (following the triplet). It was introduced in PDU volume two immobile and single movable absorbers to protect the DU250 shatter against SR, coming from the bending magnet. In addition, engineering equipment, visualization elements of SR and TV monitor were mounted on the beam lines.

INSERTION DEVICES

Works with 7.5Tt SC wiggler

Project SC wiggler parameters are presented in Table 4.

Table 4: Project SC wiggler parameters at 2.5 GeV

Max. field, T	3-7.5
Period, mm	164
N_{poles}	19+2
Elliptic liner, Cu. V*H, mm	13*120
$E_{ph\ crit}$, keV	31.2
Flux, ph/s/0.1%BW	10^{14}-10^{12}
Working spectrum, keV	5-200
Θx max, mrad	± 23.5

Energy loss/turn, keV	365
P_{tot} (100 mA), kW	36.5
Coils	NbTi

First run of SC wiggler was carried out on 2008, June, 7 with the 3 T magnetic field [2].

In November 2009, after the mounting of 3 wiggler beam lines was completed the vacuum conditions in Siberia-2 for the work with the electron beam were restored. The control code was debugged for new bipolar power units of wiggler and the ramping of magnetic field up to 7.5T was accomplished in the automatic regime. The measured shifts of betatron tunes have coincided with theoretical ones with good accuracy, Fig.4.
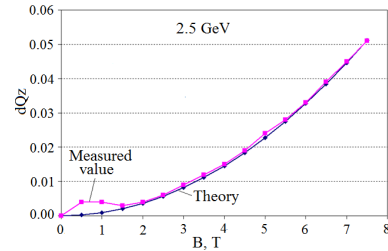
Figure 4: Measured and theoretical vertical betatron shift vs SCW magnetic field amplitude.

Hard component of SR was observed in an experimental hall with a TV camera at luminescent screens fixed on flanges, closing the ends of each of 3 tubes, Fig.5.
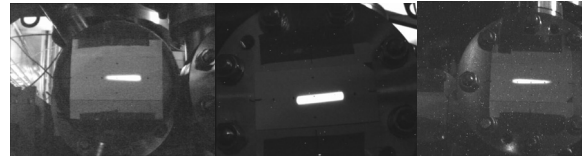
Figure 5: X-Ray beam from 7.5T SCW at output of three beam lines in the experimental hall of Siberia-2.

Measurements of position of x-ray beams relative to axes of channels and its operative adjustment have been simultaneously implemented. Besides, the card of radiation fields has been measured in an experimental hall with the deduced X-ray beams.

Unfortunately, in December 2009 the breakdown of superconductivity has occurred in the coils of the wiggler magnets at 7.5T. Under the action of resulting ponderomotive forces, the liner of wiggler - intra-vacuum thin-walled copper tube of almost elliptical cross section - collapsed, completely blocking the aperture. Therefore, the wiggler was evacuated from the ring of Siberia-2 and replaced by a spacer. In June 2010 new modified more durable liner was manufactured (BINP, Novosibirsk) and wiggler was again put on the storage ring in early July 2010.

In July-September, the vacuum chamber was degassing by means of SR. Last decade of September, after collecting the integral 2.1 A-hrs of electron current, Siberia-2 works at 2.5 GeV with 40-50 mA electron current and a lifetime of 2-4 hours. We plan to continue the work with the wiggler in October 2010.

New IDs planned at Siberia-2

The planned scheme of the insertion devices location on the Siberia - 2 storage ring is shown in Fig.6. Eight IDs are to be installed, among them 4 superconducting, 3 normal conducting wigglers and one mini-undulator. Besides that one photon line of infra-red (IR) edge radiation (ER) will be taken out [3,4]. IDs approached parameters are given in the Table 5.
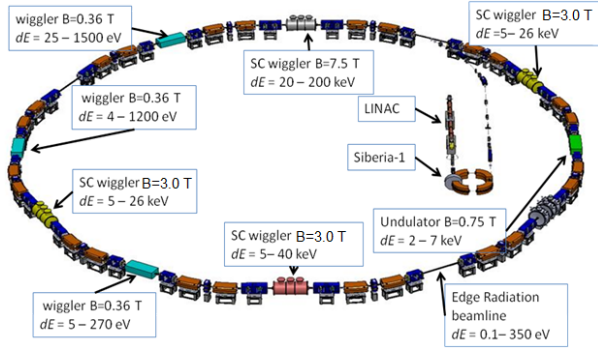
Figure 6: Plan of IDs location at Siberia-2

Table 5. Main parameters of planed insertion devices

IDs	Bmax T	λu, mm	N per	Eph	SR station, planed
1 SCW	7.5	164	10	4-200 keV	RSA, RS-MCD, Hard X-Ray
3 SCW	3.0	44	35	5-40 keV	Belok-1, Belok-2, Lengmuir-2, Standing X-Ray
3 NCW	0.36	80	51	5.5-270eV	PES microscop, PES-SH Resol., Spectro-Lumi, VUV, MR
Mini-U	0.75	7	300	2-7 keV	1.3 GeV: X-Ray holography
IR ER	-	-	-	0.1-350eV	IR, VUV, Soft-X-Ray

New experimental stations on 7.5T SCW

Now there is a progress in the creation of next 3 new experimental station based on SR from 7.5 T SC wiggler:

1. EXAFS/XANES and X-ray Magnetic Circular Dichroism (XMCD): ɋ= (13.3 ± 1) mrad, λc = 0.5 Å, P = 760 W/mrad – beam line K1.4.2;

2. Hard X-ray: λc=0.4Å, P=940 W/mrad, ɋ= (0 ± 1) mrad – beam line K1.4.3;

3. X-ray structure analysis-RSA: ɋ=(-17 ± 1) mrad, λc=0.58 Å, P = 650 W/mrad – beam line K1.4.4.

Here the SR power data correspond to 100 mA current and 2.5 GeV energy of the electron.

IMPROVEMENT OF BEAM PARAMETERS

Ultimate goal of improvements of parameters of electron and photon beams is the increase of brightness, spatial and time stability of SR source.

Diagnostics and control system [5]

- A new electronics and computer control codes were run at Siberia - 1 and Siberia – 2 for betatron tunes measurement. The betatron spectra are measured and demonstrated on operator monitor with high precision.

- A new NMR probe with auxiliary electronics and control code was installed in the calibration bending magnet of Siberia-2. New electronics serve as a part of feedback system of electron energy stabilization scheme.

- A new electronic devices (crate controllers K167), computer control codes (miniMODUL167 processor and ARTX-166 real time OS) and operator interface were elaborated and run. On the base of CC K167 and managing server of class Pentium IV several application were improved: the measuring of an electron current value in Siberia-1 and a transverse beam position in the electron transport line ETL-2 became rather simple and reliable; the modernization of synchronization system and control system of the pulse power supplies of accelerator complex were realized; new control system of Siberia–2 RF generators is developed and successfully introduced; management of power supplies of the quads and steering magnets of Siberia – 2; new operational control software and the experimental data archives in on-line mode are started in routine work.

An increasing of electron life time at Siberia-2

The lifetime at injection energy of 450 MeV is much less - not more than 30 min in single-bunch mode with a typical current in one bunch 3 - 4 mA. It is mainly determined by Touschek effect in the presence of limiting the horizontal aperture. According life time studies we have found that the most accessible method to increase the lifetime was the control of betatron oscillations coupling at low energy.

The betatron coupling was adjusted by two families of skew-quadrupole. As a result, at the injection energy an increase of lifetime was reached from 30% to 40% depending on the number of particles in one bunch. As a consequence the storage rate of electrons was increased also. Besides that, the lifetime was increased in process of the energy ramping, thus reducing the loss of current during the ramping process from 5 - 6% to 1.5 - 2% .

The lifetime of the electron beam at 2.5 GeV in Siberia-2 storage ring is determined by the vacuum conditions and is now more than 15 hrs at a current of 100 mA.

Beam lifetime $\tau(t)$ at 2.5 GeV depends on time t as follows: $\tau(t)^{-1} = \tau_0^{-1} + C \cdot I(t)$, where $I(t)$ - electron current, τ_0 - lifetime when the current approaches to zero, C - constant, τ_0 is determined by the level of vacuum in absence of the beam. The second term can be determined by the effect of Touschek or by a gas desorption stimulated by SR from the walls of the vacuum chamber. In our case, the second mechanism is running, since the values τ_0 and C depend on the collected current integral at 2.5 GeV (see Fig.7).

02 Synchrotron Light Sources and FELs

Let's note, that after closing the vacuum chamber, for the achievement of life time of 12 hours at the 100 мА electron current it was required to collect an integrated doze of 16 A*hrs, that is 10 times less, than it was required at the very beginning of SIBERIA-2 work with electron beam.
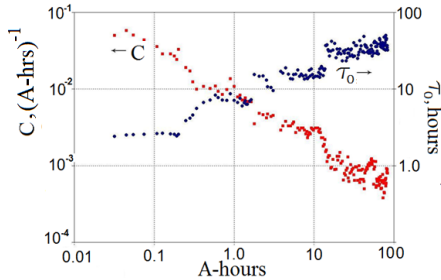
Figure 7: Parameters of τ_0(in blue) and C(in red) vs collected integral of electron current at 2.5 GeV.

MODERNIZATION OF SR SOURCE

Top-up energy injection with synchrotron [7]

In KCSR the Project of technical upgrade of accelerator complex as SR source was developed [6]. The purpose of the Project is to create SR source of 2.5÷3 generations on the base of existing accelerator complex. This will increase the spectral brightness more than in 30÷100 times in comparison with the realized project. To reach this aim means to develop the new optical structures for SIBERIA-2 with small natural horizontal emittance 6÷18 nm-rad at the electron energy 1.3 GeV and 2.5 GeV accordingly.

An achievement of the purposes means a radical improvement of an injection part of a SR complex. According to the Project, injection in Siberia - 2 will be made from a booster synchrotron (BS) with rather small natural emittance. The parameters of BS-1 and BS-2 are given in the Table 6.

Table 6: Calculated parameters of Booster Synchrotrons

Parameter	BS-1	BS-2
Injection energy, MeV	80-160	80-160
Extraction energy, GeV	2.5	2.5
Circumference, m	110.9	56.27
Cycling frequency, Hz	1	1
Emittance nm·rad	52.6	90.1
Momentum compaction	0.0107	0.032
Betatron tunes: Qx/Qy	6.83 / 4.57	5.186/2.352
Chromaticity: $\xi x/\xi y$	−14.12/−8.89	-8.85/-4.45
R.m.s. energy spread	9×10^{-4}	1.95×10^{-3}
Energy loss per turn, keV	622	622
Damping times: τ_x, τ_y, τ_s , ms	3.08, 2.97, 1.46	0.59/1.52/3.49
Beam current, mA	10	10
RF frequency, MHz	181.13	181.13
Harmonic number	67	34

BS will ramp the energy from 0.08 (0.16) GeV till 2.5 GeV with repetition rate of 1 Hz. BS will support the constant level of electron current in SIBERIA-2 and SR

for the users (an "infinite beam life time"). Now there are two schemes (BS-1 and BS-2) of the BS location relative to Siberia-2 storage ring.

In Fig.8 the modernized complex is shown. Left: an external ring - Siberia-2, an internal ring - BS-1 is in the same tunnel, the linac with a projected magnetic mirror, the small ring - a SR source Siberia -1. Right: BS-2 is outside of tunnel of Siberia-2, Siberia-1 is dismounted.
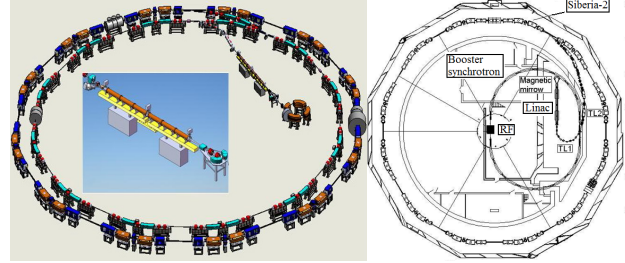
Figure 8: Two schemes of top-up energy injection.

Existing linear accelerator [8] will continue to work as injector for SIBERIA - 1 with electron energy 80 MeV. Besides, linac with a magnetic mirrow will work as injector for BS-1 or BS-2 with doubled up to 160 MeV electron energy.

CONCLUSION

We hope that the scientific and technical decisions offered in the current modernization process will provide for a scientific attractiveness and competitiveness of SR source in Russian Research Center "Kurchatov Institute".

REFERENCES

[1] V. Anashin et al., Nucl. Instr. Meth., A282 (1989), p. 369-374.

[2] V.Korchuganov,…,N.Mezentsev at al., "First Results of Siberia-2 storage ring operation with 7.5 T superconducting wiggler", RUPAC2008.

[3] A. Anoshin, E.Fomin, V.Korchuganov, S.Tomin, "Possibility to reach the diffraction limited X-ray source in Kurchatov Center of SR", RUPAC2008.

[4] V.Korchuganov, N.Smolyakov, N.Svechnikov, S.Tomin, "Radiation sources at Siberia-2 storage ring", RUPAC2010.

[5] E.Kaportsev at al., , "The expanded program tools for KSRS operation with archivation of data", RUPAC2010.

[6] V. Korchuganov at al., Nucl. Instr. Meth., A543 (2005), p.14 -18.

[7] A.Anoshin, E. Fomin, V. Korchuganov at al., "A new injection system for KSSR", RUPAC2008.

[8] A.Anoshin, E.Fomin, V.Korchuganov, S.Tomin, "Electron beam dynamics in the linac of Kurchatov source of SR with energy doubling", RUPAC2008.

[9] Proc. of the 8th EPAC, 3-7 June, 2002, Paris, p.2169-2171.

[10] V.Korchuganov, Yu.Krylov, A.Valentinov, Yu.Yupinov, "An increasing of electron beam lifetime at injection energy in SIBERIA-2 storage ring by regulating betatron coupling", RUPAC2010

RADIATION SOURCES AT SIBERIA-2 STORAGE RING

V.N. Korchuganov, N.V. Smolyakov, N.Yu. Svechnikov, S.I. Tomin,
RRC Kurchatov Institute, Moscow 123182, Russia

Abstract

In this report, two projects of radiation sources at Siberia-2 storage ring are considered. The first one is in-vacuum short period mini-undulator, which is intended for generation of bright X-ray beams. It is shown the feasibility of diffraction-limited in vertical direction X-ray source, which is to say that vertical emittance of the electron beam is equal to diffraction emittance of generated by undulator 2 KeV photon beam.

The second source will utilize edge radiation, which is generated in the fringe fields of the bending magnets. Numerical simulations show that the edge radiation is more intensive in infrared – ultraviolet spectral range as compared with standard synchrotron radiation (SR) from regular part of the same bending magnet.

INTRODUCTION

The magnetic system of Siberia-2 storage ring (electron beam energy of 2.5 GeV) consists of six mirror-symmetrical cells, each containing an achromatic bend and a gap with a zero dispersion function, see Fig.1 [1, 2]. The distance between the down- and upstream edges of the bending magnets is 5340 mm. The portion of straight section, suitable for insertion device loading, is about 3 m in length. The Siberia-2 lattice is so designed that the different requirements for wigglers and undulators are satisfied. So, the straight sections with small values of betatron functions, where electron beam has minimum sizes, provide optimum performance for wigglers, while the straight sections with large betatron functions, where the electron beam has small angular divergences, are optimum for undulators.

Now at Siberia-2 storage ring SR is mainly in use. Its flux is of the order of 10^{11}-10^{13} phot/s/mrad/(BW=0.1%) in 4 – 40 KeV spectral range. One superconducting wiggler with 7.5 T magnetic field amplitude is also installed. At the same time nearly all straight sections are planed to complete with different insertion devices in the nearest future, see Fig.1 and Table 1.
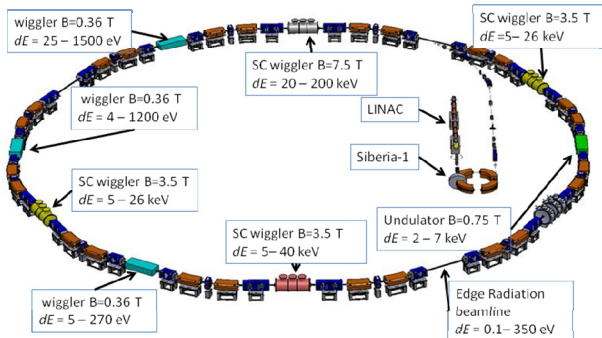
Fig.1 Siberia-2 layout with projected insertion devices.

#smolyakovnv@mail.ru

Table 1. Main parameters of insertion devices

	B_{max} T	λ_u, mm	Number of periods	Spectral range KeV
s/c wiggler	7.5	164	10	20-200
s/c wiggler	3	44	35	5-40
wiggler	0.36	80	51	5.5-270 eV
undulator	0.75	7	300	2-7
edge radiation	-	-	-	0.1-350 eV

UNDULATOR RADIATION

The most important feature of undulator radiation beam is its brilliance, which is mainly determined by the electron beam emittances and radiation diffraction phase volume, which is equel to $\lambda/4\pi$, where λ is radiation wavelength. A light source is called diffraction - limited if the electron beam emittance is smaller than that of the photon beam.

Nowadays a natural horizontal emittance of electron beam in Siberia-2 at 2.5 GeV is equal to 98 nm·rad [1]. Operating parameters of storage ring are listed in the Table 2. In addition to existing optical lattice new more brilliant lattice with horizontal emittance 18 nm·rad (at 2.5 GeV energy) has been developed (Table 2), The new lattice allows to obtain the horizontal emittance of 4.9 nm·rad at 1.3 GeV. Vertical emittance of electron beam is 49 pm·rad with a coupling factor of betatron oscillation k≈0.01 for Siberia-2. Thus, vertical emittance is equal to emittance of 2 keV photons. It is important to note that the new brilliant lattice can be obtained by changing of currents in lattice magnetic elements only.

Table 2: Siberia-2 Storage Ring Parameters

Lattice	"standard"	"brilliance"
Energy	2.5 GeV	1.3 GeV
Emittance	98 nm·rad	4.9 nm·rad
Beam size: σ_x/ σ_y	1500/78	363/17
Circumference	124.128 m	
Coupling	0.01	
Momentum compaction	0.0103	4.2×10^{-3}
Betatron tunes: Q_x/Q_y	7.775/6.695	9.707/5.622
R.m.s. energy spread	9.5×10^{-4}	5×10^{-4}
Damping times: τ_x, τ_y, τ_s	3.2; 3;1.5 ms	22;22;11 ms
Beam current	100-300 mA	

For generation of 2 KeV photons by 1.3 GeV electron beam, undulator should match rigid requirements, see Table 3. Undulator has very short 7 mm period and high peak field 0.75 T. Last years technology for undulators was greatly advanced [3, 4, 5]. It gives us a hope that production of the undulator with such record parameters will be possible.

Table 3: Main parameters of the undulator.

Gap	2.2 mm
Permanent magnet material	NdFeB
Residual field, $\mu_0 H_c$	1.2 T
Undulator period, λ_u	7 mm
Poles width, w	50 mm
Field amplitude, B_0	0.75 T
Undulator parameter, K	0.492
Number of periods	300
Undulator length, L_{ID}	2.1 m
Wavelength of fundamental, λ_1, Photon energy of fundamental, ε_1	6.06 Å 2.045 KeV

A set of computer codes SMELRAD [6] has been used for undulator radiation simulation. Flux density distributions of fundamental harmonic in horizontal and vertical directions are shown in Fig. 2. Three cases were considered: 1) electron beam with zero horizontal and vertical emittances: $\varepsilon_x = \varepsilon_z = 0$; 2) $\varepsilon_x = 4.9$ nm·rad, $\varepsilon_z = 49$ pm·rad; 2) $\varepsilon_x = 4.9$ nm·rad, $\varepsilon_z = 4.9$ pm·rad. One can see that electron beam emittance essentially influence on radiation angular distribution. At the same time a tenfold decrease of electron beam emittance in vertical direction from $\varepsilon_z = 49$ pm·rad to $\varepsilon_z = 4.9$ pm·rad does not change notably the radiation distributions. Thus we can conclude that in vertical plane the diffraction limit is achieved.
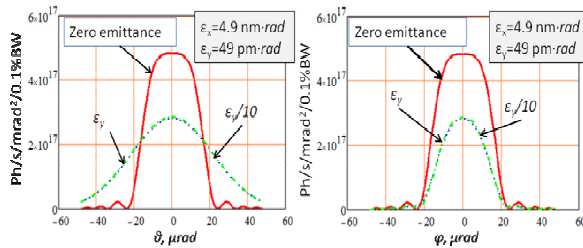
Fig.2. Horizontal (left) and vertical (right) angular distribution of fundamental harmonic.

EDGE RADIATION

The pole of each bending magnet is divided into two parts: the long one with the main field $B = 1.7$ T (bending radii of 490.54 cm) and a shorter one with a quarter field $B/4 = 0.425$ T. The shorter part of the magnetic pole with quarter field adjoins to the long straight section. The measured field of the bending magnets is shown in Fig. 3.
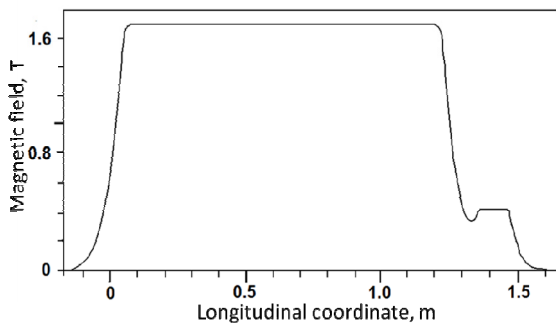
Electromagnetic edge radiation (ER) is produced by a relativistic charged particle in its passage through the fringe fields at the bending magnet edges. In long-wavelength spectral range (at radiation wavelengths much longer than synchrotron radiation critical wavelength) its intensity is much higher than corresponding intensity of synchrotron radiation from uniform magnetic field of the same bending magnet [7, 8, 9]. Measurements of long-wave ER [10, 11] strengthened the belief that electron beam ER can be used as a bright source of electromagnetic radiation in the infrared - vacuum ultraviolet spectral range. Several infrared beam lines utilizing ER are now in operation [12, 13, 14].

The photons emitted at two adjacent bending magnets bounding a straight section, appear in the same narrow cone and are subsequently synchronized by the electron itself. This leads to the interference of ER. The interference manifests itself as additional oscillations in the radiation intensity distribution [15, 16, 17].

The distance between the down- and upstream edges of the bending magnets is 5340 mm. Synchrotron radiation with 7.2 keV critical energy from the homogeneous 1.7 T field is extracted by 10x10 mrad^2 beam lines. The radiation distributions were calculated at the following beam parameters [1]: 100 mA beam current, $\sigma_x = 0.72$ mm, $\sigma_{x'} = 0.11$ mrad, $\sigma_z = 0.014$ mm, $\sigma_{z'} = 0.056$ mrad. Since $0°$ port has a mask with entrance aperture 44 mm hor. $\times$ 16 mm vert. which is installed at 1580 mm downstream from the straight section, ER distributions were calculated in the plane of this mask. The numerical evaluations are carried out with the package of computer codes SMELRAD (SiMulation of ELectromagnetic RADiation) [6]. Simulations include so-called "velocity term" and near-field effects. The program computes step by step the electron's trajectory in the given magnetic field, which should be prescribed in the input file with the magnetic field data. It makes possible to use experimentally measured data. Electron beam emittance effects are calculated via numerical convolution.

Fig.3. Magnetic field of Siberia-2 bending magnet
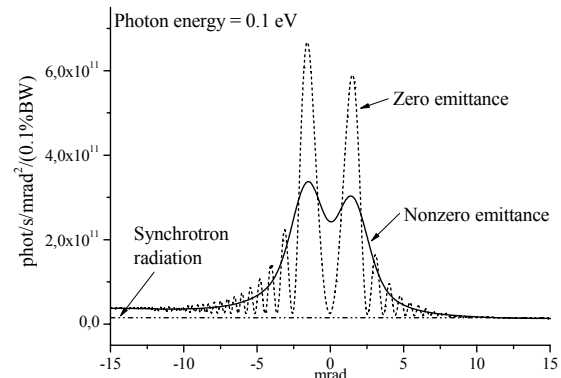
Fig. 4. Horizontal distributions of ER in the median plane.

02 Synchrotron Light Sources and FELs

Figure 4 displays the computed flux density in the Siberia-2 electron orbit plane 1580 mm downstream of a straight section. The flux density with 0.1 eV photon energy is plotted versus horizontal angle. The calculations were carried out for the electron beam with zero and nonzero electron beam emittance. One can readily see that the nonzero emittance effects smooth out the fine interference oscillations. The distributions are substantially asymmetric about the straight section axis because of the relatively short distance from the screen to the straight section. The radiation distribution tends to the correspondent SR intensity as the distance from the straight section axis in the median plane increases.
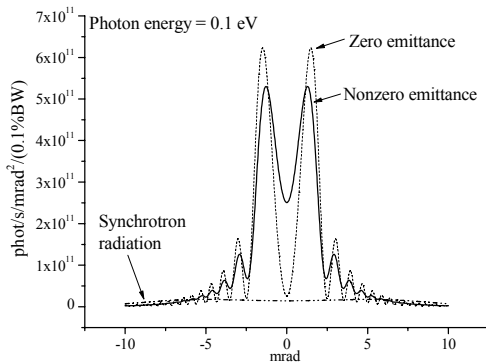
Fig. 5. Vertical distributions of edge radiation.

The vertical cross sections of 0.1 eV ER distributions along straight section axis (with zero horizontal angle) is shown in Fig. 5. For comparison the correspondent distribution of synchrotron radiation from 1.7 T bending field is also plotted in the same figure. It is easy to see from Figs. 4 and 5 that ER is much brighter than synchrotron radiation in long wavelength spectral range.

In Fig. 6, the ER and synchrotron radiation fluxes into 10×10 mrad^2 solid angle centered on the straight section axis are shown. From this figure we notice that for a given aperture the flux of edge radiation far exceeds the synchrotron radiation flux for the photon energies less than 350 eV.
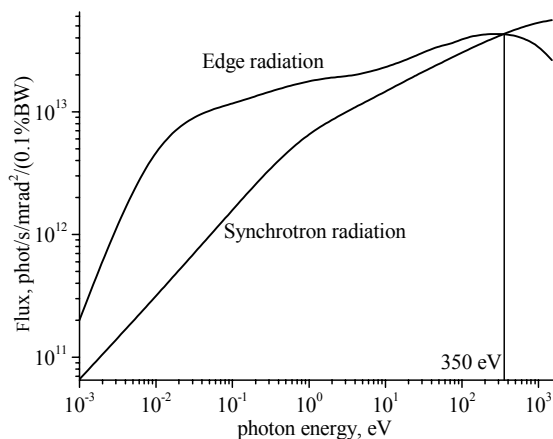
Fig. 5. ER and SR fluxes into 10×10 mrad^2 solid angle.

It is worthy of note that application of ER considerably reduces thermal and radioactive load on beam line elements. Indeed, the generation of hard X-rays is suppressed along the straight section because the magnetic field is depressed at fringe regions. The total power generated in 1.7 Tesla bending field by the 100 mA electron beam into 10×10 mrad^2 solid angle is equal to 113 W. At the same time the total power generated by this electron beam along straight section axis into 28×10 mrad^2 (entrance aperture of mask) is equal to 18 W only.

REFERENCES

[1] V.V. Anashin, A.G. Valentinov, V.G. Veshcherevich et al., Nucl. Instr. and Meth. **A282** (1989) 369.

[2] Korchuganov V., Blokhov M., Kovalchuk M. et al., Nucl. Instr. Meth. **A543** (2005) 14.

[3] Rakowsky G., Aspenleiter J.J., Graves W.S. et al. Proceedings of 1997 Particle Accelerator Conference. 1997. V. 3. P. 3497.

[4] Sasaki S. Proceedings of 2005 Particle Accelerator Conference. 2005. P. 982.

[5] Kim D.E., Park K.H., Oh J.S. et al. Proceedings of 2007 Asian Particle Accelerator Conference. 2007. P. 190.

[6] Smolyakov N.V. Nucl. Instr. and Meth. **A467-468** (2001) 210.

[7] E.G. Bessonov, Sov. Phys. JETP **53** (1981) 433.

[8] O.V. Chubar, N.V. Smolyakov, J. Optics (Paris) **24**, No. 3 (1993) 117.

[9] O.V. Chubar, N.V. Smolyakov, Proc. of the 1993 IEEE PAC Conf., Washington (1993) 1626.

[10] Shirasawa K., Smolyakov N.V., Hiraya A., Muneyoshi T. Nucl. Instr. and Meth. **B199** (2003) 526.

[11] Smolyakov N.V., Hiraya A. Nucl. Instr. and Meth. **A543 (**2005) 51.

[12] Y.-L. Mathis, P. Roy, B. Tremblay et al., Phys. Rev. Letters **80** (1998) 1220.

[13] T.E. May, R.A. Bosch and R.L. Julian, Proc. of the 1999 PAC Conf., New York (1999) 2394.

[14] R.A. Bosch, R.L. Julian, R.W.C. Hansen et al., Proc. of the 2003 PAC Conf., Portland (2003) 929.

[15] M.M. Nikitin, A.F. Medvedyev, M.B. Moiseev, Sov. Tech. Phys. Lett. **5** (1979) 347.

[16] M.M. Nikitin, A.F. Medvedyev, M.B. Moiseev, V.Ya. Epp, Sov. Phys. JETP **52** (1980) 388.

[17] M.M. Nikitin, A.F. Medvedyev, M.B. Moiseev, IEEE Trans. Nucl. Sci. **NS-28** (1981) 3130.

REVIEW OF THE DIAMOND LIGHT SOURCE TIMING SYSTEM

Y. Chernousko, P. Hamadyk, M. T. Heron, Diamond Light Source Ltd, United Kingdom

Abstract

The Diamond Light Source timing system utilises a central event generator with distributed event receivers at the equipment being controlled for all accelerator and beamline subsystems. This provides distributed fiducials with resolution of 8 nsec and stability of 8 psec. It is based on commercial hardware from Micro-Research, Finland.

This paper describes the installed timing system and summarizes 5 years' operational experience of the system. It describes the hardware and software and the distributing network, and the achieved precision and stability of the system. Developments in the timing system to support additional operational functionality of Diamond, including top-up operation, are also discussed.

INTRODUCTION

Diamond Light Source is a 3 GeV third-generation light source with a 561 m storage ring (SR), a full-energy booster and a 100 MeV pre-injector Linac [1]. The photon output is optimised for high brightness from undulators and high flux from multi-pole wigglers. The current state includes 19 photon beamlines operational, with a further three beamlines in design and construction.

The Diamond timing system is based on commercial hardware from Micro-Research Finland Oy [2] and provides an integrated timing system across the three accelerators and the photon beamlines.

DIAMOND TIMING SYSTEM STRUCTURE

The Diamond timing system is based on a central event generator (EVG) which generates events from an internal sequencer and external sources. These events are distributed over fibre optic links to multiple event receivers (EVRs) [3]. The EVRs, which are located in the control system interface layer, decode the events as hardware triggers or software interrupts. Hardware triggers are connected directly to the equipment using copper or fibre optic connections or through a four-channel timer when greater timing resolution is required. For the Linac, the decoded events are further encoded by a gun transmitter and sent over a fibre link to the gun high voltage platform. The external event sources include astronomical time derived from GPS through a Symmetricom, XLi - Time & Frequency System and a 10 MHz clock from a rubidium generator, a 50 Hz trigger and a post-mortem trigger when the beam is lost. The event clock is derived from the 500 MHz master oscillator, so that it is locked to changes in the RF frequency. The structure is shown in Fig 1.

HARDWARE

Event Generator

The EVG issues event frames consisting of an 8-bit event code and an 8-bit distributed data bus, at a rate of 125 MEvents/sec. Events can originate from several sources which are: eight external trigger events, a sequence RAM, software events and events received from an upstream event generator. Events from different sources have different priorities which are resolved in a priority encoder. A block of RAM is used to store a sequence of events. The Booster revolution clock is used to count through the sequence memory, thereby transmitting events with a time resolution of ~500nsec The 8-bit distributed data bus signals are sampled simultaneously at the event clock rate and distributed to the event receivers. The EVG is realised as a VME module.

Event Receiver

The EVR recovers the event clock signal from the event stream and splits the event frame into the 8-bit event code and the 8-bit distributed data bus. The decoded events are mapped through RAM on to: four delayed pulse outputs, with programmable delay and width (16-bit pre-scaler from the event clock, 32-bit delay and a 32-bit width register), 14 pulse outputs with programmable delay and width (32-bit delay and 16-bit width) or seven set/reset flip-flop outputs. The processed events can produce hardware outputs or software interrupts and are time-stamped with a resolution of 1 µs. The hardware outputs are routed to connectors of the rear transition board, but any of them may also be multiplexed on to the front panel connectors. The EVRs are realised as both VME and PMC modules.

Linac Gun Driver

The Linac gun driver consists of two channels, providing single- and multi-bunch injection respectively, by driving separate gun triggers. It is realised as a gun transmitter in the Linac timing crate and a gun receiver which is placed on the gun HV platform. The gun transmitter accepts trigger signals from an EVR system, delays them with a resolution of 2 ns and generates modulated optical signals which are sent to the gun receiver, where they are decoded for driving the gun. A fine programmable delay is also available and allows adjustment of the triggering position with a resolution of 10 ps over a range of 10 ns.
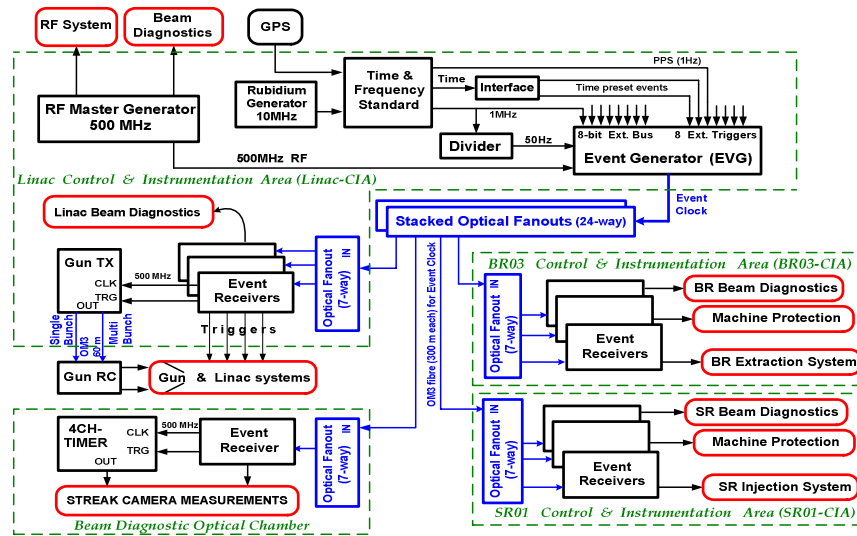
Figure 1: Structure of the Diamond Timing System

Four-channel Timer

The four-channel timer provides four independent timer channels with programmable delay and pulse width. The timer channels may be triggered individually, through a common input by PECL signals from the front panel or through a rear transition board by TTL levels. The delay and pulse width for each channel may be adjusted in a range of 8.5 sec with a resolution of 2 ns (one RF clock cycle). Further delay adjustment over a period of 10 ns with resolution of 10 ps is also provided.

Distribution

The timing distribution network delivers the event stream using OM3 multi-mode fibre. The network is structured as a two-level multi-star topology using 24 and 7 way fan-out modules. Simultaneous delivery of event messages to multiple EVRs is arranged by using fibres of equal lengths, 320m +/-0.2 m.

SOFTWARE

The timing system integrates into the EPICS based control system [4] through a number of EPICS records. The EG record configures and defines the options of a specific EVG module. These include choice of the EVG operating mode, selection of internally generated clock rates, optional transmission of software-invoked events and enable of event trigger inputs. The EGEVENT record is used to specify a single event to be placed into the sequence RAM. The ER record configures the options for the EVR, such as pulse delay, width and polarity, front panel output assignments and distributed bus enable. The EREVENT record specifies the desired actions to be performed upon receipt of a specific event code. Applications to control the timing system are built with the usual EPICS tools for databases and EDM for display panels.

Functionality to provide standard fill patterns is realised in the EPICS IOC for the EVG. This provides support for:

single bunch single shot, multi-bunch single shot, single bunch fill, multi-bunch fill, period single bunch fill, arc fill and spread fill of the SR. In all of the "fill" cases the SR is filled to a predetermined charge.

EVENT GENERATION

The Diamond SR has 936 buckets and a revolution frequency of 533.8 kHz, and the booster 264 buckets and a revolution frequency of 1892.6 kHz. The coincidence of the SR and booster revolution determines a frequency for the coincidence clock of 48.529 kHz, based on the common factors of the two frequencies. The booster clock is used for counting through the EVG sequence RAM, and the coincidence clock is used to reset to the start of the sequence, thereby locking the cycles of all accelerators. Event entries are placed in the sequence RAM to generate the necessary sequence of triggers to accelerate the electrons through the Linac and booster into the SR, as shown in Table 1. Supplementary events are produced to provide control of the diagnostics in each of the accelerators and the transfer lines, gating signals during topup, and beam loss post mortem.

Events	Time/µs	Description
T-ZERO	0	Booster cycle trigger
BR-HW-TRG	44999.8	BR Magnets trigger
LINAC-PRE	49949.6	Linac Gun pre-trigger
BR-PRE-INJ	49950.1	BR Injection trigger
LINAC-HBT	49950.6	Linac Systems trigger
BR-INJ	58312.1	Booster injection
SR-INJ-SEPT	148973.8	SR Septum
SR-PRE-INJ	148999.6	SR Kickers
BR-PRE-EXTR	149000.7	Booster pre-extraction

Table 1: Events used to accelerate electrons

OPERATIONAL EXPERIENCE

The Diamond timing system has demonstrated a relatively high level of reliability. In all cases, the failures

06 Instrumentation, Controls, Feedback and Operational Aspects

that have occurred have not led to the loss of stored beam in the SR. These failures have been associated with non-optimal driving current of optical transmitters in EVR transition modules, defective transceivers in fan-out modules and connection loss in optical fibres. In two cases individual EVRs lost their functionality and "refused" to process incoming events. Their functionality was restored after reflashing the Xilinx FPGA.

PERFORMANCE

The main performance measure of the installed system is the stability (jitter) of the decoded event with respect to the RF clock, which is 8.0 ps for the VME EVRs and 22.0 ps for the PMC EVRs [5]. The differential error of decoded events between EVRs is +/-1 ns; this is defined by lengths of fibres in distribution network. The seasonal stability (drift) is within 25-30 ps, and the drift over a 24 hour period does not exceed 10 ps. In both cases the dominant factor is the temperature stability in the experimental hall.

DEVELOPMENTS

The major development that has taken place on the Diamond timing system has been changes to support the operation of the accelerators in top-up operation, which commenced in October 2008[6]. Top-up involves injecting charge into the SR on a periodic basis, every few minutes, with photon shutters open, to maintain the fill pattern, constant current, higher overall current, constant heat load on components and hence better stability of the photon beam. The changes were: the addition of a new mode to control the EVG, the separation of triggers for the SR kickers and septum to different events, the addition of a 4 hour periodic event and the provision of new events to the photon beamlines.

The new EVG mode provides a mechanism to define a sequence of shots to take place and for the electrons to end up in the specified bunches in the SR. This enables a client application to control the top-up process by checking which bunches require charge and directing the injected charge into those bunches. This makes it possible to maintain an arbitrary bunch structure in the storage ring. An example of this is 250mA hybrid mode where there are 685 buckets filled to 0.68 nC, 125 empty buckets, 1 bucket filled to 5.6 nC and further 125 empty buckets, see fig 2. The larger bunch has a much shorter lifetime than the other bunches and so requires more frequent filling.

Originally the SR kickers and septum shared a common event; however the septum power supply requires a number of cycles before it achieves the required field. By assigning the septum to a separate event a number of pre-cycles of the septum can take place, as part of the topup cycle, without triggering the kickers and so without disturbing the stored beam.

The four-hour periodic event is used to reset the integrators on all radiation monitors, which provide an interlock based on the integrated dose over that time

period and so are sensitive to ongoing lower level radiation losses. To generate this event, an EVR local to the EVG is programmed to give an output four hours after the event. This output is then connected back into the EVG to generate the four-hour periodic event. The event is started and synchronised to the shift boundary when the IOC is restarted. To increase the reliability of this, an interface module has been developed that continues to produce the reset, every four hours, when the event from the timing systems is not produced; thus a failure of the timing system or maintenance on the timing system such that events are not produced does not result in false alarms from radiation monitors as a result of integrating the natural background radiation.

Asymmetry of the SR kicker pulses results in beam disturbance which lasts up to 12 ms. This affects the brightness of the photon beam and hence some of the beamline experiments. Two additional events were introduced for topup operation (TOP-UP-ON and -OFF) to enable the beamlines to mask the periods when the injection takes place. These events are decoded as "Short" and "Long" gate signals from the EVRs, and mask either each injection shot, or all of the multiple injections of a top-up cycle, and are provided to each photon beamline.
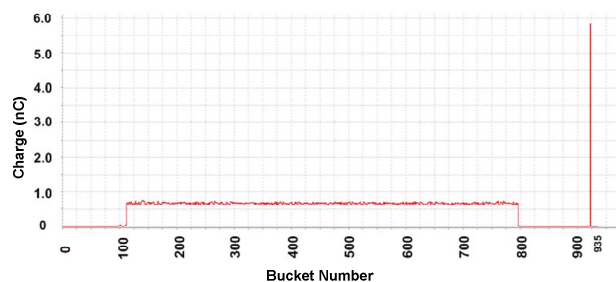
Fig 2: 250mA hybrid fill pattern

CONCLUSION

The installed timing system has functionally met the requirements for the initial operation of the accelerator and beamlines on Diamond Light Source. The system has further proved to be very reliable in operation and has proved to be flexible to accommodate additional functionality for top-up operation.

REFERENCES

[1] R.P. Walker, "Commissioning and Status of the Diamond Storage Ring", APAC 2007, Indore, India

[2] http://www.mrf.fi/

[3] Y. Chernousko, et al, "Diamond Timing System Developments", ICALEPCS'03, Gyeongju, 2003

[4] M. T. Heron, et al, "Implementation, Commissioning and Current Status of the Diamond Light Source Control System", ICALEPCS'07, Knoxville, 2007

[5] Y. Chernousko, et al, "Metrological Testing of DLS Timing System", ICALEPCS'07, Knoxville, 2007

[6] C. Christou, J. A. Dobbing, R. Fielder, I. Martin, S. J. Singleton, "The First Eighteen Months of Top-up at Diamond Light Source", IPAC'10, Kyoto, 2010

PROGRESS WITH THE 2 MEV ELECTRON COOLER FOR COSY-JUELICH/ HESR

J. Dietrich[#], V. Kamerdzhiev, FZJ, Juelich, Germany

M.I. Bryzgunov, A.D. Goncharov, V.V. Parkhomchuk, V.B. Reva, D.N. Skorobogatov, BINP, Novosibirsk, Russia

Abstract

The 2 MeV electron cooling system for COSY-Juelich was proposed to further boost the luminosity even in presence of strong heating effects of high-density internal targets. The project is funded since mid 2009. Manufacturing of the cooler components is in progress. The space required for the 2 MeV cooler was made available in the COSY ring during the summer 2010 shutdown. The design and construction of the cooler is accomplished in cooperation with the Budker Institute of Nuclear Physics in Novosibirsk, Russia. The 2 MeV cooler is also well suited in the start up phase of the High Energy Storage Ring (HESR) at FAIR in Darmstadt. It can be used for beam cooling at injection energy and is intended to test new features of the high energy electron cooler for HESR. Two new prototypes of the modular high voltage system were developed, one consisting of gas turbines the other based on inductance-coupled cascade generators. The technical layout of the 2 MeV electron cooler is described and the status of component manufacturing is reported.

INTRODUCTION

The new generation of particle accelerators operating in the energy range of 1-8 GeV/u for nuclear physics experiments requires very powerful beam cooling to obtain high luminosity. For example the investigation of meson resonances with PANDA detector requires an internal hydrogen target with effective thickness 4×10^{15} atoms per cm^2 and $10^{10} - 10^{11}$ antiprotons at 15 GeV circulating in the HESR. In this case the peak luminosities ranging from 2×10^{31} to 2×10^{32} $cm^{-2}s^{-1}$ are achievable. These experiments allow to observe meson resonances in proton-antiproton annihilations. Resolution of the experiments is limited by momentum spread in antiproton beam, which must be better than 10^{-4}.

The average momentum losses $\dfrac{dp}{pdt}$ on such a target (for 4 GeV antiprotons) will be about $4 \cdot 10^{-6}s^{-1}$ and the heating rate of momentum spread by fluctuation of ionization losses will be near $\dfrac{dp^2}{p^2 dt} = 2 \cdot 10^{-9} \, s^{-1}$. To obtain momentum spread of $10^{-5} - 10^{-4}$ cooling time in the range $\tau_{cool} = 2(dp/p)^2 /(dp^2/dt/p^2) = 0.1 \div 10s$ is needed. The 4 MeV electron cooler at the RECYCLER ring (FNAL) [1] achieves cooling time about 1 hour. The new cooler for COSY should provide a few orders of magnitude more powerful longitudinal and transverse

cooling that requires new technical solutions. The basic idea of this cooler is to use high magnetic field along the orbit of the electron beam from the electron gun to the electron collector. In this case high enough electron beam density at low effective temperature can be achieved in the cooling section. For example the electron beam density of $2 \cdot 10^8$ cm^{-3} (6 mm beam diameter and 1.5 A of current) magnetized with longitudinal magnetic field of 2 kG will have $2.7 \cdot 10^6$ cm/s drift velocity in the beam reference frame. This velocity corresponds to a cooling time near 0.1 s for the low angular spread ($\Delta p_\perp / p = 10^{-5}$) beam.

BASIC DESIGN FEATURES

The basic parameters for the COSY cooler are listed in Table 1. The length restrictions are given by the space available in the COSY ring. The height is limited to 7 m by the building.

Table 1: Basic Parameters and Requirements.

COSY 2 MeV Electron Cooler	Parameter
Energy Range	0.025 ... 2 MeV
High Voltage Stability	$< 10^{-4}$
Electron Current	0.1 ... 3 A
Electron Beam Diameter	10 ... 30 mm
Length of Cooling Section	2.69 m
Toroid Radius	1.00 m
Magnetic Field (cooling section)	0.5 ... 2 kG
Vacuum at Cooler	10^{-9} ... 10^{-10} mbar
Available Overall Length	6.39 m
Maximum Height	5.7 m
COSY Beam Axis above Ground	1.8 m

In Fig. 1 the layout of the COSY 2 MeV cooler is shown. The cooler HV terminal is installed inside the pressure vessel filled with SF_6 gas. The main features of the cooler are:

1. The design of the cooling section solenoid is similar to the ones of CSR (IMP) and LEIR (CERN) coolers designed by BINP [2, 3]. However, for the 2 MeV cooler the requirement on the straightness of magnetic field lines is so high ($\Delta\theta < 10^{-5}$) that a system for control of magnetic field lines in vacuum becomes necessary.

2. For suppression of high energy electron beam losses at IMP and LEIR coolers electrostatic bending was used [4]. The shape of the 2 MeV transport lines, however, dictates a different approach. The collector (inside the HV terminal) will be complemented by a Wien filter to suppress return flux.

[#]j.dietrich@fz-juelich.de
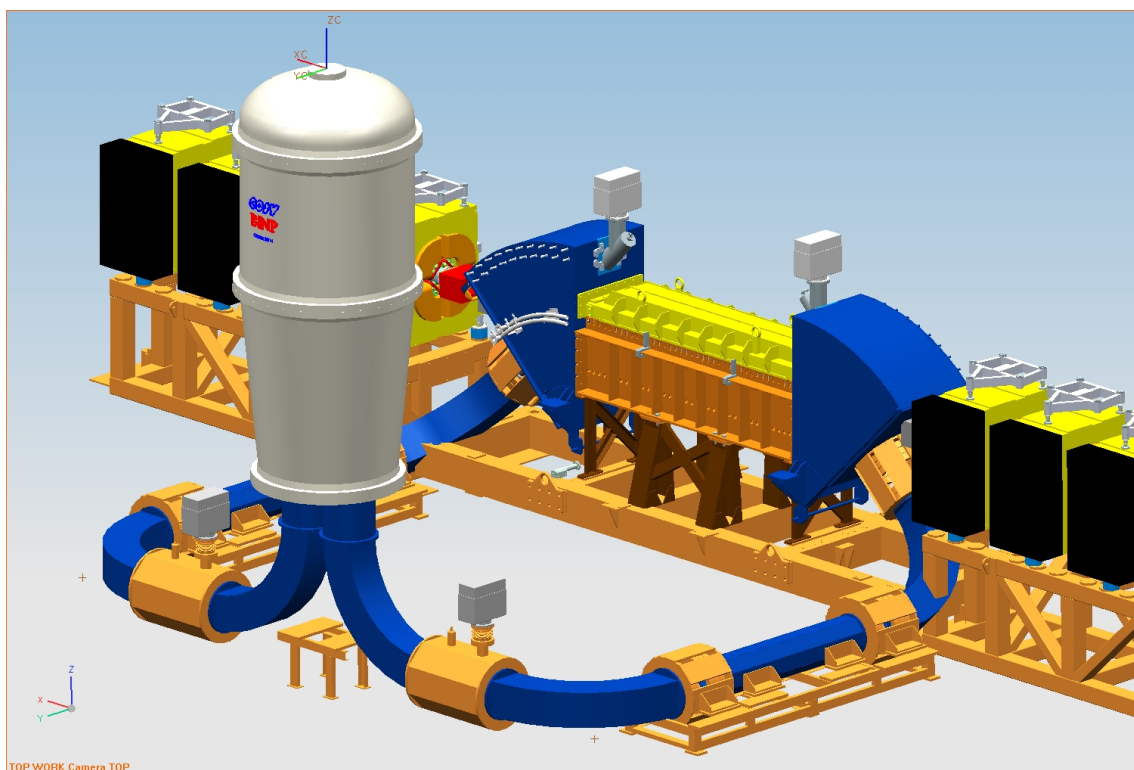
Figure 1: Layout of the 2 MeV electron cooler for COSY.

MAIN COMPONENTS

For the last few years the COSY-BINP collaboration was studying prototype elements for the magnetized cooler. The turbine electro generator driven by compressed gas feeding magnet coils along the HV column was tested. For the 2 MeV electron cooler a cascade transformer is proposed to power components at high potential. This approach benefits from the experience with ELV-8 industrial accelerator technology. It also provides necessary power for the collector. The operation range of the 2 MeV cooler is very broad from 24 keV to 2 MeV. In this case the electron optics of the accelerating tube should be very flexible. So, the continuous longitudinal magnetic field is preferable. The generation of such field demands the large number of independent solenoid coils located in each section. The solution based on a cascade transformer is expected to be more reliable because such a transformer does not contain any moving parts. For this reason the reliability of this design depends on electrical strength only. However, the cascade transformer design also has disadvantages. An issue inherent to all cascade solutions (e.g. cascade generator) is related to power transfer efficiency. The total power consumed by all sections is passed through the first one. That is why the power efficiency of the section should be extremely high in order to keep the power losses reasonable. Moreover, the required number of HV sections appears to be close to the upper limit for such systems. For 4 or 8 MeV electron cooler with lowest electron energy of about 500 keV it is possible to use smaller number of optic elements (e.g. Fermilab cooler [5] or Swedish project [6]). In this case the gas turbine has some advantages because it can be easily installed in any place of the accelerating column without complicated system of shafts. Absence of shafts and high operation frequency of the turbines (above typical mechanical resonance) makes the issues related to mechanical vibration less pronounced. This regime of the cooler operation can be easily checked with the 2 MeV COSY cooler. Turning off some power supplies of the coils in any section allows simulating the electron optics for the different regime of cooler operation, as the accelerating tube having smooth magnetic field or with some variation of it. For higher electron energies the concept of turbines will be further developed.

The power supply for the modular high voltage sections, high voltage terminal and collector consists of 34 high frequency (20 kHz) transformers with cascaded connection. The transformer column and a prototype of one section are shown in Fig. 2 and Fig. 3. The main problem of such a design is leakage of the magnetic field from the transformer that can however be resolved by adding compensative capacitors. The transformer column has a spark-gap system for safety in case of gas breakdown.

04 Hadron Accelerators
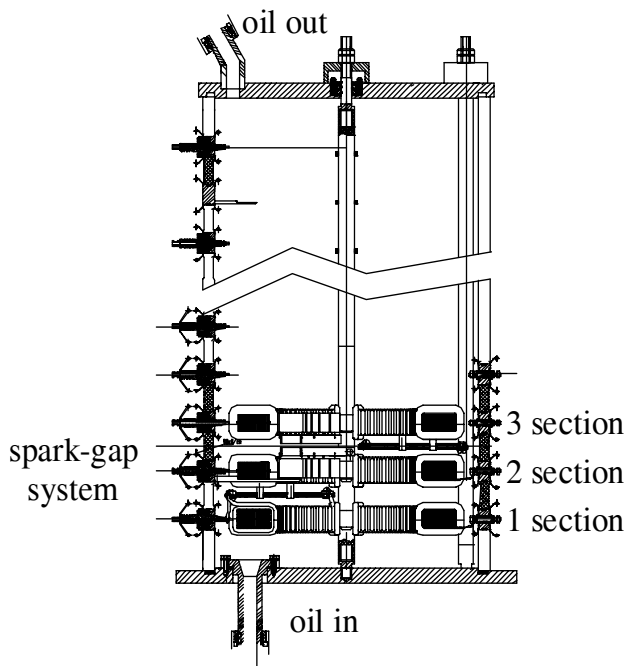
Figure 2: Transformer column.

The inner diameter of a transformer section is 20 cm, the outer diameter - 28 cm and the height 2 cm. The design value of energy-transfer power amounts to 40 kW. Oil is used as isolation and cooling medium.

Measurements of the transverse components of the magnetic field is intended to be carried out by a probe similar to the one described in [7]. The probe consists of a ferromagnetic rod and a mirror attached to it whose plane is perpendicular to the solenoidal field. This unit is installed into a gimbal that allows the magnetic body to align itself along the magnetic field lines. The sensor is mounted on a cart that can be moved along the solenoid axis. A laser beam directed along the axis of the vacuum chamber is reflected by the mirror to a position sensitive photo detector. A signal proportional to the displacement of the laser spot controls the current in corrector coils surrounding the vacuum chamber. These currents produce magnetic fields compensating the transverse components of the magnetic field. As a result the laser spot moves to the detector center and values of the transverse field components are determined from current values in compensating coils.
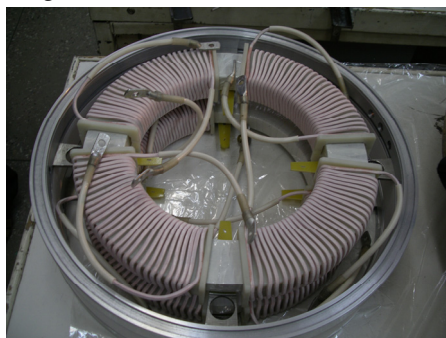
Figure 3: Prototype of the transformer section.

BEAM DIAGNOSTICS

For measurement of the electron beam position 10 pickups (5 in the beam line from gun to the cooling section and 5 from cooling section to collector) are foreseen. 2 pickups will be placed at the entrance and at the exit of the cooling section for measuring the proton as well as the electron beam position (Fig. 4). The last two ones have a special design due to the fact that the in situ magnetic field measurement needs space for the magnetic sensor which is mounted on the cart that can be moved along the solenoid axis. Each pickup consists of 4 sectors. To study the dynamics of electron cooling in a synchrotron only non-destructive instrumentation can be used. Beam diagnostics based on recombination is usually used to optimize electron cooling of protons (H^0-diagnostics). In the future HESR ring, however, this technique is not applicable due to antiprotons being accelerated. An Ionisation Profile Monitor delivers real time data in both transverse planes allowing detailed analysis of beam profile evolution in COSY. Attempts to use scintillation of residual gas to measure beam profiles were very promising. So ionisation and possibly scintillation profile monitors become vital for optimization of electron cooling of antiprotons. The IPM was designed at GSI keeping the requirements for the future FAIR machines in mind [8]. The ionisation products are guided to a position sensitive detector by transverse electric field. An arrangement consisting of an MCP stack (100x48 mm2), a luminescent screen, and a 656×494 pixel CCD camera is used to detect ions in high resolution mode. The IPM actually contains two identical units to provide simultaneous measurements in both, horizontal and vertical, planes. The IPM is installed in COSY in the arc downstream of the cooler telescope. The data acquisition software was developed at FZJ with an emphasis on real-time display of beam profiles. The software also performs fitting and plots beam width and position vs. time. The beam current measured by the beam current transformer (BCT) is also displayed. A Scintillation Profile Monitor (SPM) is being developed at COSY as a robust and inexpensive alternative to the IPM. The disadvantage of much lower event rate compared to the IPM and thus the necessity to locally add nitrogen to the residual gas is compensated by the much simpler mechanical design of the SPM. The light emitted by the gas in the vacuum chamber is focused by a lens onto a multichannel photomultiplier (PMT) array (Hamamatsu 7260-type, 32 channels, 0.8·7 mm photocathode, 1 mm pitch). The readout is performed using a multichannel current digitizer, developed at iThemba LABS [9]. A method using Thomson scattering is proposed to measure the electron beam profile in the cooling section [10].
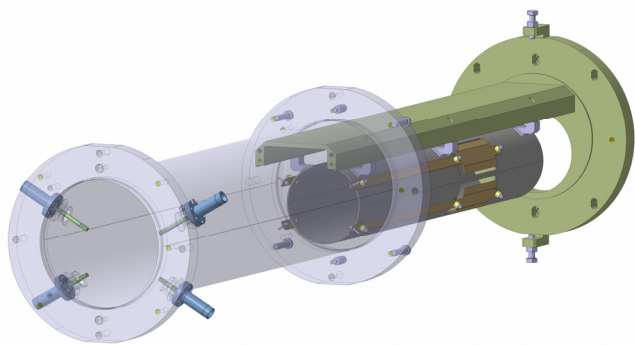
Figure 4: Prototype of the Beam Position Monitor in the cooling section.

Figure 5: High voltage vessel in BINP Novosibirsk.

SUMMARY

The 2 MeV electron cooler is under construction. The cooler components are being manufactured at BINP, Novosibirsk. The pressure vessel is now available at BINP (Fig.5). A second vessel is now under construction in Germany due to certification issues with the German TUV (Technical Inspection Agency). The HV system is modular. It is based on a resonant cascade transformer providing power to multiple HV sections at different electrical potential. A Wien filter is intended to improve collector efficiency. Since the straightness of magnetic field in the cooling section needs to be better than 10^{-5} a in-situ magnetic field measurement system is being built as well. The system will allow verification of magnetic field quality without disassembling the magnetic system or breaking vacuum. Diagnostic tools for optimisation of the electron cooling system are developed and tested. The production of the main components in the BINP workshop as magnet system, acceleration tubes, high voltage section and cascade transformer is on the way. Modifications to the COSY ring itself and its infrastructure to make space available for the cooler are in progress. Changing cabling and replacement and installing new cooling water pipes are finished.

REFERENCES

[1] L.R. Prost, A. Burov, K. Carlson, A. Shemyakin, M. Sutherland, A. Warner, Electron Cooling Status and Characterization at Fermilab's Recycler, Proceeding of COOL07, Bad Kreuznach, Germany p.49-54.

[2] X.D. Yang et al., Commissioning of Electron Cooling in CSRm, Proceeding of COOL07, Bad Kreuznach, Germany p.59-61.

[3] G. Tranquille, Cooling results from LEIR, Proceeding of COOL07, Bad Kreuznach, Germany p.55-58.

[4] E.I. Antokhin et al., Conceptual Project of an Electron Cooling System at an Energy of Electrons of 350 keV, ECOOL'99, NIM A 441 (2000) 87-91.

[5] S. Nagaitsev et al., Antiproton Cooling in the Fermilab Recycler Ring, Proceeding of COOL05, Galena, USA, p39-47

[6] HESR Electron Cooler Design Study, Uppsala,Sweden, 2009.

[7] V. Bocharov, A. Bubley, S. Konstantinov, V. Panasyuk, V. Parkhomchuk, Precision Measurements and compensation for the transverse components of the solenoids magnetic field, Instruments and Experimental Techniques, Vol. 48, Number 6, 2005, p. 772.

[8] T. Giacomini, S. Barabin, P. Forck, D. Liakin, V. Skachkov, Development of Residual Gas Profile Monitors at GSI, Proceedings BIW04.

[9] C. Böhme, T. Weis, J. Dietrich, V. Kamerdzhiev, J.L. Conradie, Gas Scintillation Beam Profile Monitor at COSY Jülich, Proceedings BIW10.

[10] T. Weilbach, University Mainz, 2010, private communication.

04 Hadron Accelerators

DEVELOPMENT OF ELECTRON COOLER COMPONENTS FOR COSY

J. Dietrich, V. Kamerdzhiev, FZJ, Juelich, Germany

M.I. Bryzgunov, V.N. Bocharov, A.V. Bubley, V.G. Cheskidov, A.D.Goncharov, A.M. Kryuchkov, V.M. Panasyuk, V.V. Parkhomchuk, V.A. Polukhin, A.A. Putmakov, V.B. Reva, D.N. Skorobogatov, BINP, Novosibirsk, Russia

Abstract

The 2 MeV electron cooling system for COSY-Juelich was proposed to further boost the luminosity even in presence of strong heating effects of high-density internal targets. The project is funded since mid 2009. Manufacturing of the cooler components has already begun with collaboration efforts of two institutes BINP(Novosibirsk) and FZJ(Juelich). The high cooling rate requires using of the high intensity electron beam with strong magnetization at the cooling section. The 2 MeV cooler also well suits in the start up phase of the High Energy Storage Ring (HESR) at FAIR in Darmstadt. At the report experimental testing results of the prototypes of the cooler elements will be discussed.

INTRODUCTION

The new generation of particle accelerators operating in the energy range of 1-8 GeV/u for nuclear physics experiments requires very powerful beam cooling to obtain high luminosity. For example the investigation of meson resonances with PANDA detector requires an internal hydrogen target with effective thickness 4×10^{15} atoms per cm^2 and $10^{10} - 10^{11}$ antiprotons at 15 GeV circulating in the HESR. In this case the peak luminosities ranging from 2×10^{31} to 2×10^{32} $cm^{-2}s^{-1}$ are achievable. These experiments allow observe meson resonances in proton-antiproton annihilations. Resolution of the experiments is limited only by momentum spread in antiproton beam, which must be better than 10^{-4}.

The average momentum losses $(dp/dt)/p$ of ion on such a target (for 4 GeV antiprotons) will be about $4 \cdot 10^{-6} s^{-1}$ and the heating rate of momentum spread by fluctuation of ionization losses will be near $\frac{dp^2}{p^2 dt} = 2 \cdot 10^{-9} s^{-1}$. To obtain momentum spread of $10^{-5} - 10^{-4}$ cooling time in the range $\tau_{cool} = 2(dp/p)^2/(dp^2/dt/p^2) = 0.1 \div 10s$ is needed. The 4 MeV electron cooler at the RECYCLER ring (FNAL) achieves cooling time about 1 hour. The new cooler for COSY [1] should provide a few orders of magnitude more powerful longitudinal and transverse cooling that requires new technical solutions. The basic idea of this cooler is to use high magnetic field along the orbit of the electron beam from the electron gun to the electron collector. In this case high enough electron beam density at low effective temperature can be achieved in the cooling section. For example the electron beam density of $2 \cdot 10^8$ cm^{-3} (6 mm beam diameter and 1.5 A of current)

magnetized with longitudinal magnetic field of 2 kG will have $2.7 \cdot 10^6$ cm/s drift velocity in the beam reference frame. This velocity corresponds to a cooling time about 0.1 s for the low angular spread ($\Delta p_\perp / p = 10^{-5}$) beam.

BASIC DESIGN FEATURES

The basic parameters for the COSY cooler are listed in Table 1. The restrictions are given by the space available in the COSY ring. The height is limited to 7 m by the building.

Table 1: Basic Parameters and Requirements.

COSY 2 MeV Electron Cooler	Parameter
Energy Range	0.025 ... 2 MeV
High Voltage Stability	$< 10^{-4}$
Electron Current	0.1 ... 3 A
Electron Beam Diameter	10 ... 30 mm
Length of Cooling Section	2.69 m
Toroid Radius	1.00 m
Magnetic Field (cooling section)	0.5 ... 2 kG
Vacuum at Cooler	10^{-9} ... 10^{-10} mbar
Available Overall Length	6.39 m
Maximum Height	5.7 m
COSY Beam Axis above Ground	1.8 m

In Fig. 1 the layout of the COSY 2 MeV cooler is shown. The cooler HV terminal is installed inside the pressure vessel filled with SF_6 gas. The main features of the cooler are:

1. The design of the cooling section solenoid is similar to the ones of CSR (IMP) and LEIR (CERN) coolers designed by BINP [2,3]. However, for the 2 MeV cooler the requirement on the straightness of magnetic field lines is so high ($\Delta\theta < 10^{-5}$) that a system for control of magnetic field lines in vacuum becomes necessary.

2. For suppression of high energy electron beam losses at IMP and LEIR coolers, electrostatic bending was used [4]. The shape of the 2 MeV transport lines, however, dictates a different approach. The collector (inside the HV terminal) will be completed by a Wien filter to suppress return the electrons flux.

MAGNETIC SYSTEM

The magnetic system has the cooling section (1) (see fig.1), where electrons and protons move at common orbit and parallel to each other. At the 45^0 toroid magnets this beams are joined and separated (2). Magnetic dipoles (3) are installed along the proton orbit for compensation of

the vertical field action on protons at toroids. There are two transport cannels for electron beam: to inlet it to cooling section and to return it at the high voltage vessel for recuperation of the electros energy. Each system has matching section (4), three 90° bending parts (5), solenoids (6), two short (7) and one long (8) transition sections and matching section (9) at entry to acceleration tube.
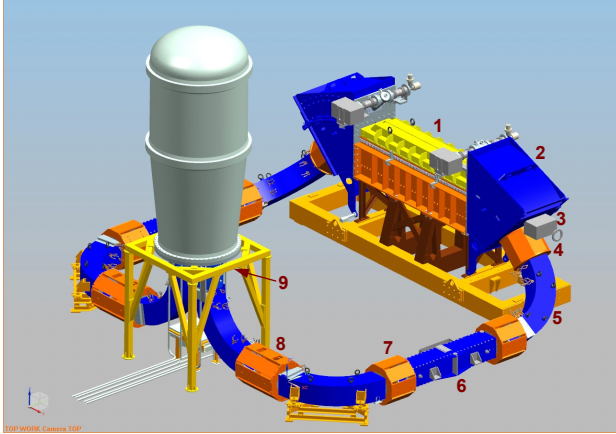
Fig.1 Schematic view of the 2 MeV COSY cooler.

The requirement on the parallelism for motion of the proton and electron beams inside cooling section is very high ($\Delta B / B = \theta < 10^{-5}$). To satisfy these requirements cooling solenoids will be made from the pancake coils with possibility to incline each on the down support points. For better compensation of transverse components of magnetic field generated by communication lines, two types of coils with opposite direction of winding are used at this cooler (in contrast to previous cooler EC-35, EX-300, LEIR). At this case neighboring coils can compensate transverse magnet components.

The toroid radius and the bending solenoid radius is 1 m (at central axis of electron beam). The value of longitudinal magnet field in toroid (B_{tor}) is up to $2kG$, and in bending solenoid (B_{turn}) is up to $1kG$. The transverse magnetic field gradient is generated by special position of the bending magnetic coils. The profile of electron trajectory and the profile of magnetic lines can be adjusted at average but at the entry and exit of a magnet the electrons will have kick by transverse component of magnetic field. The transverse magnetic field should be changed according to electron beam energy as $B_\perp \propto \gamma\beta$. We can use self compensation scheme if electron will made integer number of Larmor turns along the orbit. To keep the phase of Larmor rotation constant it is also necessary to change longitudinal component of magnetic field along electron orbit as $B_s \propto \gamma\beta$. At next figures (fig. 2, 3) an example of calculation of electron motion at the transport channel is shown. Start point is located at center of long section (8), then electrons passes bending solenoid (5), short section (7), and then enters at solenoid (6). Calculations were made using Tiunov M.A.

code MAG3D at geometry which is very close to real and magnetic parameters of iron correspond to steel 10 (Russian name type of steel)
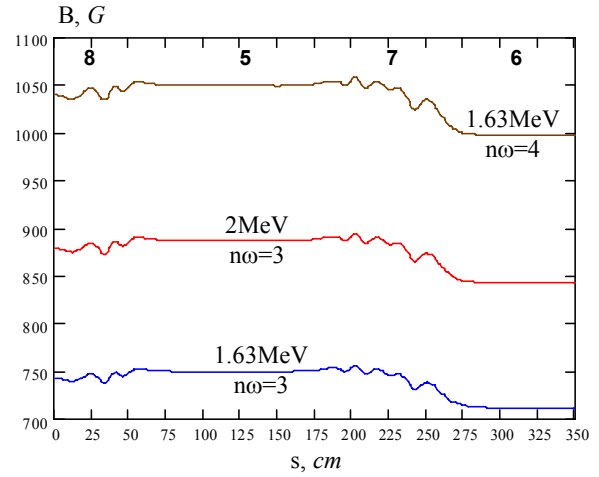
Fig. 2. The longitudinal field in the transport cannel. For this field the electron passes transport system without heating.
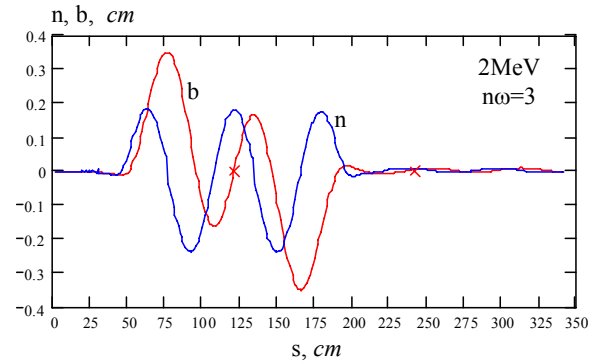
Fig. 3 The electron deflections from the axis line: **n** – at radial direction, and **b** – at perpendicular direction (drift).

Fig. 4 Coils for the cooling section

04 Hadron Accelerators

MAGNETIC LINE STRIGTHNESS

For high voltage cooler key role at cooling efficiency belongs to the quality of magnetic field at cooling section. Deviation of magnetic lines to angle θ produces motion of electrons $\Delta V = \theta \gamma \beta c$ at the electron beam rest system and, as results, decreases cooling rate. For measuring of angle of magnetic line a sensitive compass with mirror is used which reflects the laser beam along axis of the cooling section (Fig. 5). The feedback system measures back scattered laser beam and returns it to center of the system using currents at correction coils. The currents are proportional to the perpendicular components of magnetic field. Using inclining of the pancake coils the perpendicular components of magnetic field can be compensated.
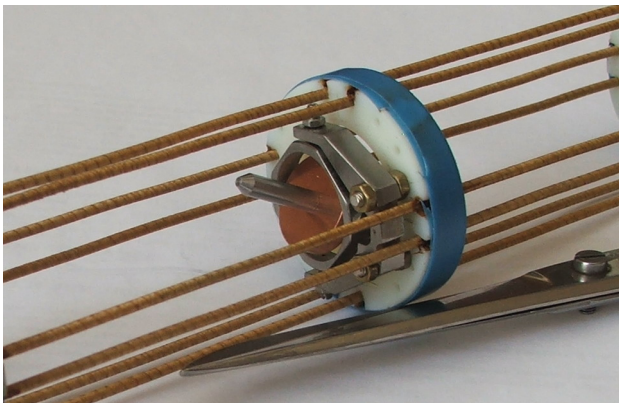
Fig.5 The compass with mirror for measuring direction of magnetic line at cooling section.

The experience of using of this system for regular control [6] demonstrated that after some period of time the deformation of line increases and procedure should be repeated. At 3 m cooling section this period for accuracy $<10^{-5}$ was about 1 week. FNAL cooler required new alignment procedure for elements of cooling solenoid after 2 months of operation [7].

HIGH VOLTAGE COLUMN

Testing of the high voltage section prototypes demonstrated that for SF_6 with 1.6 bar pressure the voltage between section achieved the project value 60 kV (Fig.6). For pressure 1.4 bar sparking events were detected. The higher pressure of SF_6 is required for suppression of sparking between the high voltage terminal and the ground potential vessel. Calculations show that the electric field on the high voltage terminal will be near 160 kV and for suppression of discharge we need more then 3 bar pressure. The really existing roughness of the high voltage terminal surface requires increasing of gas pressure to 5 bar.

Projecting high voltage vessel and column, we took the main parameters of industrial accelerator ELV-8 that works on 2.5 MV.
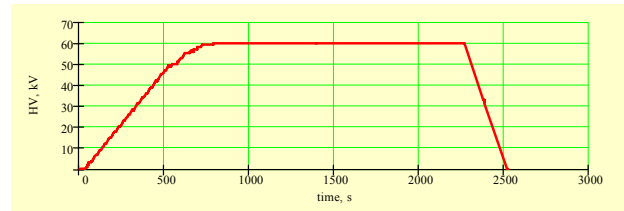
Fig. 6 Testing of the high voltage stability

The first experiments with high voltage were made with using of own BINP produced ±30 kV power supply. But later, for serial production, high voltage power supply of Japanese company MATSUSADA Precision Ink model RB30-30N will be used.

THE CASCADE TRANSFORMER

For core of the cascade transformer we will use the amorphous iron of Russian plant (http://www.amet.ru/) with small power losses for 20 kHz (at iron and winding 180 Wt/cascade). The 33 cascades will be installed at vertical column so that each core will correspond to high voltage section. Transformer oil circulated along transformer will be used for cooling and isolation (Fig. 6).
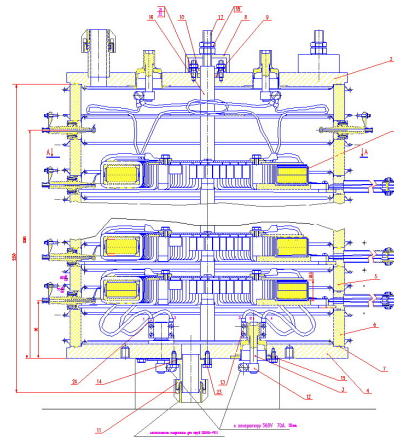
Fig. 7. The high power cascade transformer
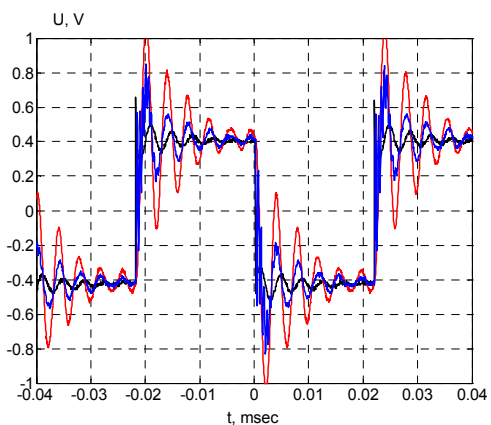
Fig 8. The voltage oscillation on 3 sections transformer if input voltage is taken from rectangular wave form generator. Measurements without resistor loading.

As is known [7] the problem in design of a cascade transformer is its own resonance mode. The high mode oscillations exiting at process of operation of high power voltage converter can limit the power transport along cascade [7]. Fig 8 shows response signals of 3 cascade transformer without resistive loading on input rectangular signal from generator. We see that own mode oscillations have frequency about 250 kHz that far from working frequency 20-25 kHz.

Table 2. Basic parameters of transformer

Size Fe (ØD1-ØD2)	28 cm–20 cm
Thickness (2 Fe rings)	2 cm
Mass	4.8kg
Magnet conductivity	26000
Cross section Fe	$8*2$ cm^2
Number winding	$2*28$
Coupling inductance	29.8 mH
Leakage inductance	160 uH
Working frequency	20kHz
Capacitance C0	1.8nF*900V
Capacitance C1	0.4 uF*280V
Voltage single winding	280 V r.m.s.
Magnet field at Fe core	2kGauss r.m.s.
Type of Fe core	5BDSR type B
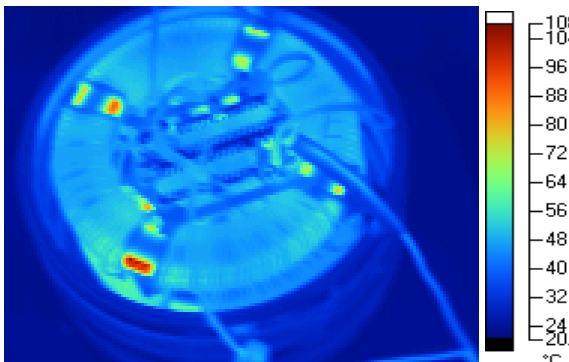
Fig 9. Thermo distribution after testing with power 15 kWt (thermo sensor photo).

After 5-10 minutes of operation of the transformer with high power 15 kWt, the photo of thermo distribution was made (Fig.9.). This measuring was made without oil cooling and we think that cooling will decrease temperature for normal value.

HIGH VOLTAGE TERMINAL

The high voltage terminal is supported by column from the 33 identical high voltage sections (fig. 10). The column with high voltage terminal is placed in special tank which can be filled with SF_6 under pressure up to 10 bar. The section contains two magnetic coils producing guiding magnetic field for acceleration and deceleration tubes and the high voltage power supply producing up to 60 kV. Each section is supplied with power from separate winding of the cascade transformer. Total power consumption of one section is about 300 W. The coils and

the electronic components are cooled with flowing transformer oil.
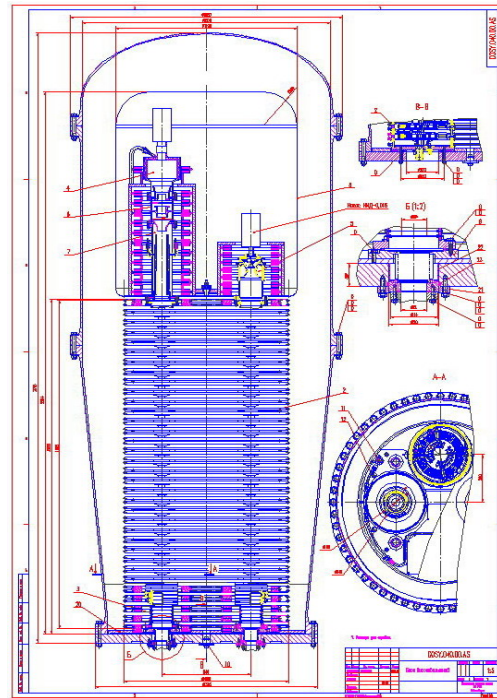
Fig. 10 The high voltage terminal with electron gun and collector

Construction of electron gun with variable beam profile is close to one which is used in previous electron cooling systems. Innovation of the gun is a controlling electrode which is split to 4 parts for independent modulation in 4 sectors of electron beam. It provides to have time modulated part of electron beam which is shifted from main beam axis. Using such modulation it is possible to control beam size and rotation with the help of pickup electrodes.

Electron collector is added with system of suppression of secondary electron flux based on Wien filter, where beam moves in crossed transverse electric and magnetic fields. In previous coolers (EC-35 CSRm, EC-300 CSRe, EC-40 LEIR) in order to achieve high recuperation special electrostatic plates, installed in bends, were used. The plates make motion of the electrons reversible. It means that electrons, reflected from the collector, move back in direction of the gun and then go to collector again where they can be absorbed by the collector. Such scheme improved efficiency of the recuperation (I_{loss}/I_{total}) from 10^{-3} to 10^{-6}.

In high energy cooler for COSY, production of such electrostatic bending plates is related with some problems. The voltage on the plates becomes too high and geometry of the cooler is too complicated: there are 6 bend with 90º and 2 bends with 45º.

Another method, based on Wien filter, was proposed for the cooler to improve efficiency of the recuperation. The idea is to collect electrons, reflected from the collector, before they are accelerated in electrostatic tube (Fig.9).

The principle of the Wien filter is based on motion in crossed transverse electric and magnetic fields. For primary beam the electrostatic and Lorenz forces are compensated, but for secondary beam they are summed and the secondary beam drifts from the primary beam to the wall of vacuum chamber with low kinetic energy 10-20 keV.

Depending on the initial displacement of electron of the primary beam, it can be accelerated or decelerated by the edge fields of the plates. It means that in homogeneous magnetic field resulting transverse force will be equal to 0 only for central particles. Consequently shape of primary beam will be changed. To avoid this, transverse magnetic field should have gradient

$$B_x = B_\perp \frac{n}{R} y , \qquad B_y = B_\perp (1 + \frac{n}{R} x) ,$$

where $R = \dfrac{pc}{eB_\perp}$, $n = \dfrac{1}{2\gamma_0^{\,2}}$. For low energy (20 keV) $n=0.5$.

Electrostatic field is produced with special plates. There are special shims on the plates to make distribution of electrostatic field in region of main beam more homogeneous.
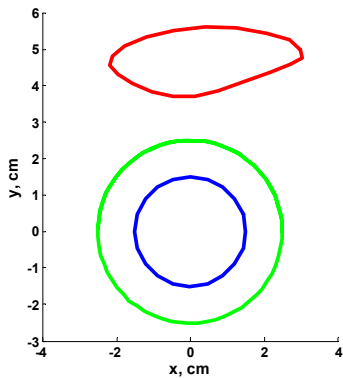
Fig. 11. Displacement of the secondary beam in Wien filter. Blue – secondary beam before filter, red – secondary beam after filter, green – internal size of diaphragm.

Transverse magnetic field in the filter is produced by permanent magnets. The magnets size and position provide average transverse magnetic field 35 G and gradient 0.5. Length of electrostatic plates is 39 cm, integral of transverse magnetic field in center 1400 G·cm, voltage on electrostatic plates ±8 kV relative to vacuum chamber. Potential of the chamber is 20 kV relative to cathode. In fig 11 displacement of the secondary beam with energy 20 keV in Wien filter is shown. As easy to see, reflected electron beam have strong deflection and can not pass limiting diaphragm.

REFERENCES

[1] Status of the 2MeV Electron Cooler for COSY Juelich, Jürgen Dietrich, V. Kamerdzhiev, FZ Juelich, Germany, M.I. Bryzgunov, A.D. Goncharov, V.V. Parkhomchuk, V.B. Reva, D.N. Skorobogatov, BINP, Novosibirsk, Russia, Proceeding COOL09, Lanzhow
[2] Commissioning of electron cooling in CSRe, X.DYang, et al. Proceeding of COOL 2009, p.173-177,
[3] Specification of new electron cooler for the low energy ion accumulation ring, LEIR, G. Tranquille, Proceeding COOL 03, NIM in Phys. Res. A 532 (2004) p.399-402
[4] Advantages of electron cooling with radially varying electron beam density, A.V. Bubley et al, Proceeding COOL 03, NIM in Phys. Res. A 532 (2004) p.303-306
[5] L.Reginato, High Frequency Cascaded Resonant Transformer Rectifier Power Supply for Neutral Beam Injection, PAC 1991, p.2918-2922.
[6] .N.Arapov, N.S.Dikansky, V.I.Kokoulin at al, Proceedings of the XIII international conference on high energy accelerators Novosibirsk, 1986, p.341-343.
[7] C. Crawford, E. Mc-Crory, S. Nagaitsev, A. Shemyakin, FNAL, V.Bocharov, A.Bubley, V.Parkhomchuk, V.Tupikov, BINP, S.Seletsky. Fermilab Electron Cooling Project: Field Measurements in the Cooling Section Solenoid. Proc. of the 2001 PAC, Chicago.
[8] V.B.Bocharov, A.B.Bubley, S.G.Konstantinov, V.M.Panasuk, V.V.Parkhomchuk, Measuring straightness magnet field line at cooler solenoid. PTE №6, 2005, pp. 78-86.

04 Hadron Accelerators

RESULTS OF ELECTRON COOLING BEAM STUDIES AT COSY*

C. Böhme, J. Dietrich, V. Kamerdzhiev[#], FZJ, Jülich, Germany
M. Bryzgunov, V. Reva, BINP SB RAS, Novosibirsk, Russia
A. Kobets[‡], I. Meshkov, A. Rudakov, N. Shurkhno, A. Sidorin, JINR, Dubna, Russia

Abstract

Beam studies dedicated to electron cooling and related problems were carried out at COSY in April 2010. The newly installed Ionization Profile Monitor was used to study the dynamics of longitudinal and transverse electron cooling. Friction force measurements were performed. Beam lifetime was measured for different injection parameters, electron currents and working points. Position and angle scans of the electron beam were also performed. Results of the recent beam studies are reported and the plans for future studies are discussed.

INTRODUCTION

The work was performed under the Helmholtz-Russia Joint Research Group (HRJRG) - HRJRG-106 "Development of a high energy electron cooler for hadron physics experiments at COSY and HESR". A long tradition of cooperation exists with the Budker Institut of Nucler Physics, Novosibirsk and the JINR Dubna in performing experiments at the low energy electron cooler at COSY Jülich.

The electron cooler was designed and constructed during the years 1989 through 1992. The design goal was a 4 A electron beam at 100 keV confined and guided in solenoidal magnetic field up to 0.15 T. Since the first cooling on May 1993 the cooler was mostly operated at injection energy of COSY, which corresponds to electron beam energy of 20 to 25 keV. Practically, electron currents up to 0.5 A are applied. Until recently the solenoid field was set to 0.08 T.

COSY INJECTION SCHEME

In this section, some of the operational features of the stripping injection into COSY are considered, see fig. 1 [1]. The stripper foil is located behind a dipole in the extraction arc, about 40 mm off the nominal orbit. For injection the COSY orbit is bumped to the edge of the foil so that it meets the incoming cyclotron beam position and direction. The injection is controlled by three main parameters, the macropulse length t_{macro}, the bumper ramp down time t_{ramp}, and the micropulsing factor f_{micro}. Controlled by a shutter at the cyclotron, H^- (or D^-) ions are delivered within a time interval t_{macro}. The orbit bumpers are de-energized in the same time. If requested, the cyclotron current I_{cycl} can be decreased by micropulsing, $f_{micro} = 1$ corresponds to 100% I_{cycl}. As injection proceeds, the betatron amplitude of the stored beam increases up to a value determined by the available

horizontal acceptance. Multiscattering due to many repeated traversals through the foil and a possible mismatch of incoming and circulating beam angles with subsequent filamentation broaden the stored beam also vertically up to the available acceptance. With the standard values $t_{macro} = t_{ramp} = 20$ ms, no micropulsing, and typically 6 µA cyclotron current, the ring is filled with $(5-10) \cdot 10^{10}$ protons, but at the expense of large emittances. Based on the aperture of the beam tubes, the optical functions, and the orbit distortions in COSY we estimate acceptances of $A_x = 80$ µm and $A_y = 20$ µm. The proton beam size (3σ emittances) is then larger than the electron beam diameter. If the macropulse is made shorter at constant ramp down time one may expect a beam with smaller emittance but also less stored beam intensity.
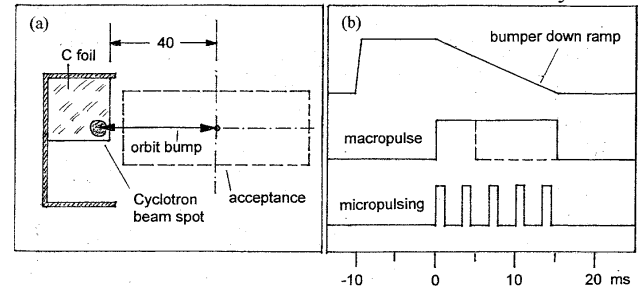
Figure 1: Principle of the stripping injection at COSY. H^- or D^- delivered by the cyclotron injector change their charge state in a carbon foil. Before injection the COSY orbit is bumped to the edge of the stripper foil (a). During the injection time, defined by the macropulse length, the orbit is moving back to its nominal position, coasting beam injection. Bumper ramp down time t_{ramp} and macropulse length t_{macro} are variable parameters (b). Micropulsing by chopping the macropulse allows to reduce the intensity I_{cycl} of the incoming cyclotron beam.

BEAM INSTRUMENTATION

Ionization Profile Monitor

The Ionization Profile Monitor (IPM), developed at GSI [2], is intended to provide fast and reliable non-destructive beam profile measurements at the future FAIR machines. The IPM was installed in COSY to test its performance and reliability and to provide routine non-destructive profile data for COSY.

The ionisation products are guided to a position sensitive detector by transverse electric field. An arrangement consisting of an MCP stack (100x48 mm^2), a luminescent screen, and a 656×494 pixel CCD camera is used to detect ions. High voltage electrodes provide the electric field for ion extraction. The IPM contains two identical units to provide simultaneous measurements in

04 Hadron Accelerators

both horizontal and vertical planes. The IPM is installed in the arc downstream of the cooler telescope. The data acquisition software described below was developed at COSY (see fig. 2).
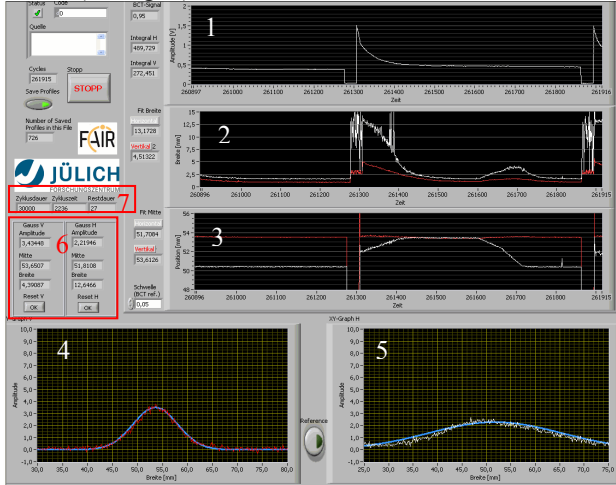
Figure 2: Display of the IPM data acquisition program. Beam Current Transformer (BCT) signal plotted over time (1); horizontal and vertical profile width (Gaussian standard deviation) (2); horizontal and vertical beam position (3); measured vertical beam profile and the corresponding fit (4); measured horizontal beam profile and the corresponding fit (5); summary of vertical and horizontal fit parameters (6); parameters of the current machine cycle (7). The data displayed in 2 and 3 is derived from the corresponding fits. The horizontal axis in 1, 2, 3 represents measurement points. The data acquisition operates at 24 profiles/s. The horizontal axis in 4 and 5 is calibrated in mm. All fits are Gaussian fits.

Beam Current Transformer

The BCT is commercially available from BERGOZ Instrumentation and is based on the CERN design of the Parametric Current Transformer [3, 4]. At injection energy at f_{rev} = 488 kHz, 10 µA of beam current corresponding to $1,28 \cdot 10^8$ protons circulating in the ring result in 1 mV at the BCT output.

EXPERIMENTAL RESULTS

Injection optimization

Prior to performing the experiments on electron cooled proton beam, injection parameters were optimized. The current in the last steering magnet of the injection beam line was varied to check for optimal injection angle from the point of view of injection efficiency and proton accumulation. For cooling experiments, injection timing was changed to minimize initial losses [5] at the very beginning of the machine cycle. Injection duration was reduced to t_{macro}= 2 ms instead of standard t_{macro}= 20 ms insuring smaller horizontal emittance of the injected proton beam and thus less beam loss. Injection delay of 5 ms was found to result in the highest injected proton current. Fig. 3 shows the proton current vs. injection delay at t_{macro}= 2 ms. The delay of 5 ms is clearly the

04 Hadron Accelerators

preferred value. Fig. 4 shows the time evolution of horizontal beam profiles in a 2.5 s cycle as contour plots for three different injection delay values.
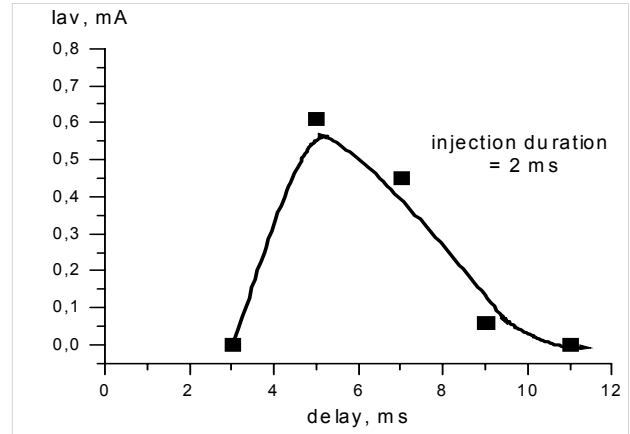
Figure 3: Injected proton current vs injection delay at t_{macro}= 2 ms.

The values 7 ms and 9 ms clearly result in double-peak profiles due to large betatron amplitudes of the injected protons.
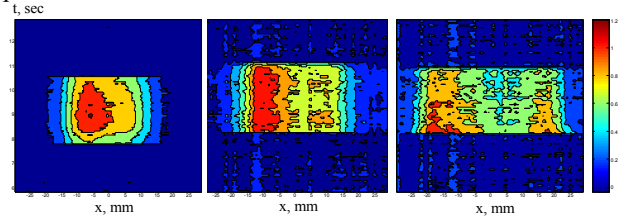
Figure 4: Contour plots representing the evolution in time of the horizontal profiles at different delay time values (5, 7 and 9 ms) at t_{macro}= 2 ms.

The majority of the further experiments were performed with the following injection settings: injection steerer magnet at 20% of maximum current, injection delay 5 ms and t_{macro}= 2 ms. Furthermore, the orbit was kept unchanged to ensure the reproducibility of the measurements. The latest experimental studies which are not described in this report show that significant improvement of beam lifetime can be achieved through orbit optimization. For the experiments reported here some standard cooling orbit was used, thus relative changes of lifetime are of interest rather than absolute values.

Proton beam lifetime and cooling time vs. electron beam position and angle

Preliminary studies of the dependence of proton beam lifetime on the angle between proton and electron beams and the position of the electron beam in respect to the proton beam were performed. The angle scan revealed no strong dependence of beam lifetime on angle within a few seconds after injection. The parallel shift of the electron beam Δx = Δy =4.5 mm resulted in lifetime improvement by about a factor of 2 (see fig. 5). This, likely, means that in the initial configuration the closed orbit did not pass through the center of the electron beam.
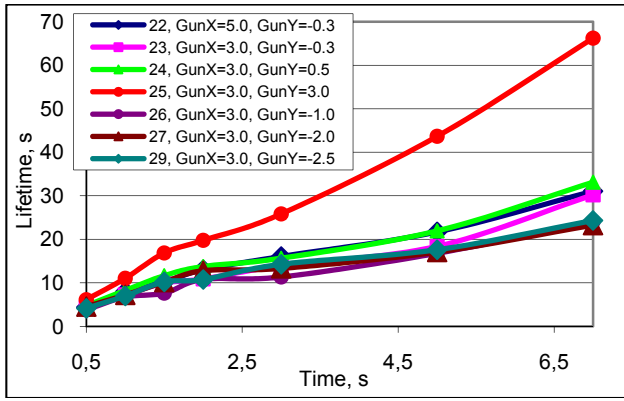
Figure 5: Instantaneous beam lifetime vs. time for different electron beam positions. The e-beam position was varied by adjusting the currents in the gun and collector corrector coils. 3 A correspond to a position change of 4.5 mm in the cooling section. $Q_x \approx Q_y \approx 3.61$.

A full scan with the electron beam across the proton beam could not be performed due to limitations in the cooler systems. These studies need to be repeated by moving the electron beam across the cooled proton beam and vice versa.
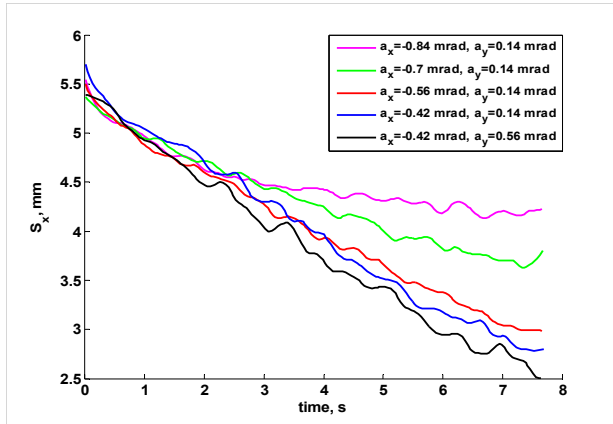
Figure 6: Proton horizontal beam width (Gaussian standard deviation) for different angles of electron beam.

During the angle scan beam profiles measured by the IPM were recorded. Result of the analysis is shown in fig. 6. Plotted is the width of the horizontal profile over time. Though there is no significant change of lifetime, an effect on cooling time was observed. After about 3 s the rate of width decrease begins to change for angles $a_x < -0.5$ mrad. This may be due to the higher effective electron temperature which begins to matter once protons have been cooled to some extent.

Varying the electron beam angle in respect to the proton beam can be used to control the beam emittance. This was done recently during the beam studies dedicated to beam lifetime optimization for PAX experiment [6].

Proton beam lifetime vs. electron current

Dependence of proton beam lifetime on electron beam current is shown in fig. 7. It was measured at optimal electron beam position and angle. If we consider the long-term lifetime, the electron current has an optimum around

110 mA. However, much higher current (290 mA) results in better lifetime on a basis of a few tens of seconds. Finally, the short-term lifetime, few seconds after injection, drops with growing electron current, being the best with no electron current at all – initial losses [5, 6]. Poor long-term lifetime at higher electron currents can be explained by the interplay of single scattering of protons on residual gas and non-linear electric field of the electron beam.
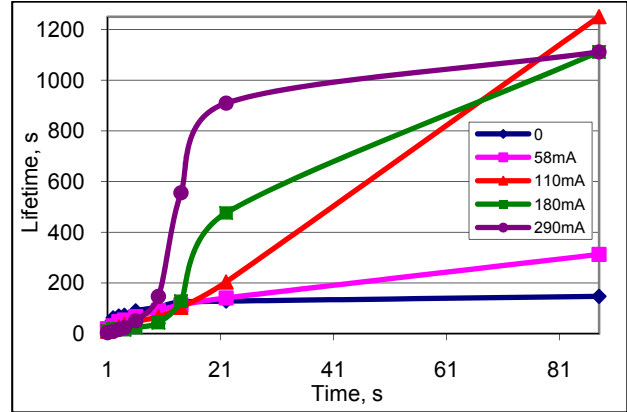
Figure 7: Variation of instantaneous beam lifetime during first 90 s for different electron currents.

Dependence of proton beam lifetime on tunes

Dependence of beam lifetime on the working point during electron cooling was measured. Although the lifetime changes fast as the cooling proceeds the change of tunes results in a change of lifetime in all timescales. The setting $Q_x \approx Q_y \approx 3.61$ was found to provide good lifetime and was used for the experiments. However, we have seen evidence that the values aside from the resonance line e.g. $Q_x \approx 3.613$, $Q_y \approx 3.607$ or $Q_x \approx 3.608$, $Q_y \approx 3.616$ may be suitable as well.

Friction force measurements

The presence of dispersion at the IPM location can be very helpful for resolving small energy changes. This technique was used to estimate the mean value of the longitudinal friction force by introducing a step to the electron acceleration voltage (see fig 8).
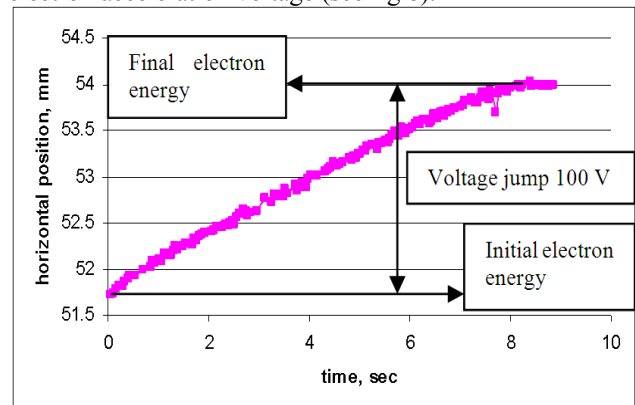
Figure 8: Change of proton beam position, as measured by the IPM, in response to the change of electron energy by 100 eV.

$$\langle F \rangle = \frac{2CE\Delta x}{l_e D\beta c\Delta t} \approx 1.9 \cdot 10^{-4} \frac{eV}{cm} \tag{1}$$

Where $E = 45\ MeV$ is the ion kinetic energy, $C = 184\ m$ the machine circumference, $l_e \approx 1.4\ m$ the effective length of the cooling section, $D = 2\ m$ dispersion at the IPM location, $\beta c = 8.97 \cdot 10^7\ m/s$, $\Delta x \approx 2.25\ mm$ the horizontal displacement at the IPM and $\Delta t \approx 8\ s$ time required to reach the new energy. This value agrees well with previous measurements based on revolution frequency shift as a result of an electron energy step.

Transverse friction force can be determined by analyzing the evolution of beam profiles during the cooling process. The experimental values of the distribution function enable to calculate the time derivative and to estimate the friction force according to equation

$$F(a_n) = \frac{1}{f(a_n)} \sum_{i=1}^{n} \frac{\Delta f_i}{\Delta t} \Delta a \tag{2}$$

where f is the proton distribution function, F is an effective friction force, a is the amplitude of betatron oscillation. The profile of the friction force can be approximated by phenomenological equation

$$F(a) = \frac{A \cdot a_{eff}^2 \cdot a}{\left(a^2 + a_{eff}^2\right)^{3/2}} \tag{3}$$

and the typical cooling rate $\lambda = dF(a)/da$ can be calculated at the point $a = 0$. Fig. 9 shows the curves of the friction force estimated according to equation (2) and the approximation curve (3). The electron current and acceleration voltage were set to 180 mA and 24.58 kV respectively. Fig. 10 shows the dependence of cooling rate on the value of electron beam current. Evidently, the maximum cooling rate of 0.25 sec^{-1} corresponds to electron current of about 300 mA.
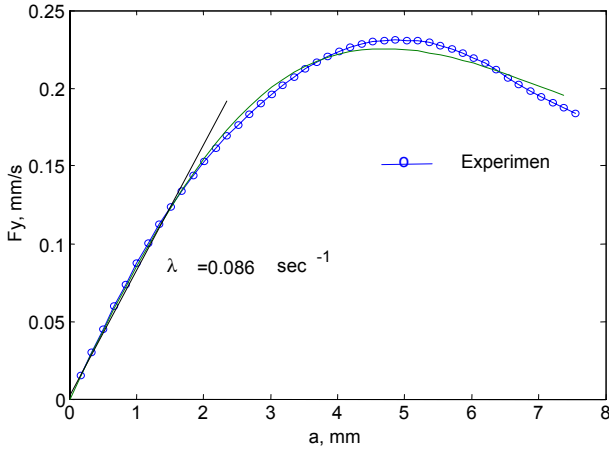
Figure 9: Experimental friction force curve (circles) according to (2) and an approximation according to (3) (solid line). The cooling rate at $a = 0$ is $\lambda = dF(a)/da$ =0.086 sec^{-1}.

Interestingly, once the final proton beam size is reached $\sigma_y \approx 1\ mm$ with electron currents above 100 mA, further increase of electron current does not result in a decrease of the proton beam size (see fig. 11). This observation does not seem to be related to the ability of the IPM to

04 Hadron Accelerators

resolve small beam size. Vertical beam size of low intensity proton beam equal to 0.67 mm has been measured before.
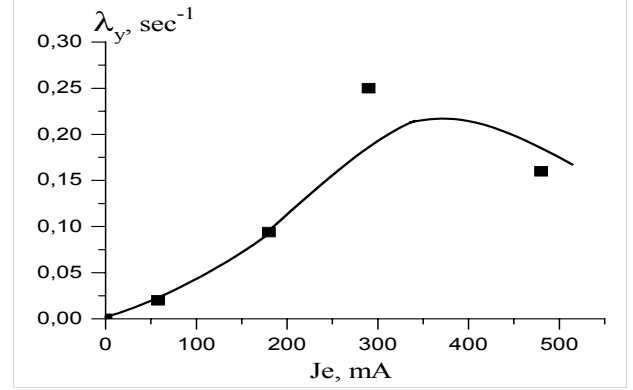
Figure 10: Dependence of cooling rate on electron current.
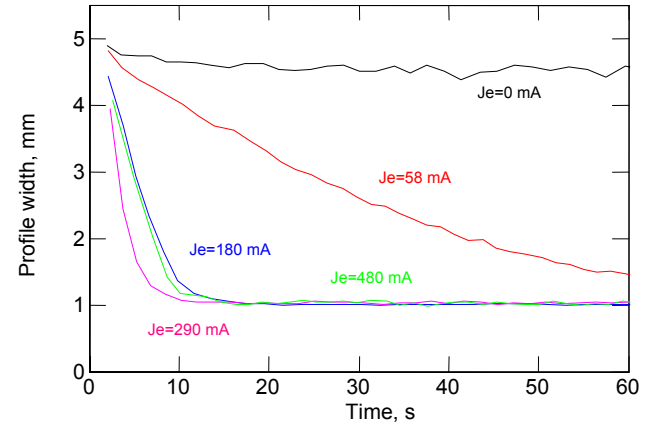
Figure 11: Evolution of the vertical beam size in time for different values of electron current.

Fig. 12 shows time evolution of the horizontal and vertical beam widths. Four regions are marked on the plot. The proton beam is injected at $t \approx 0\ s$. The initial cooling with 170 mA of electron current is shown in the first region. This process is accompanied by initial losses, so the reduction of beam width is a result of cooling and beam loss. After the beam has reached equilibrium at $t \approx 30\ s$ electron current was turned off allowing the beam size to grow (region 2). After another 30 s electron current is turned on again, leading to fast decrease of beam size (region 3). In the fourth region emittance blow-up without electron cooling is shown again. No beam losses have been observed after 10 s, corresponding to regions 2-4. An exponential fit $y = y_0 + \exp(-(t-t_0)/\tau)$ was performed in region 3 corresponding to beam cooling. In region 4 exponential and linear fits were done. Exponential beam blow up is mostly due to intrabeam scattering, whereas the linear one is due to interaction of the beam with residual gas. Significantly different slope of linear growth can be explained by the difference of mean beta functions in the ring. Fig. 13 shows three profile snapshots for the cooling-heating process indicated in fig. 12.
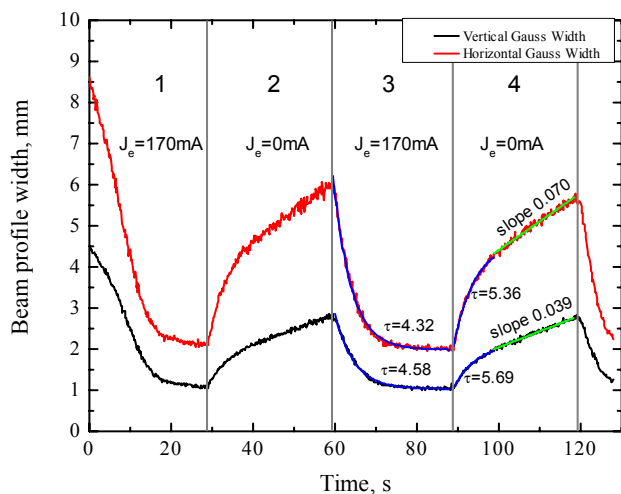
Figure 12: Horizontal and vertical beam width (Gaussian standard deviation) plotted vs. time with electron cooling on and off. Beam intensity after initial losses amounted to about $5 \cdot 10^9$ protons, average vacuum in COSY was about 10^{-9} mbar. Profile snapshots are shown in fig. 13.
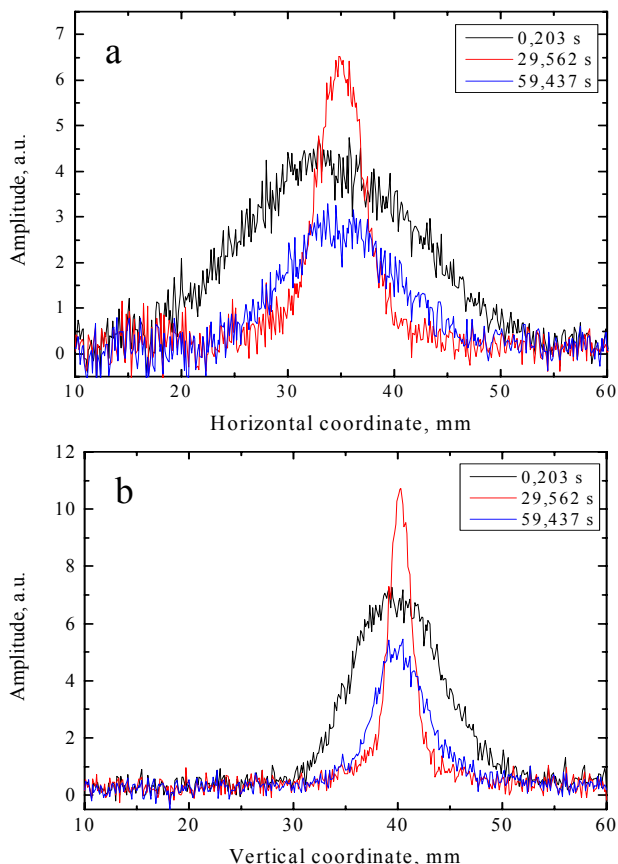
Figure 13: Horizontal (a) and vertical (b) beam profiles after injection (0.2 s), at equilibrium after cooling (29.5 s) and after 30 s without cooling (59.4 s). Continuous evolution of beam width is shown in fig. 12.

CONCLUSIONS

The dependence of cooling efficiency and proton beam lifetime on electron beam position and angle was studied.

Beam lifetime does not appear to be sensitive to the electron beam angle in presence of cooling, even though the cooling force may drop significantly and equilibrium beam size become larger. Parallel displacement of electron beam courses more effect on beam lifetime. There is one optimal position, corresponding to coaxial alignment of two beams resulting in best lifetime. The expected significant losses in the case of proton beam being at the edge of the electron beam could not be observed, partly due to limitations of electron beam positioning. This experiment needs to be performed by moving the proton beam across the electron one and vice versa. The longitudinal cooling force was estimated by detecting the change of horizontal beam position at the IPM location in response to the change of electron energy. Dependence of transverse cooling force on electron beam current was studied. The value 300 mA was found to correspond to the maximum cooling force. The short-term lifetime drops with increase of electron current supporting the explanation of initial losses offered in [5, 7]. Mid-term lifetime improves with higher electron current, whereas the long-term one has maximum at about 110 mA. This can qualitatively be explained by the beam interaction with residual gas in conjunction with non-linear field of the electron beam. The optimal working point was found for the orbit used. However, during the tune scan the orbit was not controlled. For future cooling studies more attention should be paid to orbit smoothing, using the orbit optimization techniques that recently became available at COSY. The IPM performed well and delivered very useful data. Additional functionality of the data analysis software is under discussion. Online friction force calculation would make electron cooler adjustment easier. Profile fitting with a sum of Lorentz and Gauss distributions has been proposed to improve fit accuracy.

REFERENCES

[1] H. J. Stein et al., Present Performance of Electron Cooling at COSY-Jülich, Proceedings RuPAC2002.

[2] T. Giacomini et al., Development of Residual Gas Profile Monitors at GSI, Proceedings BIW04.

[3] K.B. Unser, "Beam current transformer with DC to 200 MHz range," IEEE Trans. Nucl. Sci., NS-16, June 1969, pp. 934-938.

[4] BERGOZ Instrumentation.

[5] A. Kobets et al., Loss Phenomena of Electron Cooled Ion Beams, IKP Annual Report 2006.

[6] PAX Collaboration, Technical Proposal for Antiproton–Proton Scattering Experiments with Polarization, http://arxiv.org/abs/hep-ex/0505054.

[7] Yu. Senichev et al., Electron Cooled Beam Losses Phenomena in COSY, Proceedings HB2010.

04 Hadron Accelerators

ELECTRON COOLING EXPERIMENTS IN CSR*

Xiaodong Yang[#], Guohong Li, Jie Li, Xiaoming Ma, Lijun Mao, Ruishi Mao,
Tailai Yan, Jiancheng Yang, Youjin Yuan , IMP, Lanzhou, 730000, China
Vasily V. Parkhomchuk, Vladimir B. Reva , BINP SB RAS, Novosibirsk, 630090, Russia

Abstract

The six species heavy ion beam was accumulated with the help of electron cooling in the main ring of Cooler Storage Ring of Heavy Ion Research Facility in Lanzhou(HIRFL-CSR), the ion beam accumulation dependence on the parameters of cooler was investigated experimentally. The 400MeV/u $^{12}C^{6+}$ and 200MeV/u $^{129}Xe^{54+}$ was stored and cooled in the experimental ring CSRe, the cooling force was measured in different condition.

INTRODUCTION

Heavy Ion Research Facility of Lanzhou(HIRFL)[1] is an accelerators complex with multi-purpose, its research field includes radioactive ion beam physics, heavy ion physics, high energy density physics, super-heavy elements synthesis, atomic physics, and cancer therapy. It consists of two cyclotrons, SFC and SSC, two synchrotrons, CSRm and CSRe. It can provide the ion beam with energy range from 10 MeV/u to 1GeV/u. The ion beam delivered from SFC or SSC was injected into CSRm, after accumulation with the help of electron cooling, and acceleration, and then delivered to cancer therapy terminal and other experimental terminals, or injected into CSRe. In CSRe, ion beam was cooled by electron cooling device, and various physics experiments were completed in this ring. The ion beam with higher energy in CSRe was stripped, and higher charge state ion beam will be decelerated to lower energy, in the case of low energy of higher charge state ion beam, atomic physics experiments will be performed in CSRe.

ELECTRON COOLING DEVICES

The electron cooling devices was equipped in each ring of CSR, the purpose of electron cooling in CSRm is ion beam accumulation, the cooler was adapted as the way to increase the stored particle number in CSRm, continuous electron cooling is applied to the stored ion beam for compensation of the heating by an internal gas jet target in CSRe, the most important feature is the ability to cool ion beam to highest quality for experiments with stored highly charged ions.

In CSRm, the electron cooling device plays an important role in the heavy ion beam accumulation at injection energy. The new state-of-the-art electron cooling device was designed and manufactured in the collaboration between BINP and IMP, it has three distinctive characteristics, namely high magnetic field parallelism in cooling section, variable electron beam profile and electrostatic bending in toroids.

Continuous electron cooling is applied to the stored ion beam for the compensation of the heating by various scattering in CSRe. The most important thing is the ability to cool the ion beams to the highest quality for physics experiments with stored highly charged ions. The electron cooling devices of HIRFL-CSR were reported in many conferences[2],[3],[4],[5],[6],[7],The previous results have been given in the COOL05-P02[8], COOL07-TUM1I02[9] and COOL09-FRM1MCIO02[10].

ION BEAM ACCUMULATION IN CSRM

In order to demonstrate the performance of HIRFL accelerators complex, and satisfy the requirements of different physics experiments, ion beam with different energy, different charge state were accumulated with the help of electron cooling in CSRm. During accumulation, two injection modes were applied, in the case of lighter ion beam, stripping injection was adapted, for heavier ion beam, repeated multi-turn injection was performed. Due to the injection beam intensity, ion beam was delivered by different injector, SFC or SSC. In the case of fixed energy, choose proper injection interval, partially hollow electron beam, the direction and position of electron beam and ion beam matched well, the maximum accumulation results can be achieved.

Commissioning procedure

The CSR commissioning procedure was described as following steps:

- Obtaining high transportation efficiency in beam line and maximal beam intensity at injection point.
- Correcting the position and angle of ion beam at the injection point, Obtaining the maximal injection intensity at first Faraday cup in the ring.
- Correcting the closed-orbit globally and locally, specially in the region of electron cooler, correcting work-point (without electron beam and with electron beam), improving ion beam lifetime in the ring.
- After turned on the cooler magnetic field, compensating the influence of cooler magnetic field, correcting the position and angle of ion beam entering cooler.
- Fine tuning the energy of electron, after observe accumulation, optimizing the electron beam current and the profile, improve the lifetime of ion beam in the present of electron beam.
- Optimizing injection interval, bump amplitude and time constant.
- Optimizing the ramping data, proper time setting of trigger for RF and kicker, acceleration to high energy

04 Hadron Accelerators

and extracted from CSRm.

Table 1: Accumulation results in CSRm

Ion	E_{inj} MeV/u	Injector	M	I_{inj} µA	ΔT_{inj} s	I_{single} µA	$I_{10 sec}$ µA
$^{12}C^{6+}$	7.09	SFC	ST	12	1.0	167	700
$^{12}C^{4+}$	7.1	SFC	MI	6	1.0	20	105
$^{36}Ar^{18+}$	21.7	SFC+SSC	MI	4	0.35	6	250
$^{129}Xe^{27+}$	2.9	SFC	MI	3	0.35	6.5	70
$^{12}C^{5+}$	8.26	SFC	MI	3	0.9	11	70
$^{78}Kr^{28+}$	4.04	SFC	MI	2.4	0.2	5	80

Some accumulation results were summarized in Table. 1. The I_{inj} indicated the beam intensity in the beam line, it was limited by the capability of injector. The ΔT_{inj} is the injection interval, it depends on the transverse cooling time, the electron cooling parameters for different ion beam with different energy. I_{single} is the average ion intensity in one standard multi-turn injection, it depends on the ion beam pulse length of injector. I_{10sec} is the final ion beam intensity accumulated in 10 sec, the cycle for ion beam accumulation. A typical DCCT signal of injection results of $^{12}C^{6+}$ was displayed in Fig. 1.
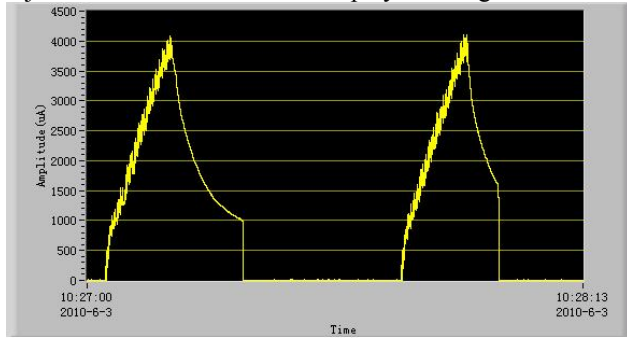
Figure 1: DCCT signal during $^{12}C^{6+}$ accumulation in CSRm.

Stripping injection

Firstly, the 7 MeV/u $^{12}C^{4+}$ was injected into CSRm from the small cyclotron SFC through a stripping foil with thickness of 15 µg/cm² placed in the first dipole of the ring, the average pulse intensity was about 8.4 µA in the injection line. In the absence of magnetic field of the electron cooler, the single-turn stripping injection beam was tested in CSRm with bumping orbit, the stored beam signal was observed from BPM signal, the closed orbit correction was done roughly, the machine parameter such as work-point was measured and tuned, and acceleration attempted. The average particle number of stored $^{12}C^{6+}$ was about 4.7×10^8 in one standard multi-turn injection. With the help of electron cooling of partially hollow electron beam, 2.5×10^9 particles were accumulated in the ring after 10 times injection in 10 seconds.

Due to intensive commissioning of Carbon ion beam in CSRm, some accumulation results were listed in Table. 2. The repeated multi-turn injection of $^{12}C^{6+}$ was attempted. $^{12}C^{4+}$ directly extracted from ECS ion source, and stripped into $^{12}C^{6+}$ in the beam line. The accumulation rate was about 3.5. In the later commissioning, the stripping injection was applied. The accumulation rate increased to 5.8 in the second row in Table 2. After fine tune the

electron cooling parameters, especially the position and angle between the ion and electron beams, shortened the injection interval, 2100µA $^{12}C^{6+}$ was obtained in 10 seconds. According to the gain formula, gain=repetition frequency×lifetime. It is helpful to increase the injection number, and to shorten the injection interval. In the latest commissioning, near 1.8×10^{10} particles were accumulated in 10 seconds.

Table 2: Accumulation parameters of ion beam

Ion	E_{inj} MeV/u	Injector	M	I_{inj} µA	ΔT_{inj} s	I_{single} µA	$I_{10 sec}$ µA
$^{12}C^{6+}$	7.09	SFC	MI	4.3	0.5	12.5	150
$^{12}C^{6+}$	7.09	SFC	ST	12	1.0	104	700
$^{12}C^{6+}$	7.09	SFC	ST	11	0.5	260	2100
$^{12}C^{6+}$	7.04	SFC	ST	8.4	0.25	400	4000

The two components accumulation fitting comparing with the experimental data was demonstrated in Fig. 2. From the results, the average intensity in one standard multi-turn injection was about 350µA, one part of ion beam decayed with the lifetime of 6 seconds, the other part of ion beam decayed with 0.35 seconds. In this condition, the measured work-point was 3.612/2.657, the improper work-point was the reason of short lifetime and fast decay of ion beam.
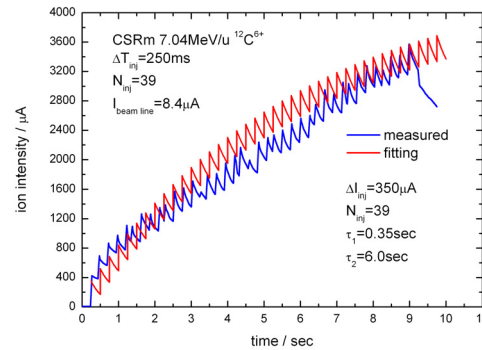
Figure 2: Two components decay fitting comparing with experimental data.

Repeated multi-turn injection

At the end of the transfer line, a magnetic septum and an electrostatic septum inflector guide the beam parallel to the ring orbit; four in-dipole coils create a DC bump of 50 mm amplitude at the electrostatic septum. For multi-turn injection four fast bump magnets produce a time dependent bump orbit to fill the horizontal acceptance of the ring.

After repeated multi-turn injection, the emittance of ion beam will be close to the transverse acceptance of the ring. And the radius of ion beam will be 3.8 cm in the cooling section. The ion beam is completely surrounded by the electron. The accumulation was improved in the case of bigger expansion factor.

Accumulation optimization experiments

The accumulation rate subjects to the cooling time and injection repetition rate. It is determined by the electron

04 Hadron Accelerators

beam parameters and injected ion beam stability. The optimum time interval between the two adjacent multi-turn injections corresponds to the transverse cooling time of ion. After observed the accumulation, the parameters related to accumulation were optimized experimentally. The dependence of accumulated ion intensity in 10 seconds on the injection interval was shown in Fig. 3. From this result, in the case of the injection interval with 0.25 seconds, the maximal ion intensity was obtained.
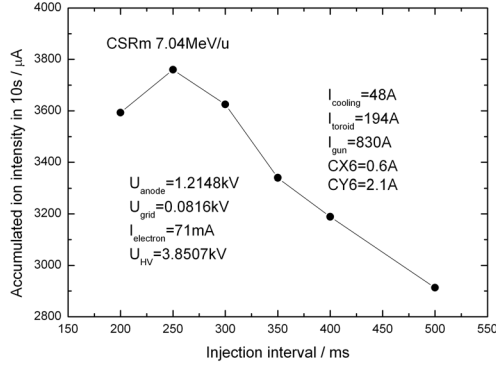
Figure 3: Accumulated ion intensity in 10s as a function of the injection interval.

The position and angle between ion and electron beams in the cooling section determined the cooling force and time. The accumulated ion intensity in 10s as a function of the current in cooling section correctors CX6 and CY6 were illustrated in Fig.4 and Fig. 5, the electron beam angles in horizontal and vertical direction with respect of ion beam were changed by these correctors. It's obvious that perfect alignment is helpful for obtaining maximum ion intensity. Due to the improper orbit of ion beam in the cooling section, the results were not as usual parabolic curve. The current regulation range of correctors was limited by the aperture of electrostatic bending plates in the toroids of cooler because of the condition of bigger expansion factor. Excessive regulation caused the fast increasing of the load current of high voltage system.
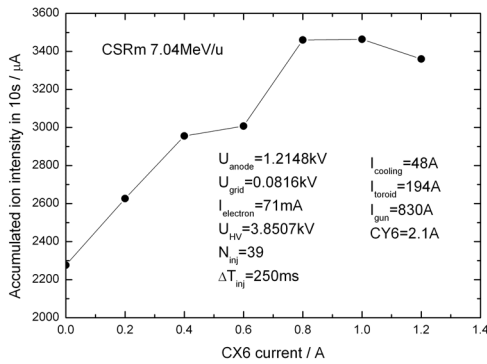
Figure 4: Accumulated ion intensity in 10s as a function of the current in cooling section corrector CX6.

The accumulated ion intensity in 10 s was measured as a function of the ratio U_{grid}/U_{anode} of electron gun at different electron current as presented in Fig. 6. It is clear

that optimum accumulation happens in the partially hollow electron beam, the ratio U_{grid}/U_{anode} is close to 0.1. In this case, the central density is less than the edge one in the electron beam. The energy of electron beam was fixed, the potential drop caused by the space charge of electron beam with a different profile was not taken into account in the experiments.
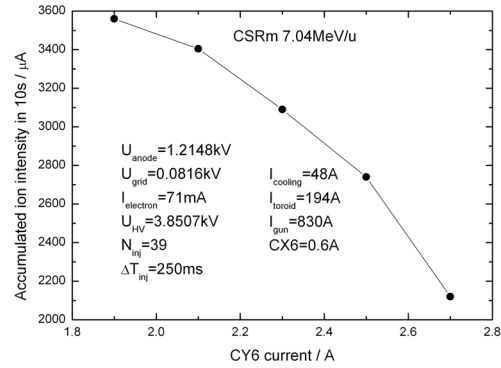
Figure 5: Accumulated ion intensity in 10s as a function of the current in cooling section corrector CY6.
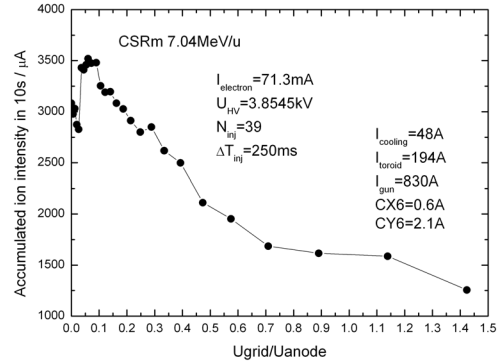
Figure 6: Accumulated ion intensity in 10s as a function of the ratio U_{grid}/U_{anode} of electron gun.
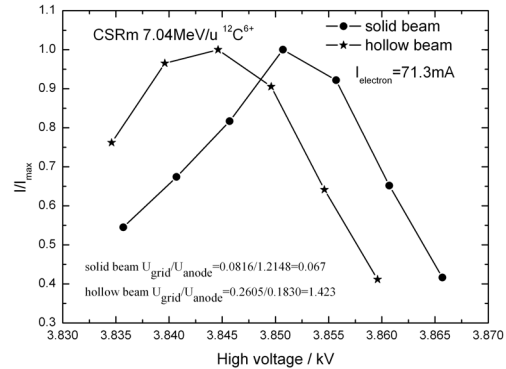
Figure 7: Accumulated ion intensity in 10s as a function of the energy for solid and hollow electron beam.

The optimal electron beam energy in the case of different electron beam profile was shown in Fig. 7. The intensity of ion beam was normalized by the maximum value. The electron beam current was kept fixed in the

experiments. It is clearly shown the effects of space charge for the solid and hollow electron beam.

ION BEAM COOLING IN CSRE

The ion beam of $^{12}C^{6+}$ was injected into CSRe from CSRm after acceleration from 7MeV/u to 200MeV/u. The magnetic field of electron cooler was set as a quarter of the maximum value. In this case, the magnetic field in the cooling section was 0.0385 T, and the electron beam current was set as 300 mA. After the global and local orbit correction and regulation of the electron beam angle and position in cooling section, the cooling was observed, but the cooling process was not fast enough. It could be caused by the poor quality of the high energy electron beam confined by a weak magnetic field in toroid, where additional transverse temperature was introduced. After increasing the magnetic field in toroid, increasing the electron beam current, improving the angle between ion beam and electron beam, about 14 seconds longitudinal cooling time was obtained. Then the ion beam was accelerated to 400MeV/u, the corresponding high voltage of electron cooler was 220kV, and the electron beam current achieved to 1A, a reasonable momentum spread of 3.2×10^{-5} was measured in the case of 600μA ion beam in CSRe. Some results have been reported in COOL'09[10].

In order to explore the minimum momentum spread, the ion beam was cut in the beam line before CSRm by means of changing the current of last quadrupole, it resulted in the DCCT in CSRm had no signal obviously. In this case, the particle number was less than 1.5×10^6 in CSRm, after acceleration, the particle number was less than 9×10^4 in CSRe, but the Sckottky monitor had the clear signal, the minimum momentum spread was measured as 1.35×10^{-5} demonstrated in Fig. 8. Generally, the measured minimum momentum spread was limited by the detection technique, stability of dipole power supply, the stability of high voltage power supply of cooler, and also the particle number stored in the ring.
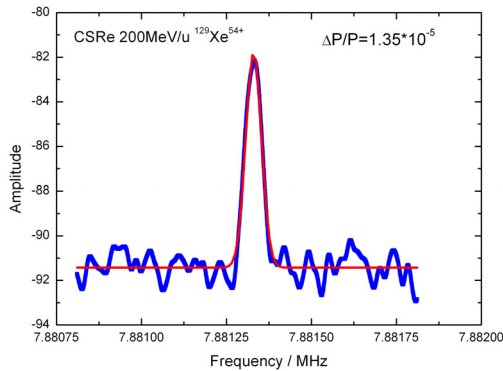
Figure 8: Measured Schottky signal of $^{129}Xe^{54+}$ in CSRe in the case of low ion beam intensity.

From the experience of CSRe cooler, the stability of dipole power supply and high voltage power supply of cooler should be improved in future. The detection technique should be upgraded to measure the momentum spread in the case of low ion intensity, and precision

calibration should be done for determine the stored particle number.
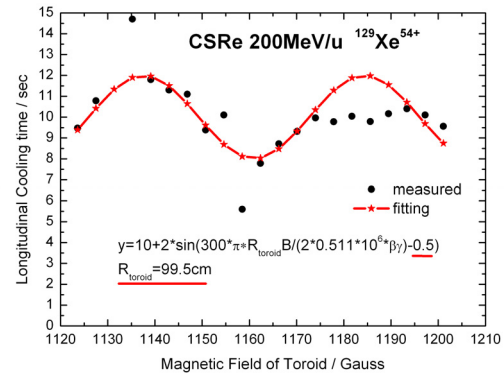
Figure 9: Longitudinal cooling time measured as a function of the magnetic field in toroid.

In the internal gas target experiments, the 200MeV/u $^{129}Xe^{27+}$ was stripped into $^{129}Xe^{54+}$ before entry of CSRe, and stored in CSRe. The longitudinal cooling time was measured as a function of magnetic field of toroid, the results was presented in Fig.9, the angle and position of the electron beam change during only regulating the current of toroid was not taken into account. From this result, one can see the dependence of cooling time on the magnetic field of toroid, it is good agreement with the results of GSI[12].
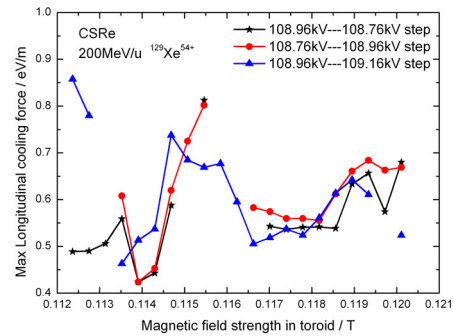
Figure 10: Maximum longitudinal cooling force as a function of the magnetic field in toroid in the case of different electron beam energy steps.

The influence of the magnetic field in toroid on the longitudinal cooling force for 200 MeV/u $^{129}Xe^{54+}$ beam was studied experimentally, longitudinal cooling forces were obtained by means of the electron energy-step method[11]. The cooling force varies with magnetic field in toroid was shown in Fig.10. The different line represents the different electron energy step. In the case of high energy, the influence of magnetic field on the electron transverse energy should be paid sufficient attention. The experimental results were in partially agreement with the experiment results in GSI[12].

From those results after the electron beam was switched off, the stability of high voltage system of CSRe cooler was derived. The data of high voltage (HV) was recorded as one file. Fig. 11 reveals the results of stability of HV of

CSRe cooler, the black line indicated the temperature from the monitor in the collector, the red line shown the signal from divider resistor 2 of HV system, one can find that as the change of temperature during 10 days, the output of high voltage changed with the temperature. From this point of view, the stability of HV system of CSRe cooler should be improved in the future.
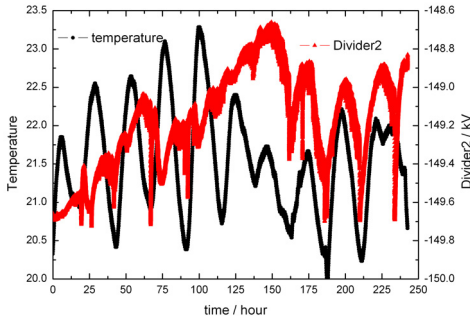
Figure 11: The temperature and divider2 voltage of CSRe cooler as a function of the time.

UPGRADE AND IMPROVEMENT

Due to the ion orbit was not in the centre of the compensation solenoid at the ends of electron cooler, when the current of compensation solenoid increased, the ion beam was not pass through the solenoid properly. It limited the increasing the working magnetic field in the cooler.

Various lifetimes were observed in different condition, it was caused by the improper setting of work-point of ring, in additional, the correction of closed-orbit was not carefully done during the operation, in this case the ion beam lost fast.

The work-point of ring varying with electron beam current of cooler was found in operation. This should be investigated experimentally in the future.

A special system of electron energy modulation was installed and tested in CSRm cooler, the energy of electron can be modulated in negative or positive deviation to the optimal value, the amplitude, pulse length and repetition frequency can be change according to the experiment requirements.

SUMMARY

- A few species heavy ion beam with different injection energy was cooled, accumulated and accelerated in CSRm.
- 400MeV/u $^{12}C6^+$ and 200MeV/u $^{129}Xe^{54+}$ was cooled with internal target in CSRe.
- Two cooling devices come into routine operation.
- Electron beam energy modulation system was installed and tested in CSRm cooler.
- Coolers were ready for physics experiments.

REFERENCES

[1] J.W Xia et al. "Heavy ion cooler-storage-ring synchrotron in Lanzhou", High Power Laser & Particle Beams, 2008, Vol.20, No. 11, 1787-1794.

[2] E. I. Antokhin, V.N. Bocharov., A. V. Bubley., et al "Conceptual project of an electron cooling system at an energy of electron of 350kV" NIM.A441(2000)87.

[3] V. N. Bocharov, A. V. Bubley, Y. Boimelstein et al "HIRFL-CSR electron cooler commissioning" NIM.A532(2004)144.

[4] E. Behtenev, V.N. Bochanov, A.V. Bubley, et al "Commission of electron cooler EC-300 for HIRFL-CSR", RuPAC XIX Dubna Russia 2004, 506-510.

[5] E. Behtenev, V.N. Bochanov, A.V. Bubley,, et al "Commission of electron cooler EC-300 for HIRFL-CSR", EPAC 2004 Lucerne Switzerland, 1419-1421.

[6] E. Behtenev, V.N. Bochanov, A.V. Bubley,, et al "Commission of electron cooler EC-300 for HIRFL-CSR", COOL'05, Galena, Illinois, U.S.A 18-23 September 2005, AIP Conference Proceedings 821 334-340.

[7] V.M.Veremeenko, R.V.Voskoboynikov, A.D. Gonchanov, et al "High voltage power supplies for ion beams electron coolers" , RuPAC 2006, Novosibirsk, Russia 97-99.

[8] X.D.Yang, V.V. Parkhomchuk, et al "Commissioning of HIRFL-CSR and its electron coolers" COOL'05, Galena, Illinois, U.S.A 18-23 September 2005, AIP Conference Proceedings 821 65-74.

[9] X.D.Yang et al. "Commissioning of electron cooling in CSRm", COOL'07, Bad Kreuznach, Germany, September, 2007, TUM1I02.pdf, 59-63.

[10] X.D.Yang, et al "Commissioning of electron cooling in CSRe" Proceedings of COOL 2009, Lanzhou, China FRM1MCIO02.pdf, 173-177.

[11] L.J.Mao, G. H. Li, J. Li et al "Cooling force measurements with variable profile electron beam at HIRFL-CSR" Proceedings of COOL 2009, Lanzhou, China THM1MCCO03.pdf, 107-110.

[12] P. Beller, K. Beckert, B. Franzke, et al "Observation of a reduction of recombination between ions and electrons" NIM.A532(2004)427.

ADVANCE IN THE LEPTA PROJECT

E.Ahmanova , V.Bykovsky, M.Eseev[*], V.Kaplin, V.Karpinsky, A.Kobets[#,**],
V.Lokhmatov,V.Malakhov, I.Meshkov, V.Pavlov, R.Pivin, A.Rudakov,
A.A.Sidorin, S.Yakovenko, JINR, Dubna

Abstract

The Low Energy Positron Toroidal Accumulator (LEPTA) at JINR is close to be commissioned with circulating positron beam. The LEPTA facility is a small positron storage ring equipped with the electron cooling system and positron injector. The maximum positron energy is of 10 keV. The main goal of the project is generation of intensive flux of Positronium (Ps) atoms - the bound state of electron and positron, and setting up experiments on Ps in-flight. The report presents an advance in the project: up-grade of LEPTA ring magnetic system, status of the construction of positron transfer channel, and the electron cooling system, first results of low energy positron beam formation with ^{22}Na radioactive positron source of radioactivity of 25 mCi.

LEPTA RING DEVELOPMENT

The Low Energy Particle Toroidal Accumulator (LEPTA) is designed for studies of particle beam dynamics in a storage ring with longitudinal magnetic field focusing (so called "stellatron"), application of circulating electron beam to electron cooling of antiprotons and ions in adjoining storage electron cooling of positrons and positronium in-flight generation.

For the first time a circulating electron beam was obtained in the LEPTA ring in September 2004 [1]. First experience of the LEPTA operation demonstrated main advantage of the focusing system with longitudinal magnetic field: long life-time of the circulating beam of low energy electrons. At average pressure in the ring of 10^{-8} Torr the life-time of 4 keV electron beam of about 20 ms was achieved that is by 2 orders of magnitude longer than in usual strong focusing system. However, experiments showed a decrease of the beam life-time at increase of electron energy. So, at the beam energy of 10 keV the life time was not longer than 0.1 ms. The possible reasons of this effect are the magnetic inhomogeneity and resonant behaviors of the focusing system.

Magnetic and vacuum system improvements

During March-May 2009 new measurements of the longitudinal magnetic field at solenoids connections were performed. According to the measurement results water cooled correction coils have been fabricated and mounted. As result, the inhomogeneity has been decreased down to $\Delta B/B \leq 0{,}02$ (Fig.1).
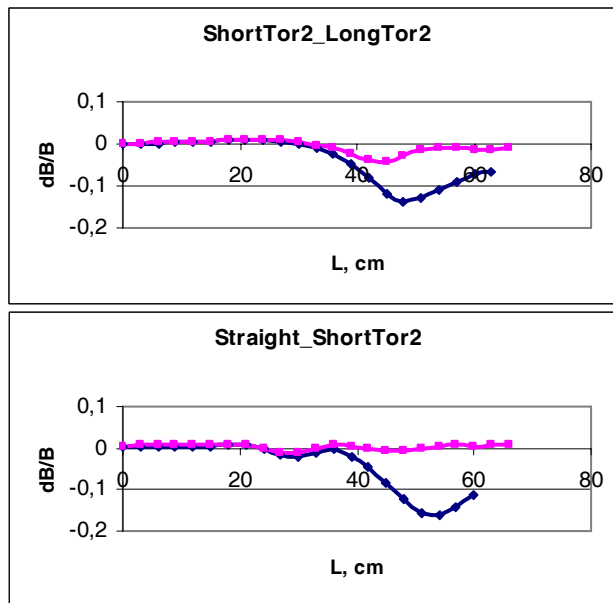
Figure 1: Magnetic field distribution along the toroidal solenoid axis.

The new water cooled helical quadrupole lens was designed and fabricated that allowed us to improve significantly the vacuum conditions in the straight section.

In old design the distance between kicker plates was off 32 mm that limited the aperture. New kicker design allows us to increase aperture up to 120 mm.

Testing after upgrading

After all the improvements and modifications the ring has been reassembled, the electron beam circulation has been obtained again and its life time has been remeasured.

Typical life time dependence on electron energy, $\tau_e(E_e)$, has two slopes (Fig.2). The left one, where τ_e increases with E_e, is defined by electron scattering on residual gas. The right slope, descending with E_e, relates to violation of electron motion adiabaticity on inhomogeneities of solenoid magnetic field.

The curves 1 and 2 were obtained in 2005, whereas the curves 3, 4 and the point 5 have been measured in June 2008. The curve 6 was measured in August 2009, after all modifications of the ring described above. One can see significant increase of the electron life time. Of the main importance is the increase of the life time (comparing with the values of the year 2005, 2008) in the energy range above 4 keV by 6÷10 times. It proves the necessity

_____
[*] M.V.Lomonosov Pomor State University, Russia.
[**] Joint Institute for Nuclear Research, Russia,
    Institute of Electrophysics and Radiation Technologies, Ukrain
[#] kobets@jinr.ru

03 Linear Colliders, Lepton Accelerators and New Acceleration Techniques

of a further improvement of the solenoid field homogeneity.
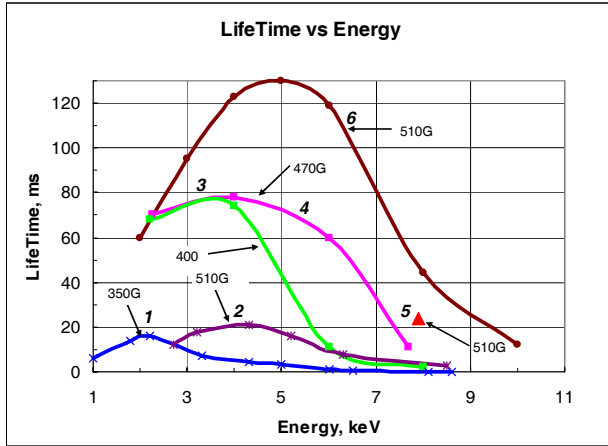
Figure 2: LifeTime vs electron energy.

An essential influence of magnetic field quality on τ_e value is demonstrated in Fig.3: the lifetime of 8 keV electrons increases significantly with correction coil current enhancement.
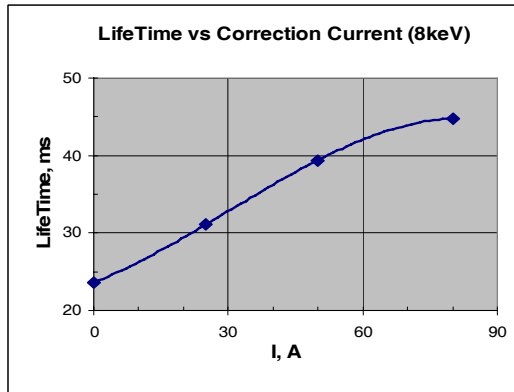
Figure 3: Lifetime vs correction coil current at electron energy of 8 keV.

Electron cooling system construction

The manufacturing of the system for generation, transportation and energy recovering of single pass electron beam has been completed. Test of the electron beam transportation from the gun to the collector begun in pulsed mode and continued in DC mode of the gun operation. Result is in Table 1.

Table 1. Parameters of electron cooling system

Electron energy	Current		
	Ie, mA	ΔIe, uA	ΔIe/Ie
3	20	230	0,011
5	50	290	0,006
7	64	620	0,01
8,7	105	430	0,004

Positron transfer channel

The channel is aimed to transport positrons extracted from the trap of the injector (see below) and accelerate them up to 10 keV (maximum) in electrostatic field in the gap between the trap and the channel entrance. The designing and manufacturing of the channel elements was completed in 2010. The manufacturing of solenoids of the positron beam transfer channel is in progress presently.

TEST OF THE NEW POSITRON SOURSE

The slow monochromatic positron flux is formed from broad spectrum of positrons from radioactive isotope ^{22}Na. The positrons with energy up to 0,54 MeV are moderated to the energy of few eV in the solid neon [2]. The neon is frozen on the copper cone surface where capsule with isotope is located (Fig.4).
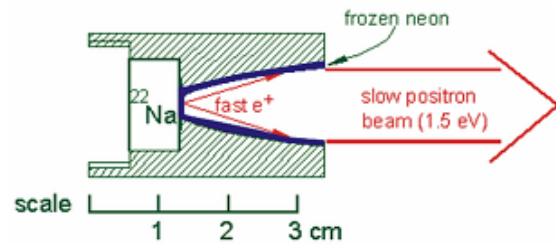
Figure 4: Positron moderation principle.

^{22}Na positron source of activity of 25mCi for LEPTA facility has been donated by iThemba LABS (RSA) and transferred to JINR in Febrary 2008. After completion of the very long procedure of formalities it was mounted in the LEPTA injector and tested.

To detect slow positron flux we used microchannel plate (MCP) detector and scintillater detector both working by coincidence scheme and independently. Integral spectra of slow positrons were measured with MCP and electrostatic analyzer - a short drift tube suspended at variable positive potential. The fitting of the experimental results are presented (Fig. 5).
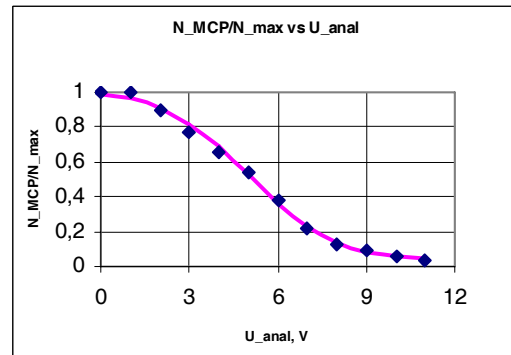
Figure 5: Gaussian fitting of positron energy spectrum curve measured at T = 7,35 K, d = 10 mcm, $(dN/dE)_{max}$ = 5.5 eV, spectrum width σ = 2.3 eV.

Maximum flux of slow positrons determined by standard method for coincidence scheme was equal:

$$N_{max} \approx 1.5 \cdot 10^5 \text{ positrons/ sec.}$$

03 Linear Colliders, Lepton Accelerators and New Acceleration Techniques

THE POSITRON TRAP

When slow positron beam is formed, it enters the Penning-Malmberg trap where the positron cloud is accumulated [3]. The trap is a device which uses static electric and magnetic fields to confine charged particles using the principle of buffer gas trapping. The confinement time for particles in the Penning-Malmberg traps can be easily extended into hours allowing for unprecedented measurement accuracy. Such devices have been used to measure the properties of atoms and fundamental particles, to capture antimatter, to ascertain reaction rate constants and in the study of fluid dynamics. The JINR positron trap (Fig. 6) was constructed to store slow positrons and inject positron bunch into the LEPTA ring.

The research of the accumulation process was carried out using electron flux. For this purpose the test electron gun allowing to emit $dN/dt = 1*10^6$ electrons per second with energy 50 eV and spectrum width of a few eV was made. These parameters correspond to slow monochromatic positron beam which we expect from a radioactive source at activity of 50 mCi.
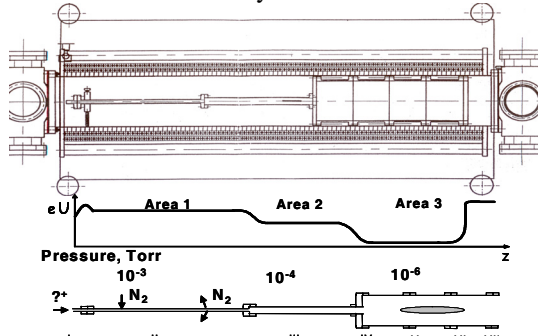
Figure 6: Assembly drawing of the positron trap (upper picture), potential and pressure distributions along the electrode system.

Electron accumulation in the trap with application of rotating electrical field so called "rotating wall" (RW)[4], was studied during December 2006 and repeated in July 2009. The test electron beam shrinking was observed when RW parameters were optimized (Fig.10).
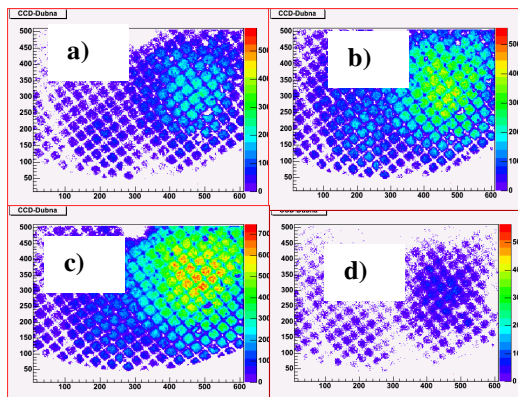
Figure 10: Profiles of the stored test electron beam at different storage time: a) 5s, RF On; b) 20s, RF On; c) 50s, RF On, d) 30s, RF Off.

THE POSITRON INJECTOR

In summer 2010 the slow positron source and the trap have been assembled. The first attempts of slow positron storage were performed (Fig.11) and stored positrons were extracted to the collector.
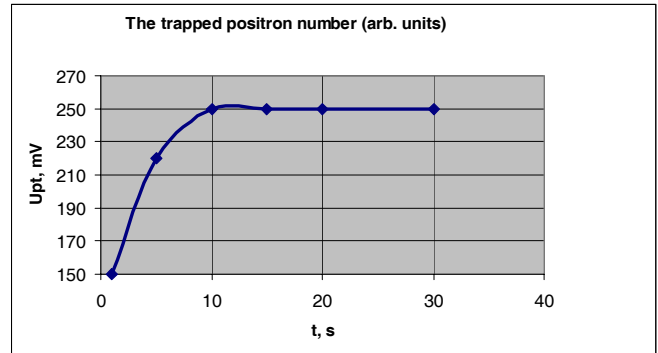
Figure 11: The trapped positron number vs storage time.

Upt is the amplitude of the signal from the phototube (PT), RW amplitude is equal to 0.5 V.

CONCLUDING REMARKS

The development of the LEPTA project is approaching the stage of experiments with circulating positron beam. All main elements of the ring and the injector are ready and have been tested.

REFERENCES

[1] A.Kobets, et. al., Status of the LEPTA project, proceeding of Beam Cooling and Related Topics, http://accelconf.web.cern.ch/accelconf/

[2] A. P. Mills, Jr. and E. M. Gullikson, "Solid Neon Moderator for Producing Slow Positrons". Appl. Phys. Lett. 49, 1121 (1986)

[3] M. Amoretti et al., The ATHENA antihydrogen apparatus, Nucl. Inst.Meth. Phys. Res. A 518 (2004) 679-711

[4] C.M.Surko, R.G.Greaves, Radial compression and inward transport of positron plasmas using a rotating electric field, Phisics of plasmas, 8 (2001), 1879-1885.

03 Linear Colliders, Lepton Accelerators and New Acceleration Techniques

ELECTROSTATIC STORAGE RINGS AT THE ULTRA-LOW ENERGIES RANGE

A.I.Papash, Max Planck Institute for Nuclear Physics, Heidelberg, Germany and
Joint Institute for Nuclear Research, Dubna, Russia
C.P.Welsch, University of Liverpool, UK and
The Cockcroft Institute for Accelerator Science and Technology, UK

Abstract

Electrostatic storage rings have proven to be invaluable tools for atomic and molecular physics at the ultra-low energy range from 1 to 100 keV/A. Due to the mass independence of the electrostostatic rigidity, these machines are able to store a wide range of different particles, from light ions to heavy singly charged bio-molecules. A so-called "reaction microscope", incorporated into the ring is considered to be a powerful tool to study fundamental effects by multiple crossing of the stored ion beam with an ultrasonic gas jet. To enable the operation of such internal experiment, one needs to provide very short beam pulses in the 1-2 nanosecond range to pave the way for kinematically complete measurements of the collision dynamics of fundamental few-body quantum systems on the level of differential cross sections. However, earlier measurements at some rings showed strong limitations depending on beam intensity, probably linked to non-linear fields that cannot be completely avoided in such machines. In this contribution, we discuss common features of electrostatic storage rings and analyze the performance of such rings.

INTRODUCTION

Magnetic storage rings operates not only in high energy range but also at low energies. In particular, the LEAR ring at CERN was the first machine to store, cool and decelerate antiprotons down to only 5 MeV [1]. $^4He^-$ and $^{12}C_{70}^-$ ions have been stored at energies of 5 and 25 keV respectively in the ASTRID magnetic ring [2].

The first electrostatic ring was built in 1953 to act as an electron analogue of the Brookhaven AGS synchrotron [3]. Ions are stored in electrostatic traps at lowest energies [4,5]. Another type of storage device complinmentary to traps and developed in response to the needs of the astro-, atomic and molecular physics communities, are Electrostatic Storage Rings (ESR) [6]. As opposed to magnetic storage rings, ESR have no lower limit on the beam energy as well as no upper mass limit on the ion mass that can be stored. Due to the mass independence of the electric fields, massive particles such as clusters and bio-molecules can be stored at lowest energies. ESR were already used to study the following problems [4,6,7]:

- Collision phenomena and plasma properties of astrophysical objects i.e.molecular clouds, quasars;
- electron impact rotational and vibrational excitation of cold molecular ions;
- quantum reaction dynamics of cold molecular ions;

- gas-phase spectroscopy of biomolecular ions;
- ultra-cold (2 K) ESR will allow to store molecular ions in their rotational ground state;
- rotational effects in the process of dissociative recombination of molecular ions with low temperature electrons (<10 K);
- molecular dynamics - to achieve Coulomb cristalli-zation for a fast strored beam and study phase transition to a cristalline beam;
- fundamental few body Coulomb problem for single as well as for multiple ionisation;
- measurements of single and multiple ionization cross-sections (total and differential) of antiprotons colliding with atoms of supersonic gas jet;
- ion-impact ionisation to benchmark theoretical predictions;
- anti-hydrogen studies by merging antiprotons with positrons;
- study of the lifetime of metastable atomic states;
- investigations of the single component plasma.

COMMON FEATURES OF ELECTROSTATIC STORAGE RINGS

ESR are in some way complimentary to ion traps and allow reducing the ion energy to almost ground state. In ESR, ions circulate in one direction while in ion traps there is no designated direction of motion. One can outline the following common features of all ES rings:

- ESR can store ions at keV energies and potentially even lower energies;
- Their fields are mass independent, i.e. –a wide range

Table 1. Electrostatic storage rings worldwide

Ring	ELISA [9,10]	ESR [11]	FRR [13]	DESIREE [14]	CSR [18,19,20]	USR [21,22,23]	AD-REC [24]
Location	Aarhus Univ. Danmark	KEK Tsukuba Japan	Frankfurt Univ. Germ	Stockholm Univ. Sweden	MPI Heidelberg Germany	FAIR-GSI Darmstadt Germany	ASACUSA CERN Switz
Ions	A ≤ 100	A ≤ 100	A ≤100	A ≤ 100	A ≤ 100	antiprotons	antiprotons
Energy, keV	(5–25)·Q	20·Q	50	(25-100)·Q	(300-20)·Q	300-20	3-30
Type	Racetrack	Race track	Race track	2 x Race tracks	quadratic	Achromat quadratic	Low beta racetrack
Symmetry	2	2	2	2 x 2	4	4	2
Perimeter, m	7.62	8.14	14.17	9.2 x 9.2	35.2	43	7.9
Revolution time, μs	3.5 (p) 93 (C_{80})	4 (p) 22 (N_2^+)	4.5 (p)	4–60	4–180	5.67–22	10–3
ES Deflectors	160°+10°	160°+10°	75°+15°	160°+10°	39°+6°	37°+8°	90°+90°
Defl.Rad mm	250	250	250	250	2000+1000	2000+1000	400
Deceleration/ acceleration	Drift tube	Drift tube	--	--	Drift tube 10 V	Drift tube 10 V	Pulsed injector
e-cool eV	NO	NO	NO	NO	10	10	NO
life time, s	10-30	12-20	--	--	10–100	~10	~20 ms
Operation modes	storage	Storage	D=0 at target	Colliding beams	Cooling storage	Short bunch Slow extr.	Low beta Low Disp.
Vac. mbar	10^{-11}	$5·10^{-11}$	10^{-12}	10^{-12} (10°K)	10^{-15} (2°K)	10^{-11}	10^{-10}
Status	operate	operate	tested	Project	manufact.	Design	Manufact.

of particles, from light protons and antiprotons to heavy molecular ions, with positive and negative charge, can be stored;

- no remanent fields and no hysteresis effects;
- Fast acceleration/deceleration can be realized because of the absence of eddy currents

A clear advantage is that in-ring experiments with the circulating ions can be done over many turns, thus multiplying the number of interactions. This is in contrary to single pass experiments realized for example behind the RFQ-D at CERN [8]. Electrostatic rings are compact and relatively cheap with respect their magnetic counterparts. The parameters of some electrostatic storage rings are shown Table 1.

The first electrostatic ring dedicated to atomic physics experiments was built in Aarhus, see Fig.1 [9]. In ELISA, two 160° cylinder deflectors and two 10° parallel plate deflectors, together with four sets of electrostatic quadrupoles form a simple racetrack structure, as seen in Fig.2 [10]. The split deflectors allow for a detection of neutral particles at the end of the straight sections and for simple injection into the machine. Initially, ELISA was equipped with 160° deflectors of spherical shape in order to provide equal focusing in both, the horizontal and vertical plane. The ring performance with spherical deflectors was rather poor. Analytical [11] and computer [12,13] studies indicated that sextupole component of the electric field distribution for the spherical deflector is four times as large as for the cylindrical one and dynamic aperture a few times smaller. Since then ESR operate with deflectors of cylindrical shape. Rings with similar lattice were built at KEK [14] and Tokyo University [15].

In the Frankfurt Storage Ring (FSR) 90° bends are split into 75° deflectors of cylindrical shape and 15° parallel plate deflectors, see Fig.3 [16]. Electrostatic triplets are located in the short sides, between two cylindrical deflectors. Quadrupole doublets in the long straight sections give rise to a low beta-function of $\beta_{x,y} \approx 0.2$ m at

Figure 3. Schematic view of the Frankfurt Storage Ring: CD–75° cylindrical deflector, PPD–15° parallel plate deflector, Q4Q5Q4 – electrostatic triplet [16]

the interaction point. The dispersion function is changing sign at this point and a sharp beam focus of 3x4 mm^2 is available in four locations around the ring.

In the DESIREE double ring project, two ESR of the same racetrack type as ELISA were overlapped, to allow for ion-molecular head-on collision studies [17].

CRYOGENIC STORAGE RING (CSR)

The Cryogenic Storage ring (CSR) at the MPI for Nuclear Physics in Heidelberg, Germany is a next-generation low energy storage ring for essentially all ion species – from hydrogen ions up to molecular ions, macro- and biomolecules, clusters, atomic ions at extreme charge states, etc. [18]. The kinetic energy of the stored ions is between 20 and 300 keV. In order to provde unique collision and blackbody radiation-free environ-ment for radiative relaxation of molecular species and for long time storage of keV beams all ring components are cooled down to ~2 K. Vacuum better than 10^{-15} mbar is anticipated [19]. Special attention had to be paid to a precise and stable ion optics alignment under the substantial thermal shrinking and displacement during cool-down of the ring. The ring has a lattice with a four-fold symmetry and accommodates a reaction microscope, electron cooling, injection, and an RF drift tube in its 2.8 m long straight sections, see Fig.4 [20].

Figure 1. Photograph of the electrostatic storage ring ELISA [9].
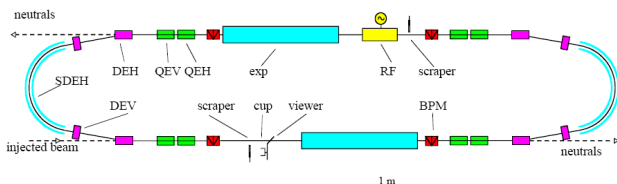
Figure 2. Layout of ELISA storage ring. Neutrals can be detected behind the 10° parallel plate deflectors - DEH [10].
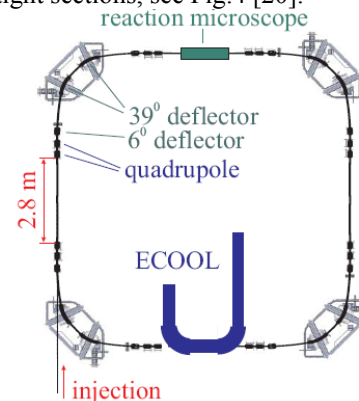
Fig.4.The CSR ring has a 4-fold symmetric lattice, each cell consists of two 39°, two 6° deflectros and two quadrupole doublets [20].

ULTRA-LOW ENERGY STORAGE RING

In the future Facility for Low-energy Antiproton and Ion Research (FLAIR) at FAIR, the USR will provide cooled beams of antiprotons down to energies of 20 keV

01 Circular Colliders

[21]. The planned experiments with both, slow and fast extracted, external beams, as well as in-ring experiments with ultra-short bunches in combination with a reaction microscope demand a very flexible ring lattice, see Fig.5 [22]. Four dispersion-free straight sections, each 4 m long, are used for the electron cooler, the decelerating drift tube, the elements for fast/slow extraction, different rf systems for the short bunch operation mode and the reaction microscope [23]. One section is kept free for a possible inclusion of a merged positron ring. Five electrostatic quadrupoles, two 8° and two 37° electrostatic deflectors form an achromatic 90° bend.
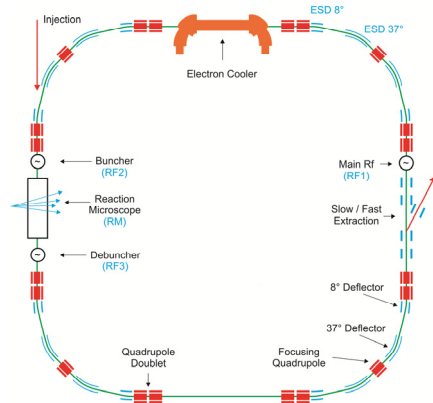
Figure 5. Layout of the Ultra-low energy Storage Ring [22].

ANTIPROTON RECYCLER (AD-REC)

A small recycling ring (AD-REC) in energy range 3 to 30 keV has been designed for use on the Musashi beamline at the CERN-AD [24]. Ring enables differential ionization cross-section measurements by incorporating the reaction microscope, see Fig.6. Four sets of ESQ triplets in the long straight sections are moved as close as possible to each other provide a sharp focus. Dispersion function in the middle of the straight section is reduced to an acceptable low value.
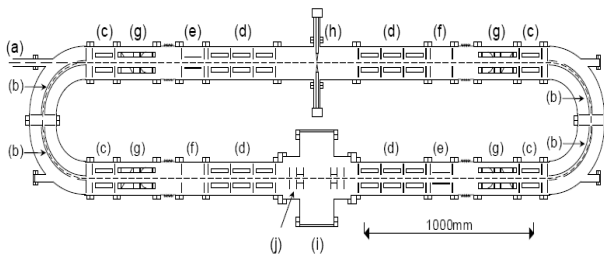
Figure 6. AD-REC cross-section: (a)-injected beam, (b)-90° deflectors, (c,d)-ES quads (e,f,j)-correctors, (g)-beam position monitors, (i)-reaction microscope chamber [24].

ACKNOWLEDGMENTS

REFERENCES

[1] P.Lefèvre, D.Möhl. "A Low Energy Accumulation Ring of Ions for LHC".CERN/PS **93-62**(DI) 259 (1993).

[2] S.Moller."The Aarhus Storage Ring for Ions and Electrons ASTRID".Proc.PAC-1993, Washington, USA (1993).

[3] M.Plotkin. "The Brookhaven Electron analogue. 1953-1957". BNL Report **45058** (1991).

[4] D.Zajfman et al. „Physics with electrostatic rings and traps". J.Phys.B: At.Mol.Opt.Phys. **37** (2004).

[5] P.Reinhed. "Ions in cold electrostatic storage devices". PhD Thesis. Stockholm University (2008).

[6] C.P.Welsch et al., "Exploring Sub-Femtosecond Correlated Dynamics with an Ultra-low Energy Electrostatic Storage Ring", C.P. Welsch, J. Ullrich, "FLAIR – A Facilty for Low-Energy Antiproton and Ion Research at GSI", Hyperfine Interactions, **172** (1-3) 71-80 (2007)

[7] D.Zaifman, J.Ullrich, C.P. Welsch. "Physics with colder molecular ions: The Heidelberg Cryogenic Storage Ring CSR". Journal of Physics. Sixth Int. Conf. on Dissoc. Recombination. V.**4**, Iss.1. (2005).

[8] R.Hayano et al. "ASACUSA Status Report-2010". CERN-SPSC-2010-005/SPSC-SR-056 (2010).

[9] S.Moller. "Design and first operation of the electro- static storage ring ELISA". EPAC, Stockholm, Sweden (1998).

[10] S.Moller and U.Pedersen. "Operational experience with the electrostatic Storage ring ELISA". PAC, USA (1999).

[11] Yu.Senichev. "Beam Dynamics in Electrostatic Rings". Proc. EPAC, Vienna, Austria (2000).

[12] A.Papash, O.Gorda, C.P. Welsch, "Simulations of Space Charge effects in Low Energy Electrostatic Storage Rings". Proc. Int. Part. Accel. Conf., Kyoto, Japan (2010).

[13] O.Gorda, A.Papash. "Non-linear fields of cylindrical and spherical deflector and their effect on beam dynamics in the ELISA ring". QUASAR Group internal report (2010).

[14] T.Tanabe, K.Noda. "Storage of bio-molecular ions in the electrostatic storage ring". NIM A, **496** (2003).

[15] T.Azuma. "Development of an LN$_2$ cooled electro-static ion storage ring". Worksh. on Atomic Collisions of Slow/ Trapped Highly-Charged Ions. RIKEN, Japan (2004).

[16] V.Aleksandrov et al. "Optical Scheme of an Electro-static Storage Ring". EPAC-2006, Edinburg, Scotland (2006).

[17] P.Löfgren et al. "Status of the Electrostatic and Cryogenic Double ring DESIREE". EPAC-2008 Genoa, Italy (2008).

[18] J.Ullrich et al., "Next-Generation Low-energy Storage rings for Antiprotons, Molecules, and Atomic Ions in extreme Charge States". Proposal to the Max Planck Society (2004).

[19] R. von Hahn et al., "CSR – a Cryogenic Storage Ring at MPI-K". Proc.EPAC-2004, Lucerne, Switzerland (2004).

[20] H. Fatil et al., "Finite elements Calculations of the Lattice and Ring Acceptance of the Heidelberg CSR". Proc.EPAC-2006, Edinburg, Scotland (2006).

[21] C.P. Welsch et al. "The Ultra-low Energy Storage Ring at FAIR: Lattice design, operating modes and beam diagnostics". Phys .Rev. Special Topics: Accelerators and Beams PRST-AB20100304 (2010), submitted

[22] A.I.Papash, C.P.Welsch. "An update of the USR lattice: towards a true multi-user experimental facility". PAC-2009 Vancouver, Canada (2009).

[23] A.I.Papash, C.P.Welsch, "Realization of nanosecond antiproton pulses in the ultra-low energy storage ring". NIM A (2010), doi:10.1016/j.nima. 2010.03.153.

[24] M.R.F. Siggel-King et al., "Electrostatic Low-Energy Anti-proton Recycling Ring".Hyperfine Interactions (2010).

RESEARCH OF PHOTON EMISSION OF 120 GEV CHANNELING POSITRONS

V.A. Maisheev, Y.A. Chesnokov, P.N. Chirkov, I.A. Yazynin, IHEP, Protvino, Russia
D. Bolognini, S. Hasan, M. Prest, Università dell'Insurbia, Milano; E. Vallazza, INFN, Trieste, Italy

Abstract

The motion of positrons in the interplanar nonlinear potential of a straight thin Si crystal and radiation spectra are calculated.

INTRODUCTION

By this time the considerable number of experimental and theoretical works is devoted to researching the radiation at plane channeling of high energy positrons in monocrystals [1, 2, 3]. This radiation arises during the motion of a charged particle under a small angle in relation to a crystallographic plane and for positrons with energies up to ~20 GeV is monochromatic enough and is characterized by high intensity. At energies of positrons more than ~20 GeV monochromaticity of the radiation strongly degrades. In September, 2009 in CERN the experiment INSURAD devoted to research of radiation at various orientations of bent monocrystals has been made at energy of positrons of 120 GeV. The radiation type of a relativistic particle depends on the value of multipole parameter ρ. When $\rho \ll 1$ it corresponds to the interference type (dipole approximation) of the radiation formed along sufficiently large length of the crystal. The case with $\rho \gg 1$ is close to the synchrotron radiation. At energies of positrons 100 GeV and more the parameter ρ can exceed 20 units for a considerable part of the particles.

In the given work we wish to receive the following results: to define characteristic parameters of motion of an ultrarelativistic particle in real plane potential of a monocrystal and to study the influence of its nonlinearities on ensemble of particles captured in a mode channeling; to calculate radiation spectrums of positrons with energies an order 100 GeV at their different entry initial conditions on an input in a monocrystal.

INTERPLANAR ONE–DIMENSIONAL MOTION OF CHANNALED POSINRONS

The motion of a charged ultrarelativistic particle in the interplanar electric field D of a monocrystal can be described by the following system of equations

$$\frac{E}{c^2}\frac{d^2x}{dt^2} = e\mathrm{D}(x), \quad \frac{d^2y}{dt^2} = 0, \quad \frac{ds}{dt} = c\left(1 - \frac{1}{2\gamma^2} - \frac{1}{2c^2}\left(\left(\frac{dx}{dt}\right)^2 + \left(\frac{dy}{dt}\right)^2\right)\right),$$

where: x, y, s - the Cartesian co-ordinates of a particle (the electric field D is directed along the axis x); E, e, γ - energy, charge and gamma factor of a particle, accordingly; t - time, c - velocity of light. The first equation describes periodic motion along x, the third equation reflects the influence of transverse motion on longitudinal one. From the above equations it is seen that the problem of finding the trajectory of a particle in three-dimensional space is reduced to finding the function $x(t)$.

We will consider periodic (generally nonharmonic) motion of positrons with energy of $E = 120$ GeV in the interplanar potential of a straight crystal Si with orientation (011). The interplanar potential is calculated for silicon at a room temperature as it is described in work [4]. The interplanar potential of interaction of a positron in a straight crystal is defined by expression [4, 5]

$$U(\xi) = -\frac{d}{2}\sum_{k=1}^{7}\frac{\alpha_k}{2k}\xi^{2k}, \tag{1}$$

where:: $\xi = 2x/d$ - normalized interplanar coordinate, $\xi \in [-1,+1]$; $d = 1.92 \text{\AA}$ - interplanar distance in (011) channel; $\vec{\alpha} = (-32.21 \; 13.86 \; -443.78 \; 234052 \; -531505 \; 481.79 \; -137513)$ in [eV/Å]; such values of $\vec{\alpha}$ provide $dU/d\xi = 0$ at $\xi = \pm 1$.

In a Fig. 1 the dependence of normalized frequency $\Omega(\xi_m) = \omega(\xi_m)/\omega_o$ on the amplitude of periodic motion is shown, where: $\omega_o = (2|\alpha_1|c^2/Ed)^{1/2} \cong 5.013 \times 10^{13}/\text{sec}$ - frequency of oscillations with small (zero) amplitudes in the potential hole $U(\xi)$. The maximum displacement of periodic motion is interpreted as amplitude ξ_m. The motion of a positron in normalized potential well $\widetilde{U}(\xi) = 2U(\xi)/|\alpha_1|d$ is described by the canonical equations

$$d\xi/d\tau = p \quad \text{и} \quad dp/d\tau = -d\widetilde{U}(\xi)/d\xi, \tag{2}$$

where: $\tau = \omega_o t$ - the dimensionless time (phase); $p^2/2 + \widetilde{U}(\xi) = \varepsilon$ - the transverse energy (integral of motion). Maximum deviation (amplitude) $\xi_m(\varepsilon)$ is defined from equation $\widetilde{U}(\xi_m) = \varepsilon$. The dependence of normalized frequency Ω on amplitude ξ_m is determined by

$$\Omega(\xi_m) = 1/\frac{4}{2\pi}\int_0^{\xi_m} d\xi/\sqrt{2(\widetilde{U}(\xi_m) - \widetilde{U}(\xi))}.$$

The multipole parameter ρ is expressed through parameters of plane periodic motion of a particle as follows [1]: $\rho = 2\gamma^2 < (\upsilon_x/c)^2 >$, where the averaging is taken over the motion period. For the channeled positron with the given ξ_m we have

$$\rho(\xi_m) = \gamma^2\kappa^2\Omega(\xi_m)\frac{4}{\pi}\int_0^{\xi_m}\sqrt{2(\widetilde{U}(\xi_m) - \widetilde{U}(\xi))}\, d\xi,$$

where $\kappa = d\omega_o/2c \cong 16.052 \cdot 10^{-6}$. In Fig. 2 (the continuous line) the exact dependence of multipole parameter on

02 Synchrotron Light Sources and FELs

amplitude ξ_m is shown. Thus, at the given potential both dipole and magnetic bremsstrahlung radiation types can be realized.

The received frequencies correspond to nonlinear (not harmonic) oscillations. The closer ξ_m to 1, the stronger difference of periodic motion from the harmonic one. Comparison at given ξ_m of the exact numerical decision of the equation of motion with approximating harmonic oscillation

$$\xi = \xi_m \cos(\Omega(\xi_m) \cdot \tau) \qquad (3)$$

with the same ξ_m and frequency $\Omega(\xi_m)$ shows that practically in all range $0 \leq \xi_m \leq 0.980$ we can consider the motion of channeled positrons to be the harmonic one. In harmonic approximation (3) the expression for multipole parameter simplifies to $\rho(\xi_m) = (\gamma \kappa \Omega(\xi_m) \xi_m)^2$ and is shown in Fig. 2 (dashed line). It is seen that the harmonic approximation of periodic motion of positrons with energy of $E = 120$ GeV is quite acceptable for calculation of the radiation spectrum of channeled particles.
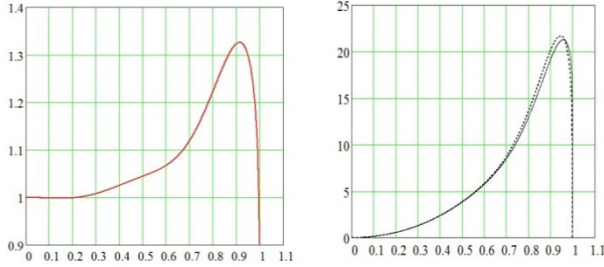
Fig.1: Dependence $\Omega(\xi_m)$.   Fig.2: Dependences $\rho(\xi_m)$.

DISTRIBUTION OF CHANNELED PARTICLES ON AMPLITUDES OF MOTION

For determining the full spectrum of radiation from all captured in the channeling positrons it is necessary to know: N - a relative part of particles of the beam, captured into the channeling; $f(\xi_m)$ - density distribution of channeled positrons on amplitudes ξ_m. We suppose that at the entry to the straight crystal positrons are distributed uniformly along x, and hence along ξ, and with the angular distribution $g(\vartheta)$. In normalized variables (ξ, p) according to (2) we have the following relation between ϑ and p : $p = \dfrac{d\xi}{d\tau} = \dfrac{\upsilon_s}{\omega_o(d/2)} \dfrac{dx}{ds} \cong \dfrac{2c}{\omega_o d} \vartheta = \dfrac{\vartheta}{\kappa}$, where $s = \upsilon_s t \cong ct$ is the longitudinal coordinate along the channel. From here the distribution of particles at the entry to the crystal on variable p becomes $\widetilde{g}(p) = \kappa g(\kappa p)$. Closed phase curve $p = p(\xi, \xi_m)$ in the plane (p, ξ) with a fixed ξ_m for a channeled particle (see Fig. 3) is given by expression

$$p(\xi, \xi_m) = \pm \sqrt{2(\widetilde{U}(\xi_m) - \widetilde{U}(\xi))} \qquad (4)$$

with $\xi \in [-\xi_m, \xi_m]$. Separatrix is (the phase curve, separating the channeled and over-barrier particles) described

by expression $p_c(\xi) = p(\xi, 1)$. The maximum value of p_L corresponds to the Lindhard angle ϑ_L, achieved at $\xi = 0$ and equal to $p_L = |p_c(0)| = \sqrt{2\widetilde{U}(1)}$. At the considered parameters of the crystal and the magnitude of the positrons energy we have: $p_L \cong 1.189$ and $\vartheta_L \cong 19.093 \times 10^{-6}$. Thus, the portion of particles captured in the channeling mode, i.e. moving inside the separatrix, is given by

$$N = \int_0^1 d\xi \int_{-|p_c(\xi)|}^{|p_c(\xi)|} \widetilde{g}(p)\,dp \quad . \qquad (5)$$
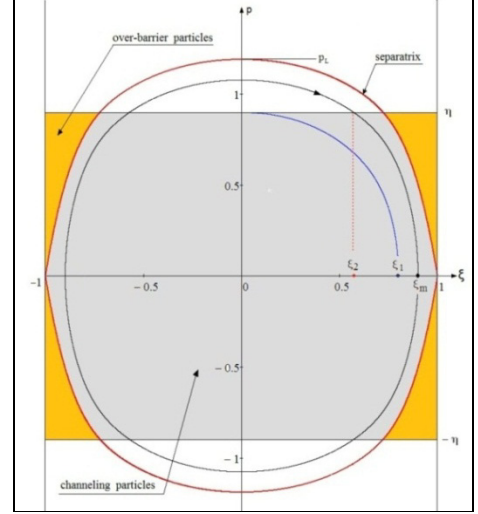
Fig.3: Phase portrait of capture of particles in the channeling.

Now we find the density function $f(\xi_m)$ of particles distribution on the amplitudes only for the particles occurring in channeling. Hereinafter we mean $p(\xi, \xi_m)$ to be a positive branch of the definition (4). The relative number of channeled particles N with amplitude $\leq \xi_m$ is equal to

$$F(\xi_m) = \frac{1}{N} \int_0^1 d\xi \int_{-p(\xi, \xi_m)}^{p(\xi, \xi_m)} \widetilde{g}(p)\,dp \quad . \qquad (6)$$

Then for the density function is determined as $f(\xi_m) \equiv dF(\xi_m)/d\xi_m$ i.e.

$$f(\xi_m) = \frac{1}{N} \frac{d\widetilde{U}(\xi_m)}{d\xi_m} \int_0^{\xi_m} d\xi \frac{\widetilde{g}(p(\xi, \xi_m)) + \widetilde{g}(-p(\xi, \xi_m))}{p(\xi, \xi_m)}. \qquad (7)$$

We confine ourselves to the simplest case of uniform and symmetric about zero angle distribution of particles, i.e. $g(\vartheta) = 1/2\vartheta_o$ if $\vartheta \in [-\vartheta_o, \vartheta_o]$, $g(\vartheta) = 0$ if $\vartheta \notin [-\vartheta_o, \vartheta_o]$. Hence, in the plane of normalized variables we have $\widetilde{g}(p) = 1/2\eta$ if $p \in [-\eta, \eta]$ and $\widetilde{g}(p) = 0$ if $p \notin [-\eta, \eta]$, here $\eta = \vartheta_o / \kappa$ is the boundary of the beam with variable p. For the case when the half-width of the angular spread is less than the Lindhard angle, $\vartheta_o < \vartheta_L$ and, hence $\eta < p_L$ (see Fig. 3), we introduce the amplitude ξ_1, for

which the phase curve has a maximum $p(0, \xi_1) = \eta$. In addition, for every phase curve with the amplitude $\xi_1 < \xi_m \leq 1$ we determine the value ξ_2 which depends on ξ_m. Dependence $\xi_2(\xi_m)$ is determined by $\sqrt{2(\widetilde{U}(\xi_m) - \widetilde{U}(\xi_2))} = \eta$.

According to the formulas (5÷7) for our case of the angular spread in the beam of positrons, we get:

$$N = \xi_2(1) + \frac{1}{\eta} \int_{\xi_2(1)}^{1} d\xi \sqrt{2(\widetilde{U}(1) - \widetilde{U}(\xi))} \; ;$$

$$f(\xi_m) = \frac{1}{N\eta} \frac{d\widetilde{U}(\xi_m)}{d\xi_m} \begin{cases} \int_{0}^{\xi_m} d\xi / \sqrt{2(\widetilde{U}(\xi_m) - \widetilde{U}(\xi))} & if \quad 0 \leq \xi_m \leq \xi_1 \\ \int_{\xi_2(\xi_m)}^{\xi_m} d\xi / \sqrt{2(\widetilde{U}(\xi_m) - \widetilde{U}(\xi))} & if \quad \xi_1 \leq \xi_m \leq 1 \end{cases} .$$

Calculated by these expressions dependence of the relative capture N in the channeling regime on the value ϑ_o is shown in Fig. 4 and density functions $f(\xi_m)$ for some values $\vartheta_o / \mu rad$ are shown in Fig. 5.
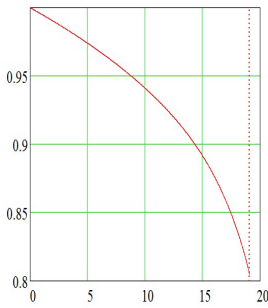
Fig.4: Function
$N(\vartheta_o / \mu rad)$.
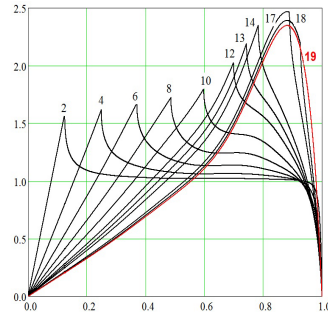
Fig.5: Functions
$f(\xi_m)$

From the above analysis it follows the further important conclusion: in the potential (1), where $d\widetilde{U}/d\xi \to 0$ at $\xi \to \pm 1$ the distribution $f(\xi_m) \to 0$ at $\xi_m \to 1$.

THE RADIATION OF CHANNELED POSITRONS IN QUASIPERIODIC MOTION

To find the radiation spectrum of channeled positrons, oscillating in the interplanar potential (1), use the formula derived in [1] (p.303) for the quasiperiodic motion of a particle at all values of ρ. The need to consider the radiation spectrum in such a very general way is due to the fact that in the potential (1) multipole parameter (see Fig. 2) covers a wide range of values ρ providing different types of radiation. The radiation spectrum of one positron per unit length of a short crystal is determined by the expression:

$$\frac{d^2 E}{dE_\gamma ds} = -\frac{\alpha E_\gamma}{c(2\pi\gamma)^2} \sum_{n=1}^{\infty} \Phi\left(n - \zeta(1 + \rho/2)\right) \int_{-\pi}^{\pi}\int_{-\pi}^{\pi} d\varphi_1 d\varphi_2 \times$$

$$\times J_o\left(2\int_{\varphi_2}^{\varphi_1} d\varphi \mu(\varphi) \sqrt{\zeta\left(n - \zeta(1+\rho/2)\right)}\right) \times \left[1 + \frac{A(E_\gamma)}{2}\left(\mu(\varphi_1) - \mu(\varphi_2)\right)^2\right] \times$$

$$\times \cos\left\{(n - \zeta\rho/2)(\varphi_1 - \varphi_2) + \zeta \int_{\varphi_2}^{\varphi_1} d\varphi \, \mu^2(\varphi)\right\} ,$$

where: $\alpha = 1/137.04$, E_γ - the energy of the emitted photon, step function $\Phi(y) = 1$ at $y \geq 0$ and $= 0$ at $y < 0$, J_o is the Bessel function, $\mu(\varphi) = \gamma(\upsilon_x(\varphi) - <\upsilon_x>)/c$, $\zeta(E_\gamma, \xi_m) = E_\gamma \, E/2\gamma^2 (\hbar\omega)(E - E_\gamma)$, $\omega = \omega_o \cdot \Omega(\xi_m)$, $A(E_\gamma) = 1 + E_\gamma^2 / 2E(E - E_\gamma)$.

The motion of a positron is presented in the form of a harmonic oscillation (3) with the frequency depending on its amplitude ξ_m. For such an approximation the spectral dependency $(d^2 E / dE_\gamma \, ds)$ on E_γ was calculated by the previous formula and shown in Fig. 6 for a single channeled positron with the following values of $\xi_m =$ 0.3, 0.5, 0.7, 0.9.
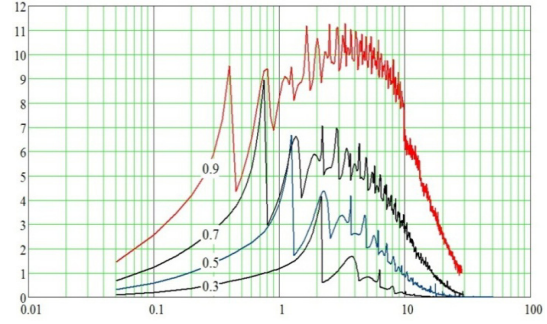
Fig.6: Dependencies $(d^2 E / dE_\gamma \, ds) \times cm$ on E_γ /GeV.

CONCLUSION

With the help of above consideration the photon spectra were calculated for the positron energy in the range of 80-120 GeV for (011) and (111) silicon planes. These spectra were inserted into the Monte Carlo program which was used for simulations of differential radiation energy losses of 120 GeV positrons at the INSURAD experiment conditions. The experiment was performed with usage of bent monocrystals with thickness of 1-2 mm. Simple estimations show: influence of crystal bending on a photon emission process is negligible at radii more than 4 m; the mean number of photons emitted by one positron in such thickness is more than 1 several times. Comparison between the energy losses measured in experiment and results of Monte Carlo simulations have shown good coincidence them [6].

REFERENCE

[1] V.N. Baier, V.M. Katkov, V.M. Strakhovenro, *Electromagnetic Processes at High Energies in Oriented Single Crystals*, Novosibirsk, Nauka, 1989.
[2] J. Bak et. al., Nuclear Physics B254 (1985), p. 491.
[3] E.N. Tsyganov, Part. & Nuclei, v. 20, part 1 (1989).
[4] V.A. Maisheev, NIM B119 (1996), p. 42.
[5] V.A. Maisheev et. al., Preprint IHEP 2009-21.
[6] S. Hasan et al., presentation at ICHEP2010, July. http://indico.cern.ch

JINR ACTIVITY IN FEL

O. Brovko, G. Chelkov, E. Ivanov, M. Kapishin, E. Matyushevskiy, N.Morozov, G. Shirkov,
E. Syresin[#], G. Trubnikov,   M. Yurkov, Joint Institute for Nuclear Research, Dubna, Russia

Abstract

Different methods for diagnostic of ultrashort electron bunches are developed at JINR-DESY collaboration within the framework of the FLASH and XFEL projects. Photon diagnostics developed at JINR-DESY collaboration for ultrashort bunches are based on calorimetric measurements and detection of undulator radiation.   The MCP based radiation detectors are effectively used at FLASH for pulse energy measurements. The new MCP detector for X-ray beam diagnostic for XFEL is under development now in JINR. The infrared undulator constructed at JINR and installed at FLASH is used for longitudinal bunch shape measurements and for two-color lasing provided by the FIR and VUV undulators.   The JINR also participates in development and construction of Hybrid Pixel Array Detector on the basis of GaAs sensors.   The JINR in collaboration with IAP RAN and DESY (Zeuthen) develops a project of laser system based on Nd laser with pulse shaper for formation of quasi 3D ellipsoidal laser pulses applied for a prototype of XFEL gun.

FLASH MCP-BASED PHOTON DETECTOR

The free electron laser FLASH has been in operation at DESY since the year 2000 [1,2]. The electron energy now reaches 1 GeV, rms bunch length is 50 μm, the FWHM radiation pulse duration is about 30 fs, the normalized emittance is 2 π·mm·mrad, the bunch charge is 1 nC, the peak power is up to 1 GW, the peak brilliance is of 10^{28} ph/s/mrad2/mm2/(0.1%bw).

Successful operation of FLASH strongly depends on the quality of the radiation detectors. The key issues are: the wide wavelength range 6-100 nm, the wide dynamic range (from the spontaneous emission level to the saturation level), and the high relative accuracy of measurements which is crucial for detection of radiation amplification and characterization of statistical properties of the radiation.

The key FLASH photon detector developed by the JINR-DESY collaboration is a micro-channel plate (MCP) detector intended for pulse energy measurements [3-5]. The MCP detector is used for measurement of statistical properties of the radiation allowing determination of the pulse length. Key element of the detector is a wide dynamic MCP which detects scattered radiation from a target. With four different targets and MCPs in combination with optical attenuators, the present FLASH detector covers an operating wavelength range 6 -100 nm, and a dynamic range of the radiation intensities, from the level of spontaneous emission up to the saturation level of SASE FEL.

The gold target is perfect for the wavelength range above 10 nm, however its reflectivity falls dramatically for shorter wavelengths, and different targets and geometries of the detector are used. We added three more targets to gold mesh: two iron meshes, and one copper mesh. This helps us to operate the detector in a range below 10 nm.
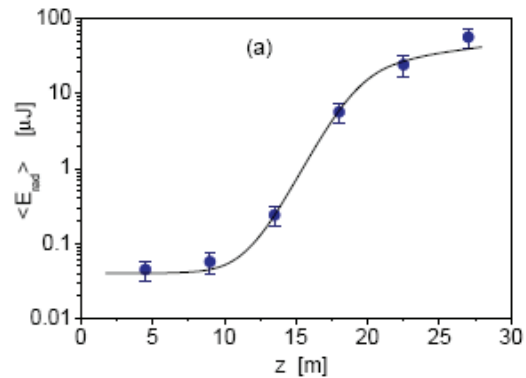
Figure. 1: Measured average energy in the radiation pulse versus the undulator length.

For tuning SASE at very short wavelengths we use movable MCPs directly facing photon beam. Light intensity variation by a factor of 50 is controlled by a mechanical attenuator of light located in the target unit. To have full control of light intensity in a wide range we installed a side MCP which detects radiation reflected by the iron mirror. The mirror serves for two purposes. One is to deflect the photon beam off- the axis, which allows placing the MCP in better background conditions.

The dependence of the measured average energy in the FLASH radiation pulse on the undulator length is shown in Fig. 1. In the saturation regime the average pulse energy is 40 μJ and the wavelength is 13.7 nm.

DEVELOPMENT OF XFEL MCP

The developed XFEL MCP-based detector consists of four main elements: attenuator, frequency filter, MCP equipped with anode as pulse energy monitor, and MCP imaging detector as a viewer of photon beam image (Fig.2). Frequency filter selects frequencies near the required harmonic of the radiation (fundamental, or higher). Technical realization of frequency filter and attenuator depends on the wavelength of interest. For operating wavelength band below 0.4 nm (fundamental harmonic of SASE1 and SASE2) Si (111) crystal (Bragg reflection) is used as a frequency filter, and attenuation is

---

[#]syresin@nusun.jinr.ru

performed by a metallic films (Be/Al/Ti). Simulated coordinate (x,z) distribution of 12.4 keV photons in SASE 1 is given in Fig.3. For wavelength above 0.4 nm (fundamental harmonic of SASE3) SiC/W multilayer mirror is used as a frequency filter and attenuation of the signal is performed by a plane SiC mirror in combination with metallic film attenuator. SiC plane mirror is installed in front of multilayer mirror thus protecting the latter one from strong synchrotron radiation background.
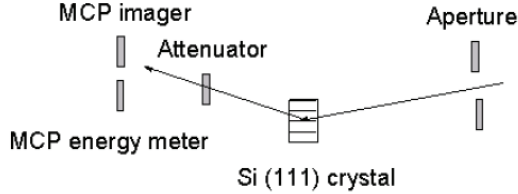
Figure 2: Schematic layout of the MCP-based photon detector at XFEL operating at wavelengths below 0.4 nm.
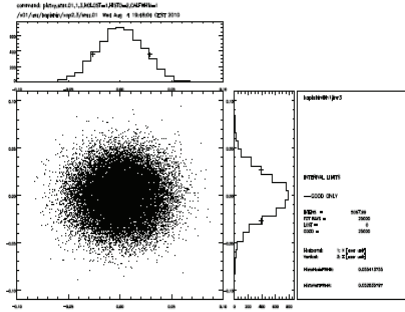
Figure 3: Simulated coordinate distribution of 12.4 keV photons in SASE 1 detected in the MCP imager plane.

FLASH FAR INFRARED UNDULATOR

The FLASH was equipped with an infrared electromagnetic undulator (Fig.4), tunable over a K–parameter range from 11 to 44, and producing radiation up to 200 μm at 500 MeV and up to 50 μm at 1 GeV [5-8]. The purpose of the device is two-fold: firstly, it is used for longitudinal electron bunch measurements, secondly, it is a powerful source of intense infrared radiation naturally synchronized to the VUV FEL pulses, as both are generated by the same electron bunches and being therefore well suited for precision pump-probe experiments.

The undulator was designed and constructed by JINR to the FLASH requirements [5-8]. The undulator period corresponds to 40 cm, the number of periods is 9, the magnetic field is varied in range of 0.1-1.1 T. Output undulator radiation has the following parameters: wavelength 5-200 μm, peak power 4 MW, micropulse energy 1 mJ, micropulse duration 0.5-6 ps. The spectrums of FLASH infrared undulator at different K-parameters are given in Fig.5.

Figure. 4: FLASH far infrared undulator constructed by JINR.

The energy radiated by the undulator is defined by the number of electrons per bunch N and a form-factor F(λ):

$$\varepsilon_{coh} = \varepsilon_e \times \left[N + N(N-1) \left| \overline{F}(\lambda) \right|^2 \right],$$

where ε_e is energy radiated by single electron. The form-factor is equal to $|F(\lambda)|^2 = \exp(-2\pi\sigma/\lambda)^2$ for Gaussian bunch with r.m.s. length σ. When the wavelength is longer than the bunch length, the coherent radiation dominates. Measuring the spectrum (Fig.5) that regime one can extract the form-factor and thus the charge distribution and the bunch leading spike length. The Gaussian fit (Fig.6) corresponds to the r.m.s. leading spike length of σ_{ls}= 12 μm.
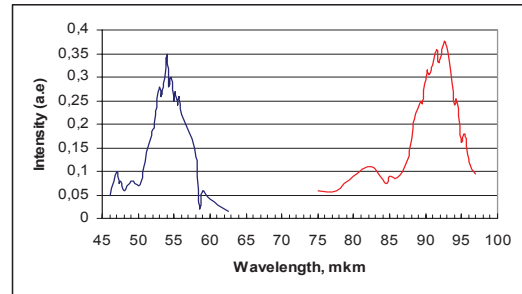
Figure 5: Spectrums of infrared undulator radiation.
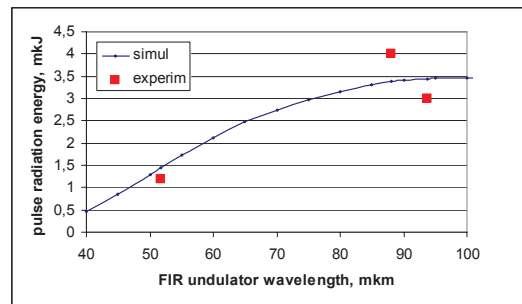
Figure 6: Dependence of the FIR undulator pulse radiation energy on the wavelength.

HYBRID PIXEL ARRAY DETECTOR

A bunched electron beam of extremely high quality is needed in the XFEL to get coherent radiation in subnanometer wavelength [10]. JINR in collaboration with Tomsk State University (TSU) and DESY design Hybrid Pixel Array Detector on basis of GaAs (Cr) detectors (Fig. 7) [11] in the frame work of the Russian-German project GALAPAD oriented on the development of the photon diagnostic systems. The technology of the pixel detector with resolution of 50 μm was developed on basis of the JINR-TSU GaAs (Cr) sensors and the Medipix (Swiss) chips. The peculiarity of the detector with Medipix chip that it measures the spectral characteristic of the X-ray radiation.

Figure 7: Spectrometric detector on basis of GaAs (Cr) pixel censor with 256×256 channels of 50 μm resolution and Medpix chip.

The sensitivity of GaAs detector is essentially improved in comparison with Si detector at photon energy larger 15 keV (Fig.8).
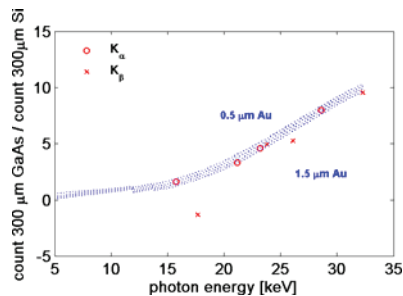
Figure 8: Dependence of ratio of counts in GaAs and Si detectors on photon energy.

FORMATION OF 3D ELLIPSOIDAL LASER PULSES

The JINR in collaboration with Institute of Applied Physics RAN and DESY (Zeuthen) develops a project of laser system based on Nd laser with pulse shaper for formation of quasi 3D ellipsoidal laser pulses applied for a prototype of XFEL gun. By optimization the main parameters of the XFEL photo injector one can simulate rather small projected normalized emittance: 0.46 mm mrad. Slice emittance of the bunch centre reduced in ~10% by applying an ellipsoid laser pulse [12]. Main reduction of the projected emittance (Fig.9) is due to significant decrease in head and tail slice emittance of the ellipsoid.
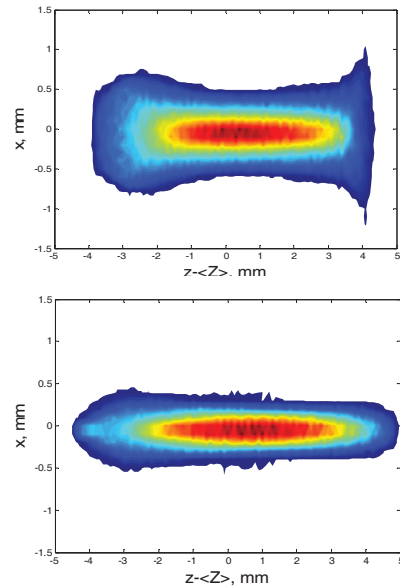
Figure 9: Transverse electron bunch shape for cylindrical (upper) and ellipsoid (down) laser shape pulses at a distance of 15 m [12].

REFERENCES

[1] J. Andruszkow et.al., Phys. Rev. Lett. 85 (2000) 3825.

[2] W. Ackerman et al., Nature Photonics. 1 (2007) 336.

[3] B. Fatz et al., Nucl.Instr. and Meth. A 483 (2002) 412.

[4] J. Bittner et al., Proc. of FEL'07, p.334 (2007); http://www.JACoW.org.

[5] O.Brovko et al, Physics of elementary particles and atomic nuclei letters, 7 (2010) 78.

[6] Y.Holler et al., FEL'07, p.318 (2007); http://www.JACoW.org.

[7] O.Grimm et al, NIM A 615, 1 (2010), 105.

[8] M.Gensh et al., Infrared physics and technology (2008) 358.

[9] O. Brovko et al., IPAC 10, TUPE040 (2010); http://www.JACoW.org.

[10] R. Abela et al., XFEL Technical Design Report, DESY 2006-097 (2006).

[11] I. Boiko et al., Nuclear Physics and Nanotechnologies, Dubna, p.198. (2008).

[12] M. Krasilnikov, Selected simulations for XFEL photo injector, Mini-Workshop on Laser Pulse Shaping, DESY Zeuthen (2006).

PROPOSAL FOR AN ACCELERATOR COMPLEX FOR EXTREME ULTRAVIOLET NANOLITHOGRAPHY USING KW-SCALE FEL LIGHT SOURCE

E.Syresin , M. Yurkov, Y. Budagov, N. Balalykin, I. Lensky, A. Olshevsky, A. Sumbaev, G. Shirkov,   G.Trubnikov, Joint Institute for Nuclear Research, Dubna, Russia.

Abstract

The project is aimed at construction of accelerator complex, based on a 0.7 GeV superconducting linear accelerator, for applications in nanoindustry, mainly for extreme ultraviolet lithography using kW-scale Free Electron Laser (FEL) light source. The project involves construction of a 0.7 GeV superconducting linear accelerator to produce coherent FEL radiation for extreme ultraviolet nanolithography at a wavelength of 13.5 nm and an average radiation power of 0.5 kW. The application of kW-scale FEL source permits realizing EUV lithography with 22 nm, 16 nm resolutions   and beyond. The project for construction of an accelerator complex for EUV lithography is based on the technology realized on FEL FLASH (Free Electron Laser in Hamburg) facility at DESY (Hamburg).

INTRODUCTION

The project is aimed at construction of accelerator complex, based on a 0.7 GeV superconducting linear accelerator, for applications in nanoindustry, mainly for extreme ultraviolet lithography using kW-scale Free Electron Laser (FEL) light source. The project involves the following activities.

Construction of a 0.7 GeV superconducting linear accelerator to produce coherent FEL radiation for extreme ultraviolet nanolithography at a wavelength of 13.5 nm and an average radiation power of 0.7 kW.

Construction of a dedicated channel for extreme ultraviolet lithography with a few nanoscanners operating simultaneously in a processing line with 22 nm, 16 nm and beyond using FEL radiation at a wavelength 13.5 nm.

Medico-biological investigations using radiation with wavelengths ranging from 2.4 nm to 4.6 nm (3rd harmonic FEL) .

Research in magnetic materials using radiation with a wavelength of about 1.5 nm (5rd harmonic FEL).

Realization of the superconducting RF linear accelerator technology for the International Linear Collider.

.

EXTREME ULTRAVIOLET LITHOGRAPHY

The development of the next generation lithography was started since the middle of 1990s. A target goal was to follow Moore's law in the reduction of a feature size by a factor of two in two years. During last two decades the progress in the feature size reduction has been provided by reducing the wavelength of lasers used.   The conventional lasers operate at wave length of 193 nm. Immersion and photoresist technologies aiming to get feature size below $\lambda/4$ limit reached their boundaries as well.

The ASML TWINSCAN NXE platform [1] (Fig.1) is the industry first production platform for extreme ultraviolet lithography (EUVL) based on the laser source LPP [2] at wave length of 13.5 nm. The resolution of NXE:3100 corresponds to 27 nm (Table 1). The resolution of NXE: 33000B is 22 nm with conventional illumination and 18 nm with of-axis illumination.

Figure 1: ASML TWINSCAN NXE industry platform for EUVL with LLP at radiation wavelength of 13.5 nm.

Table 1. Parameters of SML EUV platform.

Parameter	NXE:3100	NXE: 33000B
NA	0.25	0.32
Resolution, nm	<27	<22 (18nm off-axis illumination)
Exposition field, mm	26×33	
Illumination sigma	0.8	0.2-0.9
Overlay, nm	4.5	3.5
Productivity, wph	>60	>125

The power of LPP sources now corresponds to 75 W [2]. The exposition power is equal to 20 W that provides

production rate of 15 wafers per hour (wph) at their diameter of 300 mm. It is planed to increase the production rate up to 125 wph at the LPP power of 200 W. The LPP micropulse radiation energy corresponds to 2 mJ, micropulse repetition frequency is equal to 50 kHz, the number of micropulses is 2×10^4 per macropulse. The time duration of the macropulse is equal to 400 ms, the macropulse repetition frequency corresponds to 2 Hz, the macropulse energy is about 40 J.

EUV LITHOGRAPHY BASED ON FEL

The project for construction of an accelerator complex for EUV lithography is based on the technology realized on FEL FLASH (Free Electron Laser in Hamburg) facility at DESY (Hamburg) [3]. FLASH has produced several GW powers for EUV radiation with a wavelength of 13.5 nm, a target goal for the next generation lithography. The driving engine of FLASH facility is an L-band superconducting accelerator [3]. It is designed to operate in a pulsed mode with a pulse duration of 800 microsecond and repetition rate of 10 Hz [3]. The maximum accelerated macropulse current is 10 mA. The present analysis [4] (Fig.2-Fig.4) shows that this technology holds great potential for increasing the average power of a linear accelerator and the efficiency of conversion of electron kinetic energy into light.

Table 2. Parameters of accelerator complex for EUVL.

Acceleration complex	FLASH	EUVL-0.68	EUVL-1.25
Electron energy, GeV	0.68 (1)	0.68	1.25
FEL length	250	110	180
Macropulse frequency, Hz	10	40	10
Macropulse time duration, ms	0.8	0.14	0.8
Number of pulses per macropulse	7200	1400	8000
Micropulse frequency, MHz	9	10	10
Micropulse radiation energy, nJ	1.4	8.5	22
Macropulse radiation energy, J	10	12	176
Peak radiation power, GW	5.6	34	88
Average radiation power, kW	0.1	0.5	1.75
Number of scanners		8	10

Thus, it will be possible to construct a free electron laser facility [5-7] operating at a wavelength of 13.5 nm, an average power of up to 0.5 kW and an electron energy of 0.7 GeV (Table 2). The simulations [4] are performed at the peak current of 2.5 kA and the bunch charge of 1nC. The undulator length corresponds to 30 m, it's period is equal to 2.73 cm for a facility at 0.68 GeV and 3.5 cm for EUVL-1.25. The micropulse radiation time corresponds to 250 fs. The diameter of radiation spot at undulator exit is 0.3 mm for EUVL-0.68 and 0.2 mm for EUVL-1.25.
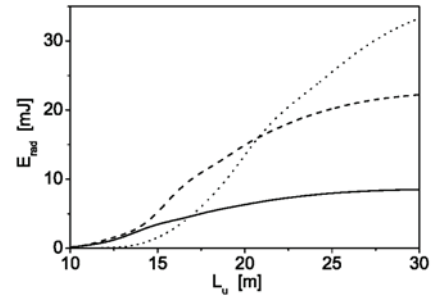
Figure 2: Dependence of radiation energy on undulator length at differen electron energies. Solid, dashed, and dotted lines correspond to the energy of driving electron beam 0.68, 1.25, and 2.5 GeV, respectively.
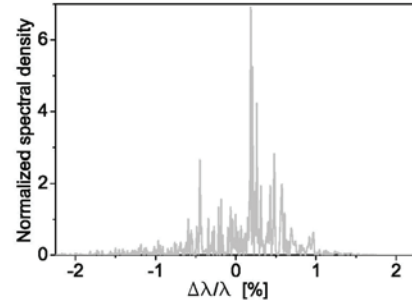
Figure 3: Normalized spectral density distribution of radiation.
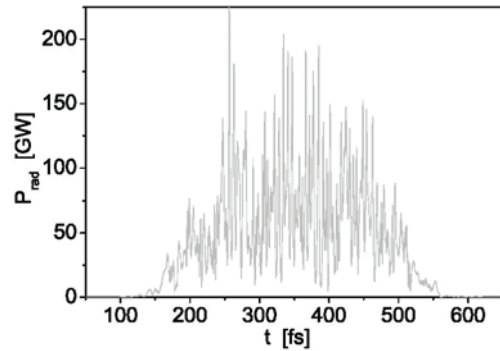
Figure 4: Dependence of peak radiation power on time at electron enrgy 1.25 GeV

Using a powerful FEL source allows this approach to be redefined as 'single source for multiple tools'. The powerful kW-scale FEL radiation can be distributed between EUV lithography 'multiple tools' operated at an average power about 60 W due to multilayer mirrors installed at the entrance of each lithography scanner and FEL time structure (Fig.5).

For powerful FEL radiation at its small angle spread and little spot size there are some peculiarities of the first defocusing SiC mirror installed at a distance of 10 m after the undulator exit. The elliptical spot sizes corresponds to 5 mm and 0.35 mm at 3^0 incident angle of the FEL radiation to the SiC mirror surface. The mirror absorbed power corresponds to 50W and absorbed macropulse radiation energy is 1J at the average FEL power of 0.5 kW and reflection efficiency of 90%.

Table.3 EUVL on basis of FEL and NXE:3100 LPP radiation.

Parameter	LPP	EUVL 0.68
Number of multilayer elements	11	
Coefficient of reflection	0.62	
Micropulse radiation energy, mJ	2 1 scan.	8.5 8 scan.
Radiation energy density, mJ/cm^2	10	
Exposition energy of chip bend	5.2	
Energy of chip exposition, mJ	83	
Wafer energy exposition, J	6	
Scanning speed, mm/ms	0.2	0.1
Average radiation power, W	100	480
Wafer average power exposition, W	0.5	0.3
Number of micropulses for band exposition	520	1250
Time of bend exposition, ms	10	0.125
Number of micropulses for chip exposition	8300	20000
Time of chip exposition, ms	160	320
Time of wafer exposition, s	14	22
Time of wafer reloading, s	22	22
Production wafer rate, w/h	100 1 scan.	640 8 scan.
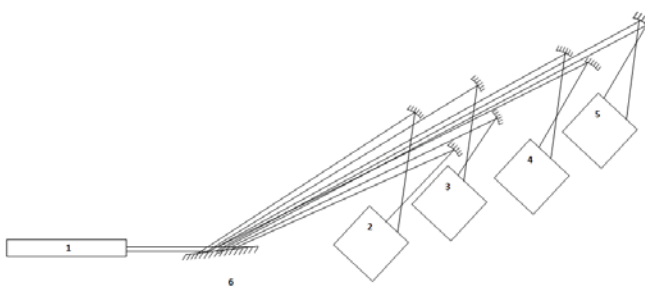
Figure 5: Distribution of FEL radiation between lithography scaners, 1- FEL, 2-5 – lithography scanners, 6 – first mirror.

The FEL radiation is divided on the 8 simultaneously operated scanners (Table 3). The FEL spot after defocusing mirror has a diameter of 50 cm which is divided on 8 concentric rings of equaled square by a special multilayer mirror system (Fig.5). The radiation from each concentric ring is pick-upped by the corresponding scanner. In each scanner a system consisted of 4 multilayer mirrors transforms the radiation ring in a bend with a size of 26×2 mm, which is exposited on chip by the 6 multilayer mirror objectives. The analogical optic for transformation of the ring in a bend is realized in NXE: 3100 platform [1] with LPP source. The full chip exposition at its size of 26×33 mm is produced at its motion across the EUV radiation flax. The radiation energy required for chip production corresponds to 16 J at wafer radiation energy density of 10 mJ/cm^2 and efficiency of EUV light transportation to the wafer of 0.5% (for 11 multilayer elements of NXE Platform). The bend exposition is produced at FEL macropulse time of 0.14s. The chip is scanned 20 ms between macropulses by FEL radiation. The chip and wafer expositions correspond to 320 ms and 22 s, correspondently. The EUVL scanner production rate is 80 wph, when the wafer exposition time is comparable with its loading time in scanner. The project production rate of full FEL EUVL complex with 8 scanners corresponds to 640 wph.

REFERENCES

[1] TWINSCAN NXE:3100 & NXE:3300B, ASML Product Catalog (2010) 8.

[2] D.C. Brandt, N.R. Farrar, Solid State Technology, v. 52, №9 (2009) 10.

[3] T.Aberg et al, Conceptual design report, DESY, TESLA-FEL 95-03, Hamburg, 1995.

[4] E.Saldin et al., FEL'09, (2009).

[5] V.S. Anchutkin et al., In proc. "Nanophysics and nanoelectronics", Nishnij Novgorod, v.1, (2010) 209.

[6] O.Brovko et al., Applied physics, 3 (2010) 46.

[7] O.Brovko et al., IPAC10, (2010).

SELF-STIMULATED UNDULATOR RADIATION SOURSES

E.G Bessonov, M.V.Gorbunkov, A.L. Osipov, Lebedev Phys. Inst. RAS, Moscow, Russia
A.A.Mikhailichenko, Cornell University, LEPP, Ithaca, NY 14853, U.S.A.

Abstract

The phenomena of self-stimulation of incoherent radiation emitted by particles in a system of undulators installed in the linear accelerators or quasi- isochronous storage rings are investigated. Possible applications of these phenomena for light sources are discussed.

INTRODUCTION

A particle passing through an undulator emits an undulator radiation wavelet (URW), the length of which in the direction of its average velocity is $M\lambda_1$, where M is the number of undulator periods, and λ_1 is the wavelength of the first harmonic. In a system of N_u identical undulators, located along straight line, the particle radiates N_u URWs with a separation l; both l and λ_1 are defined by the Doppler effect, by an angle θ between the average particle velocity in the undulator and the direction to the observer, by the distance between the undulators l_0, by the period of the undulator λ_u and by the relativistic factor $\gamma = \varepsilon / mc^2 >> 1$, m_e is the rest electron mass, ε is the electron energy [1], [2]. In the forward direction ($\theta = 0$) they are: $l = l_0 / 2\gamma^2$ and $\lambda_1 \sim \lambda_u / 2\gamma^2$. The energy radiated by a particle in a system of N_u undulators becomes modified and is N_u times larger than one radiated in just a single undulator. The spectrum of radiation emitted in an arbitrary direction also changes, appearing as a line structure. The integrated spectrum does not change much however.

Self-Stimulated Undulator Radiation (SSUR) is a kind of undulator radiation (UR) emitted by a charged particle in a field of the downstream undulator in the presence of self-fields of its own wavelets emitted at earlier times in the same or upstream undulator. These wavelets focused back to the particle's position at the entrance of the downstream undulator with mirrors, lenses and passed through the optical delay lines [3]. Below we considering two schemes based on linear accele-rators and storage rings.

One way to increase the loss rate of a particle in a sys-tem of N_u undulators by the introduction of controlled delays in the motion of the particles between undulators relative to their URWs is shown on the Fig.1.

Delays are chosen so that a particle enters the following undulator in the decelerating phase at the front edge of its URW, which was emitted from preceding one. In this case the particle will experience deceleration in its self-field generated by its instantaneous motion in the field of the undulator as well as in the field of the URW from preceding undulators (stimulated radiation in field of a

co-propagating URW). Under such conditions super-position of the wavelets occurs, which yields the electric field growth $\sim N_u$ and the growth of energy density in the emitted radiation becomes $\sim N_u^2$. Below we will name the linear system of undulators and optical elements by self stimulated undulator klystron (SSUK).
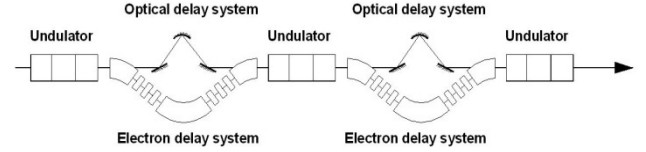
Figure 1: Schematic of the installation.

To be optimally effective, this system must use appropriate focusing elements such as lenses and/or focusing mirrors (see Figs. 1, 2). Mirrors and lenses are used to form a crossover in the middle of the undulators with the Rayleigh length of the order of the length of undulator $Z_R \cong M\lambda_u / 2$.
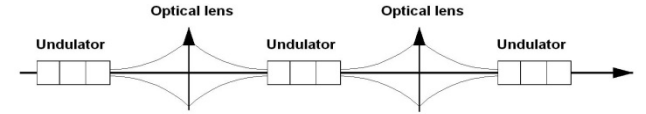
Figure 2: Equivalent optical scheme.

We considered here the case where the optical delays are tuned so that the wavelets emitted by the particle are congruent and all particles stay at the decelerating phase. For this the beam delay system must be isochronous.

Another way to increase the loss rate of a particle is the SSUR source based on a quasi-isochronous storage ring equipped with an undulator (or SSUK) installed in its straight section and the mirrors installed at both sides of the undulators outside of the closed orbits of electrons, circulating in the ring (Fig.3). So the mirrors set an optical resonator.

The scheme of the SSUR source has resemblance to the scheme of ordinary FEL with additional synchronicity condition: the oscillation period of the URW emitted by every electron in the undulator inside the optical cavity coincides with the revolution period of this electron in the storage ring in the limits of energy and transverse emittance of the beam. The URWs emitted by every electron are accumulated effectively in the optical resonator by the superposition one by another if theirs longitudinal shift per turn satisfies condition

$$\Delta l - n\lambda_m \mid \leq \lambda_m / F, \qquad (1)$$

where $\lambda_m = \lambda_1 / m$ is the wavelength of the UR emitted by the electron on the *m*-th harmonic in the direction of its average velocity, F is the finesse (quality factor) of the

02 Synchrotron Light Sources and FELs

optical resonator, $n = \pm 1, \pm 2,...,|n| \le M$, M is the number of the undulator periods.
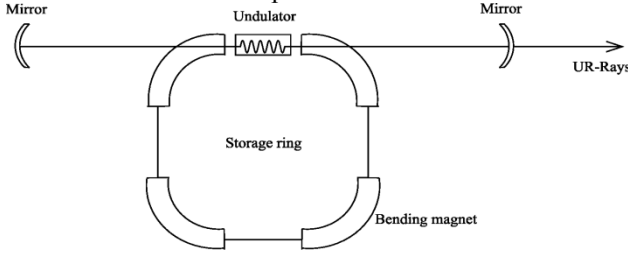
Fig.3. Schematic diagram of SSUR source built around a storage ring.

The condition (1) presents the main synchronicity condition for $n = 1$. There are $2M+1$ similar collateral synchronicity conditions corresponding to $1 < |n| < M$ (incomplete overlapping of the URWs).

The general synchronicity condition in the SSUR scheme is as the following

$$\Delta l = | c \cdot \Delta T_{e,URW} | << \lambda_m / F, \qquad (2)$$

where $\Delta T_{e,URW} = T_e - T_{URW}$ is the difference between the revolution periods of the electron in the storage ring and the UWR in the optical resonator. We are considering $T_{URW} = 2 L_{mir} / c = const$, $T_e = T_e(\varepsilon, A_b)$, where L_{mir} is the distance between mirrors, A_b is the amplitude of the electron betatron oscillations. The value $\Delta T_{e,URW}$ can be presented in the form

$$\Delta T_{e,URW} = \Delta T_\eta + \Delta T_{A_b}, \qquad (3)$$

where in the smooth approximation $\Delta T_\eta = \eta_c \cdot T \cdot \Delta \varepsilon / \varepsilon$, $c \cdot \Delta T_A = \pi^2 A_{b,x,z}^2 \nu_x^2 / C$, $\beta_{x,z} \simeq \overline{\beta}_{x,z} = C / 2 \pi \nu_{x,z}$, $\eta_c = 1/\gamma^2 - \alpha_c$ is the phase slip factor of the ring, C – is the circumference of the electron orbit, $A_{b,x,z}$, $\beta_{x,z}$, $\nu_{x,z}$ are the horizontal/vertical amplitudes, β - functions and tunes of electron betatron oscillations accordingly, α_c is the momentum compaction factor of the ring. For relativistic electron beams $\eta_c \simeq -\alpha_c$. Synchronicity condition determines the limiting energy spread, amplitudes of betatron oscillations and emittance of the electron beam:

$$\Delta \varepsilon_r / \varepsilon < \lambda_m / C F \eta_c, \ A_{b,x,z} < \sqrt{\lambda_m \ \lambda_{x,z} / F \nu_{x,z}} / \pi,$$

$$\in_{x,z} < 2 \lambda_m / \pi F \nu_{x,z}, \qquad (4)$$

where $\lambda_{x,z} = C / \nu_{x,z}$ is the wavelength of the betatron oscillations. Note that the last inequality in (4) $\nu_{x,z} F / 4 > 1$ times stronger than one for the diffraction limited electron beam

Note, that if the energy spread of the beam $\Delta \varepsilon_b$ is much bigger than the limiting one $\Delta \varepsilon_r$, then $\sim 2M+1$ collateral synchronicity conditions $\Delta l_\eta = c \Delta T_\eta = \pm n \lambda_m$ can occur simultaneously. In this case the acquired relative energy spread of the beam:

$$\Delta \varepsilon_b / \varepsilon < 2 M \lambda_m / C \eta_c. \qquad (5)$$

02 Synchrotron Light Sources and FELs

The requirements to the beam emittance for the collateral synchronicity conditions stay (4). They are less severe than ones for the limiting energy spread $\Delta \varepsilon_r$.

Requirements to the electron beam energy spread and emittance are increased with the hardness of the UR $\hbar \omega_m = 2 \pi \hbar c / \lambda_m$. It is difficult to obtain the energy spread of the electron beam $\Delta \varepsilon_r / \varepsilon$ necessary for synchronicity conditions in the X-ray region $(\lambda_m \sim 1 A^0)$, but it is possible to obtain the energy spread $\Delta \varepsilon_b / \varepsilon$ and to work with the main and collateral synchronicity conditions ($0 < |n| < M$). Remarkable part of electrons in the beam will work effectively in this case. The transient behavior of the power of the emitted undulator radiation can be used for its amplification [4].

By using a linear system of N_u pickup undulators, SSUK, (see Figures 1, 2) located along the straight section of the storage ring one can amplify this process N_u^2 times. Note that for the SSUK the requirements to the bunch parameters are much easier then (4). They are determined by (4) if we replace C on l_0, η_c on $\eta_{c,l}$, $\lambda_{x,z}$ on l_0, and suppose $\nu_{x,z} = F = 1$, where $\eta_{c,l}$ is the local slip factor do not burden by the auto phasing problem. Note that there are no problems to produce the isochronous linear system of undulators with the zero local slip factor in optical region [5].

SPONTANEOUS INCOHERENT SSUR SOURCES

Obviously, all properties of the spontaneous incoherent radiation emitted by the electrons in a SSUR source under main synchronicity condition $n = 0$ are not changed, except intensity, which becomes higher by $F / 2\pi$ times. At collateral synchronicity conditions ($|n| > 0$) the URWs emitted by an electron at each pass through the undulator are shifted by the distances $\pm \lambda_m, \pm 2 \lambda_m, ... \pm n \lambda_m$, $\cdots \pm M \lambda_m / 2$ with the gaps $\Delta l \le \lambda_m / F$ for the next URW relative to previous one and the properties of radiation are different: the intensity is dropped, but the monochromaticity is increased with the number n.

The scheme of the SSUR source requires an electron beam with ultralow transverse emittance, energy spread and an optical resonator with high finesse (quality factor). This is possible in cm to optical and UV regions. X-ray mirrors applicable for the Light Sources (LS) now are the mirrors based on the Bragg scattering. These mirrors effectively reflect radiation in a very narrow spectral range $\Delta \omega_{refl}$ ($\hbar \Delta \omega_{refl} \sim 1 \ meV$). The intensity reflection coefficient in this frequency range can be high $r_{Br} \simeq 1 - 2 \pi / F_{refl} \simeq 0.99$ and near to zero ($r_{Br} \simeq 0$) in the rest spectral region. The total energy of the URWs during round trip reflection will be decreased $r_{Br} r_{Br,tot}^{-1} = \Delta t_{refl} / \Delta t_{URW} = M_{refl} / M >> 1$ times, where

$\Delta t_{refl} = T_1 M_{refl}$ is the duration of the reflected URW, $T_1 = 2\pi / \omega_1$, $M_{refl} = \hbar\omega_1 / \Delta(\hbar\omega)_{refl} \simeq 10^6 - 10^7$ is the number of cycles in the reflected URW. The degree of monochromaticity $\Delta\omega / \omega$ and coherence length of the reflected URW $l_{refl} = c\Delta t_{refl}$ will be increased $r_{Br,tot}^{-1}$ times.

The fronts of URWs reflected by Bragg mirrors will coincide with the initial ones. Electrons will emit their URWs at different moments of time in the limits of the electron bunch current duration Δt_b. The lengths of the reflected URWs $l_{refl} = \lambda_1 M_{refl}$ can be much larger than the bunch length $l_b = c\Delta t_b$. In this case the UR bunch after reflections in the resonator will be presented by one long ($l_{refl} \gg l_b$) nearly pure sine wave except short ($\sim l_b$) head and tail parts of the beam.

SSUR SOURCES AND FREE-ELECTRON LASERS

One important peculiarity of the source suggested here is that there is no requirement for the coherence in radiation among different electrons in the bunch like it is required for the prebunched FELs including ones based on isochronous storage rings. Electrons in this source are not grouped in micro-bunches with the longitudinal dimension $\sigma_\parallel \ll \lambda_m$, separated by the distances which are integers of λ_m. Stimulated process of radiation for each electron is going in the undulator with their own URW fields only. Every electron enters the undulator together with its URWs emitted at the earlier times [3].

When we are talking about a quasi-isochronous storage ring we have in mind that round trip slip factor of the ring is set near to zero. At the same time the local slippage factor can be high in the region occupied by the undulators. It means that bunching of the beam and the emission of coherent UR can be produced by external electromagnetic wave in the undulator or in the SSUK (undulator/optical klystron mechanism). If the large number of electrons satisfying to the synchronicity conditions are located on the length of the URWs $M\lambda_1$ (coherence length, sample) then stimulation of SASE regime by high value seeding URWs from sub-regions satisfied to the synchronicity conditions will appear. Self-bunching will appear as well. In this case outside the undulator or SSUK the bunching can be lost but it will appear again and will be amplified in addition to the previous one by stored co-propagated URWs for the next turns through the same undulator or SSUK. By such way stimulation of the oscillator X-ray free-Electron laser regime under the main and collateral synchronicity conditions can be produced.

CONCLUSION

The phenomenon of self-stimulated incoherent emission of the UR in the SSUKs and quasi-isochronous storage rings is investigated. The requirements to the beam parameters and the degree of synchronicity are evaluated for the SSUR source based on a quasi-isochronous storage ring. We hope that SSUR source based on either the ordinary and compact storage rings using the static or laser undulators, electron or ion beams, ordinary or Bragg resonators will be able to generate both short and continuous, quasi-monochromatic light beams in the optical to X-ray regions.

A transient behavior of the amplitude and the power of the URWs are investigated. It was shown that these values are the quasi-periodic functions of the revolution number in the time interval determined by damping time of the URW in optical resonator. At this interval the power of emitted radiation can be much higher than its steady state value. That is why the emitted power can be increased if the energy of optical beam stored in the resonator will be extracted periodically (or, if the phase of the stored radiation in the URWs will be changed to π) for one revolution of the beam in the ring (overload conditions).

SSUKs could be used effectively both in ordinary and prebunched FELs.

More full statement of the considered and another similar questions see [4].

REFERENCES

[1] E.G.Bessonov. Undulators, Undulator Radiation, Free-Electron Lasers, Proc. Lebedev Phys. Inst., Ser.214, 1993, p.3-119, Chief ed. N.G.Basov, Editor-in-chief P.A.Cherenkov.

[2] E.G.Bessonov. Light sources based on relativistic electron and ion beams, International Con-ference on Charged and Neutral Particles Channeling Phenomena II, Channeling 2006, LNF INFN, Frascati - Rome, Italy, July 3-7, 2006 edited by Sultan B. Dabagov, published in Proc. of SPIE Vol. 6634, 66340X-1 – 66340X-14, (2007).

[3] E.G.Bessonov, M.V.Gorbunkov, A.A.Mikhailichenko, A.L.Osipov. Self-stimulated Emission of Undulator Radiation, Journal Instrumentation JINST_012P_0510, 2010, p.1-4; arXive: http://arxiv.org/abs/1003.3747.

[4] E.G.Bessonov, M.V.Gorbunkov, A.A.Mikhailichenko, A.L.Osipov. Self-stimulated Emission of Undulator Radiation and its Possible Applications. 2010. http://arxiv.org/abs/1009.3724.

[5] N.G.Gavrilov, G.N.Kulipanov, V.N.Litvinenko, I.V.Pinaev, V.M.Popik, I.G.Silvestrov, A.N.Skrinsky, A.S.Sokolov, N.A.Vinokurov, P.D.Vobly. Observation of mutual coherency of spontaneous radiation from two undulators separated by achromatic bend, IEEE Journal of Quantum Electronics, VOL. 27, No 12, 1991, p. 2569-2571.

LIGHT SOURCES IN RUSSIA

E.G.Bessonov, Lebedev Phys. Inst. RAS, Moscow, Russia

Abstract

Possible ways of development of Light Sources (LS) based on relativistic electron and ion beams in accelerators and storage rings in Russia are discussed.

INTRODUCTION

Progress in various fields of natural science, medicine, biology, chemistry and technology is closely connected with the development and use of LS based on relativistic electron and ion beams. One of the main motivations to build such sources is to have a very brilliant and bright source of monochromatic photon beams with smoothly varied frequency in a wide spectral region and varied kinds of polarization. This is achieved on one hand with the production of low emittance particle beams in accelerators and storage rings of differed energy, on the other hand with the use of a variety of undulators and on the third hand with the use of different kinds of the emitting particles (electrons, ions) which can be optimized to the special demands of a certain experiment.

By definition, the LS's are sources of powerful beams of IR to X-rays having high degree directionality, narrow bandwidth, tunability, variable photon energy and polarization. These sources are based on accelerators and storage rings and make possible basic and applied reseach in different   fields that are not possible with more conventional equipment. They are UR sources, including Backward (or Inverse) Compton scattering (BCS) sources and possibly future Backward Rayleigh scattering (BRS) sources. These sources are both spontaneous incoherent UR sources, spontaneous coherent UR sources (prebunched fel's) and stimulated UR sources (fel's) [1]. Development of LS's go on in all these directions. 3 Generations of the LSs are developed. 4th Generation of LSs is in the process.

One of the main motivations to build new generation LS is to have more bright source of photons in a wide spectral region. Brightness and brilliance [*] are determined by the equations

$$B_{rn} = \frac{1}{\hbar\omega}\frac{\partial^2 W}{\partial\omega\partial o}\Delta\omega, \qquad B_{rl} = \frac{1}{\hbar\omega}\frac{\partial^2 W}{\partial\omega\partial o\partial s}\Delta\omega,$$

where adopted $\Delta\omega/\omega = 10^{-3}$, $\hbar$ is the Planck constant, ∂s is the effective source area [2].

If the emitted UR beam is focused onto the sample, then the figure of merit of the UR source is its brilliance. In this case the smaller the particle beam dimensions and divergence, the smaller the sport size and divergence of the photon beam at the sample. The figure of merit of the

source for the unfocused UR beams is its brightness. The brilliance was chosen to be an absolute criterions for generations of LS's. But it can obscure essential distinctions between particular machines which determine if the machine is suited for a given application. Existing IR and optical FELs and future fully coherent monochromatic long duration x-ray FELs are not included in any generation of LSs. A full characterization of a LS involves specification of the brilliance, polarization, spectrum, coherence, and time structure of the emitted radiation. Third generation LSs based on storage rings can complement of forth generation LS's.

Third generation LSs based on storage rings are physically very large (~1000 meters in circumference) with a capability for 30 or more insertion-devices, and a comparable number of bend-magnets and beam lines. They are very expensive and occupy an area the size of a sports stadium. Can be such installation shrunk down to fit on the desk? Similar suggestions are discussed for a long time. Now the Compact LS (CLS) based on small storage ring (~20 – 100 MeV) and laser beam stored in high quality open resonator and propagated along   a straight section of the storage ring with zero dispersion and low beta-function is developed. Radiative cooling of the electron beam in the storage ring by high intensity laser light permits to overcome the problem of intrabeam scattering and to maintain the low emittance of the stored beam and its cross section at the IP at the average beam current I > 10 mA which permits to produce brightness enough for many experiments. Experiments will show the limiting stored currents which are determined by the laser intensity at the interaction point.

BCS and BRS sources can be considered as UR sources. In this case electron trajectories both for free electrons and for electrons bounded by nuclei (in classical approach) are undulator ones. Electrons bounded by nuclei are a very high quality oscillators. The amplitude of oscillations of an electron bounded by nuclei at resonance is much higher then for electron in free space. That is why the cross-section of the Rayleigh scattering is much higher (~10-15 orders) then Compton one [†]. Ion storage rings are much expensive then electron ones. At the same time BRS sources are fraught the ultimate in the capabilities both spontaneous and stimulatd radiation sources in X-ray and gamma-ray regions.

The energy of scattered photons is high. It can reach high value ~5 MeV at the electron energy ~ 500 MeV and the photon energy ~ 1 eV. In this case the electron will be lost at the walls of the storage ring after interaction with a laser photon. Cross section of Compton scattering is small. That is why the intensity and hardness of CLS is

---

[*] Flux refers to the number of photons/s/0.1percentBW, Brightness refers to: photons/s/unit solid angle/ 0.1percentBW and Brilliance refers to: photons/s/unit solid angle/0.1 percent BW/unit area. Forth generation LS will have average brilliance >10^{22} and peak one >10^{30} at photon energies > 1 KeV.

[†] Transition energies and equilibrium amplitudes (oscillator strengths) are calculated in the framework of the quantum theory.

limited. At the same time in case of ion beams the cross section of the Rayleigh scattering is 10 orders higher, the ion mass is much higher and equilibrium emittances in the processes of radiative ion cooling by broad band laser beams [3], [4] can be less then for electron beams, there is no loss of ions on the walls of the storage ring. The main disadvantage of the BRS source is its large dimensions at the relativistic energies and high cost. Now the relativistic ion storage rings are used in elementary particle physics and can be used later for production of BRS radiation. Dedicated BRS can be produced.

What will be 5th generation LSs? Fully coherent monochromatic (relative bandwidth < 10^-8) prebunched x-ray FELs or x-ray and gamma-ray sources based on backward Rayleigh scattering or quantum generators on moving ions?

HISTORY

In 1897, J.Larmor derived an expression for the instantaneous total power radiated by an accelerated charged particle. The following year, A.Liénard extended this result to the case of a relativistic particle undergoing acceleration in a circular trajectory. In 1907, G.Schott obtained expressions for the angular distribution of the radiation emitted by a relativistic electron in a homogeneous magnetic field as a function of the harmonic of the orbital frequency. The helical and sine-like trajectories were considered in general case as well. Nowadays they are named "undulator trajectories". His search in this field was presented in a book devoted to an attempt to explain the discrete nature of atomic spectra in 1912 [5]. In 1944 D.Ivanenko and I.Pomeranchuk showed that SR energy losses due to radiating electrons would set a limit on the energy obtainable in a betatron (~0.5 GeV). Later Schwinger in USA, I.Pomeranchuk, A.Sokolov and I.Ternov (USSR) had worked out in detail the theory of SR from accelerated relativistic electrons. For the first time the observation of SR was produced by H.Pollack in USA. In 1947, V.Ginzburg suggested the idea of spontaneous incoherent UR sources, prebunched FELs and a ring for multiple using electron beams (synchrotrons were absent that time) [6]. In 1951-1953, H.Motz produced first experiments on spontaneous incoherent UR sources and prebunched FELs based on Linear Accelerators (LA). He made an important contribution to the theory of UR sources. First experiments with UR produced in undulator installed in the straight section of a synchrotron were done at LPI RAS, Moscow (1977) [7], [8]. R.Twiss, H.Motz, M.Nakamura and other authors proved prebunched FELs and paid attention on bunching electron beams in fields of undulators and electromagnetic waves in conventional FELs by analogy with the traveling-wave tubes. First FEL based on LA was produced by R.M.Phyllips in 1960 in cm wavelengths [11], [12]. He named such devices "ubitron" (from undulator beam interaction) and suggested the idea of the undulator klystron (UK) consisting of a train of two undulators with a drift space between them for bunching. Bunching of electron beams

and harmonic generation on frequencies multiple to the frequency of the amplified wave takes place in such system. Using dispersion section between undulators of the UK for lengthening of the distance between the wavelets of the UR emitted from these undulators and increasing the gain of the FEL was suggested by N.A.Vinokurov and A.N.Skrinsky in 1977 [13]. Such system was named optical klystron (OK). First experiments with FEL in IR region was produced in 1977 (USA) [14]. High quality optical resonators were used to increase the power of prebunched fel's in [15].

BCS, in which low energy photons are scattered off high energy electrons, was first discussed by E.Feinberg and H.Primakoff in 1948 with regard to the interaction of cosmic electrons with starlight. K.Landeker, M.Lampert considered sources based on reflection of electromagnetic waves from electron beams beginning from 1952. First papers devoted to backward scattering of light from moving mirrors appeared at the beginning of the 19th edge.

Generation hard radiation through BCS in accelerators was discussed by G.Arushanov et al. in 1962 [16]. First BCS gamma-rays were generated by O.Kulikov et al. in 1964 at 680 MeV synchrotron LPI RAS [17]. BRS sources were suggested by K.A.Ispirian, A.T.Margarian in 1973 [18]. In the paper [19] the use of very powerful BRS X-ray radiation for inertial confinement fusion was suggested by N.Basov et al., LPI RAS, 1985. Quantum generators based on relativistic ion beams were suggested L.Miller in 1979 [20].

One of main problems facing the researches is the production of low emittance beams in LA's and storage rings. Cooling of particle beams in storage rings can be used. Synchrotron radiation damping (cooling) of electron beams in storage rings leads to this goal. It is originated from bending magnets of the rings due to the radiative reaction force and is limited by quantum excitation of betatron and phase oscillations. The main task of researches to find optimal magnetic lattice for the rings in this case. Strong focusing lattice with low beta- and zero dispersion functions at straight sections of the rings are required at the undulator locations to obtain high brilliance sources. Additional cooling of the electron beams in compact electron and ion storage rings based on the radiative reaction force in the fields of laser beams can be used as well [3].

LIGHT SOURCES IN RUSSIA

LSs underlies scientific and technological progress in different regions of the human activity. Now they include about 100 operating facilities in different countries. Each of them produces IR, VUV, soft- and hard X-ray beams for different applications in science and technology and γ-ray beams for high-energy physics research. Different magnetic and laser undulators are used. Dozens of photon beam transport lines allow to propagate the radiation to optical systems and experimental stations.

02 Synchrotron Light Sources and FELs

Russia in 70th had one of leading positions in theoretical and experimental investigations of the properties of both spontaneous incoherent, spontaneous coherent and stimulated UR sources. Nowadays there are 3 centres where LSs are in operation. They are in INP RAS, Novosibirsk; IAE, Moscow; and LPI, Moscow. LSs based on storage rings are constructed in Zelenograd, Moscow region. Projects of LSs are developed in JINR, Dubna, Moscow region. The most significant results are in INP, where 2 storage rings (VEPP 3 and VEPP 4) and IR FEL are in operation. Unfortunately these storage rings are very old and used for high energy physics simultaneously (2[d] Generation LSs). Projects of 3[d] and 4th Generation LSs exist. The LS in IAE is the dedicated LS. Booster for the top-up injection is needed to work in the 3[d] Generation LS regime. There are 2 synchrotrons in LPI (C-60 on 680 MeV in Moscow and synchrotron "Pachra", 1.2 GeV in Moscow region). Synchrotron "Pachra" is used for elementary particle physics and sometimes is used as LS simultaneously. It can be used as a booster for intermediary (~1GeV) dedicated LS based on a storage ring (top up energy injection).

Superconducting recirculator on the energy 1-2 GeV for the particle physics and as LS simultaneously is discussed as well.

CONCLUSION

Nowadays electromagnetic Light sources (ELS) based on emission of electromagnetic radiation by electron beams in periodic electromagnetic fields produced by undulators in vacuum stay to be highly promising. As a rule of thumb, the higher the generation of the LS, the higher the brilliance. This is not an absolute criterion and, in fact obscures essential distinctions between particular machines which determine if the machine is suited for a given application. A full characterization of a LS involves specification of the brilliance, brightness, polarization, spectrum, special-time coherence, and time structure of the emitted radiation.

REFERENCES

[1] E.G.Bessonov, Light sources based on relativistic electron and ion beams, Proc. of SPIE Vol. 6634, 66340X-1 – 66340X-14, (2007).

[2] S.Tazzari, Electron storage rings for the production of synchrotron radiation, CERN accelerator school 3-14 Sept. 1994, published in Proceedings CERN 85-19, II, Editors P.Btyant, S Turner, 1985.

[3] E.G.Bessonov, Kwang-Je Kim, Radiative cooling of ion beams in storage rings by broad band lasers, Phys. Rev. Lett., 1996, v.76, No 3, p.431; Preprint LBL - 37458, UC-414, June 1995; Proc. 5th European Particle Accelerator Conference, Sitges, Barcelona, 10-14 June 1996, v.2, pp. 1196-1198.

[4] E.G.Bessonov. The evolution of the phase space density of particle beams in external fields, Proceedings of the Workshop On Beam Cooling and Related Topics, COOL 2009, Lanzhou, China, p. 91-93, 2009.
http://cool09.impcas.ac.cn/JACoW/papers/tua2mcio02.pdf, arXiv:0808.2342v1;
http://lanl.arxiv.org/abs/0808.2342;
http://arxiv.org/ftp/arxiv/papers/0808/0808.2342.pdf.

[5] J.D.Jackson, Classical electrodynamics, 3rd edition (John Wiley and Suns, NY, 1998.

[6] V.L.Ginsburg, On emission micro radio waves and their absorption in air, Izvestia Academii Nauk SSSR, ser. Physicheskaia, 1947, v.11, No 2, p. 165.

[7] H.Motz, Applications of the radiation from fast electron beams, J.Appl.Phys., 1951, v.22, No 5, p.527.

[8] H.Motz, Thon W.Whitehurst R.N., Experiments of the radiation by fast electron beams, J.Appl.Phys., 1953, v.24, No 7, p. 826-833.

[9] D.F.Alferov, Yu.A.Bashmakov, K.A.Belovintsev, E.G.Bessonv, P.A.Cherenkov, Observation of undulating radiation with the "Pakhra" synchrotron, Phys. – JETP Lett., 1977, v.26, N7, p.385.

[10] D.F.Alferov, Yu.A.Bashmakov, K.A.Belovintsev, E.G.Bessonov, P.A.Cherenkov, The undulator as a source of electromagnetic radiation, Particle Accelerators, 1979, v.9, No 4, p.223-235.

[11] R.M.Phillips, The ubitron, a high-power traveling wave tube based on periodic beam interaction in unloaded waveguide, IRE Transactions on Electron Devices, 1960, v. ED-7, No 4, p.231.

[12] C.E.Enderby, R.M.Phillips, The ubitron amplifier-a high power millimetre-wave TWT, Proc. IEEE, 1965, V.53, No 10, p.1648.

[13] N.Vinokurov, A.Skrinsky, Optical Klystron, Preprint IYaF No77-59, Novosibirsk 1977.

[14] L.Elias, W.Fairbank, J.Madey, H.A.Shwettman, T.I.Smith, Observation of stimulated emission by relativistic electrons in a spatially periodic transverse magnetic field, Phys. Rev. Lett., 1976, v. 36, No13, p.717-720.

[15] V.I. Alexeev, E.V.Alieva, K.A.Belovintsev, E.G.Bessonov, A.V.Serov, P.A.Cherenkov, A parametric free-electron laser based on the microtron, Nucl. Instr. Meth., 1989, A282, p.436

[16] G.Arushanov, Ja. Kotov, Photon scattering by moving free electron, Izv. AN Uz. SSR, ser. Phys.-mat. Nauk, 1962, No3, c.70.

[17] O.Kulikov, Yu.Ja.Telnov, E.I.Philippov, M.N.Yakimenko, Compton-effect on moving electrons, Phys. Rev., 138 (1964), 344.

[18] K.Ispirian, A.Margarian, Lasers & resonance radiation of relativistic atoms and nuclei, Phys. Lett., v. 44A, 377 (1973).

[19] N.G.Basov, A.N.Oraevsky, B.N.Chichkov, Resonant transformation of light by relativistic ion beams, Sov. Phys. JETP, v. 62, 37 (1985).

[20] L.D.Miller, Tunable X-ray laser from high energy accelerator, Opt. Commun., v.30,87 (1979).

THE EXPANDED PROGRAM TOOLS FOR KSRS OPERATION WITH ARCHIVATION OF DATA

E.Kaportsev, Yu.Krylov, V.Korchuganov, K.Kuznetsov, K.Moseev, L.Moseiko, N.Moseiko, Yu.Yupinov, RRC Kurchatov Institute, Moscow, Russia

Abstract

The running cycle of Kurchatov Synchrotron Radiation Source (KSRS) [1] includes the injection of electrons with energy 80 MeV from the linear accelerator in the booster storage ring Siberia-1, the accumulation of a electron current up to 400 mA and, then, electron energy ramping up to 450 MeV with the subsequent extraction of electrons in the main ring, storage ring Siberia-2, and accumulation there up to 300 mA, and at last the energy ramping up to 2.5 GeV. The control system is based on the distributed network of the processors operating technological systems of KSRS. The operational level of control system is realized as a local network of the personal computer.

The database describing logic channels of the control, modes of the technological systems and the script of the running cycle of accelerating facilities is developed. The database for preservation of the received parameters of a complex is developed, the program of an archiving received with ADC data is developed. Logic channels of the control are a basis for creation of the user interface. The examples of realization of the software used in operative work KSRS are given.

OPERATIONAL MANAGEMENT OF THE COMPLEX

Network operator's machine consists of workstations running Windows XP, in the local network Ethernet (Fig. 1). [2] Program Management and diagnosis of receiving information from the database server based on MS SQL Server, where it comes from the application server. In our case, the database server and application server are located within a single machine. All executable modules, ADC and DAC combined into a CAN-network. On the application server load management program and collect data from performing devices, sensors and diagnostic tools. These servers are only three: Application server, CAMAC messaging server and Vacuum server.
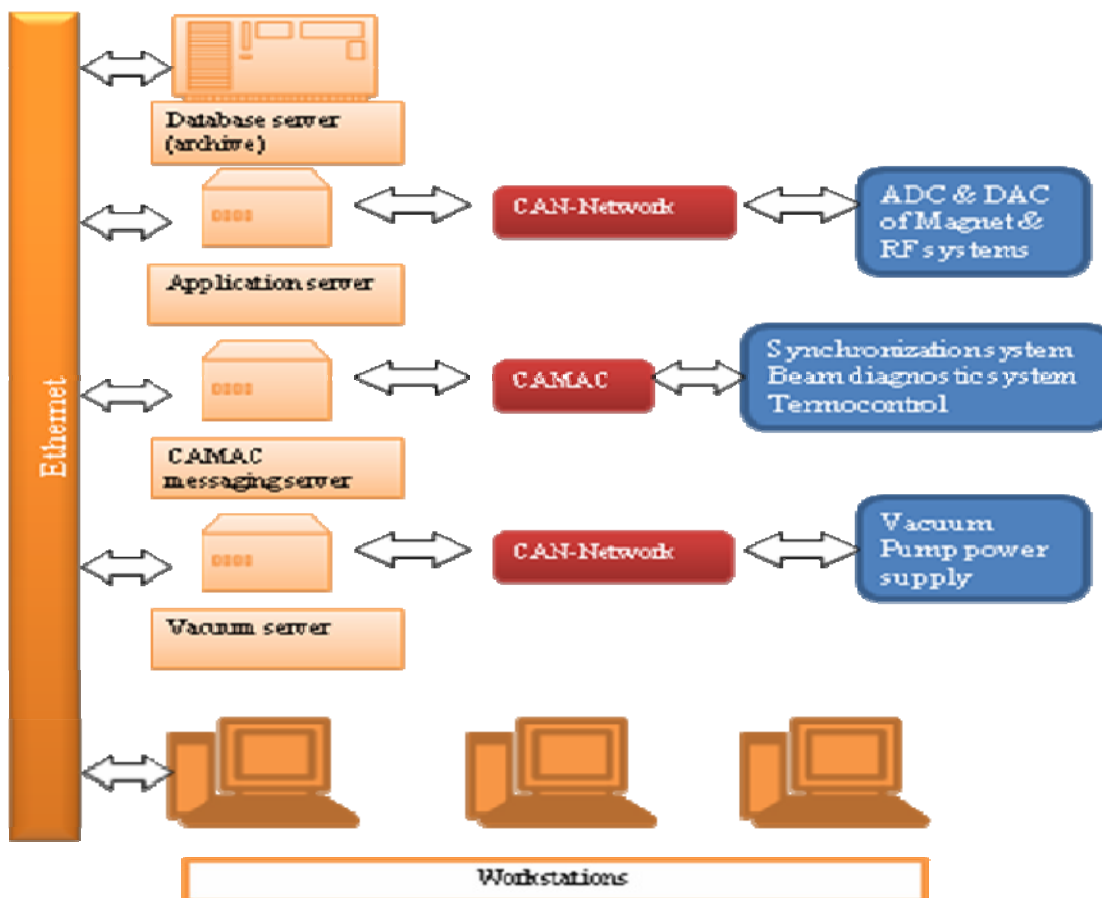
Fig. 1. Scheme of control system.

02 Synchrotron Light Sources and FELs
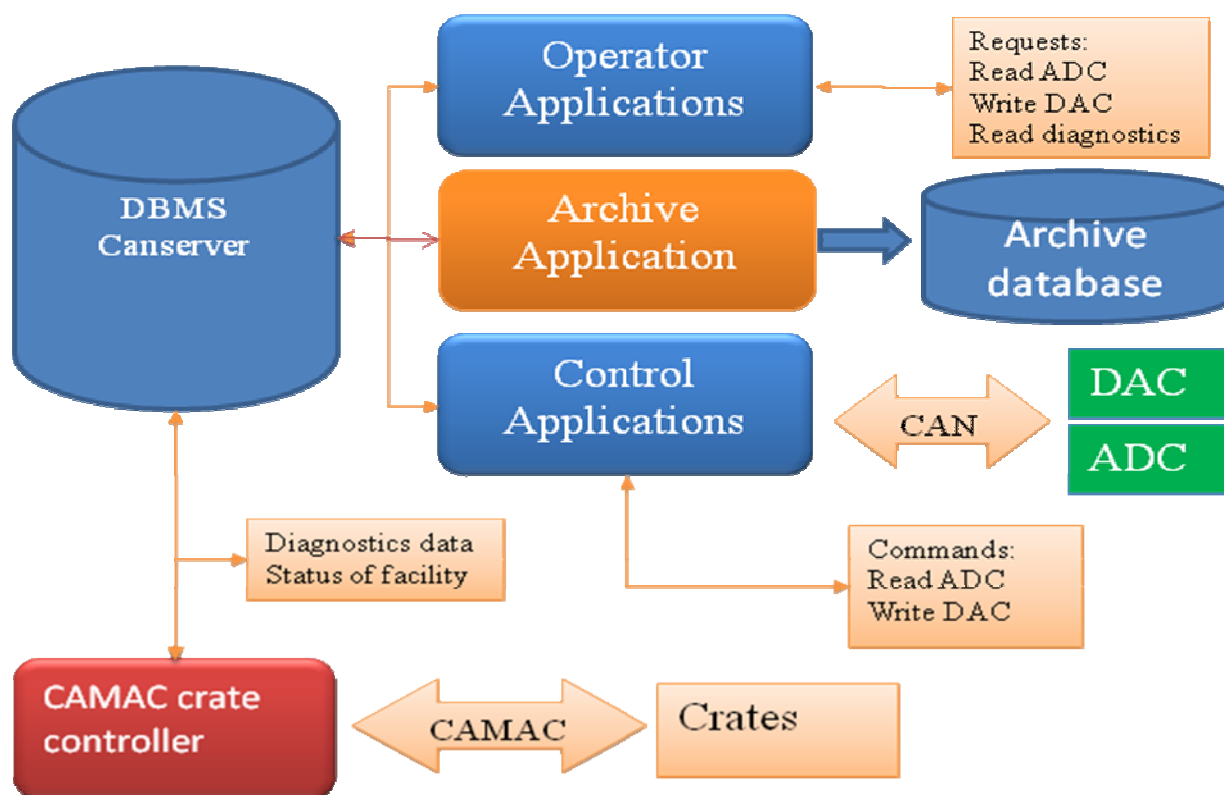
Fig. 2 Scheme for software interaction of ACS.

Canserver server used to control the DAC and ADC via the CAN network. On the application server run specialized programs, which support communication on CAN-network with executive devices, such as high-frequency generators and power of magnetic systems. [3]

Messaging Server CAMAC [4] organizes the exchange of data with CAMAC crate controller with CAN interface type of K167 [5].Through it passed all the information from the controllers and modules that have not yet adapted to the standard CAN.

Management server of vacuum system is directly in the vacuum control room. It has its own database that stores the archive currents of vacuum pumps. [6]

THE SOFTWARE OF OPERATOR

The main tasks of the operator:
- Manage the work cycle of the complex.
- The parameters of the magnetic and RF systems.
- Control of the vacuum, temperature, measurement of the orbit.

To implement these tasks, the operator uses a control system whose structure is shown in Fig. 2.

Operator programs form two types of queries: the measurement of parameters and control complex actuators. These requests come in a special table in the database. Management program read these requests and form special teams to the modules of DAC or ADC. The resulting information is delivered back to the database server, where it reads the operator application and presented to the user through the program interface example which is shown in Fig. 3.
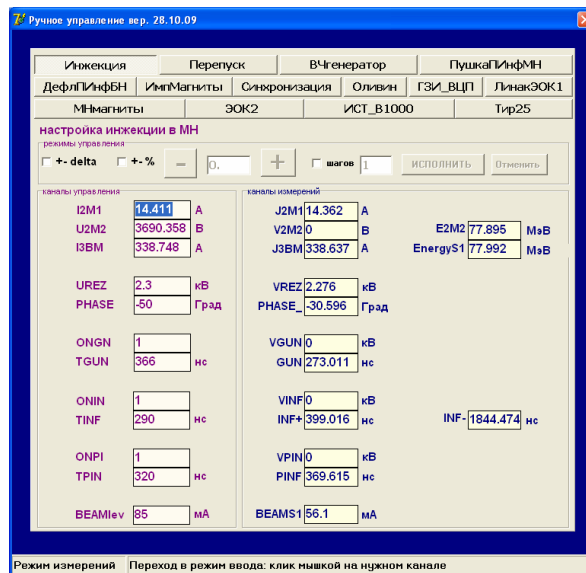
Fig. 3. Examples of operator interface software.

02 Synchrotron Light Sources and FELs
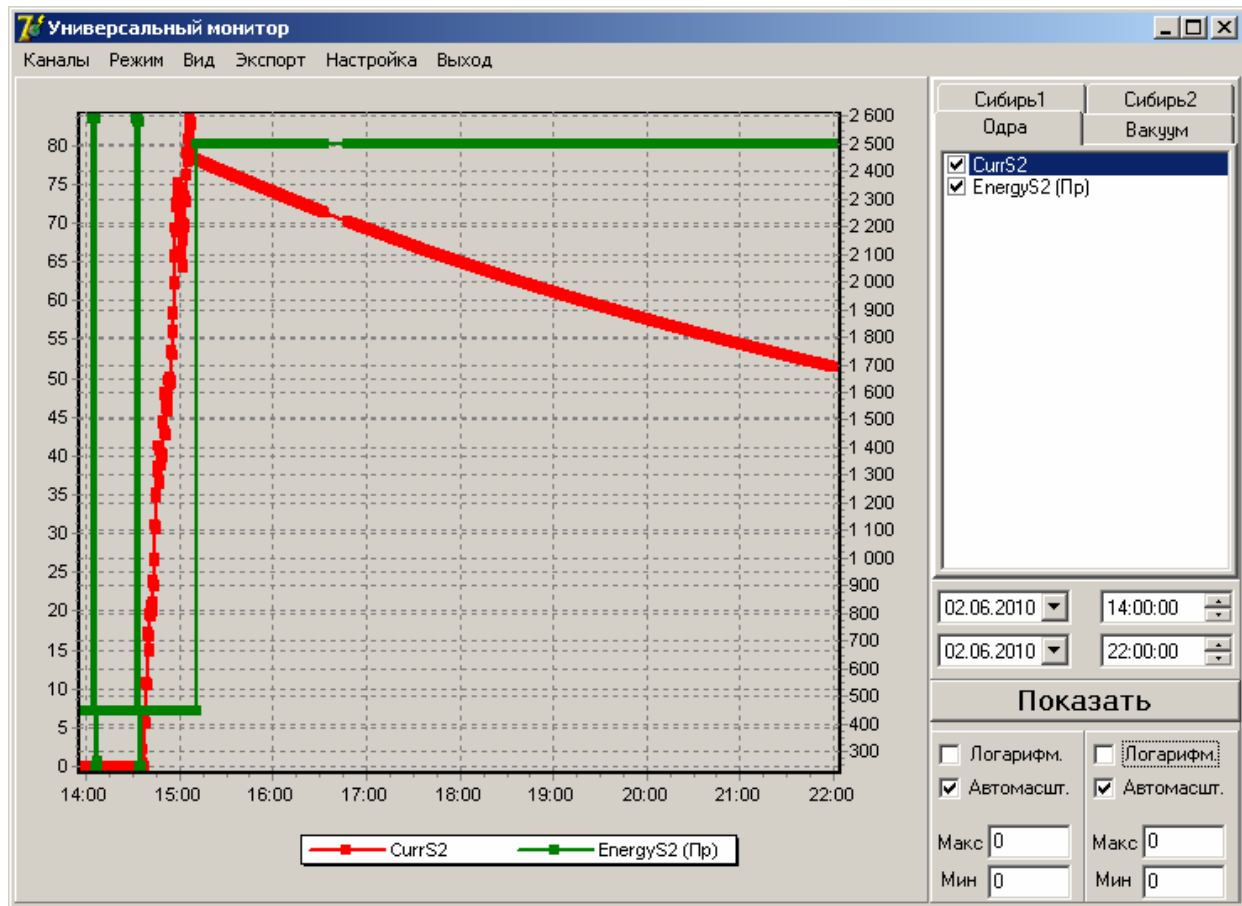
Fig. 4. Interface of Universal Monitor.

ARCHIVING AND READING INFORMATION FROM THE ARCHIVE

Subsystem of the archive is intended to store information on installation and allow subsequent analysis of stored data users. To create an archive data designed a special application. The work program is to create an archive of survey measurement channels and record the data in a database on a dedicated server with a large disk array. Programs working with archival data allows the end user to obtain the requested data in the required form.

The program produces a survey measuring channels of ACS with a period of 5 seconds., and a survey of "slow" measurement channels with a period of 15 seconds. The data obtained are checked for relevance and added to the archive table. When changing the days of creating a new archive table, and the results of the old computed value to create a daily report.

To work with archives created program "Universal Monitor (Fig. 4), which provides a graphical user interface to work with him the necessary data set. Possible to select the channel list, the time interval scale charts, etc. The program also allows you as a hard copy, and export to Excel.

Archived data allow us to get a report on the work setting for a day, week or month. In addition, a relatively simple structure of archive tables allows advanced users to use the data directly using SQL-queries.

REFERENCES

[1] V.Korchuganov et al., Modernization and Development of Kurchatov Center of Synchrotron Radiation. Proceedings of RuPAC XXI, Zvenigorod, Russia, 2008.

[2] Yu. Krylov et al., Upgrading the control system at KCSR. Proceedings of RuPAC XIX, Dubna, Russia, 2004.

[3] E Kaportsev et al., The program tools for KSRS Operation. Proceedings of RuPAC XXI, Zvenigorod, Russia, 2008.

[4] S. Kuznetsov et al., Control system of synchrotron radiation SIBERIA. NIM A352 (1994), p.161-165.

[5] L.Moseiko, N.Moseiko, A.Shirokov, INTEL-LECTUAL CRATE-CONTROLLER K167. Proceedings of RuPAC XXI, Zvenigorod, Russia, 2008.

[6] Yu. Krylov et al., Enhancement of vacuum monitoring system of KCSR accelerator facility. Proceedings of RuPAC XX, Novosibirsk, Russia, 2006.

02 Synchrotron Light Sources and FELs

ACCELERATION OF HEAVY IONS IN SPACE PERIODIC QUADRUPOLE RF FOCUSING STRUCTURE

Yu.A.Budanov, O.K.Belyaev, I.A.Zvonarev, A.P.Maltsev,
State Research Center of Russia Institute for High Energy Physics,
142281, Pritvino, Moscow Region, Russia

INTRODUCTION

Accelerators with space uniform quadrupole radio-frequency focusing (RFQ) are used for a long time already for acceleration not only protons, but also almost all spectrum of accelerated ions. In IHEP the first-ever such accelerator has been implemented, and then various accelerators with RFQ [1] have been produced some more. However, their wide application is limited only by low energy area as an initial part of the accelerator. The effective utilization of radio-frequency focusing on higher energy demands application of accelerating structure with space periodic focusing (RFQ DTL) [1], it has been carried out successfully in IHEP Protvino. Application RFQ DTL is practically realized for acceleration of protons up to 30 MeV [1]. Acceleration of heavy ions with the help RFQ DTL was never carried out, though at acceleration of heavy ions in the first sections of the linear accelerators energetically favorably use of resonators with a longitudinal magnetic field. Essential feature of space periodic focusing is dependence of focusing properties of the channel on a phase of a high-frequency field. Thus, the bunch of particles after preliminary acceleration in RFQ should be enough small in phase size, it is quite provided at acceleration of such easy ions as protons and deuterons. However at acceleration of heavy ions the phase size of the bunches changes essentially more slowly, than for protons, and its remains rather big at the reasonable sizes RFQ, used for a preliminary grouping and acceleration.

In the given report it is offered the suitable device, developed in IHEP Protvino, and parameters of section RFQ DTL. That device will consist of buncher and quadrupole lenses which allow to solve the given problem and, in general, to improve the matching of all six phase variables. Correctors of beam position in transverse plane are proposed in this matching device also.

Numerical calculations are carried out with the example of gold ions Au_{197}^{+32} at working frequency 74 MHz. Energy of transition from RFQ in RFQ DTL 0.4 MeV/u and final energy in RFQ DTL section 2 MeV/u. Calculation of section parameters for the accelerator has preliminary been carried out, determined it acceptance and separatrix. Then parameters and dynamics of a beam in the matching device have been designed. The operating mode of the described devices: $10\,\mu s$ - duration of current pulses and frequency pulses up to 10 Hz is supposed.

PARAMETERS OF RFQ DTL SECTION

The scheme of the acceleration period for RFQ DTL section is presented on fig. 1.
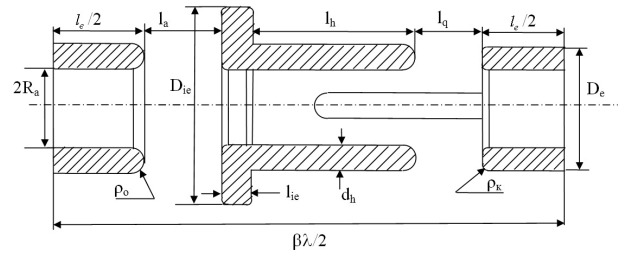
Figure 1: Acceleration period. $2R_a$ − diameter of an aperture, D_{ie} − external diameter of a space electrode, D_e − external diameter of an main electrode, d_h − diameter of a finger electrode, ρ_o − radius of a main electrode, ρ_k − radius of edges of electrodes, $\beta\lambda/2$ − length of the period of acceleration, $l_e/2$ − half of length of an main electrode, l_a − length of an axially-symmetrical gap, l_{ie} − length of an space electrode, l_h − length of a finger electrode, l_q − length of a gap between of a finger electrode and a next main electrode.

Parameters of the periods of acceleration should satisfy to a number of criteria, such as maintenance of electric strength of structure, maintenance of appropriate parameters of longitudinal and transverse movement and enough high rate of acceleration. At a choice of parameters of section RFQ DTL the special attention has been given transverse movement of particles. In this case the type of focusing FFDD has been chosen.

Acceleration and focusing of heavy ions is essentially concerned with acceptance of the channel. Dependence of focusing on phase RF field should be considered already at a preliminary stage. In this case by choice of lengths of quadrupole (focusing) electrodes l_h and lengths of axial (accelerating) gaps l_a it was possible to receive in all range of phases of acceleration such phase advance μ and the minimum value of frequency of transverse oscillation ν_{min}, which yield minimum changes μ and ν_{min}. These changes are not critical for the necessary interval phase of RF field (Fig. 2). This dependence was controlled on all length of the focusing RFQ DTL channel. It is necessary to note, that first and last period of the accelerating channel differs from the regular period (fig. 1).

05 Beam Dynamics and Electromagnetic Fields
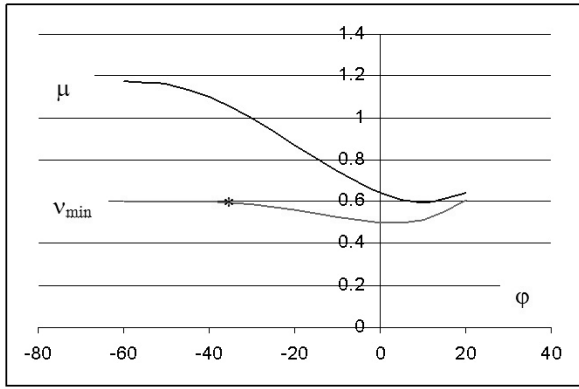
Figure 2: Phase advance μ and ν_{min} .

Under condition of preservation of transverse movement parameters presented on fig. 2 it is possible to generate geometry of the focusing channel for section RFQ DTL with the parameters presented in tab.1.

Table 1: Parameter list of RFQ DTL

Parameter	Value
Beam energy, in, KeV/u	407.113
Beam energy, out, MeV/u	2.012
Voltage across cell, kV	192÷247
Voltage across accelerating gap, kV	119÷174
Voltage across quadrupole gap, kV	73
Max. E-field on surface, kV/cm	280
Stable phase angle	-37°
Gap efficiency	0.65÷0.81
Relative frequency of longitudinal oscillation	0.07÷0.04
Trans. Phase advance	1.07÷0.901
Min. transverse frequency, ν_{min}	0.6
Norm. acceptance, mm ·mrad	2.3π

On the basis of this data the concrete geometry of section RFQ DTL has been evaluated and simulation of beam dynamics is carried out. Received separatrix and acceptance of the channel are presented on fig. 3 ÷ fig.5.

Section RFQ DTL is proposed on the basis of the sector resonator [1] with a longitudinal magnetic field. This resonator possesses good shunt impedance in a considered range of speeds of ions and experimental studies of the resonator were performed in IHEP. Essential feature of this resonator is possibility to realize variable factor of a division of voltage on length of the structure [1]. It is necessary for compensation of a decrease in acceleration rate.

Ems_long= 4.8309
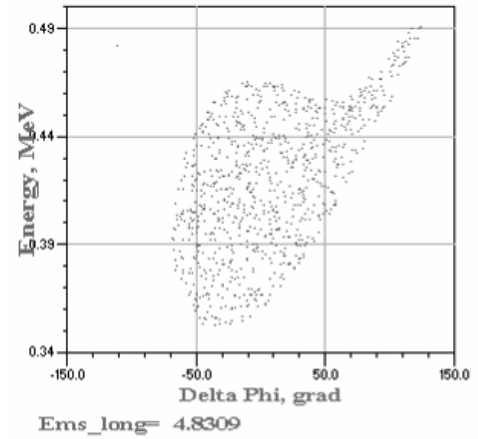
Figure 3: RFQ DTL separatrix.

Alfa=-.00104	A/B= 491.5
E(95%)= 2.188	Erms= 2.074
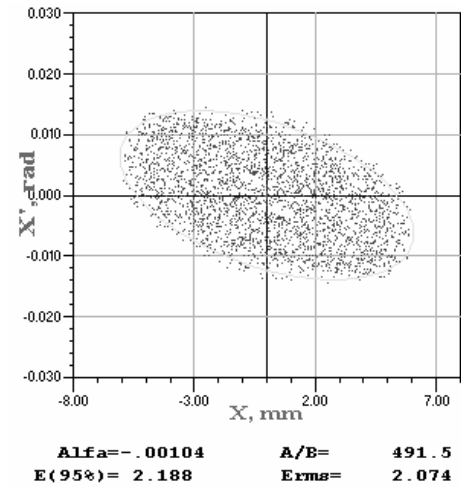
Figure 4: Acceptance x-plane.

Alfa=0.00096	A/B= 188.8
E(95%)= 2.236	Erms= 2.025
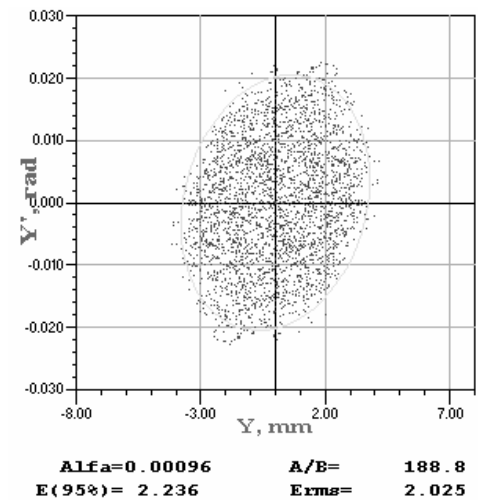
Figure 5: Acceptance y-plane.

05 Beam Dynamics and Electromagnetic Fields

MATCHING RFQ AND RFQ DTL

The received parameters of acceleration rate and acceptance in section RFQ DTL allow using it for acceleration of heavy ions and, particulars of ions Au_{197}^{+32} for which numerical calculation was produced. However, in this case the additional matching of a beam between sections RFQ and RFQ DTL on all phase variables (at acceleration of protons [1] these sections joined directly) is necessary. The example of calculation RFQ for heavy ions is considered in [2]. The scheme of matching device chosen in this report is shown on fig. 6.
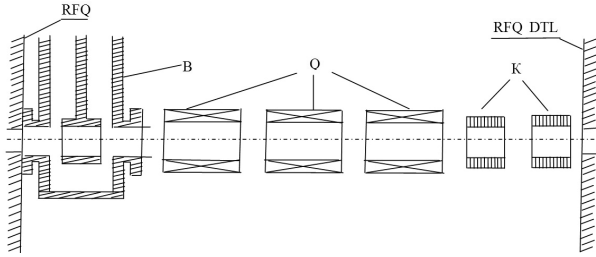
Figure 6: The scheme of matching device, B - buncher, Q - quadrupoles, K - correctors.

It is necessary to notice that for the beam matching it was applied not only the elements of the scheme represented here, but also parameters RFQ at last periods. Namely, due to a small increase of aperture radius at the output of RFQ, characteristics of a transverse movement in RFQ channel are smoothly changed and accordingly a phase portrait of a beam changes also. Such change of parameters of focusing RFQ channel already was applied in accelerator URAL 30M [1]. This part of RFQ electrodes is named by "bellmouth". Thus change of RFQ parameters and variations of magnetic field intensity in three quadrupoles Q of a matching device has allowed receiving four parameters of properties management of a beam for the matching of transverse movement for four phase coordinates.

Distance between RFQ and RFQ DTL (616 mm) is the result of the compromise between the requirement to increase this distance for placing of elements of the channel of the matching and necessity to reduce this distance to that size at which the minimum phase length of a bunch turns out. The named distance is limited by buncher in the given concrete conditions: at its further increase the phase length of a bunch increases. The distance between gaps of a buncher is equal $\beta\lambda/2$. Gradients in quadrupole lenses were estimated from matching conditions. The lengths of lenses in matching device were chosen as long as possible in order to decrease values of magnetic field gradients, but possible in the given conditions. Diameter of the aperture of lenses is chosen so that it greater than the maximum size of a beam.

The special computer program was designed for a finding of an optimum variant of the matching. It works with the help of following algorithm. In a bunch, moving in RFQ, the transverse section corresponding to a synchronous particle is selected. The rms ellipse in each of phase planes is transformed to a canonical form by turn on a angle α_i (i=1,2) and ratio of the half dimensions of ellipse is determined P_i. This procedure takes place at the RFQ DTL input. The same becomes for a corresponding acceptance ellipse of RFQ DTL. Then the functional minimum

$$F = \sum_i \left(\frac{\alpha_i - \alpha_i^0}{\alpha_i^0} \right)^2 + \left(\frac{P_i - P_i^0}{P_i^0} \right)^2$$

is solved by numerical method. The parameters designated by an index (0) concern acceptance figures. The gradients in lenses and parameters of change of transverse movement on RFQ output had been chose by the way, that was stated above. Final accurate definition of gradients in triplet lenses was provided by means of the program for numerical simulation of a beam dynamics in matching channel together with RFQ DTL. In this program all phases of a bunch, and also influence of a space charge of a bunch are considered.

The received parameters of the matching device are presented in tab.2

Table 2: Parameter list of matching device.

Parameter	Value
Length, mm	616
Aperture diameter, mm	30
Voltage, kV	202
Gap efficiency	0.89
Gradient in the first quadrupole, Tl/m	51.2
Gradient in the second quadrupole, Tl/m	60.7
Gradient in the third quadrupole, Tl/m	15.8

CONCLUSION

In the report possibility of application of structures with high-frequency quadrupole space periodic focusing for acceleration of heavy ions is shown. Developed matching device provides the beam matching in transverse phase space and reduces the longitudinal phase size of bunch for reliable capture of a beam in an acceleration mode.

REFERENCES

[1] O.K. Belyaev et al, RFQ Drift-Tube Proton Linacs in IHEP, Proceed. of LINAC 2004, Lubeck, Germany, p. 285–287.

[2] Yu.A.Budanov et al, Heavy Ion Injector for NICA/MPD Project, Proceed. Of LINAC 2008, Canada, p. 121-123.

05 Beam Dynamics and Electromagnetic Fields

METHOD TO ESTIMATE THE BEAM AND STRUCTURE PARAMETERS FOR THE DISPERSION ACCELERATOR PARTS

V.A.Moiseev , INR RAS, Moscow, Russia

Abstract

The beam dynamics parameters as the transverse emittance information, momentum spread and structure characteristics are determined by treatment of the small number of profile measurements for the dispersion accelerator parts. The reliability of measurements is estimated.

INTRODUCTION

For dispersion accelerator parts the qualitative transverse profile measurement treatment is important both for circular accelerators and aside beam lines of the linacs. On a measuring area the dispersion distorts the standard phase space ellipse description [1], where the particles with different longitudinal momentum have other transverse central orbits. For the dispersion plane the off momentum particles have a transverse moving over the central orbit defined by

$$x_c(s) = D(s) \cdot \delta \qquad (1)$$

where $D(s)$ – the dispersion function at an accelerator point s ; δ – the relative particle longitudinal momentum deviation from the nominal value.

Later for simplicity it will be supposed that there is dispersion in the horizontal plane only. The calculations will be presented for this plane.

ASSUMPTIONS AND MATHEMATICAL FORMALISM

Let is proposed the measurement area is placed between the longitudinal coordinates s_0 and s_1 of an accelerator (Fig.1). At the end point a transverse beam profilometer is located.
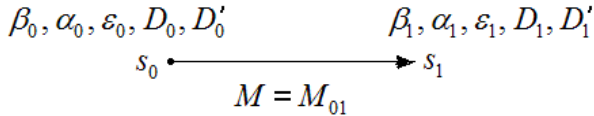
Figure 1: Measurement area

In Fig.1 at points s_0 and s_1 the $\beta_0, \alpha_0, \beta_1, \alpha_1$ are characteristic functions [1] for the beam particles with $\delta \sim 0$; ε_0 , ε_1 - rms unnormalized beam emittances of the beam particles with $\delta \sim 0$; D_0, D_0', D_1, D_1' – the values of dispersion and its derivations; M_{01} – (2×2) transfer matrix of a measurement beam line.

The basic formulas for further calculations are:

$$\overline{x^2}(s) = \overline{\xi^2}(s) + D^2(s) \cdot \overline{\delta^2} \quad ; \quad \overline{x}(s) = \overline{\xi}(s) \qquad (2)$$

where $\overline{x^2}(s) -$ the square of the rms beam profile measurements for the total beam particles; $\overline{\xi^2} = \beta(s) \cdot \varepsilon(s)$ is the standard beam phase space characteristic [1] for particles with $\delta \sim 0$. For Eq.2 the followed assumptions were done:

- the particles with deviation from nominal longitudinal momentum have the identical normalized distribution functions in transverse planes;
- the momentum distribution function is symmetrical.

For simplicity further we suggest that there are no accelerator elements and there are variation elements, for example quadrupole lenses, to change the transfer matrix M_{01} of the measurement area (Fig.1). Therefore the followed equations are valid [1]:

$$\varepsilon_0 = \varepsilon_1$$

$$\beta_1 = m_{11}^2 \beta_0 - 2 m_{11} m_{12} \alpha_0 + m_{12}^2 \cdot \frac{1 + \alpha_0^2}{\beta_0}$$

$$D_1 = m_{11} D_0 + m_{12} D_0' \qquad (3)$$

$$M = \begin{pmatrix} m_{11} & m_{12} \\ m_{21} & m_{22} \end{pmatrix}$$

By using the above formulas for the N_m profile measurement results the Eq.2 may be written in the followed form:

$$\overline{x_i^2} = \beta_i \varepsilon_0 + D_i^2 \cdot \overline{\delta^2} \quad , \qquad i = 1 \div N_m \qquad (4)$$

where index i is referred to the values at point s_1 for each measurement. In Eqs.4 there are six variables $\beta_0, \alpha_0, D_0, D_0', \varepsilon_0, \delta$. To exclude from any two Eqs.4 the variables ε_0, δ , for example by followed formulas

$$\varepsilon_0 = \frac{x_i - D_i^2 \overline{\delta^2}}{\beta_i} \quad ; \quad \overline{\delta^2} = \frac{\overline{x_i^2} \beta_j - \overline{x_j^2} \beta_i}{D_i^2 \beta_j - D_j^2 \beta_i} \quad , \quad i \neq j \qquad (5)$$

and replace these values to any third equation from Eqs.4 the next form may be derived

$$\overline{x_i^2}(\beta_j D_k^2 - \beta_k D_j^2) + \overline{x_j^2}(\beta_k D_i^2 - \beta_i D_k^2) +$$

$$+ \overline{x_k^2}(\beta_i D_j^2 - \beta_j D_i^2) = 0 \ , \quad i \neq j \neq k \qquad (6)$$

In Eqs.6 there are only four independent variables $\beta_0, \alpha_0, D_0, D_0'$. Because of the independence and equality of measurements to combine from N_m by three we get $N_1 = C_{N_m}^3$ equations like Eq.6. In Table 1 this number is presented. The equations like Eq.6 are strongly nonlinear due to the coupling in Eqs.3.

Practically this system may be solved only by numerical methods [2].

If for system of Eqs.6 the measurement results $\overline{x_i^2}$ and matrix elements of M_i are ideal, without errors, it follows that only four equations are needed in system of Eqs.6 to determine variables $\beta_0, \alpha_0, D_0, D_0'$ and as result the variables ε_0, δ from Eqs.5.

Table 1: Characteristic numbers

N_m	4	5	6	7
$N_1 = C_{N_m}^3$	4	10	20	35
$N_2 = C_{N_1}^4$	1	210	4845	52360
$N_3 = C_{N_1}^{N_m}$	1	252	38760	6724520
$N_4 = C_{N_m}^2$	6	10	15	21

REAL MEASUREMENT TREATMENT

Unfortunately the errors are presented both in the profile measurements and elements of transfer matrices for the measurement area. As result the Eqs.6 may be rewritten in form:

$$\overline{\tilde{x}_i^2}(\tilde{\beta}_j \tilde{D}_k^2 - \tilde{\beta}_k \tilde{D}_j^2) + \overline{\tilde{x}_j^2}(\tilde{\beta}_k \tilde{D}_i^2 - \tilde{\beta}_i \tilde{D}_k^2) +$$
$$+ \overline{\tilde{x}_k^2}(\tilde{\beta}_i \tilde{D}_j^2 - \tilde{\beta}_j \tilde{D}_i^2) = b_{ijk} \quad , \quad i \neq j \neq k \qquad (7)$$

where $\tilde{\beta}_i, \tilde{D}_i$ – values calculated by Eqs.3 with errors in the elements of matrix M; $\tilde{x}_i^2$ – square of rms beam profile measurements.

Solution of Basic System

To determine the solution to the basic system consisting from N_1 (Table 1) equations like Eq.7 for undefined variables $\tilde{\beta}_0, \tilde{\alpha}_0, \tilde{D}_0, \tilde{D}_0'$ it may be used the method [2] to minimize function

$$\Phi_m(\vec{y}) = \Phi(\tilde{\beta}_0, \tilde{\alpha}_0, \tilde{D}_0, \tilde{D}_0') = \sum_{m=1}^{N_1} \left| f_m(\vec{y}) \right|^2 \qquad (8)$$

where from Eq.8　　　$f_m(\vec{y}) = b_{ijk}$　　.　　　(9)

However it was proposed another method to find vector $\overline{y}$ in Eq.8. From N_1 equations like Eq.8 it was combined the systems of four equations. The total number of these systems will be $N_2 = C_{N_1}^4$ (Table 1). Each system is solved by minimization algorithm for Eq.8 and Eq.9 where $m = 1 \div 4$. The gradient method [2] and regularization algorithm [3] were used. From Table 1 it follows that for $N_m \geq 5$ the statistic treatment can be applied for solution vectors $\overline{y}_n, n = 1 \div N_2$ to get the average and rms deviations for parameters $\tilde{\beta}_0, \tilde{\alpha}_0, \tilde{D}_0, \tilde{D}_0'$. If the local minimum for Eq.9 is stable

for the different initial approach to vector $\overline{y}$ the results are accepted as final. If for high number of systems there are equalities $\Phi_4(\overline{y}) = 0$ it means there is not local minimum for Eq.8 and the exact solution was found for disturbed data of measurements. This is not correct results because in practice the experimental profile data have accuracy $\sim 10\%$. In this case one of the followed restriction algorithm is used:

- for numerical calculations the limited minimum of $\Phi_4(\overline{y})$ was entered. This limit is determined by the minimum for rms deviation for statistic treatment of solution vectors $\overline{y}_n, n = 1 \div N_2$;

- the limited minimum of $\Phi_4(\overline{y})$ is determined by the calculation of the expected exact measurement results (next section). The deviations of measurements and calculated results have to be less then 10%.

Expected Exact Measurement Results

The algorithm to estimate the quality of measurements was proposed. From previous section the averaged values $\hat{\beta}_0, \hat{\alpha}_0, \hat{D}_0, \hat{D}_0'$ for variables may be introduced to Eqs.7:

$$\overline{\hat{x}_i^2}(\hat{\beta}_j \hat{D}_k^2 - \hat{\beta}_k \hat{D}_j^2) + \overline{\hat{x}_j^2}(\hat{\beta}_k \hat{D}_i^2 - \hat{\beta}_i \hat{D}_k^2) +$$
$$+ \overline{\hat{x}_k^2}(\hat{\beta}_i \hat{D}_j^2 - \hat{\beta}_j \hat{D}_i^2) = \hat{b}_{ijk} \quad , \quad i \neq j \neq k \qquad (10)$$

Now the undefined variables are the expected exact measurement data $\hat{x}_i^2$, $i = 1, N_m$. The Eqs.10 are linear equations. From Eqs.10 the systems with N_m equations may be designed. The total number of systems is $N_3 = C_{N_1}^{N_m}$ (Table 1). For calculations the reasonable number of measurements is $N_m = 5 \div 6$. Every system is solved by minimization of the function

$$\Phi_{N_m}(\vec{z}) = \Phi(\overline{\hat{x}_1^2}, ..., \overline{\hat{x}_{N_m}^2}) = \sum_{m=1}^{N_m} \left| \xi_m(\vec{z}) \right|^2 \qquad (11)$$

where from Eq.10　　　$\xi_m(\vec{z}) = \hat{b}_{ijk}$　　　(12)

To solve Eq.11 and Eq.12 the regularization algorithm [3] for the unstable systems of linear equations must be used.

As results for the vectors $\vec{z}_n, n = 1 \div N_3$ statistical treatment may be applied to estimate the measurement reliability.

Emittance and Momentum Spread Estimation

The application of the averaged values $\hat{\beta}_0, \hat{\alpha}_0, \hat{D}_0, \hat{D}_0'$ calculated in the previous section for determination of ε_0, δ by Eqs.5 has the poor statistics (N_4 in Table 1).

Therefore it was proposed to use the solution vectors $\overline{y}_n, n = 1 \div N_2$ for every system from Eqs.7. The statistics for ε_0 and δ will be the same as for basic vectors $\overline{y}$

(N_2 in Table 1). According to the system design, the equation construction and inequality for Eqs.7, the number of measurement results for calculations, which are used, will be

$$N_5 = \begin{cases} 4 \div N_m & , \quad N_m \leq 12 \\ 4 \div 12 & , \quad N_m > 12 \end{cases} \qquad (13)$$

For determination of the variables ε_0, δ, when the parameters $\tilde{\beta}_0, \tilde{\alpha}_0, \tilde{D}_0, \tilde{D}_0'$ were found, N_5 measurement results are used. With data errors the Eqs.4 may be rewritten

$$\overline{\tilde{x}_i^2} - \tilde{\beta}_i \tilde{\varepsilon}_0 - \tilde{D}_i^2 \cdot \overline{\tilde{\delta}^2} = c_i \quad , \qquad i = 1 \div N_5 \quad (14)$$

The solution for system Eq.14 is carried out by the minimization of function

$$\Phi_2(\vec{\zeta}) = \Phi(\tilde{\varepsilon}_0, \overline{\tilde{\delta}^2}) = \sum_{m=1}^{N_5} \left| c_m(\vec{\zeta}) \right|^2 \qquad (15)$$

From Eq.13 it is evidence the number of the equations in Eqs.14 is $N_5 > 2$ (the number of variables). The regularization algorithm [3] for unstable systems of linear equations was used to solve Eqs.14 with Eq.15. The results are vectors $\vec{\zeta}_n, \ n = 1 \div N_2$ and further the standard statistic treatment may be used.

It should be noted that for Eqs.14 the expected exact measurement data $\overline{\hat{x}_i^2}$, $i = 1 \div N_m$ might be used instead of the experimental data $\overline{\tilde{x}_i^2}, i = 1 \div N_m$. It leads to the results with small differences for the average values $\hat{\varepsilon}_0$ and $\overline{\hat{\delta}^2}$ with essentially less rms deviations from these values. However the additional investigations have to be done.

Beam Centre Dynamics

According to Eq.2 and Eqs.3 the beam center dynamics with measurement errors may be described by

$$\tilde{x}_{ci} - \tilde{m}_{11i} \tilde{x}_{c0} - \tilde{m}_{12i} \tilde{x}_{c0}' = d_i \qquad i = 1 \div N_m \qquad (16)$$

where $\tilde{x}_{c0}, \tilde{x}_{c0}'$ – unknown beam centre phase space coordinates at longitudinal point s_0 (Fig.1); $\tilde{x}_{ci}$ – experimental beam centre at point s_1; $\tilde{m}_{11i}, \tilde{m}_{12i}$ – elements of matrix M for the measurement with number i.

Appling the method from previous sections the systems for two variables were constructed. The number of systems is $N_4 = C_{N_m}^2$ (Table 1). For $N_m = 5$ or 6 the statistics is poor. Therefore the minimization algorithm may be applied to the total system Eqs.16 for function

$$\Phi_2(\vec{\tau}) = \Phi(\tilde{x}_{c_0}, \tilde{x}_{c_0}') = \sum_{m=1}^{N_m} \left| d_m(\vec{\tau}) \right|^2$$

PECULARITIES OF METHOD

- The measurement area may be very shot, that permits to vary the transfer matrix parameters in the wide range without beam particle losses.
- There are possibilities to make the standard statistic treatment and to estimate the reliability of measurement data.
- The parameters of the beam and accelerator structure may easy compare with another experimental and theoretical results.

However now there are the method disadvantages:
- the number of measurements for calculations have to be not less than 5;
- at present there is not effective interactive procedure for the fast data treatments;
- from the form of Eq.2 and Eq.6 the dispersion have to be with the same sign at the point s_1 (Fig.1) for all measurements which are used for the treatments. However two series of measurements may be done for the different dispersion signs if it is possible to carry out.

CONCLUSIONS

The proposed method is valid for a small number of the transverse beam profile measurements. The information about the main beam parameters could be calculated. Simultaneously the beam line structure functions are determined for the experimental area. These data could be used to define the total beam line operation parameters.

REFERENCES

[1] E.Keil, "Single-particle dynamics – linear machine lattices", Theoretical aspects of the behaviour of beams in accelerators and storage rings, Geneva, p.22 (1977).
[2] N.N.Kalitkin, "Numerical methods", Nauka, Moscow (1978) (in russian).
[3] V.V.Voevodin, U.A.Kuznecov, "Matrices and calculations", Nauka, Moscow (1984) (in russian).
[4] S.E. Bragin, A.V.Feschenko, O.V.Grekhov, Yu.V.Kiselev, A.N.Mirzojan, V.A.Moiseev, O.M.Volodkevich, "Reconstruction of the Beam Parameters and Structure Characteristics for INR Isotope Channel", RUPAC'10, Protvino, September 2010.

05 Beam Dynamics and Electromagnetic Fields

RECONSTRUCTION OF THE BEAM PARAMETERS AND STRUCTURE CHARACTERISTICS FOR INR ISOTOPE CHANNEL

V.Moiseev, S.Bragin, A.Feschenko, O.Grekhov, Yu.Kiselev, A.Mirzojan, O.Volodkevich,
INR RAS, Moscow, Russia

Abstract

The various treatments of profile measurements have been applied to estimate both the major beam parameters and structure functions for the INR isotope channel (IC). The main problem for beam dynamics reconstruction consists in the presence of a dispersion function along the beam line studied. The reliable results were obtained and used to form the beam on the target of INR isotope complex.

INTRODUCTION

Special proton beam extraction channel is used at INR linac for isotope production for the technical and medical purposes in wide energy range (100÷160 MeV) [1]. The qualitative beam behaviour control is needed to form the beam on the isotope target. The total beam line for monitoring and forming the desired beam parameters is presented in Fig.1a (linac part) and Fig.2a (isotope channel). The deflection of the proton linac beam is carried out in horizontal plane by two bending magnets BM1 and BM2 (Fig.2a) with the total bending angle 26º.

The profile measurements for linac part (Fig.1a) are made by two 2-wire scanners WS1 and WS2. In isotope channel two-coordinate multiwire profilometer MWP

(Fig.2a) is used. The beam formation on the isotope target is made by all quadrupole doublets shown in Fig.1a and Fig.2a.

For simplicity the measurements and calculations will be discussed below only for the horizontal plane where the dispersion is taken place for the isotope complex beam line.

METHOD 1

This method is based on the measurements by the linac profilometers WS1 and WS2 only. Both monitors are operated simultaneously. The scanning time is ∼ 3 min. For each space step multiple measurements are carried out over the beam pulse. The space step is determined by 1 Hz beam pulse repetition rate, whereas the time structure is sampled at 1 MHz frequency. Any time and space region of beam intensity distribution can be taken for further treatment [1].

For the accelerator part (Fig.1a) the method [2] was realized to determine the transverse beam phase space configuration. The current variations for doublets D15 and D16 (Fig.1a) were used. The well-known beam phase space characteristics (α, β, γ) and rms emittance ε may
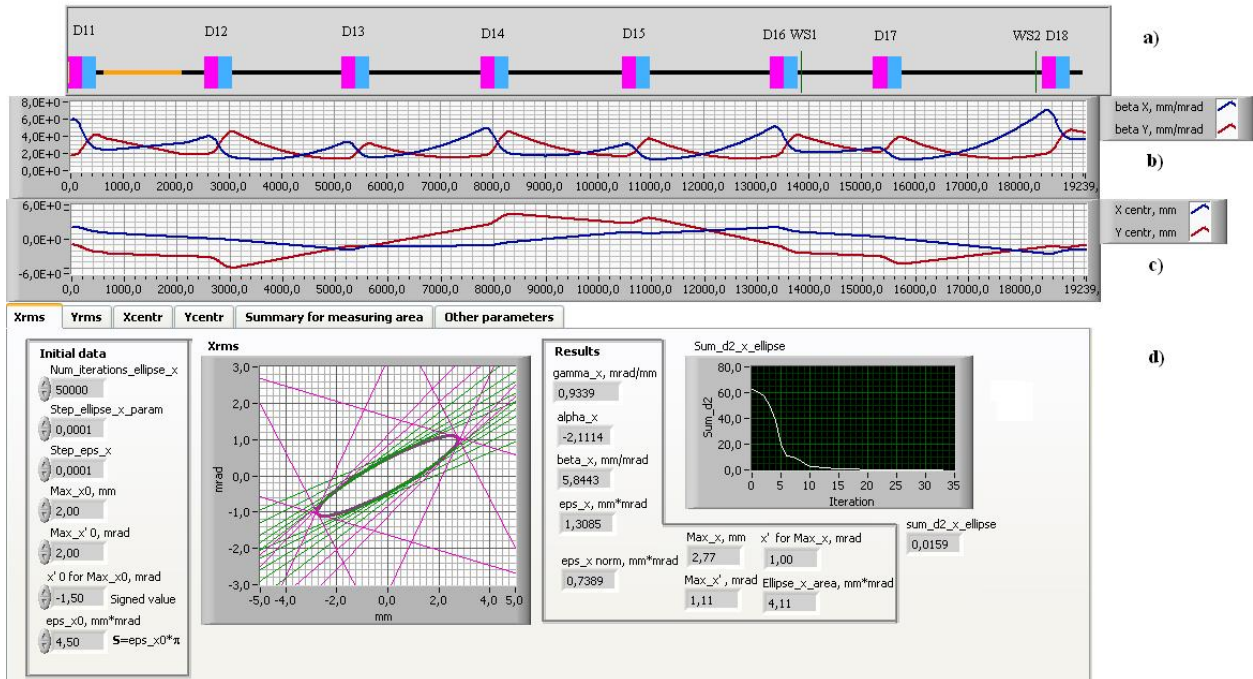
Figure 1: 160MeV beam measuring area: a) lattice: D11,…, D18 - quadrupole doublets; WS1, WS2 – 2-wire scanners; b) $\boldsymbol{\beta}$-function tracing; c) beam center tracing; d) inscribing of the beam phase ellipse and main parameters.

05 Beam Dynamics and Electromagnetic Fields
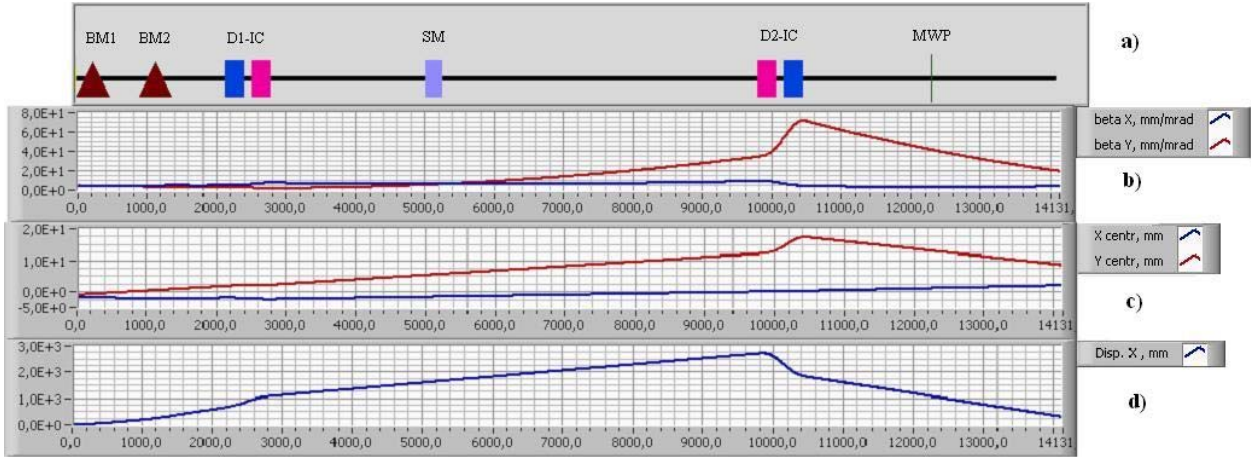
Figure 2: Isotope channel: a) lattice: BM1, BM2 – bending magnets; D1-IC, D2-IC - quadrupole doublets; SM – steering magnets; MWP – multiwire profilometer; b) β-function tracing ; c) beam center tracing; d) dispersion function.

be calculated at any accelerator point. In Fig.1(b, c, d) the Method 1 results are presented for the linac part. The calculated data for the beginning point (Fig.1d) permit to determine the beam phase space characteristics at any point of the accelerator (Fig.1b-Fig.1c) and isotope channel (Fig.2b-Fig.2c) by matrix formalism. The calculated results are used to predict the beam dynamics along any beam line including beam formation on the isotope target.

MEASUREMENTS IN ISOTOPE CHANNEL

The main isotope channel (IC) measurement area is presented in Fig.3. The multiwire profilometer MWP (Fig.2a) is used for the continuous beam size operation control. For the beam characteristic measurements the current variations are used in doublet D2-IC.
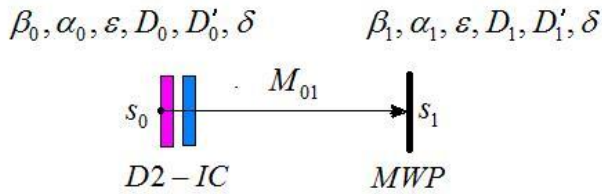
Figure 3: IC measurement area

The beam and structure parameters for proposed determination are shown in Fig.3, where δ is rms longitudinal momentum spread for the beam particles; $\beta_0, \alpha_0, \beta_1, \alpha_1$ – the beam characteristic functions at the beginning s_0 and final s_1 points for the beam particles with $\delta \cong 0$; ε – rms non-normalized beam emittance for the beam particles with $\delta \cong 0$; D_0, D_0', D_1, D_1' – dispersions and its derivations; M_{01} - varied transfer matrix for the beam particles with $\delta \cong 0$. The parameters δ and ε are constant because there are no accelerating elements in the measurement area.

Method 2

The modified Method 1 was developed [1] to treat the transverse profile measurement results for a beam lines with high dispersion. For the standard operation mode of the INR IC beam line the dispersion is ~ 2 m at MWP (Fig.2a) and ~ 3 m at D2-IC entry point. That leads to essential beam spread (~ 40 %) in a dispersion plane. It means that the ellipse presentation of a beam phase space (Method 1) is not valid. It was proposed in [1] to introduce a data correction at the measurement point with presence of high dispersion. The followed formulae were used:

$$\overline{x^2} = \overline{\xi^2} + D^2 \overline{\delta^2} \quad , \qquad \overline{x} = \overline{\xi}, \qquad (1)$$

where $\overline{\delta^2}$ – is the square of a rms longitudinal momentum deviation of the beam particles; $\overline{x^2}$ – the square of a measured rms beam size; $\overline{\xi^2}$ – the square of a rms beam size for particles with $\delta \cong 0$; D – a dispersion function at the measurement point, in our case it depends on D2-IC current and is calculated numerically; $\overline{x}$ – measured beam center; $\overline{\xi}$ – beam center for particles with $\delta \cong 0$.
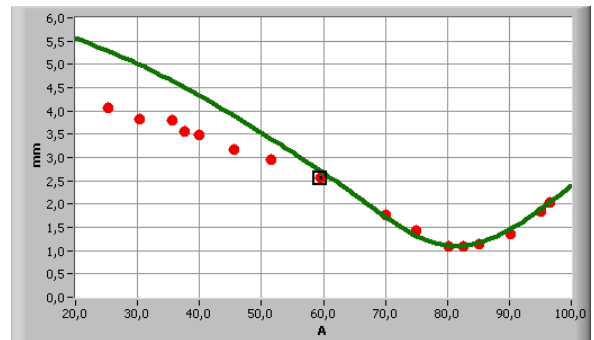
Figure 4: x_{rms} at MWP location vs. D2-IC current.

The results of Method 1 calculations for β – functions and beam sizes along the isotope channel (Fig.2a) are

used to compare with MWP measurements. According to Eq.1 the value of $\overline{\delta^2}$ was chosen to equalize the rms emittances calculated by Method 1 and by Method 2 for variable ξ. The determined rms beam size according to Method 1 results and correction Eq.1 is presented in Fig.4 by solid line. The points are the experimental data and square is the operating mode of the INR isotope channel.

Proposed Method 2 permits to predict qualitatively beam dynamics for the dispersion part of the INR isotope channel and to design beam formation on the isotope target for wide range of the beam energies.

Method 3

In [3] the analytical method is proposed to calculate the phase space beam characteristics and structure functions for beam lines without accelerating elements. The input data are the measurement results, the parameters of varying elements and the beam line information. The last one may be extremely shot to reduce the structure errors and beam losses. The developed algorithm was applied to the beam line in Fig.3 of INR isotope channel. This method includes the theory of combinations and the minimizing numerical algorithms to solve the systems of linear and nonlinear equations where there are errors of the measurement data and elements of transport matrix for the beam line under study.

Eq.1 is the basic one. The calculation results are following: the characteristic phase space parameters of the beam, the structure parameters of a beam line, the rms non-normalized beam emittance ε and rms longitudinal momentum spread δ for the beam particles. These results are averaged for the solutions of more then two hundred of linear and nonlinear equations depending on number of measurements [3]. In this case the rms deviations for calculated values may be statistically determined. Moreover the proposed method permits to estimate the measurement data quality through the calculation of assumed exact measurement data values. The determination of the characteristic parameters $\beta_0, \alpha_0, D_0, D_0'$ at the beginning point of measurement area (Fig.3) permits to define these values outside this part of beam line by matrix operations.

The disadvantages of the proposed method are following [3]:
- the necessary number of measurements must be not less than five;
- there is no fast interactive data processing algorithm now;
- for treatment it is necessary to use measurement data only for the same sign of dispersion at the measuring point (two rows for Method 3 results in Table 1).

COMPARISON OF RESULSTS

In Table 1 the results for fixed measuring cycle are presented. They were obtained for the beginning point of accelerator part in Fig.3 by means of all methods discussed above.

Table 1: Calculation Results

Parameter	Method 1	Method 2	Method 3
β_0, mm/mrad	8.90	5.47	11.65±0.24
			10.79±0.15
α_0	-0.75	-0.79	-0.64±0.10
			-0.92±0.10
D_0, m	2.705	2.705	2.34±0.22
			2.42±0.22
D_0', mrad	234.7	234.7	62.9±71.03
			29.1±147.1
ε, mm·mrad	1.29	1.27	1.11±0.21
			0.98±0.29
δ, %	earlier ~0.103	0.086	0.137±0.021
			0.120±0.019
x_{centre}, mm	-0.05	14.5	14.56±2.65
x'_{centre}, mrad	0.35	0.53	0.72±0.45

The dispersion data for Method 1 and Method 2 are equal and were estimated by tracing along the total line of isotope channel. The calculations by Method 3 were carried out for small beam line (Fig.3) only.

Only Method 3 as was mentioned above permits to estimate the quality of the profile measurements. For measuring cycle presented in Table 1 the beam rms sizes were in the range of (1.3÷2.8) mm. The deviation of expected exact measurement values is less than 0.3 mm.

CONCLUSIONS

Three methods were presented to estimate the transverse beam phase space characteristics and accelerator structure functions. All methods were implemented for the accelerator part and isotope channel to extract proton beam to isotope target. An application of any method for actual problems depends on the requirements to duration of data treatment, graphical support and results quality.

REFERENCES

[1] S.E.Bragin, A.V.Feschenko, O.V.Grekhov, Yu.V.Kiselev, A.N.Mirzojan, V.A.Moiseev, I.A.Vasilyev, O.M.Volodkevich, "Proton beam monitoring and forming on the target of isotope complex at INR linac", Problems of atomic science and technology. Series "Nuclear Physics Investigations" (47), No.2, p 96 (2010).

[2] S.E.Bragin, A.V.Feschenko, O.V.Grekhov, N.F.Lebedeva, V.N.Mikhailov, A.N.Mirzojan, V.A.Moiseev, O.M.Volodkevich, "An Interactive Procedure of the Transverse Beam Matching and Correction in INR Linac", Problems of atomic science and technology. Series "Nuclear Physics Investigations" (47), No.3, p. 116 (2005).

[3] V.A.Moiseev, "Method to Estimate the Beam and Structure Parameters for the Dispersion Accelerator Parts", RUPAC'10, Protvino, September 2010, WEPSB012, (2010); http://www.JACoW.org.

05 Beam Dynamics and Electromagnetic Fields

EXAMINATION OF CHARGED PARTICLE DYNAMICS THROUGH EMPLOYMENT OF THE FOURIER SERIES

O.E. Shishanin, Moscow State Industrial University, Moscow

Abstract

To explore a role of betatron oscillations in accelerators at the generation of synchrotron radiation it was necessary to have the continuous solutions for the Hill equation. In this case the transverse components of magnetic field were expanded in a Fourier series [1, 2]. This approach was usefully employed for the above-mentioned problem and later it has become evident that the same scheme is usable for storage rings. The procedure may even work for wigglers and undulators.

As an illustration let us consider three examples for axial betatron oscillations. The FOFDOD model can be treated as a strongfocusing system in accelerators. Here notations F and D mean focusing and defocusing magnetic fields, respectively, and symbol O is assigned to field-free section. The length L of single period successively consists of $a + l_1 + a + a + l_2 + a$, where a is the length of magnets, l_1 and l_2 are the extension of straight shifts. The path of orbit S is defined as

$$2\pi R + N(l_1 + l_2) = 2\pi R_0,$$

where

$$R_0 = R(1 + k), \ k = (l_1 + l_2)/4a, \ a = \pi R/2N,$$

N is the number of periods. Magnetic field gradient is equal to n at

$$\varphi \in (0, aT) \cup ((a + l_1)T, (2a + l_1)T),$$

where φ is the azimuth angle and $T = 2\pi/(LN)$. If

$$\varphi \in ((2a + l_1)T, (3a + l_1)T) \cup ((3a + l_1 + l_2)T, 2\pi/N),$$

gradient will be $-n$. This periodic step function may be written after expansion as

$$n(\tau) = \frac{8n}{\pi} \sum_{\nu=1}^{\infty} g_\nu \cos \nu(\tau - \tau_1),$$

where $\tau = N\varphi$,

$$\tau_1 = (2a + l_1)\pi/L, \ g_\nu = \sin^2(\pi\nu a/L) \cdot \sin(\nu\tau_1)/\nu.$$

In the middle of the first magnet $\varphi = a\pi/LN$ and after summing $n(\tau) = n$. If take one-half of the second free section $\varphi = (2a + l_1 + l_2/2)T$, then $n(\tau) = 0$. For the points with first-kind discontinuities the function $n(\tau)$ equals, by the Dirichlet theorem, $0, n/2, -n/2$. The field of single magnet H is given as br^{-n}, where b is the constant.

05 Beam Dynamics and Electromagnetic Fields

The equation of vertical oscillations in linear approximation takes the form

$$\frac{d^2z}{d\tau^2} + \frac{(1 + k)^2}{N^2} n(\tau)z = 0. \tag{1}$$

Setting $z = \exp(i\gamma_z\tau)\varphi_z(\tau)$, instead of (1) other equation for function $\varphi_z(\tau)$ may be derived as

$$\frac{d^2\varphi_z}{d\tau^2} + 2i\gamma_z \frac{d\varphi_z}{d\tau} + [\frac{(1 + k)^2}{N^2} n(\tau) - \gamma_z^2]\varphi_z = 0.$$

Putting

$$\varphi_z = \varphi_0 + \sum_{i=1}^{\infty} \varphi_i/N^i, \ \gamma_z = \sum_{i=1}^{\infty} \gamma_i/N^i$$

and exclusive of secular terms one can sequentially obtain: $\varphi_0 = b, \ \varphi_1 = b_1$ (b and b_1 are the constants);

$$\gamma_1 = 0, \ \varphi_2 = bN^2 S_1, \ \varphi_3 = b_1\varphi_2/b,$$

$$\gamma_2 = \pi n\sqrt{1 + k}/2\sqrt{3},$$

where

$$S_1 = \frac{8n(1 + k)^2}{\pi N} \sum_{\nu=1}^{\infty} \frac{g_\nu}{\nu^2} \cos \nu(\tau - \tau_1).$$

Then frequency is formed as $\nu_z = \gamma_z N$ and phase lag equals to well-known quantity

$$\mu_z = \pi^2 n\sqrt{1 + k}/N^2\sqrt{3}.$$

The first terms of asymptotics can be written as follows:

$$z = B[(1 + S_1) \cdot \cos \tau_z + \nu_z S_2 \cdot \sin \tau_z], \tag{2}$$

where $\tau_z = \nu_z\tau/N + \psi$,

$$S_2 = \frac{16n(1 + k)^2}{\pi N^3} \sum_{\nu=1}^{\infty} \frac{g_\nu}{\nu^3} \sin \nu(\tau - \tau_1).$$

Here B and ψ have been interpreted as the amplitude of axial oscillations and the initial phase. It is significant that the solution (2) is the superposition of harmonic curves with modulated amplitudes. The small parameter is n/N^2. To ease the task of estimation of an angular velocity $\dot{\varphi}$, the guiding magnetic field H_0 may be averaged over the entire period and R_0 can be conceived of as a mean radius. After that it is believed that $\dot{\varphi}$ becomes

$$\dot{\varphi} = \frac{\omega_0}{1 + k}[1 - \frac{\rho}{R_0} + \frac{3}{2}\frac{\rho^2}{R_0^2} +$$

$$\int n(\tau)(\frac{z\dot{z}}{R^2} - \frac{\rho\dot{\rho}}{R^2})dt],$$

where $\omega_0 = ceH/E$, $\rho = r - R_0$. The case discussed above was for $n(\tau)$ expansion.

By contrast, in the succeeding section let us consider a Fourier-series expansion of the magnetic field immediately for the storage ring.

In particular, Chasman-Green lattice [3, 4] has in centre focusing quadrupole. Next are magnets, defocusing and focusing quadrupoles by way of straight sections which lie on each side of the middle of period. For single lattice the length L equals $2d + 5a + 8l$, where d is the length of magnet, a is the length of quadrupoles, and l defines extension of free gaps. The path of orbit is

$$S = 2\pi R + N(5a + 8l),$$

parameter $k = (5a + 8l)/2d$.

The transverse coordinates are chose as x and z. As a consequence the quadrupole magnetic fields become

$$H_z^f = -gx, \; H_z^d = gx; \quad H_r^f = -gz, \; H_r^d = gz,$$

where g is the constant of lens, besides index f means focusing and d defocusing. The field of dipole B denotes B_z. The vertical component of magnetic field H_z after expansion is equal to

$$\frac{2d}{L}B - g\rho f(\tau) + B_a, \tag{3}$$

where

$$B_a = \frac{4B}{\pi} \sum_{\nu=1}^{\infty} \frac{(-1)^\nu}{\nu} \sin\frac{\pi\nu}{L}d\cdot$$

$$\cos\frac{\pi\nu}{L}(a + d + 2l) \cdot \cos\nu\tau,$$

$$f(\tau) = \frac{a}{L} + \frac{2}{\pi} \sum_{\nu=1}^{\infty} \frac{f_\nu}{\nu} \cos\nu\tau$$

with

$$f_\nu = \sin\frac{\pi\nu}{L}a[(-1)^\nu +$$

$$4\sin\frac{\pi\nu}{L}(a + l) \cdot \sin\frac{\pi\nu}{L}(2a + 3l)].$$

After averaging of guiding magnetic field in (3) B_a is vanished.

The second component of field takes the form

$$H_r = -gzf(\tau).$$

An equation of axial oscillations becomes

$$\frac{d^2 z}{d\tau^2} + \frac{C}{N^2}f(\tau) \cdot z = 0, \tag{4}$$

where $C = gR_0(1+k)/B$. In comparison with (1) there is constant term in last expression (4). Since sometimes a ratio $C/N^2 > 1$, asymptotics similar to (2) is unsuitable.

05 Beam Dynamics and Electromagnetic Fields

Eq. (4) is the Hill equation with periodic coefficient and large parameter. Besides series

$$\sum_{\nu=1}^{\infty} (f_\nu/\nu) \cos\nu\tau$$

cannot be differentiated. Usual methods of calculation [5] here will not work. Nevertheless if take again the asymptotic in the same form one may obtain a frequency for this model

$$\nu_z = \sqrt{\frac{Ca}{L}}(1 + \frac{\pi Ca}{6N^2 L}).$$

In this case the solution contains a set of sines and cosines with increasing amplitudes. Taking into account an injection of particles and marking off the certain points of trajectory one can enter the initial conditions and resolve the Cauchy problem for Eq. (4).

Finally let us call attention to undulators. The magnetic field strength in sinusoid case [6] is defined as

$$(0, \; 0, \; H\sin 2\pi x/l),$$

where l is the period of undulator. Here the longitudinal component of magnetic fields was neglected. Assume that the vertical part of field alternates up and down via gaps and has a rectangular shape. Using the Fourier expansion this field may be written as follows:

$$H_z = \frac{2H}{\pi} \sum_{k=0}^{\infty} \frac{1}{2k+1}[\sin(2k+1)\frac{2\pi}{l}x +$$

$$(-1)^k \cos(2k+1)\frac{2\pi}{l}x].$$

Apparently there is a need to examine the distinction between two relations. However it should be emphasized that in practice the distribution of magnetic field may not be right-angled. For the magnetic field of an arbitrary configuration one may use numerical methods of harmonic analysis.

REFERENCES

[1] O.E.Shishanin, JETP 76(1993)547.

[2] O.E.Shishanin, JETP 90(2000)725.

[3] H.Wiedemann, Nucl.Inst. and Meth. A246(1986)4.

[4] H.Wiedemann, Particle Accelerator Physics I: Basic Principle and Linear Beam Dynamics, Springer-Verlag, 1993.

[5] A.H.Nayfen, Introduction to Perturbation Techniques, John Wiley & Sons, 1981; "Mir", 1984.

[6] Editor V.A.Bordovitsyn, Radiation Theory of Relativistic Particles, Chapter 5, Moscow, Fizmatlit, 2002.

SIMULATION OF CARBON ION EXTRACTION AND LOW ENERGY BEAM TRANSPORT SYSTEM FOR RFQ AT THE LINAC I-100

B.A. Frolov

State Research Centre of Russia Institute for High Energy Physics,
142281, Protvino, Moscow Region, Russia

Annotation

For the carbon ion injection into the radio frequency quadrupole, the laser ion source and the low energy beam transport (LEBT) system has to deliver 20 mA of C_{12}^{5} ion beam with 80 keV at the input of RFQ within normalized emittance of $0.39\,\pi$ mm·mrad. An extraction system and a low energy transport line should be optimized to reduce the beam emittance as much as possible. The results of computer simulation are presented for extraction and LEBT system: the combination of the tetrode extraction system and the electrostatic focusing lens from three electrodes with middle grid electrode negative voltage.

INTRODUCTION

In the last two decades the methods of ion radiation therapy have been investigated very dynamically. The proton and especially carbon ion beams are a superior tool in treating cancer. Proton-ion radiation therapies hospital medical centers are being actively built in Japan, Germany and Italy. In the nearest future the construction of such centers is planned in the USA, France, Austria and China. For today more than 5500 patients have already been treated with carbon-ion beam at Heavy Ion Medical Accelerator in Chiba (HIMAC), Japan. Patients' treatment was first implemented at Heidelberg Ion Beam Therapy Center (HIT), Germany 2008. The project of the proton-ion beam therapy center in SRC IHEP was developed in 1998-2000 [1]. In the course of experiments held in 2000-2001 stable acceleration of carbon ion was achieved in linac I-100 [2]. In the last few years a large volume of work has been done regarding the modernization of the linear accelerator I-100 and the circular accelerator (booster) U-1.5, the transportation channel of ion beam from I-100 in the booster was built and successfully tested. Experimental researches on acceleration and accumulation of protons and deuterium ions in the circular accelerator U-70 in 2008-2009 revealed the feasibility of using IHEP acceleration complex in medical purposes: for proton-ion radiation therapies [3].

Before 1985 the linear accelerator I-100 was used as a standard proton injector directly into the big synchrotron U-70. Currently I-100 is used as injector of light ions with the energy of 16.7 MeV/u and/or as a reserve injector of protons with the energy of 72.7 MeV/u into the synchrotron-booster U-1.5 [3]. To switch to the carbon ions acceleration mode the gas-discharge source of duaplasmatron type should be replaced with the laser ion source. It seems reasonable to keep the possibility of a fast switch from the proton or deuteron acceleration mode to the carbon ions acceleration and visa versa. The scheme of carbon ion injection into the linac I-100 with the help of radio frequency quadrupole (RFQ) accelerator which is fixed at an angle to the protons injections route was developed in IHEP. The carbon ions acceleration in I-100 happens at the second multiplicity. The switch to the second multiplicity determines the number of restriction at the ratio Z/A for the accelerated ions (where Z is ion charge, A – is its mass). The work [4] shows that the ions with the ratio Z/A=0.4-0.5 can be accelerated in I-100 because of the complex of few restrictions. The percentage of carbon with Z=6 generated by the laser ion source is small [2]. That's why the RFQ parameters calculation was done for the ions beam C_{12}^{+5} at the current of 20 mA and at the injection energy of 80 keV/u. To transport the ions from the source and to modify the beam parameters in accordance with the required at the input to the RFQ the ion-optic system (IOS) of beam matching is to be design.

OPTICAL SYSTEM SIMULATION

The matching of intensive beam of highly charged ions with the input of the linear accelerator   is a complicated and not yet completely solved problem. To the large extent it is due to the strong effect of the space charge forces for the low energy region. IOS calculation is complicated by a full range of other important factors. The laser ion source is used to get the highly charged carbon ion beams. Such source was created in IHEP in 2000 [2]. The duration of multicharged ions formation is a few dozens of nanoseconds. The beam with the needed for future usage duration of a few microseconds is formed due to thermal spread of ions speed in plasma at the drift gap of L=1340 mm length from the laser focusing point till the extraction plane. The experimental investigations [2] showed that the output beam had a complicated time and charge structure. In the beam there are the ions from the first till the fifth charge inclusively. In the initial part of the current pulse ($\sim 5 \div 10$ µs) mainly there are ions with the charge Z=5 and Z=4. During the pulse the profile together with the intensity of the beam with the given charge change. Also the ratio between the currents for ions with different Z changes. As a result of the given above features of the carbon ion beam generated by the

laser ion source (complicated charge structure, plasma flow instability during the pulse, wide spread of ions energies, significant influence of the space charge effect) it is difficult to design the matching channel. It is worthy of note that the method of direct beam injection from the source into the RFQ was suggested and successfully realized in [5,6]. The stage of the target cell was at high voltage and was connected to RFQ linac directly.

IOS should provide the minimal deviation of the effective output ellipse parameters at IOS output from those of the ellipse matched with accelerator input. The calculation value of the normalized emittance of carbon beam at the RFQ input is 0.39 π mm·mrad. The beam emittance from laser ion source depends on the transverse impulse of plasma ions at drift gap output and the aberrations of beam extraction system. Due to the aberration in the matching channel the emittance increases and the beam loss at the accelerator input can be quite significant. That's why the extraction system and a low energy transport line should be optimized to reduce the beam emittance as much as possible. In course of experimental research of the laser source created in IHEP there was used the scheme of carbon ions beam extracting which consisted of a double-grid plasma diode with the voltage between the grids $10 \div 30$ kV [2]. If the beam is postaccelerated up to 80 kV using additional third electrode, the matching channel is to consist of at least two lenses. The matching beam IOS should have at least two degrees of freedom to provide the setting of two output beam parameters (radius and the angle of slope).

IOS in which the systems of beam extracting from ion emitter, acceleration till the given energy and matching are a complete union is suggested below. It is shown on the figure 1 and it consists of six electrodes. It is known that the acceptable ion optics parameters of the beam from the source are achieved upon the condition of emission uniformity over the whole area and its stability in time. The grid should be allocated to fix the plasma border in the plasma electrode surface because of plasma flow nonstationarity for the laser ion source. To extract ions from plasma and for their acceleration to the injection energy the system consisting of four electrodes is used. The length of the first gap (extraction gap) and its voltage should correspond to the given plasma density and provide the initial beam formation. In calculation the formula for optimal gap [7] can be used. In the four electrode system in distinction from the three electrode system the extraction and acceleration voltages do not depend from each other and there already is one freedom degree for the beam parameters formation (third electrode potential). Such optic system allows combining transverse beam matching with postacceleration and transportation with less aberrations. In this case for the beam matching with the RFQ it's enough using one focusing lens.

IOS calculation was done with the help of 2-D code of modeling the optics for positive ions extraction for the system with plasma emitter [8]. Current density at the extraction surface was considered constant and equal to 22 mA/cm^2 . It was suggested that plasma contained only the carbon ions with the charges Z=5 and Z=4, besides the concentration of five-charged ions was 33%, of the four-charged ions - 67%, and this balance remains unchangeable during the pulse. In real situation both ion current density incoming to the emission surface and beam charge structure change quite significantly during the pulse. As it was revealed in experiments in the head part of the beam during the first 10 μs of the current pulse there were only high-charged ions with Z=5 and Z=4. It's also worth mentioning that the approximate twice decrease of five-changed ions amount during the first 5 μs is accompanied by the increase of the four-changed ions amount (see figures [2]). As the time dependence of the current pulse charge composition is complicated, when holding on calculations the current density and percentage of five- and four-changed ions are considered constant.

Poisson equation was solved in cylindrical coordinates. When simulating the method of large particles was used (taking 1000 particles of five-charged and four-charged ions each). The initial axial ion energy (~300 eV) was distributed at a random way (the estimation of the axial velocity was done basing on the drift gap passing time [2]). The initial transverse velocities of ions were also distributed in accordance with the random normal numbers (transverse ions energy in the end of drift gap received from qualitative evaluation is ~ 10 eV).

The numerical calculations showed that the emittance value is minimal when the middle electrode of the matching lens is a grid with negative potential (Fig 1). If for the beam matching einzel lens is used, then bigger aberrations are typical of such IOS as well as the normalized emittance (at the level of 95 % particles) a few times increase the needed at the RFQ input. IOS which consisted of six electrodes was analyzed numerically. As a result of calculations IOS geometry (electrodes radiuses, distances between them) was optimized and were selected the electrodes potentials with which should be guaranteed the maximum particles entry into the calculated ellipse at the RFQ input corresponding to the optimal capture with the injection energy 80 keV. Plasma electrode aperture radius equals to 10 mm, RFQ flange radius is 18 mm, other IOS electrodes radiuses are 15 mm. Gap lengths between the first and the second, the second and the third, the third and the fourth electrodes are 8.5 mm, 20 mm and 12 mm accordingly. The distance between the grid and the electrodes is 11mm. The widths of the second and third electrodes are 4 mm, and the widths of the fourth and sixth are 20 mm. RFQ flange width is 48 mm, and the distance from the flange to RFQ electrodes is 8 mm. Carbon ions calculated trajectories and the electrodes potentials are shown on the figure 1. The figure 2 demonstrates the emittanse pattern at IOS output. The normalized 4-rms emittance for 95 % beam particles is 0.316 π mm·mrad. The emittance pattern shows that the beam is similar to the laminar one.

05 Beam Dynamics and Electromagnetic Fields

The described IOS is space effective and well manageable. It allows matching the beam with RFQ input by regulating third electrode and grid potentials in the same IOS geometry if the beam intensity changes. The extraction voltage should also be changed with the change of the current density.
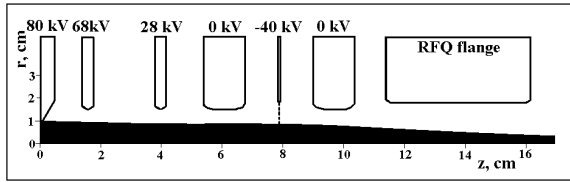
Fig.1. Geometry of the IOS and trajectory of carbon ions.
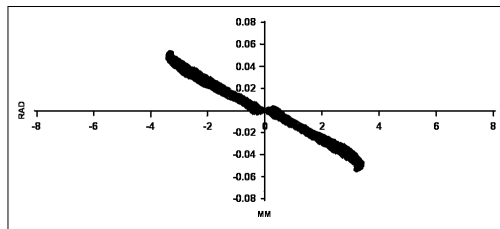
Fig.2. Emittance pattern.

REFERENCES

[1] Yu.M. Antipov, A.V. Vasilevskiy, A.P. Vorobiov et al., Proc. of XVI Charged Particle Accelerator Conference, Protvino, 1998, v. 2, p. 212-219; Yu.M. Antipov, A.V. Vasilevskiy, A.P. Vorobiov et al., Proc. of XVII Charged Particle Accelerator Conference, Protvino, 2000, v. 2, p. 302-307.

[2] Yu.M. Antipov, B.A. Frolov, Yu.P. Gorin et al., ., Proc. of XVII Charged Particle Accelerator Conference, Protvino, 2000, v. 2, p. 385-389; Yu.M. Antipov, N.E. Anferov, V.A. Batarin et al., Preprint IHEP, 2001-52, Protvino, 2001, p.10.

[3] Yu.M. Antipov, N.E. Anferov, V.A. Batarin et al., Preprint IHEP, 2003-14, Protvino, 2003, p.14.

[4] Yu.M. Antipov, S.V. Ivanov, Novosti I problemy fundamental'noj fiziki, Protvino, 2008, N3, p. 1-11.

[5] M. Okamura, H Kashiwagi, K. Sakakibara et al., Rev. Sci. Instrum. 77, № 3, Part II,03B303 (2006).

[6] H Kashiwagi, M, Fukuda, M. Okamura et al., Rev. Sci. Instrum. 77, № 3, Part II , 03B305 (2006).

[7] G.D. Alton and H. Bilheus, Rev. Sci. Instrum. 75, № 5, p.1431-1435 (2004).

[8] B.A. Frolov, Proc. of XIX Charged Particle Accelerator Conference, Dubna, 2004; Preprint IHEP, 2004-43, Protvino, 2004, p.8.

SPACE CHARGE SIMULATION USING MADX
WITH ACCOUNT OF SYNCHROTRON OSCILLATIONS

V. Kapin, MEPhI, Moscow, Russia
Yu. Alexahin, Fermilab, Batavia, IL60510, USA

Abstract

Direct space charge forces can be simulated with the 6D beam dynamics code MADX using a number of 4D BEAMBEAM elements with Gaussian transverse profile for charge density. To take into account effects of synchrotron oscillations on space charge (s.c.) forces, the amplitude of BEAMBEAM elements is modulated according to the distance between a particle and the bunch center assuming Gaussian longitudinal profile. Parameters of every BEAMBEAM element (charge and sizes) are defined by local values of beta-function and dispersion, while they are updated according to the beam intensity and beam emittances at every turn. MADX script accomplishing this method has been written for the lattice of the existing Debuncher ring. The slow extraction at the 3rd order resonance with simultaneously varying the horizontal tune and the sextupole strength is considered as one of the options for Debuncher to be used in the "mu2e" project. Our MADX simulation results are compared with results obtained by V.Nagaslaev (FNAL) using the particle-in-cell ORBIT-code. The evolutions of the phase-spaces and the beam intensity within ten thousands turns have shown a good agreement between the MADX and ORBIT results.

INTDRODUCTION

Direct s.c. forces in beam dynamics codes can be represented analytically by the bunch with elliptical cross-section. This approach has been already used with several codes, e. g. FRANKENSPOT [1], MICROMAP [2] and MAD8 [3], where the beam with Gaussian distribution is usually assumed. With the MADX code [4], which is a successor of MAD8 code, the s.c. forces can be simulated using an arbitrary number of 4D BEAMBEAM elements with Gaussian transverse profile for charge density [5,6].

In Ref. [5], the MADX with 4D s.c. has been implemented for coasting beam. In Ref. [6], effects of synchrotron oscillations on s.c. forces have been simulated assuming a prescribed Gaussian modulation of the longitudinal profile for 4D-BEAMBEAM elements.

In this report, the MADX 6D-tracking is implemented and the amplitude of 4D-BEAMBEAM is a function of the distance between an arbitrary particle and the bunch center. The example MADX-script is written for the FNAL Debuncher taking into considerations turn-to-turn variations of the lattice parameters, beam intensity and emittances during a slow extraction process.

S.C. SIMULATIOS WITH MADX

A numerical realization of the s.c. calculations with MADX deals with the s.c. force created by thin elements,

e.g., 4D-BEAMBEAM kicks, which are inserted around the ring according to some integration method. The method had been already implemented in other beam dynamics codes [1-3]. Our task is a step-by-step adaptation some of them to MADX, which is presently one of the most advanced code for nonlinear beam dynamics simulations without space-charge. The most of work is done using a language of MADX input scripts.

In our realization, s.c. kicks are inserted within every lattice thick element (e.g., BEND, QUADRUPOLE, DRIFT, etc.), according to the 2nd order ray tracing integrator [7]. At the beginning, the linear s.c. kicks represented with MATRIX elements are used for calculations of the beam sizes at the given transverse emittances, while an iteration procedure with TWISS command is used. Then, the nonlinear s.c. kicks represented with 4-D BEAMBEAM elements are inserted along the ring instead of s.c. MATRIX elements. The beam sizes of every BEAMBEAM are derived from calculations with MATRIX elements. The number of particles in every particular BEAMBEAM element is set up according to the formula presented in Ref. [3].

The benchmarking for the intense coasting beam in SIS-18 lattice has shown a good consistency with MICROMAP and SIMPSON codes [8]. The benchmarking with MADX assuming a prescribed Gaussian modulation of the longitudinal profile of 4D-BEAMBEAM elements is also showed good resuts [6,8].

6D-MADX tracking with 4D-BEAMBEAMs

To take into account effects of synchrotron oscillations on s.c. forces, the more realistic model is implemented in this report. 6D-MADX tracking determines the distance between an arbitrary particle and the bunch center. The amplitude of BEAMBEAM elements is modulated according to Gaussian longitudinal profile with a variance derived from the longitudinal emittance ε_L calculated according to a special fitting procedure [9] for the integral of distribution function $F(I) = 1 - \exp(-I/\varepsilon_L)$, where I is the action variable.

The beam sizes of 4-D BEAMBEAMs in bending magnets are corrected according to the relation $\sigma_{tot}^2 = \sigma_\beta^2 + [D(s)\sigma_p]^2$, where $D(s)$ is the dispersion.

MADX-tracking in varying lattice

Normally MADX is used for multi-turn tracking in the lattice with constant parameters. The multi-turn tracking in the lattice with turn-by-turn varying parameters can be realized via multi-runs of the one-turn tracking (TURNS=1), while changing the lattice and beam

parameters after every turn. For example, the MADX synopsis is the following one:

```
TRACK, RECLOSS, APERTURE;
        START, X, PX, Y, PY, T, PT;
        RUN, TURNS=1;
ENDTRACK;
```

MADX script accomplishing this method has been written for the lattice of the FNAL Debuncher ring. The developed MADX script has all attributes of a simple particle tracking code. At the beginning, the script accepts the coordinates of the injected particles, and then, after every turn it updates the lattice parameters according to the prescribed law, collects surviving and lost particles, calculates some "integral" beam parameters, updates the charge and sizes of every BEAMBEAM element according to new beam intensity and emittance, reads, fills and saved the tables with temporary parameters. Totally, the MADX-script consists of about 12 hundreds lines without counting the lattice file. The detailed block-diagram of the algorithm can be found in the Ref.[10].

Converting the Debuncher lattice for MADX

Two original Debuncher lattices have been used in MADX simulations: 1) the original MAD8-lattice edited by A.Werkema [11]; 2) the ORBIT-style lattice derived from the MAD8-lattice by V. Nagaslaev [12]. Of the two lattices, the latter can be used for the direct comparison of the results obtained with ORBIT and MADX, and the former for the beam dynamics in the non-linear magnets.

Firstly, the ORBIT-style lattice has been prepared for the MADX simulations. In order to accomplish this conversion, the dedicated FORTARN code has been written. It includes the following steps: 1) the acceptance of about two hundreds of the 6-by-6 sectors matrices; 2) the generation of MADX lattice with matrices and special elements (e.g., apertures, driving sextupoles); 3) the insertion of BEMBEAM elements in places between sector matrices (N_{BB}=213 for Debuncher lattice). Finally, the consistence of the linear optics has been checked with TWISS command of the MADX-code.

Secondly, the MAD8 lattice has been converted into the MADX-lattice, while preserving all relations for elements excitations existed in the MAD8 file. Then, the BEMBEAM elements (N_{BB}=642) have been inserted in the middle of every thick element according to the 2nd order ray-tracing integrator. Again, the consistence of the linear optics has been checked with TWISS commands of the MAD8 and MADX codes.

SIMULATIONS RESULTS

Simulations with ORBIT code

Beforehand the present study, the beam dynamics simulations of the slow extraction in the Debuncher ring had been performed by V. Nagaslaev with the particle-in-cell code ORBIT [12]. The slow extraction at the 3rd order resonance with simultaneously varying the horizontal tune and the sextupole strength is considered as

one of the options for Debuncher to be used in the "mu2e" project [13]. Figure 1 shows the simulation results with ORBIT code. The prescribed ramp-laws for the driving sextupoles and bare tune Q_x are shown in Fig.1,a and Fig.1,b, resp. Figure 1,c shows the tune spread used here for the evaluations of the tune-shift. Figure 1,d presents the number of survived particles (or the beam intensity) vs the turn number. Figure 2 shows evolution of the horizontal phase space $x - x'$ vs the turn number.
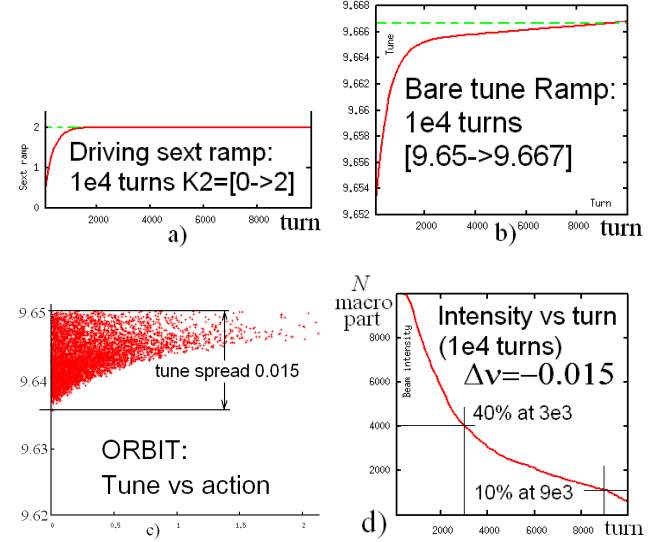
Fig.1 Simulations with ORBIT:
a) The sextupole strength $K2$ vs the turn number;
b) The bare tune Q_x vs the turn number;
c) The horizontal tunes vs the action for every particle ;
d) The number of survived particles vs the turn number.

MADX simulations for the ORBIT-style lattice

Figure 3 shows the simulation results with MADX-code for the ORBIT-style lattice. Evolutions of the beam intensity shown as the number of survived particles for MADX (Fig.3) and ORBIT (Fig.1,d) are in a good agreement. The beam intensity is equal to 42 % and 40% at the turn 3000 and 11 % and 10% at the turn 9000 for the MADX and ORBIT simulations, respectively. Evolutions of beam emittances and the number of particles involved in the evaluations of the emittance fitting are also shown in Fig.3. Evolutions of other parameter had been presented in Ref.[10].

Let's note a very similar behavior of the horizontal phase space evolutions calculated with ORBIT (Fig.2) and MADX (Fig.4).

MADX simulations for the MAD-style lattice

MADX simulations have been also performed with MAD-style Debuncher lattice converted from the original MAD8 lattice. In principle, MAD-style lattice includes many additional high-order effects in comparison with the ORBIT-style lattice, which is composed of the 6-by-6 sector matrices combining several elements included in a sector.

05 Beam Dynamics and Electromagnetic Fields

The simulations have showed that results for MAD-style Debuncher lattice are very similar to the results with ORBIT-style lattice. For example, the beam intensity is equal to 46 % at the turn 3000 and 12 % at the turn 9000. Other results can be found in [10].

CONCLUSION

MADX can be applied for s.c. simulations for coasting and bunched beams. Benchmarking test showed good agreements with other codes. Developed MADX-script for lattice with variable parameters can be used for slow-extraction simulations. Simultaneous usage of MADX and ORBIT allowed to correct possible bugs in data submitted to the codes. The slow-extraction simulations for the intense beams showed a good agreement between results obtained by MADX and ORBIT codes using either ORBIT-style lattice or MADX-style lattice.
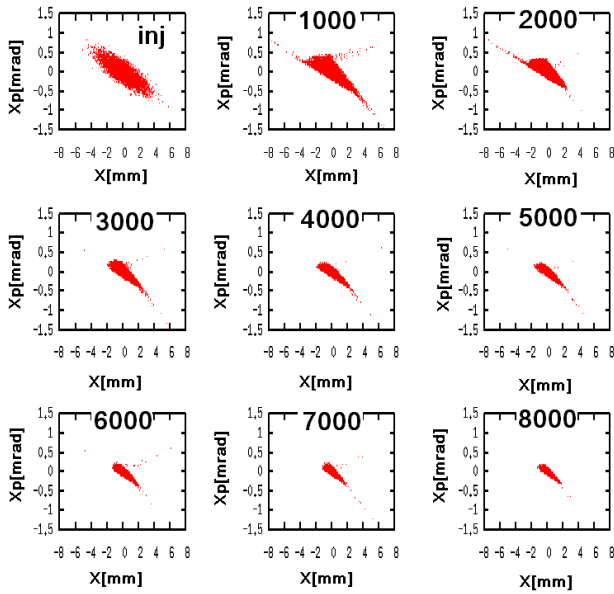
Fig.2 The horizontal phase space evolutions by ORBIT: $x - x'$ vs the turn number.
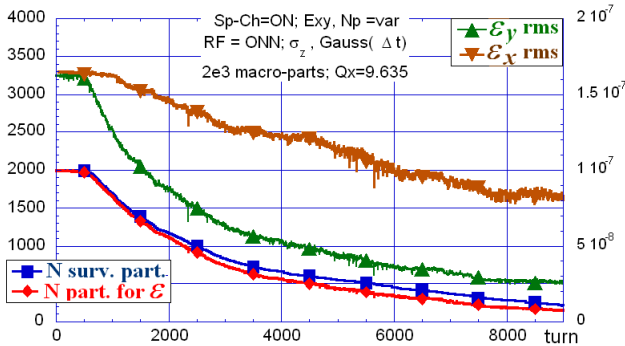
Fig.3 MADX simulations for the ORBIT-style lattice: the dependences on the turn number for the number of survived particles, the number of the emittance particles, and the horizontal and vertical rms emittances.
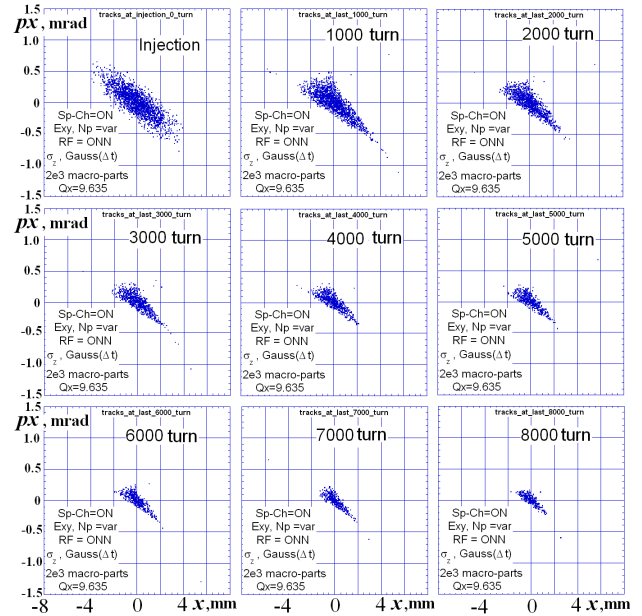
Fig.4 The horizontal phase space evolutions by MADX: $x - x'$ vs the turn number.

REFERENCES

[1] M.A. Furman, "Effect of the Space-Charge Force on Tracking at Low Energy", PAC'87[a], pp. 1034, 1987.

[2] G. Franchetti, I. Hofmann, and G. Turchetti, AIP Conf. Proc. 448, pp. 233 (1998).

[3] Yu. Alexahin, "Effects of Space Charge and Magnet Nonlinearities on Beam Dynamics in the Fermilab Booster", PAC'07[a], pp. 3474-3476 (2007).

[4] MADX home page, http://mad.home.cern.ch/mad/

[5] V. Kapin, A.. Bolshakov, P. Zenkevich, "Influence of Beam Space Charge on Dynamical Aperture of TWAC Storage Ring", RuPAC'08[a], pp.399.

[6] G. Franchetti, I. Hofmann, S. Sorge, V. Kapin, "High Intensity nonlinear dynamics in SIS100", PAC'09, poster TH5PFP023, 2009.

[7] A. Chao, "Symplectic Approximation of Maps", Lecture 7 in SLAC-PUB-9574, 2002.

[8] G. Franchetti, "Code Benchmarking…", http://www-linux.gsi.de/~giuliano/research_activity/ trapping_benchmarking/main.html

[9] Y.Alexain et al, "Simulation of direct space charge in Booster by using MAD program", Beams-doc-2609[b].

[10] V. Kapin, "Space charge simulation using MAD-X with account of longitudinal motion", slides, 31-Mar-2010, FNAL, Batavia, Beams-doc-3582.

[11] S. Werkema, Debuncher MAD8 lattice file, 2009.

[12] V. Nagaslaev, "Slow Extraction from Debuncher for mu2e project", private communications, 2010.

[13] M.J. Syphers, "Status of Mu2e Operating Scenarior", Beams-doc-3558, Fermilab, Batavia, 24-Feb-2010.

TRANSVERSE BUNCH DYNAMICS IN RECTANGULAR DIELECTRIC LOADED WAKEFIELD ACCELERATOR[*]

A.M. Altmark[#], I.L.Sheynman, S.S. Baturin, St.Petersburg Electrotechnical University «LETI», St.Petersburg, Russia
A.D.Kanareykin, St.Petersburg Electrotechnical University «LETI», St.Petersburg, Russia, and Euclid Techlabs LLC, Solon, Ohio, USA

Abstract

Beam breakup (BBU) effects resulting from parasitic wakefields provide a potentially serious limitation to the performance of dielectric structure based accelerators. We report here on comprehensive numerical studies of transverse bunch dynamics in a rectangular dielectric loaded accelerating structure. The numerical part of this research is based on a particle-Green's function beam dynamics code (BBU-3000) that we are developing. The code allows rapid, efficient simulation of beam breakup effects in advanced linear accelerators. It is shown that the LSE modes make its main contribution to the transverse deflecting force causing beam breakup in rectangular DLA structures. Results of test simulations are presented.

INTRODUCTION

A new method of wakefield acceleration of charged particles using bunches passing through the dielectric waveguide structure, is currently the subject of intense experimental and theoretical studies [1-5].

Techniques based on the Dielectric Wakefield accelerator concept are some of the most promising to date in terms of their potential to provide high gradient accelerating structures for future generation linear colliders [2-4].   High-current electron bunches in accelerator structure generate electromagnetic fields with the amplitude of the longitudinal electric field component up to 100 MV/m at GHz frequency range [2-4] and up to ~ GV/m at THz [5], which is used to accelerate the subsequent low-current bunch. The accelerated structure is a dielectric loaded waveguide with an axial vacuum channel, Fig.1. A high charge, electron drive beam propagating through the waveguide vacuum channel generates electromagnetic Cherenkov radiation (wakefields) which is used to accelerate a less intense beam following the leading bunch at an appropriate distance.

The dynamics of the beam in structure-based wakefield accelerators leads to beam stability issues not ordinarily found in other machines [6]. In particular, the high current drive beam in an efficient wakefield accelerator loses a large fraction of its energy in the decelerator structure, resulting in physical emittance growth, increased energy spread, and the possibility of head-tail instability for an off axis beam, all of which can lead to severe reduction of beam intensity. Beam breakup effects resulting from parasitic wakefields provide a potentially serious limitation to the performance of dielectric structure based wakefield accelerators as well [6,13].

The purpose of this work is research on beam dynamic simulations in rectangular waveguide (Fig. 1), providing a number of technological and constructive advantages in comparison with a traditional for DLA cylindrical waveguide. We have implemented software for rapid, efficient simulation of beam breakup effects in this type of DLA structures [13].

WAKEFIELD IN RECTANGULAR WAVEGUIDE

Transverse deflecting force in a rectangular DLA structure is a vector sum of F_x and F_y components, which can be expressed as:

$$F_x = E_x - \beta H_y , \ F_y = E_y + \beta H_x \quad (1)$$

Knowing longitudinal field component E_z one can find F_x and F_y using Panofsky-Wenzel theorem:

$$\int F_x dz = \frac{1}{k}\frac{\partial E_z}{\partial x} , \ \int F_y dz = \frac{1}{k}\frac{\partial E_z}{\partial y} \quad (2)$$

where k is a wave number, E_z – longitudinal component of electric field.

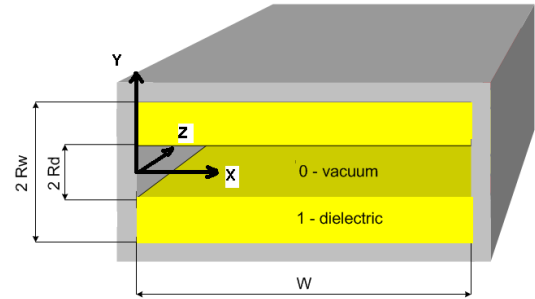Figure 1.Rectangular Dielectric Loaded Accelerating structure with axial vacuum channel: $R_d = 0.5 cm$, $R_w = 1 cm$, $\varepsilon = 10$, $W = 2.3 cm$

The complete $\vec{E}$ wakefield can be expressed in terms of *LSM* (Longitudinal Section Magnetic) and *LSE*

05 Beam Dynamics and Electromagnetic Fields

(Longitudinal Section Electric) modes, and each type of these modes consists of even and odd components correspondingly, where this wave classification is based on eigenfunctions symmetry relatively to the y coordinate [7-9].

Using the expression for the wakefields generated by a point charge in rectangular waveguide, one can write the transverse fields as:

$$Fx = \sum_{n=1}^{N_x}\sum_{m=1}^{N_y}\left(Fxo_{n,m}^{LSM}\sin\left(Kzo_{n,m}^{LSM}\zeta\right)+Fxe_{n,m}^{LSM}\sin\left(Kze_{n,m}^{LSM}\zeta\right)\right)+...$$

$$...+\sum_{n=1}^{N_x}\sum_{m=1}^{N_y}\left(Fxo_{n,m}^{LSE}\sin\left(Kzo_{n,m}^{LSE}\zeta\right)+Fxe_{n,m}^{LSE}\sin\left(Kze_{n,m}^{LSE}\zeta\right)\right)$$

$$Fy = \sum_{n=1}^{N_x}\sum_{m=1}^{N_y}\left(Fyo_{n,m}^{LSM}\sin\left(Kzo_{n,m}^{LSM}\zeta\right)+Fye_{n,m}^{LSM}\sin\left(Kze_{n,m}^{LSM}\zeta\right)\right)+...$$

$$...+\sum_{n=1}^{N_x}\sum_{m=1}^{N_y}\left(Fyo_{n,m}^{LSE}\sin\left(Kzo_{n,m}^{LSE}\zeta\right)+Fye_{n,m}^{LSE}\sin\left(Kze_{n,m}^{LSE}\zeta\right)\right)$$

(3)

where $Kzo_{n,m}^{LSM}$, $Kze_{n,m}^{LSM}$ - longitudinal wavenumbers of odd and even LSM- modes, $Kzo_{n,m}^{LSE}$, $Kze_{n,m}^{LSE}$ - longitudinal wavenumbers of odd and even LSE-modes, $Fxo_{n,m}^{LSM}$, $Fxe_{n,m}^{LSM}$, $Fxo_{n,m}^{LSE}$, $Fxe_{n,m}^{LSE}$, $Fyo_{n,m}^{LSM}$, $Fye_{n,m}^{LSM}$, $Fyo_{n,m}^{LSE}$, $Fye_{n,m}^{LSE}$ - coefficients depending on the coordinates of the bunch and observation point, the bunch charge and wave numbers, ζ -distance behind the bunch.

With this study, we present the beam breakup simulation results for the rectangular DLA structure with the parameters of Fig.1:

We assume that transverse coordinates x and y of the bunch and the observation point are equal each other. Fig. 2 shows dependence of the transverse field on the transverse coordinates x and y. With the bunch trajectory offset increasing along the y-axis, Fig.2a, one can see that all types of the modes including the parasitic ones are excited, and the odd LSE modes will prevail in its contribution to the transverse deflecting field. If the bunch offset increasing off the waveguide center along of the x axis, the deflecting force will be represented only by odd LSM and even LSE-modes. As seen from Fig.2b Maximum of transverse field is reached when offset on x is equal to w/4 value.

In this work we present numerical simulations of the transverse dynamics of the bunch with parameters [10-11]: Q=100nC, $\sigma_z = 0.4\,cm$, $\sigma_x = 0.3\,cm$, $\sigma_y = 0.01\,cm$, $\sigma_x = 0.3\,cm$, $offset_y = 0.08\,cm$, $W = 15\,MeV$ moving along the waveguide with the parameters Fig.1.

The numerical part of this research is based on a particle-Green's function beam breakup code we are developing that allows rapid, efficient simulation of beam breakup effects in cylindrical DLA structures [13]. The new capabilities of BBU-3000 emphasize features important for more accurate treatment of BBU in rectangular dielectric based accelerators [7-9,12].
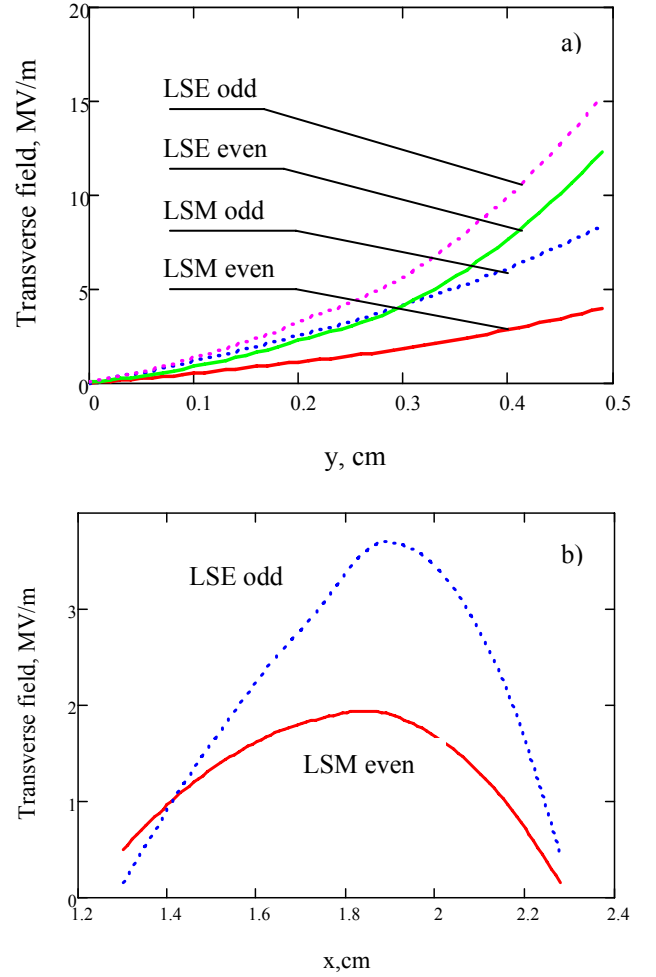
Figure 2.Transverse field as function of a) offset along y ax (with 0 offset along x ax) b) offset along x ax (with 0 offset along y ax.

For a bunch propagating in the rectangular waveguide the particles which are placed in tail of bunch experience the strongest deflecting force. Our simulations showed that the bunch with significant offset of 3mm propagated only 4 cm in the waveguide (Fig.3a) before it touched the dielectric wall, Fig.3. The cross-section of the waveguide at the X-Y plane clearly shows that the particles located around the center of bunch experience main deflecting force, Fig.3b.

At the same time, decreasing offset to 800 um would elongate the structure length up to 10 cm only. Presented test simulations show that the focusing is critical for the rectangular DLA structure the same way as it is required for the cylindrical DLAs that has been studied previously [6,13], and one have to design an external FODO channel for the control of the beam in the presence of strong transverse wakefields.

linearly tapered quad channel in controlling beam breakup is confirmed.

REFERENCES

[1] W. Gai, P. Schoessow, B. Cole, R. Konecny et al. Phys. Rev. Lett. 61, 2756 (1988).

[2] W.Gai. AIP Conference Proceedings v. 1086, pp. 3-11, 2009.

[3] M.E.Conde. Proceedings of PAC07, Albuquerque, New Mexico, USA, pp.1899-1903.

[4] A.Kanareykin. Journal of Physics, Conf. Ser., 236 (2010), 012032.

[5] M. C. Thompson, et al., Phys. Rev. Lett., 100, 214801 (2008).

[6] W. Gai, Kanareykin A. D., A. Kustov, J. Simpson. Phys. Review E 1997, v.55, №3, pp.3481-3488.

[7] L. Xiao, W. Gai, X. Sun. Physical Review E, V. 65, , pp. 1-9, (2001).

[8] C.Jing, W.Liu, W.Gai, L.Xiao, and T.Wong. Phys. Rev. E 68 016502, (2003).

[9] T-B. Zhang, J. L. Hirshfield, T. C. Marshall, B. Hafizi Phys. Rev. E. 56 (1997).

[10] A.Altmark, A. Kanareykin, I. Sheinman. Proc. PAC03, Portland, USA, pp.1897-1899 (2003).

[11] A.M.Altmark, A. D. Kanareykin, and I. L. Sheinman. Techn. Phys., 50, 1 (2005).

[12] A.Altmark, I.L.Sheynman, S.Baturin, A.Kanareykin roc. of IPAC, 2010, Kyoto (Japan), THPD057.

[13] A.Altmark, P.Schoessow, A.Kanareykin, C.Jing, A.Kustov, J.G.Power, W. Gai AIP Conf. Proc. 1086, pp.404-409, (2009).

Fig.3.Results of beam dynamics simulations for the parameters of Fig.1 (solid line show initial borders of bunch) a) Y-Z plane b) Y-X plane

CONCLUSION

The software effort is based on development of the BBU-3000 code upgrade. A number of new features have been incorporated including a rectangular dielectric based structure capabilities.

We have used the new code to model the dielectric structure BBU for the test rectangular structure and AWA electron beam parameters. The results of the simulations show that the main contribution to the transverse deflecting field is made by odd LSE-modes. It was found that the maximum of transverse field is reached at offset value on x equal quarter of the structure half-width that critically impact transverse beam stability. The structure for the tested parameters (Fig.1) can be 4-10 cm long with no focusing applied. Furthermore, the usefulness of a

RF CAVITIES HOM LONGITUDINAL INSTABILITIES AT SR SOURCE SIBERIA-2 IN KCSR

V. Korchuganov, V. Moiseev, A. Smigacheva, A. Vernov, RRC KI, Moscow, Russia.

Abstract

The electron beam parameters stability and its lifetime depend on the resonant excitation by RF cavities HOMs. The instability rising links with the temperature change, the sequent tune of RF cavities and the synchrotron tune change. Besides that the different intensity bunch distribution along the orbit influences strongly on the instability appearance. For the instability study and their identification the spectrum analyzing is used. The results of instabilities study at SR source Siberia-2 are presented in the report.

INTRODUCTION

Electron beam instabilities at high order modes of oscillations in RF cavities can appear at any storage ring and even can be used for beam parameters manipulations. In this report, situation at Siberia-2 is described. The convenient analytic model of HOM instabilities is developed. The experience of instabilities suppression and control is derived. Siberia-2 is a storage ring dedicated for electron beam storage at injection energy level 450 MeV, acceleration up to 2.5 GeV and standing over a long period of time at high energy level to generate synchrotron radiation. The beam life time can reach at high energy level a few tens of hours. Weak beam instabilities can give here the positive effect – the bunch density decrease and as a consequence the beam life time increase. The same situation is observed sometimes at injection but more often the beam instabilities at injection lead to beam losses. Nevertheless, it is not easy to avoid the resonant conditions at injection. Wide band beam current spectrum (up to 7 GHz) consists of narrow lines spaced equidistantly by comparatively low revolution frequency 2.4 MHz. Storage ring RF system (181 MHz) is based on three RF cavities. Cavities are cooled by water in common cooling circuit without precision temperature stabilization. The fundamental modes of oscillations in cavities are tuned by feedback loops in accordance with beam loading and temperature changes. The HOM frequencies are not controlled automatically. Under these conditions, the HOM frequencies may appear near the lines of densely populated beam current spectrum.

ANALITIC DISCRIPTION OF LONGITUDINAL INSTABILITIES AT HIGH ORDER MODES OSCILLATIONS IN RF CAVITIES

To examine the longitudinal stability of rigid bunches circulating in the storage ring and interacting with one of the high modes of oscillations in RF cavities, the set of the linear equations for small phase deviations φ_m of bunches from synchronous values can be written as

$$\ddot{\varphi}_m + \Omega_0^2 \varphi_m + \frac{\Omega_0^2}{V_{RF}\cos\varphi_{s0}} \cdot \mathrm{Im}\sum_{n=1}^{h} \frac{R_{shq}I_{qn}e^{iq\frac{2\pi}{h}(m-n)}}{1+i\eta_{qs}}\frac{q}{h}\times$$

$$\times\left(\varphi_m - \varphi_n + \frac{2\pi}{h\omega_s}(m-n)\left(\dot{\varphi}_m - \dot{\varphi}_n\right) + \frac{2Q_q}{\omega_q(1+i\eta_{qs})}\dot{\varphi}_n\right) = 0 .$$

The set consists of h equations ($m=1,2,..h$) where h is the RF harmonic number, V_{RF} and Ω_0 are the RF voltage and correspondingly the synchrotron oscillations frequency in absence of high order mode excitation. For problem discussed, the dominant circumstance is that some harmonic $q\omega_s$ of beam revolution frequency ω_s is almost equal to frequency ω_q of some mode in RF cavities. For this mode, the shunt impedance R_{shq}, the quality factor Q_q and the detuning factor $\eta_{qs} = 2Q_q\frac{q\omega_s - \omega_q}{\omega_q}$ are used in equations. The bunch intensities are introduced as the doubled bunch circulating currents I_{qn}, $n=1,..h$. The phase equations are worked out under the assumption that every n-th bunch excites in the cavity the field at the frequency $q\,\omega_n$ where $\omega_n = \omega_s - \frac{1}{h}\dot{\varphi}_n$ is the circulating frequency of the bunch in the ring. The complex (with respect to the bunch current) amplitude of bunch excited voltage $V_{qnn} = -\frac{R_{shq}I_{qn}}{1+i\eta_{qn}}$, where the detuning factor

$$\eta_{qn} = 2Q_q\frac{q\omega_n - \omega_q}{\omega_q} = 2Q_q\frac{q\omega_s - \frac{q}{h}\dot{\varphi} - \omega_q}{\omega_q} . \quad \text{Thus}$$

the excited voltage for the bunch is fully braking if the bunch excites the cavity at its resonant frequency, $V_{qnn} = -R_{shq}I_{qn}$. The set of the phase equations presents the standard mathematical problem and can be solved by standard methods in general. At the same time, in particular cases equations allow the simple interpretations. For example, in the particular case for one bunch on the orbit (Robinson instability when $q=h$), the set of phase equations is reduced to one equation,

$$\ddot{\varphi} + \Omega_0^2 \varphi + \frac{\Omega_0^2}{V_{RF} \cos\varphi_{s0}} \frac{R_{shq} I_q q 2 Q_q}{h \omega_q} \dot{\varphi} \, \mathrm{Im} \frac{-2i\eta_{qs}}{\left(1 + \eta_{qs}^2\right)^2} = 0.$$

The solution stability condition here is the non-negative coefficient of $\dot{\varphi}$, that is $\dfrac{-\left(q\omega_s - \omega_q\right)}{\cos\varphi_{s0}} \geq 0$. In the other case for k identical bunches oscillating in phase and under condition that bunches interact at RF frequency ($q = h$) or its harmonic (q is h multiple), the phase equation is the same as above but the instability increment (if instability arises) is proportional to the full beam current.

HOM INSTABILITIES IN STORAGE RING SIBERIA-2

Longitudinal instabilities at high order modes in Siberia-2 are not the dominant processes which can reduce such main parameters of the ring like accelerated beam current or beam life time. At the same time, the instabilities appearance or development can be continuously controlled for successful beam storage and beam energy rising. For measurements and beam diagnostics, the systems and devices are used:

- Wide band (up to 5 GHz) system for observation and measurements of bunch current distributions along the orbit.
- Optical system for integrated in time visualization of beam cross section particle distributions by TV camera.
- Dissector in stroboscope regime (50 Hz) for bunch longitudinal particle distribution measurements.
- Wide band (up to 13.5 GHz) spectrum analyser for precision measurements.

For precision spectrum measurements, signals from coupling loops in cavities and beam current monitors in vacuum chamber are used. Every RF cavity contains four tuning elements – two elements for the fundamental mode and two elements for high order modes. It is important, that elements are not rigorously independent. The fundamental mode tuning causes small changes of high order modes frequencies. The main HOMs quality factors are comparable with the fundamental mode quality factor. The example of field spectrum in RF cavity is given at Fig. 1. The field is excited by power amplifier (181.1 MHz) and beam current at harmonics of revolution frequency (2.41 MHz). The amplifier excites the RF voltage harmonics only and on the levels less then -80 dB with respect to fundamental frequency. Rich spectrum is excited by the beam. At the instability, the level of active mode can reach -10 dB with respect to fundamental mode. The narrow spectrum of beam current illustrates at Fig. 2 the development of instability. The second pair of sides may indicate the quadrupole instability rising. Instability mode is determined be dissector.

CONCLUSION

HOM instabilities appear at injection and in the narrow regions of beam currents. Practical approach here is to overcome the narrow instability regions.
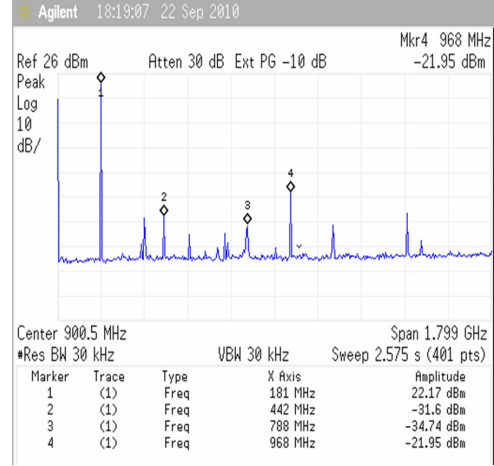
Figure 1: Field spectrum in RF cavity.

At storage ring Siberia-2, the tactics consist of: detuning of active high order modes to the optimal positions; increasing the intensity of injected bunches (to decrease
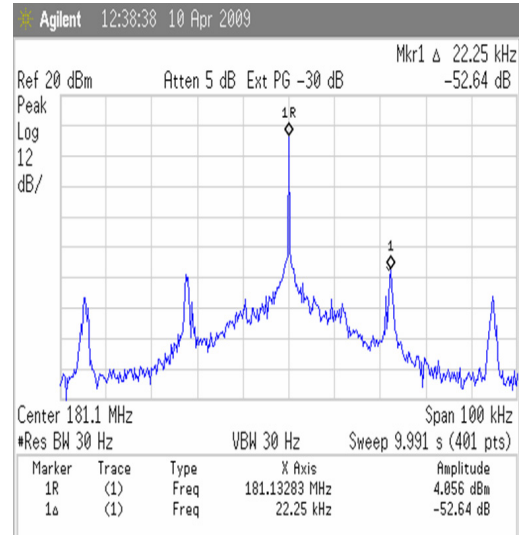
Figure 2: Beam current spectrum.

the time of being at instability regions); in the cavity with active high order mode, changing of the programmable phase (to detune the high order mode); in the cavity with active high order mode, increasing of the programmable RF voltage (to detune the high order mode), changing of bunch distribution along the orbit. As a cardinal solution of problem, the wide band feedback system is assumed at Siberia-2.

NONLINEAR ELECTRON BEAM DYNAMICS WITH LARGE ENERGY SPREAD IN THE MAGNETIC MIRROR

Ye. Fomin, V. Korchuganov, RRC Kurchatov Institute, Moscow, Russia

Abstract

One of the features of new injection system for Kurchatov source of synchrotron radiation is an energy doubling of electron beam in forinjector – linear accelerator. The magnetic mirror provides 180° turn of electron beam into acceleration structure of linac for twice beam energy increase [1]. This paper describes linear and nonlinear electron beam dynamics with energy 80 MeV and large energy spread in the magnetic mirror. The theoretical first order optical functions of the magnetic mirror and the results of computer simulation of electron beam trajectories taking into account large energy spread and curvature of trajectories are presented. The structure of the magnetic mirror providing the achromatic and isochronous 180° turn of electron beam with 7% energy spread is suggested. Mutual influence of "the head" and "the tail" of electron beam when colliding in a straight section spaced in between linac output and magnetic mirror on particle losses and on the longitudinal and transversal parameters are considered.

MAGNETIC MIRROR

The magnetic mirror is a main element of new upgraded forinjector (see Fig. 1). The magnetic mirror has to provide simultaneously the following: a) achromatic and isochronous bend, b) the saving spatial and angular beam size, c) the correction of beam position and angle. In addition, the design of magnetic mirror has to provide correction of electrons enters phase into linac after U-turn.
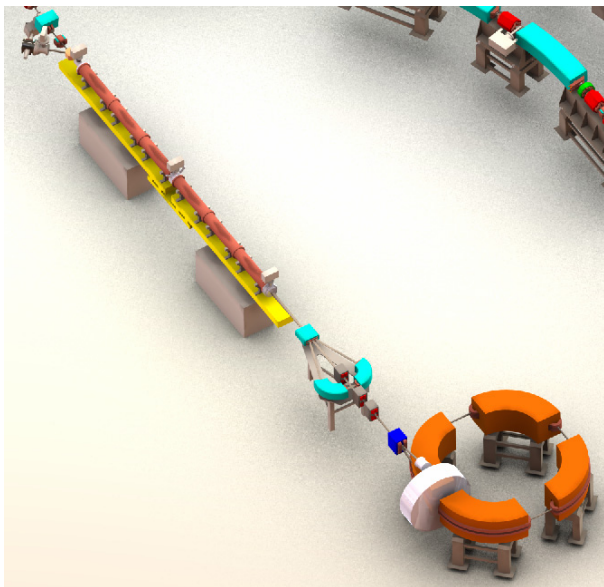
Figure 1: Upgraded forinjector.

The magnetic mirror consists from one 20° turn bending magnet and two complex mirror-symmetrical bending magnets with combined functions. This complex magnet has three components of the magnetic field (dipole, quadrupole and sextupole components) providing simultaneously 110° turn and beam focusing. Structurally the magnet consist from 3 part (see Fig. 2). The first part of magnet has all three components of magnetic fields. The central and the third parts have dipole and quadrupole components of magnetic fields. Dipole component of magnetic field in all three magnet parts is the same and quadrupole component is also the same, but has alternating values. The length of all three parts of the magnet is different.

The most important focusing property of complex bending magnet is the achievement of its length change in the sign of the dispersion function, which allowed to create on the basis of this magnet compact isochronous U-turn (see Fig. 3).
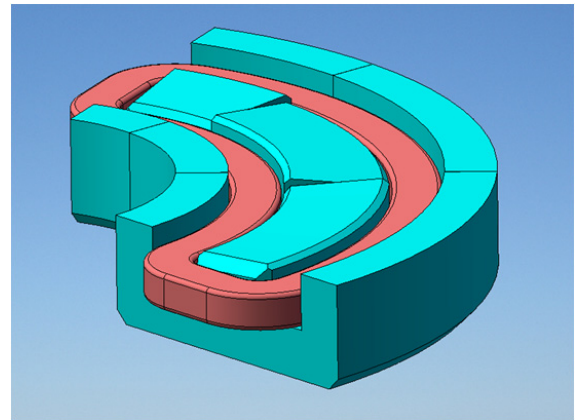
Figure 2. Bending magnet design.

The control of beam will be provided with help collimators, luminophor probes and correctors of trajectory.

LINEAR BEAM DYNAMICS

For magnetic mirror we choose mirror-symmetrical magnetic structure. This structure provides the coincidence of the initial and final values of the optical functions and their derivatives. In addition, in this structure the dispersion function and its derivative is zero and momentum compaction factor is almost zero. This provide achromatic and isochronous bend. The linear optical functions are shown in Fig. 3.

Made early calculations are not quite right for large energy spread (7%) of electrons, because they performed when electrons beam has small energy spread ($\Delta p/p \ll 1$) [1]. To improve our calculations, we take into account large energy spread into linear equations of

05 Beam Dynamics and Electromagnetic Fields

motion. But we will be use the following standard approximation:

- No space charge.
- No interaction between electrons.
- No synchrotron radiation losses.
- Magnet elements have piecewise-constant fields distribution.
- Longitudinal magnetic field component is zero.
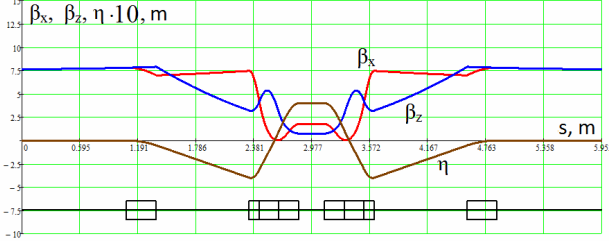
Figure 3. Linear optical functions.

For calculate linear beam dynamics into magnetic mirror we use the following linear equation of motion:

$$X''' + ((2\frac{p_0}{p} - 1)h^2 + \frac{p_0}{p})X = h\frac{\Delta p}{p_0}\frac{p_0}{p} \qquad (1)$$

where $p = p_0 + \Delta p$ - electron momentum, p_0 - momentum of reference electron, $h = B_z/B\rho$ - curvature, $k = G/B\rho$ - focusing coefficient.

Here we present electron beam dynamics only into median horizontal plane, because the motion in this plane is the determining and defining the magnetic mirror structure [1].

The initial data for tracking are the horizontal deviation of electron from reference orbit and its derivative and momentum deviation from reference momentum. This data were obtained by calculation electron beam dynamics into linear accelerator [2]. The beam in horizontal phase space at the beginning of the magnetic mirror is presented at Figure 4.
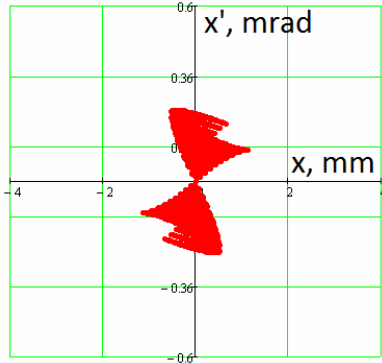
Figure 4. The beam in horizontal phase space at the beginning of the magnetic mirror.

The final data are electron trajectory into magnetic mirror (horizontal deviation of electron from reference orbit and its derivative at any point in the magnetic mirror) and trajectory length into magnetic mirror.
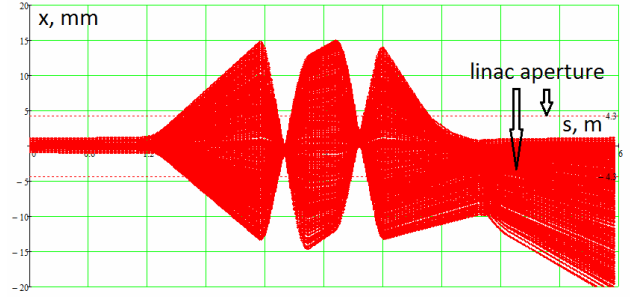
Figure 5. Electron beam trajectories.

Electron beam trajectories without corrections is presented at Figure 5. As seen, electron beam at the end of magnetic mirror have very large size and a large part of the beam will be lost.

The relative deviation of electron trajectory depending on the momentum deviation is shown on Figure 6. We can see, that both achromatic and isochronous bend are absent.
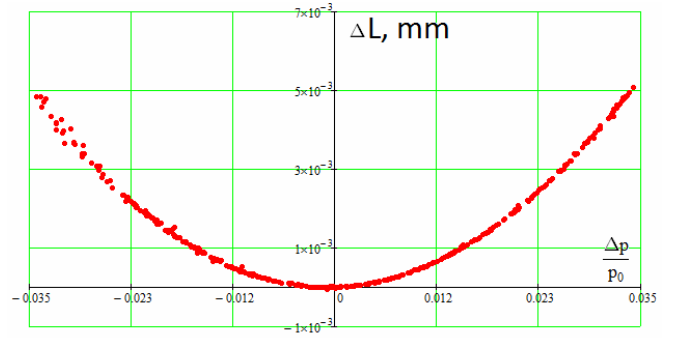
Figure 6. Relative deviation of electron trajectory depending on the momentum deviation.

For linear case we will not perform the correction of electron beam trajectories, because without the use of sextupole fields we can't good electron beam at the end of magnetic mirror.

NONLINEAR BEAM DYNAMICS

As an the linear case, we will consider the motion of electrons only into median horizontal plane. For calculate nonlinear beam dynamics into magnetic mirror we use the following equations of motion:

$$X'' - h(1 + h \cdot X) + \frac{s}{s^3}X' = -\frac{e}{p}\frac{v}{s}(1 + h \cdot X)B_z$$
$$\frac{v}{s} = \frac{dL}{ds} = \sqrt{X'^2 + (1 + h \cdot X)^2} \qquad (2)$$
$$\frac{s}{s^3} = -\frac{2h \cdot X'}{1 + h \cdot X} + \frac{1}{1 + h \cdot X}X'B_z$$

where $e = 1.6 \cdot 10^{-19}C$ - electron charge, L - the length of trajectory.

Solving the equations of motion (2) and assuming what there are only dipole and quadrupole components of magnetic field and no corrections, we get the trajectories presented at Figure 7. The magnetic fields in this case and in the case when we solving equation (1) are identical, but

electron trajectories are slightly different. We are seen an increase in betatron oscillations amplitude and the beam now has a greater asymmetry. Similarly the beam losses and beam divergence will be more essential, that in linear case.
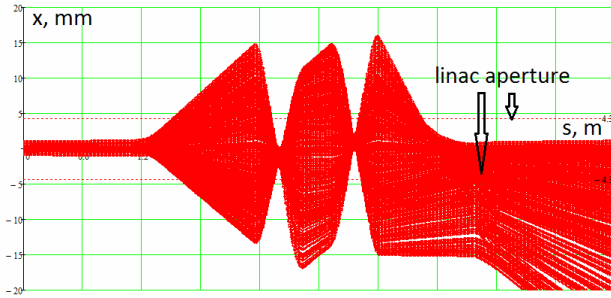
Figure 7. Electron beam trajectories.

To achieve the required parameters of magnetic mirror, we must perform correction of electron beam. We will use sextupole magnetic field component in one part of complex magnets (the part closest to separator magnet) and one quadrupole correctors in each straight sections between complex and separator magnets. Such placing sextupoles allow them to make the weaker, because phase shift is 2π. Furthermore, we shift energy deviation of electrons at the beginning of magnetic mirror from $\pm 3.5\%$ to $-3\% \div +4\%$. This allow to make the beam at the end of magnetic mirror more symmetrical.
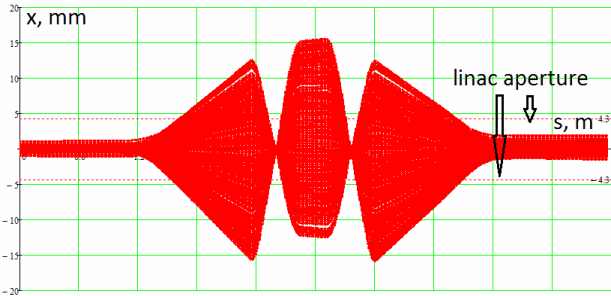
Figure 8. Electron beam trajectories.

At Figure 8 we presented the final electron beam trajectories into magnetic mirror with corrections. The beam in horizontal phase space at the end of the magnetic mirror is presented at Figure 9. Electron beam at the end of magnetic mirror after corrections will be inside the linac aperture and resulting beam divergence provides further passing of the electron beam through the linac acceleration structure.

At Figure 10 we presented relative deviation of electron trajectory depending on the momentum deviation. As in the linear case (see Fig. 6), for large momentum deviation the dominant term in the expansion of momentum compaction factor into the Taylor's series is quadratic term. Thus vanish linear term of momentum compaction factor doesn't make sense.

The maximum change in the longitudinal bunch length is about 2 mm, which is significantly less than the bunch length. The electrons with higher energy have a longer trajectory length and, hence, more magnetic mirror passage time, than the electrons with lower energy. So we will have decrease in electron microbunch length, because electrons with high energy are located into "the head" of microbanch and electrons with low energy - into "the tail" of microbunch [1].
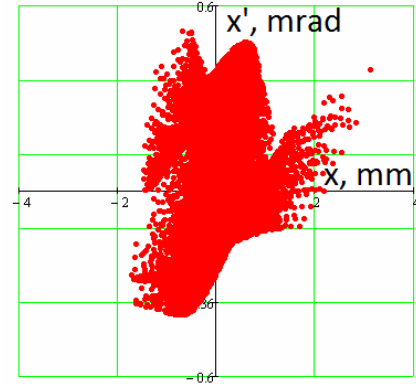
Figure 9. The beam in horizontal phase space at the end of the magnetic mirror.

In straight section spaced in between linac output and magnetic mirror "the head" and "the tail" of electron beam will be influence each other when colliding. This mutual influence in our case will be negligible, because the angles obtained by the interaction will be much smaller when available range of angles in electron beam. Note that the interface will be only 1/6 of "the head" and 1/6 of "the tail" of the beam.
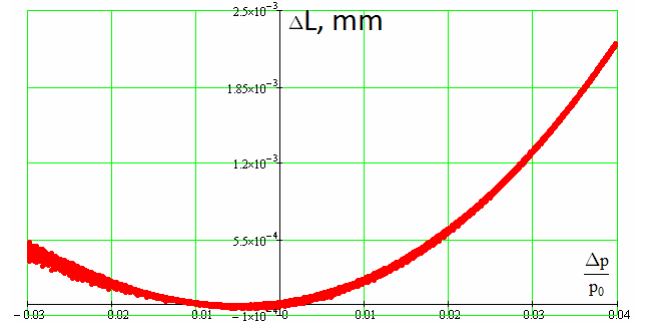
Figure 10. Relative deviation of electron trajectory depending on the momentum deviation.

Although the claim to the magnetic mirror is not satisfied, at the end of magnetic mirror we have received satisfactory to further accelerate beam without losses.

REFERENCES

[1] A. Anoshin and all, "Electron Beam Dynamics in Linac of Kurchatov Source of Synchrotron Radiation with Energy Doubling", RuPAC'08.
[2] Ya. Fomin, V. Korchuganov, "Electron Beam Dynamics with Space Charge in Linear Accelerator", RuPAC'10.

ELECTRON BEAM DYNAMICS WITH SPACE CHARGE IN LINEAR ACCELERATOR

Ye. Fomin, V. Korchuganov, RRC Kurchatov Institute, Moscow, Russia

Abstract

This paper describes electron beam dynamics with space charge in existing linear accelerator of Kurchatov source of synchrotron radiation. The linac structure operates with standing wave mode pulse power and without particle prebuncher. The results of comparison of electron beam parameters at the linac output with and without space charge consideration are presented. Electron beam shaping process starting from continuous beam to bunched beam on initial stage of acceleration under the action both of linac RF field and particle space charge field is considered. The main attention gives to calculate particle space charge field of the electron beam, which bring in essential contribution into beam dynamics on initial stage of shaping and accelerating electron bunches. The results of computer simulation of the electromagnetic field into linac structure taking with the help of ANSYS code are presented.

INTRODUCTION

Linac structure operates with standing wave mode pulse power. The pulsed diode gun with hot cathode is the electron beam source [1]. The main parameters of electron beam at the exit of a gun are given in Table 1.

Table 1: The main parameters of electron beam at the exit of a gun.

Parameter	Value
Beam current	4 A
Pulse duration	18 ns
Beam energy	40 keV
Microperveance	0.5 µA/V$^{3/2}$

Linac acceleration structure is made as biperiodic series of coupled cavities (DAW acceleration structure) [1]. It has 112 regular accelerating cells and 2 accelerating one half length cells. The special coaxial cavity, located in the center of linac, is the input of RF power. Along accelerating structure the aperture for the beam is small – a diameter of a diaphragm is 8.7 mm. The main parameters of linac are given in Table 2.

The electrons are accelerated due to stored energy which is reduced by ~10% after electron beam passage through acceleration structure.

The structure with washers and diaphragms has several advantages when working with stored energy:

- High shunt impedance.
- High coupling coefficient.
- High stored energy.

Table 2: The main parameters of linac.

Parameter	Value
RF frequency	2.797 GHz
Shunt impedance	95 MΩ/m
Q factor	28000
Time constant	1.8 µs
Length	6 m
Repetition rate	1 Hz

At Figure 1 we presented photo of existing linear accelerator of Kurchatov source of synchrotron radiation and at Figure 2 - photo and design of linac structure.

Figure 1: Linear accelerator.
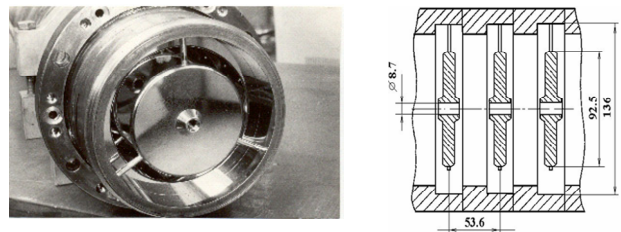
Figure 2. Linac structure.

RF FIELDS SIMULATION

For simulation rf electromagnetic field in acceleration structure we used ANSYS program code. Here we present the results of simulation.

Absolute value of electric field distribution into one cell of linac accelerating structure you can see at Figure 3. We can see that electric field has good uniformity in all volume of accelerating cell.

05 Beam Dynamics and Electromagnetic Fields
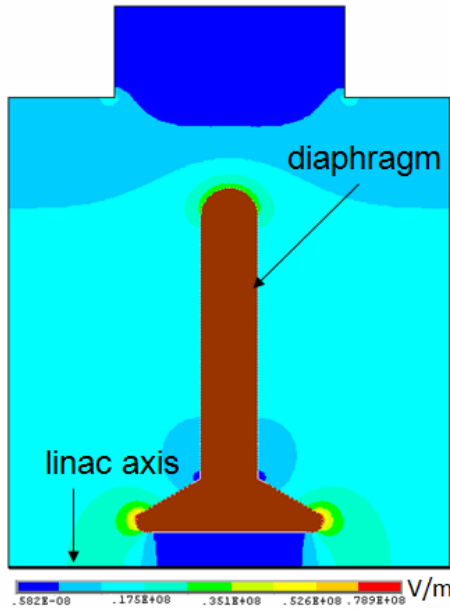
Figure 3. Absolute value of electric field into one cell of linac accelerating structure.

At Figure 4 we presented amplitude distribution of longitudinal electric field component at the linac axis ($r = 0\,mm$, red solid line) and near diaphragm aperture ($r = 4.3\,mm$, blue dotted line). Amplitude of radial electric field component (red solid line) and transverse magnetic field component multiply by speed of light (blue dotted line) near diaphragm aperture ($r = 4.3\,mm$) are presented at Figure 5. Presented amplitude field distributions are in accelerating gap, which is located between two adjacent diaphragms.
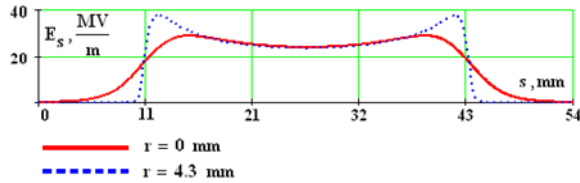
Figure 4. Amplitude distribution of longitudinal electric field component at the linac axis and near diaphragm aperture.
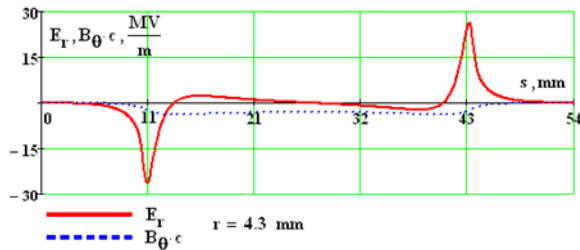
Figure 5. Amplitude of radial electric field component and transverse magnetic field component multiply by speed of light near diaphragm aperture.

At presented pictures we can see near diaphragm the increase of field amplitude, due to accelerating cell geometry.

05 Beam Dynamics and Electromagnetic Fields

ELECTRON BEAM DYNAMICS

In our calculations we used the following approximation:

- The model of macroparticle is used.
- The θ-component of the velocity of electrons is zero.
- Electron beam and linac axis are coaxial.

To calculate electron beam dynamics we use equation of motion (1):

$$\frac{d\vec{p}}{dt} = e\vec{E} + e[\vec{v} \times \vec{B}] \qquad (1)$$

The electro-magnetic fields consist of two components: RF fields and fields generated by the space charge of electron beam.

Electro-magnetic fields generated by the space charge of electron beam were obtained by solving Maxwell's equations, there the source is a spatial-temporal distribution of electron beam. And a spatial-temporal distribution of electron beam was obtained by influence the external RF fields and beam self fields. So we have self-consistent problem.

To defined self electro-magnetic fields we solve Maxwell's equations with the help of particle-mesh method. Instead of solving Maxwell's equations we will solve wave equations for scalar electric and magnetic vector potentials. Differential operators into the equations were replaced by finite-difference approximations on the mesh. Mesh-defined charge and current densities were obtained by using the "cloud-in-cell" scheme. Potentials and forces at electron positions were obtained by interpolation on the array of mesh-defined values.

The unbunched electron beam pulsed by diode gun is injected into first cell of the linac accelerating structure. The shaping of electron bunches occurs mainly during the fly through several first accelerating cells (see Fig. 6,7).
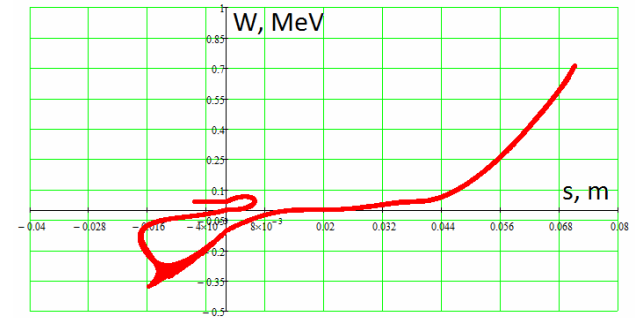
Figure 6. Electrons grouping process and bunches acceleration in the first cavity of linac.

The electrons grouping process in the first accelerating cavity is presented at Figure 6. The first cavity of linac is located at point $s = 0\,m$. The electrons with negative energy and position are moving back from linac. These electrons will be lost on the walls of vacuum chamber of channel between electron gun and linac.

The most part of electrons (about 75%) injected into linac will be lost in a few first accelerating cells on linac

aperture or on the walls of vacuum chamber of beam transfer line.
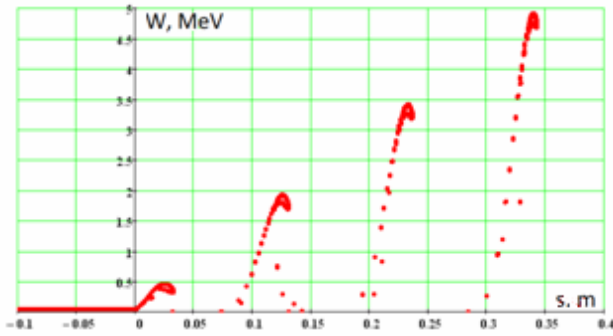
Figure 7. Electrons acceleration process in a few first cavities of linac.

At the exit of linac structure the current pulse represents a series of bunches (about 50) following each other with 2.8 GHz frequency. Average energy of accelerated electrons is 80 MeV, full beam current is about 1 A. Energy-longitudinal distribution of electron beam after acceleration is shown at Figure 8.
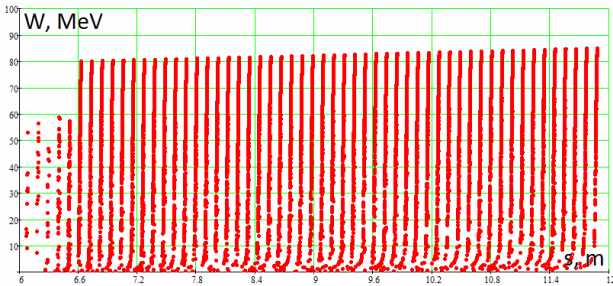
Figure 8. Energy-longitudinal distribution of electron beam after acceleration.

The first electron microbunch after acceleration is presented at Figure 9. The most part of particles are located at "the head" of microbunch and other particles are located at the long "tail" of microbunch.
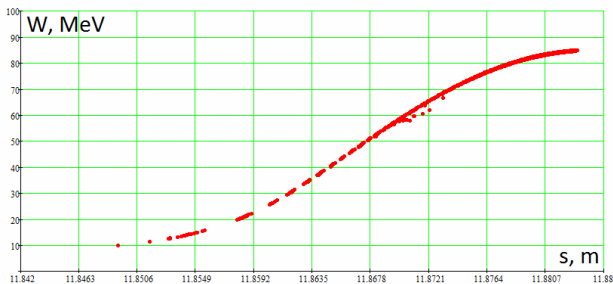
Figure 9. The first electron microbunch after acceleration.

The energy spectrum of electron beam after acceleration is presented at Figure 10. In the electron

beam the most part of particles have 80 MeV energy. The energy spread is 7% at half maximum. This result has good agreement with the measurements of electron beam properties performed at the commissioning stage [1].
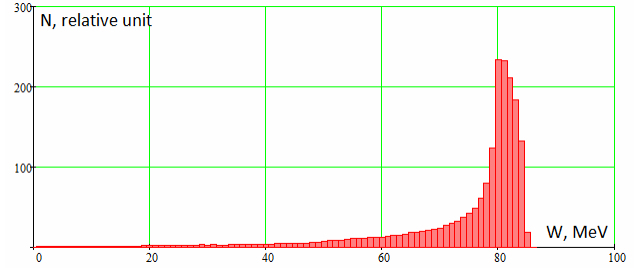
Figure 10. Energy spectrum of electron beam after acceleration.

The horizontal phase space distribution of the electron beam at the end of linac is presented at Figure 11. This phase portrait corresponds to electron beam with 7% energy spread.
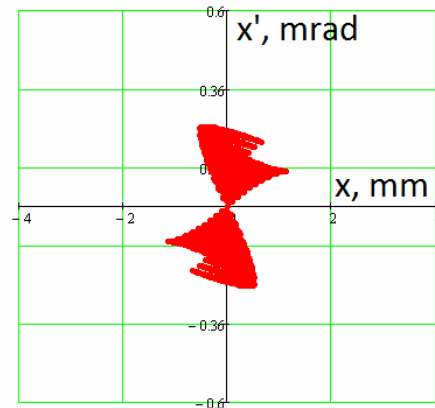
Figure 11. The horizontal phase space distribution of the electron beam at the end of linac.

The influence of space charge effect of the beam dynamics is not very strong. Taking into acount this effect we obtained the reduction of beam current by 20%. The beam dynamics is almost unchanged and is still primarily dependent on the external RF electro-magnetic fields.

REFERENCES

[1] A.G. Valentinov et al., Linac – forinjector of the dedicated synchrotron radiation source in RRC "Kurchatov Institute", Preprint BINP, 2002-29, Novosibirsk, 20p. 2002.

AN INCREASING OF ELECTRON BEAM LIFETIME AT INJECTION ENERGY IN SIBERIA-2 STORAGE RING BY REGULATING OF BETATRON COUPLING

A.Valentinov, V.Korchuganov, Yu.Krylov, Yu.Yupinov, RRC Kurchatov Institute, Moscow, Russia

Abstract

A dedicated synchrotron light source SIBERIA-2 operates at 2.5 GeV with more than 100 mA electron current. An electron beam lifetime at this energy is defined now by vacuum conditions and exceeds 15 hours for 100 mA. The lifetime at injection energy 0.45 GeV is much lower – less than half an hour for typical current value 3 – 4 mA in singlebunch mode.

An analysis of the lifetime value displayed a strong influence of Toushek effect in a presence of a horizontal aperture limitation. A dependence of the lifetime on different parameters (RF voltage, horizontal geometric and dynamic aperture, bunch current, betatron coupling value, electron energy) was analyzed.

A betatron coupling regulation was recognized the easiest way to increase lifetime value at injection energy. It was done by two families of skew-quadrupole lenses. A 30 – 40% increasing of the lifetime was observed for different values of a total current. Also a storing speed was raised because of slower decreasing of a stored current. The beam lifetime during energy ramping was also increased. It led to decreasing of current losses from 5 - 6% to 1.5 – 2% during energy rising from 0.45 GeV to 2.5 GeV.

INTRODUCTION

A dedicated synchrotron light source SIBERIA-2 [1] operates at 2.5 GeV with 100 – 150 mA electron current. An electron beam lifetime at this energy exceeds 15 hours for 100 mA that is quite enough for SR users. However the lifetime at injection energy 450 MeV is much less and not exceeds 30 minutes for typical current value 5 mA in singlebunch mode. It takes more than 30 minutes to reach 150 mA level, so current losses because of low lifetime during injection process strongly decrease injection speed. Low lifetime value is observed also at the beginning of energy ramping. It leads to additional current losses during this process. For these reasons methods of beam lifetime increasing at injection energy would be very useful. A regulation of betatron coupling is one of such methods.

BEAM LIFETIME AT 2.5 GEV

Beam lifetime $\tau(t)$ at 2.5 GeV depends on time t after energy ramping as follows:

$$\frac{1}{\tau(t)} = \frac{1}{\tau_0} + C \cdot I(t) \qquad (1)$$

where I(t) is electron current, τ_0 is lifetime for beam current close to zero and C is a constant. τ_0 is determined

by vacuum level without the beam. Second term in (1) may be determined by Toushek effect or by SR stimulated gas desorbtion from vacuum chamber walls. In our case second effect is working because values of τ_0 and C depend on current integral at 2.5 GeV. This dependence continues at least to 300 A·hours.

The Toushek lifetime depends on many parameters (2):

$$\frac{1}{\tau_{Toushek}} \propto \frac{C(\zeta) \cdot I}{\gamma^3 \cdot \sigma'_x \cdot (\varepsilon_{acc})^2 \cdot V} \qquad (2)$$

where C(ζ) is a function of $\zeta = \left[\frac{\varepsilon_{acc}}{\gamma \sigma'_x}\right]^2$, I is bunch current, γ is relativistic factor, σ'_x is RMS horizontal angular spread, V is proportional to bunch volume: $V \propto \sigma_x \sigma_z \sigma_s$ ($\sigma_z \propto \sqrt{\frac{\varepsilon_z}{\varepsilon_x}} = \sqrt{k}$, $\varepsilon_{x,z}$ – horizontal and vertical emittances, $\sigma_{x,z,s}$ – RMS bunch sizes, k – betatron coupling coefficient), ε_{acc} is the smallest of the physical, dynamic and RF acceptance. Energy acceptance is determined by total RF voltage V_{RF}. If physical aperture X determines ε_{acc}, it will obey to $\varepsilon_{acc} = X/\eta_x$ (η_x – a dispersion function on aperture limitation azimuth). Because τ depends on machine functions it should be calculated as an average value around the ring.
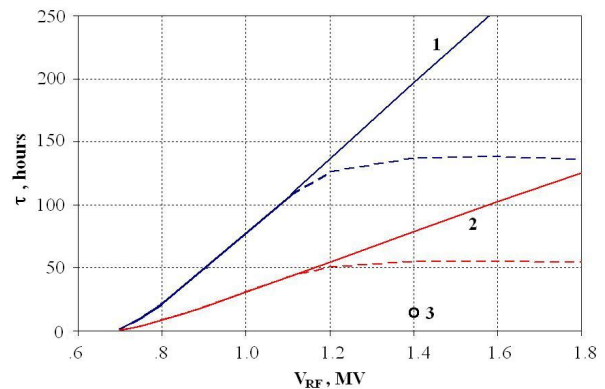
Figure 1: Calculated Toushek lifetime at 2.5 GeV as a function of the total RF voltage V_{RF}. Plots are given for two values of bunch current: **1** - 2 mA, **2** – 5 mA. An influence of horizontal aperture limitation X =20 mm is shown by dashed lines. A coupling coefficient k is equal to 0.01 (close to real value). **3** – measured lifetime value for 2 mA average bunch current and 80 A·hours total integral at 2.5 GeV.

In general, Toushek lifetime τ for particular energy and particular magnetic structure depends on four parameters: bunch current I, total RF voltage V_{RF}, coupling coefficient k and aperture limitation X. At 2.5 GeV transverse bunch sizes are independent on I, so for given V_{RF} and X Toushek lifetime is proportional to $\sqrt{k}$ and inverse proportional to I.

The Toushek lifetime calculations give mush more values than we observe in a real life. The calculations must take into account horizontal aperture limitations. In our case a distance 20 mm from injection septum to ideal orbit is a geometric limitation. A good gradient region in quadrupole lenses has slightly more dimensions. Fig.1 demonstrates theoretical dependence of the Toushek lifetime on V_{RF} for typical beam parameters.

BEAM LIFETIME AT 450 MEV

Only one bunch is added to beam for one injection cycle in SIBERIA-2. Maximal bunch current may be more than 8 mA, but it usually does not exceed 5 mA. Its value is limited by operation of booster storage ring SIBERIA-1 and stability of SIBERIA-2 RF system.

A time interval between injection cycles equals to 30 – 40 seconds. Total beam current is regulated by number of bunches. It takes 40 – 50 injection cycles to store 150 mA (number depends on injection system stability). Maximal value of total current now is determined now by RF system condition. In order to eliminate multibunch instabilities we are forced to increase V_{RF} from initial value of 200 kV up to 300 – 350 kV at the end of storing. It leads to lower injection efficiency, so average bunch current decreases during storing procedure. First bunches loose electrons because of low lifetime value. As a result the average bunch current decreases from 5 mA down to 3 - 4 mA during storage.

Beam lifetime at injection energy is determined by a number of effects such as elastic and non-elastic scattering on residual gas, Toushek effect, quantum effect due to radiation, ion storing on a beam trajectory. On SIBERIA-2 we don't see any dependence of the lifetime on vacuum conditions and outgassing duration (except the very beginning of this process). Calculated values of the lifetime due to Toushek effect were found to be very close to measured ones – from 20 to 30 minutes for 5 mA bunch.

At 450 MeV an intrabeam scattering leads to growth of energy spread and horizontal emittance with increasing of bunch current I. It makes an influence of physical/dynamic aperture limitation stronger at injection energy.

A dependence of the Toushek lifetime τ on four main parameters was analyzed for 450 MeV in order to increase τ. A value of aperture X was recognized to have the strongest influence to τ. (see Fig.2). τ is proportional to $X^{2.62}$ near X value close to 20 mm. Unfortunately we cannot increase the value of X, it is determined by distance from injection septum magnet to an ideal orbit.
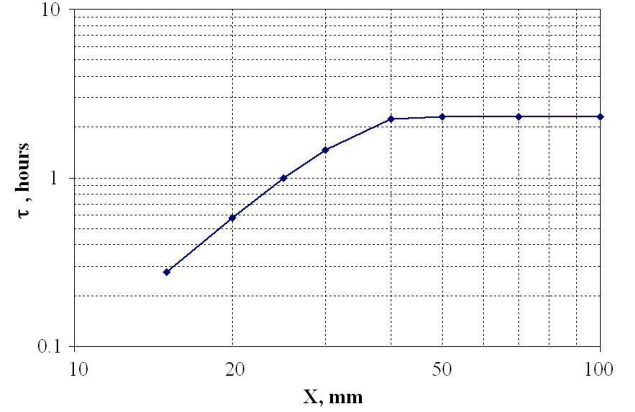
Figure 2: The Toushek lifetime at 450 MeV as a function of horizontal aperture limitation X. I = 5 mA, V_{RF} = 200 kV and coupling k = 0.01.

The RF voltage V_{RF} has weaker influence to the lifetime value. For I = 5 mA and 30 – 300 kV range of V_{RF} we observe $τ \sim V^{1.2}$. However we see strong τ dependence on X value (Fig.3). As a result Toushek lifetime is almost constant in the 80 – 300 kV range with slightly decreasing to 300 kV.
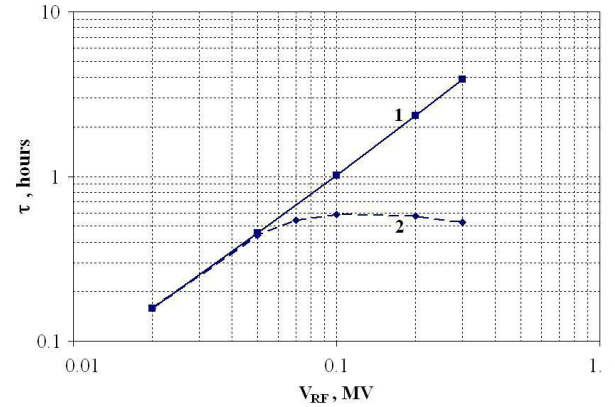
Figure 3: The Toushek lifetime at 450 MeV as a function of RF voltage V_{RF} for I = 5 mA and coupling k = 0.01 with X = ∞ (1) and X = 20 mm (2).

A dependence of τ on bunch current is shown on Fig.4 for V_{RF} = 200 kV and coupling k = .01 in a range 1 – 10 мА. Here $τ \sim I^{-0.43}$ and we see strong influence of X parameter. It seems we can increase lifetime by decreasing average bunch current. But RF harmonic number of SIBERIA-2 equals to 75. 1 mA average bunch current will correspond to only 75 mA, in addition the storing process become longer. Bunch current of 3 – 5 mA seems a good compromise between beam stability and speed of storing.

The last parameter, betatron coupling k, has the weakest influence to τ: $τ \sim k^{0.25}$ (see Fig.5). However it is the only one that can be regulated within sufficiently wide range.
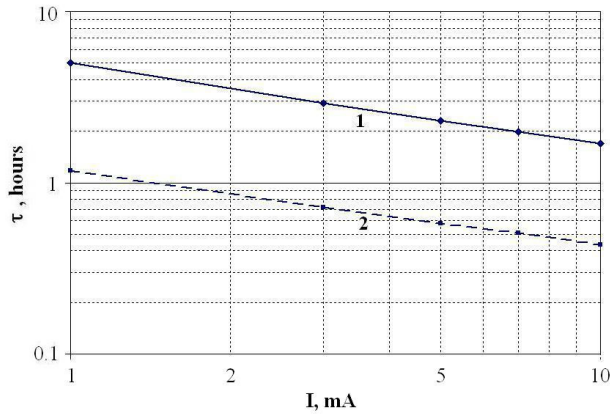
Figure 4: The Toushek lifetime at 450 MeV as a function of bunch current I for V_{RF} = 200 kV, coupling k = 0.01 with X = ∞ (1) and X = 20 mm (2).
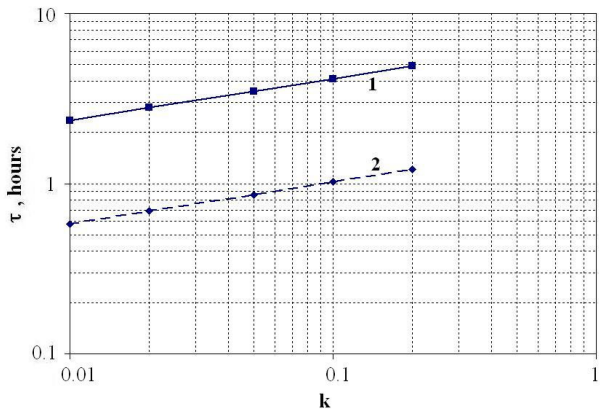
Figure 5: The Toushek lifetime at 450 MeV as a function of betatron coupling k for I = 5 mA and V_{RF} = 200 kV with X = ∞ (1) and X = 20 mm (2).

BETATRON COUPLING REGULATION

Two skew-quadrupole families are provided to regulate betatron coupling in SIBERIA-2. At 2.5 GeV they can decrease coupling coefficient k down to less then 0.001. Vertical emittance is determined by nonzero vertical dispersion in this case. At injection energy coupling is equal approximately to 0.01 without skew-quadrupoles. We can reach coupling value more than 0.3 but it causes too strong betatron tune shifts. Limiting tune shifts by 0.01 we achieve coupling coefficient value k = 0.15. It should increase lifetime approximately twice.

A behavior of lifetime value with increasing of bunch number should be mentioned here. Then number of bunches grows multibunch interactions appear. It leads to higher amplitude of energy vibrations inside every bunch. As a result energy spread becomes higher, effective density of electrons decreases and lifetime value grows even for constant average bunch current. In order to eliminate dangerous amplitude of such vibrations we are forced to increase V_{RF}. This action limits injection efficiency. So, we have several processes during storing:

increasing of V_{RF}, decreasing of average bunch current, lifetime growing due to bunch-to-bunch interactions. The last effect is strong enough – lifetime value at the end of storing may be more than twice higher than at the beginning.
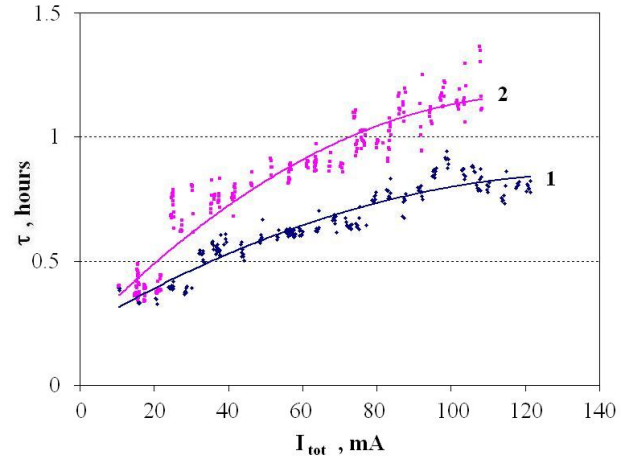
Figure 6: A measured beam lifetime at 450 MeV as a function of total electron current. 1 – without skew-quadrupoles, 2 – with skew-quadrupoles switched on.

Fig.6 demonstrates a lifetime dependence on total current during storing when skew-quadrupoles are switched off (1) and switched on (2). One may see sufficient growth of the lifetime after increasing of a betatron coupling. It achieves 30 - 40% for big number of bunches. It means shortening of the storing procedure because of slower depopulation of the stored current. The increasing of the lifetime turned out less than it was predicted. It indicates a presence of different sources of the lifetime limitation except Toushek effect.

An achieved result is useful also for energy ramping procedure. The calculated Toushek lifetime demonstrates minimum value at 700 MeV region for constant V_{RF}. The value of τ in this minimum is approximately 20% lower than at the injection energy. So the increasing of lifetime leads also to decreasing of current losses during energy ramping. It has allowed reducing such losses down to 2% from initial value 5 – 6%.

CONCLUSIONS

The analysis of the Toushek lifetime at injection energy in SIBERIA-2 storage ring lead to a conclusion of a possibility to increase the lifetime by betatron coupling regulation. As a result we could increase the lifetime on 30 - 40%. It has permitted to accelerate injection procedure because of slower current losses during storing. It also has led to lower losses during energy ramping. Their level has decreased from 5 - 6% down to 2%.

REFERENCES

[1] V.Korchuganov, M.Blokhov, M.Kovalchuk et al. "The status of the Kurchatov center of SR", *Nuclear Instruments and Methods*, A 543 (2005) pp. 14-18.

05 Beam Dynamics and Electromagnetic Fields

CENTER REGION DESIGN OF THE SUPERCONDUCTING CYCLOTRON C400

Y. Jongen, M. Abs, W. Kleeven, S. Zaremba, IBA, Belgium
G. Karamysheva, O.Karamyshev, N. Morozov, E.Samsonov, JINR, Russia.

Abstract

Compact superconducting isochronous cyclotron C400 [1] has been designed at IBA (Belgium) in collaboration with the JINR (Dubna). This cyclotron will be used for radiotherapy with proton, helium or carbon ions. The ions extracted from the source and transported with the axial line are bent into the median plane of the cyclotron by a spiral inflector. The optimal design of the inflector and cyclotron center for acceleration of the ion beams in the 4th RF harmonic mode was studied. A computer model of the dee tip geometry with the inflector and inflector housing was created. The 3D magnetic field map and 3D electric field map were used for beam dynamics simulations. Comparison between field map created in electrostatic simulation and field map from RF simulation is given. Results of the beam tracking are presented.

C400 CYCLOTRON

The last years have seen increasing interest in the particle therapy based on $^{12}C^{6+}$ ions.

IBA, the world's industrial leader in equipment of the proton therapy centers, has designed a superconducting C400 cyclotron based on the design of the current Proton Therapy C235 cyclotron.

Most of the operating parameters of the C400 cyclotron are fixed: fixed energy, fixed field and fixed RF frequency (small main field and RF frequency changes are needed for switching species). It is relatively small (6.6 m in diameter) and cost effective.
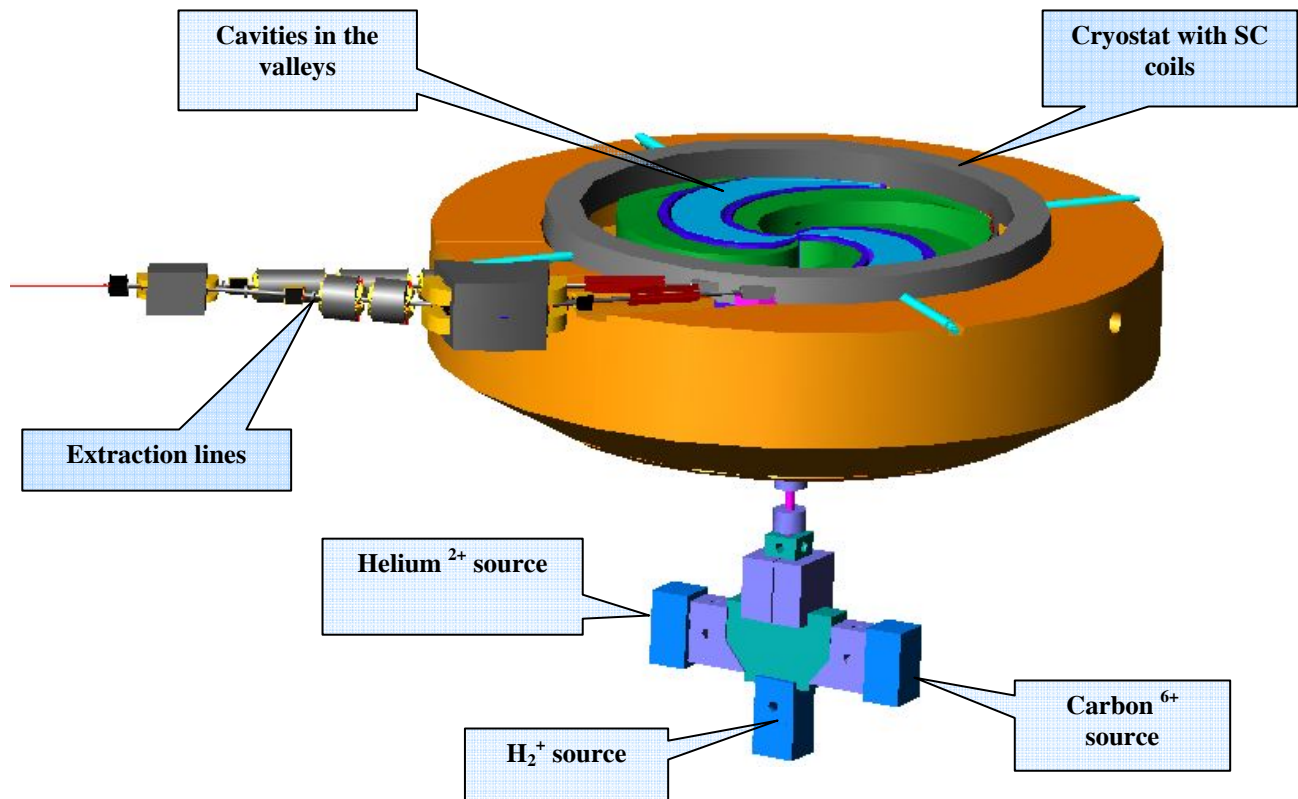
Figure 1: View of the median plane in the C400 superconducting cyclotron.

It offers very good beam intensity control for ultra-fast pencil beam scanning (PBS). But it requires an energy selection system (ESS) in order to vary the beam energy. The efficiency of the ESS for carbon is better than for

protons due to lower scattering and straggling of carbon ions in the degrader.

INJECTION

Three external ion sources are mounted on the switching magnet on the injection line located below the cyclotron. $^{12}C^{6+}$ are produced by a high-performance ECR at current 3 µA, alphas and H_2^+ are also produced by a simpler ECR source. All species have a Q/M ratio of 1/2 and all ions are extracted at the same voltage 25 kV, so the small retuning of the frequency and a very small magnetic field change achieved by different excitation of 2 parts in the main coil are needed to switch from H_2^+ to alphas or to $^{12}C^{6+}$. We expect that the time to switch species will be not longer than two minutes, like the time needed to retune the beam transport line between different treatment rooms.

Focusing in the channel (Fig. 1) is provided by three solenoid lenses (S1, S2, S3), the rotational symmetry of the beam is reestablished with the help of one quad Q placed just behind the BMR40 bending magnet. The 90º bending magnet has two horizontal and one vertical entrances, and a common exit for all ion beams.

CENTRAL REGION

A model of the dee tip geometry at the cyclotron center with the inflector placed inside the housing was developed [2] (see Fig. 2). Dee tips have the vertical aperture 1.2 cm in the first turn and 2 cm in the second and further turns. In the first turn the gaps were delimited with pillars reducing the transit time. The azimuth extension between the middles of the accelerating gaps was chosen to be 45º. The electric field in the inflector was chosen to be 20 kV/cm. Thus, the height (electric radius) of the inflector is 2.5 cm. The gap between the electrodes was taken to be 6 mm, and the tilt parameter is $k' = 0.1$. The aspect ratio between the width and the spacing of the electrodes was taken to be 2 to avoid the fringe field effect. The electric field simulation of the central region was performed.

We compared two variants of central region:
   a)   with pillars around first turn
   b)   without pillars.
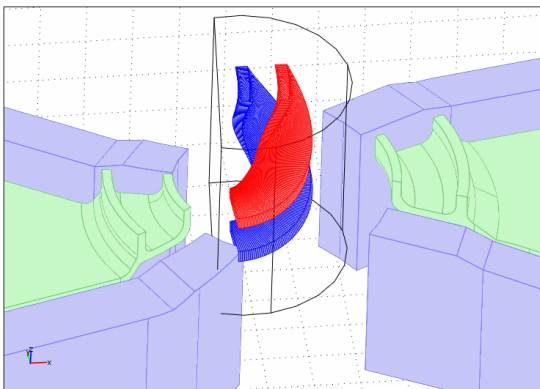
Figure 2: Central region with the spiral inflector model.

The width of the channel around the first turn was equal 1cm. Fig. 3 shows potential distribution of the both variants. Voltage distributions along radius are presented in Fig. 4. The voltage value was obtained by integrating the electric field in the median plane of the resonant cavity. It is seen that pillar increases voltage in the area of the first turn (R = 25 mm) from 55 kV (dashed blue line) to 59 kV (solid red line).
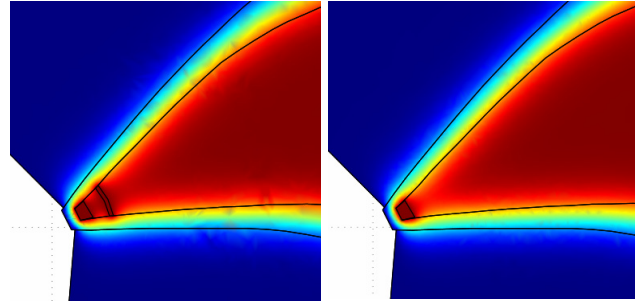
Figure 3: Dee tips with channel (left) and without channel (right).
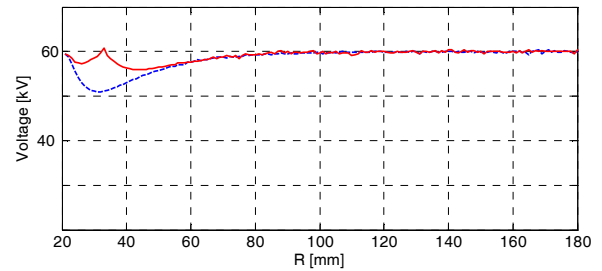
Figure 4: Voltage distribution along radius, red solid line - with channel, blue dashed line-without channel.

Beam dynamics simulations in the central region were made for particles with initial distributions in transverse phase planes obtained from the axial injection line. For all types of ions the beam diameters at the entrance into the spiral inflector are smaller than 2 mm.

The mean magnetic field against the radius is shown in Fig. 5. One can see that the value of the bump in the central region is about 200 G. At the end of our simulation (R = 8 cm) the mean magnetic field is isochronous.
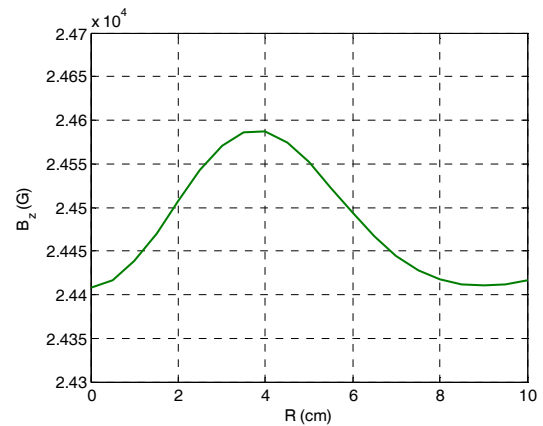
Figure 5: Mean magnetic field in the center region.

In spite of the fact that we have a magnetic field bump in the central region, it does not provide an appreciable magnetic axial focusing, but promotes electric axial focusing which plays the main role during the first turns.

Continuous beam simulation shows that when we use two phase selection slits, the injection efficiency is 12% for ions with amplitudes of radial oscillations smaller than 4 mm. The use of the buncher will increase the beam intensity at least by a factor of two.

We tested the possibility of modulating the beam intensity by changing voltage on the electrodes of the spiral inflector. We simulated ion motion through the inflector with decreasing voltage. It is necessary to decrease voltage by about 12% to lock the beam. It is clear from the simulation that this intensity modulation method has one disadvantage – radial displacement of the beam – but it is smaller than 1 mm.

COMPARISON BETWEEN RF AND ELECTROSTATIC APPROACHES

The geometric model of the double-gap delta cavity housed inside the valley of the magnetic system of the C400 cyclotron was developed. Calculations of the created model were performed using the eigenmode JD lossfree solver (Jacobi Division Method) in the CST MICROWAVE STUDIO [3]. RF cavity simulations are very time consuming therefore we usually used simplified model without pillars in the center, with vertical aperture equal 2 cm for all radii and so on. It is impossible to simulate accelerating field with good accuracy for the exact geometry of the central region from RF simulations. Usually central region model is simulated in electrostatic approach. In order to determine the margin of acceptability of this approach we compared voltage distribution from RF and electrostatic simulations in the central region. Results one can see in Fig.6 where red solid line –from electrostatic simulations and blue dotted line from RF simulations.
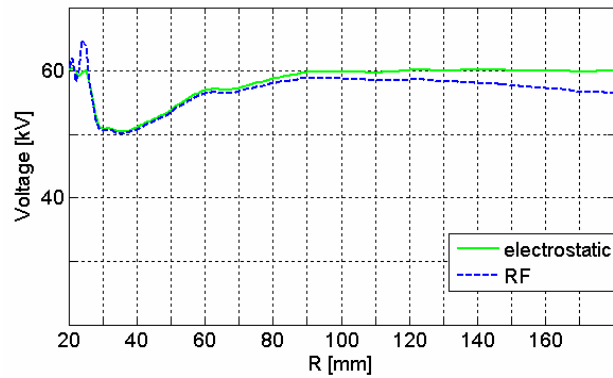
Figure 6: Voltage distribution along radius.

One can conclude that there is no difference in voltage by those approaches up to R = 60 mm. Therefore the best approach for center region design is electrostatic one because only in electrostatic approach it is possible to calculate accelerating field distribution only in the region of interest. RF approach demand modeling of the whole cavity and this is much more time consuming.

CONCLUSION

The central region of the C400 was designed using electrostatic approach in the field simulation. It is proposed to use the inflector 2.5 cm height with a gap of 6 mm between electrodes which ensures good centering (less than 1mm).

Continuous beam simulation shows that when we use two phase selection slits, injection efficiency is 12% for ions with amplitudes of radial oscillations less than 0.4 cm.

In spite of the fact that we have a magnetic field bump in the central region axial focusing is provided mainly by electric focusing.

REFERENCES

[1] Y. Jongen, etal."COMPACT SUPERCONDUCTING CYCLOTRON C400 FOR HADRON THERAPY", Nuclear Inst. and Methods in Physics Research, A, 2010.

[2] Yves Jongen et al, "Center region design of the cyclotron C400 for hadron therapy", The 18th International Conference on Cyclotrons and their Applications Cyclotrons 2007, Laboratori Nazionali del Sud, Giardini Naxos, Italy 2007.

[3] CST STUDIO SUITE http://www.cst.com

DIGITAL LONGITUDINAL FEEDBACK SYSTEMS IN SYNCHROTRONS

V. M. Zhabitsky, Joint Institute for Nuclear Research, Dubna, Russia

Abstract

The stability of a beam in synchrotrons with a digital longitudinal feedback system is treated. A longitudinal feedback system is required in synchrotrons to stabilize the high intensity beams against longitudinal instabilities and to damp the phase injection errors of a bunch. Damping rates of the digital longitudinal feedback system in dependence of its gain and delay are analysed.

INTRODUCTION

Longitudinal feedback systems are necessary in synchrotrons to reach the accuracy and stability required for reproducible beam performance [1, 2]. A digital bunch-by-bunch feedback [3] individually steers each bunch by applying electromagnetic kicks every time the bunch passes through the kicker (DK). The kick value is in proportion to the bunch deviation from the synchronus phase at the beam position monitor (BPM) location. The combiner (see Fig. 1) generates the wideband horizontal, vertical or sum signal, which is then demodulated to base-band by the detector. A stable beam rejection module removes useless
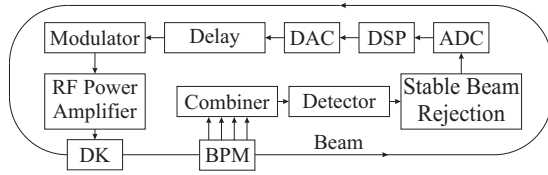
Figure 1: Block diagram of a digital feedback system

stable beam components from the signal, which is eventually digitized (ADC), processed (DSP), and re-converted (DAC) to analog by the digital processor. While in transverse feedback systems amplifier and kicker operate in base-band, longitudinal feedbacks require a modulator that translates the correction signal to the kicker operation frequency. The delay line adjusts the timing of the signal to match the bunch arrival time. Conditions for damping of the coherent synchrotron oscillations are discussed below.

BASIC NOTIONS

The RF system accelerates particles of a bunch in synchrotrons by producing a time-varying electric field in an accelerating station. The particle's energy growth per turn is given by [4, 5, 6]

$$E[n+1] - E[n] = q\widehat{V}_{\text{RF}} \sin\phi[n]\,, \qquad (1)$$

where q is the charge of the particle, $q\widehat{V}_{\text{RF}}$ is the maximal energy gain per turn and $\phi[n]$ is the phase of the RF when

05 Beam Dynamics and Electromagnetic Fields

the particle crosses the middle of the accelerating station at the point s_{RF} of the orbit in the moment $t[n]$ at the n-th turn (the origin of time for the RF phase is taken at zero crossing of the RF voltage with positive slope; s is the co-ordinate along the orbit). It is also assumed in (1) that the electric field is the even function of $(s - s_{\text{RF}})$. Details of mode structure, geometry, transit time factor, etceteras are ignored in (1) by including these features in $\widehat{V}_{\text{RF}}$.

It will be assumed further that the particle with the energy $E[n] = mc^2\gamma[n]$ passes the n-th turn with the speed $c\beta[n]$ along the orbit with the circumference $C[n]$ so that the angular frequency $\omega[n]$ and the revolution period are $T[n] = 2\pi/\omega[n] = C[n]/(c\beta[n])$; here c is the speed of light, m is the particle mass, and $\gamma = 1/\sqrt{1-\beta^2}$. In accordance with these definitions the RF phase growth per turn can be written for the particle as follows:

$$\phi[n+1] - \phi[n] = \int_{t[n]}^{t[n+1]} \widehat{\omega}_{\text{RF}}(t)dt = \omega_{\text{RF}}[n+1]\,T[n+1], \quad (2)$$

where $\omega_{\text{RF}}[n+1]$ is the average value of the angular RF frequency $\widehat{\omega}_{\text{RF}}$ during the turn $T[n+1] \equiv t[n+1] - t[n]$.

The phase $\phi[n]$ can be kept unchanged (modulo 2π) at the value ϕ_{s} when the particle returns to the same accelerating section after one revolution period. The phase ϕ_{s} is also called the synchronous phase. In what follows, the subscript "s" is used for synchronous quantities. The synchronous phase growth per turn in accordance with (2) is

$$\phi_{\text{s}}[n+1] - \phi_{\text{s}}[n] = \omega_{\text{RF}}[n+1]\,T_{\text{s}}[n+1] = 2\pi h_{\text{RF}}\,, \quad (3)$$

where $h_{\text{RF}} = (\omega_{\text{RF}}/\omega_{\text{s}})$ is the RF harmonic number. Let $\rho_{\text{s}}B_{\text{s}}$ be the momentum rigidity of the synchronous particle moving along the orbit with the circumference $2\pi R_{\text{s}}$. Then the synchronous particle's energy growth pur turn is

$$E_{\text{s}}[n+1] - E_{\text{s}}[n] = qV_{\text{RF}}\sin\phi_{\text{s}}[n] = q\,2\pi R_{\text{s}}\rho_{\text{s}}\dot{B}_{\text{s}}\,. \quad (4)$$

Eq. (3) and Eq. (4) are the system of difference equations for definition of $\phi_{\text{s}}[n]$ and $E_{\text{s}}[n]$. Let us assume that these solutions have been found. Therefore the motion of an arbitrary particle relative to a hypothetical synchronous particle can be examined.

Acceleration in presence of perturbations

Let $\delta E[n]$ and $\delta\phi[n]$ be small deviations of energy and phase of the particle from corresponding synchronous values at the n-th turn:

$$\delta E[n] \equiv E[n] - E_{\text{s}}[n]\,, \qquad \delta\phi[n] \equiv \phi[n] - \phi_{\text{s}}[n]\,.$$

Let ΔV_{RF}, $\Delta\omega_{\text{RF}}$ and ΔB_{s} be small deviations of the accelerating voltage, the angular RF frequency and the magnetic

field from designed values. Therefore the particle's energy deviation from the synchronous one gained per turn in accordance with (1) and (4) is

$$
\delta E[n+1] - \delta E[n]
$$
$$
= q(V_{\mathrm{RF}} + \Delta V_{\mathrm{RF}}[n]) \sin(\delta\phi[n] + \phi_{\mathrm{s}}) - qV_{\mathrm{RF}} \sin\phi_{\mathrm{s}}. \quad (5)
$$

In what follows, δ represents a difference taken with respect to the synchronous quantity at a given time (consequently at the given turn) and Δ represents an increment during acceleration. The phase deviation gained per turn in accordance with (2) and (3) is given by

$$
\delta\phi[n+1] - \delta\phi[n] = \int_{t[n]}^{t[n+1]} (\omega_{\mathrm{RF}}(t) + \Delta\omega_{\mathrm{RF}}(t))dt - 2\pi h_{\mathrm{RF}}
$$
$$
= \omega_{\mathrm{RF}}[n+1]\, T[n+1] - 2\pi h_{\mathrm{RF}} + \Delta\phi_{\mathrm{RF}}[n+1], \quad (6)
$$

where the phase shift due to a small modulation of the RF frequency is

$$
\Delta\phi_{\mathrm{RF}}[n+1] = \int_{t[n]}^{t[n+1]} \Delta\omega_{\mathrm{RF}}(t)dt. \quad (7)
$$

The deviation of the revolution period $T[n]$ from $T_{\mathrm{s}}[n]$ is determined by [4, 7] the energy deviation $\delta E[n]$ and the magnetic field error $\Delta B_{\mathrm{s}}[n]$:

$$
T[n] \approx \left(1 + \frac{\eta_{\mathrm{s}}\, \delta E[n]}{\beta_{\mathrm{s}}^2[n]\, E_{\mathrm{s}}[n]} - \frac{\alpha_{\mathrm{s}}\, \Delta B_{\mathrm{s}}[n]}{B_{\mathrm{s}}[n]}\right) T_{\mathrm{s}}[n].
$$

Here $\eta_{\mathrm{s}} = \alpha_{\mathrm{s}} - (1/\gamma_{\mathrm{s}}^2)$ is the phase slip factor and α_{s} is the momentum compaction factor [7]. Therefore the phase deviation gained per turn is

$$
\delta\phi[n+1] = \delta\phi[n] - \frac{4\pi^2\nu_{\mathrm{s}}^2}{qV_{\mathrm{RF}}\cos\phi_{\mathrm{s}}}\, \delta E[n+1]
$$
$$
+ \Delta\phi_{\mathrm{RF}}[n+1] - 2\pi\alpha_{\mathrm{s}} h_{\mathrm{RF}} \frac{\Delta B_{\mathrm{s}}[n+1]}{B_{\mathrm{s}}[n+1]}, \quad (8)
$$

where the synchrotron oscillation tune ν_{s} is given by [7]:

$$
\nu_{\mathrm{s}} = \sqrt{-\frac{h_{\mathrm{RF}}\eta_{\mathrm{s}}}{2\pi\beta_{\mathrm{s}}^2 E_{\mathrm{s}}}qV_{\mathrm{RF}}\cos\phi_{\mathrm{s}}}.
$$

For an adiabatic process of acceleration it is possible to neglect dependences of the coefficient before δE in Eq. (8) on time and n.

Eq. (8) and Eq. (5) are the system of difference equations for definition of $\delta\phi[n]$ and $\delta E[n]$. It corresponds to differential equations in [4] for synchrotron oscillations in presence of pertirbations and coincides with difference equations in [6, 7] in the case of $\Delta V_{\mathrm{RF}} = \Delta\phi_{\mathrm{RF}} = \Delta B_{\mathrm{s}} = 0$. The system of Eq. (8) and Eq. (5) can be solved, for example, using the Z-transform [8] in a such way that was done for the transverse feedback system in [9].

Synchrotron oscillations

If $\Delta V_{\mathrm{RF}} = \Delta\phi_{\mathrm{RF}} = \Delta B_{\mathrm{s}} = 0$ then for small $\delta\phi$ linearization of Eq. (5) in combination with Eq. (8) gives the

05 Beam Dynamics and Electromagnetic Fields

synchrotron oscillation equation as difference equations in the matrix form:

$$
\begin{pmatrix} \delta\phi[n+1] \\ \delta E[n+1] \end{pmatrix} = \widehat{M} \times \begin{pmatrix} \delta\phi[n] \\ \delta E[n] \end{pmatrix}, \quad (9)
$$

where

$$
\widehat{M} \equiv \begin{pmatrix} 1 - 4\pi^2\nu_{\mathrm{s}}^2 & -\dfrac{4\pi^2\nu_{\mathrm{s}}^2}{q\widehat{V}_{\mathrm{RF}}\cos\phi_{\mathrm{s}}} \\ q\widehat{V}_{\mathrm{RF}}\cos\phi_{\mathrm{s}} & 1 \end{pmatrix}.
$$

Consequently the particle dynamics is determined by roots z_k of the characteristic equation:

$$
\det\left(z_k\widehat{I} - \widehat{M}\right) = z_k^2 - (2 - 4\pi^2\nu_{\mathrm{s}}^2)z_k + 1 = 0, \quad (10)
$$

where $\widehat{I}$ is the identity matrix. Eigenvalues of Eq. (10) are

$$
z_{\pm} = \exp(\pm j2\pi\nu), \qquad \sin\pi\nu = \pi\nu_{\mathrm{s}}
$$

that is well known result [5].

Dipolar motion approximation

Let us consider the bunch as a statistical collection of many particles [2], each particle oscillating around the synchronous phase. Let $f(\phi, E)\, d\phi\, dE$ be the probability that the RF phase is between ϕ and $\phi + d\phi$ and the particles energy is between E and $E + dE$ when the particle crosses the middle of the RF cavity at the n-th turn with phase $\phi[n]$ and energy $E[n]$. The first order moment (centre of charge) of $\phi[n]$ at the n-th turn is

$$
\langle\phi[n]\rangle \equiv \iint \phi\, f(\phi, E)\, d\phi\, dE, \quad \iint f(\phi, E)\, d\phi\, dE = 1,
$$

where the integration covers the entire bunch. Consequently with respect to synchronous phase and energy one can write:

$$
\langle\delta\phi[n]\rangle = \iint (\phi - \phi_{\mathrm{s}}[n])\, f(\phi, E)\, d\phi\, dE; \quad (11a)
$$

$$
\langle\delta E[n]\rangle = \iint (E - E_{\mathrm{s}}[n])\, f(\phi, E)\, d\phi\, dE. \quad (11b)
$$

Let us now assume a stationary distribution so that $f(\phi, E)$ does not depend on t and n. Applying (11) to (8) and (5) for small $\delta\phi$ one can obtain:

$$
\langle\delta\phi[n+1]\rangle = \langle\delta\phi[n]\rangle - \frac{4\pi^2\nu_{\mathrm{s}}^2}{qV_{\mathrm{RF}}\cos\phi_{\mathrm{s}}}\langle\delta E[n+1]\rangle
$$
$$
+ \langle\Delta\phi_{\mathrm{RF}}[n+1]\rangle - 2\pi h_{\mathrm{RF}}\left\langle\frac{\Delta B_{\mathrm{s}}[n+1]}{B_{\mathrm{s}}[n+1]}\right\rangle; \quad (12a)
$$

$$
\langle\delta E[n+1]\rangle = \langle\delta E[n]\rangle + qV_{\mathrm{RF}}\langle\delta\phi[n]\rangle\cos\phi_{\mathrm{s}}
$$
$$
+ q\langle\Delta V_{\mathrm{RF}}[n]\rangle\sin\phi_{\mathrm{s}} + q\langle\Delta V_{\mathrm{RF}}[n]\, \delta\phi[n]\rangle\cos\phi_{\mathrm{s}}. \quad (12b)
$$

The above equations are identical to Eq. (8) and Eq. (5) describing the motion of each particle that cannot be individually observed by the instrumentation. On the other hand the motion of the centre of charge of the bunch, also called *dipolar motion*, can easily be monitored.

LONGITUDINAL FEEDBACK SYSTEMS

Let a pick-up (see Fig. 1) measure $\langle\delta\phi[n]\rangle$ for the bunch in place close to the accelerating section. The signal from the BPM can be used for the correction of the RF parameters via the modulator in the feedback loop when the same bunch crosses the accelerating section after one turn.

RF voltage modulation. Feedback is achieved passing the beam phase information through the loop to modify the amplitude at the RF cavity. Let the kick $\Delta V_{\mathrm{RF}}[n]$ be in proportion to $\langle \delta\phi[n-1]\rangle$ but $\Delta\phi_{\mathrm{RF}} = \Delta B_{\mathrm{s}} = 0$:

$$\Delta V_{\mathrm{RF}}[n] = -\frac{g_\phi \, q V_{\mathrm{RF}}}{4\pi^2 \nu_{\mathrm{s}}^2} \, u[n-1] \, \langle \delta\phi[n-1]\rangle \,. \qquad (13)$$

Here $u[n]$ is the Heaviside step function and g_ϕ is the gain of the feedback loop. Consequently Eqs. (12) can be written in the matrix form that coinsides with (9) but

$$\widehat{M} \equiv \begin{pmatrix} 1 - 4\pi^2\nu_{\mathrm{s}}^2 + \hat{g} & -\dfrac{4\pi^2\nu_{\mathrm{s}}^2(1-\hat{g})}{qV_{\mathrm{RF}}\cos\phi_{\mathrm{s}}} \\ \left(1 - \dfrac{\hat{g}}{4\pi^2\nu_{\mathrm{s}}^2}\right) qV_{\mathrm{RF}}\cos\phi_{\mathrm{s}} & 1 - \hat{g} \end{pmatrix},$$

where $\hat{g} \equiv g_\phi \tan\phi_{\mathrm{s}}$. The particle dynamics is determined by roots z_k of the characteristic equation:

$$z_k^2 - (2 - 4\pi^2\nu_{\mathrm{s}}^2)z_k + 1 - g_\phi \tan\phi_{\mathrm{s}} = 0\,. \qquad (14)$$

Eigenvalues of Eq. (14) for a small g_ϕ are

$$z_\pm = \exp\left(-\frac{g_\phi}{2}\tan\phi_{\mathrm{s}}\right)\exp(\pm j2\pi\nu)\,,$$

$$\cos 2\pi\nu = (1 - 2\pi^2\nu_{\mathrm{s}}^2)\exp\left(\frac{g_\phi}{2}\tan\phi_{\mathrm{s}}\right)\,.$$

The damping regime corresponds to $g_\phi \tan\phi_{\mathrm{s}} > 0$. It can be obtained during the B_{s} ramp only ($\tan\phi_{\mathrm{s}} \neq 0$). It should be noted that the bunch returns to the synchronous phase as quickly as possible without coherent oscillations ($\nu = 0 \Rightarrow$ *critically damped* oscillator) for

$$(g_\phi)_{\mathrm{opt}} \equiv g_\phi^* = 4\pi^2\nu_{\mathrm{s}}^2(1 - \pi^2\nu_{\mathrm{s}}^2)/\tan\phi_{\mathrm{s}}\,.$$

RF phase modulation. Let the phase shift due to a small modulation of the RF frequency in accordance with (7) is chosen in proportion to $\langle\delta\phi[n]\rangle$ but deviations $\Delta V_{\mathrm{RF}} = \Delta B_{\mathrm{s}} = 0$:

$$\langle\Delta\phi_{\mathrm{RF}}[n+1]\rangle = -g_\phi\langle\delta\phi[n]\rangle\,, \qquad (15)$$

where g_ϕ is the gain of the feedback loop. Consequently Eqs. (12) can be written in the matrix form that coincides with (9) but

$$\widehat{M} \equiv \begin{pmatrix} 1 - 4\pi^2\nu_{\mathrm{s}}^2 - g_\phi & -\dfrac{4\pi^2\nu_{\mathrm{s}}^2}{q\widehat{V}_{\mathrm{RF}}\cos\phi_{\mathrm{s}}} \\ q\widehat{V}_{\mathrm{RF}}\cos\phi_{\mathrm{s}} & 1 \end{pmatrix}\,.$$

The particle dynamics is determined by roots z_k of the characteristic equation:

$$z_k^2 - (2 - g_\phi - 4\pi^2\nu_{\mathrm{s}}^2)z_k + 1 - g_\phi = 0\,. \qquad (16)$$

Eigenvalues of Eq. (16) for a small g_ϕ are

$$z_\pm = \exp\left(-\frac{g_\phi}{2}\right)\exp(\pm j2\pi\nu),\ \sin\pi\nu = \pi\nu_{\mathrm{s}}\exp\left(\frac{g_\phi}{4}\right)\,.$$

Therefore the damping regime corresponds to $g_\phi > 0$ and

$$(g_\phi)_{\mathrm{opt}} \equiv g_\phi^* = 4\pi\nu_{\mathrm{s}} - 4\pi^2\nu_{\mathrm{s}}^2\,.$$

Feedback loop with delay. In practice there is a delay between the measurement of $\langle\delta\phi[n]\rangle$ and the RF kick. For example, one can write for (15):

$$\langle\Delta\phi_{\mathrm{RF}}[n+1]\rangle = -g_\phi u[n-\hat{q}]\,\langle\delta\phi[n-\hat{q}]\rangle\,, \qquad (17)$$

where $\hat{q}$ is the number of turns in the feedback loop delay. Applying the bilateral Z-transform [8] in Eqs. (12)

and Eq. (17) it is not difficult to obtain the characteristic equation for calculation of eigenvalues:

$$z_k^2 - (2 - g_\phi z_k^{-\hat{q}} - 4\pi^2\nu_{\mathrm{s}}^2)z_k + 1 - g_\phi z_k^{-\hat{q}} = 0\,. \quad (18)$$
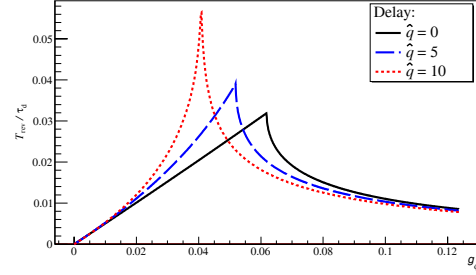
Figure 2: Dependences of maximal damping rates on g_ϕ

Dependences of maximal damping rates $T_{\mathrm{rev}}/\tau_{\mathrm{d}} = \mathrm{MAX}\,|(\ln|z_k|)|$ on feedback gains g_ϕ are shown in Fig. 2 for $\nu_{\mathrm{s}} = 0.005$. It should be emphasised that g_ϕ^* values decrease with the growth of $\hat{q}$ values.

ACKNOWLEDGEMENTS

REFERENCES

[1] W. Schnell. "Equivalent Circuit Analysis of Phase-Lock Beam Control Systems". CERN 68–27, ISR Division, CERN, Geneva, 17 July 1968.

[2] P. Baudrenghien. "Low level RF systems for synchrotrons". CAS – CERN Accelerator School: Radio Frequency Engineering, Seeheim, 8-16 May 2000, pp. 146 – 209. CERN 2005-003, Geneva, 2005.

[3] M. Lonza. "Multi-bunch feedback system". CAS – CERN Accelerator School: Digital Signal Processing, 31 May – 9 June 2007, Sigtuna, Sweden, pp. 285 – 330. CERN–2008–003, Geneva, 2008.

[4] H. Bruck. *"Accélérateurs Circulaires De Particules"*. Institute National des Sciences et Techniques Nucléares Saclay. Presses Universitares de France, 1966.

[5] I. M. Kapchinsky. *"Theory of Resonance Linear Accelerators"*. M.: Atomizdat, 1966.

[6] G. Dôme. "Theory of RF acceleration and RF noise". CAS – CERN Accelerator School: Antiprotons for Colliding-beam Facilities, 11–21 October 1983, Geneva, Switzerland, pp. 215 – 260. CERN–84–15, Geneva, 1984.

[7] Alexander Wu Chao (Editor) and Maury Tinger (Editor). *"Handbook of Accelerator Physics and Engineering"*. World Scientific, 1999.

[8] Alan V. Oppenheim and Ronald W. Schafer, with John R. Buck. *"Discrete-Time Signal Processing"*. Prentice-Hall, 2nd edition, 1999.

[9] V. M. Zhabitsky, I. L. Korenev, L. A. Yudin. "Transverse Feedback System with Digital Filter". Proceedings of the 1993 Particle Accelerator Conference, 17–20 May 1993, Washington, USA, pp. 2543–2545. IEEE, 1993.

MULTP-M CODE UPGRADE

N.P. Sobenin, V.I. Kaminskii, S.V. Kutsaev, R.O. Bolgov, I.V. Isaev, M.A.Gusarova, M.V. Lalayan,
NRNU-MEPhI, Moscow, Russia
L.V. Kravchuk, INR, Moscow, Russia

Abstract

It is obvious that for all new RF devices all issues potentially influencing on their performance and operation must be considered at design stage. Multipacting discharge is known to be one of such phenomena. This discharge occurs in vacuum areas of RF devices in case resonant conditions for electrons are met and the secondary electron emission is strong enough. The problem of effective design of multipactor-free RF devices can be solved using powerful 3D numeric simulation tool Multp-M developed at MEPhI and INR. [1].

In this paper new features of this code are presented and illustrated by several common tasks solved. Multp-M code was upgraded so it is able to simulate the external magnetic and electric fields influence on discharge behavior and transient mode simulation. Code became more user-friendly thanks to new 3D interface.

INFLUENCE OF THE EXTERNAL FIELDS

There are a lot of ways for multipactor suppression known and used in microwave techniques. Use of external magnetic or electric field is one of the most widely implemented. Besides that a lot of RF devices like electron guns and injectors operate with magnetic field applied for beam focusing. This leads to sufficient change in multipactor properties. In order to simulate these conditions at early design stage Multp-M was expanded with new modules introducing static fields in model.

Algorithms added were tested and proved to yield correct results. As the initial test single electron dynamics was simulated in simple electric and magnetic fields pattern. More comprehensive research were done and their results compared to known data.

New features were used to evaluate external focusing magnetic field in PITZ photoinjector cavity and electric bias applied in "warm" coaxial line area commonly used in high power input couplers [2]. For instance latter having inner conductor radius equals to 14.4 mm and outer of 31 mm is used in Energy Recovery Linac.

Sample results obtained for PITZ photoinjector cavity illustrating Multp-M code simulation and visualization capabilities are presented on Fig.1. For research details refer to [3]. Multipactor trajectories in cell to circular waveguide transition area were found at 27.25 MV/m on-axis field strength.

a   b
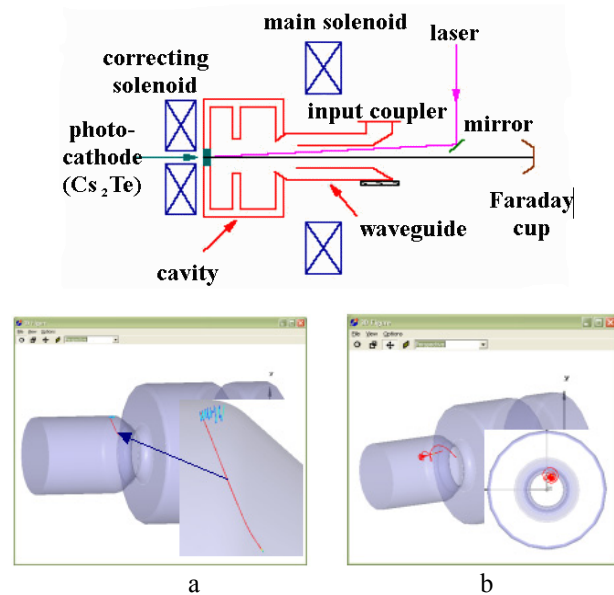
Figure 1: Sample multipactor electron trajectories

a – without external field, b – with focussing magnetic field.

Multipactor could be a severe problem for coaxial lines operation. Its suppression could be done by applying DC high voltage bias between conductors. As an example the simulated multipactor in coaxial line used in ERL high power input coupler warm part [2] is shown on Fig. 2. Coaxial line model used for simulation has inner conductor radius equal to 14.4 vv and outer one 31 mm. Fig.2 illustrates raise of electrons number vs. transmitted power for different bias applied. RF power on charts is normalized: 1 unit equals to 33 MW.

One could see that applying 3...4 KV DC lead to multipactor suppression for transmitted power up to 250 KW CW. It covers full operating range for this coupler.

Thus new computation module implemented in Multp-M code allows to make correct simulation for devices with static magnetic or electric fields and to choose of bias parameters.

0 V　　　　　　　3kV

3kV　　　　　　　4kV
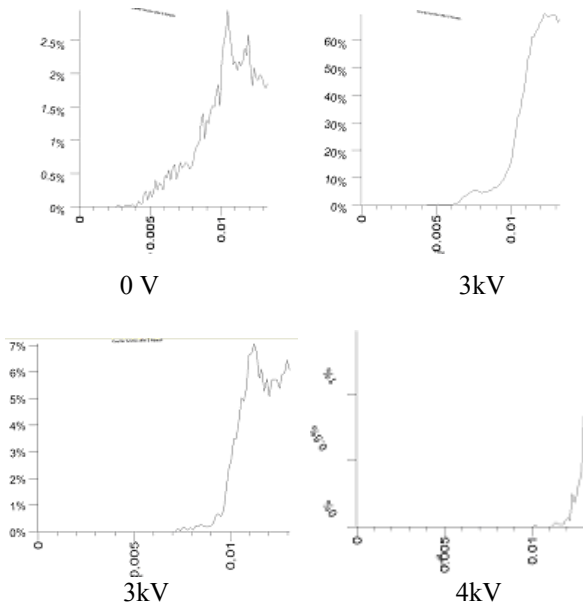
Figure 2: Multipactor electrons number in coaxial line for different DC bias applied to inner conductor.

3D – INTERFACE

Initially MultP-M had only 2D visualization mode. Both model and simulation results showed via three planes aligned to coordinate axes (see Fig. 3).
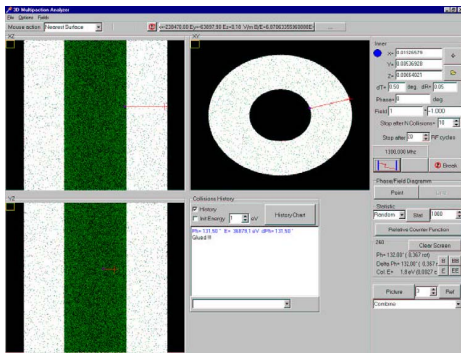
Figure 3: MultP-M: 2D interface.

However, electron trajectories analysis is very important for multipactor study. For complex models multipactor localization and its features is hard to find without true 3D figures and corresponding tools. For this reason Multp-M code was upgraded with 3D visualization module.

Code itself operates in MS Windows environment, so 3D graphics was made using OpenGL library. Fig. 4 illustrates Multp-M snapshot for disk loaded waveguide model and simulated multipactor electron trajectories.
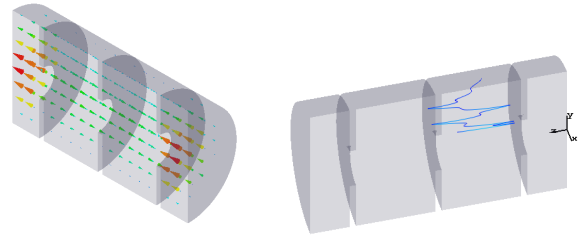
Figure 4: MultP-M: multipactor in DLW simulation results (left - electric field distribution, right – electron trajectory)

New 3D interface allows full visualization of model, electromagnetic field distributions and found electron trajectories. Panning, zoom, rotation, cut-off plane placing, transparency control and other functions are available.

TRANSIENT MODE

New simulation module for transient case development became an important code upgrade. This feature allows one to study multipactor in RF devices operating not only in steady state but also for different transient conditions occurring for example at power-on. New module for pre-calculated time-dependant fields using general purpose electromagnetic solver import was created. Transient fields distribution is interpolated using set of field matrices at different discrete time steps.

Both single and group multipacting electron trajectories simulation in transient mode made ready for use. Sample model for transient solver demonstration is rectangular waveguide of 20x40 mm cross section operating on 5712 MHz. Input signal waveform used in simulation is shown on Fig. 6. Electromagnetic field distribution along the waveguiede for 2 ns after pulse launch is shown on Fig. 6.
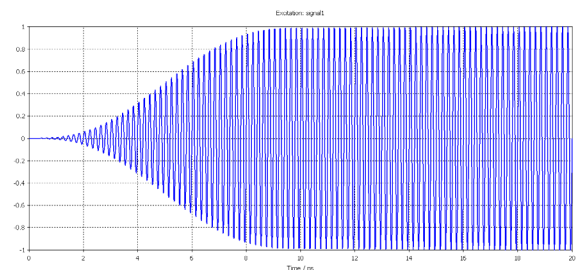
Figure 5: Transient signal waveform
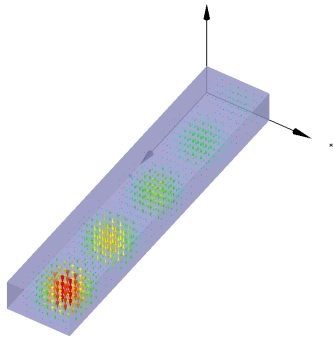
Figure 6: Electric field in waveguide distribution 2 ns after pulse rise (MultP-M).

Fig. 7 presents the rectangular wavegude operating on 5712 MHz example test simulation results. Multipacting electrons   trajectories are shown along with overall electron number vs. time.
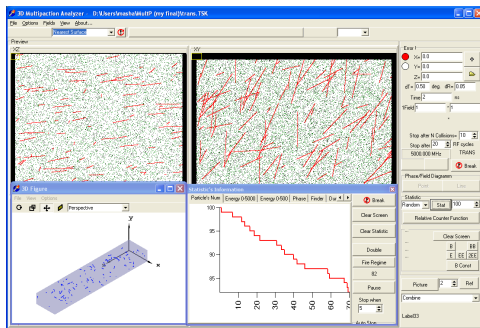
Figure 7: Multipactor electrons trajectories and   overall electron number vs. time for transient mode

CONCLUSIONS

New modules for multipactor simulation Multp-M code upgrade were developed and tested. Series of examples were presented to show code capabilities for simulation of devices with static fields and in transient conditions. 3D interface developed for this code is also.

REFERENCES

[1] M.A. Gusarova, S.V.Kutsaev, V.I.Kaminsky, M.V.Lalayan, N.P.Sobenin, L.V.Kravchuk, S.G.Tarasov, "Multipacting simulation in accelerator RF structure", Nuclear Instrument and Methods in Physics Research A, 599. P. 100-105, 2009. ISSN 0168-9002.

[2] B. Yu. Bogdanovich, M. A. Gusarova, A.A.Zavadtsev, D.A.Zavadtsev, V. I. Kaminskii, A. A. Krasnov, M. V. Lalayan, and N. P. Sobenin "High Average Power Input Couplers for Superconducting Cavities of Charged Particle Accelerators ", Instruments and Experimental Techniques, Vol. 50, No. 1, 2007

[3] M.A. Gusarova, M.V.Lalayan, S.V.Kutsaev, I.V.Isaev, R.O.Bolgov, "Multipactor discharge in accelerating cavities with external magnetic field simulation", Proc. of the   XXI International Workshop on Charged Particle Accelerators, Ukraine, Alushta, the Crimea, September 6-12, 2009

BOOSTER ELCTRON COOLING SYSTEM OF NICA PROJECT

E. Ahmanova, I. Meshkov, R. Pivin, A. Rudakov, A. Shabunov, V. Shokin,
A. Smirnov, A.Sidorin, N. Topilin, Yu. Tumanova, S. Yakovenko, JINR, Dubna, Russia

Abstract

Nuclotron-based Ion Collider fAcility (NICA) [1] is the new accelerator complex being constructed on the JINR site. A few cooling systems are considered for the NICA project – electron one for the Booster-synchrotron and for Collider rings – both electron and stochastic ones. The main goal of the Booster electron cooler is a decrease of the longitudinal emittance from the injection value to the necessary value for acceleration to Nuclotron. The designed electron cooling system for Collider rings have to prevent the emittance growth due to the intrabeam scattering and to keep the average luminosity on the constant value. The peculiarity of electron cooling systems is the using of superconducting solenoids to provide the beam transportation in cooling sections.

INTRODUCTION

The main goal of the Booster electron cooler is the decreasing of the longitudinal emittance from the injection value of about 7.5 eV·s to the necessary value of 2.5 eV·s. Cooling time is limited by the operation cycle of the Booster and can not exceed the value of 1 sec. For the transverse plane the cooling system has to keep the value of the normalized transverse emittances at the level of 1 π·mm·mrad (rms). For the stabilization of the transverse emittance the misalignment of electron and ion beam axes is proposed on the level of about 1 mrad in both transverse planes [2].

Ion energy in the Booster ranges from 6 MeV/u to 600 MeV/u that corresponds to the electron energy range 3.27 ÷ 330 keV. Choosing an optimal energy value for electron cooling one has to account the following effects:

1) beam lifetime limitation due to interaction with the rest gas ;
2) beam lifetime limitation due to recombination on the cooling electrons;
3) space charge effects appearing due to ion beam shrinking at cooling;
4) sufficiently short cooling time (≤1 sec);
5) space charge effect of electron beam on ion cooling;
6) an optimal use of the RF station;
7) cost of the electron cooler.

ELECTRON COOLER OPERATION

The maximum design ion energy of 4.5 GeV/u can be achieved in the Nuclotron with fully stripped ions only. To provide high efficiency of the ion stripping one has to accelerate them up to the energy of a few hundreds of MeV/u. For this purpose a new synchrotron ring – the Booster is planned to be used. Heavy ion injector-linac is designed for acceleration of Au^{32+} ions. The Booster has

maximum magnetic rigidity of 25 T·m that corresponds to about 600 MeV/u of the ion energy, and the stripping efficiency is no less than 80%.

The Booster is equipped with an electron cooling system that allows providing an efficient cooling of the ions in the energy range from the injection energy up to 100 MeV/u.

The magnetic system of the Booster is superconducting. Its design is based on the experience of construction of the Nuclotron SC magnetic system [3] and SC magnetic system of SIS-100 developed later at FAIR project. Therefore to avoid connections between "warm" and "cold" sections in the ring the solenoids of the cooler located along the Booster circumference are designed in the SC version (Fig. 1). This is main difference of the Booster cooler from a conventional electron cooling systems.
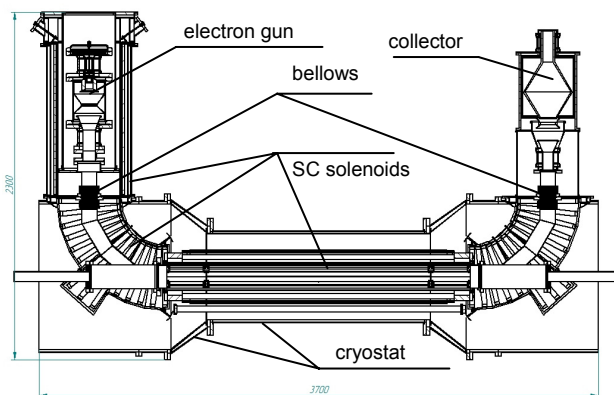
Figure 1: Booster electron cooler.

To cover total range of the ion energy in the Booster (600 MeV/u) the electron beam maximum energy has to be about 330 keV. However the cooling system at such energy is rather expensive, therefore the maximum electron energy (60 keV) is chosen as a compromise between the system price and its capability to fulfill the main project task – the ion colliding beams. A possibility to decrease the ion beam phase volume at injection energy is restricted by space charge limitations.

Another criterion for the electron energy choice is related to the frequency variation range of the Booster RF system. The ion acceleration in the Booster is proposed to be performed in two steps: on the 4th harmonics of the revolution frequency up to the cooler energy and on the 1st one after the cooling. If the cooling is performed at the ion kinetic energy ≥ 100 MeV/u, one can use the same RF system on both steps of the acceleration.

All other parameters of the Booster cooler (Table 1) are typical for conventional electron cooling systems. Design

01 Circular Colliders

of the cooler is performed by JINR electron cooling group and its construction is planned to be done at JINR workshop. Test of the cooler elements will be performed at existing test bench.

Table 1: Basic Parameters of the Booster and its Electron Cooling System

Ions	$^{197}Au^{32+}$
Booster circumference, m	211.2
Injection/extraction energy, MeV/u	6.2/600
Max. dipole field, T	1.8
Ion number	2×10^9
Beta functions in cooling section, m	8 / 8
Dispersion function in cooling section, m	0.6
Maximum electron energy, keV	60.0
Electron beam current, A	$0 \div 1.0$
Cooler overall length, m	4.0
Effective length of the cooling section, m	2.0
Magnetic field in the cooling section, kG	1.5
Magnetic field inhomogeneity in the cooling section, ΔB/B	$1\cdot10^{-4}$
Electron beam radius in the cooling section, cm	2.5
Transverse electron temperature, meV	200
Longitudinal electron temperature, meV	0.5
Cooling time, s	1
Residual gas pressure, Torr	10^{-11}

At the electron cooling of heavy ions one of the serious problems is the recombination - i.e. capture of cooling electrons by ions - resulting in loss of the ions due to change of their charge and deformation of the ion closed orbit. The recombination rate of Au^{32+} ions in the Booster cooler was extrapolated from the experimental data obtained at GSI and CERN. The estimation has shown that during 1 s of cooling the ion losses will be less than 10%. In any case the use of SC solenoid in the cooling section gives a possibility to provide the electron beam compression in order to suppress the recombination by increase of the temperature of transverse degree of freedom of the electron beam.

ELECTRON GUN AND COLLECTOR

All elements of the electron cooling system have the cryogenic temperature except the electron gun and collector which have the standard design for electron coolers (Fig.2).

The superconductive solenoids of electron gun and collector are used for the formation of the longitudinal magnetic fields The electron gun and collector are placed inside the anti cryostats and have a special bellows between "warm" and "cold" vacuum chambers (Fig.1).
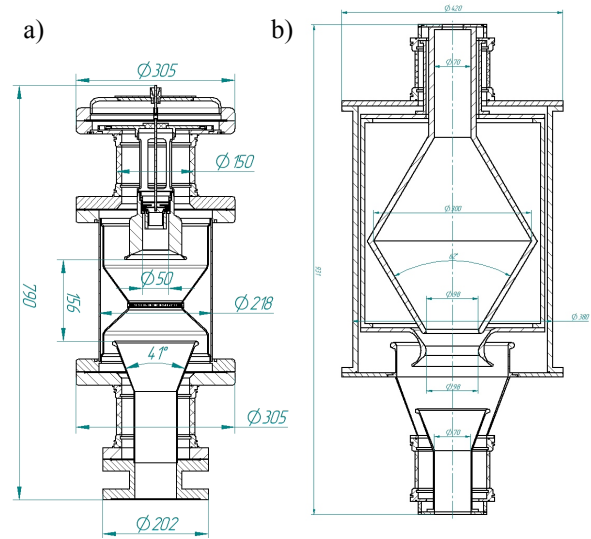
Figure 2: Electron gun(a) and collector (b) design.

For simulation of the optics of the electron guns and electron collectors both BINP and JINR electron cooling groups use mostly the special code SAM [4]. The code allows to simulate the electron trajectories taking into account the geometry of electrodes, the longitudinal magnetic field and the field of the electron beam space charge. As result of a simulation (Fig. 3) one can obtain distribution of the electron beam density and variation of the electron transverse velocity across and along the beam.
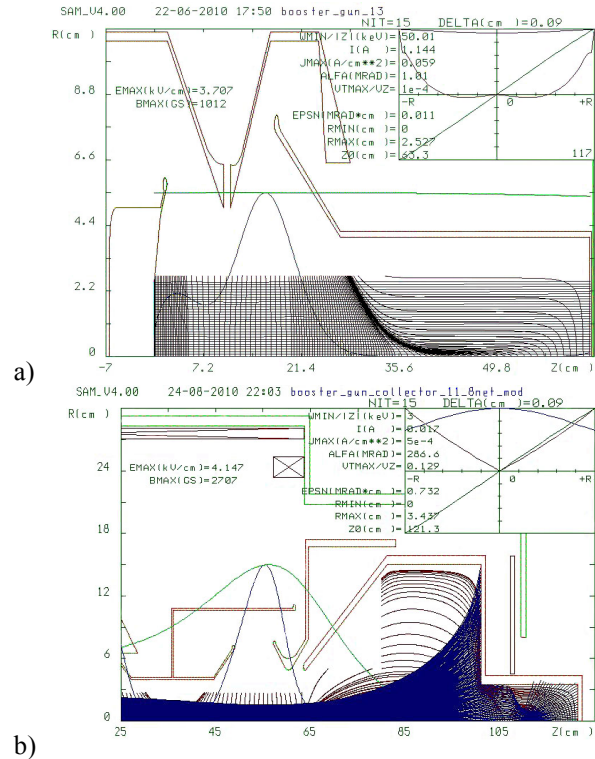
Figure 3: Simulation of electron trajectories in the gun (a) and collector (b).

SIMULATION OF COOLING PROCESS WITH BETACOOL

Main goal of the cooling of heavy ion beam is to decrease its longitudinal emittance to the value required for effective injection and acceleration in the Nuclotron and for the bunch compression in the Nuclotron before injection into the collider. Transverse beam emittance has to be stabilized at relatively large value to avoid space charge limitations in the Nuclotron and collider rings. To avoid overcooling of the transverse degree of freedom the electron beam misalignment in respect to the ion orbit can be used. Simulations of such a regime of the cooler operation performed with BETACOOL [5] code showed that during 1 second of the cooling one can decrease the longitudinal beam emittance by about 3 times at practically constant transverse emittance. That is sufficient for our goal.

The simulation of the electron cooling of $^{197}Au^{32+}$ ions in the Booster does demonstrate the effect of misalignment of the electron beam (Fig. 4-5).
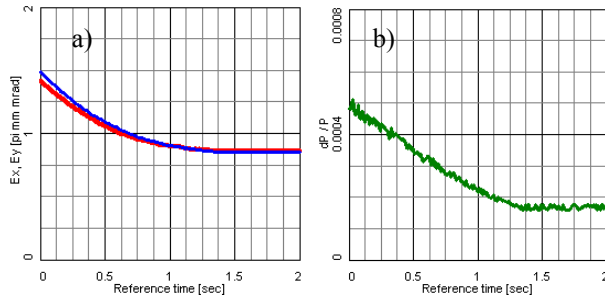
Figure 4: Evolution of the bunched ion beam parameters during the cooling process with misalignment angle of 5×10-4. a) horizontal (red) and vertical (blue) emittances, b) ion momentum spread.

One can see that after 1 sec of cooling the transverse emittance (Fig. 4a) and momentum spread (Fig. 4b) reach the equilibrium between the cooling and IBS heating. The necessary longitudinal emittance of about 2.5 eV·s can be reached in less than 1 sec of the cooling process.
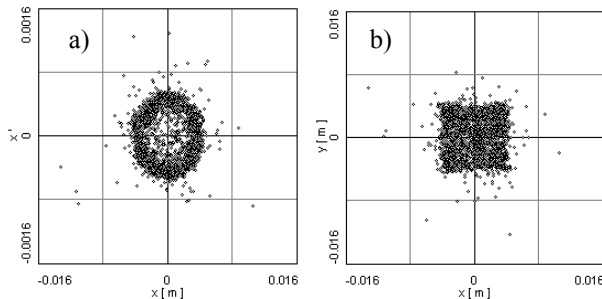
Figure 5: Ion beam density distribution after 2 seconds of the cooling: a) transverse plane and b) horizontal transverse phase space of the cooled ion beam

The beam profile at cooling with misaligned electron beam has a well pronounced double peak structure and most of the particles oscillate with equal amplitudes in the horizontal plane. (Fig.5a). Due to misalignment the transverse cross-section of the cooled ion beam has a rectangular form (Fig.5b).

The optimum regime can be found from the dependence of the cooling time on misalignment angle when the longitudinal emittance decreases from 7.5 eV·s to necessary value of 2.5 eV·s (Fig.6). The cooling time has to be less than 1 sec and the transverse emittance has to be about 1 π mm mrad. For the misalignment angle 0.5 mrad the cooling time does not decrease too much and the transverse emittance is sufficiently large to avoid a tune shift resonance.
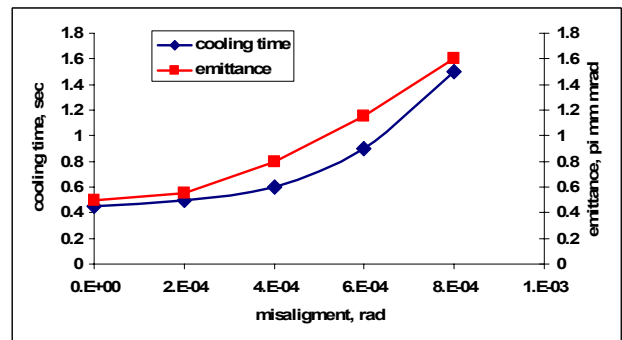
Figure 6: The dependence of the cooling time and transverse emittance after the cooling process on the misalignment angle between electron and ion beams axes; cooling time is defined as time interval when longitudinal emittance decreases from 7.5 eV·s to 2.5 eV·s.

REFERENCES

[1] G. Trubnikov, et.al., Project of the Nuclotron-based ion collider facility (NICA) at JINR, Proceedings of EPAC08, Genoa, Italy. http://www.jacow.org

[2] Design and Construction of Nuclotron-based Ion Collider fAcility (NICA). Conceptual Design Report, Dubna 2008. http://nica.jinr.ru/files/NICA_CDR.pdf

[3] H.G.Khodzhibagiyan, A.A.Smirnov. The concept of a superconducting magnet system for the Nuclotron, *Proc. of the 12th Int. Cryogen. Eng. Conf.*, 1988, pp. 841−844.

[4] Fomel B.M., Tiunov M.A., Yakovlev V.P. SAM – an Interactive Code for Evaluation of Electron Guns: Preprint № 89-159, INP, Novosibirsk, 1989.

[5] I. Meshkov, A. Sidorin, A. Smirnov, E. Syresin, G.Trubnikov, P. Zenkevich, Numerical Simulation of Particle Dynamics in Storage Rings Using Betacool Code. Proceedings of RuPAC XIX, Dubna 2004. http://betacool.jinr.ru

ELECTRON GUN AND COLLECTOR FOR 2 MEV ELECTRON COOLER FOR COSY*

A.V. Ivanov[#], M.I. Bryzgunov, A.V. Bubley, V.M. Panasyuk, V. V. Parkhomchuk, V.B. Reva
The Budker Institute of Nuclear Physics, Novosibirsk, Russia.

Abstract

COSY storage ring is planed to be upgraded in 2011 by installation of a new electron cooler [1]. Electron cooling will reduce energy spread of protons and so improve the precision of internal target experiments. Some of the most important parts of this new electron cooler are the electron gun and the collector, and they must satisfy several rigid requirements. Electron gun must provide high perveance electron beam with low transversal temperature and variable beam profile. The gun control electrode assembled of four separate sections will provide measurements of beam envelope along the transport section of the cooler. Displacement of corresponding part of the beam may be observed if alternating voltage is applied to each section. Collector should have high perveance, low secondary emission coefficient, and small dimensions. Wien filter is supposed to be installed before the collector to satisfy these requirements. In this case we can use high perveance small-scale collector with axially-symmetric magnetic field; secondary electrons will be absorbed in Wien filter. An additional vacuum pumping must be provided in the collector design.

ELECTRON GUN

The electron gun for COSY cooler is very similar to the guns for other BINP coolers, installed on CSR and LEIR rings [2]. This gun provides high-perveance electron beam with low transversal temperature. The gun design is shown in Fig. 1. The convex cathode 1 immersed into longitudinal magnetic field is used. To form the electron beam together with anode 4 control electrode 3 is used. This electrode is placed near the cathode edge and influences the emission from this area. By applying different potential on this electrode the beam with radial current density distribution from parabolic to hollow can be obtained.
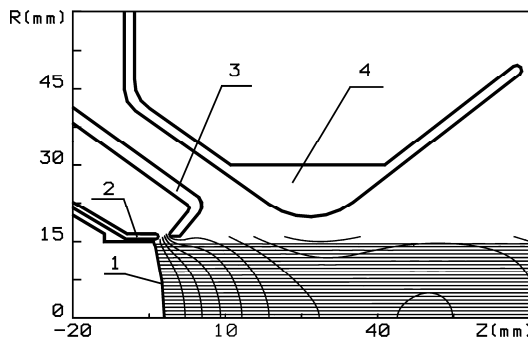
Figure 1: Electron gun for COSY cooler.

05 Beam Dynamics and Electromagnetic Fields
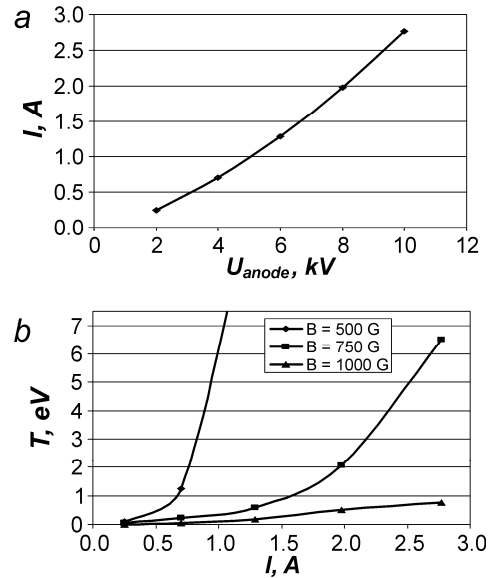
Figure 2: Current (a) and transversal temperature (b) of homogeneous electron beam.

To provide high efficiency of electron cooling at high energies one need to increase beam current density. The calculations of the homogeneous beam current as a function of anode potential (Fig. 2a) were made with UltraSAM code [3]. With the current increase the transversal temperature grows also (Fig. 2b). These calculations show that value of magnetic field should be at least 600 Gs to provide acceptable (< 2 eV) temperature of 1 A uniform beam.
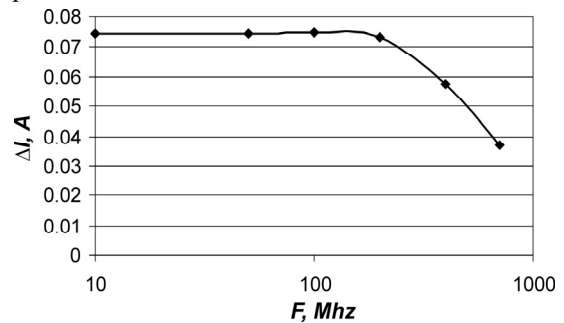
Figure 3: Electron beam current modulation at oscillation of the control electrode potential (ΔU= 50 V, U=600 V).

For beam diagnostic purposes the suggestion was made to reject axial symmetry and to divide control electrode into 4 segments. By applying small potential variation on one of these segments not only position of beam center but also beam sizes can be measured. Beam current modulation decreases at high frequencies of potential oscillation, thereby to realize this technique the cutoff

frequency must be found. The calculation results shown in Fig. 3 give 200 Mhz cutoff frequency for this gun. With help of 3D simulation it was found that modulation of emission current density at cathode opposite side from acting segment is less than 2% of the maximal current density modulation, thus this technique looks realizable.

WIEN FILTER

In order to increase efficiency of absorption of electron beam it is proposed to suppress secondary electron flux from the collector with Wien filter installed before the collector. The filter can significantly improve efficiency of recuperation (I_{loss}/I_{total}) of electron cooler. The idea of Wien filter is to suppress secondary electrons with crossed electric and magnetic fields. For main electron beam, electric and magnetic (Lorenz) forces are compensated and the beam goes to collector:

$$F_\perp = \frac{e}{c}V_\parallel B_\perp - eE_\perp = 0 \,,$$

where $V_\parallel$ is longitudinal velocity of electron, $B_\perp$ and $E_\perp$ is transverse magnetic and electric fields. For secondary beam, which is reflected from collector, the forces are not compensated and the beam drifts to wall of vacuum chamber:

$$F_\perp' = \frac{e}{c}V_\parallel B_\perp + eE_\perp = 2\frac{e}{c}V_\parallel B_\perp \,.$$

Transverse electrostatic field is produced with special plates. During entrance to the filter, electron can be accelerated or decelerated by edge fields of the plates, that depends on coordinate of an electron. It means that in the filter electrons, flying closer to positive plate, have higher velocity than in center of the beam. As a result, for homogeneous distributions of transverse fields, beam shape will be changed (Fig. 4) and it can decrease perveance of collector.
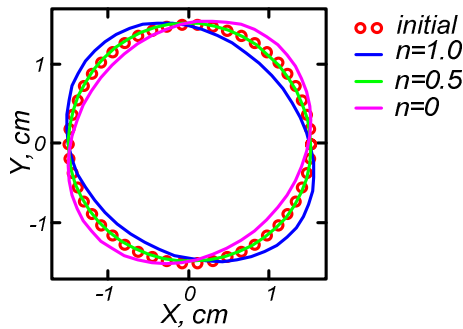
Figure 4: Change of main beam shape in homogeneous transverse fields.

In order to avoid this problem transverse magnetic field should have gradient:

$$B_x = B_\perp \frac{n}{R} y \,, \quad B_y = B_\perp \left(1 + \frac{n}{R}x\right),$$

where $R = \dfrac{pc}{eB_\perp}$, $n = \dfrac{1}{2\gamma^2}$, x and y – coordinates in transverse direction, γ – Lorentz factor.

05 Beam Dynamics and Electromagnetic Fields

Two methods of production of transverse magnetic field were investigated: with magnetic coils and with permanent magnets. Calculations show that to produce magnetic field 35-40 G the thickness of coils is about 4 cm. That is too much in order to insert it in our system without significant changes. Decreasing of size of the coil leads to increasing of its power and it becomes necessary to cool it.

System based on permanent magnets was chosen. Permanent magnets provide required value of magnetic field and their size is small enough in order to insert them in the system without significant changes in construction. Varying properties and position of the magnets one can produce required values of field and gradient. Disadvantage of such system is that it is impossible to adjust magnetic field without disassembling of the filter.

Fields in Wien filter were calculated with the help of Mermaid program. Length of electrostatic plates is 39 cm, integral of transverse magnetic field in center 1400 G·cm, voltage on electrostatic plates ±8 kV relative to vacuum chamber. Potential of vacuum chamber of the filter is 20 kV relative to cathode. Special shim is added to the plates to make homogeneous distribution of electric field.
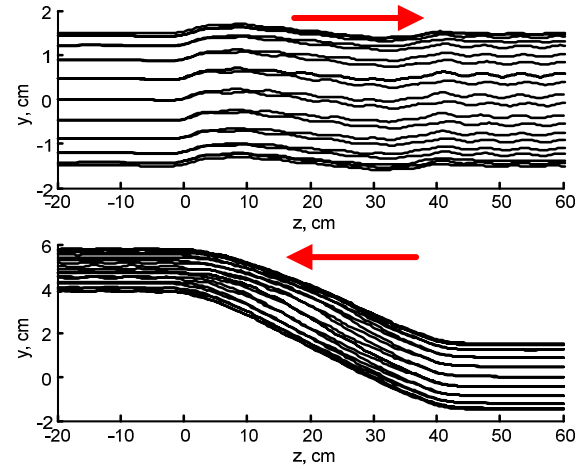
Figure 5: Electron beam motion in the filter: upper – primary beam, lower – secondary beam.

Using results of field calculations beam motion in the filter was calculated (Fig. 5). Beam radius 1.5 cm, electron energy 20 keV, longitudinal magnetic field 500 G. In the figure one can see that primary beam flies along the system with small deviation from axis which are result of mismatch between electric and magnetic fields in entrance end exit of the filter. Secondary beam is deviated from the axis to about 5 cm. Since diaphragm for secondary beam collection has inner radius 2.5 cm such deviation is enough.

Electrons moving to the diaphragm also produce secondary electrons which can make system efficiency worse. Form of the diaphragm allows decrease this flux. We expect resulting efficiency of the system will be lower then 10^{-5}.
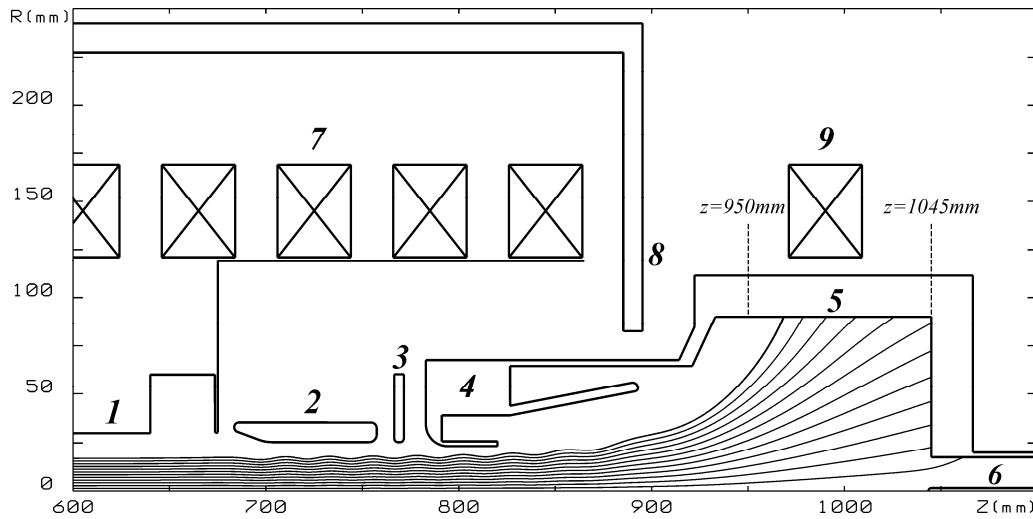
Figure 6: The collector assembly design.

COLLECTOR

The collector for high-voltage electron cooler must be small, simple design installation with high perveance and small secondary emission coefficient. To meet these requirements the suggestion was made to refuse a design with totally shielded collector as in previous BINP coolers. To weaken the magnetic field inside the collector that is needed to expand the electron beam and to form the magnetic mirror for the secondary electrons another technique was proposed – to feed one of the solenoids with opposite current.

The collector assembly design is shown in Fig. 6. The electron beam coming from drift tube 1 passes through collector anode 2 and suppressor 3 and enters inside collector 4. Due to magnetic shield 8 and coil 9 with opposite current the beam expands and deposits on cooled collector surface 5. To implement effective pumping the hole 6 is provided that connects collector with vacuum pump. To avoid electron flux into this hole in its center thin electrode under cathode potential is placed.

To optimize the collector performance current in coil 8 must be adjusted. The calculations show that with proper choice of this current most of the beam current deposits on cooled surface without local overheating (Fig. 6). The perveance of this collector with fully opened suppressor varies from 13 to 15 $\mu A/V^{3/2}$ depending on electron beam profile.

The second method to lock secondary electrons in collector is the electrostatic barrier. This barrier is formed by suppressor if its potential is lower than collector potential. Collector secondary emission coefficient is calculated as a function of suppressor potential, the results are shown in Fig. 7.

CONCLUSION

The electron gun and collector are developed for high-voltage COSY electron cooler that is under construction in BINP.
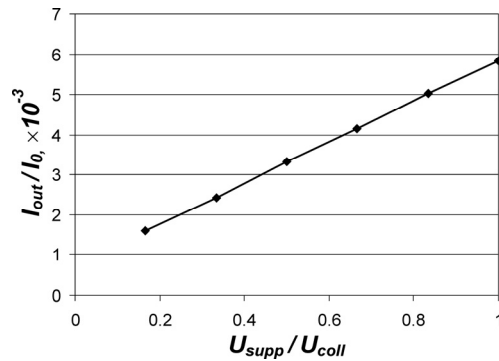
Figure 7: Secondary emission coefficient of the collector. Primary beam current $I_0 = 1$ A.

The gun can provide electron beam with current up to 3 A, low transversal temperature and variable beam profile. The beam current density can be modulated on one of the sides that will help measure the beam sizes. The collector is small and has high perveance that facilitates its placement at the top of electrostatic column. Using both electrostatic and magnetic barriers allows obtaining collector secondary emission coefficient less than 10^{-3}. Additional decrease of reverse electron flux in high-voltage system (less than 10^{-5} of the main beam) can be achieved with help of Wien filter installed before the collector that will help to increase system stability and reduce high voltage source load.

REFERENCES

[1] J. Dietrich et al., "Status of the 2 MeV Electron Cooler for COSY Juelich", Proceedings of IPAC'10, Kyoto, Japan, 2010, p. 843; http://www.JACoW.org.

[2] A. Ivanov et al., "Electron gun with variable gun profile for optimization of electron cooling of ions". Vestnik NGU, Physics, 2007, v.2, N.1, p.65-69.

[3] A. Ivanov, M. Tiunov, "ULTRASAM - 2D Code for Simulation of Electron Guns with Ultra High Precision", EPAC'02, Paris, June 2002, WEPRI050, p. 1634 (2002); http://www.JACoW.org.

05 Beam Dynamics and Electromagnetic Fields

TRANSVERSE BUNCH-BY-BUNCH DIGITAL FEEDBACK FOR THE VEPP-4M COLLIDER

V.P. Cherepanov, V. V. Oreshonok , V.V. Smaluk, D.P. Sukhanov,
Budker Institute of Nuclear Physics, Novosibirsk, Russia

Abstract

The coupled-bunch instability is the base reason of the operating current limitation at the VEPP-4M electron-positron collider. For suppression any excited transverse mode of oscillation of the accumulated beam, the transverse bunch-by-bunch digital feedback has been installed. The paper reports on the current design and status of the feedback system. The available diagnostic tools and latest operational results and beam measurements is given.

INTRODUCTION

The single-bunch beam current in the electron–positron collider VEPP-4M at the injection energy of 1.8 GeV is limited by the instability of vertical betatron oscillations caused by the transverse mode coupling or fast head-tail. At the present time, use of the consistent bunch-by-bunch scheme for the transverse feedback systems is a conventional method for suppression of any excited transverse mode of beam oscillation [1, 2].

The digital feedback system to suppress the vertical betatron oscillation of each bunch independently has been developed for VEPP-4M.

Table 1: The general parameters of the VEPP-4M collider and feedback system

Parameter	Value
Revolution frequency, f_0	818.936 kHz
RF frequency, f_{RF}	181 MHz
RF harmonic, q	222
Injection energy, E	1.8 GeV
Experiment energy, E_b	5.2 GeV
Betatron tunes, n_x/n_y	8.56/7.58
Design bunch current, I_b	40 mA
Number of bunches	$2e^-$ x $2e^+$
Number of strip-line BPMs used	1
Number of kickers	4
Feedback system bandwidth	20 MHz
Power per kicker, P_k	400 W

Figure 1 shows the block-diagram of feedback system. The system configuration and specifications are mainly determined by necessity to suppress the TMC instability in the 2×2-bunch VEPP-4M operation mode. The beam

position signals from strip-line BPM are prepared by the input front-end electronics, come to the signal processing board and are then digitized by the ADC. The kick signals formed by the digital board are converted by the DAC and, after amplification by the power amplifiers, come to the kickers.
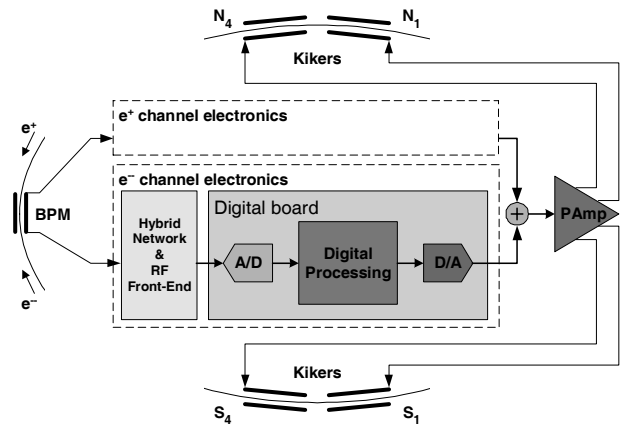
Figure 1: Block diagram of the Transverse Bunch-by-bunch Feedback system.

A more detailed description of the front-end electronics and of the power output devices is given in [3, 4]. Basic features of the presented system are the different digital part and use of the only BPM.

DIGITAL SIGNAL PROCESSING

Additional requirements for flexibility and availability of diagnostic tools have led to the development of the new digital board. The main feature of this device is use of an FPGA for the signal processing and controls (see Figure 2). The availability of several independent pipeline operations allows as to use the bunch-by-bunch feedback option and to organize different processing arrangements. This makes possible to fulfill completely the feedback system requirements and to use various diagnostic tools: detection of beam position and other possible variations of the beam parameters in real-time, betatron oscillations spectral analysis, etc. In addition, the device was developed for use in multi-bunch operation mode to satisfy the higher technical requirements in the future.

General Layout

The signal digitizing circuit includes two 12 bit pipeline ADC ADS5527, which are used to measure vertical position and intensity of the beam. Two Altera Cyclone III receive the beam position data from ADC, make DC rejection and necessary phase shift using the digital FIR filter. The correction kick data produced by the FPGA

come to the wave-shaping circuit and is converted to an analog signal by four 12 bit digital-to-analog converters TI DAC5652, one per kicker.

Figure 2: Layout and data stream for the digital board.

Kick signals for the electron and positron bunches formed by proper signal digitizing circuit are summarized for each kicker and come to the power electronics input.

The signal digitizing circuit includes digital and analog delays to synchronize the digital board operation with time of flight of each bunch through pickup and kickers.

Application of additional memory is caused by desire of temporary accumulation of the various measured and calculated data to transfer them through a network to a workstation for further analysis later. In addition, the Ethernet network is used for operative control.

Table 2: The digital board specifications

Parameter	Value
Sampling Rate	180 MHz
ADC/DAC resolution	12/10 bits
Input&Output Coupling / Impedance	AC/50 Ohm
Input/Output Analog Bandwidth	800/120 MHz
Analog&Digital Clock Shift	More 2 us
Step of Clock Programmable Shift	11 ps
Total Jitter	20 ps
Clock/Trigger signal	Diff.&CMOS
Memory	9 Mbit

Digital Filter

The basic task of the FPGA software is the calculation of the correction kick value based on the measured bunch oscillation signals. In order to reject the DC equilibrium orbit signal from the BPM and to shift all kick signals by the $\pi/2$ betatron oscillation phase with respect to the phase signal of the same bunch when it passes through the appropriate kicker, FIR filters are used. These filters

provide a necessary phase irrespective of the kicker positions in the ring.
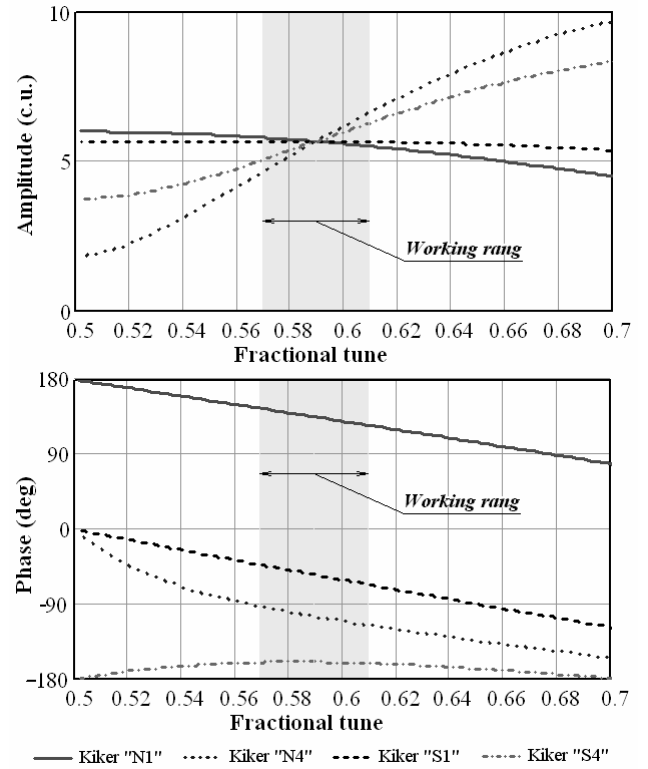
Figure 3: Transfer function of the 2-tap FIR filter.

During the energy ramping from 1.8 to 5.2 GeV the betatron tunes can vary due to dynamic mismatch of the magnet lattice elements. Since the fractional part of betatron tune is close to 0.5, complex digital filters for the tune variation compensation, which was made, for example, at ELETTRA [1], are not applicable. The simplest 2-type FIR filter successfully provides DC rejection and the appropriate phase and gain in all working frequency range. Figure 3 shows the amplitude and phase characteristics of the filter, as one can see the range of permissible deviation of betatron tune (fractional part) is $0.57 - 0.61$.

OPERATIONAL RESULTS

The new digital board is integrated into the transverse feedback system, which is successfully operates at the VEPP-4M electron-positron collider.

Figure 4 shows the turn-by-turn plots of current (left plot, top), vertical (left plot, middle), and horizontal (left plot, bottom) coordinates of the injected beam measured by the pickup in 512 turns; the figure also shows the current remaining after 512 turns I_{512}. The top plot on the right shows the spectrum of vertical beam oscillation, and the bottom plot on the right shows the spectrum of horizontal beam oscillation. It can be seen that the feedback system suppresses vertical oscillation in less than 100 turns, and current losses are not large.
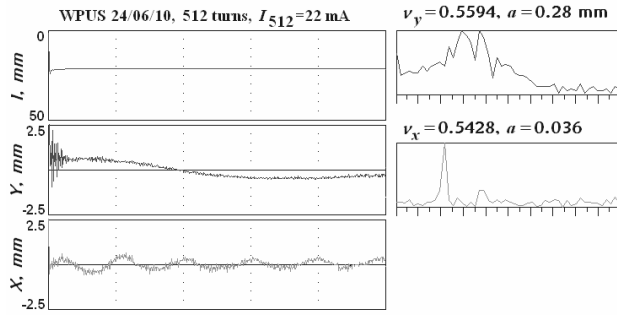
Figure 4: Beam injection with closed feedback system.
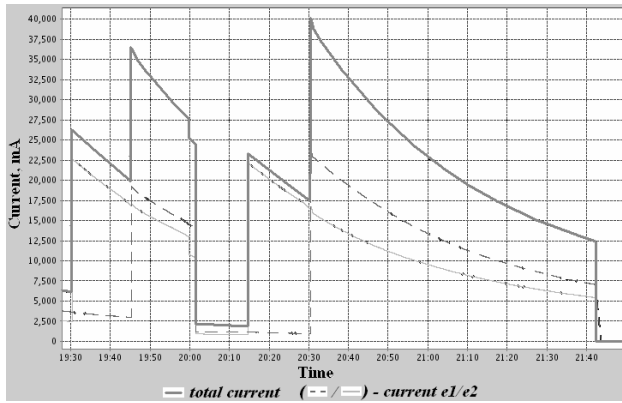
Figure 5: Time diagram of the VEPP-4M
captured beam currents.

Figure 5 shows the current of separate bunches and the total current in the two electron bunch operation mode.

At present time, for more accurate work of the feedback system during energy ramping, diagnostic tools are developed to measure possible variations of the betatron tune in real-time with closed feedback.

REFERENCES

[1] D.Bulfone et al, "The ELETTRA Digital Multi-Bunch Feedback Systems", EPAC'02, Paris, France, June 2002.

[2] M. Dehler et al, "Digital Processing Electronics for The ELETTRA Transverse Multi-Bunch Feedback Systems", DIPAC'03, Mainz, May 2003.

[3] V.P. Cherepanov, E.N. Dementev, A.S. Medvedko, V.V. Smaluk, D.P. Sukhanov, "The VEPP4-M transverse bunch-by-bunch feedback system.", RUPAC'06, Novosibirsk, Russia, September, 10-14, 2006.

[4] V.P. Cherepanov, E.N. Dementev, E. Levichev, A.S Medvedko, V. Smaluk, and D.P. Sukhanov, "Transverse Bunch-By-Bunch Feedback for the VEPP-4M Electron-Positron Collider," DIPAC'07, Venezia, Italy, 2007.

[5] V. P. Cherepanov at al, "Video Pulse Power Amplifier for Accelerator Technology Applications", RUPAC'06, Novosibirsk, Russia, September, 10-14, 2006.

TRANSVERSE FEEDBACKS
IN THE U70 PROTON SYNCHROTRON OF IHEP

O. Lebedev, S. Ivanov, N. Ignashin, and S. Sytov

Institute for High Energy Physics (IHEP), Protvino, Moscow Region, 142281, Russia

Abstract

To handle the adverse effect of transverse injection errors and resistive-wall instability in the U70, two frequency-band-separated feedback circuits are routinely employed. The first one is a narrow-band (around baseband DC) local end-to-end-analog circuit terminated by an electrostatic kicker. The second is a wide-band bandpass circuit with a variable (−10% ca) digital delay line and low-level DSP units and an electro-magnetic kicker. Both the circuits were subjected to a deep renovation during the recent 5 years, which provided a better control over transverse motion of the beam. The paper reports on technical solutions implemented, problem-oriented R&D studies, and beam observations.

INTRODUCTORY FORMULAE

In the U70, like in most of proton synchrotrons worldwide, coherent transverse beam motion, if any, is quieted by means of a relatively slow multi-turn deflecting coercion on beam. In this context [1], one can apply to a wave-to-wave cross-talk approach that involves propagating waves $\propto \exp(ik\Theta - i\omega t)$ of deflecting Lorentz force field strength (whose wave amplitude is $S_k(\omega)$) and electric dipole moment of the beam ($D_k(\omega)$). Here, k is an integer wave number, $\Theta \propto \omega_0 t$ is azimuth along the ring, ω_0 is angular rotation frequency of on-momentum particle, t is time.

Electro-dynamical properties of beam environment, either passive or active (e. g., of beam feedback circuits), are commonly described in terms of a transverse coupling impedance $Z_k(\omega)$, in Ohm/m, that is tacitly defined via

$$S_k(\omega) = i\beta\omega_0 Z_k(\omega) D_k(\omega)/L \qquad (1)$$

where L is orbit length, β is reduced velocity. This Eq. implies reflection symmetry $Z_{-k}(-\omega) = Z_k(\omega)^*$. Given *passive* components of the vacuum chamber (resistive wall, deflecting HOMs, etc.), $\omega \cdot \mathrm{Re} Z_k(\omega) \geq 0$.

Adopt, for definiteness, the upper betatron side-band convention with series $\omega \cong (k + Q)\omega_0$ where Q is betatron tune (about 9.8–9.9 in the U70). In this case, a coherent mode observable at a frequency line that probes $\mathrm{Re} Z_k(\omega) < 0$ turns unstable.

Hence, design goal for a perfect damping beam feedback is to impose *active* coupling counter-impedance with

$$Z_k^{(\mathrm{FB})}(\omega) = A_k^2 + i0 \quad \text{at} \quad \omega = (k+Q)\omega_0. \qquad (2)$$

Because of a comb nature of beam transfer function one must tailor out the appropriate function $Z_k^{(\mathrm{FB})}(\omega)$ only in a close vicinity of the frequency line (lines) $\omega = (k + Q)\omega_0$ of interest, rather than globally over the entire ω-domain, which simplifies the task from the technical viewpoint.

Let a (short) pickup electrode PU be mounted at azimuth Θ_{PU} and a (short) transverse kicker K be at Θ_{K}, their separation azimuthally being $\Delta\Theta_{\mathrm{K-PU}} = \Theta_{\mathrm{K}} - \Theta_{\mathrm{PU}}$. Following Eq. 1, one can put down

$$Z_k^{(\mathrm{FB})}(\omega) = -iG(\omega)\exp(i\omega\tau - ik\Delta\Theta_{\mathrm{K-PU}}). \qquad (3)$$

$\underline{G(\omega)}$ is in-out transfer function of electronics in the open feedback loop, reduced to units of Ohm/m,

$$G(\omega) = \frac{pc}{eJ_0}\left(\frac{\Delta y'_{\mathrm{K}}}{\Delta y_{\mathrm{PU}}}\right) = \frac{(El)_{\mathrm{K}}}{\beta(J_0\Delta y)_{\mathrm{PU}}} = \frac{c(Bl)_{\mathrm{K}}}{(J_0\Delta y)_{\mathrm{PU}}}. \qquad (4)$$

Here, y is transverse coordinate (vertical, horizontal), J_0 is average beam current, p is momentum, c is velocity of light, e is elementary charge, $(El)_{\mathrm{K}}$ and $(Bl)_{\mathrm{K}}$ are field strength integrals of electrostatic and magnetic kickers, optionally. Phase-frequency characteristic of $G(\omega)$ is assumed to have a vanishing slope averaged over the bandwidth. Time delay inherent in $G(\omega)$ (electronics + pure delay lines) is incorporated in the overall delay τ in Eq. 3.

NARROW-BAND FEEDBACK

It is a local system whose pickup, electrostatic kicker and signal-processing (analog) equipment are all housed in the same straight section SS#2 of the U70 lattice [2]. The system imposes a damping upon the dedicated spatial harmonic $-k_1 = [Q] + 1 = 10$ of beam perturbation where $[Q]$ is the integer part of Q. This harmonic is notable for the strongest destabilization by the resistive-wall wake.

The feedback signal-processing algorithm relies on tune Q being just below an integer value and reads

$$G(\omega) = -2\left(\frac{A}{1 - i\,\omega/\Delta\omega}\right)^2 \mathrm{HPF}(\omega). \qquad (5)$$

Given (i) cut-off frequency (at −3 dB) of integrator circuit $\Delta\omega$ equal to $|k_1 + Q|\omega_0$, (ii) vanishing delay time $\tau = 0$, and (iii) negligible spatial separation $\Delta\Theta_{\mathrm{K-PU}} = 0$, Eq. 3 readily turns into a sought-for damping impedance of Eq. 2 at the frequency line $(k_1 + Q)\omega_0$ in question.

Last factor in Eq. 5 denotes a high-pass filter with a roll-off frequency $\ll \Delta\omega$ that rejects a DC closed-orbit offset signal seen by the PU. Its higher-frequency translates at $\pm\omega_0$, $\pm 2\omega_0$, etc are safely smeared out by a cascade of two integrators in Eq. 5. The same mechanism suppresses residual self-excitation of the next neighbouring to k_1 base-band harmonic $k = -9$ that is inherently stable under the resistive-wall wake, with feedback off.

The system is in a routine service since 2007. Additional damping factor imposed is about 100 w. r. t. a natural decay time of harmonic k_1 due to de-coherence. Details of technical implementation are reported in [2].

WIDE-BAND FEEDBACK

Generalities

Conversely, it is a non-local wide-band band-pass system which uses two pickups, PU1, 2 at SS#107, 111 respectively, and an electro-magnetic kicker K at SS#90. In the U70, azimuth Θ of straight SS#n is $\propto 2\pi n/120$.

The kick fed back to beam proceeds from a weighted sum of two beam signals red out from PU1 and PU2. Therefore, Eq. 3 now slightly modifies to

$$Z_k^{(FB)}(\omega) = -iG(\omega)\sum_{m=1,2} w_m \exp(i\omega\tau_m - ik\Delta\Theta_{K-PUm}). \quad (6)$$

Here, three conditions to follow are set,

$$\tau_{1,2} = \Delta\Theta_{K-PU1,2}/\omega_0, \qquad Q\Delta\Theta_{K-PU0} = \frac{\pi}{2}(2j+1). \quad (7)$$

The first expressions equate beam time-of-flight to signal-processing in-out delay en routes PU1–K and PU2–K.

The rightmost of Eq. 7, where j is a positive integer, defines a virtual pickup denoted as PU0. Its location is set to an odd number of betatron quarter-wavelengths upstream of kicker K. In the U70, $j = 16$. With

$$G(\omega) = (-1)^j A^2 . \quad (8)$$

$$\begin{pmatrix} w_1 \\ w_2 \end{pmatrix} = \frac{1}{\sin Q\Delta\Theta_{PU2-PU1}} \begin{pmatrix} \sin Q\Delta\Theta_{PU2-PU0} \\ \sin Q\Delta\Theta_{PU0-PU1} \end{pmatrix} \quad (9)$$

one gets Eq. 2 that is now effective for a whole set of frequency lines occurring inside the bandwidth of $G(\omega)$.

Suppression of closed-orbit offset signal at $\omega = k\omega_0$, with DC included, is accomplished via a variable electrical center of pickup biased with balance amplifiers. Supplementary option using a one-tap periodical (with a period ω_0) digital notch FIR filter in $G(\omega)$ was also tested.

Layout

Fig. 1 shows topological layout of the feedback circuit. Lengths of cables are such as to yield $\Delta\Theta_{B-A}/\omega_0 = \tau_{C-A}$ at injection flat-bottom. Component-by-component structure is sketched in Fig. 2. There are two identical channels servicing horizontal (H) and vertical (V) directions.

Low-level signal-processing electronics is taken out of the Ring Hall to the Main Control Room. High-power RF amplifiers are housed in the technological bld. #5/3. The equipment is interconnected with high-frequency cables having low attenuation and high temperature stability.

Sensor and Actuator

Beam-position sensors are stations of skew-cut electro-static pickup electrodes followed by front-line electronics that matches pickup impedance to wave impedance of the cable traces. The pickups are mounted in straights SS#107 and 111, the latter being shown in Fig. 3 (left). Their technical performance data is reported in [2]. The difference signal is acquired and low-pass filtered (6.3 MHz cut-off at −3 dB) in the front-end electronics.

The feedback actuator is a fast electro-magnetic beam kicker (deflector) comprising a pair of air coils. Its performance data is specified in Table 1.

The kicker is installed in SS#90, refer to Fig. 3 (right). The same straight houses an auxiliary beam pickup, which is used to trim and control, mainly, the digital delay line performance. The goal for such a crucial control is to ensure simultaneous arrival to SS#90 of a bunch itself and of its signal delayed over the entire feedback path.
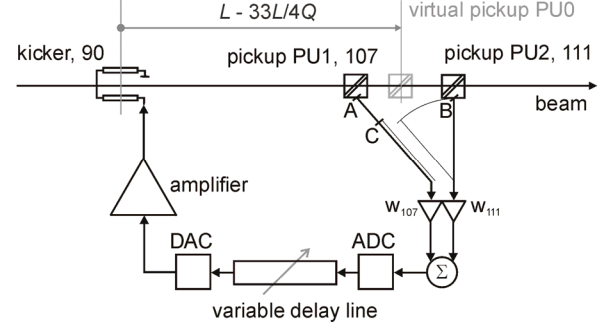
Figure 1: Layout of the wide-band feedback.
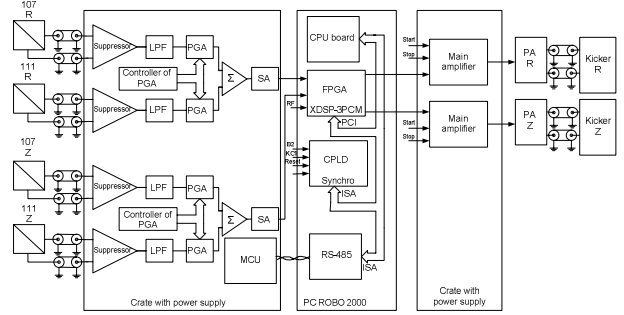
Figure 2: Block diagram of the wide-band feedback.

Figure 3: Pickup station (left). Electro-magnetic beam kicker followed by an auxiliary in-situ beam pickup (right).

Table 1: Performance data of kicker and amplifier

Length of a dipole coil	1.1	m
Coil inductance	0.6	μH
Ratio of B-field to current	6.5	μT/A
In/Out resistance of amplifier	75/37.5	Ohm
Max input voltage, peak-to-peak	1	V
Max output current	5	A
Bandwidth at −3 dB	0.1–15	MHz

Low-Level Signal Processing

The key technical problem behind this feedback is to comply with the leftmost of Eq. 7 under a varying rotation frequency $\omega_0/2\pi$= 183.9–202.0 kHz. Historically, a 1 km long hank of cable performed this task. During renovation this outdated solution was substituted by a digital delay line clocked at the 16th harmonic of acceleration frequency $\omega_{RF}/2\pi$ = 5.516–6.062 MHz.

Core of the digital system constitutes a signal-processing module XDSP-3PCM whose structure is shown in Fig. 4. It is an AT-size motherboard mounted via PCI bus into an industrial computer ROBO-2000. There are two 12-bit ADC and DAC embracing the FPGA programmable logical matrix available. The latter device implements the prescribed signal-processing algorithms, of which the simplest one being a mere delay of a signal.
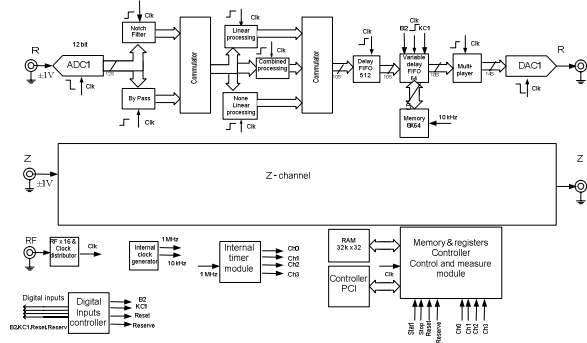
Figure 4: Block diagram of the XDSP-3PCM module.

Host processor of the ROBO-2000 computer executes Read-Write operations with service data sets that, say, govern variable gains of outer differential amplifiers whose microcontrollers acquire data through a serial optically isolated interface RS-485.

Easy implementation of variable delays is not the only profit gained on going to the DSP. Indeed, various algorithms to tailor out the feedback signal can now be accomplished by means of a straightforward high-level language coding of the DSP board free of hardware changes.

Table 2: Feedback modes

	A: linear	B: "bang–bang"
Feedback, n is turn no.	$\Delta y_n = -A y_{n-1}$, gain $A > 0$	$\Delta y_n = -B\,\mathrm{sgn}\,y_{n-1}$ kick level $B > 0$
Decay law	$y_n = y_0 \exp(-An)$	$y_n = y_0 - Bn\,\mathrm{sgn}\,y_0$ unless turning bi-polar
Decay time in turns	$\dfrac{1}{A}$	$\dfrac{|y_0|}{B} = \dfrac{|y_0|}{\max|y|}\dfrac{1}{A}$
Ultimate at $n \to \infty$	$y_n \to 0$	$y_n \neq 0$, beating with $|y_n| < B$

To this end, we have tried not only a conventional linear (proportional) feedback presented conceptually in row A of Table 2. A faster non-linear regime (row B) responding to a sign of bean offset by the utmost deflection yielded by the kicker was also tested. Regime B shortens the ini-

06 Instrumentation, Controls, Feedback and Operational Aspects

tial decay time of beam oscillations by a factor equal to a ratio of factual initial offset magnitude $|y_0|$ to a peak linear dynamic range $\max |y|$ of the feedback circuit in mode A.

As is known, contrary to linear feedback A, mode B cannot settle beam offset to zero ultimately. Therefore, a combined regime A-B with a user-selectable toggling threshold in between the two modes was adopted for a routine service. It naturally combines advantages of both the modes (shadowed cells in Table 2) and ensures a noticeably faster damping of transverse coherent motion.

Beam Observations

Since the 2nd run of 2008, the digital wide-band feedback of the U70 is in a test operation. Outcomes of its commissioning are shown in oscillograms of Figs. 5–7.
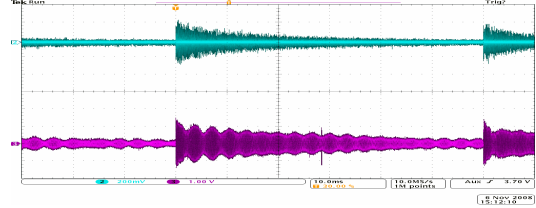
Figure 5: Natural decay (time 50 ms) of horizontal injection error with feedback off. Lower trace is the 10th harmonic of beam signal. Bunch-to-bunch gap is 60 ms.
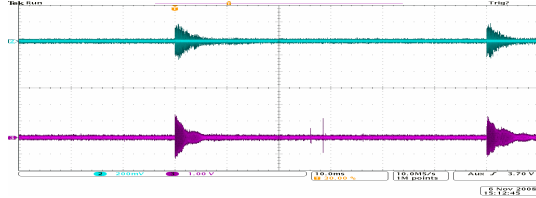
Figure 6: Forced decay (time 2–3 ms) with feedback on in a linear mode A.
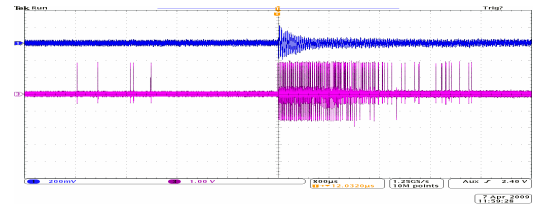
Figure 7: Forced decay (time 1 ms ca) with feedback on in a combined mode A-B. Lower trace shows driving current sent to the kicker.

CONCLUSION

The two transverse beam feedbacks in the U70 are well effective and shorten damping time by a factor of 100 for the narrow-band, and 20–25 (linear mode A) or 50 (combined mode A-B) for the digital wide-band circuits.

REFERENCES

[1] S. Ivanov, Preprint IHEP 97–64, Protvino, 1997.
[2] O. Lebedev et al, Proc. of RUPAC-2008, Zvenigorod, 2008, p. 21–23.

USER INTERFACE IN THE DIAGNOSTIC SYSTEM OF THE EXTRACTED BEAMS OF THE U-70 ACCELERATOR

N. Ivanova, V.Kovaltsov, A.Koshelev, A.Lukyantsev
V.Milyutkin, Ju.Smirnov, A.Sotnikov, IHEP Protvino, Russia

Abstract

User interface in the diagnostic system of extracted beams is described. It was developed under Linux operating system on the personal computers used as workstations.

The considered program tools provide:

- the representation on operator consoles (workstations) information about beam profiles, intensity, displacement, root-mean-square error etc. in different forms;
- the dynamic adjustment of the diagnostic system;
- web presentation of the current information about the extracted beams;
- data transfer to physical setups;
- special beam characteristics calculation by the profilometer individual units data (for research purposes);
- data archiving and web facilities for data viewing.

INTRODUCTION

The diagnostic system for the beams extracted of U-70 accelerator is intended for beam profiles, intensity and position measurement. It is a three-level hardware-software complex [1]. The structure of the lower and middle levels is described in detail in [2]. The software for the middle and upper levels was developed by EPICS toolkit [2].

This report considers software for the upper level and its important part – the user interface. The users of the diagnostic system are the beam and the accelerator specialists, experimental physicists, hardware designers and operational staff. The user interface developed in the diagnostic system provides the interaction with the system in various forms. Functionality and convenience were the main aspects of the interface design.

UPPER LEVEL OF THE DIAGNOSTIC SYSTEM

The workstations and the server are the upper level computers. The workstations take the beam data from the middle level, which is composed of so called IOCs (Input Output Controller in EPICS terms). Each IOC is connected to the lower level of the system where the data is registered. The scheme of the upper level is shown in Figure 1. The computers are linked via Ethernet by TCP/IP protocol.

One IOC is usually used for a single beam channel. From experience, it is best when single workstation corresponds to one IOC. The workstation accepts the data from this IOC and it is responsible for initial loading and parameters adjustment of this IOC.
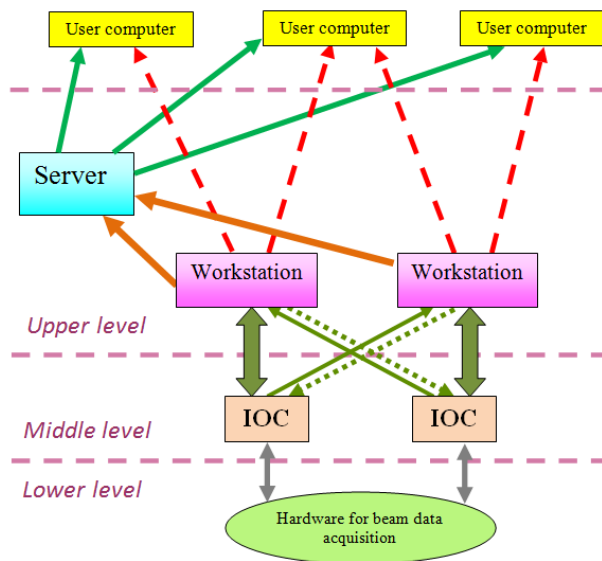
Figure 1: Upper level computers and their links. The dashed lines mean the restricted access.

However, the EPICS tools allow to monitor (and tune with small restrictions) any IOC from any workstation. For the system's reliability, we have supplied some redundancy measures. When one workstation is down another workstation is able to replace it. For this purpose the software for one workstation and "its" IOC is duplicated at another workstation and is in a non-active state. But this software can be activated if necessary and the workstation will work with two IOCs.

The current data from all workstations are transferred to the server which provides the access to information through a web-site. In addition to on-line data server keeps the information about the previous runs.

All computers of the upper level are running under Linux operating system. But user computers may be equipped with another operating system, for example, MS Windows. All one needs is a browser and an access to Internet.

SOFTWARE FOR USER INTERFACE

The upper level software includes the programs which directly realize the user interface, EPICS components needed for diagnostic system work, utilities, etc.

The main parts of the user interface software are shown in Fig. 2. The most important task of interface is to present beam data for on-line control. The appropriate software was developed by EPICS tools. It is shown by red color. This software is located on the workstation. The other part of the interface consists of utilities which are on

06 Instrumentation, Controls, Feedback and Operational Aspects

the workstation and on the server. They are marked by green color. And a set of programs provides an access to the information by web-sites (blue color).

Also, remote access to workstation by VNC (Virtual Network Computing) is provided. It gives the possibility to retransmit the workstation screen to a user computer. The access is made by Linux tools.

Some programs read data from IOC by Channel Access (CA). CA is the EPICS component which is intended for the communication between the system levels. The other way of data transfer is by our driver-program in IOC. It uses NFS protocol. The driver writes the current data to file located on the workstation in every accelerator cycle. This current data file is open for reading for all programs on the workstation.
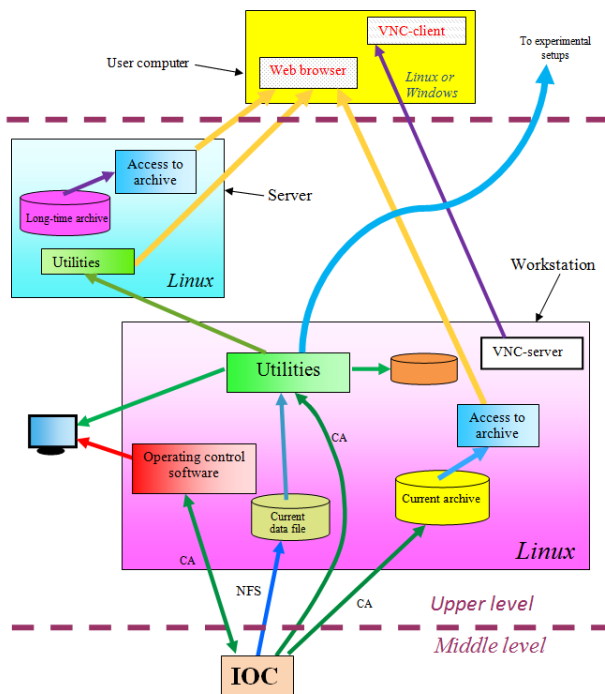
Figure 2: The user interface structure and the information flow.

ON-LINE CONTROL SOFTWARE

The on-line control software is designed for the specialists of the magnetic optics of beam channels and for the operational staff. The software is developed by EPICS and it is a graphic interface. When diagnostic system starts up an operator points out IOC and necessary graphic data presentations, so called displays. These displays contain the information about the current beam state. Two of them are presented in Fig. 3. The first picture depicts the beam profiles in the horizontal and vertical planes and some current beam features. The second display gives the operators opportunity to manage diagnostic system running. There are operator and administrator levels of management. The entry to the administrator level is paroled. It is easy to change any

display or to create a new one by means of EPICS graphical editor.
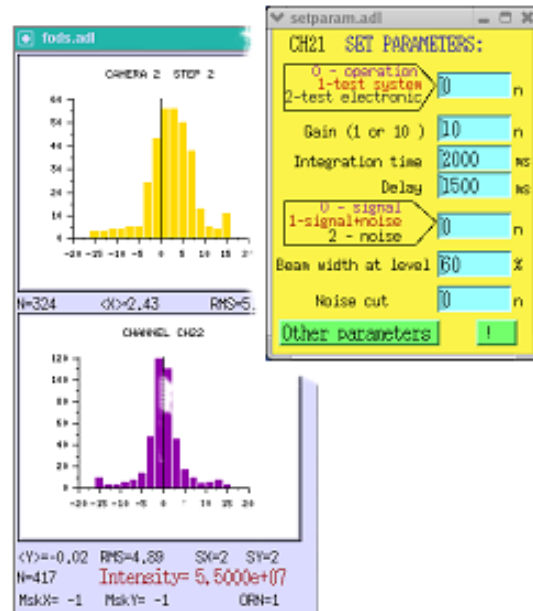
Figure 3: Examples of displays.

UTILITIES

Besides the current data visualization, the users of the diagnostic system do need the digital presentation of information, data transportation, etc. Utility programs are designed for this purpose. Fig. 4 shows the programs and related information flows. The programs are written in C. They take input data by CA or from the current data file. All the programs are running in real time. Below we describe these programs briefly.

INTEN program reads the current intensity value and computes the average and the total value of intensity during the given time period. The results are displayed and written to the file for every accelerator cycle. INTEN is used for the intensimeter calibration [2].

STAB is intended for magnetic optic specialists. It processes data acquired by the profilometer which is near the beamstopper (for OKA setup). STAB calculates the values R, Q, <Y> and RMS, where

$$R = \frac{(Pn_2 + Pn_3)}{(Pn_1 - Pn_4)} \qquad (1)$$

$$Q = \frac{(Pn_1 - Pn_4)}{(Pn_2 + Pn_3)} \qquad (2)$$

<Y> − average beam deviation,
RMS − mean-square deviation from <Y>,
Pn_i – charge of the device channel number n_i.

FRED is used for beam deviation control. It calculates value R:

$$R = \frac{(P_n)}{(Q_m)} \times coeff \qquad (3)$$

where P and Q represent the charges in X- or Y- plane, n and m – profilometers numbers, coeff – user coefficient.

FSEND reads information from the current data file and send it to FODS experimental setup. Among these data are profile measurements, intensity value etc. FSEND is running as program-client that communicates with program-server on experimental setup computer.

NTRIN is similar to FSEND program, but it is for other experimental group.
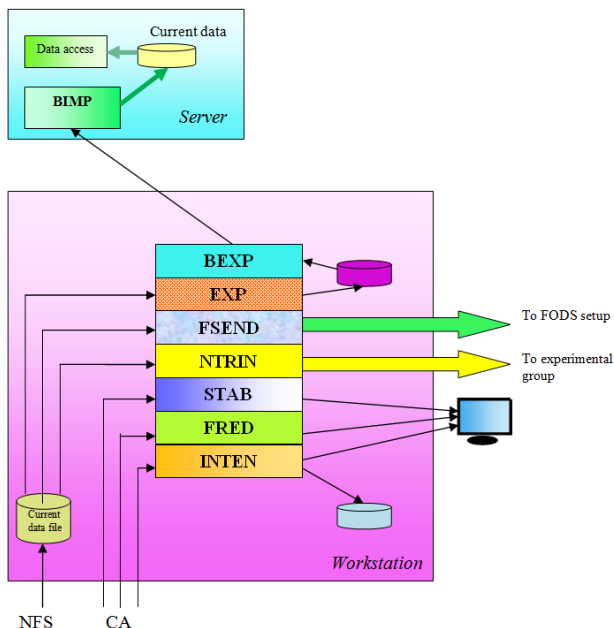
Figure 4: Utility programs.

WEB-SITES IN THE DIAGNOSTIC SYSTEM

The programs described above are for magnetic optics specialists and for physicists of some experimental groups. However, there is information that may be of interest for broader audience. Some web-sites were organized for this purpose.

One of the web-sites is located on the server. It represents the current data about extracted of U-70 beams. EXP program reads the information from the current data file and converts it into graphical form. BEXP program sends it to the server where BIMP receives this information and prepares for the web-site (Fig .4). The data on the site is refreshed in every accelerator cycle.

The acquired in diagnostic system data are archived by means of EPICS tool. The data are moved to archive immediately upon arrival. The archive for the current accelerator run is on every workstation. For access to archive the web-site is organized at every workstation.

CONCLUSION

The developed software provides user interface for different kinds of hardware and software specialists as well as for experimental setup groups. The interface is provided in various ways.

REFERENCES

[1] V.Kovaltsov, A.Matyushin, V.Milyutkin, I.Romanov, V.Seleznev, A.Sytin, M.Clausen. Upgrading of the beam diagnostic system of U-70 beam transfer lines. Proceedings of ICALEPCS-2001, San Jose, California, USA, Oct. 2001.

[2] N.Ivanova, V.Kovaltsov et al., Profiles and intensities measurements in the diagnostic system of the extracted beams of the U-70 accelerator. This Conference.

[3] http://www.aps.anl.gov/epics, 'EPICS Home Page'.

WIDEBAND BPM ELECTRONICS FOR THE VEPP-4M COLLIDER

E.A. Bekhtenev, G.V. Karpov, Budker Institute of Nuclear Physics, Novosibirsk, Russia

Abstract

New beam position monitor (BPM) FPGA-based electronics has been developed and tested at the VEPP-4M electron-positron collider. The VEPP-4M operates with two electron and two positron bunches. Compared to the old BPM electronics the new one can measure the position of each of four bunches with any BPM of storage ring including the BPMs near interaction point. Wide bandwidth of electronics (200 MHz) allows the separate measurements of electron and positron bunches with time interval between bunches up to 20 ns. BPM system works at two modes: slow closed orbit measurements and turn-by-turn measurements. We present details of system design and operation.

INTRODUCTION

The VEPP-4M is the modernized VEPP-4 collider, which had been commissioned for the first time in 1977 [1]. Conditions of high energy physics (HEP) experiments require continuous orbit measurements of electron and positron bunches. The present VEPP-4M Beam Position Monitor (BPM) system developed 25 years ago [2] can make orbit measurements only if one type of particles is circulating at storage ring: electrons or positrons. It is not capable to measure beam orbit during HEP experiments where both types of particles are at storage ring. The second disadvantage of the old BPM system is absence of turn-by-turn capability by each BPM. To satisfy modern requirements an internal R&D program has been started at BINP to develop new BPM electronics for VEPP-4M. Some of storage ring parameters are given in Table 1.

Table 1: Some parameters of the VEPP-4M collider

Beam energy	1-6 GeV
Revolution frequency F_0	0.819 MHz
RF frequency	181.8 MHz
Beam current	1-30 mA
Total number of electron and positron bunches	4
Total number of BPMs in storage ring	54
Minimal time interval between electron and positron BPM signals	20 ns

Precision requirements to BPM system are not so severe: relative accuracy of slow measurements has to be of order 50-100 microns, resolution of turn-by-turn measurements has to be of 20-50 microns.

The VEPP-4M collider operates with two electron and two positron bunches. Difference in arrival time of the electron and positron bunches is minimal for BPMs

located close to places of meeting of bunches. For example for the BPMs NEP0 and SEP0 located close to interaction point (at opposite sides of interaction point) arrival time of the electron and positron bunches differs in ~22 ns. For NEP0 the first bunch arrived is positron bunch for SEP0 – electron bunch.

New electronics design utilizes signal peak sampling with high bandwidth digitizer as it was done for CESR [3]. At the end of 2009 new BPM electronics had been developed. In January 2010 two complete sets of BPM electronics had been fabricated and installed at VEPP-4M BPMs NEP0 and SEP0.

BPM ELECTRONICS DESIGN

Functional diagram of the new BPM electronics is presented in Fig.1.
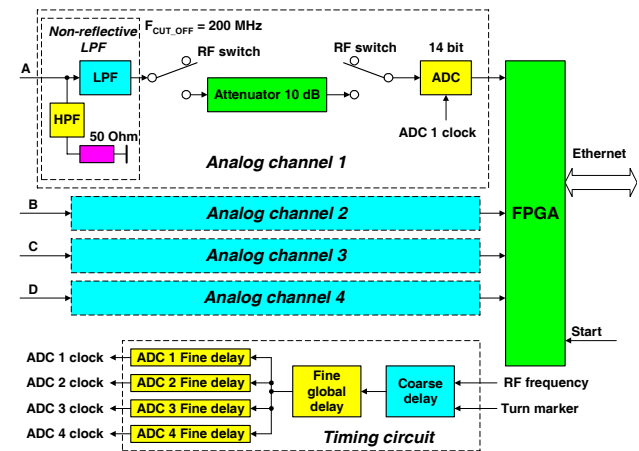
Fig.1. Functional diagram of new BPM electronics.

The electronics consists of four identical analog channels, FPGA, Timing circuit and Ethernet interface. All electronics occupies 1U 19" chassis.

In order to achieve separate measurements of electron and positron bunches the bandwidth of analog front-end electronics is chosen of 200 MHz. The bandwidth is defined by non-reflective Low Pass Filter (LPF) with cut-off frequency of 200 MHz. Pickup signal of electron bunch at the LPF output is shown in Fig2.

Amplitude of reflected from LPF signal is less than 1% of coming signal. "Tail" of the first bunch signal on the peak of second bunch signal is less than 0.5%. However such "tail" value can cause position measurement error of the second bunch up to 0.5 mm. To decrease this error program compensation of the "tail" is implemented in the system.
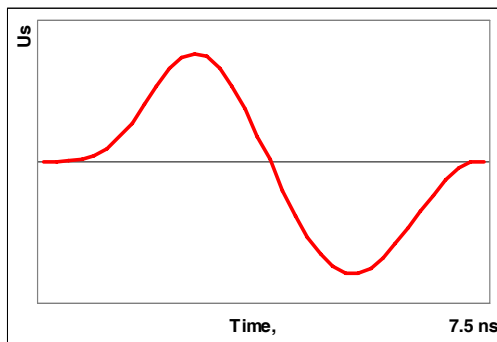
Fig.2. Pickup signal of electron bunch at the LPF output.

Pickup voltage of the second bunch is calculated with formula:

$$U_{2C} = U_{2M} - k \times U_{1M},$$

where U_{2M} and U_{1M} – are measured pickup voltages of second and first bunches correspondingly,

k – is measured relative amplitude of the "tail" of the first bunch on the peak of the second bunch.

The k value is measured experimentally one time and then is used for "tail" compensation. Such compensation decreases position measurement error of the second bunch caused by "tail" of the first bunch approximately in 10 times.

The feature of new BPM electronics is absence of any amplifier. The signal from LPF via semiconductor switches comes right to 14 bits 40 MHz ADC (AD9244). The signal amplitude for beam current of 10 mA corresponds to full scale of ADC – 1 V. For more large currents the signals pass via -10 dB passive attenuator. High voltage RF switches SW-277 of Minicircuits firm can bear peak voltages up to 20 V.

Clock frequency of ADC is revolution frequency F_0. Each turn ADC digitizes one of four bunch signals. Timing circuit provides ADC samples exactly at the top of BPM signal. Timing circuit is a three-stage delay. The first stage (coarse delay) is 8-bit programmable counter MC100EP016 with clock frequency of 181.8 MHz (RF frequency). After applying of turn marker the counter is preset by code defining coarse delay and then starts. Delay step of the first stage is one period of RF frequency ~5.5 ns. Delay range is $1/F_0 – 5.5$ ns.

The second stage (fine global delay) is 10-bit programmable delay chip MC100EP195B. It provides 10.24 ns delay range with 10 ps delay step. The third stage consists of four chips MC100EP195B, each chip for one of four ADC. As a result timing circuit provides total programmable delay range exceeding period of revolution frequency F_0 with delay step of 10 ps. Measured time jitter of ADC clock is ~10 ps.

Choosing of measured bunch is made by setting of corresponding delay code. Measurement of four bunches is carries out with multiplexing of four delay codes.

Beam position is measured each turn. Turn-by-turn data are recorded to memory (with capacity of 8192 turns) and accumulated in Accumulator (inside FPGA). Accumulated data for specified number of turns form

06 Instrumentation, Controls, Feedback and Operational Aspects

slow acquisition data (SA data). Turn-by-turn data and SA data are transmitted via Ethernet to VEPP-4M Database. SA data for all four bunches are recorded to VEPP-4M Database each second. Turn-by-turn data can be acquired on demand or on trigger after beam injection or beam kicking. The electronics can provide decimated by a factor 2-256 (programmable value) turn-by-turn data. This expands time interval of turn-by-turn data acquisition up to ~2.5 sec.

EXPERIMENTAL TESTS RESULTS

BPM electronics had been tested at test stand and at VEPP-4M storage ring. At test stand Agilent Pulse Generator was used as signal source. During some of the tests at VEPP-4M in order to exclude real beam position instability signal from one of four BPM buttons was split in four lines which was connected to four inputs of BPM electronics.

Five accuracy parameters where measured:
- Resolution of turn-by-turn data
- Resolution of SA data
- Temperature instability of the beam position measurements
- Beam-current dependence
- Dependence of measured beam position of the second bunch (electron bunch for NEP0 and positron bunch for SEP0) on the beam current of the first bunch

Results are given in Table 2. Geometric factors of BPMs NEP0 and SEP0: $K_X \approx 43$ mm, $K_Z \approx 42$ mm.

Table 2: BPM system parameters defining accuracy of measurements for average beam current 1÷10mA ($K_X \approx 43$ mm, $K_Z \approx 42$ mm).

|		
Resolution of slow measurements (SA data)	μm	3-6
Resolution of turn-by-turn data	μm	15-30
Beam-current dependence	μm	40-50
Error for the second bunch caused by first bunch "tail" when electron and positron beam currents are equal	μm	< 40
Dependence on temperature	μm/°C	4

Dependence of the result on temperature (~4 μm/°C) is caused by three main reasons:
- Inequality of the Low Pass Filters (LPF)
- Inequality of RF switches and attenuators
- Delay instability.

Delay instability is defined by delay instability of the chip MC100EP195B (10-20 ps/°C). For excluding of measurement error caused by delay instability continuous tuning of the programmable delay is carry out. Each 5-10 min delay scanning in the range of 300 ps with step of 10 ps is performed. After completing of the scanning delay code corresponding to maximal signal is found and set.

Resolution of turn-by-turn measurements is defined by two factors:

- ADC noise (~1 bit)
- ADC clock jitter (~10 ps)

ADC clock jitter generates amplitude noise of ADC data. Due to different shapes of pickup signals caused by inequality of the LPF this noise is different for different BPM buttons. This follows to degradation of resolution.

Resolution of turn-by-turn measurements for BPMs NEP0, SEP0 can be evaluated with formula:

$$\sigma \approx 30/I_b + 10 \text{ [microns]},$$

where I_b – is average beam current (for choosing bunch).

Accuracy parameters for other BPMs of VEPP-4M approximately in 2 times better than for NEP0, SEP0 due to smaller geometric factor ($K_X \approx K_Z \approx 20$ mm).

Results of slow measurements (data rate ~1 Hz) at VEPP-4M storage ring with BPM SEP0 are given at Fig.3.
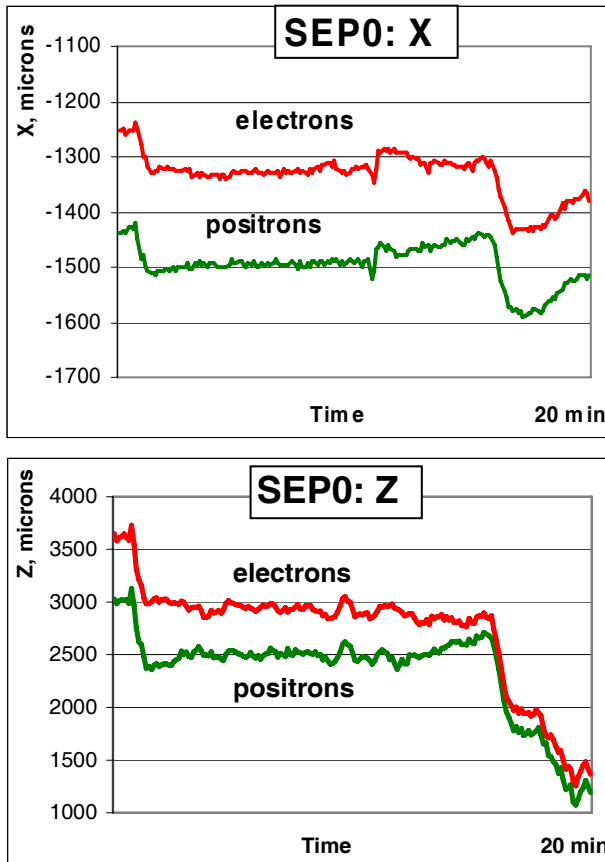
Fig.3. Results of beam position measurements at VEPP-4M with BPM SEP0 (electron and positron beam currents ~1 mA). Upper picture shows horizontal position, lower picture shows vertical position.

Measured positions of two electron bunches (two positron bunches) have good coincidence. Positions of electrons and positrons are different due to separation of the beams.

Results of turn-by-turn measurements after bunch kicking are presented in Fig.4. Turn-by-turn capability of new electronics gives new possibilities of machine study.
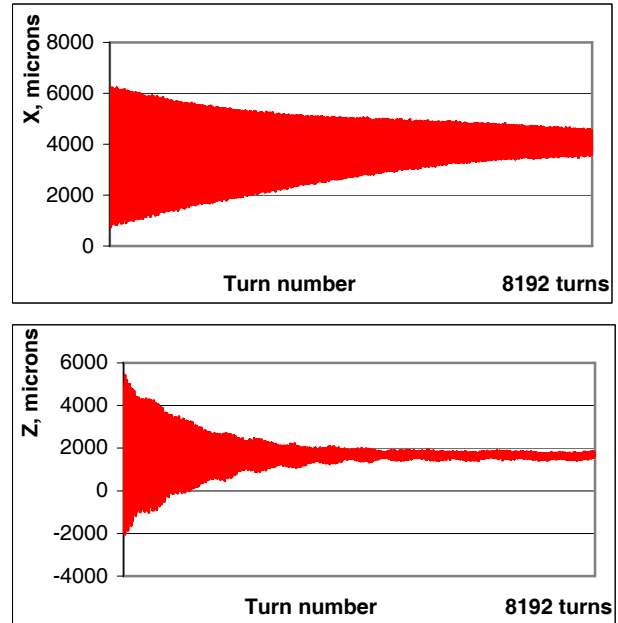
Fig.4. Results of turn-by-turn measurements of electron bunch after kicking with BPM SEP0.

SUMMARY

At present three complete sets of new BPM electronics are manufactured and installed at VEPP-4M storage ring. All software for this electronics has been written. Results achieved satisfy to machine requirements. After some period of time during which new BPM electronics will operate decision about replacement of all old VEPP-4M BPM electronics with new one will be taken.

REFERENCES

[1] V. Smaluk, for the VEPP-4 team. "Status of VEPP-4M collider at BINP". Proceeding of RuPAC-2008, Zvenigorod, p.79-81.

[2] A.N.Dubrovin et al. "Applications of beam diagnostic system at the VEPP-4", Proceeding of EPAC-96, Sitges, Vol.2, p.1585-1587.

[3] M.Palmer et al. "An Upgrade for the Beam Position Monitoring system at the Cornell Electron Storage Ring", Proceeding of PAC-2001, Chicago, p.1360-1362.

06 Instrumentation, Controls, Feedback and Operational Aspects

LOGGING ACTIONS OF OPERATORS IN THE IHEP U-70 ACCELERATOR COMPLEX CONTROL SYSTEM

V. Voevodin, IHEP, Protvino, Russia

Abstract

The control system (CS) of the U-70 accelerator complex supports distributed control rooms environment which are equipped by unified consoles. Using any console it is possible to request any action on any accelerator complex equipment in accordance with user's rights to access it. There are situations requiring knowledge of actions, was performed on some peace of equipment during defined time slot. To solve this problem the CS logs all operators' actions initialized from any consoles such as open/close session, change settings of accelerator parameters, restore settings from archives, etc.

The paper describes a logging software organization and functionalities, contents of the log files and information visualization tools.

LOGGING REASONS

The basic software architecture and organization of the CS was presented in [1]. The last steps of modernization towards homogenization of CS were discussed in [2]. As a result at present the control system supports a number of control rooms equipped with unified consoles on base of PC-compatible computers. The control rooms are distributed over different buildings and GUI is a separate software package dealing, on one side, with humans and, on other side, with descriptions in the data bases. That is why any changes and additions in the 'user–control system' interaction are made inside this package without influence on other CS software components, e. g. data processing.

Due to distribution of equal in rights consoles over number of control rooms there are necessities from time to time to know what actions on some accelerator equipment took place during the certain time slot. The knowledge helps significantly to understand complex difficult situations during simultaneous work of operators in a different control rooms with interconnected subsystems, e.g. ejection system of one accelerator and injection system of other.

We saw an acceptable decision of the problem in logging significant operator's actions with possibility of efficient visualization the information by any console of the CS. Control system users interact with it by the same unified GUI, realized as the data driven package of programs, which supports three main steps of actions:

1. User identification.
2. Menu tree - to select predefined set of parameters for observation and editing.
3. Tabular presentation of selected parameters values.

A password identifies the user and his rights to modify setting values.

'User – control system' dialogue session starts from root point of the menu tree and ends by closing the menu tree.

On selection of menu tree leaf the window with corresponding table of parameters' current values is opened. Current values of each parameter are presented by a row of a table. An operator may do next modifications on the values:

- Set new value to individual table cell.
- Set new value, add/subtract/multiply/divide all current values of selected rows or selected columns with some entered constant.
- Set new value, add/subtract/multiply/divide all current values of intersection cells of selected rows and columns with some entered constant.

So, it is possible to log most significant operator actions by modifying GUI programs only.

LOG FILES

Log files are placed in the fixed directory on the control system file server (Figure 1) and are accessed using NFS protocol inside of the CS.
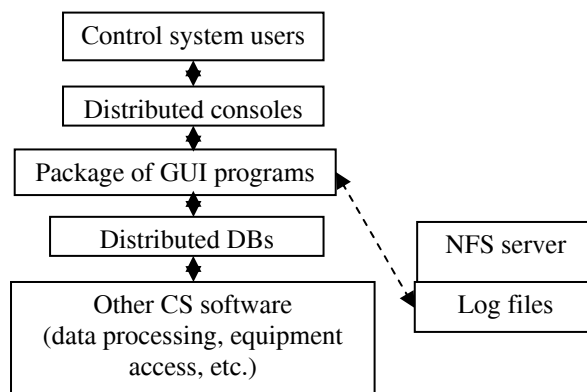
Figure 1: Location of the log files in the CS layout

There is a separate log file for each control system user containing descriptions of actins were performed by him. A log file is plane text file in Russian. A description of single action consists of two or three text lines and includes: consol computer name, date, time, menu tree path and concrete action.

A concrete action may be: open/close table corresponding to the menu tree path, restore settings from archive, one of modifications of values were listed in previous section. A table cells are addressed by row and column numbers. So, a value modification may be described like this:

pcstvn01.oku.ihep.su 09:38:40 Sat 24 Apr 2010
Table:
U1.5/ControlSystems/TimingSystem/Control/InjectionTimer/Reg.1:U-70High Intensity/Timing Delays

Set value 3900 to row = 3 column = 12

VISUALIZATION TOOLS

The GUI tools of the control system include some facilities to output contents of a log files to a separate window of consol computer. But it is too primitive and do not give a chance to find interesting operators actions and to analyze the current situation fast enough.

So, more suitable visualization tool was developed (Figure 2).
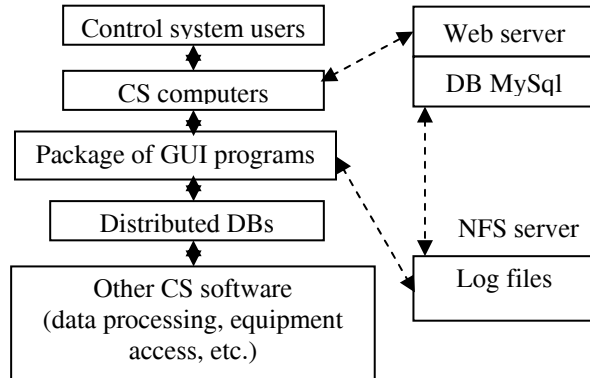
Figure 2: Layout of the logs visualization tools

First of all we decided to give any CS computer opportunity to access log files information using standard web browsers since a control system users used to work with it. More over the tool should to provide selection of desired log records by some criterions. There are next criterions one may use for events selection:

1. Consol computer name an operator used to perform actions.
2. User name.
3. Start/end date and time of interesting time slot.
4. Data table a modifications were performed on (menu tree path).

A web-browser supports the visualization window combining dialog, menu tree, comments and text areas. The dialog area of a visualization window is used to define criterions 1-3. The data table may be defined by using interactive menu tree area. The shown menu tree of this area is restored from log files contents and includes paths were really used by operators (Figure 3).

In accordance with indicated criterions the descriptions of operators' actions are showing in the text area of a visualization window. It gives sufficient easily understandable information in Russian about actions were taken on corresponding accelerator complex equipment. The comments area is used to show full path of selected data table.

To meet the requirements of log files visualization the functionalities of the control system internal web-server were broaden. To solve the problem PHP-scripts, Java-applet, HTTP and JSON protocols are used.

Between web-server and log files there is data base of MySQL. Contents of the data base are formed by processing the log files information. It corresponds to the current state of a log files always.

06 Instrumentation, Controls, Feedback and Operational Aspects

Data base is used to comply with users requests to get information in accordance with defined criterions. When user requests to show log information, the web-browser get access to descriptions of all actions were performed up to request moment.
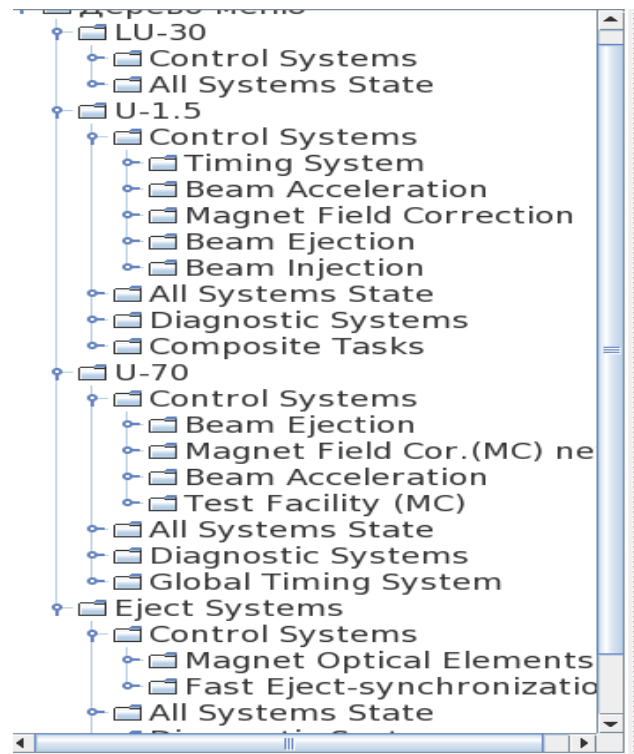
Figure 3: Menu tree is restored from log files texts

So, the control system supports the next data flow scheme (Figure 4).
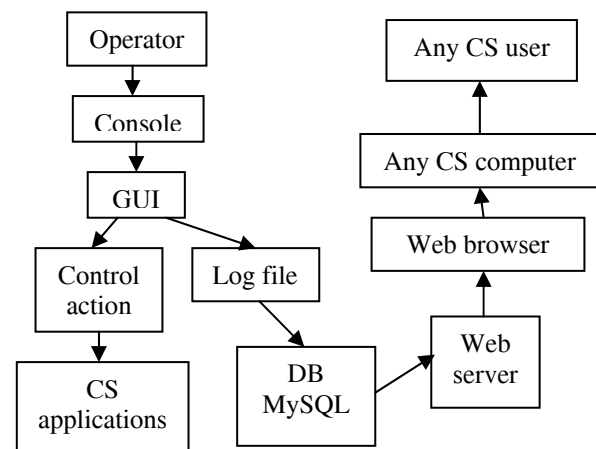
Figure 4: Data flow scheme

CONCLUSIONS

Today users of the IHEP U-70 accelerator complex control system have new very helpful tool. It is used to analyze operators' activities, to discover and understand unexpected behavior of an accelerator due to remote slightly incorrect actions of some operator.

The control system web-site is internal and log information may be seen inside of the CS only.

ACKNOWLEDGMENTS

The author would like to thank the students of the "Protvino" branch of the "Dubna" university, who participated to realization of the web visualization tool.

REFERENCES

[1] V.Voevodin, "Software Architecture of the U-70 Accelerator Complex New Control System", Proceedings of the ICALEPCS'99, Trieste, Italy, 1999, p.457.

[2] V.Voevodin, "Information technologies in the IHEP U-70 accelerator complex control system", Proceedings of the RuPAC 2008, Zvenigorod, Russia, 2008, p.270.

EXPERIENCE ON OPERATING HIGH-VOLTAGE ACCELERATORS DESIGNED IN NIIEFA ON INDUSTRIAL FACILITIES INTENDED FOR POLYMER MATERIALS' MODIFICATION

V.P. Maznev, V.P. Ovchinnikov[#], M.P. Svinin, FSUE "D.V. Efremov Scientific Research Institute of Electrophysical Apparatus", Saint Petersburg, Russia

V.I. Alexandrov, Izhevsk Plastic-Production Plant, Izhevsk, Russia

E.M. Kolchin, "Insulating Polymer Materials (IPM)" Ltd, Saint Petersburg, Russia.

Abstract

High-voltage accelerators "Aurora-5" and "Electron-10" designed and manufactured in the D.V. Efremov Institute have been operated at the plastic-production plant in Izhevsk and the joint-stock company "Terma", St. Petersburg on facilities intended for production of polymer materials with specific properties due to radiation processing. The results of accelerators' operation are considered in the paper. The annual operating time of each facility is 5-7 thousand hours, which meets the requirements for industrial equipment.

At present, electron accelerators find more and more wide industrial applications: to modify physical and chemical properties of different materials and products, to eliminate bacterial and other types of pollution as well as for other purposes. From the data given in the IAEA review, nowadays more than 1400 high-power electron accelerators are commercially used throughout the world, and the cost of the products manufactured using these machines is more than 85 billions $ per year [1].

From the diagram shown below (see Fig. 1), it can seen that a significant part of the modern industrial electron accelerators is involved in the production of articles on the basis of polymer materials, such as wires and cables, heat-shrinkage pipes, sheets, tapes and gaskets.
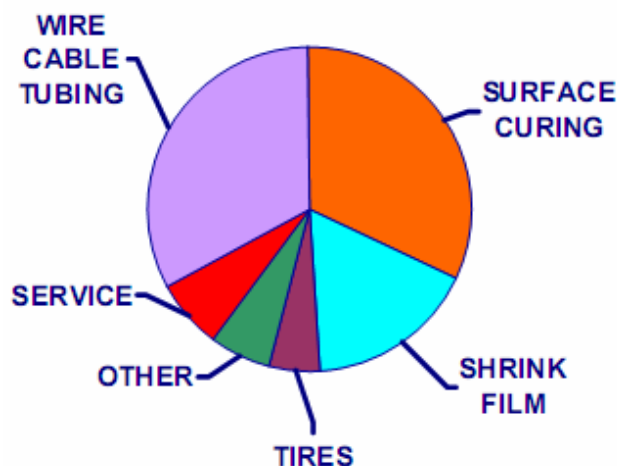
Figure 1: Industrial applications of electron accelerators

[#]npkluts@niiefa.spb.su

For many years, the development and manufacturing of high-voltage electron accelerators for radiation processing have been one of the traditional directions of activities in the D.V. Efremov Institute, NIIEFA. To date, more than fifty similar machines have been manufactured and delivered to different sites in Russia and abroad including eleven machines intended to operate in industrial processing lines for radiation curing of products made of polymers. Accelerators with an energy below 1 MeV are provided with a local radiation shielding and can be installed in conventional industrial buildings.

In 1985 the "Aurora-5" accelerator with the 400-600 keV electron energy, the beam current of 50 mA and the irradiation field width of up to 2 m was delivered to the Izhevsk Plastic-Production Plant to be used in the line producing sheets of foamed polyethylene using the manufacturing technique developed by the Japanese firm Sekisui Chemical (see Fig.2). The accelerator consisted of a separately located high-voltage generator and an irradiator with the local radiation shielding interconnected with a high-voltage cable. By using a special device, a component of the line, the material of up to 2 mm thickness was irradiated consequently from one and the other side; and the absorbed dose distribution was sufficiently uniform. The admixtures doped into the material resulted it its foaming under heating; the density decreased by 5-30 times and the heat conductance decreased as a result.

Figure 2: The "Aurora-5" accelerator in the line producing foamed polyethylene at the Izhevsk Plastic-Production Plant

The production rate of the line involving the "Aurora-5" accelerator was about one thousand tons of

06 Instrumentation, Controls, Feedback and Operational Aspects

foamed polyethylene per year, which did not satisfy the demand for this material. In this connection, the second line involving the "Electron-10" accelerator was installed at the Izhevsk Plastic-Production Plant, which allowed the material to be processed from both sides for one passage through the irradiation chamber (see Fig.3).

The schematic view of the "Electron-10" accelerator is shown in Fig.4. In contrast to the "Aurora-5"machine, its irradiator is in the horizontal position. The beam is extracted from the vacuum chamber of the accelerator in two opposite directions by using two electromagnets [3].

In 2002, the "Electron-10" accelerator was also delivered to the "IPM" Ltd, St. Petersburg to be used in the line producing double-layer heat-shrinkage coatings for underground pipelines (see Fig. 5). In 2003, the machine was put into commercial operation. Somewhat later, one more such an accelerator was installed there.

Figure 3: The "Electron-10"accelerator at the Izhevsk Plastic-Production Plant
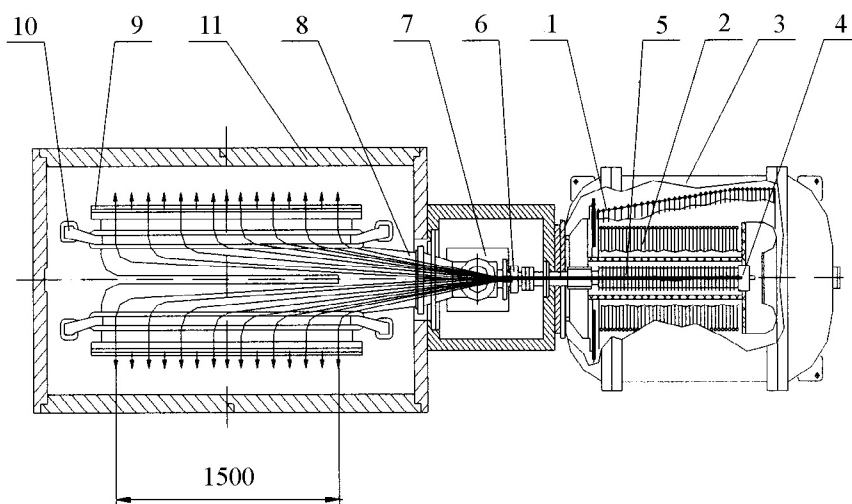
Figure 4: Schematic view of the "Electron-10" accelerator:1-primary winding, 2-secondary winding sections, 3-pressure vessel, 4-electron source, 5-accelerating tube, 6-scanning device, 7- vacuum pump, 8-vacuum chamber, 9- extraction window, 10- electromagnet,11- local radiation shielding

Figure 5: The "Electron-10" accelerator in the line for production of heat-shrinkage anti-corrosion coatings at the "IPM" Ltd, St. Petersburg

The experience gained in the process of operation of the "Aurora-5" and "Electron-10" accelerators proves their high reliability. At the Izhevsk Plastic-Production Plant in 2008 and 2009 these machines provided the fulfillment of the plan for the foamed polyethylene production; the running hours were respectively: 6170 and 3236 in 2008; 3036 and 5040 in 2009. The lifetime of the electron source cathode was 3000 hours, on average, on both the accelerators; the lifetime of the extraction window foil was 3000-4500 hours. Replacement of the cathode took 18-36 hours and of the foil -36-48 hours.

At the "IPM" Ltd, St. Petersburg since 2005 the "Electron-10" accelerator has been continuously operating in the three-shift mode with shut-downs necessary for replacement of the cathode, foil and high-vacuum pumps as well as for cleaning the filter of the water cooling system. Depending on the thickness of a material processed and the velocity of its transport, the accelerating voltage was varied from 510 up to 750 kV

06 Instrumentation, Controls, Feedback and Operational Aspects

and the beam current − from 30 up to 60 mA. The total running time of the accelerators for 5 years was 38 740 hours. During this period of time, the electron source cathode was replaced eleven times and the extraction window foils were changed twelve times. To ensure more stable operation of the accelerator and for protection of its units against corrosion, in the process of operation a system for automatic maintaining of the temperature was used, which maintained the temperature of the water cooling the extraction window and other units at a level somewhat higher than the temperature in the building. This measure reduced a possibility of corrosion of the accelerator components located in the irradiation area.

Further it seems reasonable to consider also the replacement of high-vacuum NMD pumps used in these accelerators for turbomolecular pumps or application of turbomolecular pumps at the initial stage of evacuating the accelerator vacuum chamber after the cathode/ foil replacement, which will allow the time needed for these operations to be reduced substantially.

REFERENCES

[1] Maria Helena de Oliveira Sampa, "Industrial Electron Beam Processing", IAEA, (2008).

[2] B.I. Albertinsky, N.M. Dmitrieva, D.S.Valtman et al., "Aurora-5" high voltage accelerator" Theses of the 5th All-Uninon Conference on Charged Particle Accelerators' Application in the National Economy , Moscow, (1985).

[3] A.K. Evseev, A.S. Ivanov, V.P. Ovchinnikov et al., "A Device for Electron Irradiation" Certificate of Authorship №1828380, (1991).

[4] A.S. Ivanov, V.P. Maznev, V.P. Ovchinnikov, M.P. Svinin, N.G. Tolstun, "Electron" and "Aurora" accelerators in industrial radiation technologies", EBT 2006, Varna.

06 Instrumentation, Controls, Feedback and Operational Aspects

SPECIFIC FEATURES OF AUTOMATIC CONTROL SYSTEMS FOR APPLIED CYCLOTRONS

V.P. Bagrievich, A.N. Kuzhlev, A.P. Strokach[#], FSUE "D.V. Efremov Scientific Research Institute of Electrophysical Apparatus", Saint Petersburg, Russia

Abstract

A distributed automatic control system for the MCC-30/15 compact medical cyclotron has been built on the hierarchy principle. The lower hierarchical level consists of controllers for various systems of the cyclotron, which are networked on the basis of Profibus.

An industrial Advantech-type computer has been chosen as the host computer of the system. The upper hierarchical level also contains computers to control the RF system of the cyclotron and operator workstation.

Computers of the upper hierarchical level are networked on the basis of Ethernet. The number of computers for the operator workstation is limited only by the Ethernet bandwidth and the speed of the host computer.

To measure the beam current, a multi-channel high-precision measuring current amplifier has been developed, signals from which are sent to a high-speed ADC. It is possible to view current pulse oscillograms, which makes much easier the adjustment of the cyclotron modes.

A distributed automatic control system built on the hierarchy principle has been developed for the MCC-30/15 compact medical cyclotron [1].

The lower hierarchical level consists of controllers for various systems of the cyclotron: water cooling system, vacuum system, external injection system, power supply systems for the main electromagnet and ion guide magnets and system for control of mechanical devices of the cyclotron and ion guide. Controllers of the lower hierarchical level are networked with the host computer of the automatic control system via the Profibus DP. Controllers of the external injection system are networked with the host computer via the RS-485 interface. Programmable logic controllers (PLC) of the FX3U series (Mitsubishi) and ADAM-4501controllers (Advantech) are used as controllers of the lower hierarchical level.

A high-powered industrial Advantech-type computer with a 2.4 GHz Pentium 4 Celeron processor was chosen as the host computer of the automatic control system. In addition to the host computer, the upper hierarchical level also contains a computer to control the RF system of the cyclotron and computer(s) of the operator workstation. As the RF system is one of the most complicated and important system of the cyclotron, an industrial computer similar to the host computer is used for its control. Any PC-compatible computers with the Windows XP operational system or higher may be used as the operator workstation computers. Computers of the upper hierarchical level are networked on the basis of Ethernet,

for which purpose an industrial 8-port Ethernet-switch is applied. The number of operator workstation computers is limited only by the Ethernet bandwidth and the performance of the host computer. The use of the Ethernet network allows the operator workstation to be located both in the direct vicinity of the cyclotron and in any place, provided a computer network is available. The software of the automatic control system also allows several copies of the program for the operator workstation to be executed simultaneously on one and the same computer, which makes operation of the control system much more comfortable if several monitors are connected. The host computer performs arbitration of commands and transfer of the data on the status of the cyclotron systems to the operator workstation.

Fig.1 shows a simplified structure of the automatic control system.

The information is displayed on the operator workstation monitor(s) in the form of pages; each of these pages displays status of one of the cyclotron systems. The operator can arbitrarily choose a page to be displayed. If the operator workstation contains several monitors or computers, the operator can display several different pages simultaneously. The page shown in Fig.2 is the control of the vacuum system.

The software allows all the systems of the cyclotron to be controlled in two modes. In the "Manual Remote" mode, the operator performs on/off operations and adjustment of the cyclotron devices' parameters from one of the operator workstation computers on the basis of his own experience and design parameters of the mode. The "Choose and Control" principle is applied. By clicking the mouse, the operator chooses one of the cyclotron sub-systems on the mnemonic diagram displayed on the monitor and a panel to control this system is visualized. Current operating parameters and controls of this particular device are shown on the panel. The operator can either turn on/off the device or change the adjustment of its parameters (for example, the current of the main electromagnet or radial position / angle of the stripping device, etc). In so doing, the available ACS interlocking system does not enable any unallowable operations to be done. This ACS operating mode is used at the initial stage of the cyclotron operation until the data on the cyclotron operating modes has not been stored. Parameters of the actual mode can be stored in the data base. The second operating mode of the ACS is the automatic mode. In this mode, the operator chooses an operating mode among the modes previously stored in the data base and starts automatic procedures of turning on/off the sub-systems of the cyclotron. These procedures include production of the working vacuum in the cyclotron, external injection

---

[#] npkluts@niiefa.spb.su

system and beam transport system, bringing to the working mode the main electromagnet and mechanical devices (shims and stripping devices) of the cyclotron, ion injectors, the RF system and the beam transport system. Operating parameters of all the devices are read from the chosen mode stored in the data base and are set automatically. Further an insignificant tuning of several parameters by the operator can be needed to optimize the operating mode. Sequence of the automatic procedures is defined by the system of ACS interlocks.
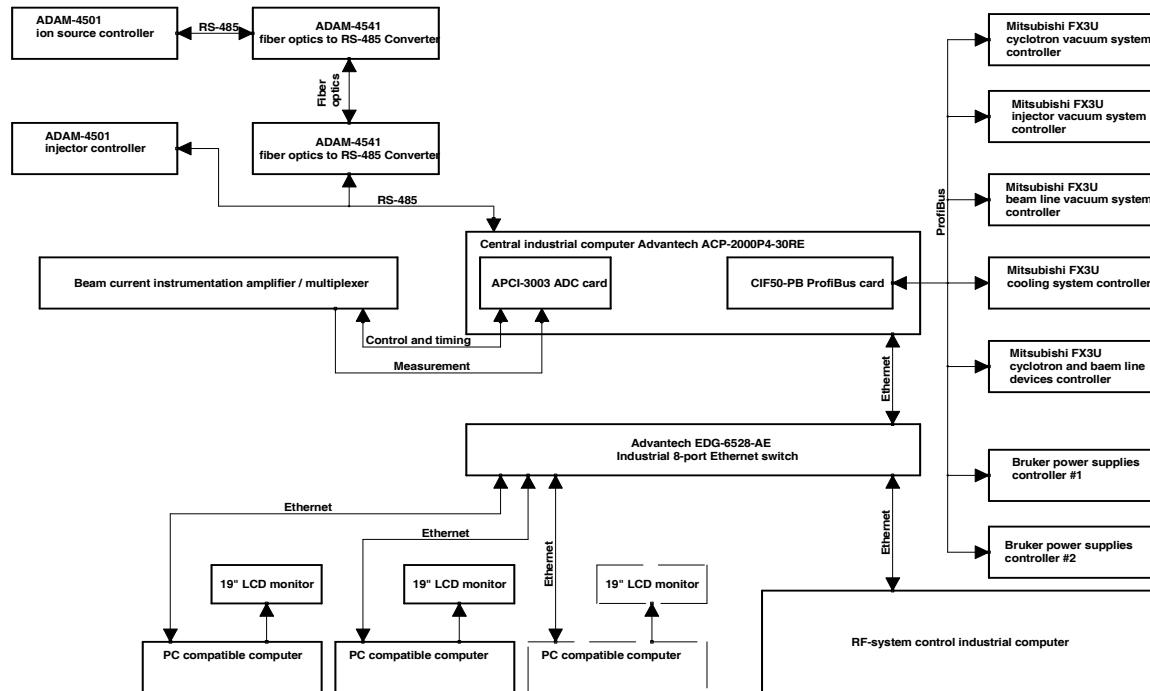
Figure 1: Automatic control system of the MCC-30/15 cyclotron. Structural diagram

Figure 2: Control of the vacuum system of the MCC-30/15 cyclotron

06 Instrumentation, Controls, Feedback and Operational Aspects
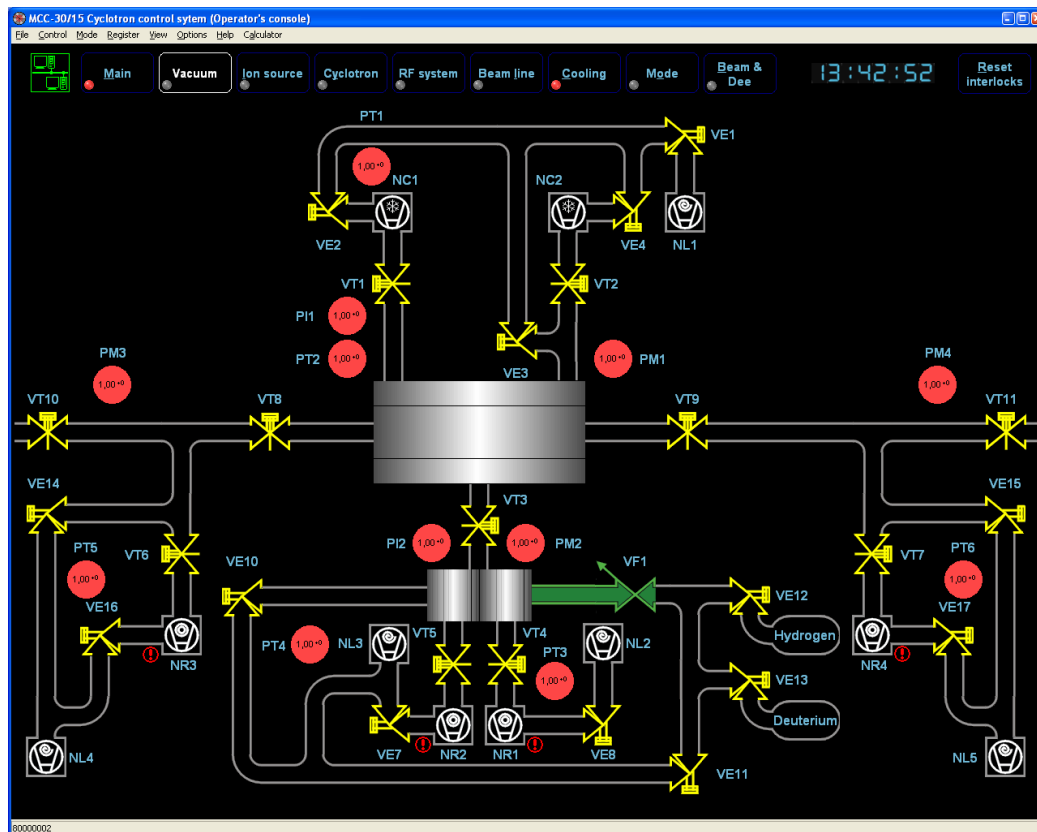
To measure the beam current, a multi-channel high-precision beam current instrumentation amplifier has been developed, signals from which are sent to a high-speed ADC. An ADC card is installed in the host computer. The ADC is started by a synchro-pulse generated in the synchronization unit of the RF system. The software of the beam current measuring system allows both average and amplitude values of current to be measured; real-time display of the current pulse oscillogram is also possible, which makes much more easier the adjustment of the cyclotron sub-systems to the mode chosen by the operator. In addition, the oscillogram of the beam current allows the cyclotron modes to be adjusted at a low pulse repetition rate and high duty cycle, that is, at a very low average beam current and as a result low radiation intensity. On completion of the mode adjustment and beam extraction to a target/Faraday cup, a necessary intensity can be easily obtained by varying the pulse repetition rate and duty cycle.

Fig.3 shows the monitor of the operator workstation with the beam current oscillogram displayed.
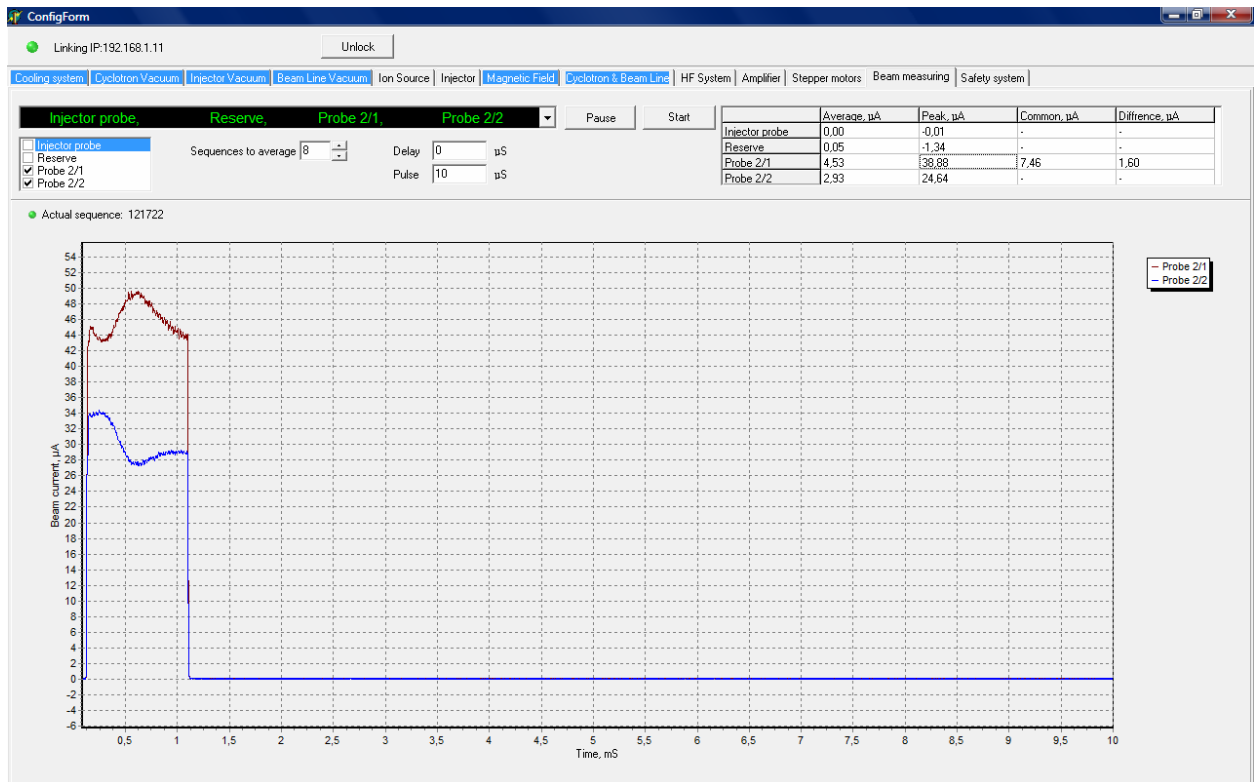
Figure 3: Oscillogram of the beam current pulse

To ensure passage of the beam through the ion guide with minimum losses, beam density scanners are used. By using these scanners, the ACS measures the beam density distribution along two coordinates of the ion guide cross-section, and a two-dimensional image obtained on the basis of two distribution curves is displayed on the monitor. Proceeding from this image, the operator can estimate necessary variation of parameters of correcting and focusing magnets of the ion guide and correct the position and size of the beam if necessary.

REFERENCES

[1] P.V.Bogdanov, M.F.Vorogushin, A.V.Galchuk, V.G.Mudroljubov, A.P.Strokach "The MCC-30/15 Cyclotron, parameters, adjusting works and their results" RuPAC-2010, Protvino (2010); http://www.JACoW.org

LABVIEW CONTROL SYSTEM OF THE CRYOGENIC COMPLEX FOR THE KAON RF-SEPARATOR AT IHEP

A.Ageyev, V.Alferov, A.Bakay, V.Fedorchenko, A.Kholkin, V.Krendelev, A.Lutchev, D.Vasiliev, Institute for High Energy Physics, Protvino, Moscow Region, 142281, Russia

Abstract

The superconducting RF separator is used for the separation of kaons at the OKA experimental setup at IHEP. The separator consists of two deflecting niobium cavities housed in the cryostats. Their cooling is provided by one large commercial helium refrigerator and two custom heat exchangers, located near cavities. The cryogenic complex for the separator provides liquid superfluid helium with the temperature of 1.8K as well as liquid nitrogen. The paper describes the arcvhitecture and the LabVIEW based software of the control system.

INTRODUCTION

The cryogenic complex comprises the vacuum system (CVS) and provides cooling of two deflecting niobium cavities RF1 and RF2 of the superconducting RF separator which is used for separation of kaons for the experiments at the OKA setup [1]-[4] at IHEP. The cryogenic helium plant KGU-500 is the main cold generating unit of the CVS. It produces both the cool and liquid helium of the same 4.6K temperature. The other parts of the cryogenic complex are: two heat exchangers located in the liquid helium baths (LHB) of intermediate cooling; large vacuum heat exchanger (HEX); heat exchangers at the entrances into the RF1 and RF2; pumping machine (PM). The control system provides measurements of about 500 analog parameters and 300 digital signals and generation of tens of commands.

ARCHITECTURE

On a lower level of the control system there are 40 custom equipment controllers based on Analog Device and Atmel programmable devices. They provide data acquisition, calculation of operating parameters, and generation of digital and analog commands for the following tasks:

-   temperature measurements with various sensors;
-   digital measurements of liquid Ni and He levels;
-   analog measurements of He level;
-   vacuum pump motors current measurements;
-   vacuum measurements;
-   turbine rotation speed measurements;
-   controls of heaters power supplies;
-   measurements of Ne contamination of gaseous He;
-   valve position measurements;
-   various measurements and generation of digital signals.

Equipment controllers are connected to three personal computers (PC) by means of CAN field buses. Each PC controls one of three physically separate groups of equipment: KGU, LHB, and HEX/RF. The fourth PC is used as a local Data Socket (DS) server. The PCs are connected by a dedicated Ethernet technology network (TLAN). Simplified block diagram of the control system is shown in Figure 1.

We use the Data Socket Connection program, which is a part of the LabVIEW package Developer Suite Core. All CAN masters are simultaneously clients and servers, so all the data are available on each console. The DS server is a client for the following users: three operator consoles; server for clients TLAN, a public LAN and SQL server hosting an archive of the CVS. As a result, all operators and other users of the TLAN can get data from both the DS and SQL servers.

CONTROLS AND DATA PRESENTATION

LabVIEW based software for control and monitoring consists of the following programs:

-   **PK09.vi** installed on the KGU PC;
-   **RF.vi** installed on the HEX/RF PC;
-   **OM.vi** installed on the PM PC;
-   **DS server.vi** installed on he DS server of TLAN;
-   **CRYOVIEWER.vi** installed on computers of clients of the DS server of TLAN.

Every program presents the main window synoptic sirquit of the equipment group with sensors and actuators as well as a parameter values. One can change parameters by putting new data into an appropriate control field. Color is a status indicator. One can draw a time graph of any parameter. Additional windows permit tuning, calibration and other manipulations with various parameters. Graphical presentation of the HEX/RF group is shown in Figure 2.

DATA ACQUISITION AND CONTROL SYSTEM

The CVS data acquisition and control system developed at IHEP allows to display on the operator's console all the main parameters required for manual or remote control. After full commissioning the system shall provide control of the following parameters:

-   temperature measurements of cryogenic components, of nitrogen and helium flows in 72 points;
-   temperature measurements of pumps of the PM in 42 points;
-   interstage pressure measurement of the PM by means of differential pressure transducers in 3 points;
-   medium and high insulation vacuum measurements by PMT-6-3 and PMT-4 sensors in 32 points;
-   liquid helium level measurement in 3 vessels;

06 Instrumentation, Controls, Feedback and Operational Aspects

- helium and nitrogen pressure measurement in 11 points;
- helium mass flow rate measurement in 2 points.
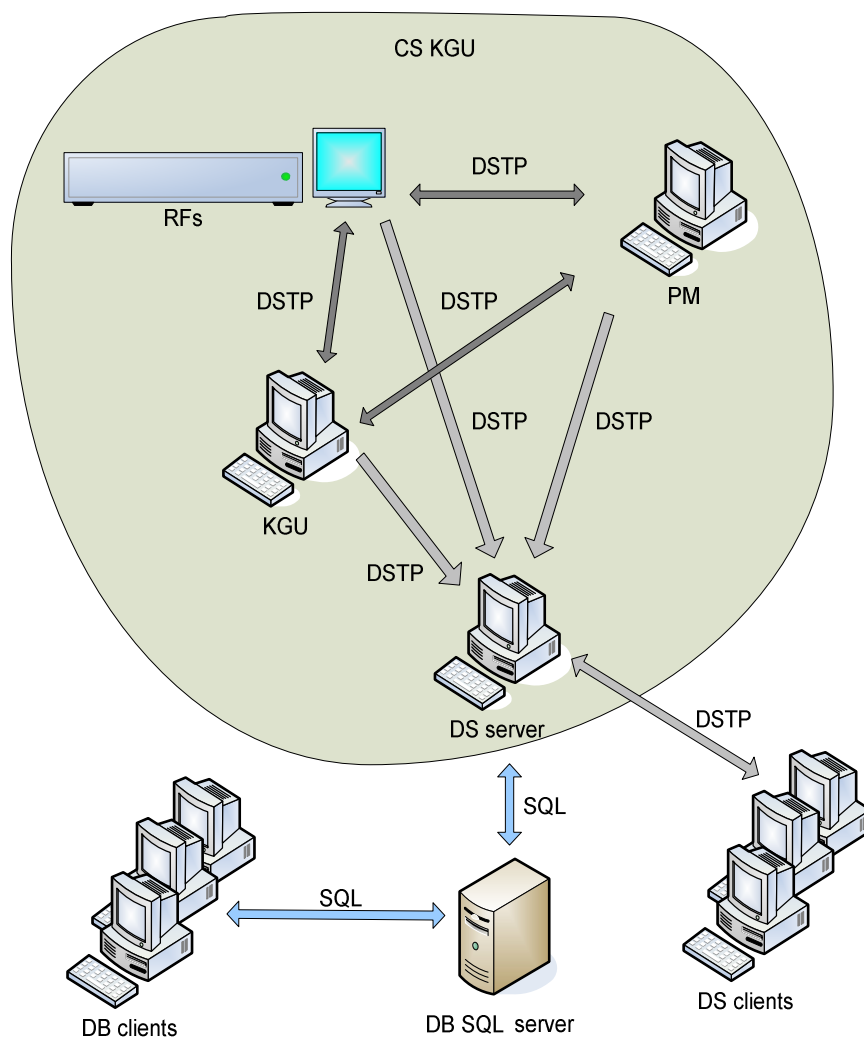
Figure 1: Block diagram of the control system
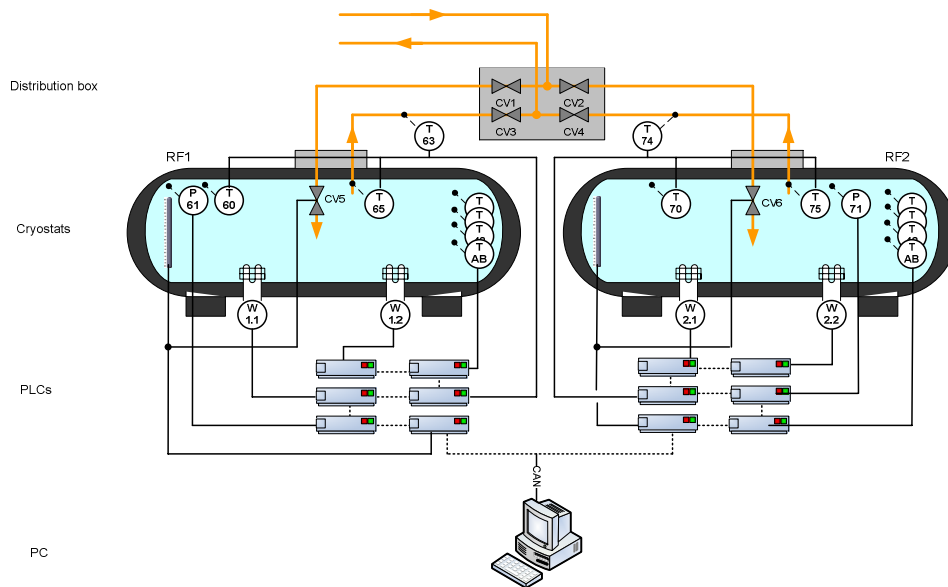
Figure 2: Data presentation of the HEX/RF equipment

CONCLUSION

The cryogenic complex for the OKA experiment at IHEP has been in operation since December 2006. It allowed to provide 1000 liters of superfluid helium at 1.8K for the RF cavities during several days of operation and thus start a research program with separated kaon beams in 2008-2009.

LabVIEW has proven to be an efficient, easy to learn and easy to use programming environment for data acquisition, monitoring and presentation. The control software is currently being refined to improve the functionality and user interface. Particularly, it is planned to implement control of closed loops by low level equipment controllers rather than mid-level computers with real time operating system.

REFERENCES

[1] E.S.Ageev et al. "Experiments with Charged Kaons on the RF Separated Kaon Beam at IHEP U-70. Proposal on the Precise Measurements of the Kaon Decays at IHEP U-70", 5 November 2003. Available: http://www.oka.ihep.su/Members/zopeadmin/oka-papers/pred.ps (in Russian).

[2] Bakay A.I. et al. "Cryogenic 1.8K Test Facility for Cryostats with Superconducting Cavities of RF-Separator". Atomic Energy, v.93, No.6, December 2002, p.p.445-448 (in Russian).

[3] Ageyev A.I. et al. "Status of Superconducting Radiofrequency Separator Cryogenic System", RUPAC-2004, October 4-9, 2004, Dubna, Russia. http://accelconf.web.cern.ch/AccelConf/r04/papers/THFO04.pdf

[4] Ageev A.I. et al. "Commissioning of Superconducting Radiofrequency Separator Cryogenic System", RUPAC-2006, September 10-14, 2006, Novosibirsk, Russia. http://rupac2006.inp.nsk.su/ready/tufo04.pdf

UPGRADE OF THE U-70 PROTON SYNCHROTRON EXTRACTED BEAM LINES CONTROL SYSTEM: MULTIPLE ACCESS AND DATA PRESENTATION

V. Alferov, I. Lobov, A. Lutchev, Y. Bordanovski, V. Lagutin,
Institute for High Energy Physics, Protvino, Moscow Region, 142281, Russia

Abstract

The U-70 extracted beam lines system includes about 130 magnet dipoles and quadrupoles, with power provided by 112 power supplies (PS). Each PS is controlled by an individual Analog Device's based controller. Since a number of used magnets may vary and exceeds the number of available PSs, the commutation is used. Controllers are connected to a front-end computer by means of four CAN field buses. The software for the controllers is tuned to a specific type of the PS and a specific inductive load of the magnet. The Dell PowerEdge T710 server is used for the PS control with multiple access from several client workstations which controls PSs for a particular beam line. All client workstations along with the server and front-end computer are connected together with a dedicated LAN.

The server grants different users a different permissions to control their own PSs only. Every four seconds the measured data are stored into an archive. Operating commands are archived as well to keep a history of all user's actions. The software is based on the National Instruments Developer Suite Core and MS Office Web Components packages.

INTRODUCTION

The Extracted Beams on the Serpukhov 70 GeV Proton Synchrotron are spread for over 1 km. They include about 130 magnet dipoles and quadrupoles. The PSs (motor-generators, silicon rectifiers and thyristor rectifiers) are installed in the special building 500m away. The total number of PSs is only 112, so, as a result, the commutation is used. The PS are characterized with the following features:

- DC current stabilization time can be as long as several minutes;
- magnet hysteresis stipulates a special procedure of installation of current,
- imperfection of the PS feedback stabilization requires to adjust the DAC reference signal to get needed current of the magnet;
- current polarity can be changed.

Intel 8051 compatible custom PSs controllers (PLCs) are uploaded before a run with accordance to features of a specific "magnet-PS" couple [1]. The following data is uploaded;

- maximum value of current,
- DAC raising rate,
- matching delay,
- minimum making step,
- number of matching steps.

CONTROL SYSTEM CONFIGURATION

A block diagram of the control system is shown in Fig.1. Front-end computer (FEC) is used as a master for PLCs. FEC acts as a CAN master and can gain the access to controllers through 4 segments of 2 CAN field buses. The total length of each bus is about 600 meters. The data transmission rate of 20 Kbit/s is used because of heavy noise conditions in order to reduce information losses down to acceptable level.

FEC reads data from PLCs periodically, one read cycle accounts for about 15 ms. Due to large number (100-120) of PLCs the polling period is 2 seconds.

FEC is a client of the MS SQL-server 2008, that is located in the beam control room on the main archive server. Any computer inside the both industrial and public LAN could be a client of this server. Each client has its own permissions. There are 3 levels in client's permissions hierarchy:

- The lowest level is occupied by «observers», who can only view the data and does not take part in any control operations. The observers may belong to both the industrial and public LAN;
- The middle level is reserved for the operators of the physical experimental installations. They are observers too, but in addition they can also operate their own magnets;
- The full permissions level is given to the operators in the main beam control room and at the PS building. They can control any magnet of any channel. In addition, they can generate a list of magnets for the current run.

Both the middle and high level operators consoles can belong to an industrial LAN only.

06 Instrumentation, Controls, Feedback and Operational Aspects
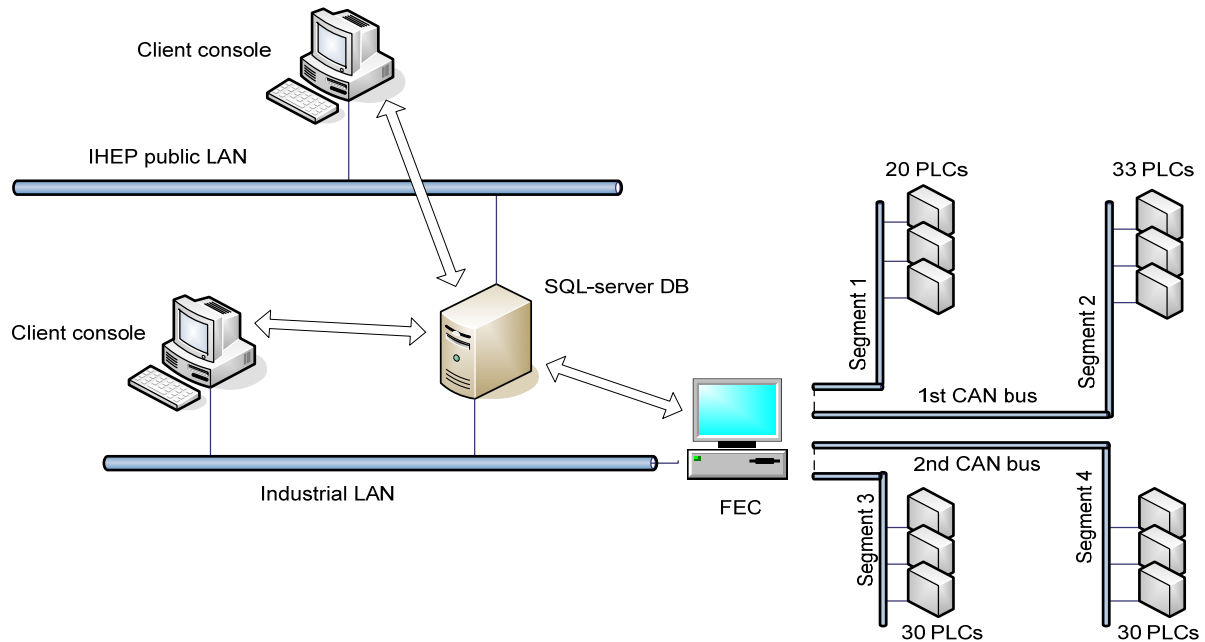
Figure 1: Control System of the Beam Lines

USER OPTIONS

The ODBC protocol is used for gaining access to SQL-server stored procedures and queries. The independence and uniformity of ODBC simplify the development of control system applications. Fig.2 and 3 show examples of web clients for selection of the channel and control operation, respectively. Internet explorer is used.

Similar examples of windows for control operations, created with the National Instruments LabVIEW environment are shown in Figures 4 and 5. Having many useful and powerful possibilities, LabVIEW is a perfect instrument for developing of control system applications.

ARCHIVING

To deal with archive data the two types of software were developed - web-pages and LabVIEW programs. Both types of applications give an opportunity to supervising (viewing) data in tabular and graphical styles as well. With any archive viewing way the operator can make data selections using different criteria.
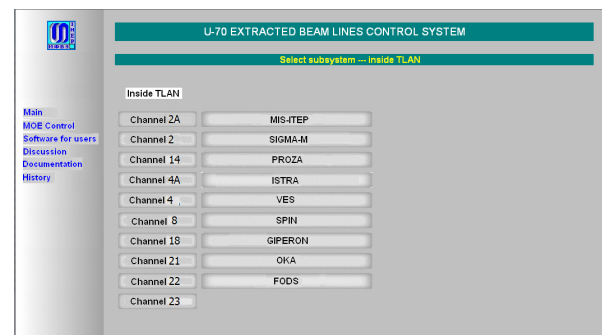
Figure 2: Web-client for channel selection. Each button corresponds one of the magnet sets – beamline or installation.

Figure 3: Web-client for magnet control operations. For every magnet the set of several operations is provided (red and green buttons)

06 Instrumentation, Controls, Feedback and Operational Aspects

The archiving gives powerful possibility for making periodical evaluation of PLC current state with the aim to find malfunctioning   PLCs or feedback stabilization systems. Fig.6 shows an example of using the archive data for monitoring of the PLC efficiency.
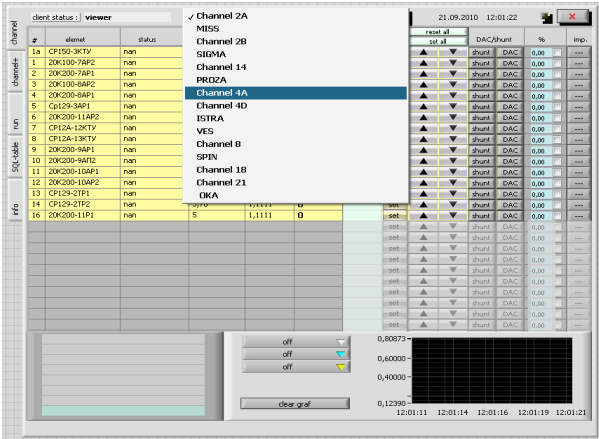
Figure 4: LabVIEW-based client for control operations
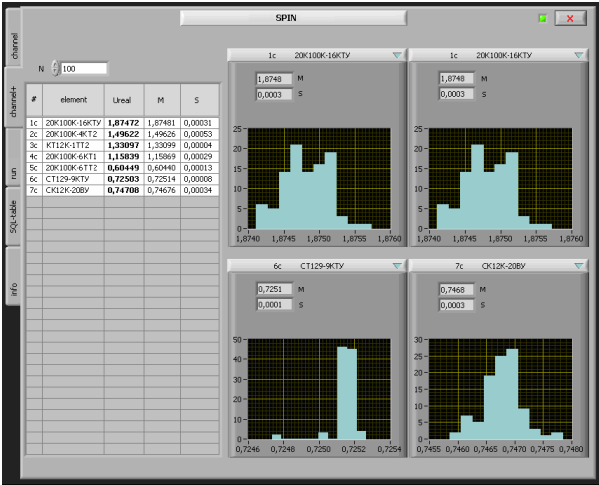
Figure 5: LabVIEW-based client for control operations
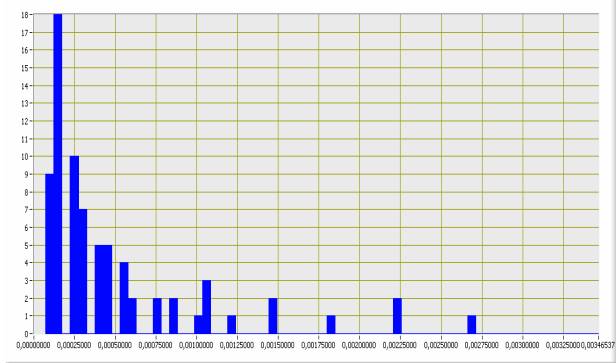
Fig 6. Histogram of the PLC distribution of self noise levels

CONCLUSIONS

The control system of the extracted beam lines at the IHEP U-70 proton synchrotron has been in operation since 2001. It provides: multiple access for different clients with different rights; data storage for quality control of   the PLCs and PS stabilization system; convenient methods of data presentation. The system can be easily expanded by adding more PLCs and more clients. We plan to make the PLC polling faster by increasing the CAN bus rate and with parallel access to two independent CAN buses.

REFERENCES

[1] V. Alferov, Y.Bordanovski, S.Klimov, V.Ilukin, V.Kuznetsov, O.Radin, A.Shalunov, A.Sytin, P.Vetrov, V.Yaryguine, V.Zapolski, V.Zaruche U-70 Proton Synchrotron Extracted   Beam Lines Control System Modernization. Proceedings of the 2001 International   Conference on Accelerator   and Large Experiment Control Systems. Los Angeles, USA, 2001.
[2] http://icalepcs2001.slac.stanford.edu; http://can.marathon.ru/

SOFTWARE SERVICE FOR CRYOGENIC DATA REPRESENTATION AND ANALYSIS

I.Lobov, A.Lutchev, M.Stolyarov, S.Sukhov

Institute for High Energy Physics, Protvino, Moscow Region, 142281, Russia

Introduction

The Cryogenic and Vacuum System (CVS) for OKA experimental complex requires reliable, fast and convenient program facilities for cryogenic data analysis – temperatures of cryogenic components, liquid helium levels, helium mass flow rates. In order to achieve that goal the software complex was developed for remote analysis and supervision of the CVS parameters with data storing ability. MS SQL-server 2008 was used for data storage and archiving. For displaying the stored data in graphic and table forms, NI Developer Suit Core software package was used. For on-line displaying current CVS parameters the dedicated web-server with xml mimic panel engine was used. The engine was developed on the base of original software created in IHEP.

THE SOFTWARE COMPLEX STRUCTURE

CVS control system has three local control rooms, which corresponds to tree main CVS machinery subsystems: pump machine (PM), bubble cell (BC) and deflector (RF). Data is transferred from control rooms to local CVS server with 2 seconds periodicity, using Data Socket protocol (National Instruments DS technology). The local CVS server supplies DS-clients with current data and then put it into its own local temporary archive.

The main task of the local CVS server is to collect the data from all CVS subsystems, build full package and transfer it to the Central Database using Open Database Connectivity (ODBC) standard. The Central Database locates on the archive server machine (Zeus) and runs MS SQL-server.

Archive server sends the data to mimic panel server (Zerver) as well. The mimic panel server put incoming data into Microsoft Access DB table and the old data is replaced by new one. This DB is used as main data source for mimic panels.
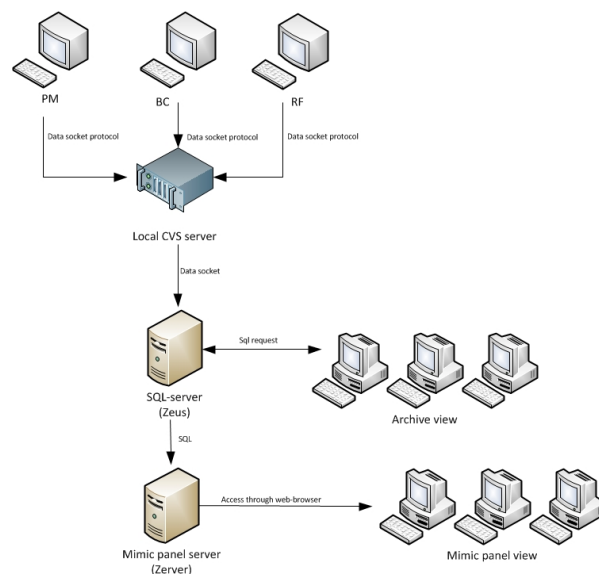
Figure 1: CVS data flow scheme.

SOFTWARE FOR CVS MIMIC PANELS

The CVS mimic panel is a web-page with graphical elements. All this web-pages are located on the mimic panel server (Zerver), and are available to users with any web-browser. The CVS operator has opportunity for supervising any parameter not only at CVS site but using any computer at IHEP site. There is no CVS control ability for mimic panels currently but it is a matter of future development.

The data for mimic panel comes from local CVS server to SQL-server as a string like:

'current data',T1,T2,T3,...Tn

where T - measured value. These original data array is represented on Figure 2.

06 Instrumentation, Controls, Feedback and Operational Aspects

parameter	unit	data	date	time
P1a	Bar	0	09.09.2010	15:31:24
S1	krpm	0	09.09.2010	15:31:24
S2	krpm	0	09.09.2010	15:31:24
	-	NaN	09.09.2010	15:31:24
Krusl	mA	0	09.09.2010	15:31:24
DD F1	Bar	0	09.09.2010	15:31:24
P2a	Bar	0	09.09.2010	15:31:24
	-	NaN	09.09.2010	15:31:24
	-	NaN	09.09.2010	15:31:24
P3a	Bar	NaN	09.09.2010	15:31:24
	-	NaN	09.09.2010	15:31:24
	-	NaN	09.09.2010	15:31:24
	-	NaN	09.09.2010	15:31:24
	-	NaN	09.09.2010	15:31:24
T32	K	287,047	09.09.2010	15:31:24
P31	Bar	0	09.09.2010	15:31:24
P34	Bar	0	09.09.2010	15:31:24
CV2	%	0	09.09.2010	15:31:24
CV3	%	0	09.09.2010	15:31:24
CV4	%	0	09.09.2010	15:31:24
HeUr	%	0	09.09.2010	15:31:24
V VPO	л	10	09.09.2010	15:31:24
v VPO	л/ч	0	09.09.2010	15:31:24
T34	K	287,983	09.09.2010	15:31:24
P32a	Bar	0	09.09.2010	15:31:24
P33	Bar	0	09.09.2010	15:31:24
-	-	0	09.09.2010	15:31:24
P51	Bar	0	09.09.2010	15:31:24
T48	K	223,15	09.09.2010	15:31:24
T41	K	23,2	09.09.2010	15:31:24
P41	Bar	0	09.09.2010	15:31:24
T45	K	23,2	09.09.2010	15:31:24
T44	K	287,047	09.09.2010	15:31:24
T42	K	288,047	09.09.2010	15:31:24
T43	K	287,047	09.09.2010	15:31:24
T46	K	23,2	09.09.2010	15:31:24
4	Om	0	09.09.2010	15:31:24
3	Om	0	09.09.2010	15:31:24
2	Om	0	09.09.2010	15:31:24
1	Om	0	09.09.2010	15:31:24
0	Om	0	09.09.2010	15:31:24
P42	Bar	0	09.09.2010	15:31:24
G1	g/s	0	09.09.2010	15:31:24
G2	g/s	0	09.09.2010	15:31:24
TRF1	K	293	09.09.2010	15:31:24
TRF2	K	0	09.09.2010	15:31:24
HV6	K	0	09.09.2010	15:31:24

Figure 2: Data from SQL server.

When the data comes onto interactive mimic panel window, it is placed opposite to schematic images of devices in accordance to corresponding CVS parameters. Every 5 seconds the data is renewed and new values are displayed on mimic panel.

The mimic panel for PK subsystem is represented at Figure 3.

SOFTWARE FOR CVS ARCHIVE

To deal with archive data the two types of software was developed. User can choose any of them at his own wish. These are web-pages and LabVIEW programs. Both types of applications give an opportunity to supervising (viewing) data in tabular and graphical   styles with data query possibility using different criteria.

Figure 4 represents the appearance of «DB reader» program window, this application designed on the base of LabVIEW. At first the user chooses subsystem, i.e. one of databases (MOE, KVU, U70, ORI),   then chooses the "run" by date. Program reads data from DB on the per day basis. Calendar applet will help to choose required date. Using drop-down menu, user can display required parameters in tabular or graphical styles. There is an opportunity to analyze   a fragment of data more carefully using loupe facility.

Figure 3: The PK subsystem mimic panel.

06 Instrumentation, Controls, Feedback and Operational Aspects
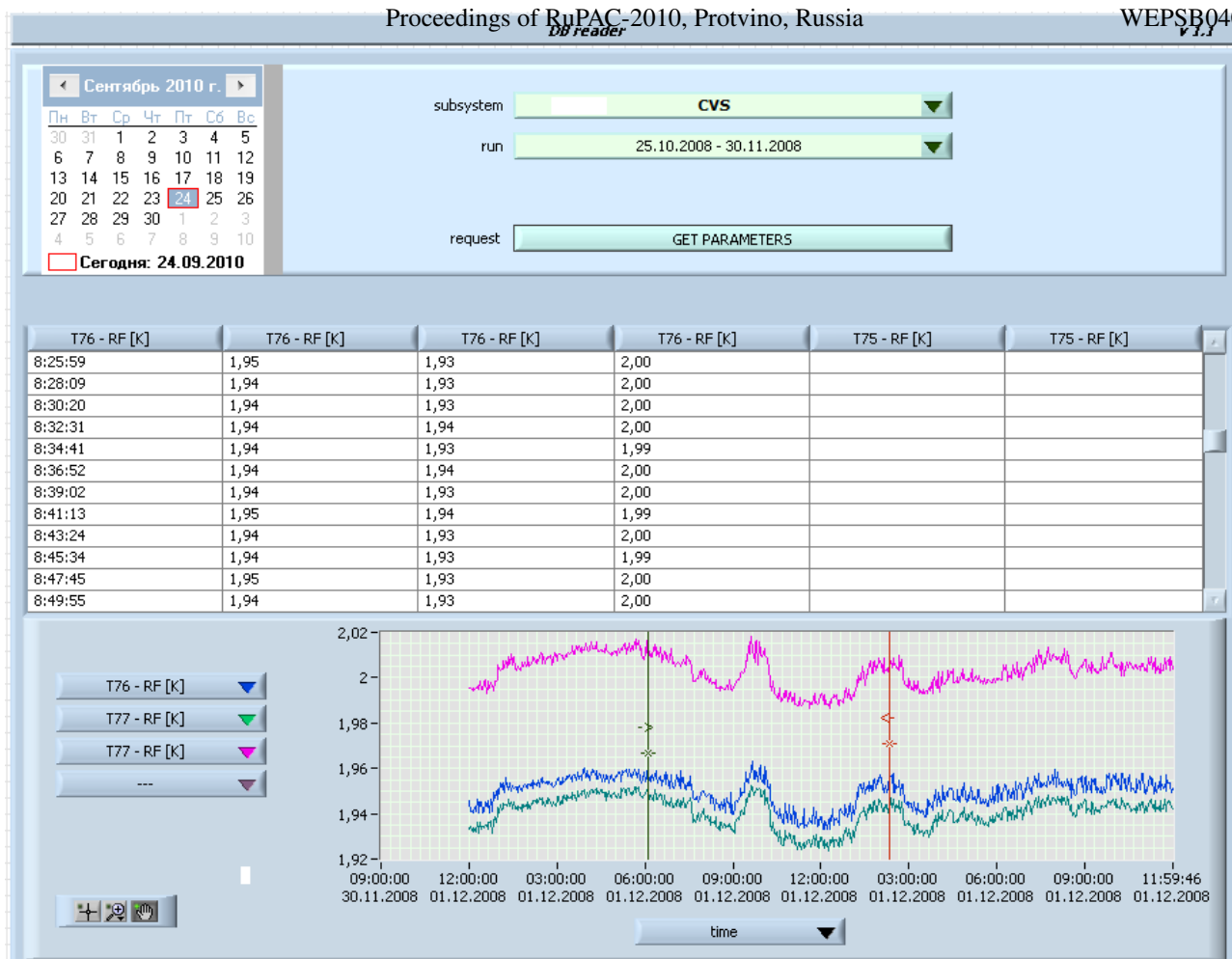
Figure 4: Archive DB reader window (screen copy).

CONCLUSIONS

The software was developed which provides a set of services for data representation and analysis for Cryogenic and Vacuum System personnel:

− viewing current CVS state using web-interface with an extendable mimic panels kit;
− viewing changes in CVS parameters during the required period of time with possibility of statistic analysis.

The software service doesn't depend on CVS parameters assignment, that's why it can be easily extended with new parameters. The service provides an access to archive data from every console inside IHEP local area network.

As a result of work the developing of united IHEP information system has been started.

REFERENCES

[1] V. Alferov, A. Bakay, V. Fedorchenko, N. Ivanova, A. Kholkin, A. Khvorostyanov, S. Klimov, S. Kozub, V. Krendelev, S. Kuznetsov, A. Lukyantsev, V. Milutkin, D. Vasiliev. A Cryo Complex Control System. Proceed of the 2005 Intern. Conf. on Accelerator and Large Experiment Control. Systems. – Geneva, 2005.

[2] Ageev A.I. et al, "Commissioning of Superconducting Radio-frequency Separator Cryogenic System", RUPAC-2006, September 10-14, 2006, Novosibirsk, Russia, http://rupac2006.inp.nsk.su/ready/tufo04.pdf

CANOPEN CONNECTED POWER SUPPLY CONTROL SYSTEMS FOR THE ELECTRON LINACS

V.N.Boriskin, A.N. Savchenko, A.A. Sarvilov, D.L. Stepin, G.N. Tsebenko National Scientific Center "Kharkov Institute of Physics and Technology", 61108 Kharkov, Ukraine

A.S. Chepurnov, I.V. Gribov, Scobeltsyn Institute of Nuclear Physics, Moscow State University, 119899, Moscow, Russia

A.F. Shamarin, "MARATHON" Ltd., Mosfilmovskaja 17b, 117330, Moscow, Russia

Abstract

Power supplies, which feed magnetic systems of electron linac, together with the control system are very critical parts of any linac. The quality of power supplies and control software defines safety of the accelerator operation, stability and cost of operation. One of the today's tendencies in power supply system architecture is to use distributed CAN-connected power supplies with high level of local intellectual properties. These properties allow to achieve high stability, high safety of operation together with the specific features such as coil temperature check without any temperature sensors. Such programmable power supplies with the intellectual CAN-bus/CANopen controller have been designed for the specific accelerator applications. The control system software was adapted to operate with CANopen protocol. "Marathon IPP-1/100" and "Marathon IPP-4/35" power supplies with CANopen are used now within the control systems of LU-60m and LU-10 linacs. 3200 hours of continues operation were achieved since the year 2008.

INTRODUCTION

Power supply development was one of the important topic in particle accelerator instrumentation since particle accelerators appeared. Wide spread of different power supplies guarantee stable, safe and long term operation of any accelerator feeding directly magnet elements and feeding other electronic equipment such as vacuum pumps, RF systems and control system. A lot of efforts were made by different groups of accelerator specialists to improve mainly circuit technology in order to achieve the stability of the output values, high degree of efficiency, adjustable limitations of current, voltage and power stability of the output. In the meantime new types of power supplies have been developed – digital programmable power supplies, which could be directly interconnected and integrated into accelerator control system via different fieldbus interfaces such as CANbus.

There are two main approaches which are used today in distributed power supplies systems. The first one is based on modular architecture when control unit is independent and could process few different power modules [1, 2]. The control unit is usually equipped with one (or several different) fieldbus interfaces and realize control logic together with precise measurement and feedback control of power modules. The power modules in such approach are usually just high power (some time very high power) amplifiers of voltage or current, depending on application.

The second approach, that we have chosen, is to develop single channel power supply module as a separate device, based on modern power supply circuits and equipped with individual smart controller and digital interface. The controller provides measurements, stabilizing and locking capabilities. Due to standardized fieldbus interface CANopen, such devices could be combined together into separate power supply control system or with other CANopen compatible sensors and actuators.

To feed beam optic of the LU-60m linac [3,4] control subsystem based on intellectual power supplies "Marathon IPP-1/100" and "Marathon IPP-4/35" have been developed. Control system of the LU-10 linac was significantly improved by replacing existing powers supplies (B5-47/B5-49) with the new ones. All this power supplies systems are based on CANbus fieldbus with CANopen higher-layer protocol and form separate subsystem but naturally integrated in to the whole accelerator control system.

INTELLECTUAL POWER SUPPLY

There are several features in the accelerator magnet optics control tasks, which make impossible to use standard industrial DC power supplies "as is" without extra efforts and use of additional hardware and control software. These features are the following:
- high long term stability and repeatability together with high accuracy;
- bipolar operation with accurate zero crossing and "true zero";
- load check function (detection of shortage, open, impedance changes) and alarm generating;
- load with high inductance;
- operation in conditions of high level of external EMI;
- flexible interface for embedding the power supply in to the existing control
- parallel operation of multiply devices.

It is also important to have a possibility of stand alone operation and operation as lab instrument to check lenses

and magnets during commissioning and repairing procedures.

All these features were completed in specially designed smart DC power supplies which Marathon Ltd manufactures. There are two versions of such a power supply up to now – "Marathon IPP-1/100" and "Marathon IPP-4/35 ". Power supplies are designed to be installed in standard 19" 3U cases in pairs in any combinations, two or one channels in one case (Fig.1). The single box version for lab applications is available also. General specifications are the following:
- two mode of operation – voltage or current tracking in the following ranges:
"Marathon IPP-1/100" – 0V - ±100 V, current 0A - ±1A
"Marathon IPP-4/35" – 0V - ±35 V, current 0A - ±4A
- Output voltage increment 1mV
- Output current increment 1mA
- Long term stability better than 0.05%
- Input voltage 220 V AC

The power supply operates in one of the three modes:
- Manual;
- RS-232/USB control;
- CANopen control.

The first mode is used for stand alone and lab applications. The second and the third modes are used for computerized control. The second one is used to control a few power supplies simultaneously, while the third mode is used to make distributed multi-channel systems with up to 127 power supplies in one network.

Advanced front panel with LCD indicator and digital encoder gives access to all features of the power supply in manual mode.

Fig.1. Power supply "Marathon IPP-1/100" – 2 channels, front and rear view.

Power supply software

Power supply firmware is distributed between three microcontrollers dedicated for different purposes. One is for internal operational control and communication via RS-232/USB interface, the second is to support man-machine interface via front panel and the third is to support CANopen [5] communication protocol over CAN-bus fieldbus.

The software has modular structure which increases reusability of the code when new versions and extensions of functionality will be needed.

06 Instrumentation, Controls, Feedback and Operational Aspects

The software of the power supply fulfills the following control commands:
- Status poll
- Set current or voltage stabilization mode
- Set current or voltage value
- Set level of maximum current in voltage stabilization mode or maximum voltage in current stabilization mode
- Store setted values in central computer and restore presetted values from central computer.

The software is developed with ANSII C and use CHAI source code and CANopen Slave source code from Marathon Ltd. to implement CANopen slave functionality[6]. Segmented SDO protocol is used, allowing transfer of ASCII commands of any necessary length via CAN-bus. All mandatory records in the Object Dictionary and NMT functionality are supported. Slave capabilities allow smooth combination of multiple power supplies into the CANopen networks. Standard configuration and analyzer tools are used to configure device behaviour in the CANbus network and trace logical network problems during whole system operation.

It is very important to notice that CANopen profile DS453 for power supplies is under development now within the activity of International organization «CAN in Automation» [7]. It could be downloaded by CiA members or requested by nonmembers from CiA web pages. Marathon Ltd. plans to implement this profile in next versions of their power supplies dedicated for accelerator control systems.

CAN-BUS BASED DISTRIBUTED POWER SUPPLY SYSTEMS

The power supplies, described above, were used to develop control subsystem for beam optics magnets of the linac LU-60m for NESTOR storage ring. The whole system consists of 10 pieces of "Marathon IPP-1/100" power supplies, 2 pieces of "Marathon IPP-4/35", one Marathon CAN-bus PCI interface board installed in IBM-PC compatible computer together with system and application control software which is integrated into the software of the whole linac control system. In addition these power supplies were used to improve control systems of LU-10 which is used for industrial application.

Measurement of the magnet elements state

The possibility to trace any changes of load parameters and measure current properties is very important especially for high current accelerators. Changes of load resistance due to shortages or breaks, when the average power of the beam is high, could cause vacuum crash and destroying of beam pipes. Presented power supplies realize a function of automatic beam breakdown and alarm signal generation at load resistance variation or at permissible voltage or current value exceeding.

Due to high accuracy of output current and voltage measurements, load resistance could be calculated, which ensures to calculate temperature of magnet elements, taking into consideration that magnet elements are constructed with copper wires The following formula, valid for $0 < T_i < 200$, was used and gives the temperature of lens or steer in Celsius degrees:

$$T_i = \frac{R_i - R_0}{R_0 * \alpha} + T_0$$, where

α - temperature to resistance coefficient for copper,

T_0 - start temperature,

R_0 - load resistance while temperature is T_0,

R_i - load resistance while temperature is T_i.
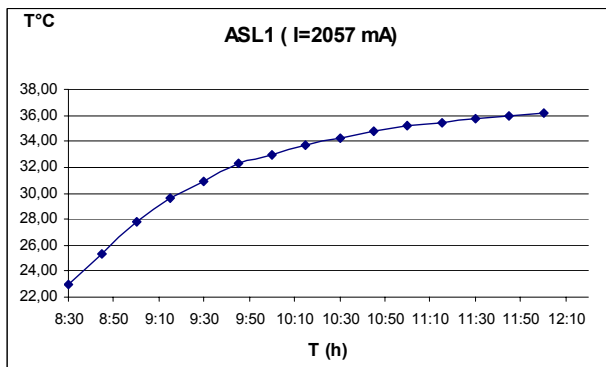
Fig.2. Magnet lens temperature variation.

Fig. 2 shows temperature variation of axis symmetric magnet lens, measured with the power supply. The lens resistance is 3.2 Ohm, inductance 0.57 Henry, current range is 0 to 3 Amp.

Power supply system operation results

Rack crate with installed power supplies is mounted in klystron room at 30 meters distance from operator's control panel. Practice of everyday operation confirmed the correct choice of CANbus for communication because of high reliability and stability of operation in very rush environment with high level of EMI. "Marathon IPP-1/100" and "Marathon IPP-4/35" power supplies operated successfully during 3200 hours within the LU-10 control system.

The commissioning of the linac LU-60m together with NESTOR storage ring is almost finished and run will start soon. The magnet elements of linac LU-60m will be feed by "Marathon IPP-1/100" and "Marathon IPP-4/35" power supplies. There are also plans to replace power supplies of running accelerator "EPOS" with these new power supplies.

CONCLUSIONS

It is possible to conclude now that circuits for power supplies together with CANopen protocol and architecture of the whole system were selected correctly and can be used in operating accelerators, as well as machines, which are under construction.

The significant advantage of the approach is the possibility to expand the CANopen network with other CANopen devices, such as power supplies or any kind of CANopen-compatible instruments. Application of internationally standardized protocols allows becoming independent on any one vendor of hardware components or configuration and diagnostic tools.

REFERENCES

[1] L. Droll Programmable power supply for high-vacuum pumps // CAN newsletter 4- 2008, p.32-34

[2] K.M. Gorchakov, S.S. Vasichev, V.F. Veremeenko, V.R. Kozak, A.S. Medvedko, R.Z. Pronik, V.P. Prosvetov, O.A. Proskurina,POWER SUPPLIES FOR THE BENDING MAGNETS OF THE BEP AND VEPP-2000 STORAGE RING// Proceedings of RuPAC 2008, Zvenigorod, Russia, 2008, pp.156-158.

[3] V.N.Boriskin, S.K. Romanovski, A.N. Savchenko, A.A. Sarvilov, D.L. Stepin, G.N. Tsebenko,A.S. Chepurnov, I.V. Gribov,A.F. Shamarin, POWER SUPPLY CONTROL SYSTEM FOR THE LINAC OF THE "NESTOR" STORAGE RING // Proceedings of RuPAC 2008, Zvenigorod, Russia, 2008, pp.252-254.

[4] M.I.Ayzatskiy, V.A.Kushnir, V.V.Mytrochenko et al. The electron injector for linac of the "NESTOR" storage ring // Problems of atomic science and technology. Ser. "Nuclear Physics Investigation". - 2(46). -2006. -p.94–96.

[5] K. Etschberger Controller Area Network, basics, Protocols, Chips and Applications, IXXAT Press, Germany, 2001   431 p. ISBN 3-00-007376-07, 1997).

[6] http://can.marathon.ru/prog/chai

[7] http:// www.can-cia.org

UNIVERSAL TIMER MODULE FOR THE TIMING SYSTEM OF THE ACCELERATING STORAGE COMPLEX ITEP-TWAC

A. Orlov, P. Alexeev, S. Barabin, D. Liakin, SSC RF ITEP Moscow, Russia

Abstract

A multipurpose synchronization module for renovating timing system of ITEP-TWAC accelerator facility is developed. A group of such modules is aimed to implement a sophisticated set of synchronization functions among four accelerators – proton LINAC I2, ion injector I3, buster synchrotron UK and accelerating and storage ring U10. This FPGA based module generates up to 16 output pulses related to timing scale (T), magnetic field scale (B), radio frequency, external events or their combination. The read back function allows controlling the pulses propagation on cycle-to-cycle basis. The structure of the module, a description of basic functions and IO interface are presented in details. Also an example of system configuration based on the developed module is discussed.

INTRODUCTION

The modernization of an accelerating complex in ITEP [1] lays new demands to the synchronization of the systems of accelerators. A new timing system should work with increasing number of synchronous elements providing more and more functionality and flexibility.
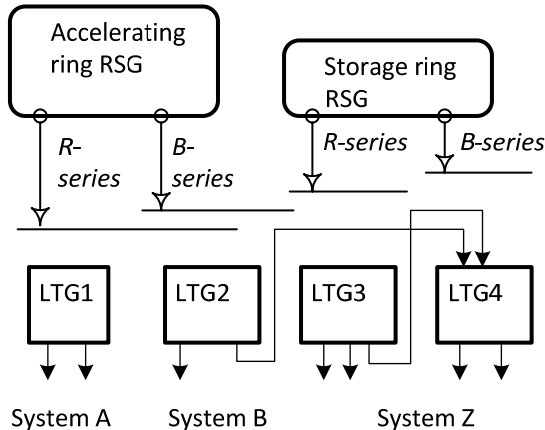
Fig. 1. A principle of organization of the timing system of the ITEP's accelerators

A principle of synchronization of the ITEP's accelerating complex shown on fig. 1.

Reference devices (reference signal generators RSG) generate **B**- and **R**- sequences of pulses synchronous to the magnetic field strength and zero phase of RF oscillations. Followed local timing generators LTGs are an assembly of properly commuted logical modules, modules of programmable time delays and fan-out modules as it shown on fig. 2. The system has a multiple hierarchy levels and distributed over the area. Some local generators are realized in the form of standalone units,

synchronized by one or two pulses from higher-level LTG. Some of local generators are placed outside of the synchrotron's control room. There are, for instance, timing systems of proton or ion sources. This allows an independent work of linacs on their own targets.
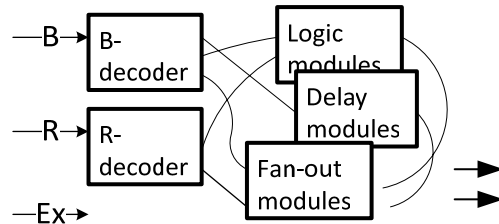
Fig. 2. A Local Timing Generator synchronizes devices with magnetic field (B), RF phase (R) and/or external events (Ex).

The tasks of the developing timing system are, in particular, unification of used modules, simplification of the process of the system setting up and extending of a system's functionality. The concept of the new timing system is based on the experience of the exploitation of the existing system in ITEP as well as other similar systems in GSI and CERN. A new timing system concept for CERN and FAIR so-called White Rabbit project [2] also has been examined. Similar to the White Rabbit the future timing system of ITEP presumed a possibility of precise delay compensation over Ethernet. But in opposition to White Rabbit, ITEP keeps a dedicated serial timing bus STB (fig.3b). The synchronized Ethernet (IEEE 1588) is an option, which is used when it is necessary without any modification of general standard. This way looks more reliable and budgetary which has the sense in present-day situation. Nevertheless, we are looking forward and in the case of successful realization of the White Rabbit project and the appearance of commercial accessible components there is a possibility of the essential incorporation of this new technology into the developed system.
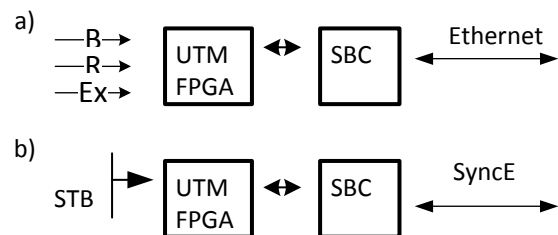
Fig. 3. Applications of the UTM: replacement of existing modules on top, using serial timing bus STB and synchronization over Ethernet on bottom.

A universal timing module UTM was developed as a key component of a new system. It intends to smoothly

06 Instrumentation, Controls, Feedback and Operational Aspects

269

replace existing timing elements in the way, shown on fig. 3.a. In the same time the UTM is a part of new technology required to fulfill new demands. It is ready to be used jointly with contemporary elements and structures like synchronized Ethernet (fig. 3b).

STRUCTURE AND THE FUNCTIONAL POSSIBILITIES OF THE UNIVERSAL MODULE

The logical structure of the module is shown in fig. 4. Element density of the contemporary programmed logic makes it possible to place several local timing generators in the single universal module. Functional modules FG give a possibility to generate complex sequences of pulses at the outputs of the device. A serial timing bus decoder's standard component is including into firmware when it is necessary to operate with STB. As a standard option, it is also possible to compensate a cable delay. A correction component, shown on the figure, could be set up after manual calibration or during automatic calibration by synchronized Ethernet.
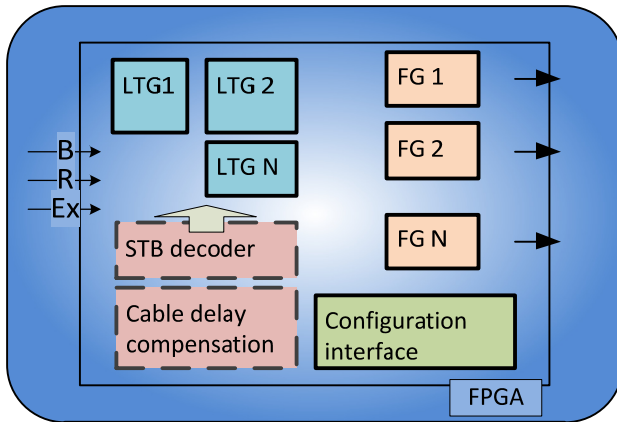
Fig. 4. Logic of the universal timer module realizes several LTG, a collection of functional blocks and series of specialized components. Numerous interfaces allow connecting via serial or parallel bus (RS485, PC104).

The accelerating facility of ITEP has different operating modes, therefore the timing must support all of them. Basic event markers for the timing system are given in fig. 5.
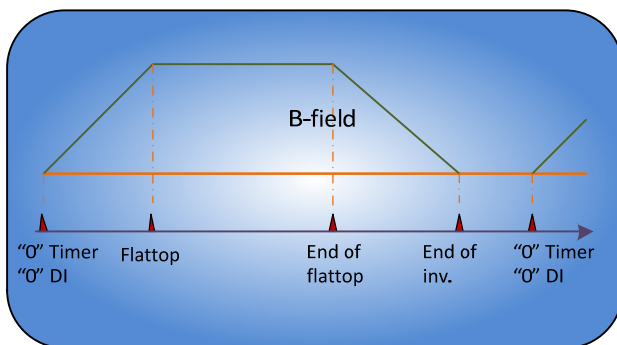
Fig. 5. Cycle of acceleration and basic event markers

Fig. 6 presents one of possible modes of operation of the timing system. The ion beam injected to and extracted from accelerating ring while rising magnetic field. A timing module starts the cycle by initiating of LEBT optics elements and main thyristor rectifier. Injection and extraction proceed when the magnetic field reaches predefined values. To initialize the extraction the module predicts magnetic field and issues HEBT start pulse little ahead of the kicker magnet start. To control timing uncertainties in technological systems the module has programmable time windows according required tolerances.
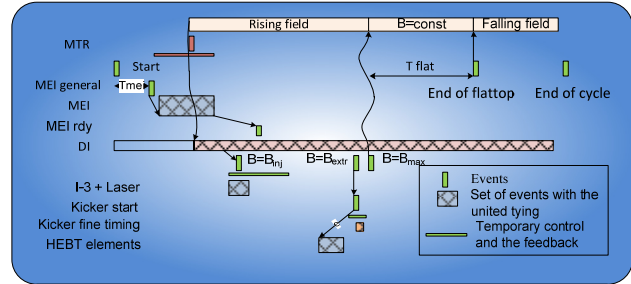
Fig. 6. A typical regime of the work of the timing system of an accelerator. Beam injected into rising magnetic field.

Abbreviations on fig. 6 are: MTR - main thyristor rectifier; MEI - magnetic elements of ion guide; MEI rdy - virtual moment of the maximum current in MEI; DI- discrete integrator, the instantaneous value of magnetic field; Kicker of fine of timing - forming by the external scheme of the precision sequence of trigger pulses with the tying to the phases HF field; HEBT - high energy beam transfer line, ionic optics of transitional channel.

REALIZATION OF THE MODULE

At the present the timing system of the accelerating facility is based on the discrete modules, similar to the one, shown on fig. 7.

The great disadvantage of such blocks is a necessity of a manual commutation while reconfiguration process.
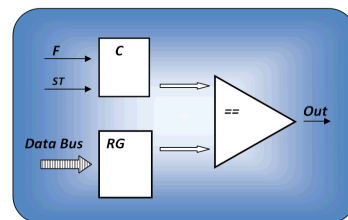
Fig. 7. A discrete block example. F – an internal frequency of 10 kHz or 10 MHz, either external frequency from the discrete integrator of the magnetic field signal or the zero-crossing pulses of the accelerating field. ST- starting of counter. Data bus - external data and address bus. Out - output of the block.

Figure 8 shows components of the UTM. On the bottom there is a single-board computer with Debian

Linux OS. It provides a remote control over Ethernet, a non-volatile storage for system setting and system default set-up during startup process. A dedicated program could be used to provide timing parameters correction in a feedback mode.

Timer module is created on the base of the microchip of the programmed logic FPGA. Use of FPGA makes possible a realization in one module of sixteen 32bit timers with programmable delay values. The selection of the counting and synchronization sources for each of sixteen timers is performed by program by setting a bitmask of an appropriate register. Four counter inputs and a 50MHz on-board oscillator could be used as counting sources. Another four inputs serve for synchronization purpose. Any input and any timers outputs could be used as a synchronization source for any timer internally. All inputs are equipped with protection and normalizing scheme. Also in the module includes a generator with the programmable period and control scheme, which makes it possible to measure the time intervals to control the time of occurrence of various events. Eighteen outputs of module can be independently commuted with the output of any of sixteen timers or with the output of the programmed generator.
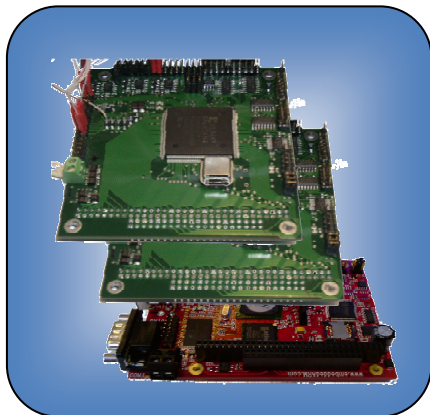
Fig. 8. Timer block, which consists of one single-board computer and two timer modules

Timer module as well as a single-board computer has several RS485 and RS232 ports, furthermore single-board computer has an Ethernet 10/100 and USB 2.0 connectors, the presence of these ports allows additional possibilities to create a distributed timing system with the use of both of the timer blocks and the separate timer modules (fig. 9).
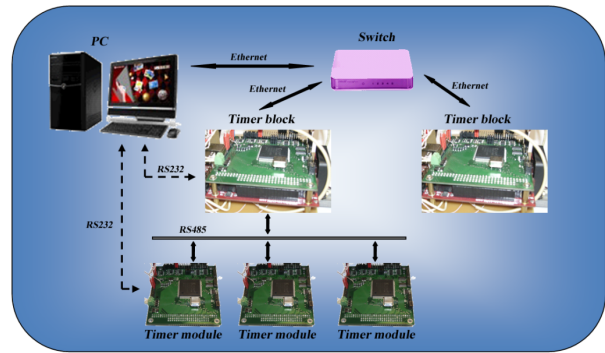
Fig. 9. Example of the creation of the distributed timing system based on timer blocks and discrete timer modules.

CONCLUSION

The Universal Timing module showed a good suitability for solving various timing problems. Behind of operation in ITEP's synchronization scheme it is used in GSI as a timing module for Ionization Profile Monitor [4][5] and as a GSI-to-CERN timing format converter in the frame of FAIR project preparations. The test exploitation of UTMs as a part of the accelerator's timing system showed the complete readiness of the module. Next stages include the reproducing of modules, the development of corresponding software and the smooth adoption of modules into the operating system.

LITERATURE

[1] N.N.Alexeev et al. ITEP_TWAC status report. Proc. RuPAC 2008, Zvenigorod, Russia, pp134..136.
http://cern.ch/AccelConf/r08/papers/TUBAU02.pdf
[2] J.Serrano et al. The White Rabbit Project, icalepcs2009, Kobe, Japan.
http://cern.ch/AccelConf/icalepcs2009/papers/tuc004.pdf

[3] IEEE 1588 Standard for a precision clock synchronization protocol for networked measurement and control systems. http://ieee1588.nist.gov/

[4] M.Schwickert et al. BEAM DIAGNOSTIC DEVEOPMENTS FOR FAIR, proc. DIPAC2009, Basel, Switzerland, pp. 424..426

[5] D.Liakin et al. EPAC08, Genoa, IT, TUPC060, p1194

CONTROL SYSTEM FOR THE NEW BEAM TRANSFER LINE AT IHEP

A.Matyushin, L.Kopylov, S.Merker, M.Mikheev, IHEP Protvino, Russian Federation

Abstract

New proton beam transfer line is study project to evaluate a possibility to use UNK injection line as an experimental facility. A wide set of accelerator equipment is involved in the test. The Control system is build on OPC and CAN technology using data driven and object oriented approach. The structure, key solution and operational experience are described in the paper.

INTRODUCTION

In IHEP on the basis of the beam transfer line (BTL) of not completed UNK ring the construction of installation for applied researches [1] is planned. Within the R&D study for finding-out of an opportunity of such decision the Prototype of such installation has been created using all spectrum of BTL equipment on the limited length of the channel: magnet optical elements, beam instrumentation, vacuum system, the radiating control. The beam, accelerated by proton synchrotron U-70 up to energy 50-70 GeV, is extracted into the channel, where it's demanded size (the maximal size allowed by the vacuum chamber) at a location of investigated object is formed.

The control system (CS) has been developed for management of the equipment, which is a subject of this report. As far as the most part of BTL equipment, and, in particular, operating electronics, has been inherited from UNK, the new CS shall be adapted for existing schemes, therefore, some of our solutions don't look very elegant. Meanwhile, as it is the prototype of essentially bigger installation, we aspired to realize CS with precise standard borders between levels. There are three such levels in our system (from bottom to top): the controller of the equipment (EqC), a front-end computers (FEC) and computer(s) in control room (CR).

As for the software solutions the object-oriented model driven by data has been chosen. It means that for all types of the equipment the corresponding data structures and methods for their handling have been designed. Corresponding objects have been developed for access to the equipment and the interface of the user.

Decisions made, experience of realization and two-year operation results are described further.

HARDWARE SOLUTIONS

The hardware of a BTL CS includes the centralized part, distributed controllers and communications (cables, repeaters, serial interfaces). The centralized part is located in CR, the embedded controllers - near to the process equipment. Communications between two parts are implemented via twisted pair cables supporting CAN protocol, timing pulses and signals of the dynamic interlocks.

Distributed part

The distributed part of a CS is based on three types of controllers: the universal controller of power supplies (PCC), the controller of the vacuum pumps (VC1) and those one for vacuum gauges (VC2). The PCC is constructed on two functional units: microcontroller CY8051F060 and programmed logic XC9536XL. Communication with upper level is carried out through microcontrollers CAN interface. There is a timing events receiver on the board as well as a driver of dynamic interlock. The controller has 16 inputs of status signals, 8 discrete outputs, two analogue inputs and one analog output.

The controller of ion pumps VC1 is embedded in a high voltage power supply. In each rack can be up to 3 high-voltage power supplies. The VC1 acquires the states of registers and transfers the status of pumps and their currents in predefined regular intervals.

Controller VC2 is used for vacuum measurement. It consists of 8-channel 24-digit sigma-delta ADC. The analogue signals proportional to pressure come from a power supply of gauges.

Means of data transmission, timing pulses and dynamic interlock of each building include repeaters boards, a twisted pairs main cable, as well as short cable taps.

The PCC develops a signal of the dynamic interlock if the current of a power supply is out of the window comparator thresholds. The inhibit signal in CAN terminology has a dominant level, and the permission signal – recessive one.

The timing controller carries out a number of service functions: calculation of number of cycles and distribution this information on CAN network, as well as management the dynamic interlock mode. The static interlock system is intended for supervision over a condition of doors of admission in a BTL tunnel, management of beam stopper and deliveries of the permission to the fast ejection system when safety requirements is fulfilled.

The BTL CS is located far away from the equipment of the proton beam fast ejection system. Communication between these two systems is done by means of timing signals generated by the fast ejection system and static interlock from BTL equipment.
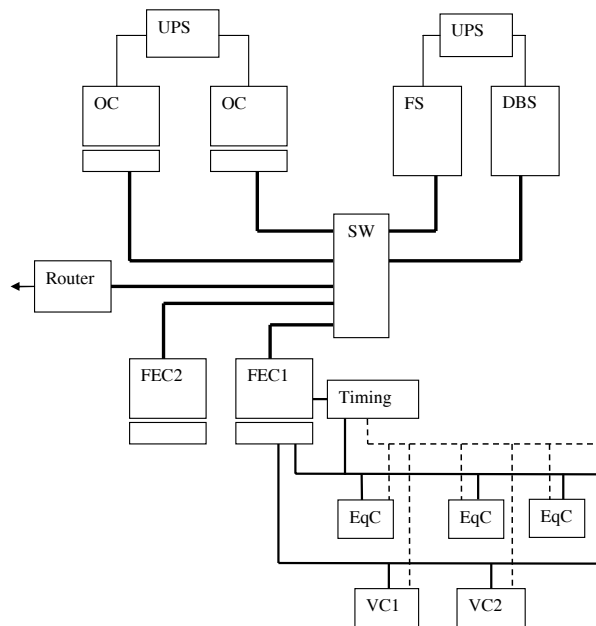
Figure 1: Hardware structure.

In addition to the static interlock the operator manually by pushbutton enables an ejection taking in account that beam intensity in the accelerator and beam quality are in proper conditions. For 300 ms till the moment of an extraction the condition of the static interlock is fixed to provide necessary time for ejection power supplies charging. At presence of the static interlock approximately for 100 μs till the moment of an extraction dynamic permission enables the experimental equipment trigger pulses.

Front-end computers

The FEC are intended for connection with the distributed level of a control system. The FEC are connected directly to a CR network through network adapters. Since few different types of EqC with different communication protocols are used, we have decided to use two types of a FEC:

- Communication FEC is intended for connecting controllers of the equipment of the bottom level. The primary goal of this type FEC – translation of the operating protocol of a CR network (Ethernet) to the operating protocol of a fieldbus (CAN). Three physical CAN buses are used in BTL, so three cards of high-speed CAN controllers are installed in such FEC.
- Specialized FEC - carries out complex equipment management directly connected to a network. In this case in FEC the necessary quantity of cards of

input/output for management of the equipment is installed. The FEC should also carry out primary processing of the information. Such FECs are used for beam instrumentation and radiation control.

Control room

CR consists of control panel, servers and the network equipment. The control panel consists of three personal computers, further called Operator Consoles (OC). Any control application can be launched on any of OCs.

Servers - computers to perform the specialized function:

- The File server (FS) is intended for the centralized storage of the software and configurations. It provides access to files from any console and a handheld computer.
- The Database Server (DBS) - storage of the systematized working parameters and data of a control system. Data are used for adjustment of system and to display the parameters of the equipment in a graphical or table view.

Network

We used one level Ethernet network to interconnect CR computers and FECs based on multiport switch. CS Network is connected to IHEP network through a router which provides access to the information on a condition and parameters of accelerator U70 and interferes with penetration into a network of the parasitic traffic.

SOFTWARE SOLUTIONS

At designing the software overall objectives were:

- To provide the homogeneous interface of access to the equipment for application programs;
- To hide differences in hardware and program realization of controllers of the equipment from application programs;
- To provide the possibility for launching any (reasonable) amount of application programs on any OC within the limits of a network of a control system;
- To provide the possibility of easy enough addition of new types of the equipment and controllers in a control system.

Figure 2: Software structure

For realization of these requirements on top level of a control system the client-server solution has been chosen, the communications between the client and a server is carried out by means of OPC [2]. One (or more) OPC servers are configured in CS which work with controllers of the equipment and provide to application programs a homogeneous way of access to any data coming from the equipment
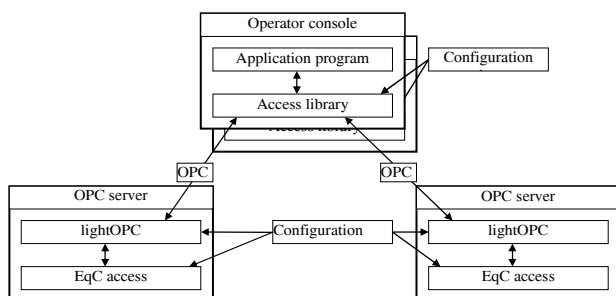
The application program accesses the parameters of the equipment using device name (unique in CS) and a name of property in this device, for example: "MKG1.MCUR" - property MCUR (the measured current in Amperes) of device MKG1. For each type of device the model of data is created - which parameters are supported by this type of the device, their types of data, a way of access (read only or read/write). While writing the applications it is necessary to know in advance names of devices in system, their types and corresponding models of data.

The access library reads a configuration of a control system (from a file) and on its basis defines where exactly (on which of server computers and under what name of OPC server) the device with the given name is accessible. When device location in CS is resolved the access library carries out OPC call(s) to corresponding OPC server.

For application programs the access library provides 3 basic modes of access to the parameters of the equipment granted by OPC servers: **Reading, Wirting, Subscription** (the code in the application program is

every time when parameter value is changed in OPC server).

CS contains one (or more) OPC servers running on one (or more) server computers. Every OPC server at start-up also finds a configuration (from a file) and on the basis of this information configures itself:

- Which devices are supervised by this OPC server
- Under what names devices data are made accessible through OPC
- What model of data is used for each device (i.e. which parameters are accessible through OPC and how to calculate these parameters from the values which have been read from the controller of the equipment)

OPC interface part is based on lightOPC library [3] developed in Institute for Problems of Informatics of the Russian Academy of Science.

OPERATIONAL EXPERIENCE

The Prototype of BTL has been put in operation in 2007. CS allows for operator to carry out all preoperational activity to get proper vacuum conditions in BTL, check security interlocks and door state. But the major task of course is setting parameters for beam optics and getting information from beam instrumentation.

Experimental facility requires very precise beam parameters and timing setting to be fulfilled. A serious effort has been spend to provide the logic to avoid incorrect extraction of the beam not matching the strict criteria of quality.

Gathering a historical data allowed to analyse the operation of equipment and improve stability and repeatability of beam parameter in the experimental point.

CONCLUSION

Presented CS has allowed maintaining successfully BTL operation for two years. Experience of development and implementation shown that multilevel structure with standard borders between layers allows to create easily configurable system. It also gives an opportunity of independently updating hardware and software components in process of appearance of new commercial products and improvements of a budgetary situation. Principles of Data driven system could be easily expanded and flexible. The object oriented approach has allowed facilitating support and development of program components

REFERENCES

[1] Ю. М. Антипов и др. Радиографическая установка ускорителя протонов
с энергией 70 Гэв ГНЦ ИФВЭ. ПТЭ, 2010, № 3, с. 1–8
[2] www.opcfoundation.org - official site of OPC foundation technology
[3] http://www.ipi.ac.ru/lab43/lopc-ru.html

BEAM TESTS OF THE LHC TRANSVERSE FEEDBACK SYSTEM

W. Höfle, G. Kotzian, E. Montesinos, M. Schokker, D. Valuch, CERN, Geneva, Switzerland
V. M. Zhabitsky, JINR, Dubna, Russia

Abstract

A powerful transverse feedback system ("Damper") has been installed in LHC in order to stabilise the high intensity beams against coupled bunch transverse instabilities in a frequency range from 3 kHz to 20 MHz and at the same time to damp injection oscillations originating from steering errors and injection kicker ripple. The LHC Damper has been also used for exciting transverse oscillations for the purposes of abort gap cleaning and tune measurement. The LHC Damper includes 4 feedback systems on 2 circulating beams (in other words one feedback system per beam and plane). Every feedback system consists of 4 electrostatic kickers, 4 push-pull wide band power amplifiers, 8 preamplifiers, two digital processing units and 2 beam position monitors with low-level electronics. The power and low-level subsystem layout is described along with first results from the beam commissioning of the LHC Damper.

INTRODUCTION

The powerful transverse feedback system ("Damper") for the Large Hadron Collider (LHC) is a joint project of the European Organization for Nuclear Research (CERN) and the Joint Institute for Nuclear Research (JINR) [1, 2]. To a large extent this project is based on the system in the SPS which has operated successfully for many years [3, 4].

The peak luminosity of 1.0×10^{34} cm^{-2}s^{-1} is achieved in the LHC with high intensity beams of low emittance. The ultimate intensities after injection into the LHC will be about 4.8×10^{14} particles for the proton beam with an energy of 450 GeV and 4.1×10^{10} ions for the ^{208}Pb^{82+} beam with an energy of 177 GeV/u. These intensities can lead to coherent transverse instabilities. The theoretical prediction for the instability rise time τ_{inst}, dominated by the resistive wall effect, is about 18.5 ms or 208 turns [5] at injection energy for the proton beam, and a significant contribution of the LHC collimators at collision energy to τ_{inst} is also predicted [6].

The normalised transverse emittance ε is expected to be smaller than 3.75 mm·mrad at collision energy. The damping time τ_{d} of the LHC transverse feedback system (TFS) was chosen to limit the emittance growth due to injection errors [7, 8]:

$$\frac{\Delta\varepsilon}{\varepsilon} = \frac{e_{\mathrm{inj}}^2}{2\sigma^2} F_\varepsilon \,; \qquad F_\varepsilon = \left(1 + \frac{\tau_{\mathrm{dec}}}{\tau_{\mathrm{d}}} - \frac{\tau_{\mathrm{dec}}}{\tau_{\mathrm{inst}}}\right)^{-2} . \quad (1)$$

Here σ is the initial RMS beam size; $e_{\mathrm{inj}} \lesssim 4$ mm $= 3.5\sigma$ is the maximum assumed amplitude of a beam deviation from the closed orbit due to displacement and angular errors at injection where the betatron amplitude function is $\hat{\beta} = 185$ m; $\tau_{\mathrm{dec}} \simeq 750 \times T_{\mathrm{rev}} = 68$ ms is the assumed

06 Instrumentation, Controls, Feedback and Operational Aspects

decoherence time (the revolution period of protons in the LHC is $T_{\mathrm{rev}} = 88.93$ μs after injection). These parameters lead to $\Delta\varepsilon/\varepsilon < 2.5\%$ the maximum admissible emittance blow-up in the LHC allocated to injection dipole errors [5] if $\tau_{\mathrm{d}} = 40 \times T_{\mathrm{rev}}$. Thus, the LHC TFS gain is $g = 2T_{\mathrm{rev}}/\tau_{\mathrm{d}} = 0.05$ and the overall damping time $(1/\tau_{\mathrm{d}} - 1/\tau_{\mathrm{inst}})^{-1}$ of the injection oscillations becomes about 50 turns or 4.4 ms.

The nominal LHC beam represents an unprecedented stored energy of 350 MJ [5]. The extremely high destructive power of such a beam imposes an external dump, where the beam must be extracted completely from the LHC, diluted to reduce the peak energy density and then absorbed in a dedicated system. A gap of 3 μs in the circulating bunch pattern is present to allow the horizontally deflecting extraction kickers to rise up to their nominal field. Since particles transiting the kickers during their field rise will not be dumped properly, the proton population in this interval must always remain below damage and quench limits. The control of the abort gap population is a problem common to high energy machines using superconducting magnets. Cleaning of the abort gap using the LHC transverse dampers should require no more than a few tens of milliseconds [9].

The LHC Damper will stabilize the beam against coupled bunch instabilities as well as damp the transverse oscillations of the beam originating from steering errors and kicker ripple. It will also be used for the purposes of tune measurement similar to the SPS system [10] and for abort gap cleaning.

GENERAL DESCRIPTION

The LHC Damper has 4 independent transverse feedback systems on 2 circulating beams (one feedback system per beam and transverse plane). Each system is a classical bunch-by-bunch transverse feedback system (see Fig. 1) [11]. It consists of 2 pick-ups (PU), a 4 section damper kicker (DK) and an electronic feedback path with appropriate signal processing and transmission from PU to DK. The DK corrects the transverse momentum of a bunch in proportion to its displacement from the closed orbit at the PU location. The digital signal processing unit (DSPU) ensures the adjustment of the feedback to the phase advance and the beam time of flight for optimum damping. The mixing of signals from 2 pick-ups allows adjustment of the betatron oscillation phase advance ψ_{PK} from the "virtual" PU to the DK to an odd multiple of $\pi/2$.

The total delay τ_{delay} in the signal processing of the feedback path from PU to DK adjusts the timing of the
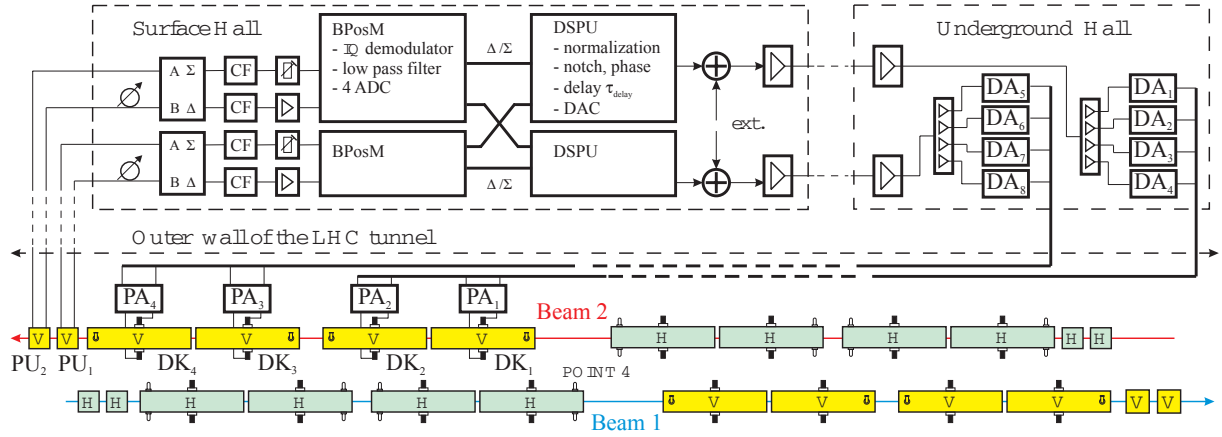
Figure 1: Layout of the LHC Damper and block diagram of the transverse feedback system for vertical oscillations.

signal to match the bunch arrival time. It equals τ_{PK}, the time of flight of the particle from PU to DK, plus an additional delay of $\hat{q}$ turns:

$$\tau_{\text{delay}} = \tau_{\text{PK}} + \hat{q} T_{\text{rev}} . \qquad (2)$$

For vertical oscillations in the LHC (see Fig. 1), the delay τ_{delay} is slightly *shorter* than one beam revolution period $T_{\text{rev}} = 88.93$ μs and $\hat{q}_{\text{v}} = 0$. For the horizontal systems, kicker *downstream* of the PU, an additional delay of one turn ($\hat{q}_{\text{H}} = 1$) is added. The delay τ_{delay} is then slightly *longer* than one turn.

The main instability that the feedback has to handle is the resistive wall instability for which the lowest frequency in the LHC is about 8 kHz ($Q_{\text{H}} = 64.28$ and $Q_{\text{v}} = 59.31$). For purposes of abort gap cleaning the unwanted beam should be coherently excited at frequencies (in accordance with the non-integer parts of the tune) gated in the 3 μs long abort gap. Consequently a lower cut-off frequency of 1 kHz was chosen for the feedback loop. The highest frequency must be sufficient to damp the dipole mode oscillation of two neighbouring bunches which corresponds to $f_{\text{max}} = 20$ MHz for the nominal bunch spacing of 25 ns. Coherent oscillations at higher frequencies are assumed to be suppressed by Landau damping. The pulse response must cope with the minimum gap between batches in the LHC (995 ns). Consequently, a rise time (1–99% V_{max}) of 720 ns was chosen for the power amplifier.

The gain g and the maximum injection error e_{inj} yield the maximum deflection $\theta_{\text{max}} = 2$ μrad required for the proton beam with energy 450 GeV and the location of the kickers at $\hat{\beta}_{\text{K}} \gtrsim 100$ m. The deflection θ_{max} is delivered by electrostatic kickers with an aperture of 52 mm. The total required deflecting length of 6 m is divided into 4 kickers to limit the capacitive loading of the power amplifiers. The nominal voltage at 1 MHz is $V_{\text{max}} = \pm 7.5$ kV [2].

Beam oscillations are measured by eight dedicated coupler type pick-ups (49 mm aperture, 15 cm in length), two per transverse plane and beam (see Fig. 1). Signals from each pick-up are transmitted by coaxial lines of 570 - 650 m length to the surface building where signals after delay equalization are combined and subtracted by a hybrid

(2 − 2000 MHz) providing Σ and Δ signals. Strip-line comb filters (CF) generate wavelets at 400.8 MHz lasting for 9 RF periods which are then passed to variable attenuators or low noise amplifiers according to the signal levels.

The signals are then processed by the Beam Position Module (BPosM) where they are IQ-demodulated, low pass filtered, sampled and digitized (16 bit analog-to-digital converter, ADC) to compute for each bunch the normalised transverse beam position Δ/Σ at 40 MS/s rate on an FPGA (field-programmable gate array).

The normalised position signal Δ/Σ is transmitted via a 1 Gbps serial link to the Digital Signal Processing Unit (DSPU) with FPGA operating at 40 MS/s rate with the following functionalities: 1) normalization of signals proportional to $\hat{\beta}^{1/2}$ at the corresponding PU locations, 2) closed orbit rejection (notch filter), 3) sample hold circuit, 4) 7 tap phase shifter, 5) phase adjustment by mixing of PU signals to obtain the "virtual" pick-up signal, 6) delay (with 10 ps resolution), 7) three 32 tap filters, 8) digital-to-analog converter, DAC, plus other built-in features allowing the user full remote operation and diagnostics. The sample hold circuit is used for damping of single bunch oscillations by holding the transverse position value in the FPGA memory for $\lesssim 255$ sampling periods in order to produce a long output pulse that allows the operation of the power amplifiers in the low frequency range up to 1 MHz. The 7 tap phase shifter allows to adjust the phase advance of the feedback loop. The 32 tap FIR (finite impulse response) filters are used to compensate the power amplifier phase response, to optimise the feedback gain for injection error damping and instability control as well as to shape the roll-off beyond 20 MHz. Overall loop gain adjustment is provided via the reference to the 14 bit DAC.

Two output analog signals from the 1 W predriver amplifier after the DACs (see Fig. 1) are transmitted via coaxial lines ($\sim$300 m) to the underground hall in a cavern outside of the LHC ring where the signal is again amplified and split to drive the eight solid state 200 W driver amplifiers (DA) per system. The signals are finally transmitted to the power amplifiers (PA) and kickers (DK).

06 Instrumentation, Controls, Feedback and Operational Aspects

16 power amplifiers are installed directly under the 16 electrostatic kickers (see Fig. 2) in the LHC tunnel on either side of Point 4 (see Fig. 1). Each pair of electrodes is driven in counter phase by one wideband power amplifier, consisting of two 30 kW grounded cathode tetrodes RS–2048–CJC (Thales®) operated in class AB (push-pull). At low frequency the amplifier works on a relatively large impedance ($\sim$1 kΩ) leading to a large kick voltage. At higher frequency the capacitance of the kicker plates shunts the impedance and consequently less kick strength is available.
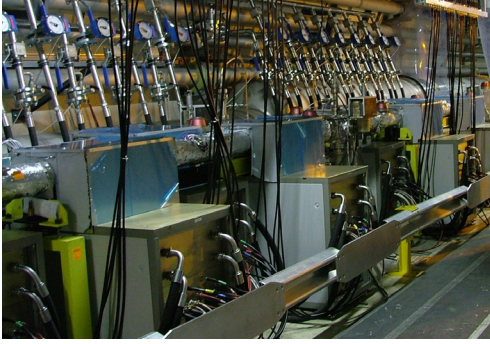

Figure 2: Kickers and amplifiers in the LHC tunnel.

The surface building also houses the 56 power converters for the power amplifiers in the tunnel at a distance of about 600 m: 8 converters for the tetrode anode voltage operating at a voltage/current of 12 kV/7 A, 16 converters of 1000 V/1 A, 32 converters of 300 V/0.2 A for the auxiliary voltage.

The hardware commissioning of the LHC transverse damper system has been successfully completed in 2008. The performance specifications and the obtained characteristics of the power amplifiers in conjunction with the 200 W driver amplifiers are shown in Tab. 1.

Table 1: Parameters of amplifiers

Parameter	Required	Achieved
nominal voltage at 1 MHz	$\pm$7.5 kV	$\pm$7.8 kV
nominal -3 dB bandwidth, kHz	3–1000	2–950
rise-time 10–90% $V_{\max}$	350 ns	410 ns
rise-time 1–99% $V_{\max}$	720 ns	760 ns
gain ripple	0.7 dB	0.5 dB

The design specifications were all met and the system has been successfully used with first beam in September 2008, exciting transverse oscillations for the purpose of tune measurement [2].

HARDWARE TUNING

Power Amplifiers

Since 2008, all the sixteen amplifiers have been in operation for, up to date (September 2010), approximately 8500 hours without any major down time. Some modifications have been implemented to the air cooling system

06 Instrumentation, Controls, Feedback and Operational Aspects

to slightly improve it, by adding two extraction blowers, reinforcing the air flow through the critical components.

However, it has been found that tetrodes offer significant different control grid U_{g1} versus anode current I_{a0} characteristics. It has been decided to arrange tetrodes by pairs, with each pair offering as similar as possible characteristics. The rearrangement of tetrodes was done during 2010 in two short technical stops. Fig. 3 shows the differences before (red dashed curves) and after (green solid curves) readjustment on one of the most significantly modified amplifiers.
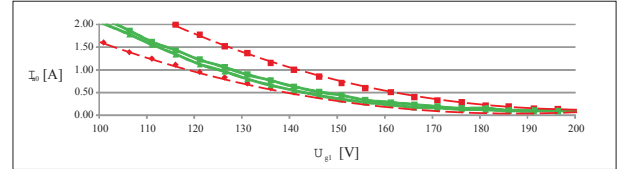
Figure 3: Anode current I_{a0} versus control grid value U_{g1} applied in an amplifier.

Since May 2010, all amplifiers now have similar characteristics, and while changing tetrodes during maintenance, it will be an important parameter to check.

The new settings for maximum operational values have been decided as follows: anode voltage of 12 kV applied with a screen grid voltage of 900 V and a biasing current of 1.2 A per tetrode that leads to peak pulse voltages of $\pm$7.5 kV at 1 MHz on the plates of kickers.

After all corrections have been applied, there were no major breakdowns due to power amplifiers, whilst amplifiers have been extensively used.

Electronics

Coefficients for mixing of pick-up signals in the DSPU were calculated in accordance with measurements of betatron phase advances between pick-ups $Q7$ and $Q9$ (PU$_1$ and PU$_2$ in Fig. 1) in horizontal (H) or vertical (V) planes for all dampers. Transverse oscillations of a bunch were
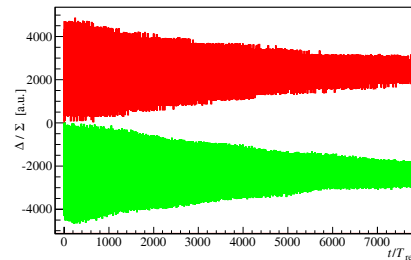
Figure 4: Signals from $Q7$ (top trace) and $Q9$ (bottom trace) pick-ups (vertical oscillations, beam 2).

induced by the Q-kicker with a pulse duration of about one revolution period, and the corresponding data (see Fig. 4) from pick-ups $Q7$ and $Q9$ were recorded at every turn. Then polar plots for the Fourier transform coefficients from the data recorded were used to determine phases at the betatron frequency that correspond to maximal amplitudes

(see Fig. 5). Measured betatron phase advances at injec-
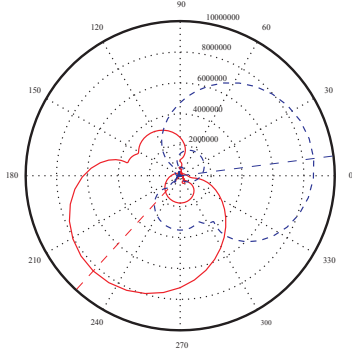
Figure 5: Amplitude–phase plot for signals from $Q7$ (solid curve) and $Q9$ (dashed curve) pick-ups.

tion between pick-ups $Q7$ & $Q9$ for all dampers are shown in Tab. 2. The values in Tab. 2 are in good agreement with data from the corresponding optics version of the LHC machine.

Table 2: Measured phase advances between pick-ups

Position of pick-ups (left or right of point 4) for beam 1 (B1) or beam 2 (B2)	Phase advance, degrees	Delta with respect to 90°
H.B1, left of 4, $Q9 \rightarrow Q7$	115	25
H.B2, right of 4, $Q9 \rightarrow Q7$	107	17
V.B1, right of 4, $Q7 \rightarrow Q9$	56	34
V.B2, left of 4, $Q7 \rightarrow Q9$	137	47

Signals from the higher order mode (HOM) couplers (50 Ω vacuum feedthrough with a small plate attached that capacitively couples to the kicker deflecting plates) was used for tuning the TFS synchronization circuit. Matching of the kick voltage generated by the feedback system and the beam voltage induced by a bunch that passes the kicker was used as a criteria for the synchronization procedure.

LHC Damper pick-ups were calibrated with data from the closed orbit pick-ups located in the same cryomodule. The calibrated pick-ups measure a deviation of the beam centre of gravity from the electrical centre of the pick-up, and data measured can be displayed in millimetres. With the present gain settings in BPosM ($< 1.3 \times 10^{11}$ protons per bunch of length > 1 ns at a saturation of ± 2 mm) an amplitude resolution of about 1 μm was obtained. A further improvement of the S/N ratio and resolution require to improve the analog circuit before digitization.

BEAM TESTS

Single Bunch Operation

First results of active damping with the LHC Damper were obtained for one bunch with an intensity of 1×10^{10} protons at 450 GeV in beam 2 in May 2010. Then all damper systems, for a single bunch injected from the SPS into the LHC, were tuned. The damping effect for injection

errors is shown in Fig. 6 for the nominal intensity of $\sim 1 \times 10^{11}$ protons per bunch.
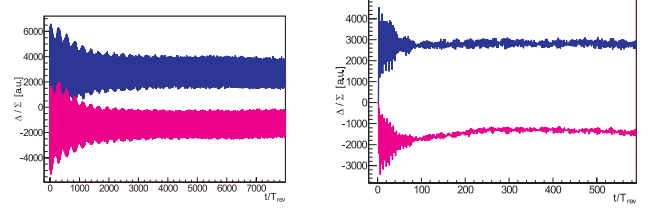
Figure 6: Damping of horizontal injection errors (beam 1): damper OFF (on the left) and ON (on the right); signals from $Q7$ (top trace) and $Q9$ (bottom trace) pick-ups.

Damping times can be modified by the feedback loop gains (see Fig. 7). A damping time of 40 turns was achieved that corresponds to the LHC Damper specification.
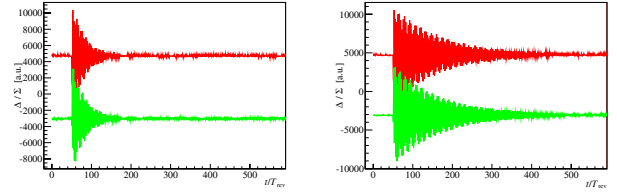
Figure 7: Damping of vertical oscillations (beam 2) induced by the Q-kicker: high (on the left) and lower (on the right) gains; signals from $Q7$ (top trace) and $Q9$ (bottom trace) pick-ups.

Table 3: Emittance measurements (20.05.2010)

Beam	ε_0, μm	ε, μm	Growth, %
H.B1	1.053	1.747	66
H.B2	1.009	1.603	59
V.B1	1.334	1.787	34
V.B2	1.305	1.487	14

Emittance measurements show better preservation for the plane for which the damper was used (V.B2, see Tab. 3, beam lifetime is > 100 hours at energy 3.5 TeV).

With the damper on the transverse emittance blow up at injection had been smaller than without the damper. Emittances of the order of 2.5–2.9 micron after injection were achieved.

The LHC Damper also has been tested during collisions with stable beam and everything worked as expected. The damping time at injection and during the ramp was approximately 70 turns, increasing to about 500 turns during collisions at 3.5 TeV. The damper is currently off during the squeeze (tune change) and for pilot bunches.

Bunch Train Operation

The LHC Damper was also used during beam tests for injection of groups of bunches (trains) from the SPS into the LHC in August–September 2010. Transverse oscillations of a whole train with four bunches (150 ns spacing) were induced by the Q-kicker. The damping effect was

measured for different bunches in the train (see Fig. 8). It was observed that the damping time was the same as for single bunch operation.
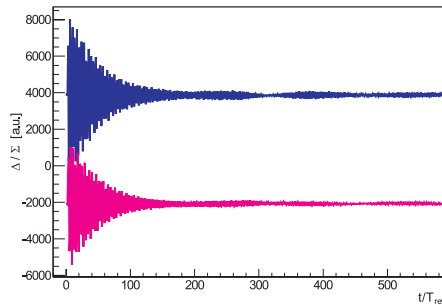
Figure 8: Damping of 150 ns bunch train excited by the Q-kicker (beam 2, horizontal oscillations); signals from Q_7 (top trace) and Q_9 (bottom trace) pick-ups, first bunch of the train.

Abort gap cleaning

The wide band power amplifiers allow the simultaneous use of the kickers for cleaning the abort gap and for feedback purposes. The flat top of the kicker pulse within the abort gap of 3 μs may be modulated as desired (see Fig. 9). Modulating the damper kicker pulse at a frequency corre-
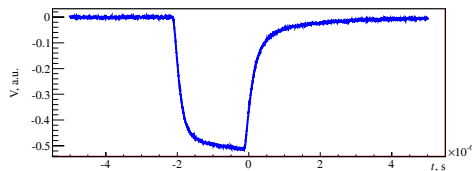
Figure 9: Signal from the kicker plates for abort gap cleaning regime (modulation at 3 kHz gives the slop at flat top).

sponding to the transverse tune will resonantly excite transverse oscillations and drive particles to larger and larger amplitudes, until they are intercepted by the betatron collimators. A specific monitor [12] to measure the particle population of this gap has been designed based on the detection of synchrotron radiation produced by protons moving through the superconducting undulator for low beam energies or the superconducting dipole for beam energies higher than 1.5 TeV. The light intensity collected by the monitor changes both in intensity and spectrum as the beam energy is ramped up. Once the cleaning is started the synchrotron light production decreased proportionally to the gap population. During 2009 a first abort gap cleaning test was carried out with encouraging results [9].

CONCLUSIONS

Beam tests and commissioning of the LHC transverse feedback system have been successfully completed. All of the 16 damper kickers, 16 wideband power amplifiers and 8 low-level subsystems have been operating continuously

06 Instrumentation, Controls, Feedback and Operational Aspects

since. The LHC Damper is now routinely used during injection, ramping and collisions for active damping.

ACKNOWLEDGMENTS

REFERENCES

[1] E. Gorbatchev et al. "Transverse Damping Systems for the Future CERN LHC". Proceedings of the 2001 Particle Accelerator Conference, 18 – 22 June 2001, Chicago, USA, pp. 1237–1239. IEEE, 2001.

[2] E. V. Gorbachev et al. "LHC Transverse Feedback System: First Results of Commissioning". XXI Russian Particle Accelerators Conference RuPAC-2008, 28 September–3 October 2008, Zvenigorod, Russia, pp. 97–100. Moscow, 2008.

[3] R. Bossart et al. "The Damper for the Transverse Instabilities of the SPS". Proceedings of the 1979 Particle Accelerator Conference, 12 – 14 March 1979, San Francisco, CA, USA, volume NS-26, No.3, pp. 3284–3286. IEEE Transaction on Nuclear Science, 1979.

[4] W. Höfle. "Progress with the SPS Damper". Proceedings of Chamonix XI, January 2001, pp. 117–124. CERN, Geneva, 2001.

[5] O. S. Brüning et al. The LHC Design Report. Vol. 1. CERN-2004-003, CERN, Geneva, 2004.

[6] E. Métral et al. ''Transverse Impedance of LHC Collimators". Proceedings of the 2007 Particle Accelerator Conference, 25 – 29 June 2007, Albuquerque, New Mexico, USA, pp. 2003–2005. IEEE, 2007.

[7] L. Vos. "Transverse Emittance Blow-up from Double Errors in Proton Machines". Proceedings of the Sixth European Particle Accelerator Conference, 22–26 June 1998, Stockholm, Sweden, pp. 1365–1367. Institute of Physics, 1998.

[8] V. M. Zhabitsky. "Transverse Emittance Blow-Up from Beam Injection Errors in Synchrotrons with Nonlinear Feedback Systems". Physics of Particles and Nuclei Letters, vol. 5, No.1(143), pp. 49–53, 2008.

[9] M. Meddahi et al. "LHC Abort Gap Monitoring and Cleaning". The First International Particle Accelerator Conference IPAC-2010, 23–28 May 2010, Kyoto, Japan, pp. 474–476. The Asian Committee for Future Accelerators (ACFA), 2010.

[10] R. Bossart and V. Rossi. "Coherent excitation of vertical beam oscillations". SPS Improvement Report No.156, CERN-SPS-ABM-RB-jf, CERN, Geneva, 29 January 1979.

[11] L. Vos. "Damping of Coherent Oscillations". NIM A, 391, pp. 56–63, 1997. CERN–SL–96-066–AP, Geneva, CERN, December 1996.

[12] T. Lefevre et al. "First Operation of the Abort Gap Monitors for LHC". The First International Particle Accelerator Conference IPAC-2010, 23–28 May 2010, Kyoto, Japan, pp. 2863–2865. The Asian Committee for Future Accelerators (ACFA), 2010.

THE NONLINEAR TRANSFORMATION OF A IONS BEAM IN THE PLASMA LENS

A.Drozdowskiy, N.Alexeev, S.Drozdowskiy, A.Golubev,
Yu.Novozhilov, P.Sasorov, V.Yanenko. ITEP, Moscow, Russia

Abstract

The focusing capabilities of a plasma lens depend on the stage of plasma development. Under certain conditions a magnetic field is linear, that allow focusing the beam to a very small spot. In other conditions, the magnetic field is nonlinear, that allow formation of hollow and others beam structures. Calculations and measurements were performed for a C+6 and Fe+26 beams of 200 MeV/a.u.m. energy. The obtained results and analysis are reported.

INTRODUCTION

The focusing properties of plasma lenses depend on the current density distribution along the radius of the
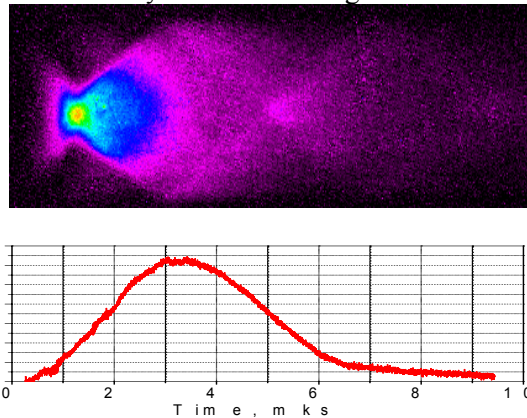
Fig. 1: Time scanning of the discharge luminescence and current.

plasma discharge [1]. Fig. 1 shows the time sweep of the luminosity of the plasma and the discharge current. The created magnetic field compresses the plasma-current cylinder. Expansion of the plasma column with a current takes place later and the discharge fills the whole tube. Current distribution across the tube changes significantly during the discharge. Therefore, plasma lens, in general, is nonlinear. Uniform current distribution longs for a limited time, so the plasma lens, as a device for sharp focusing, operates for about 1 microsecond or less. As a non-linear focusing device, the plasma lens can be used to produce beams of special shape. In particular, to create hollow beams, which can be used for the implosion of thermonuclear targets [2].

Test for sharp focusing of carbon ions has been conducted at ITEP in 2007-2008 [3]. These researches were continued in [4] to investigate possibilities of hollow beams formation. Lens parameters were as follows: capacitance - 24 µF; discharge current - 150 kA; current half-wave - 5 µs; argon pressure – 1-5 mbar; ion beam

duration – 300 ns (fig. 2). The discharge tube has radius of R = 1 cm and length of L = 10 cm. The effect of beam focusing was detected by the luminescence of a thin quartz scintillator. Fig. 3 shows crossections of the beam at position of 30 cm behind the lens as function of time during injection of the beam.
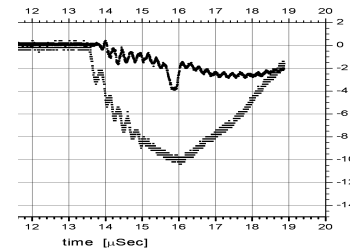
Fig. 2: Oscillograms of the discharge and the beam current.

   T=0 µs   *T=0.5 µs*   *T=1.5µs*   *T=1.7µs*   *T=2.3 µs*
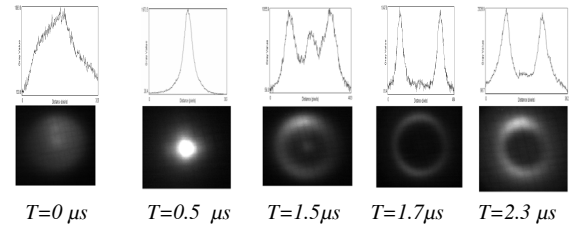
Fig. 3: The light output from a scintillator and the distribution of ion Fe^{+26} density for T > 0 behind discharge switch

FORMATION OF HOLLOW BEAMS

Possibility of transformation of ion beams with such plasma lenses has been demonstrated experimentally in GSI [5]. Researches carried out on the ITEP plasma lens confirmed this opportunities in a wide range of operating modes lens.

The paraxial beam with zero emittance is converted to a tube beam, when the distribution of azimuthal magnetic field in the plasma lens is as follows

$$B = a + br, \tag{1}$$

where a and b - constants. This distribution akes place, when distribution of the discharge current density is a superposition of a homogeneous distribution and a singular one, inversely proportional to radius r:

$$j = I_o/\pi R^2 + I_s/2\pi Rr. \tag{2}$$

Here R - plasma lens aperture, within which there are a homogeneous current, I_o and a singular one, I_s. In this notations $\quad B = B_o\,(r/R + I_s/I_o), \tag{3}$

where B_o - the field strength due to uniform current I_o of the discharge radius R. In this lens the ion beam is focused into a ring of radius

$$\rho = R \, I_s \,/I_o \qquad (4)$$

at a distance $Z_o = R \, \mathscr{R} \,/B_o L,$

(5)

where L - length of the lens and $\mathscr{R}$ – rigidity of the beam of ions. Note that Z_o is equal to the focal length of the same plasma lens in the absence of a singular component of the current. The role of the latter is to create a independent from r component of the field, which causes the coherent deflection of ion trajectories on the angle ρ / Z. The picture of trajectories of ions C^{+6} with energy of 200 MeV/a.e.m is shown in fig. 4. Radial thickness of the hollow beam at the position of the ring vanishes in this approximation.
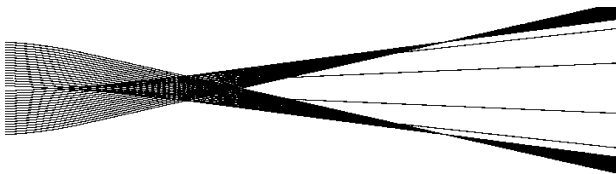
L ---|------------------Z----------------------|
Fig. 4: The picture of trajectories of a beam of ions

It is not necessary to have the extreme electric current distribution to obtain a hollow beam, satisfying the practical requirements. For real electric current distributions the annular ring will have finite thickness, and a nonzero density of particles will be inside the cavity. If real core size of the `singular' component is much smaller, than the beam diameter, then number of particles inside the cavity is negligible. Taking into account real beam phase volume leads to considerably weaker differences between the actual current distribution in the plasma lens and the ideal model introduced above. What distribution exists in reality can be estimated by comparing the characteristics of the beam obtained in the experiment with different variations of the numerical models.
Fig. 5 shows the experimental results about formation of a hollow beam of relatively small diameter, less than 1 cm.
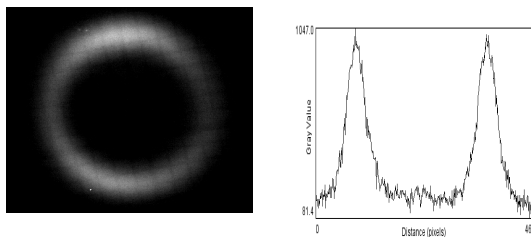
Fig. 5: Light output from scintillator and distribution of ion Fe^{+26} density at 1.7 μs after beginning of discharge at distances of 30 cm for discharge current of 150 кА. The ring diameter is 9 мм .

Our mathematical model describing the experiment gives quite similar ion beam distribution, when $Is/Io = 0.3$ (fig. 6).
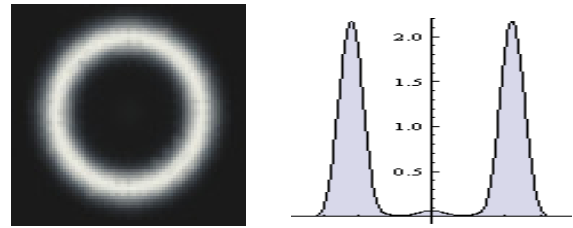
Fig. 6. The light output from a scintillator and the distribution of ion Fe^{+26} density calculated in the model approximation for the experimental condition.

FORMATION OF THE HOMOGENEOUS BEAM

Usage of ions beams for irradiation of various objects, in particular, in medical purposes, demands creation of a uniform field of an irradiation. The initial beam, as a rule, has the gaussian distribution. For alignment irradiation fields use special filters-absorbers [6]. This solution spoils however quality of irradiation fields and essentially reduces efficiency of beam. Solution of this problem is possible by means of the nonlinear focusing device. A simulation were conducted for to research opportunities of plasma lenses to solve this problem. It appears that it is possible to get uniform distribution of ion density for a case of so called 'equilibrium distribution' of a discharge current. At enough long, but quite real duration of a current pulse of <10 μs, current distribution is believed to tend to so called Bennet's distribution [7]:

$$j = I_o \,/ \pi R^2 \, (1 + (r/R)^2)^2. \qquad (8)$$

Fig. 7 shows distributions of density of ions in a beam of C^{+6} (200 MeV/n): the initial distribution and the distribution received as a result of the beam transformation in a plasma lens.
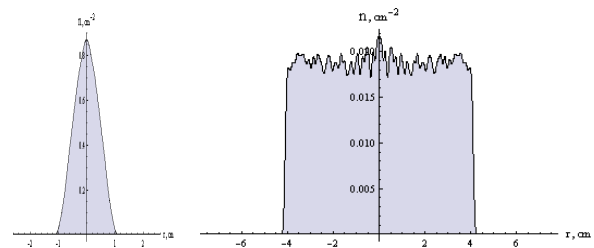
Fig. 7. The initial and transformed distributions.

Apparently, transformation can be carried out effectively, and with observance of the geometrical sizes demanded at a medical irradiation: the size of a stain and distance to it.

TWO-DIMENSIONAL TRANSFORMATION OF THE BEAM

Other possible application of a plasma lens is formation a converging conic beam by means of two plasma lens. In this case the problem of an irradiation of certain area is solved without influence in the previous zone. Fig. 8

shows results of calculations for C^{+6} (200 MeV/n) beam focused by two lenses with distributions of a discharge currents that are close to the real ones. We can see that it is possible to get a conic bunch and, as a special case, cylindrical one.
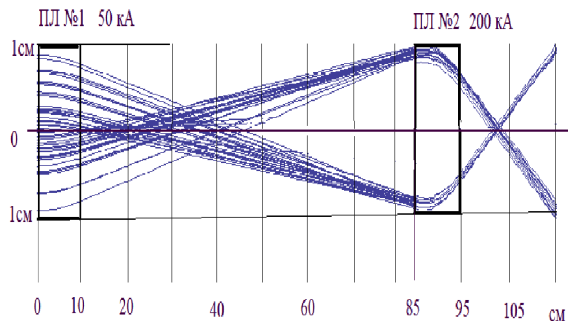
Fig. 8. Formation a converging conic beam by means of two plasma lens.

CONCLUSION

The plasma lens can carry out not only sharp focusing of ions beam with considerable reduction of their sizes. At those stages of the plasma discharge at which the magnetic field is nonlinear, formation of other interesting configurations of beams is possible.

The plasma lens provides formation of hollow beams of ions in a wide range of parameters that allows to consider it as a possible variant of a terminal lens for realization of inertial thermonuclear synthesis.

The plasma lens can be used for transformation of beams with gaussian distribution of particles density in a beams with homogeneous spatial distribution.

Application of the several plasma lenses which are in different stages of the plasma discharge, presumes to create some nontrivial spatial configurations of ions beams.

Thus, the plasma lens essentially represents the universal tool for preparation of a beams for the decision of scientific and applied technical problems.

REFERENCES

[1] D.H.H. Hoffmann et al., Nucl. Instr. Methods Phys. Res., Sect. B 161-163, p. 9, (2000).

[2] Sharkov B.Yu. et al., Nucl. Instr.Meth. A464 , p. 1-5, (2001).

[3] A. Drozdovskiy et al., European Particle Accelerator Conference EPAC'08, june, 2008, http://web.cern.ch/accelconf/

[4] A.A.Drozdovskiy e.a. INVESTIGATION OF THE FORMATION OF A HOLLOW BEAM IN THE PLASMA LENS. Internation Particle Accelerator Conference IPAC'10, june, 2010, http://web.cern.ch/accelconf/

[5] U.Neuner et al., Phys. Rev. Lett. **85**, 4518, (2000).

[6] *Haberer Th. et al.* // Nucl. Instr. Meth. A. 1993. V.330 P. 296; GSI treats cancer tumours with carbon ions // CERN Courier. V. 38, No. 9, 1998.

[7] J.D.Lawson, The Physics of Charged-Particle Beams, Oxford, 1988.

RECOVERY PROCESS STABILITY STUDY IN ENERGY RECOVERY ACCELERATOR

V.G..Kurakin, Lebedev Physical Institute, Moscow, Russia.

Abstract

Energy recovery technique in rf accelerator based applications allows to save rf power and reduce radioactive background as well. In this operation mode used beam is directed back to the accelerator in decelerating rf phase where it returns back its kinetic energy to rf field. Thus, rf generator that feeds linac covers cavities walls rf losses only and those part of beam kinetic energy that used for useful effects production as well. The sum of three fields – induced in the linac by an external rf source, accelerated and decelerated beams – determines energy and phase of the beam at linac exit, and together with beam return path optics amplitude and phase of decelerated bunches and hence third component of mentioned sum. In the case of positive sign of this feedback and sufficient amplification in the closed loop just described instability takes place.

The main equations that determine beam-rf cavity interaction in energy recovery rf accelerator are derived, single mode approximation being used. Expressions for small deviation from steady state are obtained followed by stability analysis. Results of calculations for increments of instability are presented and discussed.

INTRODUCTION

In some electron accelerator applications, only small fraction of kinetic beam energy is used, high brightness light sources of the next generation and free electron lasers being the typical examples. Keeping in mind large value of the beam energy in similar applications (it may be as large as hundreds megawatts) very fruitful idea to recover beam energy is widely discussed and already used in all over the world [1,2,3]. In recovery process used beam is guided back to the same accelerator in decelerating phase and for this reason reduces its kinetic energy along the accelerator. In other words, accelerated and decelerated bunches are spaced by half period of rf field, and in the case of lossless beam recirculation the first harmonic of total current is equal to zero and the total radiation field is equal to zero as well. The question arises whether the recovery process just described is stable in the sense that small perturbations of steady state result in such behaviour of the system that such perturbations tend to zero with the laps of time. Among the many one mechanism of feed back in the system beam – cavity may take place. Any change in beam energy results in phase shift of decelerated bunches if the longitudinal dispersion of return path is not equal to zero. This phase shift in turn results in phase shift of the voltage induced by decelerated bunches in accelerating cavity and thus in amplitude and phase of the total voltage at accelerating gap changing and as the result in energy changing acquired by the accelerated bunches. This feed back may

result in instability in the case of its positive sign and sufficient amplification in the closed feed back loop.

Following is quantitative analysis of the processes just described. Single mode approximation is used in beam-cavity interaction equations. We limit ourselves by linear approach in stability analysis.

THE EQUATIONS OF BEAM-CAVITY INTERACTION

Fig.1 represents the main features of energy recovery linac. Electron beam from injector directed into the main accelerator consisting of rf cavities. Being accelerated electron bunches are rotated by two arcs consisting of bending magnets and entered the same linac in decelerating phase. Thus, electron bunches in two beams are shifted by the angle close to 180 degrees to each others.
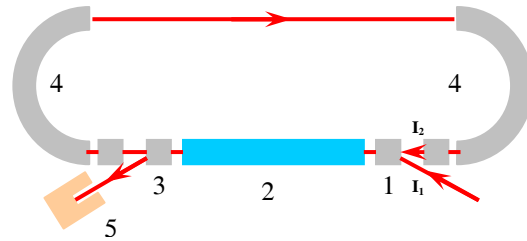
Fig.1. General layout of energy recovery linac. 1– magnet inflector, 2– main linac, 3 – magnet deflector, 4 – bending magnets, 5 – beam absorber.

While passing the main linac in decelerating phase the secondary beam looses its energy and with the help of deflector at the linac exit leaves accelerator and is directed into the beam absorber. In analysis that follows we will assume all voltage and currents being time dependent as complex exponent function $\exp(i\omega t)$ with the appropriate amplitudes which are slow functions of time t. Fig.2 represents these values on complex plane.

According to the superposition principle the total voltage $\hat{U}_\Sigma(t)$ at cavity gap is equal to the sum of three voltages – the first one $\hat{U}_e(t)$ excited by the external rf generator, while the second $\hat{U}_1(t)$ as well as the third one $\hat{U}_2(t)$ induced by the accelerated and decelerated beams:

$$\hat{U}_\Sigma(t) = \hat{U}_e(t) + \hat{U}_1(t) + \hat{U}_2(t), \qquad (1)$$

where t stands for time and "hat" symbols above letters denotes complex values. The primary (being accelerated) beam energy gain in the main linac is:

$$E = eU_\Sigma \cos(\psi) = \mathrm{Re}(e\hat{U}_\Sigma) \qquad (2)$$

Here U_Σ, ψ stand for the amplitude and the phase of accelerating voltage and Re means real part. To simplify calculations, here and in the formulae followed all voltages are understand as energies acquired by unit charge after cavity passage.
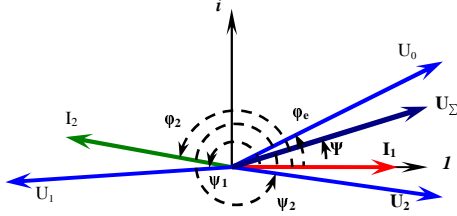
Fig.2. Voltages and currents on complex plane. I_1-accelerated beam, I_2-decelerated beam, U_0-the voltage induced in cavity by external rf generator, U_1-the voltage induced by accelerated beam, U_2-the voltage induced by decelerated beam, U_Σ-total voltage at the cavity gap.

It follows from cavity excitation electrodynamics that:

$$\frac{d^2 u}{dt^2} + \frac{\omega_0}{Q}\frac{du}{dt} + \omega_0^2 u = -\frac{\omega_0 R}{Q}\frac{dJ}{dt} \qquad (3)$$

Here $u(t)$ stands for voltage of the accelerating mode, Q are cavity quality factor, J is the first harmonic of the accelerated current, ω_0 is the cavity eigen frequency

$$Q = \frac{Q_0}{1+\beta}, \; R = \frac{R_0}{1+\beta} \; , \qquad (4)$$

where R_0 is cavity shunt impedance and β is cavity coupling coefficient respectively.

Representing beam current and induced field in the form

$$J(t) = I(t)\exp(i\omega t), \, u = U(t)\exp(i\omega t) , \qquad (5)$$

where $I(t), U(t)$ are slow functions of time one arrives to the end at the differential equation for complex amplitudes:

$$\frac{dU}{dt} + (\frac{\omega_0}{2Q} + i\Delta\omega)U = -\frac{\omega_0 R}{2Q}I \; . \qquad (6)$$

While deriving this equation we neglect the terms which are small sufficiently compared to the remaining in (6).

STABILITY ANALYSIS

We will carry out stability analysis in linear approximations. It follows from (6), that

$$\frac{d\Delta\hat{U}}{dt} + (\frac{\omega_0}{2Q} + i\Delta\omega)\Delta\hat{U} = -\frac{\omega_0 R}{2Q}\Delta\hat{I} \qquad (7)$$

where Δ means small deviation from steady state. As it has been declared in introduction we study beam phase –

cavity voltage instability mechanism and for this reason we assume that

$$\Delta\hat{I}_2 = \Delta(I_2 \exp(i\varphi_2)) = iI_2 \exp(i\varphi_2)\Delta\varphi_2 \qquad (8)$$

where I_2 and φ_2 are the amplitude and the phase of the decelerated electron bunches at the accelerator entrance. In the analysis followed these are assumed be constants, while $\Delta\varphi_2$ is a function of time. The deviation of φ_2 originates from the energy deviation ΔE at the accelerator exit followed by subsequent return path changing due to longitudinal dispersion:

$$\Delta\varphi_2(t) = \frac{2\pi\alpha L}{\Lambda}\frac{\Delta E(t-T)}{E} \qquad (9)$$

The arguments values in formula (9) reflect the fact that there is the delay T between energy changing and following appropriate phase shift of the secondary bunches. Here T is revolution period, α, L, Λ are momentum compaction factor, magnetic arcs length and accelerating voltage wavelength respectively.
As it follows from (1) and (2)

$$\Delta E = e\,\mathrm{Re}\,\Delta(\hat{U}_e + \hat{U}_1 + \hat{U}_2) = e\,\mathrm{Re}(\Delta\hat{U}_2) \quad (10)$$

The equations (7), (10) and (10) determine the behavior of the system under discussion for small deviation from steady state. These have to be rewritten in real representation for following analysis:

$$\Delta\varphi_2(t) = \frac{2\pi\alpha L}{\Lambda}\frac{\Delta E(t-T)}{E} \qquad (11)$$

$$\frac{d\Delta U_{2x}}{dt} + \frac{\omega_0}{2Q}\Delta U_{2x} - \Delta\omega\Delta U_{2y} = \sin\varphi_2 \frac{\omega_0 R}{2Q}I_2\Delta\varphi_2 \quad(12)$$

$$\frac{d\Delta U_{2y}}{dt} + \frac{\omega_0}{2Q}\Delta U_{2y} + \Delta\omega\Delta U_{2x} = -\cos\varphi_2 \frac{\omega_0 R}{2Q}I_2\Delta\varphi_2 \quad (13)$$

$$\Delta E = e\Delta U_{2x} \qquad (14)$$

Normalising all voltages by the amplitude U_Σ we have the following system after simplifications:

$$\frac{d\Delta u_{2x}}{dt} + \frac{\omega_0}{2Q}\Delta u_{2x} - \Delta\omega\Delta u_{2y} = A\sin\varphi_2\Delta u_{2x}(t-T) \quad (15)$$

$$\frac{d\Delta u_{2y}}{dt} + \frac{\omega_0}{2Q}\Delta u_{2y} + \Delta\omega\Delta u_{2x} = -A\cos\varphi_2\Delta u_{2x}(t-T) \quad (16)$$

$$A = \frac{\omega_0 R}{QU_\Sigma}I_2\frac{\pi\alpha L}{\varepsilon\Lambda} \qquad (17)$$

Hear $\Delta u = \Delta U / U_\Sigma$ for all indexes, $\varepsilon = E / eU_\Sigma$ and $\Delta\varepsilon = \Delta E / eU_\Sigma$. We will find solutions of the system (15)-(17) in the form exponential dependence of the variables. Substituting $\Delta u_{2x} = \exp(kt)$ and $\Delta u_{2y} = a\exp(kt)$ into the equations above we have:

$$k + \frac{\omega_0}{2Q} - a\Delta\omega = A\exp(-kT)\sin\varphi_2 \qquad (18)$$

$$ak + a\frac{\omega_0}{2Q} + \Delta\omega = -A\exp(-kT)\cos\varphi_2 \qquad (19)$$

The case $k = 0$ corresponds to threshold of static instability (if it takes place). Substituting this value into the system (18), (19) and resolving the system relative A one has the following expression for instability threshold

$$\frac{2\pi L}{\varepsilon\Lambda}\frac{I_2 R}{U_\Sigma}\left|\alpha(\sin\varphi_2 - \frac{2Q\Delta\omega}{\omega_0}\cos\varphi_2)\right| = 1 + (\frac{2Q\Delta\omega}{\omega})^2 \, (20)$$

For instability to take place the expression in brackets has to be positive. The instability does take place at all if longitudinal dispersion of beam return path is equal to zero or, in our notation, momentum compression factor of magnet arcs is equal to zero: $\alpha = 0$. The feed back is broken also if

$$\tan\varphi_2 = \frac{2Q\Delta\omega}{\omega_0} \qquad (21)$$

Keeping in mind that angle φ_2 (recovery angle) is close to π in energy recovery accelerator and representing this in the form $\varphi_2 = \pi + \eta$, η being close to zero, one can notice that feed back is broken when η is equal to cavity detuning angle.

If $\tan\eta > 2Q\Delta\omega/\omega_0$ the feed back becomes negative for the case $\alpha > 0$, and the static instability does not take place. But it is well known from feed back systems theory that negative in static sense feed back may become positive at definite frequency range resulting in unstable state. Let us find the solution of the system (18), (19) for $k = \text{Re}\,k + i\,\text{Im}\,k = 0 + i\Omega$ supposing zero cavity detuning. It follows from (18) that

$$\frac{\omega_0}{2Q} = A\sin\varphi_2\cos\Omega T, \; \Omega = -A\sin\varphi_2\sin\Omega T \; (22)$$

This is transcendental system relative the variables Ω and A, but simple considerations deliver us to the approximate solution

$$\Omega T \approx \frac{\pi}{2}, \; -A\sin\varphi_2 \approx \frac{\pi}{2T} \qquad (23)$$

Upper formulae determine the least roots of the system (22). It follows from (17) and (23), that instability threshold for $\alpha\sin\varphi_2 < 0$ (for zero cavity detuning)

$$\frac{2\pi L}{\varepsilon\Lambda}\frac{I_2 R}{U_\Sigma}\left|\alpha\sin\varphi_2\right| \approx \frac{\pi}{2}\frac{\tau}{T}, \qquad (24)$$

where $\tau = 2Q/\omega_0$ is cavity time constant. As compared with expression (20) instability threshold is $\frac{\pi}{2}\frac{\tau}{T}$ higher provided $\tau \gg T$, as it takes place for superconducting cavity for example.

It is worthwhile to note that instabilities just described remind those arising in racetrack microtron [4]. Mutual dependences of the kind voltage - current and injected bunches phase – current inherent to the accelerators of microtron types result in similar system behaviour.

CONCLUSION

In energy recovery rf accelerator recovered electron beam – cavity interaction takes place resulting in static or dynamics instability. The instability is coursed by mutual dependence of the accelerating voltage and the phase of bunches that entered once again the cavity to be decelerated. The instability mechanism reminds those inherent to high current racetrack microtron.

The mechanism of beam–cavity interaction just explored takes place in rf electron recirculating linac as well. Substantial difference is in shunt impedance R value for recovery and recirculating linacs. Since $R = R_0/1 + \beta$ for superconducting cavity case $R_{recirculating} \ll R_{recovery}$ for the reason that in the first case $\beta \gg 1$, while in the second case coupling is mach less (close to unity for ideal machine). That is why the threshold for beam current is shifted to mach higher value for recirculating linac.

The stability problems just described are also discussed in paper [5].

This work had been stimulated by numerous discussion concerning possible schemes of new accelerator complex realisation on the basis of superconducting cavities at Lebedev Physical Institute [6], and the author is obliged to his colleagues for these fruitful discussions.

REFERENCES

[1] U.Amaldi. Physics Letters, Volume 61B, number 3, 1976, pp. 313-315.

[2] V.E.Balakin, G.I.Budker, A.N.Skrinski. Procedings of the 6-th All union conference on charged particle accelerators, Dubna, October 11-13, 1978, v.1, pp.27-41, in Russian.

[3] ERL09 Workshop Proceedings. June 8-28, 2009. https://wiki.lepp.cornell.edu/web/bin/view/LEPP/Events/ERL09/

[4] V.G.Kurakin. High Current Racetrack Microtron as a Free Electron Laser Driver. Nuclear Instrument and Metods in Physics Research, A341(1994), pp 407-411.

[5] N.A.Vinokurov et al. Critical issues for high power FEL based on microtron recuperator/electron out coupling scheme, in Proceedings of SPIE, Vol.2988, 1997, pp. 221-231.

[6] V.G.Kurakin et al. Superconducting RF Electron Recirculator for Nuclear Physics Research at Lebedev Physical Institute, in Proceedings of the 22 Russian conference on charged particles accelerators RuPAC-2008, Zvenigorod, September 28 - October 3, 2008, pp.107-109.

A BEAM LOSS SCINTILLATOR SYSTEM FOR BACKGROUND MONITORING AT THE LHCb EXPERIMENT

V. Talanov [*], R. Dzhelyadin (IHEP, Protvino), A. Bobrov, A. Bondar (BINP, Novosibirsk),
F. Alessio, G. Corti, R. Jacobsson (CERN, Geneva), M. H. Lieng (TU Dortmund)

Abstract

The LHCb experiment at the Large Hadron Collider (CERN) has developed a complete high-speed and high-sensitivity background monitor based on a pair of plastic scintillators and a custom-made LHCb readout board to record fast LHC beam losses with time information. The system is installed close to the LHCb Vertex Locator and it has been operational since the LHC pilot run providing valuable information to the LHC Operations crew during beam commissioning and to the LHCb Control Room about the experimental conditions at the physics runs.

The system is able to record fast beam losses at a rate of 40 MHz, providing information regarding the bunch crossing of the loss and the intensity of the loss calibrated in number of Minimum Ionizing Particles. A full control and monitoring system has been developed as well within the framework of the LHCb Experimental Control System. A complete simulation of the system has been central in converting the response of the system into physical quantities.

In this paper we will describe the system in its components and functionalities, the commissioning phase, the simulation framework and the first results with real beam at the LHC.

INTRODUCTION

The Beam Loss Scintillator (BLS) detector is made of two cubic-like plastic scintillators installed 12 cm away at both sides of the LHC beam pipe on the horizontal plane, at ~ 2 m from the LHCb Interaction Point in the opposite direction to that of the spectrometer. The initial scope of the scintillators was to look at injection problems [1]. However, the opportunities of using such scintillators as a continuous detector have been exploited. It is in fact, the only instrument within LHCb which is able to measure fast losses of the beam in the experimental area. Although the instrument is not able to protect the experiment, it is however able to predict possible incidents by analyzing the behavior of the beam and the evolution of the background. Eventually the system has proved his good performance and reliability as an independent source of luminosity measurement in LHCb.

The installed system comprises two scintillators of the size $4\times4\times3$ cm^3. Each scintillator is directly attached to a PhotoMultiplier, HAMAMATSU multi-mesh R2490-05 for one side and EMI pan-type 9839A for another side. The

photocathode of each PMT is 40 mm diameter with a red light LED fast driver aside for calibration. Each scintillator itself is inserted in a steel tube and shielded against stray magnetic field. A TYVEK envelope is wrapped around each of the cubic scintillator in order to collect light. The whole tube is fixed with some rubber rings in the center of the PMT. Fig. 1 shows the position of the scintillators at the shielding wall between the LHCb Interaction Point and the accelerator tunnel.
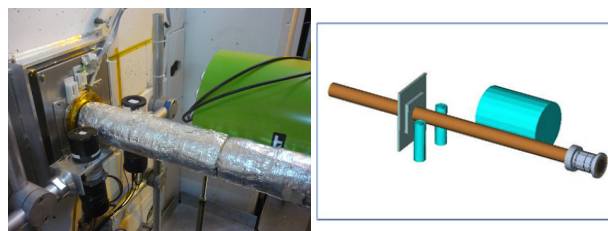
Figure 1: Left: the BLS system as installed in the LHCb cavern. The covered round pipe is the LHC beam pipe. Right: BLS model as implemented in the LHCb simulation.

The pulse generated from the PMT is then processed by an electronics limiter (LeCroy 612AM) which is able to limit the pulse between $+0.2$ and -5 V regardless of the input signal which can be as high as to -200 V. The limiter has two outputs that allow having the signal observed through an oscilloscope and a hardware readout system at the same time.

In view of the scope of the system as described earlier the readout of the BLS needs a hardware board which must be able to integrate and to read out the signal in short time scale (~ 25 ns clock cycle, 40 MHz). It is necessary to analyze the beam over a few turns (~ 5–10) at 25 ns time space just after each injection and also to monitor beam effects during a "stable" run, looking at the fine 25 ns structure of the beam. At injection, several problems — "marginal-over-injection" or "under-injection" effects, beam-beam effects (e.g. impedance effects) and misplaced bunches — can occur. It is therefore possible to predict wrong machine settings and injection timings or hardware failures. During circulating beam, misplaced bunches can surely lead to undesired effects as well as an undesired population of protons in the abort gap. LHCb is also the only detector really exposed to a possible dirty beam cleaning since the LHC betatron cleaning is located in one of the adjacent sectors.

Simulations of background estimates at injection and circulating beam are essential to know nominal rates from minimum bias p-p events and from beam halo enabling

06 Instrumentation, Controls, Feedback and Operational Aspects

to adjust the sensitivity of the instrument according to the available "dynamic range" of the readout and to set an adequate readout threshold.

THE BLS READOUT SYSTEM

In order to readout the signal generated by the scintillators complying with the requirements presented in the Introduction section, the LHCb Beam Phase and Intensity Monitor board (BPIM) has been chosen [2]. The BPIM is a custom-made board originally developed by the LHCb Online group to read out the signal generated from the beam pick-ups (BPTXs) dedicated to LHCb. Its main purpose is to measure bunch-by-bunch continuously at 40 MHz the intensity of the beam and the phase of the beam with respect to the LHC clock, allowing for a continuous monitoring of the beam. The board makes use of very fast current amplifiers and a high-performance TDC.

The board is also equipped with an ADC to digitize the analogue integration of the input pulse and an FPGA to process information and to perform online data analysis. Two FIFOs 16k deep and 16k wide will ensure an online storage of data to be retrieved by the Control System, interfaced by a server running on a Credit Card PC mounted on the board. The global LHCb bunch clock and orbit clock are fed to the board. This allows the board to identify a loss with a particular BXID. The system is aligned to the whole LHCb. The board has two general purpose ECL outputs and one general purpose 8-bit LVDS output that can be connected to the LHCb Readout Supervisor. A TTL input allows having a generic input to trigger the readout externally.

Two types of processing modes have been identified for the readout of the system:

- *Triggering on injection mode*: in this mode the BLS is triggered by an external pulse. This is the preferred mode during injection, where an LHC pre-pulse is transmitted to each board and each board records losses for more than 15 turns at 40MHz. This allows having a fine structure of the losses around the injection line.

- *Continuous readout mode*: each board continuously looks at losses measured by the scintillators. If a loss is above a programmable threshold, a running sum of 12 BXID is performed. In this mode, a full 25ns structure of each loss is recorded and the worse loss every 5 seconds is transmitted to the LHC and LHCb control room as a background estimation number.

BLS AND BACKGROUND ANALYSIS

The BLS system is not able to protect the machine from beam accidents since it is not connected to a hardware beam dump. It is however the only instrument able to observe fast losses from the beam in the LHCb experimental area whose information can be correlated with other instruments and with the detector data taking.

In the framework of a background study at the LHC, background protection and beam analysis, the LHCb experiment is publishing a series of background numbers BCKG 1-2-3 which correspond to different measurements of beam losses around the LHCb Interaction Point. BCKG1 value gives a measurement of normalized losses in the inner region of the detector, BCKG2 gives a measurement of normalized beam halo and BCKG3 gives the fraction of measured losses compared to the experiment abort threshold (so-called Dump threshold). BCKG1 and BCKG3 are constantly provided by the Beam Conditions Monitor (BCM) [3] and are the normalized (to a maximum scale of 100) measurements of beam losses respectively over 80 μs and 1280 μs and averaged over the upstream and downstream BCM stations. BCKG2 is provided by the Beam Loss Scintillator system themselves and the measurement is normalized to the beam energy in MeV and to a scale of 0–100.

RESULTS AND PERFORMANCE WITH THE FIRST LHC BEAMS

The Beam Loss Scintillator system was extensively used during first LHC beams. It was used during the commissioning of the LHC transfer lines (injection lines) for single bunch high intensity injection, multi bunch injection and trains injection, during the commissioning of the first LHC circulating and colliding beams and it is continuously used during the period of circulating beams at the LHC.

LHC Injection lines studies

Feedback to the machine was given in order to improve the settings of the injection line and to minimize beam losses around the experimental area. The background estimation was performed together with the BCM in order to cover a very large range of losses. When the losses are high, the BLS system tends to reach the saturation and the BCM becomes a more precise instruments. The two systems together exploit the full range of losses from small and fast ones (BLS) to large and accumulated ones (BCM). An example of how losses look like at injection around the LHCb experiment is provided in Fig. 2.

Background measurements

The BLS system is used for background estimation at LHCb. In particular the BLS provides the LHC machine with an estimation of the BCKG2 number which gives an indication of fast losses around the LHCb Interaction Point. This number has been decided to be calculated as the averaged loss of the two highest independent losses as detected by the two BLSs every 5 seconds.

Abort gap monitoring

By construction of the LHC machine, before each first bunch in each beam (Bunch ID = 1), there should be a 3 μs gap where no protons should be present. This gap is called

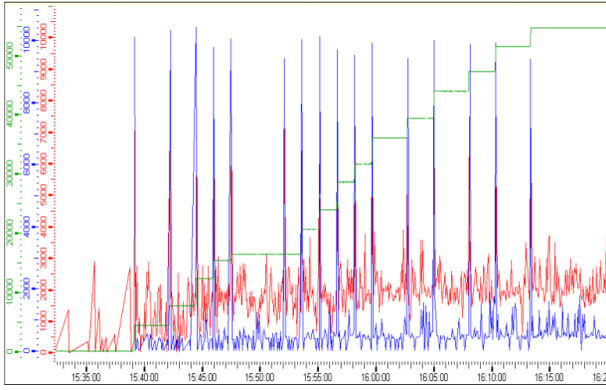06 Instrumentation, Controls, Feedback and Operational Aspects

Figure 2: The BLSs show a typical structure of losses during injection of high-intensity multi-bunch in the machine. At each step an increase in beam intensity (green line) corresponds to a loss as measured by the BLS. The X axis shows time, on the Y axis are ADC counts in a.u.

abort-gap. For the LHCb purposes, the BLS provides a continuous monitoring of this gap, looking for possible distribution which could arise during periods of beam.

Independent luminosity measurement

The BLS system is extremely sensitive to colliding beams due to its position within the LHCb detector. By definition, such device can be used as a luminometer in order to obtain an LHCb-independent measurement of luminosity, pileup corrected.

The cross-section of the BLS system, expressed in μb, is calibrated with the LHCb L0CALO trigger rate, whose cross-section is known to a precision of about 10% from Monte-Carlo simulations. The BLS cross-section can be therefore expressed as a function of the HV chosen and the ADC internal threshold in the readout board and it is automatically changed whenever the two parameters are changed. Considering these two parameters, the cross-section can then vary between 50% and 90% of the LHCb cross-section. The BLS as a luminometer is used as the official online luminosity measurement during collisions whenever the L0CALO trigger is not running.

Moreover, thanks to the 40 MHz readout capabilities of the readout board, the BLS is the only system in LHCb which is able to measure online luminosity per bunch. This allows the experiment and the machine to study possible beam-beam effects for colliding bunches at the LHC and therefore exploit possible drop in luminosity or background increase around the LHCb Interaction Point. This information is constantly fed back to the machine coordinators for complementary studies.

THE BLS SIMULATION

Simulations of the BLS response to estimate the signal rates were performed for various conditions of the machine operation, to determine the BLS settings. The BLS geom-

etry and material description, shown in Fig. 1, has been introduced in the common detector description database of the LHCb experiment. Dedicated algorithm and monitoring package have been written within the framework of the LHCb simulation application [4] based on Geant4 [5]. A digitization algorithm to produce the same signal from the BLS as the readout system is in preparation.

A couple of examples of the BLS simulation for the case of the p-p events in the IP at 450 GeV are given in Fig. 3. The figure on the left shows the distribution of the energy deposited per event in one of the two scintillators — a clear one MIP peak around 7 MeV is observed. The figure on the right shows the hit distribution vs. time, demonstrating that that most of the particles cross the BLS 7–8 ns after the collision takes place in the Interaction Point.
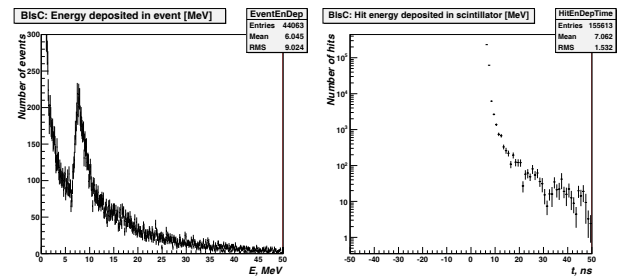
Figure 3: LEFT: Total energy deposited, MeV, in one BLS in the p-p event, RIGHT: Time profile of energy deposition.

CONCLUSION

LHCb has developed a complete system for beam and background monitoring at the LHC. The core of the system is a pair of scintillators with high speed and precision readout electronics. This system was initially intended to only look at fast losses during injection, while other uses of the system were exploited. The performance of system with the first LHC beams providing valuable information for background estimation, injection losses and behavior of the beam was described, and the results of the BLS response simulation were presented.

REFERENCES

[1] R. Dzhelyadin, "The injection beam monitor counter", EDMS document 935193, CERN, Geneva, 2010.

[2] F. Alessio et al, "A complete system for controlling and monitoring the timing of the LHCb experiment", CERN-THESIS-2008-007, Torino Univ., 2008.

[3] C. Ilgner et al, "The Beam Conditions Monitor of the LHCb Experiment", arXiv:1001.2487.

[4] The LHCb Collaboration, "LHCb Computing: Technical Design Report", LHCC 2005-019, CERN, Geneva, 2005.

[5] The Geant4 Collaboration, "Geant4 Developments and Applications", IEEE Transactions on Nuclear Science 53 No. 1 (2006) 270–278.

06 Instrumentation, Controls, Feedback and Operational Aspects

STUDY OF THE INR RAS LINAC PULSED DUOPLASMATRON

A. S. Belov, O. T. Frolov, E. S. Nikulin, V. N. Zubets and V. P. Yakushev, INR RAS,
Moscow, 117312, Russia

Abstract

Results of numerical simulation and experimental study of hydrogen ion beam from a pulsed duoplasmatron with different plasma expansion cup geometry are presented. Intensive oscillations of hydrogen ion beam current with frequency of ~ 1 MHz and amplitude up to 70% from maximum value (~ 100 mA) of ion current were observed with plasma expansion cup of different shape. It was found by direct measurements that these oscillations are formed during plasma transport through the expansion cup. Noiseless mode of operation for the pulsed duoplasmatron has been obtained with a plasma expansion cup of new design. Results of measurements of current and emittance of the hydrogen ion beam are presented

INTRODUCTION

A duoplasmatron-type ion source initially developed at NIIEFA [1] is used for injector of linear accelerator of INR RAS. The ion source has pulsed mode of operation with repetition rate of 50 Hz, pulse duration of 200 μs and pulsed ion current of 50-120 mA. During several years we study the ion source with goal to improve its reliability and increase of brightness of ion beam produced [2]. Initially, ion beam formation system of the duoplasmatron consisted from cylindrical plasma expansion cup 60 mm in diameter and gridded extraction electrode. The grid of the extraction electrode has been made from tungsten-rhenium wires 0.1 mm in diameter [1]. Hydrogen ion beam with pulsed current up to 200 mA has been obtained with this beam formation system. However, significant sputtering of the wires of the grid by beam ions has been observed after long term operation of the ion source. Relative brakes of the wires occurred which reduce reliability of the ion source. Deformation of the grid was arisen also due to its heating by the ion beam.

Additionally, significant unavoidable emittance growth of the ion beam occurred in electric field of the grid cells. This is why several gridless ion beam formation systems were used after that. The gridless ion beam formation system had high reliability and produce formation of hydrogen ion beam with relatively small normalized emittance of 0.1 π cm mrad (for 67% of ion beam current) [2]. However, ion beam obtained with the gridless ion beam formation systems had "noise" (~ 1 MHz oscillating component) which reached in some cases 70% of average value of the ion beam pulsed current. The "noise" appearance was not controlled completely by parameters of the duoplasmatron discharge and extraction voltage. Some measurements were performed to determine the "noise" origination. Then a new ion beam formation system has been developed and tested. With this beam formation system the duoplasmatron produces "noiseless"

hydrogen ion beam. Results obtained are outlined in the paper.

STUDY OF "NOISE" ORIGINATION

It was shown by direct measurements that oscillations of the ion beam current are arisen in a plasma expansion cup. Initially, total ion flux emitted from anode orifice to expansion cup has been measured. For that, a flat collector 38 mm in diameter was installed at distance of 16 mm from the anode orifice. The collector was biased by negative potential of ~ 200 V relative the anode to suppress electrons from plasma to come to the collector. The total ion flux current of 350-530 mA was recorded for the duoplasmatron discharge current of 30-50 A respectively. It was found that the ion flux current was noiseless, what means that the "noise" originated downstream the anode emission orifice. Then the ion beam current has been recorded immediately downstream the beam formation system by Faraday cup with suppression of secondary electrons and simultaneously ion beam current to the extraction electrode of the beam formation system has been recorded. It was found that oscillations already exist and that oscillations of ion beam current and of ion current to the extraction electrode are in the same phase. This result shows that oscillations of ion flux at emission plasma surface of the expansion cup are already existed. Thus, it was found that ion current oscillations arisen in the plasma expansion cup. A new ion beam formation system has been developed then with goal to eliminate the "noise" origination.

A NEW ION BEAM FORMATION SYSTEM

Extensive simulations of ion beam extraction from ion source and the ion beam transport in the proton injector were performed to optimize geometry of the ion beam formation system. Program code TRAK of Field Precision LLC [4] has been used for the simulations. The code makes possible simulation of a self-consistent emission plasma boundary of ion sources and ion beam transport with space-charge.

The new ion beam formation system designed is shown in Figure 1. A flat grid made of tungsten wires 0.1 mm in diameter is installed at output of the plasma expansion cup of the beam formation system. Diameter of the emission surface is 30 mm. A plasma electrode of the expansion cup has quasi-Pierce geometry (see Figure 1) with angle 23° relative to the emission grid surface for diameters between 30 and 40 mm. This allows to obtain flat surface of plasma with flat grid by respective choice of extraction voltage for given plasma ion flux and to minimize effective emittance growth connected with initial focusing of ions by curved emission plasma surface

at the grid cells. The plasma electrode has angle 35° relative to the emission grid surface for diameters from 40 mm to 65 mm to ensure additional focusing of the ion beam in the extraction gap. The extraction gap has shape of cuted cone with angle relative to system axis of 45°. The ion beam extracted is focused downstream into the accelerating tube by application of varied potential to a focusing electrode (see Figure 1).
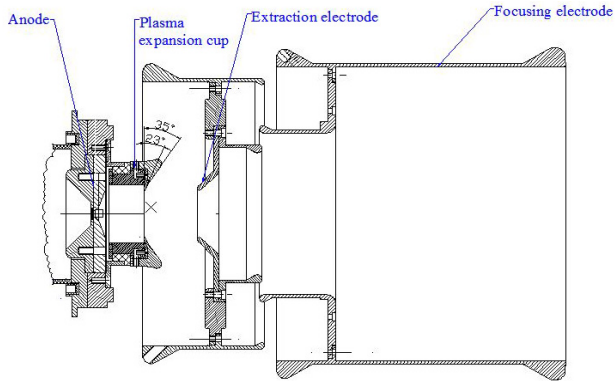
Figure 1: The ion beam formation system of the duoplasmatron.

It is worth noting that installed in the present ion beam formation system plasma electrode grid is sputtered and heated by ions in significantly less degree in comparison with system, where the grid is installed in the extraction electrode because of ions in plasma have average energy of order of 10 eV while accelerated in the extraction gap ions have more than three order of magnitude larger energy (20-40 keV).

Results of ion beam simulation with TRAK code for the ion beam formation system described are shown in Figures 2, 3.
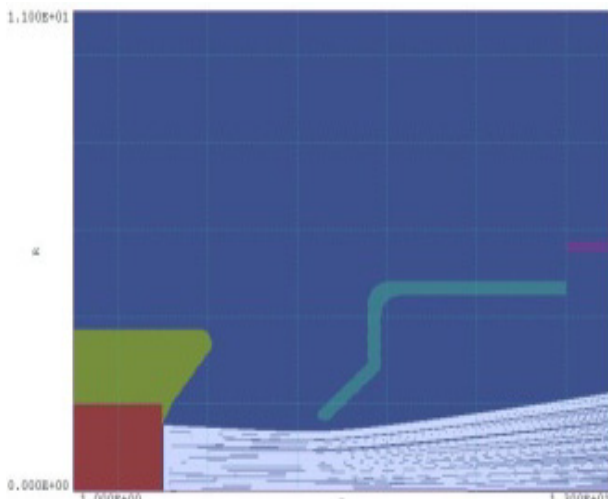
Figure 2: Results of an ion beam simulation with TRAK code. Ion beam trajectories in the beam formation system for extraction voltage of 25 kV and ion beam current of 100 mA.
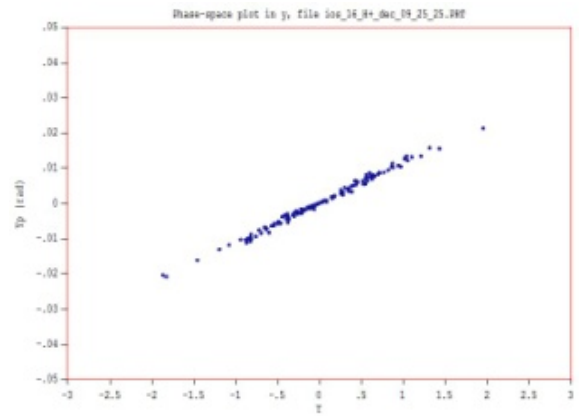
Figure 3: Results of an ion beam simulation with TRAK code. Phase space portrait of the ion beam at distance of 200 cm from the accelerating tube output.

The results show that with the given ion beam formation system aberration free ion beam extraction, acceleration and transport are achieved for an ion beam pulsed current of 100 mA. Thus the goal of the system numerical optimization is achieved.

RESULTS

The ion beam formation system described above has been incorporated into the duoplasmatron in October of 2009. The proton injector operated in five linear accelerator runs during 2009-2010 years with pulsed current at the injector output of 80 mA and repetition rate of 50 Hz. Total duration of the duoplasmatron operation since then was 1500 hrs without any failures. Evidence for sputtering or deformation of the plasma grid were not observed.

Hydrogen ion beam with pulsed current up to 180 mA has been obtained with the new ion beam formation system and recorded downstream the duoplasmatron by a Faraday cup with suppression of secondary electrons. Typical ion beam current at the injector output used for operation with linac was 80 mA. Oscillograms of the ion beam at the injector output with previous gridless ion beam formation system and with new one are shown in Figure 4a,b.

a   b
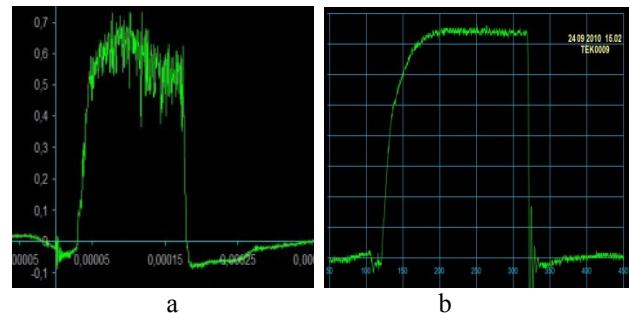
Figure 4: Oscillograms of the ion beam at the injector output, a) gridless ion beam formation system b) new ion beam formation system

The ion current has been recorded by a beam current transformer at the injector output.

Emittance has been measured at the injector output for the hydrogen ion beam with energy of 400 keV. The emittance measuring device is described in [2] and is based on "slit-slit" method. Normalized emittance of the ion beam was measured to be 0.076 π cm mrad for 63% of the total current and 0.2 π cm mrad for 90% of the total ion beam current. Typical phase space portrait measured is shown in figures 5. Percent part of the ion beam inside the given phase-space area is shown in figure 6.
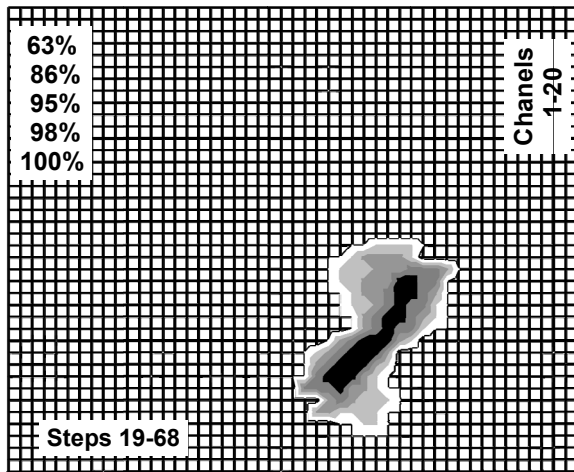
Figure 5: Phase-space portrait of the hydrogen ion beam at output of the proton injector. Ion beam energy is 400 keV, ion beam current is 85 mA. Horizontal scale is 2 mm/div and vertical scale is 2 mrad/div.
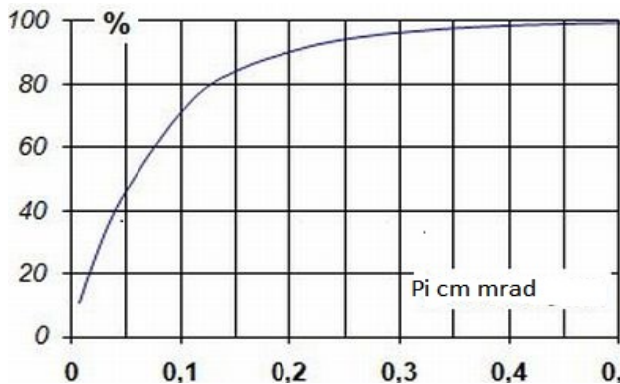
Figure 6. Percent part of the hydrogen ion beam (vertical) inside the given phase-space area (horizontal). 90% of total ion beam current is inside phase-space area of 0.2 π cm mrad.

CONCLUSION

It is shown in the present paper that oscillations of ion beam current from a duoplasmatron with typical frequencies of ~ 1 MHz which exist at some conditions are arisen in a plasma expansion cup of the duoplasmatron. Noiseless mode of the duoplasmatron operation has been obtained with the new ion beam formation system. Hydrogen ion beam with a typical pulsed ion beam current of 80 mA and normalized emittance of 0.2 π cm mrad for 90% of total ion beam current has been obtained. The duoplasmatron with these parameters of the hydrogen ion beam has been used in the INR RAS linear accelerator runs demonstrating high reliability and stability of the ion beam.

REFERENCES

[1] M. A. Abroyan et al., Duoplasmatron parameters for Optimum positive or negative ions Yield, Particle Accelerators, 1971, v.2, #2. p. 133.

[2] V. I. Derbilov et. al., Proc. of the XV International Conf. ESACCEL 2003, Obninsk-2007, p. 204-210.

[3] V. I. Derbilov et. al., Probl. of Atomic Science and Technology, Series "Nuclear Physics Investigations", (42), 2004, #1, pp 13-15.

[4] www.fieldp.com

06 Instrumentation, Controls, Feedback and Operational Aspects

SCRF DEVELOPMENT AT TRIUMF

V. Zvyagintsev, R.E. Laxdal, B. Amini, C. Beard, R. Dawson, T. Emmens, K. Fong, A. Grasselino,
P. Harmer, D. Kishi, P. Kolb, A. Koveshnikov, D. Lang, M. Laverty, R. Leewe, C. Laforge,
D. Longuevergne, M. Marchetto, A.K. Mitra, T. Ries, I. Sekachev, R. Shanks, B. Waraich, F. Yan,
Q. Zheng, TRIUMF, Vancouver, Canada
R.S. Orr, W. Trischuk, University of Toronto, Ontario, Canada
R. Edinger, PAVAC Industries, Richmond, Canada

Abstract

TRIUMF started SCRF development with the superconducting heavy ion linear accelerator project, ISAC-II, in 2000. Since that time much work has been completed for development, prototyping and testing. The ISAC-II project was successfully completed and we now have in operation 40 superconducting bulk Nb QWR cavities assembled in eight cryomodules. The last twenty cavities, just completed, were produced by PAVAC Industries Inc. of Richmond BC; the first superconducting accelerator cavities produced in Canada.

In 2007 TRIUMF started development towards a 50MeV electron superconducting linear accelerator to be used as a driver to produce radioactive ion beams through photofission. The accelerator is based on TTF/ILC elliptical bulk Nb cavities technology.

Results, experience and plans of the SCRF program at TRIUMF will be discussed.

INTRODUCTION

Motivation for SCRF development at TRIUMF was the ISAC-II heavy ion accelerator project started in 2000 and required 20 106MHz medium beta (5.7 and 7.1%) and 20 141MHz high beta (11%) superconducting QWR cavities which provide an accelerating voltage of 40MV. Medium beta cavities were developed in collaboration with LNL and fabricated by Zanon (Italy). Five cryomodules with these cavities were successfully commissioned for operation in April 2006 [1]. High beta cavities were developed at TRIUMF and produced by PAVAC Industries in Canada. Three cryomodules with high beta cavities were successfully commissioned in April 2010 [2]. An SCRF infrastructure for SC

Figure 1: TRIUMF SCRF infrastructure
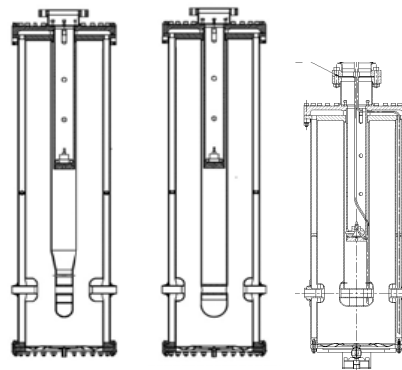
Figure 2: ISAC-II β =5.7,7.1 and 11% cavities

development including SCRF test area, clean room and chemical laboratory (Fig. 1) was created at TRIUMF.

In 2007 TRIUMF has embarked on a 1.3GHz development program to support the construction of a 50MeV 10mA e-Linac for the production of radioactive ion beams through photo-fission. A prototype cryomodule and 9 cell cavity are in conceptual design. Two copper and two niobium single cell test cavities were fabricated, and one copper model of 7 cell cavity is in fabrication at PAVAC Industries.

ISAC-II RESULTS

ISAC-II commissioning and operation results [3] provide an example of bulk Nb QWR cavities in cryomodules with common vacuum. The cavities (Fig.2) are patterned after ALPI INFN-LNL are based on a coaxial line with inner and outer conductors with diameters of 60 and 180mm. The difference between the cavities is in the beam tube region of the inner conductor. The round inner conductor shape of the beta 7.1% 106MHz is modified by squeezing to attain the 5.7% beta cavity. To provide the structure with optimum beta of 11% we went to 141MHz with corresponding decreasing of cavity length. A beam tube is added to improve the transit time factor. All cavities are specified for CW operation at 7W power dissipation with acceleration voltage 1.08MV corresponding to 30MV/m electric and 60mT magnetic peak field. Tuning of the cavities is provided with deformation of Nb plates bolted to the bottom flange. A mechanical damper installed inside of the inner conductor provides >10dB attenuation of microphonics noise. The cavities operate in strong overcoupled regime (coupling ~50-100) to provide enough bandwidth to maintain stable

07 Accelerator Technology Main Systems
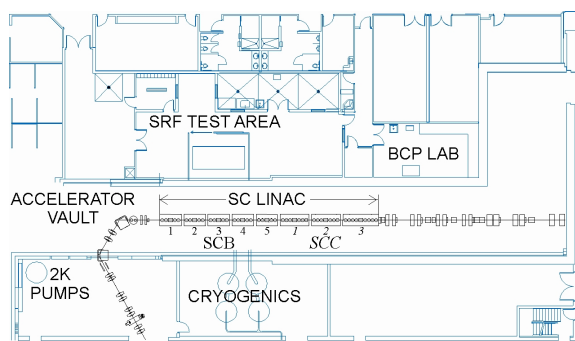
operation from microphonics. The LN2 cooled coupling loop produces <0.25W power dissipation in helium system at 200W forward power. One 9T superconducting solenoid is installed in the middle of each of the eight cryomodules in close proximity to the cavities.

Medium Beta Part (Phase I)

The performance of the SCB cavities is monitored periodically typically during start-up after shutdown (Fig. 3). The linac is warmed up once per year for three months as part of the site maintenance shutdown. In addition several of the cryomodules have been vented (SCB1 for pump replacement) and some have been taken off line (SCB2 and 4) for disassembly to repair internal faults of the coupler loop mechanical joint.

The cavities were tested in a single cavity test cryostat with average result at 7W power dissipation of Ep~37MV/m. After installation in the cryomodules average cavity performance degraded by 10% and is of Ep~33MV/m. Possible reason could be cavities contamination during cryomodule assembling. Individual cavity performance does vary somewhat but the average gradient has been maintained over four years of operation.

In 2010 we lost one cavity#11 (in SCB3 cryomodule) due to failure of the inner coupler cable connection. We already had such a problem in this cryomodule for cavity#9 in 2005 (it was 1st cryomodule in production).

Cavity#5 and #9 have custom frequency compensation puck welded to tuning plate. These cavities after experimental electro-polish had too high frequencies. Compensation puck shifts the cavity frequency down ~100kHz and cause ~30% current density increase in the tuning plate bolted contact.

During operation cryogenics failures caused cavity recoverable degradation.

- Trapped magnetic flux from short interruption of LHe supply [4]. Full recovery (~two hours activity) involves degaussing the solenoid and environs, then warming cavities and solenoid to 30K to quench all solenoid currents, then recooling the cold mass.
- Q-disease due to long interruption of LHe supply. Full recovery requires cavity warmup to room temperature.
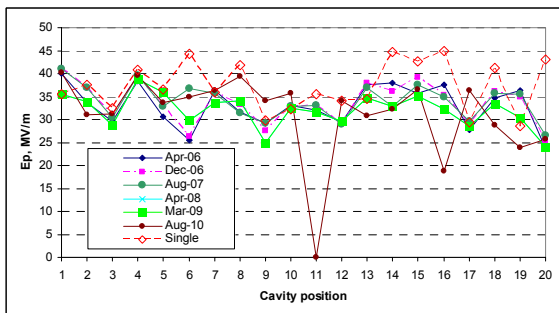
Figure 3: SCB cavities performance at 7W power dissipation over 4 years

Low level multipacting in some cavities is responsible for delay of start-up and tuning. It is three orders of magnitude less than the operational field level and doesn't

affect performance. Short pulse RF conditioning is required to start these cavities. Multipacting disappears during cavity operation and reappears after warmup.

The Phase I system uses tube amplifiers and they have been a source of downtime due to tube aging issues causing phase drift and non-linear output affecting LLRF operation. Average tube lifetime is about 10,000 hours.

High Beta Part (Phase II)

After testing of two prototype cavities in 2007 another
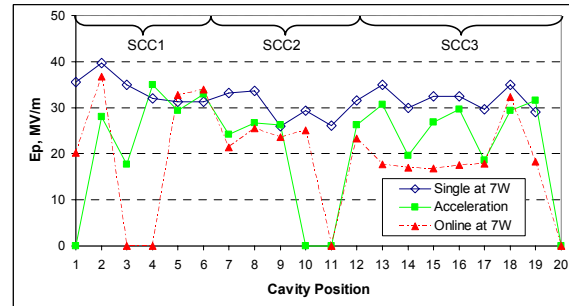
Figure 4: SCC cavities performance in single tests at 7W, 1st acceleration and current 7W levels

20 cavities were ordered from PAVAC in 2008 [5]. Four cavities were rejected due to vacuum leaks that opened in the donut weld after a final BCP of 100μm. Due to the tight schedule we limited BCP (in the beam tube region) to 60μm on subsequent cavities. All leaking cavities were successfully repaired and tested. Due to tight schedule another four cavities were installed in cryomodules without single cavity cryostat tests: three cavities were tested offline in the cryomodule SCC2 and one was installed without any test.

Fig.3 is presenting SCC cavities performance in single (offline) tests, during 1st acceleration commissioning run and recent online performance at 7W power dissipation. Average field in offline tests is 32MV/m, ~15% below Phase I performance. We speculate that this is due to the reduced etching in Phase II. The performance decreased online to 27.6MV/m, a reduction of 16%. The degradation reasons are still under investigation.

- Contamination during installation
- Q-disease. Tests show that SCC cavities start degrading performance after 1h in the range of temperatures 200-100K, for SCB cavities it occurs after 10h. It could be due to higher hydrogen content in the Nb.
- Surface pollution during rf processing
- Trapped flux due to local magnetic field penetration

We started a loop study with two spare SCC cavities to investigate the reasons of degradation and to find the ways to improve the performance [6].

During the SCC cryomodules commissioning we lost four cavities due to failure of coupler inner lines. Indirect data (TDR measurement and vacuum burst during the accidents) show that there are RF shorts formed due to breakdown in the cables. We will work on it during next

shutdowns. Since every cavity has an independent RF system, we can compensate the performance of the unavailable cavities by increasing the gradient in other cavities (at power dissipation >7W).

The solid state amplifiers work well and are more stable than SCB tube amplifiers.

SCRF DEVELOPMENT FOR ELECTRON LINAC PROJECT

In 2007 TRIUMF started developments toward an electron driver for photofission (Fig. 5) which will be independent and complementary to the 500MeV cyclotron. The linac is composed of five 9 cell elliptical cavities at 1.3GHz in 3 cryomodules with final goal by 2017 of 50MeV/10mA, 0.5MW beam power, CW operation [7].

Injector cryomodule (ICM) is under design in the collaboration with VECC (India).

The core of the driver is a 9 cell TESLA type cavity with two symmetrically opposed CPI couplers (Fig.6) and should provide at 2K nominal acceleration gradient 10MV/m in CW operation. The cavity is under development and study for higher order mode (HOM) estimations. Future developments may include a recirculating ring so that beam break-up (BBU) is also under study.
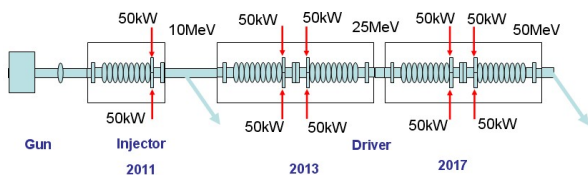
Figure 5: 50MeV e-LINAC layout

PAVAC has produced two copper and two Nb single cell test cavities. In collaboration with University of Toronto the cryostat for vertical tests of 1.3GHz elliptical cavities has been built and tested. Fig.7 shows recent results of the single cell cavity vertical tests at 4 and 2K. There is some improvement in comparison with previous
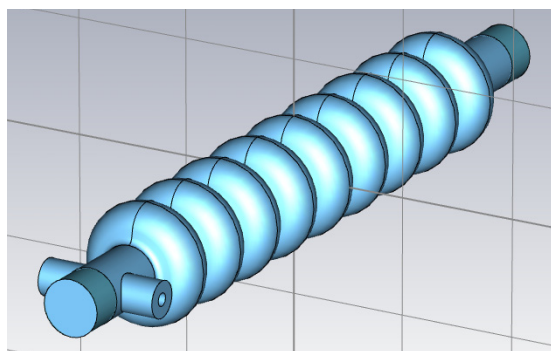
Figure 6: TRIUMF 9 cell cavity CST model

tests but factor at 2K $Qo\sim4*10^9$ is still not enough and maximum gradient $Ea\sim7.5MV/m$ is limited by field
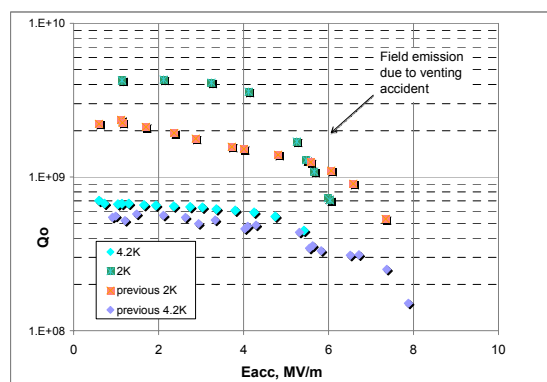
Figure 7: Test results of TRIUMF single cell cavity

emission due to a venting accident during cavity test preparation. We already have done another etching and prepared the cavity for the next test.

Fabrication of a 7 cell elliptical copper cavity model has been started at PAVAC. The goal is to develop the fabrication process of bulk Nb multicell elliptical cavities.

CONCLUSIONS

Commissioning and operational results of ISAC-II demonstrate successful operation of 20MV (20 SC QWR) from 2006. The accelerator, upgraded in 2010, now consists of 40 SC QWR cavities with independent RF systems providing high flexibility for tuning. The design goal for ISAC-II to provide 40MV acceleration voltage is achieved.

Design, production and testing of SCRF cavities towards TTF/ILC elliptical bulk Nb cavities technology are ongoing at TRIUMF.

REFERENCES

[1] R.E. Laxdal, "Initial Commissioning Results of the ISAC-II Linac", LINAC06, Knoxville, Aug. 2006.

[2] R.E. Laxdal, et al, "Operating Experience of the 20MV Upgrade Linac'', LINAC10, Tsukuba, Sept. 2010.

[3] D. Longuevergne, et al, "RF Cavity Performance in the ISAC-II Superconducting Heavy Ion LINAC", LINAC10, Tsukuba, Sept. 2010.

[4] R.E. Laxdal, et al, "Cryogenic, Magnetic and RF Performance of the ISAC-II Medium Beta Cryomodule at TRIUMF", PAC05, Knoxville, May 2005.

[5] V. Zvyagintsev, et al, "Production and Testing Results of Superconducting Cavities for ISAC-II High Beta Section", PAC09, Vancouver, May 2009.

[6] D. Longuevergne, et al, "Experimental Study of the Surface Resistance of the 141 MHz Quarter-Wave Resonator at TRIUMF", LINAC10, Tsukuba, Sept. 2010.

[7] S. Koscielniak, et al, "Electron Linac Photo-Fission Driver for the Rare Isotope Beams at TRIUMF", SRF 2009 Workshop, Berlin, Sept. 2009.

07 Accelerator Technology Main Systems

DEVELOPMENT AND PRODUCTION OF SUPERCONDUCTING AND CRYOGENIC EQUIPMENT AND SYSTEMS FOR ACCELERATORS BY IHEP

A. Ageyev, I. Bogdanov, S. Kozub, E. Kashtanov, K. Myznikov, A. Orlov, P. Slabodchikov,
V. Sytnik, P. Shcherbakov, L. Shirshov, V. Sytchev, V. Pokrovsky, K. Polkovnikov,
L. Tkachenko, S. Zinchenko, V. Zubko, IHEP, Protvino, Russia

Abstract

Superconducting and cryogenic programs at IHEP were got a powerful upsurge in the early eighties of the last century within the framework of the UNK project. More than hundred model superconducting magnets and the pilot batch of UNK superconducting dipoles and four quadrupoles were produced and tested with the help of cryogenic test facilities built for this purpose. Cooperation with international scientific accelerator centers was developed in last ten years. Two superconducting magnetic systems of Electron Lens for the Tevatron accelerator (USA) were developed, manufactured and successfully brought into operation. 42 cryogenic electrical feed boxes of various types for Large Hadron Collider (Switzerland) were developed, produced and put into commission. Results of the development of fast-cycling superconducting magnets for the FAIR project (European Research Centre of Ions and Antiprotons, Germany) are discussed. Description of the largest in Russia cryogenic system for cooling with superfluid helium of superconducting RF separator for the new beam channel of the U-70 accelerator (Russia) is presented. Design and test results of current leads as well as a dipole magnet on basis of High Temperature Superconductor are reviewed.

ITRODUCTION

In 1967 the 70 GeV proton machine of Institute for High Energy Physics (IHEP) has been commissioned. Experiments at high energies always required of cryogenic techniques (liquid hydrogen and deuterium targets, bubble chambers, cryogenic detectors). Special cryogenic plant and workshop were developed at IHEP.

RESULTS OF ACTIVITY

New generation of high energy proton accelerators is based on superconducting (SC) magnets. In the early eighties of the last century the special cryogenic and superconducting facilities have been created at IHEP in frame of UNK project (Fig.1 – 5). In collaboration with Bochvar's institute SC NbTi wire of 0.85 mm diameter with 8910 of 6 micron filaments was developed. More than 100 SC magnet models and 25 full scale 6 m dipoles (Fig. 6) and four quadrupoles were developed, produced and tested at IHEP [1] - [2]. The main characteristics of the magnets are presented in Table 1.

Figure 1: Machine for SC cable production. Nmax=28 strands of 0.3-1 mm diameter, V=1.5 m/min.

Figure 2: Machine for 6 m length SC coil winding.

Figure 3: Presses for collaring and curing of SC coil. 3800 tons, L = 7m, h = 0.67m.

Figure 4: Test facility for study of 1 m length SC magnets. 180 l/h boiling helium.

Figure 5: Test facility for study of 6 m length SC magnets and string of magnets. 120 g/s forced helium flow.

Table 1: The main characteristics of UNK SC magnets

Parameters	Dipole	Quad
Magnetic field, T	5.11	
Field gradient, T/m		97.4
Operating current, kA	5.25	5.25
Field ramp rate, T/sec	0.11	
Number of layers	2	2
Strand number in cable	19	19
AC losses, W	5.5	2
Stored energy, kJ	570	180
Inductance, mH	45	13
Coil inner diameter, mm	80	80
Length of the coil, mm	5800	3100
Length of the cryostat, mm	6420	4165
Mass of magnet, kg	6000	1600

Figure 6: UNK SC dipole magnet.

Cooperation with international scientific accelerator centers was developed in last ten years. In frame of collaboration with DESY, Germany in 1997 IHEP produced cryogenic helium vacuum heat exchanger for cooling 10g/s helium flow from 300 to 2 K temperature [3] shown in Fig. 7.

Figure 7: Cryogenic helium vacuum heat exchanger. 10g/s helium flow, 300-2 K temperature range.

In 1999 – 2000 and 2002 – 2003 two SC magnetic systems of Tevetron Electron Lens for Fermilab, USA were developed and produced. These systems were placed at TEVATRON accelerator (Fig.8) and operate up to date. The system consists of seven SC and ten copper magnets [4]. Main SC solenoid - 6.5 T nominal magnetic field, 2.5m length, 152 mm coil inner diameter. The solenoid coil was wound by the Rutherford type cable from 10 SC wires of 0.85 mm diameter. Turn number of the solenoid is 7238 and nominal current – 1800 A. Six SC steering dipoles were placed over the solenoid. Two dipoles of 1840 mm length were arranged in centre and four dipoles of 250 mm length in end parts of the solenoid. The central dipole produced 0.2 T magnetic field at 50 A current and end dipole – 0.8 T at 200 A. All dipoles were
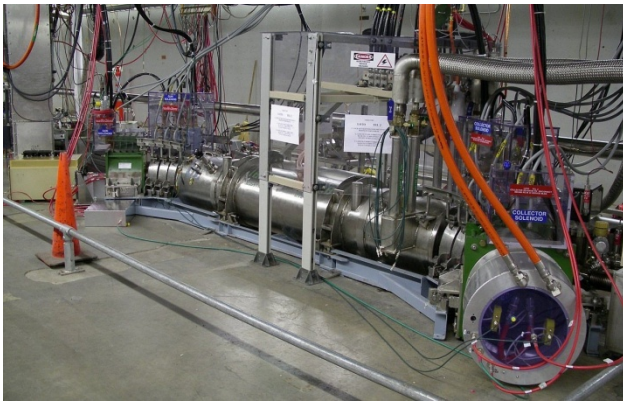
Figure 8: SC magnetic system of Tevetron Electron Lens.

wound by cable transposed from 8 SC wires of 0.3mm diameter.

The system has gun and collector solenoids with 250 mm inner diameter, 474 mm outer diameter, 300 mm length which produce 0.4 T magnetic field in aperture. Copper corrector coils are inside these solenoids. Three bending electron beam solenoids with 390 mm inner diameter, 500 mm outer diameter, 72 mm length are between cryostat and gun solenoid and the same between cryostat and collector solenoid. Turn number and nominal current of the solenoid are 48 and 357 A. Gun, collector and bending solenoids are produced from copper cable with 8.25×8.25 mm^2 cross-section with 5.5 mm diameter hole for water cooling.

At the same time activity for application of high temperature superconductor (HTS) for accelerator equipment production in collaboration with Bochvar's institute was begun. In 1998 – 2000 first in Russia 600 A HTS current leads on basis of Bi2223 were developed and successfully tested in frame of contract with CERN, Switzerland [5]. First current lead had 33 HTS tapes with Ag+10%at.Au matrix, second - 16 HTS tapes and third current leads – 14 HTS tapes with Ag+1%at.Au matrix (Fig.9).

These current leads consist of resistive part cooled by 20 K helium gas and HTS part cooled by helium vapor. The resistive part consists of 2300 copper wires of 0.13 mm diameter which are placed into stainless tube of 11 mm inner diameter and 500 mm length. HTS part is 400mm length. The third current leads had characteristics qualified LHC: Heat leak to liquid helium is 0.08W at 600A current; resistance of HTS – resistive contact equals 220 nohm, resistance of HTS – NbTi wire contact - 6nohm; helium flow cooled resistive part – 0.04 g/s; pressure drop of the helium flow – 5 kPa.

Figure 9: 600 A HTS current leads.

In 2004 – 2007 years 42 Cryogenic Electrical Feed Boxes of various types for powering of SC magnets of Large Hadron Collider (Switzerland) were developed, produced and put into commission [6]. These boxes have 2600 HTS current leads with operating current from 25 to 12500A. DFBA type box is shown in Fig. 10.

Figure 10: DFBA Cryogenic Electrical Feed Box for LHC.

The next step in application of HTS is development of first in Russian HTS dipole in 2000 – 2001 [7]. The dipole has 280x345 mm^2 cross section and 590 mm length (Fig. 11). 1 T magnetic field was reached at 25 A current and 65 K temperature in 21×70 mm^2 aperture of the dipole. "Racetrack" type coil was wound by 3.8×0.25 mm^2 HTS tape which consists of Bi2223 filaments in silver matrix. The coil was placed into yoke from electric steel.

Figure 11: HTS dipole magnet.

In 2007 the largest in Russia cryogenic system for cooling SC devices by superfluid helium was put in operation at IHEP for separated kaon beam. The system cools two SC RF cavities by superfluid helium at 1.8 K temperature [8]. Design refrigeration capacity of the cryogenic system is 250 W at 1.8 K and it should deliver 5 g/s of liquid helium per the each cavity. Main parts of the system are satellite refrigerator and KGU – 500 cryogenic plant (Fig.12), cryogenic transfer line with distribution box, pumping group. Satellite refrigerator consists of cryogenic helium vacuum heat exchanger, intercooling helium bath and two small helium heat exchangers placed near each SC RF cavity. These equipments were developed and produced by IHEP. Liquid helium plant of the KGU-500 type to feed the satellite refrigerator is commercially produced by GELIYMASH company, Moscow, and it has liquefaction rate of 150 l/hr.

Figure 12: Cryogenic plant and large helium heat exchanger of superfluid refrigerator system of 21 channel.

To reach 1.8 K the pumping group is to pump helium tanks down to 1.64 kPa. Pumping group is arranged in 3

stages: 8 Roots blowers of the 2DVN-1500 type of the first stage compress helium from 1.5 kPa to 2.5÷3.0 kPa, 8 Roots blowers of the 2DVN-500 type of the second stage compress helium to 4.0÷5.0 kPa, and the third stage of 8 slide-valve pumps of the AVZ-180 type finally compress helium up to 103 kPa.

Control system of the cryogenic system includes 240 channels of data collection and remote control, 72 electronic modules, 5 computers for inputting and outputting information in two control rooms.

Successful operation of the cryogenic system allowed to supply necessary parameters of SC RF cavities and record more than one million of kaon decay events.

From 2002 IHEP collaborated with GSI, Darmstadt, Germany. SC high field fast cycling dipole model was developed and produced for SIS300 accelerator of FAIR project (European Research Centre of Ions and Antiprotons. Special design of SC wire and cable with stainless steel core was developed for this dipole. 6.9 T magnetic field in aperture of the dipole was reached and the magnetic field value did not reduced up to 1.1 T/s ramp rate [9]. Combination of these dipole parameters is unique in world practice. The dipole is shown in Fig. 13and its parameters are presented in Table 2.

Figure13: SIS300 SC high field fast cycling dipole model.

Table 2: Parameters of the SIS300 SC dipole

Magnetic field, T	6
Operating current, kA	6.72
Field ramp rate, T/s	1
Number of layers	2
Strand number in cable	36
AC losses (calc.), W/m	4.7
In the coil	3.4
In the iron yoke	1.3
Stored energy, kJ	260
Inductance, mH	11.7
Coil inner diameter, mm	100
Length of SC coil, m	1
Mass of magnet, ton	1.8

Prototype of SIS300 fast cycling quadrupole will be produced till end of this year (Fig. 14) and tested in 2011. Design parameters of the quadrupole are 45 T/m central gradient of magnetic field, 10T/m/s ramp rate, 125 mm

07 Accelerator Technology Main Systems

inner diameter and 1 m effective length [10]. Bochvar's institute developed pilot batch of SC wire of 0.825 mm diameter, 6 km length, 3 mcm diameter SC filaments and 8 mm twist pitch.
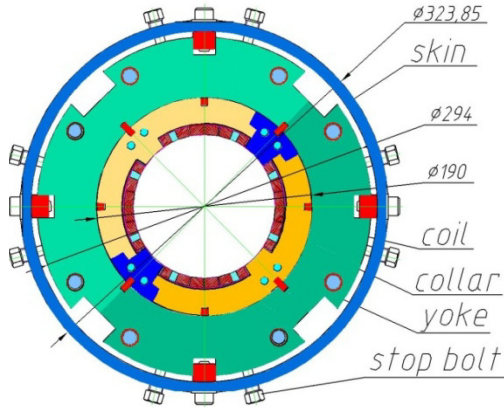

Figure 14: Cross – section of SIS300 fast cycling quadrupole prototype.

At present prototypes of SIS300 fast cycling corrector magnets are developed [10]. Main requirements to these magnets are presented in Table 3, where L is magnet length, t – time of powering to nominal magnetic force. Inner diameter of the magnets is 250 mm, operating current up to 250 A. In 2011 production of SIS300 steering magnet prototype is planned.

Table 3: Requirements to SIS300 corrector magnets

Type of corrector	Force	L, m	t, s
Chromaticity sextupole	130 T/m^2	0.78	0.21
Resonance sextupole	325 T/m^2	1	0.5
Steering magnet:			
Vertical dipole	0.5 T	0.65	2.27
Horizontal dipole	0.5 T	0.65	2.27
Multipole:			
quadrupole	1.8 T/m	0.65	2.25
Sextupole	60 T/m^2	0.65	2.18
Octupole	767 T/m^3	0.65	2.24

IHEP takes part in development of cryogenic system of SIS300. SC fast cycling magnets of SIS300 have increased AC losses as magnetic field ramp rate of the magnets is higher by order of magnitude than the ramp rate of TEVATRON, HERA, LHC magnets. According to calculation heat load for 4.5 K temperature level in SIS300 equals 4.3 kW. SIS300 magnetic ring of 1.1 km length will be halved for cryogenic strings cooled by supercritical helium [11]. UNK cryogenic scheme was took for basis but increased heat load in magnets required using of four additional helium heat exchangers in SIS300 cryogenic system in order to decrease maximal temperature of single-phase helium in cryogenic strings to 4.7 K that it necessary for stable SC magnets operation.

Proposed scheme solution allows to realize cooling SIS300 magnets up to 4.5 K during 60 hours, that is acceptable time. At present configuration and technical requirements for cryogenic system equipment are defined.

IHEP plan to use experience getting during production of LHC cryogenic electrical feed boxes for development and production of cryogenic electrical feed boxes and cryogenic holders for XFEL project, Germany. At present drawing development of the cryogenic equipment is begun.

CONCLUSION

IHEP has meaningful experience and equipment for development and production of accelerator magnets on basis of Low Temperature Superconductors and High Temperature Superconductors as well as cryogenic system for cooling superconducting devices and systems.

At present IHEP develops superconducting high field fast cycling magnets and cryogenic system for cooling these magnets.

REFERENCES

[1] N.I Andreev et al. Development and Study of the Superconducting Quadrupole Magnet for the UNK. — European Particle Accelerator Conference EPAC'94', London, June, 1994.

[2] V.I Balbekov et al. Development and Study of the UNK Superconducting Magnets. — Proc. of 1995 Particle Accelerator Conf., Dallas May, 1995.

[3] E.Kashtanov et al. Large Low Pressure Heat Exchanger for the TTF Cryogenic System. Proceedings of ICEC-18, Mumbai, India, 2000, February, p.315-318.

[4] I. Bogdanov et al. Test Results of the Magnetic System for the Tevatron Electron Lens. — European Particle Accelerator Conference EPAC 2002, Paris, France, 2002, p.p.2433-2435.

[5] I. Bogdanov et al. Design and Test of High Temperature Superconductor Current Lead. IEEE Transactions on Applied Superconductivity, March 2000, V. 10, N 1, p.p. 1485-1488.

[6] A. Perin et al. Design, production and first commissioning results of the electrical feedboxes of the LHC, Proc. of CEC-ICMC 2007 conference, Chattanooga, Tennessee USA July 16-20, 2007.

[7] I.V. Bogdanov et al. Test Results of HTS Dipole. — Proc. of XVII Int. Conf. on Magnet Technology, MT-17. Geneva, Swiss 2001.

[8] A. Ageyev et al. Starting -Up and Adjustment Works on Cryogenic AND Vacuum System of the Superconducting Radio-Frequency Separator, Proc. of RUPAC, 2008, p. 282.

[9] S. Kozub et al. SIS 300 Dipole Model, IEEE Transaction on Applied Superconductivity, V20, N3, June 2010, pp. 200- 203.

[10] L. Tkachenko et al. Development of Quadrupole, Steering and Corrector Magnets for the SIS 300, IEEE Transaction on Applied Superconductivity, V20, N3, June 2010, pp. 159- 163.

[11] A. Ageyev et al. Cooling System of the SIS300 accelerator. RUPAC, 2010, to be presented.

07 Accelerator Technology Main Systems

DEVELOPMENT OF FAST-CYCLING SUPERCONDUCTING QUADRUPOLE AND CORRECTOR MAGNETS FOR THE SIS 300

L. Tkachenko, I. Bogdanov, S. Kozub, P. Shcherbakov, P. Slabodchikov, V. Sytnik, V. Zubko
Institute for High Energy Physics, Protvino, Moscow region, 142281

Abstract

IHEP participates in the development of superconducting fast-cycling magnets for the FAIR project. In the frame of this project IHEP has developed a prototype of the main quadrupole, assigned for using in the SIS300 ring. The main parameters of the quadrupole are: 45-T/m central gradient in 125-mm ID of the coil with the useful aperture of 105 mm; the gradient ramp rate is 10 T/m/c and the length of the prototype is 1 m. The main characteristics of the designed quadrupole magnet are discussed here. The correction system consists of multipole magnets, resonance and chromaticity sextupoles and steering dipoles. The multipole magnet contains octupole, sextupole and quadrupole coils and the steering magnet involves horizontal and vertical dipoles. Geometries of corrector and steering magnets are presented as well as their main magnetic parameters.

INTRODUCTION

During the past several years IHEP has took part in the FAIR project [1]. At the moment, IHEP's main tasks are to develop a design of the main quadrupole [2], [3], [4], as well as designs of the corrector and steering magnets [3] for the SIS 300 ring. The optimized 2D and 3D geometries of the quadrupole and the main magnetic characteristics of the magnet are presented. The preliminary designs of the corrector and steering magnets for the SIS 300 as well as their main characteristics are presented too. All magnetic characteristics were calculated with a help of computer programs MULTIC [5] and HARM-3D [6].

QUADRUPOLE; REQUIREMENTS

Main quadrupole requirements are: the central gradient (G_0) is equal to 45 T/m; the inner beam pipe diameter is 105 mm; the gradient ramp rate is 10 T/m/s; the injection gradient is 10 T/m. The region of good field quality is $r_0 = 40$ mm and the effective length of the magnet is 1 m. The temperature margin has to be at least 1 K. Alterations of lower multipoles of the integral field at r_0 should be less then 2×10^{-4}. Additional requirements are: minimal geometric length; simple and reliable design; low AC losses in the magnet; minimum risks; cost reduction.[*]

QUADRUPOLE; 2D GEOMETRY

The main characteristics of the superconducting wire are: 0.825-mm strand diameter; 3.5-μm filament diameter;

---

[*] This work was completed with financial support from Rosatom, contract H4e45.03.10.1027

a 5-mm filament twist pitch, a Cu/superconductor ratio of 1.4, a critical current density of $J_c = 2.7$ kA/mm^2 (at 5 T, 4.2 K). Ratio of ρ_{300}/ρ_{10} is more than 70. Superconducting strands will have Staibrite coating.

Numerical simulations showed that it is enough to have a cable with 19 strands in order to meet given requirements for the quadrupole. Such type of cable was used for the UNK magnets [4]. The cable will be fully keystone with a width of 8.45 mm and an average height of 1.56 mm (with insulation). The cable will be insulated by polyimide tape in three layers. The radial thickness of the insulation after assembly and cool down is 125 μm and azimuth thickness is 98 μm. It is estimated that the cable will have contact crossover resistance in 0.02 mΩ and transverse resistance in 20 mΩ [6].

The 1-layer coil is divided by three blocks, allowing suppress the first three multipoles in the approximation of an infinitely high permeability in an iron yoke with the inner cylindrical surface. The geometric parameters of the coil are presented in Table 1, where N is a number of turns; φ, α are the initial and final angles of the block. The operating current is 6.262 kA. The ID of the iron yoke, made from 2212 electric steel, is 190 mm and the iron thickness is 52 mm. The iron yoke has four notches with 17×30 mm^2 dimensions for location of bus bars placed symmetrically under 45° as well as four adjusting bolts for quadrupole arrangement in the cryostat (Fig. 1).
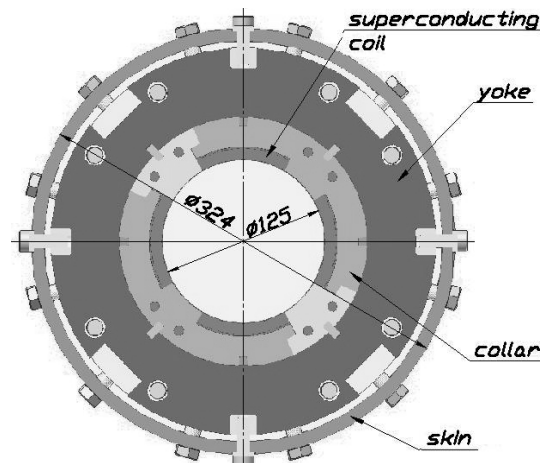
Fig. 1: General view of the cross section.

Table 1: Main Geometric Parameters of Coil Block

	N	φ	α
1	8	0.129	11.413
2	7	11.959	21.831
3	5	26.604	33.656

Field dependences for the normalized gradient and

multipole b_6 are presented in Fig. 2, 3. The initial parts of the curves show an influence of the coil magnetization and the final parts present the effects of the iron yoke saturation.
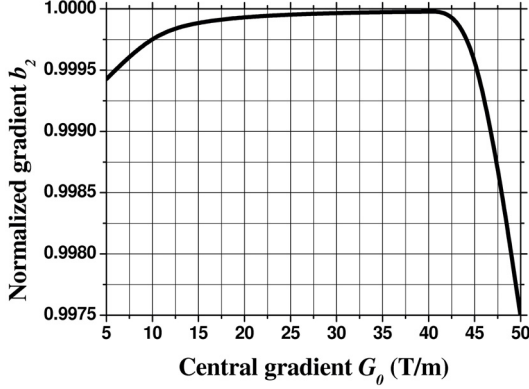
Fig. 2: Field dependence of normalized gradient.
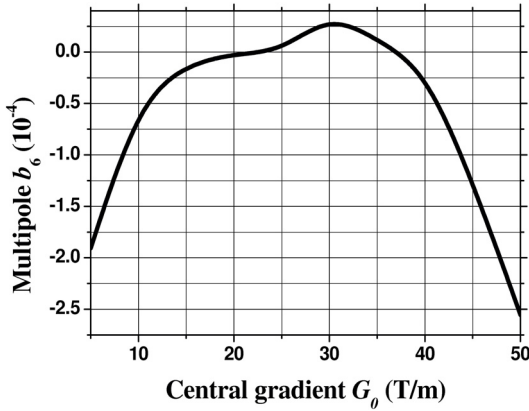
Fig. 3: Multipole b_6 versus central gradient.

QUADRUPOLE; 3D GEOMETRY

The end parts of the quadrupole have a shape that had been developed for the UNK magnets [7]. Turns in this geometry on the end parts are installed perpendicular to the generatrix of the cylinder. The geometric length of 1000 mm for the coil block was chosen because of technological considerations. The locations of spacers in the end part are chosen as a continuation of the spacers in the straight part of the coil. The thickness of the spacers in the end parts in the optimized geometry are: S_1 = 21.56 mm; S_2 = 9.42 mm. Fig. 4 shows an involute of the optimized end parts in the $\rho\theta$-Z plane.

In order to reduce the ratio of operating current I_{op} to the critical current I_C that provides a better value of the minimal quench energy, the length of the iron yoke is shorted in the end parts by 130 mm with each end. At the length of the iron yoke of 740 mm B_{max} in the end parts is equal to the maximal field in the cross section and equals 3.505 T. The temperature margin at this field is 1.54 K. The load line of the quadrupole is shown in Fig. 5. The current margin is 44%.
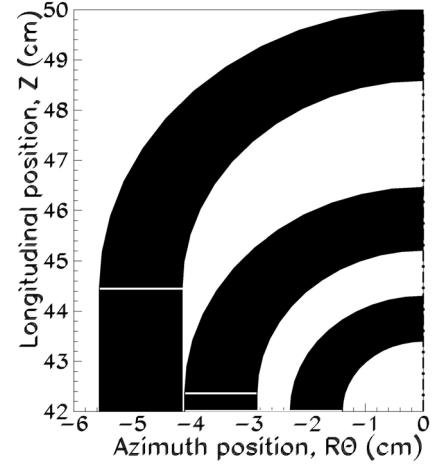
Fig. 4: Involute of optimized end parts.
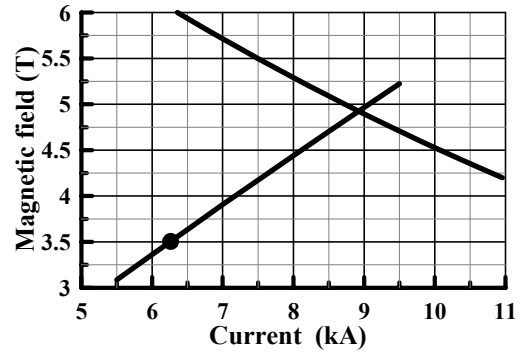
Fig 5: Load line of quadrupole.

The magnetic forces are (in kN/m): F_x = 124.2; F_y = -143.3; $|F|$ = 189.7. The stored energy is 38.0 kJ/m and the inductance is 1.94 mH/m. AC losses in the coil were calculated for the standard triangle cycle for the SIS 300: 10 – 45 – 10 T/m at the ramp rate of 10 T/m/s. The components of losses in the coil are (in J/m): hysteresis - 9.4; matrix - 3.0; cable - 0.3; total losses in the coil are 12.7. Losses in the iron yoke for 2212 steel are: hysteresis - 5.0; eddy current - 0.003, so the total losses in the magnet are 17.7 J/m.

Longitudinal distributions of the lower field multipoles in the end parts of the quadrupole are shown in Fig. 6, 7.
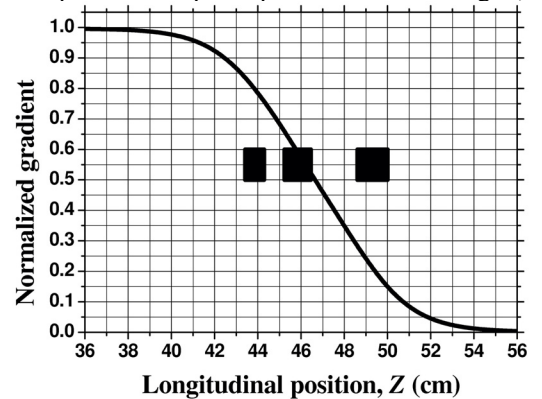
Fig. 6: Longitudinal distribution of normalized gradient. Dark rectangulars show coil blocks in end parts.
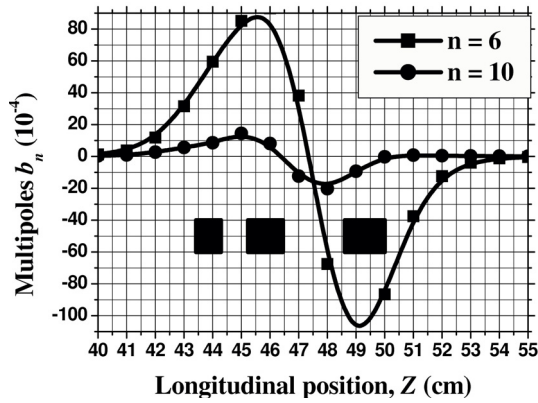
Fig. 7: Longitudinal distribution of lower multipoles. Dark rectangulars show coil blocks in end parts.

CORRECTOR AND STEERING MAGNETS

There are 4 types of corrector magnets:
1. Error compensation multipole corrector, combined magnet, which consists of quadrupole (QM), sextupole (SM) and octupole (OM) magnets;
2. Chromaticity Sextupole (CS);
3. Resonance Sextupole (RS);
4. Steering horizontal (DH) and vertical dipoles (DV), combined magnet.

The main requirements for the corrector magnets are presented in Table 2, where L_{eff} is an effective length of each magnet and t is the current-rise time. The aperture diameter for all magnets is 105 mm and the beam pipe ID is 115 mm. The CS will have series connection; there are 4 magnets in the series. The CS and RS will have bipolar power supplies. The operating current should be less than 250 A. Field quality requirements are not formulated yet, but we assume that an alteration of the first lower integral field multipole should be within 2×10^{-4} and the magnet main field deviation should not exceed 0.2%.

A wire with the following characteristics will be used for the coil winding superconducting NbTi: 0.3-mm diameter; 3-µm filaments, 3-mm twist pitch; Cu/superconductor = 1.7; RRR > 70; J_c = 2.7 kA/mm^2 (at 5 T, 4.2 K). The wires will have oxide coating. The superconducting rectangular shape cable consists of 8 strands with a transposition step of 11.9 mm. The cable will be insulated by three layers of a 25-µm polyimide film and has transverse dimensions of 0.6×1.63 mm^2.

The minimal coil ID for magnets will be 125 mm. At present only CS, RS, DH and DV magnets have been studied in more details. The coils in all magnets will be of layer type. The magnets will have classical design with an iron yoke serving directly as a supported structure for the coil. The main characteristics of the magnets are presented in Table 3, where φ, α are initial and final angles of the coil; N_w is a number of turns; R_F is the inner radius of the iron yoke; I_{op} is the operating current; L_t is the total length of the coil; S is the straight part of the coil; L_{ef0} and L_{ef} are the required and calculated effective lengths; B_{max} is the maximal field in the coil in the cross

section/end parts (T); E is the stored energy (J/m); L is inductance (mH/m); F_x, F_y, $|F|$ are components of magnetic forces (kN/m). All angular dimensions are in deg., linear dimensions are in mm.

Table 2: Main Requirements for Corrector Magnets

	Strength	L_{eff}, m	t, s
QM	1.8 T/m	0.65	2.25
SM	60 T/m^2	0.65	2.18
OM	767 T/m^3	0.65	2.24
CS	130 T/m^2	0.78	0.208
RS	325 T/m^2	1	0.5
DH, DV	0.5 T	0.65	2.27

Table 3: Main Characteristics of the Magnets

	CS	RS	DV	DH
φ	4.485	2.466	12.954	13.425
α	15.186	14.444	41.310	40.263
N_w	2×20	4×23	2×53	2×53
R_F	67.365	71.0	71.0	71.0
I_{op}	234	236	230	231
L_t	800	1040	700	700
S	741.2	973.2	611.2	610.2
L_{ef0}	780	1000	650	650
L_{ef}	780.4	1008.6	666.8	668.3
B_{max}	0.82/0.89	1.69/1.53	1.15/1.42	1.24/1.42
E	582	4358	1033	1126
L	21.3	156.5	39.1	42.2
F_x	2.8	17.6	9.2	0.3
F_y	-1.5	-13.2	-0.8	11.0
$|F|$	3.2	22.0	9.2	11.0

CONCLUSION

The design of the superconducting fast-cycling quadrupole magnet for the SIS 300 accelerator has been developed. The quadrupole magnet has a high quality of the field. The compact end parts together with two spacers provide also the high quality of the integral field. The temperature margin is 1.54 K, what guarantees a stability of the magnet. The total losses in the magnet are reduced to 17.7 J/m. The main characteristics of magnets of a correction system are presented.

REFERENCES

[1] [GSI. (2006, Sept.). Baseline technical report. [Online]. Available: http://www.gsi.de/fair/reports/btr.html

[2] L. Tkachenko, S. Kozub, V. Zubko, "Quadrupole for the SIS 300. IEEE Trans. on Appl. Supercond. vol. 19, nr. 3, pp. 1167-1179, 2009

[3] L. Tkachenko, I. Bogdanov, S. Kozub, P. Shcherbakov, V. Sytnik, A. Tchikilev, V. Zubko, "Development of Quadrupole, Steering and Corrector Magnets for the SIS 300", *to appear in IEEE Trans Appl. Supercon. 20.*

[4] L. Tkachenko, S. Kozub, P. Shcherbakov, V. Sytnik, V. Zubko. "Analysis of the Factors Affecting Field Quality and Heat Releases of the Quadrupole Magnet for the SIS 300". Presented at ASC-2010, Washington, USA, August, 2010

[5] L.M. Tkachenko. "Code Package MULTIC for Calculation of Magnetic Field with an Arbitrary Configuration". IHEP preprint 92-28, 1992, (in Russian).

[6] S.V. Purtov and L.M. Tkachenko. "HARM-3D - a Code to Calculate Magnetic Characteristics of SC Magnets". MT-15, Beijing, China, 1997, Beijing, China, Vol. 1, p.p. 1335-1338.

[7] V.I. Balbekov, L.M. Tkachenko. "Optimization of the End Parts of the UNK SC dipoles". *Preprint 82-167*, Serpukhov, 1982 (in Russian)

07 Accelerator Technology Main Systems

COOLING SYSTEM OF THE SIS300 ACCELERATOR

A. Ageev, S. Kozub, S. Zintchenko, V. Zubko, IHEP, Protvino, Russia

Abstract

The Facility for Antiprotons and Ion Research (FAIR) being under construction in Germany as an international project is a cascade of accelerators; two last accelerators from this cascade will be made with the use of superconducting magnets. The large volume of the executed work on the SIS300 superconductive equipment allowed to start the estimation of the basic parameters of SIS300 cooling system. On the base of many research notes and calculations the item-by-item heat load budget at the helium temperature level is composed. Cooling system flow diagram is proposed, the calculated single phase helium temperature profiles along the string of magnets are presented and discussed. Helium flow pressure drop along the string of magnets during cooling down is calculated on the basis of "temperature wave" model and cooling down time of the accelerator is estimated.

GENERAL COOLING SCHEME OF SC MAGNETS

According to [1], all SIS300 magnets will be divided into two equal cryogenic strings, each one to be supplied with separate flow of single-phase helium.

Based on this, following flow scheme is proposed for cryostating the string of superconducting (SC) magnets (Fig.1). In this scheme single-phase (supercritical) helium from the helium refrigerator is cooled in the subcooler and enters the string of the magnets, where it is heated due to the heat leaks and heat release, and simultaneously it is cooled in the heat exchangers located in the dipoles.
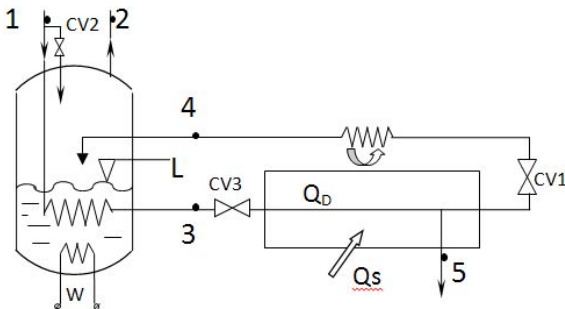

Figure 1: Flow scheme proposed for cryostating the string of SIS300 superconducting magnets.

At the end of the magnet string the single-phase helium is throttled in the J-T valve CV1, and it is converted into two-phase helium, which flows through the dipole heat exchangers of the magnet string into the subcooler. In the subcooler two-phase helium is separated to the vapor and liquid. Liquid helium is used for cooling single-phase helium in the heat exchanger of subcooler and helium vapor returns to the refrigerator.

The flow scheme is considered functional if one of the main conditions for the cryostating is satisfied: the quality

factor x of the two-phase flow of helium at the exit from the magnet string is less than or equal to 0.95 (for Fig. 1 $x_4 \leq 0.95$). This is necessary for the stable heat exchange between the two-phase and single-phase flows of helium in the heat exchangers of dipole magnets.

Heat balance equations for the flow scheme in Fig. 1 at the conditions of maintaining the fixed level of liquid helium L by the control valve CV1 (CV2 is closed) and of zero flow rate through the current leads at point 5:

$$G_1 * i_1 + Q_D + Q_S = G_1 * i_2 \qquad (1),$$
$$G_1 * i_3 + Q_D + Q_S = G_1 * i_4 \qquad (2),$$

where i - enthalpy of helium flow; G_1 – helium mass flow rate; Q_D and Q_S – AC losses and static heat leaks.

From equations (1) and (2):

$$i_4 = i_3 + i_2 - i_1 \qquad (3).$$

Equation (3) clearly shows that parameters of helium flow in point 4 at the exit from the magnet string, including its quality factor, do not depend on the heat leaks and heat release values, but depend only on the input/output parameters of the subcooler (points 1 and 2, Fig. 1). For the values given in table 10, using the thermodynamic properties of helium tables [2], one could obtain quality factor at the string exit $x_4 = 0.951$, which practically corresponds to the requirement of $x_4 \leq 0.95$. In fact, due to the presence of certain helium flow for cooling of current leads (point 5, Fig. 1), quality factor at the string exit will be below 0.95. This quality factor can be decreased by powering the electric heater W (Fig. 1).

The main part of SIS300 dipoles are about 8m length so for cooling the magnets it was decided to use single-phase (supercritical) helium, which directly washes the single-layer superconducting coil.

In the upper part of the cold mass this dipole magnet the heat exchanger is located, in which single-phase helium is cooled by two-phase helium. Thus, in each dipole magnet the heat released in the superconducting coil is removed by single-phase helium and the heat from the single-phase helium is removed by two-phase helium [3], [4].

Heat load on the cryogenic system from the cryomodules and the multipoles is considerably less in comparison with the load from the dipoles; therefore cooling of the single-phase flow by two-phase flow is not arranged in their designs. This means that in the cryomodules and in the multipoles both the heat release and the heat leak are removed only by single-phase flow.

HEAT LOAD OF SIS300 CRYOGENIC SYSTEM. PARAMETERS OF THE MAIN HELIUM FLOWS

Below we will consider the cryogenic system heat load at the helium temperature level (~4.5 K) only, as the thermal shields heat load at 50-80 K in the allowable range does not effect the functionality of SC magnets.

The heat load in question is composed of the heat release in the superconducting coils and in the iron yokes, of the heat release in the beam pipe and of the ambient heat leaks. The heat load is calculated for the most stressed SIS300 magnetic cycle presented in Table 1.

Table 1: Most stressed SIS300 magnetic cycle

Cycle time, s	Maximum field, T	Increase and reduction of magnetic field, s	Flat-top at Bmax, s
17.0	4.5	7.0	10

The specific values of heat releases and heat leaks along particular design elements are determined in different GSI reports and documents, in the communications at the SIS300 project meetings, and also in the course of mutual consultations. Calculated heat loads will be given below, first for the groups of uniform ring elements (Table 2 – Table 8) and then for the system (Table 9).

Table 2: Dipole magnets heat leaks and heat release

Type of the dipole magnet	Long	Short
AC losses	29.7 W	14.8 W
Supports heat leak	2 W	1 W
Cryostats heat leak	5.3 W	2.6 W
Total per dipole	37 W	20.1 W
Number of magnets including the reference ones	49	13
Total heat leaks and heat release	1813 W	261 W

Table 3: Cryomodules and the multipole corrector magnets (multipoles) heat leaks and heat release. Standard cryogenic module contains quadrupole magnet and one/two corrector magnets

Type of the magnet	Cryomodule	Multipole
AC losses	3 W	0.002 W
Supports heat leak	2 W	1 W
Cryostats heat leak	2 W	1 W
Total per article	7 W	2.002 W
Number of articles including two reference quadrupole cryomodule	86	12
Total heat leaks and heat release	602 W	24 W

Table 4: Heat leaks along the beam pipe cold-warm-transitions, along the connections with "warm" equipment

Single transition heat leak	2.5 W
Number of the transitions	48
Vacuum connection heat leak	1.5 W
connection heat leak vacuum connections	54
Safety valve connection heat leak	1 W
Number of the safety valve connections	40
Total heat leaks	241 W

Table 5: Heat release in the superconducting bus bars and beam pipe RF mirror current heat release

Heat release in the superconducting bus bars	566 W
Beam pipe RF mirror current heat release	450 W

Table 6: Heat leaks to the cryogenic transfer lines and to the feed and end boxes. Cryogenic transfer lines include bypass lines with the superconducting bus bars and connecting lines without the superconducting bus bars

Heat leaks to the cryogenic transfer lines	165 W
Heat leaks to the 8 boxes	54 W

Table 7: Heat load from beam position monitors, from HTS current leads and from voltage taps

42 beam position monitors	126 W
10 HTS current leads	18 W
1662 voltage taps	25 W

Table 8: Mass flow rate of liquid helium for cooling the corrector magnets current leads. Heat leaks along the corrector magnets current leads are small and they are not taken into account

Flow rate of liquid helium for cooling the 231 pairs of the corrector magnets current leads	4.53 g/s

Table 9: Total SIS300 heat load at T=4.5 K

AC losses	2472 W
Ambient heat leak	1367 W
Beam pipe RF mirror current heat release	450 W
Total heat load	4289 W
Flow rate of liquid helium for cooling the current leads	4.53 g/s

It follows from tables 2-9 that the largest heat load on the cryogenic system, almost 50%, comes from dipoles, and approximately 70% of dipole heat release is generated directly in the superconducting coil. The static heat leaks account for about 32% of the total heat load.

Table 10 presents SIS300 helium flows parameters which were defined on basis the calculated heat load.

Table 10: SIS300 helium flows parameters

Pressure of supercritical helium at the entrance into the string of magnets	3 bar
Temperature of supercritical helium at the entrance into the subcooler of the string of magnets	4.6 K
Temperature of supercritical helium at the entrance into the string of magnets	4.35 K
Pressure of two-phase helium at the exit from the string of magnets	1.105 bar
Temperature of two-phase helium at the exit from the string of magnets	4.3 K
Two-phase helium flow quality factor at the exit from the string of magnets	≤95%

COOLING DOWN THE SC MAGNETS FROM ROOM TEMPERATURE DOWN TO LIQUID HELIUM TEMPERATURE

All superconducting magnets: dipoles, quadrupoles and correctors are designed taking into account the fact that their longitudinal and transverse temperature gradient can reach the value from 4.5 K to 300 K. It allows to cool "warm" equipment of the SIS300 magnet string directly by liquid single-phase helium, which substantially simplifies the cooling down process.

Besides the equipment, depicted in Fig. 1, the quench header and the technological valves located in the SIS300 tunnel will be used in the cooling down procedure. The technological valves are installed at some intervals along the magnet string and they connect the single-phase helium channel with the quench header. In the ideal case, i.e., when at the magnets inlet is liquid helium, and at the exit is helium gas at an ambient temperature, the flow rate of helium being 100 g/s, the cooling down time will be about 60 hours, which is quite acceptable.

CRYOSTATING THE SC MAGNETS

The superconducting dipole magnet is most heat loaded. Because of this, if for any reasons the superconducting coil of dipole is warmed up to temperature of 5.7 K, then the coil will go into the normal state. Therefore the temperature of the single-phase helium, which cools the superconductive coil of dipole magnet, must not exceed 4.7 K. Experience shows that for the selected superconductor a temperature margin of 1 K is sufficient in most cases to guarantee the stable work of the superconducting dipole.

Each of the cryogenic strings contains three identical groups of magnets, the lattice is shown in Fig. 2. The alternating dipole and quadrupole magnets are located in the arc part of the ring, the separate quadrupoles - in the straight sections.
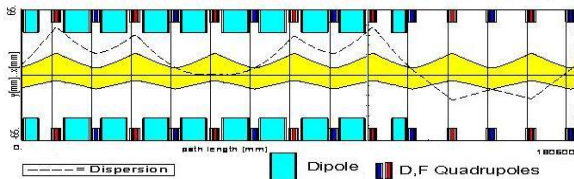

Figure 2: SIS300 magnet lattice.

For this arrangement of magnets the temperature profile of the single-phase flow along the cryogenic string was calculated for two additional heat exchangers of single-phase and two-phase helium flows into the cryogenic string. These heat exchangers (recoolers) are arranged in the first and second superperiods of magnetic structure, between the next-to-last and last quadrupoles. Temperature profile for this modernized cryogenic string is given in Fig. 3.

As it follows from Fig. 3, the temperature of single-phase helium in the dipole magnets of the modernized cryogenic string practically does not exceed value of

4.61K, which assuredly provides the condition for the stable work of dipole magnets (T<4.7 K). It is reached at the "small price" - only four additional heat exchangers for entire SIS300 ring. Moreover these heat exchangers are located in the straight sections, where space is sufficient for their convenient arrangement.
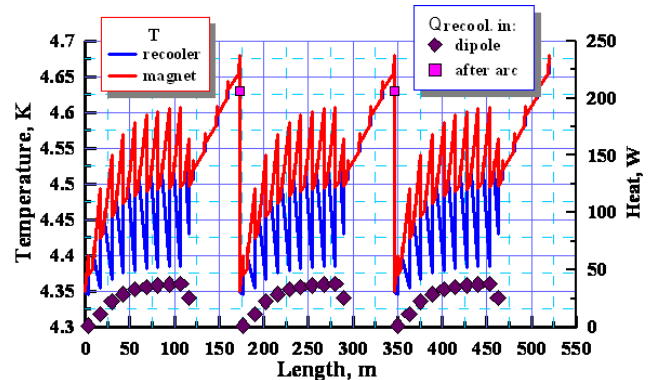
Figure 3: Temperature profile of the single-phase flow along the SIS300 modernized cryogenic string.

CONCLUSION

For the SIS300 accelerator the refined values of heat leaks and heat releases at T=4.5 K are given.

The flow scheme of cryostating the string of the SIS300 magnets is proposed, which makes it possible by sufficiently simple means to regulate the quality factor of the two-phase helium flow.

The time of cooling SIS300 magnets down to the operating temperature is estimated.

It was determined by calculations that it is enough to add to entire SIS300 machine only 4 additional helium heat exchangers (recoolers) to decrease the maximum temperature of single-phase helium flow.

REFERENCES

[1] FAIR Baseline Technical Report, Volume 2. Accelerator and Scientific Infrastructure, March 2006, http://www.gsi.de/documents/DOC-2006-Jul-40-1.pdf

[2] R. D. McCarty, Provisional Thermodynamic Functions for Helium 4 for Temperatures from 2 to 1500 K with Pressures to 100 MN/m2 (1000 Atmospheres), NBS REPORT 9762, August 1, 1970.

[3] P.Fabbricatore et al., R&D Activities Aimed at Developing a Curved Fast Ramped Superconducting Dipole for FAIR SIS300, Proceedings of EPAC08, Genova, Italy.

[4] F. Alessandria et al., Technical Design Report of a Superconducting Model Dipole for FAIR SIS300, INFN, Genova, Italy, INFN/TC-09/4, May 15, 2009.

A FAMILY OF TWENTY-AMPERES POWER SUPPLIES FOR MULTI-POLE CORRECTORS FOR ACCELERATORS AND STORAGE RINGS

O. Belikov, V. Kozak, A. Medvedko, BINP, Novosibirsk, Russia

Abstract

For decades, we at Budker Institute of Nuclear Physics SB RAS have developed precision power supplies for the electromagnets of accelerator facilities and storage ring complexes in broad range of output power. Some tasks, e.g. powering correctors, multipole magnets and low-current bending magnets, operate with up to 20A regulated current sources with an output power of about a few kilowatts [1]. Our long-term experience in the development and operation of power supplies resulted in the creation of the MPS-20 (Magnet Power Supply) family of three types of reversible power supplies. The output current of these supplies can be varied in the range of ±20A; the output voltage is ±50V, ±100V, and ±150V for MPS-20-50, MPS-20-100, and MPS-20-150, correspondingly. The power supplies developed meet the requirements of the up-to-date accelerator facilities.

INTRODUCTION

A magnetic system of the up-to-date accelerator and storage ring facilities requires a number of different regulated current sources, the large variety of which complicates the operation of a facility as a whole. That is why the goal of this work was to develop universal current sources which could be used at various accelerator facilities.

For instance, the precision experiments with colliding electron-positron beams requires a very stable magnetic field of the collider, which constrains the long-term instability of the output supply current for the magnets.

The acceleration of a charged particle beam requires good dynamic of magnetic field dynamics in an equilibrium orbit. Thus it is necessary to regulate the current in the windings of the magnetic elements in the parts of energy variation: during the energy boost in the acceleration mode and during the reduction to the injection energy. Since the impedance of corrector is the sum of the resistive impedance and the active impedance, a reverse polarity voltage is often required for regulation of the current decreasing. Thus current sources with a 4-quadrant current/voltage operation are required.

CURRENT SOURCE STRUCTURE

The circuit design was special subject to the possibility of realization of the required algorithms for the output current regulation with a high efficiency of the power supply for electromagnets. The design chosen is based on a circuit with double RF conversion (Fig. 1)
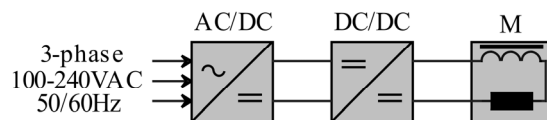
Figure 1: AC/DC and DC/DC are the Alternating current / Direct current and Direct current / Direct current convertors; M is the electromagnet.

AC/DC converters with isolated output voltage are used to get a DC buffer voltage. Those are usually conventional AC/DC converters, industrially manufactured voltage stabilizers. The output current is regulated with a DC/DC converter, a schematic diagram of which is given in Fig.2. The power part of the unit
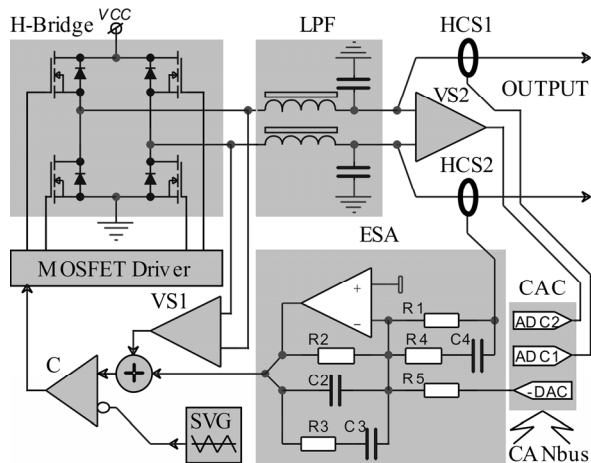
Figure 2: H-Bridge – H-Bridge inverter, LPF – Low-pass filter, HCS – Hall Current Sensors, VS – Voltage sensor, ESA – Error-signal amplifier, CAC – Controller with the CANbus interface, ADC – Analog-to-digital converter, DAC – Digital-to-analog converter, C – Comparator, SVG – Sawtooth-voltage generator.

includes the H-Bridge made on four MOSFET switches. The output current is regulated by the pulse width modulation of the output voltage of the bridge inverter. A second-order filter, LPF, is used to suppress voltage of the carrier frequency and its harmonics. Its suppression ratio is 60 dB or more.

The output current is measured with two identical noncontact Hall current sensors HCS1 and HCS2 of the current − compensating type. One sensor is used in the feedback loop; the other serves as an independent monitor for the control system.

The current-feedback loop provides the required quality of regulation. The mains ripple of 50÷360Hz is partially

suppressed by the AC/DC converter and partially by a fast voltage-feedback loop with a loop amplification factor of about 10.

The current-feedback loop contains the error-signal amplifier, ESA, including of integrating and differentiating elements. The transfer function of these elements with integral characteristics is:

$$W_1(p) = \frac{k_U \cdot (p \cdot T_3 + 1)}{p^2 \cdot T_2 \cdot T_3 + p \cdot (T_2 + T_3 + T_{23}) + 1}$$

Their time constants are:

$$T_2 = R_2 \cdot C_2, \; T_3 = R_3 \cdot C_3, \; T_{23} = R_2 \cdot C_3.$$

Such a structure makes it possible to realize a high static gain in the loop of error signal:

$$k_U = \frac{R_2}{R_1} \approx 10^3.$$

In a system with a transfer function W_1, a fast change in the driving control signal can result in an overshoot due to the delay in the regulator of the closed feedback loop system. So, an element with a differentiating characteristic is added, the transfer function of which is

$$W_6(p) = \frac{p \cdot (T_{14} + T_4) + 1}{pT_4 + 1},$$

where $T_{14} = R_1 C_4$ and $T_4 = R_4 C_4$ are the differentiation time constants.

Fig.3 presents the logarithmic gain-frequency response and the phase-frequency characteristic of the open feedback loop. The unity gain frequency (from the plot) is
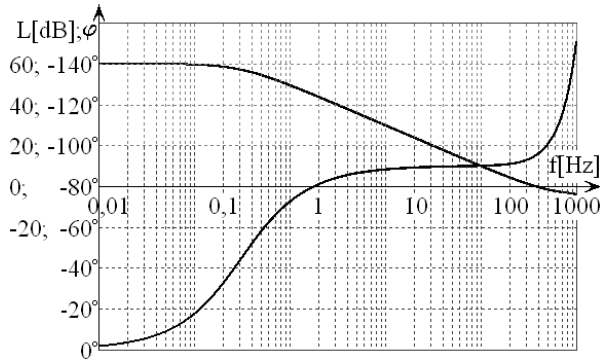

Figure 3: L is for the gain-frequency response, φ is for the phase-frequency characteristic.

about 300Hz, and the phase is approximately $\pi/2$, which corresponds to a well-damped system.

In dynamics, e.g. when the current is changing with a frequency of the order of 1Hz, the gain of the open feedback loop is approximately 100, and the time delay in the output current is about 20mS, which is quite enough for most acceleration objectives.

Parameters of the 20A current sources are given in Table 1.

Table 1: Parameters of the 20A current sources

Parameters	Magnet Power Supply
Output current	±20A
Output voltage **MPS-20-50** **MPS-20-100** **MPS-20-150**	± 50V ± 100V ± 150V
Current accuracy	≤0,1%
Output current dispersion	100ppm
Thermal drift of output current	40ppm/K
Conversion frequency	50kHz
Cooling	Air Forced

DESIGN

The 20A current sources are made in a standard "Euromechanics" crate of a 3U-subunit (432×355×133mm). The modules can be fed from both 120/208VAC and 220/380VAC, 50/60Hz mains.

The current sources are managed with the module-embedded analog-to-digital controller CEAC124, developed by BINP [2]. The controller contains 4 channels of a 16-bit bipolar analog-to-digital controller, 12 channels of a 24-bit analog-to-digital controller as well as 4 channels of input signal registers and 4 channels of output signal registers. The controller is connected with the control system via the CANbus.

The controller allows the power supply to work independently in the static and dynamic modes. In the static mode, the module works as a direct current source. In the dynamic mode, the controller can use the internal data chart. The controller approximates those data by the method of straight-line interpolation, and the current is regulated in accordance with a given time dependence with a step of about 10mS.

There are two ways of external control of the module parameters: (1) via the multichannel scanning of selected channels, (2) in the digital oscilloscope mode, which allows one to measure one selected channel with a higher time resolution of about 1mS. The multichannel scanning mode is mainly applied to control the current and voltage during the operation of the current sources. The digital oscilloscope mode is used, for instance, for the spectral analysis of the values to measure [3].

Up to two external binary signals with the ON/OFF operation command can be connected to the power supplies. Those can be signals of a thermoswitch and a water flow switch for a water-cooled load.

On the front panel of the module (Fig.4) there are digital indicators for the output current and the output voltage as well as two LED indicators informing on the availability of backup power supply and operation of the protection circuit. The protection operates when the

07 Accelerator Technology Main Systems

current in the inverter half-bridge exceeds the admissible value. In this case, the operation of the power part of the converter is blocked, a pause is sustained, and then an automatic restart occurs with a frequency of about 1Hz. The input signal register of the controller is used to notify the control computer on the protection operation.

RESULTS

About fifty of 20A current sources are now working on different BINP facilities as well as at JINR (Dubna) and other installations. Several years of operation have proved the reliability of their work.

REFERENCES

[1] O. Belikov. Current sources for the correction magnets in accelerators and storage rings. Abstract of a thesis for PhD in Technical Sciences.

[2] V. Kozak. Euromechanical device set with CANbus interface, Preprint Budker INP 2008-18, Novosibirsk (2008).

[3] O. Belikov et al. System of power supply ripples measurement for VEPP-2000 collider, RuPAC 2008, p. 178-180, Zvenigorod (2008).

Figure 4: Magnet power supply MPS-20

FIRST RADIOCARBON MEASUREMENTS AT BINP AMS

S.A. Rastigeev, A.R. Frolov A.D. Goncharov, V. F. Klyuev, S.G. Konstantinov, E.S. Konstantinov,
L. A. Kutnykova, V. V. Parkhomchuk, M.V. Petrichenkov, A. V. Petrozhitskii
BINP, Novosibirsk, Russia.

Abstract

Present status of the BINP accelerator mass spectrometry (AMS) facility is described. The results of experiments for beam selection and radiocarbon concentration analysis in trial samples are presented.

INTRODUCTION

The AMS is mainly dedicated for dating of archaeological, paleontological and geological samples by measurements of the ratio between carbon isotopes.

The BINP AMS facility [1] includes negative ion source, folded type vertical electrostatic tandem accelerator, magnesium vapors stripper [2], the high-energy and low-energy beam lines with analyzers, time-of-flight final detector [3].

The negative ion beam is horizontally extracted from the ion source. Then the beam is vertically injected into the low energy accelerating tube through injection channel with 90° magnet. The negative ions are accelerated to the positively charged high voltage terminal and stripped to charge state 3+ in magnesium vapors stripper. Then they pass through the 180^0 electrostatic bend and then again are accelerated vertically into the high energy accelerating tube to the ground potential. Then ions are horizontally put to the final detector through high-energy channel with 90° magnet.

The most distinguishing feature of our AMS machine is the use of additional electrostatic separator of ion beam, located inside the terminal. Interfering isobaric molecules are destroyed by collisions in the stripper into the terminal and are selected immediately after the stripping process. It is important to decrease the background from molecular fragments before the second stage of acceleration [4], because the energy of fragments is always less then the ion energy (at this moment). The next important distinguishing feature is magnesium vapours stripper instead of the gas stripper. The gas flow into the accelerator tubes leads to big energy spread in the beam thus limiting the sensitivity and accuracy of spectrometer. The molecular destruction and ion recharging by magnesium are localized into the hot tube of the stripper.

BINP AMS FACILITY MODIFICATIONS

Now the AMS facility created at BINP SB RAS is installed at CCU "Geochronology of the Cenozoic era". The accelerator is placed into underground room with radiation shielding. The inner size of the room is 6 x 6 x 7.5 meters. The basic parts of electronic devices are located outside of the shielding room and connected with accelerator elements. The local equipment of the water cooling, compressed air and gas transfer system has been installed.

The 500 kV terminal voltage was achieved with 1 atm atmospheric air into pressure tank (without insulating gas). The equipment for gas filling and drying was not used, but the silica gel was placed directly into the tank. Initially, the terminal voltage was limited by the water vapor condensate on the cool surface of the gas turbine feeding dielectric tube, located along the accelerator column. This tube is used for terminal turbine feeding by compressed air. The electrical conductivity of condensed water distorts the electric fields, which can induce electrical breakdown. For prevention of water condensation, the lower part of the tube (outside of the tank) was heated. Now the electrical breakdowns are occurred only during the first start after tank closing, as we assume, due to the dust accumulation when the tank is open. Recently, 1 MV terminal voltage was achieved by using low cost air-gas mixture. The tank was pumped to the 0.8 atm air pressure, and then the tank pressure was increased to 1.6 atm by four nitrogen gas-cylinder. The 4 kg of SF_6 gas was added (+0.02 atm) to increase the electrical strength of the mixture. The 1 MV has been achieved without breakdowns.

The multi-cathode (for 24 samples) sputter ion source has been recently manufactured and installed. It's needed for synchronous analysis of the samples and for comparison of the tested samples with the reference one. The negative ions are produced by bombarding graphite target with positive cesium ions. The Cs+ ions are produced on a hot tantalum ionizer (1100^0C) by cesium vapor from the oven (180^0C). The cesium ion beam is focused on the carbon sample placed on the cathode, because the working surface of ionizer is a spherical-shape cup. The copper sample holder has the inner diameter of 2 mm. The holder is water cooled to reduce sample heating. The cesium ions leaving the ionizer are accelerated by 7 kV potential. The negative carbon ions are accelerated by the same potential and extracted through the hole 6 mm in diameter in the center of the ionizer. The power consumption of the ion source does not exceed 250 W. The test sample in ion source is selected by sample wheel rotation. The stepping motor with Pi/25600 rad/step resolution is used for sample changing. The process of rotation is controlled by motor driver and checked by optoelectronic sensor system (at every turnover) and by video camera (online).

The new magnesium vapors stripper has been manufactured and installed. All hot parts of striper are located in vacuum. It prevents corrosion of striper surface by the tank gas mixture. The power consumption is about 50 W.

The electronics for time-of-flight detector (ToF) was improved. At present, the ToF channel width is 70ps. Moreover, the moment of time for ion detection can be registered with 16 μs channel width. This data is used for calculation of number of detected ions per unit time, allowing to filter the background ions from electrical breakdowns.

EXPERIMENTAL RESULTS

During the experiments, the injection energy of carbon beam was 25 keV. The carbon beam current was about 5 uA. The terminal voltage of tandem accelerator was 1 MV. The 180° electrostatic bend was set to transmit the ions with charge state 3+. The magnesium vapors stripper was heated for obtaining the equilibrium charge state distribution, but not more. The ions transmission of AMS system at this energy is about 10% (includes the stripping yield for 3+ charge state). The ^{14}C ions are counted by ToF detector. The ^{12}C ions are measured in shielded Faraday cups with secondary electron suppression. The current of the mass-12 ions can be measured immediately after the magnet of low energy beam lines (^{12}C- ions) and at the AMS exit (^{12}C^{3+}). The vacuum level in the beam line was about 10^{-6} Torr.
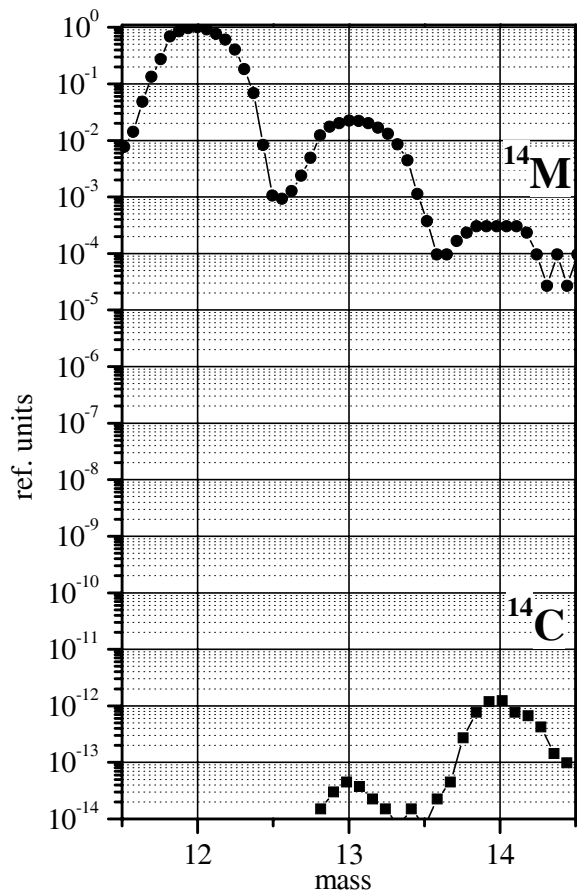

Figure 1: Mass spectrums of the injected (upper curve) and accelerated (lower curve) beams.

The typical mass spectrum of the carbon target before acceleration is shown in Fig. 1 (upper curve). The intensity of the mass-14 peak is more than 10^{-4} per ^{12}C isotope. It is mainly the ^{12}CH$_2$ and ^{13}CH molecular currents. The ToF spectrum at the exit of AMS is also shown in Fig. 1 (lower curve). The mass is calculated from ToF channels. The AMS system is tuned for radiocarbon transmission. The molecular background of the mass-14 is suppressed by the destruction process in the magnesium target and then filtered by tandem 180° bend. The small mass-13 peak is also visible in the spectrum, but the mass separation is good enough for radiocarbon measurements.
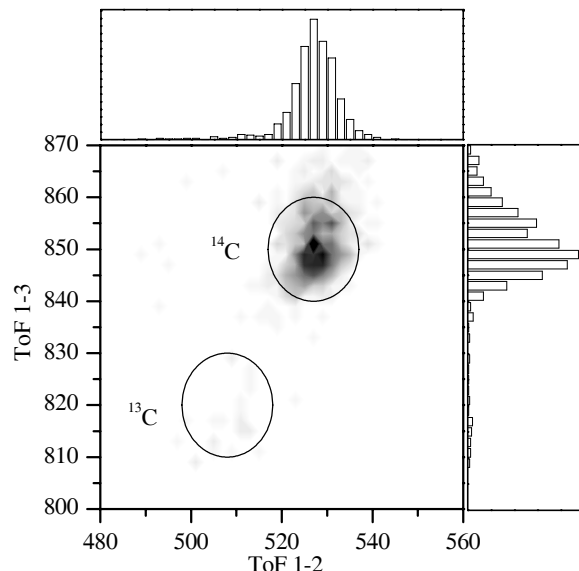

Figure 2: The 2D ToF spectrum at the exit of AMS (70 ps per channel).

The more detailed 2D ToF spectrum with the same AMS tuning is shown in Fig. 2. The solid circles show the locations of the radiocarbon and mass-13 peaks. The particles from mass-14 circle are calculated for radiocarbon concentration determination. The time-of-flight histograms for both ToF distances are also shown in Fig. 2. The peaks separation is bigger about of factor 2 than peak widths (FWHM) for each ToF distance. Such a system of several sequentially positioned detectors on the particles path allows a significantly decrease in the number of random coincidences.

The commercially available carbon fabric is used as test modern sample. The filaments of fabric are pressed into the cathode holder. The carbon fabric is made of organic materials. The radiocarbon isotope ratio of the modern organic matter is about 10^{-12} (^{14}C/^{12}C). The graphite MPG is used as test "dead" sample. The radiocarbon concentration in graphite is about 100 times lower than in modern sample.

For radiocarbon concentration analysis, the ^{12}C ions current and ^{14}C ions number are measured for each sample. During the experiments, the ^{12}C^{3+} ion current was measured one time of each 400 s interval of radiocarbon

counting. During switching between the isotopes, the magnets settings are changed. The $^{12}C^-$ ions were measured simultaneously with the ^{14}C counting. The process of isotope measuring and sample changing (wheel rotation) is fully automated.
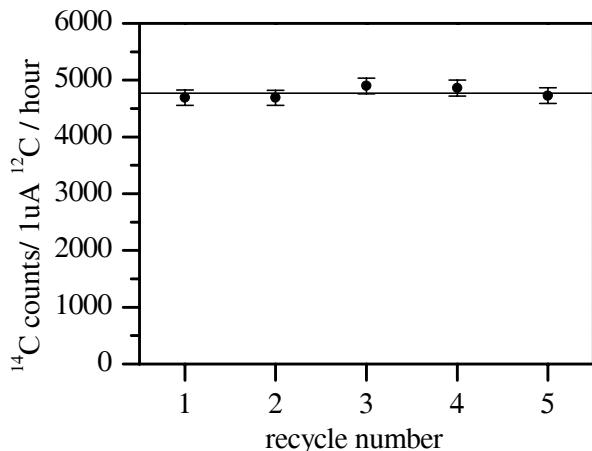

Figure 3: Radiocarbon concentration in modern sample. The sample was measured five times.

For estimation of the reproducibility of measurements, the series of five radiocarbon concentration measurements for one sample is presented at Fig.3. The solid lines show the mean concentration value. The experiment was carried out without rotation of the sample wheel. The ^{14}C counts time is 800 s for each measurement. The statistical uncertainty of radiocarbon registration is about 3% (shown by error bars). It is seen, that the results are in agreement with each other within the error ranges.
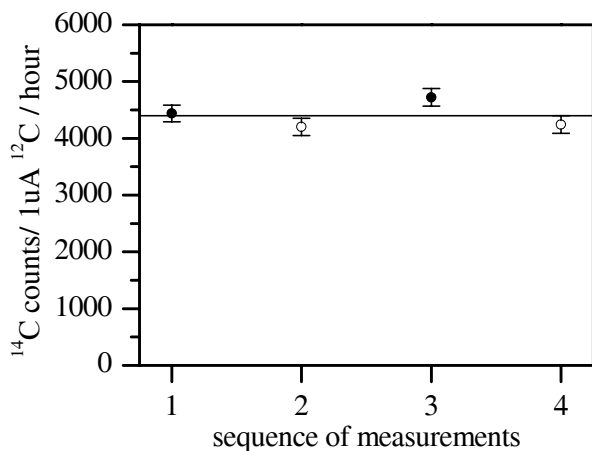

Figure 4: Radiocarbon concentration in two modern samples (measured alternately).

For testing of the reproducibility of measurements after sample wheel turning, another series of measurements is presented in Fig. 4. Here, two modern samples are measured alternately. One can see the results with wheel rotation are similar to ones presented in Fig. 3. The samples were degassed before the measurements by Cs beam. The time of degassing is about 5 min per sample.

The effect is visible by vacuum monitoring. The ion source parameters are not stable during the degas process.

For ion background estimation, the modern sample and "dead" sample are measured alternately. The results are shown in Fig. 5. The data are normalized to the radiocarbon concentration in modern sample. As seen the radiocarbon concentration in "dead" sample is about 1% of the modern sample concentration.
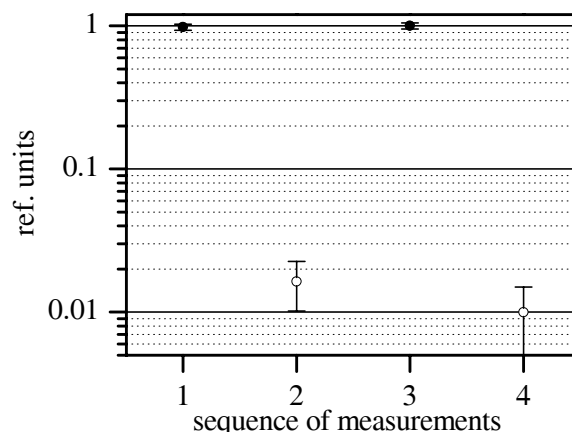
Figure 5: Radiocarbon concentration in the modern and "dead" samples (measured alternately).

For radiocarbon analysis, the samples with large content of carbon /were used. The sample preparation is needed for transformation of natural objects to such samples by combustion and graphitization. We tested more then 100 samples prepared by CCU "Geochronology of the Cenozoic era". The measured background carbon contamination during sample preparation is about 10%. This work will be continued to the reduction of contamination.

The data presented is the first preliminary estimation of BINP AMS facility for radiocarbon dating. The detailed study of the systematic errors and ion background investigation will be done soon.

SUMMARY

The accelerator complex has demonstrated the sustained performance on 1MV running. The reproducibility of first radiocarbon concentration measurements is about 3%. The measured radiocarbon concentration in "dead" sample is about 1% of the modern sample concentration.

ACKNOWLEDGMENTS

REFERENCES

[1] N.I. Alinovskii et al, Technical Physics, Accelerator mass spectrometer for the Siberian Branch of the Russian Academy of Sciences, Technical Physics, 2009, Vol. 54, No 9, p 1350.

07 Accelerator Technology Main Systems

[2] V.F. Klyuev, V. V. Parkhomchuk, S.A. Rastigeev, A magnesium vapor charge-exchange target for an accelerator mass spectrometer, Instruments and Experimental Techniques, 2009, Vol. 52, No. 2, p. 245.

[3] N.I. Alinovskii et al, A time-of-flight detector of low-energy ions for an accelerating mass-spectrometer, Experimental Techniques, 2009, Vol. 52, No. 2, p. 234.

[4] V.V. Parkhomchuk and S.A. Rastigeev, Analysis of the ion background in an acceleration mass spectrometer of the Siberian Division of the Russian Academy of Sciences, Technical Physics, 2009, Vol. 54, No. 10, p 1529.

HIGH POWER ELV ACCELERATORS FOR INDUSTRIES APPLICATION

N.K. Kuksanov, Yu.I. Golubenko, P.I. Nemytov, R.A. Salimov,
S.N. Fadeev, A.V. Lavruhin, A.I. Korchagin, D.S. Kogut, A.M.Semenov
Budker Institute of Nuclear Physics SB RAS Lavrentyev av. 11, Novosibirsk, 630090, Russia

Abstract

Beginning from 1971, the Budker Institute of Nuclear Physics Siberian Branch of Russian Academy of Science (SB RAS) started its activity in the development and manufacturing of electron accelerators of the ELV-type for their use in the industrial and research radiation-technological installations. The ELV-type accelerators were designed with use of the unified systems and units enabling thus to adapt them to the specific requirements of the customer by the main parameters such as the energy range, beam power, length of extraction window, etc.. INP proposes a series of electron accelerators of the ELV-type covering the energy range from 0.3 to 2.5 MeV with a beam of accelerated electrons of up to 400 mA and maximum power of up to 400 kW. The design and schematic solutions provide the long term and round-the -clock operation of accelerators under the conditions of industrial production processes. The ELV accelerators are especially popular accelerators not only in Russia, but in China, Korea, and etc The cross-linking technologies are applied very widely in industries. While the improved maximum operating temperature was one of the initial attractions of cross-linking, there are other important product advantages as a results of cross-linking of the polymers, such as: reduced deformation under load, improved chemical resistance, increased abrasion resistance, improved impact properties, memory characteristics. At present the electron-beam technologies are extensively used in a cable industry for cross-linking of insulation made on the basis of polymer compositions. The use of these technologies enabled to develop the manufacture of a wide range of wires, cables and heat-shrinking goods for different markets (power plant, telecommunications, electronics, oil industry, nuclear power plant, submarine and aircraft, etc). All of them are of high reliability, when being mounted and during operation as under standard and extreme operating conditions.

INTRODUCTION

The use of electron-beam technologies gave an opportunity to develop the production of wide range of wires, cables, heat-shrinking products (heating cables, power and ship cables, airborne wires and cables, as well as atomic power plant (A-plant) wires). All of them are of improved reliability at assembly and operation as in regular service and in extreme conditions. The quality of radiation treatment depends on accelerator itself as well as on under-beam equipment. Thus, the accelerators should provide stability of electron beam parameters, such as energy, beam current and width of irradiation area. In order to enhance absorbed dose azimuthal homogeneity they should be provided by 4-side irradiation system.

The main specification of the system of cable transportation through radiation zone is transportation rate of speed, which should be proportional to beam current rate. Proportionality coefficient called "specific rate" depends on the type of irradiated product and accelerator parameters. Taking into account the information mentioned above, there was developed the high-automated systems for electron-beam treatment of cable isolation. Practically, there is no necessity in permanent presence of accelerator control panel operator. Effective visualization of irradiation process (energy, beam current, cable transportation speed) allows the operators of transportation line to control and set the treatment conditions directly at working place close by pay-off and take up machines.

ACCELERATORS

The main features of ELV-accelerators are as follows:
1. High power of electron beam in wide energy range, it means high productivity of EB processing;

Fig.1 Accelerator ELV-8

2. High efficiency of conversation of electricity power to electron beam power. The efficiency is limited by frequency converter and in case of transistors frequency converter efficiency is increased up to 80-92%;

3. Simple procedure of accelerator control by operator due to control system based on computer. It allows operating accelerator in on-line mode.

4. Accelerator control system comprises a set of software and hardware covering all the accelerator units required an operative control and diagnostics.

5. Accelerator itself has simple design and high reliability. If some troubles appear our customers repair accelerator by themselves with our consulting by phone, as a rule.

6. After warranty service. It means we delivery spare parts or parts with limited lifetime or make any accelerator service after warranty period by separate contracts with the low price.

7. A set of additional equipment (such as transportation line, ring or double side irradiation system, 4-side irradiation system) increases the accelerator possibility.

8. ELV accelerators are stable in operation. The energy and beam current instabilities practically do not exceed +/-2%.

By now, over 120 accelerators had been delivered inside Russia and abroad and the total operation time exceeds 800 accelerator-years. .

4-SUIDE IRRADIATION SYSTEM

In due time the laboratory proposed to develop the system of 4-side irradiation, which allowed us to enhance dramatically the quality of cable products treatment. Fig. 2 shows the extraction device with 4-side irradiation system. Together with enhancement of absorbed dose azimuthal homogeneity this method enables to decrease accelerated electrons energy that considerably expands the range of accelerator applications in the area of irradiation of big diameter cables. New system of irradiation exchanged the traditional early applied systems of 2-side irradiation and enhanced the quality of manufactured products and raised labor productivity. The cables are laid out under the beam in such a way that at each turn (lap) the upper and lower surfaces of a cable swap their places. If beam trajectories are crossed 90^0 angularly, than, taking into account the exchange of surfaces, 4-side irradiation is achieved (Fig. 3 and Fig. 4). It is important that the cable passes the irradiation zone few times.
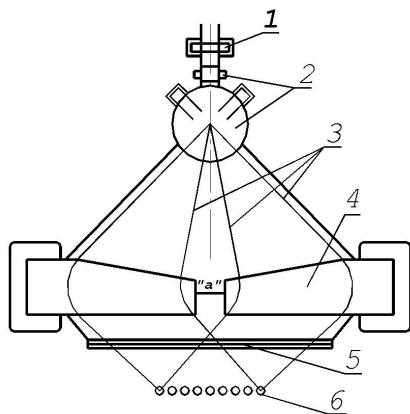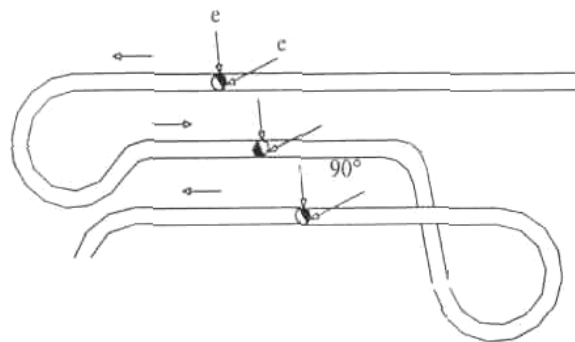

Fig.2 4-side irradiation system

Fig.3

UNDER-BEAM TRANSPORTATION SYSTEM

Universal under-beam transportation system (UBTS) was developed in our laboratory. Its design is shown in Fig. 5. UBTS consists of 2 drums, one of which is driving and another one is guided. That reduces the risk of stretching of treated product and prevents the decrease of cable cord diameter.

Fig.4

Big diameters of the drums (900 mm) allow treatment of monoconductor cable with 36 mm^2 section (Fig. 5) and exchange tape guide rollers enable to treat multiconductor cables with the diameter up to 42 mm. Minimum pitch diameter of treated wire for this facility is 1 mm, but during the experiment we successfully irradiated cable of 0.12 mm^2 Irradiated chamber with UBTS, extraction device and 4-side irradiation system delivered to "Rosskat Ltd." is shown in Figure 6. In UBTS we use the asynchronous motor (induction motor) with frequency drive. The rotation frequency is set by accelerator control system. The operation drive has a wide dynamic range, that is proportionality between transportation speed and beam current is saved within wide speed range. That enables to realize a smooth start of the technology and to refuse movable target. Irregularity of absorbed dose at UBTS acceleration from 0 right up to 250 m/min does not exceed 5%.
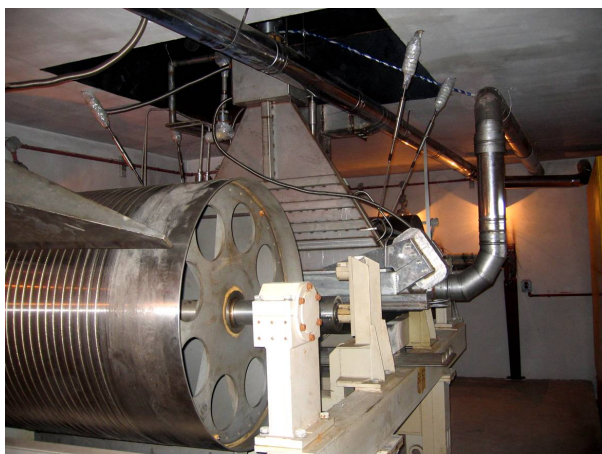
08 Applications of Accelerators, Technology Transfer and Industrial Relations

Fig.5. Cable irradiation

DATA-COMPUTING SYSTEM

The information of processing is shown on illuminated indicator board. It's dimensions allow to read information from any point of operation hall. The following parameters are continuously displayed: energy, beam current, speed of line, remainder of cable on bobbin, time to finish of bobbin (Fig. 7). The perfect quality of treatment is proved by reliable operation of cables in extreme conditions of oil industry.
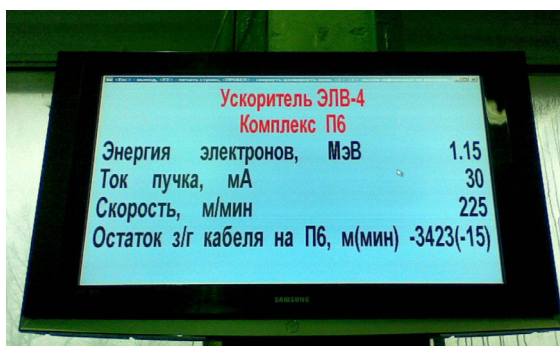
Fig.6

ACCELERATORS FOR ENVIRONMENTAL APPLICATIONS

ELV-12 accelerator with power 400 kW is used for ecological purpose. The installation for electron-beam waste water treatment was put in operation in Korea.

Simultaneously with manufacturing of high power accelerators we developed movable accelerators. Accelerator together with radiation shielding is arranged inside of trailer. Main purpose of these accelerators is to eliminate small local contamination.

Fig.7. Irradiation hall for waste water treatment with ELV-12 accelerator

Fig.8. Movable accelerator

BINP continuously improves design and increases parameters of accelerators. The set of additional equipment (such as transportation line, ring or double side irradiation system, 4-side irradiation system, focused beam extraction device) increases the accelerator possibility. Due to this circumstances and improving of economics after crisis amount of orders for accelerators extremely increased.

08 Applications of Accelerators, Technology Transfer and Industrial Relations

55 MEV SPECIAL PURPOSE RACE-TRACK MICROTRON COMMISSIONING[*]

A.I.Karev, A.N.Lebedev, V.G.Raevsky, P.N.Lebedev Physical Institute, RAS,
119991 Moscow, Russia

A.N.Ermakov, A.N.Kamanin, V.V.Khankin, N.I.Pahomov, V.I.Shvedunov, SINP MSU,
119992 Moscow, Russia

N.P.Sobenin, MEPhI, Kashirskoe shosse 31, 115409 Moscow, Russia

L.Brothers, L.Wilhide, Valley Forge Composite Technology Inc. (VFCT) 50 East Rivercenter
Blvd., Suite 820, Covington, KY, USA

Abstract

Results of Lebedev Physical Institute RAS 55 MeV special-purpose race-track microtron (RTM) commissioning are presented. RTM is intended for photonuclear detection of hidden explosives based on initiation of photonuclear activation and consequent registration of secondary gamma-rays penetrating possible screening substances.

INTRODUCTION

The purpose of the work consists in development of an effective photonuclear detector of hidden explosives to be used under stationary conditions and in mobile systems for searches of field mines. The detector consists of a source of high energy gamma - radiation and counters fixing the secondary radiation from decay of short-living isotopes formed in explosives due to reactions with nitrogen and carbon nuclei [1]. The gamma source is based on a specialized microtron (RTM) for energy of 55 MeV. A RTM photo is presented in Fig. 1, main RTM A RTM photo is presented in Fig. 1, main RTM parameters reached by commissioning are listed in Table 1.

Figure 1: RTM photo.

Table 1: RTM parameters

Output energy	55 MeV
Output pulse current	10 mA
Repetition rate	5 – 50 Hz
Number of linac passages	11
Energy gain / turn	5 MeV
Current pulse length	5 μs
Operating frequency	2856 MHz
End magnet field	1.0 T
Maximum RF power	2.5 MW
Orbit circumference increase / turn	1 λ

RTM has been built following a classical scheme with two 1 T end magnets and a standing wave linac between them providing 5 MeV energy gain per pass. A 50 keV beam from an electron gun is injected into linac through a 45^0 magnet and a solenoidal lens. The 5 MeV electron beam after the first acceleration is reflected by the end magnet field back to the linac axis and is accelerated up to 10 MeV - the energy sufficient to bypass the linac at the next turn. The beam is extracted from the last orbit [*] with a dipole of 17.5^0 deflecting angle. More details about the RTM scheme can be found in [2].

RTM SYSTEMS

RF system

The RF system is based on a multibeam klystron KIU-168 [3] with a rare earth permanent magnet focusing system providing 6 MW/6 kW pulsed/average power at 2856 MHz. The klystron is compact, its high voltage pulse amplitude is only 54 kV, so it does not need oil insulation and can be installed under the RTM table. A pumping port, a vacuum window, and a circulator are installed between the linac and the klystron.

The non-vacuum part of the waveguide tract is filled with SF_6 at 2 bars. Parameters of the vacuum window and the circulator by commissioning restricted the maximum RF power transported to the linac by 2.5 MW and thus restricted a maximum exit pulsed beam current by 10 mA. The klystron is fed by a "hard" modulator [4] with pulse duration up to 15 μs. To simplify the RF system we use a self-oscillation mode of operation with linac structure included in a feed-back loop [5]. Optimal conditions for self-oscillations and for RF power level regulation are controlled with a phase shifter and an attenuator installed in the feed-back loop. In Fig. 2 the klystron current, the high voltage and RF field pulses are shown. The 8 μs high voltage pulse duration is set externally. The delay of about 3 μs between the high voltage front and RF pulses is the time required for building-up self-oscillations from the noise. This time can be decreased by adding a low power "igniting" RF signal to the feed-back loop.
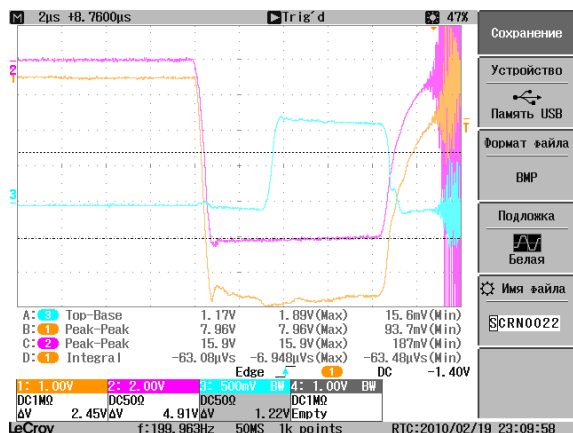
Figure 2: Klystron current (1), high voltage (2), and RF field (3) pulses.

Electron gun

A three electrodes electron gun with a 8.6 mm diameter tungsten impregnated cathode for nominal current of 400 mA and beam energy of 50 keV is used in RTM (Fig. 3(a)). By varying intermediate anode voltage the
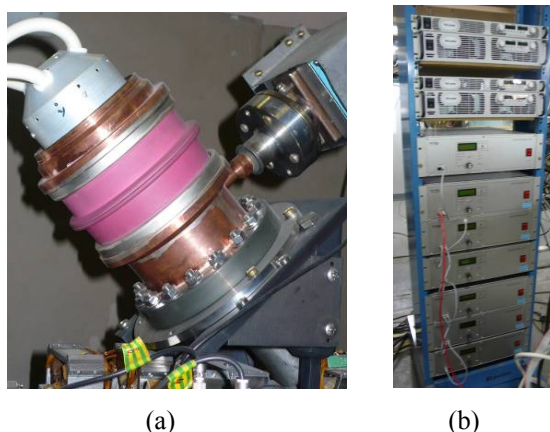

(a)   (b)

Figure 3: (a) Electron gun, (b) magnets power supply.

gun current can be controlled within ±100 mA. The electron gun is fed with the same modulator as the klystron is. A voltage at the intermediate anode regulated in discrete steps is provided from the high voltage divider installed inside the RTM table. The electron gun is pumped with 5 l/s ion pump, vacuum in the gun being better than 10^{-5} Pa.

Magnets power supply system

To feed the coils of the end magnets current sources Genesys™ type form TDK-LAMBDA [6] are used. Two GEN 12.5-60 current sources feed reverse pole coils while two GEN 60-55 sources are used for the coils of the main poles. The rest magnetic elements are fed with a multichannel current source of 42 channels designed by Protom company [7]. Magnets power supply system is shown in Fig. 3(b).

Control system and beam diagnostics

RTM control system has been built using standard National Instruments modules for signals control and LabView software [8] for user interface.

Beam diagnostic is provided by beam current monitors (BCM) of 5 mV/mA sensitivity installed at each orbit and at the linac axis, by synchrotron radiation, and by transition radiation. To observe synchrotron radiation from RTM orbits with CCD camera a glass window in the vacuum chamber was installed at the end magnets. Accelerated beam was extracted to atmosphere through 20 μm thick Ti foil. Transition radiation generated by the beam crossing the foil was registered by a CCD camera. Extracted beam absorbed in a Faraday cup provides a beam current signal.

RTM TUNING

Before RTM tuning the distance between the edges of the end magnet main poles was set according to calculated value with accuracy ±0.1 mm. The level of the main and reverse field was adjusted to calculated values using a calibrated Hall probe with accuracy 0.1% and 1%, respectively. Care was taken to decrease hysteresis phenomena influence on the field level when switching on/off current sources.

The main factors influencing on the beam propagation in the transverse plane of RTM are end magnets field errors, parasitic and strayed magnetic fields, an inaccuracy in magnets and linac positioning, an inaccuracy in longitudinal beam dynamics tuning. In longitudinal plane the main factor is uncertainty of the accelerating field level which absolute value can not be well determined by RF diode calibration or by measuring of linac dissipated RF power via cooling water temperature and flow.

To decouple longitudinal and transverse plane tuning we calibrated the RF diode signal against beam energy using end magnets combined with BCMs placed at 1st and 2^{d} orbits. To accomplish this we calculated electron trajectories in the end magnet for various currents in the coils keeping constant a ratio of the main and reverse fields. Then we found a correspondence between the electron energy and the coils current when the beam passed through the centre of the first and the second orbit tubes.

At the second step we measured the beam energy spectrum after the first acceleration using 1st orbit BCM for various settings of the accelerating field. After the first acceleration the beam is reflected back to the linac by the end magnet (M1) moving counter clockwise. In order to enter 1st orbit tube at lower magnetic field the beam must move clockwise, so to measure spectrum we reversed the polarity of the M1 coils. In Fig. 4 at the left beam spectra measured after the first acceleration at various field levels are compared with a spectrum found in RTM beam dynamics simulation (black dots). The energy resolution of spectrometer is defined by the inner diameter of the tube and is rather poor. We fixed the RF diode voltage for

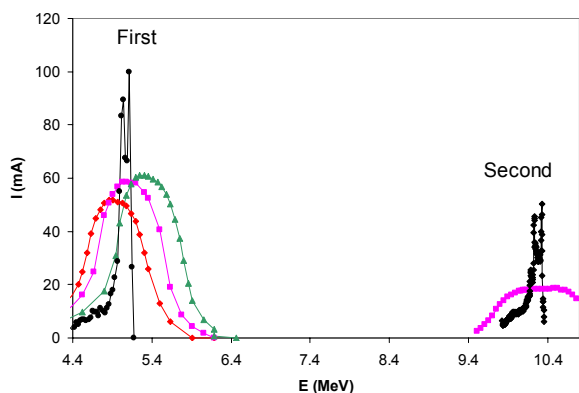pink curve as one corresponding to nominal accelerating field.

Figure 4: Measured beam spectra after first and second acceleration compared with calculated.

At the next step we set the proper polarity and level of the M1 field, so the beam was reflected back to the linac and accelerated in opposite direction. Than with second magnet (M2) and 2^d BCM we controlled beam energy (right pink points curve at Fig. 4). One can see that the measured beam spectrum maximum (~ 10 MeV) well coincides with maximum of spectrum found in beam dynamics simulation (black points). From these results it follows that the beam enters the linac after reflection by M1 in a proper phase.

Note that after the first acceleration the beam current is about 50-60 mA (this value is defined by the gun current and injection system tuning), while after the second one it falls down to about 16 mA, an essential part of the low energy tail of the beam being stopped by the linac wall. Current losses are somewhat higher than following from calculations – compare amplitudes of calculated spectra (which are in arbitrary units).
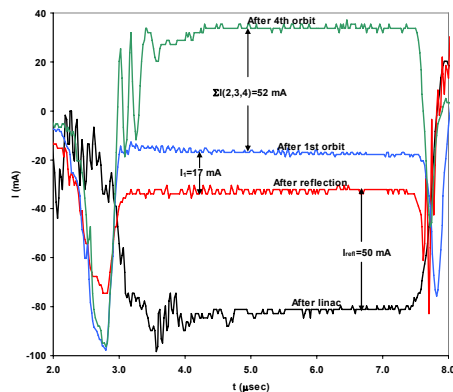

Figure 5: Signals from BCM installed at linac axis.

Additional valuable information about beam reflection by M1 and following acceleration can be obtained from BCM installed at the linac axis between the linac and M1 magnet. In Fig. 5 signals from BCM obtained under different conditions are shown. Black curve was obtained

with M1 magnet off. Beam current coming out of the linac in this case is about 80 mA. After M1 switching on a current registered by BCM decreased for about 50 mA – this was the beam current reflected from M1 and passing BCM in opposite direction. After 1st orbit the BCM signal dropped to 17 mA and after the forth additionally to 52 mA (meaning a sum of the 2,3 and 4th orbits current) changing signal polarity. From these data it follows that RTM can be tuned with minimal beam losses after 1st orbit.

In order to get beam transmission shown in Fig. 6 currents of the steering coils installed at the injection path and at RTM orbits were adjusted using information from BCM. We should note that the RF power necessary to accelerate 16 mA beam up to the last orbit exceeds the damage limit of the vacuum window and circulator. So for further RTM tuning the beam current was decreased by decreasing the gun current and by deliberate current losses in the injection path.

In succeeding RTM tuning by steering coils additional information from CCD camera viewing synchrotron radiation (Fig. 6) and from a Faraday cup was used.

Figure 6: Synchrotron radiation beam image for 4-9 orbits.

CONCLUSION

As a result of RTM tuning the pulsed beam current of 10 mA was obtained at RTM output. This value was limited by parameters of available RF elements. A new 6 MW window, and circulator have been purchased. After their installation a higher beam current is expected.

REFERENCES

[1] A.I.Karev, V.G.Raevsky, J.A.Konyaev et al, Patent RF #2226686. Filed Dates: August 14, 2002, RF.

[2] A.I. Karev, A.N. Lebedev, V.G. Raevsky et al, RuPAC-2008, p.124

[3] I.A. Frejdovich, P.V. Nevsky, V.P. Sakharov et al, Proceedings of IVEC-IVESC 2006, Report N13.5

[4] N.V. Matveev and S.F. Kravtsov, in Conference Record of the Twenty-Fifth International Power Modulator Symposium, 2002 and 2002 High-Voltage Workshop, p. 378

[5] A.N. Ermakov, D.I. Ermakov, B.S. Ishkhanov et al, Instruments and Experimental Techniques, Vol. 45, No. 4 (2002) 482–489

[6] http://www.us.tdk-lambda.com

[7] http://www.protom.ru

[8] http://www.ni.com

08 Applications of Accelerators, Technology Transfer and Industrial Relations

MAGNETIC COUPLED DISK-LOADED WAVEGUIDE

N.P.Sobenin, S.V.Kutsaev, M.A.Gusarova, M.V.Lalajan ,D.S.Kamenschikov, A.Yu.Smirnov
R.O.Bolgov
Moscow Engineering-Physics Institute, Russia.

Abstract

The results of numerical simulations of electrodynamical parameters (EDP) of magnetic coupled disk-loaded waveguide (DLS) with negative dispersion are presented in this article. Different structure variants for high and low phase velocity were considered. High order modes and multipacting discharge issues were also regarded.

INTRODUCTION

The most common accelerating structure for electron linacs is DLS at travelling wave (TW) and biperiodic accelerating structure (BAS) at standing wave (SW)
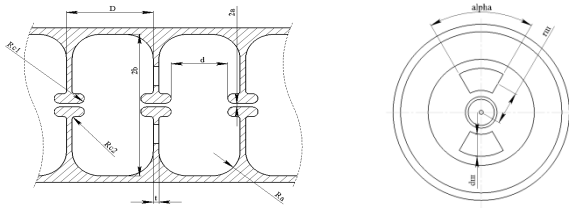
a) longitudinal section   b) transversal section

Figure 1: Magnetic coupled disk-loaded structure

TW magnetic coupled accelerating structure (DLSM) presented at Fig.1 unites the advantages of both electric coupled DLS (small fill time) and BAS (high shunt impedance). This structure is able to work in backward wave regime at the modes less than π [1].

STRUCTURE OPTIMIZATION

To design a linac which use DLSM as an accelerating structure it is necessary to find its optimal dimensions in order to obtain the best electrodynamical parameters. These parameters are the following: shunt impedance r_{sh}, normalized electric field strength $E\lambda/P^{1/2}$ and attenuation α. It is important to know their dependences on operating mode θ, group velocity β_{gr} and coupling coefficient k_c. This optimization was done for the frequency equal to 5712MHz.

Aperture Radius Optimization

First, electro-dynamic parameters dependences on aperture radius to wavelength ratio a/λ were found. At each value of a/λ the coupling holes dimensions were adjusted to make either coupling coefficient or relative group velocity equal to 1%.
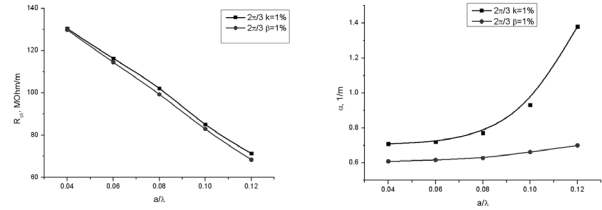
a) shunt impedance   b) attenuation

Figure 2: Parameters dependences on aperture radius

The larger aperture radius means the larger acceptance but also the larger electric coupling. To retain the chosen coupling coefficient it is necessary to increase the magnetic coupling. Besides, the large aperture reduces the electric field concentration near the axis, thus leading to shunt impedance decrease and overvoltage coefficient K_E increase. The results are presented at Fig.2. The $2\pi/3$-mode was chosen as an operating mode for DLSM.

Operating Mode Optimization

Second, it is necessary to optimize the operating mode of the structure, in order to obtain the maximum shunt impedance and normalized field strength. Also, the coupling coefficient and group velocity should be reasonable. The group velocity has the most influence on electric field among all other parameters. Thus, the coupling holes dimensions were adjusted to make β_{gr} equal to 1%.
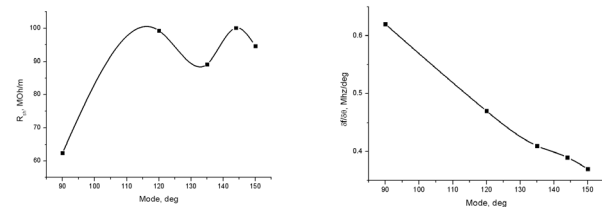
a) shunt impedance   b) frequency separation
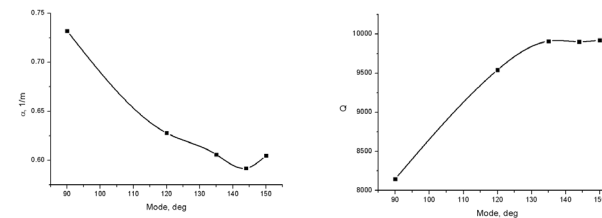
c) attenuation   d) Q-factor

Figure 3: Parameters dependences on the operating mode for DLSM

Another important parameter is a frequency separation between the nearest modes. The higher it is, the less sensitive is the accelerator to frequency deviations.

Shunt impedance, frequency separation and attenuation dependences on the operating mode are presented at Fig.3. During the optimization, a/λ was equal to 0.08. According to these results, the optimal operating mode $2\pi/3$ was chosen. Shunt impedance and normalized electric field have maximum values at these modes.

Shunt Impedance Increase

All previous results were obtained for the structure without drift tubes. But inserting a drift tube can help to concentrate the electric field near the axis and provide an RF-focusing of the particles. It is necessary to regard its influence on the electrodynamical parameters and to estimate the practicality of such an insertion. Fig.4. presents the dependencies of shunt impedance and overvoltage coefficient as functions of drift tube blending radius R_n and length L_n.

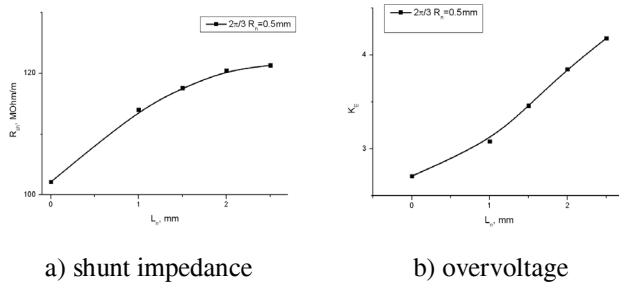a) shunt impedance　　　　　b) overvoltage

Figure 4: Parameters dependences on drift tube length

These results indicate the practicality of small dimensional drift tubes insertion, because the shunt impedance and electric field strength are slightly increased.

Low Phase Velocities

a)shunt impedance　　　　　b) attenuation
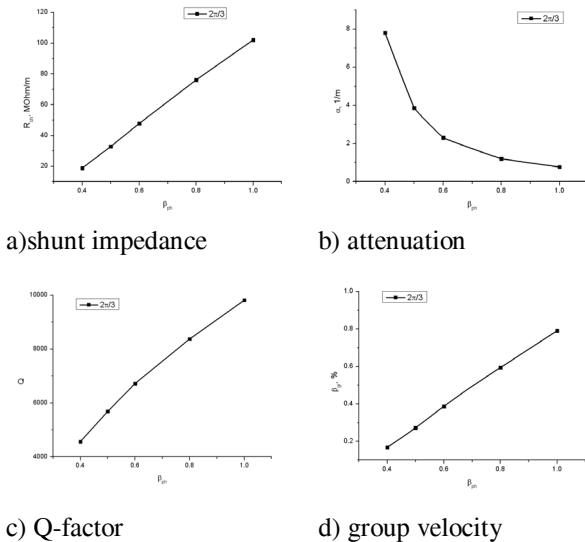

c) Q-factor　　　　　　　　d) group velocity

Figure 5: Electrodynamical parameters dependences on phase velocity

The DLS with magnetic coupling could be also designed for low beta structures without sufficient performance drop. This is important for applications like waveguide buncher with variable phase velocity for TW linear electron accelerator or heavy particle (like proton) accelerating structures. Electromagnetic parameters of DLSM were evaluated at $2\pi/3$ mode. The structure with 1% coupling coefficient operating at 5712 MHz was studied for velocities down to 0.4. Fig. 5 presents the results of r_{sh}, Q, α and β_{gr} [2] dependences on β_{ph}.

Comparison with DLS

Now it is interesting to compare electrodynamical parameters of DLSM with the same of classical electric coupled DLS. The latter structure has no magnetic coupling holes, thus only the aperture radius a/λ defines both coupling coefficient and group velocity. Fig.6 shows compared parameters of DLSM working at mode $2\pi/3$ with $a/\lambda=0.08$ and parameters of DLS working at mode $2\pi/3$ as functions of their group velocities.

a) shunt impedance　　　　　b) coupling coefficient
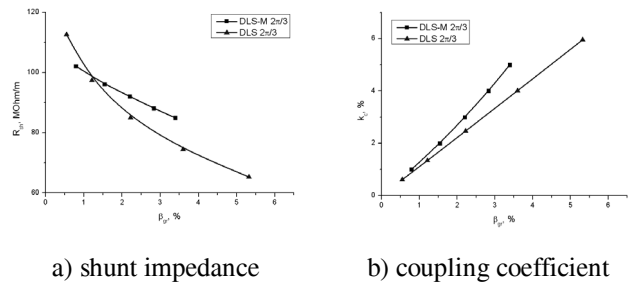
Figure 6: Parameters dependences on group velocity

These graphs show that though DLSM has better coupling coefficient, shunt impedance and is more advantageous regarding the other parameters which are important in the meaning of beam dynamics.

HIGH-ORDER MODES

The high-order modes (HOM) electrodynamical parameters were calculated for DLSM structure with $\beta_{ph}=1$ operating at $2\pi/3$ mode.

Table 1: HOM Parameters

EDC	Type	E_{110}	H_{111}	E_{111}	E_{112}
Frequency, MHz	DLS	8614.1	1041	12566	-
	DLSM	9075.0	6162.5	9885	11186
Q	DLS	13838	12809	8621	-
	DLSM	15094	12836	13128	8446
r_{sh}, MOhm/m	DLS	44.96	0.267	4.44	-
	DLSM	5.22	0.0217	1.44	0.197
k, V/(pC*m)	DLS	43.97	0.34	10.7	-
	DLSM	4.93	0.016	1.699	0.411
$W_\perp$, V/(pC*m²)	DLS	17680	113.4	2796	-
	DLSM	1882	9.2	595.5	127.2

HOM can dramatically influence on the quality of the accelerated beam. In this structure the dipole modes are presented with 2 polarizations. The values of Q-factor, transversal shunt impedance $r_{sh\perp}$, loss coefficient k and induced transversal potential $W_\perp$ for identically E_{110}, E_{111}, H_{111}, E_{112} waves of DLSM and DLS with $a/\lambda=0.1$ are presented in Table 1. The two latter parameters are given per cell. Fig.7 presents the dispersion curves of the nearest HOM.
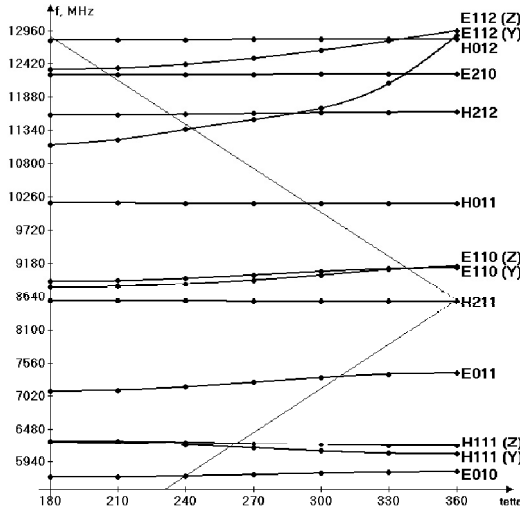

Fig.7 Dispersion curves of nearest HOM

The simulation results confirm that dipole E_{11}-like waves bring the most significant influence on a beam as they have the highest transversal shunt impedance among all HOM. This structure has a good frequency separation (over 3GHz) between operating E_{01} and dangerous E_{11} pass bands. The values of loss coefficients and transversal induced potentials are reasonable.

MULTIPACTING DISCHARGE

The calculations of multipacting discharge in DLSM structure operating at $4\pi/3$ mode with $a/\lambda=0.8$ and $\beta_{ph}=1$ were provided using MultP-M code [3]. The simulations were done for the initial phases ranges from 0 to 360 degrees with a 6 degrees step and the field strengths range from 0 to 30 MV/m. Fig.8 demonstrates the relative counter functions in DLS and DLSM structures. Only particles with 5 or more collisions were taken into account. The simulations were over after 10 RF periods. These graphs show that the increase of electrons number

occurs while the on-axis field strength is higher than 15 MV/m.

a) DLSM   b) DLS
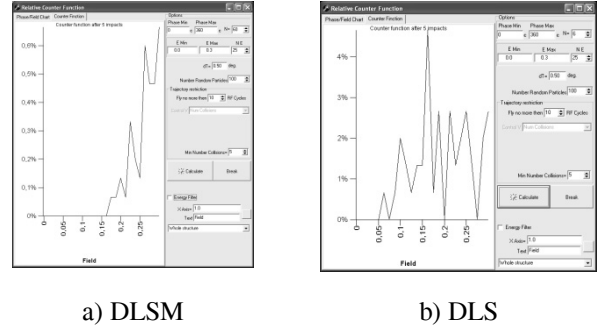
Figure 8: Relative counter functions

Comparing the results for DLS and DLSM it comes clear that the presence of coupling holes considerably improves multipacting discharge resistance.

CONCLUSIONS

The electrodynamical parameters of the magnetic coupled disk loaded structure have been calculated for negative dispersion at frequency 5712 MHz. The comparison of DLSM electrodynamical parameters with same of classical DLS shows the advantages of the described structure. Electrodynamical parameters for structures operating at lower phase velocity were studied. High-order modes parameters of this structure were calculated, which demonstrated the reasonable cell performance in meaning of HOM. The simulations of multipacting discharges proved that magnetic coupling holes help to reduce the probability of this discharge occurrence.

REFERENCES

[1] S.V.Kutsaev, N.P.Sobenin, A.A.Zavadtsev et al. "Magnetic Coupled Accelerating Structure", Problems of Atomic Science and Technology, 54 (2010), p.48-51

[2] O.A.Valdner., N.P.Sobenin, B.V.Zverev et al. Disk-Loaded Structures. 3rd ed. Energoatomizdat, Moscow, 1991, 280p..

[3] M.A.Gusarova, N.P.Sobenin, S.V.Kutsaev et al. "Multipacting Simulation in Accelerating RF structures", Nuclear Instruments and Methods in Physics Research A, 599 (2009), p.100-105

FEASIBILITY OF ALTERNATIVE PHASE FOCUSING FOR A CHAIN OF SHORT INDEPENDENTLY-PHASED RESONATORS

V.V. Kapin[*], A.V. Nesterovich, MEPhI[#], Moscow, Russia.

Abstract

Alternative phase focusing (APF) is usually realized in a long drift-tube structure with multiple acceleration gaps. The synchronous phase alternates periodically gap-by-gap according to either sinusoidal or square-wave laws. The period of synchronous phase oscillations depends on charge-to-mass ratio of accelerated ions and increases with beam energy. One period may include up to 10-20 accelerating gaps. In the case of square-wave law, the sets of 5-10 neighbouring gaps have the same synchronous phase, while whole structure consists of continuous chain such gap-sets with a constant value of synchronous phases. Therefore, every such gap-set can be formed into a separate resonator. As result a long multiple gap structure is converted into a chain of short independently-phased resonators. Such realization of APF linac allows more flexibility in a phase variation, while additional focusing-matching lenses can be set up in betweens of resonators. In this report possible parameters of such linac are evaluated and discussed.

INTRODUCTION

The APF belongs to the wide class of focusing methods by axially symmetrical RF fields provided in sequences of drift-tubes with axially symmetrical cross-sections. The original APF idea of beam focusing by a periodical alternating a synchronous phase in a sequence of the drift-tube gaps has been developed and modified since the early 50's by many authors. In the papers [1-5], there are comprehensive lists of references to the most known recipes of generating the APF drift-tube structures.

In the APF linac, the synchronous phase alternates periodically gap-by-gap according to either sinusoidal or square-wave laws. The period of the synchronous phase oscillations may include up to N_g =10-20 accelerating gaps which forming up one focusing period.

Usually, APF is considered for long multiple-gap resonators containing several tens of drift-tubes. However, APF linac also can be realized as a chain of short independently-phased resonators similar to superconductiong heavy-ion linacs [6]. For example, APF linacs consisting of the chain of *identical* short independently-phased resonators had been analyzed in Ref. [7,8], while S.A. Minaev [7] considered resonators with one and two gaps and increasing N_g along linac, and E.S. Masunov [8] considered 4-gap "fork" structures with a constant N_g =4.

The main feature of both concepts is constant number

of gaps in every short resonator. It is known [1,2], that in order to preserve a position of working point on the stability diagram, it is necessary to increase N_g along the linac. For example the approach of Ref. [7] uses an increasing number of N_g along the linac (up to 10-20). Alternatively, in the approach of Ref.[8], operating point can be stabilized by an additional focusing force.

In this paper, it is suggested to use a chain of short independently-phased resonators with increasing number of the gaps in every short resonator along a whole linac. This feature may minimize the total number of short independently-phased resonators, while preserving a position of working point on the stability diagram without an additional focusing force.

APF IN CHAIN OF RESONATORS

Method for stability analysis

The stability analysis is based on the methods developed for the asymmetrical alternative phase focusing (A-APhF), which has been proposed by V.V. Kushin in more than 30 years ago [1,2]. In the report [9], stability conditions had been extended for an arbitrary law of the synchronous phase oscillations.

Following Ref. [9], the synchronous phase sequence can be written as the step-wise function $\varphi_s(\tau) = \overline{\varphi} + \widetilde{\varphi}(\tau)$, which is the sum of the constant and varying functions $\overline{\varphi}$ and $\widetilde{\varphi}(\tau)$, respectively, while $\widetilde{\varphi}(\tau)$ is constant within every accelerating period. The focusing period of APhF linac L_f coincides with the period of phase excursions. With independent variable $d\tau = dZ_s/L_f$, small phase deviations of particle phase ψ and a linear radial motion ρ can be expressed by the following Matiew-Hill equations:

$$\begin{cases} d^2\psi/d\tau^2 + P_\psi(\tau)\cdot\psi = 0 \\ d^2\rho/d\tau^2 + P_\rho(\tau)\cdot\rho = 0 \end{cases} \quad (1)$$

where the periodical step-wise functions $P_\psi(\tau) \equiv P_\psi(\tau+1)$ and $P_\rho(\tau) \equiv P_\rho(\tau+1)$, are given by the following equations

$$\begin{cases} P_\psi(\tau) = 2B\cdot\sin[\overline{\varphi} + \widetilde{\varphi}(\tau)] \\ P_\rho(\tau) = -B\cdot\sin[\overline{\varphi} + \widetilde{\varphi}(\tau) + \psi] \end{cases} \quad (2)$$

The focusing strength B [1,2] is given by

$$B = \left(\pi q E_{\mathrm{m}} / m_o c^2\right)\left(\lambda / \beta_{\mathrm{s}}\right)\left(L_{\mathrm{f}} / \beta_{\mathrm{s}}\lambda\right)^2 \left(1 - \beta_{\mathrm{s}}^2\right)^{3/2}. \quad (3)$$

The Matiew-Hill equations with periodical step-wise functions can be solved using a well-known matrix technique [10]. The RMS and average values of functions $P_\psi(\tau)$ and $P_\rho(\tau)$ can be used to build stability diagrams [9]. In present study, the matrix technique has been performed numerically using procedures of the mathematical package MAPLE-V [11]. The MAPLE's code for APF design had been developed early in Ref.[8].

Figure 1 shows an example of the necktie stability diagram for longitudinal and transverse motion calculated for a focusing period with N_{g} =8. The curves of constant values of phase advances per period for longitudinal and radial oscillations μ_{L} and μ_{R} are shown. For the strong focusing it is usual to keep that the representative point inside the stable region near the intersection of the curves $\cos \mu_L$ =0 and $\cos \mu_R$ =0.
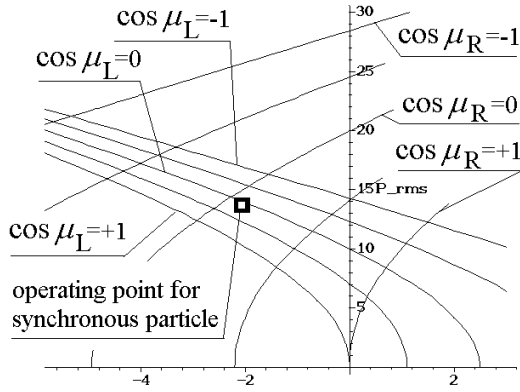

Fig. 1. The necktie stability diagram.

Figure 2 presents the radial stability diagram shown for non-synchronous particles located near synchronous with step of 5 degree. The square and cross marks are used to show positions of position of synchronous and non-synchronous particles, respectively.
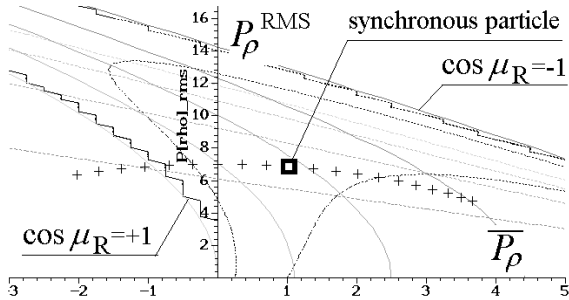

Fig.2. The radial stability diagram with synchronous and non-synchronous particles

Dependence of N_{g} on the particle velocity

The position of operating point on the stability diagrams are mainly affected by the values of focusing strength B. According to the eq. (3), with increasing the

particle velocity β_{s}, the focusing strength B is decreased. The amplitude of the accelerating wave E_{m} also depends on β_{s}, while this dependence is defined b the type of the accelerating resonator. Let's consider the case of a constant $E_{\mathrm{m}}(\beta_{\mathrm{s}})$=const, which means that the gap voltage monotonically increases along the linac. In this case, B decreases as $B \propto N_{\mathrm{g}}^2(\beta_{\mathrm{s}})/\beta_{\mathrm{s}}$.

To keep the focusing strength and a position of operating point in the center of stability diagram, it is necessary to increase N_{g} along the whole structure as square-root of β_{s}, i.e. $N_{\mathrm{g}} \propto \beta_{\mathrm{s}}^{0.5}$. It is very approximate relation neglecting variations of $\varphi_{\mathrm{s}}(\tau)$-function. The actual dependence of N_{g} on β_{s} can be calculated for a particular linac design using the considered matrix method.

Two APF designs have been calculated: 1) the 20 MeV 300 MHz proton linac; 2) the 6 MeV 150 MHz ion linac with the charge-to-mass ratio 1/8. The square-wave law for the synchronous phase variations is used.

Figures 3 and Fig. 4 show the dependence of N_{g} on β_{s} for these designs at even N_{g} values. The calculated $N_{\mathrm{g}}(\beta_{\mathrm{s}})$-dependences are approximated as $N_{\mathrm{g}} \propto \beta_{\mathrm{s}}^{0.65}$, which is close to the approximate square-root dependence. The $W(\beta_{\mathrm{s}})$-dependences are also shown in Fig.3 and Fig.4.
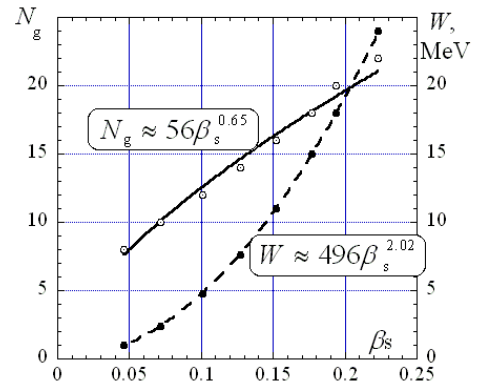
Fig.3. $N_{\mathrm{g}}(\beta_{\mathrm{s}})$ and $W(\beta_{\mathrm{s}})$ for the proton APF linac.

It seen that one period include 8-22 gaps for the 20-MeV proton linac, and 16-30 gaps for 6 MeV ion linac. The linacs contains the sets neighbouring gaps, which gaps have the same synchronous phase. Whole structures consist of continuous chain such gap-sets with a constant value of synchronous phases. Therefore, every such gap-set can be formed into a separate resonator. As result a long multiple gap structure is converted into a chain of short independently-phased resonators.

Fig.4. $N_g(\beta_s)$ and $W(\beta_s)$ for the ion APF linac.

Tables 1 and 2 shows main parameters of these APF linacs, calculated using the approach described in Ref.[9] as for a single multiple-gap resonator. The neighbouring gaps with the same φ_s can compose separate resonators of the length L with number of gaps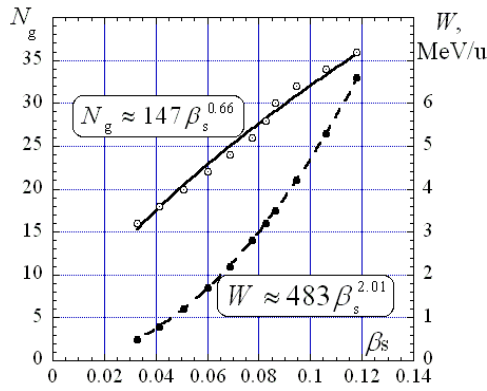 n_g. As it is suggested in the tables, the 1-20 MeV 75-gaps proton linac of the length of 4.3 m and the 0.5-6.0 MeV/u 198-gaps ion linac of the length 14 m can be decomposed into 12 and 17 independenly-phased resonators, respectively. For a comparison, the number of independenly-phased resonators in APF linacs using of 1, 2, or 4 gap resonators as suggested in Ref. [7,8] is much larger, e.g., the proton and ion linacs will consist of 19 and 50 four-gap resonators, respectively.

The suggested here realization of APF linac allow to minimize the total number of independenly-phased resonators, while keeping flexibility in a phase variation. Practically, the considered APF linac can be realized as a chain of short interdigital H-type resonators with 4-20 gaps pre resonator, while additional focusing-matching lenses can be also set up in betweens of the resonators.

REFERENCES

[1] V.V. Kushin, "Accelerator with Alternating Phase Focusing", Ch. 7 in book: "Linear ion accelerators", ed. By B.P. Murin, 1978 (in Russian), pp.173.

[2] V.V. Kushin, "Ion Acceleration in APF systems", Proc. 1994 Int. Linac Conf., Tsukuba, pp. 957.

[3] H. Okamoto, "Beam Dynamics in Alternating Phase Focusing Linac", N.I.M., A 284, 1989, pp. 233-247.

[4] W.H. Cheng et al.,"Alternating Phase Focusing Including Space Charge", Proc. 1992 Linac Conf., Ottawa, pp. 193-195.

[5] S. Minaev, U. Ratzinger, B. Schlitt, "APF or KONUS drift tube structures for medical synchrotron injectors – a comparison", Proc. 1999 PAC, New York, 1999, pp.3555-3557.

[6] K.W. Shepard, "The U.S.RIA Project SRF Linac", Proc. 10th Workshop on RF Superconductivity, 2001, Tsukuba, pp.313-317.

[7] S.A. Minaev, "Ion Beam Acceleration and Focusing in the Polyharmonical Drift Tube Systems", Proc. EPAC 1990, pp.1744-1746.

[8] E.S. Masunov, D.A. Efimov, P.N. Ostroumov, "RF focusing of Low-Charge-to-Mass-Ratio Heavy Ions in a Superconductiong Linac", Proc. EPAC 2004, pp. 1405-1407.

[9] V. Kapin, S. Yamada, Y. Iwata, "Design of APhF-IH Linac for a Compact Medical Accelerator", report HIMAC-075, 2003, 37p. (the PDF-file at site: http://cdsweb.cern.ch/).

[10] L. Smith and R.L. Gluckstern, "Focusing in Linear Ion Accelerators", The Rev. of Sci. Instrum., Vol. 26, No. 2, 1955, pp. 220-228.

[11] M.B. Monagan et al, MAPLE V – Programming Guide, 1998 by Waterloo Maple Inc.

Table 1. Parameters of the 1-20 MeV proton linac.

gap no.	φ_s, deg	L, cm	W, Mev/ inp/out	n_g	Reso nator
1-4	-45	10.0	0.9-1.1	4	1
5-8	73	16	1.1-1.4	4	2
9-13	-45	31	1.4 2.0	5	3
14-18	69	49	2.0-2.6	5	4
19-23	-44	69	2.6-3.4	5	5
24-29	65	97	3.4-4.3	6	6
30-35	-43	32	4.3-5.7	6	7
36-41	59	35	5.7-7.0	6	8
42-48	-41	46	7.7-8.9	7	9
49-56	52	61	8.9-11.8	8	10
57-65	-35	78	11.8-15.9	9	11
66-75	39	99	15.9-21.0	10	12

Table 2. Parameters of the 0.5-6.0 MeV ion linac.

gap no.	φ_s, deg	L, cm	W, Mev/u inp/out	n_g	Reso- nator
1-8	-45	20	0.46-0.54	8	1
9-16	73	28	0.54-0.60	8	2
17-25	-45	34	0.60-0.76	9	3
26-34	69	37	0.76-0.83	9	4
35-43	-44	40	0.83-0.99	9	5
44-52	65	42	0.99-1.11	9	6
53-62	-43	51	1.11-1.33	10	7
63-73	62	61	1.33-1.51	11	8
74-84	-42	65	1.51-1.80	11	9
85-95	57	71	1.80-2.04	11	10
96-107	-39	82	2.04-2.41	12	11
108-119	53	89	2.41-2.74	12	12
120-133	-35	112	2.74-3.28	14	13
134-148	40	132	3.28-3.90	15	14
152-164	-30	152	3.90-4.69	16	15
165-182	39	177	4.69-5.52	17	16
183-198	-29	192	5.52-6.53	17	17

DEVELOPMENT OF WIRE-MESHED ELECTROSTATIC LENSES FOR PROTON LINAC

V.V. Kapin[*], B.Yu. Bogdanovich, A.V. Nesterovich,
V.V. Yanenko, MEPhI[#], Moscow, Russia

Abstract

The 2-MeV 150-MHz proton RFQ linac is set up at the Radiation-Acceleration Center (RAC) of Moscow-Engineering Physics Institute (MEPhI). Its output beam-line contains doublet of the electrostatic focusing lenses with a novel design featured by the two-dimensional electric field and wire-meshed beam apertures. Every lens provides a transverse focusing effect only in one plane, while does not affect on the beam in a perpendicular plane. In this report, the analytical and numerical analysis of this lens is presented. The optics of output beam-line including these lenses is evaluated with TRACE-3D code. The experimental construction of the lens doublet is presented.

INTRODUCTION

The 2-MeV 150-MHz proton RFQ linac [1] is set up at RAC of MEPhI. It serves as a base system for the applied research works. Its output beam-line consists of doublet of the electrostatic focusing lenses, the post-accelerating 7-gap two-ridge interdigital H-resonator and a magnetic C-shaped spectrometer with vertical magnetic field.

Initially, the output beam-line with focusing doublet of two magnetic quadrupoles (instead of electrostatic lenses) had been simulated with TRACE-3D code [2]. It was shown [3] that the beam transmission is less than 10% without a focusing doublet, and it can reach 100% at the optimal magnetic field gradients of 6-7 T/m.

Although these gradients are quite moderate for a modern technology, a fabrication of quadrupoles may require impermissible efforts and resources for our small experimental setup. Therefore, the alternative focusing system based on wire-meshed electrostatic lenses had been proposed. In this report, the features and status of doublet of the electrostatic focusing lenses are presented.

WIRE-MESHED ELECTROSTATIC LENS

General Scheme of the lens

An unconventional design of the electrostatic lens featured by the two-dimensional electric field and wire-meshed beam apertures is proposed. Figure 1,a shows the ideal 2D-layout of such lens, which consists of two plane electrically-grounded wire-meshes located at planes $z=\pm l/2$ and two (upper and lower) high-voltage (U_{m}) cylindrical electrodes of radius R located at distance a from z-axis. The 3D model of the lens and the distribution of electric potential in the lens cross-section at $x=0$ are shown in Fig.1,b and Fig.1,c, respectively.
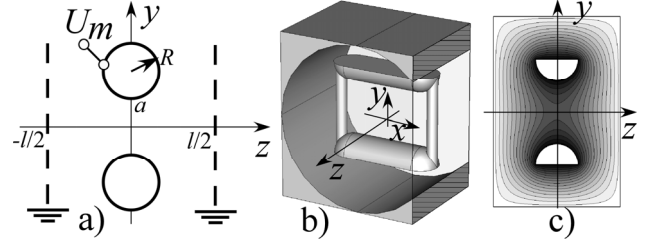
*kapin@mail.ru
[#]National Research Nuclear University "MEPhI"; http://www.mephi.ru

Figure 1: Layout of wire-meshed electrostatic lens:
a) 2D ideal layout; b) 3D model; c) potential at x=0.

Such lens provides a transverse focusing effect only in one plane (the Y0Z-plane in Fig.1), while does not affect on the beam in a perpendicular plane (the X0Z-plane in Fig.1). The pair of such lenses rotated by 90-degree relatively each other can provide an independent focusing in both transverse planes.

Focal distance evaluation

Let's evaluate the focal distance in a this-lens paraxial approximation according to the formulae

$$f_y = y_0/\mathrm{tg}(\alpha_y) \approx y_0/\alpha_y ,\qquad (1)$$

where y_0 is the transverse particle coordinate at the lens center and $\alpha_y \approx \Delta v_y/v_z$ is the angle kick provided by the lens. Let's neglect deviations of the longitudinal velocity v_z. Then, the increment of the vertical velocity Δv_y can be expressed as

$$\Delta v_y = \frac{q}{m_0 v_z} \int_l E_y \cdot dz ,\qquad (2)$$

where the integral can be treated as a transverse lens voltage U_y. Note, that the transverse voltage can not exceed the electrode potential

$$U_y = \int_l E_y \cdot dz \le U_{\mathrm{m}} .\qquad (3)$$

Finally, the angle kick α_y is expressed as

$$\alpha_y = U_y/\left(W\beta_z^2\right),\qquad (4)$$

where $W = m_0 c^2 \gamma / q$ is particle energy, and β_z is the relative velocity. Let's note that α_y strongly depends on β_z decreasing inversely as the square of β_z, and is proportional to U_y, which will be evaluated below.

Evaluation of Minimum focal distance

In linear this-lens approximation, the focusing distance of this lens can be evaluated assuming a maximum value of $U_y \approx U_m$, which can be reached at $y_0 = a$. Then, the focal distance is expressed as

$$f_y^{\min} \approx W\beta^2 a / U_m . \qquad (5)$$

Let's evaluate $f_y^{\min}$ for protons at RFQ exit. There can be two portions of protons, namely the accelerated ones with the energy of 2-MeV and the non-accelerated ones with energy of 0.1 Mev. For 2-MeV protons (the total energy W=940 MeV and β=0.066) the lens with the radius of aperture a=1cm and the voltage U_m=100kV can ensure the focal distance about 0.4 м. For 0.1 Mev protons the focal distance is much smaller and is equal to 0.05 m. It is clear that the lenses can work as supplementary energy filter for low-energy protons.

2D analytical formula for U_y

Assuming 2-D ideal geometry analytical formula for the potential distribution $U(y,z)$ can be derived [4]. Applying the boundary conditions $U(0, \pm l/2) = 0$ and $U(a, 0) = U_m$, the lowest-order potential can be written in the following form [4]:

$$U(y,z) \approx U_m \frac{\mathrm{ch}(\pi y/l)}{\mathrm{ch}(\pi a/l)} \cos(\pi z/l) . \qquad (6)$$

Then, the transverse lens voltage is expressed by the following formula:

$$U_y(y) = -2U_m \frac{\mathrm{sh}(\pi y/l)}{\mathrm{ch}(\pi a/l)} . \qquad (7)$$

Note, that the equation (7) does not take into considerations higher harmonics of a potential, which are important to express the potential distribution for a realistic configuration of the lens.

3D numerical calculations of U_y

The 3D numerical calculations has been performed for a realistic lens geometry at the electrode voltage U_m =1 kV. The horizontal electrodes with the radius R =10 mm and the length of 60 mm are located in the cylindrical tank with the radius of 45 mm and the length

l =60 mm (see Fig.1). The 3D-simulated potential and electrical field distributions along z-axis are shown in Figure 2.
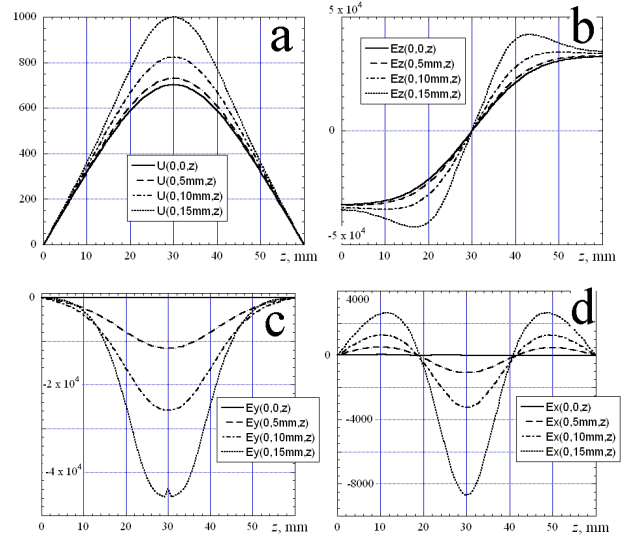

Fig.2. The potential and electrical fields vs z:

a) $U(0, y_0, z)$ at y_0 =0, 5 ,10, 15 mm;

b) $E_z(0, y_0, z)$ at y_0 =0, 5 ,10, 15 mm;

c) $E_y(0, y_0, z)$ at y_0 =0, 5 ,10, 15 mm;

d) $E_x(x_0, 0, z)$ at x_0 =0, 5 ,10, 15 mm;

The numerically calculated transverse potential distributions $U_y(y)$ and $U_x(x)$, and $U_y(y)$ calculated with eq.(7) are shown in Fig.3. Note, that $U_x \ll U_y$, and the expression (7) describes $U_y(y)$ well at $y \ll a$.
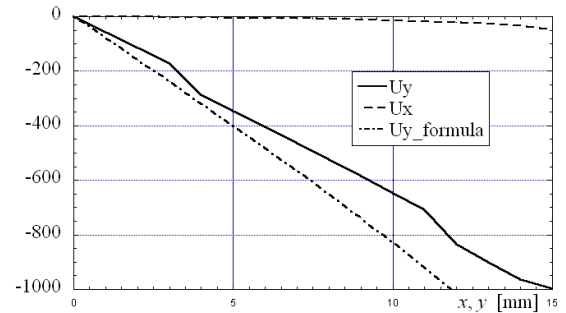

Fig. 3 The transverse potential distributions:
$U_y(y)$ -numerically and analytically calculated,
$U_x(x)$ -numerically calculated.

Beam optics evaluations

The beam transport in the output beam line has beam evaluated using the TRACE-3D code [2]. The simulated beam-line consists of two exit RFQ-cells, the wire-meshed electrostatic lenses, the 90°-bending magnet with zero field-gradient index and input and exit edges simulating the magnet fringe-fields, while all components

separated with appropriate drift-spaces. In these simulations, the focusing effects of 7-gap IH-stricture are neglected, and structure is simulated by the drift-space. Thus, beam focusing in this beam-line is ensured by electrostatic lenses and the magnet fringe-fields.

The beam dynamics simulations are shown that without any focusing (the electrostatic lenses and fringe-fields are off) the beam transmission in the whole output beam-line is very low (about 2.5%). When the fringe-focusing is used, the beam transmission is increased up to 7.5%, which is still very low. Only with usage of doublet of lenses, it is possible provide the 100% beam transmission. Figure 4 shows the beam phase-spaces at the input and output of the beam-line and the beam envelopes along the beam-line.

In the calculations, the doublet of the wire-meshed electrostatic lenses with total length of 120 mm is located near to the RFQ-exit at the distance 200 mm. The focal distances of the lenses are equal to 0.4 m, which corresponds to U_m=100kV. Practically, this voltage can be taken from high-voltage terminal of ion source.
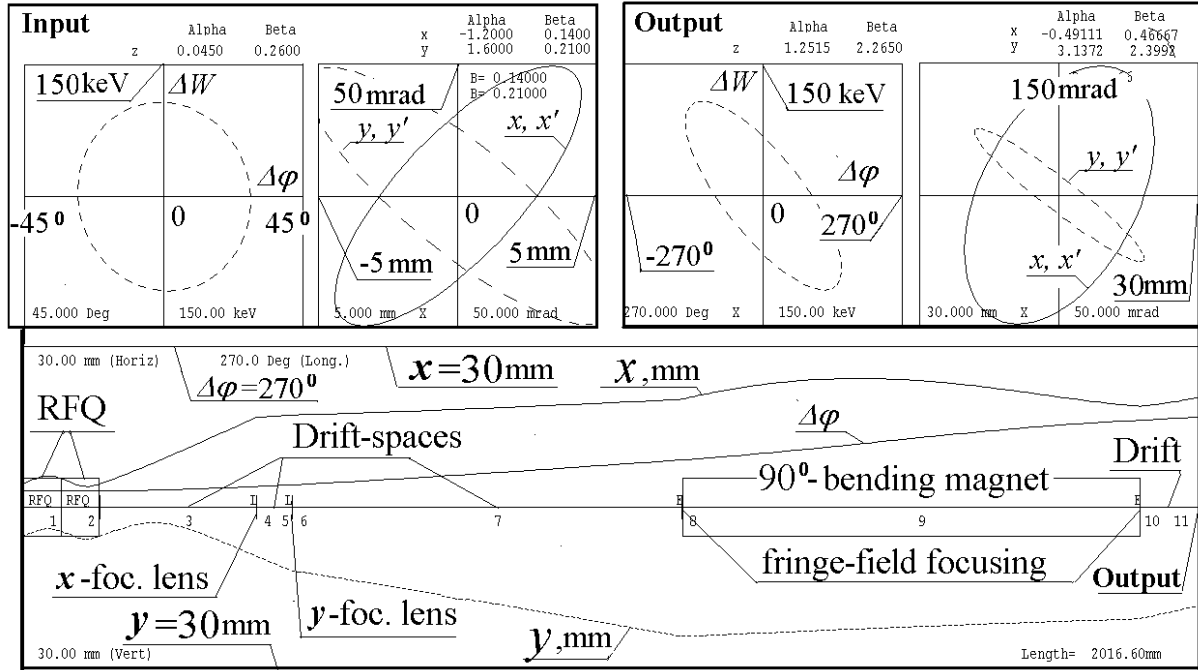

Fig.4 Beam phase-spaces and envelopes calculated by TRACE-code.

The construction of the lens doublet

The doublet of the wire-meshed lenses has been constructed, fabricated and tested at the maximal electrode voltage U_m=100kV. Figure 5 shows a general view of the fabricated doublet of the wire-meshed lenses.

REFERENCES

[1] O.K. Belyaev, O.V. Ershov, I.G. Maltsev, V.B. Stepanov, S.A. Strekalovskikh, V.A. Teplyakov, A.V. Zherebtsov, "IHEP Experience on Creation and Operation of RFQs", LINAC'2000 , MOD21, Monterey, pp. 259-262 (2000).

[2] K.R. Crandall, "TRACE: An Interactive Beam-Transport Program," Los Alamos Scientific Laboratory report LA-5332 (October 1973).

[3] B.Yu. Bogdanovich, V.V. Kapin, A.V. Nesterovich, A.N. Puchkov, V.N. Soloviev, V.P. Zubovskiy, V.V. Yanenko, "The Output Beam-line and a Novel Ion Source of 2 MeV Proton RFQ Linac", Proc. RuPAC-2008, p.307-309.

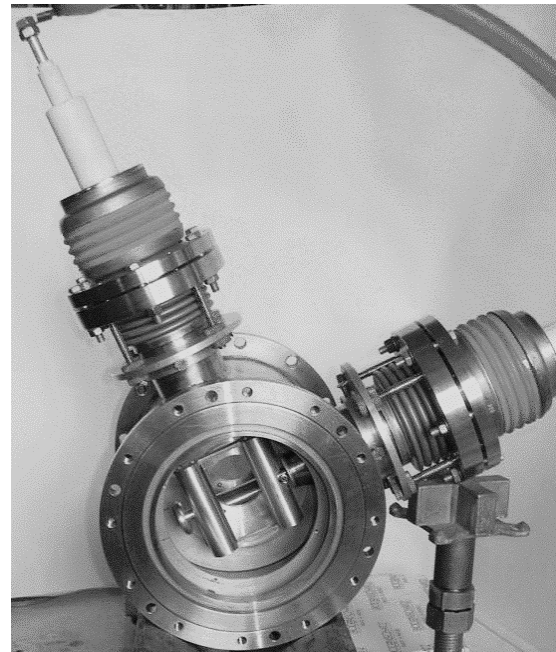[4] S.M. Molokovsky, A.D. Sushkov, "Intense Electron and Ion Beams", 2005 by Springer-Verlag.

Fig. 5 General view of the wire-meshed lenses

INPUT COUPLERS FOR THE DIPOLE MODE PERIODIC STRUCTURES

A. Anisimov, M. Lalayan, A. Smirnov, N. Sobenin,
National Research Nuclear University – MEPhI, Moscow, Russia
A. Zavadtsev, D. Zavadtsev, S. Kutsaev
Nano Invest, Moscow, Russia
L. Kravchuk, V. Paramonov
Institute for Nuclear Research of Russian Academy of Sciences, Moscow, Russia

Abstract

Three variants of the input coupler for the periodic deflecting structure, operating at hybrid dipole E_{11} mode, with the phase velocity equal to the light speed are considered: non-symmetric design and two symmetric designs with auxiliary rectangular waveguide and shorting plates in it along with auxiliary cut-off rectangular waveguide. The reflection coefficient dependences on the coupling window width and on the coupling cell diameter was been investigated for all these coupler variants. The reflection coefficient has been calculated in the whole dipole mode pass-band. The field asymmetry in the beam area has been investigated. The eigen frequency of the coupling cell has been calculated.

INTRODUCTION

Three input coupler designs have been developed for Transverse Deflecting System. 16-cell deflecting structure is shown on Fig.1 with three input coupler versions: non-symmetric coupler (a), symmetric coupler with shorting plates in additional waveguide (b) and symmetric coupler with cut-off additional waveguide. Three variants of the disk loaded waveguide (DLW), operating at 2997.2 MHz frequency and $2\pi/3$ mode, as a deflecting structure are considered: with two holes stabilizing the deflecting plane position, with two recesses at periphery cylindrical surface and with elliptical aperture hole [1].

SIMULATION MESH CHOICE

The simulation accuracy of the deflecting structure with two couplers in traveling wave operation depends on mesh used. The calculation of the TDS cell geometry has been done using 3-cell model with two coaxial couplers (Fig.2). The electric field distribution at $2\pi/3$ mode in resonant model and the tetrahedron simulation mesh in the traveling wave model are shown in Fig.2. The calculation has been done frequency band 2996.2 - 2998.2 MHz with frequency step df=0.05 MHz.

Figure 3 shows the number of mesh cells (a), reflection S_{11} (b) and tuning quality ratio K (c) depending on the number of simulation iterations for 16-cell deflecting structure with two couplers. The tuning quality ratio shows uniform distribution of the transverse electric field in the iris planes. The same mesh in 3-cell and in 16-cell models is equivalent to 64949 and 407464 tetrahedrons correspondently.
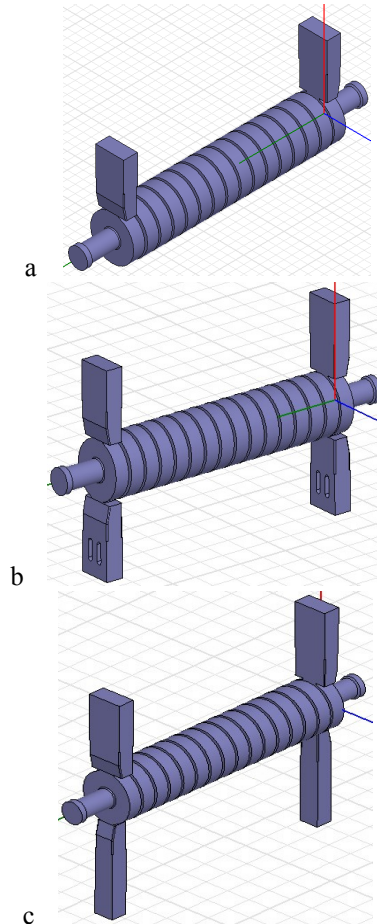

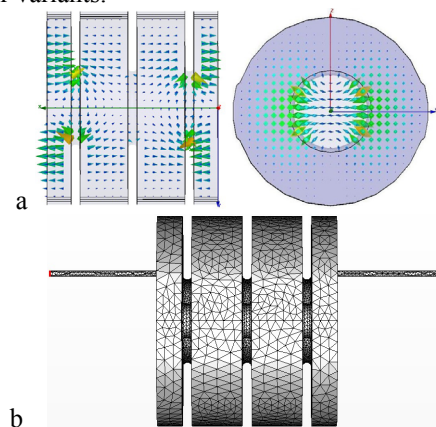Figure 1: The deflecting structure with three input coupler variants.

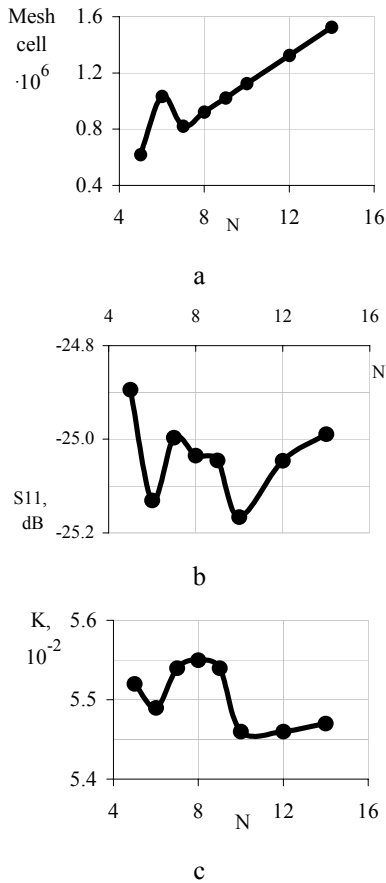Figure 2: The field distribution in resonant model (a) and the mesh in the traveling wave model (b).

07 Accelerator Technology Main Systems

a

b

c

Figure 3: Dependences on the number of mesh cells.

INPUT COUPLER TUNING

The simulation of the coupler with cut-off waveguide with 16-cell two stabilizing holes deflecting structure includes varying of the coupling window width X and the coupling cell radius R [2]. The reflection S_{11} in the input waveguide and the tuning quality ratio K are considered as tuning parameters. The reflection S_{11} in the input waveguide and the tuning quality ratio K depending on the coupling cell radius R and coupling window X are shown on Fig. 4. All dependences in f

Fig.4 presented for different X values: X = 32.15mm marked with "○", X = 32.25mm marked with "x ", X = 32.45mm marked with "+ " and X sweep X = 31.80 – 32.45mm for R = 53.68mm.

a

b
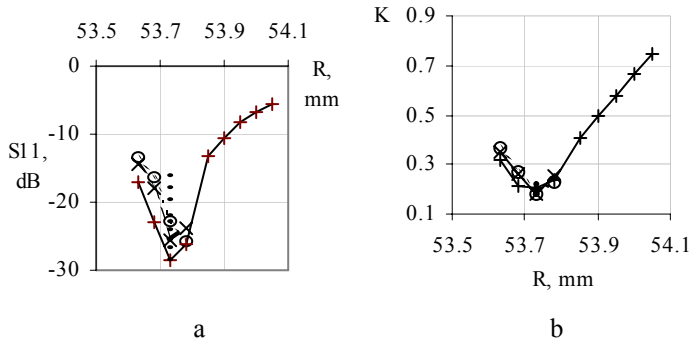
Figure 4: The reflection S_{11} in the input waveguide and the tuning quality ratio K depending on the coupling cell radius R and coupling window X.

FIELD SYMMETRY IN THE COUPLER

The transverse electric field asymmetry in the all variants of the coupler has been investigated. The field asymmetry is $\Delta E/E_1$, where $\Delta E = E_2 - E_1$, E_2 is the field in the center of the coupling cell, E_1 is the minimal field strength value (Fig.5b). The field symmetry in the coupler with the plates in additional waveguides can be tuned changing of the plates position and changing of the coupling window for the additional waveguides.

The calculation has been done in three transverse cross-sections, shown in Fig.5a.

The calculation result of the field asymmetry for the three couplers are shown in Figure 5c. For three variants there are dependences: line marked with circles "○" for structure illustrated in Fig.1.c. For structure in Fig.1.a. line marked with rhombus "◊". And for structure from Fig.1.b. pointed with triangles "Δ".

a   b

c
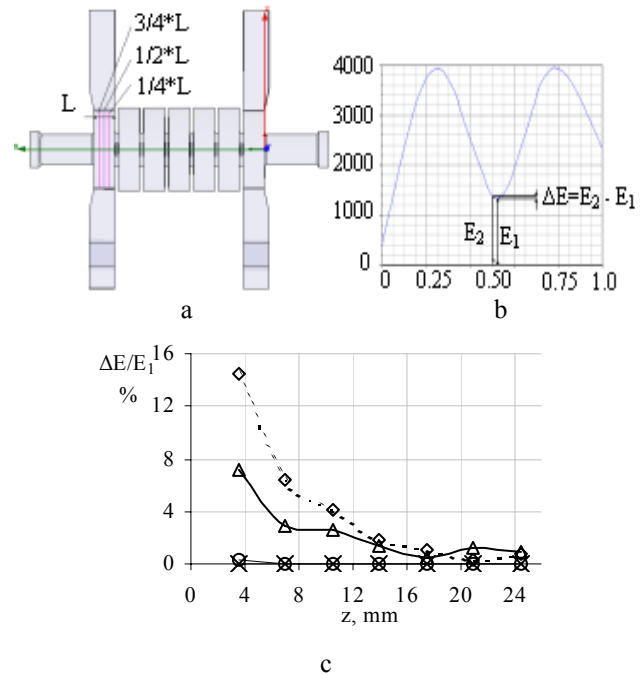
Figure 5: Cross-sections for the field asymmetry measurement (a) and the field asymmetry for the three couplers (b).

During the investigation of the coupler, shown in Fig.1b, additional resonances have been detected at the frequencies both lower than operation pass-band E_{11} and within it. The resonant frequencies depend on the plate position. The second cell has been detuned by addition plunger for the calculation of the first (coupler) cell frequency. The field distribution for two modes are shown in Fig.6.

Figure 6: Electric field distribution at two modes.

Eigen frequencies and the Q-factors of the coupler cell at two modes depending on the plate position are shown in Fig.7. The frequency of one mode is below the operating frequency, and the second one is close to it. So the cavity in the additional waveguide may be excited at operating frequency. In Fig. 7 dash line for antiphased mode, constant line for cophasal mode.
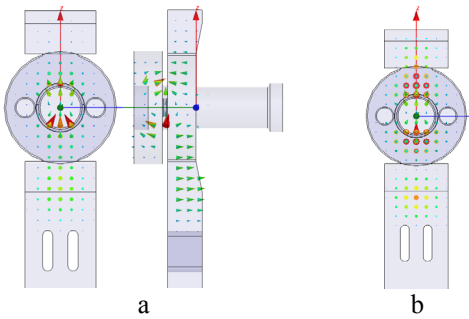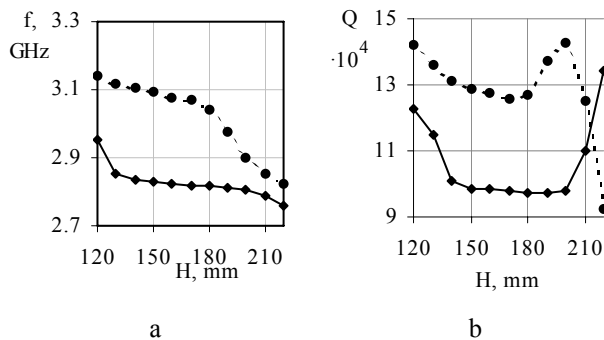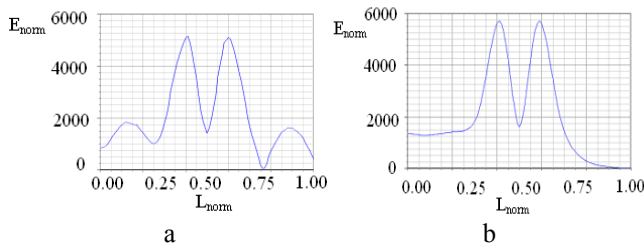

Figure 7: Eigen frequencies and the Q-factors of the coupler cell at two modes depending on the plate position.

Figure 8: Distribution of the transverse electric field in the coupler cell along the waveguide axis in the coupler with the additional waveguide and the plates (a) and in the coupler with cut-off waveguide (b). Normalized length is L_{norm}=113.57 mm.

The coupler with cut-off additional waveguide is a chosen working variant [2].

AMPLITUDE AND PHASE OF DEFLECTING FIELD DISTRIBUTIONS

The amplitude and the phase per structure period of the deflecting field at the structure axis is shown in Fig.9.

MATCHING OF THE COUPLER

The calculated reflection S_{11} in the input waveguide for the structure with the coupler, shown in Fig.1c, in the frequency pass-band is shown in Fig.10. Similar data has been got for another couplers.

CONCLUSION

Performed investigations of different variants of the input coupler shown, that the variant with cut-off additional waveguide in preferable. There is no dangerous possibility to deriving of the power part to the resonance cavity in the additional waveguide, which could lead to the elongating of the filling time in the structure.
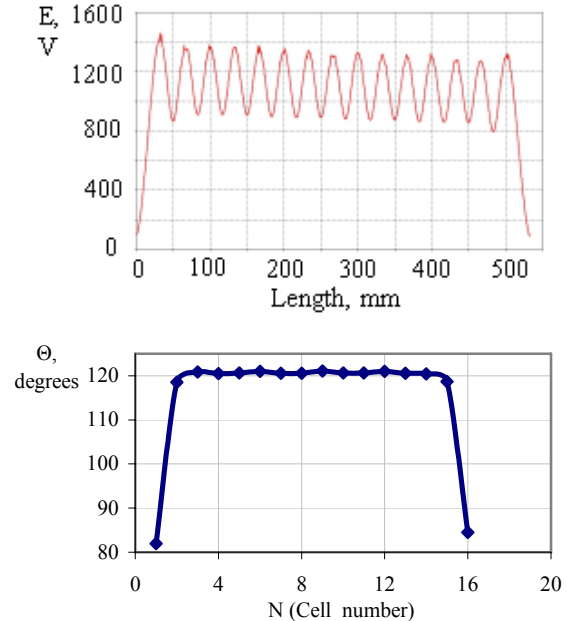
Figure 9: The amplitude and the phase per structure period of the deflecting field at the structure axis.
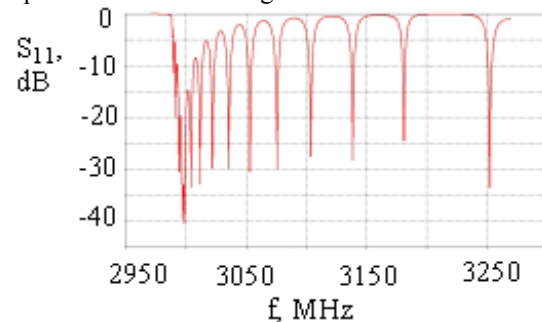
Figure 10: Reflection S_{11} in the input waveguide for the structure with the coupler, shown in Fig.1c.

REFERENCES

[1] N.Sobenin, M.Lalayan, S.Kutsaev, A.Anisimov A.Smirnov, I.Isaev, A.Zavadtsev, D.Zavadtsev. Stabilization of the Polarization Plane in Travelling Wave Deflectors, Proc. IPAC10, p.3759, 2010.

[2] L. Kravchuk, A. Anisimov et all.Layout of the PITZ Transverse Deflecting System for Longitudinal Phase Space and Slice Emittance Measurements, Proc. of LINAC2010.

07 Accelerator Technology Main Systems

MATERIALS FOR FAST CYCLING ACCELERATOR SUPERCONDUCTING MAGNETS

P. Shcherbakov, I. Bogdanov, S. Kozub, L. Shirshov, P. Slabodchikov, V. Sytnik, L. Tkachenko, V. Zubko, Institute for High Energy Physics, Protvino, Moscow region, 142281

Abstract

Development of fast-cycling superconducting magnets with high field amplitudes and ramp rate makes severe requirements especially to material properties in order to improve field quality and to reduce AC losses. Analysis of experimental and literature data is fulfilled for magnetic characteristics of electric steels at different temperatures. Susceptibilities of stainless steels of different grades are examined as well as a tolerance on the value of the magnetic permeability. Mechanical, thermophysical and technological properties at room and cryogenic temperatures are presented. Comparison of steel characteristics, selected for the SIS300 quadrupole prototype, with the steels, used in the SIS300 dipole and steels, applied in the SIS100 prototype magnets is carried out. General advices to the choice of materials for electrical and stainless steels, used in a design of fast-cycling magnets, are given. [*]

INTRODUCTION

IHEP takes part in the development of SC magnets for SIS300 from 2001 year [1]. The substantiation of steel selection for fast cycling magnets of FAIR SIS300 and SIS100 was the one of IHEP task. Accelerator dipoles work at the field ramp rates 1 T/s and 4 T/s correspondently. The main materials of SC magnet design beside the superconductor are yoke electric steels and stainless steels for collars, vacuum pipes and other elements.

In 2003 in IHEP and GSI the study of magnetic properties of steels with 1-4% Si at different temperatures have been carried out. The anisotropy of magnetic properties has been determined and hysteresis loss have been measured in symmetric, unipolar and partial cycles [2].

Main conclusions of R&D are: a) the reducing of temperature up to 4.2 K effects on magnetic properties less than in low carbon steels; b) anisotropy, obtained on the strips of one direction (in the rolling direction and transverse one) is averaged in the ring samples, and the properties of isotropic and anisotropic steel with similar Si content are approximately the same.

In this paper the emphasis is made on the technology and possibilities of industry

The selection of stainless steels for the FAIR magnets is similar to the choice in big "slow" SC projects (Tevatron,

SSC, LHC). The enormous experience in the development and study of stainless steels has been obtained during magnet development for LHC. This experience is valid for fast cycling magnets of FAIR with taking into account eddy currents at 4.2 K.

In this paper the magnetic properties of stainless steels, acceptable for the production of the collars, vacuum chambers and other elements at 300 and 4.2 K are presented.

IHEP is developing the SIS300 quadrupole, models of SIS100 magnets are developing in JINR, BINP and GSI.

ELECTRIC (ET) STEELS FOR YOKE

Severe requirements for yoke steels of SIS100 and SIS300 are given to field quality and AC losses, determined by coercivity H_c and saturation magnetization M_s, which in turn depend on Si content: H_c have to be less than 40 A/m for dipoles and 70 A/m – for quadrupole of SIS300 magnets; M_s have to be greater than 2.0 T and be as high as possible.

The carried out measurements of magnetic properties of Si steels together with analysis of literature data and steel maker catalogs allowed us to make the list of steels, which can be used as yoke material for dipole or quadrupole of the SIS 300 and SIS 100 magnets, depending on demands to field quality or acceptable AC losses. The short and full scale models of the SIS 300 and SIS 100 magnets have been made during R&D using the steels from the candidate list. The testing of these models and comparison of field quality and AC losses as well calculations with detailed models and obtained steel magnetic properties give the possibility of problem understanding and greater certainty in steel choice.

In Table 1 the steels with Si content 1.5-3% are presented [3, 4, 5]. Coercive force H_c lies in the range of 20-65 A/m, specific hysteresis loss W_h in unipolar cycles with B_{max} = 2 T at 4.2 K is in the range of 30-60 mJ/kg, saturation magnetization Ms is in the range of 2.0-2.1 T.

Table 1: Steels with 1.5-3 % of Si content

Grade	Type	Si, %	Thickness, mm	Country
M250-50	Isotropic	3	0.5	Germany
M350-50	Isotropic	1.5	0.5	Germany
2412	Isotropic	3	0.5	Russia
2212	Isotropic	1.5	0.5	Russia
M600-100	Isotropic	3	1	Germany
M700-100	Isotropic	2.4	1	Germany
M800-100	Isotropic	1.5	1	Germany
3413/3414	Anisotropic	3	0.5	Russia

It should be noted that a) isotropic steels with thickness of 1 mm are produced only in Europe in frame of standard EN 10106, b) anisotropic steels with thickness of 0.5 mm are produced only in Russia, whereas in the world the thickness is maximum of 0.35 mm.

In Fig. 1 and Fig. 2 the B-H curves and hysteresis loss dependencies, obtained on ring samples, for steels with different Si content are presented, showing the effect of Si content on magnetic characteristics. One can see that the hysteresis losses of isotropic and anisotropic steels are close, so the advantages of anisotropic steels are not obvious in the magnet circuits like dipole yoke, where there are different directions of induction with respect to rolling direction.
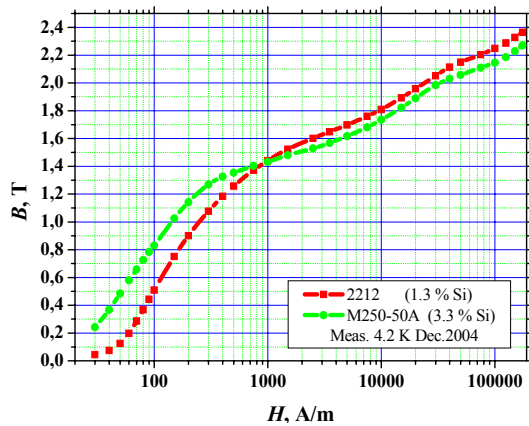

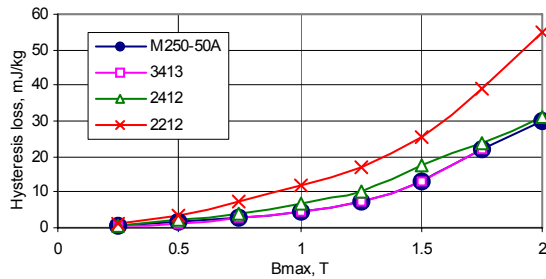Figure 1: B-H curves of M250-50 (3% Si) and 2212 (1.3% Si) steels.

Figure 2: Hysteresis loss in unipolar cycles 0 – Bмах – 0 at 4.2 K.

In Table 2 the steel grades, used in the models of the SIS 300 and SIS 100 magnets, are presented [6, 7, 8, 9].

Table 2: Steels, used in the models of magnets for FAIR

Magnet	Accelerator	manufacturer	Steel
Dipole	SIS 300	BNL (USA)	M250-50
Dipole	SIS 300	IHEP	M700-100
Quadrupole	SIS 300	IHEP	2212
Dipole	SIS 100	BNG (Germany)	M700-100
Dipole	SIS 100	JINR	3413
Dipole	SIS 100	BINP	3413

Analisys of model test results together with calculations of fields and AC losses, as well study of steelmaker possibilities allow to make the choice of steels for model production of dipoles and quadrupoles of SIS300 and SIS100. For dipoles the steels with 3% Si (M250-50, M600-100 or 2412) are preferable, for quadrupoles – steels with 1.5-2% - 2212 or M700-100.

STAINLESS STEELS

In the design of fast cycling SC magnets the stainless steels are used in different forms for production of collars, vacuum chambers, insertion in cable, shims and so on (Fig. 3, [10]).

Main requirement to steels for collars and vacuum pipes are fully austenitic with a permeability lesser than 1.005 at 4.2 K after technological processes, the permeability of cable core and structural elements has to be lesser than 1.02.
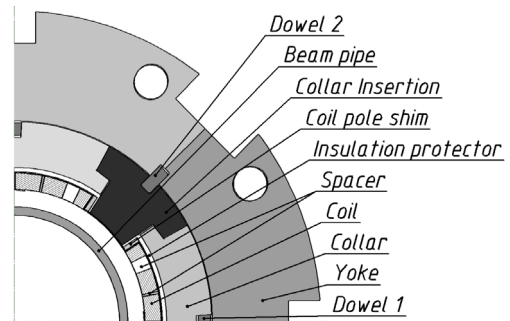
Figure 3: Main elements from stainless steels in the SIS300 quadrupole (IHEP).

Field ramp rate in the stainless steels at 4.2 K effects only on eddy currents, which restrict the thickness of sheet steels for collars and vacuum pipe. For magnets of LHC the careful selection and development of stainless steels for collars, pipes, nonmagnetic yoke end plates, beam screen has been carried out. This experience can be used for the FAIR magnets.

The main elements from stainless steels are the collars and vacuum pipe, placed near working aperture with high field homogeneity.

Collars

Stainless steels for collars have to be fully stable austenitic steels. There are two steels of this quality, Nitronic-40 and P506. Widely used at low temperature steel 316LN can show higher magnetic susceptibility at 4.2 K; steel YUS130S, used in the LHC magnets, is similar to Nitronic-40.

In Fig. 4 the dependences of permeability μ of steels Nitronic - 40 and 316LN at 300 and 4.2 K are shown [11].

In Table 3 the chemical composition, mechanical, magnetic and electric properties of studied and selected steels at 300 and 4.2 K are presented [12, 13].

Figure 4: Magnetic permeability of steels Nitronic-40 and 316L at 300 k and 4.2 K.

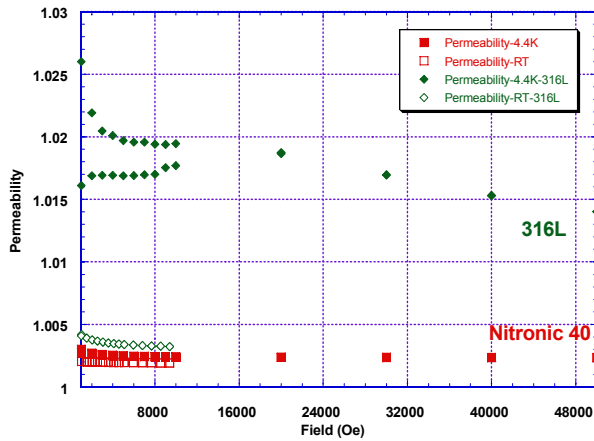Table 3: Chemical content and properties of steels for collars and vacuum chamber (0.2% yield strength $\sigma_{0.2}$; tensile strength σ; elongation δ; Young modulus E; magnetic permeability μ; resistivity ρ).

	Nitronic40	316LN	YUS130S	P506
Cr	19	16	20	19.2
Ni	6	12	6	11
Mn	9	0.8	10	12.1
C	0.03	0.02	0.09	0.01
N	0.34	0.12	0.35	0.3
$\sigma_{0.2}$,kgf/mm^2	46	35	48	41
σ, kgf/mm^2	79	65	80	73
δ, %	44	48	45	-
E, GPa, 300 K,	192	185	192	190
μ , 300 K	1.0019	1.003	1.0018	1.0026
ρ, $\mu\Omega\times$m	79	78	79	79
$\sigma_{0.2}$,kgf/mm^2	142	99	164	162
TS, kgf/mm^2	181	150	191	212
δ, %	20	43	20	-
μ , 4.2 K	1.0021	1.013	1.0018	1.0025
ρ, $\mu\Omega\times$m, 4.2K	-	55	55	50

In the model of SIS300 dipole and quadrupole the Nitronic-40 has been used with thickness 1.6 mm, in the dipole of INFN – steel P506 (3 mm). In the SIS300 quadrupole model Nitronic-40 will be used.

Vacuum chamber

Power of eddy current loss in the vacuum chamber from stainless steel is proportional to tube diameter and tube thickness as well (dB/dt)^2. The calculations show that for SIS300 and SIS100 magnets these losses at 4.2 K (ρ=50 $\mu\Omega\times$m, 4.2 К) restrict the tube thickness up 0.3-1 mm. As the tube from Nitronic-40 and P506 are not produced, steels 316L and 316LN are usually used (BNG and BINP for SIS100 dipole models)**.**

Insertion (core) in SC Rutherford cable

The core from stainless steel strip of 25 μm is introduced between layers of Rutherford keystone cable in fast cycling magnets of the SIS 300 for reducing of cable losses. Annealed steel 316L has better mechanical and magnetic properties (μ = 1.02), which do not affect field quality. Moreover the annealing provides oxide film, allowing one to avoid the preliminary cable heat treatment.

CONCLUSION

Industry offers the wide spread of electric isotropic steels with 1.5-3% Si with thickness of 0.5-1 mm and anisotropic with only 3% with thickness of 0.35 - 0.5 mm. The optimal steels are M250-50, M600-100 for the dipoles and M700-100, 2212 for the quadrupoles.

For collars of SIS300 magnets Nitronic-40 or P506 with thickness up to 3 mm can be used.

For the vacuum chamber of SIS300 quadrupoles steels Nitronic 40, YUS130S, P506 or 316L/316LN can be used.

Cable core can be made from annealed stainless steel strip 316L.

REFERENCES

[1] [GSI. (2006, Sept.). Baseline technical report. [Online]. Available: http://www.gsi.de/fair/reports/btr.html

[2] I. Bogdanov et al., "Study of Electrical Steel Magnetic Properties for Fast Cycling Magnets of SIS100 and SIS300 Rings", EPAC-2004, Lucerne, Switzerland, 2004, pp.1741-1743.

[3] Druzhinin V.V., "Magnetic properties of electric steels", Energy, 2 edition, 1974.

[4] "Cold rolled electrical steel", reference book, ed. by B.V. Molotilov, M, Metallurgy", 1989.

[5] http://www.lei.ucl.ac.be/~matagne/ELEC2311/T2007/hinNOFP.pdf

[6] P.Wanderer et al., "Initial tests of a fast ramped SC model dipole for GSI" proposed of SIS 200 accelerator", PAC, 2003, WPAB054.

[7] A.Kovalenko et al., "Design and study of a SF model dipole and quadrupole magnets for GSI fast pulsed synchrotron SIS100", EPAC, 2004.

[8] E. Fischer et al., " Magnetic field characteristics of a SIS100 full size dipole", EPAC, 2008.

[9] S.Kozub et al. , "SIS300 dipole model", MT-21, 2009.

[10] L. Tkachenko, S. Kozub, P. Shcherbakov, V. Sytnik, V. Zubko. "Analysis of the Factors Affecting Field Quality and Heat Releases of the Quadrupole Magnet for the SIS 300", presented at ASC-2010, Washington, USA, August, 2010.

[11] S. Yadav, "Magnetic Permeability of Stainless Steels at Low Temperature", TD-01-065, FNAL, Sept. 27, 2001.

[12] C. Lanza and D. Perini, "Characteristics of the austenitic steels used in the LHC main dipoles", Proceedings of MT-17, September 2001.

[13] K. Couturier and S. Sgobba, "Phase stability of high manganese austenitic steels for cryogenic applications", CERN EST/2000-006 (SM).

TEST FACILITY FOR SIS300 CRYOMODULES

A. Ageev, E. Kashtanov, S. Kozub, A. Kharchenko, A. Vlasov, S. Zinchenko,
Institute for High Energy Physics (IHEP), Protvino, Moscow region, Russia, 142281

Abstract

Within the framework of cooperation with GSI (Darmstadt, Germany), IHEP develops the superconducting quadrupole and corrector magnets, which in the specific combinations will be united into the so called cryomodules having common cryostat.

The facility for testing these cryomodules in the forced flow cooling mode, where it is intended to carry out the complex of electrical, magnetic and thermophysical tests, is examined.

The facility is based on the existing helium compression and purification equipment, helium refrigerator and research cryostats. A satellite refrigerator is added to the cryogenic system, which also works as the helium mass flow rate multiplier.

INTRODUCTION

IHEP participates in the development and manufacture of superconducting quadrupole magnets and correction (SCM) for the SIS300 accelerator project FAIR [1], in the process of implementation which need to be complex electrical, magnetic and thermal tests as a separate SCM coils and cryogenic modules (CM), which represent a cryostat with a given set of 2-3 SCM coils.

Testing of SCM coils will be held in a cryostat with boiling helium cryogenic modules - to the stocks that provides a single-phase pumping helium through the superconducting coil.

Thus, established at IHEP TF for the test of SCM coil blocks and CM products will contain helium cryogenerating setting that provides the stand with liquid helium and a circulating stream of single-phase helium, current sources and a system of magnetic and current measurements.

HEAT LEAKAGE AND HEAT RELEASE IN THE ELEMENTS OF THE TEST FACILITY

Initial data for the cryogenic system of the test facility (TF) are based on the imputation of coil blocks of SCM, the experimental data on the installation KGU cryogenic plant and test stands magnets UNK, IHEP:

- Expected heat in the quadrupole - 2 watts.
- Expected maximum heat dissipation in the corrector - 1 W.
- Expected heat leakage to the cryogenic helium cryostat module (CM) - 3 W

- Heat leakage of current leads to liquid helium - 1 W at 1 kA.
- Heat leaks to the helium pipelines with nitrogen screen - 5 watts into a single pipeline.
- Expected to helium heat leakage through anticryostat magnetic measurements - 20 W
- Critical temperature for the quadrupole - 6.7 K.
- Critical temperature for the corrector - above 6.7K.
- Operating current in the measurement of magnetic field quadrupole - 6.2 kA.
- The maximum operating current in the measurement of the magnetic field corrector - 300 A.
- Temporary temperature gradient along the length of the quadrupole is not limited to, as well as a similar gradient is not limited to magnets UNK, FNAL.
- The pressure before the valve P3 (KGU) - 7 bar.
- The temperature before the valve P3 (KGU) - 4.5 K.
- Flow through the valve P3 (KGU) - 5 g / sec.
- Consumption of liquid helium for cooling the current leads - 1 liter / hour of liquid helium at 1 kA.

HELIUM CRYOGENIC SYSTEM FOR RESEARCH SCM COILS INTO THE BOILING HELIUM

As the helium cryogenic system for the test of SCM in boiling helium using an existing cryogenic system for the test of superconducting magnet blocks corrective and quadrupole magnets in the submersible mode (boiling helium). It uses existing cryogenerating helium plant KGU 500, Kp 1/1.5 cryostat, system cryogenic and "warm" helium and nitrogen pipelines, the system of magnetic measurements, current sources feeding the system and SCM measurements of current parameters.

Additional improvement of this system is not required.

HELIUM CRYOGENIC SYSTEM FOR RESEARCH CM IN FORCED FLOW COOLING MODE

Projected helium circuit for single phase flow of helium through the corrective and quadrupole CM coils is shown in Figure 1.

Cryostatting magnets CM is as follows.

After the compressor of the cryogenic plant (CP), compressed helium goes to the KGU 500. Installing the KGU 500 is used only in the liquefier mode, supplying the liquid helium satellite refrigerator SR and

accumulating of liquid helium in a 800-liter vessel KGU. With the accumulation in the vessel, KGU 500 stops and satellite refrigerator receives liquid helium directly from the vessel of KGU 500.

The helium flow after satellite refrigerator at T ~ 4,5 K is cooled in a cryostat-recooler to T ~ 4,3 K and cools the coils of magnets CM. phase helium is divided into two streams after the CM. The first stream goes to the cooling current leads and in the gasholder with cryogenic plant, the second, after the CM, passing through the valve CV6, turns into a two-phase flow and in CR cools the main flow of helium. Next, a reverse flow of CR in the SR line cools the flow from the compressor CP.

Electric EH - phase flow of helium is used as if magnets CM in controlled Quench, and the measurement of heat and heat release.

Reverse flow of helium after SR goes into gasholder with cryogenic plant.

Application of satellite refrigerator as a multiplier allows the flow of helium to increase the multiplicity of circulation through the superconducting coil CM single-phase helium cooling capacity without increasing the system.

Thermodynamic analysis of this system [2,3] shows that for a satellite refrigerator with cold 100 W helium temperature level will require about 25 liters of liquid helium per hour. This means that the installation KGU

500, capacity 150 liters per hour will operate only one eight-hour shift for a period of 36 hours, which reduces the number of staff.

Satellite helium refrigerator is a cryogenic device, consisting only of the heat exchanger, located in the cryostat. It does not contain low-temperature expanders, which simplifies automation. With the same purpose in the scheme introduced remote-controlled valves CV1-CV7, safety valves SV and Quench receiver for effective evacuation of helium from the cryogenic module CM in Quench.

SYSTEM OF AUTOMATIC DATA ACQUISITION AND PROCESSING OF INFORMATION

Automated acquisition and processing of information generated by the TF will provide an automated and manual process of managing a booth with necessary information, which should also be displayed on the display control panel.

This information includes:
- Temperature of cryogenic units and helium and nitrogen fluxes;
- Pressure helium flows;
- The level of liquid helium in the cryostat CR;
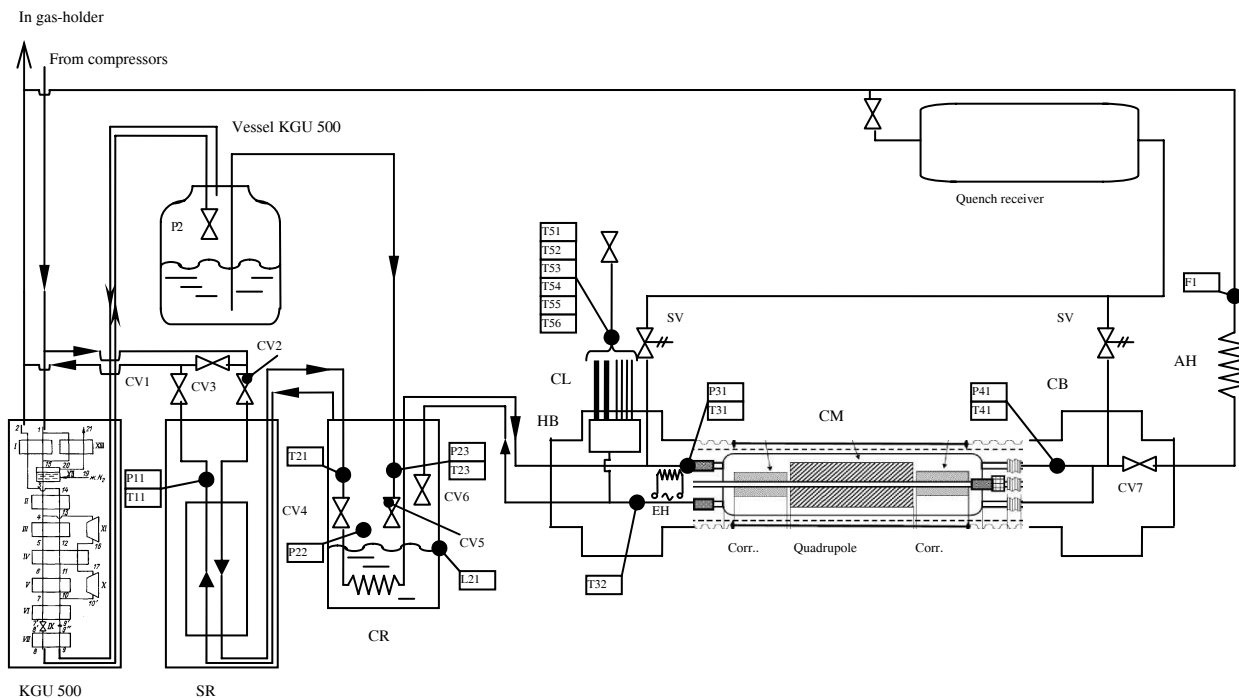
Fig.1. Test facility for research cryogenic modules in forced flow cooling mode

Symbols: HB - head box with current leads CL, CB - closing boxes, CM - cryogenic module, AH - heat exchanger to heat the helium due to atmospheric temperature, EH - an electric heater is a single-phase flow of helium, CV1-CV6 - remote-controlled valves, SR - Satellite refrigerator, CR – cryostat-recooler, SV - safety valves, T11-T56 - temperature sensors, P11-R41 - pressure sensors, F1 - flow sensor of gaseous helium.

- Position of the gas-holder;
- Position of stocks of remote-controlled valves.

Additionally, the system of collecting and processing information is to provide the operator of the TF data on vacuum insulation, the currents in the SC coils of magnets, magnetic field, the probability of the start of Quench and promptly furnish data on the pressure in the magnet and in the structural elements of the TF after Quench.

For remote control booth should be laid to move from automatic control to manual control directly from the console.

The basis of the hardware configuration of automated data acquisition and processing of information will set a three-tier organization of computing resources. This configuration includes a personal computer on the upper level, unified controllers that act as servers and computers at the front edge of mid-level and specialized hardware controllers on the ground.

VACUUM POST

Cryogenic equipment is carried out with high-vacuum insulation, working in a vacuum no worse than 10^{-5} mm Hg To ensure that the vacuum will be used positions with a backing and high-vacuum turbomolecular pumps, which

can bring the vacuum in an isolated area without leaks to 10^{-6} mm Hg.

CONCLUSION

The considered scheme of the test facility will allow efficient and low cost to conduct research cryogenic modules.

Partial automation and the use of satellite refrigerator in the scheme of the test facility will use the minimum number of staff.

REFERENCES

[1]. FAIR Baseline Technical Report, Volume 2, Accelerator and Scientific Infrastructure, March 2006, http://www.gsi.de/documents/DOC-2006-Jul-40-1.pdf

[2]. A.I. Ageev, V.N. Shamichev Thermodynamic analysis of refrigeration cycle with an excessive reverse flow: IHEP Preprint 82-159, 12 p.

[3]. A.I. Ageev, S.I. Zinchenko, S.P. Logachev, M.V. Muraviev, A.N. Shamichev. Test installation KGU-400 / 4.5 in non-standard modes: Preprint IHEP 82-158, Protvino, 1982, 7 p.

STUDY OF ELECTRODYNAMIC AND THERMODYNAMIC MECHANISMS INFLUENCING STABILITY OF SUPERCONDUCTING RUTHERFORD CABLE

V. Zubko, S. Kozub, I. Bogdanov, L. Tkachenko, L. Shirshov, P. Shcherbakov

Institute for High Energy Physics (IHEP), Protvino, Moscow region, Russia, 142281

Abstract

Stability for superconducting fast-cycling dipoles and quadrupoles plays an important role. A feature of a complex network of strands and strand-to-strand contacts, current distribution in the network has to be taken into account for superconducting cables. The coupled numerical simulation of electromagnetic and thermal processes in Rutherford superconducting cables during the initiation of a quench was carried out. The network model has been combined with thermal analysis, which allows one to model quench dynamics, including the effects of a current redistribution in strands, discontinuities and inhomogeneity, the initial heating in strand, and as a result occasional quench recovery or runaway quench propagations.

Results for the minimum quench energy for cables with core are presented and dependence the minimum quench energy from various parameters of cable is discussed.

INTRODUCTION

Russia expressed interest in the international project FAIR participation [1]. At the moment, IHEP's main tasks are to develop a design of the main quadrupole [2] for the SIS300 ring.

The main quadrupole requirements are as follows: 45 T/m central gradient; 10 T/m/s the field ramp rate; 10 T/m injection field. Maximal magnetic field in the coil is 3.5 T, the operating current I_{op} is 6.26 kA [2], working point at 70% along the load line.

As the given magnet is fast-cycling, it is necessary to have a cable with low losses and simultaneously with a good redistribution of currents between strands of the cable at a quench. For this purpose Rutherford cable has a core decreasing losses in a perpendicular magnetic field and strands, coated by a 0.5 μm thick Staybrite with low resistance for good redistribution of currents between strands.

The thickness of the core is 25 μm and the width is 6 mm. The core is made from an annealed 316L stainless steel foil. The cable with 19 strands is fully keystone, it has the 8.25 mm wide and the average thickness of 1.447 mm. The transposition length is 60 mm, all parameters are presented in [2].

The stability of the superconducting cable against local disturbance is described in general by a curve, presenting the Minimal Quench Energy MQE, as a function of the current I or ratio the current to the critical current I/I_c. If there is current redistribution between strands of cable,

normally these curves exhibits a sharp 'kink', separating two distinctive stability regimes. The current, at which the 'kink' occurs, is called I_{kink} [3, 4, 5]. Above the 'kink' MQE of the cable is equal to the single strand MQE. Below I_{kink} MQE of the cable can be more than two orders of higher than the MQE of a single strand, this current redistribution increases stability. In order to improve the stability, a shift of the 'kink' to higher current and an increase of the quench level left from the 'kink' is highly desirable. This can be achieved by increasing heat transfer to helium and the Residual Resistance Ratio of the copper RRR, and decreasing contact adjacent resistivity R_a and thermal contact.

APPROACH FOR ANALYSIS OF MQE

For the study of MQE the cable was fabricated with properties, almost the same as the original cable of quadrupole has. The cable used three types of strands with different critical current density: 2548, 2632 and 2406 A/mm^2 (5T, 4.2K), Cu/NbTi ratio of the cable is 1.45, RRR differs from 110 to 200.

Further for MQE analysis the current of the cable is used instead of the ratio I/I_c as strands have the different critical currents, so it is difficultly to calculate correctly the ratio of the current to the critical current of the cable. Other reason is impossibility to compare the working point on the load line with I_{kink}/I_c, as MQE measurements were carry out at a constant magnetic field. MQE is possible to study numerically as a function of magnetic field for turn in the high magnetic field of the magnet [5]. In this case one can compare the working point on the load line with $I_{kink}/I_c(B)$ but it is difficult to compare with measurement dates I_{kink}/I_c (constant magnetic field, therefore constant I_c)

The measurements of MQE were carried out in liquid helium (pressure of 1 atm., temperature of 4.3 K), so it is necessary to compare measured and calculated results. General experimental arrangements are described in [6].

Simulations of MQE were performed with code, developed in IHEP [7] and the CUDI program, developed in CERN [8].

These codes consist of electrodynamics and thermal parts. For electrodynamics part basic input parameter is a contact resistivity, which can be measured. For cable with core the contact adjacent resistivity R_a is about 0.2 mΩ and the crossover resistivity R_c is larger than 20 mΩ [9].

In thermal part the most difficult is correctly to define a heat transfer through thermal contact resistance between contacting strands and between strands and helium.

07 Accelerator Technology Main Systems

The thermal contact conductivity between contacting strands k_{cont} given by:

$$k_{cont} = f_{cont}\, T^{2.25}. \qquad (1)$$

Here T are temperature of strand, f_{cont} is constant. The contact surface between contacting strands is 150 mm^2 [4].

Heat transfer to Helium I consists of these regimes: the most important regime is the transient cooling regime defined by

$$\mathbf{h_{He}} = \mathbf{a_{trans}}\left(\mathbf{T_s^4} - \mathbf{T_{He}^4}\right)\mathbf{A_{He}}, \qquad (2)$$

the steady-state Nucleate boiling is defined by

$$\mathbf{h_{He}} = \mathbf{a_{nb}}\left(\mathbf{T_s} - \mathbf{T_{He}}\right)^{2.5}\mathbf{A_{He}}, \qquad (3)$$

and the film boiling is defined by

$$\mathbf{h_{He}} = 250\cdot\left(\mathbf{T_s} - \mathbf{T_{He}}\right)\mathbf{A_{He}}. \qquad (4)$$

Here T_s and T_{He} are temperatures of strand and Helium, h_{He} is coefficient of heat transfer, a_{nb} and a_{trans} are constants. The contact surface between strand and helium A_{He} is 650 mm^2 [4].

If the transient heat flow into the helium exceeds a certain limit in 20 J/m^2[10], the nucleate boiling regime starts. Nucleate boiling regimes continues until heat flow h_{lim_nb} is reached to $1.5 \ 10^4$ Wm^{-2}. Values a_{nb} is $5\cdot10^4$ Wm^{-2}K$^{-2.5}$.

Preliminary simulations of MQE by varying f_{cont} and a_{trans} parameters show that simulated results fit the measured results with $f_{cont} = 200$ Wm^{-2}K$^{-2.25}$, $a_{trans} = 200$ Wm^{-2}K^{-4}.

NUMERICAL CALCULATION OF MQE

Calculated current redistribution in the cored cable through R_a is shown, for example, in Fig. 1 and Fig. 2 without quench after current redistribution. Fig. 1 shows numbering of cable strands in the code. Some curves in these Figs are coincided. As an example Fig. 3 shows the current redistribution in the case of quench. The onset of the normal zone is in sixth strand.
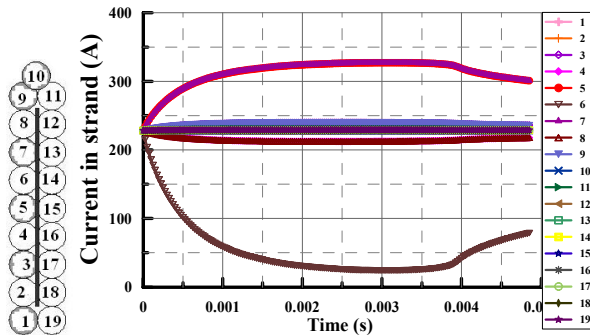

Figure 1: Current in strands of the cable during time. The onset of the normal zone is in sixth strand.
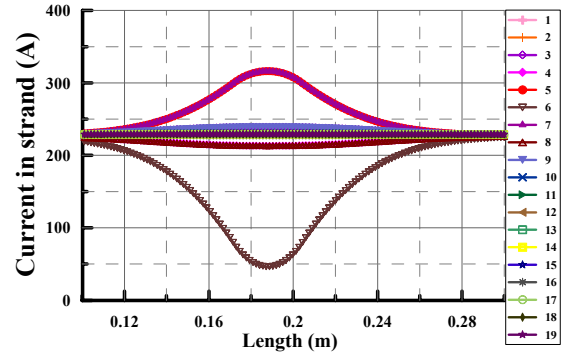

Figure 2: Current in strands of the cable along strands at 1 ms after the onset of the normal zone is in sixth strand.
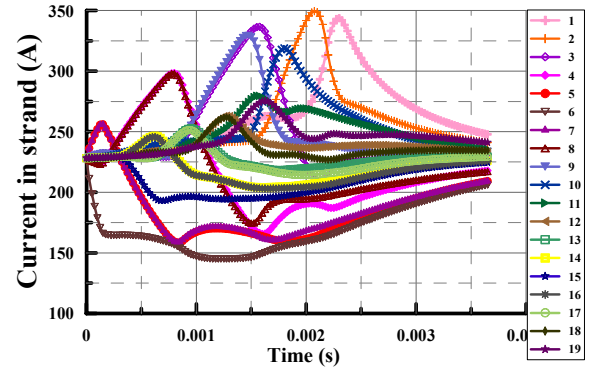

Figure 3: Current in strands of the cable during time. The onset of the normal zone is in sixth strand.

The measured dependences of MQE versus current for cored cable are presented in Fig. 4 for 3.5 T magnetic field (maximal field in the coil of the quadrupole). Also at Fig. 4 the simulated curves for RRR 110 and 200 are shown, current density 2500 A/mm^2 (5T, 4.2K) for all strands.

Using a scaling factor, which is defined by ratio between the effective quench energy and the input pulse energy [11], a good coincidence between measured curve and the simulated curves is received (Fig. 5). Scaling factor is 0.4 after I_{kink} and 0.9 before I_{kink}.
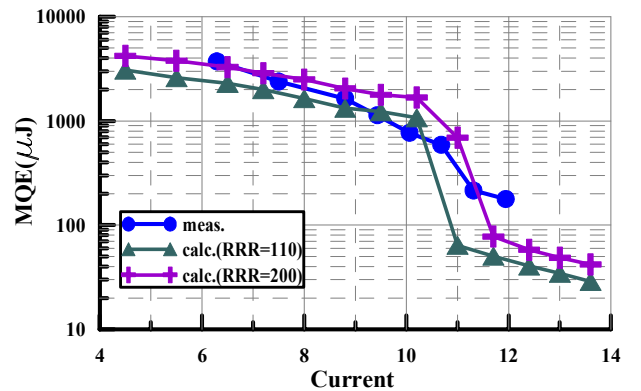

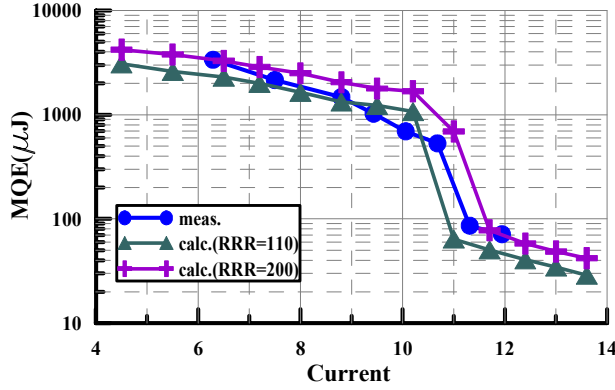Figure 4: Measured and calculated MQE versus current.

Figure 5: Measured (with scaling factor) and calculated MQE versus current.

Fig. 5 shows that I_{kink} in liquid helium is about 10.5 kA, this value is sufficiently larger than the operating current. For stability of cable I_{kink} have to be larger then I_{op}. The ratio I_{kink}/I_{op} is about 1.6.

In real condition the quadrupole will be cooled by supercritical helium. In this condition the stability is investigated by numerical calculation [5]. The coefficient of heat transfer from cable into supercritical helium is lesser then coefficient of heat transfer from cable into liquid helium, so MQE will be lesser for the cable cooling supercritical helium. MQE of cable, cooled by supercritical helium, is larger then in adiabatic condition.

The ratio of I_{kink}/I_{op} (calculated or measured) at cooling cable in liquid helium is top limit of this ratio for a magnet. I_{kink}/I_{op}, calculated for adiabatic condition, is bottom limit. If $(I_{kink}/I_{op})_{adiab} > 1$ for a magnet it will be have a good stability.

The simulated curves of MQE for RRR 110 and 200 with $f_{cont} = 200$ Wm^{-2}K$^{-2.25}$ are shown in Fig. 6 for adiabatic condition. Fig. 6 shown curves calculated both the program CUDI and code, developed in IHEP.
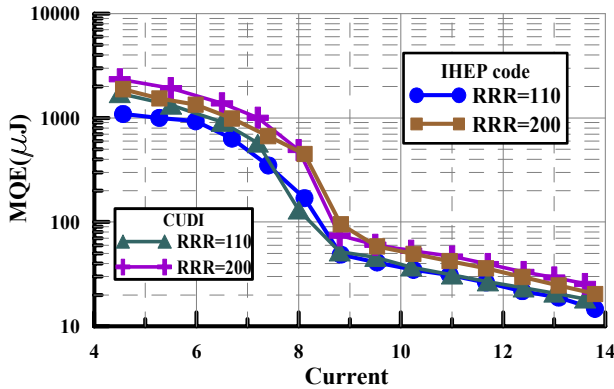

Figure 6: Calculated MQE versus current for adiabatic condition.

One can see I_{kink} in adiabatic condition is about 8 kA, this value is larger than the operating current. The ratio $(I_{kink}/I_{op})_{adiab}$ is about 1.25. It means that the cored cable, having the next parameters: RRR > 110, $R_a \approx 0.2$ mΩ, $R_c > 20$ mΩ and $f_{cont} \approx 200$ Wm^{-2}K$^{-2.25}$ for the quadrupole will have a good stability in the real conditions (cooling supercritical helium, $B_{max} = 3.5$ T).

CONCLUSION

IHEP has developed the design of the quadrupole for the SIS 300. Keystone 19-strand Rutherford cable with core is the preferred choice for the quadrupole. For estimation of stability of these cable we used ratio I_{kink}/I_{op}. This ratio has to be lager 1. For liquid helium I_{kink}/I_{op} is about 1.6. For adiabatic condition $(I_{kink}/I_{op})_{adiab}$ is about 1.25. This magnet will have a good stability in real conditions (cooling supercritical helium, B_{max} in the coil is 3.5 T).

We would like to acknowledge A.P. Verweij for accordance of CUDI program.

REFERENCES

[1] http://www.gsi.de/fair/reports/btr.html

[2] L. Tkachenko et al., "Development of Quadrupole, Steering and Corrector Magnets for the SIS 300", IEEE Trans. on Appl. Supercond. vol. 20, Is. 3, pp. 159-163, 2010

[3] M. Wilson, W. Sampson, and A. Ghosh, "Experimentally measured minimum quench energies of LHC cables", Technical report, CERN, Geneva, Switzerland, LHC project report 86, 1997.

[4] G. Willering, A. Verweij, J. Kaugerts, and H.H.J. ten Kate, "Stability of Nb-Ti Rutherford cables exhibiting different contact resistances", IEEE Trans. Appl. Supercond., 18:1263 – 1266, 2008

[5] G. Willering, "Stability of superconducting Rutherford cables", PhD Thesis University of Twente, Enschede, The Netherlands, 2009.

[6] I. Bogdanov et al., "Experimental Study of Characteristics of Cable for Fast-Cycling Superconducting Magnets", Presented in RuPAC 2010, Protvino, Russia (2010).

[7] V. Zubko et al. "Simulation of electromagnetic and thermal processes in Rutherford superconducting cables during the initiation of a quench", EUCAS 2007, September, 2007.

[8] A. Verweij, "CUDI: A model for calculation of electrodynamic and thermal behavior of superconducting Rutherford cables," Cryogenics, vol. 46, no. 7–8, p. 619, 2006

[9] M.N. Wilson et al. "Cored Rutherford Cables for the GSI Fast Ramping Synchrotron." IEEE Trans. on V.13, Issue 2, June 2003 p.:1704 – 1709

[10] C. Schmidt, "Transient heat transfer to liquid helium and temperature measurement with a response time in the microsecond region," Appl. Phys. Lett., vol. 32, p. 827, 1978.

[11] G. Willering et al., "Modeling the Heat Flow From a Graphite Past Heater Used for Cable Stability Measurements," CERN AT-MCS, intern note 2007.

SUPERCONDUCTING TRANSFORMERS FOR STUDY OF HIGH-CURRENT SUPERCONDUCTING CABLES

L. Shirshov, I. Bogdanov, E. Kashtanov, S. Kozub, P. Shcherbakov, P. Slabodchikov,
L. Tkachenko, V. Zubko, Institute for High Energy Physics (IHEP), Protvino,
Moscow region, Russia, 142281

Abstract

A facility for measurement of the critical current and minimal quench energy of Rutherford-type superconducting cables for accelerator magnets is created. The current in the sample is energized by a superconducting transformer circuit, using an inductive method, where the sample conductor is a part of the secondary circuit. Two superconducting transformers have been built; one of them is a solenoid type coil. The transformer consists of two concentric solenoids; the secondary coil is placed inside the primary coil. External magnetic field up to 6.5 T is provided by a superconducting solenoid with the aperture diameter of 60 mm. The second superconducting transformer with race-track coils has been designed and taken into operation. Short-circuited sample, fixed on a special holder, is placed in the aperture of a superconducting dipole magnet such way that the plane of sample loop is perpendicular to direction of external magnetic field, which can reach up to 6 T. The critical current of the secondary superconducting coil is 18 kA. The equipment for measurements of characteristics of a superconducting cable versus magnetic field is described.

INTRODUCTION

One of the main tasks in a development of superconducting magnets is measurements of current carrying characteristics of a superconducting (SC) cables and wires. Some equipment for measurement of the critical currents and minimal quench energy (MQE) has been development and produced in IHEP.

A direct powering of the sample by a power supply causes high losses in current leads at a level of 10 кА, what leads to large losses of liquid helium in a cold zone. The inductive method of a current input is applied for reduction losses of liquid helium and achievement of high values of currents in samples.

The description of the SC transformer design, with a help of which a study of SC cables with different coating of SC wires has been carried out, is presented in [1]. The hairpin sample and the secondary winding of transformer are fixed on the cryostat insert, can be placed into the cryostat with liquid helium, where the superconducting solenoid and primary transformer winding are fixed stationary, thus allowing one to make a fast replacement of the sample. This equipment allows one to measure characteristics of usual Rutherford type cables. The current carrying element with the stainless steel core between two layers of Rutherford type cable (cored cable) [2] will be used for the SC coils of quadrupole magnets of

the SIS 300 ring [3]. New equipment, developed and produced in IHEP, gives a possibility to study samples of different types of SC cables in an extended region of uniform magnetic fields.

Two designs of SC transformer are tested; one of them consists of solenoid coils. One of them is used a SC dipole for a creation of an external field, another one is based on a solenoid magnet.

TRANSFORMER WITH RACE-TRACK COILS

The design of equipment is shown in Fig.1 and its basic parameters are presented in Table 1. An external magnetic field with an enough large region of homogeneity is necessary for study of SC cable characteristics. From the technological reasons this magnetic field is created by SC dipole, placed into the boiling cryostat.

The part of the sample, which is being studied, is the secondary coil of the SC transformer. The measuring section of the sample is fixed in the holder at the length of 830 mm under the pressure 80 MPa. The secondary SC contour has one joint, located above the coils. The detachable insertion is put and fixed in the aperture of the dipole with a diameter of 80 mm.
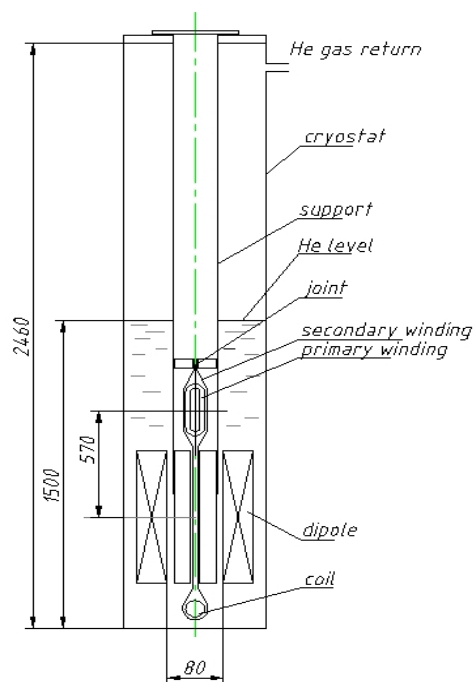

Fig.1. The general view of the equipment with SC dipole.

External magnetic field up to 6 T was created by the 1-m model of SC dipole, produced within the framework of the UNK program. The longitudinal length of the coil is 740 mm. The design of the coil block is presented in [4]. The iron yoke with a length of 500 mm was produced in order to increase the maximum magnetic field. Complete cryogenic tests have been carried out, including magnet training, the measurement of ramp rate dependence and AC losses. The longitudinal distribution of a field inhomogeneity in the dipole at radius of 30 mm is presented in Fig. 2 for the magnet with (+) and without (-) iron yoke. The point of origin coincidences with the dipole centre. It is seen the region of longitudinal 4% uniform field is 520 mm.
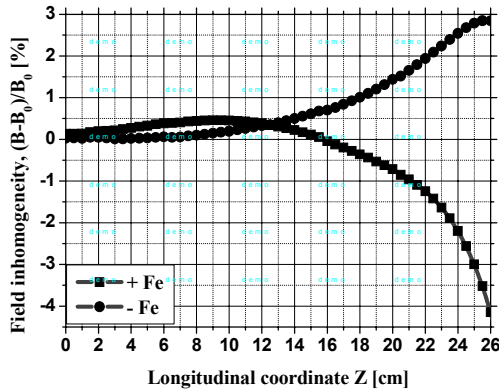

Fig. 2. The longitudinal distribution of a field inhomogeneity in the dipole at radius of 30 mm.

The magnet training was enough short and it consisted of 10 inputs of current at a rate of 100 A/s to quench. The first quench took place with the current of 6 kA (the transfer function is 0.98 T/kA), the maximum central field at quench current of 6.739 kA was 6.604 T.

Fig.3. The photo of the equipment.

The induction method of a current powering with a help of the SC transformer is used for an achievement of high values of current in the studied SC sample.

The design of the SC transformer is based on the equipment with the coil of the type race-track[5]. The primary coil of transformer contains 260 turns of the multiple strand superconductor with a diameter of 0.85 mm and has a straight part length of 230 mm. The studied cable with an overall length of 2.7 m uses as a secondary coil. It gives a possibility to use only one joint in the secondary circuit, which is placed above the transformer. The induction coil is used for the current measurements. This coil contains about 4 thousand turns of the copper wire with a diameter of 50 μm, wounded around the coil former, made from the fiberglass. The measuring circuit was calibrated by help of the direct powering SC sample with stabilized currents up to 800 A. During the calibration the voltage from the output of the analog integrator, connected to the output of induction coil, was measured in the dependence on the current in the sample.

Further the tests of SC transformer were carried out in the small cryostat with the short (less than 1 m) model of the SC cable, which was as a secondary winding. The maximum current of the primary coil was 220 A, it is possible to obtain the current above 18 kA in the secondary SC coil. The coefficient of the mutual inductance of the transformer coils was 33 μH, its own primary inductance was equal to 8 mH. Only one joint in the secondary circuit was produced by soft solder at the length of 75 mm and provides the decay time-constant of the current of secondary circuits above 100 s.

Then SC transformer was fixed on the changeable stock together with the sample. The stock was placed in the aperture of SC dipole and was fixed in the holder in order to exclude displacements. The details of the preparation of SC samples and the basic results of measurements are given in [6].

TRANSFORMER WITH SOLENOID WINDINGS

An external magnetic field in this transformer is created by SC solenoid. The primary solenoid coil and the external solenoid are fixed in the small cryostat, as it is shown in Fig. 4. The secondary coil together with the sample is fixed on the changeable stock, which is put into the cryostat. The measuring 40-mm length section of the sample in the shape of a hairpin is located in the centre of the external solenoid, which creates magnetic field up to 6.9 T.

The total length of the sample is 450 mm. It is possible to reach above 15 kA in the secondary circuit using bipolar power supply in the primary circuit. The operating current in both the external solenoid and the primary coil is not exceeding 100 A, which gives enough low expense of liquid helium.
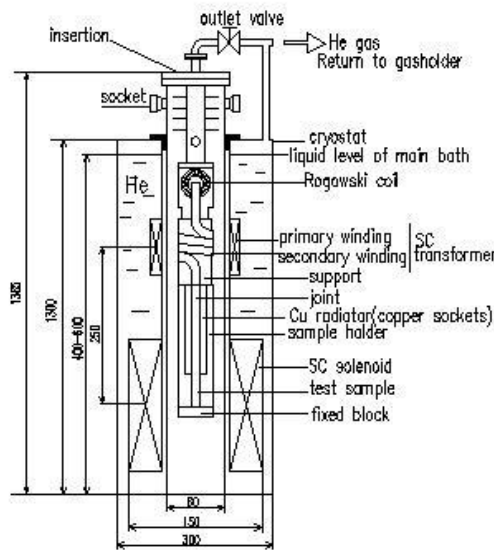
Fig.4. Scheme of equipment with SC solenoid.

The general view of the equipment is shown in Fig. 5. The suspension of SC solenoid and primary winding of the SC transformer are prepared before their arrangement in the cryostat with the neck of a 300-mm diameter.

Fig.5. The general view of equipment with solenoid coils

This equipment was used for measurements of cable samples with different coating of wires [7]. The overall dimensions of this equipment allow one to measure short samples of cables with total length lesser then 500 mm and measuring section does not exceed 40 mm.

The equipment with SC dipole gives a possibility increasing of the measuring section up to 500 mm, which

heightens instrument sensitivity. The developed facility can be used for study characteristics of high current cables up to 20 kA. For comparison the main parameters of two designs of SC transformers are presented in Table 1.

Table 1: Main of parameters of the SC transformers.

Type of coils	Race-track	solenoid
Arrangement of the SC coils	The primary coil is inside the secondary coil	The primary coil is outside the secondary coil
Number of turns in primary coil	260	960
Diameter of NbTi wire, mm	0.85	0.5
Self-inductance, mH	8	45
Maximal current of the primary coil, A	220	100
The conversion ratio	84	75
Maximal current of the secondary coil, kA	18.6	15.3

CONCLUSION

The facility is developed and created in IHEP for study samples of high current SC cables on the base of the two types of SC transformer and diverse magnets for generation of an external magnetic field. This equipment is used for measurements of the critical currents and minimal quench energy for different types of cables.

REFERENCES

[1] L. Shirshov, I. Bogdanov, S. Kozub et al, "Stability Study of High-Current Superconducting Cables for Accelerator Magnets", Proc. of RuPAC 2008, Zvenigorod, Russia, pp. 191-193 (2008), http://cern.ch/AccelConf/r08/papers/TUDPH02.pdf

[2] J. Kaugerts et al.. "Cable Design for FAIR SIS 300". IEEE Transaction on Applied Superconductivity, Vol. 17, Issue: 2, Part 2, June 2007, pp. 1477-1480. Preprint BNL-79518-2007-JA.

[3] http://www.gsi.de/GSI-Future/cdr/

[4] I.Bogdanov, V. Zubko, S.Kozub et al., "Investigations concerned with development of SC dipole for the SIS 300 accelerator", Proceedings RuPAC 2006, Novosibirsk, Russia, pp.73-75

[5] L.S.Shirshov and G.Enderlein. Apparatus for Critical Current Measurement of High Current Superconductors. - "Cryogenics", 1985, Vol.25, N 9, pp.527-529.

[6] I.V. Bogdanov, E. Kashtanov, S. Kozub et al. "Experimental Study of Characteristics of Cable for Fast-Cycling Superconducting Magnets". Presented RuPAC 2010.

[7] I.V. Bogdanov, V.V Zubko., S.S. Kozub et al. "Study of Stability of High-Current Superconducting Current-Carrying Element for Magnets of Accelerators", IHEP Preprint 2008–26, Protvino, 2008, (in Russian).

07 Accelerator Technology Main Systems

EXPERIMENTAL STUDY OF CHARACTERISTICS OF CABLE FOR FAST-CYCLING SUPERCONDUCTING MAGNETS

I. Bogdanov, E. Kashtanov, S. Kozub, P. Shcherbakov, L. Shirshov,
P. Slabodchikov, L. Tkachenko, V. Zubko
Institute for High Energy Physics, Protvino, Moscow region, 142281.

Abstract

Fast-cycling magnetic fields, produced by superconducting magnets of the SIS300 accelerator, generate cable losses, which should be reduced by increase of contact resistances between wires in the cable. For this purpose various methods of cable interstrand resistance increasing are used successfully. But the values of contact resistances have strong influence on a stability, which could be characterized by minimum quench energy (MQE).

From this point of view at IHEP it was carried out the experimental study of Rutherford type 19-strand superconducting cable with high value of contact resistances. Contact resistances and MQE measurements were performed. The description of features of samples, the measurement scheme and procedure are presented along with the experimental results.

INTRODUCTION

Last years IHEP developed the superconducting magnets for modern particle accelerators using fast-cycling magnetic fields. IHEP participates actively in FAIR project. In particular it is responsible for the development of superconducting correctors, quadrupole magnet of accelerator ring SIS300, and also for the choice of its design current carrying element [1]. Maximum magnetic field in this quadrupole coil is 3.5 T and field ramp rate is about 0.8 T/s [2].

The high and fast-ramping field in superconducting magnet generates large AC losses. For the purpose of reduction of losses try to make cable with relatively high value of the adjacent resistance Ra, which is the side-by-side resistance between adjacent pairs of strands, and the crossover resistance Rc, which is the resistance of each crossover contact. The knowledge of these resistances values, and also the ways of their control has great value already at a magnet design stage.

Two years ago we reported the results of study of cables with Ni or Cr coated surfaces of strands and it was shown that AC losses in the SIS300 quadrupole can be effectively suppressed by increasing of interstrand contact resistances by such coating. In recent time for quadrupole the cable design was chosen with stainless steel core. For such cable the interstrand resistances can be controlled independently by means of a high-resistance metallic core (Rc) and by proper oxidation of the wire surface (Ra).

Main task of this work was the study of the influence of cable curing parameters on the interstrand resistances value. Due to profound effect of these resistances on

07 Accelerator Technology Main Systems

stability against short point heat pulses the minimum quench provoking energy of cable was measured too.

INTERSTRAND RESISTANCES

The tested cable consists of 19 NbTi strands with diameter of 0.825 mm. The strands are coated by a 0.5-µm thick Staybrite. The cable has a core with thickness of 25 µm and width of 6 mm, which is made from an annealed 316L stainless steel foil. The cable is fully keystoned and it is 8.25 mm wide and has average thickness 1.447 mm without insulation. The transposition length is 60 mm.

All tested samples were made from the same original cable. The preliminary heat treatment was done in order to form the high resistive oxide layers on the surface of cable strands. The pieces of original bare cable were heat treated in air under no pressure at 200ºC during 2 and 4 hours. Then cable was insulated be three layers of polyimide tape. The last layer was PIXEO adhesive tape.

Four cable pieces were stacked with the alternation of keystone angle direction. This package was placed into the fixture mould, which consists of two massive iron block equipped by electrical heaters and temperature sensors. After the mould was placed into the hydraulic press and the curing was performed according to regime, shown in Fig. 1.
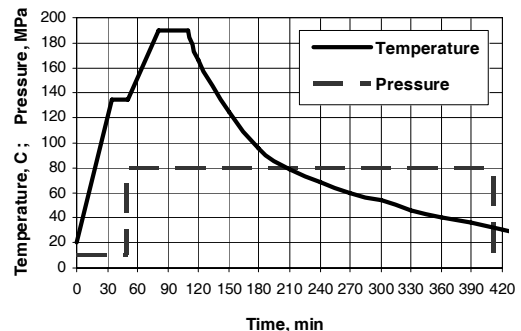

Figure 1: Curing cycle of stack of samples.

From the cured stacks the testing samples were cut, placed into sample holder and were compressed at room temperature once again up to 80 MPa on the length of 60 mm (one transposition length) and were fixed with help of bolts. Two inner layers in stack were equipped by potential taps and were used for measurement with the help of the VI method [3]. Current up to 100 A was fed into two opposite strands of cable sample (strands 1 and 10 in our case, Fig. 2 a), which was immersed into liquid helium bath. Voltage drop on strands 3, 5, 7, 9, and 10 was measured relative to strand 1. For example, the resulting profile of normalized voltage versus strand

position is presented in Fig. 2 b) for original sample without preliminary heat treatment. For other samples this profiles are closed to straight line too. That is typical for the cases, when Ra is more than two orders of magnitude lower than Rc. In this case Ra equals to 8*V/I with 5% accuracy [4], where I is a current and V is voltage drop between two opposite strand 1 and 10.
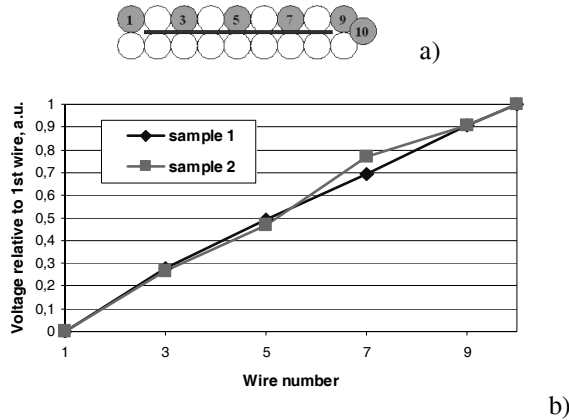

a)

b)

Figure 2: Cable sample cross section a) and the example of voltage profile across the samples b).

The dependence of adjacent resistance Ra upon the time of preliminary heat treatment is presented in Fig. 3. As evident from figure Ra = 100 µOhm is achieved even without preliminary heat treatment. This value is sufficient to restrict the Ra-specific losses by value < 5% of total quadrupole losses. Thereby Rc was measured only on the sample without preliminary heat treatment.
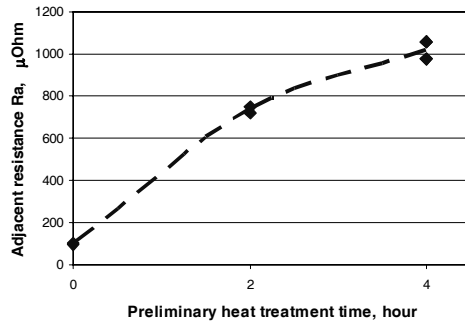

Figure 3: The influence of preliminary heat treatment on the final value of Ra.

The method of direct measurement of Rc was used. The sample was cut and prepared similarly described in [4]. That is: the small part of a cable is clamped in the central part and cable sides are cut off to interrupt the current transfer through the wire from the top to the bottom layer, the strands leaving in a longitudinal direction are untwined, all free ends of strands belonged to the same layers are soldered for maintenance of the even current distribution across the core. Thus contact between strands from different layers occurs only through the core. Described in [5] measuring procedure was used. Fig. 4 presents the dependences of crossover resistance Rc upon pressure up to 80MPa on the cable surface. Loading and unloading branch of curves are presented. Such high value is much greater than required (more than one order
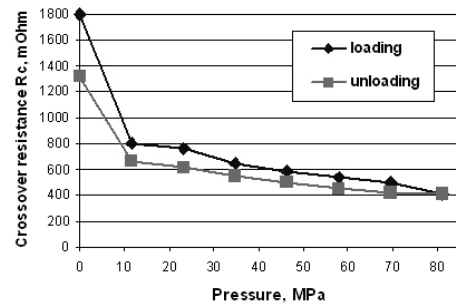

Figure 4: Rc evolution upon pressure for cored cable without preliminary heat treatment.

of magnitude).

MINIMUM QUENCH ENERGY

Measurements were performed into the liquid helium bath at the external magnetic field 6 and 3.5 T, applied normal to cable wide side on the length of 500 mm. The sample is the extended closed loop of 2.7-m cable, which forms the secondary winding of the superconducting transformer described in detail in [6]. On one end it covers current-measuring coil, and on the other it covers the primary coil of transformer. The direct and return cables in the central straight part of loop are put to the aligning flute in a special fixture along with two extra cable pieces, what provides rectangular cross section of whole stack, which are pressed on 800 mm length. Applied pressure of 80 MPa is kept by the bolt joints, uniformly distributed along the fixture. This fixture is used as a mould for curing and then as a sample holder during measurement. It is necessary to notice that in the absence of the suitable equipment for such long sample we could not reproduce curing cycle, shown in Fig. 1. Therefore, the sample, squeezed initially up to 80 MPa, was inserted in the furnace with temperature of 160ºC and then temperature was changed according to Fig. 1.

In central part on inner surface of cable loop the spot-like measuring heaters [7] were made. Heaters are allocated on the centre of broad face of cable strictly above the single strands. Thin strips of NbTi foil were put over the heater for the current delivery, whereas the cable strands are used as a current return path. The potential taps were soldered to narrow side of the cable. Simplified measuring scheme is shown in Fig. 5. Management of measurement and data acquisition are carried out through the interface bus GPIB. At current ramping the continuous registration of a sample current and voltage is performed by nanovoltmeter Agilent 34420A that provides the measuring of critical current or detecting a quench, caused by a thermal disturbance. The linear ramp of a current is used. At the appointed current the small heat disturbance with duration 50 µs was generated onto one cable strand by the measuring heater, which is fed by the power amplifier with P_{max} = 400 Wt. The amplitude of heat pulse is specified by the function generator. Short pulses of heater current and voltage are digitized with the 50 ns period by digital oscilloscope, connected via wideband insulating amplifiers.

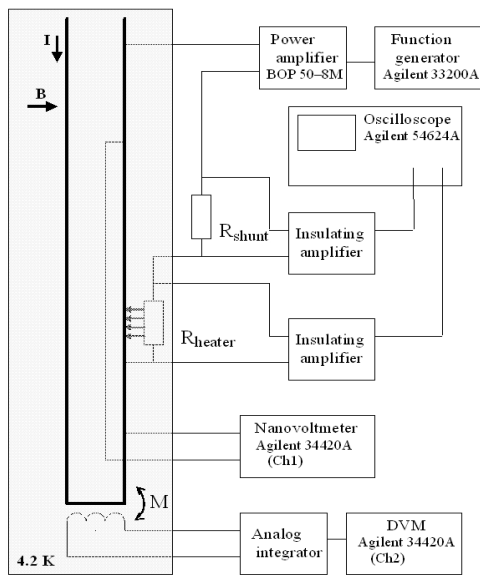07 Accelerator Technology Main Systems

Figure 5: The measuring scheme.

Then the energy, deposited in heater, is calculated. This energy is varied step by step and the minimum energy, which provoke quench, is found for every appointed current. The sharp increase of voltage over of the sample and the subsequent sharp decrease of a current in cable is a quench indicator. The cable is quenched manually for providing the same initial current distribution into the cable strands and then a new current ramp is used before each heater firing.

Such as MQE measurement is iterative process, the accuracy is determined by step of change of the heater energy, whereas the instrumental error is much lesser. In our case metering error was < 20 %. In particular for this reason the nothing scaling factors like [8] was used here. As to a first approximation, as MQE it is interpreted the dissipated into heater energy, which leads to quench of whole cable. A careful analysis is performed in [9].

The dependences of MQE versus current for the cored cable are presented in Fig. 6. For comparison the similar dependences was measured and it is shown in Fig. 7 for Ni-coated cable, whose MQE is significantly greater.

CONCLUSIONS

Preliminary heat treatment for this cable is not necessary. Adjacent resistance has enough value to reduce
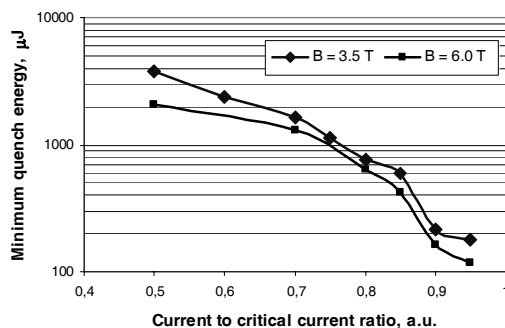

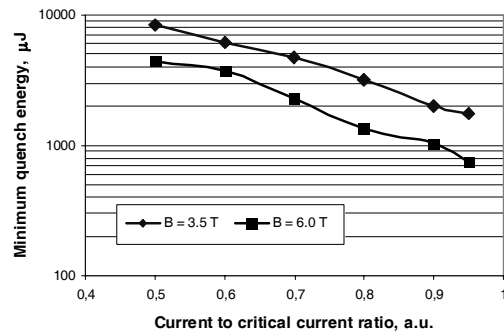Figure 6: Minimum Quench Energy for cored cable.

Figure 7: Minimum Quench Energy for Ni coated cable.

eddy current losses in cable to the reasonable level. However, very large value of Rc in cored cable is redundant from the point of view of decreasing of losses and from the other hand it makes worse the conditions of current redistribution between wires.

REFERENCES

[1] L. Tkachenko et al., "Development of Quadrupole, Steering and Corrector Magnets for the SIS 300", IEEE Trans. on Appl. Supercond., vol. 20, issue 3, pp.159-163 (2010).

[2] L. Tkachenko et al., "Quadrupole Geometry for the SIS 300", IEEE Trans. on Appl. Supercond. vol. 19, no. 3, pp. 1167-1179 (2009).

[3] A.P. Verveij, "Elecrtodynamics of Superconducting Cables in Accelerator Magnets", Ph.D. Thesis, University of Twente, Enschede, Netherlands (1995).

[4] R. Soika et al., "Inter-Strand Resistance Measure-ments in Cored Nb-Ti Rutherford Cables", IEEE Trans. on Appl. Supercond., vol. 13, pp. 2376-2379 (2003).

[5] I.V. Bogdanov et al., "Crossover Resistance of Superconducting Cable for Fast-Ramping Magnets of Particle Accelerators", Proc. of RuPAC 2008, Zvenigorod, Russia, p.p.188-190, (2008), http://cern.ch/AccelConf/r08/papers/TUDPH01.pdf

[6] L. Shirshov et al., "Superconducting Transformers for Study of High-Current Superconducting Cables", Presented in RuPAC 2010, Protvino, Russia (2010).

[7] L. Shirshov et al. "Stability Study of High-Current Superconducting Cables for Accelerator Magnets", Proc. of RuPAC 2008, Zvenigorod, Russia, pp. 191-193 (2008), http://cern.ch/AccelConf/r08/papers/TUDPH02.pdf

[8] G.P. Willering et al., "Stability of Nb-Ti Rutherford cables Exhibiting Different Contact Resistances", IEEE Trans. on Appl. Supercond., Vol.18, Issue 2, pp.1263-1266 (2008).

[9] V. Zubko et al., "Study of Electrodynamic and Thermodynamic Mechanisms Influencing Stability of Superconducting Rutherford Cable", Presented in RuPAC 2010, Protvino, Russia (2010).

THE ELECTRON LINEAR ACCELERATOR LUE-200 – DRIVER THE IREN FACILITY

Boettcher Ju., Zamriy V.N., Kayukov A.S.,
V.V. Kobets, I.N. Meshkov, V.F. Minashkin, V.G. Pyataev, A.V. Skripnik, A.P. Sumbaev,
V.G. Shabratov, V.A. Shvets, V.N. Shvetsov, JINR, Dubna, Moscow region, 141980, Russia
P.V. Logachev, V.M.Pavlov, BINP, Novosibirsk, 630090, Russia

Abstract

It is reported on startup of the first stage of the Intense REsonance Neutron source installation (IREN) at the Frank Laboratory of Neutron Physics of the Joint Institute for Nuclear Research. The general scheme and current status of the electron linear accelerator with accelerating structure on a S-band traveling wave (f = 2856 MHz) are presented. Results of adjustment of the basic functional systems of the linac and the measured parameters of the beam (pulse current of a beam – 3,0 A, electron energy - 30 MeV; duration of a pulse current - 100 ns; rep, rate - 50 Hz) are reported. The integral neutron yield from nonmultiplying target reaches $(3 \div 5) \cdot 10^{10}$ n/s.

INTRODUCTCTION

Linear electron accelerator LUE-200 [1, 2] was designed at the Budker Institute of Nuclear Physics of Siberian branch of RAS (Novosibirsk) as the driver for intense resonance neutron source IREN [3].

Accelerator consists of the pulsed electron gun, accelerating system, RF power supply system based on 10-cm range klystrons with modulators, beam focusing and transport system including wide aperture magnetic spectrometer and vacuum system. Accelerator is allocated vertically inside 3-floors building. Its designed parameters are listed in table 1. At the beginning the nonmultiplying neutron producing target will be used.

Table 1: LUE-200 designed parameters

Parameter	Value
Maximal electron energy, MeV	200
Pulse beam current, A	1.5 – 2.0
Accelerated electron pulse width, ns	≤ 250
Repetition rate, Hz	150
Accelerating rate, MeV/m	35
Beam power, kW	9 – 12

IREN FACILITY COMPONENTS

Electron sourse

LUE-200 electron source is the 2-electrode electron gun with 12 mm diameter oxide thermocathode. Cathode is fed by 200 kV pulsed transformer. The anode – wall of the vacuum chamber with hole 43 mm in diameter closed with wire frame made of stainless steel. Electron gun provides pulsed electron beam with 8 A peak current, 250-300 ns duration, 50 Hz repetition rate and $\leq 0.01 \cdot \pi \cdot$cm$\cdot$mrad emittance.

Accelerating system

Accelerating system consists of the RF buncher and 2 short (3 meters long) accelerating sections with high acceleration rate. Accelerating sections were designed and manufactured at BINP (Novosibirsk). Accelerating section represents the circular blinded waveguide with constant impedance fed by RF power. RF power comes from klystrons – RF power amplifiers of 10-cm frequency range (2856 MHz). The prototype of the accelerating system was tested at foreinjector of the VEPP-5 complex of BINP. During the tests the maximal electric field 45 MV/m and average accelerating rate 35 MeV/m were achieved [4].

Full scale accelerator project foresees two accelerating sections. At present one accelerating section is used the second one is replaced with drift section surrounded by two quadruple lenses doublets.

RF power supply

As the optimal RF power supply for LUE-200 accelerator the SLAC 5045 were chosen providing peak RF power 60 MW at average level 45 kW. RF power compression system is introduced to provide 3-4 times gain in RF power transfer to the accelerating section providing average accelerating rate up to 35 MeV/m. Main components of the RF system of the accelerator are: two-channel high frequency driving generator with possibility to set 180 degrees phase shift between channels and fast phase reversal; two RF preamplifiers for klystrons actuation; two power compression systems; waveguides, couplers etc.

At present due to the absence of SLAC 5045 klystrons only one accelerating section was put into operation with TH2129 (Thomson) klystron providing 20 MW peak power.

Beam focusing and transport system

Beam focusing and transport system provides beam transporting and trajectory correction on the way from electron gun to the nonmultiplying neutron producing target. From electron gun to the RF buncher 3 short solenoidal magnetic lenses are focusing electron beam.

Inside RF buncher and first accelerating section the beam transports due to the continuous solenoidal magnetic field provided with "short" and "long" solenoids enveloping accelerating section.

Beam transportation from the exit of accelerating section to the nonmultiplying target is provided with one separate quadruple lens, four doublets of the wide-aperture quadruple lenses and six correcting magnets distributed along the electron guide.

Nonmultiplying neutron producing target

Neutron producing target is produced with tungsten based alloy and represents cylinder 40 mm in diameter and 100 mm height spaced within aluminum can 160 mm in diameter and 200 mm height. Distilled water is circulated inside can, providing target cooling and neutron moderation. Water layer thickness in radial direction is 50 mm. Target dimensions and water moderator thickness were optimized with Monte Carlo simulation. Simulation result for neutron flux density at 10 meters flight path is shown at Figure 1.
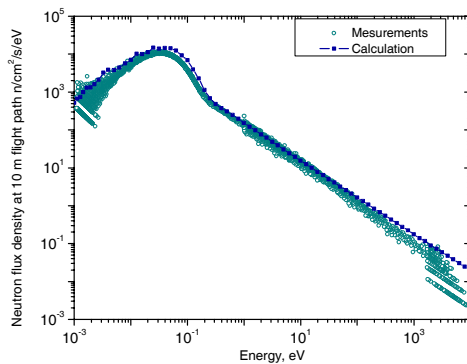

Figure 1: Neutron flux density at 10 m flight path of IREN source. Calculated (solid squares) and measured (open circles).

Accelerated electrons are penetrating inside the can through beryllium window 1 mm thick and hit the top surface of the target cylinder. One thermocouple is placed in the center of the exposed face of the target.

Neutrons are produced in the target with double stage process. At the first stage accelerated electrons stop in the target producing Bremsstrahlung gamma quanta. Energy spectrum of the gamma quanta is limited from above with the maximal energy of the accelerated electrons. At the second stage gamma quanta interacting with tungsten nuclei and neutrons are produced in reactions $^{A}W(\gamma,n)^{A-1}W$, $^{A}W(\gamma,2n)^{A-2}W$, $^{A}W(\gamma,3n)^{A-3}W$.

BEAM ADJUSTMENT AND TRANSPORTATION

Accelerator startup was carried out by subsequent adjustment of the electron gun, components of beam

focusing and transportation system and accelerating system.

During accelerator startup the beam parameters were tested at five diagnostic stations distributed along accelerator: after the electron gun, on the exit from accelerating section, at the end of the drift section, after magnetic spectrometer and in front of the target. Each diagnostic station includes: magnetic induction sensors of the beam current – Rogowski loop; beam viewer – luminescent screen with CCD camera; secondary emission wire frame profilometer. These tools let one to measure beam current and its position in each pulse.

As a result of the optimization of the operational modes of the accelerating and focusing systems at 5 A peak current from electron gun the peak current on the exit from accelerating section reaches 2.2 A and peak current on the target on the level 1.6 A.

MEASUREMENTS OF THE ACCELERATED ELECTRONS SPECTRA

To measure the spectra of the accelerated electrons the broadband magnetostatic analyzer with magnetic field perpendicular to the beam direction was used. Magnet E-core with the variable magnetic rigidity $0.166 – 0.7$ T·m is placed after the drift section. Electron beam in the spectrometer magnetic field is turned up to 90 degrees and extracted from the spectrometer vacuum chamber through 50 microns stainless steel window. Thereupon turned electrons hit the position sensitive detector which make it possible to measure electron energy with accuracy $\Delta E/E \le 5\%$.
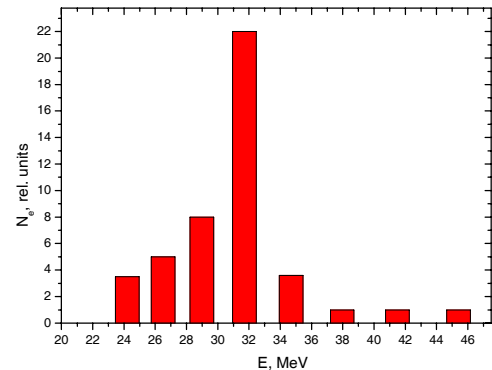

Figure 2: IREN electron beam spectra. Electron gun peak current 4 A, accelerated beam current 1 A, power compression system is on.

Electron spectra were measured at different modes of operation of the electron gun and RF power compression system. Peak current on the exit from the accelerating section varies from 0.7 A up to 2.6 A. It was found that when RF power compression system is off the maximum of the accelerated electron spectra is between 18 MeV and 20 MeV. When RF power compression system is on the maximum of the accelerated electron spectra is between

27 MeV and 31 MeV. Typical beam spectrum is visualized at Figure 2.

ESTIMATION OF THE NEUTRON YIELD AND EXTRACTED NEUTRON BEAM PARAMETERS

Actual beam parameters achieved at the middle of 2009 were: average energy of the accelerated electrons – 30 MeV; peak beam current – 1.5 A; electron pulse width 100 ns; repetition rate 25 Hz.

Estimation of the integral neutron yield realized by measurements of the neutron flux density at 10 meters distance from the target by means of the ^{3}He gaseous proportional counter SNM-16 (see Figure 1) and also with the set of activation detectors positioned on the side surface of the target can. The pressure of the ^{3}He in SNM-16 was measured beforehand by the method of transmission of the collimated neutron beam trough the counter and amounts 4.3 bar. The results of the estimation of the neutron yield for abovementioned parameters obtained with two methods are in a good agreement and amount to the value of neutron yield $(3 - 5) \cdot 10^{10}$ n/s. Corresponding neutron flux density at 10 meters from the target (shortest flight path) amounts $(2.4 - 4) \cdot 10^3$ n/cm$^2 \cdot$s.
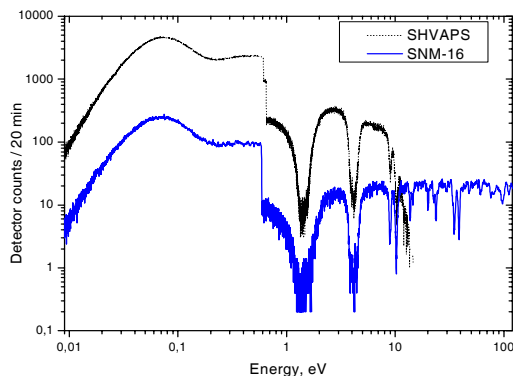

Figure 3: Transmission curves for two filters (Ta + In). Exposition – 20 minutes. Flight path – 9.3 m. Time channel widths in the energy range below 0.5 eV – 10 μs, above 0.5 eV – 2 μs.

To estimate the parameters of the extracted neutron beam the experiment on transmission of the neutrons through tantalum and indium filter samples 2 mm thick was performed. These elements have strong resonances in total cross sections in the energy region from eV to keV. Neutrons passed through the samples were detected with SNM-16 counter and another ^{3}He detector SHVAPS 38 cm in diameter and 53 cm long with 1 bar ^{3}He pressure. Time of flight spectra were registered by the DAQ system with minimal time channel width 20.83 ns. The results are presented at Figure 3.

To compare the energy resolution of the IREN source with our old IBR-30 + LUE-40 complex the experiment on measurements of the capture gamma quanta from tantalum was performed. Large volume liquid scintillator

detector consisting of 6 sections 20 liters each was placed at 60 meters flight path. Tantalum sample was installed inside the detector. Raw experimental data are presented at Figure 4. One can see valuable improvement of the energy resolution in the neutron energy range above 10 eV.
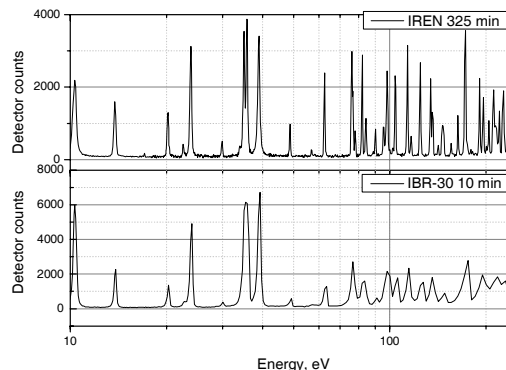

Figure 4: Liquid scintillator detector counts vs neutron energy for IBR-30 and IREN.

CONCIUSION

Physical start up of the first stage of IREN facility was performed at the beginning of 2009. Actual parameters achieved at the middle of 2009 are: average energy of the accelerated electrons – 30 MeV; peak beam current – 1.5 A; electron pulse width 100 ns; repetition rate 25 Hz; neutron yield $(3 - 5) \cdot 10^{10}$ n/s. Extracted beam parameters were estimated within the set of test experiments.

The upgrade of the facility with more powerful klystrons and modulators to reach the designed parameters is planned for the period 2010 – 2015.

REFERENCES

[1] A. Novohatsky et al., Linear accelerator for Intense Resonance Neutron source (IREN), Proc. of the 2nd Workshop on JINR Tau-Charm Factory, p. 197, D1-9-13-459, Dubna, 1994.

[2] A. Kaminsky et al., LUE200 - Driver Linac For Intense Resonant Neutron Spectrometer (IREN), Proc. of the XVIII International Linear Accelerator Conference., 26-30 August, 1996, Geneva, Switzerland, CERN, 96-07, 15 November 1996, Vol. 2, pp. 508-510.

[3] Anan'ev V.D. et al., Intense Resonance Neutron Source (IREN) – New Pulsed Source for Nuclear and Applied Investigations., Particles and Nuclei, Letters. 2005, V 2, No 3(126), 11-18.

[4] VEPP-5 Team (Budker INP, Novosibirsk, Russia) Test of accelerating structure for VEPP-5 preinjector LINAC2000 Conference. Monterey, California, August 21-25, 2000.

07 Accelerator Technology Main Systems

INVESTIGATION ON THE ELECTRON BEAM FORMATION IN THE MAGNETRON GUN WITH A SECONDARY-EMISSION CATHODE USING THE MAGNETIC SYSTEM BASED ON PERMANENT MAGNETS

A. N. Dovbnya, V.V. Zakutin, N.G. Reshetnyak, N. I. Aizatsky, V. N. Boriskin, V. P. Romas'ko, I. A. Chertishchev, N. A.Dovbnya, National Science Center "Kharkov Institute of Physics & Technology", 1 Akademicheskaya St., Kharkov, 61108, Ukraine

INTRODUCTION

The interest in the physics of processes with crossed electric and magnetic fields is aroused in connection with their wide application in the high-power vacuum electronics. Of a particular interest is the use in such devices of electron magnetic guns with secondary-emission cathodes as electron sources [1-3]. In the investigations of magnetron guns used were relatively long [1, 3] secondary-emission cathodes placed in the longitudinal magnetic field formed by the solenoid.

The present paper gives the results of investigations on the electron beam formation in the magnetron guns with secondary-emission cathodes having small longitudinal sizes in the magnetic system based on the permanent annular magnets made of NdFeB material.

EXPERIMENTAL SETUP AND INVESTIGATION METHODS

Experiments aimed to the investigation of the electron beam formation and its parameters were carried out at the facility schematically shown in Fig.1. For the electron beam powering a long (~50 μs) pulse generator was used. The present system uses a complete discharge of the storage capacitor C_1, advancing through the correcting circuit L_2R_2 to the pulse transformer. Using the low-resistance circuit: $L_2 = 134$ μHn and $R_2 \sim 3$ Ohm it is possible to decrease the voltage pulse drop during the high-current electron beam generation. The discharge of the capacitor C_2 provides a top-surge voltage pulse transmitted to cathode 4. The surge amplitude is from 10 to 45 kV, and the pulse repetition rate is from 3 to 7 Hz. Anode 5 is earth-connected via the resistor. The magnetron gun was placed in the vacuum chamber with a pressure maintained to ~10^{-6} Torr. The beam parameters were studied by means of Faraday cup 6 with 12-channel computer-assisted measuring system 7.

The investigations were carried out using the digital storage oscillograph Tektronix TDS-2014.

The cross-sectional dimensions of the beam were measured by making an indentation on the targets made of different materials.

The experiments on the electron beam formation in the magnetron gun with secondary-emission cathodes were realized using a magnetic system based on permanent annular magnets 8.
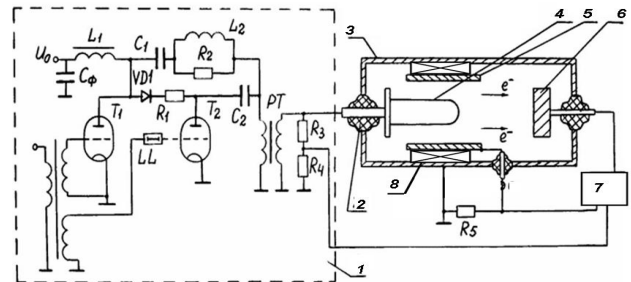

Fig.1. Schematic representation of the experimental setup: 1 – pulse generator, 2 – insulator, 3 – vacuum chamber, 4 – cathode, 5 – anode, 6 - Faraday cup, 7 – computer measuring system, 8 – permanent annular magnets.

EXPERIMENTAL RESULTS AND DISCUSSION

For experiments permanent annular magnets of NdFeB having internal diameter of 60 mm, external diameter of 80 mm and thickness of 10 mm were manufactured. The distribution of longitudinal (H_z) and radial (H_y) magnetic field components for magnetic assemblies was studied depending on the number of rings in the system. The most optimum field for the beam forming magnet system, with relation to the field homogeneity of ±5 % and its amplitude of ~750 Oe, is the magnetic system of 10 rings having 10 cm in length (Fig.2).

Since we have selected a magnetic system having the longitudinal magnetic field amplitude of ~ 750 Oe, it was necessary to select the magnetron gun geometry for realization of experiments and electron beam generation.

In the previous experiments [1] investigations were carried out using the magnetron beam with the cathode of 5 mm in diameter, the anode of 50 mm in diameter, and the maximum cathode voltage of 60 kV in the solenoidal magnetic field with amplitude of 200 Oe. It has been shown that the beam generation is reached with the drift velocity $V_D \sim cE/H \sim 0{,}15c$. At lower cathode voltages of 26…27 kV, the electron beam was formed in the magnetic field of 900…950 Oe, and the radial component was ~10 Oe.

The estimates show that in the experiments using the magnetron gun with the anode of 56 mm in diameter and cathode of 5 mm in diameter at the cathode voltage of 20 kV it is necessary to have a magnetic field of ~750 Oe for electron beam forming. The investigation of electron beam formation and its parameters was carried out for two geometries of magnetron guns: anode diameter of

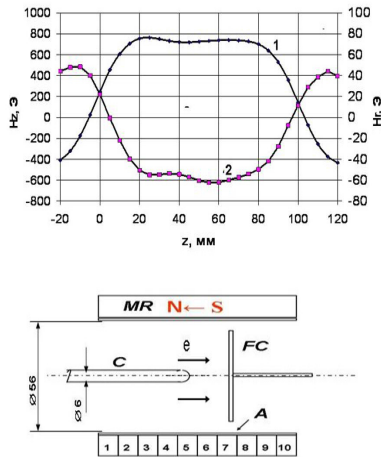56 mm and its length of 70 mm, cathode diameters of 6 and 10 mm, cathode lengths varying from 40 to 60 mm.

Fig.2. Distribution of Hz (curve 1) and Hy (curve 2) fields and the layout of the magnetron gun components
MR – permanent magnet, C – cathode, A – anode,
FC - Faraday cup.

Fig.2 shows the distribution of longitudinal and transversal magnetic fields on the radius of 3 mm along the magnetron gun axis with the cathode diameter of 6 mm. From the figure it is seen that the longitudinal component of the magnetic field is ~750 Oe, and the radial component is short and equals to ~ <60 Oe.

Also we have carried out experiments on the electron beam generation and measurement of electron beam parameters in the magnetron gun with the cathode diameter of 6 mm using the magnetic system based on permanent magnets. Experimental results have shown that at the cathode voltage of 15…25 kV the stable electron beam generation occurs. At the cathode voltage U ~ 17.5 kV the magnetron gun forms a tubular electron beam with a current of 3.5 A and duration of ~50 µs. Fig.3 represents the typical oscillograms of the cathode voltage (U) and the electron current onto the FC.
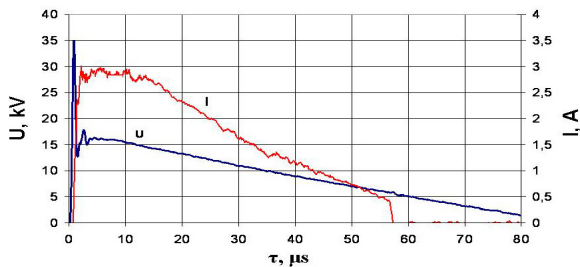

Fig.3. Oscillograms of the cathode voltage (U) and currents onto the Faraday cup (1).

As evident from Fig. 3 the electron beam generation occurs at the time of voltage surge pulse drop.

So, by the results obtained it is evident that electron beam formation was stable and the secondary-emission processes on the cathode were of long duration ~55 µs that resulted in the beam generation.

In the further experiments on the cathode diameter of 6 mm, at a distance of 4 cm from the cathode end, a reflector diameter of 16 mm, width of 5 mm was put in order to decrease the cathode length from 60 mm to 40 mm. In this case on the voltage and current pulses the rf noises were observed characterizing the electron beam generation (Fig.4). It can be assumed that because of the deficiency of primary electrons and, consequently, of the secondary ones, in the electron cloud, intense oscillations of the spatial charge density take place sufficient to sustain the secondary-emission process of electron multiplication necessary for the electron beam generation. At the cathode voltage of 19 kV the beam current was ~2.5 A, and the pulse duration was decreasing down to 15…17 µs with a sharp beam current cutoff.
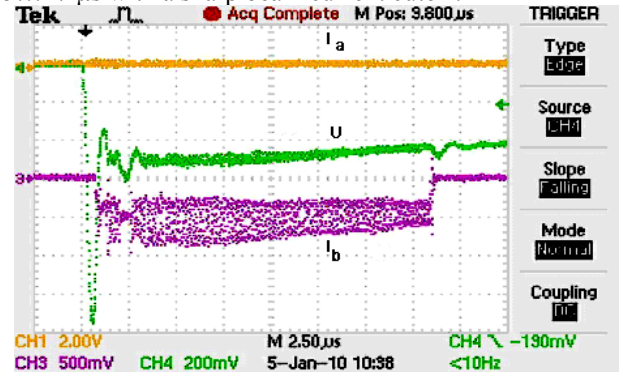

Fig.4. Oscillograms of the cathode voltage (U) and currents onto the Faraday cup (I_b) and onto the anode (I_a).

The experiments carried out in the magnetron gun with a cathode having 10 mm in diameter and the length of ~60 mm, anode diameter of~56 mm and the length of ~75 mm have shown that the magnetron gun forms a stable tubular electron beam with a duration of ~50 µs in the voltage range from 15 to 21 kV and a beam current of 3.2…6 A. The parameters of the electron beam on the aluminum target in the Faraday cup region were measured. It has been established that the internal beam diameter is ~10 mm, and the wall thickness is ~1 mm. The dependence of the beam current on the cathode voltage is shown in Fig.5. As is seen from the figure this dependence in the voltage range from 15 to 21 kV obeys to the law "3/2".
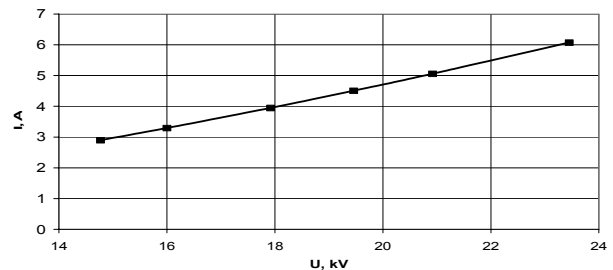

Fig.5. The beam current as a function of the cathode voltage.

The electric field influence on the electron beam formation was investigated too. According to the experimental data in the constant magnetic field the

07 Accelerator Technology Main Systems

electron beam formation keeps when the amplitude is changing by 25 % of the optimum value. If the cathode voltage approaches above and below to the boundary ΔU, the conditions of beam generation are disturbed.

It should be noted that in the both cases, when the magnetron gun was investigated in the longitudinal magnetic field formed by the solenoid [4], and when the magnetron gun was investigated before in the constant magnetic field, we observed the mode of generation of beam current- and anode current bunches with duration of ~1 µs during 20 µs at the cathode voltage ~22 kV (Fig.6).The oscillation period equals to ~1.4 µs, that is in accord with the characteristic frequency of the discharge circuit. After 20 µs, when the cathode voltage amplitude U has been decreased down to the cut-off U* [2,4], the magnetron gun operates in the usual oscillating mode.
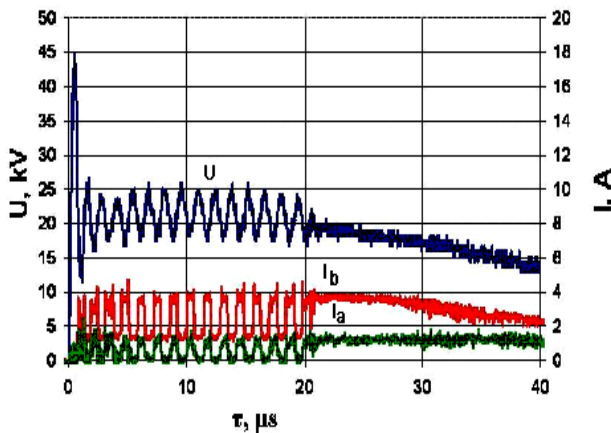

Fig.6. Oscillograms of the cathode voltage (U) and currents onto the Faraday cup (I_b) and anode (I_a).

CONCLUSION

As a result of investigations a compact magnetron gun with a secondary-emission cathode and a magnetic system on the base of annular permanent magnets was constructed.

The electron beam having a current of ~5 A at a cathode voltage ~20 kV with pulse duration ~50 µs was produced.

The mode of generation of several beam current and anode current bunches during a long-duration pulse was reached and investigated.

REFERENCES

[1] Volkolupov Yu.Ya., Dovbnya A.N., Zakutin V.V., et al. Electron bunches generation in the magnetron diode with a metallic secondary-emission cathode// Zhurnal Tekhnicheskoj Fiziki. -2002.-V.71.-No7,-P.88-91 (in Russian).

[2] Saveliev Y.M.. Sibbet W., Parkes D.M. Self-excitation and characteristics of the crossed-field emission electron source.// Review of Scientific Instruments.-1999.-V.70.-No12.-P.4502-4514.

[3] Dovbnya A.N., Zakutin V.V., Reshetnyak N.G. et al. Investigation on the azimuthal electron beam homogeneity in the magnetron gun with a secondary-emission cathode// Vestnik Kharkovskogo Natsionalnogo Universiteta, Seriya Fizika " Nucleus, particles, fields".-2004, -No 642,-Part.3(25).-P.91-96 (in Russian).

[4] Aizatsky N.I., Dovbnya A.N. Zakutin V.V. et al. Formation of electron beam bunches in the magnetron gun with a secondary-emission cathode // Vestnik Kharkovskogo Natsionalnogo Universiteta, Seriya Fizika "Nucleus, particles, fields".-2008, -No 808,-Part.1(25).-P.85-89 (in Russian).

ONE ASPECT OF THERMAL STABILITY FOR 4-VANE RFQ OPERATION WITH HIGH HEAT LOADING

V.V. Paramonov*

Institute for Nuclear Research of the RAS, Moscow, Russia

Abstract

Due to dispersion properties, 4-vane RFQ cavity without resonant coupling is a thermally unstable structure. With deterioration of balance for local detuning, especially near cavity ends, there is a possibility for runaway in the field distribution and related thermal-stress effects. It can, in principle, finish with irreversible plastic deformations and cavity frequency shift. Both the increment and the threshold of instability are proportional to the average dissipated RF power. This possibility increases for long RFQ cavities. Also particularities for the cavity ends design are important. Some general features of this effect are discussed and illustrated with simulations.

INTRODUCTION

The Normal Conducting (NC) RFQ cavity is now the imprescriptibly part of the hadron's linac. For proton linac 4-vane RFQ with operating TE_{210} mode is now prevailing. The sensitivity of the field longitudinal distribution to the shape deviations in such cavities strongly depends on the relative RFQ length $\frac{L_c}{\lambda_0}$, where L_c is the RFQ length and λ_0 is the operating wavelength. To reduce it for long RFQ cavities, $\frac{L_c}{\lambda_0} \geq 5$ the resonant coupling with special coupling cells was proposed [1], providing for RFQ properties of compensated structure in the field distribution sensitivity and stability. The shorter RFQ cavities, $\frac{L_c}{\lambda_0} \leq 5$, as a rule, are without coupling cells. It this report the stability of the longitudinal field distribution in time for RFQ without resonant coupling is considered with respect thermal induced geometry perturbations.

OPERATING REGIME STABILITY

In modern proton linac's RFQ operate with the frequency $f_0 \sim (324 \div 402.5) MHz$, maximal electric surface field $E_{sm} \sim 1.8 E_k \approx (25 \div 32)\frac{MV}{m}$, which corresponds to the maximal magnetic field at the regular RFQ surface $H_{sm} \sim 5.2 \frac{kA}{m}$. It results in the pulse heat dissipation is of $P_p \approx 100 \frac{kW}{m}$. Even for operation with duty factor $d_f \sim (1 \div 6)\%$ the average heat dissipation $P_a \sim (1 \div 6)\frac{kW}{m}$ is significant for thermal effects. The temperature of the cavity increases and f_0 decreases due to the cavity expansion. For the fixed cooling conditions the cavity frequency shift df_0 is linearly proportional to P_a.
Suppose a steady-state high RF power operation with a reference field distribution in the cavity is achieved. Let us

suppose a small local temperature deviation $\delta T > 0$ at the cavity surface due to some reasons. It may be either cooling fluctuation or electric discharge. This local temperature deviation leads to the local cavity expansion and local frequency change δf. The local frequency change δf immediately results in the change of the field distribution along the cavity and the change of the field in place of local heating. Depending on the cavity dispersion properties, two options, shown in Fig. 1, are possible.
In the first case, Fig. 1a, the local field relatively decreases.
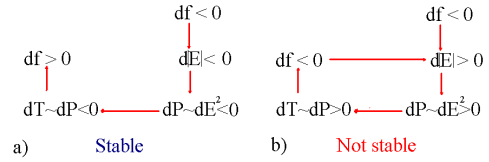

Figure 1: Thermal stable (a) and unstable (b) chain.

The local RF power dissipation decreases, the local temperature decreases, the local frequency increases, canceling or reducing initial frequency deviation δf. It is the stable case. After some time the cavity returns to operation with the reference field distribution.
In the second case, Fig. 1b, the local field, together with the local RF power dissipation, relatively increases, the local temperature increases, the local frequency decreases, amplifying initial local frequency deviation δf. Self-amplifying runaway starts and in the cavity itself there is no physical mechanism, which can stop it.
As it is shown in [10], without resonant coupling 4-vane RFQ cavity is thermal unstable.

$$\vec{E} = \vec{E}_0 - \sum_n \sqrt{8}\vec{E}_0 \frac{\delta f_0}{f_0}(1 + \frac{4L_c^2}{n^2\lambda_0^2})cos(\frac{n\pi z_0}{L_c}). \quad (1)$$

As one can see from (1), the negative local frequency deviation $\delta f_0 < 0$ at the cavity end leads to the local field increasing $\delta|\vec{E}| = |\vec{E} - \vec{E}_0| > 0$.
Most dangerous is the detuning of the cavity ends, $z = 0, L_c$. This effect linearly rises with the cavity length $\frac{L_c}{\lambda_0}$, because the relative detuning $\frac{\delta f_0}{f_0}$, caused the same absolute local deviation δf_0 is inverse proportional to L_c.

RFQ ENDS DETUNING

The RFQ vanes have undercuts in the cavity ends to return magnetic field flux, to tune the cavity frequency and tune longitudinally the field distribution. Different shapes are known - the undercut with a small tip ($N1$ in Fig. 2a,

[6]), the undercut with a moderate tip ($N2$ in Fig. 2b, [7]) and mostly distributed undercut with inclined tip, see, for example SNS RFQ, [8]. The last one can be realized both with vertical ($N3$ in Fig. 2c) and inclined ($N4$ in Fig. 2d) outputs of the vane cooling channel.

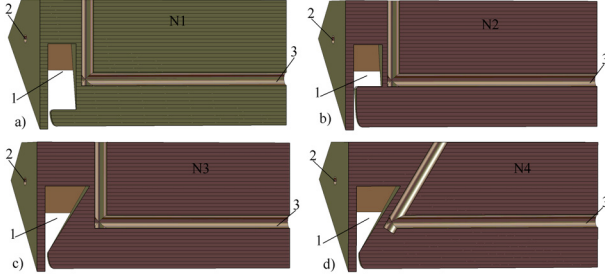For all undercut options the maximal value of magnetic

Figure 2: Different options for vane undercuts and cooling channels. 1 - vane undercuts, 2 - the channels for cavity body cooling, 3 - the vane channel.

field and related dissipated heat density takes place at the cavity ends. Additionally, the vane cooling channel may be at enlarged distance from the undercut tip, as one can see from Fig. 2. All options, shown in Fig. 2, were tuned for operating frequency and a flat field distribution along the cavity. Initial thermal-stress analysis has been performed according [9] in engineering approach assuming the duty factor of 3% ($P_a = 0.03 P_p$) and the average flow velocity $V_{av} = 1.5 \frac{m}{sec}$.

The undercuts with small and moderate tips ($N1$ and $N2$ in Fig. 2a,b) have the larger surface temperature rise $dT = T_{max} - T_w$ with respect to the temperature of cooling liquid. The smallest dT value has the undercut with inclined tip and inclined channel output, $N4$ in Fig. 2d. In more details the temperature distributions are presented in [10]. The distributions of the thermal induced displacements and related frequency shift δf_0 values are shown in Fig. 3. For δf_0 value definition it is assumed, that the detuning is localized near cavity end at the length $0.1\lambda_0$.

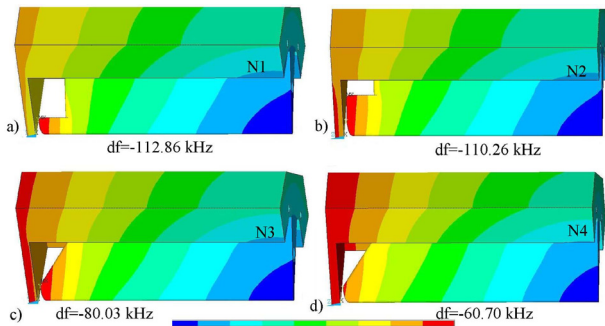Even from the qualitative displacement distributions in

Figure 3: The displacements distributions and induced frequency shift values for different undercuts options.

Fig. 3 one can see the significant difference between options $N1$, $N2$ and $N4$ - small and moderate tips move to

07 Accelerator Technology Main Systems

the cavity end plate. For the inclined undercut with inclined channel the plates moves from the tip, decreasing capacitance. More detailed analysis shows for all undercut both longitudinal and radial ($dr < 0$) displacements. The minimal δf_0 value provides $N4$ option due to better cooling and smaller induced displacements.

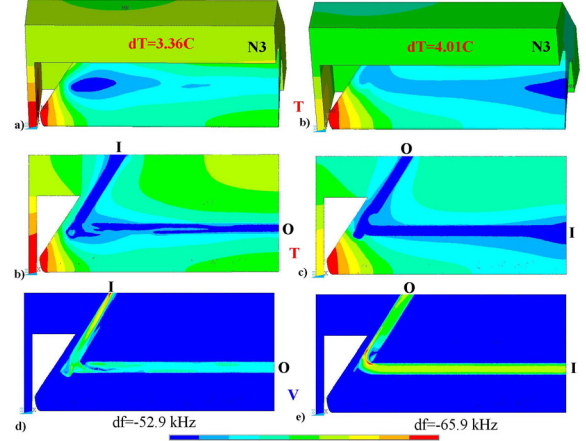The direction of cooling water is very important and can

Figure 4: The temperature distributions at the surface (a,b), in the middle of the vane (c,d) for different directions (e,f) of the cooling liquid.

be even decisive. In Fig. 4 the temperature distribution are shown for water flow direction from the cavity end and for reverse case, calculated with the extended procedure [9] starting from CFD simulations. The water input from the RFQ end results in colder vanes and reduced frequency shift. Considering in this approach more longer RFQ part, we can obtain hot region in the cavity middle and even get $\delta f_0 \geq 0$ for RFQ end with respect regular part. Depending on the design and cooling particularities, ends of RFQ cavity have different values for 'power sensitivity' $\frac{\partial f_0}{\partial P_a}$, which is **not the same** as for regular RFQ part.

INCREMENT AND THRESHOLD

The instability is the result of the coupled RF - thermal - stress - RF interaction and the increment value ζ depends on both cavity RF parameters and cavity material thermal and mechanical properties, details of the design. The precise consideration is too complicated and we can detect qualitative dependencies.

Assuming the instability development as $\delta f_0 \sim A_0 e^{\zeta t}$, and considering the sequence $d(\delta f_0) \sim \delta x \sim \delta T \sim \delta P \sim \delta E \sim \delta f_0$, in [10] the instability increment ζ is estimated as:

$$\delta f_0 \sim A_0 e^{\zeta t}, \zeta \simeq B_0 \frac{P_a}{x_i^2} \frac{L_c^2}{\lambda_0 cV} \frac{\alpha D_c}{E_c}, \quad A_0, B_0 = const \tag{2}$$

where where α and E_c are the linear expansion coefficient and Young module for copper, $D_c = \frac{K_c}{\rho_c C_c}$ is the thermal diffusivity for copper, K_c, ρ_c, C_c are the heat conductivity,

density and specific heat values for copper, respectively. The increment value ζ scales fasr with the cavity operating frequency f_0, $\zeta \sim f_0^4$.

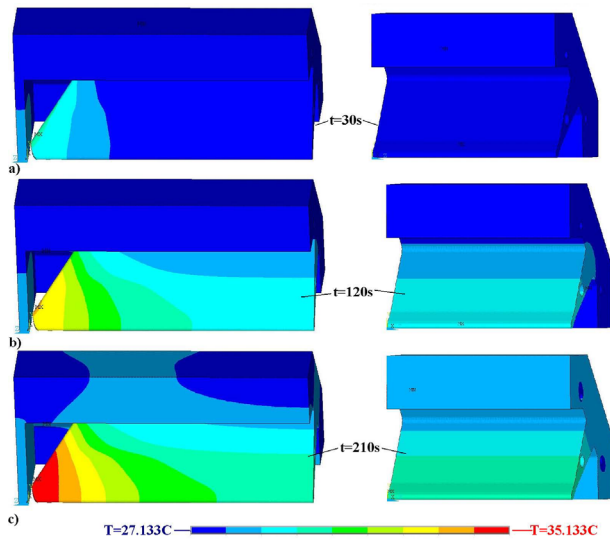The time scale of instability can be shorter, than the time

Figure 5: The transient temperature rise at the cavity and (left column) and regular RFQ part (right column) for closed vane channel.

constant of the cavity for RF power input. From Fig. 5 one can see, that local heating, for example at the cavity ends, is faster than more uniform heating of RFQ regular part.

In the frame of presented physical model, instability started when there is a powerful RF supply to support essential thermal effects, and one part of the cavity has the negative local frequency detuning with respect to total cavity. Most likely candidates are cavity ends, due to stronger effect on field distribution higher in (1) and essentially different $\frac{\partial f_0}{\partial P_a}$ value. Detuning of the segment near cavity middle at least generate 4 times lower field perturbations, have slower thermal transient and $\frac{\partial f_0}{\partial P_a}$ for middle RFQ is normally assumed for the total cavity.

The cavity tuning for frequency and field distribution is at RF power signal level, when thermal effects are absent, and results fix the initial distribution of local cavity parts detuning. With introducing RF power, sufficient for thermal effects, this distribution changes.

The RFQ cavity input and output ends, as a rule, have different design and may have different fields values. If after tuning the ends are not balanced in frequency detuning and one end has initial $\delta f_0 \leq 0$, will be even startup instability simultaneously with RF power switch on.

For balanced ends and correct cooling scheme there is a power range $0 \leq P_a \leq P_a^{cr}$ for RFQ stable operation, when the balance of local detuning is preserved. There are a lot of operating 4-vane RFQ's, but not with very high average RF power.

During the stable operation for each P_a value there is the total frequency shift of the cavity, which should be elim-

inated by frequency control system. But this system, as a rule, operates for whole cavity and can not preserve the balance of detuning. The balance of detuning is also specific for each P_a value. Due to different $\frac{\partial f_0}{\partial P_a}$ values, with P_a increasing this balance will become weaker and at some value $P_a = P_a^{cr}$ will be violated - one cavity end will get negative detuning. It will be start of instability.

In frame of presented model, the instability threshold depends on the average power, dissipated in the cavity. Additional heat sources at the 'weak' cavity part, like electric breakdowns and particle losses [8], can provoke instability or decrease threshold slightly. But original reason of instability in RFQ cavity without resonant coupling is in dispersion properties of such cavity. For stable operation with the high dissipated RF power and in CW regime, 4-vane RFQ cavity should be equipped with coupling cells to have the dispersion and stability properties of compensated structures.

In this work we can not estimate P_a^{cr} value - too many variables from cavity design, cooling, tuning and control.

SUMMARY

Consideration shows, that due to dispersion properties, 4-vane RFQ cavity without resonant coupling has the property of thermal instability. If instability started, the cavity has no own mechanism, except inelastic (irreversible) deformation to stop it. Both the increment and the threshold of instability depend on the average RF power, dissipated in the cavity and can limit possible duty factor value for each particular design. Control system for longitudinal field distribution together with fast movable tuners can dump instability.

REFERENCES

[1] M.J. Browman, L.M. Young. Coupled RFQ's as Compensated structures, Proc. 1990 Linac, p. 70, 1990

[2] V. Paramonov, Stability of Normal Conducting Structures Operation ... Proc. 2008 Linac Conf., p.61, 2008

[3] L.M. Young, J. M. Potter. CW Side Coupled Linac for the Racetrack Microtron. Proc. PAC 1981, p. 3508, 1983.

[4] B.P. Murin (ed), Ion Linear Accelerators, v.2, Atomizdat, Moscow, 1978, (in Russian)

[5] E.A. Knapp et al., Coupled cavity model for standing wave accelerator tanks. Rev. Sci. Instr., v. 38, p. 1583, 1967.

[6] A. Ueno, Y. Kondo, RF-Test of a 324-MHz, 3-MeV, H- RFQ Stabilized with PISL's, Proc. 2002 Linac, p. 545, 2002

[7] G. Romanov et al., The Fabrication and Initial Testing of the HINS RFQ. Proc. 2008 Linac, p. 160, 2009

[8] S. Kim et al., Stabilized operation of the SNS RFQ, Phys. Rev. STAB, v. 13, 070101, 2010

[9] A. Skassyrskaya et al., The complete 3-D rf-thermal-structural-rf analysis ... Proc. 2002 Linac, p. 216, 2002

[10] V. Paramonov, Possibility of Thermal Instability for 4-Vane RFQ Operation. Proc. 2010 Linac, TUP060, Tsukuba, 12-17 Sep., 2010.

THE DETECTION OF THE LEAKS LOCATION IN THE VACUUM CHAMBER ACCORDING TO SPUTTER-ION PUMPS CURRENT MEASUREMENTS

K.G. Mirzoev, A.M. Kiver, V.G. Lapygin, A.V. Larionov.

Institute for High Energy Physics (IHEP), Protvino, Moscow Region, Russia.

The present work is focused on developing methods to determine the locations of leaks in the extended vacuum chamber what is similar to chamber proton synchrotron U-70. This refers to small leaks that are difficult to detect by leak detector. Leak location is determined by measuring the air pressure in the chamber near the connectors of the diode-type sputter-ion pumps which pump out the chamber. The pumps discharge currents were used as the pressure gauges, as described in [1]. The main components of residual gas in the chamber are hydrogen and air, which come from gassing at the walls and above mentioned uncontrolled leakages, respectively. The flow and the pressure of hydrogen in the chamber were determined as described in [2], and the current of discharge corresponding to this pressure was determined as described in [1]. The discharge current corresponding to the air was determined by subtracting the current required for pumping out hydrogen from the total pump discharge current. Air pressure can be determined by the formula:

$$P = 1.67 \times 10^{-4} I^{0.92} \tag{1}$$

where the discharge current is expressed in amperes and the pressure in mm Hg. We assume that the sections of the ring between two adjacent pumps are the separate chambers. During a number of sessions of the accelerator we carried out measurements of currents in the process of alternate shutdown of neighboring pumps in six chambers. For some of these chambers the locations of leaks and air flows through them were known [3]. These observations allowed us to determine the empirical coefficients, showing what fractions of air pressure at pump connections to the chamber are the partial pressures of air components - nitrogen, oxygen and argon, as well as what are the fractions of flow of air components in the chamber and their fractions of total air discharge current. This allowed us to develop a methodology to detect a leak at its arbitrary location.
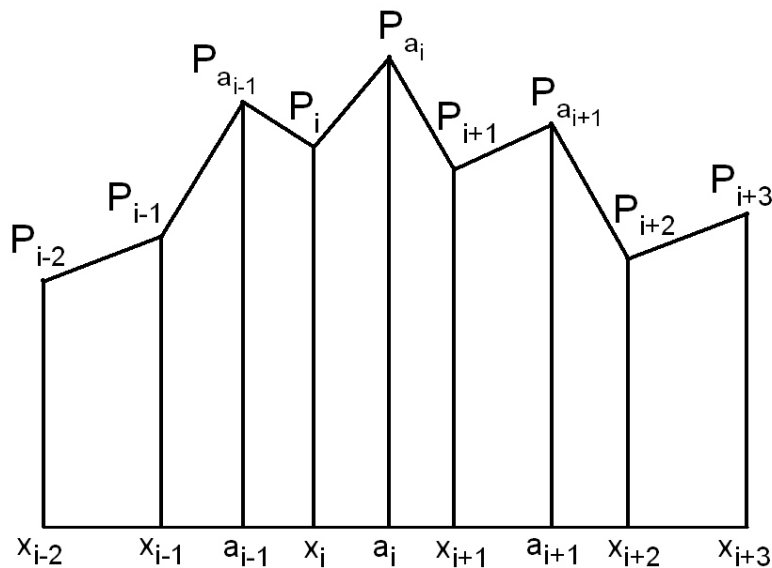

Figure.1. The diagram of pressure changes from the sites of leaks to the sites of pumps in the case of an area of three chambers having leaks, when the chambers at the beginning and the end of the area are without leaks.

07 Accelerator Technology Main Systems

Figure 1 schematically shows the change in pressure along the length of several neighboring chambers with leaks. Let us assume that the chamber i has a leak at the point a_i, the flow through which is Q_i. The geometric dimensions of vacuum leaks are very small, so the leak can be considered a point source of gas and can be characterized using the impulse δ - Dirac function [3]. Then in the interval from x_i to x_{i+1} air pressure change can be described by the following equation:

$$u_0 \frac{d^2 P}{dx^2} = -Q_i \delta (x - a_i) \qquad (2)$$

where u_0 - is the specific conductivity of the chamber for the gas of consideration. From the solution of equation (2) with boundary conditions $x = x_i$, $P = P_i$; $x = x_{i+1}$, $P = P_{i+1}$ follows:

$$P_{ai} - P_i = \frac{Q_i (a_i - x_i)}{2u_0} \qquad (3)$$

$$P_{ai} - P_{i+1} = \frac{Q_i (x_{i+1} - a_i)}{2u_0} \qquad (4)$$

where P_{ai} - is the pressure at the point of leak. By eliminating this pressure from (3) and (4), we obtain the following relation between a_i and Q_i :

$$Q_i (x_i + x_{i+1} - 2a_i) = 2u_0 (P_i - P_{i+1}) \qquad (5)$$

Applying (3) and (4) for nitrogen and oxygen separately, we obtain a system of four linear algebraic equations with four unknown parameters: $a_i, Q_i, P_{aiN_2}, P_{aiO_2}$, because the source of leak is the same for nitrogen and oxygen and the fractions of air flow (Q_{iN_2}, Q_{iO2}) and the partial pressures (P_{iN_2}, P_{iO_2}) are known from the measurements of the coefficients at the above-mentioned six chambers. This system of equations was solved using mathematical software Mathcad. There is no need for obtaining a_i in analytical form. The parameters of argon were not used due to the worst accuracy of experimental data for argon pressure as compared to nitrogen and oxygen pressure. Perhaps this was due to release of argon from the sputter-ion pumps and because of lower speed of pumping of argon compared to nitrogen and oxygen. The obtained approximate value of the root a_i was checked by equation (5) for the air. Such calculations were carried out for all the chambers what gave an idea of the ring U-70 tightness. Estimation of maximum pressure in the leaks locations allowed to determine the average pressure

of air and argon in each chamber and in the whole ring. This can be of significance for studying the scattering of protons by the residual gas. Determination of the value of leak flow is not of practical significance, except in the case of large leaks. The calculated values of a_i were compared with those obtained previously by other methods [3] and in other sessions of the accelerator. In most cases the obtained values were not significantly different (in the range of $\pm 15\%$ of difference). One can estimate the accuracy of determination of the leak location, which is at least not better than the accuracy of measurement of pressure using the discharge current pump. Therefore, an optimistic estimation of the accuracy of calculation of leak location gives a value in the range of $\pm 30cm$. This implies that the method described above so far cannot replace the search of leaks using a helium leak detector. However, compared to conventional techniques, the described method has the following important features:

 1. It allows to determine the most feasible leak location, for example, the nearest welding seam or sealing, what significantly reduces the time of searching.

 2. The leaks can be determined remotely and in advance, during a session of the accelerator by the special program without the participation of an operator.

 3. The present technique permits the detection of such leaks that are difficult to find using the conventional leak detector, for example, due to the extended time of helium passage or due to adverse conditions of helium access through a long channel.

 4. The upgrading of method of leakage determination in all chambers of the ring allows to define more accurately the value of an average pressure of air and argon during the session of the accelerator work.

In the case of improving the system of measurement of discharge currents of pumps and improving the accuracy of pressure measurements, the error of the leak determination can be reduced, which would make this method more promising.

In conclusion, the technique of determining the leak location in the vacuum chamber has been developed. This technique is of significant interest for an application to both separate and extended vacuum chambers with a large number of the same type of electro-physical pumps.

REFERENCES

[1] Kiver A.M., Lapygin V.G., Mirzoev K.G. IHEP Preprint 2001-21, Protvino, (2001).

[2] Kiver A.M., Lapygin V.G., Larionov A.V. Mirzoev K.G. IHEP Preprint 2009-10, Protvino, (2009).

[3] Kiver A.M., Lapygin V.G., Larionov A.V., Mirzoev K.G. IHEP Preprint 2009-11, Protvino, (2009).

07 Accelerator Technology Main Systems

HIGH-VOLTAGE SOURCE WITH OUTPUT VOLTAGE UP TO 60 KV WITH OUTPUT CURRENT UP TO 1A

Gusev I.A., Medvedko A.S., Protopopov A. Yu., Pureskin D.N., Senkov D.V.,
BINP Novosibirsk Russia

Abstract

The presented report contains the description of high-voltage source with output voltage up to 60kV and output current up to 1A. The source consist of the chopper with IGBT switches working with a principle of pulse-width modulation and the fill H-bridge converter with IGBT switches , both working on programmed from 15 to 25 kHz frequency, and the high voltage sectioned transformer with the rectifier and additional capacity filter. The transformer is made in oil tank with silicon oil. The additional capacity filter decreases the ripple and noise level in working range of output currents. The design of the high-voltage transformer provides preservation of working capacity at voltage up to 100kV. A nominal output voltage of the source is 60kV. The source can operate with series of high-voltage breakdowns in output voltage without risk of damage the components of source. In the high-voltage breakdown the released in load and matching circuit energy is less than 15J at maximum operating voltage 65kV. The efficiency of system is more than 80% at the nominally output power 60kW. The controller of the source is developed with DSP and PLM, which allows optimizing operations of the source. For control of the source serial CAN-interface is used. The description of the source and the test results are presented.

DESCRIPTION

The presented source was designed for some different applications at the BINP tasks. That was reason for some specific terms like: short time interval for voltage rise up to 60 kV after high-voltage breakdown, strong reliability to high-voltage breakdown, low voltage ripple for maximal power operation. The energy is dissipated in components of source and in the load during the high voltage breakdown less than 15J for 60 kV operation. The basic characteristics of high-voltage source are shown in Table1.

Overview

The circuit diagram of power part of high-voltage source is shown in Fig.1. The high-voltage source consists of the 20 kHz power converter with insulated gate bipolar transistors (IGBT) as switches (part A) and high-voltage sectioned transformer with the rectifier (part B). The power converter consists of 3-phase rectifier VD1, electromagnetic (EMI) filter F1, switch SW1, rectifier's filter capacitors C1-C2, 20 kHz chopper with IGBT switches Q1-Q2, 20 kHz inverter with IGBT switches Q3-Q6, impedance matching design L2 C5, and isolation transformer T1.

Table 1. Basic parameters of high-voltage source.

Parameter	Unit	Min	Nom	Max
Output voltage	kV	10	60	70
Output current	mA	0.1	1000	1100
Output power	kW		30	
Voltage ripple	%			0.5
Voltage stability	%			0.2
Transient time	ms		5	
Inverter frequency	kHz	15	20	25

Input rectifier

EMI filter is used to eliminate high-frequency noise to the power line from the source. 3-phase rectifier and filter C1-C4 are used to convert input AC 3-phase voltage 380V 50Hz to DC 550-600V voltage. Switch SW1 is used for soft start of converter and its consists two groups of contacts (not shown of sheet). First group of contacts is switched ON and the filter's capacitors C1-C2 are charged with 10A current. When the voltage on filter is up to 450 volts level the second group of contacts is switched ON and the rectifier is connected directly to 3-phase AC line.

Chopper

The chopper's switches Q1, Q2 are connected in parallel and operates one by one in working circle. As a result, the working frequency of each switch is the half of operated frequency of source. The chopper switches are operated with principle of pulse-width modulation on programmed from 15kHz to 25kHz frequency. The working frequency of inverter is the same. The operating frequency is selected depending on the characteristics of high-voltage transformer and the requirements to the spectrum of output high voltage ripple. The output voltage of chopper is changed from 10 to 450 volts DC by control circuit to obtain the required output high voltage of source.

Inverter

Full-bridge inverter Q3-Q6 converts DC voltage from chopper's capacitors C3-C4 to AC voltage with programmed from 15 to 25kHz frequency.
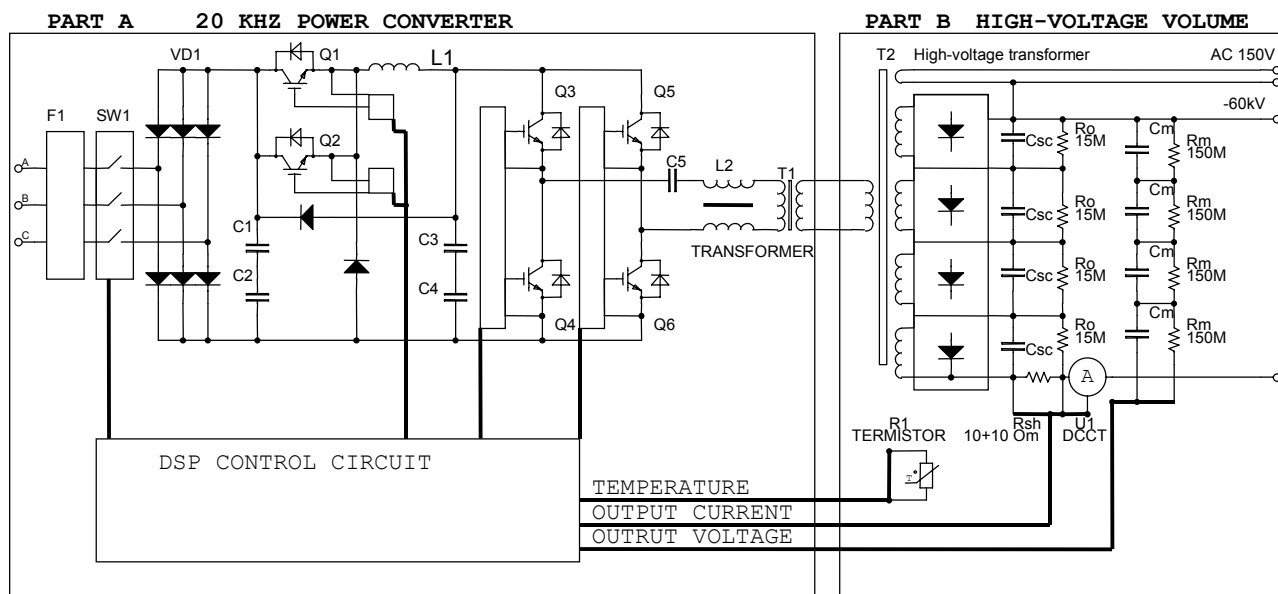
PART A   20 KHZ POWER CONVERTER   **PART B HIGH-VOLTAGE VOLUME**

Fig. 1. The high-voltage source block-diagram.

Matching circuit

The power source must work with wide range of loads, from zero current to full load. The technical conditions for this high-voltage source are: transient process time interval must be less then 5 ms with transient overvoltage less than 10kV for 60 kV operations for load switching between 20mA and 500mA (half load). The matching circuit consists of elements C5 and L2 is used for minimizing transient process and for improving efficiently of design. Magnetising inductance of high voltage transformer, its capacitance calculated to primary side and the matching circuit organize low-pass filter for all high harmonics of inverters rectangular waveform voltage. That way, sinusoidal voltage is feed in the high-voltage transformer, because all high harmonics are filtered. In other case, the presence of high harmonics causes power dissipation in the coils because of skin-effect. Also this harmonics can induce the singing in the winding of high-voltage transformer.

High-voltage transformer

Sectioned high-voltage transformer consists of four high voltage sections, joined in series. Each section is complete design and it includes winding, half-bridge rectifier, output filter capacitors and additional load resistor Ro. These additional loads improve transient process after switching OFF of the output current from 1A to zero load. Output voltage for section is 15 kV for 60 kV operations. Output filter capacity is chosen to decrease output voltage 40 kHz ripples less than 0,5% for full load operation. The top section of high-voltage transformer has addition winding with 150 volts AC 200 watts power output for supply of high side control circuits and the cathode heater. The transformer is designed in oil-filled tank (diameter 600mm, height 800mm). The silicon oil [1] is used.

Design

The converter is made in one 4U and three 6U crates in the rack of 19" Euromechanics standard. There are distilled water is used to cool IGBT switches and other elements.

The EMI-filter, input switch and input rectifier are positioned in the first 4U crate. The chopper's switches and choke are located in second crate. The chopper's capacitors, inverter and control circuit are located in the third case. And at last, there are capacitor and inductors of matching circuit located in the fourth crate.

Control circuit

The control circuit is realised in digital signal processor (DSP), programming logic matrix array (PLM), and analogue input buffers. The control and analogue grounds are isolated from external signals and grounds and, that way, in control circuit has obtained low noise level. It allows operation with better then 0.1% accuracy. All the IGBT switches are protected from short circuit and overcurrent. The controller measured seven analogue channels with 12-bits resolution. These channels are shown in Table 2. The controller has CAN-bus interface which is used to link with an external control system. The used data rates are 125, 250 and 500Kbits in second. The protocol of CAN-bus interface is compatible with devises produced in the BINP [2].

07 Accelerator Technology Main Systems

Protections and interlocks

There are two level of overcurrent protection: programmable and circuitry one. Rigid protection has a 1200mA threshold level, if the output current increases up to 1200mA or higher the converter switches OFF. The programmable threshold level is tunable. If output current is higher then programmable threshold level (from 5 to 1100mA) the converter switches OFF. Switching OFF time is less then 50 microseconds. For that reason, the breakdown energy less than 15J for 60kV operations with connected 10 meters of high-voltage cable. The converter try to switch on output voltage after 10 milliseconds with rise speed 1kV/msec. If the breakdown protection switches off the converter again rise speed is decreased to 100V/msec.

High-voltage transformer protection measures the temperature of transformer and the transformer's input current. If the input current of transformer rise up to 250A that matter the short circuit in transformer. In this case the converter is OFF.

Table2. Measured channels

Channel	Period	Range
Output voltage	50μsec	0-60.00kV
Output current (full range)	50μsec	0-1100.0mA
Output current (small current, measure with DCCT)	50μsec	0-50.00mA
Input current high-voltage transformer	50μsec	0-300A
Feedback signal	25μsec	0-3000mV
Input 3-phase voltage (r.m.s.)	1msec	0-600V
Input current (r.m.s.)	1msec	0-150A
Temperature of IGBT switches	1sec	0-70°C
Temperature of high-voltage transformer	1sec	0-100°C

Results

The high-voltage source was made and has being test with the electron beam gun for year. The power supply is tested with breakdown rate 1-2 breakdown in minute for output voltage 60kV within 3 hours. The tests are shown high reliability, efficiency better than 85% for full load operations. The long time stability of output voltage was better than 0,2%. Voltage ripple was better than 0,5%. Continues work in full load operations is 8 hours and longer.

REFERENCES

[1] http://www.sofex.ru/pdf/SOFEXIL-TCJ.pdf. Transformer fluid technical manual.

[2] V. R. Kozak, M. M. Romakch "The devices with CANBUS interface for automatic control systems of physical complexes" pre-print BINP 2004-68, 2004

[3] I.A.Gusev, A.S.Medvedko, A.Yu.Protopopov, D.N.Pureskin, D.V.Senkov, Yu.F.Tokarev, V.D.Yudin "High-voltage source with output voltage up to 60 kV with power up to 15 kW", Proceedings of RuPAC 2006, Novosibirsk, Russia, 2006 P.82.

POWER SOURCE FOR HIGH-VOLTAGE COLUMN OF INJECTOR TO PROTON SYNCHROTRON WITH OUTPUT POWER UP TO 5KW

Golubenko Yu.I., Medvedko A.S., Nemitov P.I., Pureskin D.N., Senkov D.V.,
BINP Novosibirsk Russia

Abstract

The presented report contains the description of power source with output voltage of sinusoidal shape with amplitude up to 150V, frequency 400Hz and output power up to 5kW, operating on the primary coil of high voltage transformer - rectifier of precision 1.5MV electrostatic accelerator – injector for proton synchrotron. The source consists of the input converter with IGBT switches, transformer and the synchronous rectifier with IGBT switches also. Converter works with a principle of pulse-width modulation (PWM) on programmed from 15 to 25 kHz frequency. In addition, PWM signal is modulated by sinusoidal 400Hz signal. The controller of the source is developed with DSP and PLM, which allows optimizing operations of the source. For control of the source serial CAN-interface is used. The efficiency of system is more than 80% at the nominal output power 5kW. The description of the source and the test results are presented.

DESCRIPTION

The presented source was designed as part of high-voltage power source for proton synchrotron injector, developed in BINP. The high voltage source consists of 1.5MV high voltage column with input matching circuit, operated on 400Hz frequency, and the power source with 400Hz 150V harmonic output. The block-diagram of high voltage source is shown on Fig.1. The matching circuit is necessary due to the high voltage column design feature, such as series inductance of high voltage transformer is compatible with magnetizing inductance, the capacitance of high voltage transformer calculated to primary side organize with the inductance the oscillatory circuit with 1.5kHz resonant frequency [1]. But the maximal working frequency of high voltage column consisting of sectioned transformer with rectifier is 600Hz. So the capacitor bank C1 decrease the resonance frequency of contour to operating frequency. The inductance L1 organize the partial including of the Harmonic 400Hz PS into resonance circuit, protecting the PS from large reactive currents from resonance circuit. Also L1 and C1 together are low-pass filter, which preventing the high voltage column from high frequency harmonics, from power source, where they are generated by converter and synchronous rectifier under the PWM. The basic characteristics of high-voltage source are shown in Table1.

Overview

Design of the power part of the source is shown on Fig.2. The power source consists of the 20kHz power converter with insulated gate bipolar transistors (IGBT) as switches (part A) and the isolation transformer with synchronous rectifier (part B). The design of power converter consists of 3-phase diode rectifier VD1, electromagnetic (EMI) filter F1, switch SW1, rectifier's filter L1 C1-C8, 20 kHz inverter with IGBT switches Q1-Q4, isolation transformer T1, synchronous rectifier Q5-Q8, output low-pass filter L2 C9 and three current sensors: U1, U2 and U3.
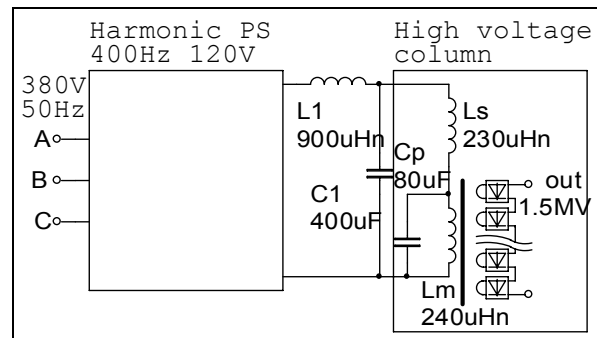

Fig. 1 High voltage source block-diagram

Table 1. Basic parameters of power source.

Parameter	Unit	Value		
		Min	Nom	Max
Output voltage	V r.m.s.	10	120	150
Output current	A r.m.s.		65	80
Output power	kW		5	7
Output voltage long time stability	%			0.1
Power source output frequency	Hz	200	400	600
Inverter frequency	kHz		20	

Input rectifier

EMI filter is used to prevent high-frequency noise from the power line from the PWM source. 3-phase diode rectifier and filter C1-C4 are used to rectifier input AC 3-phase voltage 380V 50Hz and to get DC 550-600V voltage. Switch SW1 is used for converter soft start.
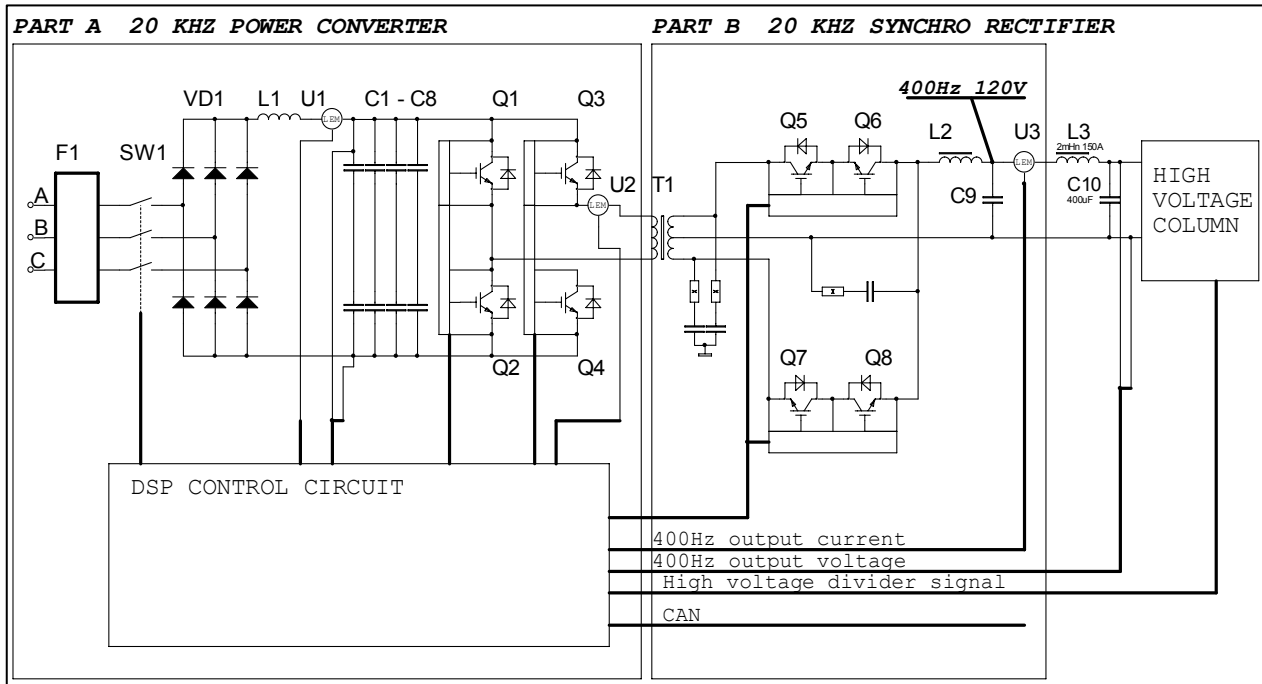
07 Accelerator Technology Main Systems
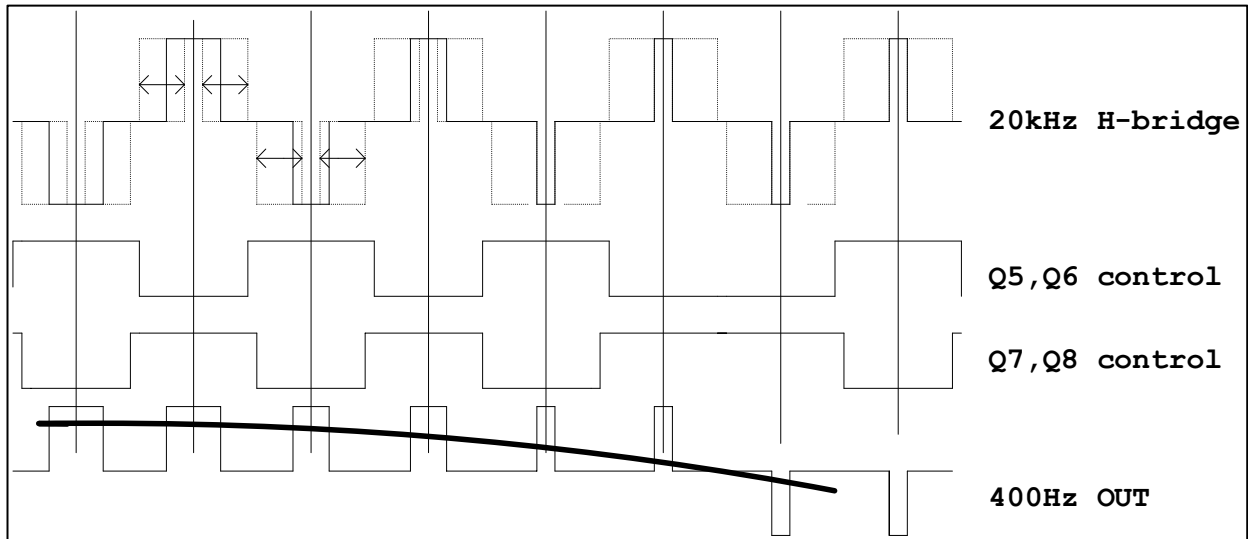
Fig. 2. The power source design circuit diagram.

Fig. 3. The power source principle of operation.

Inverter

Full-bridge inverter Q1-Q4 converts DC 550V voltage to AC voltage with 20 kHz frequency. Inverter works with principle of pulse-width modulation (PWM) with 2 circles (Fig.4): (A) freewheeling when switches Q2, Q4 are switched ON and (B) energy addition when Q1, Q4 or Q2, Q3 are ON. With this conditions the IGBT switches is in soft switching mode. As a result, the switching energy loss are minimised, the switching transient process improves. The modulation signal is 400Hz sinus, so the output signal from inverter presents 20kHz PWM AC voltage with module sin modulation

$\tau_B = Ampl \cdot T \cdot |\sin(\Omega t)|$ (Fig.4) were T is half of period 20kHz, Ω is $2 \cdot \pi \cdot 400$, $0 \le Ampl \le 1$ is amplitude of output 400Hz sin signal.
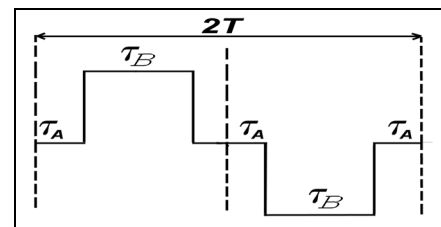

Fig. 4. PWM signal.

07 Accelerator Technology Main Systems

Synchronous rectifier

After the isolating transformer the modulated voltage feeds to synchronous rectifier switches Q5 Q6 and Q7 Q8. Each switch consists of two IGBTs in series connection, so each switch can operate with positive and negative polarity of input voltage. Switches controls by control circuit and works synchronously with inverter. The principle of obtaining 400Hz-sinusoidal voltage is shown on Fig.3. After synchronous rectifier the voltage feed to L2C9 filter. This LC circuit filtrates the 20kHz component of signal. So in the output the power source has the 400Hz-sinusoidal voltage with regulated amplitude, which feed to matching circuit L3C10 and after that on high voltage column.

The output voltage of column regulated from 10kV to 1500kV with changing amplitude of 400Hz-sinusoidal voltage with 100ppm accuracy.

Design

The power source is made in one 4U and two 6U crates in the rack of 19" Euromechanics standard. There are distilled water is used to cool IGBT switches and other elements.

There are EMI-filter, input switch and rectifier constructed in the first 4U crate. There is filter capacitors, inverter and control circuit located in the second crate. And at last, there is synchronous rectifier and low-pass filter located on third crate.

Control circuit

The control circuit is realised in digital signal processor (DSP), programming logic matrix array (PLM), and analog input matching circuits. The control and analog groundings are isolated from external signals and groundings and, that way, the control circuit has obtained low noise level. It allows to operate with better then 0.05% measurement accuracy. All the IGBT switches are protected from short circuit and overcurrent. The controller measured 7 analog channels with 12bits resolution. These channels list is shown in Table 2. The controller has CAN-bus interface which is used to link with a control system. The used data exchange rates are 125, 250 and 500Kbits in second. The protocol of CAN-bus interface is compatible with devises produced in the BINP [2].

Protections and interlocks

Breakdown protection controls output voltage from divider. If the rate of voltage variation exceeds the reference level, the high voltage breakdown is detected, and the converter switches OFF the IGBTs. Switching off time is less then 50 microseconds. The converter trays to switch on after 10 milliseconds with rise speed 1kV/msec. If the series breakdown is detected, protection decreases the rise up to 100V/msec.

High-voltage transformer protection measures the transformer's input current. If the input current of transformer increases up to 100A that matter the short circuit in transformer. In this case the converter became OFF.

Table2. Measured channels

Channel	Period	Values range
Output high voltage	50μsec	0-1500.0kV
Power source Output voltage	50μsec	0-200V
Power source Output current	50μsec	0-100A
Feedback signal	25μsec	0-3000mV
Input 3-phase voltage (r.m.s.)	1msec	0-600V
Input current (r.m.s.)	1msec	0-150A
Temperature of IGBT switches	1sec	0-70°C

RESULTS

The power source was developed and has being test with the high voltage column during last year. The tests are shown high reliability, efficiency better than 85% for full load operations. The long time stability of output voltage was better than 0.1%.

REFERENCES

[1] N.K. Kuksanov, R.A. Salimov, P.I. Nemitov, A.V. Lavruchin, Ju.I. Golubenko, S.N. Korchagin, D.S. Kogut "High power ELV electron accelerators for research and industries", proc. of 9th Intern. Conference on Electron Beam Technologies (EBT'09), Varna, Bulgaria, 1-4 June 2009.

[2] V. R. Kozak, M. M. Romakch "The devices vith CANBUS interface for automatic control systems of physical complexes" pre-print BINP 2004-68, 2004

COMPACT CYCLOTRON AS A PROTON SOURCE FOR THE DETECTION OF EXPLOSIVES BASED ON NUCLEAR RESONANCE ABSORPTION IN NITROGEN

L.M. Onischenko [#], S.B. Vorozhtsov, A.S. Vorozhtsov, Yu. G. Alenitsky, E.E. Perepelkin, A.A. Glazov, JINR, Dubna, Russia

T.J.T. Kwan, R.E.Morgado, T.F.Wang, Los Alamos National Laboratory, Los Alamos, NM, USA

Abstract

In the proposed operational implementation of the Nuclear Resonance Absorption (NRA) method for explosives detection, the inspected object is scanned by a beam of 9.17-MeV gamma rays of a precise energy to determine the fraction of the beam resonantly absorbed in the nitrogen nuclei of the explosive in the reaction, ^{14}N (gamma, p) ^{13}C. The 9.17-MeV gamma rays are most readily generated in the inverse reaction, ^{13}C (p, gamma)^{14}N, in which a 1.747-MeV proton is resonantly captured by C^{13}, followed by the emission of gamma rays from the recoiling N^{14} nucleus. To achieve the stringent requirements of a 1.747-MeV proton beam with an intensity of several milliampere and with as small as possible energy spread and angular divergence, a compact isochronous cyclotron with internal H^- ion source and current of ~2mA was considered as a stand-alone source or as an injector (with a current of ~200 microA) into a storage ring. This report describes the main cyclotron design consisting of an internal ion source, magnet, acceleration system, extraction system, and beam delivery system.

BACKGROUND

Earlier investigations [1], [2], [3], [4], [5], [6] of the beam dynamics in a cyclotron with an external H^- source resulted in the following characteristics:

maximum current (~1.8 MeV):   2.2-2.5 mA,

transverse emittances: 150-300π mm·mrad,

energy spread, $\Box E/E$:   ±8%.

Since these beam parameters do not meet the proton source requirements for nuclear resonance absorption, a cyclotron with a reduced current of ~200 $\Box$A with the transverse emittances and the energy spread reduced by an order of magnitude was proposed. This tailored beam could then be injected into a small storage ring in which the desired final beam parameters could be achieved.

To simplify the design and reduce costs, an internal ion source was examined with 6 mA of H^- ion current into the continuous mode of the cyclotron. Due to the 30-fold decrease of the average captured beam current for acceleration (from 6 mA to 200 $\Box$A), delimited by a diaphragm on the first turn, it became possible to reduce the transverse emittances and the energy spread. Calculations were performed taking into account the 3-D distributions of the electric fields of beam space charge as well as the field of the accelerating system.

BASIC CYCLOTRON PARAMETERS

The basic cyclotron parameters are listed in Table 1. The general view of the cyclotron is shown in Fig. 1

Table 1. Basic cyclotron parameters

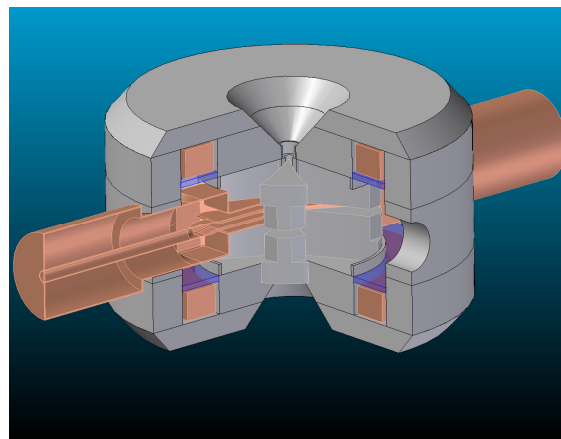| Type of ion	H^-
Extraction energy, keV	1747
Average magnetic field, T	0.64
Number of sectors	4
Number of dees	2
Betatron frequencies, Qr , Qz	1.1, 0.85
Angular span of dees, (°)	45
RF voltage, kV	60
Orbital frequency, MHz	9.76
Harmonic number	4

Fig. 1. Magnet and RF structures

MAGNET

The 4-fold type magnet with all-round yoke chosen for the cyclotron (Refs [2] and [7]) is shown in Fig. 1. The magnet poles and yoke shape the vacuum chamber for this design. The parameters of the magnet are given in Table 2.

Table 2. parameters of the magnet

magnet height	89 cm
magnet outer radius	70 cm
pole outer radius	35 cm
final orbit radius	30 cm
hill field at final radius	1.35 T
valley field	0.2 T
hill gap	3 cm
valley gap	40 cm
sector angular width	10º-30º
power consumption	10 kW

08 Applications of Accelerators, Technology Transfer and Industrial Relations

The choice of magnetic field strength (0.64 T) is a compromise between several options. The higher the field, the smaller will be the cyclotron size. A higher magnetic field also ensures a larger space-charge limit due to the effects of increased axial focusing. On the other hand, the turn separation is decreased along with the extraction efficiency.

ACCELERATION SYSTEM

The radio frequency (RF) system consists of two resonators with two 45º dees (the axial-dee aperture is 20mm) located in the opposite valleys (Fig. 1) and with two resonance lines supplied by feeders and RF voltage and phase stabilization and control.

The RF frequency ~39 MHz corresponds to the 4th harmonic of the ion orbit frequency. The accelerating voltage amplitude is U=60 kV and the peak energy gain per turn is ΔW=4U. The dissipated power in each resonator is ~5 kW.

Electric field simulation of the selected electrode structure was performed with the help of the well-known computer code "Mermaid" [8], [9]. The purpose of this calculation is to generate the spatial distribution of the acceleration electrical field to be used for the beam dynamics study.

BEAM ACCELERATION

When the cyclotron is used as an injector, the system consists of a compact cyclotron, a beam delivery system (BDS), and a storage ring [10]. Given the requirement for the beam intensity and quality, H$^-$ ions were selected for acceleration in the cyclotron with the goal of achieving high-efficiency extraction by the electrostatic deflectors(ESD1: E=28.6 kV/cm Grad=–3.7 kV/cm^2; ESD2: E=28.6 kV/cm, Grad=–14.8 kV/cm^2) and magnet(MC: B=0.45T, Grad=0 T/m).The tracking calculations in the cyclotron were performed by the homemade CBDA code [11] taking into account beam space-charge effects [12]. The main criteria imposed in the selection of the operational parameters were good centering, as high as possible energy gain of the ions in the accelerating gaps, maximum transmission through the machine, and the best possible beam quality at the final energy. Adjusting the corresponding parameters of the cyclotron optimized the overall performance of the system. Simulation of the interface between the cyclotron and the storage ring was performed in order to provide the required intensity and beam quality for injection into the storage ring.

The projections of the emittance of the extracted bunch at the entrance of the BDS are given in Fig. 2.
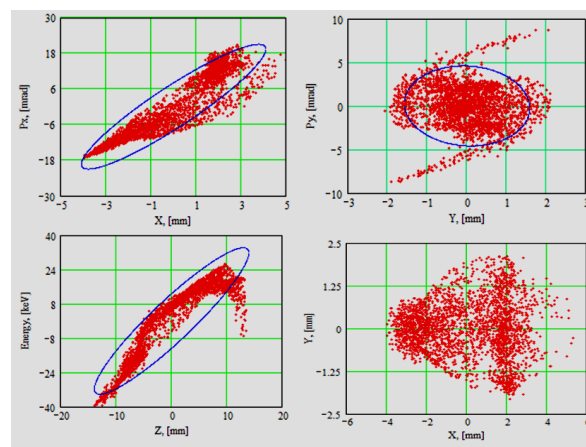

Fig. 2. Effective emittance of the beam at the BDS entrance, 260 µA beam intensity

BEAM DELIVERY SYSTEM

Dedicated structure elements in the injection channel provided dispersion control at the storage-ring injection. The optical elements were chosen to regulate the beam parameters at the target point--beta functions and dispersion. By adjusting the corresponding parameters of the cyclotron and the BDS, the required intensity and beam quality for injection into the storage ring were provided.

Figure 3 depicts the layout of the cyclotron, the BDS with the structure elements mentioned above, and the storage ring. H– ions from the cyclotron strike charge-exchange target 1 H^- -→H0 and, subsequently, charge-exchange target 2 H0→H+. The dispersion function at target 2 is controlled to provide the proper correlation between the particle momentum and horizontal position needed for injection into the storage ring. Two triplets and a bending magnet were selected to satisfy the majority of the requirements.

Estimation of the BDS parameters requires knowledge of the energy dispersion function D and its derivative $D\_$ along the beam central trajectory at the exit of the cyclotron. To define those parameters, the dependence of the particle energy on its transverse horizontal displacement from the central trajectory was calculated at two successive points along the trajectory. The results obtained at the BDS entrance, summarized in Table 3, show the impact of the space charge on the beam quality. The results were used for particle tracing through the BDS to the injection point in the cooling ring.

In order to eliminate a mismatch between the injection parameters and the beam, i.e., beam widening in the ring, the necessary energy dispersion of the beam Fig. 4 was produced in the injection channel. The improved qualities of the injected beam, compared to the previous case, permit a substantial increase _by a factor of 4, up to 40% in the intensity of the particles captured into the ring.
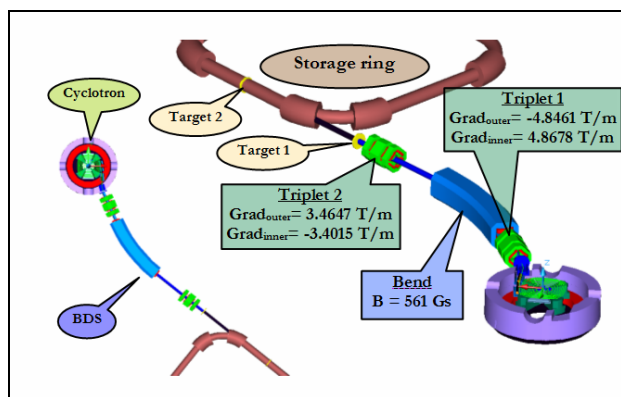
08 Applications of Accelerators, Technology Transfer and Industrial Relations

Fig. 3. General view of the facility

Table 3. Beam characteristics at the BDS entrance

Intensity, µA	100	260
Effective horizontal emittance, π•mm•mrad	24.2	33
Uncorrelated horizontal emittance, π•mm•mrad	3.1	4.9
Energy dispersion function, cm	14.3	15.3
Energy spread, keV	31	34
Axial emittance, π•mm•mrad	3.2	7.2
Longitudinal emittance, π•mm•keV	155	177
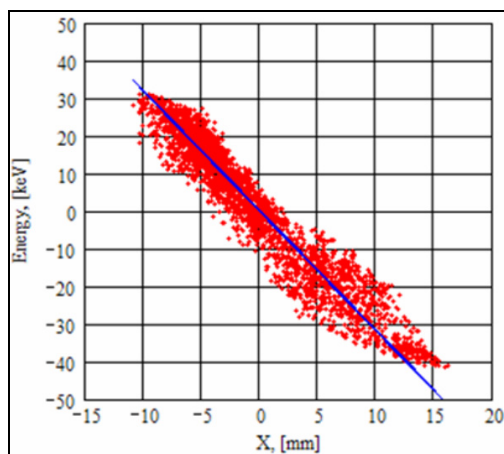
Fig. 4. Estimate of Dispersion at storage-ring injection poit,130µAbeam current

CONCLUSIONS

The beam characteristics at the point of injection into the ring approximate what is required by the storage ring designers. The injection parameters allow ~ 0.1 A of the proton current to be stored according to the numerical simulation. This current is sufficient to conduct the experiments.

The set of optical elements in the injection channel are sufficient to regulate the beam parameters at the target point (beta functions and dispersion) in order to cope with expected experimental uncertainties in the settings of the cyclotron and storage ring.

Development of the cyclotron-storage-ring accelerator system is technologically high-risk but high payoff, and it will require a dedicated experimental effort of significant

magnitude to quantify critical issues such as electron cooling and proton beam stability in the storage ring. If such cyclotron-storage-ring system can be realized, this technology will open many new possibilities for applications of high-quality and high averaged current proton beams.

REFERENCES

[1] L.M. Onischenko, Yu.G. Alenitsky, A.A. Glazov, G.A. Karamysheva, D.L. Novikov, E.V. Samsonov, A.S. Vorozhtsov, S.B. Vorozhtsov, N.L. Zaplatin, Development of Compact Cyclotron for Explosives Detection by Nuclear Resonance Absorption of Gamma-Rays in Nitrogen, RuPAC2004, Dubna, Russia.
[2] A.S.Vorozhtsov and S.B.Vorozhtsov, Magnetic Field Simulation in the Customs Cyclotron, RuPAC2004, p150,Dubna, Russia.
[3] E.E. Perepelkin, S.B. Vorozhtsov, A.S. Vorozhtsov. Dynamical Properties of the Electromagnetic Field of the Customs Cyclotron. RUPAC 2004,p147, Dubna, Russia.
[4] E.V.Samsonov, L.M.Onischenko, Computation of beam dynamics with space charge in compact cyclotron on energy ~1.8 MeV, RUPAC2004,p153, Dubna, Russia
[5] G.A. Karamysheva, L.M.Onischenko, Injection System of the Compact Cyclotron, RUPAC2004,p174, Dubna.
[6] G.A. Karamysheva, L.M.Onischenko, Spiral Inflector for Compact Cyclotron, RUPAC2004, Dubna, Russia.
[7] SIM Limited, Mermaid 2D & 3D User's Guide, SIM Limited Novosibirsk department, 1994.
[8] Dubrovin A.N. "MERMAID 3D FOR ELECTROSTATICS. Version 1.4 for DOS". Private communication. 4 Apr 2002.
[9] .S.B.Vorozhtsov, L.M. Onischenko and E. E. Perepelkin Customs Cyclotron and Beam Delivery System, Cyclotrons 2007, p421, Giardini Naxos, Italy.
[10] E.E. Perepelkin and S.B. Vorozhtsov. '**CBDA - Cyclotron Beam Dynamics Analysis code**'RuPAC2008, Zvenigorod, Russia.
[11] E.E. Perepelkin, A.S.Vorozhtsov, S.B.Vorozhtsov and L.M. Onischenko. "Beam Dynamics Simulations for the Customs Cyclotron", RuPAC2006, Novosibirsk, ,p.348.

IMPROVING OF THE DTL CAVITY RF VOLTAGE STABILITY BY MEANS OF ANODE MODULATOR FEEDBACK

A.I.Kvasha, Institute for Nuclear Research, RAS, Moscow, Russia

Abstract

In the DTL RF systems of ion pulse accelerator, operating at frequencies up to 300 MHz, are used vacuum tubes power RF amplifiers (PA). At that, the vacuum tube discharger has to be used in anode pulse modulator regardless of the PA output RF power mode of operation: RF driving or PA vacuum tube plate supply. Just these modes allow supporting an accelerating RF voltage stability by means of amplitude control system. The efficiency of the system, in particular, depends on the modulator speed of response and time delay in the feedback. The simplest and cheapest way of modulator speed of response improving is a modulator feedback.

INTRODUCTION

The subject of this paper investigation is the amplitude control system (ACS) of an accelerating RF voltage in the DTL tanks, operating at frequencies below 300 MHz. The point is that at these frequencies RF system includes in her structure vacuum tube amplifiers with the RF output power amplifier (PA), operating in B or C mode. It means that any changes of PA vacuum tube RF driving result in changes of the dc component of the anode current. Moreover, nearly all now in use powerful triodes like RCA 7835, GI-54A, GI-71A can be controlled by means of plate voltage only. As an example in fig.1 control characteristic of the INR DTL RF power amplifier are presented for cavity voltage (U/Uo) and RF power (P/Po), dissipated inside of cavity; Uo and Po correspond nominal values of cavity voltage and RF power.
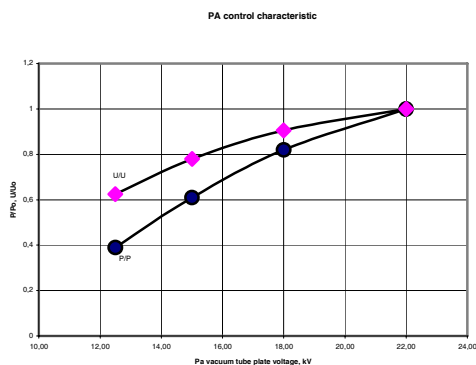

Fig.1. INR DTL power amplifier control characteristic.

That is why vacuum tube as an actuator of the DTL tank RF voltage amplitude control system is available in the PA anode pulse modulator.

At that, series connection of the modulator vacuum tube and the load (inner resistance of the PA vacuum tube over the dc component of the anode current) takes place.

Obviously, in this case the modulator vacuum tube fulfills two functions: discharge of energy storage device (capacity battery or artificial forming line) at the load and control of the discharge voltage value at the load. In turn, there are two ways of the series connection of modulator vacuum tube and load:

- The load (PA) is connected to the anode of modulator vacuum tube (MVT) by means of pulse transformer
- The load is connected to the cathode of modulator vacuum tube.

The last case opens possibilities of high-speed modulator development without powerful pulse transformer. For that it is necessary to solve a problem of the control signal transmitting at the modulator vacuum tube grid. The point is that the MVT cathode is under pulse high voltage and, hence, the control signal also has to be put up at the pulse high voltage platform. Some decisions were considered in [1, 2], and they had shown their operability.

Designers of the INR DTL RF system had chosen the simplest decision: the load connected to the cathode of MVT also, but separation of control circuit from high voltage platform was realized by means of step down pulse transformer (see fig.2) with high voltage isolation between primary and secondary windings.

In that case the modulator speed of operation is, in the main, determined by the pulse transformer parameters (leakage inductance and parasitic capacitances of transformer winding) which, in turn, depend on pulse transformer overall dimensions and passing pulse power. Certainly, the pulse transformer operation at low-resistance load – MVT grid current, allows reducing the primary inductance and, hence, the leakage inductance too. However, remarkable reducing of the primary inductance results in modulator pulse tilt, which is additional inner disturbance for the amplitude control system ACS. It isn't true as the control system has been developed to cope with outside accidental disturbances, the main of which is beam loading.

ANODE MODULATOR OF THE INR DTL RF SYSTEM

In fig.2 simplified scheme of the PA anode modulator is presented. As one can see the pulse transformer is placed directly in front of MVT that simplifies the modulator structure: with the exception of the pulse transformer only two transformers – bias and filament ones are under output pulse high voltage. On the other hand a pulse power value that comes through the transformer at the MVT grid achieves tens of kW. At that level of the pulse power it is difficult to design the pulse transformer (and the modulator as a whole) with high response speed. The simplest and cheapest way of the modulator bandwidth

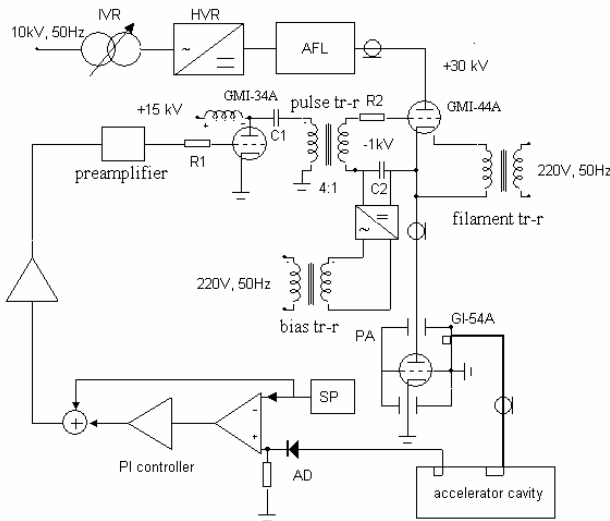06 Instrumentation, Controls, Feedback and Operational Aspects

Fig.2. Anode modulator of the RF power amplifier. IVR-induction voltage regulator, HVR-high voltage rectifier, AFL - artificial forming line, SP-ACS set point.

increasing is the modulator feedback (see fig.3). At that, it's necessary to take into consideration some peculiarities of the joint operation of the modulator and ACS feedbacks. First of all the amplitude control system becomes double-circuit and its stability depends on both modulator feedback and ACS one. In reality, the modulator feedback not only improves amplitude and phase frequency responses of the ACS, as a whole, but decreases disturbances, which appear inside of the modulator like instability high voltage supply and tilt of the modulator output pulse. Then, as can be seen from fig.2, the ACS is the automatic control system with set-point, and as DTL RF system works in pulse mode of operation the control system is subjected to 100% disturbances during every pulse due to transient in the high quality cavity. At that, the ACS feedback signal
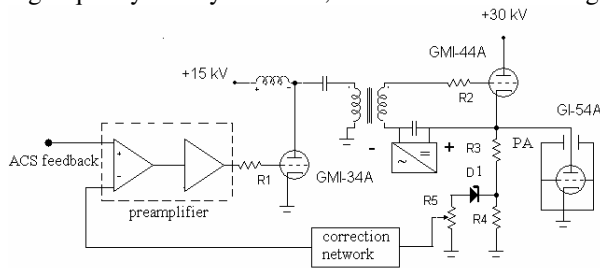

Fig.3. Anode modulator with feedback circuit.

tends to achieve the set-point level as soon as possible, but due to limited possibilities of the RF system (PA with anode modulator), the ACS feedback signal puts the anode modulator in saturation until RF envelope from the tank pickup loop won't reach the set-point value SP. To achieve the maximum value of the RF pulse flat top length, the modulator feedback has to be closed too until the modulator is in saturation. Otherwise, the modulator feedback decelerates an amplitude transient in the cavity.

That is achieved using the "dead zone" nonlinearity in the modulator feedback, which can be realized, in particular, by means of voltage-reference diode D1 in the modulator feedback circuit (see fig.3). Obviously, the modulator feedback will be closed if the condition

$$U_M \frac{R_4}{R_3 + R_4} - E_{st} > 0 \text{ is fulfilled, where } U_M - \text{amplitude}$$

of the modulator output pulse voltage; E_{st}–stabilization voltage value of the voltage-reference diode. It follows to make a note, that during the transient in the cavity when the modulator is in the saturation there is not necessity to support full dynamic range in the feedback circuit operational amplifier. The dynamic range of the amplifier operation has to ensure the modulator control, in the main, during beam pulse only. At that, realization of the amplitude control system feedback circuit is simplified. So in addition to saturation in the modulator there is another nonlinearity of the saturation type – in the feedback circuit of the amplitude control system.

To optimize ACS and modulator feedback circuits, taking into account nonlinearity listed above, a model was developed in the framework of Micro Cap 8 (MC8) program. This model has some advantages before other programs like, e.g., Vissim or Matlab Simulink:

• It is relatively simple and allows using equivalent circuits of vacuum tube amplifiers and schematic circuits of modulator feedback instead of transfer functions or differential equations.

• There is the possibility to take into account nonlinearities like "saturation", which takes place in the modulator and ACS feedback circuits and "dead zone", which takes place in the modulator feedback.

• Transient process in the high quality DTL tank and PA anode-grid cavity can be presented as the process in simple RC circuits. At that, both RF channel with the tank and the feedback circuits are arranged in the same low-frequency domain.

ACS MODEL WITH MODULATOR FEEDBACK

Model of the DTL amplitude control system with modulator feedback is presented in fig.4 where the next shorthand notations are introduced:

V2, V4 – set-points of ACS and modulator feedbacks; *V2* as well is a start pulse of modulator, which is summed up with ACS and modulator feedbacks; *V4* and diode *D3* presents voltage-reference diode parameters in the modulator feedback; *X1, X4* and *X5* present transistor
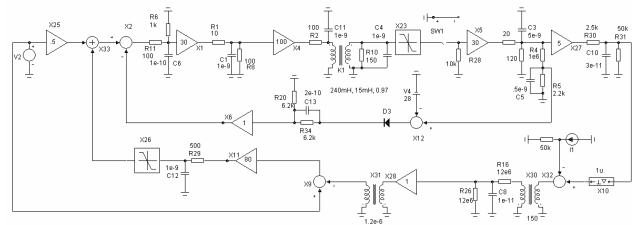

Fig.4. Model of the ACS with modulator feedback.

preamplifier, vacuum tube GMI-34A and GMI-44A amplifiers, correspondently; *X25* – amplifier, which gain is chosen so that to reach the modulator saturation level during amplitude transient in the tank; *K1*-pulse transformer between two vacuum tube amplifiers; *X27*, $T_{PA} = R30 * C10$ – present the gain and time constant of the loaded PA anode-grid cavity; *I1*- I source, presenting a beam current; *X30* and *X31* – step-up and step-down ideal transformers. Step-up transformer presents coupling between tank exciting loop RF voltage and RF voltage at the tank axis. Step-down transformer presents reduction factor of the pick-up loop; *X10* – time delay; *X23* and *X26* – nonlinearities of "saturation" type in vacuum tube GMI-44A amplifier and ACS feedback; *SW1*- T switch, which limits the modulator pulse length; *R16, R26, C8* determine the time constant of the tank; *X6* and *X11* present amplifiers in ACS and modulator feedbacks.

Both values of resistors and capacities in the model and pulse transformer *K1* parameters (inductances of transformer windings and leakage inductance) are result of measurement.

Parameters of the model, presented in fig.4, approximately correspond to the INR DTL tank # 5. Similar models can be developed for the every RF system of the DTL tank.

In fig.5 and 6, as an example, results of the amplitude control system modeling are shown. It follows from them that the modulator feedback visibly improves a quality of the amplitude control system, in result of which the beam losses are decreased at pulse edges. As for increasing of
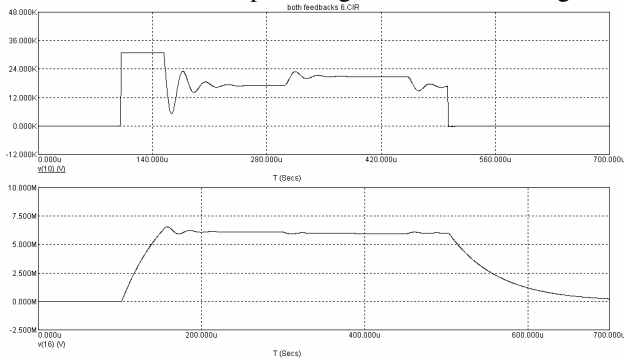

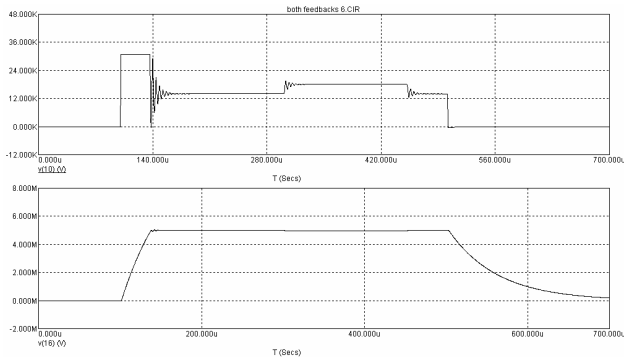Fig.5. Transients in the ACS without modulator feedback.

Fig.6. Transients in the ACS with modulator feedback.

the beam flat top stabilization factor, then it doesn't exceed 2-3 times. It follows to note that there are not so

much of degrees of freedom for modulator feedback optimization in reality. The feedback amplifier *X6* and correction network, one realization of which is shown in fig.4, are among them. At that, as mentioned above, the modulator feedback shouldn't decelerate the transient in the DTL tank, i.e. during transient in the DTL tank the modulator feedback signal mustn't take out the modulator from saturation. It can be shown that in this case the next condition has to be kept: $K_{X6} = \dfrac{V_{X26}}{V_{X23} K_{X5} K_M - V4}$,

where $K_M = \dfrac{R4}{R5}$, *V4*- modulator feedback set-point; V_{X26} – saturation voltage of the amplitude control system feedback circuit; V_{X23} – saturation voltage due to nonlinearity of the GMI-44A grid current; K_{X5} – gain of the GMI-44A amplifier. Fulfilling of the last condition allows keeping the maximum of the pulse flat top length and supporting desired stabilization of the RF voltage at the pulse flat top, where both (ACS and modulator) feedbacks are in operation.

As for the correction network parameters, presented in fig.4, they are, in the main, determined by the time constant *R5C5* of the divider in modulator feedback circuit. The capacity *C5* is that of coaxial cable between the divider, placed in high voltage area of the modulator, and transistor preamplifier, placed in engineering area.

CONCLUSION

Presented above model allows optimizing the anode modulator feedback taking into account some peculiarities of the amplitude control system, stabilizing RF voltage in the DTL tank. A result of modeling is in good agreement with the experimental data and allows successfully using the model for optimization of the modulator feedback. As follows from modeling modulator feedback solves two problems: improves quality of the amplitude control system and decreases an influence of modulator unstable operation - due to instability of modulator supply voltage and modulator pulse tilt, at the tank accelerating voltage. Use of the model can appreciably simplify the process of modulator and amplitude control system feedback circuits tuning.

REFERENCES

[1] J.Keane etc. "The prototype RF system for the 200 Mev Linac for the AGS", Proc. of the PAC1969, p.351.
[2] J. Ross Faulkner "A unique high voltage factor series hard tube modulator for use in the Los Alamos meson physics facility", Proc. of the PAC1969, p.359.

DEVELOPMENT AND APPLICATION OF ELECTRON LINAC ELECTROMAGNETIC DEVICES FOR RADIOTECHNOLOGIES

A.N. Dovbnya, A.E. Tolstoy, V.A Shendrik,. Yu.I. Akchurin

National Science Center "Kharkov Institute of Physics and Technology", Kharkov, Ukraine

.

The creation and subsequent service of modern electron linear accelerators at the NSC KIPT have brought evidence for possible successful introduction of radiotechnology processes using electron irradiation. A further extension and complication of physical problems solvable on the basis of radiotechnologies have put forward new and increased requirements for the systems of beam scanning, extraction and formation on the targets and extended irradiated objects. The results of applying our methods developed for prompt measurement of the kinetic energy of the scanned electron beam are presented. For measurement and continuous control of the electron energy the hodoscope magnetic spectrometer technique has been used. The spectrometer includes only one deflecting magnet and has no magnetic focusing. If the real field topography in the magnet is known in detail, then using the input and output coordinates of deflected particles it is possible to determine their energy, and also the chromaticity of electron beam. The step-pulse scanning of the beam is realized through the use of an air-core short-pulse electromagnet. Development and tests of separate units of the device are under way.

To realize a system of discrete-pulsed separation of the electron linac beam it was necessary to develop a series of new devices and units for electro physical equipment. The present paper considers devices of linac excitation and synchronization and a previously developed air-core short-pulse electromagnet magnet (EM). The requirements to the systems of excitation and synchronization impose that at a linac pulse repetition rate in the range from 3.125 to 300 Hz the beam-bending magnet and the accelerator were operating strictly synchronously. This condition is reached when, into the excitation source mounted by the Larionov circuit, the linac pulses of a selected frequency arrive. In the excitation source the rectified voltage transforms into the meander and then into the two-polar current pulses incoming into the bending magnet by the time of beam arrival (Fig.1).

The system of excitation and synchronization operates as is shown in Fig.2. Similarly to the linac synchronization device [1] in the source of EM excitation the positive and negative half-waves of all the three phases of the mains are rectified and fed into the amplifier-converter. At the same time in the triggering generator of the synchronization device the rectangular pulses of 2.5 μs duration are formed and fed into the injector and accelerating sections; here the excitation pulses are delayed and transformed by means of the
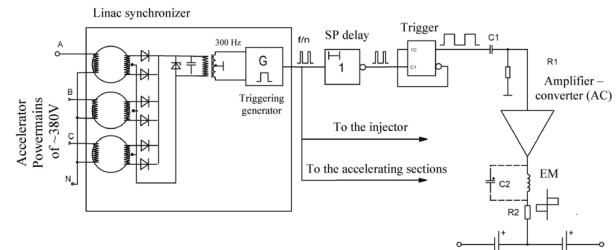

Fig.1. Block diagram of the device of excitation and synchronization

trigger into the meander of a pulse repetition frequency selected for all the linac systems, then they are amplified, transformed into the two-polar ones and enter in the bending EM. Thus, the conditions are created for, by the time of beam entering in the deflecting device (DD), the magnetic field in it be completely formed.
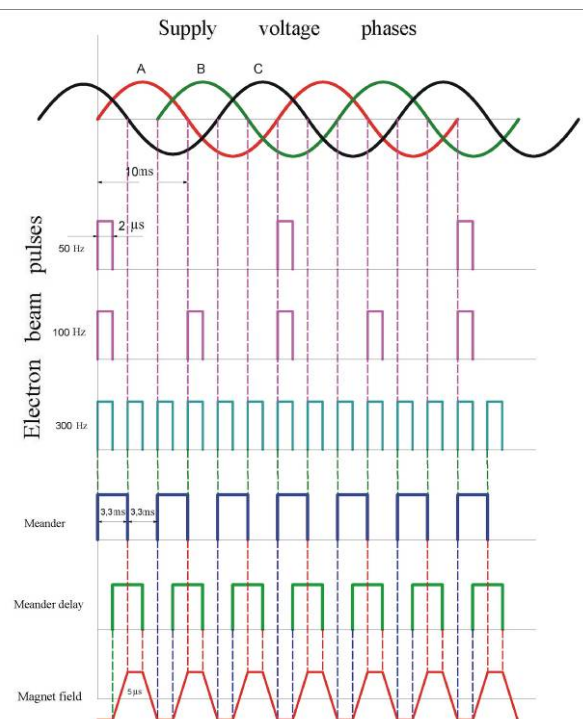

Fig.2. Diagrams of excitation system pulses.

The last state is illustrated by Fig.3 showing the magnetic field diagram in the DD at the linac pulse repetition frequency of 50 Hz.

For the DD one can apply a previously developed air-core electromagnet-transversely flat solenoid (TFS)

06 Instrumentation, Controls, Feedback and Operational Aspects

having the following parameters: L=1.3 μHn, R=0.054 Ohm, rate of rise Iout to 30 A/μs, f =10 Hz …1.25 MHz.
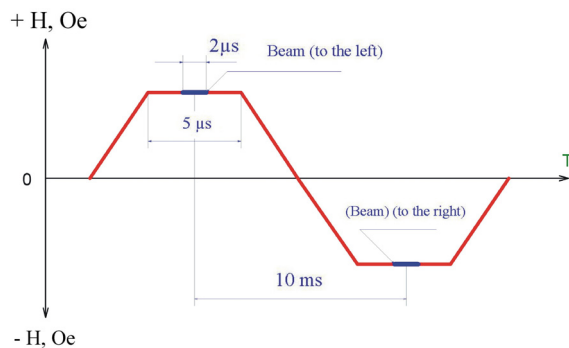

Fig.3. Excitation current signal form in the deflection magnet

By carrying out an experiment in the field of high-energy physics one uses different types of electromagnetic spectrometers. Each of elements in the magnetic circuit of the spectrometer (with iron) has the so-called operating point. It is determined by the defined value of the magnetic induction and magnetizing force in coordinates of the BH hysteresis loop (Fig.4). The operation points can be in any position inside the main hysteresis loop or on the loop itself. Therefore, before carrying out spectroscopic measurements, in particular, the precision ones, it is necessary to eliminate a residual magnetization by the outer magnetic force required for ferromagnetic domains be returned to the initial conditions of a zero equilibrium that corresponds to H= 0
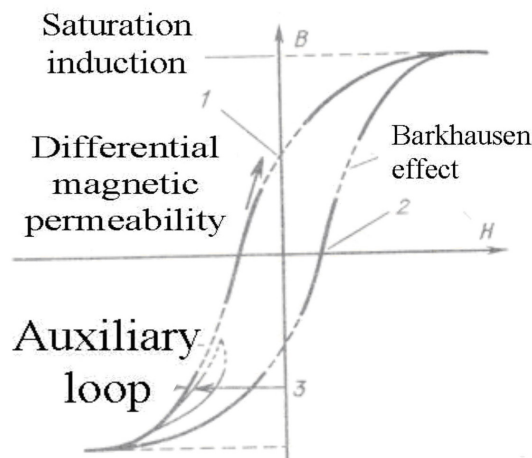

Fig.4. Hysteresis loop: 1 – residual magnetization, 2-coercive force, 3 – displacement of the operating point

Undesired magnetization can be eliminated by means of the changing magnetic field with continuously decreasing amplitude [2]. The initial field amplitude should be taken sufficiently large (two-three times more than the value of coercive force). The changing field frequency should be chosen so that the penetration depth can extend throughout the specimen. For iron at 50 Hz this depth lies between 1 and 2 mm depending on μ.

Besides, the attention should be given to the fact that because of the constant influence of the Earth the demagnetization really can take place. Therefore, to exclude the earth magnetic field influence, demagnetizing coils should be arranged in the East-West direction.

In the case of chick specimens it is recommended to perform demagnetization using, at first, the commutated direct current with decreasing amplitude and, then, the alternating current [3,4]. To perform successfully and with assurance the work upon electromagnet-analyzer demagnetization under conditions of the constantly operating linac the following requirements should be fulfilled:

- knowledge of real magnetic characteristics of the magnet used, preliminary read "on the bench" before setting it in the linac: gauge function $H_0=f(I_{excit})$ on the line of mean beam turning radius (ρ_0) in the center of magnetic track; function $H=f(s, \rho)$ along the beam trajectory for $s \approx \pm \infty$ and $\rho_0 \pm 1.5$ cm; range of operating magnetic field strength $H_0 \dots H_{max}$;

- additional (auxiliary) exciting winding with a number of ampere-turns of $\approx 10 \dots 15\%$ of the main one is used for demagnetization at the direct and alternating current (via the switch) from the independent supply source. The winding serves also as a "zero adjuster" in the process of demagnetization and during operation with the beam towards the linac exit.

- it is necessarily to have "a null indicator" with a permalloy control pickup (others do not suite). Such a device, for example, has been successfully applied at the KIPT storage ring H100 [5];

- in the magnet working gap (or at the end) one should provide for an area where a remote field control pickup can be placed in case of need during the linac operation.

- in the 'long" high-energy linacs usually one provided intermediate channels for beam extraction with the help of direct-current electromagnets. After completing the deflection process, the electromagnet is switched off and there the residual field arises distorting the rectilinear beam trajectory. Consequently, the beam cannot to hit strictly the target at the linac exit. In this case, along with the above-described demagnetization, an effective method of trajectory correction is continuous auxiliary winding current adjustment with simultaneous control of a signal from the current-and-beam position sensor being usually available at the linac exit.

REFERENCES

[1] N.V.Demidov. Synchronization system of linear accelerators. Moscow, 1984, p.29 (in Russian).

[2] E.Angerer. Physical experiment technique. Translated from German p.208. Gos.izdat.fiz.-mat lit. Moscow, 1962 (in Russian).

[3] I.A.Radkevich et al., Device for magnetic field measurement by means of permalloy sensors and its use for proton synchrotron adjustment. Pribory i Tekhnika Ehksperimenta, No 4, p.229 (1962) (in Russian).

[4] L.L. Goldin, S.V. Skachkov, K.N. Shorin. Magnetic measurements in charged-particle accelerators. p.36. Gosatomizdat, Moscow, 1962(in Russian).

[5] Tolstoj A.E. Dissertation, p. 41, Kharkov, KFTI, 1967

06 Instrumentation, Controls, Feedback and Operational Aspects

BEAM ABSORBER FOR TUNING ACCELERATOR IN THE BEAM LAYOUT OF THE EXPERIMENTAL COMPLEX

M.I. Grachev, V.A. Fedchenko, L.V. Kravchuk, E.V. Ponomareva, INR RAS, Moscow, Russia

Abstract

The absorber of a beam without moving parts in vacuum volume for tuning the high current linear accelerator is described.

INTRODUCTION

Since 2006 both the Linear accelerator and the Experimental complex at the INR have started operating with the proton beam of the current up to 100 μA [1]. The beam absorber for tuning of the accelerator, located at the beginning of the Experimental complex, was put through an upgrade. The old absorber contained by construction several moving absorbing elements in the vacuum (the copper cylinders the diameter of 20cm and the length 20cm), which required direct maintenance by people. A new beam absorber, without moving absorbing elements in vacuum, has been designed, mounted and set up in the beam tunnel.

BEAM ABSORBER

At the moment tuning of the parameters of the acceleration beam before its transport to the physical facilities in the Experimental complex is accomplished in the new beam absorption region (Fig.1). This region consists of a deflecting magnet and an absorbing part of vacuum cell, surrounded by biological shielding. The shielding decreases the level of radiation fields around the tunnel of the accelerator and surrounding rooms.
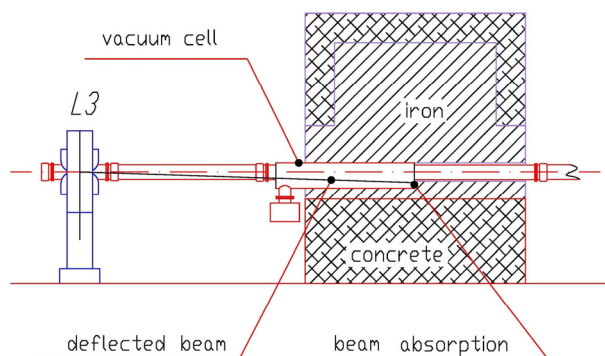

Figure 1: The beam absorber.

Beam of protons is deflected vertically downwards from the axis of the beam "red arrow" for the purpose of beam absorption during the tuning of the accelerator in the vacuum cell (as shown on Fig. 2).
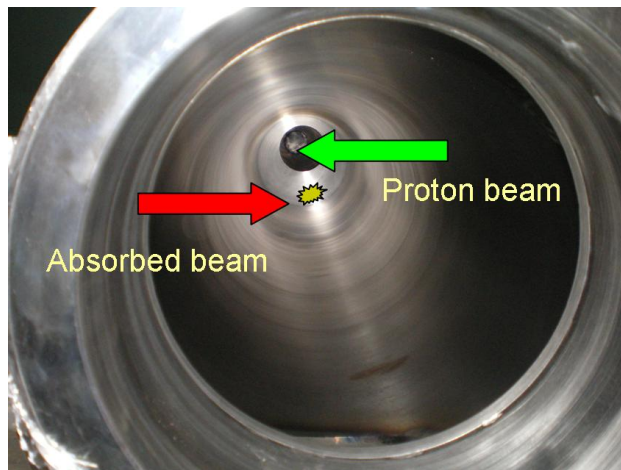

Figure 2: Inside view of the vacuum cell.

For the purposes of deflecting the beam some structural changes were made to the quadrupole lens L3 of the dipole magnet (in particular switching of lens's coils has been carried out). During the tuning of the accelerator lens L3 is used as a dipole magnet. The beam is absorbed inside a special vacuum cell, surrounded by shielding. Shielding consists of the blocks of iron and of concrete with the following dimensions: length of 4m x height 3m x width 2.5m. This ensures sufficient protection from the activation of the equipment and the air in the tunnel.

Design features of the magnetic core of this type of lens allow effective vertical deflection of the proton beam. The angle of deflection from the beam axis is 2 degrees.

Thermal calculations of absorption of the beam in the wall of the vacuum cell are implemented by JSC "N.A. Dollezal Research and Development Institute of Power Engineering" [2]. Maximum temperature of the region absorption of the beam in the vacuum cell after 16 hours of continuous work was 120C, while the maximum temperature of the near iron blocks – no more than 30C. Analysis of results of the calculations allows us to come to the conclusion of possibility of using the beam absorber without a water-cooling system.

The main factors of radiation hazard to people when the beam absorber is active are the beams of secondary photons and neutrons. These arise during interaction between proton beam and equipment of the beam absorber and channel of transportation of the beam in the Experimental complex.

Radiation safety while the beam absorber is in operation is provided by biological shielding, system of blocking doors of the Experimental complex, system of blocking of the beam of the Linear acceleration from the signal of readiness of the absorber of the proton beam of

06 Instrumentation, Controls, Feedback and Operational Aspects

the Experimental complex and automated monitoring subsystem for dose fields in the area of the beam absorption.

In November 2009 the experimental data of neutron and photon (charged) components of radiation in the absorber have been acquired. Measurements were carried out on the proton beam with energy $E_p=160MeV$, frequency $1\ Hz$, duration of an impulse of $30\mu s$ and a current in an impulse of $9\ mA$. Measurements of dozes of photon and neutron components of radiation field were collected by means of a passive dosimeter of an effective dose on the basis of a spherical polyethylene moderator with a diameter 10'' with individual dosimeters placed on its surface and a slide in the centre of a sphere [3].

CONCLUSIONS

Analysis and comparison of the received data with experimental data from the old absorber shows that the new one works more effectively as an absorber in the mode of beam absorption. Low levels of radiation are observed on the pathway of the beam after the beam absorber. During tuning of the accelerator with the beam absorber there is low activation of the equipment located in these areas and the absence of exceeding maximum permissible dose around the tunnel of the accelerator and surrounding rooms.

REFERENCES

[1] L.V.Kravchuk "Operation and Research Activities at the INR Accelerator Complex" Proc. of XXI Russian Particle Accelerator Conference RUPAC-2008, Zvenigorod, p.137-140.

[2] "The technical offer for the system of matching of parameters of the beam of the accelerator with channels of transportation beam to the Experimental Complex" by JSC "N.A. Dollezal Research and Development Institute of Power Engineering", ArXiv INR RAS (in Russian) N170, 2008.

[3] A.V.Sannikov, V.N.Lebedev, V.N.Kustarev, E.N.Savitskay, E.G.Spirov. Individual dosimeter of mixed radiation DVRN-01: development and research of characteristics. ANRI N03, 50-59(2005); preprint I 2005-6, Protvino, 2005.

LOW LEVEL RF CONTROL OF ITEP-TWAC FACILITY

P. Alekseev, S. Barabin, A. Milyachenko, V. Zavodov, ITEP, Moscow.

Abstract

Digital LLRF control system was developed to improve the RF system mobility in multimode operation of the ITEP-TWAC booster and main synchrotrons. High precision mapping of the magnetic field derivative signal to the reference function of accelerating frequency f(B) allows to accelerate ions of any type in both rings up to relativistic energies even without feedback loops. The first modification of the LLRF control module is based on a fixed point DSP, which operates with the frequency lookup table to calculate the accelerating frequency. This module is now used in the booster synchrotron. Upgraded module has a floating point DSP, which allows calculation of the accelerating frequency "on the fly". This module is in operation in the main ring. Short description of the systems is given. Some results and experience obtained at operation with the number of types of particles, such as protons and ions of carbon, aluminium, iron and silver, are presented.

INTRODUCTION

ITEP-TWAC Accelerators facility consists of two synchrotrons: УК booster and У-10 main ring [1]. At present we have two injectors:

- И-2 – for protons which are transported directly to the У-10 where they are accelerated up to 10 GeV. This is the classic mode of ITEP accelerator.
- И-3 – for ions injection into the booster. The Ions are accelerated and transported to the main ring where they may be stored or additionally accelerated up to the relativistic energies.

The RF system of the booster synchrotron consists of two accelerating cavities [2]. The first cavity operate in the range from about 700 kHz to 2.5 MHz, after that the second cavity continues operation up to 12 MHz. All five accelerating cavities of У-10 operate in the range from 1 MHz to 5 MHz. The frequency provided for each of the accelerating cavities should correspond to the beam energy at each moment of the acceleration process. The dependency is described by well known formula (see Eq. 1) that should be reproduced by the master oscillator from the available diagnostic signals.

$$f(B) = \frac{h \cdot c}{L} \cdot \frac{p}{\sqrt{\left(\frac{m_o A}{Z}\right)^2 + p^2}}, \qquad (1)$$

where h - harmonic number, c – velocity of light, L – the length of the equilibrium orbit, m_0 – atomic mass unit, A – atomic weight, Z – ion charge and p is momentum per unit charge of the ion.

Additionally independent control of phase and amplitude of the accelerating voltage should be provided for each cavity. All of the functions described are provided by digital LLRF control system of the ITEP-TWAC facility.

MASTER OSCILLATOR

The core part of the LLRF system is the master oscillator unit (see Fig. 1) based on a digital signal processor. We are using standard Texas Instruments DSK boards available on the market. Originally the master oscillator unit was based on TMS320C6211DSK with processor clock frequency of 150 MHz and 4 MB of on-board memory. Self-designed daughter board is connected to the DSK. It contains an ADC circuit and control logic for six DDS submodules.
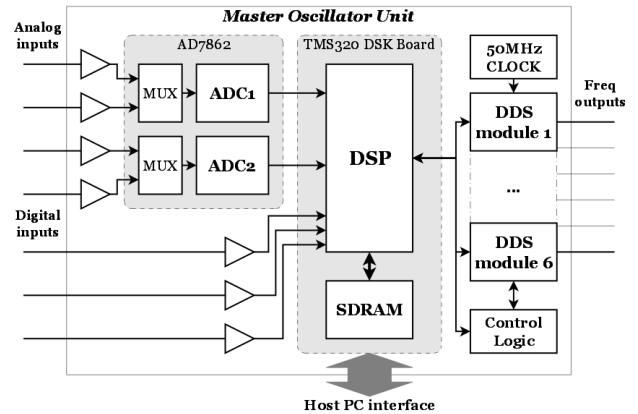

Figure 1: Master Oscillator block diagram.

All the DDS modules are connected to the common data bus. Common clock source of 50 MHz is used for all the DDS modules. All the modules could accept write commands simultaneously (on the same clock pulse) but only selected modules will store the data. Operational mode of each DDS could be selected individually by the software.

The signal of the derivative of the magnetic field induction is used as source information for producing the RF function of the magnetic field. This signal is presented in a digital form by an analog-to-digital converter with sampling frequency of 50 kHz and is integrated by a signal processor. Calculated value of the magnetic field induction then used as an address in the frequency lookup table. The table of 256 kB size should be calculated on the host computer software and stored in the SDRAM. Output frequency value is calculated by linear interpolation of the nearest tabulated values. DSP algorithm is illustrated on the figure 2.
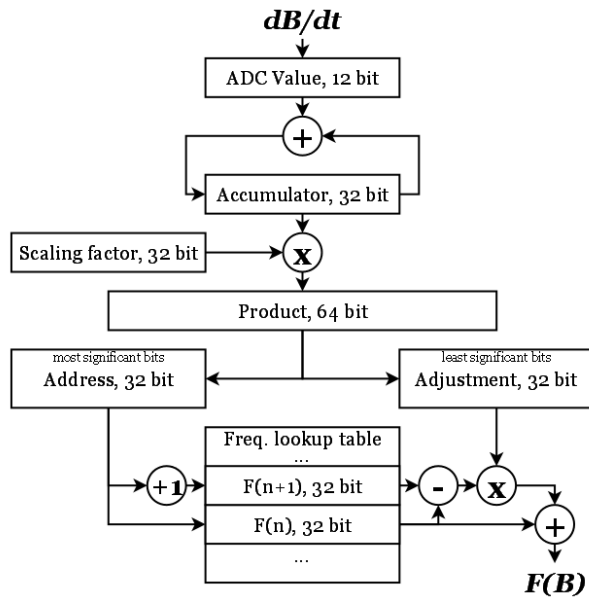
dB/dt

Figure 2: Diagram of the DSP algorithm.

The only trouble is the process of the ADC calibration. To get the first approximation of the conversion coefficient we use the signals of the B-timer which is rather well calibrated. To get better accuracy we should recalculate and reload the table several times. That takes a lot of time. On the other hand the coefficient that was found once may be used during the long time. For example presently used table for carbon ions acceleration in the booster was calculated in the October of the last year when some changes was made with the signal of test coil. Previous file is corresponds to the 2007.

AMPLITUDE CONTROL

To control the amplitude of the RF-cavities we are using the functional generators. The unit is quite simple. It's based on the ADuC814 microcontroller chip with RS485 serial interface and 12 bit DAC output (see Fig. 3).
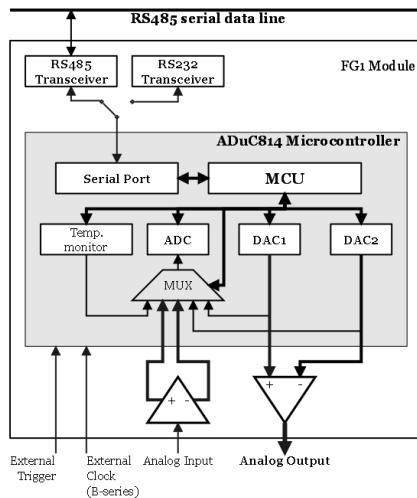

Figure 3: Functional generator block diagram.

Separate functional generators are used for each accelerating RF-cavity. All the generators are connected

to the front-end computer which provide access to them over the LAN.

Application of the master oscillator in conjunction with the functional generators allows as to easily configure and reconfigure the RF system of the booster for the acceleration of various types of ion. In addition, the system allows to implement complex modes of operation such as an adiabatic capture [3].

MODERNIZATION

This year a new DSP-board was tested in the master oscillator module of the У-10 synchrotron. Old DSK was replaced by the TMS320C6713 board. This board is the same family but improved performance. Installed processor has build-in floating point operations support. Last feature allows as to abandon of using the "frequency lookup tables". Instead of it we can calculate the frequency on-the-fly by integrating the signal of the magnetic field derivative and applying the equation 1 directly.

Upgraded master oscillator module was tested at the high energy proton cycle in У-10. It is much easy to control this module because we don't need to upload the table each time when the calibration of ADC should be tuned. We also found the significant moment in tuning of the master oscillator that was not noticed before. The length of the equilibrium orbit in the equation 1 should be carefully tuned to achieve the expected compliance between the magnetic field and the RF-frequency because orbit length L is the function of momentum offset Δp.

In the result of the tests the maximum possible energy of protons for current DSP software version was achieved even without processing of the feedback signals. This limit is the transition energy of protons in the synchrotron. So, that is the first task for the next time.

CONCLUSION

The only LLRF control system is used in the booster is digital, while the LLRF system of the У-10 still not fully functional and old analogue system is used for acceleration of protons up to the energy of 10 GeV. All the other modes of У-10 is controlled by the new digital LLRF system.

At now the work is in progress on upgrading the RF-systems of both synchrotrons. In the result four cavities will be installed in each of them. No hardware modifications should be made in the existing LLRF control system in conjunction with that upgrade. The only thing we should do is to upgrade the software of the master oscillators.

REFERENCES

[1] D.G. Koshkarev et al., XV Workshop on Charged Accelerators, Protvino, v.2 (1996) p.319

[2] V.P. Zavodov et. al., XVII Workshop on Charged Accelerators, Protvino, v.1 (2000) p.138

[3] P.N. Alekseev et al, IET, 2007, Vol. 50, No. 4, p. 437

STATUS OF HITS INJECTOR

V.G. Cherepkov, V.F. Kluev, E.S. Konstantinov, E.A. Kuper, V.R. Mamkin, A.S. Medvedko,
P.I. Nemytov, V.V. Repkov, V.B. Reva, R.A. Salimov, A.V. Semenov, D.V. Senkov,
V.A. Vostrikov. BINP, Novosibirsk, Russia.

Abstract

Ion injector for cancer therapy facility HITS was designed and assembled at BINP. Injector is based on electrostatic tandem accelerator with 1.25 MV at the high voltage terminal. The negative ion beams are injected into tandem and charge exchanged in the vapor-magnesium target with vacuum heat insulation. The results of injector tests and working with carbon ion beam are presented.

INTRODUCTION

In the BINP the facility for ion therapy of cancer based on the synchrotron with electron cooling is developed. Facility generates the therapeutic beam of carbon ions with energy up to 430 MeV/u [1, 2].

The tandem electrostatic accelerator with 1.25 MV at the high voltage terminal is used as the injector. The source of sputtering type is used for the generation of negative carbon ions C^- beam. The 10 keV beam of negative ions is transported along the low energy transport channel into the tandem accelerator. After acceleration in the first accelerating tube, negative ions charge exchange while passing the vapor-magnesium target and accelerated again at the same voltage in the second accelerating tube. Then carbon ions C^{+3} with the energy 0.417 MeV/u are injected through the transport channel into the booster synchrotron.

TANDEM ACCELERATOR

The electrostatic tandem accelerator is designed on the base of the ELV-type industrial accelerators developed in BINP [3]. The tandem assembled in a vessel with the following overall dimensions: a height is $H = 3.64$ m, a diameter is $D = 1.346$ m. The vessel can be operated at pressure up to $P = 1.0$ MPa (10 bar) of SF_6.

The tandem accelerating system consists of two ELV accelerating tubes located vertically at the vessel axis and the magnesium vapor charge exchange target between them. Operating vacuum $p = 1 \cdot 10^{-6}$ Torr in the accelerating tubes is provided by two vacuum systems placed at ground potential up and down of the vessel.

The source of high potential is the ELV type cascade voltage generator with magnetic link located in the bottom part of vessel. The alternate magnetic flux is produced by the primary winding (35 turns of double copper pipe) coiled on the cone frame. The winding is shielded by stainless steel thin strips. The shield protects the winding turns against high voltage breakdowns from the rectifying column.

The power supply voltage with the frequency 400 Hz is provided by the transistor frequency inverter. The high voltage column consists of 38 rectifying sections connected in series. Each section consists of the coil (3000 turns), rectifying circuit doubling voltage and supports for putting sections one onto another. The column outer diameter is 750 mm. The distribution of voltage among the accelerating tube sections is provided by the resistive divider.
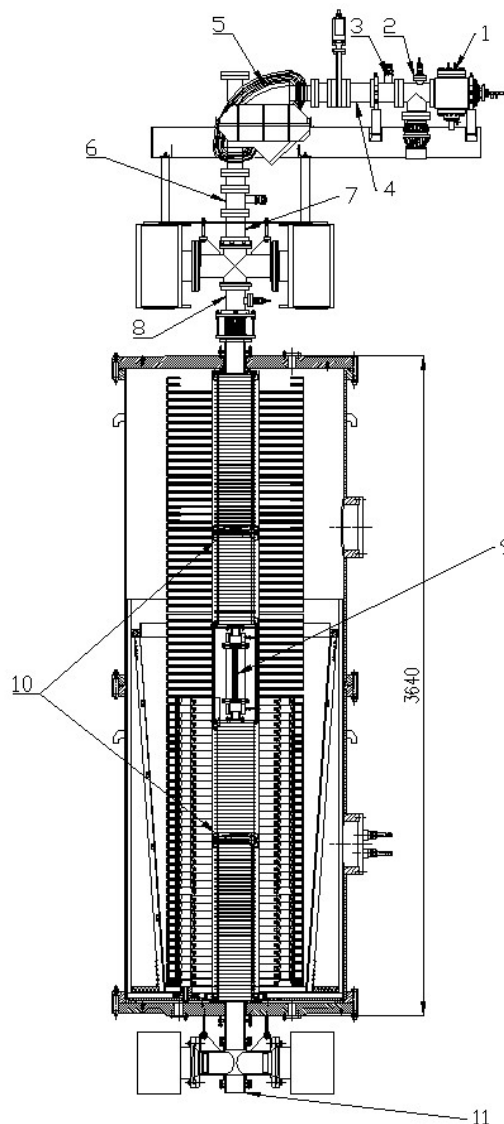

Figure 1: Injector layout: 1 – source of negative carbon ions C^- (10 keV); 2, 8 – electrostatic lenses; 3, 6 – electrostatic correctors; 5 – 90^0 bending magnet; 4, 7, 11 – Faraday cups; 9 – charge-exchange target; 10 - accelerating tubes.

In the high voltage electrode the charge exchange magnesium vapor target, the target power supply, the power supply winding for electronics, control and

08 Applications of Accelerators, Technology Transfer and Industrial Relations

measurement electronics connected via the optical wires are installed. The upper accelerating tube is surrounded by the false column made with the use of the outer shields of rectifying sections. The voltage is divided among the false column shields with the resistive divider.

NEGATIVE CARBON IONS SOURCE

The sputtering type ion source of the negative carbon ions is used. The ion source is being successfully operated in the AMS facility developed in BINP (Fig.2) [4].

The main components of the source are: a vacuum stainless steel volume, a water cooled cathode where the sputtered carbon tablet is placed, an ionizer producing the flow of cesium ions to the cathode and cesium evaporator. The operation gas pressure after bake-out is 10^{-7} Torr.
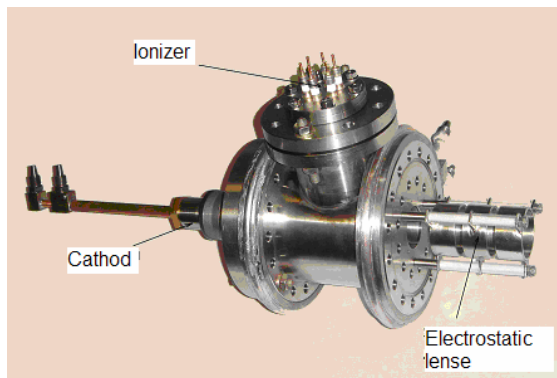

Figure 2: Prototype of the sputter source.

The ionizer working surface is a vacuum fusion tantalum spherical cup of 22 mm in diameter. The heater is laid at the opposite surface of ionizer along the spiral in two layers with connection in parallel. In order to reduce the heat loss, the heater is covered by the triple thermal shield made from the 20 µm tantalum foil. The ionizer surface temperature exceeds 1100 ^{0}C. The tube ceramic insulator is made from Beryllium oxide capable to operate at temperatures exceeding 2000 ^{0}C.

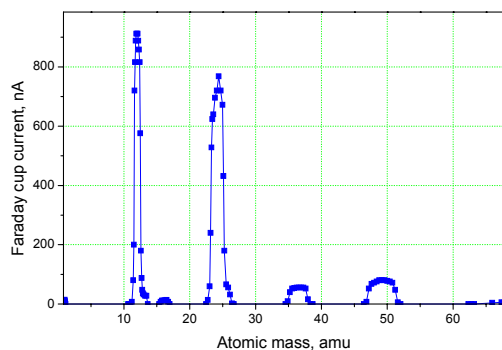Ion source spectrum at low current measured after bending magnet is shown in Fig.3.

Figure 3: Spectrum of ion source.

The lens-sensor scheme was used for transverse emittance measurements. The measured emittance is 3.5 cm·mrad.

At present, the modified design of ion source is developed (Fig. 4). A new cesium container and mechanism of changing cathode position will increase the ion source working time without reassembly. Energy of ion source will be increased up to 30 keV.
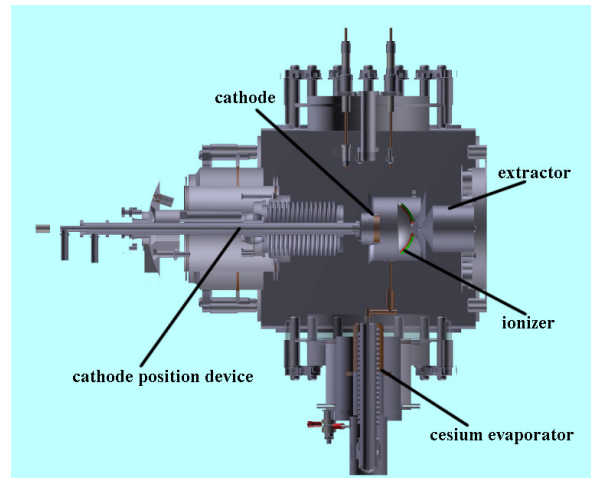

Figure 4: Layout of the new design negative ion source.

ION SOURCE-TANDEM LOW ENERGY TRANSPORT CHANNEL

The beam of carbon negative ions is transported to the tandem accelerator through the low energy transport channel (See Fig.1). The electrostatic lens installed after the ion source defines the beam size in the channel. The second lens provides matching of ion beam with the accelerating tube of tandem accelerator. The input electric field of the accelerating tube forms the effective focusing lens thus leading to the beam over focusing and limits the beam transition through the charge exchange target.

The C-shaped 90° dipole magnet with $n = 0.5$ bends ion beam in vertical plane and separates heavy clusters. Two pairs of electrostatic correctors allow correct the beam trajectory independently in two coordinates. The Faraday cups and beam position monitors control beam current, beam size and position.

VAPOR-MAGNESIUM CHARGE-EXCHANGE TARGET

The use of the vapor-magnesium charge exchange target provides the high vacuum in the accelerating tubes. The magnesium vapors are condensed in special containers at room temperature at the both sides of the charge exchange target.

The design of vapor-magnesium target developed for AMS facility has been accepted [5]. However, first experiments show inability of this design application in the atmosphere of sulfur hexafluoride. At the working temperature of target 500 ^{0}C the reaction with asbestos, glass cloth and stainless steel was observed. The heat

08 Applications of Accelerators, Technology Transfer and Industrial Relations

insulation is destroyed and target body is corroded that leads to leak opens and losing of vacuum in accelerator.

The new design of charge exchange target was proposed and successfully applied. For prevention of chemical reaction the hot part of the target has been placed inside a vacuum shield. The pumping of target is realized through the accelerating tubes. The heat radiation of target is screened by the number of layers from stainless steel foil (See Fig. 5). The maximal temperature on the external surface of target is 150^0C.

The target charge-exchange channel of 300 mm long and 6 mm in diameter is surrounded with the shell-container with the solid magnesium. When heating the container, the magnesium vapors reach the charge exchange channel through three holes of 1 mm in diameter in the middle of the charge exchange tube. Amount of magnesium in the container is sufficient for continuous operation of up to 1000 hours. The target power consumption in the stationary mode is 80 W.
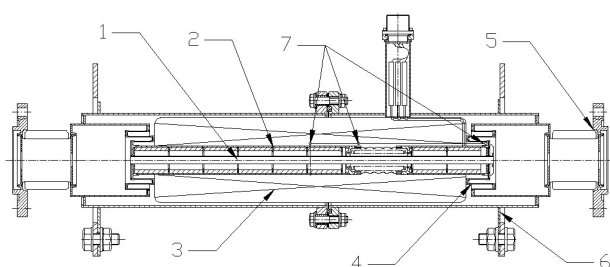

Figure5: Charge-exchange target. 1 - charge-exchange tube, 2 – container with magnesium, 3 – heat insulating layers, 4 - labyrinth, 5 - flange unit with the bellows, 6 - current inputs, 7 – control thermocouples.

EXPERIMENTAL DATA

The design of ion source prototype limits energy of ion beam not above 10 keV. Such low energy of ion beam not allows achieving the good matching of injected beam and input of accelerating tube.

With increasing of the accelerating voltage the average charge state of ion beam passed through charge-exchange target is increased. However, the experiments with different accelerating voltages show that the output current not increased according theory predictions. This phenomenon stipulated by degradation of matching conditions with increasing of accelerating voltage. The Fig. 4 shows the ratio of tandem output current I_{output} to input current I_{input} depends on temperature of charge-exchange target at different accelerating voltage.

For providing of good beam matching the increasing of ion source energy up to 30 keV is necessary.
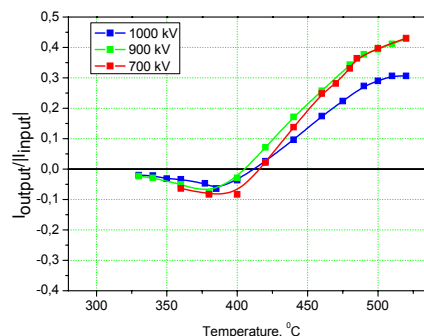

Figure 6: Charge-exchange of carbon ions depends on target temperature.

CONCLUSION

The ion injector based on tandem accelerator was designed, assembled and commissioned in the BINP. The high voltage up to 1.25 MV with stability 10^{-3} is achieved without breakdowns during long time operation with beam. New design of the vapor-magnesium charge exchange target with the vacuum heat insulation shows stable and reliable work. The measurements of transmission coefficient show necessity increasing of the ion source energy up to 30 keV. The new ion source is designed and under construction.

ACKNOWLEDGEMENTS

REFERENCES

[1] Carbon Ion Accelerator Facility for Cancer Therapy, V. Vostrikov et al., Proc. of XX RUPAC, 2006.

[2] Electron Cooling for Cold Beam Synchrotron for Cancer Therapy, V. Parkhomchuk et al., AIP Conf. Proc. 821:365-369, 2006.

[3] DC high power ELV accelerators for industrial and research application, R.A. Salimov et al., Proc. of XIX RUPAC, 2004.

[4] Accelerator mass-spectrometer for Siberian Division of RAS, V. Parkhomchuk et al., Proc. of XIX RUPAC, 2004.

[5] A magnesium vapor charge-exchange target for an accelerator mass spectrometer, S.A. Rastigeev et al., PTE, 2009, No. 2, pp. 101–104.

DUBNA PROJECT OF CYCLOTRON C250 FOR PROTON THERAPY APPLICATION

Yu.G. Alenitsky, A.A. Glazov, G.A. Karamysheva, S.A. Kostromin, L.M. Onischenko,
E.V. Samsonov, S.B. Vorozhtsov, O.V. Karamyshev, O.E. Lepkina, N.L. Zaplatin,
JINR, Dubna, Russia

Abstract

Project of the C250 – cyclotron for proton therapy is considered. Energy of the extracted from cyclotron beam was increased according to medical requirements up to 250 MeV. 4-fold and compact types of magnet yoke were studied by 3D computer magnetic field calculations. The ability of optimal combination of the magnet yoke, new form of HF systems of the cyclotron based on the dynamics of the proton beam in calculated magnetic and accelerating field is under discussion. Dubna scientific medicine canter is under development since 1967 on the base of the proton beam of LNP JINR Phazotron. Proton beam with energy Ep ~170 MeV and intensity I ~0.1 mkA is used for patients irradiation. Proposal of the cyclotron with the same beam characteristics was reported earlier at the RUPAC04 [1] ICAA05 [2], printed in the "Applied Physics" magazine [3], RUPAC06 [4], RUPAC08 [5].

Computer model of the double gap delta RF cavity with 2 stems was developed in a general-purpose simulation software CST STUDIO SUITE. Necessary resonant frequency and increase of the voltage along the gaps were achieved.

CACLOTRON MAGNETIC SYSTEM

In work [4] the various types of yoke are considered, is shown, that the magnet with four opposites yoke is more convenient for service, such design is accepted in the present project. As a material of a magnet it is supposed to use steel - 10. On the Fig. 1 one can see the lower part of magnet system of the cyclotron C250p plane view.

The magnetic system consists of sectors, poles, horizontal and vertical yokes, current coils, the circuit of a magnet is shown on Fig. 1. In opposite valleys through 90° the high-frequency resonators are located, it one can see on the Fig. 3. The key parameters of the proton cyclotron are listed in Table 1.

The variation of a magnetic field creates four pairs flat sectors located symmetrically on poles from above and below. A gap between sectors is constant size of 40 mm. The average magnetic field, growing with radius, is created at the expense of increase of the azimuth extent of sectors. The vertical stability is reached at the expense of high sectors and them spirality, the extent of sectors spirality is increased at the expense of internal border, thus, increasing spirality and, accordingly, frequency of axial fluctuations.

For the consumer the important characteristics of installation are both the sizes and a technology of manufacturing of the project, and both operational conditions - consumed energy and cost of service. We propose on the base of our results, that the offered project C250p with four symmetry return yoke (Fig. 1) is optimum and that such installation can be created as a pilot project of our institute.

Modeling of the cyclotron magnetic system was carried out by means of the code *Radia ver. 4.098* [6], which works under *Mathematica* platform and calculates magnetic field of the three-dimensional magnetic systems by a method of the integrated equations. As a material of the magnet the steel - 10 was used.
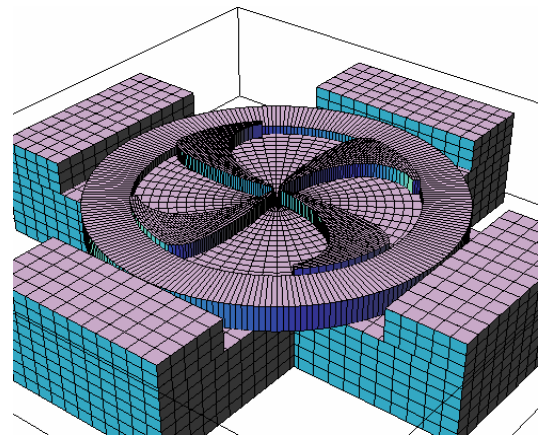

Figure 1: Magnet system of proton cyclotron C250p plane view (four symmetry return yoke).

The dynamic characteristics of beam in the magnetic field was calculated, one of them you can see on Fig. 2, all of them are in allowable limits [1, 2, 3, 4].
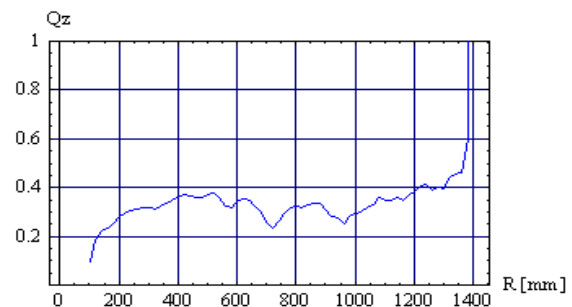

Figure 2: Dependence of frequency of axial fluctuations on radius.

Table 1: Main parameters of the cyclotron

| General properties	
accelerated particles	protons
final energy of protons	250 MeV
extraction efficiency	70 % (by deflector)
number of turns	~2000
Magnetic system	
total weight	300 tons
outer diameter	7 m
height	2.8 m
pole radius	3.0 m
Valley/hill depth	20 cm/2.5cm
hill field	2.65 T
valley field	0.95T
RF system	
number of cavities	2
operating frequency	82 MHz, 4 th harmonic
radial dimension	140 cm
vertical dimension	40 cm
dee voltage: center extraction	60 kV 80 kV
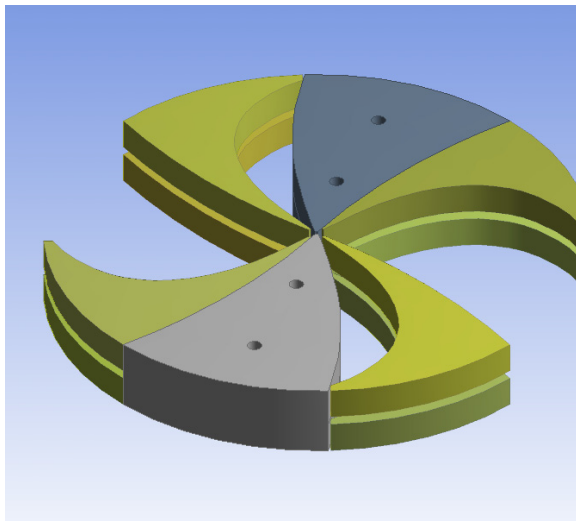
Figure 3: View of the RF-cavities in valley between of spirals.

RADIOFREQUENCY CAVITY GEOMETRY

We plan to use two RF cavities for ion beam acceleration in the C250 cyclotron (see Fig. 4). Modelling of the magnetic system and beam dynamics have determined orbital frequency of the ions equal to 20.5 MHz. As RF cavities will be operated in the 4th harmonic mode, resonance frequency must be 82 MHz.

The azimuth extension of the cavity (between the middles of the accelerating gaps) is equal to 45 deg. Cavities have a spiral shape similar to the shape of the one side of the sectors (see Fig. 3). They are located in the valleys, where the gap between poles is 400 mm. The vertical dee aperture is 40 mm. The thickness of the dee is 20 mm. The accelerating gap width is 10 mm at the center increasing to 100 mm at the extraction region. We inserted two stems with different diameter in the model. Positions of the stems determine voltage distribution along the radius of the accelerating gap. The voltage value was obtained by integrating the electric field in the median plane of the resonant cavity. For excitation of the accelerating system it is proposed to use the standard high-frequency generator on the suitable capacity and frequency 82 MHz. The active tuning system must be designed to bring the cavities to the frequency initially to compensate for detuning because of temperature variations due to RF heating.

SIMULATIONS OF THE RF CAVITY MODEL

CST STUDIO SUITE is a general-purpose simulator based on the Finite Integration Technique (FIT). This numerical method provides a universal spatial discretization scheme applicable to various electromagnetic problems ranging from static field calculations to high frequency applications in time or frequency domain. [7]. Calculations of the created model were performed using the eigenmode JD lossfree solver (Jacobi Division Method) in the CST Microwave Studio.

The computer model of the double gap delta RF cavity with 2 stems was developed, simulated and analyzed in CST Microwave Studio. The model had frequency 82 MHz and voltage value 60 – 80 kV (see Fig. 5). It was shown that the voltage behavior along the radius depends substantially on positions and diameters of the stems. The frequency value can be changed by scaling transversal dimensions of all stems without essential voltage profile modification.

Radial and azimuth electric field components and magnetic field maps in median plane were created for the beam dynamics simulation. The electric field distribution in the cavity one can see in Fig 6.

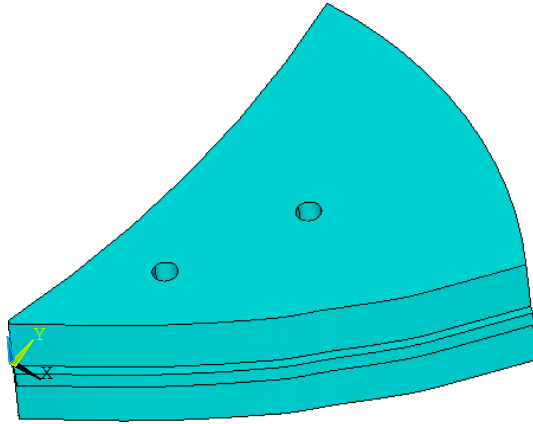08 Applications of Accelerators, Technology Transfer and Industrial Relations

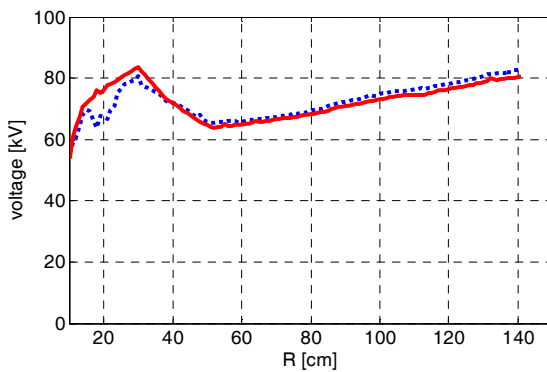Figure 4: View of the RF cavity model.

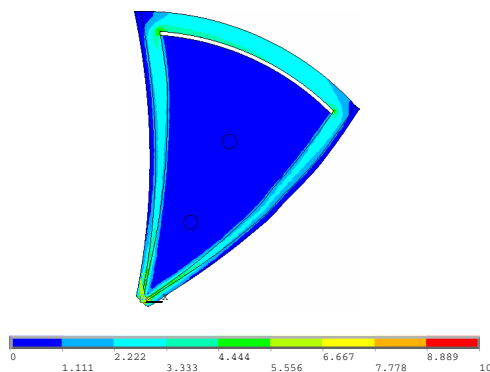Figure 5: Voltage distribution along the radius.

Figure 6: Electric field distribution.

CONCLUSIONS

The physical proposal of proton cyclotron on the energy of about $E_p \sim 250$ MeV was given. This cyclotron will provide all scientific and medical programs on the medical beam of Dzhelepov Laboratory of Nuclear Problem, Joint Institute for Nuclear Research.

REFERENCES

[1] Yu.G. Alenitsky, et al. Cyclotron for beam therapy application // XIX Russian Particles Accelerator Conf. Proc. p. 162 – 164, Dubna 2005.

[2]. Yu.G. Alenitsky, et al. Cyclotron for therapy application (in Russian) // p. 228 – 232, ICAA05 proc. SPbUniv. 2005, ISBN 5-9651-0132-5.

[3]. Yu.G. Alenitsky, et al. Cyclotron for therapy application (in Russian) // Applied Physics. 2005, №5, p. 50 – 54.

[4]. Yu.G. Alenitsky, et al. Cyclotron for therapy application (in Russian) // XX Russian Particles Accelerator Conf. Proc. Novosibirsk, 2007, p. 162 – 164.

[5] Yu.G. Alenitsky, et al. Cyclotron for beam therapy application // XXI Russian Particles Accelerator Conf. 2008.

[6] P. Elleaume, O. Chubar, J. Chavanne, "Computing 3D Magnetic Field from Insertion Devices", Proc. of the PAC97 Conference, May 1997, p. 3509 – 3511.

[7]   CST STUDIO SUITE http://www.cst.com

08 Applications of Accelerators, Technology Transfer and Industrial Relations

UEL-10-D NEW LINEAR ELECTRON ACCELERATOR FOR NON-DESTRUCTIVE TESTING

V.A. Alexeev, I.Yu. Vakhrushin[#], M.F. Vorogushin, L.Z. Kavalerchik, A.P. Klinov,
A.S. Krestianinov, K.N. Maslov, Yu.P. Schepin, FSUE "D.V. Efremov Scientific Research
Institute, of Electrophysical Apparatus", Saint Petersburg, Russia

Abstract

A compact accelerator UEL-10-D intended for radiographic inspection of steel products of up to 500 mm thickness has been designed and manufactured.

The accelerator provides the 10 MeV energy of accelerated electrons and the X-ray dose rate 1 m from target of 30 Gy/min.

The accelerator consists of an irradiator mounted on a special yoke, a heat-exchanger unit and an industrial panel-type computer. Practically all the equipment of the accelerator is mounted inside the irradiator including the HV power supply system, magnetron modulator and control system blocks. Using this yoke, the irradiator is installed on a bridge crane, which ensures its high manoerability necessary to test products of complicated geometry. Size of the irradiator without yoke is: 2040×950×950 mm.

In 2010, the accelerator was put into operation at the "Izhorskie Zavody", St.Petersburg.

The UEL-10-D accelerator can be also used in radioscopic and tomographic systems.

Requirements for reliability effective in nuclear, chemical and shipbuilding industries make necessary the non-destructive testing of large products including detection and identification of different defects such as cracks, cavities, foreign inclusions, etc. For example when manufacturing atomic reactors, 100% inspection of weld seams is necessary in compliance with requirements of Gosatomnadzor and IAEA. As the thickness of products inspected can be up to 600 mm for steel, charged particle accelerators are the only tool ensuring the required inspection quality.

A series of accelerators for NDT with energies from 2 up to 16 MeV and the photon dose rate (1 m from target) from 20 up to 120 Gy/min has been developed in the D.V. Efremov Institute [1]. Technical performances of these accelerators provide necessary quality of radiographic inspection at the 1-1T level in compliance with the international standard ASTME 142 for products with an equivalent thickness for steel up to 450 mm.

To date, more than thirty similar accelerators have been delivered to industrial enterprises in Russia and abroad. However, technological progress makes necessary updating of the delivered equipment in 10-15 years after its development. Unfortunately, in Russia deliveries of many domestically-produced component parts and units have been stopped, which impedes the process of updating. In particular, has been stopped the production

of the power klystron KIU-111 (pulse power up to 6 MW), which served as a source of the RF power in our accelerators for non-destructive inspection with an energy higher than 6 MeV. Taking into account the fact that the only our competitor in the development of accelerators for industrial radiography, VARIAN (the USA), can supply accelerators to Russia only provided a special permission of the USA government, there has been taken a solution on the designing and manufacturing a practically new domestic machine for NDT, namely UEL-10-D.

This accelerator provides the following radiation parameters: the maximum average X-ray dose rate 1m from target on the central axis is 30 Gy/min at the 10 MeV energy; the pulse repetition rates are 50 and 200 Hz; the time for the beam stabilization after its turn-on is 5 s; the range of inspected thickness for steel is 50-500 mm.

The irradiator 2040×950×950 mm in size and of 1160 kg weight is installed on the bridge crane using a specially designed yoke. The yoke enables changes of its location relative to an object under inspection: in the horizontal plane from $+180^0$ (rightwards) to -135^0 (leftwards) and in the vertical plane from $+45^0$ (upwards) to -95^0 (downwards). The irradiator is made as a support frame of aluminum section, inside which is installed practically all the equipment of the accelerator including the high-voltage power supply system, in contrast to the previous layout [1].

An electron beam with an injection energy of 50 keV is accelerated up to 10 MeV. A biperiodic standing-wave accelerating structure with axial coupling cells is applied in the accelerator. The buncher of the accelerating structure provides focusing of the electron beam under the action of accelerating RF-field, and as a result there is no need for the focusing solenoid and centering coils. The beam of accelerated electrons focused to 2 mm in diameter strikes the target wherein X-rays are produced. A water-cooled target is made of tungsten-rhenium (WRe). To measure the beam current, the target is insulated from the casing by a ceramic insulator. At the accelerator output, a collimator with a cone angle of 17^0 is installed. A laser is used to point the irradiator to a section inspected.

The MG-6090 magnetron with a power of 3 MW per a 3 µs pulse (the maximum average power is 2.5 kW) produced by an English firm is used as a source of the RF energy. The modulator of the magnetron forms the high-voltage pulse voltage up to 50 kV with a current of 100 A.

The modulator works with complete discharge of a storage device. A PFN, which is discharged through a

---

[#] npkluts@niiefa.spb.su

thyratron and the primary winding of the high-voltage step-up pulse transformer, is used as a storage. Voltage from the secondary winding of the pulse transformer is supplied to cathodes of the magnetron and electron source.

The RF power from the magnetron is transmitted to the accelerating structure through the waveguide line. To increase the electric strength, the inner volume of the waveguide line is filled with sulfur hexafluoride (SF_6) at an excessive pressure of not higher than (1.25 ±0.25) bar, which allows thin-walled waveguides to be used. To fill the waveguide with SF_6, there is provided a tank with the gas, a reduction unit, pressure gauges and adapter fittings. To match the magnetron with the accelerating structure, a phase-shifter is usually installed in the waveguide. In our case, when the accelerator operates in the fixed-energy mode, the problem has been solved by properly choosing the waveguide length.

Power is supplied to the accelerator from an AC three-phase mains 3×380 V ±10%, 50 Hz ±1% with the grounded or insulated neutral. Power consumption is not more than 25 kW. The maximum total power of the heat released into atmosphere by the accelerator equipment is not more than 6 kW. The operation mode is long-term, three-shifted with one-hour break between shifts needed to carry out visual inspection of the machine.

The power switchboard and other blocks necessary for the accelerator operation are located inside the irradiator.

The control system of the accelerator [2] is made on the basis of an industrial computer. Proper measures to provide electromagnetic compatibility of high-current devices of the accelerator and the computer control system had been taken, after which we managed to house all interface blocks of the control system inside the irradiator; only the industrial computer is located on the control desk.

Maintaining the temperature of the accelerating structure at a permanent preset level and cooling of the X-ray target and magnetron are provided by using a closed water cooling loop and a water-air heat-exchanger (RITTAL), and, as a result, the outer water cooling loop is not needed. The heat-exchanger is sufficiently compact: 640×600×670 in size and 130 kg in weight and it can be located on the bridge crane next to the irradiator.

When carrying out repair works on the irradiator connected with the depressurization of the high-vacuum volume of the accelerating line, rough evacuation of this volume should be done. For rough evacuation we use a turbo-pump unit TSH 071 E (PFEIFFER), which allows the vacuum volume to be rapidly evacuated and complete conditioning of the electron source to be performed without using standard high-vacuum pumps. On finishing the repair works, the unit is disconnected from the irradiator and can be kept separately.

The layout of the equipment allowed the irradiator parameters to be minimized; moreover the outer high-voltage cable and water-cooling hose are not needed. The length of power and control cables allow the irradiator travel in the horizontal direction up to 150 m and in the vertical direction up to 10 m. The UEL-10-D accelerator is certified and is successfully operated at the "Izhorskie Zavody" open joint stock company (see Fig. 1). Similar accelerators are in demand in the heavy engineering industry (the "Atommash", "Uralkhimmash" plants and so on) and can be also used in radioscopic and tomographic systems.

Figure 1: The UEL-10-D accelerator in a shop of the "Izhorskie Zavody" open joint stock company

REFERENCES

[1] V.P. Bagrievich, Yu.N. Gavrish, M.F. Vorogushin et al. "New Generation of Linear Electron Accelerators for Radiography", VANT, series "Electrophysical Apparatus", № 1 (27), p. 24, St.Petersburg, (2002).

08 Applications of Accelerators, Technology Transfer and Industrial Relations

THE USE OF THE ELECTRON BEAM FROM THE MAGNETRON GUN-BASED ACCELERATOR FOR ZIRCONIUM SURFACE MODIFICATION

A.N. Dovbnya , V.V. Zakutin , N.G. Reshetnyak , S.D. Aksyonova, S.D. Lavrinenko,
N.N. Pilipenko, V.N. Pelykh, NSC "KIPT", Kharkov, Ukraine, 1 Akademicheskaya St.,
Kharkov, 61108, Ukraine

INTRODUCTION

The paper reports the results from studies on metal surface irradiation with an electron beam of the accelerator based on the secondary-emission cathode magnetron gun. Presented are the results of examination of flat zirconium sample surfaces after their irradiation with an electron beam of the accelerator having the following parameters: electron energy 70 to 80 keV, pulse length – 15 μs, pulse rate – 2 pulses/s for two regimes of energy density on the samples, namely, 10 J/cm^2 and 20 J/cm^2. Experiments have been made to explore possibilities of irradiating inner surfaces of tubular items.

EXPERIMENTAL SETUP AND METHOD OF STUDIES

To irradiate zirconium surface, we have used the electron beam of the accelerator based on the magnetron gun having a secondary-emission cathode [1, 2] of diameter 40 mm and a stainless-steel cylindrical anode with a diameter of 78 mm. The accelerator diagrammatic sketch is presented in Fig. 1.
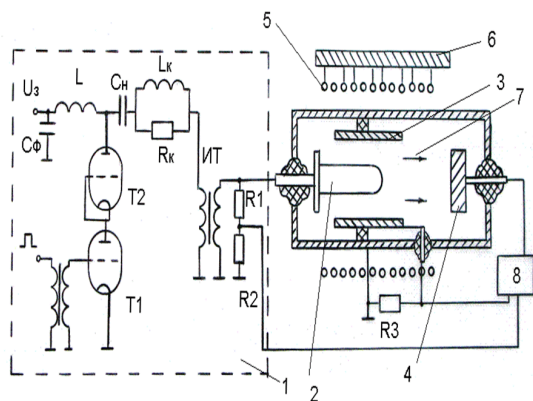

Fig. 1. Full diagram of the accelerator. 1 – impulse generator, 2 – cathode, 3 – anode, 4 – Faraday cup, 5 - solenoid, 6 - solenoid power supply, 7 – electron beam, 8 – computerized measurement system.

The accelerator consists of the following main units: an energizing high-voltage pulse generator 1; a magnetron gun with a secondary-emission cathode 2 and anode 3, located in the vacuum chamber; solenoid 5 that generates a longitudinal magnetic field; a target device with a Faraday cup (FC) 4; a computerized measurement system 8 for measuring beam parameters. The supply voltage pulse from the impulse generator 1 was applied to the magnetron gun cathode.

The impulse generator 1 provided voltage pulse shaping with a pulse overshoot amplitude of 190 kV, a pulse overshoot decay time of ~ 0.6 μs to provide the development of secondary-emission multiplication processes, and an amplitude of the voltage-pulse flat part of ~ 150 kV; the pulse length was 15 μs, the pulse-repetition rate was 2 Hz. In the impulse generator circuit, use was made of the full discharge of the storage capacitor Cs via a correcting circuit L_2R_2 to the pulse-transformer (ИТ) primary winding through two series-connected thyratrons for increasing the commutation voltage. The voltage surge was provided due to spurious inductance and capacitance of the pulse transformer.

The electron source (C – cathode, A – anode) is arranged in the vacuum chamber with an inside pressure of about 10^{-6} Torr. To produce the electron beam, the magnetron gun is used. The latter has a copper cathode (40 mm in diameter, 85 mm in length) and a stainless steel anode (78 mm in inner diameter and 140 mm in length).

The magnetic field for electron beam shaping and transport is generated by the solenoid 5 consisting of four sections, which are energized by dc sources 6. The amplitude and longitudinal distribution of the magnetic field can be controlled by varying the current value in the solenoid sections.

The measured data on the parameters of the voltage pulse, the beam current traversing the Faraday cup and their stability were processed by a computerized measuring system 9. The measurement error ranges within 1 % to 2 %. The processed data were displayed on the monitor.

EXPERIMENTAL RESULTS AND DISCUSSION

The parameters of the accelerator under discussion were investigated for the case of material surface irradiation.

The experiments have demonstrated that the maximum parameters of the beam were attained in a uniform magnetic field at a cathode voltage of ~ 120 kV. The magnetron gun formed an electron beam of current 125 A with a power density on the target ~ 4 MW/cm^2 at a pulse length of 10 μs.

The bandwidth of electron beam generation was determined by varying the magnetic field and was found to be ΔH~200 Oe. This beam generation bandwidth is of great importance in the accelerator adjustment for technological purposes.

 It has been shown that at a constant cathode voltage the change in the magnetic-field amplitude and

distribution results in the change of the beam current. Thus, with the use of this effect in the experiments on sample exposure to the accelerator beam, the beam current was changed by a factor of ~ 5 from 25 A to 135 A

at a voltage (137±12) kV. This can be seen in Table 1, which lists the beam parameter values at target irradiation conditions.

Table 1. Beam parameters

Electron energy, keV	Beam current, A	Pulse length, s	Target power density, MW/cm^2	Pulse repetition rate, Hz
120	125	12	~ 3.5	2
125	105	12	-	2
135	80	11	-	2
140	45	11	3.0	2
150	25	10	-	2

In one of the experiments, as the uniform magnetic field was varied from ~ 1200 Oe to ~ 1400 Oe, the beam current changed from 45 A up to 120 A, i.e., by 300 %, while the cathode voltage changed only by 20%, namely, from 115 kV up to 140 kV. This enables one to control the beam energy density on the target. Notice that the sputtering of target material on the cathode surface gives its contribution to the process of current variation.

The beam parameters obtained at the accelerator under consideration are close to the parameters of the facilities-analogs that are currently used for irradiation experiments [3].
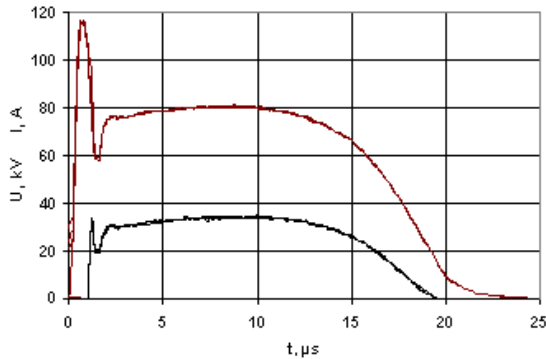

Fig. 2. Oscillograms of the cathode voltage (upper curve) and the beam current (lower curve).
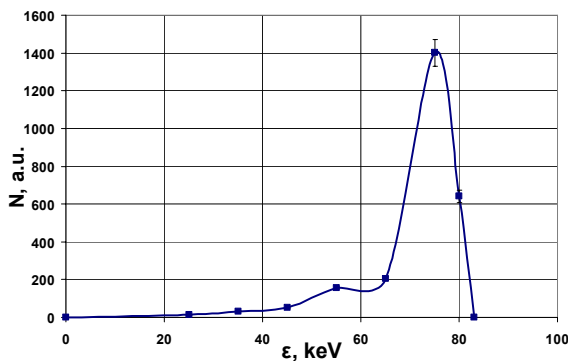

Fig. 3. Beam energy spectrum.

An important role in the experiments belongs to electron energy distribution. For this reason, based on the measurements of the beam current and the voltage amplitude we have constructed the curve of electron energy distribution in the beam. Figure 2 shows the oscillograms of the cathode voltage and the beam current, and Fig. 3 gives the beam energy spectrum in this case.

The data obtained from Fig.3 indicate that nearly 80% of particles lie in the energy range 75±10 keV (or ±10%).

The targets were irradiated at a cathode voltage of ~ 80 kV and a beam current of 85 A (the beam energy density is 20 J/cm^2) in the first case, and at ~ 70 kV and ~ 55 A (the beam energy density is 10 J/cm^2) in the second case, the number of pulses being 5. At these beam parameters the modified layer depth ranges from ~ 10 to 100 μm.

Below we give the results of metallographic examination of Zr 1%Nb samples cut out from fuel claddings and of pure zirconium samples after their exposure to a tubular electron beam of the accelerator based on the magnetron gun with a cold copper second-emission cathode. The results obtained have demonstrated that zirconium surface irradiation with electrons causes essential changes in the subsurface layer structure. Figure 4 shows the boundary surfaces of the irradiated and non-irradiated areas of zirconium materials. It is obvious that electron irradiation of zirconium surfaces causes noticeable changes in their subsurface layer. Thus, the surface texture variation caused by surface fusion and intense evaporation is clearly seen. The irradiation leads to a substantial planarization of surface roughness, the surface has become smoother and mirrored. In some cases, at an energy density of 20 J/cm^2, the areas within the irradiated region show (even at a low magnification of x100) the crater formation, the latter being due to the material expulsion as well as to gas and lightest constituents emission from the sub-surface layer (see Fig. 4 d). Microhardness tests of irradiated and nonirradiated surfaces of zirconium samples have shown changes in the microhardness values of irradiated areas, namely, the microhardness of the

08 Applications of Accelerators, Technology Transfer and Industrial Relations

Zr1%Nb alloy has changed by ~ 20 % and ~ 35 % of its initial value (19-20 MPa) at electron energy densities of 10 J/cm2 and 20 J/cm^2, respectively. This may be due to different amounts of energy imparted to the irradiated surface.
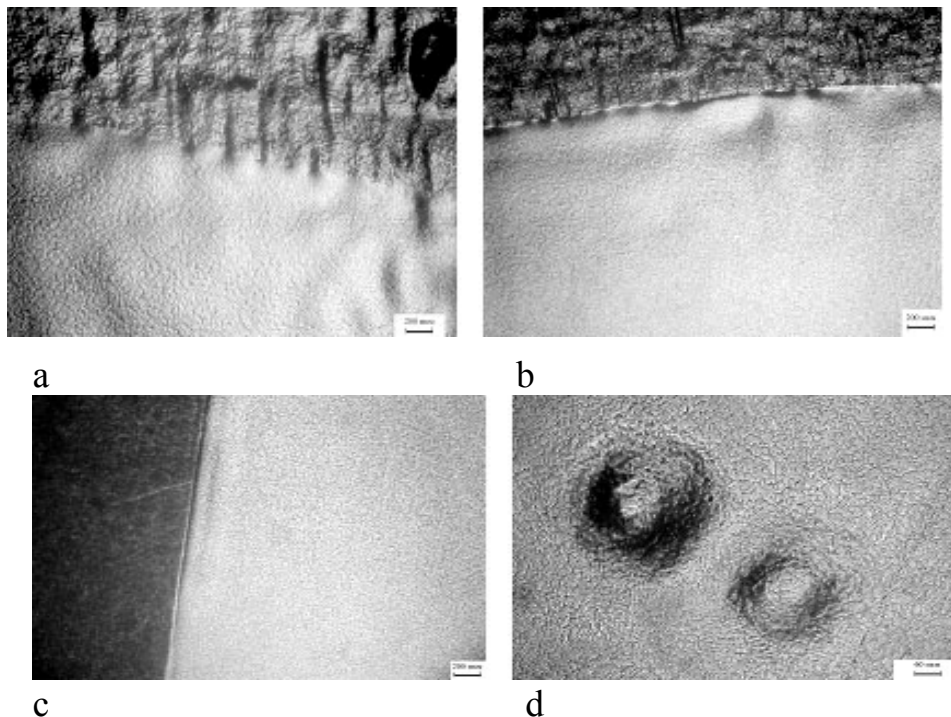

Fig. 4. Boundaries between nonirradiated and electron-irradiated Zr1 %Nb (a, b) and Zr (c) surfaces (×50), as well as irradiated Zr surface area (d) (×160), the electron beam energy density being 10 J/cm^2 (a) and 20 J/cm^2 (b, c, d). At the bottom right of the figures the mark, 200 μm in length, is shown.

The electron beam of the magnetron gun is strongly "magnetized". This enables one to increase the beam diameter as the magnetic field falls off along the beam propagation, and to provide a sufficiently precise beam entry into tubular products thereby ensuring the electron bombardment of their inner surfaces. By varying the type of falling-off magnetic field distribution it appears possible to shift the irradiation zone along the tube length.

CONCLUSION

Thus, the undertaken studies have demonstrated the possibility of using the secondary-emission-cathode magnetron gun-based accelerator for modifying planar and cylindrical surfaces.

REFERENCES

[1] N.I. Aizatsky, A.N. Dovbnya, V.V. Zakutin, N.G. Reshetnyak, at all. Studies on beam formation in the electron accelerator having a secondary-emission source. (In Russian). Vestnik of Kharkov National University, series "Yadra, chastitsy, polya" 2006, No 732, issue 2(30), pp. 96-100.

[2] A.N. Dovbnya, V.V. Zakutin, N.G. Reshetnyak at all. Surface studies of steels KhVG, KhVN10T and titanium VT-1 after exposure to the electron beam of the secondary-emission-cathode magnetron gun-based accelerator (in Russian). Proceedings of the 18th International Conference on Physics of Radiation Phenomena and Radiation Materials Science. Alushta, Crimea, Ukraine, 8-14 September, 2008, pp. 419-420.

[3] V. Engelko, G. Mueller, A. Andreyev et al, Pulsed electron beam facilities (GESA) for surface treatment of materials. 10th International Conference on Applied Charged Particle Accelerators in Medicine and Industry. Proceedings, Russia, Saint-Petersburg, 1-4 October, 2001, pp. 412-417.

08 Applications of Accelerators, Technology Transfer and Industrial Relations

ION SCANNING SYSTEM IN BEAM LINE OF U-400M CYCLOTRON FOR ELECTRONIC COMPONENTS TESTING[†]

A. Fateev[††], E. Gorbachev, G. Gulbekyan, I. Kalagin, N. Kazarinov, V. Kazacha, E. Muravyova
JINR, Dubna, Moscow region, Russia

Abstract

The beam line of the U-400M cyclotron is designed for irradiation of chips by beams of accelerated ions to determine their radiation resistance. The results of the beam transport calculations for various ion types taking into account the beam parameter changes on passing a collimator and degrader are presented. The resulting beam sizes on a target are obtained for all beam variants. The calculated beam size on the target varies in the range from 15 cm up to 30 cm. An analysis of three variants of the magnetic scanning system is carried out. The working scheme, construction and main technical characteristics of the optimal variant are presented.

INTRODUCTION

The beam line of the U-400M cyclotron is intended for the chip irradiation by flows of the accelerated ions for determination of the radiation influence upon chip work. Parameters of the ions that are supposed to be used in this beam line are presented in Table 1[1].

Table 1: Parameters of the ions

Ion	W_0 [MeV/amu]	A	Z_{ext}	A/Z_{ext}
Ne	9.2	22	+10	2.2
Ar	7.8	40	+17	2.35
Kr	8.8	86	+33	2.61
Xe	8.8	136	+49	2.78

Calculations of the beam tracing in the beam line for the beam parameters, specified in Table 1, were carried out in this work. The turned out beam dimensions on the target were defined. The different variants of the scanning system for getting demanded uniformity of the beam density distribution on the target were investigated.

BEAM LINE SCHEME

The beam line scheme is shown in Figure 1. The main beam line elements are: the correcting magnet B5CMV1 (B5CMH1), the horizontal scanning magnet B5SMH1, the vertical scanning magnet B5SMV1, the diagnostics block B5BD1 and device in the beam line end where the target is placed. The iris is placed between corrector and horizontal scanning magnet. The length of both scanners is equal to 600 mm; their bore diameter is equal to 90 mm. In the diagnostics block there is a device having the set of tantalum foils. The energy of the accelerated and extracted from the cyclotron ions can be diminished with
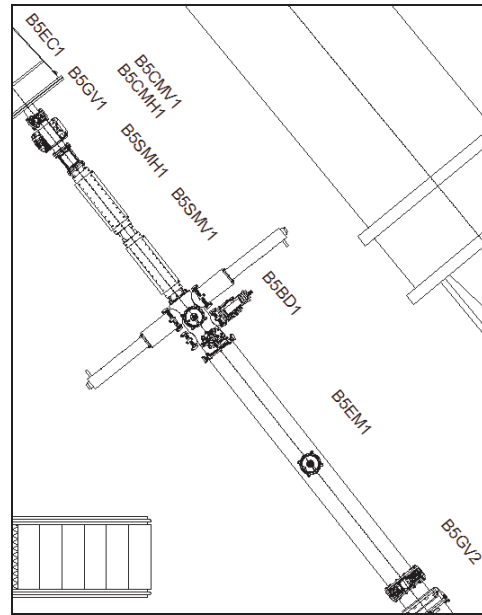

Figure 1: Scheme of the beam line

the help of these foils down to three chosen intermediate values of 6 MeV/amu, 4.5 MeV/amu and 3 MeV/amu.

Calculation of the ion movement in the beam line was carried out with the help of the code COSY INFINITY [2] in assumption that the beam has the Gaussian density distribution in its cross-section. One considered also that the magnetic fields of the scanners were switched off and the particle movement from the extraction point to the target occurs in a free space. In this case the initial data for COSY INFINITY code were calculated from the initial values of the second order moments $\overline{x^2}$, $\overline{(x')^2}$, $\overline{xx'}$, $\overline{y^2}$, $\overline{(y')^2}$ and $\overline{yy'}$ [1]. All dispersions and their derivatives were considered to be equal to zero. The magnitudes of the initial moment values for the set of ions specified in Table 1 are presented in Table 2. The value of the initial relative root-mean-square spread of the ion longitudinal momentums δ_0 is equal to $2.49 \cdot 10^{-3}$

The total length of the beam line is equal to 622 cm. There is an iris at the distance of 139 cm from the point of the beam extraction. The tantalum foil having the diameter of 90 mm is placed at the distance of 155 cm from the iris.
Evaluations show that maximum beam deviation on the foil, when the scanners are turned on, amounts ~30 mm. Therefore the beam radius before the foil must not exceed 15 mm in order the beam will not exceed the foil bounds on scanning. From these considerations the iris diameter was chosen equal to 20 mm.

---

08 Applications of Accelerators, Technology Transfer and Industrial Relations

Table 2: Initial moment values

Ion	$\overline{x^2}$ [cm²]	$\overline{(x')^2}$	$\overline{xx'}$ [cm]	$\overline{y^2}$ [cm²]	$\overline{(y')^2}$	$\overline{yy'}$ [cm]
Ne	1.95	9.31 10^{-5}	1.35 10^{-2}	6.19 10^{-3}	2.37 10^{-5}	3.65 10^{-4}
Ar	2.03	9.75 10^{-5}	1.41 10^{-2}	6.90 10^{-3}	2.57 10^{-5}	4.05 10^{-4}
Kr	1.85	7.93 10^{-5}	1.81 10^{-2}	5.74 10^{-3}	2.16 10^{-5}	-3.25 10^{-4}
Xe	2.33	9.15 10^{-5}	1.46 ``10^{-2}	2.44 10^{-2}	2.94 10^{-5}	-8.15 10^{-4}

Dimensions of the irradiated chip is equal to 50×50 mm². But because of the diagnostics, that must be placed around the target and control uniformity of the beam density distribution on it, the region where non-uniformity of the beam density distribution must not exceed the value $\pm 5\%$ was enlarged to the value of 100×100 mm².

Calculation of changes of the ion beam parameters on its passing through the iris was carried out by procedure stated in **[3]** and calculation of changes of the ion beam parameters on its passing through the degrader foil was carried out by procedure stated in **[4]**.

The calculation results of the Ne ion transportation are shown in Figure 2. The solid curves correspond to the beam horizontal dimension and dotted ones correspond to its vertical dimension. The tantalum foil thickness was selected so as to diminish the initial beam energy down to its final values W = 6, 4.5 and 3 MeV/amu.
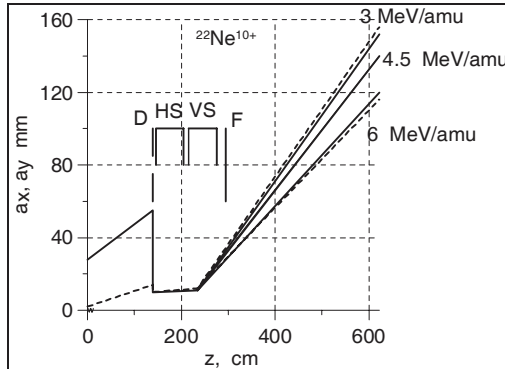

Figure 2: Calculated envelopes of the 22Ne10+ ion beams in the beam line. Here D is the iris, HS is the horizontal scanner, VS is the vertical scanner, F is the tantalum foil

For the considered ion set the calculated beam radius on the target possesses the value from ~75 up to ~159 cm. But necessary uniformity of the beam density distribution on the target can not be obtained without the scanning system.

RESULTS OF SCANNING SYSTEM WORK SIMULATION

Work of the following three variants of the scanning system was investigated:

1. The scanners having the sawtooth feed and frequencies f_x = 110 Hz, f_y = 100 Hz.
2. The scanners having the sine-shape feed at the frequencies $f_x = f_y$ = 50 Hz and the phase shift by $\pi/2$ (circular sweep).
3. The scanners having non-linear sawtooth feed and frequencies f_x = 10 Hz, f_y = 11 Hz.

The carried out analyses showed that when the beam dimensions were sizeable and determined in main by thickness and type of the foil, the variant 2 is the most optimal. Moreover, only this variant provides the necessary uniformity of the beam density distribution on the target for all ion types and energies under conditions of the mean current limitations in the magnets. Besides, the circular sweep allows one to correct small differences in width of the horizontal and vertical dimensions due to independent setting of the scanner field amplitudes.

The calculated distributions of the ^{22}Ne^{10+} ion density (W =3 MeV/amu) on the target in arbitrary units for scanners operating at the highest possible amplitudes $J(x)$ (upper curve) and also the beam density distribution on the target when the scanners are turned off $F(x)$ (lower curve) are shown in Figure 3.
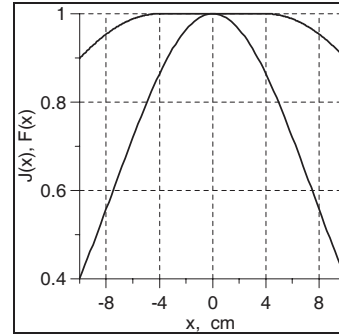

Figure 3: Calculated distributions of the ion density on the target along horizontal with (upper curve) and without (lower curve) scanning

STRUCTURE OF SCANNING SYSTEM

The scanning system consists of two deflecting magnets, power supply unit and control unit.

Construction of the deflecting magnet represents a distributed winding located directly on the ion beam line surface surrounded with compactly fitting bladed magnetic circuit made of electrical-sheet steel. The turn density of the winding vary through the azimuth according to cosine low that allows one to obtain high magnetic field uniformity in all volume of the ion beam line.

The construction of both magnets is identical but they are rotated one relative to another through an angle of 90^0. The magnetic field non-uniformity in the region of supposed beam dimensions does not exceed $\pm 5\%$. Full heat losses in the magnet do not exceed 300 W, part of

them falls on heat of the ion beam line made of thin-wall stainless steel.

Parameters: maximum deflecting magnetic field B in both magnets is equal to 400 Gs; the scanning frequency f = 50 Hz; length of both magnets along the magnetic screen l = 660 mm; maximum peak current in the windings I_{max} = 14 A; cooling of all magnet windings is carried out by the air forced method.
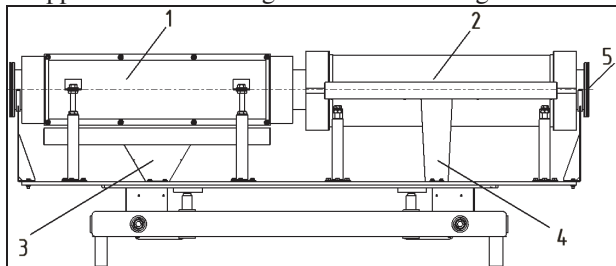
Appearance of the magnets is shown in Figure 4.

Figure 4: System of the circular sweep: horizontal scanner (1), vertical scanner (2), air conduits (3,4), vacuum ion beam line with flanges (5).

The functional scheme of the equipment power part is shown in Figure 5.
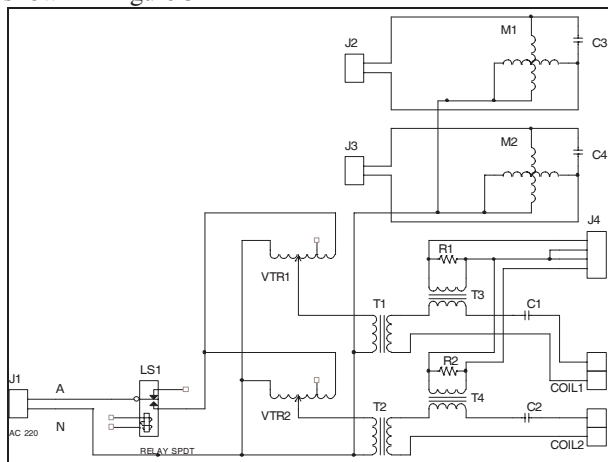
Figure 5: Power module functional diagram

Functionally power module consists of the following units: scheme of hand and remote commutation of the single-phase alternating current net; two single-phase voltage regulators remotely-operated with the help of two alternating current engines; two power step-down transformers; two measuring current transformers; phase-shifting capacities C1 and C2.

The control module is fulfilled as a printed circuit board 220×100 mm^2 where all module components are placed. The printed circuit board is located in the standard module Euro-191 Rack Mount having the width of the front panel 42TE and its height 3U. Access to the inputs and outputs of the module is carried out through contacts of two D-SUB9 and one D-SUB25 connectors placed on the back module panel.

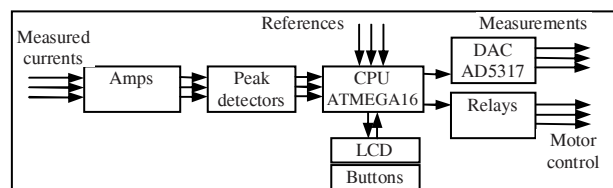Functionally the module consists of (Figure 6):

Figure 6: Control module functional diagram

microcontroller Atmel ATMega16 with built-in analog-digital converter (ADC); amplifiers of the current signals in the windings; peak detectors with control; digital-analog converter AD5317; LCD display, buttons and toggles on the front panel; electromagnetic relays.

Sine-shaped signals with frequency 50 Hz from the current transformers, inserted in the deflecting magnets windings, are filtered, amplified by factor 40 and detected by peak detectors controlled by CPU. The microcontroller program initiates ADC measurements every 25 ms measuring current amplitudes in the windings and references specified by external control system. After carrying out measurements, microcontroller discharges the peak detectors providing detection of the current amplitudes in the next measurement cycle. The measured values of the current amplitudes in the deflecting magnet windings are compared with references specified by the outside control system or manually by knobs placed on the front panel. In accordance with measurement results the microcontroller switches on the proper relay to commutate AC voltage to corresponding auto transformer engine, attaining the necessary current amplitude in the windings.

SUMMARY

The scanning system was successfully tested in the cyclotron run for the chip irradiation during more than three weeks. Measurements of the ion density distribution uniformity on the target showed its agreement with the calculations.

REFERENCES

[1] O. Borisov, "Extraction of Xe, Kr, Ar, and Ne Ion Beams from Cyclotron U-400M Having the Energies 4 – 10 MeV/amu for Irradiation of Films", JINR LNR Report TOT-SFU-07-20, Dubna, 2009..

[2] K. Makino and M.Berz. COSY INFINITY versin 9. NIM, 258 (2005) p.p. 346 -350.

[3] N. Kazarinov, V. Kazacha, "Calculation of Ion Beam Transportation in Channel B5 of Cyclotron U-400M", JINR LNR Report TOT-SFU-234, Dubna, 2009.

[4] N. Kazarinov, V. Kazacha, "Calculation of Second Order Moments of Ion Beam in Degrader", International Particle Acceleration Conference (IPAC10),Japan, 2010, http://ipac10fs2. kek. jp/ ipac10/MOPEC041

COMPROMISE SYSTEMS FOR TRANSPORT PROTON AND ION BEAMS IN MEDICAL AIMS

Mark Kats, ITEP, 25, B.Cheremushkinskaya, Moscow, Russia

Abstract

A center of treatment by proton and ion beams must be equipped by a few (4-6) treatment rooms and in most of them must be used equipment for choose optimal directions of irradiation. Usually it is gantry. In gantry patient is immovable and any directions of irradiation are possible. But any modern gantry are so large, complex and expensive, that it is necessary to suggest new solutions – more compact, less heavy, less expensive, but with enough wide choose of direction of irradiation. Similar system can be designed only with compromises: with displacement of treatment coach at horizontal position of the patient and at limited directions for irradiation. Planar systems are seems as most suitable for treatment centers. Layouts of proton and ion centers with 5-6 treatment rooms equipped by planar systems at hot magnets are suggested.

INTRODUCTION

The number of patients requiring beam therapy is very high. Future centers for medical irradiation by proton or ion beam should be highly effective and it requires 5-6 treatment rooms that use one accelerator and are able to have high quality irradiation for every room.

It is necessary for successful treatment in most cases to choose direction of irradiation and change this direction several times within one fraction of treatment. The second important condition of optimal irradiation is to use active dose distribution on the target volume (3-D scanning by the narrow beam).

Equipment used today to provide these conditions is called gantry. Gantry consists of a beam transport channel with magnets for beam scanning placed on the rotatable frame. Classical gantry, according to the medical requirements, assumes that horizontally fixed patient is placed immovable with center of the target at center of irradiation, at the axis of frame rotation Any directions of irradiation are available via frame rotation. But any modern gantry are so large, complex and expensive, that it is necessary to suggest new solutions – more compact, less heavy, less expensive, but with enough wide choose of direction of irradiation. Similar system can be designed
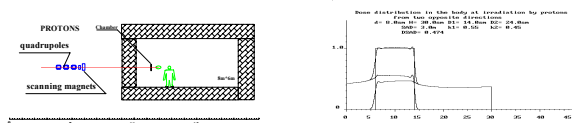

Figure 1. Scheme of treatment room with horizontal beam and scheme of doses distribution at irradiation from two opposite directions.

only with compromises: with displacement of treatment coach at horizontal position of the patient and at limited

directions for irradiation. It is important to highlight that availability of any direction (as it is using gantry) is not necessary. Three versions of compromise solutions were observed.

EQUIPMENT WITH FIXATED DIRECTIONS OF THE BEAM

Simplest equipment with fixated direction is a horizontal beam. There is clear defect of similar system. Doses level in healthy parts of the body is comparable to doses into the target at irradiation in only one direction targets with large sizes. So, it is very useful to produce irradiation from two or three directions. At horizontal beam doses level can be decreased two times at irradiation by two opposite directions after rotation of treatment table around of vertical axis (see Figure1). But volume of irradiated healthy parts of the body will be increased more then two times. Sometimes the second direction of irradiation at horizontal beam is closed by value of maximal range (30cm) or by medical reasons.

There are systems with beam transport to patient from vertical or bent directions. Sometimes the beam can be transport from two directions in one room, in one common iso-center. Two directions have more possibilities in comparison with one direction, but quantity of possible directions are small and magnetic channel for similar system has magnetic optic and volume of the room comparable to gantry. Increasing of quantity of transport channels with different fixated directions of irradiation to one iso-center does not seem as optimal solution.

ECCENTRIC GANTRY

For decreasing diameter of rotated heavy equipment in gantry it was suggested to rotate it around of the axis which pass through center of heavy mass and displaces treatment table with horizontally fixed patient around of magnets in order to direction of bended beam pass through the target center (see Figure 2).
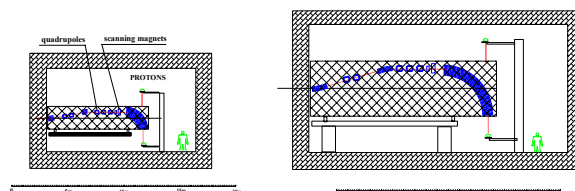

Figure 2. Spatial schemes of eccentric gantry for proton and ion beams.

In such eccentric gantry design diameter of heavy rotated equipment is like to radius of particles bend in magnetic field (at 1.6Tl R=1.4m for protons and R=4m

08 Applications of Accelerators, Technology Transfer and Industrial Relations

for ions). So, in comparison with usual gantry mechanical difficulties will be significantly decreased. Treatment table must be displaced in vertical plane around of circle with radius like R/2+1.5m (2.2m for protons, 3.5m for ions). An industrial manipulator or similar device can be used in all versions of transport system for precision displacement of horizontally fixated patient. As result, direction of the beam after bends into gantry must pass through center of the target. Optical scheme of eccentric gantry is similar to usual gantry and any directions can be used for irradiation. Of course, it is compromise solution with displacement of treatment table on significant distances.

EQUIPMENT WITH BENDS OF A PATIENT BODY

Transport systems with bends of treatment coach or table around of vertical axis, which pass through center of the target, are well known and it used usually for targets placed into the head. Only like 10% of targets placed into the head.

V.Balakin suggested rotation patient in vertical position around of the vertical axis. For treatment by such equipment each patient must be in rather good condition and specific "vertical" tomography is necessary.

B.Astrachan suggested fixation of the patient into rigid thin cylinder between two air bags and then rotation of this cylinder. Unfortunately, such fixation is very uncomfortable to the patient.

Those methods are not universal.

SIEMENS company suggested bends of treatment table with fixated patient around of horizontal longitudinal axis on limited angles for increase possibility of transport systems with fixated directions of the beam (see Figure 3). But even at rotation like 10 degrees there are displacements of inner parts of the body. Therefore firm SIEMENS suggested after each rotation to use additionally movable tomography and recalculation of plan of irradiation. Similar systems will be installed in two new centers of ion therapy in Germany. But each tomography and planning take some time in treatment room, and some unnecessary irradiation will be caused by every tomography (after each rotation into each fraction). Of course, it is interesting compromise solution.
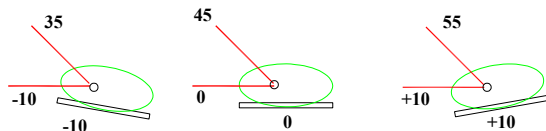

Figure 3. Scheme of possible directions of irradiation at two fixated directions of the beam and at rotation of treatment table.

PLANAR SYSTEMS

Planar systems are based on bends of the beam by immovable magnets only in vertical plane simultaneously

with displacements of treatment table with a patient, which fixated horizontally. Bended beam is directed to the center of a target and plan of irradiation is saved.

SIMPLE PLANAR SYSTEM, SPS(F)

A magnet with increased gap is placed in a room with initially horizontal beam just in front of patient for bend of the beam only in vertical plane. Size working gap of the magnet is equal to maximal sizes of the target (20cm*20cm). The beam can be bend from horizontal plane at any angle f according of magnet strength, in limits –F < f < F. Treatment table with horizontally fixated patient is displayed in vertical plane after any changes of beam direction (see Figure 4). Angel F is main compromise of SPS(F). As bigger F the efficiency of SPS(F) is close to gantry, but with large magnet and large treatment table displacements. The second compromise is displacements of treatment table with patient.
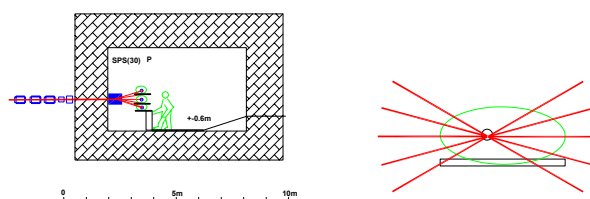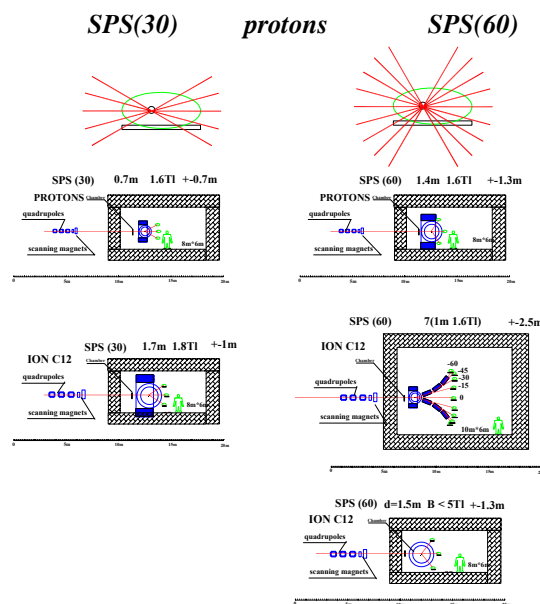

Figure 4. Scheme room with SPS(F).

SPS(F) can be designed with hot magnets for proton and ion beams in many versions. Super conductive magnet with $B \leq 5Tl$ can be useful for decreasing sizes and weight of SPS(60) for ion beam (see Figure 5).

SPS(30)   ions C12   SPS(60)
Figure 5. Spatial schemes of Simple Planar Systems.

Optical scheme of SPS(F) in comparison with gantry optical scheme is rather simple. Symmetrical input beam is not necessary.

PLANAR SYSTEMS WITH PRELIMINARY BENDS OF INITIAL BEAM IN VERTICAL PLANE

Spread of directions for irradiation by SPS(F) can be changed by preliminary bends of the beam on angle H in vertical plane from -F < f < F to -F+H < f < F+H by using additional magnet with small gap. In such conditions SPS(F) must be installed along of direction of bended initial beam (see Figure 6).
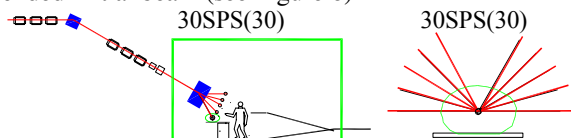

Figure 6. Scheme a room with SPS(F) and preliminary bend of initial beam.

Preliminary bends of the beam can be used for transport beam to a few treatment rooms placed on different levels. Preliminary bends of the beam can be used for increasing total spread of directions in systems with a few treatment rooms equipped by SPS(F) with small value of F. For example, it is possible to design two treatment rooms with SPS(30) into each. Initial beam direction in the first room is horizontal. Initial beam direction in the second room is H. Total spread of directions for irradiation in system of two rooms is (-F < f < F) + (-F+H < f < F+H). Each room can be used as separate treatment room with its spread of possible directions for irradiation. It can be useful at design of ion transport system at hot magnets.

CENTER OF PROTON THERAPY WITH 5 ROOMS EQUIPPED BY SPS(60)

For center of proton therapy with high productivity at enough high quality it was suggested to use 5 treatment rooms near one accelerator (see Figure 7). Magnet for protons SPS(60) can have the length like 1.3m at maximal field ≤1.8Tl and working gap 20cm. For displacement of treatment table (±1.4m) each room must be equipped with specific (industrial) manipulator. Each room equipped by scanning system. Approximately the same scheme can be used for center of ion therapy at using in each SPS(60) super conducted magnet (diameter 1.3m, gap 20cm, maximal field less 5Tl).

CENTER OF ION THERAPY WITH 6 ROOMS EQUIPPED BY SPS(30)

Radius of ion with maximal energy rotation in field 1.8Tl is 3.5m. Therefore sizes, weight, power of hot magnet for SPS(60) will be unsuitable. It was suggested to use pairs of rooms on two levels with SPS(30) into each. Spread of directions into each room (60 degree from two sides) is enough large for using each room as independent treatment room in most fractions for any patients. For center therapy with high productivity at enough high quality it was suggested to use 3 pairs of

treatment rooms near one accelerator (see Figure 8). Magnet for ion SPS(30) can be with length like 1.7m and maximal field like 1.8Tl at gap like 20cm For displacement of treatment coach (dZ < ±0.9m) each room must be equipped with specific (or industrial) manipulator. Each room equipped by scanning system.
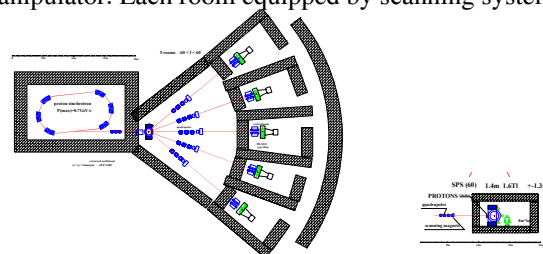

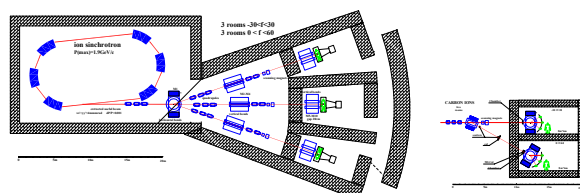Figure 7. Scheme of transport system for proton therapy center with 5 treatment rooms.

Figure 8. Scheme of transport system for ion therapy center with 6 treatment rooms.

Medical ion accelerator and its transport system (P/Z≤1.9GeV/c) can be used for acceleration and transport of proton beam (P/Z≤0.7GeV/c). But using more complex and more expensive equipment, than necessary, does not seems to be the best solution.

Two different accelerators with its two different transport systems need for optimal center of therapy by protons and ions beams.

Next possibility is using two extraction directions from common ion accelerator and two different transport systems with 5-6 treatment rooms in each (see Figure 9).
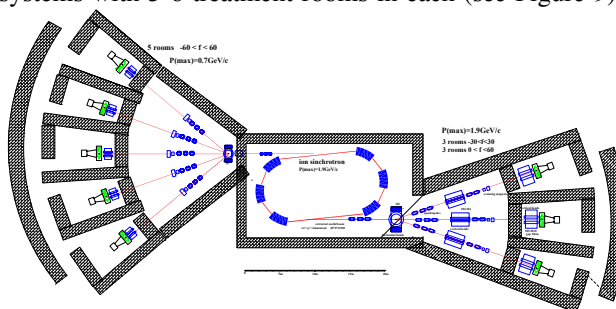

Figure 9. Scheme of transport system for proton and ion therapy center.

CONCLUSIONS

The most perspective solutions of transport systems for center proton and ion therapy are based on planar systems in its various modifications.

COMPACT SUPERCONDUCTING SYNCHROCYCLOTRONS AT MAGNETIC FIELD LEVEL OF UP TO 10 T FOR PROTON AND CARBON THERAPY

A.I.Papash, G.A.Karamysheva, L.M.Onischenko,
Joint Institute for Nuclear Research, Dubna, Russia

Abstract

Based on brief analysis of accelerators widely used for proton-ion therapy and patient cure during last 20 years the feasibility and importance of compact superconducting synchrocyclotrons operating at magnetic field level up to 10 T is outlined. The main component of modern commercial facility for proton-ion therapy is an isochronous cyclotron with room temperature or superconducting coils accelerating protons up to 250 MeV as well as synchrotron accelerating carbon ions up to 400 MeV/A. Usually ions are delivered from accelerator into the treatment room by transport lines. Irradiation is done by system of pointed to the patient magnets, collimators, energy degraders which are attached to the rotating Gantry. To greatly reduce price of facility (almost one order of magnitude) and to simplify operational conditions of hospital personal it is proposed to provide iso-centric rotation of compact superconducting synchrocyclotron around the patient. Main physical and technical parameters are described in the paper.

INTRODUCTION

During 60 years proton beams are being used for radiation therapy[1]. Proton resistive tumours are treated by carbon beams [2]. Dedicated commercial facilities for proton/ion therapy are based on 250 MeV synchrotron build by FERMILAB [3] and 400 MeV/A carbon synchrotron HIT [4]. Room temperature cyclotron C235 from Company IBA [5] and superconducting isochronous cyclotron SC250 built by ACCEL [6] are basic accelerator units on the international market. The field level of C235 magnet is 2.17 T and weight is 200 tons while field of SC250 is 3 T and weight is 90 tons. Modern commercial proton therapy complex includes accelerator, beam lines, rotating Gantries and auxiliary equipment. Basic price of Complex is 100-150 M\$ and cyclotron cost is only 15% of total price. Special buildings and services are required for such Facility for extra cost.

COMPACTNESS LIMIT FOR 250 MEV ISOCHRONOUS CYCLOTRONS

If one could locate accelerator on rotating carousel platform then ions might be delivered to patient directly – without beam lines and gantry. Compact neutron therapy system with superconducting cyclotron on the rotating platform has been built at NSCL MSU [7,8]. Weght of 50 MeV Deuteron cyclotron is 20 tons. Main condition for

rotation of 250 MeV proton machine is the reduction of cyclotron dimensions and weight. Of course one may build rotating platform with 100 tons accelerator on it but there is no commercial interest on such equipment.

Beam energy in cyclotron is $T_k \sim (B_{ext} \cdot R_{ext})^2 Q^2 / A$. Magnet weight is $\sim R^2$ (coefficient $\sim R^3$ leads to overstated results). Increasing of field will reduce magnet pole radius and weight. Magnet for 250 MeV cyclic accelerator is weighting 65 tons at field level B=5.5 T and only 20 tons at level B=9 T. Magnet is saturated at high field levels and maximum contribution from iron sectors is ~2 T. Thus flutter is inversely proportional to $F \sim B_{av}^{-2}$ and at the field level of 10 T flutter is only F=0.01.Using of sectors with high spirality $\delta \approx 80°$ ($tg\delta \approx 5$) to improve focusing properties might cause nonlinear instabilities. It is hardly possible to build compact 10 T isochronous cyclotron.

SYNCHROCYCLOTRONS FOR PROTON/ION THERAPY

Main operational principles of synchrocyclotron with weak focusing $0<n<1$ do not impose any limit on the level of magnetic field. In contrast to isochronous cyclotrons there is a possibility to operate synchro-cyclotron with superconducting colis (SC-SC) at high fields. Prof.H.Blosser has proposed to install 5.5T SC-SC on rotating platform [9] and theoretical studies have been performed in NSCL MSU [10,11]. In 2007 Dr. T.Antaya has proposed design of the SC-SC at significantly higher level of magnetic field − up to 10 T (Fig.1) [12]. Private company "Still River" has built "single room" unit for proton therapy "Monarch250" (Fig.2) where compact 9T SC-SC roundabout patient (Fig.3) [13]. The first beam was extracted in May 2010 [14].
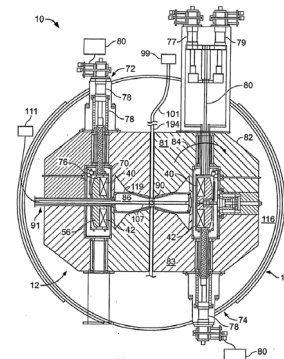

Fig.1. Vertical cross-secion of 9T Synchrocyclotron **[12]**: (81,82,83)−magnet, (40)−Superconducting coils from Nb_3Sn, (70)−cryostat, (119)−Dee, (114)−magnetic shield.
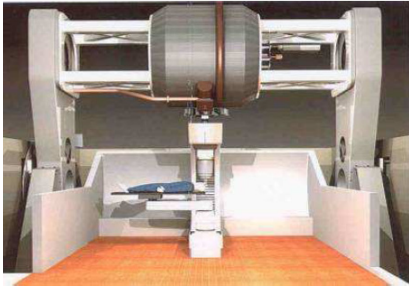
Fig.2. Single room proton therapy unit Monarch250 [13].

Fig.3. Superconducting Synchrocyclotron with 9 T field built by "Still River". Weight is 20 tons. [14].

Another version of compact "single room" proton therapy unit is being built by company ACCEL [15]. Common features of "single room" SC-SC units are:

- High level of magnetic field – 9 T
- Flat poles, azimuthal symmetry
- Weak focusing due to low efficiency of Flatter
- Field slightly drops with radius to ensure axial focusing during acceleration
- RF frequency is reduced to follow relativistics
- Operation by cycles – phase stability
- Low amplitude of Dee voltage
- Moderate beam current but enough for PT

PARAMETERS OF SUPERCONDUCTING SYNCHROCYCLOTRONS

Based on [11,12], we analyse possible parameters of compact superconducting synchrocyclotrons to accelerate protons up to 250 MeV as well as Carbon ions up to 400 MeV/A. In this paper we do not discuss problems related to superconductors at 10T field level. Modern technologies would allow to operate superconductors at 11 T field level and current densities up to 1000A/mm^2 providing A15 Nb$_3$Sn superconductors of type II cooled down to 4.5° K will be used.
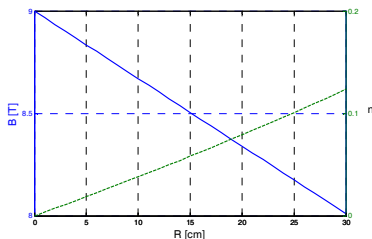

Fig.4. Range of variation of field (1) and field index (2) in the proposed Proton superconducting synchrocyclotron

01 Circular Colliders

Table 1. Parameters of synchrocyclotrons for proton/ion therapy

Parameter	Synchro-cyclotron NSCL MSU [4]	Proton Synchro-cyclotron JINR	Carbon Synchro-cyclotron JINR
Ion	protons	protons	C +6
Energy, MeV/A	250	250	400
Beam current, nA	200–400	100–300	100-200
Field, T	5.5-- 4.9	9.1--8	5.8-5
Field index	0.12	0.12	0.12
Radial tune	0.94	≈0.94	≈0.94
Axial tune	0.35	≈0.35	≈0.35
Extr.radius, cm	45	~31	~1.2
Magnet size, cm	264 x 173	185 x 100	420 x 200
Magnet weight, tons	65	25	220
Field azimuthal	symm	4 sectors	4 sectors
Type of Focusing	weak	Weak	Weak
Pole gap-centre, mm	60	25-30	
Pole gap–edge, mm	120	~200	
Flutter	0	0.01	0
Dees	1	2	2
RF harmonic	1	2	4
RF freq.range, MHz	84 / 62	276 /192	178/125
Capture time, μs	~4.5	8	
Repetition rate, kHz	1	1	1
RF voltage, kV	20	20	20
Dee gap, mm	20 / 13	20 / 13	20 / 13
Dee-ground gap,mm	2	2	2
Ion Source	Cold PIG	Cold PIG	ECR
Beam current, mA	1.8	1.8	0.003e

Main parameters of NSCL MSU SC-SC Project as well as our estimations are listed in Table 1. To provide adequat focusing field is reduced from 9 to 8 T and field index is growing to n=0.12 (Fig.4). Axial betatron tune is ν_z≈0.35 (fig.5). Extraction radius of 250 MeV protons is 31 cm. Magnet weight is 20 tons. We propose to reduce gap between poles in the center to 25-30 mm with respect to 60 mm in the NSCL MSU design. 180° Dee will not be fitted in such small gap and we consider option to machine azimuthal profile in the magnet pole – 4 straight sectors and 4 valleys. Two 42° Dees will be located in free opposite valleys. 70-100 mm gap in valleys should be enough to allow stable RF operation. In the center field bump is created for axial focusing as well as field profile is shaped to maximize index n in order to improve RF capture efficiency. Regeneratvie type of extraction by exciting of ν_r = 2/2 resonance is used.

Radius of first turn at Dee voltage 20 kV is 2.7 mm. Diameter of ion source Chimney is 3.2 mm and ions of phase band 50° RF will clear central region. Gap between source slit and puller is reduced to 1.5 mm in order to minimize time-of-flight effect. For same reason Dee-Dummy Dee gaps are decreased to 2 mm. Ion source was tested at NSCL MSU and proton beam current is 1.8 mA.

SC-SC will operate at the second harmonic of RF. Span of RF frequency modulation is 84 MHz (fig.6). Repetition rate of cycles is F_{rep}=1000 Hz
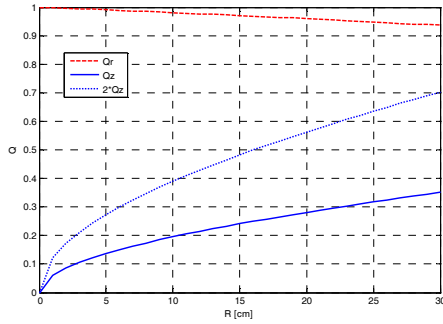
Fig.5. Range of betatron tunes variation: 1–radial tune ν_r, 2 – axial tune ν_z, 3–double axial tune $2\nu_z$. Coupling resonance $\nu_r = 2\nu_z$ should not be expected.
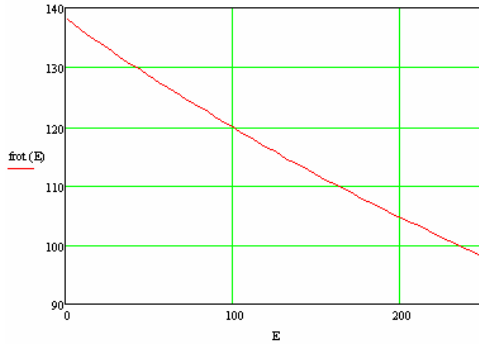

Fig.6. During each operation cycle orbital frequency is reduced from 138 to 96 MHz.

During capture stage the required speed of RF frequency variation is $df/dt = 70$ MHz/ms and maximum slip of RF frequency when ions are still captured into the RF Buckets is 1.9 MHz. Thus capture time of ion bunches into the stable synhrotron oscillations is $\Delta t \approx 5\text{-}9$ μs. Beam intensity is proportional to capture efficiency in cyclotron $\eta_{cyc} \approx 10\%$ averaged over capture time Δt and repetition rate of RF cycles F_{rep}

$$I_{synchr} = I_{source} \times \eta_{cyc} \times F_{rep} \times \Delta t \times \eta_{extr}$$

Extraction efficiency is $\eta_{extr} \approx 20\text{-}40\%$ and average proton beam current from SC-SC should be $I_{synchr} \approx 100-300$ nA. During each acceleration cycle speed of RF frequency variation is being optimized. Acceleration might be done in a constant amplitude of RF voltage mode either in a constant energy gain per turn mode i.e. with constant area of separatrix. At fixed amplitude $V = 20$ кB speed of RF frequency change is adiabatically reduced from 100 to 75 MHz/ms. Acceleration time is ~300μs. In constant energy gain per turn mode $dE/dN = 10$ keV/turn and amplitude of RF voltage is decreased from 20 to 14 kV. Speed of RF frequency modulation is reduced from 100 to 50 MHz/ms. Acceleration time is ~400μs.

SUMMARY

Estimations of possible parameter of Proton and Carbon Synchro-Cyclotrons at 10T field level and comparison with commercial "single room" units being built in USA and Germany allow us come to the conclusion that

design of accelerators is feasible and perspective. In case if positive decision will be made to launch projects one has to provide significant amount of simulations and experimental studies. Authors are appreciated to Pr. D.Johnson from "BestCyclotrons" (Canada) for general remarks and Pr. H.Blosser from NSCL MSU (MSU) for kind opportunity to explore results of intensive studies of his students.

REFERENCES

[1] V.Dzhelepov et al. „Theory and modelling of ring Phazotron with spiral structure of magnetic field". *Nucl.Instr.Meth. v.21, No.1* (Holland, 1963). pp.85-88.

[2] G.Kraft et al. "First patients' treatment at GSI Heavy-Ion Beams". in *Proc. of the Europian Part.Accel.Conf. EPAC-2006.* (Edinburgh, Scotland, 2006). pp.212-216.

[3] F.Cole. et al. "Loma-Linda Accelerator Project". in *Proc. of the Part.Accel.Conf. PAC-1989.* (Chicago, USA, 1989). pp.737-741.

[4] H.Eickhoff. "HICAT - The German Hospital-Based Light Ion Cancer Therapy Project". *in Proc.of the Europian Part.Accel.Conf.EPAC-2004.*(Lucern, Switzerland, 2004). pp.290-294

[5] Y.Jongen. et al. "New Cyclotron developments at IBA". in *Proc. of the Int. Conf. on Cycl.* (Tokyo, Japan, 2004). pp.87-91.

[6] A.Geisler et al. "Status Report of the ACCEL 250 MeV Medical Cyclotron". in *Proc. of the Int. Conf. on Cycl.* (Tokyo,Japan,2004).pp.87-91.

[7] H.Blosser et al. "Medical Accelerator Projects at Michigan State University". *In Proc.of the Part.Accel.Conf.* (USA, 1989), pp.742-746.

[8] H.Blosser et al. "Superconducting Cyclotron for Medical Application". *IEEE, Vol.25, Issue 2*. (USA, 1989). pp.1746-1754.

[9] H.Blosser, X.Wu. "Compact Superconducting Synchrocyclotron Systems for Proton Therapy at PSI". *Nucl. Instr.Meth.* **B40/41**. (USA, 1989), pp.1326-1330.

[10] Gordon M., Wu X. "Extraction Studies for a 250 MeV Superconducting Synchrocyclotron". *In Proc.of the Part.Accel. Conf. (*USA, 1987*)*, pp.1255-1257.

[11] X.Wu. "Conceptual Design and Orbit Dynamics in a 250 MeV Superconducting Syncrocyclotron". *PhD Thesis Michgan State University*. (USA, 1990). 172 p.

[12] T.Antaya. "High-field Superconducting Synchrocyclotron". *Patent , PCT/US2007/001628.* (USA, 2007). 26 p.

[13] Pedroni. "Status of Hadron Therapy facilities worldwide". *Presentation at Europ. Part. Accel. Conf. EPAC-2008.*(Genoa, Italy, 2008). 42 p.

[14] M.Miller. „Announcement. 14 May 2010". www.StillRiverSystems.com (2010). 1p.

[15] www.varian.com

01 Circular Colliders

TUNING OF THE INR THERAPEUTIC PROTON BEAM

S.V. Akulinichev, V.N. Vasiliev, Yu.K. Gavrilov, M.I.Grachev, E.V. Ponomareva, INR RAS,
Moscow, Russia

V.N. Zapolsky, IHEP, Protvino, Russia

Abstract

   The medical proton beam channel of the INR Experimental Complex and the therapeutic beam formation system are described (see also Refs. [1,2]). Parameters of the 209 and 160 MeV proton beams were investigated and dose distributions in matter were measured.
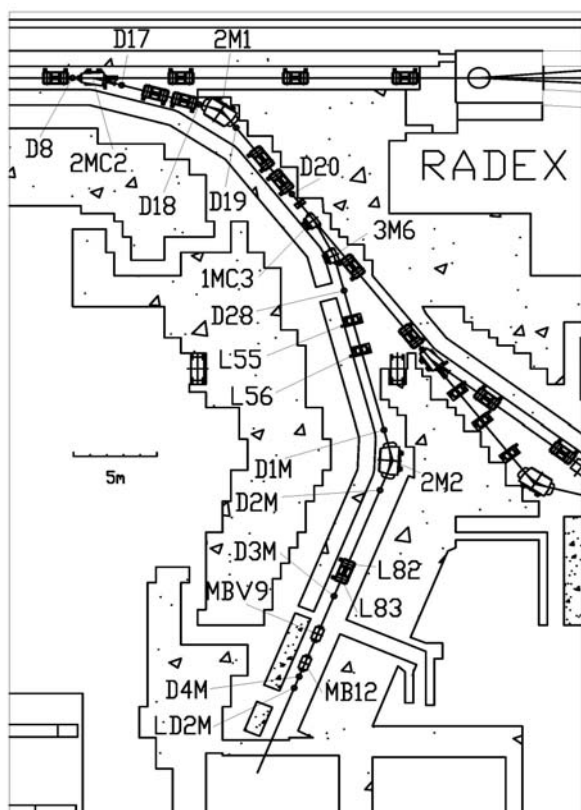
MEDICAL PROTON BEAM CHANNEL

Figure 1: The layout of the proton beam channel for proton therapy. 2MC2, 2M1, 1MC3, 3M6, 2M4, MBV9, MBV12 – bending magnets; L55, L56, L82, L83 – quadrupole lenses; D8, D17, D18, D19, D20, D28, D1M, D2M, D3M, D4M, LD2M – profile detectors.

   A special channel of INR Experimental Complex was built for radiotherapy needs [3]. The layout of the optical elements and profile detectors along this proton beam channel is illustrated in Fig.1. The length of this channel is about 50 metres [4].

   The distinguishing feature of optics, operated during the last session in April 2010, is that only 4 quadrupole lenses have been used in the channel. Five magnets ensure beam bending on 112 degrees. The lenses L55, L56 are responsible for compensation of angular and linear dispersion of the beam after the bending magnet 2M4. The lenses L82, L83 form a beam on the scatterer with the required angular divergence of less than 2mrad and the dimensions $\sigma_x=\sigma_y=5$mm. Alignment of the beam with the axis of the treatment room is provided horizontally by magnets 3M6 and 2M4, and vertically by magnets MBB9 and MBB12. Each element in the channel is supplied by its own power source with the current fluctuations of $\sim 10^{-4}$. The electrical power consumption of the channel with the proton energy of 209MeV is equal to ~ 87.5kW. This amount is just a small fraction of the total energy consumption of both the accelerator and the experimental complex.

   For the purposes of beam tuning there are ten 16-channel secondary-emission profile detectors, with a step of 2 and 4mm [3]. Profile detectors allow us to measure the position and the spot size of the proton beam during the tuning of a channel. A luminescent detector (item LD2M in Fig. 1) is installed at the end of the channel, just before the treatment room. This detector enables us to monitor on-line position and dimensions of the beam.

   The principal aim of the tuning of the channel during the April 2010 session was the analysis of the parameters of the beam with proton energies of 160 and 209 MeV. This has been carried out with the aid of the profile detectors. As it follows from the analysis, the energy spread of protons was very small, approximately 10^{-3}. Therefore a strict achromaticity of the channel is not necessary for the required parameters of the beam. This eliminates the constraints on the regimes of the lenses L55-56 that are used for the focusing of the beam. Fig.2 shows the profiles of the beam at the entrance to the channel (distance from the accelerator is about 150 m), before the magnet 2M4 and at the end of the channel.

   It is worth highlighting the details of the profile of the beam in front of the magnet 2M4. We have managed to focus the beam into dimensions $\sigma_x=1.6$mm, $\sigma_y=1.5$mm by means of the lenses L55-56.

   The profile of the beam, at the end of the channel and before the scatterer, is obtained using the adjusted regime of lenses L55-56 for the beam focusing of lenses and the computed value of the regimes of the lenses L82, L83. This beam was used for forming the dose field.

   One of the main properties of the medical channels is the time required to tune the channel. In the last session the tuning process took 1.5 hours. Similar time was required for the tuning of the beam during the transfer to another beam energy (without taking into account the time of re-tuning of the accelerator).
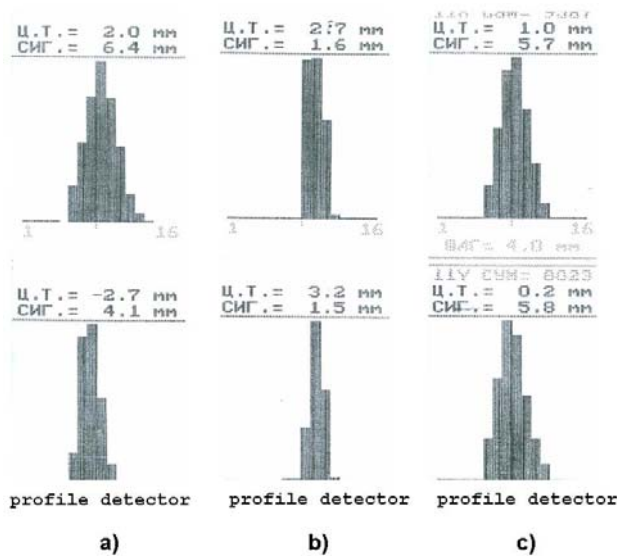
Figure 2: a) Beam profiles at the entrance of the forming proton channel (profile detector D8), b) before the magnet 2M4 (profile detector DM1) and c) at the end of the proton channel (profile detector D4M).

EXPERIMENTAL EQUIPMENT AND METHODS

The design of the end of medical channel is shown in Fig. 3. The beam is delivered to the treatment room via the vacuum transport system and passes through an output window (1.04 mm Al), a graphite collimator with the window of 10 mm and thickness 17 cm, additional 0.1 mm copper foil and a special profiled scatterer-degrader. Dose distributions in water were measured with the dose analyzer Wellhöfer WP600, including an acrylic water phantom of 60x60x30 cm, a high accuracy 3D detector positioner, two 0.14 cm^3 ionization chambers IC-10, a double channel electrometer, a control computer and electronics. A plane-parallel chamber PPC05 (Scanditronix-Wellhöfer) has been used for precise depth dose measurements.
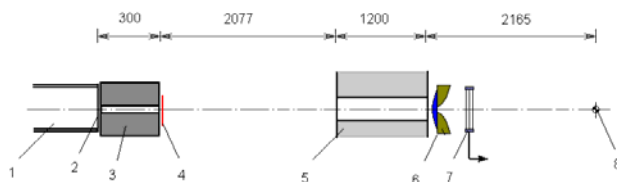

Figure 3: The individual beam formation system (160 MeV, all sizes are in mm). 1 – the end of vacuum channel; 2 – the Al window; 3 - the graphite; 4 – the primary scatterer; 5 – a 120 cm biological shield, the channel of diameter 10 cm; 6 – the secondary profiled scatterer/degrader; 7 – the monitor chamber; 8 – the isocentre of the treatment room.

Along with the ionization methods, the Bragg curve was measured inside a Plastic Water LR solid state

phantom (CIRS Inc., USA) with strips of radiochromic film Gafchromic MD-55.

RESULTS AND DISCUSSION

First, the Bragg curve in water for 209 MeV protons was determined and the proton range and energy were estimated. During these measurements, the collimator and scattering system were removed from the beam line (items 3, 4, 6, 7 in Fig. 3). The curves (Fig.4) were measured using the IC-10 ionization chamber, a standard deviation over a group of 5 measurements was 1.5%.
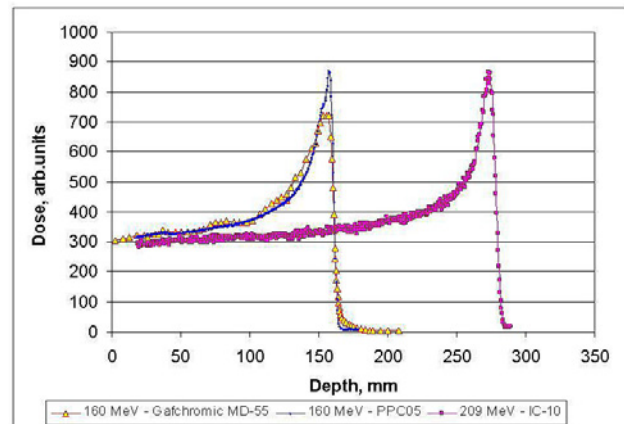

Figure 4: The Bragg curves in water.

The CSDA range in water, estimated as the depth of the Bragg curve where the dose was reduced to 80% of its maximum, was 275.6±0.2 mm. Mean proton energy was estimated as 207.5±0.1 MeV using the ICRU49 [6] range-energy relation.

On the basis of the 160 MeV proton beam earlier measured parameters, a beam spread out system was designed and manufactured. This system was simulated with the utility NEU [7] and included a flat primary scatterer (1.04 mm Al + 0.1 mm Cu) and a profiled secondary scatterer made of tin. To compensate the energy losses, a profiled PMMA energy degrader was set after the scatterer.

The beam profiles in water without using the secondary scatterer are presented in Fig.5. Both profiles are close to each other, symmetric and well aligned relative to the beam axis. The FWHMs were 101 and 99 mm respectively in horizontal and vertical directions.

The complete set of scattering system was carefully investigated: we measured vertical and horizontal profiles at depths 19, 69, 119, 157 (the Bragg peak) and 164 mm (Fig. 6 and 7), depth dose data along the beam axis (Fig. 4).

The profiles at low and medium depths demonstrated reasonable dose uniformity within a few percents. Most serious profile skewness, up to 10%, was found in the vertical profile at the Bragg peak. It can be resulted from a little energy variation across the beam and, respectively, a little Bragg peak depth variation. In this case, the skewness can be compensated in further spread-out Bragg peak formation by ridge filters.
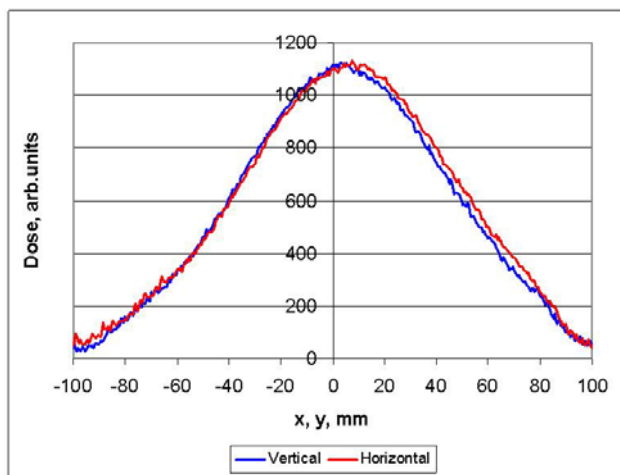
06 Instrumentation, Controls, Feedback and Operational Aspects

Figure 5: Horizontal and vertical dose profiles formed by the primary scatterer at a depth of 20 mm, E = 160 MeV.

The depth dose distribution measured along the beam axis with the PPC05 plane-parallel ionization chamber is shown in Fig. 5. The proton range calculated on the base of eight measurements was 159.6±0.07 mm and mean proton energy was 151.02 MeV.

It follows that the 160 MeV beam, formed by the double scattering system, meets the medical requirements under the condition of stability of main parameters.

Direct depth dose measurements in a water equivalent plastic phantom were performed using the Gafchromic MD-55 film. Two strips of the film of 127 x 15 mm were placed and aligned between the Plastic Water LR slabs. The water equivalence of the Plastic Water substitute material was verified previously [5]. The films were scanned and converted to the Bragg curve (Fig. 4). The resulting proton CSDA range was 159.2 mm, it agrees with the PPC05 data within the 0.4 mm.
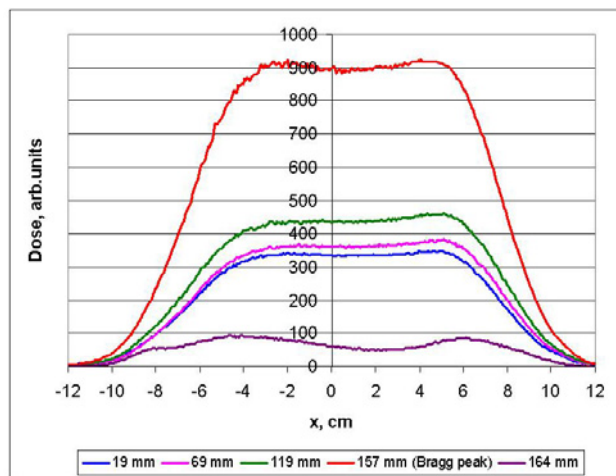

Figure 6: Horizontal dose profiles in water at depth from 19 to 164 mm, E = 160 MeV, double scattering system
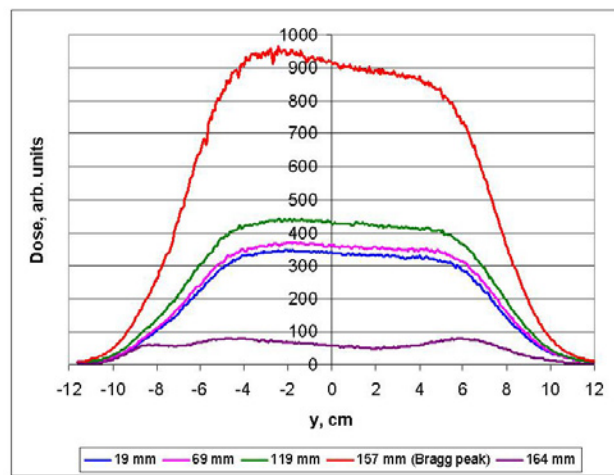

Figure 7: Vertical dose profiles in water at depth from 19 to 164 mm, E = 160 MeV, double scattering system.

CONCLUSION

The last session of the proton beam supply to the Complex of proton therapy of INR has demonstrated that medical requirements of the beam can be fulfilled with the existing beam channel and beam formation system. However, before the patient treatment will take place, further test sessions with different proton energies, as well as the installation of additional equipment in the channel and in the treatment room, should be carried out.

REFERENCES

[1] L.V.Kravchuk "Development of nuclear physics medicine at the Institute for Nuclear Research, RAS" Uspekhi Fisicheskih Nauk, V.180, N6, June 2010, pp.665-670.
[2] S.V.Akulinichev "Status and perspectives of the radiological center in Troitsk, Medical Physics" (in Russian) №4 (v. 39, 2008).
[3] M.I. Grachev, E.V. Ponomareva, L.V. Kravchuk, V.K. Gorbunov, V.C. Seleznev, "Transportation of the proton beam at the Experimental complex of linear accelerator INR of the RAS", XXI-RUPAC, September-October 2008.
[4] M.I. Grachev, E.V. Ponomareva, L.V. Kravchuk, V.K. Gorbunov, V.M. Skorkin, V.N. Zapolsky, "System of preliminary formation of the beam for the channel of proton therapy", XXI-RUPAC, September-October 2008.
[5] V.N. Vasiliev, V.I. Kostjuchenko, O.B. Riazantsev, V.G. Khaybullin, S.I. Samarin, A.S. Uglov, "Tissue equivalence of some phantom materials for proton beams", PTCOG 48, Heidelberg, September 28th - October 3rd, 2009. arXiv:1005.4389. http://arxiv.org/abs/1005.4389
[6] Stopping powers and ranges for protons and alpha particles. ICRU Report 49, ICRU, Bethesda, 1993.
[7] B. Gottschalk, "NEU User Guide", 2006, Harvard University; http://huhepl.harvard.edu/˜gottschalk

THE HIGH-CURRENT DEUTERON ACCELERATOR
FOR THE NEUTRON THERAPY

V. Skorkin, S. Akulinichev, A. Andreev, INR RAS, Moscow, Russia.

Abstract

Physical project of neutron sources for the neutron therapy and neutron activation analysis is proposed. The neutron sources are based on beam provided by the high-current deuteron accelerator. The fast neutrons with intensity up to $5 \cdot 10^{12}$ n·s^{-1} are produced using T(D,n)^{4}He reaction at the energy of deuteron beam about 430 keV and average current up to 20 mA. Neutron source can be used for the fast neutron and neutron capture therapy. Liquid-crystalline DNA-Gd nanoparticles, as a potential biomaterial for the neutron capture therapy were investigated on a thermal neutron beam.

INTRODUCTION

Progress in the physics and technology of linear accelerators ion promotes the wider use in various sectors of the linear accelerators of protons and deuterons at low energies. In particular, such accelerators are used for the production of medical radioisotopes, neutron activation analysis, fast neutron therapy and neutron capture therapy of cancer [1]. Creation of fast and thermal neutrons through nuclear reactions (d, n), (p, n) without the use of fissile materials is a safe alternative to nuclear reactors. At low deuteron energy for high intensity neutron fluxes is most preferable DT and DD fusion reactions.

Currently in Russia powerful neutron generators (NG) using DT reaction produces NIIEFA. One of them, NY-12-2, provides a flow of 14 MeV neutrons of about $2 \cdot 10^{12}$ n·s^{-1} at an accelerating voltage of 250 kV and a current of 10 mA of deuterium ions. From foreign producers should be noted the firm "IRELEC" (France), which produces NG with fast neutron flux of about $5 \cdot 10^{12}$ n·s^{-1} at an accelerating voltage of 430 kV and a deuteron current of 20 mA. In the INR, was assembled and tested a NG based on high-current accelerator of deuterons (HCAD). The impact of a 20 mA deuteron beam accelerated at 430 kV on tritium target produces a neutron flux of $2 \cdot 10^{11}$ n·s^{-1}·cm^{-2} for a neutron output of $5 \cdot 10^{12}$ n·s^{-1}.

DEUTERON ACCELERATOR

The machine consists of: an electrostatic particle accelerator, supplying a 20 mA/430 kV beam of monoatomic deuterium ions, a target assembly, an ISU type high voltage DC power supply, providing the 400 kV acceleration voltage, a control and monitoring system.

The electrostatic particle accelerator consists of a high voltage electrode with the injector and associated power supplies, accelerating tube, quadrupole focalization double, an extension tube, leading to the targets assembly (see Fig. 1). The high voltage (HV) electrode is mechanical assemble designed to house the high voltage components (400 kV) and supported by three insulated legs.
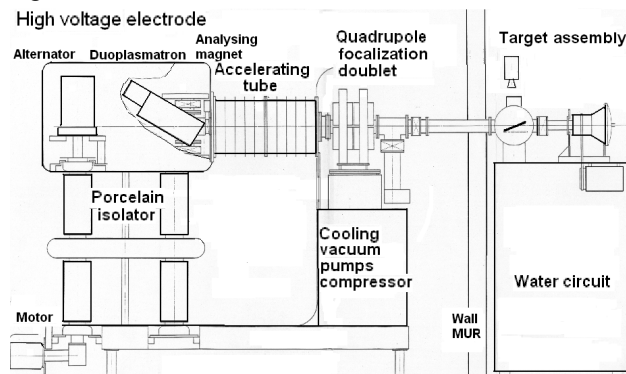

Figure 1: Deuteron accelerator.

The HV electrode includes the vacuum chamber of the injector with deflecting magnet and associated power supplies, the magnet enclosure auxiliaries, the ion source equipment, the alternator supplying power to the HV electrode. The injector has the ion source (the duoplasmatron type), beam extraction optics, atomic ion analysing magnet. A low pressure discharge is created between a hot cathode and an anode. The plasma expands through the anode into a expansion cup. Oven-heated oxide cathode has lifetime greater than 300 hours for discharge current of 15 A and discharge voltage of 150 V. The beam extraction optics (the pierce type) has maximum deuterium beam current of 55 mA.

Accelerating tube fixed to the high voltage head and consists of two half-length tubes, each made up of 5 porcelain rings and electrodes bonded together, providing a 12.5 kV/cm outside the accelerating space. A rated voltage, diameter and length of the tube are 400 kV, 0.5 m and 1.03 m respectively. The beam hits the target at a distance of 3.3 m. To compensate for divergence and to adjust the impact dimension, a quadrupole doublet is located. A throat diameter and a nominal gradient of the doublet are 102 mm and 1.9 T/m respectively.

The target assembly consists of the retractable target designed for beam adjustment, the rotating target containing the tritiated layer, representing the neutron source, a cryopump, the target water cooling system.

The retractable target used to focus the beam by examining the impact dimension on a tantalum network through a window using a video camera. The power of the beam is determined by a calorimetric measurement of the cooling water. Considering the angle of 18° between the target and the horizontal plane, it can receive a maximum power of 8.6 kW for a 20 mm beam diameter.

The rotating target consists of a 345 mm diameter spherical sector, a double rotating seal to ensure an air-tight vacuum, an insulated tube, DC motor rotating the target at 1500 rpm. The axis of rotation is shifted by 30° with respect to the beam axis. The target and the rotating seals are water cooled.

The ISU DC power supply consists of a transformer set enclosed in cylindrical tank. In the ISU 400 kV – 30 mA single – phase configuration, multi-turn induction system is powered directly from a motorized variable auto-transformer connected to mains power. The control and monitoring system includes the Control Bay, centralizing the controls, adjustments for the various beam parameters, operating modes, fault indications and safety; the information transmission system, the power box, centralizing the power components.

Overall dimensions of the deuteron accelerator are 6.8×1.7×3 m. A power consumption is about 60 kW. Dangers related to the use of the accelerator is 400 kV high voltage of the HV electrode, X-rays of secondary electrons at the entrance to the accelerating tube, neutron radiation, radiation from neutron activation, the high radioactivity of the target (1000 curies).

NEUTRON THERAPY FACILITY

The physical project of compact neutron sources for the fast neutron therapy (FNT), the neutron capture therapy (NCT) and the neutron activation analysis (NAA) is proposed. The layout neutron sources based on HCAD for FNT, NCT and NAA is illustrated in Fig. 2. This sources can be used to investigate neutron scattering (NSF).
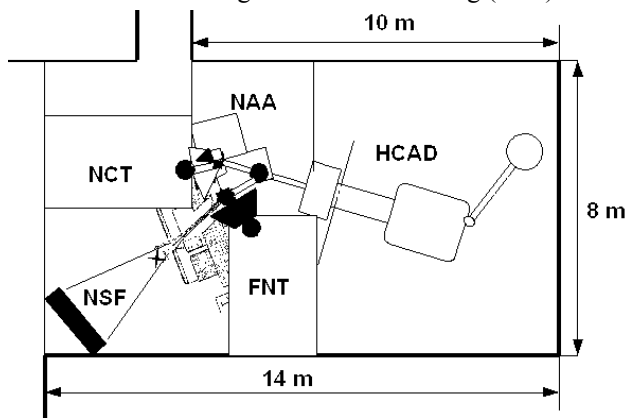

Figure 2: The layout neutron sources and facilities for the FNT, NCT, NAA and NSF.

Thermal neutron flux at moderation DT neutrons is of $1 \cdot 10^{10}$ n·s^{-1}·cm^{-2}. This neutron flux can be used for the NAA and will allow several times the sensitivity of NAA in the determination of quantitative properties of the element in the sample (1 ng) [2]. Fast neutron flux is equal to $1 \cdot 10^{8}$ n·s^{-1}·cm^{-2} can be obtained for FNT. The neutron source could be employed for NCT experimental investigations by using an irradiation facility consisted of the tungsten neutron converter, a bismuth reflector, a

graphite and polyethylene moderator. The thickness of W converter and Bi reflector is about 10 cm. Thickness of graphite moderator is about 20 cm.

A Monte-Carlo transport program, NCNP4B, was used to calculate the neutron fluxes from such a system. Thermal neutron flux is equal to $1 \cdot 10^{9}$ n·s^{-1}·cm^{-2} can be obtained at the facility for NCT (see Fig.3).
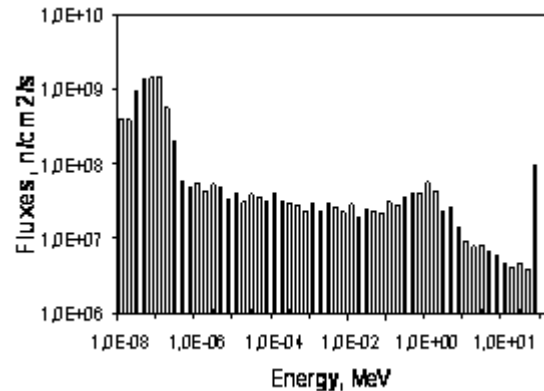

Figure 3: Spectrum of the neutrons from moderator system of the neutron sources for NCT.

THE DNA-GD RBE RESEARCH

In [3] have proposed particles of liquid-crystalline dispersions formed by the cholesteric double-stranded DNA and Gd ions as a potential platform for NCT. We have investigated the radiobiological effectiveness (RBE) of the secondary photon and electron radiation, generated after the thermal neutron capture by the DNA-Gd particles. Each particle contains 10^{8} gadolinium atoms and the corresponding natural gadolinium concentration in the biomaterial is about 250 mg/g. The conversion electrons, X-rays and gamma rays have a range in tissue about of 50 μm and can induce a tissue dose and DNA double strand breaks in cell nucleus when the DNA-Gd particles located on the surface of cells.

The biological samples containing cell suspension and DNA-Gd particles has been irradiated into the polyethylene phantom by neutrons from generator NG-400. The thermal and fast neutron fluxes for each biological sample were measured by means of the neutron activation analysis. The killing of a major part of tumor cells in biological samples with nanoparticles was produced the thermal neutron fluence about 10^{11}cm^{-2} for a nanoparticle density of the order of 10^{3} particles per cell. In our experiment samples were irradiated inside the polyethylene phantom of the size 20×20×20 cm^{3}. We have identically irradiated two sets of samples: one is the cell culture added with the solid particles of (DNA-gadolinium) complex, and another one is the cell culture without these particles. In the latter case, the killing effects can be caused only by fast neutrons. Therefore the difference in the cell killing efficacy for the two sets of samples might be due to the thermal neutron capture by

the solid particles only. The irradiation time was about 1 h and the thermal neutron fluence of about $5 \cdot 10^{11}$ $n \cdot cm^{-2}$. The thermal and fast neutron fluence was measured by means of the activation method. The fast neutron (~ 1 MeV) fluence of about $1 \cdot 10^{11}$ $n \cdot cm^{-2}$. The absorbed dose of the thermal neutron was ~ 20 Gy. The absorbed dose of the fast neutron was ~ 2 Gy and the effect of this types of radiation was smaller and did not produce the cell killing. The examination of irradiated samples has proved it: the tumor cells in the samples with gadolinium were killed while the cells in control samples survived under the same conditions.

REFERENCES

[1] B.F. Bayanov, V.P. Belov, E.D. Bender et al., Nucl. Instr. and Meth. A 413 (1998) 397.

[2] C. Zhang, Z.Y. Guo, A. Schempp, et al., Nucl. Instr. and Meth. A 521 (2004) 326.

[3] Yu.M. Yevdokimov, V.I. Salyanov, O.V. Kondrashina et al., Int. J. Biol. Macromol. 370 (2005) 165.

DEVELOMPENT OF ACCELERATORS AND DETECTOR SYSTEMS FOR RADIACIAN MEDICINE IN DLNP JINR

E.M. Syresin[*], N.V. Anphimov, G.A. Chelkov, G.A. Karamysheva, M.Yu. Kazarinov, C.A. Kostromin, G.V. Mytzin, N.A. Morozov, A.G. Olshevsky, V.M. Romanov, E.V. Samsonov, N.G. Shakun, G. D. Shirkov, S.G. Shirkov, Joint Institute for Nuclear Research, Dubna, Russia.

M.Abs, A. Blondin, Y. Engen, S. Zaremba, D. Vandeplassche, IBA, Belgium.

Abstract

The DLNP JINR activity is aimed at developing two directions in radiation medicine: development of accelerator technique for proton and carbon treatment of tumors and new types of detector systems for spectrometric computed tomography (CT) and combined magnetic resonance tomography (MRT)/positron emission tomography (PET).

JINR-IBA realized the development and construction of proton medical cyclotron C235-V3. At present time all basic cyclotron systems were constructed. During 2011 we plan to assemble this cyclotron in JINR and in 2012 perform tests with extracted proton beam.

A superconducting isochronous cyclotron C400 has been designed by IBA-JINR collaboration. This cyclotron will be used for radiotherapy with proton, helium and carbon ions. The $^{12}C^{6+}$ and $^4He^{2+}$ ions will be accelerated to the energy of 400 MeV/amu, the protons will be extracted at the energy 265 MeV. The C400 construction was started in 2010 in frame work of the Archarde project (France).

Modern CT require modification to allow determining not only density of a substance from the X-ray absorption coefficient but also its chemical composition (development of spectrometric CT tomographs with colored X-ray imaging). JINR develops the principle new pixel detector systems for the spectrometric CT. A combined MRT/PET is of considerable interest for medicine, but is cannot be made with the existing PET tomographs based on detectors of compact photomultipliers. Change-over to detectors of micropixel avalanche photodiodes (MAPDs) developed in JINR allows making a combined PET/MRT .

PROTON THERAPY

Dubna is one of the leading proton therapy research centers of the in Russia [1]. The modern technique of 3D conformal proton radiotherapy was first effectuated in Russia in this center, and now it is effectively used in regular treatment sessions [1-2]. A special Medico-Technical Complex was created at JINR on the basis of the synchrocyclotron (phasotron) used for proton treatment. About 100 patients undergo a course of fractionated treatment here every year. During last 10 yeas were treated by proton beams about 660 patients .

PROTON CYCLOTRON C235-V3

A cyclotron C235–V3, superior in its parameters to the medical proton cyclotron IBA C235 installed in 10 proton treatment centers of the world, has been design and manufactures by JINR-IBA collaboration. This cyclotron design is an essentially modified version of IBA C235 cyclotron [3-4] (Table 2).

Table 2 JINR-IBA cyclotron C235-V3

Parameter	C235	C235-V3
Optimization of magnetic field at modification of sector		Modification of sector azimuthal angle at R>80
Vertical betatron frequency at R>80	Qz=0,25	Qz=0,45
Vertical coherent beam displacement related to median plate effects	6-7 mm	1,5-2 mm
Beam losses at proton acceleration	50%	15%
Beam losses at extraction	50%	25%
Reduction of radiation dose of cyclotron elements		by 2-3 times

The one goal is to modify the sectors spiral angle at R>80 cm for improving of the cyclotron working diagram (Fig.1) and reduction of coherent beam losses at acceleration. The coherent beam displacement z from median plane is defined by vertical betatron tune Q_z: $z \propto Q_z^{-2}$. At $Q_z \approx 0.2$ the coherent beam displacement

08 Applications of Accelerators, Technology Transfer and Industrial Relations

corresponds to 7 mm and at amplitude of free axial oscillations of 2-3 mm can became to beam losses at reduction of the sector gup in the C235-V3 cyclotron. An increase of vertical betatron tune from $Q_z \approx 0.2$-0.25 to $Q_z \approx 0.4$ in C235-V3 permits to reduce by 3-4 times the coherent losses at proton acceleration (Table 2).
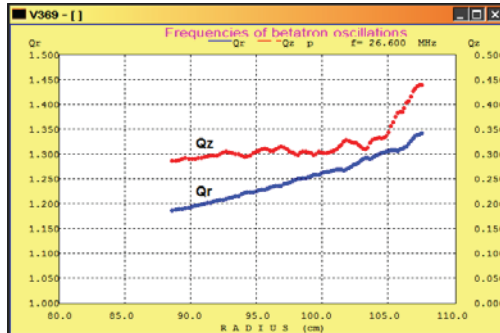

Figure.1: Dependence of betatron tunes on radius in cyclotron C235-V3.

The modification of extraction system is other aim of new cyclotron C235-V3 [4]. The main peculiarity of the cyclotron extraction system is rather small gap (9 mm) between sectors in this area. The septum surface consists of several parts of circumferences of different radii. The septum thickness is linearly increased from 0.1 mm at entrance to 3 mm at exit. The proton extraction losses essentially depend on septum geometry. In proposed JINR septum geometry when minimum of septum thinness is placed on a distance of 10 cm at entrance the losses were reduced from 25% to 8%. Together with an optimization of deflector entrance and exit positions it leads to increasing of extraction efficiency up 80%. The new extraction system was constructed and tested on IBA cyclotron C235. The experimentally measured extraction efficiency was improved from 60% for old system to 77% for new one (Fig.2).
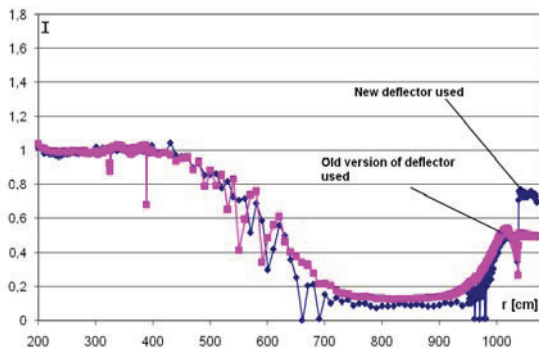

Figure 2: Proton beam extraction in cyclotron C235 with old IBA deflector and new electrostatic deflector developed in JINR.

Advantages of the medical proton cyclotron are simplicity, reliability, small size, and most importantly,

the ability to modulate rapidly and accurately the proton beam current (Fig.3). The current modulation of the extracted proton beam at a frequency up to 1 kHz [5] is most advantageous with Pencil Beam Scanning and Intensity Modulated Proton Therapy. The energy of the extracted beam in cyclotron is fixed. However the fast proton energy variation at a rate of 15 MeV/s is easily performed during active cancer treatment by using a wedge degrader. This energy variation rate is few times faster than for typical synchrotron regime.
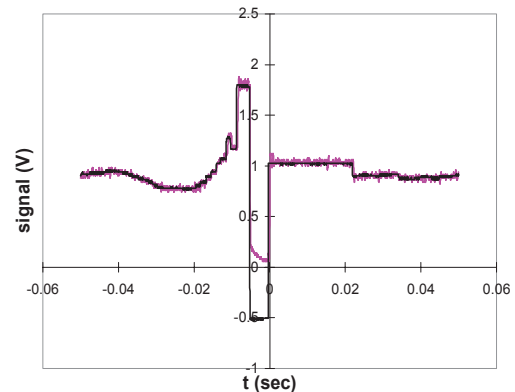

Figure.3: Beam intensity variation at the IBA C235 proton cyclotron.

SUPECONDUCTING CYCLOTRON C400 APPLIED FOR CARBON THERAPY

Carbon therapy is the most effective method to treat the resistant tumors. A compact superconducting isochronous cyclotron C400 (Fig.4) was designed by JINR-IBA collaboration (Table 3) [4-8]. This cyclotron will be used for radiotherapy with protons, helium and carbon ions. The $^{12}C^{6+}$ and $^{4}He^{2+}$ ions will be accelerated to the energy of 400 MeV/amu and H_2^+ ions will be accelerated to the energy 265 MeV/amu and protons will be extracted by stripping.

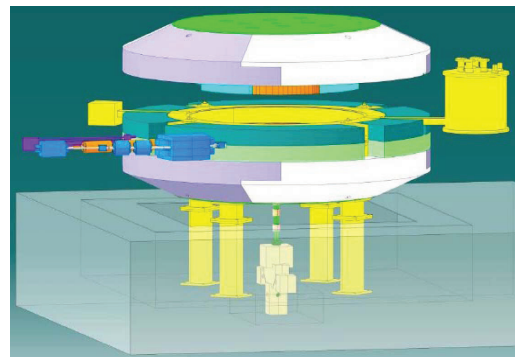Figure. 4: Common view of C400 cyclotron.

Table 3: Main parameters of the C400 cyclotron

General properties	
accelerated particles	H_2^+, $^4He^{2+}$, $^6Li^{3+}$, $^{10}B^{5+}$, $^{12}C^{6+}$
Injection energy	25 keV/Z
Final energy of ions, Protons	400 MeV/amu 265 MeV
Extraction efficiency	~70 % (by deflector)
Number of turns	~1700
Magnetic system	
Total weight	700 tons
Outer diameter	6.6 m
Height	3.4 m
Pole radius	1.87 m
Valley depth	60 cm
Bending limit	K = 1600
Hill field	4.5 T
Valley field	2.45 T
RF system	
Radial dimension	187 cm
Vertical dimension	116 cm
Frequency	75 MHz
Operation	4 harmonic
Number of dees	2
Dee voltage: center extraction	80 kV 170 kV

DETEECTORS FOR TOMOGRAPHY

The developed spectrometric CT tomographs of next generation should measure not only density of a substance but also its chemical composition. Colored X-ray imaging CT will ensure high-contrast imaging of a structure with different chemical compositions (tomography at different gamma ray energies selected near the K-edge of absorption lines of such elements as Ca, C, Fe, etc.) allowing, for example, clear-cut image of blood vessels including those behind bone structures with considerable shadowing of these structures. The gamma ray energy in the spectral CT tomography based on the JINR-TSU GaAs pixel detector [9] is determined by a special chip involving a comparator of eight signal levels (eight colors) that allows spectrometry and determination of gamma ray energy from this information thus implementing colored X-ray imaging. The detecting systems of the spectrometric CT tomography are based on the semiconducting heterostructures. Together with spectrometric possibilities the pixel detectors on basis of GaAs(Cr) have a high space resolution(~100 μm), their sensitivity is one order of magnitude better comparing with Si detectors at photon energy of 30-35 kev.

A combined MRT/PET tomograph is under consideration in many research centres. The application of micropixel avalanche photodiodes (MAPDs) allows making a combined PET/MRT tomograph. This photodiode [11] consists of many microcells, micropixels, each working in the yes/no Geiger mode with a high internal gain (up to 10^5) and being capable of detecting single photons. A special shop for assembly and testing of micropixel detectors is built at JINR. MAPDs are more and more widely used in nanoindustry (laser location, optical-fiber communication, optical information transmission lines, systems for optical readout of super high-density information from various carriers on the nanostructure basis, luminescence of quantum dots) and in development of medical diagnosis equipment (PET, combined PET/MRT, single-photon emission tomograph). The MAPD advantages comparing with photomultipliers [10] are high dynamic range (pixel densities of up to 4×10^4 mm^2); photon detection efficiency up to 30%; gain up 10^5; insensitivity to magnetic field; better radiation hardness; compact and rigid; low voltage supply (<100 V).

REFERENCES

[1] O.V. Savchenko, "40 years of proton therapy on synchrocyclotron and phasotron of LNP JINR", J. Medical physics (2007), № 3-4.

[2] A.V. Agapov et al, "Methodic of 3D conformal proton therapy", Particle and Nuclei Letters, №6 (2005), 80-86.

[3] G. Karamysheva et al, "Simulation of beam extraction from C235 cyclotron for proton therapy", Particle and Nuclei Letters, v.7, №4 (2010).

[4] E.M. Syresin, Centers of hadron therapy on the basis of cyclotrons, RUPAC 08, Zelenograd, 2008, p.316.

[5] Y. Jongen, "Design of a K=1600 SC cyclotron for Carbon therapy" ECPM, Nice, 2006.

[6] Y. Jongen et al., "Design Studies of the Compact Superconducting Cyclotron for Hadron Therapy", EPAC 06, p. 1678, 2006.

[7] Y. Jongen et al., "IBA C400 Cyclotron Project for hadron therapy", Cyclotrons 2007, Italy, p. 151.

[8] Y. Jongen et al.," Current status of the IBA C400 cyclotron project for hadron therapy" , EPAC 08, p.1806, 2008.

[9] Tlustos, G. Chelkov, O.Tolbanov "Characterization of GaAs(Cr) Medipix2 hybrid pixel detectors" in Proc. of iWoRid, Prague, 2009.

[10] Z. Sadygov et al. "Three advanced designs of micro-pixel avalanche photodiodes: Their present status, maximum possibilities and limitations", NIM A567(2006)70-73.

ELLUS-6M LINEAR ELECTRON ACCELERATOR FOR RADIOTHERAPY

A.A. Budtov, M.F. Vorogushin, V.A. Shyshov[#], FSUE "D.V. Efremov Scientific Research Institute of Electrophysical Apparatus", St. Petersburg, Russia
S.V. Kanaev, N.N. Petrov Scientific Research Oncology Institute, Pesochny, St. Petersburg, Russia

Abstract

"ELLUS-6M", a compact medical accelerator of new generation, has been designed and manufactured for radiotherapy by 6MeV photons in the multi-static and arc modes. The gantry of the accelerator can be rotated through $\pm185^{0}$ and ensures setting accuracies of the irradiator rotation velocity and positioning sufficient for the IMRT mode. The computerized control system is compatible with the treatment planning system and allows upgrading by adding new modules.

To realize the conformal radiotherapy, the following additional medical equipment has been developed: a multi-leaf collimator, a portal vision system for the dose field verification during irradiation and an upgraded treatment table made as a semi-pantograph.

In 2010, it is planned to finish clinical tests of the "ELLUS-6M" accelerator with the additional medical equipment carried out in the N.N. Petrov Scientific Research Oncology Institute, Pesochny, St.Petersburg.

In countries with a highly-developed economics, radiotherapy is used for treatment of more than 70% of oncological patients, and more than 60% of such patients are usually successfully cured of cancer. In Russia, this method is used for treatment of less than 20% of the whole number of oncological patients, which mainly depends on insufficient up-to-date radiotherapeutic equipment available in oncologic institutions in our country Linear accelerators, which can be used for the conventional beam therapy, are about 80 in number, and only 20 machines are used for the conformal treatment. It is highly insufficient to satisfy the needs for these machines; for comparison, the international standards are 1 machine for 250-300 thousand people.

Nowadays in Russia have appeared all necessary prerequisites to change critically the status of radiotherapy. The Government of the Russian Federation has taken a decision on the financial support of activities aimed at the advancement of oncological treatment of the population and fitting out of oncological clinics with up-to-date equipment.

Development of electrophysical equipment for radiotherapy is one of high-priority lines of activity of FSUE "D.V. Efremov Scientific Research Institute of Electrophysical Apparatus". Several generations of accelerators and cyclotrons for medicine have been developed since the foundation of the Institute [1, 2]. A new generation of linear electron accelerators for radiotherapy has been developed by specialists of the Institute, one of these machines is a 6 MeV "ELLUS-6M" shown in figure 1.
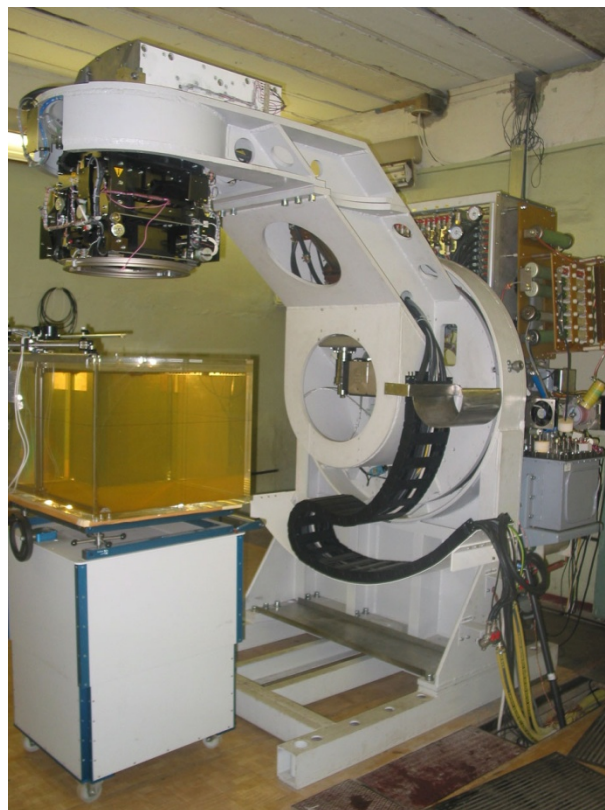

Figure 1: The "ELLUS-6M" accelerator under technical tests; dose fields are being measured in a water phantom

The new accelerator is equipped with a computerized control system, demountable multileaf collimator to form bremsstrahlung fields with a high accuracy and a portal image-based verification system. The system for radiotherapy developed on the basis of the "ELLUS-6M" accelerator allows the most advanced technologies of the radiation oncology to be realized.

The main block of the accelerator is an irradiator, which includes systems and units for an electron beam generation and acceleration, its transport and forming in compliance with a particular treatment plan, as well as dose monitoring and verification of treatment prescription.

The beam is generated in a three-electrode electron source and injected into the accelerating structure, which is a chain of coupled cavities. A standing-wave accelerating structure is used in the "ELLUS-6M" accelerator. Simultaneously, the RF energy is supplied to the accelerating structure by a magnetron via the waveguide line.

[#]npkluts@niiefa.spb.su

08 Applications of Accelerators, Technology Transfer and Industrial Relations

From the accelerating structure, electrons reach a deflection-focusing system where they are deflected by a magnet to an angle of 130° and focused to a tungsten target. Rectangular radiation fields, which are necessary for radiotherapy, are formed by radiation head collimators.

The irradiator can be rotated through an angle of $\pm 185^0$; the servo drive of the gantry ensures variation of angular velocity and necessary irradiator positioning accuracy.

Mechanical travels of the gantry, radiation head and treatment table can be controlled both from the manual control console and automatically from the host computer located in the control console room.

The computer control system supports DICOM 3, DICOM RT and HL4 communication protocols with the treatment planning and topometric systems.

The accelerator is also equipped with a multileaf collimator (see Fig. 2, 3), which allows individual radiation fields to be formed (see Fig. 4).

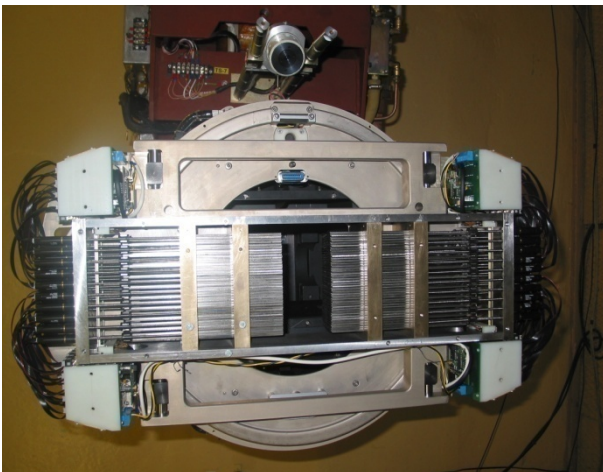Figure 2: Multileaf collimator mounted on the SL-75-5 accelerator
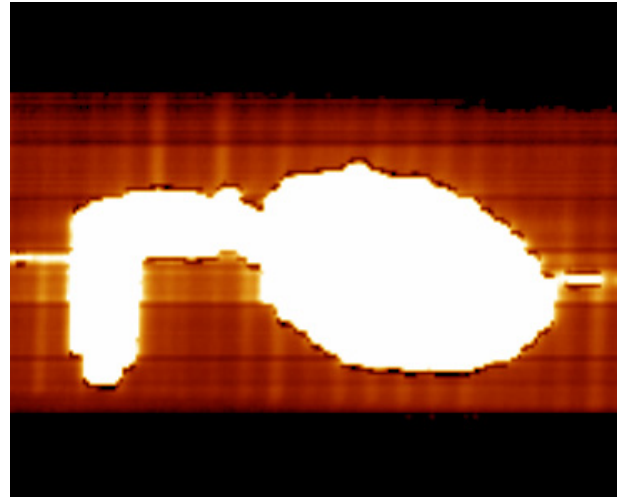

Figure 3: Multileaf collimator without casing

Figure 4: Radiation fields of required configuration formed with the MLC; the field image is obtained by using the portal image-based verification system

Prior to irradiation with an irregular field, an anatomic and topometric preparation is done with an X-ray topometric system TSR-100 [3], which is a component of the radiotherapeutical system developed in NIIEFA.

Fig. 5 shows the preparation of a patient for treatment. On the image of a patient's body a radiologist chooses an area to be treated (on the right of the figure); after that the treatment planning system performs computations of the leaves' position, which most accurately describes a preset contour (on the left of the figure). The data file comprising coordinates of the leaves is transferred to the MLC control system of the accelerator. In the process of patient's set up, the portal image system is used to verify the accuracy of the formed radiation field and the coincidence of the planned treatment area with the actual patient treatment position.
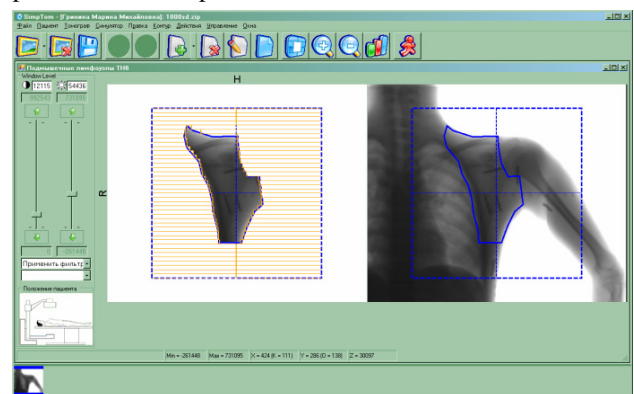

Figure 5: Irregular field chosen for treatment by a radiologist on the basis of a patient body projection image (right) and computations of MLC leaves' coordinates (left)

The collimator is a demountable device; it is so mounted on the accelerator radiation head so that to keep the possibility of the radiation head to rotate around the central axis of the beam. The collimator drive ensures independent travel of leaves and verification of their

position. The width of the area covered with one leaf is 0.5 cm 1m from target. The transmission between the ends of the closely connected leaves is less than 50% and between the neighboring leaves is 5%.

The MLC leaves' positioning system ensures the formation of the field boundary 1 m from target accurate to not worse than ±1mm. Depending on the leaf position, the penumbra width changes less than for 3 mm.

The MLC developed can also be used with SL-75-5 accelerators for conformal and IMRT irradiation techniquesIn addition to the MLC, the accelerator is equipped with an independent patient treatment prescription verification system, which allows us to verify the compliance with the treatment prescription of the patient position relative to the beam of the accelerator.

The portal image device is an advanced tool contributing to higher efficiency of radiotherapy due to verification of the most important stages of the treatment process, namely a patient's set up and radiation field formation.

The portal image-based verification system is located directly on the rotating gantry of the accelerator (see Fig. 6). The system visualizes projected images of a patient's treatment position by recording the beam passing through the body of the patient (the portal image device). The dose field verification system developed for the "ELLUS-6M" accelerator can also be used on SL-75-5 accelerators.

As an example, Fig. 7 shows an image of a calf head obtained with the TSR-100 topometric system by using the beam of the SL-75-5 accelerator.

Figure 6: The portal vision system with beam-forming block

The delivery set of the "ELLUS-6M" accelerator includes a treatment table. The table top vertical travel is from 650 up to 1900 mm (above the floor); the table top horizontal longitudinal travel is 800 mm and its transversal travel is ±200 mm. The table can be rotated around the vertical axis passing through the isocenter for ±95⁰.

The treatment table travels are actuated by servo drives with a smoothly regulated velocity. The table travels can

be controlled both manually from a local control desk and automatically from the accelerator control system.

The table top is equipped with components to secure fixing accessories. On both sides of the table top, universal rails are made and emergency-off buttons for the whole radiotherapeutic facility and to stop the table traveling are located.
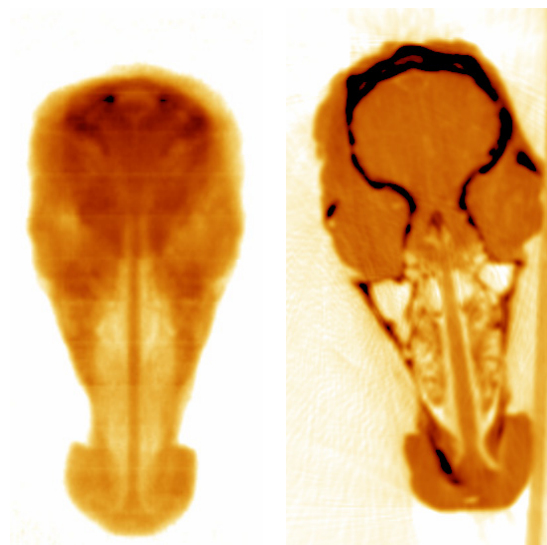

Figure 7: Calf head as a tested object.The image obtained with the therapeutic beam of the SL-75-5 accelerator (left) and a longitudinal tomogram obtained on the TSR-100 topometric system (right)

In addition, the accelerator is equipped with laser isocentor pointers, a TV treatment-room monitoring system and an intercom. The delivery set in addition to the accelerator includes the equipment necessary for maintenance/repair works.

So, the radiotherapeutic system on the basis of the linear electron accelerator "ELLUS-6M" equipped with the multileaf collimator, portal vision system for treatment verification, treatment table and other auxiliary devices allows the main problems of radiotherapy to be successfully solved satisfying the requirements of modern beam therapy techniques.

REFERENCES

[1] M.F. Vorogushun, A.S. Tikhomirov, "High-tech medical equipment for radiotherapy", Latest commercial techniques, TSNILOT Minatom RF, Moscow, № 1(312) p. 42 (2003).

[2] S.V. Kanaev, M.F. Vorogushun, A.S. Tikhomirov, V.A. Shishov, "Characteristics of the domestic system for radiotherapy of oncological patients", Voprosy Onkologii, V. 49 № 5, p. 668 (2003).

[3] S.V. Kanaev, M.F. Vorogushun, A.S. Tikhomirov, V.A. Shishov, "Anatomic and topometric preparation of oncological patients with the TSR-100 topometric system used in radiotherapy", Voprosy Onkologii, V. 49 № 5 p. 676 (2003).

MCC-30/15 CYCLOTRON – PARAMETERS, ADJUSTING WORKS AND THEIR RESULTS

P.V. Bogdanov, M.F. Vorogushin, A.V. Galchuk, V.G. Mudrolubov, A.P. Strokach[#],
FSUE "D.V. Efremov Scientific Research Institute, of Electrophysical Apparatus",
Saint Petersburg, Russia

Abstract

The Medical Compact Cyclotron MCC-30/15 is intended for acceleration of hydrogen and deuterium negative ions in the energy control range. The Cyclotron was designed in the frame of the Contract for the delivery of the MCC-30/15 cyclotron equipment to the Accelerator Laboratory of the Jyvaskyla University, Finland.

The Cyclotron is built up on the basis of a shielded-type electromagnet with a pole diameter of 140 cm. The Cyclotron is equipped with the external injection system of negative hydrogen and deuterium ions.

Particles are accelerated at a fixed frequency (the 2nd and 4th harmonics). The beam current of 30-18 MeV protons and 15-9 MeV deuterons extracted into two beam lines is more than 100 µA and 50 µA, respectively.

The Cyclotron equipment has been delivered to the Buyer; the commissioning works were finished on April 30, 2010.

THE MAIN DESIGN FEATURES OF THE CYCLOTRON

The designing of the MCC-30/15 cyclotron was started in 2007 after signing the Contract for the cyclotron delivery to the Jyvaskyla University, Finland. The main cyclotron characteristics were agreed upon with the Customer: the cyclotron must be equipped with an external ion injection system, the negative ions of hydrogen and deuterium must be accelerated up to an energy of 30/15 MeV with an energy control range of 60-100% of the ions maximum energy, the cyclotron beam are to be extracted by negative ion stripping on thin carbon foils to two beam lines with a possibility to irradiate two targets simultaneously. The maximum beam current was defined to be 100 microamperes for protons and 50 microamperes for deuterons.

When designing the cyclotron, the positive experience gained when designing and commissioning the CC-18/9 cyclotron at the Abo Academy PET Center (Turku, Finland) in 2006 was used. A series of basic engineering solutions were applied, in particular, the external multicasp source of negative hydrogen and deuterium ions, the RF field frequency similar for both types of ions, the vertical location of the beam acceleration and extraction plane, which gives an operator an easy access to in-chamber units and injection system for maintenance/repair in the process of exploitation. A software package previously applied on the CC-18/9 cyclotron was used for 3D calculations of the cyclotron magnetic and accelerating RF systems.

While elaborating the Technical Project, a Planning Information document for the layout of the cyclotron equipment was worked out. On the basis of this document, the works on elaboration of construction documentation and on building the rooms to house the cyclotron equipment have been finished by the Finnish side for two years.

THE CYCLOTRON MAGNETIC FIELD

3-D calculations of the cyclotron magnetic field were performed to provide isochronous magnetic fields required for the acceleration of two particles, hydrogen and deuterium ions. The calculations were carried out by the method of successive iterations. The magnet pole geometry and corresponding magnetic field in the acceleration area were defined from the beam dynamics calculations [1].

Two magnetic fields needed for isochronous acceleration of hydrogen and deuteron ions were formed in the following way. The rotating shims placed into two cyclotron valleys free of dees were used when changing from one accelerating mode to another. In the acceleration mode of deuteron ions, these shims were placed completely inside the magnet pole. The pole sector sides were provided with plates of small azimuth length, which shape was chosen when forming the isochronous field for the deuteron ion acceleration. If hydrogen ions are accelerated, the magnetic shims are rotated so that the magnetic masses enter the magnet gap thus providing the magnetic field increase along the radius. The required isochronous radial dependence was provided by adjusting the shim generatrix.

Use of the shims located in two cyclotron valleys free of dees results in the appearance of the 2nd harmonic of the magnetic field. To decrease its value, two fixed shims were additionally placed into two other valleys. In the deuteron ion acceleration mode with these fixed shims, the 2nd harmonic of the magnetic field appeared and the 2nd harmonic in the hydrogen ion acceleration mode decreased respectively.

The carried out calculations of the beam dynamics have shown that the 2nd harmonic of the magnetic field of the 500 Gs amplitude does not affect the accelerated beam stability and does not increase the radial emmitance of the beam.

Radial distributions of the measured average magnetic field are shown in figs. 1-2.
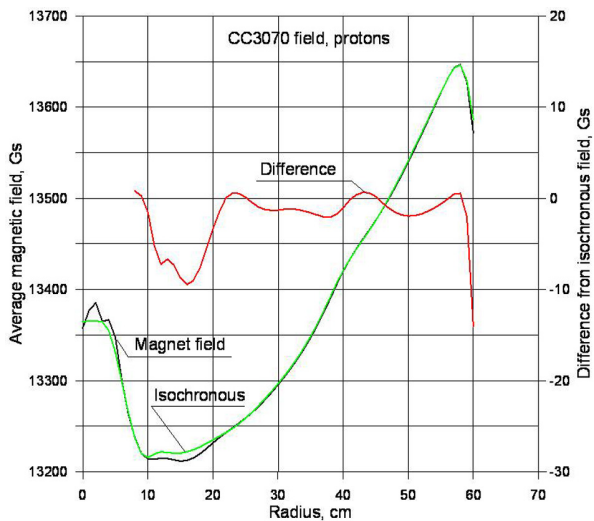

[#] npkluts@niiefa.spb.su

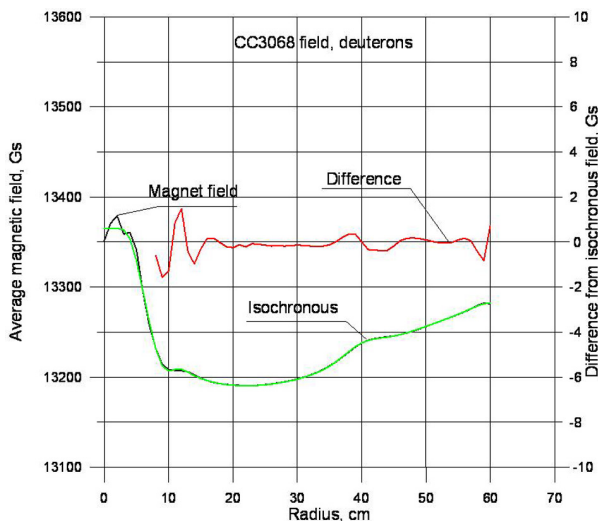Figure 1: Isochronous field for the deuterium ion acceleration.

Figure 2: Isochronous field for the hydrogen ion acceleration.

THE CYCLOTRON ELECTROMAGNETIC FIELD

The MCC-30/15 cyclotron operates at a fixed frequency of 40.68 MHz. The hydrogen and deuteron ions are accelerated by the 2nd and 4th harmonics, respectively. The similarity of the ion orbits is not applicable in this case; therefore when calculating the beam dynamics, much attention was given to the beam centering in order to achieve optimum conditions for two-particle acceleration.

An electric field map obtained as a result of 3-D calculations [2] was used in the beam dynamics calculations. The map of the cyclotron central region was 16×16 cm in size in the acceleration plane and ±8 mm in the axial direction with a step of 0.5 mm for each of three coordinates. The resultant electric field map was obtained after several iterations. The electric field corrections were made from the results of the beam dynamics calculations.
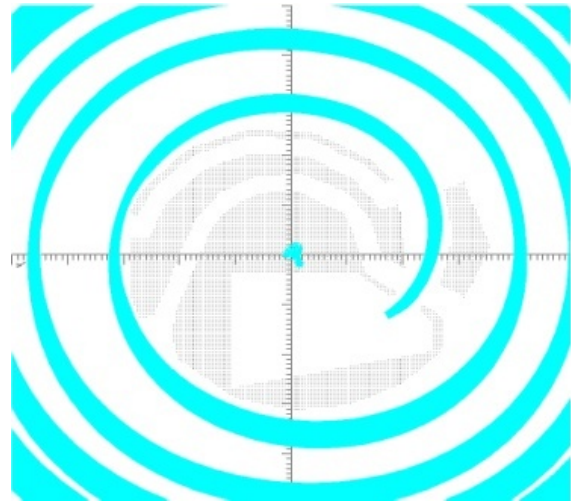

Figure 3: Centering of accelerated hydrogen ions. Phase range is ±0.25 rad. Accelerating voltage is 37.5 kV.

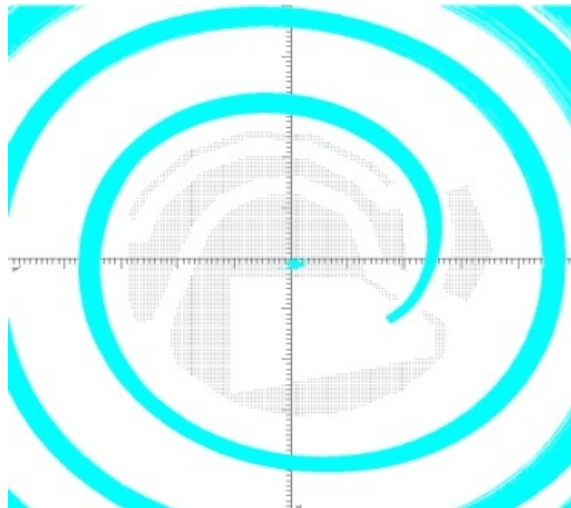

Figure 4: Centering of accelerated deuterium ions. Phase range is ±0.25 rad. Accelerating voltage is 25.5 kV.

When calculating the beam centering, the beam characteristics at the inflector output were taken as the key parameters of the cyclotron central region. These characteristics were corrected when calculating the beam dynamics to obtain the maximum acceptance in two perpendicular planes: the acceleration plane (the maximum phase range for the minimum orbit center zone) and the axial plane (the dee aperture restricted at the maximum axial emittance).

From the calculations, the following output parameters of the helical inflector were defined: hydrogen ion injection energy of 19 keV (for deuterium ions it was 9.5 keV), initial radius of 20.5 mm, central trajectory output angle of 23 degrees, tilt parameter of 0.28, radial emittance of 50π mm. mrad and axial emittance of 50π mm. mrad [2].

EXTERNAL BEAM ENERGY RANGE

In the MCC-30/15 cyclotron, the beam is extracted by carbon foil stripping of negative ions with control of the

extracted beam energy. Strippers are placed symmetrically relative to the cyclotron dees, which allow external beams in two beam lines to be vertically shifted relative to each other and located 1350 and 1582 above the ground. The extracted beam energy range is provided by changing the stripper radial position by 120-130 mm and its azimuth position by 2-3 degrees.

The matching magnets installed at the cyclotron outputs allow the difference in the output beam angles of different particles with different energies to be compensated up to approximately 11º. The diagram of the beam extraction is shown in Fig 5. Fig. 6 shows the results of numerically simulated beam acceleration and extraction. The initial particle (500 pcs.) parameters were chosen randomly from the phase range of ±0.25 rad and amplitudes of radial and axial betatron oscillations (the radial emittance of 50 π mm.mrad and the axial emittance of 50 π mm. mrad).
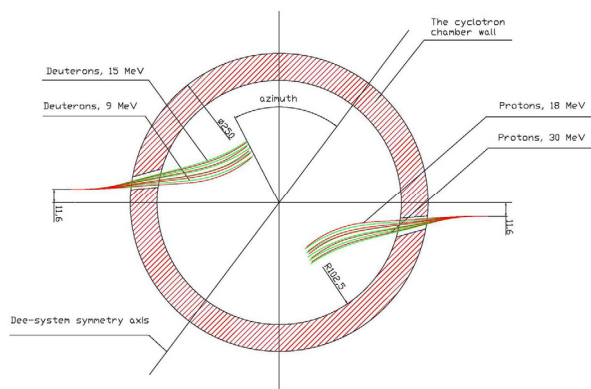

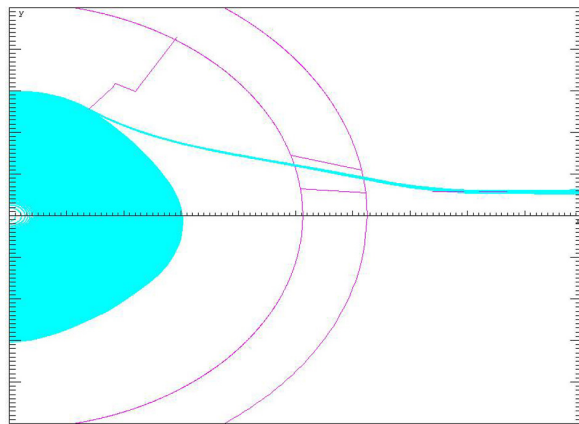Figure 5: The cyclotron beam extraction.

Figure 6: The results of numerically simulated acceleration and extraction of the beam. A small division value is 2 cm.

STARTUP AND COMMISSIONING OF THE CYCLOTRON

In August 2009, the MCC-30/15 cyclotron equipment was shipped to Finland and installed at the Accelerator Laboratory of the Jyvaskyla University. Works on the installation and adjustment of separate cyclotron systems: power supplies, water cooling, pneumatic, vacuum, ion source, injector, RF power supply and control systems were carried out during September-October. In October-December 2009, the adjusting of the cyclotron as a whole system and preliminary cyclotron tests were carried out, in the process of which the design cyclotron parameters were obtained. External proton beam with the maximum energy and current of more than 200 µamps per pulse and deuteron beams with the maximum energy and current of more than 60 micro µamps per pulse were obtained. From the results of the cyclotron preliminary tests, definite measures were planned to be taken to improve the RF power supply in-feeding unit and power filter. Final acceptance tests were planned for spring 2010.

Prior to the commissioning works, the isochronism of the particle acceleration was checked once more when the cyclotron RF system operated in the dee voltage stabilization mode. Measured resonance curves for the deuterium ion acceleration mode (see Fig. 7) show a negligible phase drift and no phase losses when passing the main acceleration area.

A list of the cyclotron operating modes (10 modes) to undergo the acceptance tests was agreed upon with specialists of the Accelerator Laboratory of the Jyvaskyla University. At the end of April 2010, during one week all the agreed upon modes were demonstrated, and on May 1, 2010 the MCC-30/15 cyclotron was put into operation.
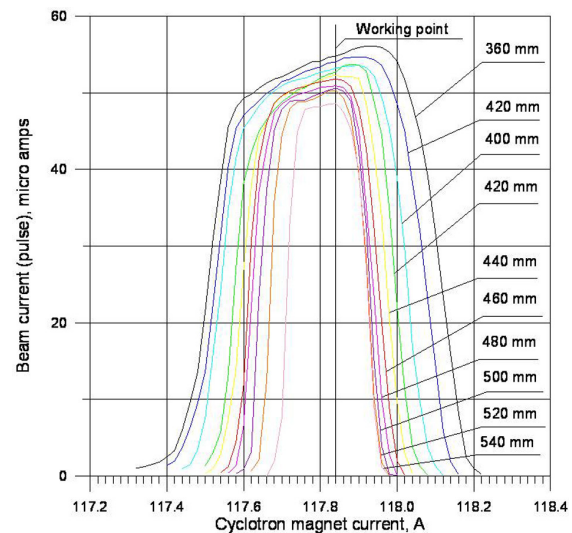

Figure 7: Resonance curves for deuterium ion aceleration modes.

REFERENCES

[1] V. Kukhtin, T. Belyakova, P. Bogdanov, I. Gornikel, E. Lamzin, A. Strokach, S. Sytchevsky, M. Vorogushin. "Numerical synthesis of CC18/9 and CC30/15 isochronous cyclotrons magnetic systems with moving shims", ECPM 2009, Groningen, The Netherlands 28-31 October (2009).

[2] A. Galchuk, S. Grigorenko, Yu Zuev, S. Silaev, A. Strokach. "Simulation of Electromagnetic Fields and Computations of the Beam Dynamics in Compact Cyclotrons", The paper of the current Conference.

08 Applications of Accelerators, Technology Transfer and Industrial Relations

STATUS OF ILU-14 ELECTRON ACCELERATOR

V.S.Podobaev[#], V.V. Bezuglov, A.A. Bryazgin, K.N. Chernov, V.G. Cheskidov, B.L. Faktorovich,
V.A. Gorbunov, I.V. Gornakov, A.V. Ivanov, E.N. Kokin, M.V. Korobeynikov, A.N. Lukin,
I.G. Makarov, N.V. Matyash, S.A. Maximov, G.N.Ostreiko, A.D. Panfilov, V.M. Radchenko,
N.D. Romashko, G.V. Serdobintsev, A.V. Sidorov, V.V. Tarnetsky, M.A. Tiunov, V.O. Tkachenko
BINP SB RAS, 630090, Novosibirsk, Russia.

Abstract

A new high power (up to 100 kW) industrial linear electron accelerator ILU-14 for energy of 7.5–10 MeV is under construction at Budker INP. The accelerator operates at 176 MHz with total efficiency of 26 %, its modular structure allows the electron energy and beam current to be varied within certain limits by changing the modular arrangement. The 5 MeV prototype of the accelerator was created and successfully tested in 2009. The designed average beam current of 600 mA with pulsed power of 2.5 MW and accelerating structure electron efficiency of 68 % were obtained during experiments. Applying an additional RF voltage to the electron gun cathode-grid gap allowed a beam current passing of 96 % with minor beam energy spread. The paper presents results of the numerical and experimental study of the accelerator systems together with the latest tests on the accelerator prototype.

INTRODUCTION

A new powerful (up to 100 kW) industrial electron accelerator with energy range from 7.5 to 10 MeV was designed in BINP SB RAS [1-3]. This model was named ILU-14 and can be used in electron and bremsstrahlung modes. This accelerator has all basic features of ILU-type accelerators like internal injection type and using of autogenerator for RF power feeding, but has also some its own features. On the base of ILU-14 it planned to produce a line of simple and effective accelerators, which can compete with existent industrial accelerators in this energy range.
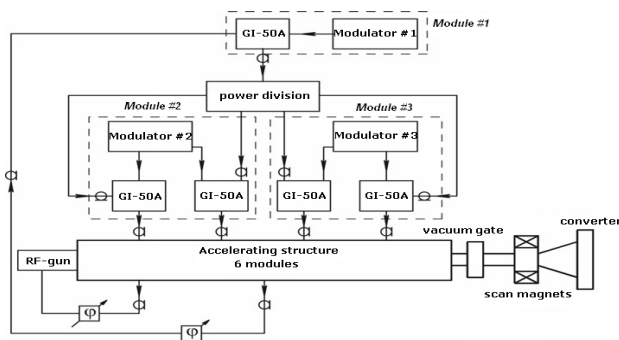
IDEA OF ILU-14 ACCELERATOR

Fig.1. Block scheme of ILU-14

The main elements of the accelerator are: accelerating structure, triode RF-gun, two-cascade autogenerator, feeder system, RF power inputs, modulators, scan magnets system and converter (in the case of bremsstrahlung mode operating) (Fig.1).

In ILU-14 (in comparison with other powerful impulse linear accelerators) some features were realized.

The first feature of it is using of low-frequency many-resonator structure on standing wave with coupling resonators on the axis. The accelerating structure is assembled from separate modules with using of indium vacuum seals. The module consists of one coupling resonator and two half accelerating resonators (Fig. 2-A). Accelerating structure, used for electron accelerating to the energy up to 10 MeV, consists of 6 such modules (Fig.2-B).

The structure is excited by autogenerator, based on powerful pulse triodes GI-50A, which provide competitive efficiency to the accelerator.
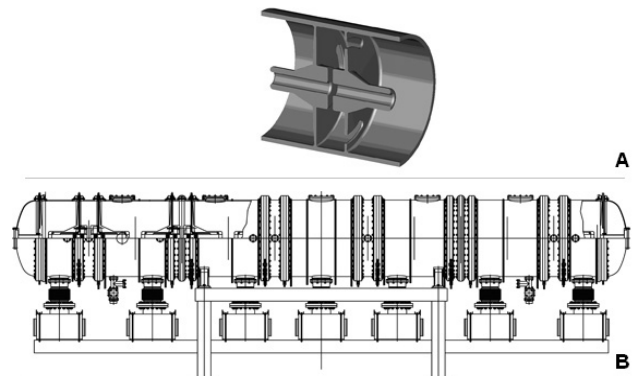

Fig.2. ILU-14 units. A-The module of accelerating structure. B-General view of accelerating structure

The second feature of the low-frequency accelerator is the using of triode RF-gun with specially designed for it grid with high transmissivity as an injector. RF-gun is placed directly in the first accelerating gap. Narrow energy spectrum of electron beam, which is necessary for effective conversion its power to bremsstrahlung and beam conducting through the structure with small losses are provided by feeding of grid-cathode unit of the RF-gun by additional RF-voltage.

The third feature is using of two-cascade autogenerator with feedback through accelerating structure. This feature allows operating of the accelerator without frequency stabilization system of structure or generator. As a result, the generator and accelerator control system are simple enough.

The fourth feature is the module construction of ILU-14. Separate modules are assembled by using of serial units, designed in the experimental plant of BINP.

This conception allows simplify the construction, decrease the cost of the accelerator, raises its safety and diminishes the operating costs.

ACCELERATING STRUCTURE AND DYNAMICS OF ELECTRON BEAM

Accelerating structure operates on frequency of 176 MHz on standing wave mode (quality factor is equal to 22000, shunt resistance – to 27.3 MΩ). Magnetic field coupling is provided through coupling slots (coupling coefficient is equal to 0,078). Every resonator side has two coupling slots. The slots on opposite sides of resonator are located from each other at the angle of 90^0 for prevention of slot-through-slot coupling.

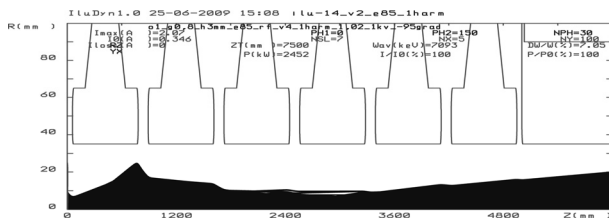On Fig. 3 the forms of electron trajectories in ILU-14 are presented [5].

Fig.3.Typical electrons trajectories in the accelerating structure.
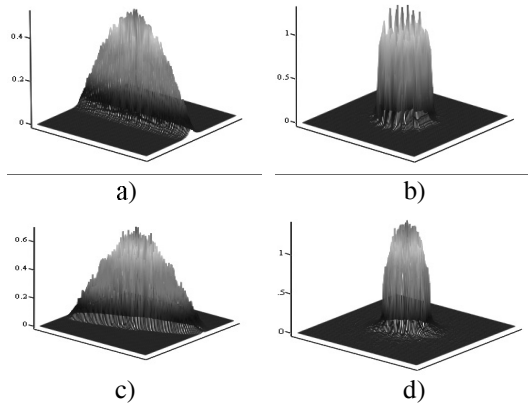

a)

b)

c)

d)

Fig.4. Profiles of average beam current density: a) – on the input to the second accelerating gap; b) – on the distance of 3000 mm from cathode; c) – on the output of accelerating gap; d) – after magnet lens focusing.

Electrons, which fly out from slot center in the grid perpendicularly to the cathode, form beam core. Around the core there is a visible halo, formed by electrons, flown out from slots borders under the angle to the perpendicular. Calculations showed a possibility of beam conduction through accelerator at the expense of aperture increase and RF focusing effect only [4-5].

On Fig. 4 calculated profiles of average current density during the macroimpulse width are presented.

Because of spread of injection transverse velocities across grid slots density profile of beam current obtains elliptic form on the input to the second accelerating gap (Fig. 4a). RF focusing gradually diminishes this effect (Fig. 4b), but at the same time overfocuses the extreme

particles (Fig. 4c). This effect can be removed by additional magnet lens focusing of the beam in magnet scan system on the output of accelerator (Fig. 4d).

ACCELERATOR PROTOTYPE

In radiation protected bunker the 5 MeV electron energy accelerator prototype was assembled for main elements tests. RF system of the prototype includes 4 module accelerating structure (Fig.2), triode RF-gun and two-cascade autogenerator on the pulse triodes GI-50A.

Fig. 5. ILU-14 prototype. A - two-cascade RF feeding system with coaxial feeders. B - accelerating structure with scan system.

For positive feedback of the autogenerator the part of RF power is withdrawn from accelerating structure by feedback loop, goes through coaxial phase-shifting line to the input of first cascade cathode circuit and, two parts divided, is delivered to the inputs of second cascades (Fig.5-A). Cascades power is delivered by two 2λ feeders to the power inputs and summarized in the structure (Fig.5-B). The amplitude of 30 kV anode voltage pulse of 450 μs width is provided by ILU-10M modulator [2]. Repetition rate is up to 50 Hz.

TEST OF PROTOTYPE STRUCTURE

Experimentally frequencies of structure coupling and Q-factor of working mode were measured by RF circuits analyzer (Fig.6). Also measurements of working mode

08 Applications of Accelerators, Technology Transfer and Industrial Relations

fields amplitudes relative values were carried out by method of dielectric ball small perturbation. Measurements results were in good agreement with results of 3D calculations by Microwave Studio program [6].
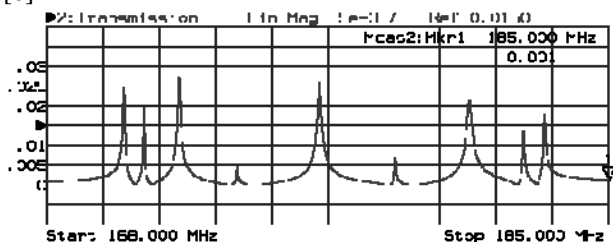

Fig.6. Spectrum of working mode oscillation.

After structure assembling it was needed 6 hours for obtaining of vacuum of 10^{-7} torr. On the repetition rate from 1 to 25 Hz it was needed about 3 hours of structure training for multipactor suppression. On the 4-module structure accelerating voltage level of 7.5 MV was obtained during 2 hours. So, 6-module accelerating structure will be possessed of enough electric strength to accelerate electron beam up to 10 MeV.

Current transmission of electron beam through accelerating structure without RF voltage feeding of gun cathode is equal to 80%. After the feeding of cathode-grid gap with optimal by amplitude and phase RF voltage cathode pulse current with current transmission coefficient of 96% was obtained.

Average power of electron beam was estimated:

a) as multiplying of average energy (which was defined after results of beam spectrum measurements) to average current of collector;

b) by calorimetric method.

At the energy of accelerated electrons of 5 MeV, impulse amplitude of accelerated current on the collector of 480 mA (injection current from gun cathode was equal to 500 mA), pulse duration of 420 µs, repetition rate of 33 Hz, power, measured by calorimetric method, was equal to 33±2 kW. Power, measured as multiplying of average energy and average current, was equal to 34.2±1 kW. This agreement is satisfactory.
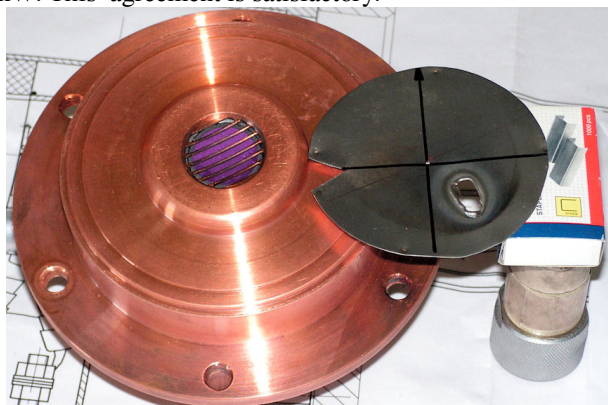

Fig.7. Cathode-grid unit and the burned foil (grid diameter is 20 mm).

Measurement of accelerated electrons energy was carried out by magnet spectrograph with inhomogeneous magnet field (n=0.5), turn angle, equal to 148º, and turn radius, equal to 200 mm. Beam current was fixed on the Faraday cup, placed after spectrograph.

Measurement of beam size on the output of accelerating structure was carried out by the method of spot burning in 0.25 mm-wide foil (Fig.7).

CONCLUSION

In the BINP SB RAS prototype of the powerful industrial electron accelerator passed the development tests in impulse regime successfully. Achieved parameters are presented in the Table 1.

Table 1: Achieved parameters of the prototype

Maximum accelerating voltage, MV	7,5
Maximum impulse beam current, mA	600
Beam current transmission coefficient, %	96
Impulse beam power at the 5 MeV electron energy, MW	2,5
Impulse duration, µs	420
Average beam power (at the repetition rate of 33 Hz), kW	33

At the impulses repetition rate of 50 Hz, average power of the beam will be 50 kW. Also impulse of accelerated current, equal to 300 mA, at the electron energy, equal to 6.7 MeV, was obtained.

Tests results confirm a possibility of ILU-14 accelerator at the energy up to 10 MeV and the power up to 100 kW on the base of designed modules creation. Accelerated structure in that case must be formed from 6 modules. Necessary RF power is provided by summation of 4 output cascades on the GI-50A triodes power.

Narrow energy spectrum of accelerated electrons allows use ILU-14 in the electron regime and the regime of bremsstrahlung. This fact increases application field of the accelerator in the industry.

REFERENCES

[1] V.L. Auslender et al., Instruments and experiment techniques. 2009, № 3, с. 98–103.

[2] V.L. Auslender et al., Problems of Atomic Science and Technology. (47). 2006, № 3, с. 163–187.

[3] V.L. Auslender et al., Problems of Atomic Science and Technology. (49). 2008, № 3, с. 20–24.

[4] V.L. Auslender et al., Problems of Atomic Science and Technology. (47). 2006, № 3, с. 3–5.

[5] M.A.Tiunov et al., Nucl. Instrum. and Meth. 2006, v. A 558, p. 77–88.

[6] http://www.cst.de.

08 Applications of Accelerators, Technology Transfer and Industrial Relations